IFMBE Proceedings

Ibrahim · Abu Osman · Usman · Kadri (Eds.)

Volume 15

3rd Kuala Lumpur
International Conference
on Biomedical Engineering 2006,
11–14 December 2006,
Kuala Lumpur, Malaysia

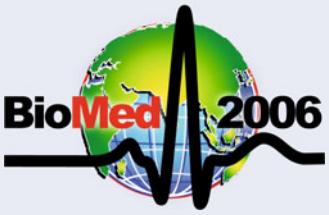

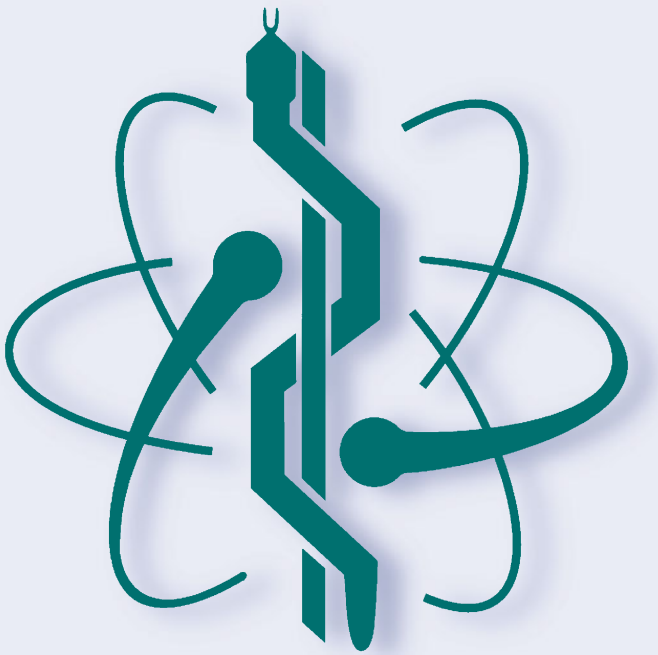

Springer

IFMBE Proceedings Volume 15

Series Editors: R. Magjarevic and J. H. Nagel

The International Federation for Medical and Biological Engineering, IFMBE, is a federation of national and transnational organizations representing internationally the interests of medical and biological engineering and sciences. The IFMBE is a non-profit organization fostering the creation, dissemination and application of medical and biological engineering knowledge and the management of technology for improved health and quality of life. Its activities include participation in the formulation of public policy and the dissemination of information through publications and forums. Within the field of medical, clinical, and biological engineering, IFMBE s aims are to encourage research and the application of knowledge, and to disseminate information and promote collaboration. The objectives of the IFMBE are scientific, technological, literary, and educational.

The IFMBE is a WHO accredited NGO covering the full range of biomedical and clinical engineering, healthcare, healthcare technology and management. It is representing through its 58 member societies some 120.000 professionals involved in the various issues of improved health and health care delivery.

Previous Editions:

IFMBE Proceedings WC 2006 "World Congress on Medical Physics and Biomedical Engineering",
Vol. 14, 2006, Seoul, Korea, DVD

IFMBE Proceedings BSN 2007 "4th International Workshop on Wearable and Implantable Body Sensor Networks",
Vol. 13, 2006, Aachen, Germany

IFMBE Proceedings ICBMEC 2005 "The 12th International Conference on Biomedical Engineering",
Vol. 12, 2005, Singapore, CD

IFMBE Proceedings EMBEC'05 "3rd European Medical & Biological Engineering Conference, IFMBE European Conference on Biomedical Engineering", Vol. 11, 2005, Prague, Czech Republic, CD

IFMBE Proceedings ICCE 2005 "The 7th International Conference on Cellular Engineering",
Vol. 10, 2005, Seoul, Korea, CD

IFMBE Proceedings NBC 2005 "13th Nordic Baltic Conference on Biomedical Engineering and Medical Physics",
Vol. 9, 2005, Umeå, Sweden

IFMBE Proceedings APCMBE 2005 "6th Asian-Pacific Conference on Medical and Biological Engineering",
Vol. 8, 2005, Tsukuba, Japan, CD

IFMBE Proceedings BIOMED 2004 "Kuala Lumpur International Conference on Biomedical Engineering",
Vol. 7, 2004, Kuala Lumpur, Malaysia

IFMBE Proceedings MEDICON and HEALTH TELEMATICS 2004 "X Mediterranean Conference on Medical and Biological Engineering", Vol. 6, 2004, Ischia, Italy, CD

IFMBE Proceedings 3rd Latin – American Congress on Biomedical Engineering "III CLAEB 2004",
Vol. 5, 2004, Joao Pessoa, Brazil, CD

IFMBE Proceedings WC2003 "World Congress on Medical Physics and Biomedical Engineering",
Vol. 4, 2003, Sydney, Australia, CD

IFMBE Proceedings EMBEC'02 "2nd European Medical and Biological Engineering Conference",
Vol. 3, Parts 1 & 2, 2002, H. Hutten and P. Kroesl (Eds.), Vienna, Austria

IFMBE Proceedings 12NBC "12th Nordic Baltic Conference on Biomedical Engineering and Medical Physics",
Vol. 2, 2002, Stefan Sigurdsson (Ed.) Reykjavik, Iceland

IFMBE Proceedings MEDICON 2001 – "IX Mediterranean Conference on Medical Engineering and Computing",
Vol. 1, Parts 1 & 2, 2001, R. Magjarevic, S. Tonkovic, V. Bilas, I. Lackovic (Eds.), Pula, Croatia

For ordering Proceedings from the IFMBE Proceedings Series, please contact the IFMBE Secretariat at: office@ifmbe.org.

IFMBE Proceedings Vol. 15
F. Ibrahim, N. A. Abu Osman, J. Usman and N. A. Kadri (Eds.)

3rd Kuala Lumpur International Conference on Biomedical Engineering 2006

Biomed 2006, 11 14 December 2006
Kuala Lumpur, Malaysia

Springer

Editors

Fatimah Ibrahim
Department of Biomedical Engineering
Faculty of Engineering
University of Malaya
50603 Kuala Lumpur, Malaysia
E-Mail: fatimah@um.edu.my

Juliana Usman
Department of Biomedical Engineering
Faculty of Engineering
University of Malaya
50603 Kuala Lumpur, Malaysia
E-Mail: juliana_78@um.edu.my

Noor Azuan Abu Osman
Department of Biomedical Engineering
Faculty of Engineering
University of Malaya
50603 Kuala Lumpur Malaysia
E-Mail: azuan@um.edu.my

Nahrizul Adib Kadri
Department of Biomedical Engineering
Faculty of Engineering
University of Malaya
50603 Kuala Lumpur, Malaysia
E-Mail: nahrizuladib@gmail.com

Library of Congress Control Number: 2007924600

ISSN: 1680-0737
ISBN: 978-3-540-68016-1 Springer Berlin Heidelberg New York

The IFMBE Proceedings is an Offical Publication of the International Federation for Medical and Biological Engineering (IFMBE)

Springer is a part of Springer Science+Business Media
springer.com

Typesetting: Data supplied by the authors
Production: Le-Tex Jelonek, Schmidt & Vöckler GbR
Cover design: deblik, Berlin

Printed on acid-free paper SPIN 11945857 60/3100/YL – 5 4 3 2 1 0

About IFMBE

The International Federation for Medical and Biological Engineering (IFMBE) was established in 1959 to provide medical and biological engineering with a vehicle for international collaboration in research and practice of the profession. The Federation has a long history of encouraging and promoting international cooperation and collaboration in the use of science and engineering for improving health and quality of life.

The IFMBE is an organization with membership of national and transnational societies and an International Academy. At present there are 52 national members and 5 transnational members representing a total membership in excess of 120 000 worldwide. An observer category is provided to groups or organizations considering formal affiliation. Personal membership is possible for individuals living in countries without a member society The International Academy includes individuals who have been recognized by the IFMBE for their outstanding contributions to biomedical engineering.

Objectives

The objectives of the International Federation for Medical and Biological Engineering are scientific, technological, literary, and educational. Within the field of medical, clinical and biological engineering it s aims are to encourage research and the application of knowledge, and to disseminate information and promote collaboration.

In pursuit of these aims the Federation engages in the following activities: sponsorship of national and international meetings, publication of official journals, cooperation with other societies and organizations, appointment of commissions on special problems, awarding of prizes and distinctions, establishment of professional standards and ethics within the field, as well as other activities which in the opinion of the General Assembly or the Administrative Council would further the cause of medical, clinical or biological engineering. It promotes the formation of regional, national, international or specialized societies, groups or boards, the coordination of bibliographic or informational services and the improvement of standards in terminology, equipment, methods and safety practices, and the delivery of health care.

The Federation works to promote improved communication and understanding in the world community of engineering, medicine and biology.

Activities

Publications of IFMBE include: the journal *Medical and Biological Engineering and Computing*, the electronic magazine *IFMBE News*, and the Book Series on Biomedical Engineering. In cooperation with its international and regional conferences, IFMBE also publishes the IFMBE Proceedings Series. All publications of the IFMBE are published by Springer Verlag. The Federation has two divisions: Clinical Engineering and Health Care Technology Assessment.

Every three years the IFMBE holds a World Congress on Medical Physics and Biomedical Engineering, organized in cooperation with the IOMP and the IUPESM. In addition, annual, milestone and regional conferences are organized in different regions of the world, such as Asia Pacific, Europe, the Nordic-Baltic and Mediterranean regions, Africa and Latin America.

The administrative council of the IFMBE meets once a year and is the steering body for the IFMBE: The council is subject to the rulings of the General Assembly, which meets every three years.

Information on the activities of the IFMBE can be found on the web site at: http://www.ifmbe.org.

Preface

The Kuala Lumpur International Conference on Biomedical Engineering (BioMed 2006), was held from 11 to 14 December 2006 at the Palace of the Golden Horses, Kuala Lumpur, Malaysia. This international conference was jointly organised by the Department of Biomedical Engineering, University of Malaya, Malaysia; Department of Biomedical Engineering, Inje University, Korea; and Malaysian Society of Medical and Biological Engineering.

The papers presented at BioMed 2006 cover the following areas: Artificial Intelligence, Biological effects of non-ionising electromagnetic fields, Biomaterials, Biomechanics, Biomedical Sensors, Biomedical Signal Analysis, Biotechnology, Clinical Engineering, Human performance engineering, Imaging, Medical Informatics, Medical Instruments and Devices, Physiological Modelling, simulation, and Control, Prostheses and artificial organs, Regulations and Organisations, Rehabilitation Engineering, Telemedicine, Tissue Engineering, and Virtual Reality in Medicine.

The conference program included invited plenary sessions by Joachim Nagel, the President of IUPESM; Makoto Kikuchi, the President of IFMBE; John G. Webster from the University of Wisconsin-Madison, United States; Metin Akay from Arizona State University, United States; Marc Madou from University of California, United States; and Yilin Cao from Shanghai s 9th People s Hospital, China.

The conference also featured pre-conference tutorial sessions. There are four sessions altogether, and the topics are Bioinstrumentation, by John G. Webster; MEMS by Marc Madou; Biomedical Informatics and Neural Engineering by Metin Akay; and Biomedical Image Analysis by Bart ter Haar Romeny.

Thanks are due to the members of the organising committee for their support and assistance in ensuring a successful BioMed 2006. Particular thanks go to Healthtronics, without whose financial support the conference could not have been successfully organised.

Assoc. Prof. Dr. Fatimah Ibrahim
Chairperson
Kuala Lumpur International Conference on Biomedical Engineering 2006

Contents

Biological effects of non-ionising electromagnetic fields

Biomaterials

Biomechanics

Biomedical engineering education

Biomedical imaging

Biomedical sensors

Biomedical signal analysis

Biotechnology

Clinical engineering

Medical informatics

Medical instruments and devices

Physiological modelling, simulation and control

Prostheses and artificial organs

Rehabilitation engineering

Telemedicine

Tissue engineering

Dart-to-Heart Distance when Taser® Causes Ventricular Fibrillation in Pigs

Jiun-Yan Wu[1], Hongyu Sun[1], Ann P. O Rourke[2], Shane Huebner[3], Peter S. Rahko[4], James A. Will[5], and John G. Webster[6]

[1]Department of Electrical and Computer Engineering, University of Wisconsin, Madison, WI 53706 USA
[2]Department of Surgery, University of Wisconsin, Madison, WI 53792 USA
[3]Department of Nutritional Sciences, University of Wisconsin, Madison, WI 53706 USA.
[4]Department of Medicine, University of Wisconsin, Madison, WI 53792, USA
[5]Department of Animal Health and Biomedical Sciences and the
Department of Animal Sciences, University of Wisconsin, Madison, WI 53706 USA.
[6]Department of Biomedical Engineering, University of Wisconsin, Madison, WI 53706 USA

Abstract—**Electromuscular incapacitating devices (EMDs), such as Tasers, deliver high current, short duration pulses that cause muscular contractions and temporarily incapacitate the human subject. Some reports suggest that EMDs can kill. To help answer the question, "Can the EMD directly cause ventricular fibrillation (VF)?," ten tests were conducted to measure the dart-to-heart distance that causes VF in anesthetized pigs (mass = 64 kg ± 6.67 (SD)) for the most common X26 Taser. The dart-to-heart distance that caused VF was 17 mm ± 6.48 (SD) for the first VF event and 13.7 mm ± 6.79 (SD) for the average of the successive VF events. The result shows that when the stimulation dart is close enough to the heart, X26 Taser current will directly trigger VF in pigs. Echocardiography of erect humans shows skin-to-heart distances from 10 to 57 mm (dart-to-heart distances of 1 to 48 mm). These results suggest that the probability of a dart on the body landing in 1 cm^2 over the ventricle and causing VF is 0.000172.**

I. Introduction

The use of electromuscular incapacitating devices (EMDs) such as the Taser has been controversial (also called electromuscular disruption devices (EMDs), human electromuscular incapacitation (HEMI) devices, and conducted electrical weapons (CEWs)). Some suggest that EMDs can kill [1]. If the EMD directly electrocutes the heart, ventricular fibrillation (VF) would cause the heart to stop pumping, the blood pressure would decrease near zero in about 5 s, and the subject would faint within 30 s. However many deaths following EMD use occur much later and may be caused by drug overdose, positional asphyxia, or other causes [2]. To help answer the question, Can the EMD directly cause VF?, we have measured dart-to-heart distances that cause VF in pigs for the X26 Taser, and measured skin-to-heart distances in erect humans.

Electromuscular incapacitating devices (EMDs), such as Tasers, deliver high current, short duration pulses that cause muscular contractions and temporarily incapacitate the human subject. Their risk in causing VF has been studied and their safety margin has been discussed [3 5]. The risk of inducing VF for a 60 Hz power source and leakage current of cardiac pacemakers has been widely studied [6 9]. Previous studies used 60 Hz data to examine the Taser [10] and calculated the safety factor for the human body ranging between 24 and 53 for the M26 and between 18 and 39 for the X26 [11]. However, EMDs operate with short duration pulses and 60 Hz power source data may not apply. This study obtained data independent of 60 Hz data by experimentally measuring the dart-to-heart distances causing VF for the X26 Taser on anesthetized pigs. All experiments were approved by the appropriate Institutional Animal Care and Use Committee and adhere to all applicable laws and standards of the NIH and USDA as well as the policies of the APS.

Medium sized pigs were subjects because they are about the size of humans and have similar physiology. The mass of the ten normal healthy pigs ranged from 53.8 to 74.4 kg. The pigs were anesthetized and intubated. The blood pressure, oxygen saturation, respiration, heart rate and ECG of the animal were monitored throughout the experiment. The thoracic fat and muscle were reflected to expose the sternum and nearby ribs. The heart dart was placed over the right ventricle, which is the most susceptible region of the heart [12]. The distances between the heart dart tip and the right ventricle were sequenced from long-to-short distances to determine the threshold distance for VF.

II. Materials and Method

Equipment: Anesthesia Monitor: The Datex-Ohmeda s/5 compact Anesthesia Monitor was used to measure physiological parameters during the experiments. Physiologic parameters of blood pressure, electrocardiogram, respiration rate, O_2 saturation (SO_2), and end-tidal CO_2 (ET) were recorded continuously.

Defibrillator: The Hewlett Packard 7802D defibrillator was applied to defibrillate the pig.

F. Ibrahim, N.A. Abu Osman, J. Usman and N.A. Kadri (Eds.): Biomed 06, IFMBE Proceedings 15, pp. 1-5, 2007
www.springerlink.com ' Springer-Verlag Berlin Heidelberg 2007

EDM device: The X26 Taser delivered peak current pulses of about 2 A for a duration of about 150 μs. The stimulation lasted about 5 s with 15 to 19 pulses per second. The typical X26 Taser current waveforms were recorded by an oscilloscope across a precision resistor.

Stimulation darts: In all experiments, the two stimulation darts setup was used to deliver Taser current to pigs. The stimulation darts were made to match the standard Taser probes which were 9 mm long and 0.7 mm in diameter [13].

The heart dart was placed inside a standard French 7 catheter with a conductive lead installed inside to deliver current. One end of the lead was connected to the heart dart and the other end was connected to the X26 Taser. Fig. 1 shows that the heart dart in the catheter was attached to a syringe to provide a stable ground for dart-to-heart distance adjustments. The heart dart was placed inside a virtual tunnel through the intercostal muscle between the 3rd and 4th ribs right above the right ventricle. The plunger of the syringe formed an adjustable stop. It was placed against the ribs next to the virtual tunnel to provide a firm surface to maintain the dart-to-heart distance constant during the vibration caused by the stimulation.

The remote dart, a standard Taser probe, was placed on the abdominal surface ranging from 15 to 54 cm caudal from the stimulation dart.

Muscle-impedance matching gel: The virtual tunnel was made by bluntly dividing intercostal muscle wall tissue between the external surface of the ribs and the heart. The virtual tunnel in the muscle created the possibility of an air gap. This air gap between the stimulating electrode and the heart could change the current density distribution due to the higher impedance of the air compared to muscle. In order to maintain a normal electric current distribution, muscle-impedance matching gel was injected into the virtual tunnel to fill the air gap. The gel was fabricated from NaCl, water and agar. In order to match the 3.0 Ω•m resistance of intercostal muscle [14], concentration 0.2 % saline was used as electrolyte and consolidated by agar (10 g agar with 500 ml saline).

Experimental procedures: Anesthetization process: The pigs were premedicated with Telazol for immobilization. Isoflurane was administered via a mask to induce a surgical plane of anesthesia. A tracheostomy was performed and placement of the endotracheal tube allowed connection to a Harvard respirator. The tidal volume was set to 15 20 ml/kg body weight. Isoflurane was set at 5% for induction and decreased to 3 4% when the surgical plane was achieved. The level of anesthesia was monitored by heart rate, end-tidal CO_2 and testing the corneal reflex, jaw tone, and limb withdrawal. If any of these reflexes were elicited, the concentration of anesthetic was increased until the response subsided. Animals were euthanized with intracardial injections of a saturated solution of KCl while under anesthesia.

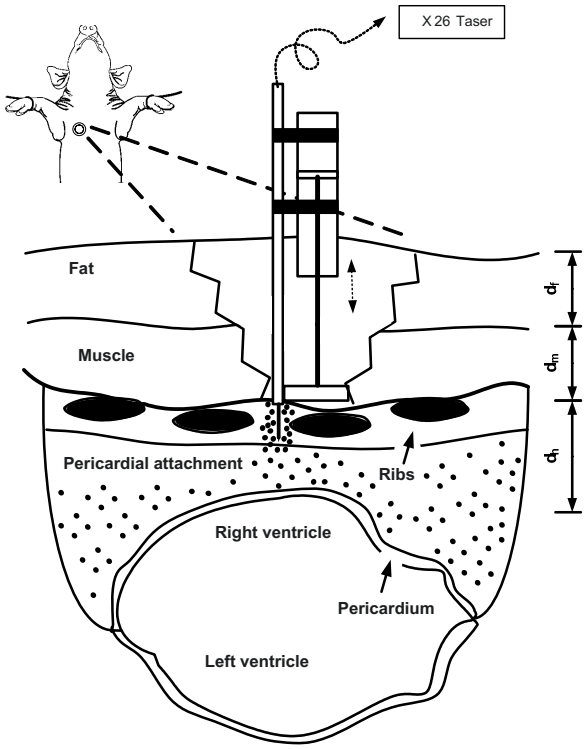

Fig. 1 A midsternal dissection exposed the ribs. Above the external intercostal muscles were muscle layers about 30 mm (d_m), and fat layers about 20 mm (d_f) that were resected to provide the intercostal approach. A virtual tunnel (d_c) contained the heart dart. The heart dart was inserted into a standard F7 catheter with a syringe attached to provide a stable ground to keep the dart-to-heart distance stable during the Taser discharge vibrations. We held the plunger of the syringe against the exposed ribs, which were 30 to 35 mm (d_h) from the pericardium of the heart. Gel is represented by the black dots.

Determination of stimulation location: Once the pharmacologic procedures were complete and the animal was in a homeostatic condition, the sternum was exposed up to the external surface of the intercostal muscle layer. The most sensitive region of the heart for external stimulation has been found to be close to the midpoint of the right ventricle [12]. This region was under the 3rd and 4th ribs. Thus, we placed the heart dart at this region over the right ventricle. A virtual tunnel was made by blunt dissection through the external intercostal muscle between the 3rd and 4th ribs as shown in Fig. 1. The muscle impedance matching gel was injected into the virtual tunnel to fill the potential air gap.

F. Ibrahim, N.A. Abu Osman, J. Usman and N.A. Kadri (Eds.): Biomed 06, IFMBE Proceedings 15, pp. 1-5, 2007
www.springerlink.com ' Springer-Verlag Berlin Heidelberg 2007

Stimulation procedure: After the dissection, the heart dart setup was inserted into the virtual tunnel and advanced toward the pericardium of the right ventricle. The remote dart was placed caudally into the abdominal skin separated from the stimulation dart setup. The distance d_h from the external intercostal muscle to the heart was measured to determine the dart-to-heart distance. The dart-to-heart distance was the distance from the tip of the heart dart to the heart. Current was applied from long-to-short distances to determine the distance threshold of VF. In each experiment, the dart-to-heart distance was started at 20 mm to prevent causing VF immediately. (However in pig 10, VF occurred at 20 mm, so the distance was increased to 24 mm to continue the dart-to-heart protocol.) Then the Taser current was applied through the heart dart for about 5 s with 15 to 19 pulses per second.

After the stimulation, the ECG was verified to check if the heart was beating normally. If the heart beating was normal, the dart-to-heart distance was decreased by 2 mm for each step closer to the heart. Then the stimulation current was applied again. The same process was applied until the first VF occurred. Immediately, the defibrillator with increasing energy from 100, 200, 300, 400 J was used to defibrillate the pig. After the defibrillation, a 5 min recovery period was given to return the pig to a homeostatic condition. After the first VF event, the dart-to-heart distance was increased 2 mm to a less hazardous distance. Then the same process was applied to gather at least 3 VF dart-to-heart distances or the pig was euthanized. After euthanasia, we inserted a different catheter with a detachable barbed tip like a harpoon. This stuck in the heart wall and permitted verification of where the heart dart had been in relation to the ventricle. During the experiment, the impedance matching gel was refilled whenever an air gap in the tunnel was suspected.

Human skin-to-heart distance study: After IRB approval, 150 adult patients scheduled for a clinical echocardiogram were studied. The ultrasound systems used were Philips 5500, Siemens Sequoia c512 and General Electric Vivid-7 with Aquasonic 100 gel. Patients were scheduled for clinical studies and were approached by sonographers in the laboratory to participate. After informed consent was obtained, the patient was asked to stand and images were obtained during quiet respiration. Two views were obtained, the first being the best possible parasternal (sternal border between the ribs with the transducer resting on the ribs) long axis (vertical) view of the heart, and the second being the best apical (tip) four chamber view of the heart (with the transducer resting on the ribs). We did not use the subcostal (under ribs) four chamber view because the transducer distorted the skin in a way that would not occur for a Taser dart. For each imaging location an average of 10 beats were obtained during quiet respiration. The data were digitally stored for further analysis.

To measure skin-to-heart distance, the entire in-digital loop was scanned. A linear measurement was made from the apex of the sector scan, which represents the skin transducer interface to the shortest distance to the epicardial surface of the heart in the given view. Respiratory variation and location of the heart through the cardiac cycle were observed and the point in the loop when the heart was closest to the skin was used for the measurement. In the parasternal long axis view, the shortest distance was from the skin to the right ventricular free wall. In the apical four chamber view the shortest distance to the skin was at the left ventricular apex.

III. Experimental results

Ten animal tests were performed to study the VF dart-to-heart distance of X26 Taser using the two stimulation darts configuration. Except for pigs 1 and 3, the separation of two stimulation darts was fixed at 54 cm in all other tests.

The dart-to-heart distances of all stimulations including VF and no VF events were recorded. Fig. 2 shows only VF dart-to-heart distances of all pig experiments. The first VF distance ranged from 14 to 24 cm except for pig 2. The average first VF distance is 17 mm ± 6.48 (SD). The average VF distance for each experiment ranges from 9.3 to

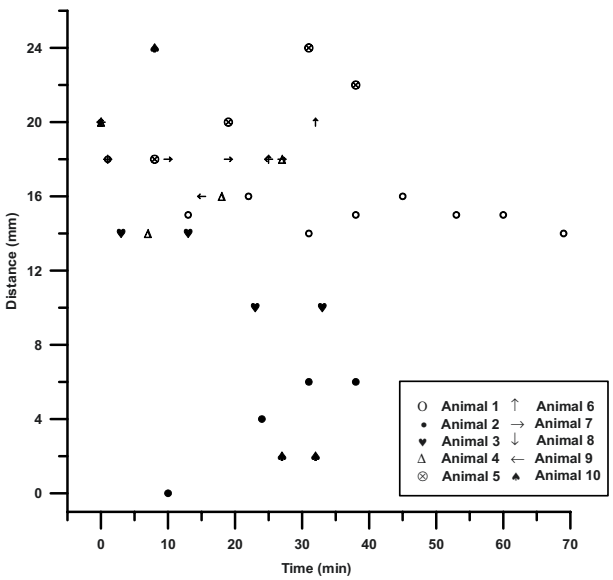

Fig. 2 The VF dart-to-heart distances in all 10 experiments. All symbols represent VF events. The shortest VF distance was 0 mm and the longest VF distance was 24 mm. The first VF distance ranged from 14 to 24 cm except for pig 2. The average of the first VF distance was 17 ± 6.48 mm (SD).

F. Ibrahim, N.A. Abu Osman, J. Usman and N.A. Kadri (Eds.): Biomed 06, IFMBE Proceedings 15, pp. 1-5, 2007
www.springerlink.com ' Springer-Verlag Berlin Heidelberg 2007

21 mm except for pig 2. The overall average is 15.16 mm ± 5.25 (SD).

All animals remained physiologically stable throughout the experimental procedures; however, blood pressures were depressed after the first episode of VF. Generally, the first VF dart-to-heart distances were longer than the following VF distances. At necropsy, we looked specifically at the gel distribution. It was found that the tunnel seemed to be sealed and the remainder of the gel was apparently spread evenly in a barely discernable film over the surface of the pericardium and the pericardial attachment supporting the porcine heart. There were no accumulations detected.

Among 10 experiments, very different VF behavior in pig 2 and pig 10 was observed. Pig 2 was less susceptible to the stimulation current than the other pigs. The first VF distance of pig 2 was 0 mm with average VF distance 4 mm – 2.83 (SD). For pig 10, the first VF distance was 24 mm. However, after the first VF event, pig 10 became less susceptible to the stimulation current and the following two VF distances were shortened to 2 mm.

Human skin-to-heart distance study: Fig. 3 shows that the skin-to-heart distance was 10 to 57 mm in 150 subjects. The skin-to-heart distance increases with body mass index (BMI).

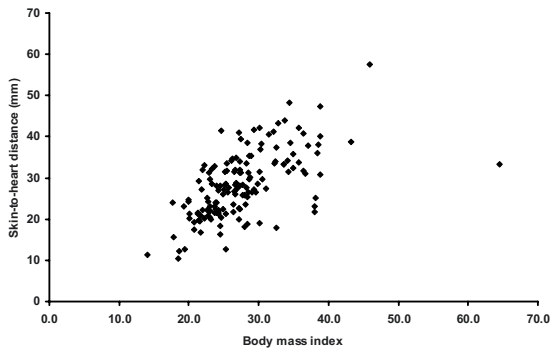

Fig. 3 Echocardiograpy of erect humans shows skin-to-heart distances from 10 to 57 mm.

IV. Discussion

Ten animal experiments, yielded dart-to-heart distances that cause VF in anesthetized pigs for the X26 Taser. The dart-to-heart distance that causes VF is 17 mm ± 6.48 (SD) for the first VF event and 13.7 mm ± 6.79 (SD) for the average of the successive VF distances. Data from only the first VF event were used because each successive defibrillation damages the heart muscle and changes the VF threshold. No meaningful relation between the weight of the pig and the VF threshold distance was observed. Standard Taser darts that stimulate a pig may not cause VF because the normal skin-to-heart distance of pigs is 70 to 80 mm, which is much farther than the sum of the maximum (most dangerous) VF threshold distance 24 mm plus dart length 9 mm equals 33 mm. Assuming the human heart is as vulnerable as the pig s heart, it is more dangerous for human subjects than pig subjects due to the shorter human skin-to-heart distance. The Visible Human Project [15] shows that a typical human skin-to-heart distance is 30 mm, which is much shorter than that of pigs. However Fig. 3 shows that thin humans have still shorter skin-to-heart distances.

McDaniel et al. [3] were unable to cause VF when applying the Taser to the skin of pigs. However pigs have a layer of fat (~20 mm) plus a layer of muscle (~30 mm) over the sternum whereas most humans do not. This causes a lower cardiac current density in the pig heart than in the human heart. Thus, we sought to determine the dart-to-heart distance that causes VF in pigs. Ho et al. [4] were unable to cause VF in humans when applying the Taser to the human back and cites 100,000 applications to the back of Taser class participants with no reported VF. However application from the back causes a lower cardiac current density because of the long distance from the back to the heart.

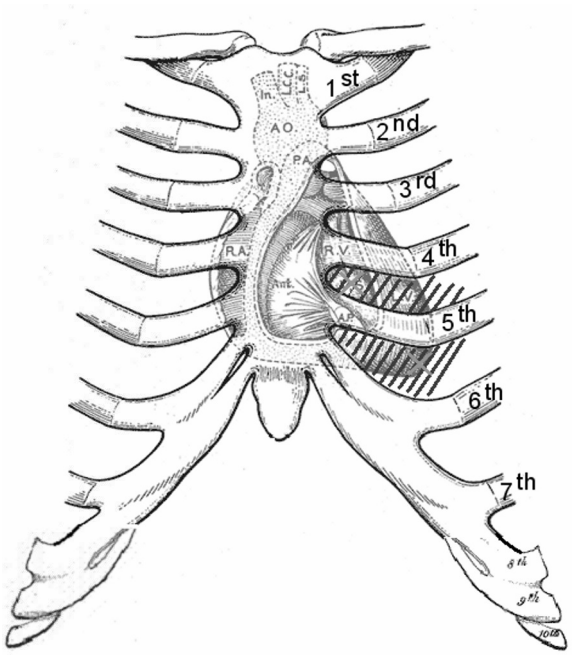

Fig. 4. The ventricle of the heart lies behind the ribs. Slanted lines show the most dangerous locations for dart penetrations between the ribs.

F. Ibrahim, N.A. Abu Osman, J. Usman and N.A. Kadri (Eds.): Biomed 06, IFMBE Proceedings 15, pp. 1-5, 2007
www.springerlink.com ' Springer-Verlag Berlin Heidelberg 2007

Taser International has gathered statistics on dart hit locations [16]. They report that 373 out of 3039 hits were in a 20 by 15 cm rectangle on the upper chest. The probability of a hit in this area = 373/3039 = 0.123. The probability of a hit in 1 cm^2 = 0.123/300 = 0.00041. This probability is multipled by the fraction of humans with skin-to-heart distance less than a chosen distance, from Fig. 3 data. Thus for the dart-to-heart distance of 17 mm found in this study, the probability of a dart on the body landing in 1 cm^2 over the ventricle and causing VF is 0.000172. This probability would be decreased if the dart approached the heart at an angle. Also, if air did penetrate the space between the pericardium and the pleura, this space could distort and modify the distances. The slanted lines in Fig. 4 show that a dart in more than 1 cm^2 could cause VF. These must be added to yield the total probability. We are developing a finite element method (FEM) model of pathways of electric current through the human torso, which has complicated anatomy. Results from this model will provide an estimate of the total probability of human VF. Results should help law enforcement jurisdictions decide appropriateness of use for Tasers (which have a very low probability of death) or bullets (which have a high probability of death) when apprehending violent offenders.

Limitations of this study are that there is a possibility that the virtual tunnel may have permitted air to enter the thorax and thus distorted normal anatomy, and that the conductive gel may have permitted a change in the density of current transmitted to the heart than would occur through the intact tissue.

Necessary, but not sufficient, conditions for concluding that the heart was directly electrocuted are (1) dart landing in a small frontal region over the heart, and (2) collapse of the subject within 30 s after Taser firing. Coroners should seek to confirm these conditions before ascribing Tasers as a contributing cause of death. These results suggest that all Taser training should be done on the back, thus avoiding the front of the torso.

Acknowledgement

This project was supported by Grant No. 2004-IJ-CX-K036 awarded by the National Institute of Justice, Office of Justice Programs, US Department of Justice. Points of view in this document are those of the author and do not necessarily represent the official position or policies of the US Department of Justice.

References

[1] Amnesty International (2006): http://news.amnesty.org/index/ENGAMR51039

[2] Laur D. (2004) 'Excited Delirium and its Correlation to Sudden and Unexpected Death Proximal to Restraint', (Canada: Victoria Police Department), Internet site address: http://www.taser.com/facts/medical_info.htm.

[3] McDaniel W. C., Stratbucker R. A., Nerheim M., Brewer J. E. (2005): Cardiac safety of neuromuscular incapacitating defensive devices', *PACE, Suppl. 1*, **28**, S284-7

[4] Ho J. D., Milner J. R., Lakireddy D. R., Bultman L. L., Heegaard W. G. (2006): 'Cardiovascular and physiologic effects of conducted electrical weapon discharge in resting adults', *Acad. Emerg. Med*., **13**, 589-95

[5] Stratbucker R., Roeder R., Nerheim M. (2003): 'Cardiac safety of high voltage TASER X26 waveform', Proc. Annu. Int. Conf. IEEE Eng. Med. Biol. Soc. **4** 3261-2

[6] Reilly J. P. (1998): 'Applied bioelectricity', (Springer, New York)

[7] Geddes L. A., Baker L. E. (1989): 'Principles of Applied Biomedical Instrumentation, 3rd ed.', (John Wiley & Sons, New York), pp. 458 61

[8] Geddes L. A. (2004): Accuracy limitations of chronaxie values', *IEEE Trans. Biomed. Eng*., **51** 176-81

[9] Jones M., Geddes L. A. (1977): Strength duration curves for cardiac pacemaking and ventricular fibrilllation', *Cardiovasc. Res. Center Bull*. **15** 101-12

[10] Webster J. G. (2005) Electromuscular incapacitating devices', IFMBE Proc. **9**.

[11] Sun H., Wu J.-Y., Abdallah R., Webster J. G. (2005): Electromuscular incapacitating device safety', IFMBE Proc., **11**(1)

[12] Roy O. Z., Scott J. R., Park G. C. (1976) '60-Hz ventricular fibrillation and pump failure thresholds versus electrode area', *IEEE Trans. Biomed. Eng*. **23** 45-8

[13] TASER International. Inc. (2006): Taser cartridge specification - 15', 21' and 25' XP , Internet site address: http://www.taser.com/law/download/specs.htm

[14] Duck F. A. (1990): 'Physical Properties of Tissue: A Comprehensive Reference Book', (Academic Press, San Diego)

[15] U.S. National Library of Medicine, National Institutes of Health, (2003): 'Visible Human Project', Internet site address: http://www.nlm.nih.gov/research/visible/visible_human.html

Author: Jiun-Yan Wu
Institute: Department of Biomedical Engineering,University of Wisconsin
City: Madison
Country: USA

F. Ibrahim, N.A. Abu Osman, J. Usman and N.A. Kadri (Eds.): Biomed 06, IFMBE Proceedings 15, pp. 1-5, 2007
www.springerlink.com ' Springer-Verlag Berlin Heidelberg 2007

Advances and Challenges in Neural Engineering: Neurogenesis, Neurocontrol and Neurochips

Metin Akay

Harrington Department of Bioengineering, Fulton School of Engineering,
Arizona State University, Tempe, Arizona 85287

Abstract–**Neural engineering is an emerging discipline to understand the organizational principles and underlying mechanisms of the biology of neural systems and to study the behavior dynamics and complexity of neural systems in nature.**

It coalesces the engineering including electronic and photonic technologies, computer science, physics, chemistry, mathematics with the molecular, systems, cellular, cognitive and behavioral neuroscience. Therefore, the neural engineering deals with many aspects of basic and clinical problems associated with neural dysfunction including the representation of sensory and motor information, the electrical stimulation of the neuromuscular system to control the muscle activation and movement, the analysis and visualization of complex neural systems at mutli-scale from the single-cell and to the system levels to understand the underlying mechanisms, the development of novel electronic and photonic devices for experimental probing, the simulation studies, the design and development of human-machine interface systems and artificial vision sensors and neural prosthesis to restore and enhance the impaired sensory and motor systems and functions.

In this presentation, we will briefly overview the recent developments in this emerging field, Neural Engineering from neurogenesis to neurochips. Then, we will discuss the ongoing research activities at the Neural Engineering and Informatics Lab at ASU, AZ, USA.

First, we will discuss our recent finding about the relative contributions of maturation to the dynamical behavior of respiration during ontogeny in the neonate and the underlying mechanisms of the respiratory network.

Acknowledgements

This research was supported in part by NIH HL.

F. Ibrahim, N.A. Abu Osman, J. Usman and N.A. Kadri (Eds.): Biomed 06, IFMBE Proceedings 15, p. 6, 2007
www.springerlink.com ' Springer-Verlag Berlin Heidelberg 2007

Nanotechnology Impact Towards Innovative Biomedical Engineering

Makoto Kikuchi

National Defense Medical College Research Institute / Department of Medical Engineering, National Defense Medical College, JAPAN

Abstract:
Nanotechnology is emerging as a new field enabling the creation and application of materials, devices, and systems at atomic and molecular levels and the exploitation of novel properties that emerge at the nanometer scale. Many areas of biomedical engineering are expected to benefit from nanotechnology including sensors for use in the laboratory, the clinic, and within the human body, new formulations and routes for drug delivery, and biocompatible, high-performance materials for use in implants. Examples of potential uses of nanotechnology in biomedical engineering include the early detection and treatment of disease. Recently, enormous researchers with this notice have been launched to encourage the applications for research, in the general areas of nanoscience and nanotechnology as related to

1) The development of new research tools for elucidating biological principles essential for the design and implementation of nanostructured materials for use in biomedical engineering, and
2) The transfer of nanotechnology advances in other fields of science and engineering to develop new ways to help prevent, detect, diagnose, and treat disease and disorders.

Nanostructures offer a new paradigm for materials manufacture by submicron-scale assembly (ideally, utilizing self-organization and self-assembly) to create entities from the bottom up rather than the top down ultraminiaturization method of chiseling smaller structures from larger ones. Each significant advance in understanding the physical/chemical bio properties and fabrication principles, as well as in development of predictive methods to control them, is likely to lead to major advances in our ability to design, fabricate and assemble the nanostructures and nonodevice into a working system being applicable to healthcare technology.

F. Ibrahim, N.A. Abu Osman, J. Usman and N.A. Kadri (Eds.): Biomed 06, IFMBE Proceedings 15, p. 7, 2007
www.springerlink.com ' Springer-Verlag Berlin Heidelberg 2007

3-D Reconstruction of Nasopharyngeal Airways in Malaysian Subjects

G.D. Singh[1], M.H. Rozihan[2], M.T.M. Nidzam[3], A.K. Shamim[3], A.R. Samsudin[2], D. Suhaimi[3]

[1] BioModeling Solutions, San Juan, PR, USA
[2] USM School of Dental Sciences, Kota Bharu, Malaysia
[3] Hospital USM Dept. of ORL-HNS, Kota Bharu, Malaysia

Abstract— **Objectives: To develop 3-D nasopharyngeal airways from 2-D acoustic rhinometer data for diagnostic purposes. Methods: Rhinometer readings were taken from 285 Malaysian subjects. Data from the right (R) and left (L) nostrils were stratified according to age and sex. The sample comprised: 88 Female Teenagers (FT); 77 Female Adults (FA); 70 Male Teenagers (MT), and 50 Male Adults (MA). New algorithms were developed and encoded in C++ using Air-Ex3™ software. Mean 3-D left and right nasopharyngeal airways were computed for each group, and subjected to finite-element scaling analysis and principal components analysis, using statistical tests for dependent groups. Results: Comparing the corresponding 3-D mean left nasopharyngeal airway with the right side for all four groups, no statistical differences were found. When comparing left sides by age and sex, however, significant differences were detected for the following groups: MAL vs. FTL, MAL vs. FAL, MAL vs. MTL, MTL vs. FTL ($p < 0.05$). Similarly, for the right side, significant differences were detected for the following groups: MAR vs. FTR, MAR vs. FAR, MAR vs. MTR ($p < 0.05$), but MTR was not significantly different from FTR. Therefore, the adult Malay male 3-D nasopharyngeal airway differs from females (both teenagers and adults) and teenage males, bilaterally. Specifically, the adult Malay male nasopharyngeal airway is narrower in the anterior nasal valve region closer to the nostril and wider in the distal regions of the 3-D nasopharyngeal airway. Conclusions: This protocol may useful for the diagnosis, treatment planning and assessment of nasopharyngeal conditions, such as snoring, sleep disordered breathing and obstructive sleep apnea. As well, a similar methodology can be applied to 2-D acoustic pharyngometry data.**

Keywords— **3-D airway, acoustic rhinometry, pharyngometry**

I. Introduction

There are many clinical reasons why the upper airway needs to be imaged. For example, for intubation prior to general anesthesia, an appropriately sized nasopharyngeal airway tube needs to be selected, but traditional methods used to assess the airway may not correlate with the anatomy of the airway, and are unreliable[1]. Two-dimensional methods of assessing pharyngeal airways include cephalometric radiography and nasopharyngeal videoendoscopy[2]. While these methods have some advantages, both procedures are invasive, involving either exposure to ionizing radiation or requiring good patient compliance, which may be less easy in children with asthma, for example. For three-dimensional imaging of the upper airway, Computerized-Tomography (CT) is often employed[3]. Alternatively, airway models can be made from multi-sectional in vivo Magnetic Resonance Imaging (MRI) scans[4]. However, both of the above techniques are time-consuming, expensive, and require specialized technical training and personnel.

Due to the various difficulties of assessing the nasopharyngeal airway, it is necessary to find an accurate method of measuring this region using a non-invasive, non-ionizing technique. Modrzynski et al.[5], as well many previous clinical studies, have used Acoustic Rhinometry (AR) for this purpose. Tarhan et al.[6] found the differences between AR nasal volumes and CT nasal volumes were small, and concluded that AR measurements of healthy adult nasal cavities are reasonably accurate. Similarly, Nurminen et al.[7] reported that reproducibility correlation coefficients were fair for both nasal volume measurements and for nasal minimal cross-sectional area measurements. Therefore, AR is a clinically-reliable method for nasal airway assessment, and recent studies have validated the use of AR to objectively assess nasal patency[8]. However, currently AR data is used to provide a 2-D curve of cross-sectional areas against distance. Clinicians are more accustomed to visualization of patient data. Therefore, the purpose of this article is to develop 3-D nasopharyngeal airways from 2-D acoustic rhinometer data for diagnostic purposes, using a new method of 3-D reconstruction in Malaysian subjects.

II. Materials and method

Sample:

After obtaining appropriate consent, AR readings were taken from 285 Malay subjects at Hospital USM, Dept. of ORL-HNS. Data from the right and left nostrils were strati-

F. Ibrahim, N.A. Abu Osman, J. Usman and N.A. Kadri (Eds.): Biomed 06, IFMBE Proceedings 15, pp. 8-11, 2007
www.springerlink.com ' Springer-Verlag Berlin Heidelberg 2007

fied according to age and sex. The sample comprised: 88 Female Teenagers (FT); 77 Female Adults (FA); 70 Male Teenagers (MT), and 50 Male Adults.

Methods:

New algorithms were developed and encoded in C++ using Air-Ex3^{TM} software, which converted the 2-D AR data into 3-D objects. From there, the mean 3-D left and right nasopharyngeal airways were computed for each group, and subjected to finite-element scaling analysis (FESA) and principal components analysis (PCA), using statistical tests for dependent groups.

III. Results

For the left side, using 3-D finite element analysis Fig.1 illustrates MAL vs FAL (shown on the left) and MAL vs FTL (shown on the right). Using the pseudo-color scale, mean adult male nasopharyngeal airways are narrower in the regions closer to the nostril (blue color) and wider in the regions deep to it (yellow-orange color), relative to both adult and teenage females.

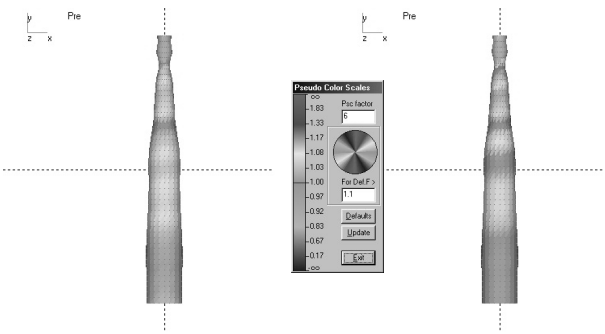

Fig. 1 Results of MAL vs. FAL (shown on left above) and MAL vs. FTL (shown on right above) obtained with FESA.

Using principal components analysis, significant differences were detected for MAL vs. FAL using the first two eigenvalues, which accounted for the majority of the shape-change noted ($p < 0.001$). Similarly, when MAL vs. FTL were compared (Fig. 2), PCA of the first two eigenvalues, which accounted for most of the shape-change, indicated significant differences ($p < 0.001$).

For the right side, using 3-D finite element analysis Fig. 2 illustrates MAR vs. FTR (shown on left) and MAL vs. MTR (shown on right). Using the pseudo-color scale, the mean adult male nasopharyngeal airways are again narrower in the regions closer to the nostril (blue color) and wider in the regions deep to it (yellow-orange color), relative to both male and female teenagers.

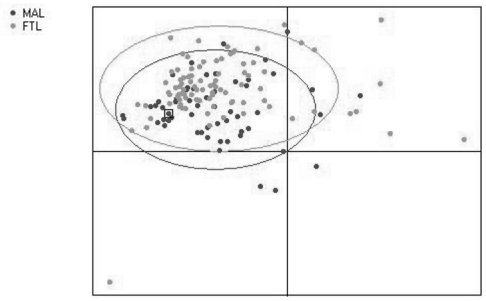

Fig. 2 Results of MAL (red) vs. FTL (green) obtained with PCA are shown above. The x, y axes represent the first two eigenvalues, which encompass the majority of the shape-change information.

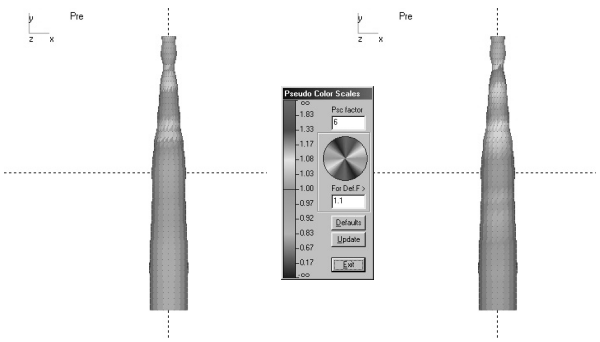

Fig. 3 Results of MAR vs. FTR (shown on left above) and MAR vs. MTR (shown on right) obtained with FESA.

Using principal components analysis, significant differences were detected for MAR vs. FTR using the first two eigenvalues, which accounted for the majority of the shape-change noted ($p < 0.001$). Similarly, when MAR vs. MTR were compared (Fig. 4), PCA of the first two eigenvalues, which accounted for most of the shape-change, indicated significant differences ($p < 0.01$).

F. Ibrahim, N.A. Abu Osman, J. Usman and N.A. Kadri (Eds.): Biomed 06, IFMBE Proceedings 15, pp. 8-11, 2007
www.springerlink.com ' Springer-Verlag Berlin Heidelberg 2007

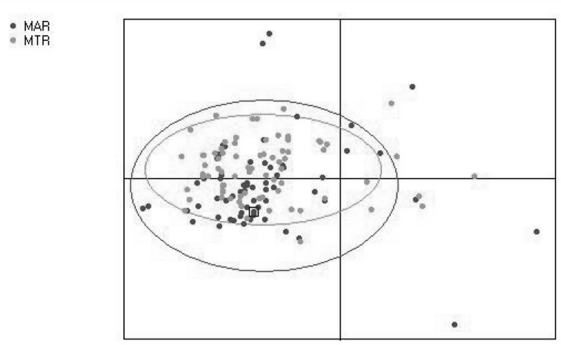

Fig. 4 Results of MAR (red) vs. MTR (green) obtained with PCA are shown above. The x, y axes represent the first two eigenvalues, which encompass the majority of the shape-change information.

Table 1 summarizes the entire statistical findings of this present study. (N.S. = Not Significant).

Groups compared	p value	Significance
FAL vs. FTL	0.681	N.S.
MTL vs. FTL	0.049	*
MTL vs. FAL	0.122	N.S.
MAL vs. FTL	**0.000**	**
MAL vs. FAL	**0.000**	**
MAL vs. MTL	**0.005**	*
FAR vs. FTR	0.599	N.S.
MTR vs. FTR	0.157	N.S.
MTR vs. FAR	0.069	N.S.
MAR vs. FTR	**0.000**	**
MAR vs. FAR	**0.000**	**
MAR vs. MTR	**0.004**	*

Table 1 Statistical findings indicating the adult male nasopharyngeal airways (**in bold**) are significantly different from the other three groups.

Therefore, the adult male nasopharyngeal airways are consistently different from female (teenagers and adults) and teenage male airways on both the left and right sides.

IV. Discussion

Acoustic rhinometry is a well-established method for evaluation of nasal patency, but further improvement of the technique is required[9]. It has several attractive features, as it is non-invasive, non-ionizing, quick and easy to use, and reliable[10, 11]. Mamikoglu et al.[12] suggested that the diagnosis of nasal septal deviation can be supported by AR, and in this present study we found that other nasal morphologic features, particularly in the anterior region of the nasal cavity, can be identified in 3-D. Numminen et al.[13] found strong statistically-significant correlations between AR and CT volumes in the anterior parts of the nasal cavity. Therefore, our present results indicating differences in the anterior nasal valve region are reliable. However, Cankurtaran et al.[14] suggest that AR does not provide reliable information about the cross-sectional areas of the nasal cavity distal to a significant constriction, such as narrowing the nasal valve area. Nevertheless, our primary finding is constriction of the nasal valve area in adult Malay males, which might explain the increased tendency for snoring, sleep disordered breathing and sleep apnea in adult males more generally. Indeed, Ahmad and Gendeh[15] consider that AR is a good tool to evaluate nasal patency in cases of sinonasal surgery. Furthermore, Terheyden et al.[16] using 3-D reconstruction from CT scans found a reasonable agreement of AR and CT volumes in the anterior nose with a mean error at the nasal valve of <5% and at the nasal isthmus of <2%. Thus, measurements up to the turbinate head are reasonably accurate for diagnostic use. In a further 3-D study using MRI data, Djupesland and Rotnes[17] reported that volume estimates based on the smallest cross-sectional areas at points along the acoustic pathway correlate well with acoustically derived volumes. Therefore, the methodology developed in this current study is warranted.

Huang et al.[18] found no differences in the normal range of AR measurements among Chinese, Malay and Indian ethnic groups, but AR was able to determine structural abnormalities of the nasal cavity, such as septal deviation and inferior turbinate hypertrophy. In our present study, we were able to identify narrowing in the nasal valve region of adult Malay males, and this contention is supported by the earlier findings of Cakmak et al.[19], who showed that AR is a valuable method for measuring nasal valve area. Indeed, Yang et al.[20] suggest that AR can be used to define the exact location for nasal surgery. Later, Capone and Sykes[21] reported an increase in both the internal and external nasal valve cross-sectional areas at after rhytidectomy. Therefore, localization and quantification of internal nasopharyngeal airways is possible using the methods described in the present study.

V. Conclusions

The adult Malay male nasopharyngeal airway differs from female (teenagers and adults) and teenage male airways on both the left and right sides. The adult Malay male nasopharyngeal airway is narrower in the anterior nasal valve region closer to the nostril and wider in the distal regions of the 3-D nasopharyngeal airway. These morphol-

F. Ibrahim, N.A. Abu Osman, J. Usman and N.A. Kadri (Eds.): Biomed 06, IFMBE Proceedings 15, pp. 8-11, 2007
www.springerlink.com ' Springer-Verlag Berlin Heidelberg 2007

ogic differences might explain the increased general tendency for snoring, sleep disordered breathing and obstructive sleep apnea in adult males. This protocol may useful for the diagnosis, treatment planning and assessment of snoring, sleep disordered breathing, obstructive sleep apnea, and other nasopharyngeal conditions. For future studies, a similar methodology could be applied to 2-D acoustic pharyngometry data.

Acknowledgment

We would like to thank J. Lourido for developing the source code and computing the results reported.

References

1. Roberts K, Porter K. (2003) How do you size a nasopharyngeal airway. Resuscitation 56:19-23
2. Filho DI, Raveli DB, Raveli RB et al. (2001) A comparison of naso pharyngeal endoscopy and lateral cephalometric radiography in the diagnosis of nasopharyngeal airway obstruction. Am J Orthod Dento facial Orthop 120:348-352
3. Nuhoglu Y, Nuhoglu C, Sirlioglu E at al. (2003) Does recurrent sinusitis lead to a sinusitis remodeling of the upper airways in asth matic children with chronic rhinitis? J Investig Allergol Clin Immu nol 13:99-102
4. Cheng YS, Holmes TD, Gao J et al. (2001) Characterization of nasal spray pumps and deposition pattern in a replica of the human nasal airway. J Aerosol Med 14:267-280
5. Modrzynski M, Mierzwinski J, Zawisza E et al. (2004) Acoustic rhinometry in the assessment of adenoid hypertrophy in allergic children. Med Sci Monit 10:CR431-8. Epub 2004 Jun 29.
6. Tarhan E, Coskun M, Cakmak O et al. (2005) Acoustic rhinometry in humans: accuracy of nasal passage area estimates, and ability to quantify paranasal sinus volume and ostium size. J Appl Physiol 99:616-623. Epub 2005 Mar 31.
7. Nurminen M, Hytonen M, Sala E. (2000) Modelling the reproducibil ity of acoustic rhinometry. Stat Med 19:1179-1189
8. Gosepath J, Belafsky P, Kaldenbach T et al. (2000) The use of acous tic rhinometry in predicting outcomes after sinonasal surgery. Am J Rhinol 14:97-100
9. Hilberg O. Objective measurement of nasal airway dimensions using acoustic rhinometry: methodological and clinical aspects. (2002) Allergy 57:5-39
10. Djupesland P, Pedersen OF. (2000) Acoustic rhinometry in infants and children. Rhinol Suppl 16:52-58
11. Lal D, Corey JP. (2004) Acoustic rhinometry and its uses in rhinology and diagnosis of nasal obstruction. Facial Plast Surg Clin North Am 12:397-405
12. Mamikoglu B, Houser S, Akbar I et al. (2000) Acoustic rhinometry and computed tomography scans for the diagnosis of nasal septal deviation, with clinical correlation. Otolaryngol Head Neck Surg 123:61-68
13. Numminen J, Dastidar P, Heinonen T. (2003) Reliability of acoustic rhinometry. Respir Med 97:421-427
14. Cankurtaran M, Celik H, Cakmak O et al. (2003) Effects of the nasal valve on acoustic rhinometry measurements: a model study. J Appl Physiol 94:2166-2172
15. Ahmad RL, Gendeh BS. (2003) Evaluation with acoustic rhinometry of patients undergoing sinonasal surgery. Med J Malaysia 58:723-728
16. Terheyden H, Maune S, Mertens J et al. (2000) Acoustic rhinometry: validation by three-dimensionally reconstructed computer tomo graphic scans. J Appl Physiol 89:1013-1021
17. Djupesland PG, Rotnes JS. (2001) Accuracy of acoustic rhinometry. Rhinology 39:23-27
18. Huang ZL, Wang DY, Zhang PC et al. (2001) Evaluation of nasal cavity by acoustic rhinometry in Chinese, Malay and Indian ethnic groups. Acta Otolaryngol 121:844-888
19. Cakmak O, Coskun M, Celik H et al. (2003) Value of acoustic rhi nometry for measuring nasal valve area. Laryngoscope 113:295-302
20. Yang Y, Lang J, Wu J et al. (2004). Acoustic rhinometry measure ment from the patients with deviation of nasal septum. Lin Chuang Er Bi Yan Hou Ke Za Zhi 18:225-226 [Article in Chinese]
21. Capone RB, Sykes JM. (2005) The effect of rhytidectomy on the nasal valve. Arch Facial Plast Surg 7:45-50

Address of the corresponding author:

Prof Dr GD Singh DDSc PhD BDS
BioModeling Solutions
3508 Paseo del Bosque, Las Cumbres Ave
San Juan, PR 00926-6643
USA
Email: info@biomodelings.com

F. Ibrahim, N.A. Abu Osman, J. Usman and N.A. Kadri (Eds.): Biomed 06, IFMBE Proceedings 15, pp. 8-11, 2007
www.springerlink.com ' Springer-Verlag Berlin Heidelberg 2007

A Hierarchical Artificial Neural Network Model for Giemsa-Stained Human Chromosome Classification

Jongman Cho

Department of Biomedical Engineering, Inje University, Gimahe, 621-749, Korea

Abstract— **A hierarchical multi-layer neural network with an error back-propagation training algorithm has been adopted for the automatic classification of Giemsa-stained human chromo-somes. The first step classifies chromosomes data into 7 major groups based on their morphological features such as relative length, relative area, centromeric index, and 80 density profiles. The second step classifies these 7 major groups into 24 sub-groups using each group classifier. The classification error decreased by using two steps of classification and the classify-cation error was 5.9%. The result of this study shows that a hierarchical multi-layer neural network can be accepted as an automatic human chromosome classifier.**

Keywords— **Chromosome Classification, Hierarchical Artificial Neural Network**

I. Introduction

Human chromosome analysis is an essential task in cytogenetics, especially in prenatal screening and genetic syndrome diagnosis, cancer pathology research and environmentally induced mutagen dosimetry [1]. Cells used for chromosome analysis are taken mostly from amniotic fluid or blood samples. The stage at which the chromosomes are most suitable for analysis is the metaphase in cellular division. One of the aims of chromo-some analysis is the creation of a karyotype, which is a layout of chromosome images organized by decreasing size in pairs. The karyotype is obtained by all of procedures for cell culture, preparing slides, selection of best-observable chromosome image, analysis and classification.

However, even today, chromosome analysis and karyotyping are manually performed in most cytogenetics laboratories in a repetitive, time consuming and therefore expensive procedure [2]. So, efforts to develop automatic chromosome classification techniques have been made during the last 20 years. The use of features rather than the picture itself makes the classification procedure easier and faster. All the efforts to make the chromosome analysis automatic had limited success and poor classification results compared to those of a trained cytotechnician [1], [6].

An artificial neural network (ANN) makes it possible to overcome most of these limitations. This is mainly because it allows application of expert knowledge and experience through network training. And it is suitable for automatic chromosome classification because the human chromosome images have nonlinear properties [3]. Finally, it is well known that the problems best solved by neural networks are those that humans do well, and classification of chromosomes is one of them [2].

In this study, a hierarchical multi-layer neural network was employed as a human chromosomes classifier. The first step classifies chromosomes data into 7 major groups based on their morphological features such as relative length, relative area, centromeric index, and 80 density profiles. The second step classifies these 7 major groups into 24 subgroups using each group classifier.

1.1 Morphological Features of Human Chromosomes

A centromere is important in the activities of the chromosomes during cellular division and can be located in one of four general positions in the chromosome. A metacentric chromosome has the centromere in approxi-mately the center of the chromosome so that it appears to have two approximately equal arms. Submetacentric chromosomes have one arm longer than the other, acrocentric chromosomes have one arm with a stalk and often with a satellite on it, and telocentric chromosomes have only one arm, since the centromere is at the end [4].

1.1.1 Relative Length

One of the significant morphological features used to identify a chromosome is a length characteristic. However, the length must be normalized before the identification of the chromosome because the length varies according to the phase of the cellular division.

1.1.2 Relative Area

The relative area is one of the significant morphological features used to identify a chromosome, too. The area must be normalized like the relative length.

1.1.3 Centromeric Index

The centromeric index (CI) is the ratio of the length of the short arm to the whole length of a chromosome. It is another significant morphological feature used to identify the chromosome. But it is difficult to get the location of the

F. Ibrahim, N.A. Abu Osman, J. Usman and N.A. Kadri (Eds.): Biomed 06, IFMBE Proceedings 15, pp. 12-15, 2007
www.springerlink.com ' Springer-Verlag Berlin Heidelberg 2007

centromere and the centromeric index for telocentric chromosomes in Group-D (No. 13, No. 14 and No. 15) and Group-G (No. 21, No. 22 and Y).

1.1.4 Features of Banding Pattern of a Giemsa-Stained Chromosome

The Giemsa-stained chromosome has a sequence of banding patterns that are perpendicular to the medial axis of the chromosome. This feature is important to identify chromosomes because each chromosome has its own banding pattern.

II. Methodology

2.1 Chromosome Data

The suggested methodology was applied to Edinburgh database. The chromosome database was provided by Dr. Piper and exported from the Medical Research Council Human Genetic Unit, Edinburgh, UK.

2.2 Experimental Tool

In this study, Microsoft Visual C++ .Net was used to implement the application program for feature extraction and NeuroShell 2.0 (The Ward Systems Group) was used to train and test as a neural network simulator.

2.3 Feature Extraction

2.3.1 Medial Axis

The thresholding operation to the chromosome image was applied before getting the medial axis or line. If the pixel is in the chromosome, the pixel value is set to 1 and otherwise, 0 . The medial line of a chromosome could be obtained by applying the medial axis transformation (MAT) algorithm. The MAT is widely used as a convenient transformation for the representation of elongated objects, for example in character recognition or chromosome analysis, where the width of the objects contains little useful information [7]. In addition, the thinning algorithm that iteratively deletes edge points of a region subject to the constraints that deletion of these points does not remove end points, does not break connectedness, and does not cause excessive erosion of the region was used [4]. After applying the MAT, the skeletonized line was extended to the boundary and the extended medial line of the chromosomes could be obtained.

2.3.2 Relative Length

After getting the medial line, it is common to use Euclidean distance to get the distance between two points. This method was not used because most chromosomes are not exactly straight. Instead, the length of each chromosome could be calculated by counting the number of pixels along the medial line.

The relative length of the i-th chromosome (l_{ri}) can be obtained by normalizing the medial axis length using the following equation, where l_i (i = 1,2, ,24) is the length of i-th chromosome and l_t is the total length of all 46 chromosomes of one cell.

$$l_{ri} = \frac{l_i}{l_t} \tag{1}$$

2.3.3 Relative Area

The relative area of the *i*-th chromosome (A_{ri}) can be obtained by counting the pixels of the chromosome body and by normalizing the areas using the following equation, where A_i (i = 1,2, ,24) is the area of *i*-th chromosome and A_t is the total area of all 46 chromosomes of one cell.

$$A_{ri} = \frac{A_i}{A_t} \tag{2}$$

2.3.4 Centromeric Index (CI)

The CI is the ratio of the length of the short arm to the whole length of a chromosome. It is another significant morphological feature used to identify the chromosome and can be calculated using the following equation, where C_i is the CI of *i*-th chromosome, l_{si} (i = 1,2, ,24) is the short arm length of *i*-th chromosome and l_i is the whole length of *i*-th chromosome.

$$C_i = \frac{l_{si}}{l_i} \tag{3}$$

2.3.5 Normalized Density Profile

The Giemsa-stained human chromosome has a sequence of banding pattern that is perpendicular to the medial axis of the chromosome. Density profile (DP) is a one-dimen-sional graph of the banding pattern property of the chromosome computed at a sequence of points along the possibly curved chromosome medial axis. The DP for a chromosome is obtained from measurements made along a transverse line, perpendicular to the tangent of the medial axis. Each profile value (I_i) results from the summing properties of points spaced at unit distance apart along each transverse line. To reduce the variation of the density values due to the different cell culturing conditions, this DP is normalized three times by three different methods. First, this profile ($d_w(i)$) is normalized in the direction of the perpendicular to the medial axis of the chromosome to reduce the variation of width of a chromosome.

F. Ibrahim, N.A. Abu Osman, J. Usman and N.A. Kadri (Eds.): Biomed 06, IFMBE Proceedings 15, pp. 12-15, 2007
www.springerlink.com ' Springer-Verlag Berlin Heidelberg 2007

In the above equations, m is the number of pixel on the line of perpendicular to the tangent of the medial axis, d(i,j) is the pixel value on the line of perpendicular to the tangent of the medial axis, and w(i) is the width of i-th point in a chromosome.

$$I_i = \sum_{j=0}^{m-1} d(i,j) \qquad (i = 0,1,\ldots,n-1) \qquad (4)$$

$$d_w(i) = \frac{I_i}{w(i)} \qquad (i = 0,1,\ldots,n-1) \qquad (5)$$

Next, histogram equalization is applied to the profile to reduce the effect of non-homogeneous illumination conditions of the microscope. Finally, the profile is normalized along the medial axis to obtain the same number of normalized density values ($d_N(i)$) regardless of chromosome length shown as the following equation, where $d_{wMIN}(i)$ is the minimum density value and $d_{wMAX}(i)$ is maximum density value [3].

In this study, the number of DP was set to 80 because the length of each chromosome in a cell varies and the length of No. 1 chromosome was about 80.

$$d_N(i) = \frac{d_w(i) - d_{wMIN}(i)}{d_{wMAX}(i)} \qquad (i = 0,1,\ldots,n-1) \qquad (6)$$

2.3.6 Chromosome Data Sets

Ten cells (460 chromosomes) were selected for training and another ten cells were prepared for test at random from the database. Some studies have used the relative length, CI and DP as features [2], [3] but two sets were prepared as the input vectors to multi-layer neural network to compare the classification errors. One used the relative length, CI and DP like some studies, the other used the relative length, the relative area, CI and DP.

2.3.7 Chromosome Classifiers

Chromosome classification was done in two steps and multi-layer neural networks were used in each step and the error back-propagation training algorithm was applied for training them.

A. The First Step Classifier

Chromosomes are classified into seven subgroups (Group A-G) in this step. The optimal number of processing elements (PEs) in the hidden layer of this neural network was determined so that it showed the best classification result.

B. The Second Step Classifiers

Seven neural networks were used to classify chromosomes of each subgroup into individual chromosome. Parameters for the neural network for each subgroup were different according to the subgroups and selected as the same method as the first step classifier.

III. Results

3.1 Number of Processing Elements in Each Step

The optimal numbers of PEs in the hidden layer of the neural networks were determined through training phase. The number of PEs of the first step classifier was selected as 35 and the others for the second step classifiers were selected as shown in Table 1.

Table 1 Number of processing elements in the hidden layer of the second step classifiers

Group	*Number of PEs*
A	7
B	7
C	11
D	15
E	11
F	7
G	11

3.2 Classification Result of the First Step

The best trained neural network showed the smallest error was selected as the first step classifier and the test data set that was not used for the training phase was applied as input vectors to the classifier. The classification result was shown in Table 2.

Table 2 Classification result of the first step classifier

Classification result by expert	*Classification result by the trained neural network*							
	A	**B**	**C**	**D**	**E**	**F**	**G**	**Sum**
A	59		1					60
B		38	2					40
C	2	1	152					156
D			1	58	1			60
E			1		59		1	60
F						39	1	40
G						5	39	44
Sum	61	39	157	58	60	44	41	460

F. Ibrahim, N.A. Abu Osman, J. Usman and N.A. Kadri (Eds.): Biomed 06, IFMBE Proceedings 15, pp. 12-15, 2007
www.springerlink.com ' Springer-Verlag Berlin Heidelberg 2007

Table 3 Classification result of the 2nd step

		Classification By Trained Neural Network																								
		A			B		C								D			E			F		G			Sum
		1	2	3	4	5	6	7	8	9	10	11	12	X	13	14	15	16	17	18	19	20	21	22	Y	
A	1	19		1																						20
	2		19																							19
	3			20																						20
B	4				19																					19
	5				1	18																				19
C	6						18																			18
	7							19																		19
	8								19	1																20
	9								1	18				1												20
	10										20															20
	11									1		20														20
	12												19													20
	X												1	15												16
D	13														20											20
	14															19	1									20
	15																18									18
E	16																	20								20
	17																		19							19
	18																			19						19
F	19																				20					20
	20																				1	19				20
G	21																						17	2	1	20
	22																						1	15		16
	Y																							1	3	4
Sum		19	19	21	20	18	18	19	20	20	20	20	20	16	20	19	19	20	19	19	21	19	18	18	4	460

3.3 Classification Result of the Second Step

Only the correctly classified chromosome data in the first step were used in the second step classification by using seven different classifiers and showed 3.1% of classification error as shown in Table 3.

IV. Discussion and Conclusion

Sixteen chromosomes were misclassified in the first step classification and the error rate was 3.4 %; especially, the group G showed the highest classification error. On the other hand, 11 chromosomes were misclassified in the second step classification and the error rate was 2.4 %.

In this study, two-step hierarchical multi-layer neural network was employed to classify Giemsa-stained human chromosomes. It showed 5.9 % of overall classification error and is better than the previous result that used single-step multi-layer neural network. However, chromosomes of group G showed relatively higher classification error in the first step, so new chromosome features that can improve classification accuracy in the first step should be studied in the future work.

Acknowledgment

This work was supported by Inje Research Foundation.

References

1. Carothers A, Piper J (1994) Computer-Aided Classification of Human Chromosomes. A Review. Stat. Comput. Vol. 4. 161-171
2. Lerner B (1998) Toward a Completely Automatic Neural-Network-based Human Chromosome Analysis. IEEE Tran. Systems Man. and Cybernetics. Vol. 28. 544-552
3. Cho J.M. (2000) Chromosome Classification Using Backpropagation Neural Network IEEE Med. and Bio. Magn. Vol. 19. 28-33
4. Peter J, Russell (1998) Genetics. Addison Welsley Longman Inc., New York Chapter 3
5. Gonzalez R.C, Woods R.E. (1992) Digital Image Processing. Addision-Wesley, MA Chapter 8
6. Groen F.C.A, Kate T.K, Smeulders A.W.M, Young I.T (1989) Human Chromosome Classification based on Local Band Descriptors. Pattern Recognit. Lett., Vol. 9 211-222
7. Lerner B, Guterman H, Dinstein I, Romen Y (1995) Medial Axis Transform-based Features and a Neural Network for Human Chromosome Classification. Pattern Recog., Vol. 28, No. 11 1673-1683

Address of the corresponding author:

Author: Jongman Cho
Institute: Department of Biomedical Engineering, Inje University
Street: 607, Obang-dong
City: Gimhae
Country: Korea, South
Email: minerva@ieee.org

F. Ibrahim, N.A. Abu Osman, J. Usman and N.A. Kadri (Eds.): Biomed 06, IFMBE Proceedings 15, pp. 12-15, 2007
www.springerlink.com ' Springer-Verlag Berlin Heidelberg 2007

Fluid Micromixing Technology and Its Applications for Biological and Chemical Processes

Y.T. Chew, H.M. Xia and C. Shu

Department of Mechanical Engineering, National University of Singapore, Singapore 117576

Abstract— **In recent years, there have been intensive investigations on various microfluidic devices and integrated microfluidic systems, such as lab-on-a-chips (or micro total analysis system— μ -TAS) and microreactors. They have been increasingly applied for the biological and medical processes such as genetic analysis, disease diagnosis, chemical synthesis, etc. One involved problem is to mix fluids at microscopic scales. Due to the reduced feature size, the micro flow is usually viscosity dominant laminar flow, and the fluid mixing is limited to diffusion. However, in many applications, the fluid mixing is of crucial importance. The mixing efficiency may directly affect the performance of the whole system. In this paper, the techniques to enhance fluid micromixing are reviewed. A brief introduction of their applications for various biological and medical processes is also presented.**

Keywords— **Fluid Micromixing, Biochip, Microreactor**

I. Introduction

In the past decade, the advent in the microfabrication techniques has greatly enhanced the trend of miniaturization of the fluidic devices. Intensive studies have been reported on the individual microfluidic components, such as micropump, microvalve and micromixer, etc., as well as the integrated systems [1-4]. They are increasingly being applied for various biological and chemical process, leading to the new concepts such as Bio-MEMS, Bio-chip (DNA-Chip, RNA-Chip, Protein-Chip, etc.), Lab-on-a-chip (or micro-total-analysis systems, μ -TAS) and Microreactor.

Bio-chips and Lab-on-a-chips are integrated systems with various components. They are usually fabricated with glass, silicon or polymer materials. All the procedures for bio-analysis, including sample injection, mixing, reaction and information extraction, etc. can be completed on this single platform. Compared with traditional laboratory work, these systems promise some apparent advantages such as (1) less material, sample and reagent, and consequently lower cost; (2) less waste and contamination; (3) fast response time and high efficiency; (4) reduced size, portability and on site applications; (5) easy automation and operation, etc.

The microreactor is an advanced technology for modern chemistry [5, 6]. Microfabricated reactors have high surface-to-volume ratio, and so excellent mass/heat transfer properties. This is an advantage for many chemical processes. Its production flexibility through parallel operation also makes it attractive for chemical engineering.

The feature size of a microfluidic device is typically from several tens to several hundred micrometers. Fluid flow at such a micro scale introduces some new characteristics due to its large surface to volume ratio. There is increased influence of the surface tension, and the dominance of fluid viscous forces at the expense of inertia force. Thus all micro flows fall in the low Reynolds (Re) number laminar regime. The involved Re is usually below 100, and may be far below 1. The laminar nature of the micro flow increases the difficulty for fluid mixing. Due to the lack of turbulence, the mixing solely depends on the molecular diffusion, which is slow and usually not sufficient. But on the other hand, for many biological and chemical processes, the rapid mixing of the cells, viscous organic solutions or reactants could be of crucial importance. The mixing efficiency may directly determine the overall performance of the whole system.

As a solution to this problem, appropriate micromixers are usually applied to meet the relevant mixing requirements. This paper presents a review on the fluid micromixing technology and its applications for biological and chemical processes. It also presents the newly designed micromixers by the authors that are based on three-dimensional chaotic advection through a stretching and folding process. The new micromixers are capable of achieving good mixing at Re below 1.

II. Techniques to enhance fluid micromixing

The mixing rate through diffusion can be expressed as

$$V = A\sqrt{Dt} \tag{1}$$

where V is the volume of the mixed fluids after time t, A is the contact area between the fluids and D is the diffusion coefficient. From equation (1), to promote the mixing, we need to increase the material interface A or to reduce the diffusion length V/A.

In the past few years, many micromixers have been reported. Basing on their working principles, they are usually categorized into two types: the active mixer and the passive mixer.

F. Ibrahim, N.A. Abu Osman, J. Usman and N.A. Kadri (Eds.): Biomed 06, IFMBE Proceedings 15, pp. 16-20, 2007
www.springerlink.com ' Springer-Verlag Berlin Heidelberg 2007

Active micromixers use external resources to stir the fluids. Some relevant methods are illustrated in Fig.1. The actuator could be made of piezoelectric (PZT) material [7, 8]. It can be used to cause ultrasonic vibration of the fluids to achieve good mixing. Electro-hydrodynamic (EHD) [9] and Magneto-hydrodynamic (MHD) [10] effects can also be applied basing on the electrical and magnetic properties of the fluids. Stirrings of the fluids are achieved through changing the electrical/magnetic fields. Another method is to apply pressure perturbations through side channels [11]. The branch flow can cause the stretching and folding of the fluids, and the material interface is greatly increased.

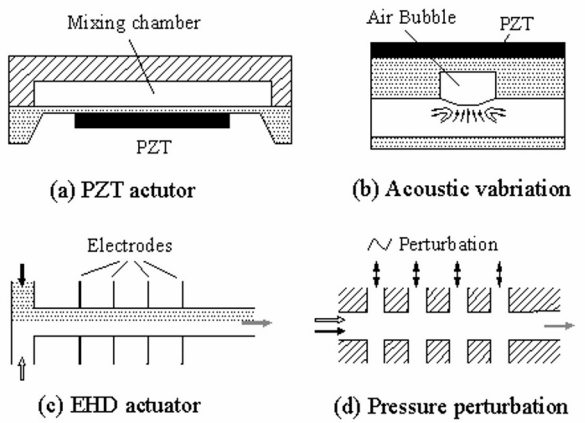

Fig. 1 Stirring methods used for various active micromixer designs.

Passive micromixers utilize the geometric structure of the flow channel to apply perturbations on the fluids. Some examples are shown in Fig. 2. (1) Mixer using fluid lamination. One typical design is the LIGA mixer as shown in Fig. 2(a) [12]. The fluids are driven into the mixing chamber from opposite directions. And they are laminated into thin stream layers through narrow microchannels that are arranged in an alternate manner. The fluids are then driven perpendicular to the direction of the feeding flow and the stream layers are in contact with each other. As a result, the material interface is significantly increased. (2) Split-and-Recombine (SAR) Mixer [13]. In this design, the fluids are first flattened through changing the cross-sectional shape of the channel. Then, they are split into two streams using branch channels before being folded together through the merging of the branch channels. The merged fluids are then flattened and the process repeats again. Through this splitting and recombination process, the diffusion length between the fluids is continuously reduced. (3) 2D Planar Mixer using twisted channel, such as zigzag [14] or wavy converging-diverging channel. When the Reynolds number exceeds a certain value, recirculation flow or vortices occur in the wandering channel and promotes the mixing. (4) Chaotic Mixers shown in Figs. 2(d) to (f). This type of mixer applies chaotic advection to enhance the mixing. In a chaotic flow, even simple velocity field solution can lead to very complex flow patterns. Two initially close fluid particles may diverge exponentially and concentrated materials can be quickly dispersed into the whole flow region. One example is the 3D serpentine mixer [15] shown in Fig. 2(d). At moderate Re, the serpentine channel can cause a secondary flow which further leads to chaotic mixing. The SHM (Staggered Herringbone Mixer) mixer shown in Fig. 2(e) is also well known [16]. On one wall of a rectangular channel, there laid a series of asymmetric herringbone-like grooves. While the fluids are driven through the channel, two recirculation streams occur and chaotic advection is produced through the interactions between them. Another design is the TLCCM (Two-Layers Crossing-Channel Mixer) mixer shown in Fig. 2(f) developed by us [17]. This mixer adopts a structure of two-layer crossing channels. The interactions between the two branch flows facilitate the fluid manipulations. Fluid stretching and folding, together with the splitting and recombination can be easily achieved, which further lead to chaotic mixing. As shown in Fig. 2(f), while the cross-sectional distribution of the fluids keep a similar shape, the thickness of the stream layers are continuously reduced along the mixer.

Among the above mentioned mixers, the LIGA mixer can be applied at low Re, but the diffusion length is confined by the width of the microchannel. Both the 2D planar design and the 3D serpentine mixer rely on the fluid inertial forces. The former works at a typical Re range of several hundred and the latter can be applied at a lower Re range of several tens. The SAR mixer involves complex structure, and it works well at Re<15. At higher Re, its performance is affected by the secondary flow. Comparatively, the SHM and TLCCM mixers are more efficient. Both of them are independent of the fluid inertial effects to generate chaotic advection. They are capable of mixing highly viscous fluids and applicable at extremely low Re (<<1).

Compared with the passive design, the active mixer usually provides fast mixing. But as external resources, such as moving parts and power supply are required, it is more complex and less reliable. The passive mixer is relatively simple and can be easily realized. It is also more convenient to be integrated into microfluidic systems. On the other hand, the active mixer is mainly applied for chamber mixing while the passive mixer is more suitable for in-line continuous processing.

F. Ibrahim, N.A. Abu Osman, J. Usman and N.A. Kadri (Eds.): Biomed 06, IFMBE Proceedings 15, pp. 16-20, 2007
www.springerlink.com ' Springer-Verlag Berlin Heidelberg 2007

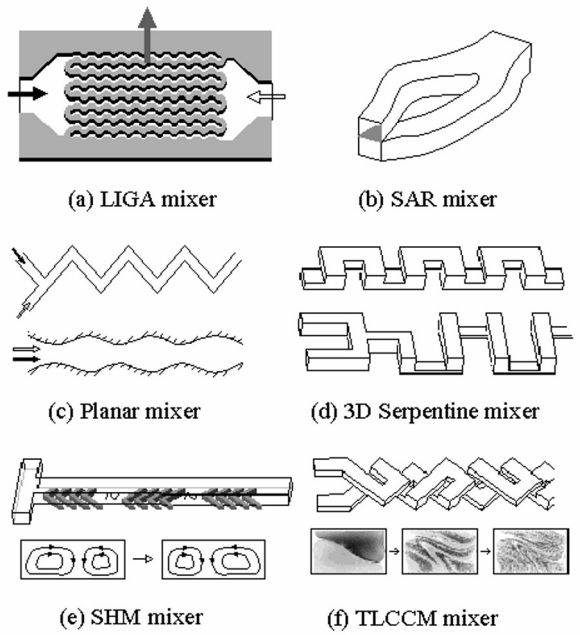

Fig. 2 Schematic illustrations of various passive micromixers.

III. Applications for Biochemical Analysis

One important application of the microfluidic devices is for biological processing, for which rapid mixing is usually an important step. The followings are some examples.

The DNA analysis plays an important role in biological studies. The DNA sample preparation, polymerase chain reaction (PCR) and DNA hybridization etc., all require efficient mixing. Lee et al. [18] performed the DNA purification using a passive micromixer as shown in Fig. 2(d). It adopts a 3D serpentine channel with some segments flattened to reduce the diffusion length. Through the repeated fluid twisting and flattening processes, efficient mixing can be achieved. The mixer was integrated with an SPE-based (solid phase extraction) DNA purification micro-column. The DNA purification from a biological sample was demonstrated by a rapid change of the salt concentration. In this way, the DNA preparation process can be greatly simplified.

Lee et al. developed an electrokinetically driven active micromixer [19] and applied it for DNA amplification [20]. The mixer includes several shielding electrodes that are buried along the side of a microchannel. They are used to apply an electrical potential to drive an electro-osmotic flow (EOF). Through changing the voltage applied on the electrodes, perturbation of the EOF flow can be achieved, leading to efficient mixing. They further integrated this mixer into a microfluidic system for DNA amplification. The cell lysis is first performed in a micro cell lysis reactor. Then, the extracted DNA samples, primers and reagents are driven electro-osmotically into the mixer, where they are well mixed. Next, the homogeneous mixture is driven into a micro-PCR chamber for DNA amplification. Results show that this system performs well and automates the sample pre-treatment operation in DNA detection applications.

Liu et al. introduced a bubble-induced acoustic mixing technique, and applied it for DNA hybridization [8, 21]. In their design, a number of air pockets are laid on the cover slip of the hybridization chamber (see Fig. 1(b)) to trap air bubbles in the reaction solution. A PZT disk is attached to the external surface of the cover slip. It is applied to generate a sound field and cause the vibrations of the bubbles. This further leads to a recirculation flow around the air bubble, which can efficiently promote the mixing. They applied this mixer to promote the DNA hybridization. Results show that, compared with the conventional static method, the new technique led to a 5-fold increase in the hybridization rate. The uniformity of the signal across the whole chip is also significantly improved.

In kinetic studies of in vivo biological reactions, it requires the rapid mixing of crowded solutions, which should be completed faster than the reaction. However, the highly concentrated solutions of crowding agents (such as bovine serum albumin and haemoglobin) are very viscous and extremely difficult to mix. Liau et al. proposed a micromixer which is suitable for such kinetic studies [22]. The mixer adopts a serpentine channel and protrusions are laid out on the channel wall. At the inlet, parallel streams of crowded solutions first pinch off into droplets through intersection with the two oil streams. They are then driven into the bumpy serpentine channel. The protrusions on the channel wall can generate oscillating interfacial shear within the droplets, and mixing can be completed within milliseconds.

In another study by He et al., a picoliter-volume mixer was applied for enzyme assays [23, 24]. In this mixer, the mixing bed consists of multiple intersecting channels. The main channel is arranged in a zigzag manner, while several narrower microchannels form cross-links between different sections of the main channel. This structure can cause substantial convective flow when driven by electro-osmosis and mixing is promoted. The mixer was applied for enzyme assays on a chip in the stopped-flow mode. Their study showed that the enzyme assays can be performed within 60s with roughly 6 nL liquid volume. Relevant results compare well with that using conventional apparatus.

F. Ibrahim, N.A. Abu Osman, J. Usman and N.A. Kadri (Eds.): Biomed 06, IFMBE Proceedings 15, pp. 16-20, 2007
www.springerlink.com ' Springer-Verlag Berlin Heidelberg 2007

IV. Applications for chemical processing

Besides biological analysis, another application field of the fluid micromixing technology is in microreactor, which may bring revolutionary influence on modern chemistry. According to Reberge et al. s report, 50% of reactions in the fine chemical and pharmaceutical industry could benefit from the continuous process basing on microreactor technology [6]. In various microreactor systems, micromixer is also a key component. The mixing efficiency of the reactants greatly influences the reaction time, the yield, as well as the quality of the final products.

In Nagaki et al. s study [25] of the Friedel-Crafts reactions, micromixers (including the LIGA mixer) were applied to improve the chemical selectivity. In macroscale batch reactors, the slow mixing process may disguise the chemical selectivity. The rapid micromixing in a microreactor system can provide a solution to this problem, and result in a much higher yield. Another example is demonstrated by Hessel et al [26]. In their investigation, micromixers were applied in a microreactor for *Phenyl Boronic Acid Process.* With efficient mixing, a high yield of 89% was reported, nearly 25% higher than the performance with stirred tank process. Reduced side products, higher purity of the products, as well as less energy consumption were also reported.

For more discussions of the influence of fluid mixing on various chemical processing, one can refer to Pennmann et al. s review paper [27].

V. Summary

In microfluidic systems, fluid mixing is an important step but becomes more difficult due to the laminar nature of most micro flows. In this paper, various techniques to enhance fluid micromixing and their applications for biological and chemical processing are introduced. The integrated lab-on-a-chips will facilitate the bio-analytical process, such as DNA analysis, disease diagnosis, drug development etc., and the microreactor technology may bring revolutionary changes to the fine chemical and pharmaceutical industry. In future, this research field is expected to benefit from the progress of micro-fabrication techniques and the theoretical guidance of so called micro fluid dynamics .

References

1. Stone HA, Stroock AD, Ajdari A (2004) Engineering flows in small devices: microfluidics toward a lab-on-a-chip. Annu. Rev. Fluid Mech. 36:381-411
2. Beebe DJ, Mensing GA, Walker GM (2002) Physics and applications of microfluidics in biology. Annu. Rev. Biomed. Eng. 4:261-286
3. Verpoorte E, DE Rooij NF (2003) Microfluidics meets MEMS. Proceedings of the IEEE, 91(6):930-953
4. Ng JMK, Gitlin I, Stroock AD et al. (2002) Components for integrated poly(dimethylsiloxane) microfluidic systems. Electrophoresis 23: 3461-3473
5. Ehrfeld W, Hessel V, Löwe H (2000) Microreactor: New technology for modern chemistry. Wiley-VCH, Boston.
6. Roberge DM, Ducry L, Bieler N et al. (2005) Microreactor technology: a revolution for the fine chemical and pharmaceutical industries?. Chem. Eng. Technol. 28(3):318-323
7. Yang Z, Goto H, Matsumoto M et al. (2000) Active micromixer for microfluidic systems using lead-zirconate-titanate (PZT)-generated ultrasonic vibration. Electrophoresis 21:116-119
8. Liu RH, Lenigk R, Druyor-Sanchez RL et al. (2003) Hybridization enhancement using cavitation microstreaming. Anal. Chem. 75:1911-1917
9. Moctar AOE, Aubry N, Batton J (2003) Electro-hydrodynamic microfluidic mixer. Lab Chip 3:273-280
10. Bau HH, Zhong JH, Yi MQ (2001) A minute magneto hydrodynamic (MHD) mixer. Sens. Actuators B 79:207-215
11. Niu X, Lee YK (2003) Efficient spatial-temporal chaotic mixing in microchannels. J. Micromech. Microeng. 13:454-462
12. Ehrfeld W, Golbig K, Hessel V et al. (1999) Characterization of mixing in micromixers by a test reaction: single mixing units and mixer arrays. Ind. Eng. Chem. Res. 38:1075-1082
13. Schönfeld F, Hessel V, Hofmann C (2004) An optimised split-and-recombine micromixer with uniform chaotic mixing . Lab Chip 4:65-69
14. Mengeaud V, Josserand J, Girault HH (2002) Mixing processes in a zigzag microchannel: finite element simulations and optical study. Anal. Chem. 74:4279-4286
15. Liu RH, Stremler MA, Sharp KV et al. (2000) Passive mixing in a three-dimensional serpentine microchannel. J. Microelectromech. Syst. 9:190-197
16. Stroock AD, Dertinger, SKW, Ajdari A et al. (2002) Chaotic mixer for microchannels. Science 295:647-651
17. Xia HM, Wan SYM, Shu C, Chew YT (2005) Chaotic micromixers using two-layer crossing channels to exhibit fast mixing at low Reynolds umbers. Lab chip 5:748-755
18. Lee NY, Yamada M and Seki M (2005) Development of a passive micromixer based on repeated fluid twisting and flattening, and its application to DNA purification. Anal. Bioanal. Chem. 383:776-782
19. Lee CY, Lee GB, Fu LM et al. (2004) Electrokinetically driven active micro-mixers utilizing zeta potential variation induced by field effect. J. Micromech. Microeng. 4:1390-1398
20. Lee CY, Lee GB, Lin JL, et al. (2005) Integrated microfluidic systems for cell lysis, mixing/pumping and DNA amplification. J. Micromech. Microeng. 15:1215-1223
21. Liu RH, Yang J, Lenigk R et al. (2004) Self-contained, fully integrated biochip for sample preparation, polymerase chain reaction amplification and DNA microarray detection. Anal. Chem. 76:1824-1831

F. Ibrahim, N.A. Abu Osman, J. Usman and N.A. Kadri (Eds.): Biomed 06, IFMBE Proceedings 15, pp. 16-20, 2007
www.springerlink.com ' Springer-Verlag Berlin Heidelberg 2007

22. Liau A, Karnik R, Majumdar A et al. (2005) Mixing crowded biological solution in milliseconds. Anal. Chem. 77:7618-7625
23. He B, Burke BJ, Zhang X et al. (2001) A picoliter-volume mixer for microfluidic analytical systems. Anal. Chem. 73:1942-1947
24. Burke BJ and Regnier RE (2003) Stopped-flow enzyme assays on a chip using a microfabricated mixer. Anal. Chem. 75:1786-1791
25. Nagaki A, Togai M, Suga S et al. (2005) Control of extremely fast competitive consecutive reactions using micromixing. Selective friedel-crafts aminoalkylation. J. Am. Chem. Soc. 127:11666-11675
26. Hessel V, Hofmann C, Löwe H et al. (2004) Selectivity gains and energy saving for the industrial phenyl boronic acid process using micromixer/tubular reactor. Org. Proc. Res. Dev. 8:511-523
27. Pennemann H, Watts P, Haswell SJ et al. (2004) Benchmarking of microreactor applications. Org. Proc. Res. Dev. 8:422-439

F. Ibrahim, N.A. Abu Osman, J. Usman and N.A. Kadri (Eds.): Biomed 06, IFMBE Proceedings 15, pp. 16-20, 2007
www.springerlink.com ' Springer-Verlag Berlin Heidelberg 2007

Implantable and Wearable Bionics

N. Lovell

Graduate School of Biomedical Engineering, University of New South Wales, Sydney, Australia

Abstract- **The role of telemetry and communications technology will be explored in a number of medical devices developed at the Graduate School of Biomedical Engineering, University of New South Wales. Topics discussed will include clinical measurement devices used for home telecare, triaxial acceleromters for personal alarming in the elderly, implantable heart pumps and vision prostheses.**

In particular, a review of the state-of-art with regards vision neuroprostheses, with an emphasis on retinal prostheses, will be presented. Through an examination of the neurobiology and biophysics at the electrode tissue interface and by drawing heavily on biologically-inspired designs, critical areas that require concentrated research and development will be described. Brieflycovered are topics relating to application specific integrated circuits (ASIC), appropriate image processing for prosthetic vision, the psychophysics of prosthetic vision, and models of parallel stimulation at multiple electrode sites.

Address of the corresponding author:

Author:	Nigel Lovell
Institute:	Graduate School of Biomedical Engineering, University of New South Wales
City:	Sydney, NSW 2052
Country:	Australia
Email:	n.lovell@unsw.edu.au

F. Ibrahim, N.A. Abu Osman, J. Usman and N.A. Kadri (Eds.): Biomed 06, IFMBE Proceedings 15, p. 21, 2007
www.springerlink.com ' Springer-Verlag Berlin Heidelberg 2007

Surface Modification of Biomaterials and Tissue Engineering Scaffolds for Enhanced Osteoconductivity

Min Wang

Department of Mechanical Engineering, The University of Hong Kong,
Pokfulam Road, Hong Kong

Abstract— **The majority of currently used implant materials in orthopaedics lacks osteoconductivity. This paper reviews our efforts of using a number of surface modification techniques (hydrothermal-electrochemical deposition, plasma spraying, spraying-and-sintering, ion beam assisted deposition, and biomimetic deposition) to improve the osteoconductivity of metallic, polymeric and ceramic biomaterials. Furthermore, biomimetic processes have been employed to render non-bioactive polymer tissue engineering scaffolds osteoconductive. Surface modification has an important role to play in the development of materials for human tissue repair and regeneration.**

I. Introduction

With the help of advances in biological and medical sciences, materials science and engineering has triumphed in the past few decades in providing useful implant materials for human tissue repair for millions of patients all over the world. Nowadays, various materials including metals, polymers, ceramics and composites are used clinically for implants in orthopaedics, dentistry, etc. [1]. Even they have served their roles relatively well, some of the currently used implant materials that were not originally developed for medical applications have shortcomings in their biological environment. One example is the bioinertness of orthopaedic alloys such as stainless steel and Co-Cr alloys, which results in the fibrous tissue formation on implants of these materials in the body [2]. On the other hand, bioceramics such as hydroxyapatite (HA, $Ca_{10}(PO_4)_6(OH)_2$) are known to be bioactive (osteoconductive), which form chemical bonding with bone after implantation [3]. The prerequisite for a material to be bioactive is its ability to form (or induce to form) apatite on its surface after coming into contact with bone in the body. The implant made of an bioactive material is bonded to bone through this intermediate apatite layer [4, 5]. Therefore, since the 1980s, various techniques have been investigated to form an apatite layer on metals such as titanium in an attempt to make them osteoconductive. Some of these surface apatite-forming techniques for metals can also be applied to polymers. Furthermore, investigations have also been made to coat bionert bioceramics such as alumina with an apatite layer in order to achieve bioactivity. Surface modification of existing, accepted biomaterials improves/enhances their biological performance and is thus an important area in biomaterials R & D.

Tissue engineering, since the definition and use of the term appeared in open literature in 1988 [6], has attracted great attention in science, engineering, medicine, and the society. As a new and multidisciplinary endeavor, tissue engineering holds the promises of (a) eliminating re-operations by using biological substitutes, (b) using biological substitutes to solve problems of implant rejection, transmission of diseases associated with xenografts, and shortage in organ donations, (c) providing long-term solutions in tissue repair or treatment of diseases, and (d) potentially offering treatments for medical conditions that are currently untreatable such as fulminant hepatic failure. It has made rapid advances over the last two decades due to more knowledge being gained in biology and medicine, the advancement in physical sciences and technology, and more willingness for collaboration and actual deeper collaboration among clinicians, engineers and scientists [7]. Synthetic scaffolds are considered an important part of a successful tissue engineering strategy. The scaffolds are designed to provide a structural framework as well as a microenvironment for the seeded cells and to facilitate the formation of new tissues. In bone tissue engineering, it is desirable that the tissue engineering scaffolds are osteoconductive. Currently, tissue engineering scaffolds are mainly made of biodegradable polymers such as poly(lactic acid) (PLA), which are non-osteoconductive, and there are various methods to fabricate tissue engineering scaffolds [8, 9].

Our strategy in R&D in the biomaterials and tissue engineering field is to design and develop new, synthetic biomaterials and structures according to clinical requirements, and at the same time to improve current, accepted biomaterials. With such a strategy, our group has invstigated a few techniques for modifying biomaterial surfaces for osteoconductivity. Our group is also conducting research into fabricating osteoconductive scaffolds for bone tissue engineering.

F. Ibrahim, N.A. Abu Osman, J. Usman and N.A. Kadri (Eds.): Biomed 06, IFMBE Proceedings 15, pp. 22-27, 2007
www.springerlink.com ' Springer-Verlag Berlin Heidelberg 2007

II. Materials and Methods

A. Surface Modification of Ceramics, Metals and Polymers for Osteoconductivity

Hydrothermal-electrochemical Deposition

One of our earliest attempts to form an apatite coating on biomaterials was achieved through hydrothermal-electrochemical deposition [10-12]. In this process, brushite single crystals were used as seeds for the deposition of HA via hydrothermal-electrochemical treatment. An acellular simulated body fluid (SBF) [13] was used as the electrolyte and the seed crystal was fixed as one of the electrodes. Experiments were performed at a temperature from 80 to 200°C. A relatively thick layer of HA on the brushite single crystal was obtained at 140°C for a growth time of 30 minutes by passing 100mA current (Fig.1). This deposition technique may be good for the scientific investigations into transformations between various calcium phosphates but it may not be suitable for the surface modicication of actual implant materials.

Fig. 1 Apatite coating deposited on brushite through a hydrothermal-electrochemical treatment

Plasma Spraying

For cementless hip replacement, plasma spraying has been the industry's choice for coating prostheses with a so-called hydroxyapatite coating [3]. Our work on plasma spraying of calcium phosphate coatings has concentrated on producing toughened coatings with high bonding strength with the Ti substrate [14-17]. As HA is a brittle and relatively weak ceramic, some tough but bioinert ceramics such as TiO_2, Al_2O_3 and ZrO_2 can be used to form bioactive ceramic composite coatings for improved mechanical performance. Other calcium phosphates such as tricalcium phosphate (TCP, $Ca_3(PO_4)_2$) can also be considered for toughened bioactive coatings. Additionally, due to its biodegradability, TCP in the HA-based coatings can gradually dissolve after implantation so that enhanced osseointegration is promoted. For achieving good adhesion between the coating and the substrate, a three-layer functionally graded coating (FGC) structure was be employed (Fig.2). The sub-layer which bonds with the substrates should be a mechanical support for the whole coating system. In the mean time, the sub-layer on the surface of the FGC should be bioactive (or biodegradable) in order to obtain good osteoconductivity. The sub-layer which is located between the aforementioned layers may have a compromised mechanical/biological performance.

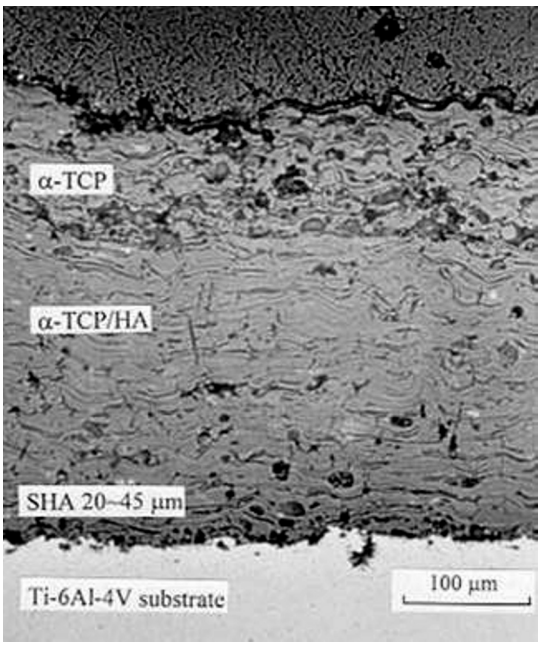

Fig. 2 An FGC produced by plasma spraying

Spraying-and-Sintering

HA decomposes at high temperatures, which causes the loss of osteoconductivity that is desired of the material [3]. To overcome the problem of HA decomposition due to high temperatures in the plasma spraying process, composite bioceramic coatings containing HA can be produced using the spraying-and-sintering technique [18-22]. The spraying-and-sintering technique is a very simple and effective method for producing composite coatings containing HA and HA FGC. Using this technique, the FGC was manufactured by spraying composite powders of different compositions layer by layer onto Ti-6Al-4V plates at room temperature using an airbrush under controlled pressure. The FGC on Ti-6Al-4V was sintered at 900°C which is

F. Ibrahim, N.A. Abu Osman, J. Usman and N.A. Kadri (Eds.): Biomed 06, IFMBE Proceedings 15, pp. 22-27, 2007
www.springerlink.com ' Springer-Verlag Berlin Heidelberg 2007

much lower than the plasma spraying temperature. The coatings had a dense structure (Fig.3). XRD analysis revealed that no HA decomposition was encountered with this coating technique and the FGC retained functional groups for its bioactivity as shown in the FTIR spectra.

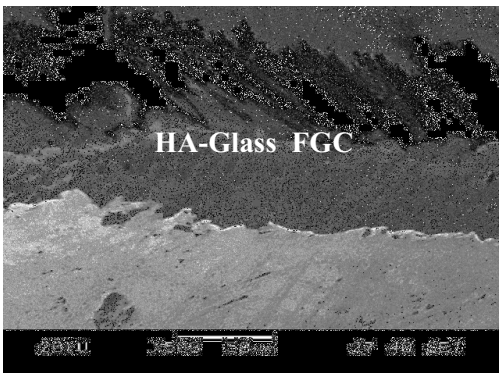

Fig. 3 An HA composite coating fabricated using the spraying-and-sintering technique

Ion Beam Assisted Deposition

Commercially available HA-coated metal implants are manufactured mainly through plasma spraying. A variety of other coating techniques, such as electrochemical deposition, radio-frequency magnetron sputtering, excimer laser deposition, pulsed laser deposition, and dipping, have also been investigated for producing calcium phosphate coatings on metallic substrates. Ion beam sputter deposition was studied as a potential method for producing biocompatible ceramic coatings on metallic implants due to its various advantages which include the production of thin coatings with high density and superior adhesion. In this process, the ionized argon gas was used to sputter atoms from a ceramic target. The sputtered atoms built up on the metallic substrate that was placed in the path of the sputtered material.

In one series of investigations, the ion beam sputtering/mixing deposition technique was employed to produce thin calcium phosphate (Ca-P) coatings on titanium substrate and the structure and *in vitro* properties of these coatings were studied [23]. In other investigations, ion beam assisted deposition techniques were used to produce calcium phosphate FGCs [24, 25] and bioactive glass coatings [26]. It was shown that the Ca-P coating produced promoted the proliferation of osteoblastic cells (Fig.4).

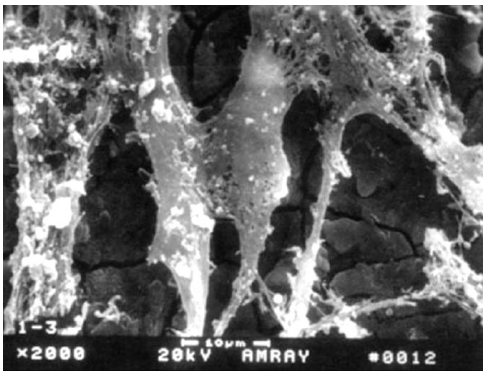

Fig. 4: Osteoblastic cells on a Ca-P coating

Biomimetic Deposition

A few metals including Ti and its alloys can induce the formation of bone-like apatite on their surfaces after they have undergone suitable chemical and thermal treatments. Surface modification of implantable metals through the surface apatite formation via biomimetic processes appears to be a good approach for improving the use of these metals in the medical field. The biomimetic processes take place at human body temperature and do not require harsh reaction conditions, high (or low) pressure, or high temperature, which avoids major disadvantages of other surface apatite-forming techniques such as hydrothermal-electrochemical deposition, plasma spraying and ion beam assisted deposition. Furthermore, as these are low-temperature processes, they can be used to form apatite on polymer surfaces and hence provide non-bioactive polymers with osteoconductivity [27].

Mechanisms and kinetics of biomimetic apatite formation on metal surfaces were studied using a variety of analytical techniques [28-31]. It was found that *in vitro* apatite formation depended on the solution and the procedure that were used. In a recent series of studies, a low-temperature process was employed to treat metal substrates prior to biomimetic deposition of the apatite layer [32-34], thus totally eliminating the detrimental thermal treatment of substrates which is required in the biomimetic processes used by other researchers. Fig.5 shows the apatite coating on Ti produced through the low-temperature biomimetic deposition route [33]. Fig.6 is a high magnification SEM micrograph of biomimetic apatite formed on a surface treated PTFE [27].

F. Ibrahim, N.A. Abu Osman, J. Usman and N.A. Kadri (Eds.): Biomed 06, IFMBE Proceedings 15, pp. 22-27, 2007
www.springerlink.com ' Springer-Verlag Berlin Heidelberg 2007

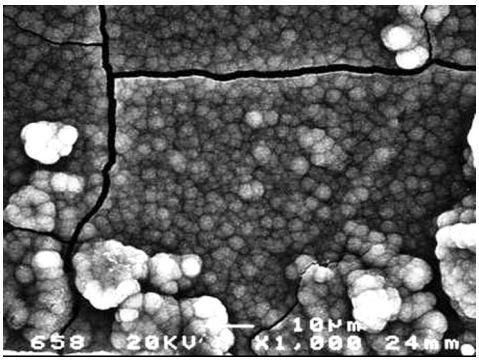

Fig. 5 Apatite coating formed on Ti through biomimetic deposition

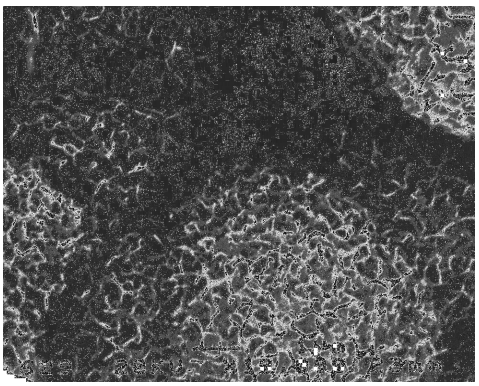

Fig. 6 Apatite coating formed on a surface treated PTFE polymer

B. Fabrication of Osteoconductive Tissue Engineering Scaffolds Using Biomimetic Processes

There are two main routes for the manufacture of polymer-based osteoconductive scaffolds for tissue engineering: (1) incorporating bioceramic particles in the scaffold through a variety of techniques [35-37], and (2) coating a polymer scaffold with a thin layer of apatite through biomimetic processes [38-40]. The two routes have respective advantages and disadvantages and the latter can be used to make osteoconductive the non-bioactive polymer scaffolds readily fabricated.

Incorporating bioceramic particles into biodegradable polymers to form bioactive scaffolds can be successful. But there is an upper limit for the amount of the particles to be incorporated. It has been shown that bone-like apatite could form *in vitro* on the composite scaffolds [35], indicating osteoconductivity of these scaffolds. This route of making bioactive bone tissue engineering scaffolds is being explored, with several manufacture techniques being currently investigated actively.

Biomimetic apatite formation on biodegradable polymer scaffolds provides an alternative route. In the classical biomimetic process to form an apatite layer on metal or ceramic surfaces, normal-strength SBF is commonly used and it usually takes 1-4 weeks to form the apatite layer. However, as scaffolding materials such as PLLA are easily hydrolyzed in water, a much shorter coating time must be used in the biomimetic deposition process in order to avoid hydrolysis of the biodegradable polymer scaffolds. Therefore, an accelerated biomimetic process which employed higher-strength SBF (5 times stronger: 5SBF) was used for PGA fiber meshes and PLLA scaffolds [38]. Apatite formed on their surfaces within 24 hours (Fig.7). Moreover, complex structures such as apatite/collagen coatings could be built up on pore surfaces of tissue engineering scaffolds using biomimetic processes [39] and such coatings enhance adhesion of seeded cells on the scaffolds (Fig.8) [40]. The biomimetically formed apatite layer also reinforced the scaffold structure [38].

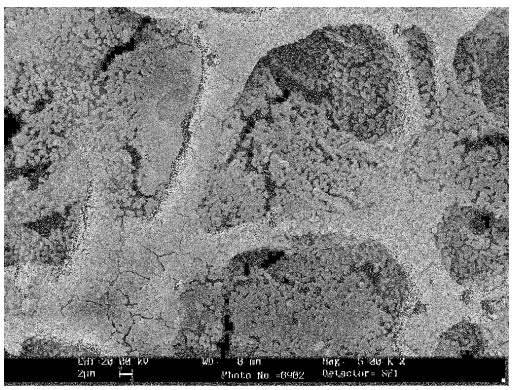

Fig. 7 Bone-like apatite formed on pore surfaces of a PLLA scaffold through an accelerated biomimetic process

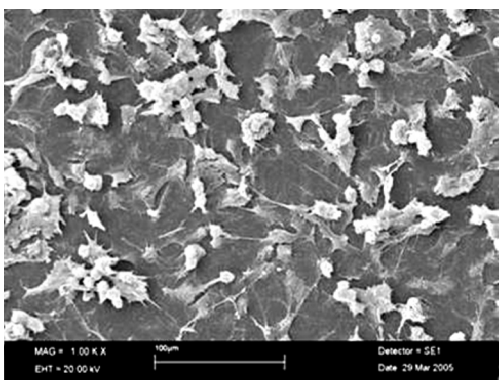

Fig. 8 Osteoblast-like cells attaching to the biomimetic apatite/collagen composite coating

F. Ibrahim, N.A. Abu Osman, J. Usman and N.A. Kadri (Eds.): Biomed 06, IFMBE Proceedings 15, pp. 22-27, 2007
www.springerlink.com ' Springer-Verlag Berlin Heidelberg 2007

III. Conclusions

For existing bioinert implant materials, there are several surface modification techniques that can be used to deposit an apatite or bioactive bioceramic layer on their surfaces in order to make them osteoconductive. The selection of a particular surface modification technique for such a purpose depends on a number of factors. The biomimetic deposition route appears to be increasingly used in biomaterials development. The biomimetic deposition of apatite on polymeric tissue engineering scaffolds provides a simple means to render the scaffolds osteoconductive. The biomimetic processes can also be used to add or enhance other functions of tissue engineering scaffolds.

Acknowledgment

The author thanks his research staff and students for conducting the experimental work and also thanks his collaborators for support. Financial support for his research from various funding agencies (MOE in Singapore, RGC in Hong Kong, etc.), universities and industrial sponsors is gratefully acknowledged.

References

[1] J.Black, G.Hastings, (Eds.), *Handbook of Biomaterial Properties*, Chapman & Hall, London, 1998

[2] B.D.Ratner, A.S.Hoffman, F.J.Schoen, J.E.Lemons, (Eds.), *Biomaterials Science: An introduction to materials in medicine*, 2nd Edn., Academic Press, San Diego, 2004

[3] L.L.Hench, J.Wilson, (Eds.), *An Introduction to Bioceramics*, World Scientific, Singapore, 1993

[4] L.L.Hench, "Bioceramics: from Concept to Clinic", *Journal of the American Ceramic Society*, **74** (1991), 1487-1510

[5] T.Kokubo, "Bioactivity of Glasses and Glass-Ceramics", in *Bone-Bonding Biomaterials*, Edited by P.Ducheyne, T.Kokubo and C.A.van Blitterswijk, Reed Healthcare Communications, Leiderdorp, 1992

[6] R.Skalak, C.F.Fox, (Eds.), *Tissue Engineering*, Alan R.Liss Inc., New York, 1988

[7] L.V.McIntire, (Ed.), *WTEC Panel on Tissue Engineering Research: Final Report*, Academic Press, San Diego, 2003

[8] R.P.Lanza, R.Langer, J.Vacanti, (Eds.), *Principles of Tissue Engineering*, 2nd Edn., Academic Press, San Diego, 2000

[9] A.Atala, R.P.Lanza, (Eds.), *Methods of Tissue Engineering*, Academic Press, San Diego, 2002

[10] R.R.Kumar, M.Wang, "Hydrothermal-Electrochemical Deposition of Hydroxyapatite on Brushite Single Crystals Grown by the Gel Technique", *Proceedings of the 4th Asian Symposium on Biomedical Materials*, Singapore, 1999, 31-32

[11] R.R.Kumar, M.Wang, "Growth of Single Crystals of Brushite by Gel Technique and Subsequent Biomimetic Deposition of Hydroxyapatite on Brushite Crystals", *Transactions of the 6th World Biomaterials Congress*, Hawaii, USA, 2000, 1310

[12] R.R.Kumar, M.Wang, "Biomimetic Deposition of Hydroxyapatite on Brushite Single Crystals Grown by the Gel Technique", *Materials Letters*, **49** (2001), 15-19

[13] T.Kokubo, H.Kushitani, S.Sakka, T.Kitsugi, T.Yamamuro, "Solutions Able to Reproduce *in vivo* Surface-structure Changes in Bioactive Glass-Ceramic A-W", *Journal of Biomedical Materials Research*, Vol.24 (1990), 721-734

[14] X.Y.Yang, M.Wang, K.A.Khor, Y.Wang, "Mechanical and Structural Characterisation of Bioactive Coatings", *Bioceramics*, **11** (1998), 227-230

[15] M.Wang, X.Y.Yang, K.A.Khor, Y.Wang, "Preparation and Characterisation of Bioactive Monolayer and Functionally Graded Coatings", *Journal of Materials Science: Materials in Medicine*, **10** (1999), 269-273

[16] X.J.Ye, M.Wang, K.A.Khor, "Influence of Surface Conditions on Adhesion of Hydroxyapatite Coating to Titanium Substrate", *Proceedings of the 8th International Conference on Processing and Fabrication of Advanced Materials*, Singapore, 1999, 291-298

[17] M.Wang, X.J.Ye, K.A.Khor, "Assessing Interfacial Properties of Plasma Sprayed Bioceramic Coating on Metal Substrate Using Indentation Techniques", *Transactions of the 7th World Biomaterials Congress*, Sydney, Australia, 2004, 1789

[18] R.R.Kumar, M.Wang, "Manufacture and Characterisation of Functionally Graded Bioactive Coatings", *Proceedings of the 8th International Conference on Processing and Fabrication of Advanced Materials,* Singapore, 1999, 133-140

[19] R.R.Kumar, M.Wang, "Developing Hydroxyapatite/Glass Functionally Graded Coating for Clinical Applications", *Proceedings of the 10th International Conference on Biomedical Engineering*, Singapore, 2000, 265-266

[20] R.R.Kumar, M.Wang, P.Ducheyne, "Production and Evaluation of Hydroxyapatite/Tricalcium Phosphate Functionally Graded Coating", *Key Engineering Materials*, **192-195** (2001), 231-234

[21] R.R.Kumar, M.Wang, "Functionally Graded Bioactive Coatings of Hydroxyapatite/Titanium Oxide Composite System", *Materials Letters*, **55** (2002), 133-137

[22] R.R.Kumar, M.Wang, "Modulus and Hardness Evaluations of Sintered Bioceramic Powders and Functionally Graded Bioactive Composites by Nano-indentation Technique", *Materials Science and Engineering A: Structural materials: properties, microstructure and processing*, **338** (2002), 230-236

[23] C.X.Wang, Z.Q.Chen, M.Wang, Z.Y.Liu, P.L.Wang, "Ion-Beam-Sputtering/Mixing Deposition of Calcium Phosphate Coatings: I. Effects of Ion Mixing Beams", *Journal of Biomedical Materials Research*, **55** (2001), 587-595

[24] C.X.Wang, Z.Q.Chen, M.Wang, Z.Y.Liu, P.L.Wang, S.X.Zheng, "Functionally Graded Calcium Phosphate Coatings Produced by Ion Beam Sputtering/Mixing Deposition", *Biomaterials*, **22** (2001), 1619-1626

[25] C.X.Wang, Z.Q.Chen, L.M.Guan, M.Wang, Z.Y.Liu, P.L.Wang, "Fabrication and Characterisation of Graded Calcium Phosphate Coatings by Ion Beam Sputtering/Mixing Deposition", *Nuclear Instruments and Methods in Physics Research*, **B 179** (2001), 364-372

[26] C.X.Wang, Z.Q.Chen, M.Wang, "Fabrication and Characterisation of Bioactive Glass Coatings Produced by the Ion Beam Sputter Deposition Technique", *Journal of Materials Science: Materials in Medicine*, **13** (2002), 247-251

[27] J.M.Wu, M.Wang, S.Hayakawa, K.Tsuru, A.Osaka, "Direct Deposition of Rutile Layer on Polymer Substrates to Induce Bioactivity *In Vitro*", *Key Engineering Materials*, **309-311** (2006), 419-422

F. Ibrahim, N.A. Abu Osman, J. Usman and N.A. Kadri (Eds.): Biomed 06, IFMBE Proceedings 15, pp. 22-27, 2007
www.springerlink.com ' Springer-Verlag Berlin Heidelberg 2007

[28] C.X.Wang, M.Wang, "Electrochemical Impedance Study of the Nucleation and Growth of Apatite on Titanium Pretreated with NaOH Solution", *Transactions of the Society For Biomaterials 27th Annual Meeting*, Minnesota, USA, 2001, 101

[29] C.X.Wang, M.Wang, "Mechanism of Apatite Formation on Titanium Treated with Alkaline Solution", *Transactions of the Society For Biomaterials 27th Annual Meeting*, Minnesota, USA, 2001, 317

[30] C.X.Wang, M.Wang, X.Zhou, "Electrochemical Impedance Spectroscopy Study of the Nucleation and Growth of Apatite on Chemically Treated Titanium", *Langmuir*, **18** (2002), 7641-7647

[31] C.X.Wang, X.Zhou, M.Wang, "Mechanism of Apatite Formation on Pure Titanium Treated with Alkaline Solution", *Bio-Medical Materials and Engineering*, **14** (2004), 5-11

[32] J.M.Wu, M.Wang, S.Hayakawa, K.Tsuru, A.Osaka, "*In Vitro* Bioactivity of Hydrogen Peroxide Modified Titanium: Effects of Surface Morphology and Film Thickness", *Key Engineering Materials*, **309-311** (2006), 407-410

[33] J.M.Wu, M.Wang, Y.W.Li, F.D.Zhao, X.J.Ding, A.Osaka, "Crystallization of Amorphous Titania Gel by Hot Water Aging and Induction of *In Vitro* Apatite Formation by Crystallized Titania", *Surface & Coatings Technology*, in press

[34] J.M.Wu, F.Zhao, Y.Li, S.Zhang, M.Wang, A.Osaka, "Influence of Film Thickness on *In Vitro* Bioactivity of Thin Anatase Films Produced through Direct Deposition from an Aqueous Titanium Tetrafluoride Solution", *Surface and Coatings Technology*, in press

[35] J.Weng, M.Wang, J.Chen, "Plasma Sprayed Calcium Phosphate Particles with High Bioactivity and their Use in Bioactive Scaffolds", *Biomaterials*, **23** (2002), 2623-2629

[36] N.Sultana, M.Wang, "Fabrication and Characterisation of Polymer and Composite Scaffolds Based on Polyhydroxybutyrate and Polyhydroxybutyrate-co-hydroxyvalerate", *Key Engineering Materials*, in press

[37] W.Y.Zhou, S.H.Lee, W.L.Cheung, M.Wang, W.Y.Ip, "Selective Laser Sintering of Porous Scaffolds from Poly(L-Lactide) Microspheres and its Nanocomposite with Carbonated Hydroxyapatite Nanospheres", *20th European Conference on Biomaterials (ESB2006)*, Nantes, France, 2006, accepted

[38] Y.Chen, A.F.T.Mak, J.Li, M.Wang, A.W.T.Shum, "Formation of Apatite on Poly(α-hydroxy acid) in an Accelerated Biomimetic Process", *Journal of Biomedical Materials Research Part B: Applied Biomaterials*, **73B** (2005), 68-76

[39] Y.Chen, A.F.T.Mak, M.Wang, J.Li, "Composite Coating of Bone-like Apatite Particles and Collagen Fibers on Poly L-lactic Acid Formed through an Accelerated Biomimetic Coprecipitation Process", *Journal of Biomedical Materials Research Part B: Applied Biomaterials*, **77B** (2006), 315-322

[40] Y.Chen, A.F.T.Mak, M.Wang, J.Li, M.S.Wong, "PLLA Scaffolds with Biomimetic Apatite Coating and Biomimetic Apatite/Collagen Composite Coating to Enhance Osteoblast-like Cells Attachment and Activity", *Surface and Coatings Technology*, **201** (2006), 575-580

Address of the corresponding author:

Author: Min Wang
Institute: Department of Mechanical Engineering, The University of Hong Kong
Street: Pokfulam Road
Country: Hong Kong
Email: memwang@hku.hk

F. Ibrahim, N.A. Abu Osman, J. Usman and N.A. Kadri (Eds.): Biomed 06, IFMBE Proceedings 15, pp. 22-27, 2007
www.springerlink.com ' Springer-Verlag Berlin Heidelberg 2007

Warping a Neuro-Anatomy Atlas on 3D MRI Data with Radial Basis Functions

H.E. Bennink, J.M. Korbeeck, B.J. Janssen, B.M. ter Haar Romeny

Eindhoven University of Technology - Department of Biomedical Engineering, Group Biomedical Image Analysis
Eindhoven, the Netherlands

Abstract— **Navigation for neurosurgical procedures must be highly accurate. Often small structures are hardly seen on pre-operative scans. Fitting a 3D electronic neuro-anatomical atlas on the data assists with the localization of small structures and dim outlines. During surgery also brainshifts occurs. With intra-operative MRI the pre-operative MRI can be warped to the real 3D situation. The paper describes a general 3D landmark-based warping method, based on radial basis functions (thin plate splines) for data of any number of dimensions, including all code in *Mathematica*.**

Keywords— **Brain atlas, image warping, radial basis functions, neurosurgery, computer vision**

I. Introduction

Neurosurgical operations require very precise navigation. Not only during resection surgery of brain tumors, also for deep brain stimulation (DBS), i.e. the placement of electrodes for the electrical stimulation of some specific deep-brain structures. In particular, the placement of electrodes for stimulation of the Nucleus Subthalamicus (STN) in the deep brain may enable Parkinson patients to reduce their spontaneous tremor, which is often invalidating them.

Today, with Magnetic Resonance Imaging and Computed Tomography scanners it is possible to image the patient in three dimensions at high resolution, typically 0.5-1 mm in each direction.

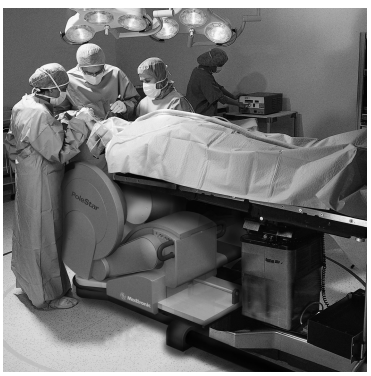

Fig. 1 Open MRI scanner on the neurosurgical theatre enables imaging during surgery (Medtronic - Odin N20, 0.15 Tesla, Maastricht University Hospital, the Netherlands).

However, two major problems exist:

- it is often difficult to find the many individual brain nuclei on these scans due to the low contrast and the noise. The mapping of an electronic brain atlas on the scans substantially helps the navigation (Fig. 2) [3]. The atlas is based on a mean patient, and will not fit the data. So a 3D warping method is necessary.

- When the skull is opened, brain shift occurs due to pressure changes and loss of liquids. The pre-operative data do no longer correspond to the real situation, making precise navigation, e.g. with avoidance of bloodvessels, difficult. Recently, an open mobile low-field MRI scanner (Fig. 1) has been installed in the Maastricht University Hospital (the first in the Netherlands), to image the patient after the trepanation. Due to the lower image quality of the intra-operative scans, registration and warping of the pre-operative scans is necessary.

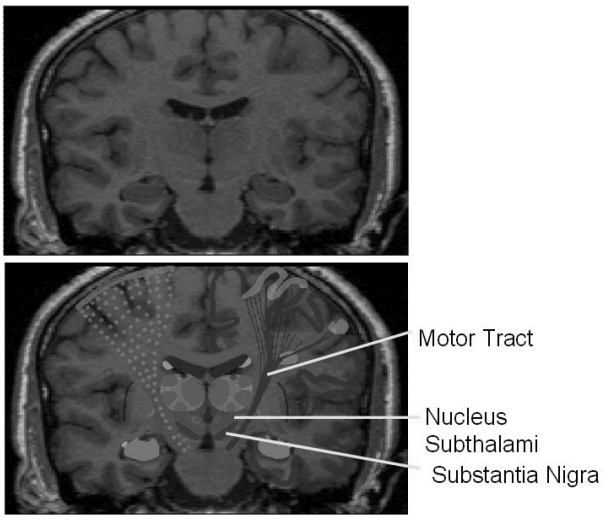

Fig. 2 Electronic brain atlas mapping on Magnetic Resonance slices.

Fully automatic registration and 3D warping on the gray-scale images is difficult, if not impossible. In this paper we describe a warping based on registration of manually selected anatomical landmarks in 3D. Neurosurgeons are very familiar with such landmarks, and good descriptions [6][7] and neuro-anatomical atlases [8] exist. The 3D deformation

F. Ibrahim, N.A. Abu Osman, J. Usman and N.A. Kadri (Eds.): Biomed 06, IFMBE Proceedings 15, pp. 28-32, 2007
www.springerlink.com ' Springer-Verlag Berlin Heidelberg 2007

field is constructed by means of an interpolation based on thin plate splines [1],[2], a special form of the radial basis functions. In Mathematica [16] the code is very short, readable and efficient.

II. Thin plate splines

In order to warp a brain atlas onto an MRI scan of the brain we identify so called landmarks of which the correspondence between the atlas and the scan is known. Because of this correspondence we can find the vector field that can be used for the warping procedure. The vector field is found by interpolating the know vectors at the location of the landmarks. Hence we first introduce interpolation of arbitrarily spaced points in multiple dimensions.

Imagine a thin metal plate of infinite extent that is fixed at certain points $\vec{x}_i = \{x_i, y_i\}$ at the heights $f_i, i \in \mathrm{I}$ (and neglect gravity). The metal plate has a shape such that its surface is minimally bent. The bending energy of such a plate $s(x, y)$ equals

$$E_{bend}(s) = \int_{\Re^2} \frac{\partial^2 s(x,y)}{\partial x^2} + 2\frac{\partial^2 s(x,y)}{\partial x \partial y} + \frac{\partial^2 s(x,y)}{\partial y^2} dxdy$$

This is an instance of a semi-norm proposed by Jean Duchon. In order to find the shape of a plate that is fixed at the points mentioned above we will have to find the minimizer of this equation such that the constraints, $s(\vec{x}_i) = f_i, \forall i \in \mathrm{I}$ are met. The shape can be approximated by finding that *s* that minimizes

$$E(s) = \sum_{i \in \mathrm{I}} | s(\vec{x}_i) - f_i |^2 + \lambda E_{bend}(s)$$

The first part of this convex energy functional makes sure the constraints are met and the second part smooths the result. $\lambda \in \Re$ is a parameter that controlls the quality (deviation from the constraints) of the approximation. A smaller value of λ results in a better approximation, ultimately achieving interpolation when λ tends to 0. Duchon was one of the first who recognised that the solution of the variational problem can be written in the form

$$s(\vec{x}) = \sum_{i \in \mathrm{I}} w_i \varphi(\| \vec{x} - \vec{x}_i \|) + p(\vec{x}) \qquad (1)$$

Here $\varphi(r)_{k=2} = \begin{cases} r^{2k-d} \log(r) & if\ 2k-d\ even \\ r^{2k-d} & if\ 2k-d\ odd \end{cases}$

is a so called radial basis function. We neglect *k*, which is a setting for the order of the norm that will be minimized $(k = 2)$. *d* sets the number of dimensions, for our fiducial metal plate $d = 2$. $p(\vec{x})$ is a polynomial that lies in the null space of the differential operator that appears in the bending energy. In our example it thus takes the form $p(x) = a_1 + a_2 x + a_3 y$. In order to find the interpolating (or approximating) function of the form of equation (3) we can simply solve a linear system of equations. We are searching for the solution of

$$\begin{pmatrix} B + \lambda I & Q \\ Q^T & O \end{pmatrix} \begin{pmatrix} \vec{w} \\ \vec{a} \end{pmatrix} = \begin{pmatrix} \vec{f} \\ \vec{0} \end{pmatrix} \qquad (2)$$

where $\{B\}_{i,j} = \varphi(\| \vec{x}_i - \vec{x}_j \|)$, $\{Q\}_{i,j} = \{1, x_i, y\}$, I is the identity matrix and $O = \begin{pmatrix} 0 & 0 & 0 \\ 0 & 0 & 0 \\ 0 & 0 & 0 \end{pmatrix}$. Those $\vec{w}$ and $\vec{a}$ that solve the linear system of equation (2) can be plugged into equation (1) in order to find the expression for the shape we are looking for.

III. The landmarks

Well-known neuro-surgical atlases exist, such as by Talairach-Tournoux [11][12]. Recently, a family of electronic atlases has been brought to market, such as the Cerify series of atlases [8] by Nowinski et al. In these atlases landmark coordinates can conveniently be found [6],[7]. In this study we selected 148 well-defined landmarks in coronal, sagittal and transversal slices in the atlas and in 3D in the patient's MRI dataset. Some examples are shown in Fig. 3.

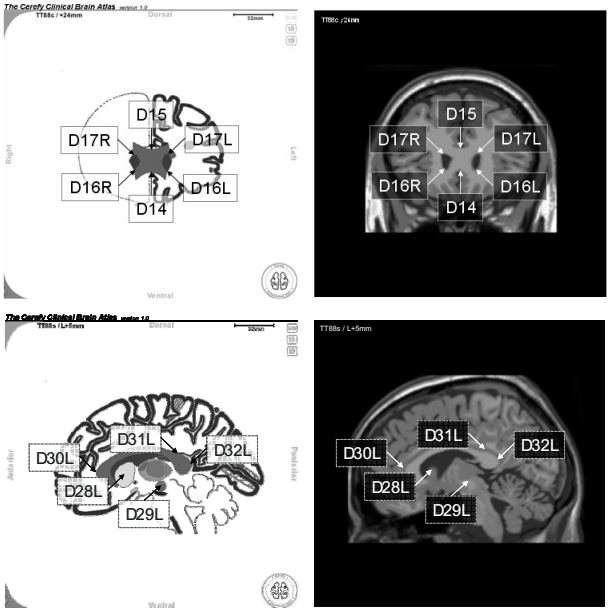

Fig. 3 Examples of landmark points in coronal slice TT88c / +24mm (top) and in sagittal slice TT88s / R-4mm (bottom). In total 148 landmarks were set.

F. Ibrahim, N.A. Abu Osman, J. Usman and N.A. Kadri (Eds.): Biomed 06, IFMBE Proceedings 15, pp. 28-32, 2007
www.springerlink.com © Springer-Verlag Berlin Heidelberg 2007

IV. Implementation

We implemented the method that is outlined above (for a 2D image/metal plate) for N dimensions in *Mathematica* [16] (code: see Appendix). The module takes input similar to the built-in Interpolation function and returns a compiled function.

There is a great advantage to design this method in the high level software system *Mathematica*. The code is amazingly compact, and can be easily transferred and made public.

A 2D EXAMPLE

The *Mathematica* code for the radial basis function interpolation is given in the Appendix. Below, the example code (Fig. 4) shows the local warping on a 2D image by randomly moving a small set of 7 randomly chosen landmark points. The radial basis function is a Bessel function in this case (to show the versatility).

```
source = Table[Random[Real, {10, 90}], {7}, {2}];
target = source + Table[Random[Real, {-5, 5}], {7}, {2}];
grid = Table[{x, y}, {x, 1, 100, 2.5}, {y, 1, 100, 2.5}];
Show[Graphics[{Gray, Line /@ grid, Line /@ grid^T, Blue,
    PointSize[0.02], Point /@ source, Red,
    Circle[#1, 2] & /@ target}], AspectRatio → 1,
  Frame → True];

rbn[v_] := If[# == 0, 0.5, BesselJ[1, 1/5 Sqrt[#]] / (1/5 Sqrt[#])] &[v.v];

rbi = RadialBasisInterpolation[{source, target}^T,
  RadialBasisNorm → rbn];
newgrid = Map[rbi @@ #1 &, grid, {2}];
Show[Graphics[{Gray, Line /@ newgrid, Line /@ newgrid^T,
    PointSize[0.02], Blue, Point /@ (rbi @@ #1 &) /@ source,
    Red, (Circle[#, 2] &) /@ target}], AspectRatio → 1,
  Frame → True];
```

Fig. 4 Mathematica code to warp a grid based on 7 random location shifts. The main code, which is suitable for data of any dimensionality, is given in the Appendix.

After the warping the full new image is interpolated towards the new coordinates. The new points are placed exactly at the location of the old points, the environment is smoothly deformed by radial basis interpolation. The deformation of the coordinate grid can be clearly appreciated (Fig. 5).

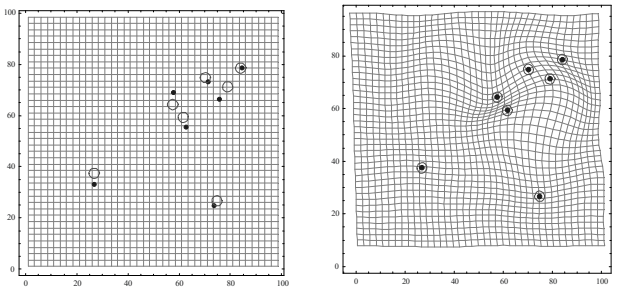

Fig. 5 Radial basis interpolation of a regular grid, based on the random motion of 7 landmarks.

V. Results

In total 148 landmarks were set in both the 3D MRI data and the electronic atlas, in coronal, sagittal and tranversal slices. After 3D warping by thin plate splines, the result was good around the set landmarks, but unsatisfactory in regions far away from the landmarks. New points were added in those regions (typically 3-10) for a second warping iteration. After three iterations the result was satisfactory. Some examples of the warped atlas on the data are shown in Fig. 6.

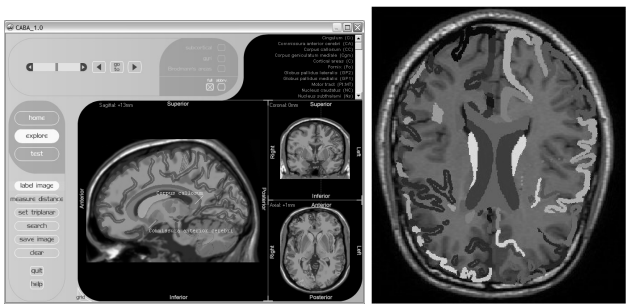

Fig. 6 Left: integration of the warping result in the Cerefy students atlas. Right: one of the transversal slices of the final result.

VI. Conclusions

An elegant and efficient method is described to warp data in any dimensions based on sets of corresponding landmarks. Automated landmark extraction should be rthe next step. Fast implementations of this method are appearing, based on graphics card hardware, and splines interpolation. Code in *Mathematica* [16] is short, easily transferable, educational and applicable to data of any dimension.

F. Ibrahim, N.A. Abu Osman, J. Usman and N.A. Kadri (Eds.): Biomed 06, IFMBE Proceedings 15, pp. 28-32, 2007
www.springerlink.com ' Springer-Verlag Berlin Heidelberg 2007

ACKNOWLEDGEMENT

The authors like to thank the A*Star Bio-Informatics Institute in Singapore for making available the Cerify Student brain atlas, and invaluable help in the landmark allocation. We thank Markus van Almsick for the MathVisionTools library (www.mathvisiontools.net).

REFERENCES

[1] Bookstein, F. (1989) Principal warps: thin-plate splines and the decomposition of deformations. IEEE Trans. Pattern Analysis Machine Intelligence 11(6): 567-585.
[2] Carr J.C., Fright W.R., Beatson R.K. (1997) Surface interpolation with radial basis functions for medical imaging. IEEE transactions on medical imaging, Vol. 16, No. 1.
[3] Free S.L., O Higgins P, Maudgil D.D., Dryden I.L., (2001) Landmark-Based morphometrics of the normal adult brain using MRI. NeuroImage 13 801-813.
[4] Grachev I.D., Berdichevsky D., Rauch S.L. (1999) A method for assessing the accuracy of intersubject registration of the human brain using anatomic landmarks. NeuroImage 9, 250-268.
[5] Levin D., Dey D., Slomka P.J. (2004) Acceleration of 3D, nonlinear warping using standard video graphics hardware: implementation and initial validation. Computerized Medical Imaging and Graphics 28: 471-483.
[6] Nowinski W.L., Thirunavuukarasuu A. (2001) Atlas-assisted localization analysis of functional images. Medical Image Analysis 5, 207-220.
[7] Nowinski W.L., (2001) Technical Report: Modified Talairach Landmarks. Acta Neurochir 143: 1045- 1057 Wien.
[8] Nowinski W.L., Belov D. (2003) The Cerefy Neuroradiology Atlas: a Talairach-Tournoux atlas-based tool for analysis of neuroimages available over the internet. NeuroImage 20, 50-57.
[9] Rizzo G., Scifo P., Gilardi M.C. (1997) Matching a computerized brain atlas to multimodal medical images, NeuroImage 6, 59-69.
[10] Talairach J., Tournoux P. (1988) Co-planar stereotactic atlas of the human brain. Georg Thiem Verlag/Thieme Medical Publishers, Stuttgart New York.
[11] Talairach J., Tournoux P. (1993) Referentially oriented cerebral MRI anatomy. Atlas of stereotaxic anatomical correlations for gray and white matter. GeorgThieme Verlag/Thieme Medical Publishers, Stuttgart New York.
[12] Verard L., Allain P., Travere J.M. (1997) Fully automatic identification of AC and PC landmarks on brain MRI using scene analysis. IEEE transactions on medical imaging, Vol. 16, No. 5.
[13] M.Arigovindan,M.Sühling,P.Hunziker,and M.Unser. Variational image reconstruction from arbitrarily spaced samples:A fast multiresolution spline solution. IEEE-TIP,14(4):450-460,April 2005.
[14] J. Duchon, in Constructive theory of functions of several variables,W. Schempp and K. Zeller, editors. Splines minimizing rotation-invariant semi-norms in Sobolev spaces. Springer Verlag, 1976.
[15] J. Kybic, T. Blu, and M. Unser. Generalized sampling: a variational approach, part I: Theory. IEEE Transactions on Signal Processing, 50:1965, 1976, August 2002.
[16] *Mathematica* 5.2, URL: www.wolfram.com.

APPENDIX: *MATHEMATICA* CODE

RadialBasisInterpolation[{x_1,y_1},{x_2,y_2}, ,{x_n,y_n}]] constructs a compiled approximate function that interpolates the *y*-value at any given *x*-value. x_i and y_i can be tensors in any number of dimensions. The interpolation function is a function of the form: $y(x) = ax + \sum_{i=1}^{n} w_i \varphi(x - x_i)$. Here a is the linear part of the interpolation function, w_i is the weight of basis x_i and φ is a function that calculates the vector norm of the vector $(x - x_i)$. The implemented radial basis norm functions φ are:

ThinPlateSplineNorm[p] (Fig. 7) with $p = 2k - d$ and GaussianNorm[σ]. Thin plate splines are fundamental solutions of $\Delta^k \varphi = 0$. In d dimensions these solutions are given by $\varphi^{(d)}(r) = r^{2k-d} \log r$ for $k \geq d$ and d even and $\varphi^{(d)}(r) = r^{2k-d}$ for $k \geq d$ and d odd.

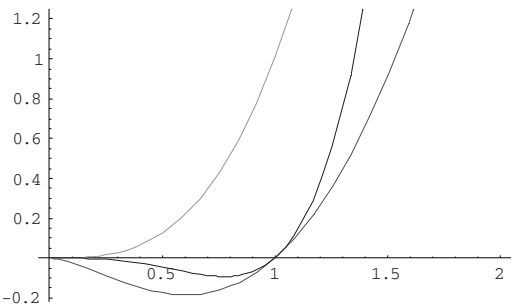

Fig. 7 **ThinPlateSplineNorm[p]** functions for p = 2 (red), p = 3 (green) and p = 4 (blue).

The Gaussian norm function is implemented as a compiled function calculating a Gaussian weighted vector norm $\varphi(r) = e^{-\frac{r^2}{2\sigma^2}}$.

Mathematica code:

```
Options[RadialBasisInterpolation] =
  {RadialBasisNorm → Automatic, Smoothness → 0.};
ThinPlateSplineNorm[1] =
  Compile[{{#1, _Real, 1}}, √#1.#1];
ThinPlateSplineNorm[2] =
 Compile[{{#1, _Real, 1}},
  (If[#1 > 0., #1 Log[√#1], 0.] &)[#1.#1]];
ThinPlateSplineNorm[p_?OddQ] =
 Compile[{{#1, _Real, 1}}, (#1.#1)^(p/2), {{p, _Integer}}];
ThinPlateSplineNorm[p_?EvenQ] =
 Compile[{{#1, _Real, 1}},
  (If[#1 > 0., #1^(p/2) Log[√#1], 0.] &)[#1.#1],
  {{p, _Integer}}];
GaussianNorm[σ_] = Compile[{{#1, _Real, 1}},
   (If[#1 > 0., e^(-#1/(2 σ^2)), 1.] &)[#1.#1], {{σ, _Real}}];
RadialBasisInterpolation[data_List, opts___?OptionQ] :=
 Module[{points, values, n, pointDim, valueDims,
   valueRank, ϕ, B, Q, O, A, λ, x, w, a, slots},
  {ϕ, λ} = {RadialBasisNorm, Smoothness} /. {opts} /.
    Options[RadialBasisInterpolation];
  {points, values} = N[Transpose[data]];
  If[Depth[points] == 2, points = List /@ points];
  {n, pointDim} = Dimensions[points];
  valueDims = Rest[Dimensions[values]];
  valueRank = Length[valueDims];
  If[ϕ === Automatic,
   ϕ = ThinPlateSplineNorm[Max[2, pointDim]]];
  O = Table[0., {pointDim + 1}, {pointDim + 1}];
  B = Outer[ϕ[#1 - #2] &, points, points, 1];
  Q = (Prepend[#1, 1] &) /@ points;
  A = MapThread[Join,
    MapThread[Join, ((B - λ IdentityMatrix[n]  Q
                      Q^T                      O))]];
  b = PadRight[Transpose[values,
     RotateRight[Range[valueRank + 1]]],
    Append[valueDims, n + pointDim + 1], 0];
  x = Map[LinearSolve[A, #1] &, b, {valueRank}];
  w = Map[Take[#1, n] &, x, {valueRank}];
  a = Map[Take[#1, -(pointDim + 1)] &, x, {valueRank}];
  slots = Array[Slot, {pointDim}];
  (Compile[#1, #3.#4 /@ Transpose[#5 - #6] + #2,
      {{#4[_], _Real, 0}}] &)[({#1, _Real} &) /@ slots,
   a.Prepend[slots, 1], w, ϕ, slots, Transpose[points]]]
```

Address of the corresponding author:

Author: Bart M. ter Haar Romeny
Institute: Eindhoven University of Technology
Street: Den Dolech 2 WH2.108
City: NL-5600 MB Eindhoven
Country: the Netherlands
Email: B.M.terHaarRomeny@tue.nl

F. Ibrahim, N.A. Abu Osman, J. Usman and N.A. Kadri (Eds.): Biomed 06, IFMBE Proceedings 15, pp. 28-32, 2007
www.springerlink.com ' Springer-Verlag Berlin Heidelberg 2007

Ex vivo magnetic resonance spectroscopy method for the diagnosis of human stomach cancer

ChiWoong Mun

Dept. of Biomedical Engineering, Inje University, Gimhae, Gyongnam, South Korea

Abstract— **This study was performed to evaluate the characteristics of the spectral peak intensities and T2-relaxation times of the biochemical metabolites related to cancerous gastric tissue using ex vivo proton MR spectroscopy (^{1}H MRS) method, and to assess its clinical usefulness. The volume of interest data results from MRS measurement was extracted from proper muscle (MUS) layer and the composite mucosa/submucosa (MC/SMC) layer and their spectral peak intensities and T2-value were quantitatively analyzed. In this study, we present that both of spectral peak analysis and T2-relaxation time measurement using MRS method may be very useful for the diagnosis of the gastric cancer.**

Keywords—**Magnetic resonance spectroscopy (MRS), Chemical shift imaging (CSI), Gastric cancer, Spectral peak intensity, T_2-relaxation time**

I. Introduction

Gastric cancer is one of the most common malignant tumors in Asian countries. And its prevalence rate and mortality rate in this region are higher than those of western countries [1,2]. This is very suggestive that early detection and treatment of gastric carcinoma is very important [3]. Accurate preoperative staging and local resectability of gastric carcinoma are important to ensure proper treatment and prognosis [1,3]. Various methods were used to diagnosis the stomach disease. However, a limitation of these techniques is that layers of the gastric wall cannot be clearly depicted, and therefore, the degree of the serosal infiltration, which is one of the most important factors in the staging of gastric carcinoma, cannot be reliably evaluated. MR imaging techniques has recently been used to diagnose the gastric carcinoma [4-6], and so far his method has not achieved clinical importance. To further investigate the potential of MR investigation for the staging of gastric carcinoma, basic experimental studies such as MR spectroscopy are needed to define normal and pathological MR morphology of the gastric wall [7-8].

There are two main hurdles for studying or diagnosing the gastric disease using MR apparatus. One is the inherent artifact due to peristaltic motion of stomach wall, pulsations and respiration, and the other is that the thickness of the gastric tissue layer is too thin to examine the extent of the invasion of the carcinoma cells into each layer. These are the reason why the number of studies on MR imaging of gastric carcinoma [4-6] is still small even though stomach cancer is one of the most common malignant tumors in Asian country. It is well known that proton (^{1}H) magnetic resonance spectroscopy provides clinical importance that allows non-invasive access to metabolic information about human body organs [9-10].

In this study, we attempted to (a) ascertain MRS peak characteristics of the stomach layers, (b) distinguish MRS peaks between normal and abnormal gastric specimens, and (c) study the effects of formalin fixation on the signal intensities of the MR spectroscopy peaks. This study demonstrates the feasibility of in vitro ^{1}H MR spectroscopy technique to diagnose gastric carcinoma and to categorize the spectrum according to histological type.

II. Materials and methods

Thirty-two stomach tissue specimens, resected during gastric cancer surgery at Pusan Paik Hospital Inje University and Gospel Hospital Kosin Colleg, were obtained from twelve patients between March and September 2005. These patients consisted of ten male and two female aged for 49 to 75 years old (mean 62). Nineteen were diagnosed as cancerous tissue, while the others were noncancerous specimens as confirmed by histopathological examination. These specimens were put in a refrigerator immediately after the gastrectomy and the MR data was obtained in 24 hours to prevent metabolic changes in the specimens.

High-resolution NMR spectroscopic experiments were performed at 400 MHz for ^{1}H on a Bruker DSX 400 spectrometer system (Bruker Analytische GmbH, German) equipped with a ^{1}H probe able to provide a magnetic field gradient. Ex vivo ^{1}H NMR spectra were obtained from four gastric tissue specimens, two of them from cancerous tissue with ulceration and the others from normal tissues. All tissue samples from selected layers of the gastric specimens, i.e., the mucosa/sub-mucosa (MC/SMC) and muscle (MUS), were cut to the size of 4×10 mm^2 for NMR spectroscopy. And the T2-relaxation time in ^{1}H NMR experiments was obtained by spin echo sequence and measured at thirteen spectra of different echo times from 10 μs to 200 *ms*.

F. Ibrahim, N.A. Abu Osman, J. Usman and N.A. Kadri (Eds.): Biomed 06, IFMBE Proceedings 15, pp. 33-36, 2007
www.springerlink.com ' Springer-Verlag Berlin Heidelberg 2007

Magnetic resonance scans were performed with a 64-MHz (1.5-T) MRI system (Echo Speed, General Electronics Co., Milwaukee, WI, USA) at the Pusan Paik Hospital using the custom-made volume coil [8]. Subjects were 19 cancerous- and 13 normal-gastric tissues. And each specimens were dissected into the sections measuring 25×50 mm^2 and placed in polyethylene tubes (inner diameter, 30 mm) filled with normal saline solution within four hours after they were resected at surgery. Spin echo T_1 weighted images (repetition time: TR = 300 msec and echo time: TE = 15 msec) in the oblique plane were obtained using 70 mm field of view (FOV), matrix size of 256×256, slice thickness of 3 mm, slice gap of 0.1 mm, and number of excitations (NEX) of 4. These images were used mainly for localizer images of CSI. The CSI data were obtained by CSI point-resolved spectroscopy (CSI-PRESS) sequence, repetition time (TR) = 1500 msec, matrix size = 24×24, NA = 1, and voxel size of 2.2×2.2×4 mm^3. Two sequential measurement using echo times (TE) of 35 and 144 msec were performed in order to calculate the T2-relaxation time in each voxel. ROI was placed to cover the both MC/SMC and MUS layers of the specimens. Auto-gradient shimming was performed before all data acquisitions. All calculations were performed on a Pentium IV PC (3 GHz and 2 Gbytes RAM), running Windows XP using a Visual C++6.0 (Microsoft, U.S.A.) and Matlab (MathWorks, Massachusetts, U.S.A.) based custom designed software and commercial SPSS software package (version 11.0, ISP Inc., Chicago, IL, USA).

The T2-relaxation times were measured from spectral peaks of each metabolite using CSI processing software developed by the author. The measurements of T2-relaxation time in selected two layers of the gastric tissue were performed in three metabolite peaks such as Lipid, NANA and Cho. The selected two layers were the muscle (MUS) layer and the composite of mucosa/submucosa (MC/SMC) layer because the thickness of MC and SMC layer (less than 2 mm) is usually thinner than the voxel size.

After analysis of MR data, all specimens were fixed in 4% para-formaldehyde at 4˚C for 24 hours and embedded in paraffin for histological examination. The sections 4 to 6 ㎛ in thickness in the same direction as the MR imaging, were then prepared. The sections were deparaffinzed in xylene, rehydrated through graded ethanol and stained with hematoxylin-eosin (H-E) for microscopic examination using an inverted microscope. Histopathological sections were selected for comparison and for determination of cancer invasion. The cancer invasion into each layer of the human gastric tissue was diagnosed by a pathologist, blinded to the findings of the MR study.

III. Results

Both 9.4-T NMR and 1.5-T single voxel MRI spectra of non-cancerous and cancerous gastric tissue were obtained and shown in Figure 1. Two upper spectra were measured from the 9.4-T NMR system, and the two lower spectra were obtained using the 1.5-T clinical MRI/S system. Fig. 1(a) and 1(c) are representative spectra from the MUS layer of normal gastric tissue, while Fig. 1(b) and (d) are representative spectra from the MUS layer of cancerous gastric tissue. With the exception of the choline peak at 3.2 ppm, the intensities of all metabolite peaks were decreased in the cancerous gastric tissue. In comparison with the 9.4-T NMR spectra, the resonance peaks of the 1.5-T MR spectra were broad and featureless.

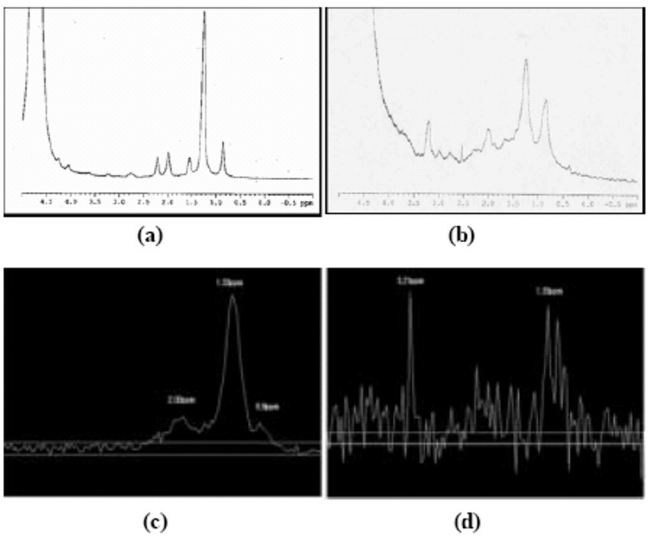

Fig. 1. Spectra of (a) normal gastric tissue in 9.4-T NMR, (b) cancerous gastric tissue in 9.4-T NMR, (c) noncancerous gastric tissue in 1.5-T MRS, and (d) cancerous gastric tissue in 1.5-T MRS.

The histopathological analysis of the H-E stained sections of 12 patients with human gastric carcinoma indicated that 11 specimens were tubular adenocarcinomas. The twelfth sample was a signet ring cell carcinoma mixed with tubular and papillary adenocarcinoma. These histological examination results were used as references to categorize MR spectroscopy data according to the infiltration of the tumor cells into gastric tissue.

Using the 9.4-T (400-MHz) NMR instrument, ex vivo ^1H high-resolution NMR spectra were obtained from two gastric tissue layers (MC/SMC and MUS). Prominent resonance peaks were found at the approximate peak positions of 0.87 ppm (lipid: $-CH_3$), 1.26 ppm (lipid: $-CH_2$), 1.54 ppm (alanine: $-\beta-CH_3$), 2.0 ppm (NANA or sialic acid, $-CH_3$) and

F. Ibrahim, N.A. Abu Osman, J. Usman and N.A. Kadri (Eds.): Biomed 06, IFMBE Proceedings 15, pp. 33-36, 2007
www.springerlink.com ' Springer-Verlag Berlin Heidelberg 2007

2.2 ppm (glutathione) in both non-cancerous layers. In the measurements of cancerous gastric tissue, similar resonance peaks 9 were found at 0.87 ppm (lipid: -CH_3), 1.25 ppm (lactate or lipid: -CH_2), 2.0 ppm (NANA), 2.54 ppm (Citrate: -CH_2), and 3.2 ppm (choline) in both the MC/SMC and MUS. The choline peak was not clearly shown in the spectra of normal specimens but was prominent in the cancerous specimens. Though the other spectral peak intensities in the cancerous specimens were clearly decreased, the choline peak intensity increased slightly. The results of these peak measurements are summarized in Table 1.

Table 1 Metabolite peak intensities of ex vivo 400-MHz NMR spectra of gastric tissue

Metabolite	MC/SMC (arbitrary unit)		Tumor	MUS (arbitrary unit)		Tumor
(ppm)	normal	abnormal	remark	normal	abnormal	remark*
0.87	2.2×10^6	7×10^5	↓	1.3×10^6	5.7×10^5	↓
1.25	9.1×10^6	1.1×10^6	↓	4.2×10^6	1.0×10^6	↓
1.54	1.4×10^6	-	-	7.3×10^5	-	-
2.0	1.8×10^6	5.9×10^5	↓	9.7×10^5	5.0×10^5	↓
2.2	1.6×10^6	-	-	7.8×10^5	-	-
2.54	-	8.1×10^5	-	-	3.8×10^5	-
3.2	6.2×10^5	7.2×10^5	↑	5.0×10^5	5.6×10^5	↑

* ↑ indicates the increase of metabolite peak intensity and ↓ represents the decrease of the metabolite peak intensity.

T2-relaxation times in non-cancerous specimens were measured at each metabolite peak of lipids (-CH_3 and CH_2), alanine (-β-CH_3), NANA and glutathione. The T2 values of the choline peak (3.2 ppm) in the MC/SMC layers and the lipid peak (1.25ppm) in the MUS layer were the longest. The T2 values of the alanine (1.54 ppm) from the MC/SMC layers and NANA (2.0 ppm) from the MUS layer were short.

T2-relaxation times in cancerous specimens were measured at each metabolite peaks of lipids (-CH_3 and -CH_2), NANA, Citrate (-CH_2) and Choline. The T2-relaxation times of the choline and lipid peak at 1.25 ppm and 3.2 ppm, respectively, were clearly decreased with respect to normal tissue. In summary, the T2-relaxation times of all resonance peaks of cancerous specimens became shorter than the non-cancerous ones. (Table 2)

Table 2 T2-relaxation time of ex vivo ^{1}H high-resolution NMR spectra

Metabolite	MC/SMC (ms)		Tumor	MUS (ms)		Tumor
(ppm)	Normal	Abnormal	remark	Normal	Abnormal	remark*
0.87	20.66	8.55	↓	19.05	13.48	↓
1.25	28.57	15.65	↓	34.36	16.03	↓
1.54	14.71	-	-	20.00	-	-
2.00	15.9	11.67	↓	13.62	11.01	↓
2.2	16.72	-	-	15.67	-	-
2.54	-	14.07	-	-	10.36	-
3.2	37.45	14.37	↓	27.55	19.38	↓

* ↑ indicates the increase of metabolite peak intensity and ↓ represents the decrease of the metabolite peak intensity.

In 64-MHz (1.5-T) ^{1}H -MR spectroscopy, the prominent resonance peaks in non-cancerous gastric specimens were found at 0.90 ppm (-CH_3 of lipid methyl), 1.33 ppm (-CH_2 of lipid methylene), and 2.02 ppm (N-CH_3 of NANA, sialic acid) (Fig. 1(c)). In comparison with the 9.4-T NMR spectra, the observed resonance peaks of the 64-MHz MR spectra were broad and featureless. The statistical peak positions of the non-cancerous gastric tissue, average (number of peak /number of total measurements)–SD, were 0.90 ppm–0.037 ppm (12/13), 1.31–0.038 ppm (11/13), and 2.04 –0.039 ppm (10/13), respectively. The observed resonance peaks did not show statistically significant spectral differences between the MC/SMC and MUS layers.

Two strong resonance peaks in cancerous gastric specimens were observed at 1.30 ppm and 3.19 ppm (Fig. 1(d)). The statistical peak positions of cancerous gastric tissue, average–SD, were as follows; 1.30–0.068 ppm (17/19), and 3.19–0.043 ppm (15/19). Due to the poor signal-to-noise ratio (SNR), resonance peaks in two cancerous gastric specimens were not observed. In comparison to the spectra of non-cancerous specimens, the lipid peak at 1.30 ppm was significantly decreased and split, while the choline peak at 3.19 ppm increased. This trend was the same as that observed in the 9.4-T NMR results. This experiment indicated that decreases in the intensities of lipid peaks and increases in the choline and lactate peak intensities are markers of infiltration of carcinoma cells into the gastric tissue.

T2-relaxation times of cancerous gastric tissue in the 1.5-T MRS experiments were higher than those from the 9.4-T NMR spectral peaks and do not exhibit significant differences between the MC/SMC and the MUS layers.

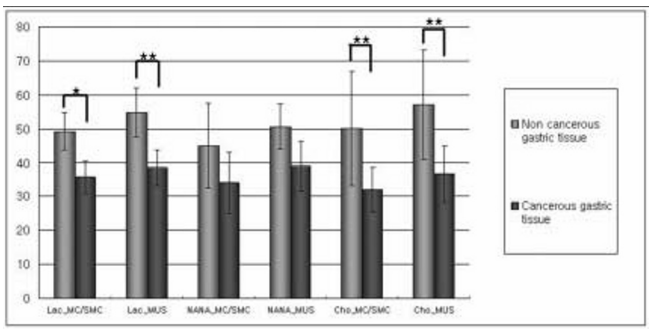

Fig. 2. The statistical analysis results from the measured T2-relaxation times obtained at 64-MHz (*: $p<0.05$, ** : $p<0.01$)

However, the T2-relaxation times of the three metabolite peaks in cancerous specimens were significantly shorter than the non-cancerous times. As shown in Fig. 2, a statistical analysis (one-away analysis of variation: ANOVA) of the choline and lipid peaks indicated that the differences be-

F. Ibrahim, N.A. Abu Osman, J. Usman and N.A. Kadri (Eds.): Biomed 06, IFMBE Proceedings 15, pp. 33-36, 2007
www.springerlink.com ' Springer-Verlag Berlin Heidelberg 2007

tween the corresponding T2-relaxation times in non-cancerous and cancerous gastric specimens were statistically significant (choline peak: $p < 0.01$, lipid peak: $p < 0.05$).

IV. Conclusions

In cancerous gastric tissue, we found two strong resonance peaks, lipid at 1.30 ppm and choline at 3.2 ppm (Table 2). The observed resonance peaks did not have any statistically significant spectral differences between the MC/SMC and MUS layers in either the 9.4-T or 1.5-T instruments. In comparison with normal gastric tissue, the intensity of the choline peak at 3.2 ppm was increased and the intensities of the lipid and NANA peaks at 1.3 ppm and 2.0 ppm were decreased in abnormal gastric tissue. In cancerous gastric tissues, choline peak intensity increases, while lipid peak intensity decreases and splits. It has been shown that the proton MR spectra of invasive carcinoma of human organs show strong signal intensity peaks from lactate/lipid (di-/triglyceride) at 1.2 1.3 ppm, arising primarily from methylene protons of acyl chains in mobile neutral lipid, with additional contributions from the methyl protons of lactate and threonine [11]. Understanding the cellular origin of the MR signal, therefore, must be undertaken for each individual organ and compared with established histological, biological, and genetic criteria in order for MRS to be used as a robust method for determining human tumor development and progression. In conclusion, the peak intensity variation of the choline and lipid peaks in MR spectra can used as an index of gastric cancer disease.

We found that all measured T2 relaxation times at metabolite peaks in cancerous gastric tissue were decreased in both of 9.4-T and 1.5-T spectra. However, these studies have not quantitatively measured the T2 relaxation time of metabolites. Nevertheless, we found significantly different T2 value between normal and abnormal stomach tissue. In the statistical analysis shown in Fig. 2, the T2-relaxation times of choline and lipid peaks in 1.5-T MR spectra were clearly decreased in cancerous gastric tissues. We suggest that the T2-relaxation times of the choline and lipid metabolite peaks can be used as a marker of invasion of gastric cancer cells. However, there were no statistically significant differences in T2 relaxation times between the MC/SMC and MUS layers.

The results of this study represent fundamental data which may be useful in overcoming the limitations of in vivo MR spectroscopy to diagnose gastric tissue disease.

Acknowledgment

This work was supported by the Inje Research and Scholarship Foundation in 2005.

References

1. Yoo KY(1998) Epidemiologic features and perspective of stomach cancer in Korea (in Korean).Medical Postgraduates. Korea Green Cross Co. 26(2):9-64
2. Kim SK, Jung JM (1988) Clinical review of gastric cancer in Korea (in Korean). Medical Postgraduates. Korea Green Cross Co. 26(2):8-70
3. Hong WS (2004) Chemoprevention of Gastric Cancer (in Korean). Journal of Korean Association of Cancer Prevention 9(1): 1-7.
4. Auh YH, Lim TH, Lee DH, et al. (1994) In vitro MR imaging of the resected stomach with a 4.7-T superconducting magnet. Radiology 191:129-34
5. Matsushita M, Oi H, Murakami T, et al. (1994) Extraserosal invasion in advanced gastric cancer evaluation with MR imaging. Radiology 192:87-91
6. Du X M, Roeren T, Kuntz C, et al. (1997) MRI for staging of gastric carcinoma: first, results of an experimental prospective study. J Compute Assist Tomogr 21:66-72
7. Bloch R, Hansen WW, Rackard M. (1946) Nuclear induction. Phys Rev, 69 : 127
8. Vlaardingerbroek M.T., den Boer J.A. (1999) Magnetic Resonance Imaging, 2nd Ed., Springer 331～47
9. NessAiver M. (1997)About MRI Physics, UMSM, 2-1～9-10. 18
10. Stewart C. Bushong (1996) Magnetic Resonance Imaging 2nd : Physical and Biological Principles, Mosby
11. Mun CW, Cho JY, Shin W-J, Choi K-S, et al. (2004) Ex vivo MR spectroscopy (1H-MRS) for evaluation of human gastric carcinoma. Magn Reson Imag 22:861-70

Address of the corresponding author:

Author: Chi-Woong Mun
Institute: Inje University
Street: 607 Obang-dong
City: Gimhae
Country: South Korea
Email: mcw@inje.ac.kr

F. Ibrahim, N.A. Abu Osman, J. Usman and N.A. Kadri (Eds.): Biomed 06, IFMBE Proceedings 15, pp. 33-36, 2007
www.springerlink.com ' Springer-Verlag Berlin Heidelberg 2007

A Comparative Analysis of Zernike moments and Principal Component Analysis as Feature extractors for Face Recognition

A.J. Nor aini[1], P. Raveendran[1], N. Selvanathan[2]

[1] Department of Electrical Engineering, Faculty of Engineering University Malaya 50603, Kuala Lumpur
[2] Department of Artificial Intelligence, Faculty of Computer Science and Information Technology, University Malaya, Kuala Lumpur

Abstract— **This paper describes the comparison between Principal component analysis (PCA) also known as eigenfaces and Zernike moments (ZM) as feature extractors, used in face recognition. These feature extraction methods are still being research until today even though the techniques may either be hybrid or fusion. The study look into the capability of these two feature extraction methods to recognize face due to changes in illumination condition, pose, facial expression and others. The experiment carried out utilizes the earliest eigenfaces technique adopted from Turk and Pentland [1] and ZM polynomials [2]. The classification technique employed in the recognition stage is a simple Euclidean square distance classifier or nearest neighbor (NN). The experiments utilized database face images from Olivetti research laboratory (ORL) consisting of 40 subjects of 10 images each where none of them are identical [3]. They vary in position, rotation, scale and expression, with and without glasses. From the comparative study, the outstanding feature extraction method is considered for face recognition system.**

Keywords— **Zernike moments, Principle component analysis, Eigenface, nearest neighbor, orthogonal moment.**

I. Introduction

Face recognition has been actively research over a decade and now it is still being research although many of the latest work are either the improvement of existing techniques or hybrid techniques whereby several available techniques are incorporated to become one system. The face recognition systems have wide range of applications such as access control systems, content-based video browsing, building or office security, criminal identification and authentication in secure systems like computers or bank teller machines [4].

Constraints such as poses, illumination conditions, facial expressions, aging and many others are still the main problem to achieve high classification accuracy. A successful face recognition system however depends heavily on the particular choice of feature extraction methods. Regardless of the method used, extracted features must minimize the within-class face variability and maximize between-class face variability in order to provide sufficient discrimination among different faces [5].

Orthogonal moment based feature extraction methods like ZM, Legendre moments (LM), Pseudo Zernike moments (PZM) and others have gain attention lately. They have proven to be suitable for handling images with binary patterns such as pattern recognition, palm print verification and etceteras [7]. These moments may acquire the characteristic of translation, scaling and rotation invariance and thus can be chosen for image analysis and pattern recognition application [7].

Hybrid features that are the combination of orthogonal moments with other feature extractors like Principle Component Analysis (PCA), Fourier descriptors and others have also gain attention and use to represent faces. For instance, A. Saradha et al, who combines Fourier descriptors with ZM and classifies the face images using Linear Discriminant Analysis (LDA) [5]. J. Haddadnia et al utilizes ZM on localized and segmented faces and classifies using Radial Basis function neural network [4], and N.H.Foon et al combines Wavelet Transforms (WT) and ZM as a feature vector using Euclidean distance as the classifier [8].

The technique that functions by projecting face images onto a feature space and spans the significant variations among known face images is known as eigenfaces technique since they are the eigenvectors or principal components of the set of training faces [1]. This technique was popular way back in early nineties and was extended not only to face images but also to other face features such as eyes, mouth and others. For instance P. Quintiliano and A. Santa-Rosa proposed an eigeneyes technique to perform face recognition from fragments of face images approximately 20% of the face [6].

In this paper the classification results from the experiments utilizing feature vectors extracted from ZM order 2 to 12 and PCA are presented and analyzed. The data input consists of 40% train images and 60% test images. The rest of the paper is organized as follows. Section 2 describes the theory of ZM and PCA. Section 3 detailed out the classifier used for face recognition. Experimental results are presented in section 4. Section 5 analyses the performance of the feature extractors and finally section 6 concludes the paper.

F. Ibrahim, N.A. Abu Osman, J. Usman and N.A. Kadri (Eds.): Biomed 06, IFMBE Proceedings 15, pp. 37-41, 2007
www.springerlink.com ' Springer-Verlag Berlin Heidelberg 2007

II. Feature extractors

A. Zernike moments

The kernel of Zernike moments are orthogonal Zernike polynomials defined over the polar coordinates inside a unit circle. The Zernike moment of order p is defined as,

$$Z_{pq} = \frac{(p+1)}{\pi} \int_0^{2\pi} \int_0^1 V_{pq}^{*}(r,\theta) f(r,\theta)\, r\, dr\, d\theta \quad (1)$$

where, $V_{pq}(r,\theta)$ denote Zernike polynomials of order p and repetition q and is written as

$$V_{pq}(r,\theta) = R_{pq}(r) e^{jq\theta} \quad (2)$$

while $*$ denotes complex conjugate. The radial polynomial, $R_{pq}(r)$ is expressed as

$$R_{pq} = \sum_{s=0}^{(p-|q|)/2} (-1)^s x A \quad (3)$$

$$A = \frac{(p-s)!}{s!\left(\frac{p-2s+|q|}{2}\right)!\left(\frac{p-2s-|q|}{2}\right)!} r^{p-2s}$$

where p is a non-negative integer, and q is an integer such that $p-|q|$ is even, and $|q| \le p$. The discrete approximation of the continuous Zernike integral of equation (1) is written as follows

$$Z_{pq} = \lambda(p,N) \sum_{i=0}^{N-1} \sum_{j=0}^{N-1} R_{pq}(r_{ij}) e^{-\hat{j} q \theta_{ij}} \times f(i,j), \quad (4)$$

$$for\ 0 < r_{ij} < 1$$

where, $\lambda(p,N)$ is the normalizing constant based on the mapping transformation [2][9].

Zernike moment is used as the feature extractor whereby the order is varied to achieve the optimal classification performance.

B. Eigenfaces

Consider a face image $I(x,y)$ be a two dimensional NxN array of (8-bit) intensity values. This can be expressed as a vector of dimension N^2, in other word a typical image of size 100x100 becomes a vector of dimension 10,000 or equivalent to a point in 10,000 dimensional spaces [1][10].

To compute the eigenfaces, first compute the average face from the training set, Γ_1, Γ_2 , Γ_3, .. Γ_M using the expression

$$\psi = \frac{1}{M} = \sum_{n=1}^{M} \Gamma_n \quad (5)$$

where, M is the number of training images. The difference between each face and the average face is then computed as

$$\phi_i = \Gamma_i - \psi, \quad for\ i = 1,2.....M \quad (6)$$

A covariance matrix of the training images is constructed as,

$$C = AA^T, \quad (7)$$

where $A = [\phi_1, ..., \phi_M]$. The basis vector of the face space that is the eigenfaces is the orthogonal eigenvectors of the covariance matrix C [1][10]. To find the eigenvectors of NxN matrix C is a difficult task for typical image size, hence a simplified way of calculation is adopted. Considering the number of training images is very much less than the number of image pixel ($M<N$), therefore there will only be $M-1$ meaningful eigenvector instead of N. Due to this, the eigenfaces are computed by first finding the eigenvectors $v_l (l = 1,....., M)$ of MxM matrix L, where.

$$L = A^T A \quad (8)$$

This means that only M eigenvectors is determined. The eigenfaces, $u_l (l = 1,...., M)$, of matrix C are then expressed as

$$u_l = \sum_{k=1}^{M} v_{lk} \phi_k, \quad l = 1,...., M \quad (9)$$

which is the linear combination of the difference face images , $\phi_i (i = 1,...., M)$ weighted by $v_l (l = 1,....., M)$ [8]. With this, the calculations are greatly reduced, from the order of the number of pixels in the images (N^2) to the order of the number of images in the training set (M) [1].

Normally a smaller set of M' where $M'<M$ eigenfaces is sufficient for face identification. In other words, M' significant eigenvectors of L corresponding to the largest M' eigenvalues are selected for the eigenface computation [10].

III. Nearest neighbor classifier

Nearest neighbor is regard as the simplest and powerful classification method and it has wide applications. It is used to compare the feature vector of the prototype image and the feature vectors stored in the database. This is obtained by calculating the Euclidean square distance between the prototype image and the database. For instance let $C_1, C_2, C_3 \ldots C_k$ be the K clusters in the database. The class is found by measuring the distance $d(x^{(q)}, k)$ between $x^{(q)}$ and the K th cluster C_k. The feature vector with minimum difference is found to be the nearest matching vector [5][11]. The expression for the minimum distance is given by

$$d(x^{(q)}, C_k) = \min\left\{ \left\| x^{(q)} - x \right\| : x \in C_k \right\} \quad (10)$$

In the experiments, the square distance is computed to determine the minimum difference that best match the feature vector of the stored database.

F. Ibrahim, N.A. Abu Osman, J. Usman and N.A. Kadri (Eds.): Biomed 06, IFMBE Proceedings 15, pp. 37-41, 2007
www.springerlink.com ' Springer-Verlag Berlin Heidelberg 2007

IV. Experimental study

The experiments were conducted on various numbers of subjects from ORL database of 40 subjects, where each subject consists of 10 different orientations of the images. Each image is of size 92x112 and in order to reduce the complexity in computation, the images are resized to 64x64. Fig. 1 shows the some of the train images from ORL database with different orientation used in the experiments.

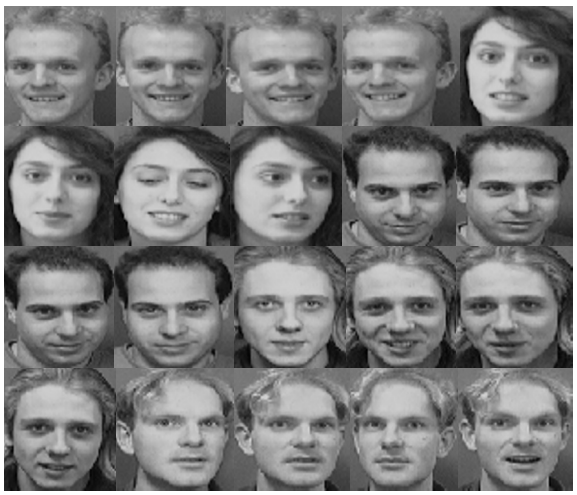

Fig 1. Some of the train images from ORL database

The experiments are not restricted to one set of train images but the train images are picked at random as tabulated in Table 1 and 2 respectively and 4 from each subject are considered as train images and the other 6 as test images.

The number of subjects considered in these experiments is 5, 20, 25, 30 and 40. Experiments conducted on 5, 20 and 25 subjects do not include those wearing spectacles while 30 and 40 subjects include those with spectacles but they are all subjected to constraints as mentioned earlier. The number of subjects wearing spectacles in the experiment of 30 subjects is 5 and increased to 15 when 40 subjects are considered.

The objective of the experiments is to make comparison between ZM, which is the moment based method and PCA, an eigenface based method in terms of their classification accuracy and also which feature extractor is suitable for face recognition.

A. Experiment 1

The first experiment utilizes ZM of order 2 to12 and the extracted original feature vector is of size 47. The reason for excluding order 0 and 1 is that moments at lower order are basically noise and this may creates confusion in face recognition. For this reason order 2 to 12 is considered in the experiment and the percentage classification accuracy for the random combination of train images is tabulated in Table 1 with the best overall performance being highlighted.

Table 1. Percentage classification accuracy of ZM order 2 to 12

			Classification. accuracy (%)				
		Train images	image1-image4	image5-image8	image9,10,1,2	image3-image6	image7-image10
No. of subjects/images	No. of train images	No. of test images					
5(50images) w/o spects.	20	30	100.00	100.00	100.00	100.00	100.00
20(200image) w/o spects.	80	120	91.67	95.83	95.83	90.83	96.67
25(250images) w/o spects.	100	150	89.33	94.67	96.00	90.67	94.67
30(300images) with spects.	120	180	89.44	95.00	96.11	90.00	94.44
40(400images) with spects.	160	240	84.17	91.25	92.50	87.08	83.75

F. Ibrahim, N.A. Abu Osman, J. Usman and N.A. Kadri (Eds.): Biomed 06, IFMBE Proceedings 15, pp. 37-41, 2007
www.springerlink.com ' Springer-Verlag Berlin Heidelberg 2007

Table 2. Percentage classification accuracy of PCA

			Classification accuracy (%)				
		Train images	image1-image4	image5-image8	image9,10,1,2	image3-image6	image7-image10
No. of subjects/images	No. of train images	No. of test images					
5(50images) w/o spects.	20	30	96.67	100.00	93.33	100.00	100.00
20(200image) w/o spects.	80	120	90.00	82.50	90.83	87.50	92.50
25(250images) w/o spects.	100	150	81.33	88.67	84.67	84.00	83.33
30(300images) with spects.	120	180	82.78	84.44	84.44	78.33	82.78
40(400images) with spects.	160	240	75.00	82.50	80.00	78.33	75.83

B. Experiment 2

In experiment 2, PCA method is applied by selecting the highest eigenvalues that correspond to the eigenvectors that are used to project the images on to the face space. The eigenvectors are varied to obtain the best classification accuracy. Fig. 2 shows the eigenfaces from the train images of Fig. 1 while Table 2 tabulates the percentage classification accuracy with the best overall performance being highlighted.

Fig 2. Eigenfaces from the train images

V. Performance analysis

Comparing the results obtained in Table 1 and 2, the best performance of 5 subjects is similar for both ZM and PCA that is 100%. At 20 subjects, ZM achieves classification accuracy of 96.67 % while PCA at 92.50% where ZM is 4.17 % higher. When 25 subjects are considered, classification accuracy of 96% is achieved for ZM while 88.67% for PCA. This shows that the performance of ZM is 7.33 % higher than PCA. 5 subjects with spectacles are included in the experiment with 30 subjects. The best classification accuracy obtained for ZM and PCA is 96.11% and 84.44% respectively. ZM outperforms PCA by 11.67%. The number of subjects with spectacles is increased to 15 at 40 subjects for both methods. ZM shows 92.50% classification accuracy while PCA shows 82.50% classification accuracy that is 10% higher.

From the results above, it is pretty obvious that ZM performs better compared to PCA as number of subjects is increased. The reason being PCA is sensitive to scale, pose and illumination but robust when dealing with glasses and facial expressions [10]. The ability of ZM to better recognize face image is due to its characteristics that are invariant to rotation and insensitive to noise [2].

VI. Conclusion

From the results, ZM possess the best features that illustrate the face compared to PCA. However, the percentage classification accuracy achieved for both methods is very subjective since it is very dependent on the choice of database that is either the database has less constraints or otherwise, the combination techniques employed and choice of the classifiers. It is also dependent on the number of train images. In general, the performance of either ZM or PCA methods as feature extractor requires supporting technique that able to improve the overall performance of the face recognition system [4][5][8]. This can be done either looking in terms of preprocessing of the images before extracting the features or combining other feature extraction methods. Nevertheless, lots of factors need to be investigated to achieve high classification accuracy and able to develop a robust and effective face recognition system.

References

1. M.Turk, A. Pentland, Eigenfaces for recognition , Journal of Cognitive Neuroscience,Vol.3,No. 1,pp71-86, 1991.
2. R. Mukundan, K.K.Ramakrishnan, Fast computation of Legendre and Zernike moments , Pattern Recognition, vol 28, no9,pp1433-1442,1995.
3. Olivetti Research Laboratory, http://www.uk.research.att.com:pub/data/att_faces.zip
4. Javad Haddadnia et-al, Neural Network Based face Recognition with moment invariants, IEEE transaction, 2001.
5. A. Saradha, S. Annandurai, A Hybrid Feature Extraction Approach for Face Recognition Systems , International Journal on Graphics, Vision and Image Processing, Vol.5, 2005.

F. Ibrahim, N.A. Abu Osman, J. Usman and N.A. Kadri (Eds.): Biomed 06, IFMBE Proceedings 15, pp. 37-41, 2007
www.springerlink.com ' Springer-Verlag Berlin Heidelberg 2007

6. P. Quintliano, A.Santa-Rosa, Face RecognitionBased on Eigeneyes , Pattern Recognition and Image Analysis, Vol. 13, No.2, 2003, pp. 335-338.
7. Y.C.Chin, A.A.Kassim, Y.Ibrahim, Character recognition using statistical moments , *Image Vision computing*, Vol. 17, pp 299-307, 1999.
8. N.H.Foon et al An efficient Method for Human Face Recognition using Wavelet Transform and Zernike Moments , Proceedings of the International Conference on Computer Graphics, Imaging and Visualization (CGIV 04).
9. Belkassim S. O, Pattern Recognition with moment invariants- A comparative study and new results , Pattern Recognition, Vol. 24 No. 12(1991), pp1117-1138.
10. S. Wei, A shape Analysis in Computer Vision Final project report: Face recognition , Department of Electrical Engineering McGill University, Canada, December 21, 1998. http://www.cim.mcgill.ca/~wsun/sa/project/report.html, 30 March 2004.
11. D. Barber, Learning from data: Nearest neighbor classification , http://www.anc.ed.ac.uk/~amos/lfd/, pg. 2-6, 2001-2004.

Author: Nor aini Abd. Jalil
Institute: University Malaya Kuala Lumpur
Country: Malaysia
E-mail: nonie183@yahoo.com

F. Ibrahim, N.A. Abu Osman, J. Usman and N.A. Kadri (Eds.): Biomed 06, IFMBE Proceedings 15, pp. 37-41, 2007
www.springerlink.com ' Springer-Verlag Berlin Heidelberg 2007

Application of Artificial Neural Network for Estimation of Fetal Weight

Y.C. Cheng[1], C.J. Hou[2], F.M. Cheng[3] and K.C. Chung[1]

[1]Institute of Biomedical Engineering, National Cheng Kung University, Tainan, Taiwan
[2]Department of Electrical Engineering, Southern Taiwan University of Technology, Tainan, Taiwan
[3]Department of Obstetrics and Gynecology, National Cheng Kung University Medical College and Hospital, Tainan, Taiwan

Abstract— **Accurate estimation of fetal weight is crucial for deciding which mode is the best for babies to be delivered. With the advancement of ultrasonic technologies, sonographic parameters of the fetal can be used to estimate fetal weight. Fetal weight estimated by regression methods is relatively acceptable in the clinical Obstetrics, but the accuracy of estimated fetal weight remains to be improved. This study was aimed to develop a group-based artificial neural network model to improve the accuracy of fetal weight estimation through sonographic parameters. Stepwise regression analysis was used to examine and extract the significant parameters. The input layer in the artificial neural network model included seven significant parameters such as biparietal diameter, occipito-frontal diameter, abdominal circumference, gestational age, femur length, gender, and fetal presentation. A total of 2,107 consecutive singleton fetuses were divided into training group with 1,411 samples and testing group with 696 samples. The results show that the accuracy of fetal weight estimated by the artificial neural network model is significantly better than those by regression methods. The importance of this study is to consider and control the heterogeneity among the high variability and broad ranged parameters by statistics, and to choose scientific parameters as reasonable input variables of artificial neural network to improve the estimation of fetal weight. This study has proved the accuracy of fetal weight estimation by artificial neural network model is better than those of previous models.**

Keywords— **estimated fetal weight, sonographic parameter, artificial neural network**

I. Introduction

Accurate estimation of fetal weight is very important in modern Obstetrics. It helps the clinicians to decide which mode is the best for babies to be delivered. In clinics, real-time high-resolution ultrasound (US) is a major tool for estimating fetal weight. In the literature, most published formulas for fetal weight estimation were derived from 2-D US measurements such as biparietal diameter (BPD), occipitofrontal diameter (OFD), abdominal circumference (AC) and femur length (FL). Fetal weight estimated by regression methods is relatively acceptable in the clinical Obstetrics, but the accuracy of estimated fetal weight remains to be improved [1-2]. In recent studies, the accuracy of fetal weight estimated by artificial neural network (ANN) model has been improved as compared with regression methods [4]. However, the estimation error of fetal weight will be raised by regression methods or previous ANN model as an actual fetal weight is higher than 4 kilograms or lower than 2.5 kilograms. The purpose of this study was to develop a group-based ANN model to improve the accuracy of fetal weight estimation through sonographic parameters.

II. Materials and Methods

A. Data collection

A total of 2,107 consecutive singleton fetuses within 3 days before delivery were conducted into the study. Fetal evaluations and examinations based on the clinical protocol were performed at the delivery room in National Cheng Kung University Hospital. Fetal biometric measurements were quantified by US (Aloka SSD-680, Aloka Inc., Japan) with a 3.5 MHz linear array transducer. Criteria excluded from the study were anomalous fetuses, multiple gestations and fetuses not delivered within 3 days of US examination. Stepwise regression analysis was used to extract significant features from fetal biometric measurements.

B. Modified ANN Modeling

In this study, the back propagation network (BPN) algorithm was applied to develop the group-based ANN model for fetal weight estimation. In order to solve the problem of high estimation error, a group-based ANN model was established according to fetal AC size which was divided into three groups. Seven significant features including BPD, OFD, AC, GA, FL, gender, and fetal presentation were used as input parameters in the group-based ANN model. The total cases were further divided into training and testing groups. A total of 1,411 fetuses were randomly assigned to the training group for training the group-based ANN model, and 696 fetuses were used to validate the ANN model. The architecture of the group-based ANN model in this study was composed of an

F. Ibrahim, N.A. Abu Osman, J. Usman and N.A. Kadri (Eds.): Biomed 06, IFMBE Proceedings 15, pp. 42-44, 2007
www.springerlink.com ' Springer-Verlag Berlin Heidelberg 2007

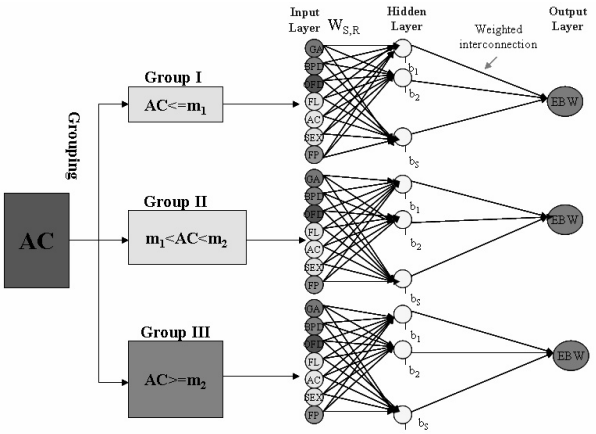

Fig. 1 The architecture of group-based ANN model.

input layer with seven inputs, a hidden layer and an output layer, as illustrated in Figure 1.

C. Experiments

An experiment with Friedman test was designed to investigate the accuracy of fetal weight estimation in this study. The difference of fetal weight estimation among four methods was statistically analyzed by comparing mean absolute error (MAE) and mean absolute percent error (MAPE) of estimated fetal weight in the group-based ANN model with that in three regression methods reported by Hsieh et al. and Hadlock et al. [1-2].

III. Results

The results show the MAPE of estimated fetal weight is 5.53% with standard deviation of 4.35% and the MAE of estimated fetal weight is 160.55g with standard deviation of 119.06g in the group-based ANN model. The accuracy of fetal weight estimation in this study is significantly better than that in regression methods, as shown in Table 1. The group-based ANN model in this study could reduce errors between estimated fetal weight and actual fetal weight, and improve the accuracy of fetal weight estimation.

Table 1 Comparison of MAPE and MAE of fetal weight estimation among four methods (n = 696)

Formula	MAPE (%, mean ± SD)	Significance (p<0.05)	MAE (g, mean ± SD)	Significance (p<0.05)
Group-based ANN modeling	5.53 ± 4.35%	-	160.55±119.06g	-
Hsieh et al. (1987) formula 1B	6.12 ± 4.76%	0.000*	181.99±128.81g	0.000*
Hsieh et al. (1987) formula 2B	6.59 ± 6.80%	0.000*	185.23±131.73g	0.000*
Hadlock et al. (1985)	7.68 ± 5.57%	0.000*	181.99±128.81g	0.000*

*Friedman Test, $p < 0.05$

Group-based ANN model used as a comparison,
MAPE: mean absolute percent error; MAE: mean absolute error

IV. Discussion

The ANN model has been widely used in many fields such as pattern recognition, classification, image analysis and prediction model construction [5]. The first study using ANN to estimate fetal weight was reported by Farmer et al. [3]. Their study was focused mainly to the macrosomia group in which fetal weights ranged between 3,360 and 5,260 grams and 13 variables were inputted into the ANN model. Their report showed the MAPE of estimated fetal weight was 4.7% with standard deviation of 3.9% estimated from 102 fetuses. The MAPE in the group-based ANN model is 4.8% with standard deviation of 3.2% in the macrosomia group with fetal weights ranged from 3,400 to 4,295 grams. This improved accuracy of estimated fetal weight in our study agrees with that in Farmer s study.

V. Conclusions

In conclusion, the importance of this study is to consider and control the heterogeneity among the high variability and broad ranged parameters by statistics, and to choose the best parameter as a reasonable classified group to improve the estimation of fetal weight. This study has proved the accuracy of fetal weight estimation by the group-based ANN model is better than those of previous models. The results of this study may contribute to the best choice of how to deliver a baby safely and thus lower down the maternal-fetal morbidity and mortality.

F. Ibrahim, N.A. Abu Osman, J. Usman and N.A. Kadri (Eds.): Biomed 06, IFMBE Proceedings 15, pp. 42-44, 2007
www.springerlink.com ' Springer-Verlag Berlin Heidelberg 2007

REFERENCES

1. Hsieh F.J., Chang F.M., Huang H.C., Lu C.C., Ko T.M., Chen H.Y.(1987) Computer-assisted analysis for prediction of fetal weight by ultrasound: comparison of biparietal diameter, abdominal circumference and femur length. J Formosan Med Assoc 86:957 964
2. Hadlock F.P., Harrist R.B., Sharman R.S., Deter R.L., Park S.K.(1985) Estimation of fetal weight with the use of head, body and femur measurements a prospective study. Am J Obstet Gynecol 151:333 337
3. Farmer R.M., Medearis A.L., Hirata G.I., Platt L.D. (1992) The use of a neural network for the ultrasonographic estimation of fetal weight in the macrosomic fetus. Am J Obstet Gynecol 166: 1467 1472
4. Chuang L., Hwang J.Y., Chang C.H., Yu C.H. , Chang F.M.(2002) Ultrasound estimation of fetal weight with the use of computerized artificial neural network model. Ultrasound in Medicine and Biology 28:991 996
5. Cross S.S., Harrison R.F., Kennedy R.L.(1995) Introduction to neural networks. Lancet 346:1075 1079

Address of the corresponding author:

Author: Y.C. Cheng
Institute of Biomedical Engineering,
National Cheng Kung University,
No.1, University Road,
Tainan City 701,
Taiwan (R.O.C.)
Email: chengyc@mail.ncku.edu.tw

F. Ibrahim, N.A. Abu Osman, J. Usman and N.A. Kadri (Eds.): Biomed 06, IFMBE Proceedings 15, pp. 42-44, 2007
www.springerlink.com ' Springer-Verlag Berlin Heidelberg 2007

Classification of Breast Lesions Using Artificial Neural Network

M.Y. Mashor[1], S. Esugasini[2], N.A. Mat Isa[2] and N.H. Othman[3]

[1]Electronic & Biomedical Intelligent Systems (EBItS) Research Group, School of Mechatronic Engineering
Kolej Universiti Kejuruteraan Utara Malaysia, 02600 Jejawi, Arau, Perlis, MALAYSIA
[2]Control and ELectronic Intelligent System (CELIS) Research Group, School of Electrical & Electronic Engineering, Universiti Sains Malaysia, Engineering Campus, 14300 Nibong Tebal, Pulau Pinang, MALAYSIA.
[3]Pathology Department, School of Medical Science, Universiti Sains Malaysia
Medical Campus, 16150 Kubang Kerian, Kelantan, MALAYSIA.

Abstract— **This paper presents a study on classification of breast lesions using artificial neural networks. Thirteen morphological features have been extracted from breast lesion cells and used as the neural network inputs for the classification. Multilayered Perceptron, Radial Basis Function and Hybrid Multilayered Perceptron networks were used to perform the classification task. Unlike the previous studies that only classify the lesion into benign and malignant, this study extends the breast lesions classification into four categories that are malignant, fibroadenoma, fibrocystic disease and other benign cells. The three neural networks were trained and compared using 1300 data samples. The classification results indicating that all the networks give good overall diagnostic performance. However, only Hybrid Multilayered Network that provides 100% accuracy, sensitivity and specificity.**

Keywords— **Breast Cancer, Neural Network, Classification, RBF Network, HMLP Network**

I. Introduction

There are various techniques that were used to interpret the cancerous cells or the lesions suspected to be cancerous in the medical field. The conventional or manual ways of interpreting the cells are microscopic diagnosis by cytopathologists or based on mammogram images by oncologists. Mammography has high sensitivity in screening of breast cancer, however, it normally produces high rate of false positive prediction that will lead to large number of biopsies of benign lesions, Starita *et al*. [1]. The application of artificial intelligence in the medical field has revealed many computer aided diagnostic (CAD) systems to assist medical experts to produce faster and more accurate diagnosis for the increasing incidence of breast cancer cases. Giger and Huo [2] used artificial neural network (ANN) to develop a CAD that incorporates various computer-extracted image features from mammogram images to differentiate malignant from benign masses. The performance of the computer aid with 100% sensitivity was appreciable with a positive predictive value of 83%, which was 12% higher than an experienced mammographer. Wu *et al.* [3] used Multi-layered Perceptron (MLP) network to differentiate between malignant and benign mammographic patterns based on radiographic features extracted by radiologists. The ability of neural network classification was then compared to classification by mammographers and the results showed that the capability of the neural network to do classification is better than that of a mammographer alone.

Other researches in neural networks implementation in cancer diagnosis have been done by Kok *et. al*. [4], Mitra *et. al*. [5] and Mashor *et. al* [6] for cervical cancer and Yao & Liu [7] and Kates *et. al*. [8] for breast cancer. Yao & Liu [7] defined two neural network approaches for breast cancer diagnosis, evolutionary and ensemble. The evolutionary approach was used to design compact neural networks automatically by evolving network architectures and weights, while the ensemble approach was aimed at tackling large problems that may not dealt with efficiently by a monolithic neural network. Kates *et. al* [8] presented the potential contributions of neural network to a clinical decision support framework for the prediction of breast cancer therapy response.

Most of the previous studies of breast cancer diagnosis are based on the mammograms images. The limitation of these neural network based breast cancer diagnostic systems are that they only capable of classifying the breast lesions into two categories which are benign and malignant tumours. The current study, neural network will be used to classify the breast lesion into four categories, which are malignant, fibroadenoma, fibrocystic disease and other benign cases. The classification is based on smear slides of fine needle aspirate (FNA) cells of breast lesion.

II. Breast Lesion Classification Using Neural Network

Multilayered Perceptron (MLP), Hybrid Multilayered Perceptron (HMLP) and Radial Basis Function (RBF) networks were tested to screen breast lesion cells. The inputs to the network are some features of the breast lesion cells. The images of breast lesion cells have been captured from smear slides using a computerized microscope.

F. Ibrahim, N.A. Abu Osman, J. Usman and N.A. Kadri (Eds.): Biomed 06, IFMBE Proceedings 15, pp. 45-49, 2007
www.springerlink.com ' Springer-Verlag Berlin Heidelberg 2007

Thirteen features have been manually extracted from the computer images of breast lesion cells. The 13 features are cellularity, background, cohesiveness, cell in cluster, significant stromal component, clump thickness, nuclear membrane thickness, bare nuclei, normal nucleoli, mitosis, nucleus stain, uniformity of cell and fragility. The neural networks receive these features as the inputs and classify the cells into four categories which are malignant, fibroadenoma, fibrocystic disease and other benign cells. Sample of fibroadenoma, fibrocystic disease, malignant and other benign cells are shown in Figure 1.

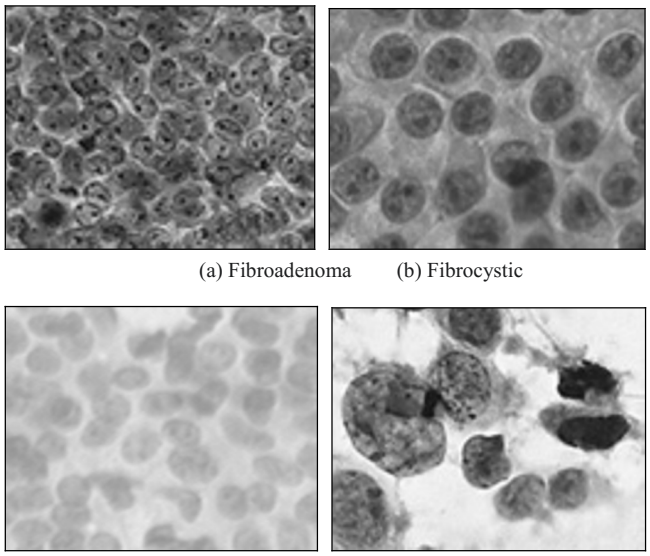

(a) Fibroadenoma (b) Fibrocystic

(c) Other benign (d) Malignant

Fig. 1 Four categories of breast lesion cells

The features of the samples are extracted and interpreted into numerical data sets by experienced cytotechnologists with assistance and supervision by experienced pathologists. All the data were bypassed and checked thoroughly by minimum of three pathologists per sample. A total of 1300 data were collected from Hospital University Sains Malaysia and Penang General Hospital. First the captured images were revised by pathologists to determine the appropriateness of the breast lesion images. Then, thirteen features were extracted from the revised images with the pathologists supervision, and the interpreted data were again compared with the respective medical reports of the cases. If there are any mismatches in the information, the cases were again referred and discussed with experienced pathologist and the medical report keeper before a decision is made. The data collection methodology was carefully revised and approved by the experienced pathologist before it was used to train and test the networks. The 1300 data were divided into 800 training data and 500 testing data sets, where the distributions of the data are as shown in Table 1.

All the networks have 13 input nodes that would accept the 13 features from the breast lesion cells. Then the networks will classify the lesion cells into four categories that are fibroadenoma, fibrocystic disease, other benign and malignant cells. Therefore, the network would have four output nodes to represent those four categories of breast lesion cells. The number of hidden nodes for the networks were determined based on their best classification performance respectively. In the current study, MLP and HMLP networks were trained using Recursive Prediction Error (RPE) Algorithm and Modified Recursive Prediction Error (MRPE) Algorithm, respectively. RBF network was trained using a hybrid algorithm [15].

Table 1 Distribution of training and testing data sets

Category of Breast Lesion	Training data	Testing data
Fibroadenoma	240	150
Fibrocystic Disease	240	150
Other Benign	50	30
Malignant	270	170
Total	800	500

A. Multilayered Perceptron Network

Multilayered perceptron (MLP) network is a feed forward neural network with one or more hidden layers. Cybenko [9] and Funahashi [10] have proved that the MLP network is a general function approximator and one hidden layer networks will always be sufficient to approximate any continuous function up to certain accuracy. In the current study, the MLP network with a single hidden layer is used. With this simplification the network can be expressed as:

$$y_k(t) = \sum_{j=1}^{n_h} w_{kj}^2 F\left(\sum_{i=1}^{n_i} w_{ji}^1 v_i(t) + b_j^1 \right) \quad \text{for } 1 \le k \le n_o \qquad (1)$$

where w s, b s, n_h, n_i, n_o, $v_i(t)$ and $F(.)$ are the weights, thresholds, number of nodes in hidden layer, number of nodes in the input layer, number of nodes in output layer, inputs and an activation function respectively.
The activation function $F(.)$ is selected to be:

$$F(v(t)) = \frac{1}{1 + e^{-v(t)}} \qquad (2)$$

F. Ibrahim, N.A. Abu Osman, J. Usman and N.A. Kadri (Eds.): Biomed 06, IFMBE Proceedings 15, pp. 45-49, 2007
www.springerlink.com ' Springer-Verlag Berlin Heidelberg 2007

The weights *w*'s and threshold *b*'s are unknown and should be selected to minimise the prediction errors defined as

$$\varepsilon_k(t) = y_k(t) - y_k(t) \tag{3}$$

where $y_k(t)$ represents the actual outputs and $y_k(t)$ denotes the network outputs.

In the current study, MLP network was trained using RPE algorithm [12]. Recursive prediction error algorithm (RPE) was originally derived by Ljung and Soderstrom [11] and modified by Chen et al. [12] to train MLP networks. RPE algorithm is a Gauss-Newton type algorithm that will generally give better performance than a steepest descent type algorithm such as back propagation algorithm.

B. Hybrid Multilayered Perceptron Network

A hybrid multilayered perceptron (HMLP) network with one hidden layer is shown in Figure 2. HMLP network with one hidden layer can be expressed by the following equation, [13]:

$$y_k(t) = \sum_{j=1}^{n_h} w_{jk}^2 F\left(\sum_{i=1}^{n_i} w_{ij}^1 v_i^0(t) + b_j^1\right) + \sum_{i=0}^{n_i} w_{ik}^3 v_i^0(t); \quad \text{for } 1 \le k \le m \tag{4}$$

where w_{ij}^1, w_{jk}^2, w_{ik}^3 denote the weights between input and hidden layer, weights between hidden and output layer, and weights between input and output layer respectively. b_j^1 and v_i^0 denote the thresholds in hidden nodes and inputs that are supplied to the input layer respectively; n_i, m and n_h are the number of input nodes, output nodes and hidden nodes respectively. $F(.)$ is an activation function that is normally be selected as sigmoidal function. In this paper, sigmoidal function was used for the activation function of the HMLP network.

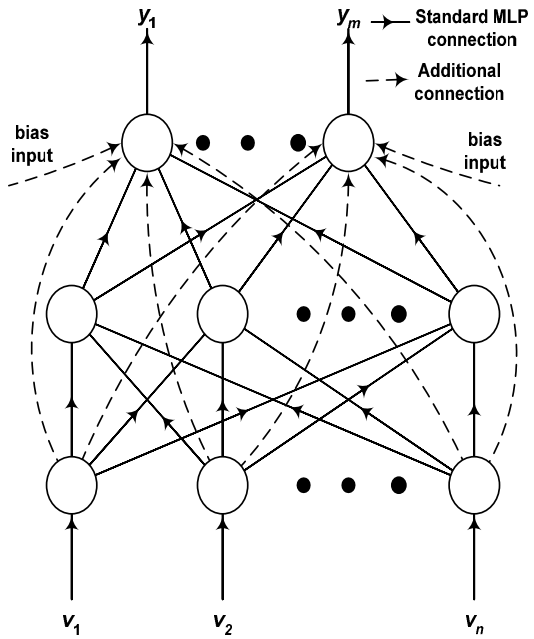

Fig. 2 One-hidden node HMLP network

The weights w_{jk}^2, w_{ik}^3, w_{ij}^1 and threshold b_j^1 are unknown and should be selected to minimise the prediction error defined as:

$$\varepsilon_k(t) = y_k(t) - y_k(t) \tag{5}$$

where $y_k(t)$ and $y_k(t)$ are the desired outputs and network outputs respectively. In the current study, the HMLP network has been trained using MRPE algorithm and the description of MRPE algorithm could be found in Mashor [14].

C. Radial Basis Function Network

A RBF network is a one-hidden-layered feed forward neural network. The first layer consists of input nodes connected to a hidden layer via a set of unity connections. A RBF network with n_o outputs and n_h hidden nodes can be expressed as:

$$y_i(t) = w_{i0} + \sum_{j=1}^{n_k} w_{ij}\phi\left(\left\|v(t) - c_j(t)\right\|\right) \quad i = 1, \cdots, n_o \tag{6}$$

where w_{ij}, w_{i0}, $c_{j(t)}$, n_h and n_o are the connection weights, bias connection weights, RBF centres, number of hidden nodes and number of outputs respectively; $v(t)$ is the input vector to the RBF network and $\phi(\bullet)$ is a non-linear basis function. The notation $\|\bullet\|$ denotes a distance measure that is normally taken to be the Euclidean norm.

In the present study, the thin-plate-spline function has been selected as the non-linear function because this function has a good modelling capability. Thin-plate-spline is given by:

$$\phi(a) = a^2 \, log(a) \tag{7}$$

where $a = \left\|v(t) - c_j(t)\right\|$. In the current study the RBF network is based on Chen et al. [15] that is trained using on-line recursive hybrid training algorithm.

F. Ibrahim, N.A. Abu Osman, J. Usman and N.A. Kadri (Eds.): Biomed 06, IFMBE Proceedings 15, pp. 45-49, 2007
www.springerlink.com ' Springer-Verlag Berlin Heidelberg 2007

III. Results and Discussion

After some simulation analyses, the MLP, RBF and HMLP network with 80, 40 and 10 respectively, seem to provide the best classification performance for the networks. All the networks were trained using 300 epochs. The classification performances of the networks are shown in Table 2 and 3 for training and testing data sets, respectively. The overall classification performances are shown in Table 4.

Table 2 Classification performance for training data set.

Network Model	MLP	RBF	HMLP
Accuracy	93.33%	84.24%	100.00%
Sensitivity	100.00%	100.00%	100.00%
Specificity	89.90%	81.94%	100.00%
False Negative	0.00%	0.00%	0.00%
False Positive	10.10%	18.06%	0.00%

In general the performances over the testing data set are slightly lower than the ones for training data set. All the networks provide good classification performance with accuracy, sensitivity and specificity above 80% for all data sets. However, HMLP network proved to be the best with 100% accuracy, sensitivity and specificity with no false negative and false positive. HMLP network also has more efficient structure, where only 10 hidden nodes are required to produce the classification results. MLP and RBF networks on the other hand require 80 and 40 hidden nodes respectively to produce their best results, which are not as good as the HMLP.

Table 3 Classification performance for testing data set.

Network Model	MLP	RBF	HMLP
Accuracy	91.89%	81.82%	100.00%
Sensitivity	97.47%	100.00%	100.00%
Specificity	89.07%	79.87%	100.00%
False Negative	2.59%	0.00%	0.00%
False Positive	10.93%	20.13%	0.00%

Table 4 Overall classification performance of the neural networks

Network Model	MLP	RBF	HMLP
Accuracy	92.78%	83.31%	100.00%
Sensitivity	99.03%	100.00%	100.00%
Specificity	89.58%	81.14%	100.00%
False Negative	1.00%	0.00%	0.00%
False Positive	10.41%	18.86%	0.00%

IV. Conclusion

MLP, RBF and HMLP networks were used to classify breast lesions into four categories that are malignant, fibroadenoma, fibrocystic disease and other benign cells. Thirteen morphological features have been extracted from breast lesion cells and used as the neural network inputs for the classification. All the networks give good overall diagnostic performance. However, only HMLP network could provides 100% accuracy, sensitivity and specificity with no false negative and false positive. It is also noticeable from the results that HMLP network has more efficient structure compared to MLP and RBF networks, where much smaller hidden nodes are required to produce better results.

References

1. Starita, A., S. La Manna, D. Majidi, D. Caramella and A. Cilotti (2000). Magnetic resonance in mammography: A quantitative evaluation tool of contrast-enhanced magnetic resonance of the breast. Advances in Medical Signal and Information Processing, 2000, First International Conference on (IEE Conf. Publ. No.476), pp. 200 205.
2. Giger, M.L., and Huo, Z., (1999). Artificial Neural Networks in Breast Cancer Diagnosis: Merging of Computer-Extracted Features from Breast Images. Proc. of. IEEE Conference on Soft Computing, vol., pp. 1768-1769.
3. Wu, Y., Giger, M.L., Doi, K., Vyborny, C.J., Schmidt, R.A., Metz, C.E. (1993). ANNs in mammography: Application to decision making in the diagnosis of breast cancer, Radiology. pp. 81-87.
4. Kok M.R., Schreiner-Kok P.G., Veen V.D., and Boon M.E., (1999), Potentially difficult smears of women with squamous cell carcinoma pose fewer problems when PAPNET is used for primary screening, Cytopathology, vol. 10, no. 5, pp 324-34.
5. Mitra P., Mitra S. and Pal S. K., (2000), Staging of Cervical Cancer with Soft Computing, IEEE Trans. on Biomedical Eng., vol. 47, no. 7, pp. 934-940.
6. Mashor, M. Y., Mat-Isa, N. A. & Othman, N. H., (2004), Classification of Pap Smear Tests Using Neural Networks, Proceedings of Kuala Lumpur International Conference on Biomedical Engineering (BioMed2004). Kuala Lumpur, Malaysia, 2-4 September, 2004, pp. 21-24.
7. Yao, X. & Liu, Y., (1999), Neural Networks for Breast Cancer Diagnosis, Proc. of. IEEE Conference on Soft Computing, vol. 3, pp. 1760-1767.
8. Kates, R., Harbeck, N., Schmitt, M. (2000), Prospects for clinical decision support in breast cancer based on neural network analysis of clinical survival data, Proceedings of the 4th international Conference on Knowledge-Based Intelligent Systems & Allied Technologies. pp. 764-767.
9. Cybenko, G., (1989), Approximations by superposition of a sigmoidal function, Mathematics of Control, Signal and Systems, vol. 2, pp. 303-314.
10. Funahashi, K., (1989), On the approximate realisation of continuous mappings by neural networks, Neural Networks, vol. 2, pp. 183-192.
11. Ljung, L. & Soderstrom, T. (1983). Theory and practice of recursive identification. Cambridge: MIT Press.

F. Ibrahim, N.A. Abu Osman, J. Usman and N.A. Kadri (Eds.): Biomed 06, IFMBE Proceedings 15, pp. 45-49, 2007
www.springerlink.com ' Springer-Verlag Berlin Heidelberg 2007

12. Chen, S., Cowan, C.F.N., Billings, S.A., and Grant, P.M., (1990), A parallel recursive prediction error algorithm for training layered neural networks, International Journal of Control, vol. 51, no. 6, pp. 1215-1228.
13. Mashor M.Y., (2000), Hybrid Multilayered Perceptron Networks, Int. Journal. of System and Science, vol. 31, no. 6, pp. 771-185.
14. Mashor M.Y., (1999), Performance Comparison Between Back Propagation, RPE and MRPE algorithms, Journal of The Malaysian Tecnologist, vol. 2, pp. 22-29.
15. Chen, S., and Billings, S.A., (1992), Neural networks for non-linear dynamic system modeling and identification, Int. J. of Control, vol. 56 no. 2, pp. 319-346.

Address of the corresponding author:

Author: Mohd Yusoff Mashor
Institute: Kolej Universiti Kejuruteraan Utara Malaysia
Street: Kompleks Pusat Pengajian KUKUM
City: Jejawi
Country: Perlis, Malaysia
Email: yusoff@kukum.edu.my

F. Ibrahim, N.A. Abu Osman, J. Usman and N.A. Kadri (Eds.): Biomed 06, IFMBE Proceedings 15, pp. 45-49, 2007
www.springerlink.com ' Springer-Verlag Berlin Heidelberg 2007

Classification of Risk in Dengue Fever and Dengue Haemorrhagic Fever using Rule Based Expert System

[1]F. Ibrahim, [1]M.I Mohamad, [1]S.N. Makhtar, and [2]J. Ibrahim

[1]Department of Biomedical Engineering, Faculty of Engineering, University of Malaya, 50603, Kuala Lumpur, Malaysia
[2]Power Engineering Society, IEEE Malaysia Chapter

Abstract— **This paper describes the development of a rule based expert system to classify risk in dengue infections using bioelectrical impedance analysis (BIA). This system is able to classify three types of risk groups in dengue infections; higher risk, lower risk and no risk (healthy) groups. The classification process was done according to gender, reactance value of the BIA and 'day of fever' on a daily basis diagnosis. BIA measurements have been conducted on 209 serological confirmed dengue patients during their hospitalisation in University Kebangsaan Malaysia Hospital (HUKM), and 223 healthy subjects in Malaysia. The rules were developed based on the 95% confidence interval ranges of reactance value for each risk group obtained from the univariate analysis of variance (ANOVA) analysis. The system was designed and programmed via Visual Basic 6.0. Graphical user interface were employed, in order to enhance user interaction with the system. The system is able to classify the risk in dengue patients non-invasively with total classification accuracy of 66.7%.**

Keywords— **Dengue haemorrhagic fever, expert system, univariate analysis of variance, classification, risk**

I. Introduction

Dengue fever (DF) and Dengue Hemorrhagic Fever (DHF) have caused significant morbidity and mortality in tropical and subtropical region in the world. DF is always associated with fever, headache, myalgia and arthralgia. A small percentage of DF patients will progress to a more severe form of disease, known as dengue haemorrhagic fever (DHF)[1]. The major pathophysiological change of DHF are plasma leakage resulting in increasing haematocrit (20% absolute rise from the baseline) leading to haemoconcentration, and a serous effusion that may lead to shock [1-3].

The current gold standard technique in monitoring risk in dengue patients is to take the patient s blood sample for the measurement of total haematocrit (HCT), haemoglobin (Hb) concentration, platelet count and liver function status [1,4]. This technique is invasive and regular blood sampling will cause further injury to the subcutaneous tissue and potentially risky to dengue patients [5]. Hence, non-invasive approaches in classifying and monitoring the risk in dengue patients are very crucial to be developed as alternatives to the conventional practices.

Even though, Ibrahim *et al* [5] have proven that the gender, day of fever, and reactance values were significant predictors in classifying risk, it is not yet appropriate for the real application in the hospital. Thus, this paper describes the development of rule based expert system for dengue fever and dengue haemorrhagic fever to classify the daily risk in patients using bioelectrical impedance analysis (BIA) for future clinical application.

II. Subjects and methods

A. Subjects

A database obtained from [5,6], a total of 209 adult patients aged 12 years old and above, serologically [1] confirmed dengue patients during their hospitalisation in University Kebangsaan Malaysia (HUKM) and a total of 223 voluntary healthy subjects were analyzed. The database is divided into 2 sets: i) clinical data ii) BIA data

i) Clinical data

The clinical blood investigation database comprises of information pertaining patient information and 27 blood investigation parameters such as: platelete (PLT), Hematocrit (HCT), Aspartate aminotransferase (AST), alanine aminotransferase (ALT) and Hemoglobin (Hb).

The blood investigation data was taken for 5 days with reference to the day the fever subsided (fever day +0). Fever day +0 is defined as the day the fever subsided, i.e., when the body temperature fell below 37.5°C. Fever days after fever day +0 are fever days +1 and onwards. The blood measurement was taken from fever day +0 until the fever day +4 (fourth day after fever subsided)[5,6].

ii) BIA data

The BIA database comprises of patient information and 17 BIA parameters including the resistance, reactance, body capacitance, fat mass, intracellular water and etc. The BIA information was also taken for 5 days with reference to the day of fever subsided to the fourth day after fever subsided i.e. from fever day +0 to fever day +4 [5,6].

F. Ibrahim, N.A. Abu Osman, J. Usman and N.A. Kadri (Eds.): Biomed 06, IFMBE Proceedings 15, pp. 50-53, 2007
www.springerlink.com ' Springer-Verlag Berlin Heidelberg 2007

B. Methods

The severity of dengue risks criteria were determined based on the blood investigations conducted by Ibrahim et al [5,6]:

1. Platelet (PLT) count was less than or equal to 30000 cells per mm3 [7, 8]
2. Hematocrit (HCT) increase by more than or equal to 20% [1]
3. Aspartate aminotransferase (AST) and Alanine aminotransferase (ALT) levels rose by 5-fold the normal upper limit for AST and ALT [4].

The risk quantification was performed on daily basis where blood information of the patient was evaluated for each day and formed into 2 groups [5,6]:

1. Group 2 (Lower risk group) accounted for the DHF patient who did not experienced any of the defined risk criteria, or experienced only 1 of the 3 risk criteria.
2. Group 3 (Higher risk group) accounted for DHF patient who experienced 2 or more risk criteria.

Patients were then classified according to their groups and subsequently, the corresponding patient BIA data were obtained and quantified.

The healthy subjects were automatically grouped as Group 1(Control data) which is the control group for healthy female and male subjects without taking any blood evaluation, however based on their BIA measurements.

III. Statisical analysis

The statistical analysis was performed using Statistical Package for Social Sciences (SPSS) statistical package version 12 for Window XP. Simple linear regression and Kolmogrov-Sminorv Z test were used to examine the normality assumption and for test of significant. The clustered error bar chart displaying 95% confidence interval for reactance value was drawn. Univariate Analysis of Variance (ANOVA) was used to estimate the mean and standard error as well as the 95% confidence interval for all the BIA parameters. The results were considered statistically significant if the p-value was ≤ 0.05.

IV. Development of a rule based expert system

The development of the rule based expert system in this study involved as followings:

Identifying the objective of the expert system development
Designing the tree structure of the problem domain.
Developing the user interface, inference engine and patient database
Testing the performance of the database

A. Identifying the problem

The objective of the development of this expert system is to build a ruled based expert system that can classify risk in dengue patients according to their reactance value, gender and day of fever [5, 6].

B. Tree Diagram

The tree structure of an expert system visualizing the flow of decision making is based on the ANOVA result of the 95% confidence interval (CI) for the reactance value. In this study, the 95% CI of reactance value as shown in Table I, was an improved version from study conducted by Ibrahim et al [5] from 183 dengue patients in [5] to 209 dengue patients. While, for the healthy subjects from 142 in [5] to 223 subjects.

Table 1 Reactance mean values for each group and gender (Gender (G) coding, Female = 0, Male = 1)

Risk	Days	No of sample	Gender	Mean– Std. Error (Ω)	95% CI Min-Max
1	Control	158	0	69.37–0.94	67.51-71.22
2	0	25	0	58.03–2.37	53.37-62.70
2	1	34	0	58.92–2.04	54.92-62.91
2	2	29	0	61.31–2.20	56.98-65.64
2	3	26	0	61.43–2.33	56.85-66.00
2	4	13	0	54.95–3.29	48.49-61.42
3	0	20	0	55.54–2.65	50.33-60.76
3	1	37	0	50.09–1.95	46.25-53.92
3	2	34	0	48.25–2.04	44.25-52.25
3	3	26	0	49.52–2.33	44.95-54.10
3	4	15	0	45.81–3.06	39.79-51.83
1	Control	65	1	72.79–3.43	66.04-79.53
2	0	35	1	55.12–4.68	45.93-64.31
2	1	44	1	55.07–4.17	46.87-63.27
2	2	44	1	56.28–4.17	48.09-64.48
2	3	29	1	58.55–5.14	48.45-68.65
2	4	12	1	59.95–7.98	44.25-75.65
3	0	28	1	52.71–5.23	42.43-62.99
3	1	44	1	53.81–4.17	45.61-62.01
3	2	46	1	54.65–4.08	46.63-62.67
3	3	32	1	55.28–4.89	45.67-64.59
3	4	16	1	58.03–6.91	44.43-71.62

F. Ibrahim, N.A. Abu Osman, J. Usman and N.A. Kadri (Eds.): Biomed 06, IFMBE Proceedings 15, pp. 50-53, 2007
www.springerlink.com ' Springer-Verlag Berlin Heidelberg 2007

However, the 95% confidence intervals for the classification of risk group in Table I was not continuous. There were many gaps and overlapping reactance value in between the intervals in which not included in the classification intervals, leaving holes in the output probability. Hence, to resolve the problem, the new cutoff midpoint between the upper and lower limit of each interval was reconstructed. These new value was used as threshold limit to eliminate the gap intervals for developing the expert system production rules.

C. Rule Based Expert Sysytem

Rule based expert system is a computer program that represents the knowledge of experts in a narrow and specialized domain. Expert system was built based from the idea that human solves problem by applying their knowledge expressed as rules to a given problem represented by problem specific information [9]

Basic structures of the rule based expert system include the knowledge base, database, inference engine, explanation facilities and user interface. In this study, the expert system was developed using Microsoft Visual Basic (VB) 6.0. The VB 6 was chosen because it is very powerful and yet very easy and simple to program [10].

The Visual basic programming process includes starting the visual basic, create new application or load the existing application wizard, test the application by using the VB Debugging tool and compile program into the final application [11].

D. Architecture of the Expert System.

The Dengue expert system comprise of 5 user interface frames include:

Index or main frame
Daily Analysis Frame
Information frame and
About frame.

The index frame provides links to the analysis systems and contains dialog boxes to request for patients clinical data. The Daily Basis analysis frame provides interface to support calculation by requesting the day of fever and reactance value. Information frame and About frame both provide information on dengue fever and the information about the Expert system developer respectively.

E. Structure of the Patient Database

The patient database was developed using Microsoft Access. Microsoft Access is a program that is used to create databases and programs to manage information. The patient s form which contents the following information:

Patient ID (auto generated)
Patient s number
Patient s name
Gender
Reactance value
Category of Risk
Day
Date

were stored in the database soon after the inference engine has completed each calculation. The database was queried and administered by using Win SQL. This feature is very vital as complement to expert system since physicist and researcher may need the information to further investigate the disease in the future.

V. Results and discussions

The rule based expert system for classifying DF and DHF using BIA has been developed and tested. The testing data comprises of 15 control data, 15 lower risk and 15 higher risk dengue patients data. The system is able to classify the risk in dengue patients with total accuracy of 66.67%. The detail testing results is tabulated in Table II.

Table 2 Dengue s expert system testing results.

Risk	No of testing samples	Classification	Accuracy
Normal	15	10/15	66.67 %
Lower risk	15	9/15	60%
Higher risk	15	11/15	73.33 %
		Total Acuracy	66.67%

The expert system rules that used the reconstruction of the 95% confidence interval of patient s reactance value were not precise. Moreover, certain ranges in the 95% confident intervals of reactance value were overlapping which contributes to a significant drop in the expert system s risk classification accuracy.

VI. Conclusion and future work

The rule based expert system for DF and DHF risk classification findings showed that the system is a non-invasive, rapid and safe that makes it practical for future clinical application. Future work is to improve and increase the classification accuracy of the system by employing a non-linear modeling technique such as the artificial neural network (ANN). ANN is a powerful non-linear statistical paradigm for recognition of complex patterns with the ability to maintain accuracy even when some input data are missing.

F. Ibrahim, N.A. Abu Osman, J. Usman and N.A. Kadri (Eds.): Biomed 06, IFMBE Proceedings 15, pp. 50-53, 2007
www.springerlink.com ' Springer-Verlag Berlin Heidelberg 2007

Acknowledment

This research was supported by University of Malaya, and Sultan Iskandar Johore Foundation Greatest appreciation to all the dengue patients involved the authorities and the staff of HUKM for hosting and supporting this research. HUKM Ethics approval code D-004-2002.

References

1. WHO (1997), Dengue Haemorrhagic Fever, Diagnosis, Treatment, Prevention & Control. Second Edition. Geneva: World Health Organization, 2nd ed., World Health Organization (WHO), Geneva.
2. S Nimmannitya, S, Halstead, SB, Cohen, Margiotta, MR, Dengue and chikungunya virus infection in man in Thailand, 1962-1964. I. Observations on hospitalised patients with haemorrhagic fever (1969) *American Journal of Tropical Medicine and Hygiene,* **18**,954-971
3. Nimmannitya, S, (1987) Clinical spectrum and management of dengue fever *Southeast Asian Journal of Tropical Medicine and Public Health*, **18**,392-397
4. Kuo, C.H, Tai, D.I, Chang-Chein, C.S, Lan, C.K, Chiou, S.S., and Liaw, Y.F., (1992) Liver Biochemcial test and Dengue fever, *American Journal Tropical Medicine Hygiene,* **47(3)**, pp. 265-270.
5. Ibrahim, F., Taib, M.N., Wan Abas, W. A. B., Chan, C.G. and Sulaiman, S. (2005), A Novel Approach to Classify Risk in Dengue Hemorrhagic Fever (DHF) Using Bioelectrical Impedance Analysis (BIA). Proceeding of IEEE Transaction on Instrumentation and Measurement , **54(1)**, pp. 237-244.
6. Ibrahim F.,(2005) : Prognosis of Dengue Fever and Dengue Hemorrhagic Fever Using Bioelectrical Impedance . Ph.D Thesis, Department of Biomedical Engineering, Faculty of Engineering, University of Malaya,
7. Chua, M.N, Molanida, R, Guzman, M.D, and Laberiza, F, Prothrombin Time and Partial Thromboplastin Time As A predictor of Bleeding in Patients with Dengue Hemorrhagic Fever, *Southeast Asian Journal Tropical Medicine Public Health,* **24**, pp. 141-143, 1993.
8. D.Y.H Tai, Y.C. Chee, and K. W. Chan, The natural history of dengue illness based on a study of hospitalized patients in Singapore, *Singapore Medical Journal*, **40**, pp. 238-242, 1999.
9. Negnevitsky, M (2002): Artificial Intelligence, A Guide to Intelligent Systems , (Addison-Wesley)
10. Mann, A.T.(1995): Real World Programming with Visual Basic 4.0, 2nd Edition, SAMS Publishing,
11. Perry G, and Hettihewa, S, (1998): Teach yourself Visual Basic 6 in 24 Hours . SAMS Publishing,

Author: Fatimah Ibrahim
Institute: Department of Biomedical Engineering,
Faculty of Engineering, University of Malaya
Country: Malaysia
Email: fatimah@um.edu.my

F. Ibrahim, N.A. Abu Osman, J. Usman and N.A. Kadri (Eds.): Biomed 06, IFMBE Proceedings 15, pp. 50-53, 2007
www.springerlink.com ' Springer-Verlag Berlin Heidelberg 2007

Comparison of MLP and Elman Neural Network for Blood Glucose Level Prediction in Type 1 Diabetics

S.A. Quchani, E. Tahami

Biomedical Engineering Department of Azad University, Mashhad, Iran

Abstract— **One of the most dangerous symptoms of Type 1 diabetes is the frequent and grate oscillation of blood glucose level that can lead the patient to unconscious and coma states . So being able to predict and finally prevent these two symptoms would simplify the management of the diabetic patients. This paper attempts to comparison the performance of MLP and Elman neural networks to predict the blood glucose levels in type1 diabetics. Data set, used in this paper consists of the protocol of a 10 Iranian type1 Diabetic women and include features such as type and dosage of injected insulin, The period of time (in hour) between two consecutive measurements of the blood glucose level, carbohydrate intake , exercise and the blood glucose level measured at start of the given period of time. Finally we concluded that the usage of Recurrent Neural Network such as Elman can be an appropriate model to predict the long term blood glucose level in type 1 diabetics also we could successfully increase the accuracy of prediction and reduce the number of layers and neurons used in the construction of Neural Networks.**

Keywords—**Diabetes, Blood glucose prediction, Elman, MLP, Neural Network**

I. Introduction

Diabetes mellitus is one of the most widespread chronic diseases known in the world that mostly extending in developed and developing countries, so that it is forecasted 220 million people will have this disease till 2010. Now Diabetes mellitus is one of the most common chronic diseases with approximately 1.5 million affected people, just in Iran [1] .

Most dangerous and basic symptoms associated with this disease are related to the frequent and grate oscillation of blood glucose level known as a hypoglycemic and hyperglycemic which can lead the patient to unconscious or coma states and finally some other complications such as heart attack , blindness, diabetics foot and mental disturbance.

Because of this, the methods that can reduce the number of blood glucose level registration and also predict and prevent these two fundamental symptoms are the best ways to control and cure the diabetes.

Different computer-assisted approaches have been attempted to predict blood glucose levels and insulin requirements such as mathematical minimal models [2-12] Most of these models also incorporate prediction of the patient s response to insulin and recommendations on supplements, adjustments, or dietary modification. These approaches have been based on complicated algorithms or mathematical models or combinations of the two. Still, there are many detectable and undetectable factors that are difficult to measure and incorporate into a model, making the model more or less uncertain. The ideal prediction tool should minimize the impact of such factors.

In this paper we attempted to compare the performance of MLP and Elman neural networks in blood glucose levels prediction and improved the accuracy of prediction and also reduce the number of layers and neurons used in the construction of neural network in comparison with previous researches in this case.

II. Data and Method

A. Data

Dataset used in this paper consists of the protocols of a 10 Iranian type1 Diabetic women with the ages between 17 and 26 that include features such as:

- Dosage of injected short acting insulin (unit)
- Dosage of injected long acting insulin (unit)
- Period of time between two consecutive measure ments of the blood glucose level(hour)
- Stress level (unit)
- Carbohydrate intake (gr)
- Exercise(unit)
- Blood glucose level measured at the start of the given period of time(FBGL) (mg/dlit)

The recorded data that was used covers a continuous period of 75 days for some of patients and 135 days for another. For each day we have recorded data just in the morning and afternoon and during this interval. 75% of this recorded data is used to train the neural network and 25% is used to test the neural.

It is noticeable that the carbohydrate intake was an estimate in grams. Exercise is expressed on a four step scale from one to four, which one means doing nothing and four expresses heavy exercise. A scale from one to four was also

F. Ibrahim, N.A. Abu Osman, J. Usman and N.A. Kadri (Eds.): Biomed 06, IFMBE Proceedings 15, pp. 54-58, 2007
www.springerlink.com ' Springer-Verlag Berlin Heidelberg 2007

used for stress, which one means relaxing and four expresses heavy stress .In this paper First, Blood Glucose Level (FBGL) has been recorded before breakfast and Next, Blood Glucose Level (NBGL) has been recorded before launch in each day. A sample of data is shown in Table 1.

Table 1 Sample of dataset

FBGL	Short Acting Insulin	Long Acting Insulin	Stress Level	Exercise Level	Carbohydrate	Time Interval	NBGL

B. Methodology

Designed algorithm for prediction of e blood glucose level has five steps. In first step data are divided in two groups of testing and training sets. In second step data must be normalized for using in neural network. In third step data are fed into the neural network and finally in forth step the output of neural network must be renormalized to return in the correct blood glucose ranges. Block diagram of our designed algorithm has shown in Fig. 1.

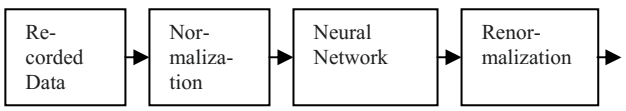

Fig.1 Block diagram of designed algorithm for prediction of blood glucose level in type one diabetics

It must be emphasized that the present method results in an individual model , valid for that particular patient under a limited period of time because the blood glucose affected by some physiological conditions such as age, weight, sex and even some other non physiological factors . However, the method itself has general validity, since the blood glucose variations over time have similar properties in any diabetic patient.

C. Multilayer neural networks

Multilayer perceptron neural networks are capable of learning and parallel processing, which are valuable specifications; and commonly are being used for solving complicated problems. In these networks, learning process is accomplished by specific algorithms which adjust existing weights between neuron connections.

Neural network used in proposed intelligent algorithm, is a 3 layer MLP which has a hidden layer with 5 neuron and 1 neuron in output layer. Learning criteria is based on back propagation. MATLAB is used to design MLP neural network. Neuron active functions of each layer are used to determine the threshold of output layer. For output layer logsig activation functions and for hidden layer tansig activation functions have been used

Neural network weights, by considering back propagation algorithm , are improving automatically in iteration stages calculated by (2) , in other words weight x in each moment equals to weight in previous moment plus gradient error function g_k in each stage, which is multiplied by learning rate a_k and this will repeated so many times until the weights vector reaches its optimal degree which is calculated by (3), versus this optimal degree, error criterion reaches its minimum. Error criterion is mean square error MSE here.

$$X_{k+1} = X_K - a_k g_k \tag{1}$$

$$MSE = \frac{1}{N}\sum_{k=1}^{N}(t(k) - a(k))^2 \tag{2}$$

t(k) is expected output , a(k) is real network output and N is number of iterations.

It should be pointed out that in initializing the algorithm, some initial quantities are being chosen randomly for weights and then these quantities will improve during performance of the algorithm. Bias quantity which adjust the activation function also designate and shift the threshold amount of each activation function. As the initial quantities were random for weights, initial quantities for bias are also random. The entire network construction and parameters is tabulated in Table 2.

Table 2 MLP Neural Network construction

Number of input	7
Network Configuration	[5 1] tansig pure line
Learning Rate	0.01
Number of epochs	300
Training goal accuracy	0.1

Fig. 2 shows the results of blood glucose level time series prediction with the MLP neural network for one of diabetics. Finally the mean absolute error between recorded and predicted blood glucose levels for testing and training sets is tabulated in Table 3.

F. Ibrahim, N.A. Abu Osman, J. Usman and N.A. Kadri (Eds.): Biomed 06, IFMBE Proceedings 15, pp. 54-58, 2007
www.springerlink.com ' Springer-Verlag Berlin Heidelberg 2007

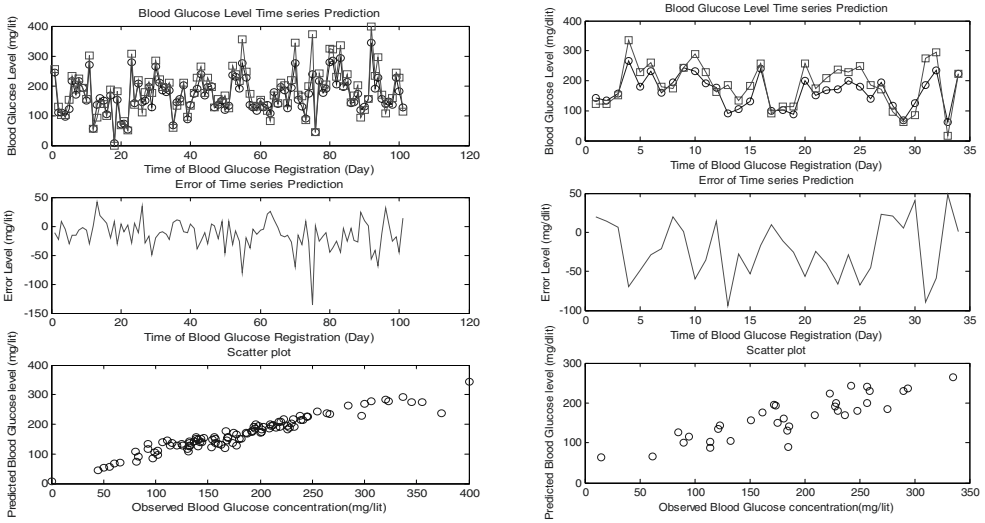

Fig.2 The plots show the blood glucose level time series prediction for two parts which part (A) is related to the training set and part (B) is related to the testing set. At the top of each part the small circles indicate real recorded blood glucose levels and the small squares indicate predicted blood glucose levels. Predicted Error and scatter function are plotted in the next terms.

Table 3 Mean of prediction Errors for training and testing of MLP Neural Network

Steps of prediction	Mean absolute error of prediction
Training step	22.5289 (mg/dlit)
Testing step	24.1449 (mg/dlit)

D. Recurrent Neural Network

In contrast to feed-forward networks partially recurrent neural networks, especially the Elman net, offer a good compromise between complexity and capability. After modifying the network by introducing additional feedback loops in the context layer of the Elman net as shown in figure 3 it is able to learn the process that their current state heavily depends on events that took place in the past.

The Elman Recurrent Neural Network is used in this paper has an identical construction with the MLP Neural Network in number of neurons, number of layers, Type of activation functions and also training algorithm .The only difference between two types of neural network is just related to the delays used in the feedback loops of Elman Recurrent Neural Network .The Elman Neural Network we used in this paper is shown in Fig. 3.

According to the Fig. 3 the outputs of the Elman Recurrent Neural Network at each time step can be calculated as follows where $a_j(k)$ is the output of the hidden layer, IW_{ij} are the weights of the input layer, LW_{ij} are the weights of the feed back and V_j are the weights of the output layer.

$$a_j(k) = \tan sig(X_i \cdot IW_{ij} + a_j(k-1).LW_{ij}) \quad (3)$$

$$BGL = pureline(a_j(k) \cdot V_j) \quad (4)$$

Fig. 4 shows the results of blood glucose level time series prediction with the Elman Recurrent neural network for one of diabetics.

The mean absolute error between observed and predicted blood glucose levels for testing and training sets are shown in Table 4.

Table 4 Mean of prediction Errors for training and testing of Elman Recurrent Neural Network

Steps of prediction	Mean absolute error of prediction
Training step	5.4597 (mg/lit)
Testing step	10.4023 (mg/lit)

F. Ibrahim, N.A. Abu Osman, J. Usman and N.A. Kadri (Eds.): Biomed 06, IFMBE Proceedings 15, pp. 54-58, 2007
www.springerlink.com ' Springer-Verlag Berlin Heidelberg 2007

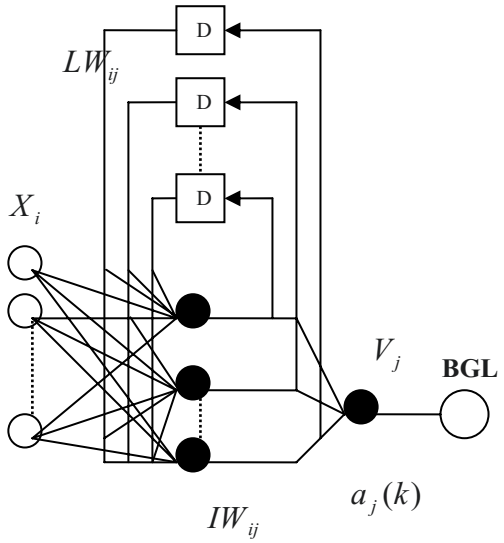

Fig.3 Elman Recurrent Neural Network

By comparing Tables 3 and 4 we can conclude that the Elman Recurrent Neural Networks have more appropriate accuracies than the MLP Neural Networks in the blood glucose level prediction process.

This result adapted to the real blood glucose regulatory system of the body because the glucose metabolism is characterized by the fact that the current state heavily depends on events (meals, insulin injections , exercise) that took place in the past and this factor an be provided with time delays in the construction of Elman Recurrent Neural Networks.

III. Conclusions

On of the most dangerous and basic symptoms associated with the diabetes disease are related to the frequent oscillation of blood glucose level known as a hypoglycemic and hyperglycemic that can lead the patient to unconscious and coma states .For this reason it is necessary to use, methods which can decrease the registration number of blood glucose level and also predict and prevent these two fundamental symptoms.

In this paper we could successfully compare the performance of MLP and Elman neural networks and then we conclude that the performance of Elman Recurrent Neural Network is better than the MLP Neural Network for blood glucose levels prediction also we could increase the accuracy of prediction and reduce the number of layers and neurons used in the construction of neural network in comparison with previous researches in this case which make the algorithms faster and simpler. To improve the accuracy of blood glucose time series prediction we suggest that the number of effectiveness features must be increased and the intervals between data registration must be decreased also optimization of Neural Network construction with other intelligent methods such as Genetic algorithms or Fuzzy Logics are another ways to achieve this goal.

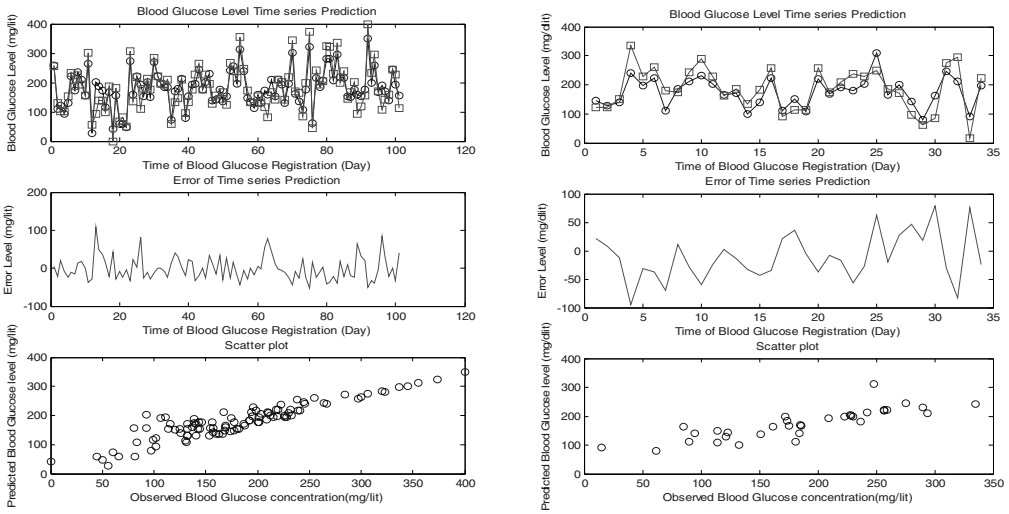

Fig.4 The plot show the blood glucose level time series prediction for two parts that part (A) related to the training set and part (B) is related to the testing set. At the top of each part the small circles indicate the recorded blood glucose levels and the small squares indicate the predicted blood glucose levels. Predicted error and scatter function are plotted in the next terms.

F. Ibrahim, N.A. Abu Osman, J. Usman and N.A. Kadri (Eds.): Biomed 06, IFMBE Proceedings 15, pp. 54-58, 2007
www.springerlink.com ' Springer-Verlag Berlin Heidelberg 2007

References

1. B. Larijani, M.D; F. Zahedi, M.D; Sh. Aghakhani, M.D Epidemiology of Diabetes Mellitus in Iran Shiraz E-Medical Journal , Vol. 4, No. 4, October 2003
2. Martin H. Kroll, "Biological variation of glucose and insulin includes a deterministic chaotic component" BioSystems 50 (1999) 189 201
3. E.Carson et al. , 1992 A Spectrum of Approaches for Controlling Diabetes , IEEE Transactions onControl Systems, No.12 Andreassen, S., Benn, J., Hovorka, R., et al. A probabilistic approach to glucose prediction and insulin dose adjustment: Description of metabolic model and pilot evaluation study. Comput.Methods Programs Biomed. 41, 153, (1994).
4. Deutsch, T., Lehmann, E. D., et al. Time series analysis and control of blood glucose levels in diabetic patients. Comput. Methods Programs Biomed. 41, 167, (1994).
5. Lehmann, E. D., Deutsch, T., et al. AIDA: An interactive diabetes advisor. Comput. Methods Programs Biomed. 41, 183, (1994)
6. A. De Gaetano, O. Arino, Mathematical modelling of the intravenous glucose tolerance test, J. Math. Biol. 40 (2000) 136 168.
7. R.N. Bergman, Pathogenesis and prediction of diabetes mellitus: Lessons from integrative physiology, in: Irving L.Schwartz Lecture, Mount Sinai J. Medicine 60 (2002) 280 290.
8. D.L. Bennett, S.A. Gourley, Asymptotic properties of a delay differential equation model for the interaction of glucose with plasma and interstitial insulin, Appl. Math. Comput. 151 (2004) 189 207.
9. J. Li, Y. Kuang, C. Mason, Modeling the glucose-insulin regulatory system and ultradian insulin secretary oscillations with two time delays, submitted for publication.
10. Leaning M. S. and Boroujerdi M. A., "A system for compartmental modeling and simulation," Comput. methods programs biomed., vol. 35, 1991
11. Tresp V., Moody J., and Delong W.-R., \Neural modeling of physiological processes," Computational Learning Theory and Natural Learning Systems, vol. 2, 1994, S. Hanson et al., eds., MIT Press.
12. A. Drozdov, H. Khanina, A model for ultradian oscillations of insulin and glucose, Math. Comput. Modeling 22 (1995) 23 38.

Address of the corresponding author:

Author: Ehsan Tahami
Institute: Biomedical Engineering of Azad university of mashhad
Street: Ghasem abad ostad usefi
City: Mashhad
Country: Iran
Email: ehsantahami@yahoo.com

F. Ibrahim, N.A. Abu Osman, J. Usman and N.A. Kadri (Eds.): Biomed 06, IFMBE Proceedings 15, pp. 54-58, 2007
www.springerlink.com ' Springer-Verlag Berlin Heidelberg 2007

Electroglottographic Signal Acquisition and Neural Network based classification for pathology

G.Subramanya. Nayak and Jagdish Nayak

Manipal Institute of Technology/E&C Engineering, MAHE, Manipal , INDIA

Abstract— **The method is used to register the laryngeal behavior indirectly by measuring change in the electrical impedance across the throat during speak or voice. The RF carrier signal is amplitude modulated by the modulating speech/ voice signal and the dc component from the demodulated signal is extracted. The variations in the dc component corresponds to the vocal fold abduction/laryngeal movement. For normal and pathology conditions the results are recorded. These values form a feature vector which reveal information regarding pathology. Then a classical multilayer feed forward neural network with back propagation algorithm is employed to serve as a classifier of the feature vector, giving 100% successful results for the specific data set considered.**

Keywords— **Electroglottography (EGG), Artificial Neural Network (ANN) , Back propagation algorithm**

I. Introduction

The voice pathology are very common in all over the world. In the current study the vocal fold abduction /laryngeal movement of normal and pathology patients have been recorded in terms of dc component of demodulated signal and MATLAB @6.1 supported neural network algorithms are used for classification.

II. Instrumentation

The electrodes are made of steel. They have the form of rectangles covering an area of 8.75 cm^2.It may be designed as a separate electrode or as a ring electrode encircling each of the two other electrodes. The electrodes are mounted on a flexible band whose length may be adjusted to hold the electrodes in a steady position and to still allow the subject to comfortably speak and breathe naturally.

The electrodes are mounted on a small holder which is pressed against the throat by hand. A signal generator supplies an AC sinusoidal current usually ranging from 300 KHz to 5 MHz as shown in Figure 1.

The frequency selected for the above test is 1 MHz. This frequency is sufficiently high, so that the current capacitancively bypasses the less conductive skin layer without the use of additional conductive paste [1]. The generator may produce constant voltage or constitute constant current source [1]. The supplied current is different for each particular device, but is not stronger than several milliamperes. The voltage between the electrodes depends on the tissue impedance [1-3].The power dissipation of only several microwatts occurs at the level the subject 's vocal folds.

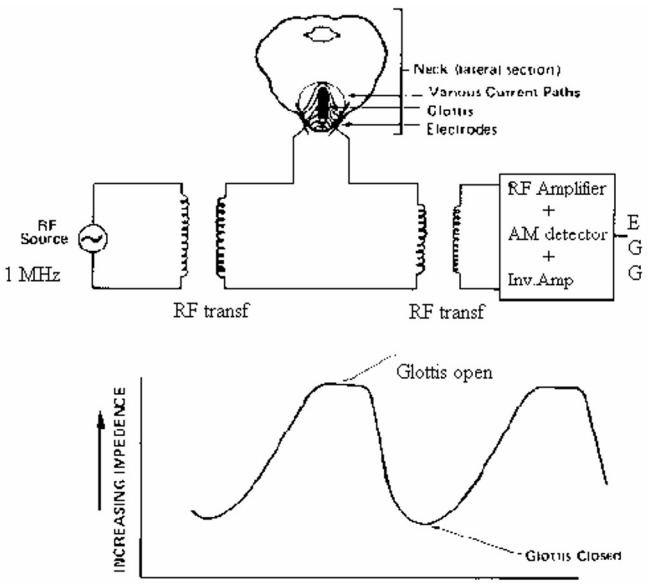

Fig. 1 Instrumentation for EGG

An integral part of the electroglottographic signal is the varying component generated by the vertical movement of the whole larynx. Therefore, the signal of rapid movements of the vocal folds is superimposed on the signal produced by the slower movements of the other structures. Fourcin & Abberton proposed the name Gx for the waveform of larynx movement and the name Lx for the vibration component. The Gx component originates, for example can be observed in swallowing, but it is caused by the vertical movement of the larynx which is related to the voice quality setting of the raised/ lowered larynx. Gx to calculate vocal fold abduction[1]

F. Ibrahim, N.A. Abu Osman, J. Usman and N.A. Kadri (Eds.): Biomed 06, IFMBE Proceedings 15, pp. 59-62, 2007
www.springerlink.com ' Springer-Verlag Berlin Heidelberg 2007

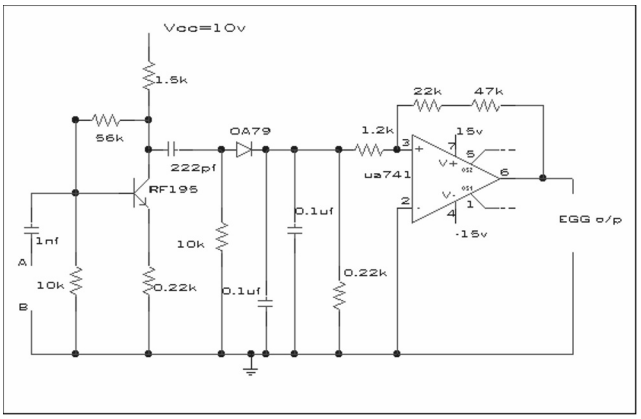

Fig. 2 RF Amplifier and diode detector

The DC offset changes (Gx) can be evened out because, the effects of the varying larynx height are compensated by the use of additional electrodes or high pass filtering of the registered signal. The sensing electrode detects the current as it passes through the skin and the throat .The percentage of amplitude modulation of the received signal reflects the percentage change in tissue impedance in the current s path. The output from the second RF transformer is then amplified using the above RF amplifier circuit. The output is demodulated using a diode detector circuit (Gx + Lx) .The DC component of the output is then amplified using a OPAMP inverting amplifier (Gx) as shown in Figure. 2. The output readings were recorded.

III. ANN IMPLEMENTATION

An ANN structure is employed for the classification of speech/voice pathology. It consists of four modules as shown in Figure 3.

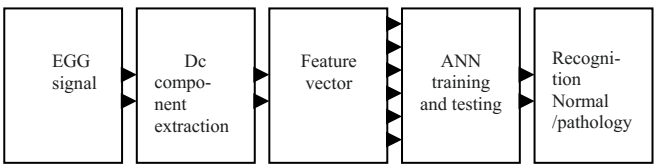

Fig. 3 The model of ANN

A. Design of ANN with Back Propagation Algorithm:

Three layer networks are sufficient to design any nonlinear network. [4, 5].Input is a layer of nodes with four feature vectors as input. Single second and third layers have same activation function for all neurons. Activation function is a tan sigmoid function as shown in Figure 4.

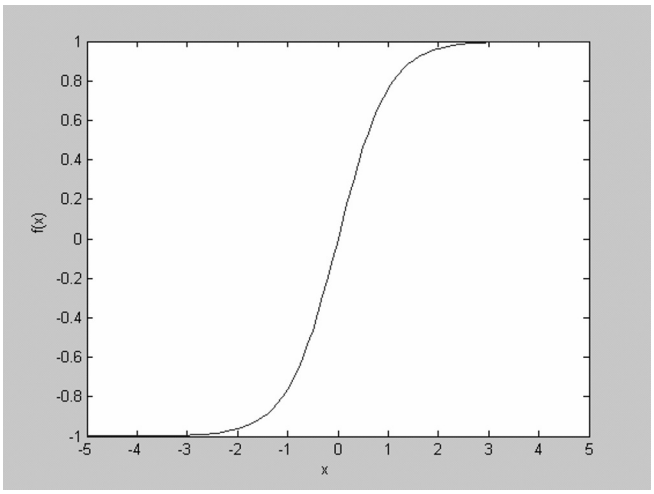

Fig. 4 Activation function Tan sigmoid

Single hidden layer is considered. An optimum number of seven neurons are considered in hidden layer and one neuron in output layer. The performance goal is set at 0.0001accuracy. Number of epochs is set for 15,000. The learning cycle updates the weights of output layer and progress backwards. Error function is MSE and updating in negative gradient [6 -8].Hence it is a gradient descent algorithm.

Gradient descent is a standard Back propagation Algorithm. But it is too slower and convergence depends on learning rate. Hence high performance algorithm (Levenberg Marquardt algorithm) which operate in batch mode is used.

B. Training of ANN:

Data from normal and pathology were obtained from Kasturba Medical College Hospital, Manipal Academy of Higher Education, Manipal. Data of 12 normal and 12 pathology are used to train the network.

Feature vector is constructed and training program is executed. The training of ANN stops once the performance goal is met, as shown in Figure 5. The convergence is achieved in 131 epochs.

F. Ibrahim, N.A. Abu Osman, J. Usman and N.A. Kadri (Eds.): Biomed 06, IFMBE Proceedings 15, pp. **59**-62, 2007
www.springerlink.com ' Springer-Verlag Berlin Heidelberg 2007

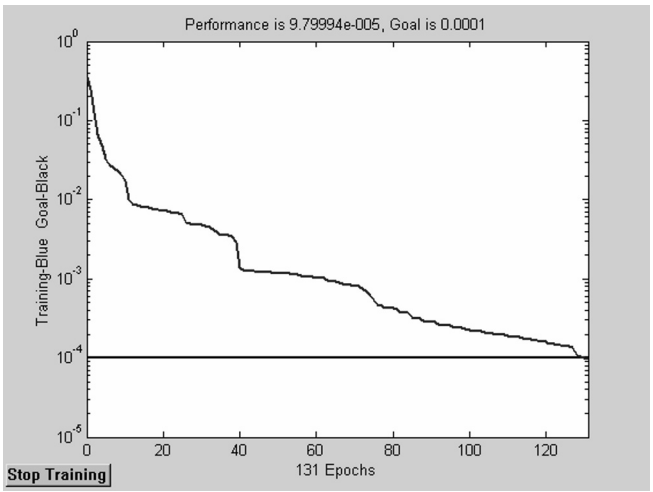

Fig 5. Training of ANN

IV. Results and discussion

Feature vector of 09 test data of *Normal* and 09 test data of *pathology* are given to network to classify. The results are shown in Table 1.

Table 1 Classification results

Test data	Desired output	Classifier output	Output Characterization
N1	1	1.0000	normal
N2	1	1.0000	normal
N3	1	1.0000	normal
N4	1	1.0000	normal
N5	1	1.0000	normal
N6	1	1.0000	normal
N7	1	1.0000	normal
N8	1	1.0000	normal
N9	1	1.0000	normal
P1	-1	- 0.9025	pathology
P2	-1	-0.9008	pathology
P3	-1	- 0.8025	pathology
P4	-1	-0.9078	pathology
P5	-1	-0.8070	pathology
P6	-1	-0.1000	pathology
P7	-1	- 0.8970	pathology
P8	-1	-0.8033	pathology
P9	-1	0.9776	normal

The ANN is trained with the data of 12 normal and 12 pathology each. The network is then tested with the feature vector of 09 test data of normal and 09 test data of pathology. The results obtained show 100% specificity, 90.0% sensitivity and 94.4% accuracy. Furthermore, a small time needed to acquire and analyze the fluorescence spectra together with the high rates of success, proves our method very attractive for real time applications. As less number of features is used, computational delay in training the ANN is reduced.

The amplitude of the signal changes because of permanently varying vocal fold contacts. It depends on the configuration and placement of electrodes, the electrical contact between the electrodes and the skin, the position of the larynx and the vocal folds within the throat, the structure of the thyroid cartilage, the amount and proportion of muscular, glandular and fatty tissue around the larynx, the distance between the electrodes.

It may happen that the impedance fluctuation caused by the vocal fold movements is too weak to be registered.[1,9].It also has to be noted that EGG signals of acceptable quality are harder to obtain from women and children than from men. This is related to the smaller mass of vocal folds, the wider angle of the thyroid cartilage and different proportions between different types of tissue [10,11].

The DC offset changes are to be taken for large number of data set of normal and pathologies and further analysis can be done on vertical movement of the larynx which is related to the voice quality setting of the raised /lowered larynx. This gives us to firmly decide on the pathological condition. Suitable addition to the standard configuration of the device consists of instruments for measuring the signal strength (e.g. LED) [12].

V. Conclusions

Despite the problems just mentioned, electroglottography has established itself as a valuable method for evaluating laryngeal behavior. In comparison to other methods of glottography, Frokjaer - Jensen observed as early as 1969 that electroglottography allows for a better representation of the closed and closing phases of vocal fold movement, especially of the vertical contact area. The EGG is superior to all other methods and is not uncomfortable to speakers as it is completely non-invasive. (it exerts no influence at all on the articulation and production of sounds).

Acknowledgment

We are thankful to Dr. G.K.Prabhu for his valuable suggestions during ANN analysis.

F. Ibrahim, N.A. Abu Osman, J. Usman and N.A. Kadri (Eds.): Biomed 06, IFMBE Proceedings 15, pp. **59**-62, 2007
www.springerlink.com ' Springer-Verlag Berlin Heidelberg 2007

REFERENCES

1. http: // www.ims.uni stuttgurt de /phonetic/EGG/Page1.htm
2. Krishnamurthy, Childers (1986) Two Channel Speech Analysis. IEEE Transactions on Acoustics, Speech and Signal Processing. ASSP-34:730-743
3. Robert F.Orlikoff.(1991) Assessment of Dynamics of vocal Fold contact From the Electroglottogram. Journal of Speech and Hearing Reaserch 34:1066 -1072
4. G.S.Nayak, Sudha Kamath et al. (2006) Principal Component Analysis and Artificial Neural Network Analysis of oral Tissue Fluorescence Spectra: Classification of Normal, Premelignant and Malignant Pathological Condition Biopolymers 82:152-166
5. Sigurdur Sigurdsson et al.(2004) Detection of skin cancer by classification of Raman spectra, IEEE transactions on Biomedical Engineering 51: 1784-1793
6. George A.Rovithakis and Michail Maniadakis(2001) Artificial Neural Networks for discriminating Pathologic from Normal Peripheral Vascular tissue *IEEEtransactionsonBiomedicalEngineering*,48:1088-1097
7. Rudra P (2000) Getting started with MATLAB@ 5. Oxford University Press New Delhi
8. Jacek M. Zurada (2002) Introduction to Artificial Neural Systems Jaico Publishing House Mumbai
9. http:// www.lam.jussieu.fr
10. http:// www.ins.uni-stuttgart.de
11. http:// www.glottal.com
12. G.Subramanya Nayak and Gopallakrishna Prabhu K (2004) Analysis of Electroglottographic Signal for Measurement of Vocal Fold Abduction / Larynx Movement ,using Amplitude Modulation Technique,ECCS-2004 Proc. National Conference on Electronic Circuits and Communication Systems, Patiala, India, 2004,pp 463-465

Address of the corresponding author:

Author: G.Subramanya Nayak
Institute: Manipal Institute of Technology
Street: Manipal
City: Karnataka State
Country: India
Email: gs.nayak@manipal.edu / gs_nayak@rediffmail.com

F. Ibrahim, N.A. Abu Osman, J. Usman and N.A. Kadri (Eds.): Biomed 06, IFMBE Proceedings 15, pp. **59**-62, 2007
www.springerlink.com ' Springer-Verlag Berlin Heidelberg 2007

Expert System for Non-Invasive Classification of Total Cholesterol Level Using Bioelectrical Impedance

M.S Mohktar[1], F.Ibrahim[1] and N.A Ismail[2]

[1] Department of Biomedical Engineering, Faculty of Engineering, University Malaya, Kuala Lumpur, Malaysia
[2] Department of Applied Statistics, Faculty of Economics and Administration, University of Malaya, Kuala Lumpur Malaysia.

Abstract—**This paper describes the development of a Rule Based Expert System (ES) to classify the Total Cholesterol (TC) level using Bioelectrical Impedance Analysis (BIA). A total of 199 voluntary subjects were recruited in the study. The BIA parameters that are statistically significant predictors are body capacitance (BC), basal metabolic rate (BMR) extracellular mass (ECM) and lean body mass (LBM). The ES was developed using Bayesian reasoning method. The developed ES is able to classify subjects' TC level between normal (<=5.2 mmol/L) and abnormal (>5.2 mmol/L). From the analysis using 40 testing data, the system total accuracy for classifying TC level at 0.6 probability cut-off prediction was only 70.0%. The sensitivity was 67%, and specificity of 74%. From the validation data, this ES system can classify 6 from 10 subjects correctly.**

Keywords— **Total Cholesterol, expert system, bioelectrical impedance**

I. Introduction

Cholesterol is a substance that can be found in the cell membranes of all body tissues [1]. This substance is important for normal body functioning. It is used for cellular functions, production of hormones and plays a central role in many biochemical processes. Moreover, cholesterol is best known for its association with cardiovascular disease [2].

One of the major cholesterol profiles is total cholesterol (TC). TC is the sum of all the cholesterol in the blood. Recently, to obtain the TC value, blood is to be withdrawn from one of the subject's vein. This procedure is invasive that may carry risk in developing a bruise, or hematoma. [2]. Therefore finding some painless methods would be a need. Hence, this paper describes the development of an expert system (ES) that can classify the TC level using bioimpedance analysis data (BIA) that were measured non-invasively.

II. Methodology

A. Understanding the problem domain and objective

The objective of this expert system is to classify total cholesterol (TC) level according to the subjects age, body mass index (BMI), and the significant predictors from BIA parameters [9].

B. Data Collection

Subjects were recruited through the advertisement of Wellness Programme, University Malaya Students Health Clinics, Kuala Lumpur. A total of 199 subjects were volunteered. They had to fast for 9 to 12 hours and were asked to abstain from doing any exercise in the 9 to 12 hours prior to attendance at the clinic. All subjects were given a consent form for the study. Of the 199 individuals studied, 149 collected data were used for training purpose 40 were used for testing the system and 10 were used for system validation.

C. Anthropometric and Bioimpedance Analysis Measurements

Anthropometric measurements were taken with the subjects in light clothing and without shoes. Height was measured to the nearest 0.1 cm and weight was measured to the nearest 0.1 kg. Body mass index (BMI) was calculated BMI by divided subjects weight in kilograms to height in meters squared (BMI=kg/m^2).

Subjects were asked to lie face up on a bed in a supine position. Two pairs of sensor electrodes were placed on the subject's right hand and wrist, and right foot and ankle. A cable was connected between the analyzer and the sensor electrodes.

The measurement was performed by passing a constant current less than 1 mA at a single frequency of 50 kHz using the biodynamic Model 450 bioimpedance analyzer [6]. The results provide the measurement of bioelectrical tissue conductivity (resistance (R), reactance (Xc), body capacitance (BC) and phase angle (PA)), mass distribution (body cell mass (BCM), extracellular mass (EM), lean body mass (LBM), fat mass (FM) and basal metabolic rate (BMR)), and water compartments (intracellular water (IW), extracellular water (EW), total body water (TBW), TBW/Lean Body Mass (TBW/LBM) and TBW/total weight (TBW/TW)).

F. Ibrahim, N.A. Abu Osman, J. Usman and N.A. Kadri (Eds.): Biomed 06, IFMBE Proceedings 15, pp. 63-66, 2007
www.springerlink.com ' Springer-Verlag Berlin Heidelberg 2007

D. Total cholesterol measurement

Subjects serum was collected for measurement of TC. Patient serum samples were tested for TC using the Dade Behring Clinical Chemistry System machine. TC method was based on the principle described by Stadtman [7]. Subjects were grouped according to their TC level and divided into two groups: Group 1 consists of normal subjects with TC<=5.2 mmol/L while Group 2 consists of the abnormal subjects with TC >5.2 mmol/L [8].

E. Statistical analysis

Statistical analyses were performed using SPSS version 13.0 for window XP. Data were tested for normal distribution using the Kolmogorov-Smirnov test. Differences between TC groups and anthropometric and BIA parameters were tested using *t*-test. When correlation exists between independent variables, one or more variables were excluded to avoid multicollinearities problem. Then the mean and standard deviation (SD) were calculated to obtain the classification evidence in the expert system.

F. Rule based Expert system using Bayesian reasoning.

Rule based expert system is a computer program that represents the knowledge of experts in a narrow and specialized domain [15]. Expert system was built based from the idea that human solves problem by applying their knowledge expressed as rules to a given problem represented by problem specific information [4]. Using the Bayesian reasoning, the rules are represented as follow [12]:

IF E is true

THEN H is true {with probability p}

This rule implies that if evidence E occurs, than the probability that event H will occur is p [3]. In this study, the hypothesis is; H; the subject has abnormal TC. If the probability (p) < cutoff prediction, then our hypothesis H is not true and can be written as; H; the subject has abnormal TC is not true. Since the hypothesis; H; the subject has abnormal TC, the evidences were obtained using the mean and SD for group 2. Then, the probability p for 40 testing data set was calculated using equation 1 [3].

$$p(H_i|E_1E_2..E_n)=\frac{p(E_1|H_i)\times p(E_2|H_i)\times..\times p(E_n|H_i)\times p(H_i)}{\sum_{k=1}^{m} p(E_1|H_k)\times p(E_2|H_k)\times..\times p(E_n|H_k)\times p(H_k)} \quad (1)$$

Where;

p(H) : the prior probability of hypothesis H being true

p(E|H) : the probability that hypothesis H being true will result with evidence E

n: number of evidence

m: number of hypothesis.

To find the cutoff prediction, the receiver operating characteristic Curves (ROC) was plotted for the sensitivity with respect to 1-specificity for each of the 21 cutoff values [13, 14]. Sensitivity is the number of correctly classified subject with abnormal cholesterol level (True Positive) divided by the number of all subjects with abnormal cholesterol level. Specificity is defined as the number of correctly classified subjects with normal cholesterol level (False Negative) divided by the number of all subject with normal cholesterol level. The developed ES was programmed using MATLAB version 7.1.

G. Expert system validation

The ES system was validated using 10 new data. The validation data comprises of 4 (40%) male and 6 (60%) female. Of the 10 subjects; 6 subjects were having abnormal and 4 subjects with normal TC, respectively.

III. Results and discussions

The training dataset (n=149), consist of 67 (44.97%) males and 82 (55.03%) females. Group 1 consists of 70 subjects and Group 2 with 79 subjects.

The means and SD for the parameters that were predictors to TC level were presented in Table 1 [9] while Table 2 presents the 6 evidences obtained.

Table 1 Summary of significant predictors to TC

Variables (units)	Means ± standard deviation	
	Group 1(n=70)	Group 2 (n=79)
Age (years)	37.4 – 10.67	42.6 – 8.55
BMI (kg/m^2)	26.6 – 6.11	28.9 – 5.35
BC (pF)	635.5 – 164.41	707.6 – 178.50
BMR (cals)	1488.8 – 273.79	1623.8 – 306.72
EM (%)	38.6 – 10.67	37.0 – 3.56
LBM (%)	72.3 – 9.08	69.4 – 8.47

Table 2 Evidence Statement for the hypothesis.
H; the subject has abnormal TC

Evidence	Statement
E1	34.05 ≤ Age ≤ 51.15 (years)
E2	23.55 ≤ BMI ≤ 34.25 (kg/m^2)
E3	529.1 ≤ BC ≤ 886.1 (pF)
E4	1317.08 ≤ BMR ≤ 1930.52.0 (%)
E5	33.44 ≤ EM ≤ 40.56 (%)
E6	60.93 ≤ LBM ≤ 77.87 (%)

F. Ibrahim, N.A. Abu Osman, J. Usman and N.A. Kadri (Eds.): Biomed 06, IFMBE Proceedings 15, pp. 63-66, 2007
www.springerlink.com ' Springer-Verlag Berlin Heidelberg 2007

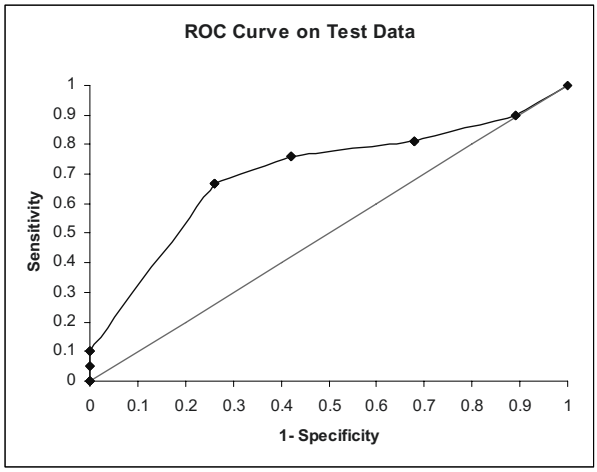

Fig. 1 ROC Curve on Test Data

Fig. 1 shows the ROC curve for sensitivity with respect to 1-specificity. The highest sensitivity was 90% when the cutoff predictions were 0.68 and 0.69. However, at this cutoff point, the specificity was 11%. Meanwhile 0.59, 0.60 and 0.61 cutoff points gave the highest specificity of 74% and acceptable sensitivity of 67%. Hence, the 0.6 probability cutoff point was selected which gave a total accuracy of 70.0%.

The ES rules were written and the examples for the rules based used are as follow;

Rule A

If $23.55 \leq BMI \leq 34.25\ (kg/m^2)$
and $529.1 \leq BC \leq 886.1\ (pF)$
and $1317.08 \leq BMR \leq 1930.52.0\ (\%)$
and $33.44 \leq EM \leq 40.56\ (\%)$
Then the subject has abnormal TC {0.78}

Rule B

If $33.44 \leq EM \leq 40.56\ (\%)$
Then the subject has normal TC {0.56}

If a subject have the criteria in rule A, then the probability was obtained from equation 1 is 0.78, therefore the hypothesis of the subject having abnormal TC is true. Meanwhile, if the subject only has the criteria in Rule B, with probability of 0.56, the hypothesis of the subject having abnormal TC is not true.

The developed ES system has been validated using 10 new subjects. The system is able to correctly classified 6 subjects out of 10 and the detail result is shown in Table 3.

Table 3 Results from the validation data of determining the TC level

TC level	Group 1(n=4)	Group 2(n=6)
Abnormal	3 (FN)	3 (TP)
Normal	1 (TN)	3 (FP)

TP=True positive, FN=False negative, FP=False Positive, TN=True Negative

IV. Conclusions and Future Works

From the analysis, it can be concluded that the developed ES is able to classify TC at 70% of total accuracy. For future work, a nonlinear modeling technique will be used for a better classification.

Acknowledgment

M.S. Mohktar would like to express her gratitude to all the subjects that involved in the studies and University Malaya for supporting the research. Special thanks to Dr. Caroline and her laboratory assistant in the University Malaya Student Clinic for their valuable support.

References

1. N. Paul Durrington Hyperlipidemia Diagnosis and Management. 2 nd Edition (1994)
2. Anthony E. Douglas, M.D, Cholesterol Test Department of Primary Care Internal Medicine Hospital of the University of Pennsylvania, Philadelphia. (2001),
3. Negnevitsky, M. Artificial intelligence, a guide to intelligent system, First Edition, Pearson education, ISBN: 0201711591(2002)
4. Arie Ben-David, Leon Sterling, Generating rules from examples of human multiattribute decision making should be simple. Expert Systems with Applications 31 (2006) 390 396
5. Eraim Turban, Jay E. Aronson Decision Support System and Intelligent Systems, Sixth Edition, Prentice Hall, ISBN: 0130327239 (2001)
6. BIODYNAMIC 450-Biodynamics Model 450 Bioimpadance Analyzer user s guide, Basic Principles of Bioimpedance Testing , First edition, copyright Biodynamics Corporation, pp. 1-22.
7. Stadtman, TC , Methods in Enzymology, Vol III, Colowick, SP, and Caplan, NO(Eds.), Academy Press New York, NY, 1957, pp 392-394,678-6
8. Lim TO et al. Clinical Research Centre Distribution of Blood Total Cholesterol in a National Sample of Malaysian Adults. (2000)
9. MS Mohktar, F. Ibrahim, NA Ismail, Effects of Abnormal Total Cholesterol Level on Bodycomposition Parameters, World Congress on Medical Physics and Biomedical Engineering, August 27-September 1, 2006, Seoul, Korea, Pages: 3628-3630.
10. Jerrold H. Zar, (1999) Biostatistical Analysis (Fourth Edition), Prentice Hall.
11. Marcello Pagano, Kimberlee Gauvreau (2000) Principles of Biostatistics, Duxbury, Thomson Learning.

F. Ibrahim, N.A. Abu Osman, J. Usman and N.A. Kadri (Eds.): Biomed 06, IFMBE Proceedings 15, pp. 63-66, 2007
www.springerlink.com ' Springer-Verlag Berlin Heidelberg 2007

12. Editorial, Bayesian networks in biomedicine and health-care, Artificial Intelligence in Medicine 30 (2004), 201 214
13. J.H. Orallo, C.Ferri, N. Lachiche, P. Flach, (2004), The 1st Workshop on ROC Analysis in Artificial Intelligence (ROCAI-2004), Volume 6, Issue 2 - Page 159-161
14. Peter Lucas, Bayesian Networks in Medicine: a Model-based Approach to Medical Decision Making, University of Aberdeen, Scotland, UK, (2000)
15. K.S Metaxiotis, J.E Samouilidis, (2000), Expert System in Medicine: Academic Illusion or Power, Information Management & Computer Security, 8/2, Page 75-7

Address of the corresponding author:

Author:	Mas Sahidayana Mohktar
Institute:	Department of Biomedical Engineering, Faculty of Engineering,University of Malaya
Street:	50603,
City:	Kuala Lumpur
Country:	Malaysia
Email:	mas_dayana@um.edu.my

F. Ibrahim, N.A. Abu Osman, J. Usman and N.A. Kadri (Eds.): Biomed 06, IFMBE Proceedings 15, pp. 63-66, 2007
www.springerlink.com ' Springer-Verlag Berlin Heidelberg 2007

Genetic Algorithm for Various Face Emotions Classification

M. Karthigayan, Mohamed Rizon, Sazali Yaacob, R. Nagarajan

School of Mechatronics Engineering, Northern Malaysia University College of Engineering Jejawi, Perlis, Malaysia

Abstract—**The eye feature plays a vital role in classifying the face emotion using Genetic Algorithm. The acquired images have gone through few preprocessing methods such as grayscale, histogram equalization and filtering. Among the edge detection methods, Sobel method performed very well in segmenting the image. The projection profile is found to be suitable feature extraction method comparing with other two methods in respect of time of processing. The second part discusses a Genetic Algorithm methodology of estimating the emotions from eye feature alone. Observation of various emotions lead to a unique characteristic of eye, that is, the eye exhibits ellipses of different parameters in each emotion. Genetic Algorithm is adopted to optimize the ellipse characteristics of the eye features. A new form of fitness function is proposed for the Genetic Algorithm. It is ensured through several experiments that the optimized parameters of ellipse reveal various emotional characteristics. Processing time for Genetic Algorithm varies for each emotion.**

Keywords—**Feature extraction, Ellipse fitness function, Genetic algorithm, Emotion recognition.**

I. Introduction

In recent years, there has been a growing interest in improving all aspects of interaction between humans and computers especially in the area of human emotion recognition through facial expression. Ekman and Friesen developed the most comprehensive system for synthesizing facial expression based on what they call as action units [1]. In the early 1990 s the engineering community started to use these results to construct automatic methods of recognizing emotion from facial expression in still or video images [2]. Human beings possess an ability of expressing their emotion through eyes in day to day interactions with others. One set of category of emotions has attracted most of the interest in human computer interaction environments. The universally accepted category of emotions, as applied in human computer interaction is: Sadness, Anger, Joy, Fear, Disgust or Dislike and Surprise. This paper consists of mainly two parts. The first part of this paper describes various stages in image processing towards applying the techniques of emotion determination. The processing stages include preprocessing, filtering and edge detection. Three methods of extracting face features (eyes and lips) are proposed and their characteristics towards determining the emotions are compared. The second part of this paper discusses a Genetic Algorithm (GA) based approach for estimating the emotion through eye feature alone. A new form of fitness function adopting the characteristics of ellipse is suggested. It is ensured through several experimentation that the eye feature is well suited in finding the emotions through GA.

II. Methods

Face features are unique to one face thus vary from one person to another. Any emotion determining parameters derived from face features cannot be the same within any two persons. For example, the eye features of a Chinese are totally different from those of ASEAn. Hence, the determination of emotion is personalized and hence suitable to one person only. Figure 1 indicates an ASEAn face expressing the emotion anger . Figure 2 describes the block schematic of image processing and emotion determination stages that is to be undertaken in this paper.

In this work, a digital camera with 3.2 Mega pixels has been used to acquire face image. The region of interest (ROI) has been selected in the acquired image. The ROI is then converted into grayscale image (0-256 range) as the first stage of image processing.

Fig. 1 The Angry Emotion

Before applying the filter to the grayscale image, a histogram equalization method is applied. Histogram equalization [3] improves contrast and achieves the goal of this equalization method which is to obtain an uniform histogram. The histogram equalization method also helps

F. Ibrahim, N.A. Abu Osman, J. Usman and N.A. Kadri (Eds.): Biomed 06, IFMBE Proceedings 15, pp. 67-71, 2007
www.springerlink.com ' Springer-Verlag Berlin Heidelberg 2007

the image to reorganise the intensity distributions. New intensities will not be introduced into the image. Existing values will be mapped to new values but the actual number of intensities in the resulting image will be equal or less than the original number of intensities.

The histogram equalized image is filtered using average and median filter to make the image smoother. Finally, Sobel edge detection method is applied to the filtered image. Due to the problem of light intensity variations, the segmentation process applied to entire image was not successful. In the edge detected image of the whole face, the eyes are properly segmented where as the lip segmentation is poor as shown in Figure 3. So the histogram equalized image is split into eyes ROI (region of interest) and lip ROI regions.

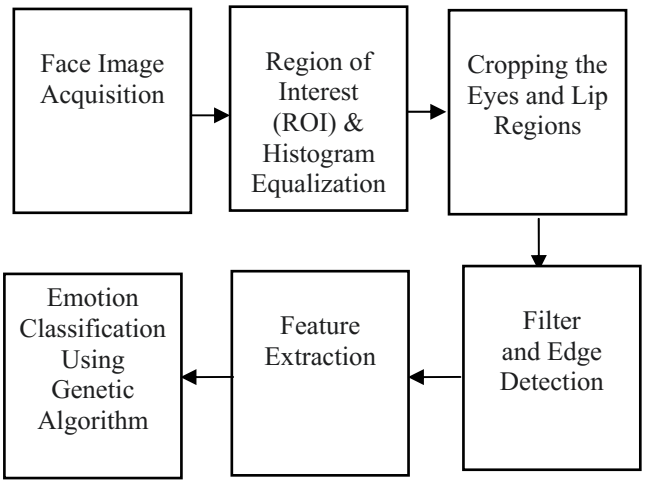

Fig. 2 A General Process Flow of face emotion recognition

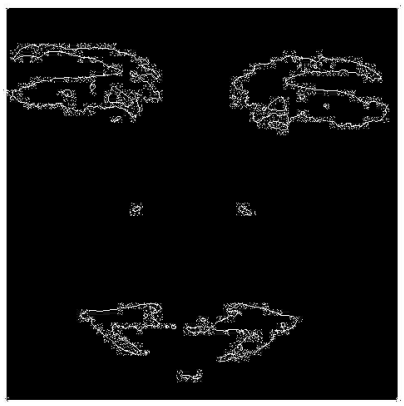

Fig. 3 Sobel Edge Detection for ROI Face

Noises are added to the cropped ROI eyes and lip regions. The salt and pepper noise are added to the image. This type of noise consists of random pixels being set to black or white. The application of the filter such as average filter and median filter to the noise added image is to remove the unwanted noise. The Average filter thus creates a two-dimensional filtered image and returns with a correlation kernel. Median filtering [4] makes each output pixel set to an average of the pixel values in the neighborhood of the corresponding input pixel. However, with median filtering, the value of an output pixel is determined by the median of the neighborhood pixels, rather than the mean. The median is much less sensitive than the mean to extreme values (called outliers). Median filtering is therefore better in its ability to remove these outliers without reducing the sharpness of the image. The median filter with various matrix sizes such as 3*3, 4*4, 5*5, 6*6, 7*7 and 8*8 are applied. The 5*5 size matrix has been found to be suitable to the image.

Thresholding is then performed to the filtered image by selecting a suitable threshold value. Then, various edge detection methods such as Sobel, Prewitt, Canny, Roberts and Log have been applied to the image. A comparison has been made among the edge detection methods and it is found that the Sobel edge detection method [4] performed well compared to other four methods. The sobel edge detection applied to eyes region and lip region are as shown in Figure 4 and Figure 5 respectively.

Fig. 4 Sobel Edge Detected Eyes Region

Fig. 5 Sobel Edge Detected Lip Region

The processing time for all these methods such as preprocessing, filtering and edge detection of the face image is in the range of 1.03 to 1.23 seconds. The processing time is based on a PC with Pentium Mobile processor 1400 MHz.

F. Ibrahim, N.A. Abu Osman, J. Usman and N.A. Kadri (Eds.): Biomed 06, IFMBE Proceedings 15, pp. 67-71, 2007
www.springerlink.com ' Springer-Verlag Berlin Heidelberg 2007

III. Feature extraction

A feature extraction method is now to be applied to the edge detected image to extract features. Three feature extraction methods are considered and their capabilities are compared for adopting the one that is suitable for the proposed face emotion recognition problem. They are projection profile [6], contour profile [6] and moments [5].

The performance of each feature extracting methods can be compared with respect to processing time using the edge detected image of eyes and lip. The processing time includes the image reading, preprocessing, filtering, edge detection and feature extraction processes. Table 1 shows the processing time (including eyes and lip features) of all three feature extraction methods. The projection profile is found to perform well in feature extraction with regards to the processing time and is adopted here.

Table 1 Processing Time for Feature Extraction (SEA)

Feature Extraction Method	Processing Time (Seconds)
Projection Profile	1.06 - 1.23
Moments	1.24 1.28
Contour Profile	50.43 68.90

IV. Face emotion recognition using genetic algorithm

In the early 1970s, John Holland, one of the founders evolutionary computations, introduced the concept of Genetic Algorithm [7]. Genetic algorithm (GA) is a heuristic method used to find approximate solutions to solve problems through application of the principles of evolutionary biology. GA adopts biologically-derived techniques such as inheritance, mutation, natural selection, and recombination (or crossover). GA is a particular class of evolutionary algorithms. A population containing a number of trial solutions each of which is evaluated (to yield fitness) and a new generation is created from the better of them. The process is continued through a number of generations with the aim that the population should evolve to contain an acceptable solution. GA is well known as an optimizing method. It offers the best optimized value for any fitness and objective function. It can be used in minimization or maximization problems.

GA has been applied in various applications such as in image processing, control, design of aircraft, robot trajectory, multiple fault diagnosis, engineering design optimization, the traveling salesman, sequence scheduling and so on [8]. The GA is applied to extract the facial features such as the eyes, nose and mouth, in a set of predefined sub regions. Some simulations have been carried out using GA [4]. A method has been suggested to extract regions of eyes out of facial image by GA in order to detect one s eye [9].

The human eye shape is of more towards ellipse. The preprocessed eye image can be considered as an ellipse. The major axis of this ellipse is more or less fixed for the eye of a particular person Then, the minor axis of the eye feature can be related to the emotion.. The whitened area of edge detected eye image for a particular emotion is shown in Figure 6. The ellipse can be parameterised by its minor and major axes. The major and the minor axes are 2a (more or less fixed) and 2b (to be computed) respectively. This is shown in Figure 7. The ellipse is defined by its equation as

$$\frac{x^2}{a^2} + \frac{y^2}{b^2} = 1 \qquad (1)$$

A fitness function, to be described latter, for applying GA is derived to optimally compute minor axis, b, such that the emotions can be easily related to the values of b.

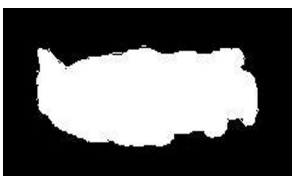

Fig. 6 Image Processed Eye

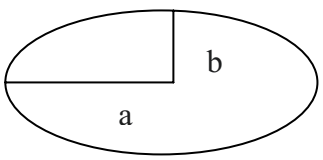

Fig. 7 Ellipse with Minor and Major Axis

V. The fitness function

A fitness function is a particular type of objective function that quantifies the optimality of a solution (that is, a chromosome) in the GA. This particular chromosome may be ranked against all the other chromosomes. A fitness

F. Ibrahim, N.A. Abu Osman, J. Usman and N.A. Kadri (Eds.): Biomed 06, IFMBE Proceedings 15, pp. 67-71, 2007
www.springerlink.com ' Springer-Verlag Berlin Heidelberg 2007

value reflecting the amount of overlapping between the regions covered by the overlaid boundaries is computed for each chromosome. A pair of individuals are selected with a probability proportional to their fitness and mated to reproduce their next generation. The process is performed in a repetitive manner with the same number of individuals of the previous epoch is formed. The fitness function, Equation (2), as shown below, is developed based on the general ellipse Equation (1). The proposed fitness function is to find the minor axis of the eye feature using GA. The fitness function is derived as

$$f(x) = \Big(\sum_{i}^{m} \sum_{j}^{n} col(j) - 2\sqrt{X^2(1 - \frac{row(i)^2}{a^2}} \Big)^2 \quad (2)$$

where col(j) is the sum of white pixels occupied in each column, row(i) is number of rows and X is expected optimized value of b . The constant a is a measure of major axis. The values of m and n represent the number of rows and the number of columns respectively.

VI. Results and discussion

In this analysis, a subject (South East Asian) expressing 6 different emotions and the neutral face is considered. The eye feature is given as input to the GA to compute the optimized value of b. The optimization is performed for more than 5 times for each emotion in reaching consistent minor axis value of b. Table 2 indicates one set of parameters used in the process of obtaining the optimized values of b. Table 3 illustrates the values of b for each emotion. The experiment results demonstrate that the minor axis of the eye feature is different for each emotion. This is the advantage of using GA to get the optimized values of b from unpredicted shapes of processed images towards classifying the emotions. Table 3 concludes that each emotion has unique minor axis values. Table 3 also indicates the number of rows (m, as a measure of minor axis) and the number of columns (n, as a measure of major axis).

VII. Conclusion

In this paper, a set of suitable preprocessing, filtering, edge detection and feature extraction methods for applying Genetic Algorithm have been proposed. Three different feature extraction methods are suggested and compared for their individual performances. Projection profile method of feature extraction has been adopted for its speed of response and for its requirement of less complex computations. All these image processing stages work favorably well even when the face image is obtained under uneven lighting. GA has been applied to get the optimized values of the minor axis using the proposed fitness function to classify the emotion. These optimized value of minor axis show that the eye can express the emotion based on changes in the minor axis. The new method has shown successful classification of emotion of unique person. Genetic Algorithm is then applied for estimating the emotions. Eye is used as the emotion determining feature. The developed fitness function for applying the Genetic Algorithm exhibits its capability in identifying the emotions. The fitness function is derived from the theory of ellipse in which a measure of minor axis, b, is related to the emotions. It is to be indicated here that a mean value of b for an emotion is obtained through several experiments. However, variations of b do occur from one experiment to another. These variations can give information on real time changes of emotions from one to another. The processing time for classification time for each emotion is calculated.

Table 2 Parameter Settings

Generation	200
Population size	20
Fitness scaling	Rank
Selection Function	Roulette
Mutation	Gaussian
Crossover	Scattered
Stall generation	50
Stall time	20

Table 3 Classification of Emotion

Emotions	**n**	**m**	**Optimized Mean Value of "b"**	**Duration of Emotion Recognition by GA (sec)**
Neutral	202	72	33.7993	142
Fear	184	70	37.8598	162
Happy	176	60	27.6636	118
Sad	186	66	33.8305	149
Angry	192	50	22.4746	99
Dislike	162	50	25.2514	113
Surprise	210	78	39.9059	172

Acknowledgment

This research is financially supported by KUKUM Short Term Grant 9001-00026.

F. Ibrahim, N.A. Abu Osman, J. Usman and N.A. Kadri (Eds.): Biomed 06, IFMBE Proceedings 15, pp. 67-71, 2007
www.springerlink.com ' Springer-Verlag Berlin Heidelberg 2007

REFERENCES

1) Haibo Li. 2001. Computer Recognition of Human Emotion, In Proceedings of International Symposium on Intelligent Multimedia, Video and Speech Processing, Hong Kong, 2-4 May 2001, pp. 490-493.
2) Nicu Sebe, Michael S. Lew, Ira Cohen, Ashutosh Garg and Thomas S. Huang. 2002. Emotion Recognition Using a Cauchy Naïve Bayes Classifier, In Proceeding. of Sixteenth International Conference on Pattern Recognition, Vol. 1, 11-15 August 2002, pp. 17-20.
3) Rafael C Gonzalez and Richard E Woods. 2002. Digital Image processing: Pearson Education, Inc, India,
4) Gary G. Yen and Nethrie Nithianandan 2002. Facial Feature Extraction Using Genetic Algorithm, Proceedings of Congress on Evolutionary computation, Vol. 2, 12-17 May 2002, pp. 1895-1900.
5) M. Karthigayan, Mohammed Rizon, Sazali Yaacob and R. Nagarajan. 2006. An Edge Detection and Feature Extraction Method Suitable for Face Emotion Detection under Uneven Lighting, The 2nd Regional Conference on Artificial Life and Robotics (AROB 06), July 14 - July 15, 2006, Hatyai, Thailand.
6) R. Nagarajan, Sazali Yaacob, Paulraj Pandiyan, M. Karthigayan, Marzuki Khalid and Shamsudin H Amin. 2006. Real Time Marking Inspection Scheme for Semiconductor Industries. International Journal of Advance Manufacturing Technology (IJAMT), Springer Publisher. (Accepted for publication).
7) Michael Negnevitsky. , 2002. Artificial Intelligence: Addison Wesley, Pearson Education Limited, England
8) 27 Nov 1997, Citing Internet sources URL http://neo.lcc.uma.es/TutorialEA/semEC/cap03/cap_3.html
9) Hideaki Tani, Kenji Terada, Shunichiro Oe and Junichi Yamaguchi. 2001. Detecting of One s Eye from facial Image by Using Genetic Algorithm. The 27thAnnual Conference of the IEEE Industrial Electronics Society, pp. 1937-1940.

Address of the corresponding author:

Author: M. Karthigayan
Institute: School of Mechatronics Engineering Northern Malaysia University College of Engineering
City: Perlis
Country: Malaysia
Email: karthigayan@ieee.org

F. Ibrahim, N.A. Abu Osman, J. Usman and N.A. Kadri (Eds.): Biomed 06, IFMBE Proceedings 15, pp. 67-71, 2007
www.springerlink.com ' Springer-Verlag Berlin Heidelberg 2007

Hybrid Method for Digits Recognition using Fixed-Frame Scores and Derived Pitch

Rubita Sudirman[1], Sh-Hussain Salleh[1], Shaharuddin Salleh[2]

[1]Center for Biomedical Engineering, Faculty of Electrical Engineering
[2]Mathematics Department, Faculty of Science
Universiti Teknologi Malaysia, 81310 UTM Skudai, Johore, Malaysia

Abstract— **This paper presents a procedure of frame normalization based on the traditional dynamic time warping (DTW) using the LPC coefficients. The redefined method is called as the DTW frame-fixing method (DTW-FF), it works by normalizing the word frames of the input against the reference frames. The enthusiasm to this study is due to neural network limitation that entails a fix number of input nodes for when processing multiple inputs in parallel. Due to this problem, this research is initiated to reduce the amount of computation and complexity in a neural network by reducing the number of inputs into the network. In this study, dynamic warping process is used, in which local distance scores of the warping path are fixed and collected so that their scores are of equal number of frames. Also studied in this paper is the consideration of pitch as a contributing feature to the speech recognition. Results showed a good performance and improvement when using pitch along with DTW-FF feature. The convergence rate between using the steepest gradient descent is also compared to another method namely conjugate gradient method. Convergence rate is also improved when conjugate gradient method is introduced in the back-propagation algorithm.**

Keywords— **dynamic warping, pitch coefficients, back-propagation neural, conjugate gradient**

I. Introduction

NN has attracted researchers interest for speech recognition since more than half century ago and the phenomena still growing to improve either ASV or ASR system. Minute avenues are explored because there are possibilities that the system can be refined for more accurate tuning. Areas like dynamic warping has been among the popular methods to accomplish the ASR or ASV system tuning in which they were first introduced by [1].

In this paper, the motivation to the study is initiated after looking at the massiveness of input data presented into the NN and the computation complexities especially when parallel processing is intended. A common avenue that researcher looked into is the speech timing between samples [3][4][5]. Realizing the importance of samples timing relationships, an alignment/normalization method using DTW is investigated and feature vectors manipulations are performed to suit the back-end proposed recognition engine. In our study, back-propagation neural network algorithm is used. The aim is to simplify the input which previously was using the LPC coefficients and produce a faster convergence to the network. By doing this, a new form of input is derived and used into our NN speech recognition system.

Traditionally automatic speech recognition used derived features which represent the vocal tract system characteristics, and leaving the knowledge of voice source characteristics, namely as pitch because pitch is not an ideal source of information for automatic speech recognition [2]. Pitch contains a lot of information such as information about the speaker, it can tell whether the sound is a voiced or unvoiced, as well as it contains prosodic information [6] [7]. In our study, we are considering pitch as another input feature into the NN so that a supra-segmental feature of the vocal tract can be included.

The remainder of this paper is organized according to the flow of the experiments conducted which is arranged as follows: Section II describes the approach and methods used in the study, Section III presents of the results and discussion of the study, while section IV summarizes and concludes the findings of the study.

II. Approach and methods

A linear time alignment is the simplest method to overcome time variation, but it is a poor method since it does not account important feature vectors when deleting or duplicating them to shorten or lengthen the pattern vectors. However, it is a typical method to interpolate input signal into a fixed size of input vector which is intended in this study. In this particular study, a hybrid method involves the combination of DTW and NN back-propagation algorithm, utilized DTW to normalize all input patterns with respect to the template pattern of digits utterances for NN recognition.

According to the warping path type 1, three slope conditions are set to perform the compression and expansion to the speech frames [8][9][10]: (i) horizontal slope, (ii) vertical slope, and (iii) diagonal slope. The frame compression and expansion processing used a modified

F. Ibrahim, N.A. Abu Osman, J. Usman and N.A. Kadri (Eds.): Biomed 06, IFMBE Proceedings 15, pp. 72-76, 2007
www.springerlink.com ' Springer-Verlag Berlin Heidelberg 2007

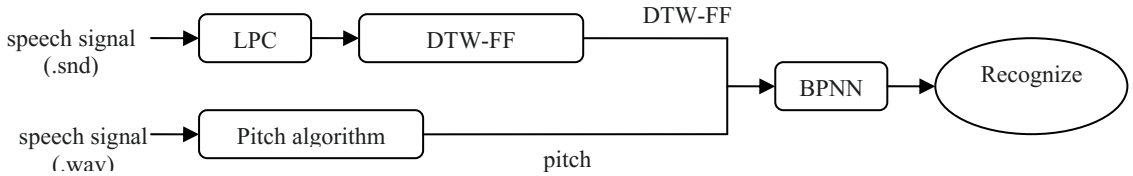

Fig. 1 The experiments process flow

version of DTW matching technique which is renamed as DTW frame fixing (DTW-FF) algorithm. The DTW-FF is utilized to fix the input frames to a fix number of input frames: the source frames are aligned to the template frames. During the frame fixing, the source and template frames are adjusted so that they have the same number of frames. In addition to that, we retained and used the local distance scores (which is called as the DTW-FF coefficient) of the fixed frames as inputs into the MLP neural network instead of using the global distance score which were used by many researchers [3][8][9].

The speech recognition is performed using the back-propagation neural network (BPNN) algorithm to enhance the recognition performance and their results are compared between using the DTW with LPC coefficients to BPNN with DTW-FF coefficients.

The acoustical feature generated caused by the vibration of the vocal fold in the vocal tract, namely pitch is introduced as another input feature into the NN. This is because LPC feature vectors itself sometimes does not give an overall high percent of recognition, pitch feature itself does not give high recognition rate indeed.

The pitch feature is optimized using pitch-scaled harmonic filter algorithm to reduce glitches during the voice activity. The overall approach of the study is illustrated in Fig. 1 which also portrays the flow diagram of the recognition process.

The result for BPNN with DTW-FF plus pitch feature achieved its high recognition rate faster than the combination of BPNN and DTW-FF feature only.

A. The DTW-FF Algorithm - Feature Extraction

The method of time alignment is based mostly on dynamic time warping and part of trace segmentation approach. The method is called the DTW-FF algorithm in which this is a part of feature extraction. In this research, the time normalization is done based on DTW method by warping the input vectors with reference pattern vectors represented by LPC coefficients.

If an input frame has almost similar feature vectors as the reference within a frame (a frame consists of 10 feature vectors), then they will have almost similar local distances. For this condition, vectors expansion of the input will take place, i.e, reference vectors shows a vertical movement; shares same feature vectors for a feature vector frame of an unknown input. If compression vector takes place, the input frames will be compressed and take only a copy the reference feature vector frame, in other words compression is compressing multiple similar input frames into one frame with respect to the reference. The rules are based on the following slopes [10][11]:

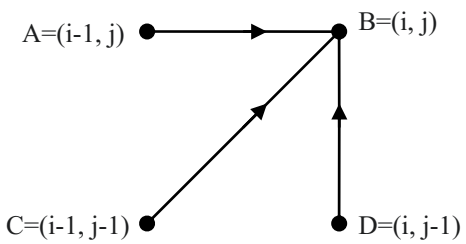

Fig. 2 The warping path type 1

Referring to Fig. 2,

- Slope is 0 (horizontal line)
  If the warping path moves horizontally from one frame to another (example: from point A to B or from point C to D), the frames of the speech signal are compressed. The compression process takes place by taking the minimum calculated local distance amongst the distance set in the frames involved: compare *w(i)* with *w(i-1), w(i+1)* and so on, and choose the frame with minimum local distance.
  Consider the frame vectors of LPC coefficients for input as *i…I*, and reference as *j…J*, while *F* denotes the frame. Frame compression involves searching minimum local distance out of distances in a frame set within a threshold value, it is represented as

$$F^{-} = F(\min\{d_{(i,j)} \quad _{(I,J)}\}) \tag{1}$$

F. Ibrahim, N.A. Abu Osman, J. Usman and N.A. Kadri (Eds.): Biomed 06, IFMBE Proceedings 15, pp. 72-76, 2007
www.springerlink.com ' Springer-Verlag Berlin Heidelberg 2007

- Slope is ∞ (vertical line)
  If the warping path moves vertically from one frame to another (example: from point C to A or from point D to B), the frame of the speech signal is expanded. This time the reference frame gets the identical frame as *w(i)* of the unknown input source.

  Frame expansion involves duplicating a particular input frame to multiple reference frames of *w(i)*, represented as

$$F^{+} = F(w(i)) \tag{2}$$

- Slope is 1 (diagonal)
  When the warping path moves diagonally (from point C to B), the frame is left as it is because it already has the least local distance compared to other movements.

The normalized sample has being tested and compared to the traditional DTW algorithm and results showed a same global distance score [10]. Also, from the frame fixing experiment, the fixed frames, N_{ff} is calculated as

$$N_{ff} = N_{if} - N_{cf} + N_{ef} \tag{3}$$

where N_{if} = number of input frame
N_{cf} = number of compressed frame
N_{ef} = number of expanded frame

After collection of DTW-FF coefficients, the second feature accounted in this study which is pitch, is extracted [10][11] and introduced into the NN along with the DTW-FF coefficient. This is because pitch feature itself cannot give a good representation of speech signal when used for speech recognition.

B. Experimental Setup

In this paper, the experiments are conducted using 11 subjects. Each subject uttered digits 0-9 for five sessions, each digit is uttered fives times in each session giving a total of 50 utterances in each session. The network is tested using different number of hidden nodes with constant momentum rate, α=0.9 and learning rate, η = 0.1 in which these parameters are determined from experiment carried out to the same data. The experiments are described as follows along with their respective results and discussions.

III. Results and Discussion

A. Traditional DTW vs. BPNN with DTW-FF Feature

The purpose of this experiment (*Experiment A*) is to find the recognition rate when DTW-FF is fed into traditional DTW and also into the NN. Results of the experiment are illustrated in Fig. 2. It is clearly shown that the BPNN using the DTW-FF coefficients outperformed the traditional DTW for all subjects. Traditional DTW gives an average recognition of 90% while BPNN is 97%, however the average improvement is about 6.45% per subject. In earlier experiments reported in [10] and [11], traditional DTW showed same recognition performance when using both features, either LPC or DTW-FF features. One way or the other this proved that no information loss occurred during feature interpolations from LPC to DTW-FF [10][11]. Indeed the used of DTW-FF feature in BPNN has outperformed the traditional DTW. The results are collected from an average of 20 hidden nodes NN where most of the networks have learned sufficiently.

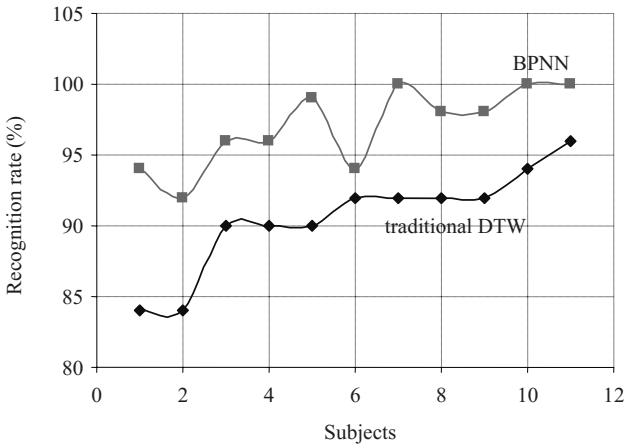

Fig. 3 Comparison of typical DTW and BPNN when using the DTW-FF feature.

B. DTW-FF and Pitch Feature into BPNN

In the NN experiment of DTW-FF combined with the pitch feature (*Experiment B*), the same network setting is use so that it will produce a fair result when compared to *Experiment A*.

The same experimental setup as *Experiment A* is used for *Experiment B* except this time *Experiment B* is using only the last 6 subjects. Observation to this experiment found that a faster network convergence is achieved when the network has learned sufficiently using only 10 hidden nodes, compared to 20 hidden nodes in *Experiment A,* refer

F. Ibrahim, N.A. Abu Osman, J. Usman and N.A. Kadri (Eds.): Biomed 06, IFMBE Proceedings 15, pp. 72-76, 2007
www.springerlink.com ' Springer-Verlag Berlin Heidelberg 2007

to Fig. 4. This proved that pitch feature is an attractive feature if it is used along with other feature namely the DTW-FF feature to produce a higher recognition and faster convergence. During the experiment, some of the subjects start to show drastic improvement as early as 5 hidden nodes. These have proven that better recognition can be achieved when taking pitch feature into account particularly in isolated digits speech recognition. This method also has been tested on a number of words obtained from TIMIT database. However, the result is not very encouraging: only around 65-70% accuracy, this might due to a speaking variation, intonation and dialect that have been used by the speakers during the recordings of the words in the sentences.

The statistical test, called as T-Test has been conducted to the data in Fig. 3 in which this test assesses weather the means of two groups are statistically different from each other. The hypothesis is set such that: H_0: $\mu_{before}=\mu_{after}$ and H_1: $\mu_{before}<\mu_{after}$. From the test with a level of significance of α=0.05, it is found that the value of t for DTW-FF in traditional DTW is smaller than the in BPNN. In that case, the results reject the null hypothesis which states that $\mu_{before}=\mu_{after}$. Since H_1 is true where $\mu_{before}<\mu_{after}$, then it can be concluded that by using DTW-FF coefficients into traditional DTW and BPNN the recognition is significantly improved.

In addition, a lot of network complexity and amount of connection weights computations during forward and backward pass have been reduced due to replacement of LPC coefficients with DTW-FF coefficients. Besides fixing to equal number of frames between the unknown input and the reference, this activity have also tremendously reduced the amount of inputs presented into the back-propagation neural networks. The percentage of number coefficients reduced is calculated as follows:

$$\%\ \text{coefficients reduced} = \frac{\text{Input}_{\text{LPC}} - \text{Input}_{\text{LD}}}{\text{Input}_{\text{LPC}}} \text{x}100\% \qquad (4)$$

For example, the input size reduction for 50 samples of 49 frames with LPC order-10 is 90% when using the local distance scores instead of the LPC coefficients. Nevertheless, this percentage will be higher if higher LPC order was used. For 12-order LPC the reduction is about 92%. This means a simpler calculation for connection updates in the NN thus giving faster convergence for the same sample under testing.

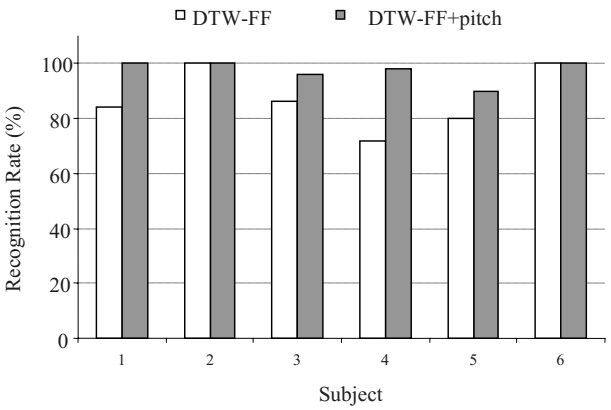

Fig. 4 Before and after pitch addition for 10 hidden nodes

C. Convergence Test

The back-propagation neural network experiments are utilizing the steepest gradient method. The recognition rate achieved is acceptable with their high percentage, sometimes reached to 100%. However, we are looking for a faster convergence time, so the data are tested using other search engine for the back-propagation part, namely the conjugate gradient method. The forward pass mechanism is the same for all architecture except for the backward-pass, so the backward pass is replaced with the conjugate gradient algorithm (CG) [12]. The results using this algorithm are compared to the results using the steepest gradient algorithm obtained in the previous experiments.

In Fig. 5, the curves tell how the search for optimal global minimum behaved for each type of the gradient search. In comparison, the steepest gradient descent (SG) seems to reach the convergence at a faster rate, but not to the optimal value. However, the CG converged at the slower rate but smaller error which determines its optimal global minimum between the methods tested. The result suggested that for a large number of weights like in this experiment, the conjugate gradient is the more efficient compared to other gradient search methods for an optimal global minimum. The oscillation in CG during the early stage shows the search of optimal global minimum in the golden section interval.

F. Ibrahim, N.A. Abu Osman, J. Usman and N.A. Kadri (Eds.): Biomed 06, IFMBE Proceedings 15, pp. 72-76, 2007
www.springerlink.com ' Springer-Verlag Berlin Heidelberg 2007

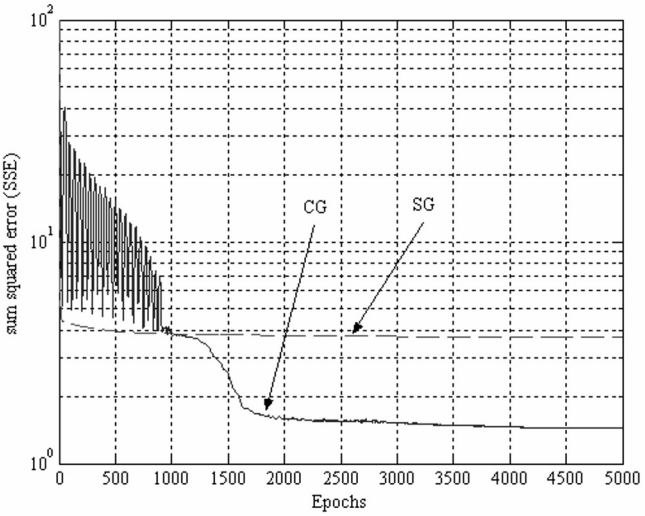

Fig. 5 The convergence comparisons between the steepest gradient descent (SG) and conjugate gradient method (CG).

IV. Summary and conclusion

In this paper, the frame fixing of speech signal based on DTW method for processing LP coefficients into another form of compressed data called DTW-FF coefficients have been described. These coefficients are used as input into BPNN. Initial observation from the experiment conducted leads to a resolution that the DTW-FF algorithm is able to produce a better way of representing input features into the neural networks. These have been proven that the reformulation of the LPC feature into DTW-FF coefficients do not affect the recognition accuracy although the coefficients size is reduced by 90% from using an order 10 of LPC to using the DTW-FF coefficients. As a result, the computation and network complexity have been greatly reduced indeed still gain a high recognition rate than the traditional DTW. This is a new approach of feature representation and combination that can be used into the back-propagation neural networks.

A higher recognition rate is achieved when pitch feature is added to the DTW-FF feature. It can be concluded that even though pitch itself cannot provide a good recognition, eventually it can be an added feature to another very reliable feature to form a very good recognition.

Performance optimization showed that the recognition does not produce higher percentage except that network converged to a better optimal global minimum after an extra of 500 epochs for these particular samples. This is due to the line search technique and followed by the golden section search which only focused on the global point vicinity based on the interval defined from the line search process.

Acknowledgements

An appreciation goes to MOSTI and Universiti Teknologi Malaysia, Skudai for supporting this study.

References

[1] Sakoe H and Chiba S (1978). Dynamic Programming Algorithm Optimization for Spoken Word Recognition, IEEE Transactions on Acoustics, Speech and Signal Processing. ASSP-26(1): 43-49.

[2] M. Magimai-Doss M (2003). Using Pitch Frequency Information in Speech Recognition. Proceedings of 8th European on Speech Communication and Technology. Geneva, Switzerland. 4: 2525-2528.

[3] Abdulla W H, Chow D and Sin G (2003). Cross-Words Reference Template for DTW-based Speech Recognition System. IEEE Technology Conference (TENCON). Bangalore, India, 1: 1-4.

[4] Creany M J (1996). Isolated Word Recognition using Reduced Connectivity Neural Networks with Non-Linear Time Alignment Methods. PhD Thesis, University of New Castle-Upon-Tyne, UK.

[5] Uma S, Sridhar, V, and Krishna G (1992). Time-Normalization Techniques for Speaker-Independent Isolated Word Recognition. Proceedings of Pattern Recognition Conference: Image, Speech and Signal Analysis. 3: 537-540.

[6] Prasanna S R M, Zachariah J M, and Yegnanarayana B (2004). Neural Network Models for Combining Evidence from Spectral and Suprasegmental Features for Text-Dependent Speaker Verification. Proceedings of International Conference on Intelligent, Sensing, and Information Processing. pp 359-363.

[7] B. R. Wildermoth. 2000. Text-Independent Speaker Recognition using Source Based Features. Master of Philosophy Thesis Griffith University, Australia.

[8] Botros N M and Premnath S (1992). Speech Recognition using Dynamic Neural Networks. International Joint Conference in Neural Network. 4: 737-742.

[9] Soens P and Verhelst W (2005). Split Time Warping for Improved Automatic Time Synchronization of Speech. Proceeding of SPS DARTS, Antwerp, Belgium.

[10] Sudirman R., Salleh S-H, and Ming T C (2005). Pre-Processing of Input Features using LPC and Warping Process. Proceeding of 1st International Conference on Computers, Communications, and Signal Processing, Kuala Lumpur. pp 300-303.

[11] Sudirman R, Salleh S-H and Salleh S (2006). Local DTW Coefficients and Pitch Feature for Back-Propagation NN Digits Recognition. IASTED International Conference on Networks and Communications, Chiang Mai, Thailand. pp 201-206.

[12] Hagan M T, Demuth H B, and Beale M (1996). *Neural Network Design*. Boston: PWS Publishing Company.

Multiple neural networks for Human Face Recognition

Muhammad Firdaus Hashim[1], Mohamed Rizon[2], Puteh Saad[1] and Noor Azuan Abu Osman[3]

[1]School of Computer and Communication Engineering, Kolej Universiti Kejuruteraan Utara Malaysia (KUKUM), Perlis, Malaysia
[2]School of Mechatronic Engineering, Kolej Universiti Kejuruteraan Utara Malaysia (KUKUM), Perlis, Malaysia
[3]Department of Biomedical Engineering, University of Malaya, 50603 Kuala Lumpur, MalaysiaE-mail: firdaush@gmail.com

Abstract—**In this paper, a computational model has been developed to identify a face of an unknown person's by utilizing eigenfaces as unique features and backpropagation Neural Network for recognition. The features of a basic human face are extracted using eigenfaces. These features are then used to identify an unknown face by using multiple numbers of backpropagation neural networks. Samples of 15 human faces are obtained from The ORL database. The experiments are compared to the effects of changes size of face images, different face images combination and different neural network parameter. The classification more than 90% for trained classes and 18% for untrained classes were achieved.**

Keywords— **Feature Vector, Eigenfaces, eigenvalues and Eigenvector**

I. Introduction

The developing of face recognition system is difficult because human faces is complex, multidimensional and alter according to environment changes. For that reason the human machine recognition of human faces is a challenging problem due the changes in the face identity and variation between images of the same due to illumination and viewing direction. The issues here are what are the suitable features to be adopted in order to represent a face under environmental changes and how an unknown face image is identified based on the chosen representation. Human faces recognition systems have been applied in various applications such as security system, mug shot matching and model-based video coding.

The eigenfaces is a well known method for face recognition. Sirovich and Kirby [1] had efficiently representing human faces using principle component analysis. M.A Turk and Alex P. Pentland [2] developed the near real-time eigenfaces systems for face recognition using eigenfaces and Euclidean distance.

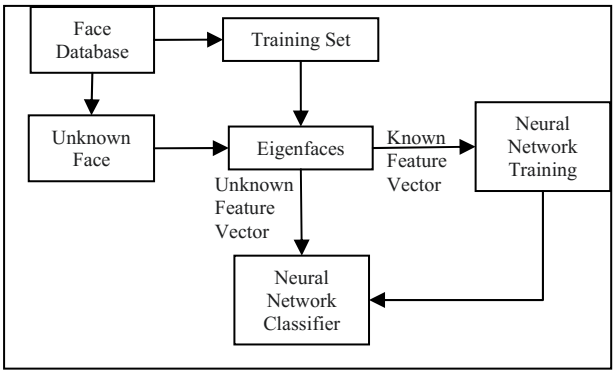

Fig. 1 Proposed Face Recognition System

The research is focused on the development of the computational model of face recognition that is fast, simple and accurate in different face environments. Here, the eigenfaces method is first described and then it is demonstrated that the features vectors obtained from the eigenfaces can easily be used for classification and recognition using neural network. Figure 1 shows the design model of face recognition system.

II. Eigenfaces method

The basic idea of eigenfaces is that all face images are similar in all configurations and they can be described in its basic face images. Based on this idea, the eigenfaces procedures [2, 3] are as follows:

a) We assume the training sets of images are $\Gamma_1, \Gamma_2, \ldots, \Gamma_m$ with each image is $I(x, y)$. Convert each image into set of vectors and new full-size matrix $(m \times p)$, where m is the number of training images and p is $x \times y$ (Figure 2).

F. Ibrahim, N.A. Abu Osman, J. Usman and N.A. Kadri (Eds.): Biomed 06, IFMBE Proceedings 15, pp. 77-81, 2007
www.springerlink.com ' Springer-Verlag Berlin Heidelberg 2007

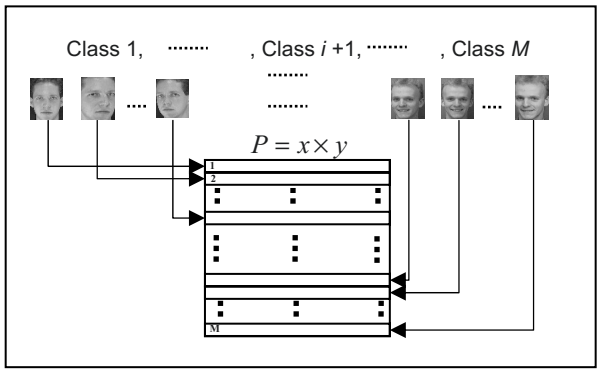

Fig. 2 Training set

b) Find the mean face by:

$$\Psi = \frac{1}{m}\sum_{i=1}^{m}\Gamma_i \tag{1}$$

c) Calculated the mean-subtracted face:

$$\Phi_i = \Gamma_i - \Psi, i = 1, 2, \ldots, m \tag{2}$$

and a set of matrix is obtained with $A = [\Phi_1, \Phi_2, \ldots, \Phi_m]$ is the mean-subtracted matrix vector with its size A_{mp}.

d) By implementing the matrix transformations, the vectors matrix is reduced by:

$$C_{mm} = A_{mp} \times A_{pm}^T \tag{3}$$

where C is the covariance matrix and T is transpose matrix.

e) Find the eigenvectors, V_{mm} and eigenvalues, λ_m from the C matrix using Jacobi method [4, 5, 6 and 7] and ordered the eigenvectors by highest eigenvalues. Jacobi s method is chosen because its accuracy and reliability than other method [8 and 9].

f) Apply the eigenvectors matrix, V_{mm} and adjusted matrix, Φ_m. These vectors determine linear combinations of the training set images to form the eigenfaces, U_k by:

$$U_k = \sum_{n=1}^{m}\Phi_n V_{kn}, k = 1,2\ldots, m \tag{4}$$

Instead of using m eigenfaces, $m' < m$ which we consider the image provided for training are more than one for each individuals or class. m' is the total class used.

g) Based on the eigenfaces, each image have its face vector by:

$$W_k = U_k^T(\Gamma - \Psi), k = 1, 2, \ldots, m' \tag{5}$$

and mean subtracted vector of size $(p \times 1)$ and eigenfaces is $U_{pm'}$. The weights form a feature vector:

$$\Omega^T = [w_1, w_2, \ldots, w_{m'}] \tag{6}$$

h) A face can reconstructed by using its feature, Ω^T vector and previous eigenfaces, $U_{m'}$ as :

$$\Gamma' = \Psi + \Phi_f \tag{7}$$

where $\Phi_f = \sum_{i=1}^{m'} w_i U_i$.

III. Classification and Recognition

In previous section the obtained feature vectors, Ω^T is used as inputs through backpropagation neural network for classification and recognition. The number of inputs is equally to m' and number of patterns is m. The feature vector is normalized to a range of (0, 1) using Improve Linear Scaling (ILS) normalization technique

$$x' = \frac{\left(\frac{x-\mu}{3\sigma}+1\right)}{2} \tag{8}$$

Where:

$$\mu = \frac{\sum x_n}{n},\ \sigma = \sqrt{\frac{\sum (x_n - \mu)^2}{n-1}}$$

the normalization is needed to meet the input scaling input data that is required by the backpropagation neural network and to avoid computational problems and to facilitate learning [10].

- Neural network consist several layers such as input layer, hidden layer and output layer [11, 12, 13]. In this paper, the number is relying with the total number of classes affected in the training phase with each network has as output neuron which the target is set into 0 or 1[14] (Figure 3). ff

F. Ibrahim, N.A. Abu Osman, J. Usman and N.A. Kadri (Eds.): Biomed 06, IFMBE Proceedings 15, pp. 77-81, 2007
www.springerlink.com ' Springer-Verlag Berlin Heidelberg 2007

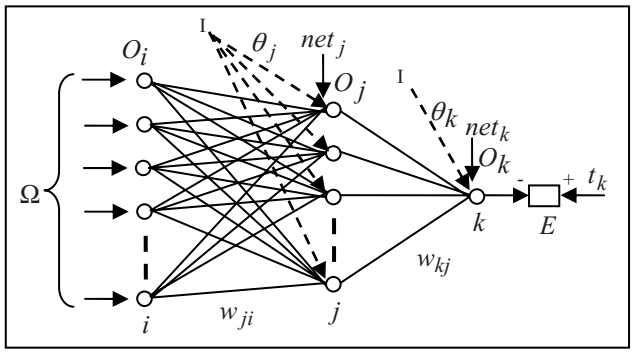

Fig. 3 MLP with single Output Neuron

Each pattern is trained separately into its neural network but the number of hidden layer is synchronized within neural network. In each training session, the patterns corresponding to its neural network are set as 1 and other are 0 for their output target. After all neural networks are fully generalized the optimal weight, the test samples are used for recognition purposes.

IV. Discussion

The eigenfaces procedure described in section 2 is coded using Visual C++. The eigenvectors and eigenvalues play a major role in producing eigenfaces. The results in terms of eigenfaces obtained using the procedures that is developed are compared with the output generated by MATLAB and by eigenvalues and eigenvectors java applet [15].

The experiments have been conducted using the Olivetti Research Laboratory (ORL) database (see Figure 2). 15 classes with 10 face images in each class are used in the experiments. In order to examine the generalized performance of backpropagation neural network, the cross validation technique is used. Thus the classes is divided in to three group which first and the second group are the from the same class but only first group is used in the training phase and second group is include unknown face images but still the same trained class (Figure 4). The third group is consists the unknown person and surely different class from first and second group (Figure 5). In this experiment, the second and third group is used as the testing pattern.

The research hypothesis, the second group should give high recognition rate and the third group should be lower as it was difference person or class from the training classes.

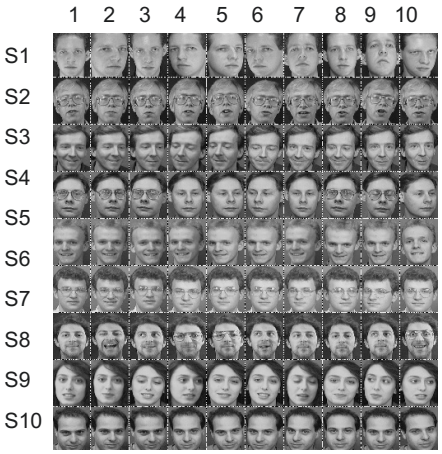

Fig. 4 Sample Trained Face Images

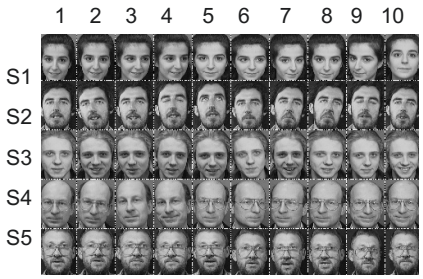

Fig. 5 Sample Untrained Face Images

In the experiments, seven face images for each class is taken in training phase. The different combination of face images and different face images sizes are used (see Table 1, 2 and 3). The results show the performance of recognition is almost 90% for trained classes and 18% of untrained classes. Although the changing of face images sizes, it is shown the capability of eigenfaces to extract the significant data.

Table 1 Recognition result with face image size 92 x 112

Face index in training set	Face index in testing set	Trained Class Recognition rate (%)	Untrained Class Recognition rate (%)
1,2,3,4,5,6,7	8,9,10	90.00	26.00
2,3,4,5,6,7,8	1,9,10	80.00	26.00
3,4,5,6,7,8,9	1,2,10	90.00	18.00
4,5,6,7,8,9,10	1,2,3	90.00	36.00

F. Ibrahim, N.A. Abu Osman, J. Usman and N.A. Kadri (Eds.): Biomed 06, IFMBE Proceedings 15, pp. 77-81, 2007
www.springerlink.com ' Springer-Verlag Berlin Heidelberg 2007

Table 2 Recognition result with face image size 41 x 50

Face index in training set	Face index in testing set	Trained Class Recognition rate (%)	Untrained Class Recognition rate (%)
1,2,3,4,5,6,7	8,9,10	90.00	20.00
2,3,4,5,6,7,8	1,9,10	80.00	52.00
3,4,5,6,7,8,9	1,2,10	90.00	22.00
4,5,6,7,8,9,10	1,2,3	93.33	52.00

Table 3 Recognition result with face image size 20 x 24

Face index in training set	Face index in testing set	Trained Class Recognition rate (%)	Untrained Class Recognition rate (%)
1,2,3,4,5,6,7	8,9,10	90.00	22.00
2,3,4,5,6,7,8	1,9,10	83.33	28.00
3,4,5,6,7,8,9	1,2,10	83.33	32.00
4,5,6,7,8,9,10	1,2,3	80.00	56.00

Table 4 shows the results of different combination of neural network parameter (learning and momentum rate). When the learning rate is set lower than momentum rate, the success rate shows outstanding performance with 90% of recognition although with different number of hidden layer.

Table 4 Different Combination Neural Network Parameter with image size 41 x 50

Learning vs Momentum Rate	Hidden Neurons	Recognition Rate (%)	
		Trained Class	Untrained Class
0.2 - 0.7	7	90	20
0.5 - 0.7	7	90	32
0.7 - 0.2	7	90	24
0.7 - 0.5	7	90	24
0.8 - 0.5	7	90	34
0.9 - 0.7	7	76.66	24
0.2 - 0.7	5	90	24
0.5 - 0.7	5	93.33	30
0.7 - 0.2	5	90	22
0.7 - 0.5	5	90	26
0.8 - 0.5	5	90	24
0.9 - 0.7	5	93.33	36
0.2 - 0.7	8	90	26
0.5 - 0.7	8	90	32
0.7 - 0.2	8	90	18
0.7 - 0.5	8	90	36
0.8 - 0.5	8	90	40
0.9 - 0.7	8	86.66	28

However with momentum is higher than the learning rate, the success rate performance become unstable because some information might be lost [16]

V. Conclusions

In this paper, the eigenfaces are used to represent the features vectors for human faces. The features are extracted from the original image to represents unique identity and then used as inputs into neural network for learning and recognition.

The result shown that the feature vectors obtained from the eigenfaces method can be used to classify the human face and recognize them reasonably good up to 90% accurate of trained classes and 18% of untrained classes.

Acknowledgements

Portions of this research use the Olivetti Research Laboratory (ORL) databases. The authors would like to acknowledge IRPA-UTM (Project vote 74133) and KUKUM for supporting this research work.

References

[1] Kirby et al. 1990, Application of the Karhunen-Loeve procedure for the characterization of human faces, IEEE Transactions on Pattern analysis and Machine Intelligence, Vol 12(1), pp. 103-108.

[2] M.A. Turk and A.L. Pentland 1991, Face Recognition using Eigenfaces, Proceeding of IEEE Computer Society Conference on Computer Vision and Pattern Recognition, pp. 586-591.

[3] Zhujie,Y.L.Yu. 1994, Face Recognition with eigenfaces, Proceedings of the IEEE International Conference on Industrial Technology, pp. 434-438.

[4] M.Firdaus et al. Dec 2005 , An Approach of Feature Extraction for face recognition, Proceeding of the Conference on Intelligent Systems and Robotics (iCISAR2005): Malaysia..

[5] M. Firdaus et al Dec 2005, Face Recognition using Neural Network, Proceeding of the International Conference on intelligent Systems (ICIS): Malaysia.

[6] M.Firdaus et al. Jan 2006, Dimensions Reductions for Face Recognition using Principal Component Analysis, Proceeding of the 11th International Symposium on Artificial life and Robotics (AROB 11th 06): Japan.

[7] J.H. Mathew 2003, Eigenvalues and Eigenvectors, pp. 612-621, Dept. of Mathematics, Univ. of California.

[8] J. Demmel and K.Veselic 1989, Jacobi s method is more accurate than QR, Technical Report: UT-CS-89-88, pp. 1-60,. Courant Institute, New York.

[9] M.T Health. 2002, Scientific Computing: An Introductory Survey, McGraw-Hill, pp. 191-200.

[10] Puteh Saad et al. 2001, A Comparison of Feature Normalization Techniques on Complex Image Recognition, Proceeding of the 2nd Conference on Information Technology in Asia, pp. 397-409.

[11] S.C Debipersand and A.D Broadhurst 1997, Face Recognition using Neural Network, Proceedings of the IEEE Communication and Signal Processing (COMSIG 97), pp.33-36.

[12] Nazish et al. 2001, Face Recognition using Neural Network, Proceeding of the IEEE INMIC 2001, pp. 277-28.

[13] Marzuki Khalid, Multilayer Neural Network and Backpropagation Algorithm. Citing internet sources URL www.cairo.utm.my

[14] Q. Jiang, Thesis: Principal Component Analysis and Neural Network Based Face Recognition. Citing in internet source URL: http://people.cs.uchicago.edu/~qingj/ThesisHtml

[15] Java applet for Eigenvalues and Eigenvectors, Citing internet sources URL:http://users.ugent.be/~mvdaele/cgiin/ILONA/theorie/Applets/Jacobi/Jacobi.

[16] R.J. Schalkoff. 1997, Artificial Neural Network, McGraw Hill.

Address of the corresponding author:

Author: Muhammad Firdaus Hashim
Institute: School of Computer and Communication Engineering, Kolej Universiti Kejuruteraan Utara Malaysia (KUKUM)
City: Perlis
Country: Malaysia
E-mail: firdaush@gmail.com

F. Ibrahim, N.A. Abu Osman, J. Usman and N.A. Kadri (Eds.): Biomed 06, IFMBE Proceedings 15, pp. 77-81, 2007
www.springerlink.com ' Springer-Verlag Berlin Heidelberg 2007

Recognition of Lower Limb Muscle EMG Patterns by using Neural Networks during the Postural Balance Control

Jaehoon Jeong, Wonhak Cho, Yongchul Kim, and Hyeonki Choi

School of Mechanical Engineering, Sungkyunkwan University, Suwon, Korea

Abstract— **The purpose of the study was to recognize EMG signal patterns of lower limb muscles by using neural networks during the recovery of postural balance of human body. Surface electrodes were attached to several lower limb muscles. EMG signals were collected during the postural balance recovery process after a perturbation without permitting compensatory stepping. A waist pulling system was used to apply transient perturbations in five horizontal directions. The EMG signals of fifty repetitions of five motions were analyzed for 10 subjects. Twenty features were extracted from EMG signals of one event. By using neural networks, EMG signals were classified into five categories, such as forward perturbation, backward perturbation, lateral perturbation and two oblique perturbations. As results, motions were recognized with mean success rates of 75 percent. With the neural network classifier of this study, the EMG patterns of lower limb muscles during the recovery of postural balance could be classified with high accuracy of recognition.**

Keywords—**EMG, Lower limb muscle, Pattern recognition, Postural balance**

I. Introduction

Balance recovery is the most basic human movement during gait and dynamic activities of daily life and the complex process to adjust body posture by various joints, muscles and bones. Loss of balance caused by the degeneration of the balance recovery control system in the elderly and in many pathologies is becoming ever more critical with the increase in our ageing population [1]. Falls due to loss of balance result in injuries and loss of life. Virtually it has been estimated that one third of older people 65 years and over experience one or more falls each year. And older people are hospitalized for fall-related injuries 5 times more often than they are for injuries from other causes [2]. A serious health threat facing the older adult population is an increasing susceptibility to loss of balance resulting in a fall and possible injury. On the one hand, several system using bio-signals that assist humans for their incomplete activities and lost senses have been developing.

There are various bio-signals, such as EMG, EEG, EOG and ECG. Recently, bio-signals have been paid a great deal of attention due to their potentiality to provide new communication and control channels between human and machine, or, more specifically, between the disabled and the computer/robot in rehabilitation engineering [3]. The EMG signal reflects the level of electrical activity of muscles and therefore provides insight in their coordination in movement and in their role in a specific task. The studies on EMG signal can be classified into two groups: the control of human-assisting robots and rehabilitation systems by using EMG pattern recognition; and an automatic diagnosis in a clinic. As examples of the former, Sankai [4] developed HAL (Hybrid Assistive Leg) which was performed according to the operator s intention by using EMG signal as the primary command signal. Later, there are researches on diagnosis of neuromuscular system by evaluating the degree of muscle fatigue [5].

Studies concerning falls and balance recovery mechanisms have been developed using surface sway, slipping, waist pulling, pushing and setting an obstacle artificially [6-8]. Especially, surface sway has been most frequently used for understanding postural balance recovery mechanism [6]. One of the researcher, Runge et. al. presented a fact that movement analysis by using joint torque is useful method for understanding of postural balance recovery mechanism [7]. Recently, Pai et. al. and Rosers et. al. compared postural balance recovery mechanism between the older adults and the young during waist pulling at standing [8].

Many studies on EMG signal pattern recognition have been reported. During the first stage of this research, linear prediction models for EMG signal, such as the autoregressive (AR) model, were frequently used. Graupe et al. [10] reported on discriminating EMG signal measured from one pair of electrodes using this model. In pattern recognition problems, neural networks are of particular significance because of their learning capability and have already been successfully applied to a wide range of bio-signal analysis and classification problems. As examples of application, there are the research of Michael [9] and Fukuda et al. [3].

The purpose of the study was to recognize EMG signal patterns of lower limb muscles by using neural networks during the recovery of postural balance of human body. The schematic diagram of this study is shown in Fig. 1.

F. Ibrahim, N.A. Abu Osman, J. Usman and N.A. Kadri (Eds.): Biomed 06, IFMBE Proceedings 15, pp. 82-85, 2007
www.springerlink.com ' Springer-Verlag Berlin Heidelberg 2007

II. METHODS

In this study, 10 male adults (age range: 23-30; height range: 167-181cm; weight range: 59-86kg) participated who have no history of otologic, neurologic, or orthopedic abnormality. We used EMG system (MyoSystem 1400, Noraxon USA, Inc.) and waist pulling system. Waist pulling system consisted of air cylinder, compressor and switching module. The waist pulling system pulls and pushes the rope, which is connected to subject's waist, with, respectively, from 8psi to 12psi for applying transient perturbations in five horizontal directions, such as forward, backward, oblique (45°), oblique (135°) and lateral perturbation. We used switching module to develop natural sway of subjects. In the experiments, we used eight surface electrode attached to lower limb (ch. 1 Tibialis anterior m.; ch. 2 Castrocnemius m.; ch. 3 Peroneus longus m.; ch. 4 Vastus medialis m.; ch. 5 Rectus femoris m.; ch. 6 Vastus lateralis m.; ch. 7 Biceps femoris m.; ch. 8 Gluteus m.) [Fig. 2].

Experimental procedure, which is followed, is that first, subjects stood with bare feet on the ground. They loosely tethered at the waist to the perturbation system. To initiate the perturbation, the air cylinder was activated by a compressor. EMG signals were collected during the balance recovery process form a perturbation without permitting compensatory stepping. EMG signals of fifty repetitions of five motions were analyzed for five subjects. Data collection was started from the balance recovery of the subject after the onset of pulling for 1 second.

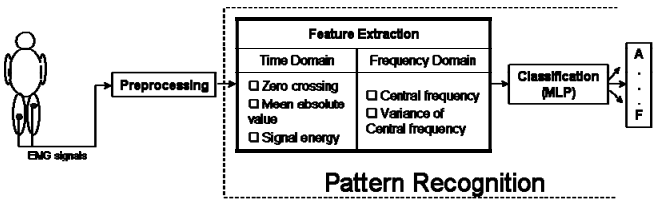

Fig. 1. Schematic diagram

Feature extraction

Feature extraction is an important step in process of pattern recognition. Generally, there are two major approaches to extracting feature: a) temporal approach, and b) spectral approach.

A. Temporal approach

Temporal approach in feature extraction identifies the attributes of the raw EMG signal that characterize it temporal structure relative to a specific muscular function [11]. The features used in this research are listed below:

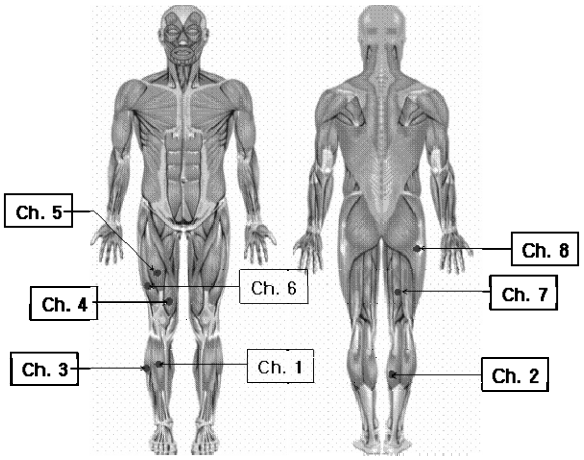

Fig. 2. Electrode position

1) Zero crossing (ZC): Zero crossing is the number of times that the signal passes the zero amplitude axes. It is calculated as

$$ZC = \sum_{i=1}^{N} \mathrm{sgn}(-x_i x_{i+1})$$

$$\mathrm{sgn}(x) = \begin{cases} 1 & \text{if } x > 0 \\ 0 & \text{otherwise} \end{cases}$$

2) Integral of absolute value (IAV): The IAV of EMG is calculated as

$$IAV = \frac{1}{N} \sum_{i=1}^{N} |x_i|$$

3) Variance (VAR): The variance is a measure of the signal power and calculated as

$$VAR = \frac{1}{N-1} \sum_{i=1}^{N} x_i^2$$

In each, x_i is the i th sample of EMG signal and N is the window size for computing the features.

B. Spectral approach

Spectrum analysis has been applied to EMG studies. Various feature extraction methods based on the spectral analysis are experimented [14]. The using of information contained in frequency domain could lead to a better solution for encoding the EMG signal.

A traditional way to characterize the spectral properties of a time sequence $s[n]$ is through its power spectral density (PSD) function $P(f)$. If the available observations of

F. Ibrahim, N.A. Abu Osman, J. Usman and N.A. Kadri (Eds.): Biomed 06, IFMBE Proceedings 15, pp. 82-85, 2007
www.springerlink.com © Springer-Verlag Berlin Heidelberg 2007

$s[n]$ constitute a truncated sequence $s[0]$, $s[1]$, , $s[N-1]$ then $P(f)$ can only be estimated through some estimator. The simplest and oldest estimator of PSD is the periodogram:

$$P(f) = \frac{1}{N}\left|S(f)\right|^2 = \frac{1}{N}\left|\sum_{n=0}^{N-1} s[n]e^{-j2\pi fn}\right|^2$$

In order to decrease the spectral leakage caused by truncation, the sequence is often windowed, i.e. $s[n]$ is replaced by $s[n]w[n]$ where $w[n]$ is some time windowing function, for example the popular Hamming window.

Since the estimated PSD, $P(f)$, is itself a random function, it is convenient to define the spectral-based features as some averaged values of $P(f)$. A simple choice is the spectral magnitude averages defined over L equidistant frequency intervals:

$$P_m = \frac{1}{f_m - f_{m-1}} \int_{f_{m-1}}^{f_m} P(f)df, \quad m = 1,2,...,L$$

These averages help reduce the effect of a considerable variance of periodogram. An alternative possibility to extract the features from a PSD estimate are the spectral moments:

$$M_m = \int_0^w f^m P(f)df, \quad \text{m} = 0,1,...,L$$

where W is bandwidth of the spectrum. As will be shown later, the spectral moments have given much better results in the case of classification of prehensile EMG patterns than the magnitude averages.

The most important spectral moments are the first three moments.

Energy:

$$E = M_0 = \int_0^w P(f)df$$

Central frequency (spectral center of gravity):

$$f_c = \frac{\int_0^w P(f)fdf}{\int_0^w P(f)df} = \frac{M_1}{M_0}$$

Variance of central frequency:

$$\sigma_f^2 = \frac{1}{M_0}\int_0^w P(f)(f-f_c)^2 df = \frac{M_2}{M_0} - \left(\frac{M_1}{M_0}\right)^2$$

III. Results and discussion

We conducted experiments with ten subjects. EMG signal is amplified by 1000 times, and filtered by using sixth Butterworth band pass filter (10-500 Hz). Because the meaningful frequency range is 0-500 Hz with most energy concentrated from 50-150 Hz [De Luca, 1997], the sampling rate set up to 1 KHz.

First, Fig. 3 illustrates patterns of EMG activity during forward perturbation. Biceps femoris m. and Gluteus m., corresponding respectively to ch. 7 and ch. 8, rarely activated and Peroneus longus m., corresponding to ch. 3, simultaneously activated with Gastrocnemius m. (ch. 2). So three muscles mentioned above, such as Biceps femoris m., Gluteus m. and Peroneus longus m., excepted from the process of feature extraction. Twenty features, such as IAV, SE, CF and VCF, were extracted from EMG signals (five ch.) of one event and used as input parameter of classifier. MATLAB (Math Works, V 7.0) was used for programming feature extraction and classification.

The classifier system consisted of 20 neurons in input layer, 10 neurons in hidden layer and 5 neurons in output layer. Training of neural network was able to be finished with 100 patterns in the training set and within a few hundred epochs by error-backpropagation algorithm. Test set size is fixed at 150 patterns. Then the classifier after learning could identify distinct types of EMG signals that were generated by five perturbations.

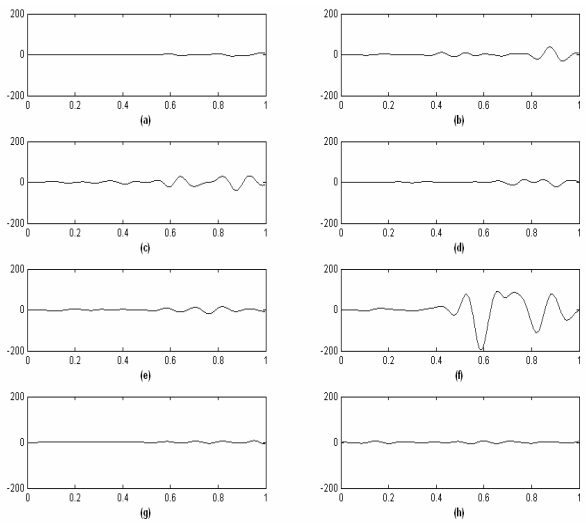

Fig. 4. Filtered EMG signal during forward perturbation. X-axis: time (s), Y-axis: amplitude (μV*1000), (a): ch. 1, (b): ch. 2, (c): ch. 3, (d): ch. 4, (e): ch. 5, (f): ch. 6, (g): ch. 7, (h): ch. 8

F. Ibrahim, N.A. Abu Osman, J. Usman and N.A. Kadri (Eds.): Biomed 06, IFMBE Proceedings 15, pp. 82-85, 2007
www.springerlink.com ' Springer-Verlag Berlin Heidelberg 2007

Table 1. Mean recognition rates (%). FP, BP, LP, OP1 and OP2 is forward, backward, lateral, oblique 45° and oblique 135° perturbation, respectively.

Motion / Subject	FP	BP	LP	OP1	OP2
a	87	85	86	84	83
b	83	77	78	75	73
c	74	79	69	60	63
d	77	74	70	63	61
e	76	71	77	72	70
f	81	84	74	75	70
g	79	80	81	70	60
h	84	81	82	75	74
i	84	80	82	70	65
j	71	73	70	62	64

Mean recognition rates during forward, backward and lateral perturbation are 80%, 78% and 77%, respectively, but mean recognition rate is 71% for oblique (45°) perturbation (Table 1) and 69% for (135°) perturbation. In case of subject-a as shown in Table 1, mean recognition rate is 85%. Whereas, in case of subject-j, mean recognition rate is 68%. We considered the causes of results are that the EMG patterns are changed according to differences among individuals, different locations of the electrodes and time variation caused by fatigue or sweat. Mean recognition rate on total subjects is 75%. For further recognition rate improvement of the system, several techniques such as feature selection method for reducing feature space dimension and combining multiple classifiers must be applied.

IV. Conclusions

The goal of this research is to perform the EMG pattern recognition during postural balance control of human body. We proposed an EMG pattern recognition method to classify motions of lower limb. Mean recognition rate during forward, backward and lateral perturbation is 80%, 78% and 77%, respectively, but in case of oblique perturbations, mean recognition rate is 70%. And mean recognition rate on ten subjects is 75%. For more accurate results, a larger training database is required and further improvement of the system may be achieved by several techniques such as feature selection method for reducing feature space dimension and combining multiple classifiers.

.

References

[1] P. Kannus, J. Parkkari, S. Koskinen, S. Niemi, M. Palvanen, M. Jarvinen, and I. Vuori,, (1999) Fall-induced injuries and deaths among older adults. JAMA, Vol. 281, 1895 1899.

[2] M. E. Tinetti, M. Speechley, and S. F. Ginter, Risk factors for falls among elderly persons living in the community. N. Engl. J. Med., Vol. 319, no. 26, 1701-1707.

[3] Osamu Fukuda, Toshio Tsuji, (2003) A human-assisting manipulator teleoperated by EMG signals and arm motions. IEEE Transactions on Robotics and Automation, Vol. 19, No. 2, 210-222.

[4] Kawamoto H., Sankai Y., (2002) Comfortable Power Assist Control Method for Walking Aid by HAL-3. IEEE International Conference on System, Man, and Cybernetics, 3877-3882.

[5] M. Maranzana Figini, M. Fabbro, (1981) A simulation model for the study of EMG signals in normal and pathological conditions. Electroencephalography and clinical neurophysiology, Vol. 52, No. 4, 378-381.

[6] C. F. Runge, C. L. Shupert, F. B. Horak, and F. E. Zajac, (1999) Ankle and hip postural strategies defined by joint torques. Gait and Posure, Vol. 10, 161-170.

[7] Y. C. Pai, M. W. Rogers, J. Patton, T. D. Cain, and T. A. Hanke, (1998) Staic versus dynamic predictions of protective stepping following waist-pull perturbations in young older adults. J. Biomechanics, Vol. 31, 1111-1118.

[8] M. W. Rosers, L. D. Hedman, M. E. Johnson, K. M. Martinez, and M. L. Mille, , (2003) Triggering of protective stepping for the control of human balance: age and contextual dependence. Cognitive Brain Research, Vol. 16, 192-198.

[9] Michael F. Kelly, Philip A. Parker, Robert N. Scott, , (1990) The application of neural network to myoelectric signal analysis: a preliminary study IEEE Trans. On Biomedical Engineering, Vol. 37, No. 3.

[10] Daniel Graupe, Jan Magnussen, Aloysius A. Beex, (1978) A microprocessor system for multifunctional control of upper limb prostheses via Myoelectric signal identification. IEEE Trans. On Automatic control, vol. Ac-23, no. 4.

[11] Bernard Hudgins, Philip Parker, (1993) A new strategy for mulitifunction myoelectic control. IEEE Transactions on Biomedical Engineering, vol. 40, No. 1.

[12] Willis J. Tonpkins, (1993) Biomedical Digital Signal Processing. Prentice Hall International Editions.

[13] D. L. Davies, D. W. Bouldin, (1979) A cluster separation measure. IEEE Trans. Pattern Anal. Machine Intell., Vol. PAMI-1, 224-227.

[14] B. Hannaford, S. Lehman, (1986) Short Time Fourier Analysis of the Electromyogram: Fast Movements and Constant Contraction. IEEE Transactions on Biomedical Engineering, Vol. BME-33, 1173-1181.

[15] Omid O., Judith D., (1998) Neural networks and pattern recognition. Academic Press, Inc.

Address of the corresponding author:

Author: Hyeonki Choi
Institute: Sungkyunkwan University
Street: 300 Chunchun-dong, Jangan-gu
City: Suwon
Country: Korea
Email: hkchoi@skku.edu

F. Ibrahim, N.A. Abu Osman, J. Usman and N.A. Kadri (Eds.): Biomed 06, IFMBE Proceedings 15, pp. 82-85, 2007
www.springerlink.com ' Springer-Verlag Berlin Heidelberg 2007

Biological Effects of EMF in Engineering Teaching Laboratories: A Review

W.N.L. Mahadi[1], N.A. Rashid[1], N. Md Ali, N. Soin[1], S.Z. Md Dawal[2]

[1]Department of Electrical Engineering, Faculty of Engineering, University of Malaya, Kuala Lumpur Malaysia
[2]Department of Manufacturing, Faculty of Engineering, University of Malaya, Kuala Lumpur Malaysia

Abstract— **Over the past two decades, there has been concern about potential adverse effects of EMF radiations on humans due to widespread use of electrical appliances. Reports have shown sufficient scientific evidence regarding the impact of electromagnetic field on the human health. This paper aims at reviewing the EMF effects particularly in higher education engineering laboratories. Several relevant methods on estimating EMF radiation has been studied and analyzed.**

Keywords— **Electromagnetic radiation, magnetic field, electric field, effects of EMF**

I. Introduction

Electromagnetic field or EMF is referred to as the presence of electromagnetic radiation, which consists of waves of electric and magnetic energy moving together through space at the speed of light. EMF is generated when an electric current runs through a wire or an appliance. These fields are characterized by a pair of vector fields of electric field, E (V/m) and magnetic field, H (A/m).

Many technological applications use or produce electromagnetic energy as found in electrical lighting and appliances, computers, computer monitors, and microwave ovens, radios, TVs, and cellular phones, broadcast stations, surveillance systems and communications satellites. It has been reported[1], that this technology has its harmful effects, not only for humans but also for every living thing. Electromagnetic fields and radiations cause cellular changes that may lead to health risks. It is believed that the association of electromagnetic fields increases behavioral changes and health problems such as epilepsy, leukemia, cancer, brain tumor, fatigue, headache, and loss of appetite, decreased blood pressure and itching. Many scientists and physicians suggest a link between these disorders and long-term exposure to EMF [2,3].

A. EMF in a typical engineering teaching laboratory

The static and time-varying magnetic fields from man made sources commonly have much higher intensities than the naturally occurring fields. At the present, many of man made sources; operating at the power frequencies of 50 or 60 Hz are to be found in laboratories at university, research, industrial and medical centre. The sources most frequently found at laboratories that cause EMF radiation are net currents; fluorescent lights; air conditioners; ceiling fans, distribution lines; electrical experiment apparatus for instance electronic devices, oscilloscopes, frequency generators; office equipment such as faxes, printers, copy machines, computers; and security systems.

In general, current flows from the power source to the appliance and back to the power source. Net current is generated when the forward and return currents have different intensities. It is important to note that the net currents is the most frequent source of EMF radiation since they are solely the result of wiring which does not conform to the wiring code.

Security systems for electronic surveillance in laboratories operate at frequencies ranging between 0.1 and 10 kHz. It requires a person to carry an identification magnetic strip to pass through the coil and the maximum magnetic flux generated by the coil is about 1 mT at the ground [4].

Stray fields generated by apparatus such as incubators, heaters, motors in laboratory systems can contribute to background exposure and yield ohmic heating and contribute to the temperature effects. The widespread use of computers and video display terminals (VDT) in laboratories have increasing concerns about potential effects from emissions of low level radiations since EMFs radiates from all sides of the computers. Magnetic fields as high as 0.9 μT under worst-case condition have been measured close to the surface of the screen (Bureau of Radiological Health, 1981).

Fluorescent ceiling lights produce more EMFs than incandescent bulbs. Typical fluorescent lights of an office ceiling have readings of 0.5 to 2 μT at 30 cm distance away [5]. At 6 inches away, the typical median magnetic field strength measurement for fax machine, copy machine, air cleaner are 6 mG, 90 mG and 180 mG, respectively [6].

B. Biological Effects of EMF in the laboratories

In the laboratories, students and researchers using the electrical and electronic equipments are constantly being exposed to EMF radiation since electrical appliances that run on electricity pose EMF radiation risks. Fluorescent light emits EM radiation with wavelengths between 380 800 nm. Wavelength of UV radiation is 100-400 nm, that is known to alter DNA sequences and gene expression.

F. Ibrahim, N.A. Abu Osman, J. Usman and N.A. Kadri (Eds.): Biomed 06, IFMBE Proceedings 15, pp. 86-88, 2007
www.springerlink.com ' Springer-Verlag Berlin Heidelberg 2007

Some human show greater sensitivity to electromagnetic radiation, after being exposed in multiple ways from the surrounding electrical equipments as some researchers show symptoms of extreme stress, chronic fatigue syndrome (CFS), attention issues, and allergies, depression and sleep disturbances. CFS is depressed immune system associated to exposure to extremely low frequency electromagnetic fields.

Studies have also shown that both high and low frequency EMFs are capable of impairing resistance to infection.

II. Measurement of EMF in Laboratories

There are five methods to measure EMF exposure that are commonly used in the majority of published epidemiological studies of EMF exposures which are; wire codes, spot measurements, personal monitor and calculated historical fields [7].

Wire codes, is a classification of homes based on the types of power lines outside the house and their distance from it. The system of wire codes estimates the magnetic field levels from the visual assessment of the characteristics features of power lines (such as thickness of wire, wire configuration, etc.) and distance of power lines nearby to home. Several studies have shown that wire codes can be used consistently to rank home crudely according to the median magnetic field intensity. However, wire codes are not preferable in estimate of exposure to electric fields within homes.

Spot measurements were the basis of a standardized protocol for measuring magnetic fields in home over a short time period. The spot measurements involve the measurement of actual levels and could capture exposure from sources such as appliances and home wiring. Instantaneous measurements are taken at body locations or work areas, generally with simple metrics such as the rms vector magnitude of the ELF magnetic field. Previous studies had involved a variety of protocols, for instance 24-hour recordings and spot measurements taken in several areas, to measure magnetic fields.

Personal monitors or dosimeters measure EMF exposures over an hour, a shift, a day or longer. The rationale reason for using personal measurements was to ascertain human s EMF exposure from all sources (such as residential, school, etc.) and to afford more detailed information about characteristics of individual spatial and temporal variation in exposure [8].

A calculated historical field is estimation method based on a theoretical calculation of the magnetic field emitted by power lines using historical electrical loads on those lines. An important feature of historical method was that a computer model was used to calculate magnetic fields from the transmission lines in residential area around the time of diagnosis, rather than depending on cotemporary measurements. Table 1 shows examples on typical field strength of laboratory equipments.

Table 1 Typical magnetic field strength of equipments in the laboratory[6]

Electric equipments	**Spot Measurement (mG)**			
	6 inches	**1 foot**	**2 feet**	**4 feet**
Fluorescent lights	40	6	2	-
Video Display terminals	14	5	2	-
Ceiling Fans	50	6	1	-
Fax Machines	6	-	-	-
Copy Machines	90	20	7	1
Air Conditioners	3	1	-	-
	Measured 6 inches and away			
Power cables in floor	15-170			
Other electrical Equipments	10-200			
Drills	20			

Magnetic field measurement unit is milliGauss (mG) and taken as the median value.

III. Evaluation of EMF

Based on [9], exposure assessment for low frequency fields was performed at large, different locations and facilities of utilities. In this study, EMDEX II was used to measure EMF characterizations. The instrument measures magnetic flux densities using three orthogonal mounted sensors and gives the individual spatial components and the recorded field magnitude range averaged over the sampling interval. Magnetic field spot measurement obtained using the EMDEXII meter during the initial walk-through survey in utilities facilities are summarized in Table 2.

F. Ibrahim, N.A. Abu Osman, J. Usman and N.A. Kadri (Eds.): Biomed 06, IFMBE Proceedings 15, pp. 86-88, 2007
www.springerlink.com ' Springer-Verlag Berlin Heidelberg 2007

Table 2 Magnetic Flux densities Measured During Utilities Facilities Walk-Through Survey

Location	Magnetic Flux Density(mG)
(a)Ground floor *	
Entrance	0.8 1.0
Lobby	1.0 1.2
Hall	1.2 3.2
Computer rooms	1.6 5.0
(b) Second Floor	
Wall power panel	
Adjacent offices*	14 - 16
Hallways*	8 - 35
Power utility room*	50 - 75
Computer rooms**	
Tape Drive	25 - 30
VDT(side)	30 - 35
VDT(front)	2 - 6
Printer	20 - 35
Work station monitor	4 - 8

* 1 m above floor level ** 0.2m away from source

In general access area, magnetic fields were approximately 2.5 mG and appear to represent background levels. On the other hand, magnetic fields measured near power supply panels in these areas ranged from 8 mG to 75 mG. The highest values measured were near computer tape drives, printers and near power supply systems it was found to be around 75 mG. Most of the electronic equipment was found to generate magnetic fields throughout the low frequency but with varying characteristics frequencies.

The equipments in the laboratories may not contribute extremely high EMF radiation as in power lines [10,11]. However the cumulative effect after prolong exposure to these equipments may contribute to more serious health risks.

IV. Conclusion

This paper has identified the electromagnetic field radiation in laboratories. Studies of EMF have been based on measurements at one point in time, stationary monitoring over time or area measurements involving mapping of the spatial characteristics of fields. The biological effects of EMF in such an enclosed environment were also reviewed. The interactions of humans with EMF is complex, and undoubtedly continue to be of public concern.

References

1. Miller A. B, To T, Agnew D. A**,** Wall C and Green L M (1996). Leukemia Following Occupational Exposure To 60 Hz Electric And Magnetic Fields Among Ontario Electric Utility Workers. *Epidemiology* (144) 150-160.
2. Gudnel, P., Nicolau J., Imbernon E, Chevalier A and Goldberg M. (1996) Exposure to 50 Hz Electric Field and Incidence of Leukemia, Brain Tumors, and Other Cancers among French Electric Utility Workers. *Epidemiol*ogy (144) 1107-2.
3. International Programme on Chemical Safety, Environmental Health Criteria 69. World Health Organization , Geneva , 1987.
4. Mixon P. D. (1998) Power Line Electromagnetic and The EMF Issue : An Update For 1998 . Papers presented at the 42nd Annual Conference on Rural Electric Power Conference. Pg: 1-6.
5. WHO International EMF Project , http://www/who.int/peh-emf/project.
6. EMF In Your Environment . http://www.web-pub.com
7. Electric and Magnetic Field Exposure Assessment of Powerline and non-Powerline Sources for california Public School Environments . http://www.dhs.ca.gov/ps/deodc/ehib/emf.
8. Qabazard A.M, Elhirbawy M.A (2005) Physical Measurements and Calculation Approach of Extremely Low Frequency Electromagnetic Field. International Symposium on Electromagnetic Compatibility, EMC 2005 (2)509-514.
9. Farag A.S, Dawoud M.M, Cheng T.C, Cheng J.S, (1997) Occupational Exposure Assessment For Power Frequency Electromagnetic Fields. *Proceedings of the 32nd Intersociety on Energy Conversion Engineering Conference*. (3)2107-2113.
10. Azzuhri S.R, Mahadi W.N.L (2004), Power transmission Line Magnetic Fields: A Survey on 120 kV Overhead Power Transmission Lines in Malaysia , *IEEE TENCON 2004*, Chiang Mai, Thailand, paper 0770.
11. Mahadi W.N.L, Md.Ali N., Soin N, Hj.Siraj S.F (2000), Biological Effects of Electromagnetic Fields: A Review , National Conference on Biomedical Engineering Malaysia, pg. 74-77.

Address of the corresponding author:

Author: Wan Nor Liza Mahadi
Institute: University Malaya
Street: Jalan Pantai Baru
City: Kuala Lumpur
Country: Malaysia
Email: wnliza@um.edu.my

F. Ibrahim, N.A. Abu Osman, J. Usman and N.A. Kadri (Eds.): Biomed 06, IFMBE Proceedings 15, pp. 86-88, 2007
www.springerlink.com ' Springer-Verlag Berlin Heidelberg 2007

Theta Burst Transcranial Magnetic Stimulation Can Modify Cortico-Muscular Coherence in Humans

M. Saglam[1], K. Matsunaga[2], H. Yanagida[1], Y. Hayashida[1], T. Igasaki[1], N. Murayama[1] and R.Nakanishi[2]

[1] Dept. of Graduate School of Science and Technology, Kumamoto University, Japan
[2] Dept. of Neurology, Kumamoto Kinoh Hospital, Kumamoto, Japan

Abstract **Previous studies have shown that repetitive transcranial magnetic stimulation (rTMS) can modify cortical excitability in humans, and particularly that a recently-proposed rTMS protocol, "theta burst stimulation" (TBS) can induce the long-lasting effects with the stimulation duration much shorter than those of conventional rTMS protocols. However, in those studies, the effects of rTMS were assessed mainly by means of motor evoked potential, and how the rTMS affects functional coupling between cortex and muscle was least studied. Here, we examined the coherence between electroencephalographic (EEG) and electromyographic (EMG) signals during isometric hand (first dorsal interosseous muscle) contraction, before and after application of TBS to primary motor area (PMA). Magnitude of the EEG-EMG coherence at beta band (13-30Hz), localizing for the C3 scalp site, significantly decreased 30-60 minutes after TBS and, in 90-120 minutes, gradually recovered to the control level before TBS. The present results suggested that TBS applied to PMA can suppress the cortico-muscular synchronization.**

Keywords **Theta Burst Transcranial Magnetic Stimulation, Electroencephalogram, Electromyogram, Coherence, Primary Motor Area.**

I. Introduction

Transcranial magnetic stimulation (TMS) on motor cortex can activate cortico-spinal tract with a short pulse [1], eliciting field potentials from the descending motor pathways. Thus, the cortex-to-muscle signal transmission can be examined by measuring motor evoked potentials (MEP) in response to single TMS pulse. On the other hand, functional coupling between the cortex and the muscle can be assessed by the coherence analysis on electroencephalographic (EEG) and electromyographic (EMG) signals recorded during voluntary isometric muscle contraction [2, 3, 4]. In previous studies, both the MEP measurements and the EEG-EMG coherence analysis were used to reveal the circuit configurations of motor cortex and cortico-muscular pathways [2, 3], and it was demonstrated that those circuit configurations can be modulated by repetitive TMS (rTMS) to motor cortex [5,6,7,8,9] as well as externally applied sensory stimulations [10]. Recently, theta burst stimulation (TBS) was proposed as a promising substitute for conventional protocols of rTMS [11]. TBS applied to primary motor area (PMA) can produce a decrease/increase in the amplitude of MEP for a period of time longer than those with conventional rTMSs [e.g. 1 hr with TBS vs. 15 min with 0.9-Hz rTMS], despite its relatively less number of the pulses applied and short–stimulation duration [e.g. 600 pulses for 40 sec with TBS versus 810 pulses for 15 min with 0.9-Hz rTMS]. In the present study, we examined if the TBS to PMA can modulate–the EEG-EMG coherence during isometric hand contraction.

II. Materials and Methods

A. Experimental Procedures

Subjects: 6 healthy right-handed volunteer subjects participated and gave written informed consents.

Determination of PMA: High Power Magstim 200 machine (Magstim, Whitland, Dyfed, UK) and figure-of-8 coil with a mean loop diameter of 90 mm were used to apply single monophasic (width of 100μs) TMS pulses to evoke MEPs. PMA was determined by moving the coil in 1 cm steps around the presumed PMA and simultaneously observing the MEP response of the first dorsal interosseous (FDI) muscle. The stimulation site that gave maximum MEP was assumed to be PMA.

Stimulation Intensity: Magstim Super Rapid (Magstim, Whitland, Dyfed, UK) and figure-of-8 coil with a mean loop diameter of 90 mm were used to apply single biphasic (width of 300μs) TMS pulses to evoke MEPs. Pulse strength was gradually decremented to find lowest stimulus intensity (Active Motor Threshold-AMT) that elicited MEPs around 200μV.

Theta Burst Stimulation: TBS was delivered to PMA using the same setup for determination of stimulation intensity. Each single TMS pulse is biphasic and has an intensity of 80% AMT and 600 pulses constitute the pattern shown in figure 1.

F. Ibrahim, N.A. Abu Osman, J. Usman and N.A. Kadri (Eds.): Biomed 06, IFMBE Proceedings 15, pp. 89-93, 2007
www.springerlink.com ' Springer-Verlag Berlin Heidelberg 2007

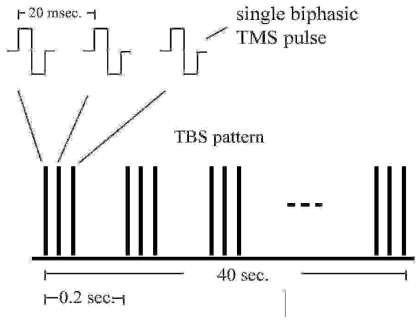

Fig. 1 Graphical illustration of 40 s-train of TBS paradigm (Totally 600 pulses).

EEG and EMG Recording: EEG signals were recorded with ear lobe reference from 19 surface electrodes placed according to International 10-20 electrode method. EMG was recorded from right FDI muscle with the contraction level of 15–5 % of the maximum. A digital device gave visual feedback to subjects prior to the experiment to maintain constant contraction. EMG and EEG signals were recorded with 1 kHz sampling frequency and band-pass filtered with 0.5-200 Hz and 5-300 Hz, respectively.

EEG and EMG signals were recorded as a set of 4 trials each of which lasts 1 minute. Subjects were asked to rest 30 seconds between two trials in order to avoid fatigue. Two sets of experiment were performed 30 minutes (pre30) and just prior (pre0) to the TBS stimulation. Hot spot and intensity determination for TBS was performed between first and second sets prior to TBS. In order to assess after-effects of TBS, 0 (just after), 30, 60, 90, 120 minutes-after-recordings were done respectively.

B. Data Analysis

Coherence: Synchronization level between EEG and EMG signals was investigated with the coherence analysis. Data was divided into 1024 point-long epochs and FFT was calculated for coherence function given below:

$$0 \le \kappa_{xy}^2(f) = \frac{\left|S_{xy}(f)\right|^2}{\left|S_{xx}(f)S_{yy}(f)\right|} \le 1 \qquad (1)$$

Here, $S_{xy}(f)$ stands for the estimated cross-spectral density function. $S_{xx}(f)$ and $S_{yy}(f)$ represent auto-spectral density of the signals x(t) and y(t), respectively. Coherence function always takes values between 0 and 1 where $\kappa_{xy}(f)$=0 indicates lack of dependency and $\kappa_{xy}(f)$=1 represents perfect linear correlation between two signals [2]. 95% (α=0.95) confidence limit which can be calculated using the following formula:

$$CL(\alpha) = 1 - (1-\alpha)^{1/M-1} \qquad (2)$$

where M is the number of epochs used for coherence calculation.

III. Results

Figure 2 shows two samples of 1024 msec.-long segments of EEG and EMG signals recorded 30 minutes before and 60 minutes after TBS from subject 1. Significant EEG-EMG coherence was observed on the beta band (15-30 Hz for 30 minutes before and 20-25 Hz for 60 minutes after). Peak values were significantly decreased (0.08 vs. 0.03) and the peaks were at 19 and 21 Hz, respectively.

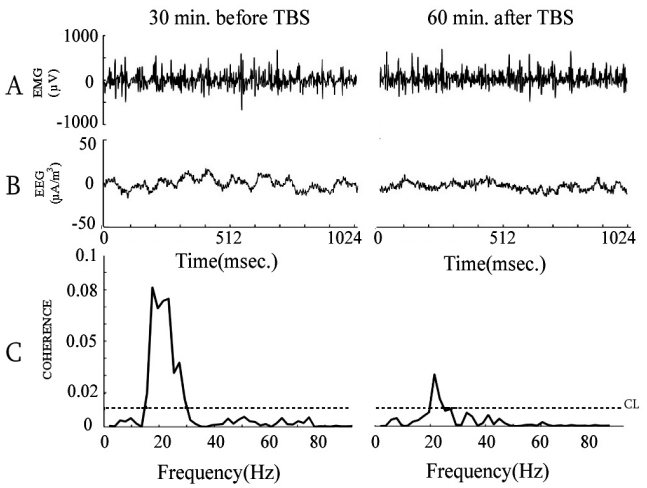

Fig. 2 1024msec.-long segments of (A) EEG (C3) and (B) EMG (FDI) recorded 30 min. before and 60 min. after the TBS. (C) EEG-EMG Coherence of the 4 minute-long respective data set.

Averaged peaks (6 subjects) are shown in figure 3 where spatial distribution of EEG-EMG coherence is also given. Peak coherence occurred only at beta band (21.9 – 0.94 Hz) at left PMA (5 subjects on C3, 1 subject on F3). The mean peak coherence value at C3 is observed as 0.038–0.011 where the confidence limit is 0.01. EEG-EMG coherences from other scalp sites are found insignificant; they remain below the confidence limit.

F. Ibrahim, N.A. Abu Osman, J. Usman and N.A. Kadri (Eds.): Biomed 06, IFMBE Proceedings 15, pp. 89-93, 2007
www.springerlink.com ' Springer-Verlag Berlin Heidelberg 2007

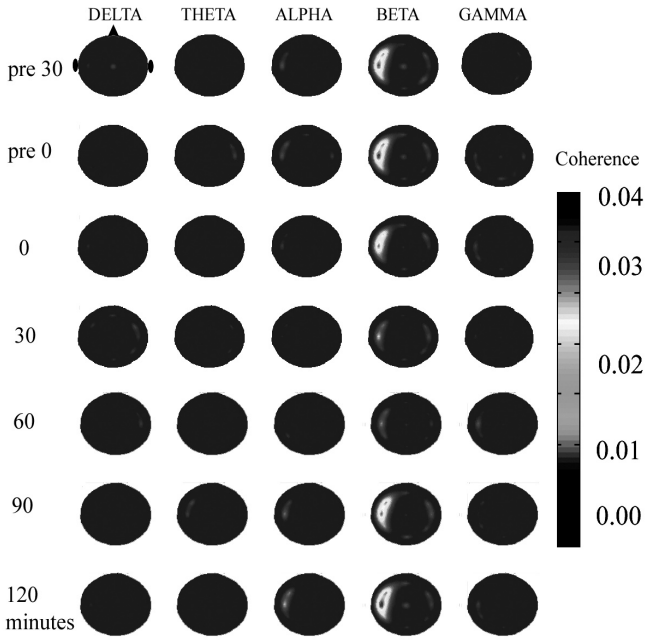

Fig. 3 Topography of EEG-EMG coherence at delta (1-4 Hz), theta (4-8 Hz), alpha (8-12 Hz), beta (13-30 Hz) and gamma (30-40 Hz) bands. Pre30 and pre0 are the recordings of 30 minutes and 0 minutes before TBS.

In figure 4, temporal and spectral distribution of EEG (C3)-EMG (FDI) coherence is illustrated. Initial coherence was significantly suppressed by TBS. Suppression started just after the stimulation and maximum effect took place between 30-60 minutes after the delivery of TBS (0.048 – 0.013 vs. 0.018 – 0.005). Recovery to the baseline value was observed (0.018 – 0.005 vs. 0.048 – 0.014) 90-120 minutes after TBS.

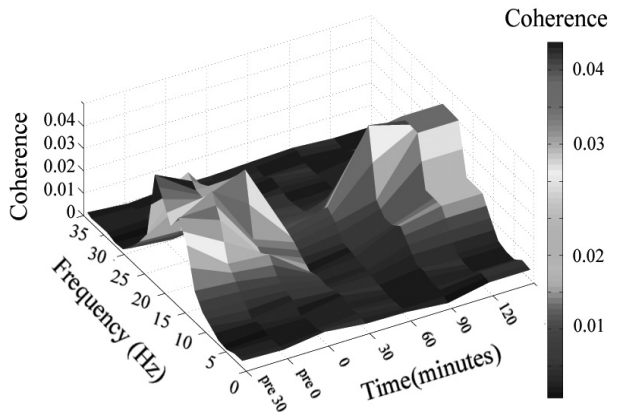

Fig. 4 EEG (C3)-EMG coherence. Hot-spot search was made between pre 30 (30 minutes before) and pre 0 (just before) recordings. Stimulation applied between pre 0 and 0 minute (just after) recordings.

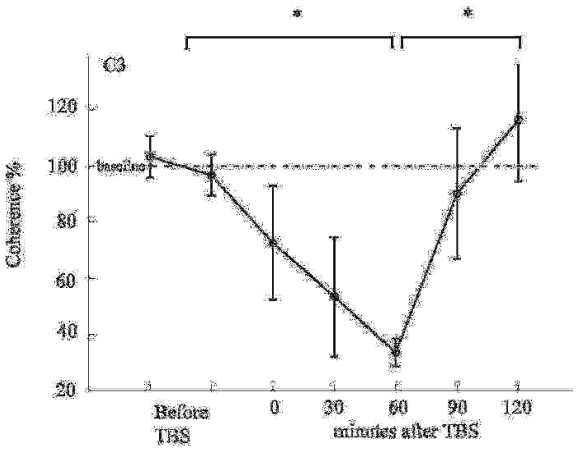

Fig. 5 Beta EEG (C3)-EMG coherence percentage changes. Pre-stimulation values were taken as baseline. Coherence change (P<0.01; post-hoc testing using the Bonferroni multiple comparison tests) was observed between (*) 'Before TBS and 60 min. after TBS' and '60 min. after TBS and 120 min. after TBS'. Error bars indicate standard error of mean (–SEM).

Figure 5 shows the percentage change of the EEG(C3)-EMG coherence after TBS. Mean of the coherences 30 min. and 0 min. before TBS was taken as the baseline (100%). Coherence percencantage was significantly (P<0.01; post-hoc testing using the Bonferroni multiple comparison tests) supressed. Maximum supression occured 60 min. after TBS (33%). Recovery was observed after 90 and 120 minutes.

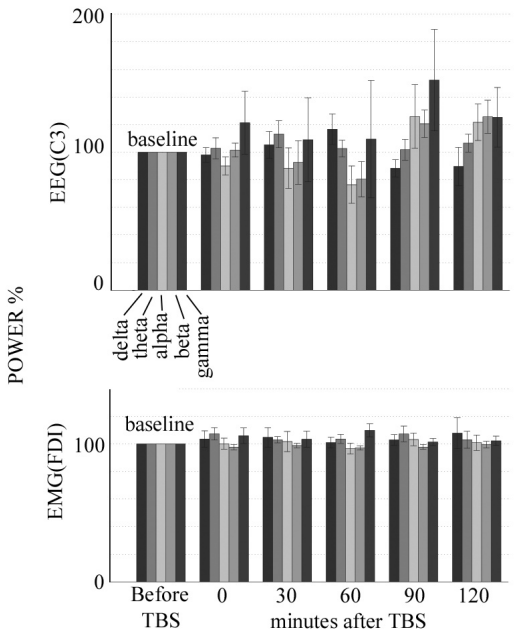

Fig. 6 Percentage distribution of spectral EEG (C3) and EMG (FDI) powers. Power distribution ratio of post 0, 30, 60, 90, 120 minutes recordings to the baseline (before TBS) are given. Vertical bars represent the distribution in respective order: delta, theta, alpha, beta and gamma bands.

F. Ibrahim, N.A. Abu Osman, J. Usman and N.A. Kadri (Eds.): Biomed 06, IFMBE Proceedings 15, pp. 89-93, 2007
www.springerlink.com ' Springer-Verlag Berlin Heidelberg 2007

Alpha power percentage of EEG (C3) decreased 30 and 60 minutes and recovered 120 minutes ($P<0.05$; post-hoc testing using the Bonferroni multiple comparison tests) after the stimulation where beta coherence suppressed most (Fig. 6). On the other hand, EMG (FDI) power percentage distribution did not change in response to TBS.

Reproducibility of the effect of TBS on EEG-EMG coherence was investigated by performing the same experiment on different days for 3 subjects. The suppression and the following recovery demonstrate the reproducibility of the experiment (Fig.7).

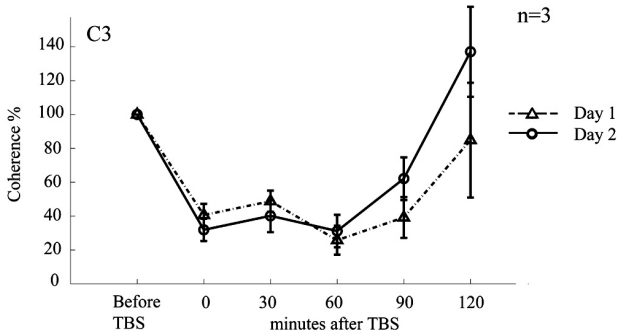

Fig. 7 Reproducibility of TBS. Beta EEG (C3)-EMG coherences from Day-1 and Day-2 experiments were compared. Error bars indicate SEM.

IV. Discussion

Our results first indicate that peak coherence values occur strictly within the beta band (21.9 – 0.94 Hz). This is consistent with the reports on the EEG-EMG coherence during isometric contraction of the FDI [10, 12, 13, 14].

We found clear results where EEG-EMG coherence is suppressed by 40 second-long TBS on PMA. Suppression after 30-60 minutes advocates that TBS inhibits motor cortical excitability. In previous studies motor cortex excitability (by means of MEP amplitude) was suppressed for the first 60 minutes (max. suppression at 10-20 min.) [11]. Here one may claim that EEG-EMG coherence is a different output measure of the motor cortex-muscle interaction than MEP. Maximum coherence suppression occurs later then MEP suppression (10-20 min. vs. 30-60 min.) however the duration of the effect is similar (0-60 min. vs. 0-60 min.). Huang et al. [11] introduced TBS as a longer-lasting substitute for 1 Hz rTMS. We confirmed this idea by comparing EEG-EMG coherence suppressions. It was reported that EEG-EMG coherence was suppressed by using 0.9 Hz rTMS [6]. Our results confirm that TBS effect persists longer than rTMS (15 min. vs. 60 min.).

We showed that EMG power distribution within all frequency bands did not change with respect to TBS. However EEG (C3) alpha power percentage was decreased 30 and 60 minutes after TBS (Fig. 6). This result may arouse the idea of the correlation between C3 alpha power and EEG-EMG beta coherence. In [10], EEG-EMG coherence was investigated in response to visual stimulation during isometric FDI contraction. Coherence was enhanced on beta band during the visual stimulation while alpha power at EEG (C3) was increased and EMG power remained unchanged. Here we could speculate that some cortical activity at alpha band drives the synchronization between EEG (C3) and EMG on beta band during isometric contraction. This driving factor could be enhanced by the visual stimulation [10] or inhibited by magnetic stimulation.

V. Conclusions

We demonstrated that TBS can be a substitute to 1 Hz rTMS not only by means of MEP decrease but also EEG-EMG coherence suppression; because TBS requires shorter stimulation and provides longer effect of coherence suppression than 1 Hz rTMS.

References

1. Rothwell JC (1997) Techniques and mechanisms of action of transcranial stimulation of the human motor cortex. J. Neurosci. Methods 74(2), 113-122.
2. Mima T, Hallett M (1999) Corticomuscular coherence: a review J. Clin Neurophysiol., 16(6), 501-511.
3. Mima T, Hallett M. (1999) Electroencephalographic analysis of cortico-muscular coherence: reference effect, volume conduction and generator mechanism. Clin Neurophysiol., 11, 1892-1899.
4. Salenius S, Portin K, Kajola M et al. (1997) Cortical control of human motoneuron firing during isometric contraction. J. Neurophysiol. 77(6), 3401-3405.
5. Todd G, Flavel S C, Ridding M.C. (2006) Low intensity repetitive transcranial magnetic stimulation decreases motor cortical excitability in humans , J. Appl. Physiol. In press.
6. Safri N M, Murayama N, Igasaki T et al. (2006) Effects of visual stimulation on cortico-spinal coherence during isometric hand contraction in humans. Int. J. Psychophysiol. 61(2), 288-293.
7. Chen W H, Mima T et al. (2003) Low-frequency rTMS over lateral premotor cortex induces lasting changes in regional activation and functional coupling of cortical motor areas. Clin. Neurophysiol. , 114(9), 1628-1637.
8. Matsunaga K, Maruyama A, Fujiwara T et al. (2005) Increased corticospinal excitability after 5 Hz rTMS over the human supplementary motor area. J. Physiol. 562(1), 295-306.
9. Oliviero A, Strens L H A., Lazarro V et al. (2003) Persistent effects of high frequency repetitive TMS on the coupling between motor areas in the human, Exp. Brain Res., 149, 107-113.
10. Rizzo V, Siebner H R, Modugno N et al.(2004) Shaping the excitability of human motor cortex with premotor rTMS. J. Physiol. 554(2),483-495
11. Huang Y Z , Edwards M J, Rounis E et al. (2005) Theta Burst Stimulation of the Human Motor Cortex, Neuron, 45,201-206.
12. Murayama N, Lin YY, Salenius S, Hari R et al. (2001) Oscillatory interaction between human motor cortex and trunk muscles during isometric contraction. Neuroimage, 14, 1206-1213.

F. Ibrahim, N.A. Abu Osman, J. Usman and N.A. Kadri (Eds.): Biomed 06, IFMBE Proceedings 15, pp. 89-93, 2007
www.springerlink.com ' Springer-Verlag Berlin Heidelberg 2007

13. Conway B.A., Halliday D.M., Farmer S.F., Shahani U., Maas P., Weir A.I., Rosenberg J.R. (1995) Synchronization between motor cortex and spinal motoneuronal pool during the performance of a maintained motor task in man. J. Physiol. 489(3), 917-924.
14. Safri N.M., Tanaka M., Murayama N., Igasaki T.(2004) The influence of visual stimuli on cortico-muscular synchronization during isometric contraction in human., Kuala Lumpur International IFMBE Proc.2004, 7, 149-152

Address of the corresponding author:

Author: Prof. Nobuki Murayama
Institute: GSST, Kumamoto University
Street: Kurokami 2-39-1, 860-8555
City: Kumamoto
Country: Japan
Email: murayama@cs.kumamoto-u.ac.jp

F. Ibrahim, N.A. Abu Osman, J. Usman and N.A. Kadri (Eds.): Biomed 06, IFMBE Proceedings 15, pp. 89-93, 2007
www.springerlink.com ' Springer-Verlag Berlin Heidelberg 2007

Cell Adhesion and Degradation Behaviors of Acetylated Chitosan Films

S.M. Lim[1], D.K. Song[1], K.J. Cho[1], S.H. Oh[1], D.S. Lee-Yoon[2], E.H. Bae[2] and J.H. Lee[1]

[1]Department of Advanced Materials, Hannam University, Daejeon 306-791, Korea
[2]Regen Biotech, Ltd, Seongnam 462-120, Korea

Abstract— **Chitoan, which is derived from chitin, is a linear heteropolysaccharide composed of β-1,4-linked D-glusosamine (GlcN) and N-acetyl-D-glucosamine (GlcNAc) with various compositions of these two monomers. The degree of acetylation (DA) represents the portion of GlcNAc units to total number of units. DA of chitosan influences not only the physicochemical characteristics, but also the biodegradability and biocompatibility. We synthesized DA-controlled chitosans (from 10% to 90%) by the acetylation reaction of deacetylated chitosan (DA ~ 10%) and acetic anhydride with different ratio. The DA value of the chitosans was characterized by solid state 13C NMR and FT-IR spectroscopies. Surface properties of chitosan films with different DA value were investigated by the measurements of water contact angle and Zeta potential. The cell compatibility of the acetylated chitosans was estimated by cell culture using NIH/3T3 mouse fibroblasts and C28/I2 human chondrocytes. It was observed that the cell adhesion and growth decreased on the acetylated chitosan film surfaces with increasing DA value, probably owing to the increased number of acetyl groups leading to the increased hydrophobicity and reduced positive charge on the film surfaces. The degradation behavior of the acetylated chitosan films was also investigated in the solutions of lysozyme and/or N-acetyl-β-D-glucosaminidase, which are enzymes for chitosan existed in the human body. The degradation rate of the films with different DA value was observed as follows: 50 % > 30 % ≈ 70 % > 90 % > 10 %. Modifying the DA of chitosan provides a powerful means for controlling biodegradation and biocompatibility and can be optimized for tissue engineering applications.**

Keywords— **Chitosan, Degree of acetylation (DA), Surface properties, Cell adhesion, Degradation**

I. Introduction

Chitosan is a non-toxic and biocompatible cationic polymer derived from chitin which exhibits numerous interesting physicochemical and biological properties. Chitosan is a linear heteropolysaccharide composed of β-1,4-linked-D-glucosamine (GlcN) and *N*-acetyl-D-glucosamine (GlcNAc) with various compositions of these two monomers [1, 2]. The degree of acetylation (DA) represents the proportion of *N*-acetyl-D-glucosamine units with respect to the total number of units. It allows us to define the two terms, chitin and chitosan. In the case of chitosan, DA value is usually considered to be below 50 %. This value also determines the solubility limit of the polymer in dilute acidic solutions ($2 < pH < 6$) [2]. Commercially available chitosans have been obtained by the deacetylation of chitin in a concentrated alkali with high temperature. However, their low solubility (thus processing difficulty) in common solvents caused by block-type (heterogeneous) distribution of the GlcNAc residues and low DA reproducibility which leads non-uniform physicochemical properties and biodegradability are still remained as some limitations. To overcome these problems, DA-controlled chitosans (from 10% to 90%) were synthesized by the acetylation reaction of deacetylated chitosan (DA ~ 10%) and acetic anhydride with different ratio in this study. The acetylated chitosans seem to have random-type (homogeneous) distribution of the GlcNAc residues. The films fabricated from the chitosans with different DA value were investigated by the observations of surface properties, cell compatibility, and the enzymatic degradation behavior.

II. Materials and methods

A. Materials

Chitosan (Mw, 160,000; DA, ~10 %) was supplied by Regen Biotech Inc. (Korea). Acetic anhydride was purchased from Junsei (Japan). Lysozyme (human milk) and *N*-acetyl-β-D-glucosaminidase (bovine kidney) were purchased from Sigma (USA). All other chemicals used were reagent grade.

B. Preparation and characterization of chitosans with different DA

Chitosan (DA, ~10 %) was dissolved in 0.1 M acetic acid. Acetic anhydride (predetermined amount for controlling DA from 10 to 90 %, respectively) was added into the chitosan solution and was kept at room temperature for 1 hr with agitation. Subsequently, synthesized acetylated chitosan was precipitated in NH_4OH solution. The precipitated acetylated chitosan was filtered and neutralized in 75 % methanol and the following deionized water.

The DA value of the acetylated chitosans was determined by solid-state ^{13}C NMR (Unity Inova 200, Varian, USA) and FT-IR (1000 PC, Perkin-Elmer, USA) spectroscopies. From the NMR spectroscopy (applied integral ratio of 6

F. Ibrahim, N.A. Abu Osman, J. Usman and N.A. Kadri (Eds.): Biomed 06, IFMBE Proceedings 15, pp. 94-97, 2007
www.springerlink.com ' Springer-Verlag Berlin Heidelberg 2007

carbon and new CH_3 in saccharide ring), DA was calculated using the following equation [3]:

$$\text{Degree of acetylation (DA)} = \frac{I_{CH3}}{(I_{C1} + I_{C2} + I_{C3} + I_{C4} + I_{C5} + I_{C6}) / 6}$$

From the FT-IR spectroscopy (using amide III band (C-N stretching coupled with N-H in plane deformation) at 1320 cm^{-1} as the analytical band and the band at 1420 cm^{-1} as the internal reference band), DA was calculated as follows [3]:

$$\text{Degree of acetylation (DA)} = 31.92 \times (A_{1320}/A_{1420}) - 12.2$$

C. Preparation and characterization of acetylated chitosan films

Acetylated chitosan films were prepared by casting acetylated chitosan solutions (in 0.1 M acetic acid) onto glass Petri dishes. The prepared films were dried at room temperature and neutralized by washing in NH_4OH aqueous solution. Then the films were repeatedly washed with deionized water and finally dried again. The thickness of the prepared films was about 200 μm.

The acetylated chitosan film surfaces were characterized by measuring water contact angles using an optical bench type contact angle goniometer (Model 100-0, Rame-Hart, Inc., USA) to examine the surface hydrophilicity/hydrophobicity or wettability of the films. The acetylated chitosan film surfaces were further characterized by measuring Zeta-potentials in PBS (with polystyrene latex monitor, 520 nm) using an electrophoretic measurement apparatus (ELS-8000, Otsuka electronics, Japan) with a plate cell to investigate the surface charge character of the films.

D. Cell culture on acetylated chitosan film surfaces

The acetylated chitosan films (DA, 10, 30, 50, 70, and 90 %) sterilized by ethylene oxide (EO) were placed on 6-well polystyrene (PS) plate (Corning, USA). Fibroblasts (NIH/3T3 mouse embryo fibroblasts, Korean Cell Line Bank, Korea) and chondrocytes (immortalized human costal chondrocyte cell line C-28/12, Beth Israel Deaconess Medical Center, USA) were used as model cells to estimate cell adhesion and growth behaviors on the acetylated chitosan film surfaces. A cell suspension in RPMI (for fibroblasts) or DMEM (for chondrocytes) containing 10 % fetal bovine serum (FBS, Gibco, USA), 0.1 % gentamicin sulfate (Sigma, USA), and 1 % penicillin G (Sigma) was seeded to the each film surface (cell density, 4×10^4 cells/specimen). The cell-seeded films were maintained for 1 day at 37 °C in an incubator with humidified 5 % CO_2 atmosphere for cell adhesion to the films. After that, the cells on the films were cultured up to 4 days with mild shaking (about 50 rpm). The viable cell numbers on the film surfaces were estimated by a hemacytometer.

E. Degradation test of acetylated chitosan films

The acetylated chitosan films (DA, 10, 30, 50, 70, and 90 %; about 100 mg) were placed in polypropylene conical tubes, each containing 50 mL PBS dissolving 10 mg/L lysozyme and/or 5 U/L *N*-acetyl-β-D glucosaminidase, which are enzymes in the human body inducing chitosan degradation [4, 5]. The tube was sealed and kept at 37 °C with mild shaking (about 50 rpm) for up to 56 days. Periodically, 2.0 mL of the enzyme solution was taken and mixed with 5.0 mL of ferricyanide solution (0.5 g of potassium ferricyanide in 1 L of 0.5 M sodium carbonate). The solution color intensity (absorbance) was measured at 420 nm using UV spectroscopy (Lambda14, Perkin-Elmer, USA) [6]. The molar concentration of *N*-acetyl-D-glucosamine residues formed by degradation of the chitosans was determined from the calibration curve. The calibration curve was obtained using *N*-acetyl-D-glucosamine (end group of chitosan; 99 %, Aldrich, USA) as a standard. The degradation behavior of the chitosan films was also evaluated by the measurement of weight loss. The chitosan film in enzyme solution was taken out, washed extensively with deionized water, freeze-dried, and then weighed.

III. Results and Discussion

A. DA analysis of chitosans

Table 1 compares the DA values of acetylated chitosans measured by solid-state ^{13}C NMR and FT-IR spectroscopies and theoretically calculated values. The results clearly showed that the DA values measured by both spectroscopies are closely matched with the theoretically calculated ones indicating that the synthetic method for chitosan acetylation used in this study as well as the DA analysis methods are suitable.

Table 1 Analysis results of DA values of acetylated chitosans

DA(Theo.)(%)*	10	30	50	70	90
Solid state ^{13}C NMR	10.9	28.91	48.84	67.83	81.57
FT-IR	11.9	27.65	46.58	63.39	83.23

*Theoretically calculated DA

F. Ibrahim, N.A. Abu Osman, J. Usman and N.A. Kadri (Eds.): Biomed 06, IFMBE Proceedings 15, pp. 94-97, 2007
www.springerlink.com ' Springer-Verlag Berlin Heidelberg 2007

B. Surface characterizations of chitosan films

Figure 1 shows the water contact angles and Zeta potentials of the acetylated chitosan film surfaces with respect to the DA values. As the DA value increased from 10 to 90 %, the water contact angles decreased from 95° to 72°, while the Zeta potential gradually increased. These are possibly owing to the increased number of acetyl groups on the film surfaces leading to the increased hydrophobicity and decreased positive charge character (NH_3^+).

C. Cell adhesion and growth behavior

Fibroblasts and chondrocytes were seeded on EO-sterilized acetylated chitosan films (DA, 10, 30, 50, 70 and 90 %) with the cell seeding density of 4.0 x 10^4 cells/film. The cells were cultured on the film surfaces for given periods (1, 2 and 4 days), and viable cell numbers attached on each film surface were estimated (Figure 2). The cells were adhered and grown on the film surfaces, regardless of cell types. However, the film surfaces with different DA value showed different cell adhesion and growth behaviors; the film surfaces with increased DA value showed gradually decreasing cell adhesion and growth, possibly owing to the increased hydrophobicity and decreased positive charge character (NH_3^+), as discussed earlier.

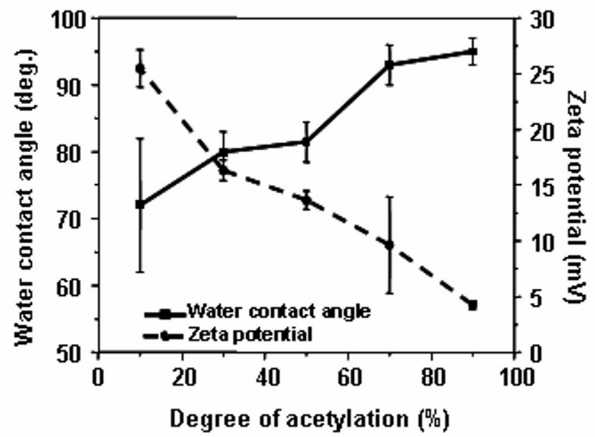

Fig. 1 Water contact angles and zeta potentials of acetylated chitosan film surfaces with various DA value.

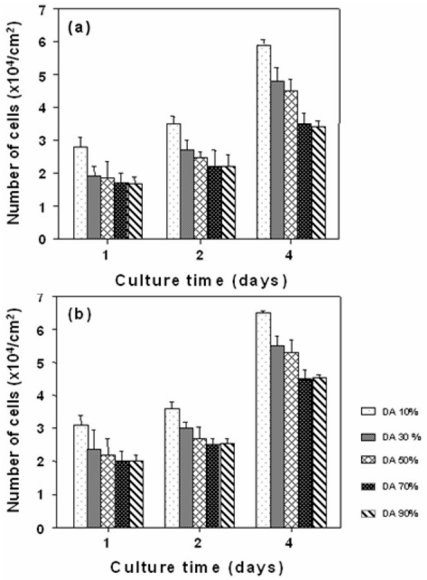

Fig. 2 Number of cells adhered and grown on the acetylated chitosan film surfaces; (a) fibroblasts and (b) chondrocytes.

D. Degradation behavior

Enzymatic degradation behaviors of the acetylated films were examined using lysozyme and *N*-acetyl-β-D-glucosaminidase. Lysozyme is found in various human body fluids and tissues, in concentrations from 4 to 13 mg/L in serum and from 450 to 1230 mg/L in tears [4]. *N*-acetyl-β-D-glucosaminidase is also found in human serum in concentrations of 16.8 – 2.2 U/L [5]. It was recognized that chitosans are degraded by both lysozyme and *N*-acetyl-β-D-glucosaminidase in the body [7]. Lysozyme degrades the chitosans from high molecular weights to oligimers, and *N*-acetyl-β-D-glucosaminidase degrades the oligomers to monomer forms. Until now, in vitro degradation studies of chitosans were mostly carried out only in lysozyme solution. In this study, we compared the degradation behaviors of the acetylated chitosan films in the solutions of lysozyme and *N*-acetyl-β-D-glucosaminidase (separaterly and both together). Figure 3 shows the degradation behavior of the acetylated chitosan films in lysozyme (10 mg/L in PBS). The degradation rate of the films with different DA value was observed as follows: 50 % > DA 30 % ≈ DA 70 % > DA 90 % > DA 10 %. An accelerated mass loss was also observed for the films having intermediate DA values, particularly for DA, 50 %. The enzyme degrades the polysaccharide by hydrolyzing the glycosidic bonds present in the chemical structure. Lysozyme contains a hexameric binding site, and hexasaccharide sequences containing 3-4 or more acetylated units contribute mainly to the initial degradation of *N*-acetylated chitosan [4]. The pattern of chitosan degra-

F. Ibrahim, N.A. Abu Osman, J. Usman and N.A. Kadri (Eds.): Biomed 06, IFMBE Proceedings 15, pp. 94-97, 2007
www.springerlink.com ' Springer-Verlag Berlin Heidelberg 2007

dation can be explained by this mechanism of enzymatic degradation. The lack of consecutive *N*-acetyl glucosamine residues is responsible for the slow degradation of chitosans with low DA. However, the chitosan films having a high DA also showed a decreasing degradation rate with increasing DA relative to those films with intermediate DA. The *N*-acetyl groups seem to affect faster degradation of chitosans. The chitosan film with DA 50 % was degraded the fastest. Figure 4 compares the degradation behavior of the acetylated chitosan film with DA 50 % in lysozyme, *N*-acetyl-β-D-glucosaminidase and lysozyme/*N*-acetyl-β-D-glucosaminidase mixture solutions. The chitosan film in lysozyme/*N*-acetyl-β-D glucosaminidase mixture solution was degraded faster and more larger than that in lysozyme solution. The chitosan film in *N*-acetyl-β-D glucosaminidase solution was not degraded at all. As a result of this, it can be explained that chitosan degradation is initiated by lysozyme to oligomers and then followed by *N*-acetyl-β-D-glucosaminidase to monomer forms.

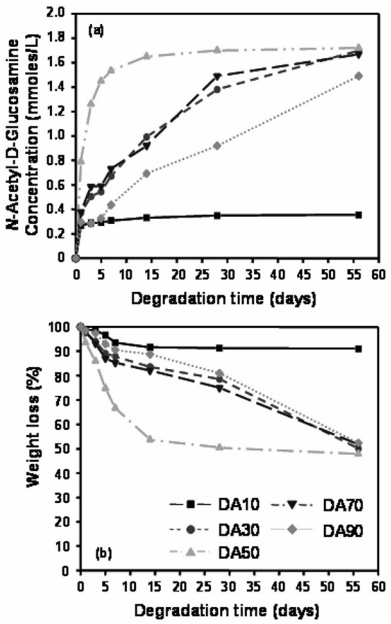

Fig. 3 Degradation behavior of acetylated chitosan films in lysozyme solution; (a) end group analysis (using UV) and (b) weight loss.

Acknowledgment

This work was supported by a grant from Korea Ministry of Commerce, Industry and Energy (Grant No. 10011366) and a post BK-21 program.

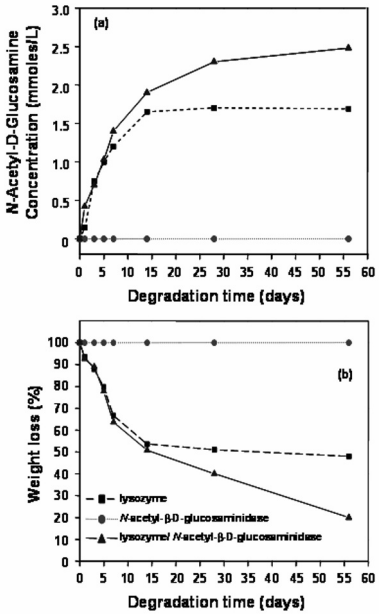

Fig. 4 Degradation behavior of chitosan film (DA, 50 %) in lysozyme, *N*-acetyl-β-D-glucosaminidase, and lysozyme/*N*-acetyl-β-D-glucosaminidase mixture solutions; (a) end group analysis (using UV) and (b) weight loss.

References

1. Freier T, Koh S, Kazazian K, Shoichet MS (2005) Controlling cell adhesion and degradation of chtosan films by *N*-acetylated. Biomaterials 26:5872-5878
2. Ottoy MH, Varum KM, Smidsord O (1996) Compositional heterogeneity of heterogeneously deacetylated chitosans. Carbohyd polym 29:17-24
3. Brugnerotto J, Lizardi J, Goycoolea FM, Aruelles-onal W, Desbrieres J, Rinaudo M (2001) An infrared investigation in relation with citin and chitosan characterization. Polymer 42:3569-3580
4. Muzzarelli R (1994) In vivo biochemical significance of chitin-based medical items. Polymeric Biomaterials 179-197
5. Perwaiz lqbal M, et al. (2003) Experimental & Molecular Medicine, 35: 275
6. Imoto T, Yagishta K (1971) A simple activity measurement of lysozyme. Agr Biol Chem 35:1154-1156
7. Henry JB (1991) Clinical diagnosis and management by laboratory method. Saunder, Philadelphia

Address of the corresponding author:

Author: Jin Ho Lee
Institute: Department of Advanced Materials, Hannam University
Street: 133 Ojeong Dong, Daedeog Gu
City: Daejeon 306-791
Country: Korea
Email: jhlee@hannam.ac.kr

F. Ibrahim, N.A. Abu Osman, J. Usman and N.A. Kadri (Eds.): Biomed 06, IFMBE Proceedings 15, pp. 94-97, 2007
www.springerlink.com ' Springer-Verlag Berlin Heidelberg 2007

Degradation of Magnesium Alloys in Biological Solutions and Reduced Phenotypic Expression of Endothelial Cell Grown on These Alloys

S.K. Lu[1], H.I. Yeh[2], T.Y. Tian[2] and W.H. Lee[1]

[1] Institute of Mechatronic Engineering, National Taipei University of Technology, Taipei, Taiwan
[2]Department of Medical Research, Mackay Memorial Hospital, Taipei, Taiwan

Abstract—**Generally, inflammatory response to the metal stents contributes to the formation of in-stent restenosis. Howerver, recent development of biodegradable stents made of magnesium alloys has a potential to overcome this drawback. Nevertheless, the degradation profile of such stents and the influence on the endothelial cells remained unclear.**

In this study, the flat magnesium alloyed sheets cut by wire electrical discharge machine were immersed in distill water or culture medium. In addition, human aortic endothelial cells (HAEC) were seeded (800 cells/mm^2) onto various magnesium alloyed sheets, including Mg-Al-Zn alloys (AZ31, AZ91) and Mg-Al-Mn alloy (AM60). Cells seeded onto tissue culture treated polystyrene dish coated with gelatin were used as controls. Forty-eight hours later, the cells were examined by immunofluorescence microscopy.

The results were shown that content of Mg^{2+} within 15 weeks gradually increased to more than 40 mg/dL in the culture medium, but remained less than 10 mg/dL in the water. For all magnesium groups the cellularity at 48 hours was less than 60% of that of the controls ($p<0.01$). Comparison among the magnesium alloyed groups showed that both AZ31 and AM60 have lower values of cellularity, compared to the AZ91 (AZ31: 164 cells/mm^2; AM60: 318 cells/mm^2; AZ91: 442 cells/mm^2; AZ91 vs either AZ31 or AM60, both $p<0.05$). Immunfluorescence microscopy showed that cells grown on such magnesium metals expressed less amounts of Von Willebrand factor (VWF), connexin43 (Cx43) gap junctions, and endothelial nitric oxide synthase (eNOS).

The conclusion suggested that degradation of magnesium alloys are enhanced in culture medium, in which HAEC's had a retarded growth and protein expression profile grown on the metal. Otherwise, it also suggested that strategies to improve the biocompatibility of stents made of magnesium alloy are necessary.

I. Introduction

Although endothelial cells play a critical role during neointima formation post vascular stenting, the behavior of endothelial cells on coated stent surface was unclear.

Basically, laboratory investigation has demonstrated that endothelial cells are involved in the regulation of thrombosis and proliferation of subjacent smooth muscle cells. In addition, complete coverage of endothelial cell is associated with attenuation or even stop of the growth of neointima in the injured segment.

Although, in-stent restenosis after stenting in the coronary artery is a major drawback of percutaneous coronary intervention using stent, inclusive of drug-eluting stent (DES), owing to the dysfunction of endothelial cells are affected by the local environment. Therefore, in order to realize the biocompatibility of cells grown on magnesium alloyed materials, we examined the growth profiles of HAEC in the present study. The expression of Cx43 gap junctions, eNOS, and endothelial marker VWF were evaluated. Previous studies have shown that eNOS expressed usually in the endothelial cell of vascular tissue. Otherwise, adequate generation of nitric oxide by the eNOS is essential to the homeostasis of circulation. In addition, reduction of the eNOS and hence its product nitric oxide (NO) is well known to signify endothelial dysfunction

II. Materials and methods

Metal Sheets: Those metallic sheets, measuring 5 mm × 5 mm × 0.1 mm, made of various magnesium alloys were used. Afterward the surface of magnesium sheet was polished by 600 grit enamel paper and down to 0.3μm Al_2O_3 powder and cleaned by ethanol.

Cell Culture: HAEC cells of passage 4 were seeded (800 cells/mm^2) onto the metallic sheets, which were placed at the center of a 35 mm tissue culture treated polystyrene dish filled with 8 ml of culture medium (Medium 200 (GIBCO)). Forty-eight hours later, the cells were examined by immunofluorescence microscopy. For immunolabeling, cells grown on gelatin-coated (Merck, Darmstadt, Germany) glass coverslips were used as control.

Immunocytochemistry: For Cx43 and VWF double immunolabeling, cells grown on the metallic sheets were fixed with methanol at -20 °C for 5 minutes. After blocking with 0.5% BSA for 15 minutes, the cells were incubated with the anti-VWF antibody (1:50) and anti-Cx43 antibody (1:100) at 37 °C for 2 hours, followed by incubation with a CY3 conjugated donkey anti-mouse antibody (1:500; Chemicon) for 50 minutes in the dark. The cells next were incubated with bisbenzamide (1□g/ml; Sigma) for 15 minutes in the dark. Moreover, for eNOS immunolabeling, cells grown on the metallic sheets were fixed with 4% PFA

F. Ibrahim, N.A. Abu Osman, J. Usman and N.A. Kadri (Eds.): Biomed 06, IFMBE Proceedings 15, pp. 98-101, 2007
www.springerlink.com ' Springer-Verlag Berlin Heidelberg 2007

for 5 minutes. After blocking with 0.5% BSA, the cells were incubated with the mouse anti-eNOS antibody (1:100) in the dark overnight, followed by incubation with a CY3 conjugated donkey anti-mouse antibody (1:500; Chemicon). Then, the cells were incubated with bisbenzamide. All phenotypes were mounted, examined, and recorded using an epifluorescence microscope equipped with a digital camera.

Degradation: The degradation test was carried out at room temperature using a culture medium 200 of 50 ml tube (Falcon USA). The samples, measuring 20 mm × 20 mm × 0.1 mm, made of various magnesium alloys were cleaned before testing using ethanol and immersed in the medium. Then, at each time-critical observation, 1.5 ml medium was drawn out to determine the concentration of Mg^{2+} ion within 15 weeks.

Analysis: For comparison of cellularity, cells were stained with bisbenzamide to make the nucleus visible under fluorescence microscope and were observed in x160 magnification. Images of 10 randomly selected rectangular fields. The images were then analyzed using QWIN image analysis software (Leica) to count the nucleus. For this purpose, 4 separate experiments of cell culture for all types of materials were conducted. Data, expressed as mean values (±SD), were compared statistically by t-test. A p value < 0.05 was considered to be significant.

III. Results

Determination of magnesium degradation: The content of Mg^{2+} within 15 weeks gradually increased to more than 40 mg/dL in the culture medium, but remained less than 10 mg/dL in the water (Fig. 1). The images expressed that magnesium alloy AZ31 was degraded faster than AM60 and AZ91 in medium (Fig. 2). Othetwise, these images also showed that all magesium alloys in medium were found some crystal products on the surface. On the contrary, the magesium alloys just resulted a gray film upon the surface in the water group (Fig. 3).

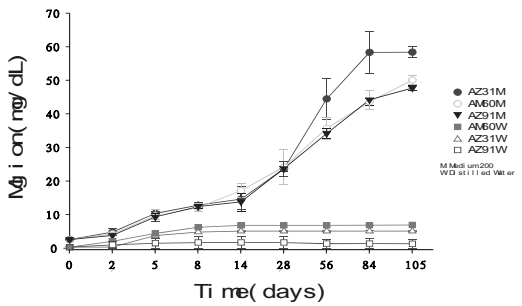

Fig. 1 Degradation rate of magnesium alloys in solution within 15 weeks.

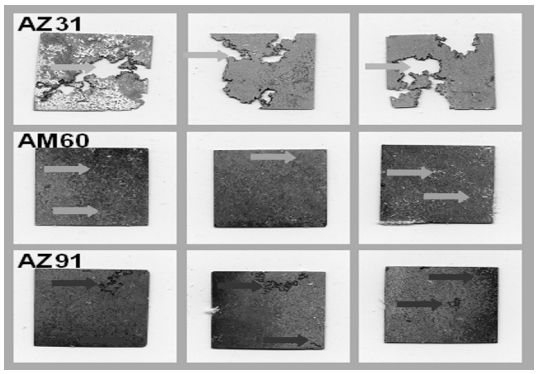

Fig. 2 The expression of magnesium alloys in culture medium 200. White small grains on the surface are crystal products.

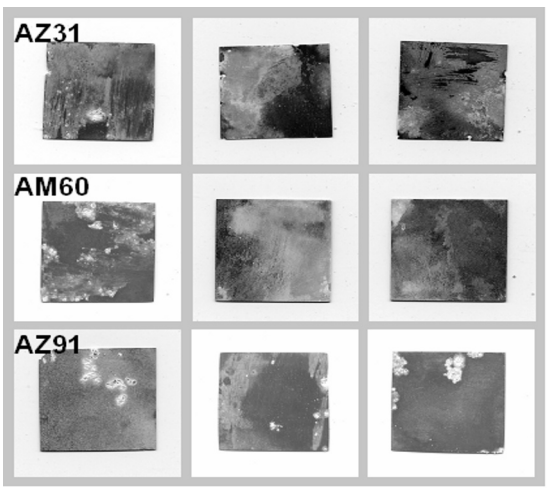

Fig. 3 The expression of magnesium alloys in the water. Gray films on the surface are oxides.

Cell Proliferation Assays: After seeding, cells were able to attach and grow on the surface, but the cell proliferation at 48 hours following the seeding varies widely, according to the magnesium alloys (Fig. 4 and Fig. 5). Regarding the magnesium alloys, for seeding of 800 cells/mm^2, all magnesium alloys have comparable or lower values of cellularity, compared to the control (all vs control, $p<0.05$). Otherwise, comparison among the magnesium alloyed groups showed that both AZ31 and AM60 have lower values of cellularity, compared to the AZ91. Generally, for the seeding of 800cells/mm^2, the cellularity on each of magnesium groups is less than 60% of control groups.

Immunofluorescence microscopy: Typically Cx43 gap junctions, seen as punctate labelngs at cells borders, were abundant in the control group, but less expressed in the remaining groups (Fig. 6). A similar pattern of expression levels was seen for VWF (Fig. 6), the labellings of which are located in the cytoplasmic compartment. Moreover,

F. Ibrahim, N.A. Abu Osman, J. Usman and N.A. Kadri (Eds.): Biomed 06, IFMBE Proceedings 15, pp. 98-101, 2007
www.springerlink.com ' Springer-Verlag Berlin Heidelberg 2007

typically eNOS, located in the cytoplasmic compartment, was more abundant in the control group, but less expressed in the remaining groups (Fig. 7).

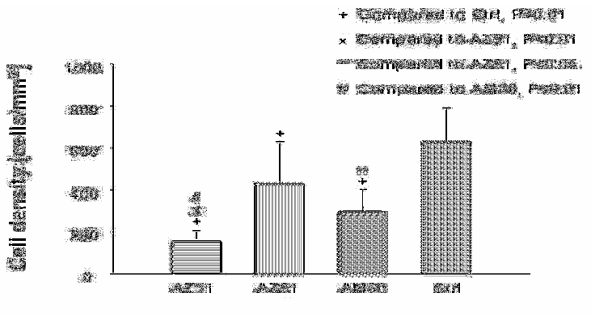

Fig. 4 Cellularity, expressed as mean ± SD, were averaged from at least 3 separate experiments and compared statistically by t-test.

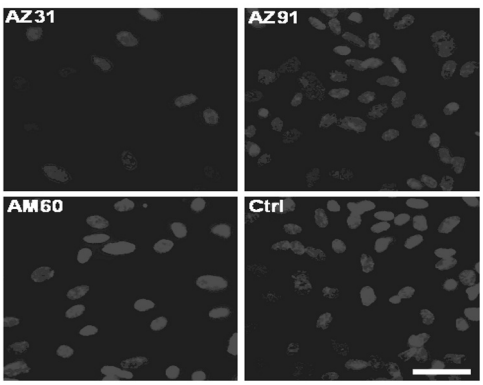

Fig. 5 Blue signal is nucleus. Bar, 100μm.

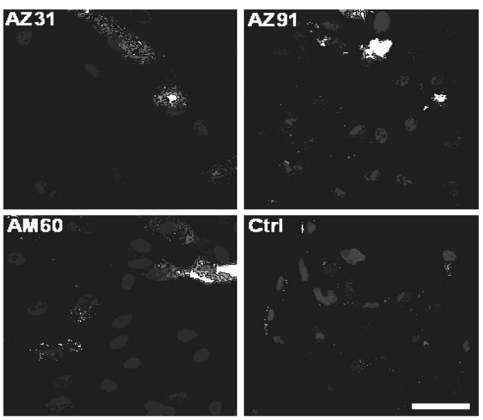

Fig. 6 Red signal is Cx43, green signal is VWF, and blue signal is nucleus. Bar, 100μm.

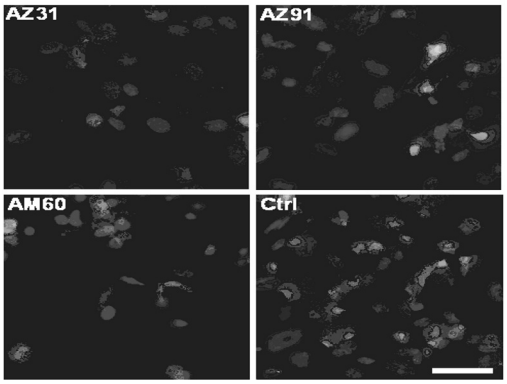

Fig. 7 Red signal is eNOS and blue signal is nucleus. Bar, 100μm.

IV. Discussion

This study demonstrates that the phenotypic features of endothelial cells, including growth profile and expression of proteins are altered when grown on the biodegradable magnesium surface. However, the finding that cells seeded on all magnesium metals, regardless of the alloyed compounds, express a small amount of Cx43, VWF, and eNOS suggest that the overlying endothelial cells have functional defects.

In addition, the corrosion rate of magnesium in such environment is very according to the magnesium percentage of alloy and it s immersed component of solution. Furthermore, when magnesium exposed to a typical atmosphere will develop a gray oxide film of magnesium hydroxide ($Mg(OH)_2$) on the surface of magnesium. However, if chloride ions are present at levels on the order of 150 mmol/L in aqueous environment, $Mg(OH)_2$ will react with Cl^- to form the magnesium chloride and hydrogen gas. Previous studies showed that pitting of magnesium was observed for Cl^- concentrations exceeding 30 mmol/L.

V. Conclusions

The degradation of magnesium alloys are enhanced in culture medium, in which HAEC s grown on the metal had a retarded growth and protein expression profile, suggesting that strategies to improve the biocompatibility of stents made of magnesium alloy are necessary. In this present study, HAEC grown on magnesium sheets vary widely in growth profile and protein expression according to the alloys. Endothelial cells grown on magnesium materials showed growth retardation and phenotypic changes, furthermore, down-regulation of Cx43, VWF, and eNOS are the common phenomena in the cells in such environments.

F. Ibrahim, N.A. Abu Osman, J. Usman and N.A. Kadri (Eds.): Biomed 06, IFMBE Proceedings 15, pp. 98-101, 2007
www.springerlink.com ' Springer-Verlag Berlin Heidelberg 2007

These suggest the endothelial cells in the stented vessels were functionally impaired, which potentially contributes to the formation of in-stent restenosis and thrombosis post biodegradable magnesium stent implantation. Therefore, improve the biocompatibility of stents made of magnesium alloy are necessary.

REFERENCES

[1] Heublein B., Rohde R., Kaese V., Niemeyer M., Hartung W. and Haverich A. (2003): Biocorrosion of magnesium alloys: a new principle in cardiovascular implant technology? , Heart. 89 p.p. 651-656

[2] Carlo D M., Huw G., Omer G., Nicolas P., Jan V., Marc B., Koen D., Bernhard H., Roland R., Victor K., Charles I. and Raimund E. (2004): Drug-eluting bioabsorbable magnesium stent , J Interven Cardiol. 17 p.p. 391-395

[3] Witte F., Kaese V., Haferkamp H., Switzer E., Meyer-Lindenberg A., Wirth C J. and Windhagen H. (2005): In vivo corrosion of four magnesium alloys and the associated bone response , Biomaterials 26 p.p. 3557-3563

[4] Maier J A, Bernardini D, Rayssiguier Y and Mazur A. (2004): High concentrations of magnesium modulate vascular endothelial cell behaviour in vitro , Biochim Biophys Acta 6-12

[5] Maier J A, Malpuech-Brugere C, Zimowska W, Rayssiguier Y and Mazur A. (2004): Low magnesium promotes endothelial cell dysfunction: implications for atherosclerosis, inflammation and thrombosis , Biochim Biophys Acta p.p. 13-21

[6] Witte F, Kaese V, Haferkamp H, Switzer E, Meyer-Lindenberg A, Wirth C J and Windhagen H. (2005): In vivo corrosion of four magnesium alloys and the associated bone response , Biomaterials 26 p.p. 3557-3563

[7] Michael B, Esthie R, Iris B, Arie R, Gad K and Jacob G. (2004): Zinc reduces intimal hyperplasia in the rat carotid injury model , Atherosclerosis 175 p.p. 229-234

[8] Yeh H I., Lu S K., Tian T Y., Hong R C., Lee W H. and Tsai C H. (2006): Comparison of endothelial cells grown on different stent materials J Biomed Mater Res 76A p.p. 835-841

[9] Lu S K., Yeh H I., Huang C W., Tian T Y., Chen C Y. and Lee W H. (2005): Phenotypic change of HUVEC grown on stent material coated with Titanium (Ti) and Tantalum (Ta) compounds , ICBME Int. Conf. 4A3-10 Singapore

[10] Yeh H I., Lu S K., Tian T Y., Chiang C L., Lee W H. and Tsai C H. (2004): Down-regulation of connexin43 Gap Junctions, eNOS, and VWF in endothelial cells grown on stent materials , Int J Cardiol. S29 Taiwan

[11] Tian T Y., Lu S K., Yeh H I., Chiang C L., Lee W H. and Tsai C H. (2003): Phenotypic change of endothelial cells grown on stent materials of various properties , Acta Cardiol Sin. 19:S200 Taiwan

[12] Mark P S., Alexis M P., Jerawala H. and George D. (2006): Magnesium and its alloys as orthopaedic biomaterials: A revies , Biomaterials 27 p.p. 1728-1734

[13] Frank W., Jens F., Jens N., Horst A C., Volker K., Alexander P., Felix B. and Henning W. (2006): In vitro and in vivo corrosion measurements of magnesium alloys , Biomaterials 27 p.p. 1013-1018

Address of the corresponding author:

Author: S.K. Lu
Institute: Department of Physics, University of Indonesia
City: Taipei
Country: Taiwan

F. Ibrahim, N.A. Abu Osman, J. Usman and N.A. Kadri (Eds.): Biomed 06, IFMBE Proceedings 15, pp. 98-101, 2007
www.springerlink.com ' Springer-Verlag Berlin Heidelberg 2007

Fabrication of 316L stainless steel parts by Injection Moulding for Biomedical Application using a Novel Binder

R Ibrahim[1], M A Omar[2], W C Goh[3], M Mohamad[4],
S Muhamad[5], N A Yahya[6], Z Radzi[7], N H Abu Kasim[8]

[1,2,4]Structural Materials Programme, Advanced Materials Centre (AMREC), SIRIM Berhad, Malaysia
[3]Material Science Programme, School of Applied Physics, Malaysia
Faculty of Science and Technology, Universiti Kebangsaan Malaysia, Malaysia
[5]Herbal Medicine Research Centre (HMRC), Institute of Medical Research (IMR),
50690 Kuala Lumpur, Malaysia
[6,7,8]Faculty of Dentistry, University of Malaya, 50603 Kuala Lumpur, Malaysia

Abstract— **This paper focuses on the usage of a novel binder system base on palm oil product to produce sintered parts of stainless steel 316L produced by vertical injection molding technique for biomedical application. The stainless steel 316L powder was mixed using z-blade mixer with the thermoplastic binder system comprising of polyethylene, paraffin wax, stearic acid and palm stearin which was derived from palm oil at different volume percent (%). The feedstock then was studied in term of viscosity and shear rate using capillary rheometer. The feedstock was molded using vertical injection molding machine. After molding, the green molded part was immersed into the solvent to extract part of the binder system followed by sintering under vacuum atmosphere at the temperature of 1360°C. The physical and mechanical properties of the sintered part such as density, hardness, shrinkage, ultimate tensile strength and elongation were measured. Biocompatibility study of *in vitro* test using cell osteosarcoma MG-63 was observed and discussed.**

Keywords— **binder system, palm stearin, stainless steel 316L, injection molding**

I. Introduction

Powder Injection Molding (PIM) is one of the prime processes of manufacturing complicated shapes of metals. In this process a large volume of metal is mixed with small amount of sacrificial binder to give sufficient fluidity during injection molding. In order to produce consistent products with the process, it is essential to understand the flow characteristics of PIM.

Binder system is an important key component, which provides the powder with the flowability and formability necessary for molding [1,2,3]. Binder system commonly used for injection molding technique based on thermoplastic materials such as polyethylene, paraffin wax and stearic acid. Thermoplastic material can also be derived from palm oil. A novel binder was formulated and in the process of being patented; palm stearin has been evaluated as a possible binder system. The content of palm stearin is shown in Table 1. The reason for using palm stearin as a binder system is due to its contents that can be advantages during debinding process. It is important that the removal of binder be performed gradually to maintain the shape of the debound part. At different heating temperature, the binder melts leaving different impurities at different melting point. The remaining impurities help form capillary holes for the removal of the rest of the binder material. Therefore, the selection of palm stearin as a possible binder system fulfills the important criteria of a binder system in PIM process as its components exhibit various melting points as illustrated in Table 1.

Table 1. Contents of Palm Stearin with the Melting Temperature

CONTENTS	PERCENTAGE (%)	MELTING (°C)
Palmitic Acid	54.3	62.0
Oleic Acid	32.5	16.3
Linoleic	7.0	85.0
Stearic Acid	4.7	70.0
Myristic	1.3	54.0
Linolenic	0.1	44.0

II. Experimental details

Stainless steel 316L powder from ANVAL (Sweden) was used in this work and its composition and characteristic are illustrated in Table 2.

F. Ibrahim, N.A. Abu Osman, J. Usman and N.A. Kadri (Eds.): Biomed 06, IFMBE Proceedings 15, pp. 102-105, 2007
www.springerlink.com ' Springer-Verlag Berlin Heidelberg 2007

Table 2. Stainless Steel (SUS 316L) Powder Chemical Composition and Characteristic

Powder Identification: SUS316L
Powder Source: Anval 316 Stainless Steel, Sweden

Powder Chemistry	*By Manufacturer*	*By ICP*
%C	-	0.026
%Si	0.36	0.580
%Mn	1.44	1.430
%P	0.01	0.030
%S	-	0.012
%Cr	16.11	16.40
%Ni	9.97	10.40
%Mo	1.92	2.080

Tap density, g/cm^3	4.09
Apparent density, g/cm^3	2.82
Pynometer density, g/cm^3	7.96

In this study, two different composition of binder systems, A and B were developed and the volume percentage (vol. %) of binder composition of polyethylene (PE), paraffin wax (PW), stearic acid (SA) and palm stearin (PS) was formulated as shown in Table 3.

Table 3. Three Different Composition of Binder Systems

Binder	**System A (vol.%)**	**System B (vol.%)**
Polyethylene	35	35
Paraffin Wax	55	55
Palm Stearin	10	-
Stearic Acid	-	10

The melting temperature of each of the binders system was measured using Differential Scanning Calorimetry (DSC) is shown in Table 4.

Table 4. Melting Temperature of each Binder System

Binder	Melting Temperature (^{o}C)
Polyethylene	125.86
Paraffin Wax	63.60
Palm Stearin	54.22
Stearic Acid	57.79

Determination of critical and optimum solid loading of the mixture powder/binder was measured using Brabender Plasti-Corder. The weight of stainless steel powder of 218 gram was poured into mixer bowl at different volume percent of oleic acids.

The rheological study of the compatibility and homogeneity of the mixture was measured in term of torque value, viscosity and shear rate using Brabenda Plastic-Corder and Capillary Rheometer. The mixture of the powder and binder so called as feedstock was mixed using z-blade mixer at the temperature range between 130 to 160^{o}C for 2 hour. The feedstock was then adapted into the mold using Vertical Injection Molding (VIM) machine. After molding, two types of debinding was implemented in order to remove the binder system. The green molded parts were first subjected to a solvent extraction where approximately two third of the volume fraction of the binder was removed. Followed by immersion in heptane for 4 hours at 60^{o}C. Thermal debinding process were then carried out to remove completely all the organic binder. The parts were heated up to 440^{o}C at the rate of 1^{o}C/min and maintained at that temperature for 2 hours. Followed by continuous heating in High Temperature Control Atmosphere Furnace (HTCAF) at 10^{o}C/min until the temperature of 1360 ^{o}C was reached. The density, hardness and strength of each of the sintered part were measured using Densimeter ED-120T, Vicker Hardness Tester and Instron-Universal Testing Machine respectively. Scanning Electron Micrograph (SEM) was used to observe and evaluate the bio-]compatibility of *in vitro* test using cell osteosarcoma MG-63.

III. Results and Discussion

A.Rheology study

The homogeneity of the feedstock was determined using Brabender Plastic-Corder and Capillary Rheometer. Figure 1 shows the torque value versus time of the feedstock of system A and B. From the results, the feedstock of system B has the best of homogeneity follow by feedstock system A. Both of the system seems to be homogenous after 30 min in the torque value range of 2.0 to 3.0Nm.

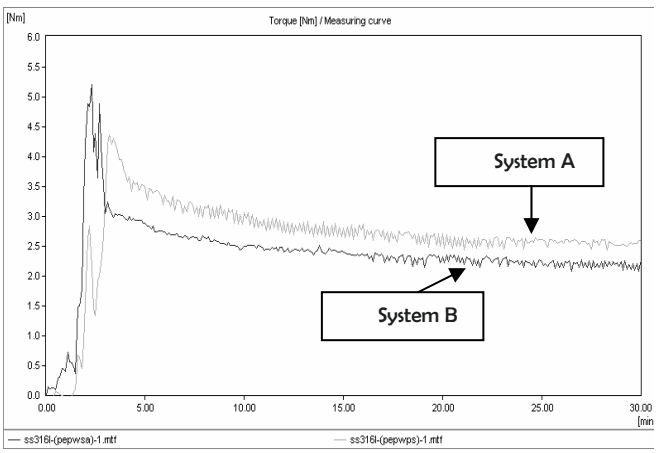

Figure 1. The Torque Value versus Time of the Feedstock System A and B.

F. Ibrahim, N.A. Abu Osman, J. Usman and N.A. Kadri (Eds.): Biomed 06, IFMBE Proceedings 15, pp. 102-105, 2007
www.springerlink.com ' Springer-Verlag Berlin Heidelberg 2007

Figure 2 (a) and (b) show the viscosity versus shear rate of the feedstock system A and B using capillary rheometer at different temperature range of 120°C to 160°C. The results show that the viscosity of the feedstock exhibit pseudo-plastic behavior, which is common for PIM feedstock. The variation of viscosity versus shear rate in log-log scale graph is almost linear, which is an indicator of feedstock stability. Besides, as the temperature of feedstock increases, the viscosity decreases. In order to make the feedstock flow nicely into injection molding machine, the shear rate and viscosity should be in the range of $100s^{-1}$ to $10000s^{-1}$ and 1000 Pa s. Table 5 shows the recommended temperature range that can be injected for the feedstock of system A and B.

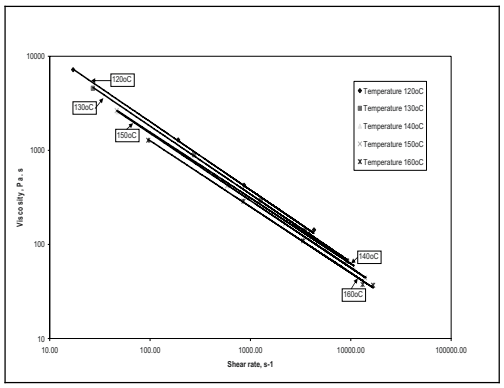

(a) Binder System A

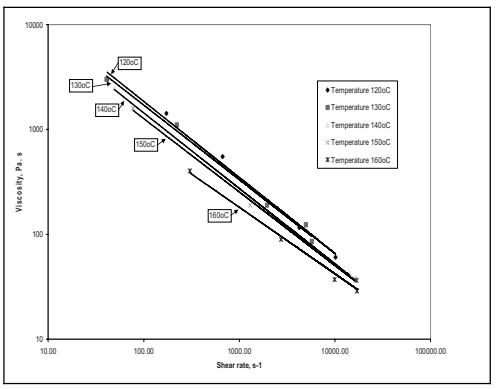

(b) Binder System B

Figure 2 (a) and (b). The Viscosity Versus Shear Rate of the Feedstock System A and using Capillary Rheometer at Different Temperature Range of 120°C to 160°C

Table 5. Temperature Range of the Feedstock System A and B

Feedstock System	Temperature range (°C)
A	120 to 160
B	130 to 150

B. Physical and Mechanical Properties and Micrograph Observation

The physical and mechanical properties of the sintered tensile test part were shown in Table 6. The results show that the sintered parts have achieved the minimum requirement for sintered PIM parts compared with Standard Metal Powder Industries Federation (MPIF) 35. SEM of system A and B (Figure 5) clearly showed the attachment of cells osteosarcoma MG-63 to the stainless steel 316L parts. It can be seen that cell growth on system B was more than system A. However no explanation can be offered at this juncture for this observation. Further studies need to carried out.

Table 6. The Physical and Mechanical Properties of the Sintered Tensile Test Part of System A and B

Properties	System A	System B
Density (g/cm^3)	7.845	7.853
Hardness (Hv)	162.5	160.1
Shrinkage (%)	14.17	13.88
Strength (MPa)	511.87	511.23
Elongation (%)	21.74	21.63

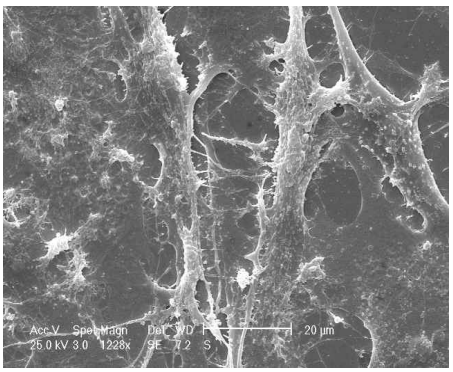

(a) System A- Stearic Acid

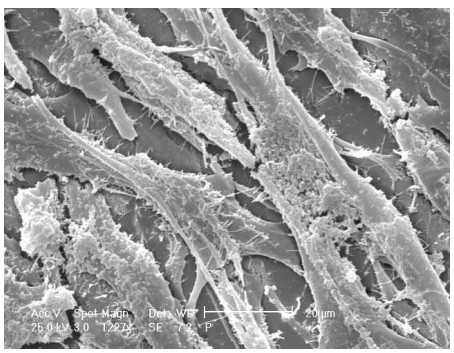

(b) System B- Palm Stearin

Figure 5. The Micrograph Observation on the Attachment of Cell Osteosarcoma of the System A and B.

F. Ibrahim, N.A. Abu Osman, J. Usman and N.A. Kadri (Eds.): Biomed 06, IFMBE Proceedings 15, pp. 102-105, 2007
www.springerlink.com ' Springer-Verlag Berlin Heidelberg 2007

IV. Conclusion

The feedstock made using palm stearin binder exhibited good homogeneity. Its physical and mechanical properties of the sintered parts achieved the minimum requirement for sintered PIM parts compared with Standard Metal Powder Industries Federation (MPIF) 35. Attachment of MG63 cell on the stainless steel 316L fabricated using palm stearin binder system confirmed its biocompatibility.

Acknowledgment

This work partly was supported by Internal Seed Funding of SIRIM Berhad: (4-497-010924).

References

1. Chung C. I., Rhee B. O., Requirements of Binder for Powder Injection Molding. Compending Metal Injection Molding 1987;2(5):269-77
2. Norhamidi M., Muhammad H. I., Nor H. M. N., Ahmad K. A. M. I. and Jaafar S., Improtance of Rheological Behaviour in Metal Injection Moulding for Prediction of Injected Parts , ICAST 2000, pg. 169-174
3. Norhamidi M., Iriany, Ahmad K. A. M. I. and Jaafar S., Rheological Study of Feedstock for Metal Injection Molding Process , ICAST 2000, pg. 97-106

Address of the corresponding author:

Author: Dr Rosdi Ibrahim
Address: Structural Materials Programme, Advanced Materials Centre (AMREC), SIRIM Berhad, Lot 34, Jalan Hi-Tech 2/3, Kulim Hi-Tech Park, 09000, Kulim, Kedah, Malaysia
Email: rosdi@sirim.com.my

F. Ibrahim, N.A. Abu Osman, J. Usman and N.A. Kadri (Eds.): Biomed 06, IFMBE Proceedings 15, pp. 102-105, 2007
www.springerlink.com ' Springer-Verlag Berlin Heidelberg 2007

Hardness Evaluation of Porous Hydroxyapatite Coating

A. Behnamghader[1], B. Farsadzadeh[2], D. Najjar[3], A. Iost[3]

[1] Materials and Energy Research center, Tehran, P.O. Box 14155-4777, Iran
[2]Biomedical Department, Azad Islamic University, P.O. Box 14665-1445, Tehran, Iran
[3] ENSAM/LMPGM CNRS UMR 8517, 8 Bd . Louis XIV, 59046 Lille Cedex, France

Abstract– **The extensive use of appropriate coatings to improve wear resistance, friction coefficient, electrical properties, corrosion resistance and biomedical application has stimulated a growing interest in their mechanical properties and especially hardness testing that is routinely used for coating evaluation. In this study Jönsson and Hogmark model is applied for the porous hydroxyapatite produced by plasma spraying on Ti6A14V substrate. Firstly, the effect of indentation load on hardness values of coating and substrate are studied. The modified Jönsson and Hogmark model is used to explain the composite hardness behavior and the effect of coating porosity.**

Keywords– **Hardness, Coating, Hydroxyapatite, Plasma-spray, porosity**

I. Introduction

The hardness test, because of its simplicity, is commonly used to estimate the mechanical properties of coatings. There are several approaches to measuring coating hardness. For thin coatings, a modeling approach can be used to determine the coating hardness and indentation size effect (ISE) behavior. For the Vickers pyramid indenter, the hardness is defined as the load divided by the surface area of the impression. The Vickers hardness number (VHN) is defined as the ratio of load to the total area of impression. According to the usual practice VHN is expressed in $kgfmm^{-2}$ and the units are omitted.

Two main problems arise when this technique is applied to coated materials:

a) The coating thickness varies typically between 2000A° for an ion-implanted substrate to 20 micron for the hard coatings used to improve the wear resistance of tool steels. To obtain the bulk hardness value for the film it is necessary to satisfy requirement that the film thickness should be ten times greater than the penetration depth [1]. As the indentation depth is D=d /7, the substrate hardness generally influences the measured hardness values.

b) In the load range commonly used in microhardness characterization (typically 5-1000 gf) the hardness number varies with the applied load. This situation is called the indentation size effect (ISE) and has been attributed to a wide variety of mechanisms [1, 2]. ISE can be modeled in two ways. The first is empirical and corresponds to a power law.

$$P = a\, d^n. \qquad (1)$$

This equation is called Meyer relationship. The second is a linear relationship between hardness and the reciprocal length of the impression [3]:

$$VHN = H_0 + B/d. \qquad (2)$$

Where H_0 is the absolute hardness and B is a constant. This equation corresponds to a variation of the indentation diagonal with the applied load [4]:

$$P = a_1 d + a_2 d^2. \qquad (3)$$

With $a_2 = H_0$ and $B=1.8544\ a_1$. Some attempts have been made to give a physical significance to Eq. (3) [5]. In our opinion, the size effect in hardness is due to the formation of a pile-up at the immediate edge of the impression [6]**.** This is confirmed by the investigation of Chaudhri and Winter [7], which show that the pile-up supports a part of the indenter load.

Many attempts have been made to establish a quantitative correlation between the hardness of composite material and that both of coating and substrate. The main models developed are based on the area law-of-mixture [8-15] or the volume law-of-mixture [16-18]. Jönsson et al. proposed that the composite hardness H_C can be expressed as a weighted mean of the film hardness H_f and the substrate one H_S:

$$H_C = (A_f/A)\, Hf + (A_s/A)\, Hs. \qquad (4)$$
$$A_f/A = 2kt/d-(kt/d)^2.$$

Where A is total projected area of the impression, equal to the sum of the projected areas of the rim, A_f, and the interior, A_S.

The objective of this study was to evaluate the hardness of porous hydroxyapatite coated onto Ti6A14V substrate.

F. Ibrahim, N.A. Abu Osman, J. Usman and N.A. Kadri (Eds.): Biomed 06, IFMBE Proceedings 15, pp. 106-108, 2007
www.springerlink.com ' Springer-Verlag Berlin Heidelberg 2007

II. Experimental procedure

Plasma spraying is used to produce the composite of hydroxyapatite coating on Ti6A14V substrate. Before spraying, the samples were sandblasted in order to obtain a favorable random surface roughness for mechanical bonding in the coating/substrate interface. Surface roughness (R_a) was 2.29 micrometers and coating thickness varies between 100 and 120 micrometers. Indentation were made using a Vickers diamond indenter at peak contact loads between 50 gf and 2000 gf on the surface prepared by the way of polishing. The indentations were made and measured in ambient air and approximately 1 minute elapsed between indenting and measuring.

III. Results and discussion

The hardness values of substrate (H_S) and of composite (HV_C) were determined according to general equation of Vickers hardness. The particular points of model are shown in the table 1.

The measured hardness values were to be dependent on coating thickness. The hardness values are plotted in Fig. 1 as a function of the reciprocal indentation depth 1/d.

Table 1. Some particular points of composite, substrate and coating hardness.

d (mm)	Kt/d	A_f/A	H_c (Kgf/mm^2)	H_s (Kgf/mm^2)	H_f (Kgf/mm^2)
High	0	0	233	233	209
60	1	1	277	314	277
30	2	0	395	395	344

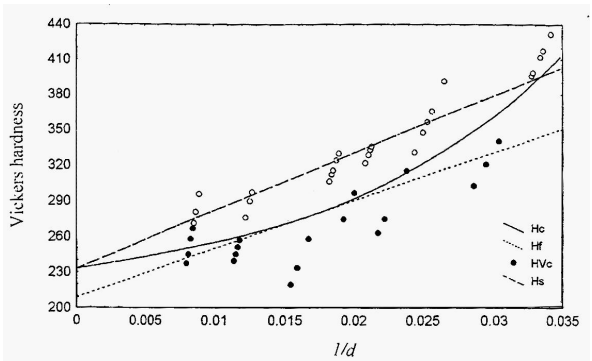

Fig. 1. A Schematic representation of the composite hardness versus 1/d. Tangent at H_C, Model, H_f, H_s.

At each load, more than six experimental data are recorded to calculate the hardness value.Interpretation of the model based on the area law-of-mixture:

Iost and Bigot [19] consider the relation (4) without the Jönsson and Hogmark simplifications. Taking into account the second- and third-order 1/d terms, composite hardness can be expressed using the following expansions:

$$H_c = H_{0s} + A_1/d + A_2/d^2 + A_3/d^3. \quad (5)$$

with
$$A_1 = 2kt\,(H_{0f} - H_{0s}) + B_S$$
$$A_2 = 2kt\,(B_f - B_S) - k^2t^2\,(H_{0f} - H_{0s})$$
$$A_3 = -k^2t^2\,(B_f - B_S)$$

A mathematic analysis shows that the form of equation (5) depends on the product of $\Delta = (H_{0f} - H_{0s})/(B_f - B_S)$ and kt.

For our experimental data, $\Delta = 0.03$ and k = 0.5 since cracks formation occur at the corners of the indentation print. This product is less than 0.5.The substrate hardness measured at different applied load after removal of the coating is:

$$H_s = 233 + 4871/d \quad (6)$$

Application of Eq. 5 and 6 with the experimental results of the composite hardness aim to obtain the film hardness and its variation with the applied load :

$$H_f = 209 + 4061/d \quad (7)$$

It is worth noting that a hardness intrinsic value of 484 *VHN* has been measured for dense HA.

IV. Conclusions

One of the most important particularities of hardness measurement is that they are load dependent. In order to obtain an intrinsic value of hardness for the coating/substrate systems, it is possible to use the Jönsson et al. Model. The model based on the area law-of-mixture is suitable at condition that Kt/d is less than 1. Values higher than 1 for kt/d correspond to an indent diagonal length less than the coating thickness, and consequently the measured hardness equal the coating one. From the above discussion it is not so difficult to obtain an absolute hardness because the influence of substrate has been found effective only for the highest load. It is also to be noticed that the hydroxyapatite hardness of the coating is less than the bulk hydroxyapatite and substrate ones. This result is a consequence of the presence of porosity in the plasma-sprayed hydroxyapatite coating.

F. Ibrahim, N.A. Abu Osman, J. Usman and N.A. Kadri (Eds.): Biomed 06, IFMBE Proceedings 15, pp. 106-108, 2007
www.springerlink.com ' Springer-Verlag Berlin Heidelberg 2007

References

1. H. Bückle, in Wesbrook and Conradd (eds), ASM, Metals park, Ohio, (1997), P. 453-491.
2. D. Chicot and J.Lesage, Thin Solid Film, 254, (1995), P. 123.
3. F. Frohlich, P. Grau and W. Grellmann, Phys. Stat. Solidi A, 42, (1977), P. 79.
4. H. Li and R.C. Bradt, J. Mater. Sci., 28, (1993), P. 917.
5. A. Iost, J. Aryani-Bouffette and J. Foct, Mem. Sci. Rev. Met. 11, (1992), P. 681.
6. A. Iost and R. Bigot, J. Mater. Sci., 31, 1996, 3573-3577..
7. M. Chaudhri and M. winter, J. Phys. D: Appl. Phys., 21, (1988), P. 370.
8. B. Jönsson and S. Hogmark, Thin Solid Film, 114 , (1984) , P. 257.
9. A. Thomas, surf. Eng., 3, (1987), P. 117.
10. L. J. Bredell and J.B. Malherbo, Thin Solid Film, 125, (1985), P. 125.
11. P. A. Engel, E.Y. Hsue and R. G. Bayer, Wear, 162-164, (1993), P. 538.
12. P. A. Engel, A. R. Chitsaz and E.Y. Hsue, Thin Solid Film, 207, (1992), P. 144.
13. S. Betsofen, Russ. Metall. 2, (1993), P. 156.
14. O. Vingsbo, S. Hogmark, B. Jönsson and A. Ingemarsson, (P.J. blau and B.R. Lawn eds.). ASTM, STP, 889, Chap. 15, Philadelphia, (1986), P. 257-271.
15. P. Nemac and V. Navratil, J. Mater. Sci. Lett., 13, (1994), P. 1179.
16. J. R. Tuck, A. M. Korsunsky, D. G. Bhat and S. J. Bull, Thin Solid Film, 148, (1987), P. 51.
17. P.J. Burnett, and D.S. Rickerby, Thin Solid Film, 148, (1987), P. 41.
18. S.J. Bull and D.S. Rickerby, Surf. Coat. Technol., 42, (1990), P. 149.
19. A. Iost and R. Bigot, Surf. Coat. Technol., 80, (1996), P.117.

Address of the corresponding author:

Author:	Aliasghar BEHNAMGHADER
Institute:	Materials and Energy Research center
P.O. Box:	14155-4777
City:	Tehran
Country:	Iran
Email:	a_behnamghader@merc.ac.ir

F. Ibrahim, N.A. Abu Osman, J. Usman and N.A. Kadri (Eds.): Biomed 06, IFMBE Proceedings 15, pp. 106-108, 2007
www.springerlink.com ' Springer-Verlag Berlin Heidelberg 2007

Hydroxyapatite Formation on Acrylic Acid-grafted Porous PLLA Scaffolds in Simulated Body Fluid

Hyun Jung Jung, Kwideok Park, Jun Sik Son, Jae-Jin Kim, and Dong Keun Han*

Biomaterials Research Center, Korea Institute of Science and Technology,
P.O. Box 131, Cheongryang, Seoul 130-650, Korea

Abstract— **This study focused on the effect of surface-modification of 3D poly(L-lactic acid) (PLLA) scaffolds in the formation of hydroxyapatite (HA) crystals in simulated body fluid (SBF). PLLA scaffolds were subjected to plasma treatment and simultaneous grafting of acrylic acid (AA). When three different substrates, such as PLLA control, PLLA-HA, and PLLA-PAA-HA were analyzed, HA crystals on the surface of AA-grafted PLLA were identified better in size and distribution. The major compositions of HA, calcium and phosphorus were confirmed in the ESCA analysis of PLLA-PAA-HA. Significantly reduced water contact angles were identified with PLLA-HA and PLLA-PAA-HA as compared to PLLA control. When osteoblasts were cultivated in different 3D PLLA scaffolds, good cell attachment was seen from scanning electron microscopy (SEM) micrographs and osteoblasts appeared to be well spread and aggregated on the HA-formed scaffold. Once the total cell number was determined, the highest cellularity was noted with the PLLA-PAA-HA during 4-week culture. The difference was statistically significant between PLLA-PAA-HA and PLLA control or PLLA-HA. This study indicates that functional carboxylic groups could greatly facilitate HA crystal formation and that HA-formed polymer scaffolds can find favorable applications in bone tissue engineering.**

Keywords— **Tissue engineering, PLLA scaffold, acrylic acid (AA), hydroxyapatite (HA), osteoblast adhesion**

I. Introduction

Reconstruction of skeletal defects represents a major clinical challenge that often requires bone grafting. As an alternative of auto/allograft, tissue-engineered bone grafts that utilized inorganic/organic biomaterials have been developed and tested *in vitro* and *in vivo* [1-3]. One of the key ingradients of building a bone-like structure is scaffold that can mimic the natural bone in structure and composition. Hydroxyapatite (HA) has drawn much attention as a scaffold material or a bone substitute, because of its similar chemical composition to the inorganic part of human bone. Meanwhile, Li et al. reported that apatite formation was possible on the hydrated silica gel in a simulated body fluid (SBF) [4]. This was also proven feasible with highly porous 3D polymer scaffolds. Zhang et al. proposed biodegradable polymer/apatite composite as a new type of scaffold for bone tissue engineering [5]. In their scheme, the bone-like apatite was grown on the surface of pore walls of poly(L-lactic acid) (PLLA) foams in SBF. Use of deposited HA on porous polymeric scaffold can have a wide range of application for bone tissue regeneration. To induce more HA formation, polymer surface needs to be properly modified, because carboxylic or hydroxyl group can facilitate HA nucleation and growth. In the previous work, we found out that carboxyl groups could be introduced in the porous PLLA scaffold using plasma treatment and *in situ* acrylic acid (AA) grafting [6]. It is assumed that grafted functional groups may play a significant role to induce more HA crystals and as a result this can affect osteoblasts behavior. In this study, once PLLA surface was surface-modified with AA using plasma treatment, the effects on HA formation and osteoblast response were evaluated.

II. Materials and Methods

A. Materials

PLLA (Mw 250,000) was purchased from Boehringer Ingelheim (Germany). Sodium bicarbonate and citric acid crystals were purchased from Aldrich (USA). Solvents are chloroform and methylene chloride (MC). Acrylic acid (AA) was obtained from Aldrich (USA). Organic reagents for SBF, including NaCl, $NaHCO_3$, KCl, $K_2HPO_4 \cdot 3H_2O$, $MgCl_2 \cdot 6H_2O$, HCl, $CaCl_2$, Na_2SO_4, and $NH_2C(CH_2OH)_3$ were purchased from Wako (USA).

B. Preparation of PLLA film and porous PLLA scaffold

PLLA film was made using solvent casting technique. PLLA was dissolved in chloroform and this solution (8 wt%) was transferred to a glass dish to make thin film by evaporation. For biodegradable porous scaffold, PLLA were dissolved in MC to become 13 wt% polymer solution. Sodium bicarbonate and citric acid that have various size distribution (10-50 and 200-300 μm) were mixed homogeneously with the polymer solution. The ratio of porogens-to-polymer was 20:1 by weight. The mixture was filled in a disc-shaped silicon mold and then freeze-dried to remove solvent. During gas foaming process, the polymer disks

F. Ibrahim, N.A. Abu Osman, J. Usman and N.A. Kadri (Eds.): Biomed 06, IFMBE Proceedings 15, pp. 109-112, 2007
www.springerlink.com ' Springer-Verlag Berlin Heidelberg 2007

were immersed in 50% aqueous ethanol solution and briefly sonicated at room temperature. When the disks were put in the water, base (sodium bicarbonate) and acid (citric acid) reaction could liberate carbon dioxide gas, an effervescence proceeds. After that, the obtained porous PLLA scaffolds were washed with distilled water, vacuum-dried, and then stored in a moisture-free dessicator.

C. Preparation of simulated body fluid (SBF)

SBF with nearly 1.5 times more concentrated than the inorganic ion concentrations in human blood plasma was prepared by dissolving the reagent grade salts of NaCl, $NaHCO_3$, KCl, $K_2HPO_4\ 3H_2O$, $MgCl_2\ 6H_2O$, HCl, $CaCl_2$, Na_2SO_4, and $NH_2C(CH_2OH)_3$ in water. Its pH was adjusted to 7.4 at 37℃ with tris-(hydroxymethyl)aminomethane [$NH_2C(CH_2OH)_3$] and hydrochloric acid (HCl). The final concentrations of inorganic ions were 213.0 mM Na^+, 7.5 mM K^+, 3.8 mM Ca^{2+}, 2.3 mM Mg^{2+}, 221.9 mM Cl^-, 6.3 mM HCO^{3-}, 1.5 mM HPO_4^{2-} and 0.75 mM SO_4^{2-}, respectively.

D. Surface modification of PLLA

The surface of PLLA films and porous PLLA scaffolds were modified through a graft-polymerization of hydrophilic monomer, AA onto the PLLA surface as described in the previous work [6]. Briefly, PLLA films and scaffolds were fixed between radio frequency generating electrodes located in the chamber of plasma-discharging device (Model PTS-003IDT, I.D.T. ENG., Inc., Korea). Once all valves were closed and internal pressure was set to 10^{-3} torr, Argon was first injected into the chamber, followed by AA injection in a gas phase, while RF power (50 W) and pulse type negative voltage were being applied. The discharging was lasted for 60 s to obtain PLLA-PAA.

E. Hydroxyapatite formation in SBF

Films and scaffolds of PLLA and PLLA-PAA were immersed in 5 and 10 mL of SBF, respectively at 37 ^{O}C. A series of evacuation/repressurization cycles were applied to force the SBF solution into the pores within the scaffolds. The solution was renewed every 5 days. The specimens were incubated for up to 10 days and taken out, then washed overnight in 10 ml of deionized water to remove the soluble inorganic ions. Finally, PLLA-HA and PLLA-PAA-HA were obtained.

F. Surface characterization

Surface morphology of the films and scaffolds was examined by scanning electron microscopy (SEM; Hitachi, Tokyo, Japan). They were gold-coated using a sputter coater (Eiko IB3, Tokyo, Japan) before observation. Surface contact angle was measured using contact angle machine (VCA Optima XE Video Contact Angle System, Crest Technology Ltd., Singapore). Five different sites of each film were tested. An XRD spectrum of each specimen was obtained using Phillips X-ray diffractometer. Using S-Probe Surface Science ESCA instrument, surface elemental compositions were determined.

G. Cell culture and assay

For cell experiment with different PLLA scaffolds, osteoblasts (MG6) were used. The cells were grown in α-MEM containing 10% fetal bovine serum (FBS) and 1% antibiotics. The culture was maintained at 37℃ in a humidified atmosphere with 5% CO_2 supply and medium was replaced every 3 days. For cell seeding at $3x10^5$/ml, HA-formed PLLA scaffolds were placed at the bottom of the 24-well plates and cultivated for up to 4 weeks. For SEM observation, the PLLA scaffolds were completely dehydrated by a series of ethanol solution after fixation with 2.5% glutaraldehyde for 24 h at 4℃. Changes in the total cell numbers were evaluated using WST-1 assay kit.

H. Statistical analysis

The data were presented as means ± standard deviation (SD). Statistically significant difference was determined using the Student *t* test. The difference was considered significant when *p* value is less than 0.05.

III. Results

When the surface of PLLA and PLLA-PAA was exposed to SBF solution, the HA crystal formation was clearly observed in the SEM images (Fig. 1). No HA particles in the control PLLA were noticed without SBF. The size and distribution of HA crystals on the surface of PLLA-PAA were found significantly better than those on the PLLA. The water contact angle of PLLA control was 74 degree, a typical hydrophobic surface, whereas that of PLLA-HA and PLLA-PAA-HA was significantly reduced (Fig. 2), indicat-

F. Ibrahim, N.A. Abu Osman, J. Usman and N.A. Kadri (Eds.): Biomed 06, IFMBE Proceedings 15, pp. 109-112, 2007
www.springerlink.com ' Springer-Verlag Berlin Heidelberg 2007

ing more hydrophilic surface. When wide-angle XRD was used to characterize the PLLA films, a characteristic peak of HA was detected on the surface of PLLA films incubated in the SBF (Fig. 3). The amplitudes of the peaks increased with incubation time in SBF solution. Analysis of elemental compositions using ESCA also presented a notable difference on the surface with the HA crystal formation (Table 1). While the surfaces of PLLA control showed two peaks, C1s and O1s, those of PLLA-HA and PLLA-PAA-HA presented three other peaks, Cl, Ca, and P peaks, which were indicative of HA components, along with C1s and O1s. Upon the ESCA analysis, the Ca/P ratio was ranged from 1.36 to 1.40. When osteoblasts were cultured on 3D PLLA scaffolds that have different substrate property, cell attachment was witnessed in the SEM images and osteoblasts appeared to be well spread and aggregated on the surface-modified scaffold (Fig. 4). Once the total cell number on the various PLLA scaffolds was determined, the highest cellularity during 4-week culture was found in the PLLA-PAA-HA (Fig. 5). The difference was statistically significant between PLLA-PAA-HA and PLLA control or PLLA-HA. The same was also witnessed between PLLA-HA and PLLA control.

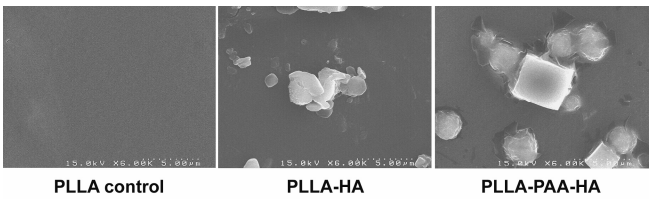

Fig. 1 SEM observation of HA crystals formed on PLLA and PLLA-PAA films (x6,000). HA particles were clearly formed in SBF solution.

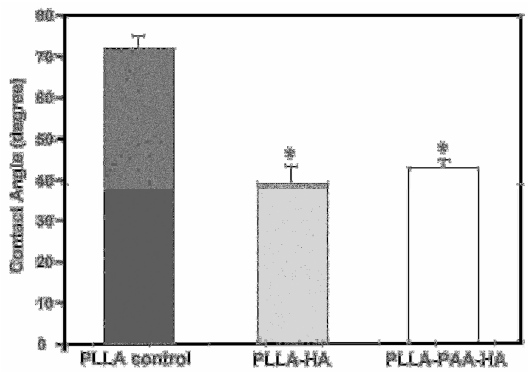

Fig. 2 Comparison of water contact angles on different PLLA surfaces. HA-formed surfaces have significantly lower contact angles. Asterisk (*) indicates statistically significant difference ($p<0.05$) as compared to PLLA control.

Table 1 ESCA analysis of PLLA film surfaces

Material	Atomic %				
	C	O	Cl	Ca	P
PLLA control	67.5	32.5	-	-	-
PLLA-HA	67.3	31.0	0.7	1.0	-
PLLA-PAA-HA	65.8	29.1	1.5	2.1	1.5

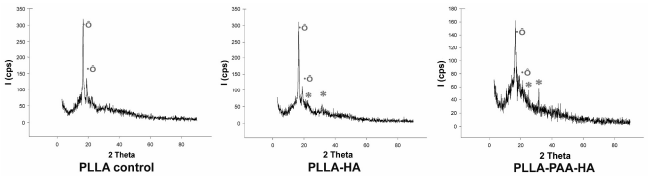

Fig. 3 XRD analysis of HA-formed PLLA surfaces.

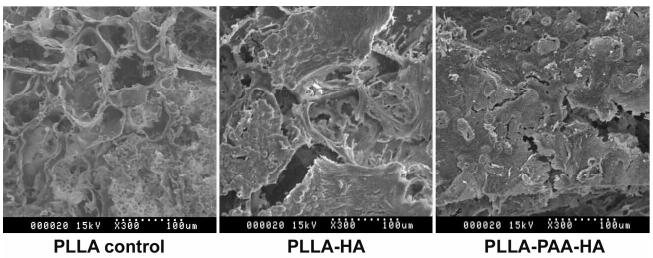

Fig. 4 SEM observation of osteoblast-seeded PLLA scaffolds cultivated for 1 week.

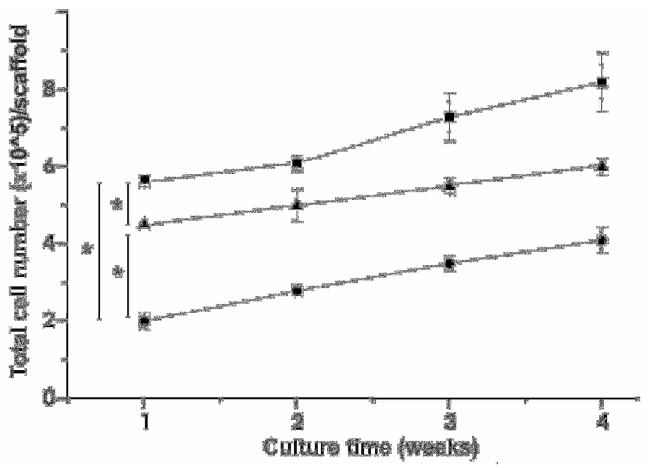

Fig. 5 Total cell numbers in the PLLA control (●), PLLA-HA (▲), and PLLA-PAA-HA (■). Asterisk (*) indicates statistically significant difference ($p<0.05$) among the tested specimens.

F. Ibrahim, N.A. Abu Osman, J. Usman and N.A. Kadri (Eds.): Biomed 06, IFMBE Proceedings 15, pp. 109-112, 2007
www.springerlink.com ' Springer-Verlag Berlin Heidelberg 2007

IV. Discussion

Introduction of more carboxylic groups onto PLLA surface was found very effective in the HA formation. The AA-grafted PLLA surface could significantly accelerate the nucleation and growth of HA crystals in SBF as compared to the unmodified PLLA, PLLA control. While lower density of smaller crystals was found on the PLLA surface, denser and larger crystals were noticed after 10-day incubation of AA-grafted PLLA in SBF. The mechanism of HA crystal induction seemed to be related to chemical interactions between functional groups and apatite components in SBF solution. In general, the ester linkages of PLLA break due to hydrolysis and as a result, carboxylic acids and hydroxy groups are exposed on the surface. The carboxylic groups are then turned into carboxylate anions at a buffer solution (pH 7.4), providing negatively charged surface to adsorb positive calcium ions from saturated SBF solution. Locally excessive calcium ions can induce apatite nucleation and crystal growth in reaction with phosphate ions. From the results of this experiment, the quality of HA itself appeared better in the AA-grafted PLLA, because both calcium and phosphate atoms were found in the ESCA analysis but only calcium was identified in the PLLA-HA.

Interestingly, HA crystals may have significant implications on osteoblast behavior. During 4-week culture, osteoblast proliferation was greatly improved with the HA-formed surfaces, PLLA-HA and PLLA-PAA-HA. Although the principle is unclear at this time, it is postulated that cell-substrate adhesion was stronger with the HA-formed substrate as compared to PLLA control. Regarding the extent of hydrophilicity of each specimen, this may be indirectly explained from the different contact angles, in which the HA-formed films carried much lower ones than PLLA control. It is generally believed that cell adhesion is better on relatively hydrophilic surface. Due to the HA crystals, the initial surface topography of PLLA could also be largely changed, as a result, influencing cell behavior. In addition, size and distribution of HA might be anther factor in osteoblast proliferation, as contrasted in SEM observation between the two HA-formed surfaces.

V. Conclusion

AA-grafted PLLA (PLLA-PAA) surface can induce HA formation better in size and distribution than unmodified one, due mainly to the functional carboxylic groups that were responsible for crystal nucleation and growth. HA-formed surface was able to affect osteoblast behavior, leading to the improvement of cell adhesion and proliferation. HA-formed polymer scaffolds should find many applications in bone regeneration using tissue engineering technique.

Acknowledgment

This work was supported by KIST grants, 2E19220 and 2E19362, from Ministry of Science and Technology, Korea.

References

1. Chou YF, Dunn JCY, Wu BM (2005) *In vitro* Response of MC3T3-E1 Preosteoblasts within Three-Dimensional Apatite-Coated PLGA Scaffolds. J Biomed Mater Res 75B:81-90.
2. Lu HH, El-Amin SF, Scott KD, Laurencin CT (2003) Three-dimensional, bioactive, biodegradable, polymer-bioactive glass composite scaffolds with improved mechanical properties support collagen synthesis and mineralization of human osteoblast-like cells *in vitro*. J Biomed Mater Res 64A:465-474.
3. Li H, Chang J (2004) Preparation and characterization of bioactive and biodegradable Wollastonite/poly(D,L-lactic acid) composite scaffolds. J Mater Sci:Mater Med 15:1089-1095.
4. Li P, Ohtsuki C, T. Kokubo T et al. (1992) Apatite formation induced by silica gel in a simulated body fluid. J Am Ceram Soc 75: 2094 2097.
5. Zhang RY, Ma PX (1999) Porous poly(L-lactic acid)/apatite composites created by biomimetic process. J Biomed Mater Res 45:285 293.
6. Jung HJ, Ahn KD, Han DK (2005) Surface Characteristics and Fibroblast Adhesion Behavior of RGD-Immobilized Biodegradable PLLA Films. Macromol Res 13:446-452.

Address of the corresponding author:

Author: Dong Keun Han
Institute: Biomaterials Research Center,
Korea Institute of Science and Technolgy
Street: P.O. Box 131, Cheongryang
City: Seoul
Country: Korea
Email: dkh@kist.re.kr

F. Ibrahim, N.A. Abu Osman, J. Usman and N.A. Kadri (Eds.): Biomed 06, IFMBE Proceedings 15, pp. 109-112, 2007
www.springerlink.com ' Springer-Verlag Berlin Heidelberg 2007

Inhibitive Effect of Antibiotic-Loaded Beads to Cure Chronic Osteomyelitis in Developing Country: Hand-made vs Commercial Beads

Hermawan N. Rasyid[1,3], Jim R. Van Horn[2], Henny C. Van der Mei[1], Soegijardjo Soegijoko[3], Henk J. Busscher[1], and Dani° lle Neut[1,2]

Departments of Biomedical Engineering[1] and Orthopaedic Surgery[2], University Medical Center Groningen, and University of Groningen, The Netherlands; Biomedical Engineering Program[3], School of Electrical Engineering and Informatics, Institut Teknologi Bandung, Indonesia

Abstract— **Local antibiotic-loaded beads have been approved for standard treatment of orthopaedic pathogens, especially chronic osteomyelitis. Septopal®, the only commercial local antibiotic bead available on the market, is expensive and contains only gentamicin. This study aimed to compare the *in vitro* inhibitive effect of hand-made antibiotic-loaded beads (fosfomycin-sodium) with Septopal® for ten bacterial strains of chronic osteomyelitis by diffusion technique at various indicated time points. The results showed that Septopal® could inhibit all bacterial strains except CNS 7334 and CNS 7391. Hand-made fosfomycin beads were only slightly effective in two of the ten bacterial strains is used (*Staphylococcus aureus* 7323 and CNS 7391). In conclusion, this study demonstrated that Septopal® can inhibit common orthopaedic pathogens better than hand-made beads *in vitro* study, however, fosfomycin concentrations required to kill orthopedic implant related bacterial strains are high and its release from hand-made beads is too low to be considered efective when compared with Septopal beads.**

I. Introduction

The uses of polymethylmethacrylate (PMMA) for delivery of local antibiotics for the treatment of musculoskeletal infection has become increasingly popular for a variety reasons.[1,2,3] *In vitro* and *in vivo* study have shown amounts of the antibiotics incorporated in bone cement are actually released.[4] High local levels of antibiotics facilitate delivery of antibiotics by diffusion to avascular areas of the bone and hypovascular areas of surrounding soft tissue that are inaccessible by systemic antibiotics and in many circumstances of organisms that are resistant to drug concentrations achieved systemically.[5,6]

The concept of antibiotic delivery by incorporation of gentamicin into acrylic bone cement was introduced in 1970.[5] This concept has been approved for their efficacy and effectiveness for treatment of orthopaedic infections, especially chronic osteomyelitis, which is caused mostly by Gram positive bacteria such as *Staphylococcus aureus*.[5]

In developing countries, such as Indonesia there are many poor people that always make use of the service of traditional medicine like bonesetter when dealing with open factures of the bone. In treating these fractures, initially they reduce the fracture without cleaning the wound, then directly covered the wound by herbals, then, fixed them using wood as a slab. After several months, the patient comes to the orthopedic clinic with persistent sinus tract and active pus, meaning that chronic osteomyelitis occurred

Chronic osteomyelitis in developing countries is generally treated by clearing the cavity of infected materials, systemic administration of antibiotics and planting a chain of hand-made antibiotic-loaded beads. These beads are left *in situ* for about fourteen days, after which the cavity is filled with bone graft.

Antibiotic-loaded PMMA beads are commercially available under the name Septopal , but the price of these beads is far too high for most patients. Fosfomycin is the commonly used antibiotic in these bone cement beads, because of its low costs, wide antibacterial spectrum, small molecular weight (138 Da) and its ability to remain stable up to the high temperatures as reached during polymerization of the bone cement.[7]

The treatment of osteomyelitis in Indonesia generally yields satisfactory clinical results, but it is unknown up to what extend the fosfomycin-loaded, hand-made beads contribute to these results. The aim of this study is to evaluate the *in vitro* antibacterial efficacy and kinetics of antibiotic release of several currently used, hand-made fosfomycin-loaded beads. All results will be compared with those of commercially available gentamicin-loaded PMMA beads (Septopal).

II. Materials and methods

Antibiotic-loaded beads preparation

A number of orthopedic surgeons in Indonesia were requested to describe their personal concepts developed to prepare antibiotic-loaded beads. In general, PMMA bone cements were used, in combination with a variety of different mixing techniques and sometimes templates. Fosfomycin-sodium was the general antibiotic included. Based on this inventory, six concepts were selected for further research and the participating surgeons were asked to submit an extensive protocol of their concept, as summarized in Table 1, together with samples of their beads.

F. Ibrahim, N.A. Abu Osman, J. Usman and N.A. Kadri (Eds.): Biomed 06, IFMBE Proceedings 15, pp. 113-117, 2007
www.springerlink.com ' Springer-Verlag Berlin Heidelberg 2007

Antibiotic-loaded PMMA beads are commercially available under the name Septopal (Biomet Deutchland, Darmstadt, Germany). It consists of 30 beads threaded on surgical wire several threads thick.

Table 1. Six different local concepts developed by Indonesian orthopedic surgeons for preparing hand-made antibiotic-loaded beads. All beads contained fosfomycin and mixing was done by hand using a spatula.

Beads	Cement base	Fosfomycin content [g]	Shaping	Size [cm]	Area/volume ratio [cm^{-1}]
#1	Zimmer, 40 g	4	Template	1.7	1.8
#2	Simplex P, 40 g	2	Handrolled	2.8	1.0
#3	Simplex P, 40 g	2	Handrolled	1.6	1.8
#4	Simplex P, 40 g	2	Handrolled	2	1.5
#5	Simplex P, 40 g	2	Handrolled	1.6	1.8
#6	Simplex P, 40 g	2	Handrolled	1.6	1.9

Antibacterial efficacy

Beads#1 to #6 and Septopal beads were immersed in 10 ml of sterile phosphate buffer saline (PBS) and incubated at 37^0C. After 24 h of incubation 15 µl samples were taken and these were placed on bacterial streaked trypton soya brooth (TSB) agar plates. The zones of inhibition were established by measuring the diameters of the clear areas around one drop of elution fluid. Absence of an inhibition zone was taken as a sign that the antibiotic concentration was too low to inhibit bacterial growth. For this study we used ten clinical strains isolated from patients with an implant-related infection of the University Medical Center Groningen, The Netherlands. Distribution of the different strains and species chosen are in accordance with those reported to be involved in the occurrence of osteomyelitis.[8,9] Each strain was diluted in 4 ml of 0.9% saline to concentration approximately of 10^8 bacteria/ml. After overnight incubation at 37^0C on agar plates, the inhibition zone diameters (mm) were scored.
In addition, the minimal inhibitory concentration (MIC in µg/ml) of the isolated bacteria against fosfomycin and gentamicin were determined by an E-test (AB Biodisk, Dälvagen, Sweden).

Kinetics of antibiotic release

Six different hand-made beads and Septopal beads were immersed in 10 ml sterile PBS and incubated at 37^0C. At indicated time points (24 h, 48 h, 72 h, and 144 h), beads were transferred to fresh 10 ml PBS and again incubated at 37^0C. The kinetics of antibiotics release was established by taking four 15 µl elution fluid samples at the indicated time points and placing the droplets on the four quadrants of a bacterial streaked TSB agar plate. Kinetics of antibiotic release was only studied with strains toward which antibacterial efficacy could be established, as described above. After 24h incubation at 37^0C the inhibition zone diameters were scored in all four quadrants.

Scanning electron microscopy

For scanning electron microscopy (SEM), beads were exposed overnight to an osmium tetroxide vapor. Samples were dehydrated in air and sputter-coated with gold/palladium (~3 nm). Examination was done at 5.0 kV in a JEOL field emission scanning electron microscope type 6301F.

III. Results

Minimal Inhibitory Concentration (MIC value)

The effect of fosfomycin and gentamicin on the growth of 10 bacterial strains (see Table 2). The MIC values for these isolates ranged from 0.19 to over 1024 µg/ml for fosfomycin and 0.38 to over 256 µg/ml for gentamicin. Resistant sub-population could be observed within inhibition zones in both strains. The efficacy of fosfomycin is effective in *S. aureus* 7323, CNS 7391 and *E.coli* BS 6202 (MIC value 0.19, 0.50 and 1.5 µg/ml). Two bacterial strains were gentamicin resistant. Efficacy of gentamicin on the growth of 10 bacterial strains was evaluated, it has MIC value ranged from 0.75 to over 256 µg/ml and effective in all bacterial strains except for CNS 7334, CNS 7391, *P. aeruginosa* 5148, and *P. aeruginosa* 7348.

Table 2. MIC values of 10 bacterial strains used in this study for fosfomycin and gentamicin.

No.	Bacterial strains	MIC value (µg/ml)	
		Fosfomycin	Gentamicin
1	*S. aureus* 5298	96	0.75
2	*S. aureus* 7323	0.19*	1.5
3	CNS 7368	48	0.38
4	CNS 7334	24	6
5	CNS 7391	0.50*	>256
6	*Micrococcus* 7397	192	0.5
7	*P. aeruginosa* 5148	>1024	2
8	*P. aeruginosa* 7348	32	4
9	*E. coli* BS 6206	1.5*	1.0
10	*Klebsiella* 333257	>1024	1.0

* resistant sub-populations could be observed within the inhibition zones

F. Ibrahim, N.A. Abu Osman, J. Usman and N.A. Kadri (Eds.): Biomed 06, IFMBE Proceedings 15, pp. 113-117, 2007
www.springerlink.com ' Springer-Verlag Berlin Heidelberg 2007

The efficacy of fosfomycin was also evaluated on the growth of 20 bacterial strains of chronic osteomyelitis patients from Indonesia after incubation *in vitro*. Results of MIC values for these isolates ranged from 1.5 to over 1024 µg/ml. Fosfomycin is effective with low MIC values (1.5µg/ml) in three bacterial strains of *S. aureus (S. aureus InB1; InP4; In B4 and InB7)*. Resistant sub-populations could not be observed in these inhibition zones.

Antibacterial efficacy

Table 3 shows that hand-made fosfomycin-loaded beads were only slightly effective and never against more than two of the ten bacterial strains is included. Nearly all beads are effective against *S. aureus* 7323 and CNS 7391, which appears resistant against gentamicin.

Table 3. Zones of inhibition around droplets of elution fluids from hand-made fosfomycin-loaded PMMA beads and gentamicin-loaded Septopal beads.

Bacterial Strains	Beads						
	#1	#2	#3	#4	#5	#6	Sept
S. aureus 5298	-	-	-	-	-	-	+
S. aureus 7323	-	+	-	+	+	+	+
CNS 7368	-	-	-	-	-	-	+
CNS 7334	-	-	-	-	-	-	-
CNS 7391	-	+	+	+	+	+	-
Micrococcus 7397	-	-	-	-	-	-	+
P. aeruginosa 5148	-	-	-	-	-	-	+
P. aeruginosa 7348	-	-	-	-	-	-	+
E. coli BS 6206	-	-	-	-	-	-	+
Klebsiella 333257	-	-	-	-	-	-	+

- =no zone; + = clear inhibition zone; Sept = Septopal

Antibiotic release

Table 4 presents the diameter of the inhibition zones in millimeters achieved with elution fluid from the hand-made fosfomycin-loaded beads after different elution periods. None of the beads showed antibacterial efficacy against *S. aureus* 7323 extending beyond 24 h, whereas beads#1 and #3 were not effective at all. This is all in sharp contrast with the inhibition zones achieved with elution fluid from Septopal beads, showing sustained release against *S. aureus* 7323 for at least 144 h. Due to its gentamicin-resistance, no inhibition zones could be measured against CNS 7391.

Table 4. Diameters of clear zones of inhibition (mm).

Beads	*S. aureus 7323*				*CNS 7391*			
	24h	*48h*	*72h*	*144 h*	*24h*	*48h*	*72h*	*144h*
#1	-	-	-	-	20	20	15	20
#2	16	-	-	-	25*	20	20	20
#3	-	-	-	-	15*	15	-	15
#4	11	-	-	-	20*	20	20	20
#5	7	-	-	11	25*	20*	-	20*
#6	13	-	-	-	25*	20	20	20
Sept	16	12	11	14	-	-	-	-

- = no zone; * resistant sub-populations could be observed within the inhibition zones

Scanning electron microscopy

We utilized scanning electron microscopy (SEM) to investigate the homogenicity and porosity of the polymer antibiotic complexes. We have shown that the addition of antibiotic renders the polymer texture more homogen in Septopal beads compared to beads#2 (Fig. 1 A and B).

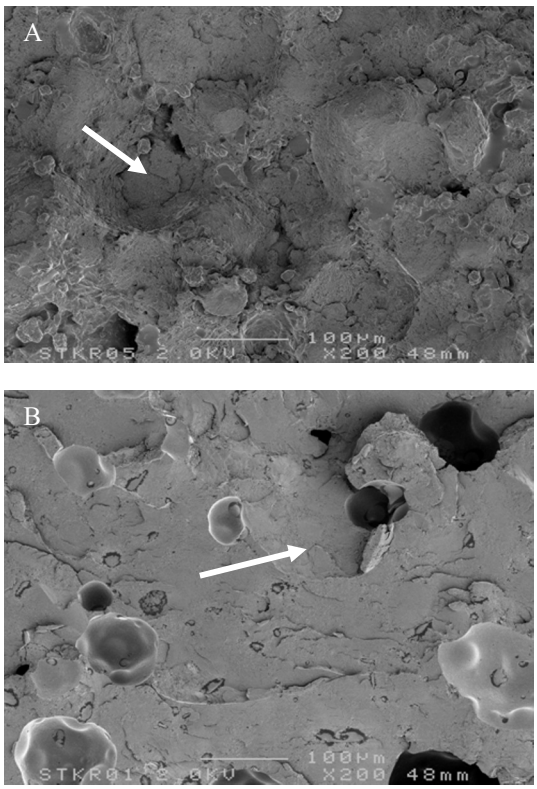

Fig. 1 SEM images of the PMMA with gentamicin Septopal beads and fosfomycin beads in different magnifications. **(A)** High magnification of fracture surface): SEM of a Septopal bead. **(B)** Fracture surface in high magnification: SEM of beads#2, which is the broadest antimicrobial efficacy.

F. Ibrahim, N.A. Abu Osman, J. Usman and N.A. Kadri (Eds.): Biomed 06, IFMBE Proceedings 15, pp. 113-117, 2007
www.springerlink.com ' Springer-Verlag Berlin Heidelberg 2007

IV. Discussion

Currently, antibiotic-loaded PMMA beads were successfully used as local antibiotic delivery systems, however, these compounds are not degraded or absorbed in the body, they must be removed by further operation and their long-term implantation is difficult. Various operative techniques have been adopted in the management of this disease.[8,9,10] Chains of antibiotic-loaded cement PMMA beads are an effective drug delivery system for local antibiotic therapy in bone and soft-tissue infections. The antibiotic concentrations at the site of infection are far higher than after systemic application of the same antibiotic and far above the minimal inhibitory concentrations of most common pathogens. Elution of antibiotics from PMMA is dependent on the access of fluid to the depths of the cement that contains the antibiotic.[11]

The elution of fosfomycin-loaded beads were only effective in two of the ten bacterial strains tested, while the elution of Septopal beads were effective against eight of the ten strains used. An E-test determined the MIC values of the clinical strains for both fosfomycin and gentamicin. Four of the ten clinical strains turned out to be fosfomycin resistant, meaning a MIC value above 64 µg/ml. On the other hand two of the ten strains were considered gentamicin resistant as their MIC value was above 4 µg/ml. Accordingly, the fosfomycin-loaded beads did not show efficacy against four of the fosfomycin sensitive bacteria. In a large beads surface, they were able to release more antibiotics as antibiotic release is mostly a surface phenomenon (van de Belt 2001).[12] Moreover, prolonged release from bone cement is only possible when the cement is very porous.[13] Release rate of antibiotic from PMMA is important clinically. Porosity/permeability of the PMMA is an important factor in determining the release rate. Known factors that influence antibiotic release from PMMA are surface roughness and porosity. Van de Belt *et al*, demonstrated that porosity corresponded best with the eventual amount of release. It make sense since the evaluation of SEM, the broadest beads#2 revealed homogenicity of the surface texture and more porous, and there are many craters and cracks as well. It means that antibiotics are leached from this type of beads. Space inside the beads and particle size has to be noticed. Pores should be large enough in order to release process of the antibiotic to the medium without obstacle. The evaluation of fosfomycin loaded beads is using clinical strains isolated from patients with an infected joint replacement in Dutch patients, these situations mostly due to deep infection. This situation will be different with clinical strains focused on chronic osteomyelitis hematogenously. Retrospective study was done in 56 osteomyelitis patients at the Dept. of Orthopedic and Traumatology dr. Hasan Sadikin Hospital, Bandung, Indonesia. The microorganism pattern of osteomyelitis is *S. aureus* 26.9% of all cases, and *P. aeruginosa* 11.0% of all cases.[14]

The microorganism pattern of osteomyelitis and the treatment results can be contradictory. It seems that the efficacy of fosfomycin loaded beads did not appear, but standard surgical debridement and systemic antibiotic administration should have an important role to treat this disease. We conclude from the presented observations that a mixture of fosfomycin and PMMA bone cement is not an effective one. Efficacy could only be seen in two of the ten bacterial strains. We assume that the hand-made beads were not porous enough as porosity of bone cement is the key to high antibiotic release. Therefore we have to try other procedures to increase the porosity, like adding glycine as in currently done in the Septopal beads.[15] Also trying an other antibiotic is an option, together with changing the antibiotic carrier from PMMA bone cement to calcium phosphate.[16] One big advantage of calcium phosphate above PMMA bone cement is that calcium phosphate is biodegradable, so no second operation is needed to remove the beads.

V. Conclusions

Fosfomycin concentrations required to kill orthopedic implant related bacterial strains are high and its release from hand-made beads is too low to be considered effective when compared with Septopal beads.

Acknowledgements

The author would like to thank to Mr. Ietse Stokroos, Department of Cell Biology and Electron Microscopy for his help with the electron microscopy. This work is funded in part by Eric Bleumink Fund, University of Groningen, The Netherlands.

References

1. Buchholz, H.W., and Engelbrecht H. Uber die Depotwirkung einiger Antibiotica bei Vermischung mit dem Kunstharz Palacos. Chirurg 1970;41:511-5.
2. Klemm, K. Gentamicin-PMMA-Kugeln in der Behandlung abszedierender Knochen und Weichteilinfektionen. Zentral bl. Chirurg 1979;104:934-42.
3. Brinker, M.R. Antibiotic beads in general principles of trauma, in: Review of orthopaedic trauma 2001:31-43.
4. Patzakis, M.J., Wilkins, J., Kumar, J., Holtom, P., Greenbaum, B., and Ressler, R. Comparison of the results of bacterial cultures from multiple sites in chronic osteomyelitis of long bones: A prospective study. *J Bone Joint Surg Am* 1994;76:664-6.

F. Ibrahim, N.A. Abu Osman, J. Usman and N.A. Kadri (Eds.): Biomed 06, IFMBE Proceedings 15, pp. 113-117, 2007
www.springerlink.com ' Springer-Verlag Berlin Heidelberg 2007

5. Walenkamp, G.H.I.M., Coombs, R., and Fitzgerald, R.H. Gentamicin PMMA beads: Pharmacokinetics and toxicology in: Infection in the orthopaedic patient 1989:163-66.
6. Wahlig, H., Dingeldein, E. Antibiotics and bone cements. Experimental and clinical long term observations. *Acta Orthop Scand* 1980;51:495.
7. Goto, S. Fosfomycin, antimicrobial activity *in vitro* and *in vivo* in: *Chemotheraphy* 1977;23:65-74.
8. McLaughlin, R.E., Reger, S.I., Barkalow, J.A., Allen, M.S., and Difazio, C.A. Methylmethacrylate: A study of teratogenicity and fetal toxicity of the vapor in the mouse. *J Bone Joint Surg* 1978;3:355-58.
9. Klemm, K.W. Antibiotic bead chains. *Clin Orthop* 1993;295:63-76.
10. Seligson, D., and Henry, S.L. Newest knowledge of treatment for bone infection: antibiotic-impregnated beads. *Clin Orthop* 1993;295:2-18.
11. Hanssen, A.D. Local antibiotic delivery vehicle in the treatment of musculoskeletal infection in: Local antibiotic delivery systems. *Clin Orthop* 2005;437:91-6.
12. Van de Belt, H., Neut, D., Van Horn, J.R., Van der Mei, H.C., Schenk, W., and Busscher, H.J. *Staphylococcus aureus* biofilm formation on different gentamicin-loaded polymethylmethacrylate bone cements. *Biomaterials* 2001;22:1607-11.
13. Van de Belt, H., Neut, D., Uges, D.R., Schenk, W., Van Horn, J.R., and Van der Mei. H.C., Busscher, H.J. Surface roughness, porosity and wettability of gentamicin-loaded bone cement and their antibiotic release. *Biomaterials* 2000;21:1981-7.
14. Saragih, J.R. Microorganisms pattern and its sensitivity in osteomyelitis case at the Dept. of Orthopedic Surgery Dr Hasan Sadikin Hospital, Bandunng, Thesis 1999:50-1.
15. McLaren, A.C., Nelson, C.L., McLaren, S.G., and DeClerk, G.R. The effect of glycine filler on the elution rate of gentamicin from acrylic bone cement. A pilot study. *Clin Orthop* 2004;427:25-7.
16. Wichelhaus, T.A., Dingeldein, E., Rauschmann, M., Kluge, S., Dieterich, R., Schäfer, V., and Brade, V. Elution characteristics of vancomycin, teicoplanin, gentamicin and clindamycin from calcium sulphate beads. *J Antimicrobial Chemotherapy* 2001;48:117-9.

Address of the corresponding author:

Author: Hermawan N. Rasyid
Institute: Departments of Biomedical Engineering[1] University of Groningen
Country: The Netherlands
Email: hermawan_nr@yahoo.com

F. Ibrahim, N.A. Abu Osman, J. Usman and N.A. Kadri (Eds.): Biomed 06, IFMBE Proceedings 15, pp. 113-117, 2007
www.springerlink.com ' Springer-Verlag Berlin Heidelberg 2007

Nanostructure in Bone Apatite

Y.W. Sari[1 2], D.S. Soejoko[1] and K.Dahlan[2]

[1]Department of Physics, University of Indonesia, Kampus UI Depok 16424, Indonesia
[2] Department of Physics, Bogor Agricultural University, Kampus IPB Darmaga Bogor 16680, Indonesia

Abstract– **The mineral component of bone is a form of calcium phosphate known as hydroxyapatite. Due to the presence of significant amount of foreign ions, biological apatites have a poor crystallinity and are non-stochiometric. Size and shape of mineral particles change with species, age, and disease. This work studied the relationship between rat bone mineral and the age of rat. Analysis was carried out by using an X-ray diffraction (XRD) and a scanning electron microscopy (SEM). It was found that bone apatite has a nano sized crystal (14, 70 – 24,49 nm). Bone apatite crystalinity has a nonlinear relation to the age, however younger rats is more crystalline than older. SEM micrograph has shown that bone apatite, which is a nanostructure material, composes two phase, amorphous and crystalline.**

Keywords– **bone mineral, carbonate apatite, hydroxyapatite**

I. Introduction

Bone is a unique composite composed of 50 % wt minerals, 25% wt matrix, and 25% wt water[1]. Matrix occurs as a template for bone mineral deposition. Bone matrix is formed by type I collagen. Besides as a unique composite, bone is a living tissue due to its cellular content. The difference between bone and other tissues is its mineralization over the matrix[2]. This mineralization provide bone hardness to support its function as levels for locomotion. The mineral component of bone is a form of calcium phosphate known as apatite crystals, which is idealized as $Ca_{10}(PO_4)_6(OH)_2$[2-5]. The incorporation and/or substitution of foreign ions, other than calcium and phospahte, tends to modify the basic hydroxyapatite and produce great amount of various calcium phosphates. Some of them enter the hydroxyapatite crystal lattice while others are only adsorbed on the surface[6]. Several studies have shown carbonate ions are located inside the bone apatite. Carbonate ions can occupy two different anionic sites. The minor carbonate substitutes for the OH^- sites, leads to type A cabonated apatite, while the mayor carbonate substitutes for PO_4^{3-}, leads to type B carbonated apatite.

Bone trauma or disease, such as defects and fractures, have led to an increase in the use of bone substitutes. Currently available bone substitutes show a variety of composition and properties. The use of calcium phosphate ceramics has become relatively commonplace[7-8]. SEM and XRD analyses of several commercially available calcium phosphate powders have shown them to vary considerably with respect to morphology[8]. Behave as bone substitutes, there is a needed to compare comercially available calcium phosphates with natural bone apatite. The purpose of this research was to provide further knowledge about the microscopic character of the natural bone apatite.

II. Materials and methods

Sample Preparation: The mineral bone used in this experiment were obtained from Sprague-Dawley rats. The rats were anasthesized using ether, afterwards the femur and tibiae were dissected. Using normal saline, the marrow and the remain flesh were removed. To extract the organic matters, the bone samples were deproteinated with hysdrazine solution. The samples were immersed into 5 ml hydrazine at room temperature in a crucible for 3 hours. To increase the extraction, the reagent was changed after one hour. After 2 hours of this treatment, the reagent was changed and preparation was performed in incubator with temperature 60°C for 25 hours. After the first hour, the reagent was changed and further stored in incubator for the remaining hours. Samples were then serially washed with 50%, 75%, 85%, 96% ethanol and aquades. Samples were heated at 110°C for 10 hours to release the adsorbed water before ground to become a powder.

Analyses: Structure of bone hydroxyapatite was analyzed by LEO scanning electron microscope and XD 610 SCHIMADZU X-ray diffractometer. Powder X-ray diffraction analysis was carried out at a scanning speed $1°min^{-1}$ covering the range of scattering angles (2θ) from 20° - 50° .

III. Results

SEM examination showed the bone apatite to be a plate shaped morphology (Figure 1 and 2). The grain was shown clearly since in the first month. The X-ray diffraction profile (Figure 3) showed that crystal phase in rat bone mineral are attributed to apatite crystal which are rich of carbonates. The presence of peak at about 25°, 28°, 31°, 39°, and 46° indicated

F. Ibrahim, N.A. Abu Osman, J. Usman and N.A. Kadri (Eds.): Biomed 06, IFMBE Proceedings 15, pp. 118-121, 2007
www.springerlink.com ' Springer-Verlag Berlin Heidelberg 2007

the presence of apatite crystals. X-ray diffraction profile of early age rat bone initiated with decline pattern at about 20° to 25°. The crystal size was calculated using Scherrer equation[9]:

$$D = \frac{K \cdot \lambda}{\beta \cdot \cos\theta}$$

where λ is the X-ray wavelength, which is Cu-Kα 1,5406 , θ is the diffraction angle, K is a constant warying with crystal habit and chosen as 0,9 for the apatitic crystallites of bone. The degree of crystallinity can be determined as the ratio of area under the curve of crystalline to cystalline plus amorphous.

IV. Discussion

Bone apatite was a nonstochiometric due to the presence of foreign ions, such as carbonate, magnesium, fluor, etc. The major ions that substitute and/or incorporate the hydroxyapatite are carbonates. The presence of natrium bicarbonate as the buffer solution of body acidity plays significant role. The substitution and/or incorporation in the body is due to the interaction of carbonate with calcium and phosphate as they precipitate on to the matrix. This precipitation takes place as wet reaction and in low temperature. Therefore major of bone apatite presents as a type B carbonated apatite. Type B carbonated apatites results as the substitution of phosphate by carbonate from wet reaction in low temperature atmosphere[10]. Carbonates will disturb the precipitation and impede the growth of hydroxyapatite crystal[11]. Stochiometrical hydroxyapatite crystal is in the form of closed-packed hexagonal with lattice parameters a = b = 9,422 and c = 6,883 [11-13]. This crystal consists of calcium ions surrounded by phosphate and hydroxil ions. Due to its larger size compare to calcium and hydroxil, phosphate will take most of hexagonal space. Phosphate substitution by carbonate leads to smaller crystal size in the dirrection of c axis. Therefore, bone apatite has plate shaped morphology.

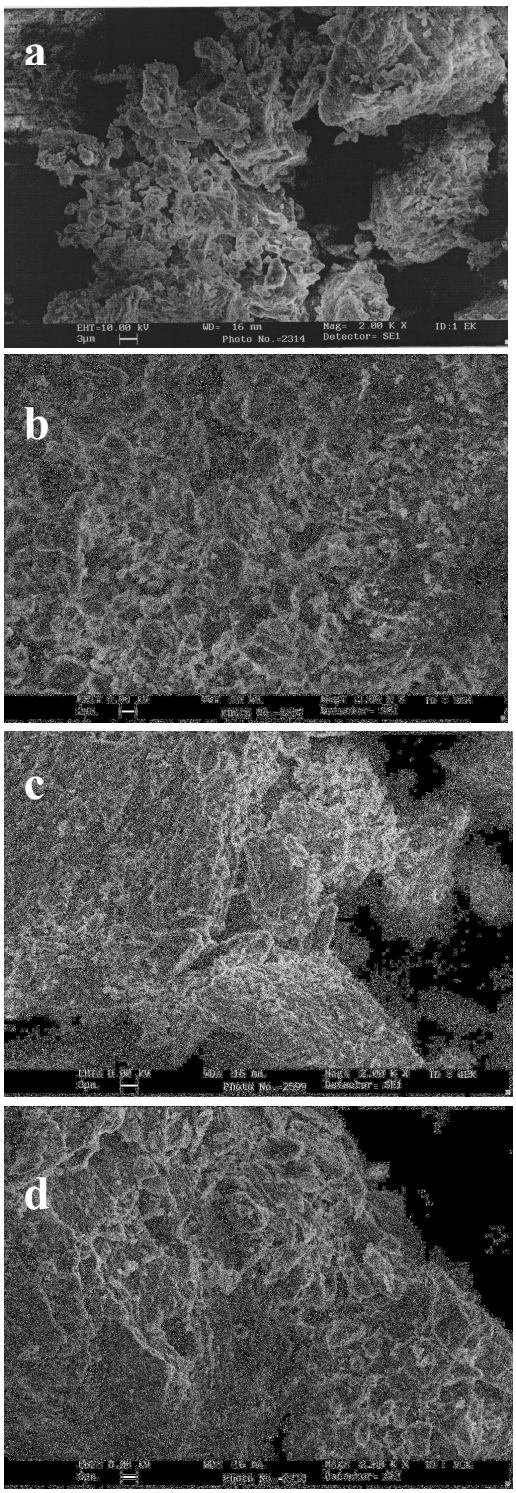

Fig.1 SEM Morphology of rat bone hydroxyapatite for the age of **a,** 1 month **b**, 2 month **c**, 4 month and **d**, 7 month

F. Ibrahim, N.A. Abu Osman, J. Usman and N.A. Kadri (Eds.): Biomed 06, IFMBE Proceedings 15, pp. 118-121, 2007
www.springerlink.com ' Springer-Verlag Berlin Heidelberg 2007

SEM micrograph of rat bone apatite has also shown that bone apatite crystal is a nano sized material. This result was emphasized by crystal size obtained from XRD analyses. The crystal size ranged from 14,70 - 24,49 nm (Table 1). It is an interesting phenomenon that there is a nonlinearity in the crystal size of bone apatite. The crystal size increase in the early age and then decrease in the 7th month. Of the three stages of apatite crystalization, there is an Ostwald ripening stage. In this stage, the small sized crystals will be dissoluted into free ions and then be deposited again in the epitaxial. This redeposition leads to higher size of apatite crystal. If there was a linear correlation between crystal sizes and ages, the highest crystal would be belong to the 7th months old rat.

Table 1 Crystal size of rat bone hydroxyapatite

Age (Month)	2θ (°)	β (mrad)	Crystal Size (nm)
1	25,568	9,430	14,70
2	25,839	5,734	24,18
4	25,839	5,661	24,49
7	25,595	8,185	16,94

Bone classifies into a living tissue due its cellular contents. Bone cells, via osteoclast, remove old bones and replace it with the new one. The active metabolism makes nonlinearity in bone apatite s size. As a living tissue, bone is governed by the hormonal signal. In the younger, the hormone apparantly signals the bone to absorb more minerals due to bone growth. After bone growth maximum, there is possibility of estrogen deficiency to play a role that will cause reduction in osteoblast ability to form matrix for minerals apatite deposition[14]. This disability governs the small crystal size of old rat bone.

Table 2 Crystal size of rat bone hydroxyapatite

Age (Month)	Crystalinity (%)
1	74
2	75
4	65
7	66

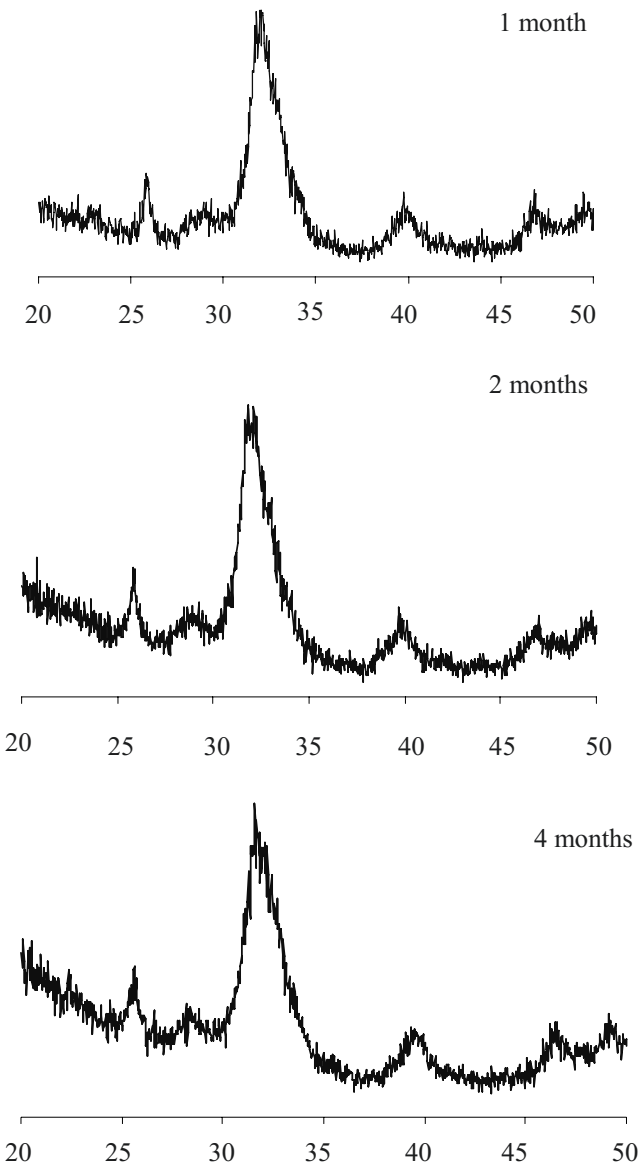

Fig. 2 XRD Profile of Rat Bone Hydroxyapatite

SEM micropgraph support the statement that crystal size of rat bone apatite was very small. Although there was a crystaline since the first month, SEM micrograph did not show crystaline grain clearly. There was another phase, which is an amorphous, existence with the bone apatite morphology. An amorphous calcium phosphate particles have a size in range of 200 2000 . The obtained crystal sizes were among this range, therefore the micrograph couldn t differentiate between amorphous and crystalline phase. However, the decline of XRD profile in the range of 20°-25° indicates the presence of amorphous phase[15]. Through metabolism activity, the highest

F. Ibrahim, N.A. Abu Osman, J. Usman and N.A. Kadri (Eds.): Biomed 06, IFMBE Proceedings 15, pp. 118-121, 2007
www.springerlink.com ' Springer-Verlag Berlin Heidelberg 2007

crystallinity was obtained in the early age. High crystalinity of apatite show lower biodegradation[16]. As a calcium reservoir, if it is needed, bone should be able to supply the calcium inside the body. Younger rat is able to gain enough calcium from food supply. As the increase of the age, disability to absorb calcium from food supply, will cause calcium demands will be provided by bone s calcium. Lower crystalinity in the older support this function.

Compared to commercially hydroxyapatite, natural bone is different, there is a bit difference between it and the natural one. If synthetics hydroxyapatite is well crystallized, while bone minerals is a mixture of amorphous and crystalin phase. The small size and low crystalinity of bone minerals supports bone function as calcium reservoir.

V. Conclusions

We studied bone apatite from rat femur bone. Bone apatite composes two phase, amorphous and crystalline. Higher crystalinity was obtained in the early age. Research on nanostructure in bone material is important in understanding biodegradation of bone hydroxyapatite and in the design a comercially hydroxyapatite

References

[1] JONATHAN, B, GARTH H. (1998): Handbook of biomaterial properties , (Chapman and Hall, USA)

[2] CARVALO G.V, GUARINO A, GONZALES G. (2004): Mineralization of hydroxyapatite over collagen type I , *European Cell and Materials*,**7**, pp. 58-9

[3] BIGI A, GANDOLFI M, KOCH MHJ, and ROVERI N. (1996): X-ray Diffraction study of in vitro calcification of tendon collagen . *Biomaterials*,**17**, pp. 1195-1201

[4] WALSH WR, GUZELSU N. (1994): Compressive properties of cortical bone: mineral-organic interfacial bonding . *Biomaterials,***15**, pp. 137-9

[5] BIGI A, GANDOLFI M, ROVERI N, and VALDRE G. (1997): In vitro calcified tendon collagen:an atomic force and scanning electron microscopy investigation. *Biomaterials,***18**, pp. 657-65

[6] NANCOLLAS GH. (1982): Biological mineralization and demineralization , Proc. Dahlem Konferenze, Berlin, 1982

[7] SCHNETTLER R, STAHL JP, ALT V, PAVLIDIS T, DINGELDEIN E, and WENISH S. (2004): Calcium phosphate-based bone substitutes . *European Journal of Trauma*, **4**, pp. 219-29

[8] KIESWETTER K, BAUER TW, BROWN SA, VAN LENTE F, and MERRITT K. (1994): Characterization of calcium phosphate powders by ESCA and EDXA . *Biomaterials*, **15**, pp. 183-8

[9] BIGI A, FORESTI E, GREGORINI E, RIPAMONTI A, ROVERI N, and SHAH JS. (1992): The role of magnesium on the structure of biological apatites . *Calc.Tiss.Int*, **50**: pp. 439-44

[10] AOKI H. (1991): Science and medical application of hydroxyapatite , (JAAS, Tokyo)

[11] AHMIARTI S, SOEJOKO DS. (2002): Pengaruh ion karbonat dalam proses presipitasi senyawa kalsium fosfat . *Makara Seri Sains*, **6**, pp. 55-8

[12] HANSOS B. 150.000.000:1 model of hydroxyapatite: http://www.stolaf.edu./

[13] CALDERIN L, SCOTT MJ, RUBIO A. (2003): Electronic and crystallographic structure of apatites . *Phys. Rev. B*, **67**, pp. 1341061-7

[14] FREY GD, YETSER MV. (1991): Why, when, and how to measure bone mass: a guide for the beginning user-expanding the role of medical physics in nuclear medicine . *AAPM Med. Monograph*, **18**, pp. 254-6

[15] DANILCHENKO SN, MOSEKE C, SUKHODUB LF, SULKIO-CLEFF B. (2004): X-ray diffraction studies of bone apatite under acid demineralizatin . *Cryst. Res. Technol*, **39**, 71-7

[16] CHEN J, WOLKE JGC, and DE GROOT K. (1994): Microstructure and crystallinity in hydroxyapatite coatings . *Biomaterials*, **15**, pp 396-8

Address of the corresponding author:

Author: Y.W. Sari
Institute: Department of Physics, University of Indonesia
City: Depok
Country: Indonesia

F. Ibrahim, N.A. Abu Osman, J. Usman and N.A. Kadri (Eds.): Biomed 06, IFMBE Proceedings 15, pp. 118-121, 2007
www.springerlink.com ' Springer-Verlag Berlin Heidelberg 2007

PCL Electrospun Sheet-Embedded Microporous PLGA Membrane For Effective Guided Bone Regeneration

W.J. Cho[1], J.H. Kim[1], S.H. Oh[1], H.H. Nam[2], J.M. Kim[2] and J.H. Lee[1]

[1]Department of Advanced Materials, Hannam University, Daejeon 306-791, Korea
[2]Department of Pathology, Chungnam National University Hospital, Daejeon 301-131, Korea

Abstract— **Bone healing is one of the importance phenomena in various clinical fields. The rapid appearance of fibrous connective tissue in bone defect during the healing, which can lead to the incomplete bone formation, has been considered as a major problem. To solve this, guided bone regeneration (GBR) membranes which can prevent fibrous connective tissue infiltration and thus promote bone healing have been used as a simple therapy. In this study, we fabricated a novel GBR membrane by the immersion precipitation of PCL/Tween 80 electrospun sheet filled with PLGA/Pluronic F127 solution. The top surface of prepared membrane had nano-size pores (~100 nm) which can effectively prevent from fibrous connective tissue invasion but permeate nutrients, while the bottom surface had micro-size pores (~ 40 μm) which can improve adhesiveness with bone and provide osteoconductivity. The morphology, mechanical (tensile and suturing) strengths and model nutrient permeability of the prepared membrane and its bone regeneration behavior using a rat model (skull bone defect) were compared with those of PLGA/F127 membrane, PCL/Tween 80 electrospun sheet, and a commercialized GBR membrane, Bio-Gide®. From the result, the PCL electrospun sheet-embedded PLGA membrane (hybrid membrane) seems to be a good candidate as a GBR membrane for the effective permeation of nutrients and osteoconductivtity as well as the good mechanical strength to maintain a secluded space for the bone regeneration.**

Keywords— **Guide bone regeneration membrane, poly(glycolic-co-lactic acid), polycaprolactone, electrospun nanofiber, selective permeability**

I. Introduction

Guided bone regeneration (GBR) method is a well established therapy to repair mandible and alveolar bone defects infected by periodontal diseases. The principle of GBR method is to prevent an invasion of non-functional scar tissues. GBR membranes also have an important function which encourages bone growth. GBR membranes as physical barriers create a space around the defect, prevent fibrous connective tissue invasion into the defect space, and thus can promote bone healing. Until now, various materials, including non-degradable expanded-polytetrafluoroethylene (ePTFE: Gore-Tex) [1] and degradable polylactic acid (Guidor) [2] and Collagen I/III (Bio-Gide) [3], have been used as GBR membranes. Although non-degradable ePTFE membrane has achieved excellent clinical results, second surgery is required to remove the membrane after new bone generation. On the other hand, degradable GBR membranes have a benefit to avoid second surgery which lightens the burden of patients. However, there are still challenges with respect to (1) barrier of tissue invasion associated with rapid degradation of membranes, (2) selective permeability to prevent fibrous connective tissue invasion but allow nutrient and oxygen supplies and (3) mechanical stability of membrane to sustain surgery treatment. The fast degradation and poor mechanical strength of natural polymers, and low permeability caused by hydrophobicity and brittleness of biodegradable synthetic polymers are also considered as critical problems for clinical applications [4].

In this study, we prepared a novel GBR membrane with selective permeability and good mechanical stability using the immersion precipitation of poly(glycolic-co-lactic acid) (PLGA)/Pluronic F127 solution embedded with polycaprolactone (PCL)/Tween 80 electrospun sheet (called PCL/PLGA hybrid membrane). The morphology, mechanical (tensile and suturing) strengths, model nutrient permeability and bone regeneration behavior of the prepared membrane were compared with those of PLGA/F127 (5 wt%) membrane (called PLGA membrane), PCL/Tween 80 (3 wt%) electrospun sheet (called PCL electrospun sheet), and a commercialized GBR membrane, Bio-Gide .

II. Materials and method

A. Materials

PCL (Mw, 80,000; degradation time, ~ 24 month) and PLGA (lactic to glycolic acid mol ratio, 85:15; Mw, 123,000; degradation time, ~ 10 month) were purchased from Aldrich (USA) and Alkermes (USA), respectively. Tween 80 and Pluronic F127 were used as a hydrophilic additives to PCL (3wt% addition, PCL base) and PLGA (5wt% addition, PLGA base), respectively. Commercialized GBR membrane, Bio-Gide was purchased from Geistlich Pharma AG (Switzerland).

F. Ibrahim, N.A. Abu Osman, J. Usman and N.A. Kadri (Eds.): Biomed 06, IFMBE Proceedings 15, pp. 122-125, 2007
www.springerlink.com ' Springer-Verlag Berlin Heidelberg 2007

B. Fabrication of GBR membranes

For prepare electrospun sheet, PCL was dissolved in a mixed solvent (MC/DMF, 85/15 (v/v); 10 wt%) and then Tween 80 was added in the PCL solution with 3 wt%. The solution was placed in a syringe whose needle inner diameter size is 21gauge. Using a high voltage supply (CPS-60 K02v1, Chungpa EMT, Co., Korea), 15 kV voltage was applied to the needle tip at room temperature. Electrically charged polymer solution formed Taylor cone from the tip of the needle to the ground collector plate with a fixed distance 100 mm. During this traveling, solvent is evaporated in the air and randomly oriented nano-fibrous mesh was finally fabricated on the collector plate. The fabricated samples were vacuum-dried overnight at room temperature. The prepared PCL electrospun sheet was placed on a mold (50 mm x 50 mm x 0.4 mm) and then PLGA/F127 solution (in tetraglycol, 10 wt%) was filled into a mold and immersed into water for 1 hr at room temperature. The hybrid membrane was produced after washing the solidified PLGA/F127 mixture in excess water to remove residual tetraglycol and the following vacuum drying. Characteristics of the prepared PCL/PLGA hybrid membrane were compared with PLGA membrane, PCL electrospun sheet and a commercial membrane (Bio-Gide).

C. Characterization of GBR membranes

Morphology Observation: Surface and cross-section morphologies of the GBR membranes were observed by a scanning electron microscope (SEM; S-3000N, Hitachi, Japan). The average pore sizes of the membrane surfaces were measured using an image analysis program (*i*-solution, IMT, Korea).

Measurement of Mechanical Properties: For the measurement of tensile strength, the specimens (width, 10 mm; length, 25 mm) were attached in an ultimate tensile test machine (AG-5000G, Shimadzu, Japan) equipped with a 50 kg_f load cell and was pulled at a crosshead speed of 10 mm/min. The stress-strain curves were obtained from the specimens. For the measurement of suture strength, a 5-0 nylon suture was passed through the specimens (width, 10 mm; length, 20 mm), 2 mm from the top edge. A knot was made to produce a loop for the attachment to the hold of the tensile test machine. The specimen was pulled like a tensile strength measurement. The ultimate strength at the time of pullout of the suture was recorded. All samples (tensile and suture) were prepared in dry and wet (soaking in saline solution) condition.

Permeability Experiment: The fluorescein isothocyanate-bovine serum albumin (FITC BSA, Sigma) was chosen as a model nutrient. The permeability experiment was performed using side-by-side diffusion cells with a 3 ml volume in each compartment. The GBR membranes clamped between the cell-halves. The donor chamber was filled with 3 ml of FITC-BSA solution (1 mg/ml in PBS, pH ~7.4), while the receptor chamber was filled with PBS. The diffusion cells in triplicate were incubated at 37 ^{o}C for 12 hrs and continuously agitated with magnetic stirrers. At predetermined time intervals, the whole PBS in the receptor cell was collected and replaced with a fresh one. The amount of permeated FITC-BSA was determined by a fluorescence spectrophotometer (RF-5301 PC, Shimadzu, Japan).

D. Preliminary animal study

Sprague-Dawley (SD) rats were chosen as the animal model to evaluate the bone regeneration behavior of the membranes. After exposure of the parietal calvaria, a full-thickness skull defect was made by using an 8-mm trephine hand instrument (Leibinger, Germany). Subsequently, the defect was covered with the membrane (12 x 12 mm in size) with the micro-pore side of the membrane facing the bone defect. After the application of the membrane, the periosteum was closed over the membrane. The blank (without membrane) was also examined as a control group. At predetermined periods (1, 2 and 4 months) after surgery, euthanasia was performed with an overdose of pentobarbital sodium. For histological study, the defects with surrounding cranial tissues were removed. The specimens were fixed with 4 % formaldehyde in PBS and decalcified in 10 % formic acid. After dehydration in a graded series of alcohol, the specimens were embedded in paraffin wax and cut into 5 μm transverse sections in the center of the bony defects. These sections were stained with hematoxyline and eosin (H & E) for the observation by light microscopy (Model BX50F4, Olympus, Japan).

III. Result and discussion

A. Morphology observations

Fig. 1 shows the SEM photographs showing the morphologies of GBR membranes. Bio-Gide is a bilayer membrane consisting of porcine collagen type I and III [3]. The bilayer structure of Bio-Gide show a compact, dense top surface (~300 nm pore size) and the porous bottom surface (~5 μm pore size). PCL electrospun sheet had very compact structure with micro-size pores of ~3 μm on top surface and ~2 μm on bottom surface. PLGA membrane showed an asymmetric column-shape porous structure having nano-size pores (~50 nm) on top surface and micro-size pores (~40 μm) on bottom surface. The morphology of PCL/PLGA hybrid membrane was similar to that of PLGA membrane

F. Ibrahim, N.A. Abu Osman, J. Usman and N.A. Kadri (Eds.): Biomed 06, IFMBE Proceedings 15, pp. 122-125, 2007
www.springerlink.com ' Springer-Verlag Berlin Heidelberg 2007

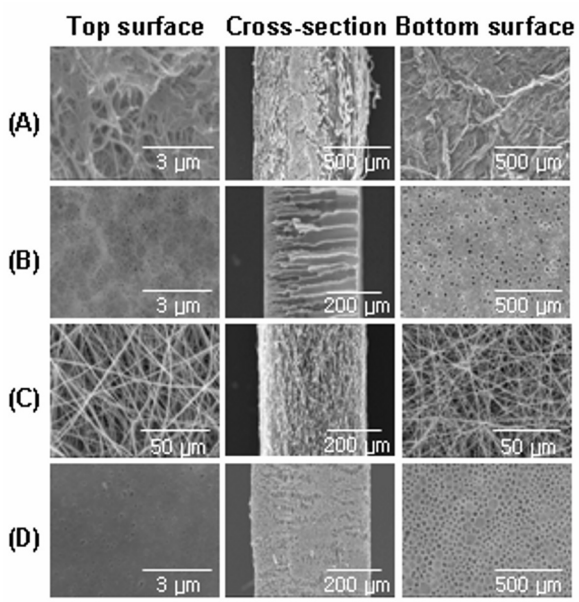

Fig. 1. SEM photographs showing the morphologies of top, cross-section, and bottom surfaces of (A) Bio-Gide , (B) PLGA membrane, (C) PCL electrospun sheet, and (D) PCL/PLGA hybrid membrane.

for both top and bottom surfaces. The smaller pores of top surface are formed by the precipitation of the polymer through a higher initial polymer concentration at the contact side and the delay of water diffusion into PLGA/F127 solution at the initial contact of water, while the larger pores of sublayer are formed by the precipitation of the polymer having much lower polymer concentration compared to the contact side.

B. Mechanical property

The mechanical strengths of the PCL/PLGA hybrid membrane were better (for tensile strength) than or similar (for suturing strength) to the Bio-Gide in wet condition (Fig. 2). Excellent mechanical strengths of the PCL/PLGA hybrid membrane compared to others are probably owing to the hybrid of PCL electrospun nanofabric property (toughness) and PLGA property (brittleness). Bio-Gide showed significantly different mechanical strengths between dry and wet conditions, probably owing to the swelling of collagen in wet condition, leading to weak mechanical strengths.

C. Permeability behavior

The permeability through the membrane is important for the supply of nutrients and oxygen which are essential factors for bone regeneration. The cumulative permeation profiles of FITC-BSA through the membranes was observed in

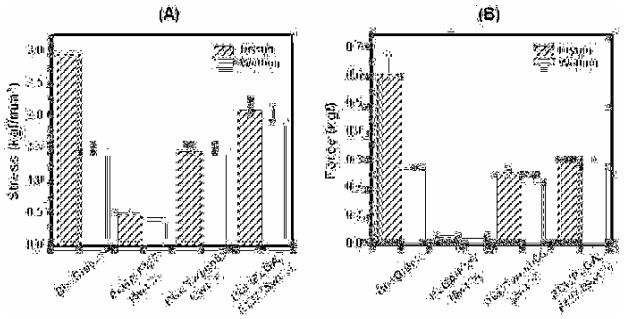

Fig. 2. Mechnical properties of GBR membranes. (A) Tensile strength and (B) suture strength.

the order of PCL/PLGA hybrid membrane > PCL electrospun sheet > Bio-Gide > PLGA membrane, regardless of permeation directions (top surface into bottom or bottom surface into top) (Fig. 3). Although the amount of permeated BSA was different each other, all the membranes permeated the BSA continuously over time. This continuous permeation of nutrient may be very helpful for bone regeneration. From the result, it was recognized that all the membranes can permeate growth factors, bone morphogenetic proteins and nutrients, etc, but prevent fibrous connective tissue invasion.

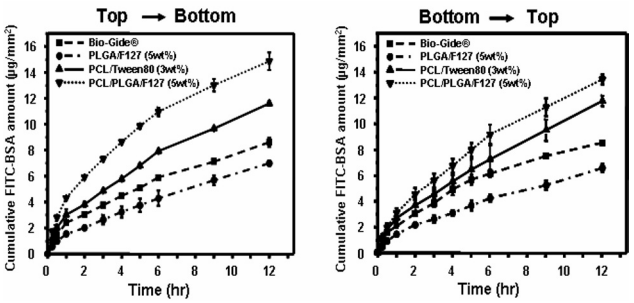

Fig. 3. Cumulative FITC-BSA permeation profiles through GBR membranes (n=3).

D. Bone regeneration behavior

A SD rat model was used to investigate the bone regeneration behavior of the membranes. Eight mm diameter, which is a critical size defect of rat [4], was created for each animal and the defect was covered with the membranes. Fig. 4 shows bone regeneration behavior in the defect covered by the membranes with time. In the blank control group (without membrane), the fibrous connective tissues were rapidly filled into the bone defect and thus the new bone formation was inhibited, as expected. However, in the membrane groups, the new bone was continuously grown from the margin to center of the defect with time. Particularly, the PCL/PLGA hybrid membrane showed fastest bone regen-

F. Ibrahim, N.A. Abu Osman, J. Usman and N.A. Kadri (Eds.): Biomed 06, IFMBE Proceedings 15, pp. 122-125, 2007
www.springerlink.com ' Springer-Verlag Berlin Heidelberg 2007

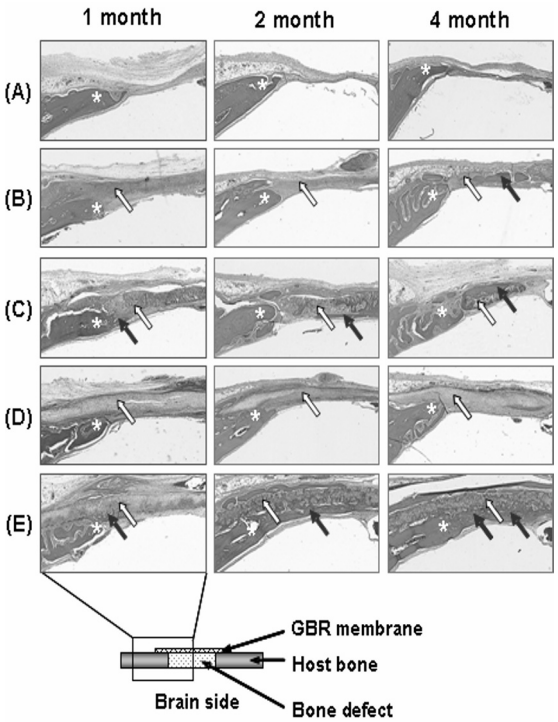

Fig. 4. Histological sections of bone defect and surrounding cranial tissue covered without membrane (blank control) (A), covered with Bio-Gide membrane (B), PLGA membrane (C), PCL elctrospun sheet (D) and PCL/PLGA hybrid membrane with different periods. (*, host bone; white arrow, GBR membrane; black arrow, new bone; H&E staining, x 40).

eration than other membrane groups, probably owing to the osteoconductivity provided by extended inner spacing of PCL electrospun sheet layer by the swelling of PLGA matrix when it is degraded. Also, slow degradation of PCL electrospun sheet provides bone regeneration space for a long time in the contrast with the PLGA membrane. On the other hand, the PCL electrospun sheet and Bio-Gide showed slow bone regeneration due to their compact structure. The GBR membrane can function as a scaffold which can improve osteoconductivity. The bone growth along the porous substrate which can permits attachment of osteogenic cells was already reported by some research groups [5]. From the results of this study, it can be concluded that the PCL/PLGA hybrid membrane can be a good candidate as a GBR membrane for the selective permeability, sufficient mechanical strengths as well as osteoconductivity.

Acknowledgment

This work was supported by a grant from the Korea Research Foundation (Grant No. KRF-2004-202-D00768).

References

1. Piattelli A, Scarano A, Paolantoni M (1996) Bone formation inside the material interstices of e-PTFE membranes: a light microscopical and histochemical study in man. Biomaterials 17:1725-1731
2. Imbronito AV, Todescan JH et al. (2002) Healing of alveolar bone in resorbable and non-resorbable membrane-protected defects. A histologic pilot study in dogs. Biomaterials 23:4079-4086
3. Hillmanan G, Steinkamp-Zucht A, Geursen W et al. (2002) Culture of primary human gingival fibroblasts on biodegradable membranes. Biomaterials 23:1461-1469
4. Maeda H, Kasuga T et al. (2006) Preparation of poly(L-lactic acid)-polysiloxane-calcium carbonate hybrid membranes for guided bone regeneration. Biomaterials 27:1216-1222
5. Kellomäki M, Niiranen H, Puumanen K et al.(2000) Bioabsorbable scaffolds for guided bone regeneration and generation. Biomaterials 21:2495-250

Address of the corresponding author:

Author: Jin Ho Lee
Institute: Department of Advanced Materials, Hannam University
Street: 133 Ojeong Dong, Daedeog Gu
City: Daejeon 306-791
Country: Korea
Email: jhlee@hannam.ac.kr

F. Ibrahim, N.A. Abu Osman, J. Usman and N.A. Kadri (Eds.): Biomed 06, IFMBE Proceedings 15, pp. 122-125, 2007
www.springerlink.com ' Springer-Verlag Berlin Heidelberg 2007

Physicochemical Properties and Biological Response of Titanium Surface Modified by Anodic Spark Deposition for Dental Implants

L. Sarinnaphakorn[1], P. Mesquida[2], C. Giordano[3], E. Sandrini[3], R. Chiesa[3], A. Cigada[3], M. Fenlon[1], and L. Di Silvio[1]

[1] King s College London Dental Institute, Biomaterials and Biomimetics Group, London, UK
[2] King s College London, Material Group, Department of Mechanical Engineering, London, UK
[3] Giulio Natta, Politecnico di Milan, Department of Chemistry, Materials and Chemical Engineering, Milan, Italy

Abstract—**Surface modifications play a significant role in the interaction and success of implants to adjacent tissues. This study evaluated the surface topography and in vitro cellular response of surface treatments on titanium performed by multiphase anodic spark deposition (ASD). The titanium surfaces examined were: BioSpark (BS) and OsseoSpark (OS), obtained by ASD method; BioRough™ (BR), a chemical etching treatment used for comparison; and commercially-pure grade-2 titanium (cpTi) used as a control. The samples were cut in discs (12 mm diameter; 0.5 mm thickness) and sterilised by γ-irradiation prior to use. All samples were imaged using Scanning Electron Microscopy (SEM) (Hitachi S-3500N, Hitachi High-Technologies) to characterise the surface in 2 dimensions. Atomic Force Microscopy (AFM) (Topometrix Explorer SPM, Veeco Metrology LLC, CA, USA) was performed in contact mode to investigate topography in 3 dimensions and qualitatively analyse the surface roughness. Physicochemical analysis was also performed using energy dispersive X-ray spectroscopy (EDS) (Oxford Instruments Microanalysis, UK). A human osteosarcoma cell line (HOS TE85) was used for in vitro analysis; MTT assay to determine cell metabolic activity and Alamar Blue™ (Serotec) for assessing cell proliferation. SEM images indicated that ASD treatment created a microrough surface with a web-like nanostructure. AFM images illustrated the 3-dimensional topographies and quantitatively analysed surface roughness by ranging from the roughest to the smoothest which were Br > OS > BS > cpTi, respectively. Cellular response results showed no toxic leachables released from the test samples, thus indicating all sample were biocompatible. A good level of cell proliferation compared to the control was observed indicating a favourable attachment surface. This study has indicated that the ASD treatment surface has a nanostructure topography favouring cell attachment and proliferation and can potentially be used to improve titanium performance by enhancing osseointegration for use in dental implantology.**

Keywords—**surface modification, surface roughness, titanium implant, osseointegration, anodic spark deposition**

I. Introduction

Surface modifications play a significant role in the interaction and success of implants to the adjacent tissues. Current research has focused on the effect of different chemical and electrochemical treatments on the bioactivity of titanium [1]. Thus, the aim of this study was to evaluate the surface roughness characteristic and *in vitro* cellular response of two surface treatments on c.p. titanium, performed by multiphase anodic spark deposition (ASD). The treatments aim to obtain a thickened titanium oxide layer doped with calcium (Ca) and phosphorus (P), known to potentially enhance osseointegration properties of titanium implants [2]. A commercially available surface treatment named BioRough was chosen for comparison.

II. Materials and Methods

A. Sample preparation

Four different titanium surfaces were used in this study: BioSpark (BS), and OsseoSpark (OS), obtained by ASD method [3]; BioRough (BR), chemically etched titanium surfaces; and commercially-pure grade-2 titanium (cpTi) used as a control. All samples except cpTi (Loterious SpA, Italy) were made and supplied by Nanosurfaces s.r.l., Italy. The samples were supplied as discs (12 mm diameter; 0.5 mm thickness) and sterilised by γ-irradiation prior to use.

B. Surface characterisation

All samples were imaged using Scanning Electron Microscopy (SEM) (Hitachi S-3500N, Hitachi High-Technologies) at an accelerating voltage of 15 kV to obtain the surface topography in 2 dimensions. Physicochemical property analysis of each surface was performed by energy dispersive X-ray spectroscopy (EDS) using the Oxford Instruments X-ray Analysis Inca System (Oxford Instruments Microanalysis, UK). Furthermore, Atomic Force Microscopy (AFM) (Topometrix Explorer SPM, Veeco Metrology LLC, CA, USA) was performed in contact mode on each surface, to investigate surface topography in 3-dimension and quantitatively analyse the surface roughness.

F. Ibrahim, N.A. Abu Osman, J. Usman and N.A. Kadri (Eds.): Biomed 06, IFMBE Proceedings 15, pp. 126-129, 2007
www.springerlink.com ' Springer-Verlag Berlin Heidelberg 2007

C. *In vitro cellular response*

A human osteosarcoma cell line (HOS TE85) was used for the *in vitro* cellular response. Elutions were obtained by placing each test sample (n=3) in Dulbecco's Modified Eagle Medium (DMEM) and left on a rotating mixer for 24 and 72 hours. 96 well-plates were seeded with $1.5x10^4$ cells/well and cells were allowed to adhere for 24 hours at 37˚C with 5% CO_2. Cellular viability was then assessed using the MTT assay and exposing cells to the collected elutions at 24, 48, and 72 hours. The Alamar Blue™ (Serotec) assay was performed for assessing cell proliferation. Cells were seeded at a density $1x10^5$ cell/ml directly onto the test discs (n= 3 replicates) in 24 well plates and incubated at 37˚C with 5% CO_2 for six time points; 1, 3, 7, 14, 21 and 28 days, using Thermanox® (NY, USA), as a negative (non-toxic) control and polyvinylcholride (PVC) as a positive (toxic) control.

III. Results

A. *Surface characterisation*

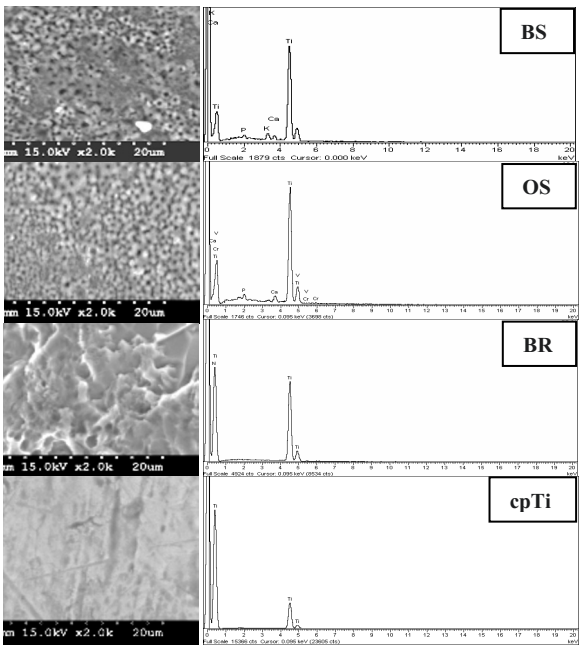

Fig. 1**: SEM images and EDS results**

SEM images on the right column show EDS analysis on the left column of BS, OS, BR, and cpTi, consecutively. BS and OS surfaces were similar with micropore texture roughness, while BR surface showed irregularity roughness with gen eralised sharp edge, the typical acid etched surface. Contrast to the previous described surfaces, cpTi surface was relatively smoother with some scratches and crack appearances. EDS diagrams revealed Ca and P peaks on both BS and OS surfaces rather than Ti peaks, while both BR and cpTi surfaces composed of pure Ti peaks.

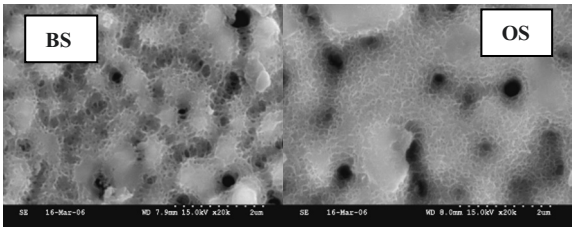

Fig. 2: **SEM of BS and OS at higher magnification**

SEM at a higher magnification (X20 k, and 2 μm measurement bar) showed web-like structure on both BS and OS surface. The web-like micro-structure with honeycomb appearance in BS was much smaller (<50%) and had a more open-network structure than the OS structure.

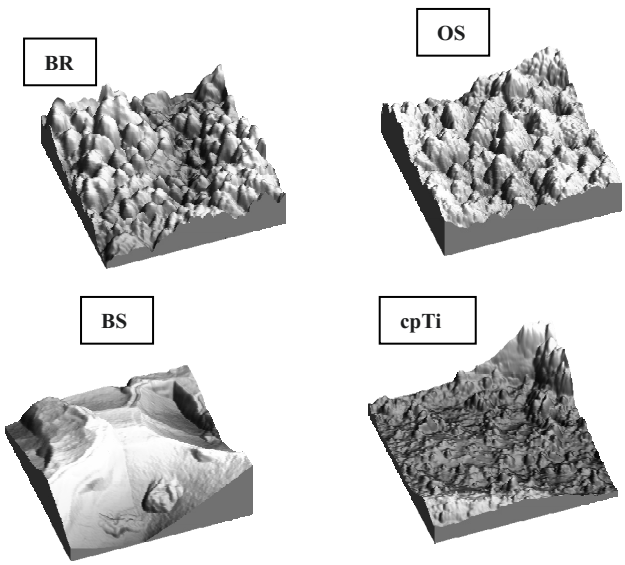

Fig. 3: **AFM images**

AFM images (10 μm x 10 μm) of each surfaces showed different topographies in 3 dimensions. The topographic images between BS and OS were similar as also previously indicated by SEM images. Each surface roughness in both 1-d roughness (Ra) and 2-d roughness (Sa) was analysed and shown in Table 1 as followed.

F. Ibrahim, N.A. Abu Osman, J. Usman and N.A. Kadri (Eds.): Biomed 06, IFMBE Proceedings 15, pp. 126-129, 2007
www.springerlink.com © Springer-Verlag Berlin Heidelberg 2007

Table 1: Surface roughness analysis

Surfaces	1-d roughness Ra (nm)	2-d roughness Sa (nm)
BS	**140±14**	**190±20**
OS	**180±40**	**200±50**
BR	**470±180**	**530±130**
cpTi	**80±1**	**130±20**

B. In vitro cellular response

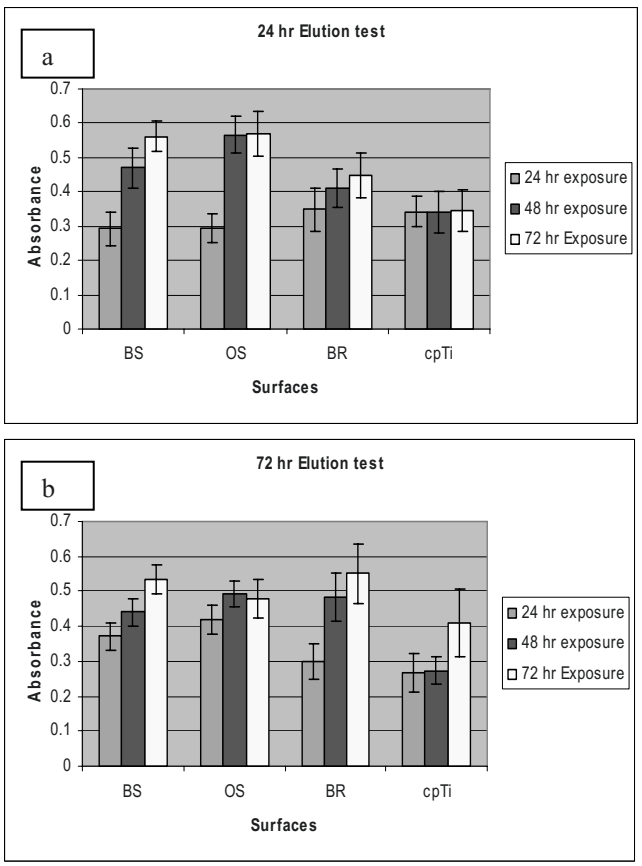

Fig. 4: **MTT assay at 24 hr (a) and 72 hr (b) elution test**

Elution study results showed an increase in metabolic activity of cells with exposure times on both 24hr and 72hr elution study, thus indicating no toxic effect on the cells. A low response of cellular activity was observed with cpTi.

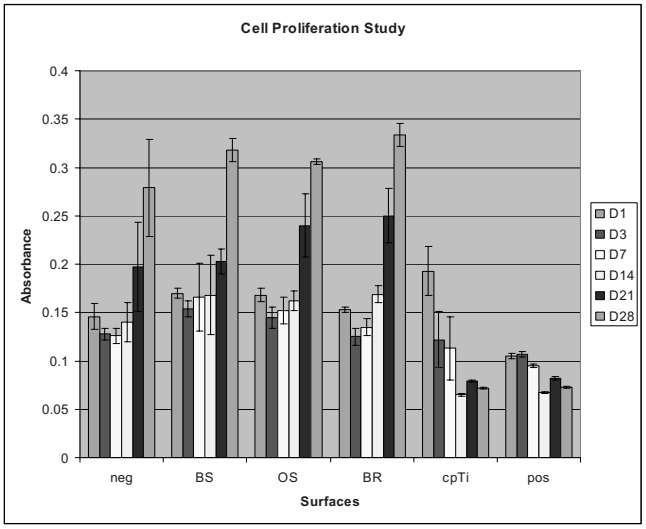

Fig. 5**: Alamar Blue™ assay**

Cell proliferation as indicated by Alamar Blue results showed a good proliferation on Day 1 (D1) for all test materials compared to the cell culture control. The cpTi has the highest proliferation, followed by the BS and OS. A slight drop in proliferation was observed on Day 3 (D3), but generally this was seen to increase again in BS, OS and BR test samples on Day 7 (D7) and D14 (D14), consecutively, except in cpTi showed continuous decrease of the absorbance which indicated slower cellular activity from the first day.

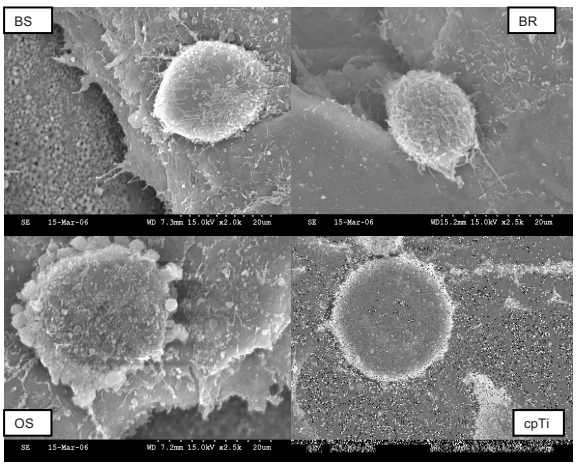

Fig. 6: **Cell adhesion and morphologic study**

SEM images showed HOS cells at Day 7 on BS, OS, BR, and cpTi surfaces. Cell layers on each surface were observed. The cells on all surfaces exhibited normal cellular

F. Ibrahim, N.A. Abu Osman, J. Usman and N.A. Kadri (Eds.): Biomed 06, IFMBE Proceedings 15, pp. 126-129, 2007
www.springerlink.com ' Springer-Verlag Berlin Heidelberg 2007

activity with filopodia attaching to the surfaces. Rounded cells were also observed, with filopodial extensions stretching on cell layers and in some cases, to the surface of the test materials. In the cpTi, fewer cellular processes were observed, and a less pronounced cell layer. It was noticed that on OS surface, cellular activity was enhanced, with vesicles observed in some rounded cells, indicating a high level of cellular activity.

IV. Discussion

The surface analysis results indicated that ASD treatment created a microrough surface with a micropore texture on both BS and OS, which was different compare to BR rough surface. AFM images illustrated the 3-dimensional topography of these rough surfaces and quantitatively analysed surface roughness by ranging from the most to the least roughness which were BR > OS > BS > cpTi, respectively. In addition, the higher magnification (x20 k) SEM images showed a web-like nanostructure with a honeycomb appearance on both BS and OS surfaces. An open-network structure was also observed on the BS surface, but not on the OS surface.

Surface characterisation and physicochemical property results from ASD treated surfaces indicated that the two ASD modified titanium surfaces evaluated had a microstructure topography enriched in Ca and P which enhanced cellular response and may potentially benefit osseointegration. The web-like microstructure with honeycomb appearance of both BS and OS surfaces, especially the open-network microstructure of BS may have a specific effect on protein adsorption and hence enhances cellular response.

No deterioration in cell viability was observed following incubation in elution extract, thus indicating that all samples were biocompatible. A good proliferation activity of cellular response *in vitro* was exhibited on the modified surface when compared to cpTi. This study has indicated that the BS and OS showed promising biological response *in vitro*. Further studies are ongoing to specifically probe favourably adsorbed proteins onto surfaces and to clarify the rate of cell adhesion, cell spreading, proliferation and also differentiation of cells on these modified surfaces.

V. Conclusions

The results have shown that the ASD modified titanium surfaces produced a nanostructure topography favouring cell attachment and proliferation. This study has indicated that the BS and OS surface treatments can potentially be used to improve titanium performance by enhancing osseointegration for use in dental implantology.

Acknowledgment

Research project is supported by King s College London Dental Institute, London, UK and the author is funded by Royal Thai Government Scholarships, Thailand.

References

1. Giordano C et al (2005) Physiological and biological characterisation of a novel multiphase anodic spark deposition coating to enhance implant osseointegration. J Mater Sci Mater Med. Dec;16(12):1221-9
2. Giordano C et al (2004) Titanium for osseointegration: comparison between a novel biomimetic treatment and commercially exploited surfaces. Journal of Applied Biomaterials and Biomechanics. 2: 35-44
3. Sandrini E et al (2005) *In vitro* assessment of the osseointegrative potential of a novel multiphase anodic spark deposition coating for orthopaedic and dental implants. J Biomed Mater Res partB: Appl Biomater 73B:392-399

Address of the corresponding author:

Lertrit Sarinnaphakorn
King s College London Dental Institute
Biomaterials and Biomimetics, Floor 17, Guy s Tower
St Thomas Street, SE1 9RT
London
UK
Email: lertrit.sarinnaphakorn@kcl.ac

F. Ibrahim, N.A. Abu Osman, J. Usman and N.A. Kadri (Eds.): Biomed 06, IFMBE Proceedings 15, pp. 126-129, 2007
www.springerlink.com ' Springer-Verlag Berlin Heidelberg 2007

Poly (lactic–co–glycolic acid) and hydroxyapatite composite films for cartilage reconstruction

J. B. Lee[1], C. W. Mun[1], H. H. Choi[1], J. C. Park[2], J. B. Choi[3] and J. K. Kim[1]

[1]Dept. of Biomedical Engineering, Inje University, Gimhae, Korea
[2]Dept. of Medical Engineering, College of Medicine, Yonsei University, Seoul, Korea
[3]Dept. Mechanical Systems Eng., Hansung University, Seoul, Korea

Abstract— **PLGA (75:25)/hydroxyapatite (HA) composite films were fabricated by solvent-casting method to investigate the effect of various hydroxyapatite content ratio to the PLGA for mechanical properties, cellular attachment and proliferation. Mechanical property of the composite film was characterized by tensile test. The ultimate tensile strength of 10 wt% HA content film was two-fold higher than control group. Surface of the film was characterized by contact angle measurement and scanning electron microscope (SEM). The PLGA/HA composites were more hydrophilic than control. Chondrocyte responses to the composite films were measured *in vitro* by cellular attachment and proliferation test. The attached and proliferated cells were significantly higher on PLGA/HA (10 wt%) composite film than control group (1.44 times higher in attachment test and 1.31 times higher for 6th-day at culture in proliferation assaying, p<0.05).**

Keywords— **Poly (lactic–co–glycolic acid) ; Hydroxyapatite; Composite; Chondrocyte**

I. Introduction

It is well known that articular cartilage has a limited regeneration capacity [1]. Hence, there are many studies about approaches to generate cartilage *in vivo/vitro* from cells and films/scaffolds [2]. The approach of cultivating cells in films/scaffolds for cartilage regeneration has been developed with different polymeric scaffolds for bone and cartilage [3]. Among the polymers, poly(lactic acid), poly(glycolic acid), poly(ε-caprolactone), and their copolymers have been attracted in wide attention for their biodegradability and biocompatibility. However, the mechanical strength, toughness and elastic modulus of these polymers were lower than those of natural bone and cartilage tissue. Thus, for improving mechanical properties, inorganic fillers were introduced into biodegradable polymers to fabricate filler/polymer composites. Hydroxyapatite (HA, $Ca_5(PO_4)_3OH$, Ca/P: 1.67) is used as a bone substitute, non-toxic, which can offer stability with host bone [4, 7]. In this manner, PLGA/HA composite is expected to offer improved biocompatibility from biological and mechanical view point [5-7]. Practically, regarding the PLGA/HA composites were reported mainly on mechanical properties and bone cells [2-7].

In this study, we fabricate PLGA (75:25)/hydroxyapatite composite films with various HA contents to investigate optimum HA ratio that is effective on cell attachment and proliferation for cartilage reconstruction as well as enhancement of mechanical properties.

II. Materials and methods

A. Preparation of PLGA and Hydroxyapatite composite

PLGA (M_w = 113kD) was purchased from lakeshore-biomaterials. (Brookwood Pharmaceuticals, Inc., U.S.A.) Hydroxyapatite powder was obtained from Sigma-Aldrich. (Sigma-Aldrich, Inc., U.S.A.) PLGA/HA composite films were fabricated by solvent-casting method. PLGA (with HA 5, 10 and 15 wt%) powder was dissolved in chloroform, the solution was cast into a mold. The solvent was evaporated overnight at ambient atmosphere, and vacuum freeze-dried during 48 hrs. PLGA film without HA were also fabricated by the solvent-casting, for control group.

B. Characterization of composite films

Static contact angle measurement of the PLGA/HA composite specimens was performed and characterized by contact angle analyzer (Phoenix 150).

Morphology study of the PLGA/HA composite film had done by the FE-SEM (HITACHI S-4300DSE., Japan) at 5 kV.

For mechanical property of the prepared specimens, tensile test were performed with a Micro-Load System (R & B INC. Korea). For tensile testing, the samples (15 × 10 mm) were cut from PLGA/HA films with 0.14 – 0.02 mm (n=5) thickness. Measurement was carried out at a cross-head speed of 2 mm/min with 5 kgf load [7]. The specimen was elongated until failure occurred. The elastic modulus was determined from the slopes in the initial elastic portion of the stress-strain diagram.

F. Ibrahim, N.A. Abu Osman, J. Usman and N.A. Kadri (Eds.): Biomed 06, IFMBE Proceedings 15, pp. 130-133, 2007
www.springerlink.com ' Springer-Verlag Berlin Heidelberg 2007

C. Chondrocyte isolation and culture

Full-thickness articular cartilage was obtained from the joint of porcine rear leg and chipped into small pieces at the size of 0.5 x 0.5 x 0.2 mm. Chondrocytes were isolated by trypsin treatment of cartilage for 10 min, followed by type II collagenase (GIBCO) (2 mg/ml) digestion for 8-12 hrs, and filtered through a nylon sieve (cell strainer, Falcon) with an 80 μm pore size. The cells were rinsed three times with Hank s balanced salt solution (HBSS) by centrifugation at 1000 rpm for 3 min. Then, cultured in cell culture flasks in a density of $2.0 \times 10^4/cm^2$ with Dulbecco s modified Eagle s medium (DMEM, Sigma) supplemented with 10 % FBS (GIBCO), 120 mg/L penicillin and 200 mg/L streptomycin, in a humidified incubator at 37 ℃ and 5 % CO_2. The medium was changed every 3 days.

D. Cellular attachment and proliferation

Cellular attachment and proliferation on PLGA/HA composite films at different time intervals were investigated. The films were cut (φ =12 mm) and placed into 24-well plates (Falcon), washed three times with PBS. The 2nd-passage chondrocytes were used for cell attachment test with 1.3×10^5 cells/film. The plates were incubated at 37 ℃ and 5 % CO_2 for 4hrs. After that, the medium was added by 1 ml for next another 4 hrs incubating. The attached cells on film were measured by Cell Counting Kit (CCK-8, Dogindo Lab, Kumamoto, Japan). After adding 10 μl CCK-8 solution to 24-well plate for 4hrs, the CCK-8 solution which reacted with cells on the film had changed in color from pink to orange. Hence, the absorbance of the solution was measured at 450 nm using a micro-plate reader (synergy HT, BIO-TEK).

For cell proliferation assaying, 1.3×10^4 (cells/film) initial cell density of the chondrocytes were cultivated in a humidified incubator containing 5 % CO_2 at 37 ℃. The proliferated cells were measured at 1st, 3rd and 6th days. The specimens of 6th-day harvest were fixed by addition of 1 ml of 3.0 % formaldehyde solution for cell distribution analysis. The cells were stained with hematoxylin and eosin (H&E) and observed by optical microscope (BX51, OLYMPUS).

E. Statistical analysis

The results were expressed as mean – standard error (S.E.) for all comparisons. The one-way analysis of variance (ANOVA) method was used to determine the significance of difference among multiple times. A difference was considered statistically significant at $p<0.05$.

III. Result and disscusion

A. Analysis of films

The contact angles of all PLGA/HA composite groups were more decreased than control group, as presented in Table 1. Therefore, the PLGA/HA composite made more hydrophilic surface of the film than PLGA film itself ($p < 0.05$), because HA was more hydrophilic material than PLGA substitute.

The SEM observation had been done in order to investigate the dispersion homogeneity of HA particles in the PLGA matrix. In the 15 wt% HA composite, there many clots colony were observed throughout the specimen (Fig. 1 (c)), and a fine fracture surface was detected in the HA clots (Fig. 1 (d)). On the other hand, for 5 and 10 wt% HA composite, no clots were found in the specimens (Fig. 1 (a), (b)). Moreover, it had shown that fine HA particles were spread throughout the 5 and 10 wt% HA composite. This meant that the mixed HA powders were dispersed on the film very evenly. It is expected to increase the chances of cells to make contact with HA, which was believed enhancing osteo-like cells to grow [4, 8].

The ultimate tensile strength and Young s modulus of HA content composites were given in Table 1. Compared with control group, PLGA/HA composite showed improved tensile strength and young s modulus at the particle content of 5 and 10 wt%. The HA particles were reinforced to the PLGA matrix successfully to produce composite film. On the other hand, the 15 wt% of HA composite showed high young s modulus, but significantly decreased in tensile strength. This may be caused by weak adhesion between the HA and the polymer interface (Fig. 1 (d)). The 5 and 10 wt% HA composite films offered mechanical stability for cell attachment and proliferation [5]. They are suitable for cartilage tissue regeneration in the mechanical property aspect among the groups.

B. Cell studies

The results of cell attachment and proliferation on PLGA and PLGA/HA films were shown in Fig. 2. Compared with each group, PLGA/HA (10 wt%) group showed 1.44 times more cells were attached on film than control. ($p<0.05$)

F. Ibrahim, N.A. Abu Osman, J. Usman and N.A. Kadri (Eds.): Biomed 06, IFMBE Proceedings 15, pp. 130-133, 2007
www.springerlink.com ' Springer-Verlag Berlin Heidelberg 2007

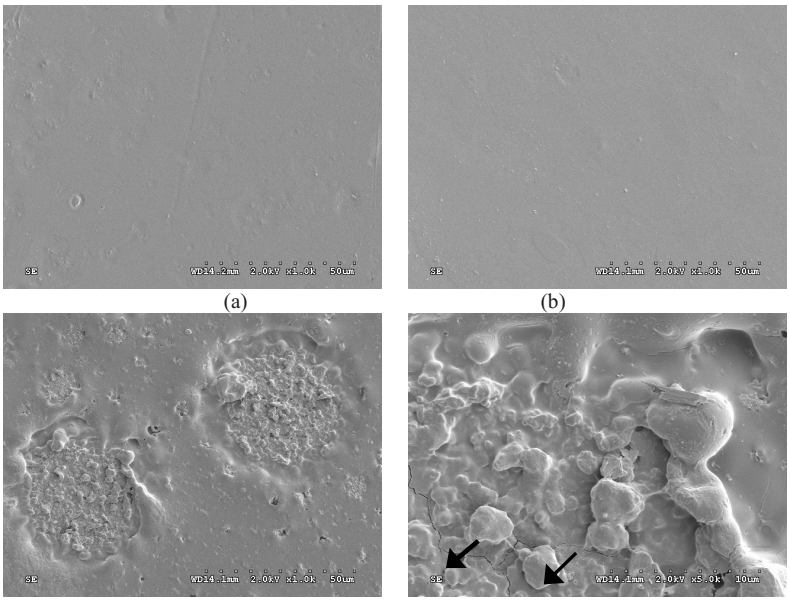

Fig. 1 SEM image PLGA/HA composite films (a) PLGA/HA5 wt%; (b) PLGA/HA10 wt%; PLGA/HA 15 wt% (c) x 1000 and (d) x 5000

For cell proliferation assaying, cell quantity of PLGA/HA (10 wt%) composite group showed 1.3 times higher than control group at 6th-day of culture. It showed significantly improved in the statistical analysis. ($p<0.05$) However, compared with 10 and 15 wt% HA composite group, there was no significant differences in statistics. Strangely, in the 5 wt% HA composite, less cells were proliferated than control at 6th-days. It is necessary to investigate about it.

The HA within the polymer matrix improving cell growth, beyond some amount of HA, as evidenced in the chondrocyte cell attachment and proliferation. However, beyond 10 wt% of HA particle content caused degradation and destruction of the film and seemed to give damage on attached and proliferated cells.

Table 1 Properties of PLGA/HA composites determined by contact angle and tensile tests (n=5)

	Contact angle	Ultimate tensile strength (MPa)	Young's modulus (MPa)
PLGA	68	1.89–0.4	3.09–0.30
PLGA/5%	61.75–4.06	3.4–0.3	7.2–0.28
PLGA/10%	58.125–2.1	3.9–0.37	10.4–0.62
PLGA/15%	56–1.51	1.77–0.1	8.5–0.53

C. Cell distribution

The H&E assayed chondrocytes through out the various composite films were demonstrated in Fig. 3. Compared with 10 and 15 wt% HA composites, there were no dramatic differences in the histological appearance of the chondrocytes-seeded composite films. But, the chondrocytes in the 15 wt% HA composite films were distributed unevenly throughout the specimens (Fig. 3 (d)). A homogeneous distribution of attached cells is important and necessary for the development of tissue engineering [9]. The 10 and 15 wt% HA composite films were effective in chondrocytes proliferation with an evenly distribution, in this study.

IV. Conclusions

The PLGA/HA composite material enhanced chondrocyte adhesion and proliferation *in vitro*. Also, the composite showed improved mechanical property as well as surface property of the film. The enhancement of cell attachment and proliferation may result from the exposed/embedded bioactive HA particles on PLGA film surface which were biocompatible and similar to the mineral phase of native bone tissue in chemical and structural point of view. Especially, 10 wt% HA composite film showed a maximum cell attachment and proliferation among the groups.

F. Ibrahim, N.A. Abu Osman, J. Usman and N.A. Kadri (Eds.): Biomed 06, IFMBE Proceedings 15, pp. 130-133, 2007
www.springerlink.com ' Springer-Verlag Berlin Heidelberg 2007

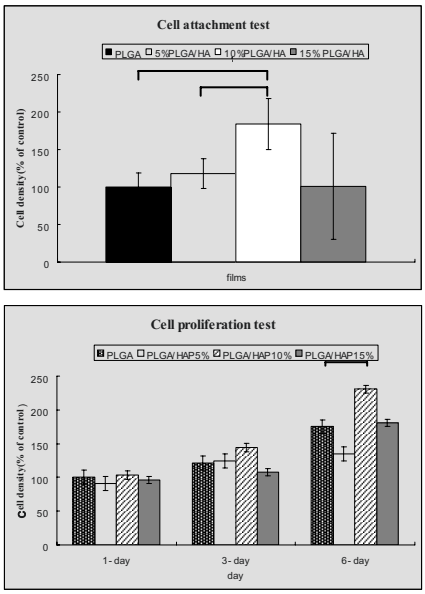

Fig. 2 Effect of hydroxyapatite on attachment (1.3x105 cells/film) and proliferation (1.3x104 cells/film) of chondrocytes (n=5)

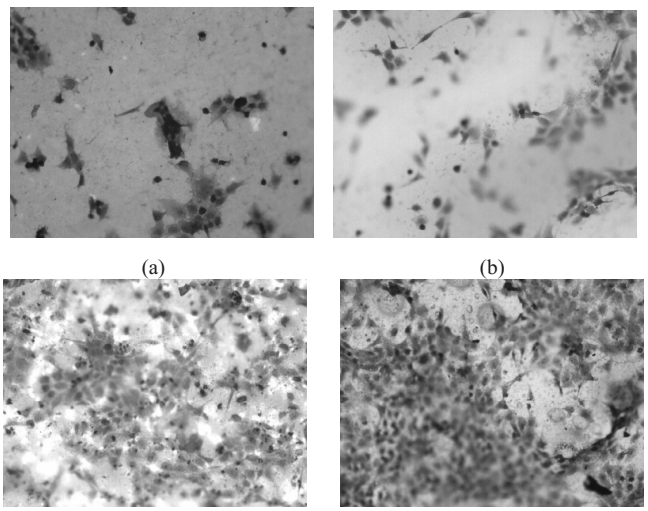

(a) (b)

(c) (d)

Fig. 3 H&E image of PLGA/HA composite film at 6th-day culture in proliferation test (a) PLGA (b) PLGA/HA 5% (c) PLGA/HA 10% and (d) PLGA/HA 15% film

The mechanical properties of 5 and 10 wt% HA composites are enough to implant and regenerate articular cartilage among the groups.

Conclusively, the PLGA/HA 10 wt% composite film could enhance the cartilage regeneration efficiently for chondrocyte attachment and proliferation for the treatment of cartilage defect, as compared with PLGA/various content of HA films.

Acknowledgment

This work was supported by the Korea Research Foundation Grant funded by the Korea Government (MOEHRD) (D00615)

References

1. Dietmar W. Hutmacher : Biomaterials 21 (2000), p.2529
2. Hunziker EB: Osteoarthritis Cartilage Vol. 10 (2002), p. 423
3. A. Sinha, G. Das, B. K. Sharma, R. P. Roy, A. K. Pramanick, S. Nayar : Mater Sci and Eng 2006
4. Kikuchi M, Suetsugu Y, Tanaka J, Akao M. : J Mater Sci Mater Med Vol. 8(1997), p. 361
5. Z. Hong, P. Zhang, C. He, X. Qiu, A. Liu, L. Chen, X. Chen, X. Jing: Biomaterials Vol. 26 (2005), p. 6296-6304
6. C. Durucan, P. W. Brown.: Journal of Biomedical Materials Research Vol. 51 (2000), 717-725
7. Kacey G. Marra, Jeffrey W. Szem, Prashant N. Kumata, Paul A. Dimilla, Lee E. Weiss. Journal of Biomedical Materials Research (1999) Vol. 47, Issue 3, p. 324-335
8. Sang-Soo Kim, Min Sun Park, Oju Jeon, Cha Yong Choi: Biomaterials Vol. 27(2006), p. 1859
9. Chih-Hung Chang et al. : Biometerials 24 (2003), p4853-4858

Address of the corresponding author:

Author: Jeong Koo Kim
Institute: Biomedical engineering, Inje University
Street: Obang-Dong
City: Gim-hae
Country: Korea
Email: jkkim@inje.ac.kr

F. Ibrahim, N.A. Abu Osman, J. Usman and N.A. Kadri (Eds.): Biomed 06, IFMBE Proceedings 15, pp. 130-133, 2007
www.springerlink.com ' Springer-Verlag Berlin Heidelberg 2007

Silverfil: Its Physical Characterization

N H Abu Kassim[1], N A Yahya[2], Z Radzi[3], W J Basirun[4], A A Ghani[5]

[1,2,3]Faculty of Dentistry, University of Malaya, 50603 Kuala Lumpur, Malaysia
[4,5]Faculty of Science, University of Malaya, 50603 Kuala Lumpur, Malaysia

Abstract— **This article focuses on the physical characterization of Silverfil® amalgam. Analysis of the amalgamated material semi-quantitatively showed that Silverfil® comprised of approximately two thirds mercury and one third silver. No other elements were detected. Examination of the amalgamated material by x ray mapping and metallographically showed no evidence of free mercury present. Silverfil® has strong affinity towards the mercury ion. X-ray Diffraction analysis showed that the amalgamated Silverfil® is similar to a mineral in nature called "Moschellandsbergite". The advantages of Silverfil® over conventional amalgam were highlighted.**

Keywords— **Amalgam, Silverfil®,Physical characterization**

I. Introduction

These are the instructions for preparing papers for the Biomed 2006 Proceedings Series. English is the official language. Please, do not forget to prove the spelling with your spell checker. Set the language to English (U.S.). Read the instructions in this sample paper carefully before typing. Dental amalgams have been used continuously in dentistry for nearly 200 years to reconstruct decayed teeth. Mercury is one of its component that combines readily with other metals to form solid amalgams. However, the usage of mercury in dentistry has been controversial since at least the middle of the 19th Century. This controversy has intensified over the last 25 years, since sensitive analytical chemistry techniques showed continuous release of mercury from dental amalgams [1}. International and regulatory agencies have evaluated the potential of amalgam fillings to cause health effects, usually concluding no evidence of harm and, therefore, no reason to advise against their use [2,3,4]. Amalgam fillings currently compromise about 50% mercury, with the remainder principally silver, plus smalls amounts of copper, tin, or zinc [5].

Table 1: Constituents of a typical dental amalgam

Constituent	% of total
Ag	67-74
Sn	25-28
Cu	0-6
Zn	0-2
Hg	0-3

Chemical reaction of low copper amalgam

Ag_3Sn (γ) + Hg (mercury) → Ag_3Sn (γ)+ $Ag_2Hg_3(\gamma_1)$+ $Sn_7Hg(\gamma_2)$

Chemical reaction of high copper amalgam

The first reaction is the same as for the low copper amalgam, but this is followed by the second reaction:

γ_2 + Ag-Cu → Cu_6Sn_5 + γ_1

Although other filling materials are available, popularity of amalgam is maintained by its relative cheapness, durability, and ease of use. In many countries amalgam is still the most commonly used filling material in posterior teeth [6].

In the past 10 years, development has been carried out to produce a Hg free silver amalgam, and Silverfil (Dunia Perwira Manufacturing Sdn Bhd, Malaysia) was recently introduced into the Malaysian market. It is manufactured purely from reactive silver particles (60%) and silver-mercury in powder form (40%).It does not contain any tin, copper or zinc. Following amalgamation, scientific studies have proven that it does not contain any free or unreacted mercury.

Chemical reaction of Silverfil

Ag_3Hg_2 + Ag_3 + Hg → Ag_3Hg_2 + Ag_3

It was the purpose of this study to quantify any excess Hg after amalgamation of Silverfil and its physical characterization after amalgamation.

II. Materials and methods

A. Assessment of free mercury

Two methods were used to assess the presence of excess Hg after the amalgamation of Silverfil .

F. Ibrahim, N.A. Abu Osman, J. Usman and N.A. Kadri (Eds.): Biomed 06, IFMBE Proceedings 15, pp. 134-136, 2007
www.springerlink.com ' Springer-Verlag Berlin Heidelberg 2007

Metallographic examination

Electron beam bombardment in the electron microscope was used to create an x-ray map of the spectra from Silverfi[l] to enable semi-quantitaive analysis of Silverfi[l] . Metallographic examination was carried out to determine excess Hg.

Optical absorption

Silverfil powder and mercury in various mixing proportions (1:1.3 to 1:6) were mixed by using pestle and mortar. Optical absorption examinations with Shidmadzu UV-3000 were carried out.

B. Hg diffusion rate

A three headed electrochemical cell was used to determine the rate of Hg diffusion into Silverfil particles. Ag/AgCl was used as the reference electrode, Silverfil as the working electrode and the counter electrode was made from platinum wire. Two different mixing electrodes were fabricated using mixing proportion of Ag_3:Ag_3Hg_2 ; 1:1.13 and 1.25.

The Randles-Sevcik equation was used to calculate the diffusion rate.

$J = -0.4436\ nF\ (nF/RT)^{1/2}\ cD^{1/2}\ v^{1/2}$

where:

n = the number of electrons transferred in the electrochemical step.

F = Faraday constant 96,500 C mol^{-1}

R = gas constant 8.3142 J mol^{-1} K^{-1}

T = Kelvin temperature K.

c = concentration of electro-active species.

v = scan rate / V s^{-1}

Two different current at scan rates were used in this experiment, 400mVs^{-1}/A and 100mVs^{-1}/A.

C. X-ray Diffraction Analysis (XRD)

XRD method was used to further characterized the amalgamated Silverfil . The Silverfil fine grain sample of < 0.2 mm across was analysed to determine its characteristic d-spacing by noting the angle of θ at which peak reflection were present.

III. Results and discussion

A. Assessment of free mercury

The semi-quantitative analysis revealed that Silverfil contained about 33% of silver and about 67% of mercury. No other elements were present in detectable amounts. Examination of the amalgamated material by X-ray mapping showed no evidence of free mercury present as if areas rich in one particular constituent existed they would show up on the map . This observation was further substantiated by work carried out using the optical absorption method. Free or colloidal mercury is known to have an optical absorption band at 285nm and it is intense enough for detection by the optical absorption method in concentrations of about 100 ppm. When excess mercury is present it tends to form aggregate colloids which can be seen to have an optical band characteristic of the colloids at 310 nm. Only in the samples prepared with mixing ratio of 1:1.6 and above, an optical absorption band with observable intensity begins to appear indicating the presence of free mercury. For samples prepared with less mercury no detectable optical band was found. The mixing ratio of the commercially available Silverfil is 1:1.15.

The decades-long issue of excess mercury in dental amalgam fillings may has been finally overcome. Silverfil® has been shown to have no excess mercury,. Tests revealed small amounts of un-reacted or free silver within Silverfil® fillings. This further infers that there is no excess mercury at all as there is insufficient mercury to completely react with all the silver. Conventional Silver-Tin-Copper amalgams waste are to be stored in a sulphite solution as recommended by the American Dental Association (ADA). The sulphite chemically reacts with the excess mercury to prevent its vaporisation. Silverfil® waste does not require any special storage as there is no excess mercury.

B. Hg diffusion rate

When amalgamating Silverfil using mortar and pastel, the Hg disappeared fast into the silver alloy which leads to calculation of Hg diffusion rate. The diffusion constant for Ag_3:Ag_3Hg_2 ratio of 1:1.13 and 1:1.25 were 7.87 X 10^{-8} m^2s^{-1} and 7.09 X 10^{-9} m^2s^{-1} respectively. Both values are considerably greater than diffusion constant for simple redox reaction such as the reduction and oxidation of Fe^{3+}/Fe^{2+} which are in the orders for 10^{-10} m^2s^{-1}. One such explanation is that the amalgamated Silverfil has huge affinity towards the Hg^{2+} ion, that by increasing the scan rates will not significantly increase the currents. The reduction of Hg^{2+} ions is not only facilitated by the linear diffu-

F. Ibrahim, N.A. Abu Osman, J. Usman and N.A. Kadri (Eds.): Biomed 06, IFMBE Proceedings 15, pp. 134-136, 2007
www.springerlink.com ' Springer-Verlag Berlin Heidelberg 2007

sion of Hg^{2+} ions to the amalgamated Silverfil electrode but by also by the affinity of the amalgamated Silverfil towards the Hg^{2+} ions.

The high diffusion constant is likely to be attributed to the porosity present in the reactive silver and Ag_3Hg_2 particles.

C. X-ray Diffraction Analysis (XRD)

Analysis on Silverfil® was done after mixing the Silverfil® powder with mercury and the XRD recorded (Table 2). It was found that after 30 minutes and 1 hour after mixing, the XRD diffractograms matched exactly to that of Ag_2Hg_3 which is also known as gamma-Moschellandsbergite and there was no free mercury in the amalgam as the XRD diffractograms didn t resembled to those of the free mercury. It can be concluded that there were no free mercury in the amalgam after 30 minutes and 1 hour of mixing and all the mercury existed in the amalgam form of gamma-Moschellandsbergite which has the molecular formula Ag_2Hg_3.

Table 2: Results of Silverfil® XRD analyses

CuKα radiation 2θ angle SILVERFIL	d-spacing SILVERFIL®	d-spacing MOSCHELLANSBERGITE
21.5	4.08	4.08
24.95	3.53	3.53
30.65	2.88	2.88
33.12	2.67	2.67
37.85	2.36	2.36
40.10	2.24	2.24
42.4	2.13	2.13
44.1	2.05	2.05
46.1	1.965	1.965
49.7	1.828	1.828
54.9	1.667	1.667
62.5	1.478	1.478
64.5	1.447	1.447
*65.7		
68.5	1.365	1.365
*74.2		
77.1	1.236	1.236

Note: At 2θ angle 65.7 and 74.2 for Silverfil®, there is no corresponding d-spacing values for published moschellansbergite in the data. Therefore values (d-spacing) for silverfil and moschellansbergite are left blank.

Silverfil® is similar to a mineral in nature called "Moschellandsbergite", which is found in the district of Landsberg in Germany. This infers that Silverfil® fillings are very stable and are also environmentally friendly. No worries of water contamination in dental spittoons from waste amalgam as Silverfil® has no mercury that can leach out and contaminate the water system. Thus no need for special separators or filters. Many countries have now started classifying silver-tin-copper amalgam waste as 'hazardous waste', and the recovery and refining of this amalgam waste is relatively complex. Silverfil® waste, however, being similar to a mineral in nature, is not hazardous to the environment and can be disposed of with relative ease.

IV. Conclusion

Analysis of the amalgamated material semi-quantitatively showed that Silverfil® comprised of approximately two thirds mercury and one third silver. No other elements were detected. Examination of the amalgamated material by x -ray mapping and metallographically showed no evidence of free mercury present. Silverfil® has strong affinity towards the mercury ion. Analysis from geology XRD found that Silverfil® is similar to a mineral in nature called "Moschellandsbergite".

References

1. Gay DD, Cox RD, Reinhardt JW. (1979) Chewing releases mercury from fillings. Lancet 1 (8123):985-986.
2. World Health Organisation. (1997) Dental amalgam and alternative dental direct restorative materials.
3. Department of Health and Human Services: Public Health Service, 1997. Dental amalgam and alternative restorative materials. An update from the Working Group on Dental Amalgam, Washington (http://www.health.gov/environment/amalgam2/Contents.html).
4. US Food and Drug Administration, Department of Health and Human Services. 2002. Consumer Update: Dental Amalgams (http://www.fda.gov/cdrh/consumer/amalgams.html).
5. Fredin B. 1994. Mercury release from dental amalgam fillings. Int J Risk Saf Med 4; 197-208.
6. Newman SM. 1991 Amalgam alternatives: what can compete? JADA 122, 67-71.
7. Radhakrishna S. 1992. Optical absorption and SEM studies on Silverfil. Technical report.
8. Walker JDR. 1990. Tests to determine free mercury on Silverfil filling material. Technical report.
9. Basirun WJ. 2003 Analysis on Silverfil using X-Ray Diffraction. Technical report.
10. Ghani AA. 2003. Silverfil XRD analysis. Technical report.
11. Pletcher D. 1991. A first course in electrode processes. Electrochemical consultancy.

Address of the corresponding author:

Dr Noor Azlin Yahya
University Malaya
50603 Kuala Lumpur, Malaysia
Email: nazlin@um.edu.my

F. Ibrahim, N.A. Abu Osman, J. Usman and N.A. Kadri (Eds.): Biomed 06, IFMBE Proceedings 15, pp. 134-136, 2007
www.springerlink.com ' Springer-Verlag Berlin Heidelberg 2007

Sinterability Of Hydroxyapatite Compacts Prepared By Cold Isostatic Pressing For Clinical Applications

C.Y. Tan[1], S. Ramesh[2], A.S. Hamdi[1]and I. Sopyan[3]

[1] Department of Engineering Design & Manufacture, Faculty of Engineering, University Malaya, 50603 Kuala Lumpur, Malaysia.
[2] Department of Mechanical Engineering, College of Engineering, University Tenaga Nasional, 43009 Kajang, Selangor, Malaysia.
[3] Department of Manufacturing and Materials Engineering, Faculty of Engineering, International Islamic University Malaysia (IIUM), Kuala Lumpur, Malaysia.

Abstract— **The effect of cold isostatic pressing (CIP) on the sinterability of synthesized hydroxyapatite (HA) powder was investigated. The starting powder was initially uniaxially die-pressed at about 1.3-2.5MPa to form disk and rectangular green compacts. Two batches of green samples were prepared, i.e. one batch was in the as-compacted state (Un-CIP) and another batch samples was subjected to cold isostatic press at 200 MPa (CIP). The latter samples exhibited a linear shrinkage of ~16% prior to sintering. All the samples were sintered in air at temperatures ranging from 700°C to 1400°C. The densification behaviour of HA was evaluated in terms of linear shrinkage, phase stability, bulk density, Vickers hardness and Young's modulus. The results revealed that green samples subjected to cold isostatic pressing exhibited better sinterability and possessed excellent mechanical properties. This effect is more pronounced particularly for the low temperature sintering regime i.e. ≤ 1100ºC.**

Keywords— **hydroxyapatite, cold isostatic pressing, sinterability, mechanical properties**

I. Introduction

The use of hydroxyapatite (HA) or $Ca_{10}(PO_4)_6(OH)_2$ as a potential bioactive calcium phosphate ceramics has gained popularity in recent years in clinical applications due to its close chemical resemblance with the mineral components of natural bone and teeth [1-4]. Several studies have been carried out and the results demonstrated that HA can accelerate initial biological response with host tissues at the implanted site in the body and improves the bone-implant adhesion [3, 4]. Nevertheless, the applicability of HA as a biomaterial in clinical orthopaedic and dental applications is limited to only non-stressed loaded regions owning to the brittle nature and low fracture strength (< 120 MPa)[5,6] accompanied by low fracture toughness (0.8-1.2 $MPam^{1/2}$) of the bioceramic as compared to 2-12 $MPam^{1/2}$ for the human bone [2, 5]. As a result, a great number of studies have been devoted to improve the mechanical properties of HA materials [7,8].

The success of HA ceramic in biomedical application is largely dependent on the availability of a high quality, sintered HA that is characterized having fined microstructure and improved mechanical properties [9]. In general, fine powder with greater surface area allows higher sinterability that leads to the use of lower densification temperature [9]. On the other hand, the presence of agglomerates, especially of the hard form, tends to disrupt the densification process resulting in the formation of defects (e.g. porosity, grain growth, microcracks, etc.) in the microstructure and thus limiting the strength of the sintered material [9]. Although numerous results to improve HA powder have been reported, nevertheless, literatures on the effect of cold isostatic pressing on the sinterability of HA are rather scarce.

Thus, in the present work, the effect of cold isotatic pressing (CIP) on the sinterability/densification of HA powder that was produced by wet chemical technique was investigated.

II. Experimental procedures

Stoichiometric HA was prepared using the precipitation reaction at room temperature between calcium hydroxide and orthophosphoric acid where the pH was maintained above 10 by the addition of ammonium hydroxide solution. After completion of titration, the suspension was aged overnight. The resulting precipitate was filtered, washed, dried and then ground to a powder of high purity, which composed of single phase stoichiometric HA [10].

The as-received powder was die-pressed at about 1.3-2.5 MPa into disc and rectangular green compacts. Two batches of green samples, i.e. in the as-compacted condition (Un-CIP) and samples that were CIP at 200 MPa (Reiken Seiki Japan), were prepared. The compacts were sintered in air atmosphere at temperatures ranging from 700°C to 1400°C, at ramp rates of 2°C/min with holding time of 2 hours.

The phase compositions of the synthesized powder and the sintered compacts were analyzed by X-ray diffraction (XRD) (Rigaku GeigerFlex, Japan) using Cu-Kα as the radiation source with a scan speed and step scan of 0.5°/min and 0.02° respectively to determine the phases present in the

F. Ibrahim, N.A. Abu Osman, J. Usman and N.A. Kadri (Eds.): Biomed 06, IFMBE Proceedings 15, pp. 137-140, 2007
www.springerlink.com ' Springer-Verlag Berlin Heidelberg 2007

samples. Identification of phases was achieved by comparing the diffraction patterns of HA with ICDD (JCPDS) standards [11].

The sintered densities of the samples were obtained by water immersion technique for dense compacts (above 95% of the theoretical density) and from the measurement of geometric dimensions and sample mass for low-density samples (below 95%). For low-density samples, the former method allows water to penetrate the pores, resulting in an overestimate value of the sample density. The relative density was calculated by taking the theoretical density of HA as 3.156 gcm^{-3}. The Vickers hardness (H_v) of the sintered polished samples was determined using a Matsuzawa microhardness indenter. A loading time of 10 seconds was employed and average hardness value was taken from at least five indents made for each sample. The Young s modulus by sonic resonance was determined for rectangular samples using a commercial testing instrument (GrindoSonic: MK5 Industrial , Belgium). The modulus of elasticity is calculated using the experimentally determined resonant frequencies, according to standard test method [12].

III. Results and Discussion

The XRD analysis of the synthesized powder in this study exhibited peaks that corresponded to stoichiometric HA [11]. Thus, it is evident that the filtered crystals were mainly single-phase HA and is believed to be very small. Estimates of crystal size from peak broadening [13] for the synthesized powder gives about 110 from the (2 1 1) reflection and about 350 from the (0 0 2) reflection.

The XRD analysis of all the sintered samples, regardless of pressing conditions and sintering temperature, produced only peaks that correspond to stoichiometric HA. This results indicate that HA did not decompose to secondary phases upon sintering and the phase stability was not affected by the pressing conditions prior to sintering. In addition, phase decomposition was not observed for both batches of samples even when sintered at high temperature above 1300℃ as typically shown in Fig. 1.

Decomposition of HA phase was not observed in the present material even for the high temperature (i.e. 1400℃) sintered samples. This observation is not in agreement with other workers, which have reported that decomposition of HA starts at about 1300℃ [14-16]. The difference in result in the present work could in part be attributed to the relatively high humidity content present in the sintering atmosphere and the nature of the synthesized powder. It is believed that the high humidity content slows down decomposition rate by preventing dehydration of the OH group from the HA matrix [14].

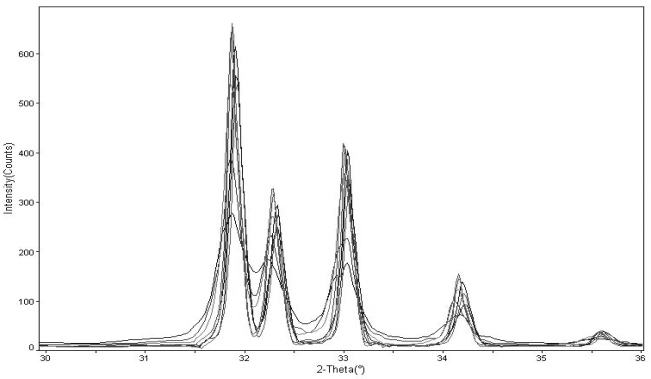

Fig. 1 XRD signatures of sintered (700℃ 1400℃) CIP HA. Similar results were obtained for the Un-CIP HA. All peaks correspond to the hydroxyapatite phase.

In general, sintering HA can lead to the partial thermal decomposition of HA into tricalcium phosphate (TCP) and/or tetracalcium phosphate. The thermal decomposition is accompanied in two steps i.e. dehydroxylation and decomposition. Dehydroxylation to oxyhydroxyapatite proceeds at temperatures about 850℃ to 900℃ by the fully reversible reaction in accordance to equation 1 [15, 16]:

$$Ca_{10}(PO_4)_6(OH)_2 \rightarrow Ca_{10}(PO_4)_6(OH)_{2-2x}O_x + xH_2O_{gas} \quad (1)$$

The decomposition to TCP and tetracalcium phosphate occurs at temperatures greater than 900℃ according to the reaction given in equation 2 [15, 16]:

$$Ca_{10}(PO_4)_6(OH)_2 \rightarrow 2Ca_3(PO_4)_2 + Ca_4P_2O_9 + H_2O_{gas} \quad (2)$$

Since both the dehydroxylation and decomposition reactions include water vapour as a product, the rates at which these reactions proceed depend on the partial pressure of H_2O in the furnace atmosphere. Thus, the secondary phase formation during sintering could be control by simply controlling the sintering atmosphere.

Since no attempt was made in the present work to control the sintering atmosphere, the present results indicate that the minimum moisture content for maintaining phase stabilization must be low. However, it is not clear if the loss of water during sintering plays a role in suppressing dehydroxylation.

Further results indicated that CIP HA exhibited higher linear shrinkage due to improved densification resulting from intimate powder particle contact from cold isostatic pressing. This was more evident for samples sintered below 1200℃. For example, the CIP HA recorded shrinkage of approximately 20% at 700℃, whereas the UN-CIP HA required a higher temperature of about 1150℃ to achieve similar shrinkage value. The final linear shrinkages for both sets of HA, regardless of pressing condition, were between 34% 35%.

F. Ibrahim, N.A. Abu Osman, J. Usman and N.A. Kadri (Eds.): Biomed 06, IFMBE Proceedings 15, pp. 137-140, 2007
www.springerlink.com ' Springer-Verlag Berlin Heidelberg 2007

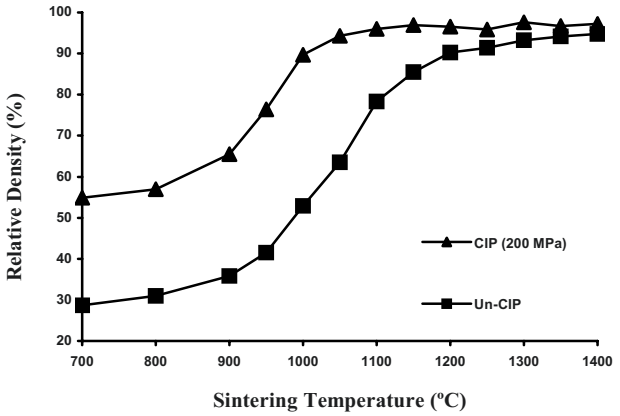

Fig. 2 The effect of pressing condition and sintering temperatures on the relative density of HA.

The effect of sintering temperatures on the bulk density of HA is shown in Fig. 2.

In general, the bulk density increases with increasing sintering temperature regardless of pressing condition. However, the beneficial effect of CIP in enhancing the bulk density of HA throughout the sintering regime employed has been revealed. The effect is more pronounced at lower temperatures ≤ 1100℃ where the density of the CIP samples was higher by more than 150% as compared to the Un-CIP samples when sintered at the same temperature. In addition, the CIP samples achieved > 95% of the theoretical density when sintered at temperature as low as 1050°C as compared to the Un-CIP HA which required a higher sintering temperature, above 1300°C.

The effect of sintering temperature on the Vickers hardness of HA is shown in Fig. 3. A linear relationship was observed for both sets of HA. The hardness of CIP HA decreases linearly with increasing sintering temperature whereas the opposite trend was observed for the Un-CIP HA.

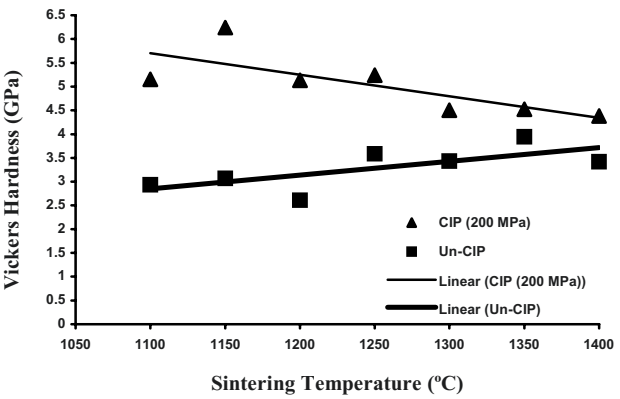

Fig. 3 Effect of sintering temperatures on the Vickers hardness of HA.

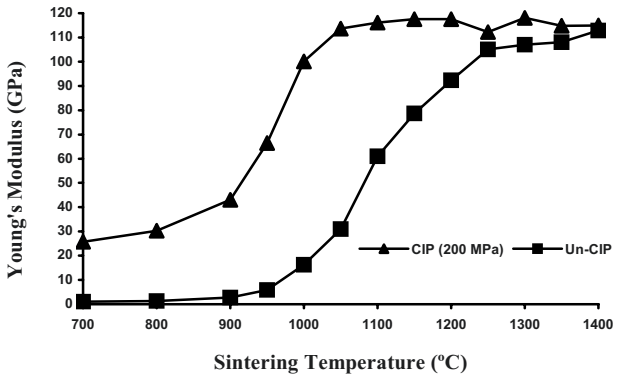

Fig. 4 The effect of sintering temperatures on the Young s modulus of HA.

The relationship between the Young s modulus (*E*) of the HA (CIP and Un-CIP) and sintering temperature is shown in Fig. 4.

Generally, it was found that the Young s modulus of the HA gradually increase with increasing sintering temperature up to about 1350℃. The variation in the Young s modulus is in good agreement with the bulk density as observed in Fig. 2. The CIP samples exhibited higher matrix stiffness than the equivalent Un-CIP samples, particularly at lower sintering temperatures. The results showed that the CIP HA achieved a Young s modulus above 100 GPa at approximately 1000℃, whereas the Un-CIP sample requires a sintering temperature of approximately 1250℃ to reach a similar modulus of elasticity. This result further emphasize the importance of cold isostatic pressing prior to sintering of the HA product. However, this improvement is more pronounced at lower temperatures as the maximum Young s modulus obtained for both HA was almost similar, i.e. approximately 115 GPa (CIP HA) and 111 GPa (Un-CIP HA) sintered at 1300℃ and 1350℃ respectively.

Attempts to correlate the Young s modulus with bulk density revealed a different trend for the CIP and Un-CIP HA as shown in Fig. 5. It was found that Young s modulus varied almost linearly for the CIP HA as compared to the Un-CIP HA, which exhibited a polynomial relationship. Clearly, the use of cold isostatic pressing treatment prior to sintering of the green samples plays a significant role in determining the densification behaviour of the synthesized HA, more particularly when sintered at low temperature regimes.

F. Ibrahim, N.A. Abu Osman, J. Usman and N.A. Kadri (Eds.): Biomed 06, IFMBE Proceedings 15, pp. 137-140, 2007
www.springerlink.com ' Springer-Verlag Berlin Heidelberg 2007

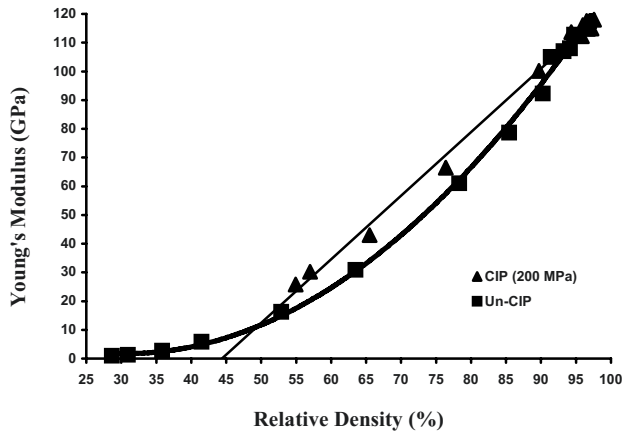

Fig. 5 Relationship between the relative density and Young s modulus of CIP HA and Un-CIP HA.

IV. Conclusions

Decomposition of HA phase to secondary phases was not observed in the present work. The effect of cold isostatic pressing (CIP) on the sinterability of HA was reflected in the sintered densities and Young s modulus values. The study revealed that CIP, among other parameters such as sintering temperature, plays an important role in enhancing the densification and stiffness of the HA matrix. Samples that were cold isostatic pressed at 200 MPa sinters more readily and required a much lower temperature (~ 1050℃) to achieve densities above 95% of theoretical value and a Young s modulus above 100 GPa, whereas the Un-CIP samples required a sintering temperature of above 1250℃ to achieve similar results. In general, the present work revealed that the CIP samples exhibited superior properties than the equivalent Un-CIP samples and this effect is more pronounced when samples sintered below 1150℃.

Acknowledgment

The authors gratefully acknowledge the support provided by UNITEN and SIRIM Berhad.

References

1. Hench L L (1998) Biomaterials: A forecast for the future. Biomaterials 19: 1419-1423.
2. Suchanek W, Yoshimura M (1998) Processing and properties of hydroxyapatite-based biomaterials for use as hard tissue replacement implants. J Mater Res 13: 94-117
3. Gross K A, Berndt C C (1998) Thermal processing of hydroxyapatite for coating production. J Biomed Mat Res 39: 580-587
4. Cook C D, Thomas K A, Kay F J, Jarcho M (1988) Hydroxyapatite coated titanium for orthopaedic implant applications. Clin Orthop 232: 225-243.
5. Muralithran G, Ramesh S (2000) Sintering behaviour and properties of commercial hydroxyapatite. Ceram Inter 26: 221-230.
6. Arita I H, Wilkinson D S, Mondragon M A, Castano V M (1995) Chemistry and sintering behaviour of thin hydroxyapatite ceramics with controlled porosity. Biomaterials 16: 403-408.
7. Suchanek W, Yashima M, Kakihana M, Yoshimura M (1997) Hydroxyapatite ceramics with selected sintering additives. Biomaterials 18: 923-933.
8. Fang Y, Agrawal D K, Roy D M, Roy R (1995) Fabrication of transparent hydroxyapatite ceramics by microwave processing. Mater Lett 23: 147-51.
9. Gibson I R, Ke S, Best S M, Bonfield W (2001) Effect of powder characteristics on the sinterability of hydroxyapatite powders. J Maters Sci: Mater in Med 12: 163-171.
10. Kutty M G, Ramesh S, Malaysia Patent, 2000 (PI. 20000349).
11. PDF Card no. 9-432, ICDD, Newton Square, Pennsylvania, USA.
12. ASTM E1876-97 (1998) Standard test method for dynamic Young s modulus, shear modulus and poisson s ratio by impulse excitation of vibration, Annual Book of ASTM Standards.
13. Culity B D, Stock S R (2001) Elements of X-Ray diffraction. 3rd Edition, Prentice Hall, Inc: 167-170.
14. Van Lunduyt P, Li F, Keustermans J P, Streydio J M, Delannay F, Munting E (1995) The influence of high sintering temperature on the mechanical properties of hydroxylapatite. J Mater Sci: Mater in Med 6: 8-13.
15. Royer, Viguie J C, Heughebaert M, Heughebaert J C (1993) Stoichiometry of hydroxyapatite: influence on the flexural strength. J Mater Sci: Mater in Med 4: 76-82.
16. Wang P E, Chaki T K (1993) Sintering behaviour and mechanical properties of hydroxyapatite and dicalcium phosphate. J Mater Sci: Mater in Med 4: 150-158.

Address of the corresponding author:

Author: Tan Chou Yong
Institute: Universiti Malaya
City: Kuala Lumpur
Country: Malaysia
Email: chouyong@perdana.um.edu.my

F. Ibrahim, N.A. Abu Osman, J. Usman and N.A. Kadri (Eds.): Biomed 06, IFMBE Proceedings 15, pp. 137-140, 2007
www.springerlink.com ' Springer-Verlag Berlin Heidelberg 2007

Standardization of Distance and Angulation of Light Curing Unit Tip Using Distometer

Z Radzi[1], N H Abu Kasim[1], N A Yahya[1], N A Abu Osman[2], N L Kassim[3]

[1] Faculty of Dentistry, University of Malaya, 50603 Kuala Lumpur, Malaysia
[2]Department of Biomedical Engineering, Faculty of Engineering, University of Malaya, 50603 Kuala Lumpur, Malaysia
[3]Centre for Language Studies, International Islamic University, Malaysia

Abstract **The purpose of this study was to investigate the light intensity of selected light curing unit with varying distance and angulation of the light curing tip and lightmeter.**

Four types of light units; Spectrum 800 (Dentsply), Coltulux 3 (Coltene), Elipar FreeLight 2 (3M Espe) and Starlight Pro (Mectron) were evaluated for light intensity at various distance between the light curing tip and the lightometer Cure Rite Denstply (0, 1, 3, 5, 10 and 15 mm). The light curing units were angulated at 45°, 60° and 90° at a standardized 5 mm distance.

The intensity of light curing is affected by the distance between the light curing tip and the lightmeter. However, the decrease in light intensity of the light curing unit was found not to obey the inverse square law for the distances 0 to 15 mm.

The study found that there was no significant difference between 45° and 60° angulation between the light curing tip and the lightmeter. However, the decrease in light intensity is significant when compared to the light tip is placed perpendicular (90°) to the aperture of the light meter.

Keywords— **Distance, Angulation, Light curing unit, Light intensity, Composite resin.**

I. Introduction

Light activated composite resin is the most commonly used restorative material on the anterior teeth as it fulfills the requirements of excellent esthetics and durability (1). Light activation is accomplished with blue light at peak wave length of about 470 nm, which is absorbed usually by photo-activator, such as camphorquinone (2).

Initiation system starts the polymerization process through the formation of free radicals. When a free radical collides with a carbon double bond (C=C) in resin monomer, the free radical pairs with one of the electrons of the double bond, converting the other member of the pair to a free radical, and thus the reaction continues. In light cured systems, a light source of 468 nm (+/- 20) excites camphorquinone or another diketone into a triplet state that interacts with a non-aromatic tertiary amine, such as N,N-dimethylaminoethyl methacrylate. Ideally, this process continues until all of the monomers become polymerized. Polymerization is directly related to the wavelength, intensity and time of exposure (3).

For maximum curing, which is about 50% to 60% monomer conversion, a radiant energy influx of approximately 16 joules/cm^2 is required for a 2-mm thick layer of resin. This can be delivered by a 40-sec exposure to a lamp emitting 400 mW/cm^2. The same result can be produced by a 20-sec exposure at 800 mW/cm^2, or an exposure of ~13 sec with 1200-mW/cm^2 lamp. Thus increasing the power density of the lamp increases the rate and degree of cure (4).

The degree of polymerization also varies according to the distance from the surface of the composite to the light source. Depth of cure decreases significantly as this distance increases. The potential for activation declines exponentially as a function of the distance from the surface of the filling. The intensity of the light I_x at a distance x from the surface is given by the function

$$I_x = I_o\, e^{-\mu X}$$

Where I_o is the light intensity at the surface and μ is the absorption coefficient of the material. Since certain level of intensity is required to cause activation it follows that light activated materials have a limited depth of cure (3).

Van Noort (2002) stated that the light intensity on unit surface area drops off with inverse square of the distance between the light source and the resin (5).

The ideal distance of the light source from the composite is 1 mm, with the light source positioned 90° from the light composite surface. As the angle diverges from 90° to the composite surface, the light energy is reflected away and penetration is greatly reduced (6,7). Although the 90° position has always been emphasis, no study has been done on the effect of angulation as this situation is usually seen in the clinical practice.

Therefore, the purpose of this study was to investigate the light intensity of selected light curing units with varying distance and angulation of the light curing tip.

F. Ibrahim, N.A. Abu Osman, J. Usman and N.A. Kadri (Eds.): Biomed 06, IFMBE Proceedings 15, pp. 141-143, 2007
www.springerlink.com ' Springer-Verlag Berlin Heidelberg 2007

II. Materials & method

Four types of light curing units; Spectrum 800 (Dentsply), Coltolux 3 (Coltene), Elipar FreeLight 2 (3M Espe) and Starlight Pro (Mectron) were evaluated for light intensity at various distance between the light curing tip and the lightmeter (Cure Rite Caulk, Denstply).

In this study, a specially designed distometer (8) was used to standardize the distance between the light curing tip and the lightmeter. This distometer consist of; base, sliding platform mounted on the box, protractor, ruler, height gauge (Mitutoyo) and light curing holder (Fig.1).

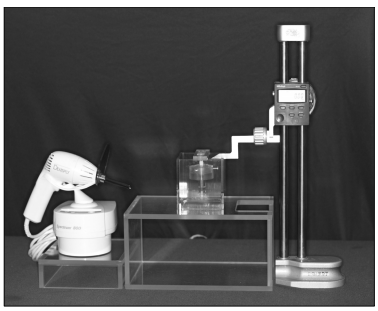

Fig. 1 Distometer

The light curing unit was fastened to a vertical support so that the tip was parallel to the table surface. The digital visible lightmeter was fixed to the mounting table coaxially with the light tip. The light tip was angulated at 90^o to the light aperture and held at five different distances -0 mm (surface contact), 1mm, 3mm, 5mm, 10mm and 15mm from the lightmeter aperture. These distances were standardized using the gauge height (Mitutoyo, Japan) that was attached to the distometer. Light tip were adjusted to ensure the light emitted is transmitted to the centre of the lightmeter aperture. Intensity of the light source is measured in mW/cm^2. The light intensity was measured 5 times for 10 seconds.

In another part of the study, the distance was standardized at 5 mm and the light curing tip were angulated at 90^o, 60^o and 45^o to the lightmeter aperture. Similar set-up of the distometer was used. The light output was measured 5 times for 10 seconds.

Statistical analysis was performed using Two-Way ANOVA (SPSS version 12.0).

III. Results & discussion

Fig. 2 shows that the highest light intensity is obtained when the tip of light curing unit is in contact with the lightmeter aperture. It is illustrates that the intensity of all light curing units decrease as a function of distance.

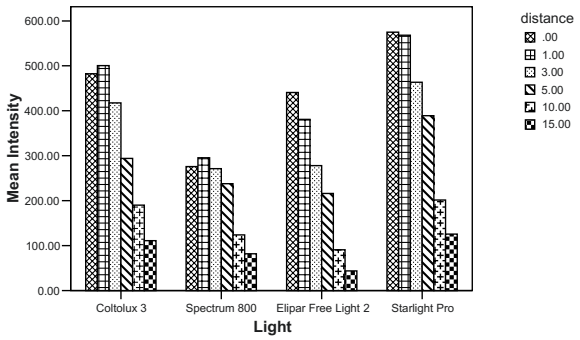

Fig. 2 Histogram of Light curing units vs Intensity with varying distances

Descriptive statistics showed that all data were normally distributed. Two-way ANOVA showed that there was a significant interaction between light and distance. Dunnett s T Post Hoc tests were used to compare the differences between groups as Levene s test revealed that equal variance across all groups could not be assumed. The box plot in Fig. 3 shows that light intensity decreased significantly when light tip was placed 5mm, 10mm and 15mm away from the lightmeter aperture. However, no significant differences were detected between 0mm, 1mm and 3mm.

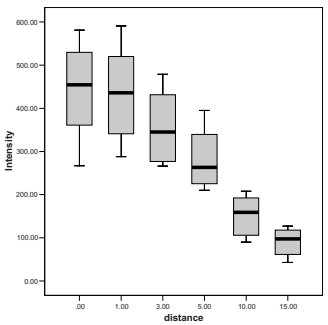

Fig. 3 Box plot illustrating mean and std deviation of all test groups with varying distances.

Results of this study confirmed that distance has an effect on the intensity of light curing units (9,10,11). However this study measured light intensity directly using a lightmeter. Others evaluated surface hardness, depth of cure and bond strength of composite resin (9,10,11). No attempt was also made to ensure that the distances between light tip and composite is standardized.

Fig. 4 illustrates a decrease in light intensity when light tip is angulated to 45^o and 60^o except for Coltolux 3. Descriptive statistics showed that all data were normally distributed. Two-way ANOVA showed that there was a significant interaction between light and angulation. Dunnett s T Post Hoc tests were used to compare the differences be-

F. Ibrahim, N.A. Abu Osman, J. Usman and N.A. Kadri (Eds.): Biomed 06, IFMBE Proceedings 15, pp. 141-143, 2007
www.springerlink.com ' Springer-Verlag Berlin Heidelberg 2007

tween groups as Levene s test revealed that equal variance across all groups could not be assumed. The box plot in Fig. 5 shows that light intensity decreased significantly when light tip was angulated at 45° and 60° from the light-meter aperture.

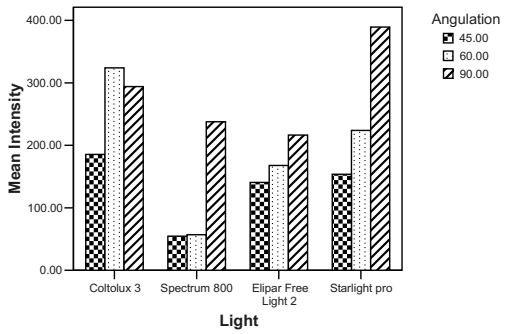

Fig. 4 Histogram of Light curing units vs Intensity with different angulation of light tip

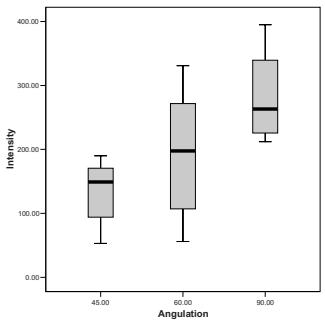

Fig. 5 Box plot illustrating mean and std deviation of all test groups with varying angulation.

In everyday clinical work dentist invariably angulate the light curing unit s tip when polymerizing composite resin. Sometimes angulating light tip cannot be avoided as access to the restoration may be limited by the tooth or cavity s position. It may also be due to poor hand control of the operator or assistant. The findings of this study elucidated that it is important to maintain 90° angulation of the tip of light curing unit to the surface of the restoration. Further studies need to be carried out to ascertain it effect on composites. Therefore the curing times recommended by the manufacturer may need to be extended whenever the tip of the light curing unit could not be placed perpendicular (90°) to the surface of the composite resin.

IV. Conclusions

The intensity of light curing is affected by the distance between the light curing tip and the lightmeter. However, the decrease in light intensity of the light curing unit was found not to obey the inverse square law for the distances 0 to 15 mm.

The study found that there was no significant difference between 45° and 60° angulation between the light curing tip and the lightmeter. However, the decrease in light intensity is significant when compared to the light tip is placed perpendicular (90°) to the aperture of the light meter.

Acknowledgment

We would like to express our appreciation to Mrs Yvonne Padmini, Miss Kasmaliza Kassim and Mr. Zaini Abdul Wahab for their invaluable contribution to this project.

References

1. Murchison, D.F., Roeters, J., Vargos, M.A, Chan, D.C.N. (2006).Direct Anterior Restorations in Fundamentals of Operative Dentistry. A Contemporary Approach. 3rd Edition. Quintessence
2. Powers, J.M., Sakaguchi R.L. (2006) Craig s Restorative Dental Materials. Mosby Elservier
3. McCabe, J.F., Walls, A.W.G. (1998). Applied Dental Materials. 8th Edition. Blackwell Publishing
4. Anusavice K.J. (2003). Philips Science of Dental Materials. Eleventh Edition. Saunders
5. Van Noort, R. (2002) Introductions to Dental Materials. Mosby-Year Book, Inc.
6. Kelsey, W.P., Shearer, G.O., Cavel, W.T., Blankenau, R.J. (1987). The effects of wand positioning on the polymerization of composite resin. J Am Dent Assoc 114:213-215
7. Radzi, Z., Yahya, N. A., Zamzam, N., Wood, D.J., (2004) Light Curing Units in Orthodontics. Annals of Dentistry 11: 13-23
8. Radzi, Z., Yahya, N. A., Kasim, N.H., Abu Osman, N.A., Aziz, Z.A. (2006) Light Composite Distometer. Abstract University of Malaya Research and Innovation Expo.
9. Rueggeberg, F.A., Jordan, D.M. (1993). Effect of light tip distance on polymerization of resin composite. The Int Jour Prosthod 6: 364-370
10. Pires, J..A.F., Cvitko, E., Denehy, G.E., Swift, E.J. (1993) Effects of curing tip distance on light intensity and composite resin microhardness. Quintessence Int; 24: 517-521
11. Cacciafesta, V., Sfondrini M.F., Scribante, A., Jost-Brinkmann, P.G. (2005). Effect of light-tip distance on the shear bond strength of composite resin. Angle Orthod; 75: 386-391

Address of the corresponding author:

Author: Dr Zamri Radzi
Institute: University of Malaya
Street: Lembah Pantai
City: Kuala Lumpur
Country: Malaysia
Email: zamrir@um.edu.my

F. Ibrahim, N.A. Abu Osman, J. Usman and N.A. Kadri (Eds.): Biomed 06, IFMBE Proceedings 15, pp. 141-143, 2007
www.springerlink.com ' Springer-Verlag Berlin Heidelberg 2007

Structural and conductivity studies in Ag-rich AgI-ZnI_2 solid solutions

Mohd Heazill Nordin[1], Zawawi Abdul Rahman[1], Mohd Rafie Johan[1], S. Anandan[2], Abdul Kariem Arof[3]

[1]Department of Mechanical Engineering, University of Malaya, Kuala Lumpur 50603, Malaysia
[2]Department of Biomedical Engineering, University of Malaya, Kuala Lumpur 50603, Malaysia
[3]Department of Physics, University of Malaya, Kuala Lumpur 50603, Malaysia

Abstract – **Compositions of solid solutions $xAg1-(1-x)ZnI_2$ ($0.5 \leq x \leq 1$), had been synthesized. The characterization studies of the materials using x-ray diffraction at room temperature and conductivity measurements by using impedance spectroscopy. The investigations were carried out for determination of the structure of materials and the conductivity for different composition in order to establish the relationship between the material structure and the conductivity. Samples with more AgI content are more crystalline. The conductivity of the compound will be increased with the decreases of crystalline structures.**

Keywords– **ionic conductivity, impedance spectroscopy, x-ray diffraction, crystalline**

I. Introduction

Study of ionic conductivity in solid electrolytes has been attracted over the last few decades due to their various important technological applications like solid state battery, chemical sensor, fuel cell and others. It was reported that the research progress in nano-technology, synthesis of silver iodide (AgI) particle from dilute solution and many others ways [1]. Solid state ionic is deal with materials and devices based on the flow of ions in solid instead of electron flow. Solid with high ionic conductivity also known as super ionic conductors can achieve electrical conductivity as high as 10^{-1} to 10^{-4} S/cm.

Batteries fabricated with solid electrolytes could surmount many limitations of conventional liquid electrolyte batteries such as, low self life, corrosion, leakage, instability towards temperature variation. Different types of (crystalline, glasses, polymers and composite) super ionic conductors with various mobile ions like Li^+ ,Na^+ ,Ag^+, Cu^+, $Pb2^+$, etc. have been synthesized and characterized [2]. Among them, silver based glasses show high ionic conductivity and high stability at ambient temperature [2]. Hence, silver based glass solid electrolytes have been synthesized to attain high ionic conductivity, which could be used for better ionic device applications. Research of new amorphous and polycrystalline ion conductive materials has been carried out. The aim is to synthesize a new material, exhibiting high ionic and mixed conductivity for application in solid state ionic devices. Investigations were on glass and crystalline phase formation regions and the structure of various systems. Via the use of diffraction methods as well as impedance spectroscopy a correlation between the composition, structure and properties of the obtained materials is found. According to several numbers of reports, conduction occurs in the amorphous region [3]. The increase in electrical conductivity can therefore be partially understood if upon some modification, let the addition of salt to material, makes the final material more or less amorphous than before any salt was added.

In this research, silver iodide (AgI) and zinc iodide (ZnI_2) has been used for study the performance of ionic conductivity of the mixture by controlling the composition between the two materials. While AgI is already an ionic (Ag^+) conductor at ambient temperature, ZnI_2 is a mixed. Solid solutions of AgI and ZnI_2 were prepared so as to change the property of the material in a single component. AgI has been of interest as a model compound for the study since there are several discoveries of large silver ionic conductivity [3]. It is also prove that AgI show the highest electrical conductivity at room temperature. As stated before our aim is to search a new material, so we decide to use ZnI_2 as a combination material in order to improve the ionic conductivity of silver ion.

To our knowledge, there are no research had been done in these combinations of materials. The combination is possible because of the extended mutual solid solubility range of AgI and ZnI_2 despite their unequal ionic radius (radius Ag = 144pm and radius Zn = 133.2pm). The large size mismatch in a mobile cation size points to the possibility of a mixed mobile ion effect which controlled the ionic conductivity in the AgI ZnI_2 system.

II. Experimental methods

AgI was prepared by chemical reaction of silver nitrate ($AgNo_3$) aqueous with potassium iodide (KI) aqueous. $AgNo_3$ is dissolve in water with a ratio of one mol $AgNo_3$ (166 gram) with 1000ml water. KI also dissolve in water with a ratio of 1 mol KI (169 gram) with 1000ml water. The dissolved of $AgNo_3$ and KI is then mixed together and

F. Ibrahim, N.A. Abu Osman, J. Usman and N.A. Kadri (Eds.): Biomed 06, IFMBE Proceedings 15, pp. 144-148, 2007
www.springerlink.com ' Springer-Verlag Berlin Heidelberg 2007

produced sediment of AgI and solution of KNO_3. The chemical equation of this reaction is shown below:

$$AgNO_3 + KI \rightarrow AgI + KNO_3 \quad (1)$$

AgI is dried in furnace at temperature 35 ℃ for one day before use. Calculation was carried out in order to determine the weight of AgI and ZnI_2 before mixed. The AgI powders were mixed with ZnI_2 powder at various different compositions using ball milling at room temperature for 4 hours and 350 rpm.

$$AgI + ZnI_2 \rightarrow (x)\ AgI\text{-}(1\text{-}x)\ ZnI_2 \quad (2)$$

The powder samples then palletized by using 25 ton hydraulic cylindrical die at pressure 4 tons in a stainless steel die at room temperature in order to form a circular pallet. Each of the samples was prepared for a 4 gram of one pallet. The pallets had an area of 0.79cm^2 and 5mm thickness for electrical conductivity measurement. The palletized samples were kept in drying cabinet in order to prevent any reaction.

Structural characterizations on these samples were performed using X-ray diffractometer. Sample pellets of 0.79cm^2 area and 1.5mm thickness were used. Through the XRD results we studied the phase transition which influences the conductivity in AgI-ZnI_2. As expected, there will be a reduction of the crystalline peak but increasing of amorphous nature of the sample. The degree of crystalline was calculated using Scherer equation:

$$L = \frac{0.9\lambda}{\Delta 2\theta_b (\cos\theta_b)} \quad (3)$$

Impedance measurements in the frequency range, 50Hz - 1MHz and temperature 25° C, respectively, were carried out using Hioki 353I-01 LCR Hi - Tester. The samples were sandwiched between two stainless disk electrodes which acted as a blocking electrode for ion. The imaginary impedance is usually negative indicating the sample to be capacitive. A plot of negative imaginary impedance versus real impedance on a graph with horizontal and vertical axes having the same scale will give a semicircle if the sample has a Debye nature. From the complex impedance plot, the bulk resistance can be obtained. The ionic conductivity is determined by equation:

$$\sigma = \frac{L}{R_b A} \quad (4)$$

where σ is conductivity, L is sample of length, R_b is the bulk resistance and A is the cross section of contact area.

III. Results and Discussion

The sharp and intense diffraction peaks occured at 2θ = 24° as shown in Fig. 1 indicating the crystalline nature of AgI. The peak are varies greatly as ZnI_2 salt was added to AgI as shown in Figs. 2 - 6. These suggest that part of AgI were remained salt-free and another part of AgI were salt-contained. As a result, it will transform into amorphous phase and hence depressed crystallinity.

In Fig. 2, an additional diffraction peaks had been observed in 0.9AgI - 0.1ZnI_2 composition at 2θ = 22.5°, 23.5°, 25.5°, 33°, 43° and 46°. These indicate the existence of ZnI_2 in a crystalline phase of AgI and suggested the co-existence of amorphous phase with dissolve ZnI_2.

Figs. 1, 2, 3 and 4 shows the XRD patterns of the prepared sample.

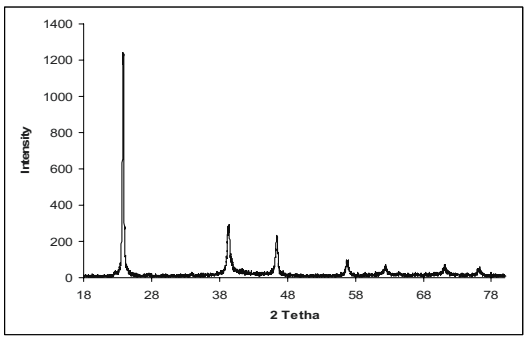

Fig. 1 XRD result of pure AgI

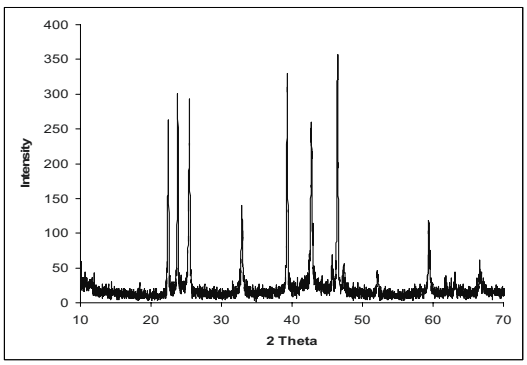

Fig. 2 XRD result of 0.9 AgI-0.1 ZnI_2

F. Ibrahim, N.A. Abu Osman, J. Usman and N.A. Kadri (Eds.): Biomed 06, IFMBE Proceedings 15, pp. 144-148, 2007
www.springerlink.com ' Springer-Verlag Berlin Heidelberg 2007

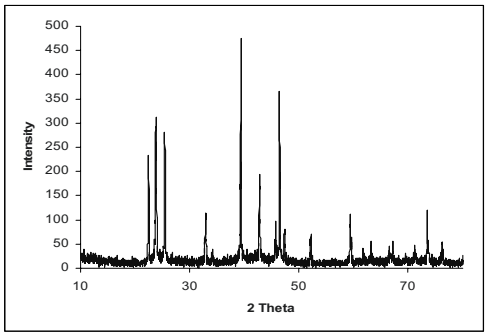

Fig. 3 XRD result of 0.8 AgI-0.2 ZnI_2

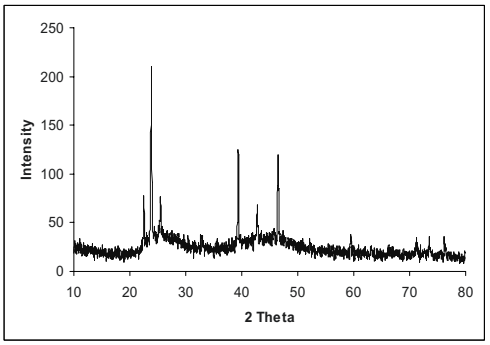

Fig. 4 XRD result of 0.7 AgI-0.3 ZnI_2

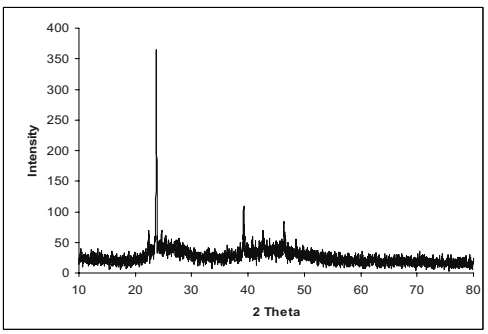

Fig. 5 XRD result of 0.6 AgI-0.4 ZnI_2

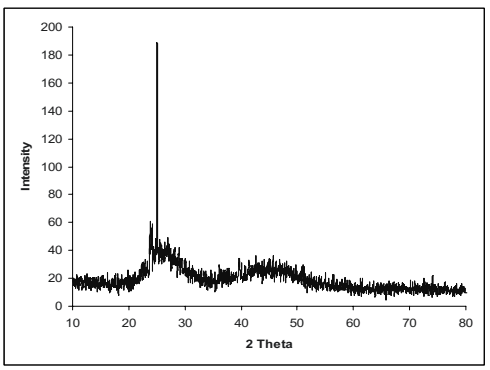

Fig. 6 XRD result of 0.5 AgI-0.5 ZnI_2

The existence of amorphous phase in the complexation materials is evident from the appearance of broaden peak between $2\theta = 20^{\circ}$ and 60° at 0.7AgI - 0.3ZnI_2 as shown in Fig. 4. From the figures, it can be conclude that at higher ZnI_2 content ($ZnI_2 \geq 30\%$), most of the salt were dissolved within the amorphous phase of AgI. This will strongly increase the non-crystalline fraction. However, by lowering the addition of ZnI_2 ($ZnI_2 \leq 30\%$) will give a rise to the gradually formation of crystalline phase. This fact is proven by existence of diffraction peak at $2\theta = 22.5^{\circ}$, 24.5°, 25.5°, 33°, 43° and 46.5° ($x \leq 0.8$) (see Figs. 3 - 6). These peaks were absent with higher concentration of ZnI_2. A complex amorphous with a several peaks which are shifted from the original position and reducing the intensity are indicates that the complexation between AgI and ZnI_2 has been taken place. The salt added in AgI form complexation disrupted the crystalline of AgI and converting them into an amorphous phase. When the salt concentration exceeding the amount of which contributed to the maximum conduction, the conductivity will decrease as the mobile or the number of free charge carrier of ion decreases. The degree of crystalline is related to the coherent or Scherer length. For AgI - ZnI_2, the coherent length of each composition was evaluated from the diffraction peak at $2\theta = 23^{0}$.

Table 1 Coherent length of (x)AgI-(1-x)ZnI_2.

x	Coherent length (L)
AgI	6.97
0.9AgI-0.1ZnI_2	7.713
0.8AgI-0.2ZnI_2	9.918
0.7AgI-0.3ZnI_2	6.97
0.6AgI-0.4ZnI_2	9.98
0.5AgI-0.5ZnI_2	8.67

Table 1 shows that the sample with x = 0.7 has the smallest coherent length and therefore is the most amorphous sample. Coherent length will decrease with increases of the amorphous nature of the sample. The larger the coherent length, the more crystalline are the materials. The amorphous / crystalline nature will affect the electrical conductivity of the samples. In general, the conductivity is increases as the degree of crystallinity decreases.

The impedance spectroscopy results revealed the electrical properties of AgI-ZnI_2 at room temperature and had been used for determination of electrical conductivity dependence are shown in Fig. 7. The interception of the depressed semicircle will give the bulk resistance, $R_{b,}$ value which then used to calculate the electrical conductivity of each composition as display in Table 2.

F. Ibrahim, N.A. Abu Osman, J. Usman and N.A. Kadri (Eds.): Biomed 06, IFMBE Proceedings 15, pp. 144-148, 2007
www.springerlink.com ' Springer-Verlag Berlin Heidelberg 2007

Table 2 Results of conductivity

Mol fraction	Thickness (L) cm	Resistance bulk (Rb)	Conductivity s/cm
AgI	0.778	2816.8	$3.5x10^{-4}$
	0.834	2817.5	$3.7x10^{-4}$
	0.834	2908.95	$3.6x10^{-4}$
0.9AgI-0.1ZnI_2	1.082	410.65	$9.7x10^{-4}$
	1.051	1352.9	$9.8x10^{-4}$
	1.067	1316	$1.0x10^{-3}$
0.8AgI-0.2ZnI_2	1.041	3106.5	$1.4x10^{-4}$
	1.00	2293.2	$5.5x10^{-4}$
	1.14	3009	$4.7x10^{-4}$
0.7AgI-0.3ZnI_2	0.53	136	$5.1x10^{-3}$
	0.57	130	$5.6x0^{-3}$
	0.61	117	$6.6x10^{-3}$
0.6AgI-0.4ZnI_2	0.927	1033.5	$1.13x10^{-3}$
	0.888	669	$1.7x10^{-3}$
	0.89	831	$1.4x10^{-3}$
0.5AgI-0.5ZnI_2	0.935	2041.8	$5.5x10^{-4}$
	0.883	2192.85	$5.1x10^{-4}$
	0.887	1575	$7.1x10^{-4}$

From the table it shows that a sample with the highest conductivity $6.6x10^{-3}$ S/cm was contained 0.3ZnI_2. In pure AgI, the conductivity is lower. Therefore the initial rise in ZnI_2 contained can be attributed to the increasing in the number of charge carriers and also to the decreasing in crystalline of the system.

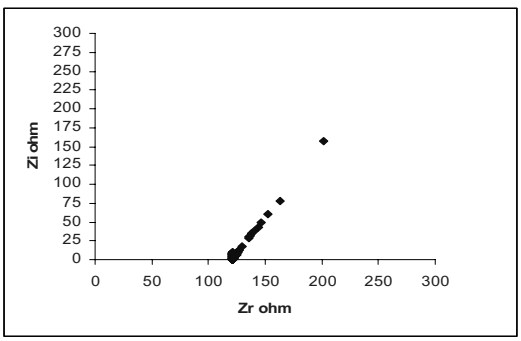

Fig. 7 Impedance plot of 0.7AgI-0.3ZnI_2

Meanwhile, the decreases in the conductivity for higher ZnI_2 concentration can be explained as the decreases either in mobility or in the number of free charges carrier or both. 0,9 chFig. 8, show some variation of conductivity. The trend of conductivity can be explained in term of the degree of crystallinity of the sample. It is well known that the ionic conductivity occurred in the amorphous region. Hence the increasing the amorphous region will increase the conductivity of material. The conductivity was maximum at x = 0.7.

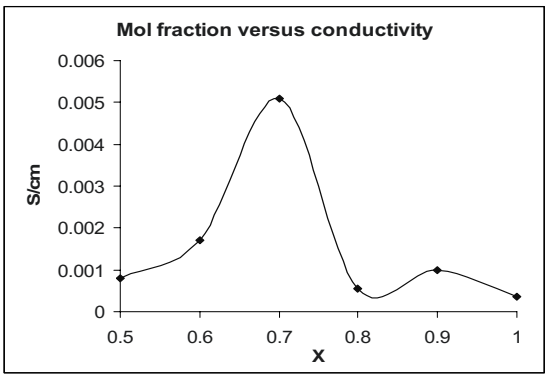

Fig. 8 Mol fraction versus ZnI_2 content in AgI

IV. Conclusion

At a room temperature, the mixture of (x)AgI - (1-x)ZnI_2 show some improvement in the ionic conductivity. It is shown that by adding a certain amount of ZnI_2 will give certain value of conductivity. Therefore, the ionic conductivity in a material can be increase/decrease by controlling the amount of composition of the material. From the results it is shown that the highest conductivity in xAgI - (1-x)ZnI_2 at chemical composition 0.7AgI-0.3ZnI_2 at room temperature with the value is $6.6x10^{-3}$S/cm. This will confirm that the ionic conductivity will be increase with increases of the amorphous region but the conductivity in amorphous region was limited by the charges carrier or by mobility of ions.

F. Ibrahim, N.A. Abu Osman, J. Usman and N.A. Kadri (Eds.): Biomed 06, IFMBE Proceedings 15, pp. 144-148, 2007
www.springerlink.com ' Springer-Verlag Berlin Heidelberg 2007

References

1. A. Dalvi , K. Shahi b. (2004) Formation of superionically conducting amorphous phase in mechanically-milled AgI Ag2O V2O5 system. *J. Non-Cryst. Solids.* **341 (2004)** 124 132.
2. M. A. Urena, A. A. Piarristeguy, M. Fontana, B. Arcondo. Ionic conductivity (Ag+) in AgGeSe glasses. *J. Sol. State Ionics* **176 (2005)** 505 512
3. A. K. Arof. Characterization of silver ion conductors and battery performance (1996) *Ph.D Thesis,* Universiti Malaya.

Author: Mohd Rafie Johan
Institute: Department of Mechanical Engineering
University of Malaya, 50603
Kuala Lumpur, Malaysia
Email: mrafiej@um.edu.my

F. Ibrahim, N.A. Abu Osman, J. Usman and N.A. Kadri (Eds.): Biomed 06, IFMBE Proceedings 15, pp. 144-148, 2007
www.springerlink.com ' Springer-Verlag Berlin Heidelberg 2007

Synthesis and characterization of nanocrystalline hydroxyapatite powder via sol-gel method

A. H. Rajabi, A. Behnamghader, A. Kazemzadeh, F. Moztarzadeh

Materials and Energy Research Center, Tehran, Iran

Abstract— **Nanocrystalline hydroxyapatite (HAP) powder was synthesized by a non-alkoxide sol-gel method. The prepared powder was characterized with STA, X-ray diffraction, Zetasizer and SEM microscopy. The effect of aging for 24h and heating time at 550ºC on crystallity, crystallite and particle size were studied through XRD, zetasizer and SEM. Results showed that the powder obtained after heating at 550ºCfor 6h was composed of pure HAP with the estimated crystallite size and particle size of 9.3 nm and 503.6 nm.**

Keywords— **Hydroxyapatite, sol-gel, Nanocrystalline powder**

I. Introduction

Bone is a composite of an organic collagenous tissue and an inorganic phase which is mainly composed of hydroxyapatite $Ca_{10}(PO_4)_6(OH)_2$. Hydroxyapatite (HAP) is a calcium phosphate material with little bioresorbablity and therefore suitable for long term clinical applications [1]. For the synthesis of HAP, different techniques have been developed including mechanochemical [2], combustion preparation [3], co-precipitation [4], electrochemical deposition [5], hydrothermal synthesis [6], emulsion or micro-emulsion routes [7] and sol-gel process. The latter method is a new wet chemical route having significant advantages in comparison with the other methods. Increased homogeneity due to molecular mixing of the component ions, lower sintering temperatures resulted from small particle sizes and the ability of preparing thin bioactive films on hard tissue implants are some of the advantages of this method [8]. In this research sol-gel method has been used to prepare HAP powder.

II. Experimental procedure

Analytical grade calcium nitrate tetrahydrate $Ca(NO_3)_2.4H_2O$ was dissolved in medical grade ethanol (96%) to form a 1.67 *M* solution. Analytical grade phosphoric pentoxide P_2O_5 was also dissolved in the same alcohol to form a 0.5 *M* solution. The solutions were mixed to achieve the Ca/P ratio of 1.67. The color of the mixture changed to white as soon as the precursors were mixed whereas they were absolutely colorless before being mixed. The mixture was stirred at ambient temperature for 30 minutes and subsequently heated in water bath at 60 C for 1 h. During heating the viscosity of the gel increased while its transparency decreased. The gel was then divided to two parts. The first part dried in an electric oven at 80 C for 24 h and the second part was aged in ambient temperature for 24 h and dried in the same way. The samples were next heated in an electric furnace at 550 C for 1h and 6 h. The produced powders were finally crushed with an agate mortar and pestle.

To study the thermal behavior of the gel, the as-dried gel was analyzed through thermogravimetric and differential thermal analyses (DTA/TG) using a PL-1640 in air and with the heating rate of 10 ^oC/min up to 900^oC. Phase characterization was studied with X-ray diffraction using Siemens D-500 with Cu K ά radiation (λ=1.5405Å) and the evaluation of the particle size was done with Malvern 3000 HSA Zetasizer using the wavelength of 633.0 nm at ambient temperature.

III. Results and discussion

DTA/TG analyses: Fig.1 shows the differential thermal analysis/thermo gravimetric analysis of the dried gel. The weight loss happened at ~200 C can be related to the evaporation of the crystalline water in $Ca(NO_3)_2.4H_2O$. The differential thermal analysis also shows a broad endotherm at this temperature. The sharp endothermic reaction illustrated at about 530 C could be related to the removal of the NO_3 groups [9]. Since no significant weight loss appeared above 530 C, all the dried gels were heated at the same temperature i.e. 550℃for 1h and 6h to compare the effect of heating time on the phase formation and crystallity.

XRD Patterns: Fig. 2 shows the XRD patterns of the gel aged in ambient temperature for 24h and dried at 80℃ for 24h show the presence of $Ca(NO_3)_2.4H_2O$, P_2O_5 and a very small amount of HAP phases. In contrast the samples prepared in the same way and heated in the electric furnace at 550℃ for 1h and 6h show a pure HAP phase. Similar results have also been reported by Seok [11]. It can be seen that as the time of heating differs from 1h to 6h the intensity

F. Ibrahim, N.A. Abu Osman, J. Usman and N.A. Kadri (Eds.): Biomed 06, IFMBE Proceedings 15, pp. 149-151, 2007
www.springerlink.com ' Springer-Verlag Berlin Heidelberg 2007

of HAP lines increases showing the increase of the crystallite degree whereas no new phase has been appeared.

Fig. 3 illustrates the XRD patterns for two different aging times. The crystallite size can be estimated from broadening of XRD peaks using Scherer's formula [10].

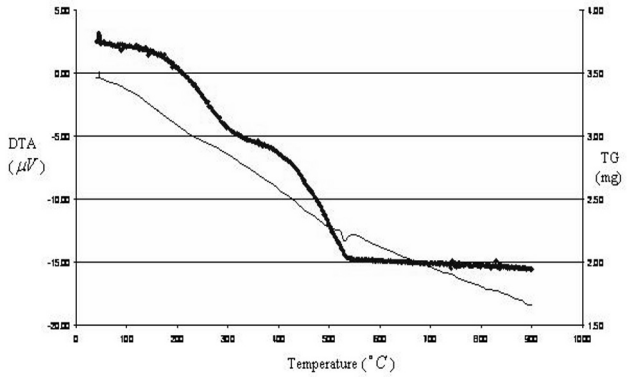

Fig. 1. Differential thermal analysis/thermo gravimetric analysis of the 24 h aged dried gel.

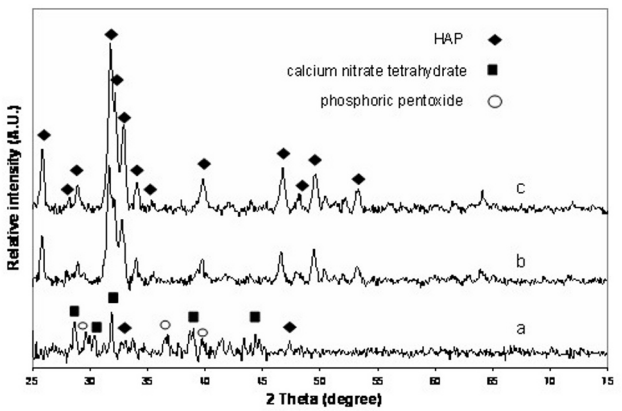

Fig. 2. XRD patterns for the dried gel (a), and the powders heated at 550℃ for 1h (b) and 6h (c).

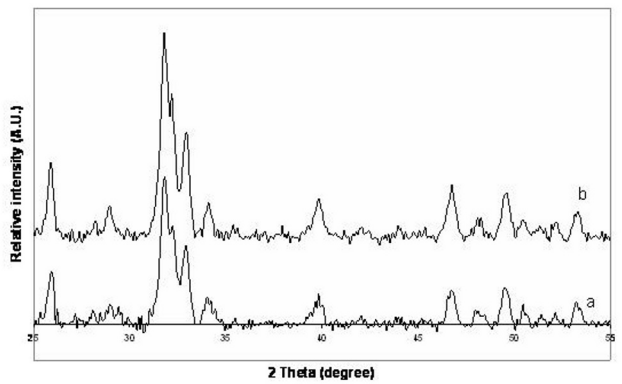

Fig. 3. XRD patterns of the samples heated for 6h at 550℃ with different aging times: 24h (a) and not aged (b).

$$t = \frac{0.9\lambda}{BCos\theta}$$

While t is the average grain size,λ the wave length, B the diffraction peak width of the half maximum intensity and θ is the Bragg diffraction angle. Through this method the crystallite sizes were estimated to be about 8.1 nm for the aged powder and about 9.3 nm for the powder without aging. According to the results of the XRD analysis and Scherer's estimation, it can be concluded that for aging periods in this study no significant change can take place in the crystallite size of the powder. TEM images reported by Feng [8] show that increasing the aging time from 4h to 48h increases the crystallite size from 10-15nm to 15-25 nm. Thus it seems that it could be better to use Scherer's estimation and direct observation via transmission electron microscopy simultaneously.

Particle size measurements: The zeta particle size distribution of the powder heated for 6h at 550℃without aging and aged for 24h are shown in Fig. 4 and 5 respectively. Aging time has increased the mean size of the particles from 503.6 to 788.6 nm that can be related to its effect on the powder growth and agglomeration.

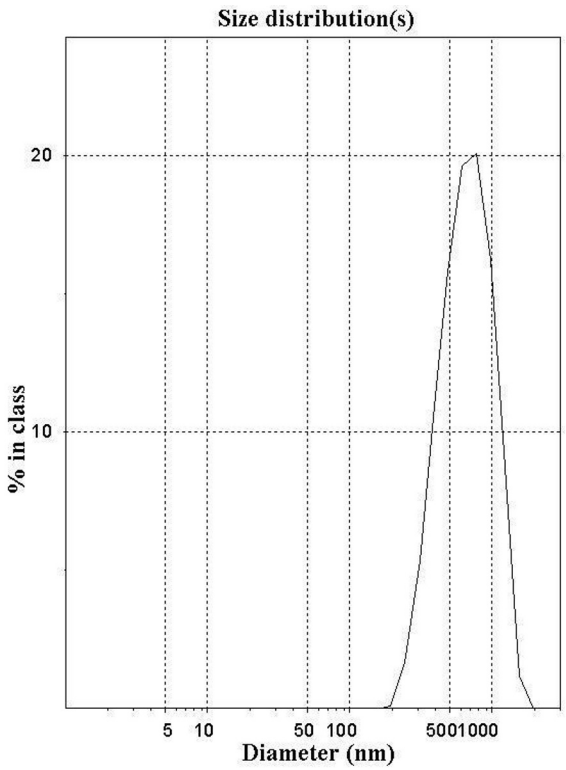

Fig. 4. Particle size distribution of the powder heated for 6h at 550℃without aging.

F. Ibrahim, N.A. Abu Osman, J. Usman and N.A. Kadri (Eds.): Biomed 06, IFMBE Proceedings 15, pp. 149-151, 2007
www.springerlink.com ' Springer-Verlag Berlin Heidelberg 2007

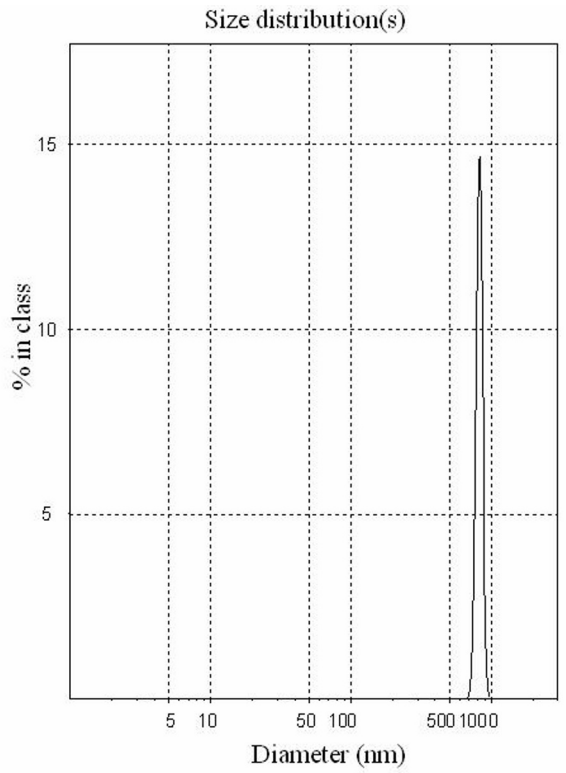

Fig. 5. Particle size distribution of the powder heated for 6h at 550℃ with the aging time of 24h

IV. Conclusions

HAP is synthesized through heating the dried gel formed by mixing $Ca_{10}(PO_4)_6(OH)_2$ and P_2O_5 in ethanol medium. Heating the dried gel at 550℃for 1h causes the formation of pure nanocrystalline HAP and the increase of heating time to 6h increases the crystallity of the pure HAP phase.

Aging the gel for 24h causes no significant change in the crystallite size of the powder whereas it increases the mean size of the particles. Controlling the labratorial conditions, refluxing the precursures, modifying the mixing procedure, stirring time and speed and the amount of the gel can be effective on the repeatability and the results of the experiment. It seems that longer aging periods need to be studied to define its effect on the crystallite and particle size. Achieving pure nanocrystalline HAP in this study suggests that through coating titanium implants with HAP via sol-gel, the oxidation of the substrate can be prevented due to low sintering temperatures.

References

[1] Bengt Sanden, Ph.D. thesis, " Clinical and Experimental Studies on the Effects of Hydroxyapatite Coating", Uppsala University, Faculty of Medicine, 2001.
[2] C.C. Silva, A.G. Pinheiro, R.S. de Oliveira, J.C. Go·es, N. Aranha, L.R. de Oliveira, A.S.B. Sombra, Materials Science and Engineering C 24 (2004) 549.
[3] A.C. Tas, J. Eur. Ceram. Soc. 20 (2000) 2389.
[4] A. Cuney Tas, F. Korkusuz, M. Timicin, N. Akkas, J. Mater. Sci. Mater. Med. 8 (1997) 91.
[5] L.Y. Huang, K.W. Xu, J. Lu, J. Mater. Sci., Mater. Med. 11 (2000) 667.
[6] H. S. Liu, T. S. Chin, L. S. Lai, S.Y. Chiu, K. H. Chung, C. S. Chang, M. T. Lui, Ceram. Int. 23 (1997) 19.
[7] G.K. Lim, J. Wang, S.C. Ng, L.M. Gan, J. Mater. Chem. 9 (1999) 1635.
[8] Wang Feng, Li Mu-sen, Lu Yu-peng, Qi Yong-xin, Materials Letters 59 (2005) 916.
[9] D.-M. Liu, T. Troczynski, W.J. Tseng, Biomaterials 22 (2001) 1721.
[10] B.D.Cullity, Elements of X-ray diffraction, 2nd ed., Addison- Wesley publishing , 1977.
[11] Il-Seok Kim, Prashant N. Kumta, Materials Science and Engineering B 111 (2004) 232.

Address of the corresponding author:

Author: Aliasghar BEHNAMGHADER
Institute: Materials and Energy Research center
P.O. Box: 14155-4777
City: Tehran
Country: Iran
Email: a_behnamghader@merc.ac.ir

F. Ibrahim, N.A. Abu Osman, J. Usman and N.A. Kadri (Eds.): Biomed 06, IFMBE Proceedings 15, pp. 149-151, 2007
www.springerlink.com ' Springer-Verlag Berlin Heidelberg 2007

The effect of sample preparation and calcination temperature on the production of hydroxyapatite from bovine bone powders

J.A. Toque[1, 2], M.K. Herliansyah[1, 3], M. Hamdi[1], A. Ide-Ektessabi[4], M.W. Wildan[3]

[1]Department of Engineering Design and Manufacture, Faculty of Engineering, University of Malaya, Kuala Lumpur, Malaysia
[2]Department of Mechanical Engineering, University of the Philippines, Diliman, Quezon City, Philippines
[3]Department of Mechanical Engineering, Gadjah Mada University, Yogyakarta, Indonesia
[4] International Innovation Center, Kyoto University, Sakyo-ku, 606-8501, Kyoto, Japan

Abstract— **The production of hydroxyapatite (HA) from bovine bones was studied in this paper. Bovine hydroxyapatite (BHA) was produced from bovine bone powders by calcination without compaction. The powders were calcined at temperatures ranging from 700-1100ºC. It was discovered that sample preparation has some influence on the calcination behavior of the bovine bone powders. XRD results confirmed that HA has been successfully produced but traces of α-TCP and β-TCP were also found. The Ca/P ratios of the BHA powders produced from the process have values greater than 2.0.**

Keywords— **bovine bone, hydroxyapatite, cortical bone, calcination**

I. Introduction

Hydroxyapatite [$Ca_{10}(PO_4)_6(OH)_2$] is a calcium phosphate-based compound classified as a bioceramics. Various studies showed evidence that HA has good biocompatibility and bioactivity [1-2]. It is generally accepted that the human bone is composed of 70% mineral and 30% organic compounds, where 95% of the mineral phase is HA [3]. This greatly contributes to the performance of HA in biological studies.

HA can be used either as a bone graft or a coating material. In coating application, it is normally deposited as a thin-film on to metallic implants using various coating techniques (i.e. PVD, CVD, etc.). As a bone graft, it is being used either as dense or porous grafts. However, due to its poor mechanical property, its application is limited to non-load bearing applications. Therefore it is a must to find ways how to resolve this issue.

Due to the attractive properties of HA, various techniques have been and are being developed to produce hydroxyapatite. It can either be through chemical synthesis such as wet-precipitation [4-5], sol-gel method [6], hydrothermal method, thermal deposition, continuous precipitation [7], etc. It can also be synthesized from natural source such as corals [8], egg shell [9] and bovine bone [10].

This paper focuses on producing hydroxyapatite from bovine source, especially cow bone since it is readily available in Malaysia and has been proven to be a good source of quality HA. Two important process parameters such as bovine bone preparation and calcination temperature were studied. The result of this study has been compared to other studies done previously that utilized a different way of sample preparation.

II. Materials and methods

A. Sample Preparation

Cortical bovine bones were collected from the local slaughter houses. The procured bone samples were cleaned using boiling method to remove organic substances and collagen. This was done to avoid soot formation in the material during the calcination process. Raw bone was boiled in water for 30 minutes at 99.5ºC, and then the water was removed and the bones were washed using fresh water. This process was repeated trice until it yielded white and clean samples. Before boiling, the macroscopic adhering impurities and substances, which include the ligaments and tissues that stick on the bone were shaved and removed. After boiling, the bone samples were sun-dried for 3 days. The dried cortical bone samples were cut into shape using hacksaw. The bone powders from cutting chip or sawdust were collected and used for this experiment.

The bone powders were calcined in a box furnace at the following temperatures: 700ºC, 800ºC, 900ºC, 1000ºC, and 1100ºC; with a temperature rate of 5ºC/min. The temperature was maintained for 2 hours to remove the organic matrix. The bovine bone powders were cooled to room temperature by slow furnace cooling.

B. Evaluation and measurement

The bone powders calcined at various temperatures were analyzed using XRD with a monochromated CuKα radiation. A scan speed of 7" per minute and a step scan of 0.02" were employed. The chemical elements of calcined specimens were analyzed by EDX. The Ca/P ratio was determined by calculating the calcium and phosphorous content

F. Ibrahim, N.A. Abu Osman, J. Usman and N.A. Kadri (Eds.): Biomed 06, IFMBE Proceedings 15, pp. 152-155, 2007
www.springerlink.com ' Springer-Verlag Berlin Heidelberg 2007

of the identified compounds containing both elements and compared with the stoichiometric ratio.

III. Results and discussion

A. Bovine hydroxyapatite and other CaP phases

The XRD pattern of the specimens (Fig 1.a) showed peaks characteristic of that of HA (JCPDS 9-432). Majority of the peaks belong to HA. However the result of characterization of the specimen produced some intriguing results. The XRD patterns, shown in Figure 1.a of the specimen calcined at different temperatures indicate traces of α-TCP and β-TCP even when sintered at relatively low temperature. This means that the decomposition of HA to other phases happened at a lower temperature of what is expected. Previous studies showed that these phases start to transform at temperature above 1000℃ [11-12]. In the XRD result, these phases are detected to have been present with temperature as low as 700℃. Several reasons are believed to have caused this so-called untimely transformation.

One of the reasons would be specimen preparation. Previous studies used different means in preparing the sample. In those studies, commercial HA powders were used. They were compacted and then sintered at different temperatures. Those can be considered as bulk samples [11-13].

The present study used bovine powders which are not compacted. Since the powders were not compacted, it facilitated the transfer of heat more effectively. This owes to the fact that powders have bigger surface area to volume ratio. This may not seem significant on a large scale but since powders are on the scale of microns to sub-microns, this has tremendous effect. The ratio could go up to an order of as high as 10^6-10^9. Having a large ratio means that the effect of heating can occur at much lower temperature than expected. In addition, since the specimens were in powder form, the organic components of the bone can easily be removed and therefore will require lower temperature and lesser time to initiate the growth of HA phase

It should be noted that the bovine powders in these experiment were calcined to produce the HA whereas in the previous studies, the commercial HA were heated to sinter the compacted powders and not to produce it. The intents of utilizing the heating process were different but the some similar phenomenon can be observed.

Figure 1.b supports the argument presented. It shows the XRD pattern of bulk bovine bone calcined at the same conditions from a previous study [14]. It can be seen that the transformation of HA to β-TCP for the samples in Fig.1b started to occur at a calcination temperature of 1100℃ which is in agreement to other previous studies.

The experiment of Fig.1a and Fig.1b differs in the sample preparation. In the latter, the bulk bovine bone was calcined without prior defatting. On the other hand, the powders used in this experiment were collected from defatted bovine bones. Defatting was done by successive boiling and washing.

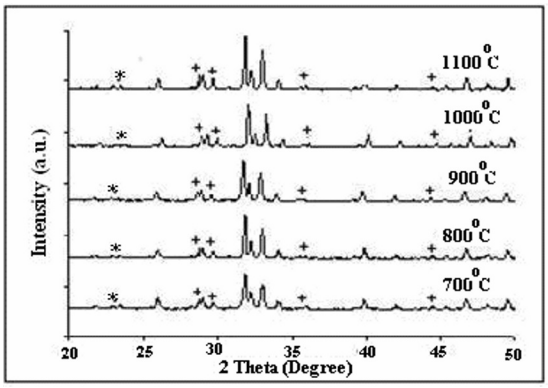

(a)

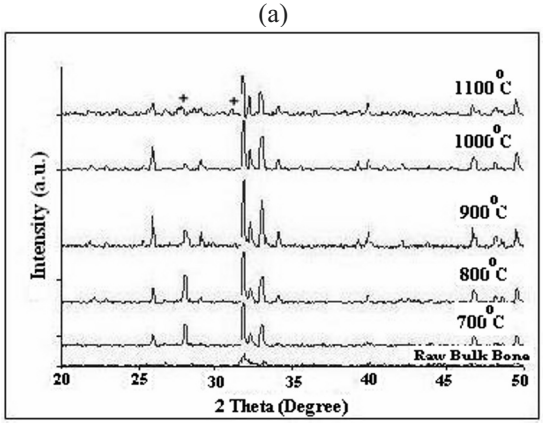

(b)

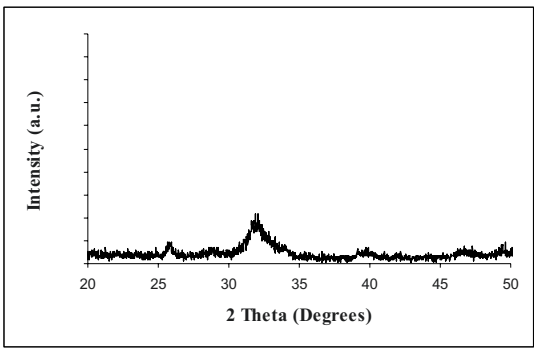

(c)

Fig. 1 XRD patterns of the calcined and as received bovine bone. (a) calcined bovine bone powders; (b) calcined bulk bovine bone [14]; (c) as received bovine bone powder (Key: + = β-TCP; * = α-TCP; unmarked peaks belong to BHA).

F. Ibrahim, N.A. Abu Osman, J. Usman and N.A. Kadri (Eds.): Biomed 06, IFMBE Proceedings 15, pp. 152-155, 2007
www.springerlink.com ' Springer-Verlag Berlin Heidelberg 2007

Moreover, Figure 1.c shows the XRD pattern of the raw bovine bone powders. It resembles a pattern of that of an amorphous phase. It can be seen that the peaks which manifested after subsequent heating was not present from the starting material and that the calcium phosphate phases identified after heating resulted from the calcination process.

In addition, the presence of other calcium phosphate phases may not be all bad. Some recent studies revealed that biphasic calcium phosphate produced good results in biological studies [15-20], while other studies showed that the presence of these other phases contribute to the rapid dissolution when implanted in to the body [21]. These phases coexisting with HA might provide better anchorage for bony tissues since they dissolve faster in physiological fluid. The next step of this study is to evaluate the mechanical properties and biological properties of the bovine HA powders.

B. Calcium to phosphorous ratio

The chemical composition of the bovine bone powders were characterized using EDX. The results are able to confirm the presence of the inorganic contents found in a bovine bone. Among the elements identified, calcium and phosphorous are the most abundant. Base on the spectra of the results, the Ca/P ratios were calculated from the weight percentage [11].

Figure 2 shows the graph of the Ca/P ratio of the bovine bone powders calcined at different temperatures. The ratios of the powders produced from this experiment deviates significantly from that of the theoretical Ca/P ratio of stoichiometric HA which is 1.67. There is no general pattern on the ratio plot as function of temperature. However it is interesting to note that the lowest ratio was achieved at 900℃ calcination temperature. This temperature have been previously identified in other bovine bone HA studies as the temperature where HA yielded good results from characterization [14].

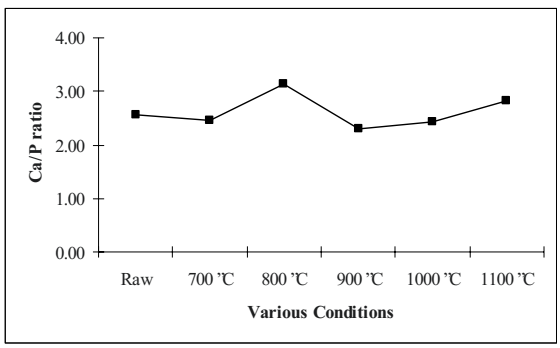

Fig. 2 Plot of the Ca/P ratio as a function of calcination temperature.

The significant difference in the Ca/P ratio acquired from this study compared to the theoretical ratio may be due to the fact that significant amounts of non-HA phases nucleated from the process. The abundance of these other CaP phases (i.e. α-TCP, β-TCP and other CaP phases in smaller quantities) may have contributed to the seemingly contentious behavior of the Ca/P ratio plot. These other phases may have resulted from the way the samples were prepared. Other similar studies on the production of bovine HA were produced using bulk bones cut into cubic shapes while the present study was fabricated from bovine bone powders.

In addition, in the study of Kitty van Dijk et al, they proposed that the high Ca/P ratio of magnetron sputtered CaP coating may have been due to the presence of other calcium-rich phases or phosphorous-poor phases which may not be as dominant as the other expected CaP phases [22].

Another factor that may have an impact on the Ca/P ratio was the source of the bovine bone used in the experiment. It is possible that different nourishments, origin and age of the bone source affected the amount of inorganic compounds and minerals found in it. Calcination only removes the organic compound of the raw bone and facilitates the transformation of other compound phases, but it does not initiate the growth of new elements or components which were not initially present.

IV. Conclusions

Bovine hydroxyapatite (BHA) was successfully produced by calcinating bovine bone powders. The results showed that BHA can be harnessed at a much lower temperature when calcined as a powder without compaction as compared to calcination of the bulk bones. This finding may be quite promising since this will lessen the time of BHA preparation and will also enable it to be produced at lower temperatures.

It was also found out that calcinating in powder form lowers the temperature by which α-TCP and β-TCP start to decompose which may be due to the higher surface to volume ratio of powders as compared to bulk form.

The results of this study confirm that raw material preparation has significant effect in the calcination behavior of bovine bone in producing hydroxyapatite.

Acknowledgment

This work was supported by a grant from the JICA-AUN SEED Net collaborative research program. The authors are very grateful to Mrs. Halipah and Mr. Shahril of the University of Malaya for the assistance in the preparation and characterization of samples in EDX.

F. Ibrahim, N.A. Abu Osman, J. Usman and N.A. Kadri (Eds.): Biomed 06, IFMBE Proceedings 15, pp. 152-155, 2007
www.springerlink.com ' Springer-Verlag Berlin Heidelberg 2007

References

1. Yildrim O, Aksakal B, Celik H, Vangolu Y, Okur A (2005). An investigation of the effects of hydroxyapatite coatings on fixation strength of cortical screws. Medical Engineering & Physics 27: 221-228.
2. Jun Y-K, Kim W, Kweon O-K, Hong S-H (2003). The fabrication and biomedical evaluation of alumina reinforced calcium phosphate porous implants. Biomaterials 24: 3731-3739.
3. Toque J, Hamdi M, Ide-Ektessabi A (2006) A review on hydroxyapatite coating using magnetron sputtering, ICMM Proc. Vol. 1, 1st International Conference & 7th AUN/SEED-Net Fieldwise Seminar on Manufacturing and Material Processing, Kuala Lumpur, Malaysia, pp 603-608.
4. Kothapalli C, Wei M, Vasiliev A, Shaw M (2004). Influence of temperature and concentration on the sintering behavior and mechanical properties of hydroxyapatite. Acta Materialia 52: 5655-5663.
5. Narasaraju T and Phebe D (1996). Some physico-chemical aspects of hydroxylapatite. J Mat Sci 31: 1-21.
6. Breme J, Zhou Y, Groh L (1995). Development of a titanium alloy suitable for an optimized coating with hydroxyapatite. Biomaterials 16: 239-244.
7. Herliansyah M, Hamdi M, Ide-Ektessabi A, Wildan M (2006). Fabrication of hydroxyapatite bone graft for implant application: a literature study, ICMM Proc. Vol. 1, 1st International Conference & 7th AUN/SEED-Net Fieldwise Seminar on Manufacturing and Material Processing, Kuala Lumpur, Malaysia, pp 559-564.
8. Roy D, Linnehan S (1977). Hydroxyapatite formed from coral skeletal carbonate by hydrothermal exchange. Nature 247: 2012 2014.
9. Lee S and Oh S (2003). Synthesis of biocompatible calcium phosphate powders by using egg shell. Key Eng Mats 240-242: 35-38.
10. Huffman E and Keil R (2003). Determination of trace organic carbon and nitrogen in the presence of carbonated in anorganic bovine bone graft materials. Microchemical Journal 74: 249-256.
11. Muralithran G, Ramesh S (2000). The effects of sintering temperature on the properties of hydroxyapatite. Ceram Int 26: 221-230.
12. Tampieri A, Celotti G, Szontagh F, Landi E (1997). Sintering and characterization of HA and TCP bioceramics with control of their strength and phase purity. J Mat Sci: Mat Med 8: 29-37.
13. Rao W and Boehm R (1974). A study of sintered apatites. J Dent Res 53: 1351-1354.
14. Ooi C.Y (2005). Fabrication of calcium phosphate bioceramics by using bovine bone. Masters Thesis, University of Malaya, Kuala Lumpur Malaysia.
15. Kalita S, Bhardwaj A, Bhatt A (2006). Nanocrystalline calcium phosphate ceramics in biomedical engineering. Mat Eng C (In Press, Corrected Proof).
16. Trojani C, Boukhechba F et al (2006). Ectopic bone formation using an injectable biphasic calcium phosphate/Si-HPMC hydrogel composite loaded with undifferentiated bone marrow stromal cells. Biomaterials 27: 3256-3264.
17. Nihouannen D, Guehennec L et al (2006). Micro-architecture of calcium phosphate granules and fibrin glue composites for bone tissue engineering. Biomaterials 27: 2716-2722.
18. Santos E, Farina M, Soares G (2006). Specific proliferation rates of human osteoblasts on calcium phosphate surfaces with variable concentrations of α-TCP. Mat Sci & Eng C (In Press, Corrected Proof).
19. Goyenvalle E, Aguado E et al (2006) .Osteointegration of femoral stem prostheses with a bilayered calcium phosphate coating. Biomaterials 27:1119-1128.
20. Curran J, Gallagher J, Hunt J (2005).The inflammatory potential of biphasic calcium phosphate granules in osteoblast/macrophage coculture. Biomaterials 26: 5313-5320.
21. Yang Y, Kim K-H, Ong J (2005). A review on calcium phosphate coatings produced using a sputtering process an alternative to plasma spraying. Biomaterials 26: 327-337.
22. Dijk K (1997). RF magnetron sputter deposition and characterization of Ca5(PO4)3OH- coatings. Doctoral Disseration, Katholieke Universiteit Nijmegen.

Address of the corresponding author:

Author:	Jay Arre Toque
Institute:	Department of Engineering Design and Manufacture, Faculty of Engineering, University of Malaya
City:	Kuala Lumpur, 50603
Country:	Malaysia
Email:	jayarre81@gmail.com

F. Ibrahim, N.A. Abu Osman, J. Usman and N.A. Kadri (Eds.): Biomed 06, IFMBE Proceedings 15, pp. 152-155, 2007
www.springerlink.com ' Springer-Verlag Berlin Heidelberg 2007

Topological Analysis of a Polymer Based Contraceptive Using Atomic Force Microscopy

Sunil Kumar[1], Koel Chaudhury[1], Prasenjit Sen[2] and Sujoy K. Guha[2]

[1]School of Medical Science and Technology, Indian Institute of Technology, Kharagpur 721302, India
[2]School of Physical Sciences, Jawaharlal Nehru University, New Delhi-110067, India

Abstract— **A novel injectable male contraceptive (RISUG®: an acronym for Reversible Inhibition of Sperm Under Guidance) has been developed by our research group and is currently in the advanced clinical trial stage. RISUG® consists of a copolymer styrene maleic anhydride dissolved in dimethyl sulfoxide of a particular formulation and is injected into the lumen of the vas deferens using a no-scalpel approach. Its polyelectrolytic nature induces a surface charge imbalance on the sperm membrane system leading to the leakage of enzymes essential for sperm-egg interaction. In the present study, surface characterization of the contraceptive using atomic force microscopy (AFM) is proposed. RISUG® gel was spin coated on glass sides and hydrolyzed with saline and seminal plasma to mimic *in vivo* conditions. Contact mode atomic force microscopy (AFM) has been used to analyze quantitatively the micro-structural properties of RISUG® and its precipitate in various systems. Hydrolysis of the contraceptive gel resulted in the formation of pores of varying dimensions. RISUG® being a highly charged molecule, as evident from zeta potential measurements, has a tendency to form a complex with ionic biomolecules present in the seminal plasma. This is supported by the experimental observations using AFM. This RISUG® - biomolecule complex possibly acts as an ionic trap for spermatozoa passing through the vas deferens. Micro-structural properties of RISUG® including amplitude (root mean square, peak-to-valley distance, skewness, and kurtosis) and spatial roughness have been studied to understand its response to various physiological conditions.**

I. Introduction

A polymer-based contraceptive, given the name RISUG (an acronym for *R*eversible *I*nhibition of *S*perm *U*nder *G*uidance), injected into the lumen of the vas deferens has been developed by our research group [1]. It requires minimal surgical intervention and its action can last for long [2]. The injection essentially causes a partial blockage of the vas deferens with a regular flow of functionally inactive cells [3]. Sperm production is not blocked; hence there is no significant rise in anti-sperm antibody titres [4]. Non-invasive reversal can be achieved by dissolving the contraceptive in an appropriate solvent and flushing it out of the lumen [5] or by stimulating the vas deferens percutaneously for expulsion of the contraceptive [6].

RISUG consists of a copolymer styrene maleic anhydride (SMA) dissolved in dimethyl sulfoxide (DMSO) of a particular formulation. Evidence indicates that when RISUG comes in contact with the spermatozoa, its polyelectrolytic nature induces a surface charge imbalance on human sperm membrane system. Subsequently, the head swells up and ruptures resulting in leakage of enzymes necessary for fertilization [1, 7]. Spermatozoa breakdown products, as well as whole but damaged spermatozoa, are present in the ejaculate of RISUG injected subjects [5].

AFM has been largely utilized to study biomaterials [8, 9] including polymers [10] and hydrogel [11]. Besides providing a better visualization of surfaces due to its higher sensitivity, AFM allows one to distinguish surface areas of different physical properties. Surface micro-domain structure and characterization of biomaterials roughness are important aspects of biomaterials assessment for their potential biological responses when interfacing with physiological media since protein adsorption, biocompatibility, etc. are influenced [12]. In the present study, surface topography and roughness of RISUG are assessed and nature of micro-domain structures investigated using AFM.

II. Materials and Methods

A. *Zeta Potential Measurements*

10mg SMA / 1 ml DMSO was taken and the zeta potential analyzed using a zeta potential analyzer (ZetaPlus, Brookheaven Instruments Corp, US). Next, RISUG hydrogel was prepared by dissolving 60mg SMA / 120 µl DMSO which was then precipitated with PBS (pH - 7.2). 1 mg of this precipitate in 1ml of PBS was taken and sonicated for 30 min. at 4^0C and zeta potential measured.

B. *Atomic Force Microscopy*

RISUG gel was prepared by dissolving 60mg SMA in 120µl DMSO. This gel was then spin coated on glass sides at 2000 rpm for 30 s. Next, the slides were divided into three groups: Group I consisted of the RISUG gel; Group II and III represented RISUG hydrolyzed with saline and

F. Ibrahim, N.A. Abu Osman, J. Usman and N.A. Kadri (Eds.): Biomed 06, IFMBE Proceedings 15, pp. 156-159, 2007
www.springerlink.com ' Springer-Verlag Berlin Heidelberg 2007

seminal plasma, respectively to mimic *in vivo* conditions. Contact mode scanning was carried out on all the three groups using AFM (ThermoMicroscopes, CP Research Model, Sunnyvale, CA, USA). Silicon Nitride cantilever, 50 μ in length, with a force constant of 0.050 N/m was vibrated near its resonance frequency of ~30 kHz to scan the samples.

C. *Data Analysis*

It is necessary to employ mathematical tools for extracting quantitative information on surface roughness from AFM images. Several amplitude parameters were used. The arithmetic average roughness (R_a) and the root mean square (RMS) roughness (R_q) are given by:

$$R_a = \frac{1}{n_x n_y} \sum_{i=1}^{n_x} \sum_{j=1}^{n_y} \left| Z(i,j) - Z_{ave} \right| \quad (1)$$

$$R_q = \sqrt{\frac{\sum_{i=1}^{n_x} \sum_{j=1}^{n_y} [Z(i,j) - Z_{ave}]^2}{n_x n_y}} \quad (2)$$

where $Z(i,j)$ denotes the topography data for the surface after specimen tilt-correction, Z_{ave} is the average surface height, i and j correspond to pixels in the x and the y direction. The maximum number of pixels in the two directions are given by n_x and n_y [13].

D. *Roughness Analysis*

Statistical analysis of the roughness scaling behavior was performed using the power spectrum (PS) which is the Fourier transform of the height auto-correlation function [14].

$$PS(\ ) = \frac{1}{L} \left| \int_0^L dx e^{i2\pi\ x} [h(x) - < h >] \right|^2 \quad (3)$$

where $PS(\ )$ is the power of the surface wave of frequency , L is the total scan length in μm and x is the spatial variable. The power spectrum of a single image *i.e.* 5 different line spectra on sperm head was recorded and averaged.

*Skewness and Kurtosis:*AFM images were imported in ASCII format to commercial mathematical software, Matlab 7.0 for statistical analysis. Data from the images was used to calculate skewness and kurtosis to describe the probability distribution.

III. Results

Figure 1A and B show the 2D image of RISUG and its saline precipitate, respectively. The height profile in Figure 1C indicates the pore dimensions. Figure 2A and B represent the 3D images of RISUG precipitate in saline and seminal plasma, respectively. Figure 2C shows the 2D image of RISUG precipitate in seminal plasma and its height profile is indicated in Figure 2D. Various roughness parameters calculated for AFM images are tabulated in Table 1. Figure 3 represents the average power spectrum of RISUG and its precipitate in saline and seminal plasma.

IV. Discussion

As sperm cells mature and flow through the epididymis towards the ejaculatory duct, they interact with RISUG , injected into the vas deferens, in the presence of the spermatic fluid rich in biomolecules. The presence of breakdown products of spermatozoa in the ejaculate of subjects injected with RISUG is reported in previous studies [5]. Hence, topological analysis of RISUG in saline and seminal plasma using AFM was studied to understand the *in vivo* mechanism underlying these observations.

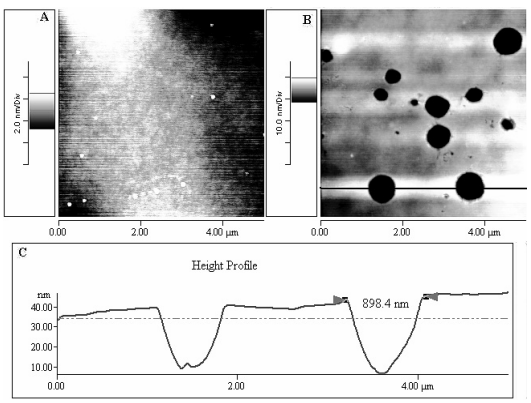

Figure 1: 2D image of RISUG gel spin coated on a glass slide and B) RISUG precipitate in saline. C) Height profiles indicating the width of the pores observed in the RISUG -saline precipitate.

Pores on the surface of thin films are observed in both the systems, saline and seminal plasma precipitate. This may be attributed to phase separation process, wherein a homogeneous polymer film phase separates into regions deficient of the polymer (i.e. pores) and regions rich in the polymer. This observation is in good agreement with the report of Faldi et al. who have shown the formation of holes in the dewetting of one polymer layer from another [15].

F. Ibrahim, N.A. Abu Osman, J. Usman and N.A. Kadri (Eds.): Biomed 06, IFMBE Proceedings 15, pp. 156-159, 2007
www.springerlink.com ' Springer-Verlag Berlin Heidelberg 2007

Since thermal modulation is an important external factor inducing the formation of pores during dewetting process of homopolymers [16], RISUG film development and hydrolysis in saline and seminal plasma was carried out at room temperature. Hence, surface pattern changes in RISUG film may be associated with the intrinsic properties of the copolymer in the films.

A probable theory for the underlying contraceptive mechanism of RISUG is proposed on the basis of the AFM images of RISUG -saline and RISUG -seminal plasma precipitate. High surface charge density of RISUG as indicated by the zeta potential measurements allows the formation of a complex with ionic biomolecules of seminal plasma as observed in Figure 2. This complex has a significant effect on the surface roughness and further restricts the movement of the sperm cells through the vas deferens. It has been reported that cone-shaped nanopores with charged surfaces are ion selective [17]. An electrostatic interaction occurs between the sperm cell and the surface charge on the pore walls. This non-zero surface charge on pores creates an internal electrostatic potential, with a profile dependent on pore shape and size. In a conical pore, this profile resembles an asymmetric ratchet tooth [18], which gives rise to an electrostatic trap for ions at the pore tip [19]. The electrostatic interaction of RISUG with sperm cells subsequently increases the overall surface roughness of the sperm cell which destabilizes its acrosomal membrane. This is followed by the rupture and release of enzymatic fluid rendering the spermatozoa incapable of fertilization [7, 20].

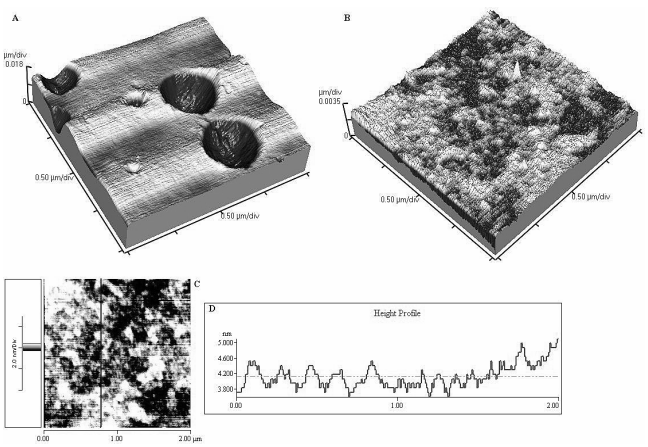

Figure 2: A) 3D image of RISUG precipitate in saline showing pores B) 3D image of RISUG precipitate in seminal plasma showing attached seminal proteins on it. C & D) 2D of RISUG precipitate in seminal plasma and its height profile respectively.

Table 1: Roughness parameters of RISUG and its precipitate in saline and seminal plasma.

Groups	*Rp-v* (nm)	Rq (nm)	Ra (nm)	Mean Height	Volume (μm^3)
RISUG	1.417 –0.43	0.290 –0.10	0.228 –0.07	4.407 –0.778	0.363 –0.104
RISUG - saline precipitate	21.38 –6.94	5.94 –3.26	4.85 –3.0	57.61 –9.849	5.893 –1.280
RISUG - seminal plasma Precipitate	1.997 –0.52	0.3660 –0.04	0.3002 –0.03	38.55 –4.779	3.925 –0.480

Surface roughness parameters affect the real area of contact and hence the friction in micro/nanoscale systems [21]. Therefore, quantitative surface roughness parameters have been calculated from different surfaces. Significant increase in the average, RMS and Rp-v values is observed in the RISUG - saline precipitate. Surfaces with positive skewness and higher kurtosis are known to exhibit lower real area of contact and hence lower friction [22, 23]. High kurtosis (13.283) and negative skewness (-2.6348) of RISUG -saline precipitate indicates the increased resistance to sperm movement trying to pass through the vas deferens injected with the contraceptive. Similarly, increased kurtosis (4.5552) in RISUG - seminal plasma precipitate shows increased micro/ nanoscale friction.

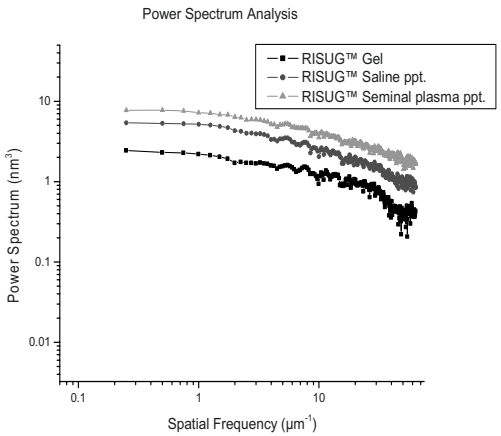

Figure 3: Average power spectrum of RISUG and its precipitate in saline and seminal plasma on a log scale.

Further, power spectrum (PS) analysis has been carried out which provides quantitative information not only on the height deviation of the roughness profile, but also on its lateral distribution (the spatial extent of the height variations in the roughness profile). Decreasing power law dependence of the PS is an indication of the fractal nature of a real surface profile and provides the overall magnitude of the

F. Ibrahim, N.A. Abu Osman, J. Usman and N.A. Kadri (Eds.): Biomed 06, IFMBE Proceedings 15, pp. 156-159, 2007
www.springerlink.com ' Springer-Verlag Berlin Heidelberg 2007

micro-roughness profile. Considerable increase in the spatial roughness of the RISUG seminal plasma precipitate has been observed (Figure 3). This increase in the total surface roughness imparts high resistance to the sperm movement through the vas deferens injected with RISUG .

V. Conclusion

Topological alterations associated with the precipitation of RISUG have been analyzed through AFM, which show the formation of pores with varying dimensions. These pores act as ion traps for sperms cells trying to pass through the vas deferens. Formation of complex between the ionic biomolecules present in the seminal plasma and RISUG indicate an increase in the total surface roughness. This is determined on the basis of the amplitude (average, RMS, and R*p-v*, skewness and kurtosis) and spatial parameters (power spectrum) which show high real area of contact. Increased friction and resistance to sperm movement through the vas deferens by the RISUG complex is, therefore, concluded. The electrostatic interaction between the sperms cells and the charged RISUG complex, in turn, leads to the breakdown of the sperm cells rendering the spermatozoa infertile.

References

1. Guha S K (1996) Contraceptive for use by a male, US Patent (1996): 54880705.
2. Guha S K (2005) RISUG (reversible inhibition of sperm under guidance) An antimicrobial as male vas deferens implant for HIV free semen. Med. Hypotheses 65: 61-64.
3. Chaudhury K, Sharma U, Jagannathan N R, Guha S K (2002) Effect of a new injectable male contraceptive on the seminal plasma amino acids studied by proton NMR spectroscopy. Contraception 66: 199-204.
4. Mishra P K, Manivannan B, Pathak N, et al. (2003) Status of Spermatogenesis and Sperm Parameters in Langur Monkeys Following Long-term Vas Occlusion with Styrene Maleic Anhydride. J Androl 24: 501-509.
5. Koul V, Srivastav A, Guha S K (1998) Reversibility with sodium bicarbonate of styrene maleic anhydride, an intravasal injectable contraceptive in male rats. Contraception 58: 227 231.
6. Guha S K (1999) Non-invasive reversal of intraluminal vas deferens polymer injection induced azoospermia technology. Asian J Androl 1: 131 134.
7. Kumar S, Chaudhury K, Sen P, Guha S K (2006) Topological alterations in human spermatozoa associated with the polyelectrolytic effect of RISUG . Micron 37: 526-532
8. Garrison M D, Ratner B D (1997) Scanning probe microscopy for the characterization of biomaterials and biological interactions. Ann N Y Acad Sci 31: 101-113.
9. Siedlecki C A, Marchant R E (1998) Atomic force microscopy for characterization of the biomaterial interface. Biomaterials 19: 441-454.
10. Glomm B H, Grob M C, Neueschwander P et al. (1994) Characterization of Fibers from poly- (2-Fluorophenylene-2-Fluoroterephthalamide) by A Combination of Waxd and AFM Studies. Polymer 35: 878-881.
11. Han D K, Park K D, Hubbell J A, Kim Y H (1998) Surface characteristics and biocompatibility of lactide-based oly (ethylene glycol) scaffolds for tissue engineering. J Biomater. Sci. Polym. Edn. 9: 667.
12. Schmidt J A, Von Recum A F (1991) Texturing of polymer surfaces at the cellular level. Biomaterials 12: 385-389.
13. Lindseth I, Bardal A (1999) Quantitative topography measurements of rolled aluminium surfaces by atomic force microscopy and optical methods. Surf Coat Tech. 111: 276 286.
14. Voss R F, Pynn R, Skjeltorp A (1985) Scaling Phenomena in Disordered Systems. Plenum 1-11.
15. Faldi A, Composto R J, Winey K I (1995) Unstable polymer bilayers. 1. Morphology of dewetting. Langmuir 11:. 4855-61.
16. Wang M, Zhu X, Wang S, Zhang L (1999) Surface pattern in thin poly(styrene maleic anhydride) films. Polymer 40: 7387-7396.
17. Apel P, Korchev Y E, Siwy Z, Spohr R, Yoshida M (2001) Diode-like single ion-track membrane prepared by electro-stopping. Nucl. Instr. Meth. 184: 337-346.
18. Siwy Z, Fulinski A (2002) Fabrication of a synthetic nanopore ion-pump. Phys. Rev. Lett. 89: 198103.
19. Siwy Z, Heins E, Harrell CC, Kohli P, Martin C R (2004) Conical-Nanotube Voltage-Gated Ion Channel Mimics - The Role of Surface Charge. J. Am. Chem. Soc. 126: 10850-10851.
20. Kumar S, Chaudhury K, Sen P, Guha S K (2004) AFM study of surface structure changes in human spermatozoa treated with RISUG: a new male contraceptive ISAMAP2K4, IIT Kharagpur, India, 2004: 701-08.
21. Chandrasekaran S, Sundararajan S (2004) Effect of microfabrication processes on surface roughness parameters of silicon surfaces Surf. Coat. Tech. 188 189: 581 87.
22. Maboudian R, Howe R T (1997) Critical review: adhesion in surface micromechanical structures J. Vac. Sci. Technol. B 15: 1-20.
23. Chilamakuri S K, Bhushan B (199) A Comprehensive Kinetic Meniscus Model for Predication of Long-Term Static Friction J. Appl. Phys. 86: 4649 4656.

Address of the corresponding author:

Author: Sunil Kumar
Institute: School of Medical Science and Technology, Indian Institute of Technology
City: Kharagpur
Country: India
Email: sunilkumar1@gmail.com

F. Ibrahim, N.A. Abu Osman, J. Usman and N.A. Kadri (Eds.): Biomed 06, IFMBE Proceedings 15, pp. 156-159, 2007
www.springerlink.com ' Springer-Verlag Berlin Heidelberg 2007

Rolling Ball Contact as a method for Testing Surface Fatigue of Resin Based Restorative Materials

N H Abu Kasim[1], J F McCabe[2], Z Radzi[1] and N A Yahya[1]

[1]Faculty of Dentistry, University of Malaya, 50603 Kuala Lumpur, Malaysia
[2]School of Dentistry, University of Newcastle upon Tyne, England

Abstract— **It has been recognised that compressive, tensile and flexural strength do not accurately determine the durability of dental restorations and that fatigue induced failure plays an important role. Fatigue caused by cyclic loading is thought to be responsible for the failure of composites restorations described by chipping, localized or generalized wear and fracture. The main aim of this work is to develop and evaluate the rolling ball contact as a method for testing surface fatigue of resin-based restorative materials. The results showed that material loss during the testing period mimic that of a fatigue failure process occurring in rolling elements. The rolling ball contact method proved to be a simple and reproducible method for testing fatigue in dental composites.**

Keywords— **Fatigue, Rolling ball contact, Composite**

I. Introduction

Failures have occurred since man first built structures and devices. Many failures occurred in components in which the static load bearing capacity was exceeded and the material failed by rupture, buckling and bending. Other failures involved the dynamic application of load causing resonant reaction in a structure, leading to failure. Where cyclic loads were applied, other failures occurred and this was attributed to the material becoming tired, so the term fatigue was coined. Fatigue can be defined as a process of progressive localized permanent structural change occurring in a material subjected to conditions which produce fluctuating stresses and strains at some point or points and which may culminate in cracks or complete fracture after a sufficient numbers of fluctuations. Fatigue is often a surface related phenomenon and consists of several distinct processes including cyclic damage, crack initiation, crack growth and final failure.

In the oral cavity, restorative materials such as dental composites are subjected to a combination of movements and loadings in a hostile biological environment, and therefore subject to fatigue. It is now widely recognised that the deterioration of composite restorative materials may be related to fatigue.

Since fatigue plays a major role in the durability of composite restorations, it is therefore important to gain more information on the fatigue behaviour of these materials. Various methods have been used for testing fatigue in general however only two methods have been commonly used for testing of fatigue of dental materials. Firstly, the compressive fatigue testing method and secondly the flexural fatigue testing method (McCabe et al, 1990; Bream et al, 1993; Azer et al, 2001; Frankenberger et al, 2005 and Kuijs et al, 2006). It is the aim of this work to assess a newly developed rolling ball contact fatigue as a method to test surface fatigue for composites, which is less time consuming and possibly used a smaller number of specimens.

II. Materials and Method

The rolling ball contact fatigue test apparatus is illustrated schematically in Figure 1. The test apparatus consists of a balanced beam, ie a quartz rod pivoted by a frictionless hinge mounted on a drill stand. This enables a 200g load be mounted on one end of the rod to apply a compressive load to the other end, where the specimen is located. The specimen which is embedded in polyester resin is held on a PTFE mounting jig with the aid of two screws. The other main component of this apparatus is the V grooved stainless steel rotor which is held in the chuck of an electric motor. When testing a specimen, a 2 mm diameter ruby ball is placed between the V grooved rotor and the specimen surface.

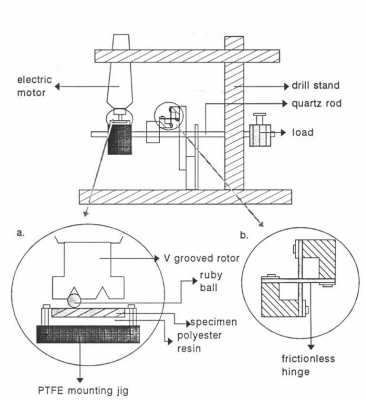

Fig.1 Schematic diagram of the rolling ball contact fatigue apparatus

F. Ibrahim, N.A. Abu Osman, J. Usman and N.A. Kadri (Eds.): Biomed 06, IFMBE Proceedings 15, pp. 160-162, 2007
www.springerlink.com ' Springer-Verlag Berlin Heidelberg 2007

The speed of the rolling ruby ball is determined using a strobe light. A digital tachometer was also used to confirm the speed of rotation of the rotor in order to rule out any harmonic effect from the strobe light.

Discs specimens were prepared using metal washers of approximately 1.5mm thick and 12mm in diameter. The mould is slightly overfilled with the material and a matrix strip was placed over it. Hand pressure was used to press down the matrix strip using a Perspex block, thus expressing the excess material. The specimens were polymerized using a visible light curing unit for 40 seconds. The first cured surface was then polished using 800grit carborandum paper followed by polishing cloth with 7 micron alumina. All specimens were stored in distilled water at 37°C for 24 hours. Prior to testing the specimens were mounted in a polyester resin blocks.

Tests were carried out to assess the reproducibility of the rolling ball contact apparatus using composite P50 3M, USA) using a load of 200g at 17 cycles per seconds. The effect of varying load (175g and 225g) and its reproducibility was also investigated. Specimens tested were profiled using surface profilometer 6 times at intervals (5 X 10^3 cycles up to 2 x 10^4 cycles and every 2 x 10^4 cycles up to 15 x 10^5 cycles) during testing giving a total of 12 equidistant points (Fig. 2) for each fatigue track. All specimens were profiled before testing to provide the baseline data.

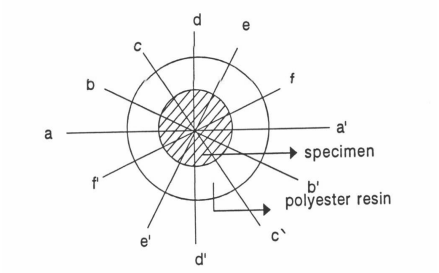

Fig.2 Fatigue track depth measurements

III. Results and discussion

A graph of mean depth (μm) against number of cycles for P50 tested up to 15 x 10^5 cycles. The reproducibility of the results in all the three runs is illustrated in Fig. 3. This graph showed 2 distinct different regions. There was virtually no material loss in the early stages and marked loss of surface material occurred later. This phenomenon is characteristic of a fatigue failure which occurred in rolling elements as described by Scott (1979).

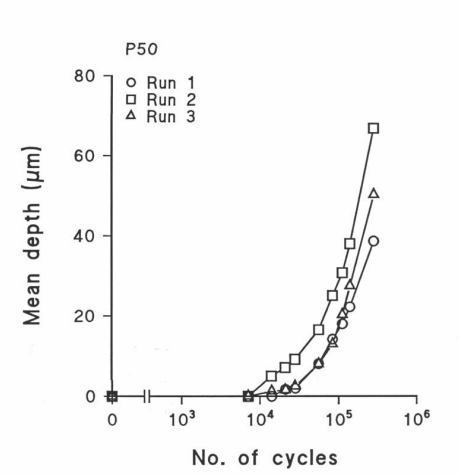

Fig.3 Depth of fatigue track vs. No. of cycles

The effect of varying load was also studied and the result is shown in Fig 4. The reproducibility of the rolling ball contact fatigue test is further substantiated. The standard deviations of each fatigue track depth measurements were also low.

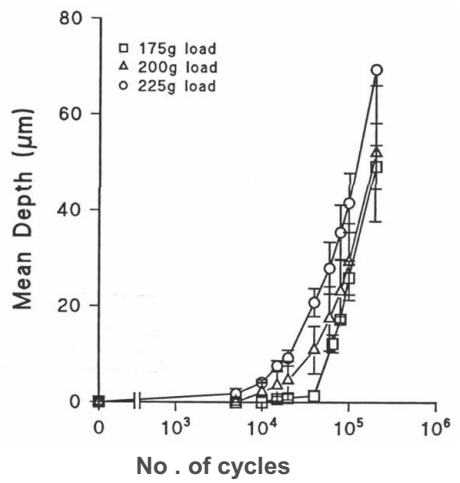

Fig.4 Depth of fatigue track vs. No. of cycles for varying loads

Fig. 5 shows the fatigue track after a specimen was tested up to 4 x 10^4 cycles. It is obvious that is a single track with definite boundaries.

F. Ibrahim, N.A. Abu Osman, J. Usman and N.A. Kadri (Eds.): Biomed 06, IFMBE Proceedings 15, pp. 160-162, 2007
www.springerlink.com ' Springer-Verlag Berlin Heidelberg 2007

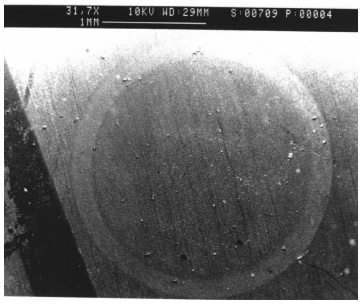

Fig. 5 A single fatigue track generated after completing 4 x 10^4 cycles

Fig. 6 shows a higher magnification at the boundary of the fatigue track. The rolled area (A) appears to be granular with the filler particles being dislodged from the resin matrix. No scouring can be seen in this area indicating a rolling process had taken place throughout the test while polishing lines is evident in the untested area (A). The dislodged filler particles can be seen clearly at higher magnification micrograph in Fig 7.

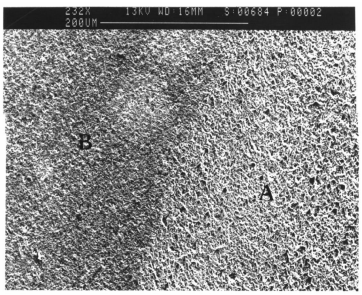

Fig.6 SEM at boundary of fatigue track at 232X

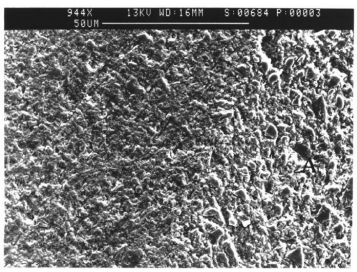

Fig.7 SEM at boundary of fatigue track at 944X

IV. Conclusions

The rolling ball contact test method is a simple and reproducible method of testing fatigue for resin-based restorative materials. Results can be obtained in a short period of time.

Acknowledgment

We would like to appreciate the following people for their contributions to this work; Mr. TE Carrick, Mr. M Gross and Mr. V Wiley.

References

1. Scott D (1979) Rolling contact fatigue. Treatise on Materials Science and Technology 13: 321-361
2. McCabe JF, Carrick TE, Chadwick RC et al (1990) Alternative approaches to evaluating fatigue characteristics of materials. Dent. Mater 6:24-28
3. Bream MJ, Davidson CL, Lambrechts P et al (1993) In vitro fatigue limit testing of dental composites. J. Dent Res. 72:178 Abstr. No. 593
4. Azer SS, Drummond JL, Cambell SD et al (2001) Influence of core buildup material on the fatigue strength of an all-ceramic crown. J Prosthet Dent 86: 624-631
5. Frankenberger R, Garcia-Godoy F, Lohbauer U et al (2005) Evaluation of resin composite materials. Part I: in vitro investigations. Am J Dent 18:23-27
6. Kuijs RH, Fennis WM, Kreulen CM, et al (2006) A comparison of fatigue resistance of three materials for cusp-replacing adhesive restorations.J Dent. 2006 Jan;34(1):19-25

Address of the corresponding author:

Author: Noor Hayaty Abu Kasim
Institute: Faculty of Dentistry, University of Malaya
City: Kuala Lumpur
Country: Malaysia
Email: nhayaty@um.edu.my

F. Ibrahim, N.A. Abu Osman, J. Usman and N.A. Kadri (Eds.): Biomed 06, IFMBE Proceedings 15, pp. 160-162, 2007
www.springerlink.com ' Springer-Verlag Berlin Heidelberg 2007

A Model of Impact Forces during Landing from a Jumping Smash Activity

A.S. Rambely[1], W.A.B. Wan Abas[2]

[1]Centre of Mathematical Sciences, Faculty of Science & Technology, National University of Malaysia, Bangi, Selangor, West Malaysia
[2]Biomedical Engineering Department, Faculty of Engineering, University of Malaya, Kuala Lumpur, West Malaysia

Abstract - **The study discusses a model for impact forces produced during landing from a jumping smash activity. The objectives are to investigate the magnitude of the forces during landing, to observe the angles at the hip and knee joints, as well as the forces in the horizontal axis. The Newton-Euler equation is applied to develop a model that represents the lower limb of a human body. World class badminton player are chosen as subjects during the Kuala Lumpur Thomas Cup 2000. Results show that during landing, the impact forces produced on the landing foot is lower than that of the other foot. Change of the angles on the shank and hip segments shows that subjects flexed their feet when landing to minimize injury.**

Keywords - **Jumping Smash, biomechanics, human movement model, Newton-Euler Equation**

I. INTRODUCTION

A lot of biomechanical studies relating to jumping, either vertical jumping (for example, high jump and counter movement jumping) or horizontal jumping (long jump) have been researched by Bobbert & van Soest [1], Linthorne et al [2], Hatze [3], and Pandy et al [4]. In vertical jumping, researchers interested in the contribution of the human lower limb with height of jump [1] and parameters that can guarantee the height performance [5], whilst in the long jump activity, researchers look at the jumping performance, such as optimal take-off angle [6],[2], run speed [7][8] and jump techniques [9].

Jumping smash in badminton is categorized as vertical jumping. However, limited studies are found regarding a jumping smash model. Thus the objective is to develop a skeletal human model that can be used to observe the impact forces during landing phase in a jumping smash activity. It is hypothesized that landing with both feet will stabilize a body thus decreases the potential injury especially at the lower limb segments. However, the relatively high number of landings using the one-foot pattern might lead to loss of balance and subsequent injury, especially to the ankle and knee joints. Therefore the paper intends to investigate the impact forces during landing and how these forces, during landing, are distributed to the other foot, as well as to look at the angles at the thigh and shank segments.

II. METHOD

The development of the mathematical model uses the Newton-Euler equation to produce a system of linear equations. Kinematic data collected through video capture of landing phase during jumping smash is taken as input in the system of linear equations. The inverse kinematic approach is applied in order to calculate the forces and moments produced during landing from a jumping smash activity.

Video data are collected on badminton games during the men s singles and doubles semi-final and final events of the Thomas/Uber Cup 2000 competition held in Kuala Lumpur, Malaysia, from 11 May to 21 May 2000. Two male players in the single competition are chosen as subjects. The video recording is cropped and jumping activity from take off to landing is edited. The best smash strokes made by each player during the games are selected. The stroke referred to what is perceived, through manual observation, to produce the fastest shuttlecock speed. For each selected player, eight trials in the semi-finals are used in the analysis. Thus a total of 16 trials are involved. Each trial consists of, on average, 60 frames starting from the action of getting ready to the landing position after the smashing stroke. By using Peak Motus 2000, the recoding is analysed and digitized.

III. MATHEMATICAL MODELLING FOR TWO SEGMENTS

In this section, a mathematical model that represents a skeletal model of lower extremities of a body in a horizontal plane is developed using the Newton-Euler equations. This equation describes the forces ($F = m\,a$) and moments ($M = I\ddot{\theta}$) acting on the joints through horizontal and vertical components when a person is in an anatomical position. The two-segment model will be broken up into two separate segments and the modeling process will assume as two separate rigid bodies. The inverse dynamic method is employed for the kinematic data through experimental process which is used as input for the known variables to obtain the unknowns such as the forces and the angular velocities.

F. Ibrahim, N.A. Abu Osman, J. Usman and N.A. Kadri (Eds.): Biomed 06, IFMBE Proceedings 15, pp. 163-166, 2007
www.springerlink.com ' Springer-Verlag Berlin Heidelberg 2007

The model of the lower extremities used in this study is a branching 2-link kinematic chain (Fig. 1). We described the dynamics of this model in mathematical terms, making the following assumptions: (1) The problem can be solved in two dimensions (x-y plane); (2) The model consists of two rigid segments. The first segment is the shank and the second corresponds to the thigh; (3) Each segment has a length, l_i. The width of the segment (the bone) is assumed to be very small compared to the other geometrical measures, so the value can be neglected; (4) There is no influence of the muscles; (5) The movements of interest is the landing phase from an activity of a jumping and landing during a smash motion; (6) The movements of the two segments are illustrated as the movements of two simple pendulum; (7) The first and second links are connected by frictionless spherical joints; (8) The end point is considered free and its position is given by coordinate (x,y); (9) The length l_i , is rigid. For this model the length are, l_1 (rigid) = 0.435 meter (shank) and l_2 (rigid) = 0.410 meter (thigh), which represent a person with height 1.8 meter and weight 74 kg (Winter, 1979); (10) Moment of inersia, I_i, is known by calculation; (11) The joints are assumed to be frictionless and (12) The symbols used in this model are:

F_{ij}^{x} = a force component in x direction exerted by system j on system i
F_{ij}^{y} = a force component in y direction exerted by system j on system i
F_{cgi}^{x} = a force exerted by gravitational force on segment i in horizontal component (x-axis)
F_{cgi}^{y} = a force exerted by gravitational force on segment i in vertical component (y-axis)
m_i = mass of segment i.
l = distance from the joint to the segment s center of mass
I_i = moment of inersia of segment i with respect to the center of mass of segment i.
M_i = moments exerted on the end point nearest to segment i.
M_{cgi} = moments exerted on the end point nearest to center of mass of segment i.
x = horizontal component
y = vertical component
$\dot{x}$ = linear velocity in x-direction
$\dot{y}$ = linear velocity in y-direction
$\ddot{x}$ = linear acceleration in x-direction
$\ddot{y}$ = linear acceleration in y-direction
θ = segment angle in horizontal axis
$\dot{\theta}$ = segment angular velocity
$\ddot{\theta}$ = segment angular acceleration
g = acceleration of gravity

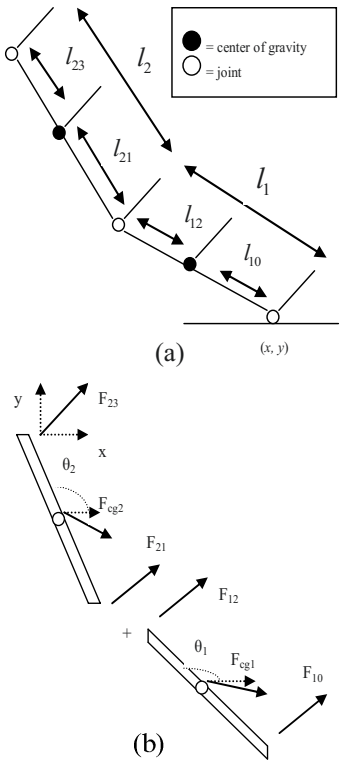

Fig. 1 (a) A model of two segments (b) A system of forces and moments acting on the two segments.

The system in Fig. 1(a) involves two moments. If the simple pendulum above represents a human body, it will show the summation of moments at three joints while a person is in an upright position. In Fig. 1(b), the system shows the forces and moments acting on and exerted by each segment when the pendulum are break up into two separate pendulum. When the two segments is combined, the system will produce two forces acting oppositely on each other at the same joint. Because the force exerted by j on i is the same as that exerted by i on j then $F_{ij} = F_{ji}$ (I = 1, 2).

F. Ibrahim, N.A. Abu Osman, J. Usman and N.A. Kadri (Eds.): Biomed 06, IFMBE Proceedings 15, pp. 163-166, 2007
www.springerlink.com ' Springer-Verlag Berlin Heidelberg 2007

The *x*-component of force for the first and second segments are given by

$$F_{10}{}^{x} - F_{12}{}^{x} + F_{pg1}{}^{x} = m_1 \ddot{x} - m_1 l_{10} \dot{\theta}_1^2 \, kos\, \theta_1 - m_1 l_{10} \ddot{\theta}_1 \, sin\, \theta_1$$

$$F_{10}{}^{x} - F_{12}{}^{x} + m_1 l_{10} \ddot{\theta}_1 \, kos\, \theta_1 = -F_{pg1}{}^{x} + m_1 \ddot{x} - m_1 l_{10} \dot{\theta}_1^2 \, kos\, \theta_1 \quad (1)$$

$$F_{21}{}^{x} - F_{23}{}^{x} + F_{pg2}{}^{x} = m_2 \ddot{x} - m_2 l_1 \dot{\theta}_1^2 \, kos\, \theta_1 - m_2 l_{21} \dot{\theta}_2^2 \, kos\, \theta_2 - m_2 l_1 \ddot{\theta}_1 sin\, \theta_1 - m_2 l_{21} \ddot{\theta}_2 sin\, \theta_2$$

$$F_{21}{}^{x} - F_{23}{}^{x} + m_2 l_1 \ddot{\theta}_1 sin\, \theta_1 + m_2 l_{21} \ddot{\theta}_2 sin\, \theta_2 = -F_{pg2}{}^{x} + m_2 \ddot{x} - m_2 l_1 \dot{\theta}_1^2 \, kos\, \theta_1 - m_2 l_{21} \dot{\theta}_2^2 \, kos\, \theta_2 \quad (2)$$

Similarly, the *y*- component of force for the first segment and second segment is,

$$F_{10}{}^{y} - F_{12}{}^{y} - F_{pg1}{}^{y} = m_1 \ddot{y} - m_1 l_{10} \dot{\theta}_1^2 sin\, \theta_1 + m_1 l_{10} \ddot{\theta}_1 \, kos\, \theta_1$$

$$F_{10}{}^{y} - F_{12}{}^{y} - m_1 l_{10} \ddot{\theta}_1 \, kos\, \theta_1 = -F_{pg1}{}^{y} + m_1 \ddot{y} - m_1 l_{10} \dot{\theta}_1^2 sin\, \theta_1 \quad (3)$$

$$F_{21}{}^{y} - F_{23}{}^{y} + F_{pg2}{}^{y} = m_2 \ddot{y} - m_2 l_1 \dot{\theta}_1^2 sin\, \theta_1 - m_2 l_{21} \dot{\theta}_2^2 sin\, \theta_2 + m_2 l_1 \ddot{\theta}_1 \, kos\, \theta_1 + m_2 l_{21} \ddot{\theta}_2 \, kos\, \theta_2$$

$$F_{21}{}^{y} - F_{23}{}^{y} - m_2 l_1 \ddot{\theta}_1 \, kos\, \theta_1 - m_2 l_{21} \ddot{\theta}_2 \, kos\, \theta_2 = -F_{pg2}{}^{y} + m_2 \ddot{y} - m_2 l_1 \dot{\theta}_1^2 sin\, \theta_1 - m_2 l_{21} \dot{\theta}_2^2 sin\, \theta_2 \quad (4)$$

The momen for the first and second segment is given by,

$$(l_{10} sin\, \theta_1) F_{10}{}^{x} + (l_{12} sin\, \theta_1) F_{12}{}^{x} - (l_{10} \, kos\, \theta_1) F_{10}{}^{y} - (l_{12} \, kos\, \theta_1) F_{12}{}^{y} - I_1 \ddot{\theta}_1 = -M_{cg1} - M_1 + M_2 \quad (5)$$

$$(l_{21} sin\, \theta_2) F_{21}{}^{x} + (l_{23} sin\, \theta_2) F_{23}{}^{x} - (l_{21} \, kos\, \theta_2) F_{21}{}^{y} - (l_{23} \, kos\, \theta_2) F_{23}{}^{y} - I_2 \ddot{\theta}_2 = -M_{cg2} - M_2 + M_3 \quad (6)$$

Now equations (1), (2), (3), (4), (5) and (6) consists of 6 equations with 6 unknowns which are $F_{10}{}^{x}, F_{12}{}^{x}, F_{10}{}^{y}, F_{12}{}^{y}, \ddot{\theta}_1$ and $\ddot{\theta}_2$. Rewrite the equation in a matrix form taking $F_{23}{}^{x} = F_{23}{}^{y} = M_3 = 0$ for the third link does not exist, then

$$\begin{bmatrix} 1 & -1 & 0 & 0 & m_1 l_{10} sin\theta_1 & 0 \\ 0 & 1 & 0 & 0 & m_2 l_{1} sin\theta_1 & m_2 l_{21} sin\theta_2 \\ 0 & 0 & 1 & -1 & -m_1 l_{10} kos\theta_1 & 0 \\ 0 & 0 & 0 & 1 & -m_2 l_{1} kos\theta_1 & -m_2 l_{21} kos\theta_2 \\ l_{10} sin\theta_1 & l_{12} sin\theta_1 & -l_{10} kos\theta_1 & -l_{12} kos\theta_1 & -I_1 & 0 \\ 0 & l_{2l} sin\theta_2 & 0 & -l_{21} kos\theta_2 & 0 & -I_2 \end{bmatrix} \begin{bmatrix} F_{10}{}^{x} \\ F_{12}{}^{x} \\ F_{10}{}^{y} \\ F_{12}{}^{y} \\ \ddot{\theta}_1 \\ \ddot{\theta}_2 \end{bmatrix} \quad (7)$$

$$= \begin{bmatrix} -F_{pg1}{}^{x} + m_1 \ddot{x} - m_1 l_{10} \dot{\theta}_1^2 \, kos\, \theta_1 \\ -F_{cg2}{}^{x} + m_2 \ddot{x} - m_2 l_1 \dot{\theta}_1^2 \, kos\, \theta_1 - m_2 l_{21} \dot{\theta}_2^2 \, kos\, \theta_2 \\ -F_{cg1}{}^{y} + m_1 \ddot{y} - m_1 l_{10} \dot{\theta}_1^2 sin\, \theta_1 \\ -F_{cg2}{}^{y} + m_2 \ddot{y} - m_2 l_1 \dot{\theta}_1^2 sin\, \theta_1 - m_2 l_{21} \dot{\theta}_2^2 sin\, \theta_2 \\ -M_{cg1} - M_1 + M_2 \\ -M_{cg2} - M_2 + M_3 \end{bmatrix}$$

IV. RESULT AND DISCUSSION

Table 1 shows antropometric and kinematic data produced based on anatomical location of markers and anthropometric data given by Winter [10]. The anatomical position is based on a body of 1.8 m height and the kinematic data is based on a body with mass 74 kg.

Referring to Table 1, kinetic data such as forces at the ankle and knee is produced using matrix (7). Result in Figure 2 shows that while landing, the force at the knee is higher than that of the ankle in *x*-direction. On the other hand, force at the ankle is higher than that of the knee in *y*-direction. When a subject is airborne, the force at the ankle is higher than that at the knee in *x*-direction, while the force acting at the ankle in *x*-direction is higher than that in *y*-direction.

Table 1 Anthropometric data for a body with height 1.8 m and weight 74 kg, kinematic data and moment produced from the calculation of mass of two subjects.

Anthropometric Data		
Length of shank l_1	0.435m	
Length of thigh l_2	0.410m	
Length of shank from ankle to cg, l_{10}	0.247m	
Length of shank from knee to cg, l_{12}	0.188m	
Length of thigh from knee to cg, l_{21}	0.232m	
Length of thigh from hip to cg, l_{23}	0.178m	
Segment Length		
proximal	0.567	
distal	0.433	
Segment weight/Total body weight -shank	0.0465	
Segment weight/Total body weight -thigh	0.1	
Radius of gyration for shank cg	0.302	
Radius of gyration for thigh cg	0.323	
Distance from mass center to knee	0.131m	
Distance from mass center to hip	0.132m	
Distance of shank at cg	0.075m	
Distance of thigh at cg	0.075m	
Kinematic Data	**AJC**	**PGC**
Weight	75kg	73kg
Mass first segment m_1	3.488kg	
Mass second segment m_2	7.500kg	7.300kg
Moment of Inersia of shank I_1	0.060kgm^2	0.058kgm^2
Moment of Inersia of thigh I_2	0.131kgm^2	0.127kgm^2
Moment of Inersia at cg of shank Icg_1	0.020kgm^2	0.019kgm^2
Moment of Inersia at cg of thigh Icg_2	0.042kgm^2	0.041kgm^2

From Fig. 2, it can be seen that during landing the forces acting at the ankle and knee joints are lower on the landing foot compare to that of the other foot in both *x*- and *y*-directions. On the other hand, during airborne phase those forces are higher on the landing foot than that of the other foot. This shows that there exists transfer of forces from the landing foot to the other foot during airborne and landing phases.

F. Ibrahim, N.A. Abu Osman, J. Usman and N.A. Kadri (Eds.): Biomed 06, IFMBE Proceedings 15, pp. 163-166, 2007
www.springerlink.com ' Springer-Verlag Berlin Heidelberg 2007

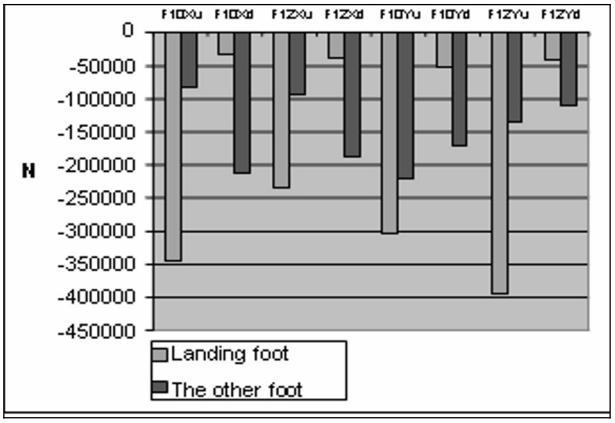

Fig. 2 The forces acting on the ankle (F10) and knee (F12) on both feet while the subject is airborne and during landing

Looking at the angles at thigh and shank, subject tends to flex their foot before landing. This can be seen through change of angles at those segments. The angle at shank is smaller than that of the thigh, which indicates that flexion of the landing foot occurs during landing. Fig. 3 shows an example of change in angles at the two segments.

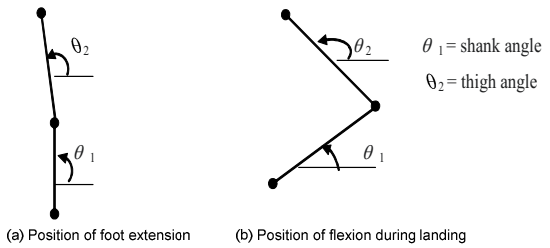

Fig. 3 Change of angles on foot extension and flexion during landing from a jumping activity

The objective of flexion at the knee is to extend the time before landing. The time span can reduce a high impact on the foot during landing from a jumping activity. A maximum impact force is one of the causes of serious injury to the lower limb.

Hypothetically, for those who land on one foot, they might experience a greater injury compare to those land on both feet, for landing with both feet are known to provide a wide base of support. However, Rambely et al has shown that most of the jumping and landing performed by professional players are done using a one-foot technique [11]. Therefore, based on this research, flexion of the landing foot might be one of the techniques adopted by the professional players in order to minimize injury during landing while performing the jumping activity.

V. CONCLUSION

In conclusion, during landing, the impact force produced from the landing foot is smaller compare to that of the other foot. This shows that there exists a transfer of force to the other foot to reduce the potential injury to the landing foot. Furthermore, a flexion of the landing foot plays a significant role in minimizing the risk of injury.

ACKNOWLEDGMENT

The first author is grateful to Faculty of Science and Technology, UKM for the short grant ST-034-2005.

REFERENCES

1. Bobbert, M.F. & van Soest, A.J. (1994). Effects of muscle strengthening on vertical jump height: A simulation study. *Medicine and Science in Sports and Exercise,* **26**, 1012-1020.
2. Linthorne, N.P., Guzman, M.S. & Bridgett, L.A. (2002). The optimum takeoff angle in the long jump. In: Gianikellis, K.E., 20th International Symposium on Biomechanics in Sports, 126-129, Universidad de Extremadura, Spain.
3. Hatze, H. (1981a). A comprehensive model for human motion simulation and its application to the take-off phase of the long jump. *Journal of Biomechanics*, **14**, 135-142.
4. Pandy, M.G., Zajac, F.E., Eunsup, S. & Levine, W.S. (1990). An optimum control model for maximum-height human jumping. *Journal of Biomechanics*, **23**, 1185-1198.
5. Greg, M.P. & Yeadon, M.R. (2000). The influence of touchdown parameters on the performance of a high jumper. *Journal of Applied Biomechanics*, **16**, 367-378.
6. Lees. A., Fowler, N. & Derby, D. (2000). Optimum take-off techniques and muscle design for long jump. *Journal of Experimental Biology*, **203**, 741-750.
7. Bridgett, L.A., Galloway,M., & Linthorne, N.P. (2002). The effect of run-up speed on long jump performance. In: Gianikellis, K.E., 20th International Symposium on Biomechanics in Sports, 80-83, Universidad de Extremadura, Spain.
8. Hay, J.G. (1993). Citius, altius, longius (faster, higher, longer): the biomechanics of jumping for distance. *Journal of Biomechanics*, **26** (Suppl. 1), 7-21.
9. Hay, J.G., Miller, J.A. & Canterna, R.W. (1986). The techniques of elite male long jumpers. *Journal of Biomechanics*, **19**, 855-866.
10. Winter, D.A. (1979). *Biomechanics of human movement*. John Wiley and Sons: New York.
11. Rambely, A.S., Wan Abas, W.A.B and Yusof, M. S. 2005a The analysis of jumping smash in the game of badminton. In: Wang, Q. (ed.) *Scientific Proceedings of the XXIIIth International Symposium on Biomechanics in Sports,* Beijing. Vol. 2 Pp 671-674.

Adress of the corresponding author:

Azmin Sham Rambely
Centre of Mathematical Studies,
Faculty of Science and Technology,
National University of Malaysia,
Bangi 43600 Selangor DE
Email: asr@pkrisc.cc.ukm.my

F. Ibrahim, N.A. Abu Osman, J. Usman and N.A. Kadri (Eds.): Biomed 06, IFMBE Proceedings 15, pp. 163-166, 2007
www.springerlink.com ' Springer-Verlag Berlin Heidelberg 2007

A New Modification of Adjustable standing Frame for children with Cerebral Palsy

Alice M.K. Wong[1], Y.C. Pei[1], H.W. Chang[2], J.W. Chen[3], S.W. Chou[1] and Y.C. Lau[1]

[1] Department of Physical Medicine and Rehabilitation/Chang Gung Memorial Hospital and Children Hospital, Taoyuan, Taiwan
[2] Institute of Rehabilitation Science/Chang Gung University, Taoyuan, Taiwan
[3] Department of Mechanical Engineering/Oriental Institute of Technology , Taipei, Taiwan

Abstract—**Standing frame is commonly used in rehabilitation training for children with cerebral palsy (CP), but the design and clinical effectiveness were rarely investigated. In this study we modified the standing frame with adjusted footplate with a separate control, a linear acurator, high-density durable foam and adjusted table surface with Acme lead screew and sliding block. Six spastic quadriplegic CP children (aged 4.6±1.3y/o) were recruited and received electromyographic (EMG) evaluation on using both the traditional and modified standing frame for 15 minutes, with a two-week interval. A questionnaire was obtained after the evaluations.**

EMG studies showed significantly lowered activities of bilateral anterior tibialis and gastrocnemius after using the modified standing frame for 6 to 15 minutes. The questionnaire also showed significant increased adjustment and satisfaction index with the modified frame. This modification reduces spasticity and muscle tone in CP children and helps to enhance the efficacy of rehabilitation program.

Keywords—**cerebral palsy, design and manufacture, posture, surface electromyography, standing frame**

I. Introduction

Postural control is related to righting and equilibrium reactions. The ability to stand erect and maintain posture against gravity is acquired through maturation and learning, and needs repetition for a period of time. The learned patterns of postural control are programmed centrally and specify statokinetic postural reactions of motor neuron activity to all involved muscles and inputs. Pathological influence after brain damage can generate an irrelevant motor program leading to abnormal posture [1,2,3].

The training of standing posture is very important in rehabilitation of people with physical disabilities. Standing in the upright position is proposed to be necessary in the continued growth and development of children with or without physical disabilities. Standing provides those children to develop vestibular and spatial experiences. It can also improve bony development, circulation, respiration and digestion function [4, 5].

Cerebral palsy (CP) refers to a group of disorders characterized by abnormal control of movement or posture, and is due to damage to the immature brain before, at or shortly after birth [6]. Upper motor neuron syndrome usually results in paresis, loss of dexterity, or spasticity due to velocity-dependent disinhibition of tonic stretch reflexes and lack of selective motor and postural control. The types of CP are defined according to neuromotor deficits, including spastic, dyskinetic, ataxic, or mixed CP [7, 8].

CP children require support to maintain a satisfactory upright posture by adaptive device, to facilitate their function or learn standing balance. There are many commercially available standing frame for children.

However, these standing frames may not adequately fulfill the diversity of CP children with changing tone and muscleskeletal deformity. They require a more individual approach to adjust to their problems.

Although studies had been conducted to investigate the function of standing frame for CP children, few qualified its effectiveness in normalization of muscle tone, or user adaptability.

In this study, we designed a new adjustable standing frame for CP children and compared its advantage and disadvantages with the contemporary standing frames, the needs of therapists and care givers of CP children in our hospital. We hypothesized that this new standing frame could provide better adjustment to fullfil the clinical needs than the commercial available standing frame.

II. Method

A. Design

To improve the function of support and posture control in contemporary prone standing frames, we design a new adjustable prone standing frame with the following modification from the contemporary design (Fig. 1):

a) for the adjustment of the footplates, a screw was used to adjust the angle, to accommodate the delicate change footplate tilt in which the contemporary standing frame could provide by wedges.

b) a separated control was adopted for bilateral feet by Acme lead screw and sliding block in the new standing frame to adjust the height of footplate.

F. Ibrahim, N.A. Abu Osman, J. Usman and N.A. Kadri (Eds.): Biomed 06, IFMBE Proceedings 15, pp. 167-170, 2007
www.springerlink.com ' Springer-Verlag Berlin Heidelberg 2007

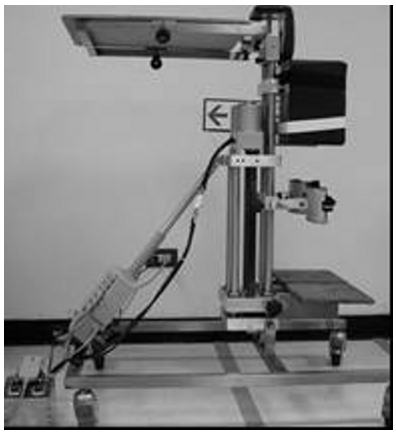

Fig.1. A new designed standing frame.

c) linear acturator instead of the screw type was applied in new frame for the adjustment of supporting frame.

d) Acme lead screw and sliding block were used for the adjustment of table surface.

e) high density durable foam was used for better support and comfort in the new frame.

B. Subjects

The inclusion criteria of the present study were CP children with spastic quadriplegia. Exclusion criteria were CP children with athetosis , ataxia, severe cognitive impairment, uncorrectable visual impairment or fixed contractive in lower extremities. Six spastic quadriplegic CP children, 3 boys and 3 girls, aged 4.6–1.3 y/o, participated in this study.

C. Measurements

Each CP child received two evaluations with a two-week interval, one for standing on a contemporary and another for the new standing frames in randomized order. Each CP child was put upright position on the standing frame after optimal adjustment of the standing frame and standing posture.

Each evaluation, the CP child stand on the standing frame for a total of 15 minutes. EMG data were collected for 15 seconds, in each of 0, 3, 6, 9, 12 and 15 minute.

a) EMG data were collected by Myosystem 2000 (Noraxon USA, Arizona) from 8 channels. Surface electrodes were placed in biceps femoris, rectus femoris, medial head of gastrocnemius and tibialis anterior of bilateral lower extremities . The raw EMG electrical signals were band-pass filtered (20~200 Hz) and sampled at 1000 Hz. The sampled signals were then low pass filtered (with a cutoff frequency of 6 Hz) off-line. The filtered EMG activities were analyzed by root mean square value (RMS) for each recording period.

b) The questionnaire for standing frame

A questionnaire was developed to document subjective evaluation provided by the patients and physical therapists. The questionnaire consisted of three indexes, each comprising several topics. Reliability in terms of internal consistency was checked to ensure that internal consistency is adequate for each item.

(1) Adjustment index: the adjustment of moving parts in standing frames (7 topics).

(2) Satisfaction index: the trunk stability, movement of head and upper extremities of the children, acceptance and tolerance by the child, comfort and fatigue of prolong standing of the child (13 topics).

(3)Transportability index: the stability, weight and transportability of the standing frame (3 topics).

D. Statistics

Cronbach alpha was applied to evaluate the internal consistency in each item of the questionnaire. Wilcoxon signed ranks test was adopted to compare the EMG activities expressed in RMS(mV) in different muscles on two different standing frames, as well as the total score in each item in the questionnaire. A value of $P < 0.05$ was considered statistically significant.

III. Results

The comparison of EMG activities of lever limbs. There were significant lower in EMG activities of tibialis anterior and gastrocnemius muscles in bilateral lower limbs from 6 minutes to 15 minutes when CP children stand in the new designed standing frames than the conventional frame. However, the difference was not significant in biceps femoris and rectus femoris muscle when positioned on the contemporary and new designed standing frame were in Tab. 1 and Fig. 2(shown right leg).

Internal reliability of subordinate indexes of the questionnaire for the standing frame were cross examined from 2 physiatrist, 2 physical therapist, 2 bioengineers and 1 occupational therapist. All three indexes of the questionnaire demonstrate adequate internal consistency (Cronbach alpha > 0.8).

Questionnaire for the standing frame: The newly designed standing frame scored better in adjustment and satisfaction indexed than the contemporary standing frame ($p<0.05$). No difference was noticed in transportability index between the two standing frames (Fig. 3).

F. Ibrahim, N.A. Abu Osman, J. Usman and N.A. Kadri (Eds.): Biomed 06, IFMBE Proceedings 15, pp. 167-170, 2007
www.springerlink.com ' Springer-Verlag Berlin Heidelberg 2007

Table 1 The comparison of EMG activities (RMS, mV) of lower limbs in two different standing frames.

		LE	0 min	3 min	6 min	9 min	12 min	15 min
Rectus femoris muscle	conventional	left	12.1–10.4	9–7.7	11.7–6.9	6.3–5.1	10.6–6.7	10–8.5
		right	11.4–8.2	12.2–10.5	14.1–7.1	10.6–9.6	9.8–5.4	8.7–5.3
	new designed	left	5.4–2.8	6.5–5.1	4.9–2	4.9–2.5	7–3.4	4.8–2.7
		right	6.7–7.2	5.9–6.8	3.6–1.6	3.3–0.9	4.7–4.1	3.7–1.6
Biceps femoris muscle	conventional	left	12.2–9.6	11–7.5	11.6–8.4	10.8–6.3	13.3–8.6	11.3–8.5
		right	12.8–5.9	13.8–11.7	15.7–10.1	15.4–10.1	13.4–8.2	13–9.7
	new designed	left	5.9–3.4	6.2–4.2	3.9–1.7	3.7–1.5	4.8–3.1	3.3–2
		right	8.8–5.7	7.1–6.4	3.6–2.1	3.9–2.6	5.8–4.2	4–2.1
Tibialis anterior muscle	conventional	left	12.2–9.4	11–9.1	12.1–6.1*	10.5–6.2*	10.4–5.3*	16.5–7.8*
		right	13.5–7.9	12.5–7.6	12.2–5.9f	11.8–8.5f	14.2–9.8f	13.3–7.6f
	new designed	left	7–4.5	8.2–8.3	4.9–2.1*	3.9–0.7*	5.1–2.3*	4.1–2.5*
		right	7.5–3.8	5–5.1	4–1.5f	4–2.1f	3.7–2.5f	4.4–3.8f
Gastrocnemius muscle	conventional	left	21–14.2	19.3–17	23.5–13.4*	14.8–16.2*	17.5–12.8*	17.2–12.8*
		right	14.5–7.3	13.5–8.7	16.8–7.1f	13.5–11.6f	15–10.2f	12.8–10.1f
	new designed	left	7.9–4.9	5–5.6	4.4–1.8*	2.7–0.9*	3.4–1.5*	2.8–1.3*
		right	6–6	5–4	3.8–0.8f	3–1.1f	4.2–3.1f	3.2–1.8f

*: $p<0.05$ for muscle in left leg for two different frames.
f: $p<0.05$ for muscle in right leg for two different frames.

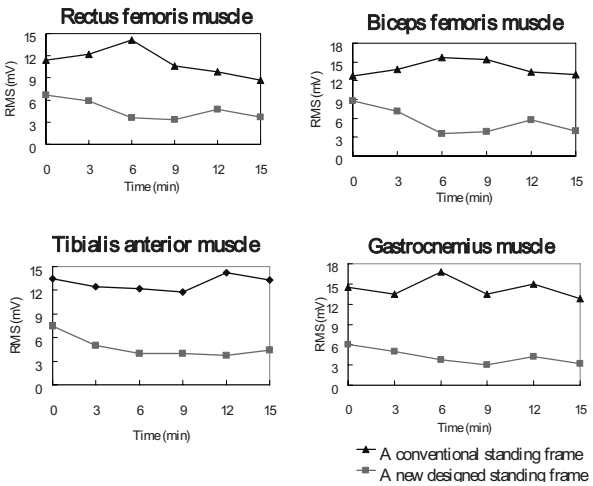

Fig. 2 The activity of right leg muscle affected by the conventional and a new design standing frame during CP children standing.

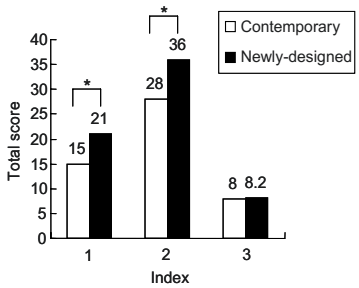

Fig 3. Comparison of three domains between the conventional and newly-designed standing frames. 1: Adjustment index; 2: Satisfaction index; 3: Portability index. *: significant difference between two standing frames.

IV. Discussion

There are many upright standing frames to provide the child maintaining an erect posture. They may offer many potential benefits for the child, such as sustained muscular stretch, decrease of muscle tone, maintenance of trunk and lower limb straight, facilitation cocontraction of muscle, and improvement of head and trunk control [9].

To selecting a standing frame for different standing position, such as supine, prone or vertical type, many points should be considered. The supine standing frame is recommended for a child with significant extensor tone and posture with poor head control. Prone standing frame supports the children anteriorly to improve antigravity head control and to promote bilateral upper extremity weight bearing in additional to trunk and leg blocks. Vertical standing frame mimics a normal standing position, permits the child to work on head control and upper extremity strengthening. It has no head support and only limited trunk support with a tray in front and a strap around the child s back. It is preferred for the children with fair to good control in trunk and upper limbs, but still not able to stand independently.

This study showed that children with cerebral palsy stand considerably better in the new designed prone standing frame than they were put in the contemporatory standing frame since its flexible adjustment better fulfill the clinical needs. Before the design for this standing frame, twenty CP children from 2-10 year old were invited for arthropometric measurement, to accommodate the children from 88 to 140 cm in height and 10 to 40 kg in weight. This new standing frame had passed the evaluation of TIPO in Taiwan, with patent NO. M 260258.

F. Ibrahim, N.A. Abu Osman, J. Usman and N.A. Kadri (Eds.): Biomed 06, IFMBE Proceedings 15, pp. 167-170, 2007
www.springerlink.com ' Springer-Verlag Berlin Heidelberg 2007

As reports of previous studies, prone standing frame supports the child anteriorly. Postural support is supplied through trunk laterals, hip guides, abductor blocks, knee blocks and shoe holders. In this study, the surface EMG signals in RMS(mA) in lower limb were recorded including rectus femoris, biceps femoris, tibialis anterior and gastrocnemius muscles. The comparison of EMG in children between this new standing frame to contemporary prone standing frame in supporting standing over 5 minutes to 15 minutes. The EMG signals were significantly lower than in the contemporary frame ($p<0.05$) which might imply the reduce of spasticity and the decrease of muscle tone .The same results was also obtained from our questionnaire submitted by parents of CP children [10-15].

However, there was only 6 children joint this study, all of them were spastic CP. Further, studies including the increase of case number, types of CP (eg. athetoid, hypotonic, ataxic, or mixed type), or functional task of upper limbs, may be investigated.

V. Conclusions

This new design prone standing frame might provide a more accurate and flexible adjustment to fulfill the clinical needs, and also reduce spasticity and muscle tone in CP children. All these together might enhance the effectiveness of physical therapy and rehabilitation in the facility.

Acknowledgment

This study was supported by grant NSC from National Science Committee of Taiwan No. NSC 93-2314-B-182A-064 & No. NSC 94-2314-B-182A-007.

References

1. Nashner LM, Woollacott M.(1979) The organization of rapid postural adjustments of standing human: an experimental conceptual mode. In: Talbott RE, Humphrey DR, eds. Posture and movement. New York: Raven Press pp 243-57.
2. Brooks VB.(1983) Motor control: How posture and movements are governed. Phys Ther 63(5):664-73
3. Wang A MK, Lee MY, Kuo JK, Tang FT.(1997) The development and clinical evaluation of a standing biofeedback trainer. J Rehabil Rev Dev 34(3):322-7.
4. Tolley B, Cohen L, Nogi J.(1982) In-house modification of variety village standing frame. J Assoc child Prosth Orthotic Clin 18(2):5.
5. Matjacic Z.(2000) A multi-purpose rehabil frame: an apparatus for experimental investigations of human balance and postural control. J Med Eng Tech 24(6):250-4.
6. Bax MCO.(1964) Terminology and classification of cerebral palsy. Dev Med Child Neurol 6:295-6.
7. Albright AL.(1996) Spasticity and movement disorders in cerebral palsy J Child Neurol 11:S1-S4.
8. Filloux FM.(1996) Neuropathophysiology of movement disorders in cerebral palsy. J Child Neurol, 11: S5-S12.
9. Rose J, Wolff DR, Jones VK, et al.(2002): Postural balance in children with cerebral palsy. Dev Med Child Neurol 44(1)58-63.
10. Bond WT, Wajed A(1979): The Carshalton standing frame for physically handicapped children. Physiotherapy 65(6):185.
11. Hom C, Whistler B, Heisler K (1972): Adjustable prone standing table. Phys Ther 52(10): 1058-9.
12. Hueter A, Blossom B (1967) A prone-stander. Phys Ther 47(5):386.
13. Ivey A, McDaniel C, Perkins, et al: Supine stander for severely handicapped child. Physical Therapy 1981;61(4):525-6.
14. Taylor AG, Rocca L (1982): Standing frame--the Salford design. Physiotherapy. 68(12):399.
15. Wilton SM (1977): Standing frame. Physiotherapy 63(8):258.

Address of the corresponding author:

Author: Alice MK Wong, MD
Institute: Department of Physical Medicine and Rehabilitation/ Chang Gung Memorial Hospital and Children Hospital
Street: No 5, Fu Hsing Street
City: Kuei Shan, Taoyuan
Country: Taiwan, R.O.C.
Email: walice@adm.cgmh.org.tw

F. Ibrahim, N.A. Abu Osman, J. Usman and N.A. Kadri (Eds.): Biomed 06, IFMBE Proceedings 15, pp. 167-170, 2007
www.springerlink.com ' Springer-Verlag Berlin Heidelberg 2007

A Preliminary Study of Acceptable Load Carriage for Primary School Children

H.N. Shasmin, N.A. Abu Osman, R. Razali, J. Usman and W.A.B Wan Abas

Department of Biomedical Engineering, Faculty of Engineering, University of Malaya, 50603 Kuala Lumpur, Malaysia.

Abstract—**This study investigated the changes in Ground Reaction Forces, GRFs and trunk inclination among primary students when carrying heavy backpacks. A randomised controlled experimental study was conducted on seven boys aged between 9 and 11 years old with similar Body Mass Index. Observations were done when the boys were carrying school bags of 0 (as control), 10, 15 and 20% of their own body weight whilst normal walking. Data acquisition was carried out using force platforms and 3-D motion analysis system. A significant difference in Ground Reaction Forces at load of 20% of body weight was found. The vertical GRF increased almost three times when loads increased up to 20% of body weight compared to 10% of body weight. The anterior-posterior GRFs were asymmetrical when loads were increased. When carrying load of 15% of body weight, the subjects adopted a compensatory trunk inclination. If Ground Reaction Forces and trunk inclination are important as the criteria to determine the acceptable backpack loads for children, those loads should not exceed 15% of body weight.**

Keywords- **Gait, Children, Load carriage, GRF, Trunk**

I. Introduction

School children lugging bags packed with books have been a perennial problem. In Malaysia, Ministry of Education has introduced periodic table and serial textbooks to reduce the weight of school backpacks. The changes were done when many teachers and parents voiced their concern about the load in school bags especially in early 2002.

However, heavy school bags remain a yearly problem as some subjects, especially the language ones, require five or six exercise books, not counting the textbooks. The bags could weight some 10 kg each which is about 50% of student body weight. The rolling backpacks have been recommended by United Kingdom professionals, but these bring their own array of challenges, such as difficult manipulation on stairs, storage within school and passage through crowded hallways and buses [1].

The main idea of this project was to analyze the load carriage effect among students. The effect would be viewed on children s gait and posture from full biomechanics analysis. At the end of this study, a safe load limit for children would be suggested. In other country, many researches about load carriage among students had been done. The majority of biomechanical studies with children s backpacks have examined the effect of different loads on three main parameters: trunk forward lean, cranio-vertebral angle, and gait [2]. The studies suggested that the suitable load carry by the students is 10-15% from their body weight. When load is carried more than that, a student probably will have changes in his or her physical such as bad posture and shoulder depression [3].

II. Methods

Questionnaires: The methodology of this study can be divided into 2 main steps. The first step was to find the right school boys to be the subjects. Apart of this, proposal paper was send to a school. First of all, the questionnaires were distributed to students from Primary 3 to Primary 5. The questionnaires were important to review what types of bag the student were currently used and the school children s subjective perceptions of their backpack loads. After students weight and height were measured, some of them were selected to participate in the experiment.

Subjects: Seven boys with a mean age of 10.28 ± 0.72 years were selected from the local primary school to participate in this study. The boys were best represented their age group in terms of their Body Mass Index. The body mass and height of the subjects were 28.7 ± 0.73 kg and 134.7 ± 5.30 cm. All experiments were conducted at the Motion Analysis Laboratory, Department of Biomedical Engineering, Faculty of Engineering, University of Malaya, Kuala Lumpur, Malaysia. During the experiments, the subjects need to walk on a floor with four different load conditions; without a bag and with a school bag of 10, 15 and 20% of body weight. The most popular school bag, a two straps, rigid backpack was employed in the experiment.

Experimental Procedure: The children wore dark uniforms with socks and shoes. After consents were obtained from the subjects parents, anthropometric measurements of the subjects including body height and weight were taken and reflective markers were attached to their body segments. These reflective markers represented specific bone landmarks such as ankle, knee and shoulders.

Afterward, the children were required to walk in a straight line along 5 m distance at their own comfortable speed on the floor which was equipped with Kistler® Force Platform Type 9281C to detect their Ground Reaction Forces. The stance phase of the subjects were filmed by

F. Ibrahim, N.A. Abu Osman, J. Usman and N.A. Kadri (Eds.): Biomed 06, IFMBE Proceedings 15, pp. 171-174, 2007
www.springerlink.com ' Springer-Verlag Berlin Heidelberg 2007

four sets of 50 Hz shuttered CCTV cameras. Before the experiment started, a calibration procedure was conducted using 17-points calibration frame and the Global Transformation Frame, GTF. The GTF marked the x, y and z axis. This procedure was important when digitizing purpose. The reflective markers that attached to the subjects from recorded video tapes were digitized on a motion analysis system by using a human body model. Afterwards, full biomechanical analysis was done using PEAK Motus ® 7.2.4 software. A Butterworth low-pass filter from the software was used to smooth the data for anatomical landmarks and Ground Reaction Forces.

Measurement: One stance phase was deemed to contain the foot strike, opposite foot strike, foot flat, mid-stance, heel off and toe off [4]. Stance phase was defined as the period during the foot make contact with the ground [5]. For kinetic measurement, analysis was done on three components of Ground Reaction Forces, (GRF. The Ground Reaction Force is the propulsive force in the walking. According to the previous studies [6-9] all components of Ground Reaction Forces are proportional to the load increment. The stance duration was also measured in this study.

Statistics: One-way ANOVA (analysis of variance) from SPSS ® version 12.0 software was used to test for significant differences. If this calculation was significant, a univariate one-way ANOVA was performed on each different load conditions to determine those which possessed significant variance. Statistical significance level of 0.05 was set.

III. Results

Questionnaires: The questionnaires that were distributed to the school had three sections. The sections were demographic information, school bag use and the student perceptions of their backpacks. The questionnaires were answered by 77 school boys; 37 students from Primary 3 and 40 students from Primary 5. In the section of school bag usage; about 95 percent of the children used a standard two rigid, straps backpack and about 80 percent from them were reported using both straps on their shoulders. From the questionnaires, 31% students said that their backpacks were uncomfortable and heavy.

*Ground Reaction Forces:*The results in this study showed that in vertical Ground Reaction Force, GRF, when the load was increased the force also increases. This condition aroused in all the subjects. The shapes of vertical ground reaction force from other boys were almost similar to each other between every load conditions respectively, except the forces varied. The forces varied according to the subject mass and percentage load of body weight carried by the boys. Fig. 1 shows an example of vertical GRF from the subjects. There was no significant difference, (P>0.05) between load carriage of 0% and 10% of body weight.

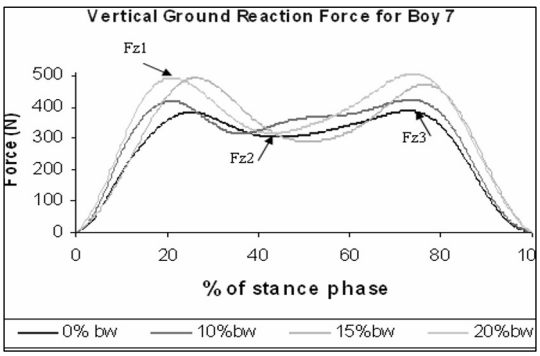

Fig. 1: Vertical Ground Reaction Force from a subject. The force is increased when load increases. Fz1 and Fz2 are peak values. Fz3 is trough values

For the anterior-posterior GRF, some of the boys showed decrement in force at 15% load conditions but their force increased again at the 20% load condition. Fig. 2 represents an example for some anterior-posterior GRF. Carrying backpack of 20% body weight resulted in significant increase in medial-lateral force for four boys. Significant differences (P< 0.05) were found only on one or two boys for other load conditions. This result almost similar to the vertical and anterior-posterior GRF statistical analysis.

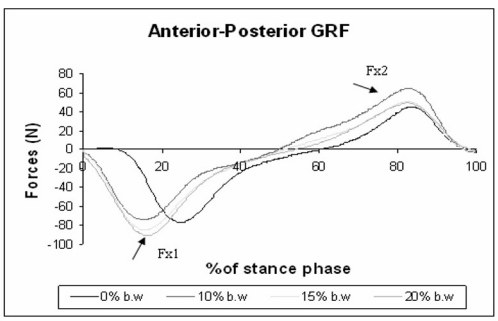

Fig. 2: an example of Anterior-Posterior Ground Reaction Force from a subject. The force is increased when load increases. Fx1 is breaking force and Fx2 is propulsion force.

Trunk Inclination: Fig. 3 shows mean changes in trunk forward lean angle when the load in the school bags increased. Some increment was found on trunk forward lean angle at load of 10% and 15% body weight (Fig. 4). At the load of 20% of body weight, the children s trunks lean forward more than 45° from the vertical plane.

F. Ibrahim, N.A. Abu Osman, J. Usman and N.A. Kadri (Eds.): Biomed 06, IFMBE Proceedings 15, pp. 171-174, 2007
www.springerlink.com ' Springer-Verlag Berlin Heidelberg 2007

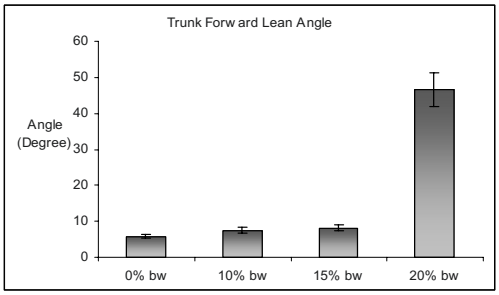

Fig. 3: Mean trunk forward lean angle of male subjects. Significant difference occurred at 20% load conditions.

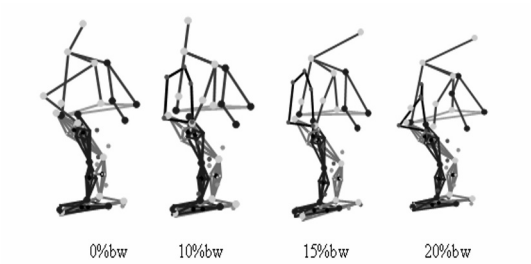

Fig. 4: Changes in trunk forward lean angle of a male subject.

IV. Discussions

Ground Reaction Forces measurements during locomotion are necessary to study the mechanical properties of the lower limbs during the contact phase [10]. The kinetic data obtained from this study demonstrated the same results as obtained by Cottalorda et al (2003) and Ren et al. (2005) [6,8], the GRFs was proportional to the load increment. Carrying load at more than 15% of body weight induced an asymmetric gait for breaking and propulsive anterior-posterior forces for some boys. This probably due to some alteration that was made by the boys to balance their body while carrying the load on their school bags.

In this study, the ground reaction forces data from all the boys were not averaged for the analysis purpose. Averaging the Ground Reaction Force data from different subjects without normalizing the subjects weight would change the identity of a person [11-12]. This was possible as the peak of vertical ground reaction force was usually about 112 percent of subject s body weight at the 25 percent of stance phase [13-15].The slope from the heel strike (0 percent of stance phase) to the first peak force measures the rate of load acceptance of the limb [14,16]. From the results, the loads acceptance for the boys from the 10% and 20% load conditions was in range 116 percent to 129 percent of body weight which was much higher from the standard value of vertical peak force. Standard value in this study was referred to the GRF shape that was obtained from previous study on more than 60 subjects in both genders [15,17].

The anterior-posterior graphs for the boys in this study did not have similar shape to each other. Although, each subject had the shape of standard anterior-posterior graphs but the forces did not have standard arrangement either decrease or increase with respect to the load increment. This was probably due to subjects did not walk at same speed for every trials.

All of the boys increased the Medial-Lateral GRFs when the load was increased from 0 to 20 percent of their body weights except Boy 4.

The increased load carried on the back would bring the center of gravity of the body-load system closer to the rear limit of the base of support, thus reducing stability in the walking direction [9,18,20]. In response to this change, children were leaning forward to bring center of gravity over their base of support to maintain their walking stability. The results in this study are in agreement with the previous findings [9,10,20].

V. Conclusions

In conclusion, based on the statistical analysis, the safe load carriage for children aged between 9 and 11 years old is not exceed 15% of their body weight. From this study, the vertical GRF increased almost three times when loads increased up to 20% of body weight compared to 10% of body weight. The anterior-posterior GRFs were asymmetrical when loads were increased. When carrying load of 15% of body weight, all the seven subjects adopted a compensatory trunk inclination. This study suggested that the safe load carriage for children under twelve years old is not exceed 15% of body weight.

References

1. Furjuoh SN, Lane BL and Schuchmann JA. Percentage of Body Weight Carried by Students in Their School Backpacks, 2003. Am J Phys Med Rehabil. 82,261-266.
2. Brackley and Joan M. Stevenson. Are Children s Backpack Weight Limits Enough? A Critical Review of the Relevant Literature. SPINE No. 19, 2184-2190.
3. W. Whittle,1996. Gait Analysis: An Introduction, first ed. Butterworth Heinimann.
4. White LJ, Frasure HE, White P.Weight of backpacks carried by school children: Students or Sherpas (abstract). Acad Emerg Med 2000; 7:487.
5. Hamill and M. Knutzen, 1995. Biomechanical Basic of Human Movement, first ed. Williams and Wilkins.
6. Cottalorda and Jerome, Rahmani. Influence of School Bag Carrying on Gait Kinetics, 2003. Journal of Pediatric Orthopaedics. 12(6), 357-364.
7. Hong and C.K Cheung. Gait and Posture Responses to Backpack Load During Level Walking in Children, 2003. Gait and Posture. 17, 28-33.

F. Ibrahim, N.A. Abu Osman, J. Usman and N.A. Kadri (Eds.): Biomed 06, IFMBE Proceedings 15, pp. 171-174, 2007
www.springerlink.com ' Springer-Verlag Berlin Heidelberg 2007

8. Ren, Richard K Jones and David Howard. Dynamic Analysis of Load Carriage Biomechanics During Level Walking, 2005. Journal of Biomechanics. 38, 853-863.
9. Hong and G.P Brueggemann. Changes in Gait Pattern in 10-year-old boys with increasing loads when walking on a treadmill, 2000. Gait & Posture.11, 254-259.
10. Hong and J.X. Li. Influence of Load and Carrying Methods on Gait Phase and Ground Reactions in Children s Stair Walking,2005. Gait & Posture. 22,63-68.
11. Pui-Han Lai and Alice Yee-men Jones. The effect of shoulder-girdle loading by a school bag on lung volumes in Chinese primary school children, 2001.79 86.
12. Grimmer Karen, Brenton Dansie, Steve Milanese and Patricia Trott. Adolescent Standing Postural Response to Backpack Loads: A Randomised Controlled Experimental Study, 2002. BMC Musculoskeletal Disorders; 3:10.
13. Perry J,1992. Gait Analysis: Normal and Pathologic Function. SLACK Incorporated.
14. Stansfield, S.J. Hillman, M.E. Hazelwood, J.E. Robb. Regression analysis of gait parameters with speed in normal children walking at self-selected speeds, 2006. Gait & Posture, 288 294.
15. Spivack B. S., 1995. Evaluation and Management of Gait Disorders. New York: Marcel Dekker, Inc.
16. Stansfield, Ben W., Hillman, Susan J., Hazelwood, M. Elizabeth, Lawson, Alastair A., James E. Sagittal Joint Kinematics, Moments, and Powers are Predominantly Characterizes by Speed of Progression, Not Age, in Normal Children. Journal of Paediatric Orthopaedics 2001, 21(3); 403-411.
17. Keller T. S., Weisberger A. M., Ray J. L., Hasan S. S., Shiavi R. G., & Spengler D. M. (1996). Relationship between vertical GRF and speed during walking, slow jogging, and running. Clinical Biomechanics. 11(5). 253 259.
18. Smidt Gary, 1990.Gait in Rehabilitation, First ed Churchill Livingstone.
19. Chow Daniel. The effect of load carriage on the gait of girls with adolescent idiopathic scoliosis and normal controls, 2005. Gait & Posture.
20. Hamish W. Mackie, Joan M. Stevenson, Susan A. Reid and Stephen J. Legg. The Effect of Simulated School Load Carriage Configurations on Shoulder Strap Tension Forces and Shoulder Interface Pressure, 2005. Applied Ergonomics. 36, 199-206.

Address of the corresponding author:

Author: Hanie Nadia Shasmin
Institute: Department of Biomedical Engineering,
Faculty of Engineering, University of Malaya
City: Kuala Lumpur
Country: Malaysia
Email: hanie_nadia@um.edu.my

F. Ibrahim, N.A. Abu Osman, J. Usman and N.A. Kadri (Eds.): Biomed 06, IFMBE Proceedings 15, pp. 171-174, 2007
www.springerlink.com ' Springer-Verlag Berlin Heidelberg 2007

A Preliminary Study of EMG Measurements on Biceps Brachii Muscles During Repetitive Task at Automotive Industry

S.Z. Dawal[1], N. Soin[2], W.N.L. Mahadi[2], N.M. Ali[2],N.A. Abu Osman[1], S.A. Aziz[1], M. Yusof[1] and Z. Ismail[3]

[1]Department of Engineering Design and Manufacture, Faculty of Engineering, University Malaya, Kuala Lumpur, Malaysia
[2]Department of Electrical Engineering, Faculty of Engineering, University Malaya, Kuala Lumpur, Malaysia
[3]Department of Civil Engineering, Faculty of Engineering,, University Malaya, Kuala Lumpur, Malaysia

Abstract— **A preliminary study is conducted to investigate the effect of task activity on Biceps brachii muscles response during repetitive task at automotive industry in Malaysia. The aim of the study is to analyze time to fatigue of bicep brachii muscles during repetitive task at a tyre assembly in an automotive industry. Thirty electromyography (EMG) measurements were taken from three selected samples at the tyre assembly line. Measurements were taken in duration of two hours and thirty minutes. The results indicate that similar root-mean-square (RMS) patterns were obtained for the three samples. Regression method was used for the analysis. In addition, the regression analysis also gives similar prediction on the subject. One explanation is that time to fatigue for a particular task can be predicted.**

Keywords **Muscle fatigue, EMG, repetitive task, regression analysis, automotive industry**

I. Introduction

Muscle fatigue is defined by S. Marthur et. al [1] as a reduction in the force generating capacity of a muscle due to previous activity. Several other definitions suggest fatigue occurs when there are changes in EMG readings, or changes in perceived effort level for a given force level [2][3][4].

The presence of work-related musculoskeletal disorders (MSDs) including disorders or injuries of the back, trunk, upper extremities and lower extremities in automotive industrial employees is commonly recognized. According to Salvendy et. al [5], the evidence that chronic muscular skeletal disorders of the upper extremities are work related is fast expanding. Since most manual work requires the active use of the arms and hands, the structures of the upper
extremity are particularly vulnerable to soft tissue injury. Work related upper extremity disorders are typically associated with repetitive manual tasks with forceful exertions, such as those performed at assembly lines. Repetitive manual tasks impose repeated stresses to the upper body, i.e the muscles, tendons, ligaments, nerves tissues and neurovascular structures. In this study, the possibility risk of work related musculoskeletal disorder to the upper extremity are tendon disorder (such as tendonitis), nerve disorder (such as Carpal tunnel syndrome), and neurovascular disorder (such as thoracic outlet syndrome) [5].

Therefore, repetitive task in modern industry has proven to be one of the factors that could cause musculoskeletal disorder amongst correspondent workers. The aim of the study is to investigate muscle fatigue pattern during repetitive task at a tyre assembly in an automotive industry.

II. Methods

A Sample

Three samples were selected from the tyre assembly for the study. The sample is very small as this is a pilot study

B Procedures

EMG surface electrodes were used to measure bicep brachii muscles activity. Bicep brachii was selected because it is one of the primary muscles used in repetitive task at the tyre assembly. Data were collected throughout the second job rotation within two and a half hours job duration. Ten measurements were taken for each sample within the duration. Electromyographiy (EMG) recordings were obtained using DataLab 2000 system.

C Statistical analysis

Regression analysis is carried out to examine the relationship between a dependant variable (time) and one independent variable. The following shows the general linear regression equation:

$$Y = \beta_0 + \beta_1 x + \in \qquad (1)$$

F. Ibrahim, N.A. Abu Osman, J. Usman and N.A. Kadri (Eds.): Biomed 06, IFMBE Proceedings 15, pp. 175-177, 2007
www.springerlink.com ' Springer-Verlag Berlin Heidelberg 2007

III. Results and Discussions

A RMS results

Figure 1,2 and 3 show the RMS versus time for the three samples. The results indicate that the RMS measurements decrease with time mainly reflect the fatigue pattern for the task under study. It can be seen that the rate of fatigue obtained for individual sample varies and these could be the consequence of a change in muscle temperature [6] and difference in fibre types or differences in muscle fibre recruitment pattern [7][8].

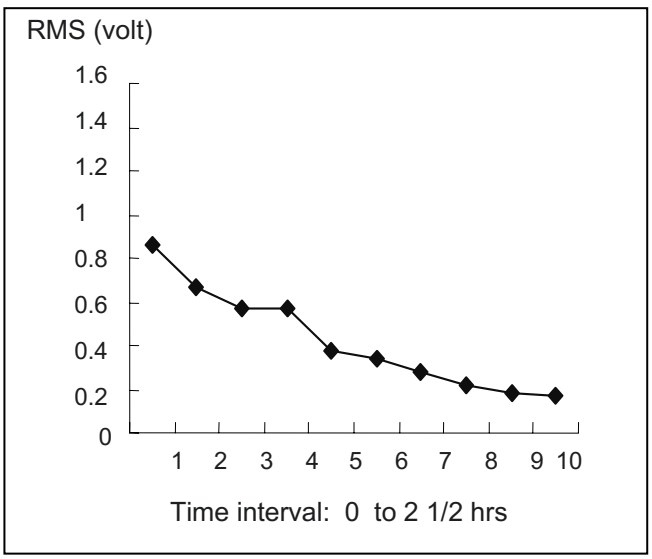

Fig. 1 RMS for sample 1

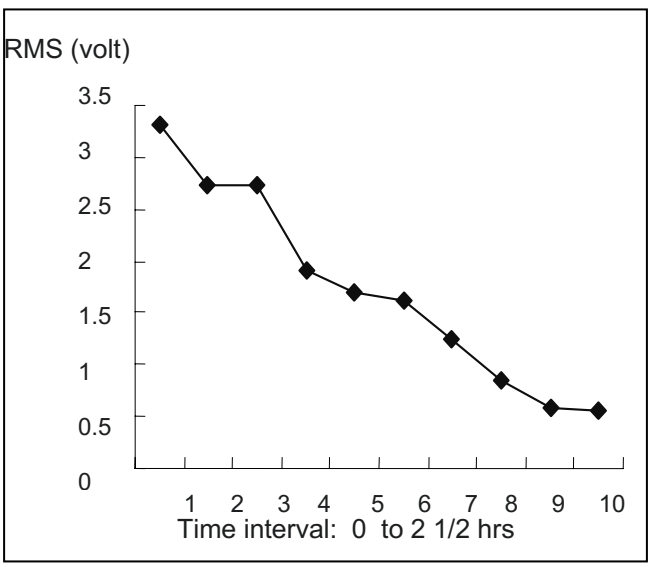

Fig. 2 RMS for sample 2

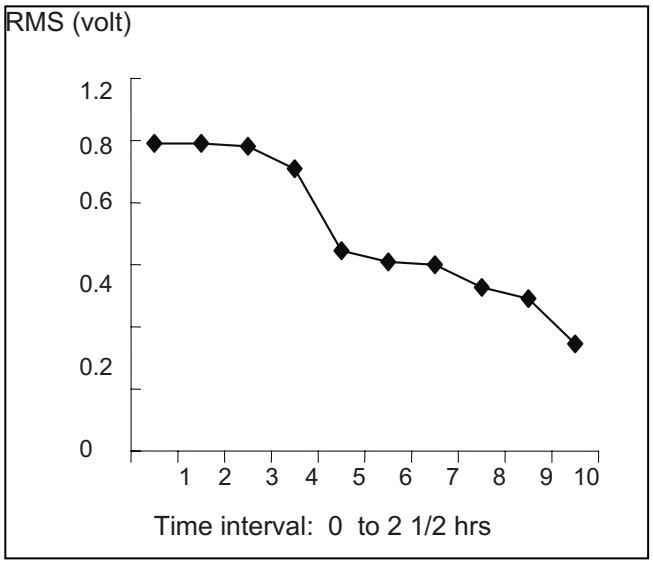

Fig. 3 RMS for sample 3

B Regression analysis on biceps brachii musles

Table 1 Model summary of regression analysis for the three samples

Model	R	R Square	Adjusted R Square	Std. Error of the Estimate
Sample 1	0.972	0.946	0.939	0.74943
Sample 2	0.992	0.983	0.979	0.44325
Sample 3	0.994	0.989	0.986	0.36184

Table 1 summarized the regression analysis model for the three samples. The regression analysis R represents the absolute value of the correlation coefficient and to see how well the model fits a set of data, Pearson correlation R is most frequently used. Adjusted R Square values are very large for the three samples (0.939, 0.979 and 0.986) indicating that the linear regression models can be predicted from independents variables.

IV. Conclusions

The conclusions derived from this investigation highlight that time to fatigue for bicep brachii muscle in repetitive work can be analyzed and predicted. Further studies will be conducted to determine the validity of the model with increase samples and to compare its fatigue pattern with other muscles. It can be deduced that there is a general trend in an exponential decrease in muscle strength for bicep brachii muscle due to prolong repetitive activity.

F. Ibrahim, N.A. Abu Osman, J. Usman and N.A. Kadri (Eds.): Biomed 06, IFMBE Proceedings 15, pp. 175-177, 2007
www.springerlink.com ' Springer-Verlag Berlin Heidelberg 2007

REFERENCES

1 Marthur S. et. al (2005) Reliability of Surface EMG during sustained contractions of the quadriceps , *Journal of Electromyography and Kinesolog,* Vol. 15. pp. 102-110.

2 Esposito, D. Malgrati, A. Veicsteinas, C. Orizio (1996) Time and frequency domain analysis of electromyogram and sound myogram in the elderly, Eur. J. Appl. Physiol. 73 503-510.

3 Nagata, S., Arsenault, A.B., Gagnon, D., Smyth, G. and Mathieu , P. A. (1990) EMG power spectrum as a measure of muscular fatigue at different levels of contraction, Med. Biol. Eng. Comput. 28 (4) 374-378.

4 Silverstein, B., Fine, L. J.,Armstrong, T. J. (1986) Hand wrist cumulative trauma disorders in industry, Brit. J. Ind. Med. 43 (1986) 779-784.

5 Salvendy, G. (1997) Handbook of Human Factors and Ergonomics. 2nd edition. John Wiley & Sons.

6 Duchene, J and Goubel, F. (1993) Surface Electromyography during voluntary contraction : processing tools and relation to physiological events, Crit. Rev. Biomed. Eng. 21 313-397.

7 Gerdle,B., Henriksson-Larsen, K., Lorentzon, R. and Wretling, M. L. (1991) Dependence of the main power frequency of the electromyogram on muscle force and fiber type, Acta Physiol, Scand. 142 457-465.

8 Kupa, E. J., Roy, S. H., Kandarian, S. C. and DeLuca, C. J. (1995) Effects of muscle fiber type and size on EMG median frequency and conduction velocity, J. Appl. Phys. 79(1) 23-32.

Address of the corresponding author:

Author: Siti Zawiah Md. Dawal
Institute: University Malaya
Street: Jalan Pantai Baru
City: Kuala Lumpur
Country: Malaysia
Email: sitizawiahmd@um.edu.my

F. Ibrahim, N.A. Abu Osman, J. Usman and N.A. Kadri (Eds.): Biomed 06, IFMBE Proceedings 15, pp. 175-177, 2007
www.springerlink.com ' Springer-Verlag Berlin Heidelberg 2007

Analysis of Stress on Inflation of Balloon Catheter using Finite Element Method

Solehuddin Shuib[1], M.I.Z. Ridzwan[1], M.N.M. Ibrahim[2], M.A.F.M. Ariffin[1], and A.B. Abdullah[1]

[1] School of Mechanical Engineering, Engineering Campus, Universiti Sains Malaysia, 14300 Nibong Tebal, Seberang Perai, Malaysia
[2] School of Chemical Sciences, Universiti Sains Malaysia, 11800 Penang, Malaysia

Abstract— **Urinary catheter has been widely used as a solution for urinary incontinence problem. But it can induce pressure stress at the human bladder neck. However, owing to the complexities in balloon geometries, material properties and interactions in bladder, analyses of the complete stress inflation of balloon are limited. This study describes some numerical simulations of the expansion phase of catheter balloon on bladder and to study the stress distribution at the balloon. In order to investigate the mechanical characteristics of inflation catheter balloon, a three-dimensional model of the complete catheter balloon were developed, which made the simulation well close to the real situation. Finite element analysis (FEA) ABAQUS 6.4-PR11 was used to simulate the balloon inflation and deflation. The hyperelastic behavior of the Mooney-Rivlin model is considered. Mechanical properties of the balloon have been taken from the literature. Simulated results showed that the stress distributed on the surface of the balloon. The maximum Von Mises stress for natural rubber from the analysis is 5.11 MPa. High stress concentrates on the center of it. In conclusion, FEM can help illustrate and quantify some mechanical characteristics of the balloon and it would be helpful for the general understanding of inflation of urinary catheter balloon.**

Keywords— **Urinary Catheter, Finite Element Analysis, Mooney-Rivlin, ABAQUS, Hyperelastic Behavior**

I. Introduction

A. Catheter

A catheter is a small flexible tube inserted into some part of the body that provides a channel for fluid passage or a medical device. Depending on some situation, a catheter removes waste fluids (urine) from the body after a transurethral resection [1].

A balloon catheter was developed in 1853, using rubber or woven fabric, dipped in linseed oil and baked [2]. The modern day equivalent, originally manufactured from latex and known as the Foley catheter, as shown in Figure 1, was first introduced in 1920s, by Dr. Frederick B. Foley. Fredrick Foley designed a catheter with an inflatable balloon to keep it positioned inside the bladder. Today it is one of the most commonly used devices employed for the management of urinary incontinence by catheterization [3].

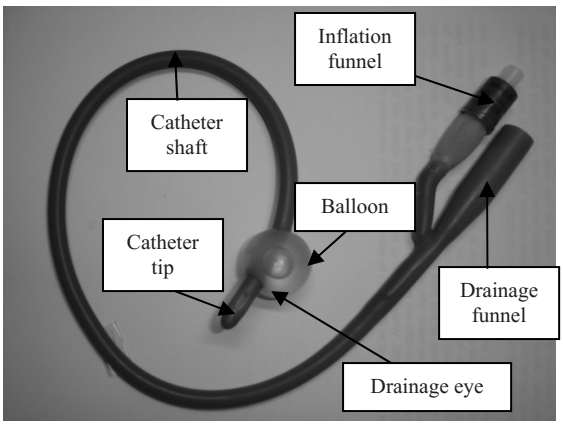

Fig. 1 A latex Foley catheter with the balloon inflated

The catheter is inserted into the bladder, via the urethra, and is held in place by inflating the balloon, just below the drainage eye in the tip, with sterilized liquid. Once the catheter is inside the urinary bladder and urine is draining, the catheter balloon has to be inflated using sterile water to the correct amount indicated on the packaging to keep the catheter *in situ*.

B. Urinary catheter balloon

Balloon sizes vary from 2.5 ml for children to 30 ml. Large balloon catheters (30 ml) weigh approximately 48 g, causing pressure on the bladder neck and pelvic floor and potential damage to these structures [3; 4].

Figure 2 shows the diameter of the balloon, D. Care should be taken to use the correct amount of water or air to fill the balloon because too much or too little may cause distortion of the catheter tip. This may result in irritation and trauma to the bladder wall consequently causing pain, spasm, bypassing and haematuria. If under inflated, one or more of the drainage eyes may become occluded or the catheter may become dislodged. Over inflation risks rupturing the balloon and leaving fragments of balloon inside the bladder [3; 4]. This study describes some numerical simulations of the expansion phase of catheter balloon on bladder and to study the stress distribution at the balloon.

F. Ibrahim, N.A. Abu Osman, J. Usman and N.A. Kadri (Eds.): Biomed 06, IFMBE Proceedings 15, pp. 178-181, 2007
www.springerlink.com ' Springer-Verlag Berlin Heidelberg 2007

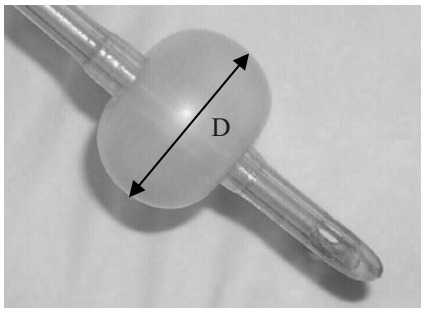

Fig. 2 Inflated balloon

II. Materials and Methods

A. Balloon modeling

A study was performed using ABAQUS 6.4-PR11. The model of balloon was shown as in Figure 3 and its geometry was taken from Tyco Healthcare. This study makes the following assumptions; the material behavior is elastic, isotropic, incompressible and the simulation will include non-linear geometric effects.

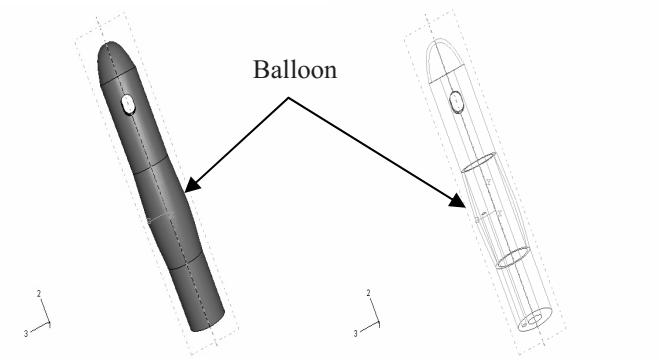

Fig. 3 Balloon model

B. Meshing and boundary conditions

The tube was constraints at both of balloon side. The membrane will be given 92.5kPa of air pressure inside (natural rubber material) (Figure 4(a)). The balloon will inflate due to pressure given. It will inflate until it reaches the maximum value of stress. If the pressure given is too high the analysis will aborted. The cylindrical surface was modeled as a solid and homogenous surface. Its mesh consisted of 4-noded linear tetrahedron elements (C3D4) since this is a geometric nonlinear contact mechanics problem. The total number of elements in the mesh was 16061 in the surface of rubber catheter with minimum element size about 0.8 mm was used as shown in Figure 4(b).

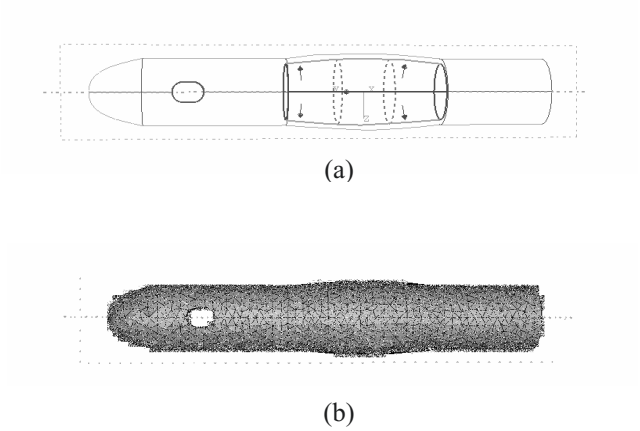

(a)

(b)

Fig. 4 (a) Loading and boundary condition and (b Finite element mesh

Three materials have been chosen for analysis purposes as shown in Table 1.

Table 1 Material property for urinary catheter

Material	Density, ρ (kg/mm³)	Young Modulus, E (MPa)	Mooney-Rivlin constant	
			C_{10} (N/mm)	C_{01} (N/mm)
Natural Rubber	9.20×10^{-7}	1.90	0.14	0.14
Silicone	2.33×10^{-3}	127×10^{3}	0.10	0.90
Polyure-thane	1.07×10^{-6}	34.47×10^{-3}	0.10	0.37

III. Results and Discussions

Figure 5 showed the step of inflated balloon that given 92.5kPa pressure of fluid. For inflating the balloon, the ABAQUS CAE needed 7 steps from the initial condition until the balloon inflated. The radius of balloon was slowly increasing depended on the time step. This simulation was using natural rubber as its properties.

These pictures were taken for each time of step. The time was increasing from 0 second until 1 second. To inflate the balloon, it took 7 steps from 1 second. The balloon slowly inflated. From the initial condition (Figure 5(a)) until the maximum pressure (Figure 5(h)). The stress was different depending on the size of balloon and it could be differentiated by its color. The catheter has given different of pressure until it reached the maximum value of stress. The analysis started with 10kPa fluid pressure. From the observation that have been made, the size of balloon was different for each pressure given. The size for the 10kPa pressure of fluid was small than the size of 30kPa of air. The load from the pressure of fluid has made the balloon filled with fluid (air or water). The surface of the balloon would tightly stretch and inflate.

F. Ibrahim, N.A. Abu Osman, J. Usman and N.A. Kadri (Eds.): Biomed 06, IFMBE Proceedings 15, pp. 178-181, 2007
www.springerlink.com ' Springer-Verlag Berlin Heidelberg 2007

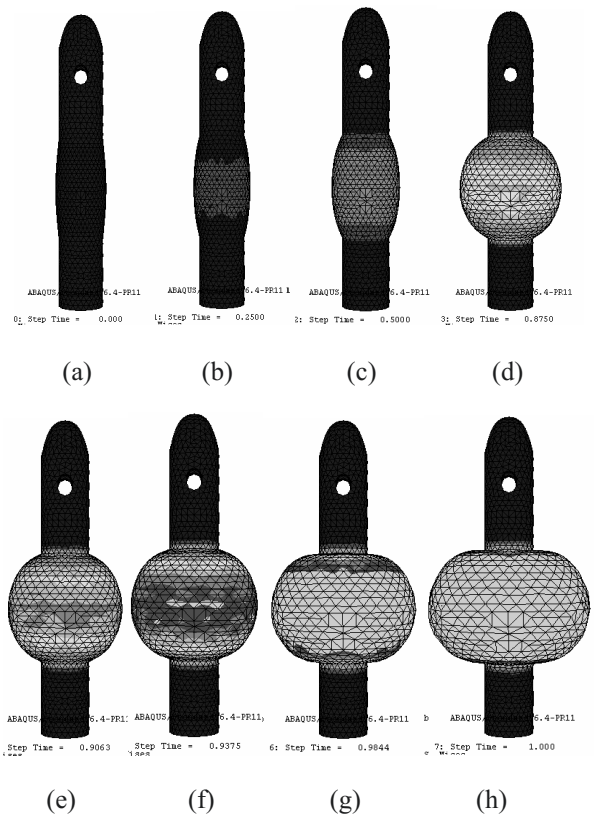

Fig. 5 Time step of inflation a catheter for 92.5kpa fluid pressure

From the analysis we could get the maximum load of fluid pressure given inside the catheter. The differences of load were because of the materials properties of the catheter. If the load given was beyond the maximum value, the balloon will be burst. For summarization, Table 2 illustrated the maximum load given and its material property. The maximum load value could be increased if the catheter has higher Mooney-Rivlin constant. This simulation test was important in designing catheter material. For further design, this catheter could be mixed with other material that has bigger elasticity. The material also needed to be coated with other polymer to get bigger inflation. But, the size of the balloon it s not important than the stress distribution. The balloon with low stress distribution has longer life than balloon that has high stress distribution.

Table 2 Maximum load for different material

Material	Maximum load (kPa)
Natural rubber	92.5
Silicone	271
Polyurethane	155

The maximum pressure load given inside the natural rubber catheter was 92.5kPa. It was smaller than silicone and polyurethane catheter. These catheters have bigger Mooney-Rivlin constants than rubber due to different in mechanical properties. From Figure 6 showed that the different load might produce different in stress distribution. This load has different of pressure and it caused the balloon inflate depending on its pressure.

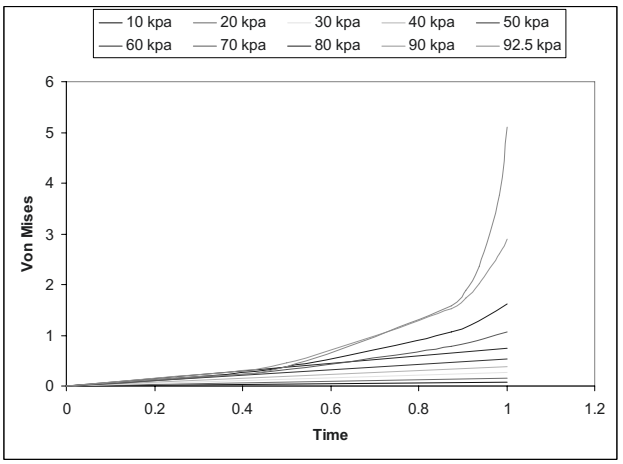

Fig. 6 Von Mises stress for different load against time

This graph was based on element 208 because it produced the maximum value of stress during the simulation. The highest stress was belongs to 92.5kPa, followed by 90kPa, and 80kPa. The 10kPa has the minimum value of stress distribution on the balloon. For 10kPa, 20kPa, 30kPa, 40kPa, 50kPa and 60 kPa, there only have one step time. For 70kPa and 80kPa, both were have 4 step time involved. While for 90kPa and 92.5 kPa its have 7 step time increments. The stress distribution is depending on the pressure given. From the analysis, the diameter of the balloon will inflate depending on the pressure given. Different material has different elasticity, it would inflate depending on it strain energy. Table 3 showed different material and its diameter when given maximum load. The size of the infill balloon was compared to the size of balloon that given maximum load of pressure.

Table 3 Comparison of diameter

Material	Experiment [5] (diameter, mm)	Simulation (diameter, mm)
Natural rubber	26	24.43
Silicone	25	19.55
PTFE	25	17.48

F. Ibrahim, N.A. Abu Osman, J. Usman and N.A. Kadri (Eds.): Biomed 06, IFMBE Proceedings 15, pp. 178-181, 2007
www.springerlink.com ' Springer-Verlag Berlin Heidelberg 2007

There were differences in the value of diameter. The actual condition has bigger diameter than simulation. It was about 2-7 mm different from the actual experiment. This happened because of the FEA simulation did not consider a few things. In FEA, the catheter were assign as solid homogenous, but for better element type it should be consider as membrane type.

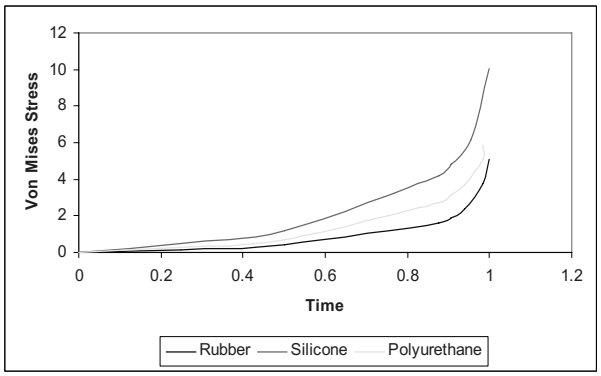

Fig. 7 Von Mises stress for three different materials against time

Figure 7 showed Von Mises stress against time for these three type material. From the graph, silicone has the highest value of stress than polyurethane and rubber. The maximum value of stress for silicone was 10.07MPa, followed by polyurethane (5.86MPa) and natural rubber (5.11MPa). The differences of stress value were because of the mechanical properties of the catheter.

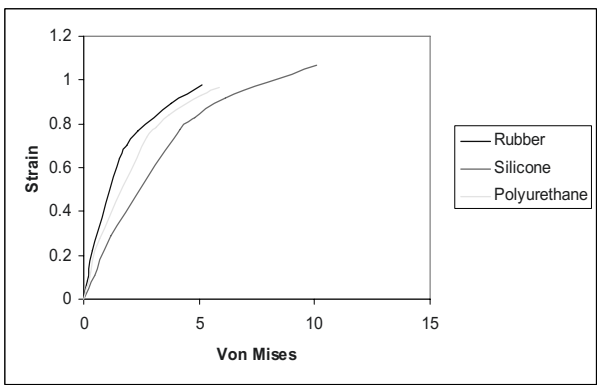

Fig. 8 Von Mises stress against strain for three different materials

The Figure 8 showed Von Mises stress against strain for these 3 different catheter materials. It was shown that silicone has the highest Von Mises value than other type of catheter.

IV. Conclusions

The purpose of this paper was to analyze the stress distribution on catheter inflation. A three dimensional finite element method analysis was carried out using the Mooney-Rivlin material model. The value of stress obtained from the analysis is 5.11 MPa for natural rubber. For silicone and polyurethane material, the values are respectively 10.07 MPa 5.86 MPa. Generally, the properties of the catheter are the main factor in designing the urinary catheter. Different types of material can give different result on the analysis. The size of the catheter also different even the load given is still same. For further improvement of catheter, the material properties of the catheter must be study first. The polymer coated catheter is a way in improving the catheter. The less value of stress distribution on the catheter can give a long life to the catheter. The catheter also can deflate to the initial condition without cuffing, ridges and creased.

References

1. Lawrence E.L., Turner I.G (2004) Materials for urinary catheters: a review of their history and development in the UK. Medical Engineering & Physics 27:443 453
2. Carr H.A (2000) A short history of the Foley catheter: from hand-made instrument to infection-prevention device. J Endourol 14:5 8
3. Pomfret I (2000) Catheter care in the community. Nursing Standard 14:46 51
4. Robinson J (2001) Urethral catheter selection. Nursing Standard 25:39-42
5. Robinson J (2003) Deflation of a Foley catheter balloon. Nursing Standard 27:33-38

Address of the corresponding author:

Author: Solehuddin Shuib
Institute: School of Mechanical Engineering
Street: 14300 Nibong Tebal
City: Penang
Country: Malaysia
Email: meshuib@eng.usm.my

F. Ibrahim, N.A. Abu Osman, J. Usman and N.A. Kadri (Eds.): Biomed 06, IFMBE Proceedings 15, pp. 178-181, 2007
www.springerlink.com ' Springer-Verlag Berlin Heidelberg 2007

Design of an automated Rapid Maxillary Expansion (RME) appliance. A Preliminary Study.

A.A. Sharizli, N.A. Abu Osman, Z. Radzi, N.A. Yahya, A.A.Shaifizul

University Malaya / Department of Mechanical Engineering, Kuala Lumpur, Malaysia

Abstract - **Expansion of the maxilla is used to correct skeletal and dental transverse discrepancies between the maxilla and mandible. These discrepancies are corrected through a combination of skeletal expansion (separation of the maxillary midpalatal suture) and dental expansion (lateral tipping of the maxillary posterior teeth). The rapid maxillary expansion appliance is a tooth-borne appliance that consists of a midpalatal jackscrew. Appliances currently on the market for expanding the maxillary dentition vary from simple tooth tipping devices to rigid orthopedics expanders. These devices vary widely from active implants with springs and/or screw, to passive acrylic molds and simple medical tape. The problem with current devices is they need to be manipulating manually multiple times to readjust the screw, which requires a considerable time commitment from the family and the physicians. Therefore the goal of project is to design the new automated Rapid Maxillary Expansion (RME) appliances, which encompasses the benefits of current devices and is easily adjustable.**

Keywords – **Rapid Maxillary Expansion, automated appliances, micro gear, micro motor, microcontroller**

I. Introduction

Maxillary expansion used to correct maxillomadibular transverse discrepancies occurs through a combination of skeletal (orthopedic) expansion, which involves separating the maxilla at the midpalatal suture, and dental (orthodontic) expansion, which results from buccal tipping of the maxillary posterior teeth. The proportional of the skeletal and dental movement is dependent on the rate of expansion (rapid or slow) and the age of the patient during treatment.[1-4] The goal of palatal expansion is to maximize the skeletal movement and to minimize the dental movement,[5,6] while allowing for physiological adjustment of the suture during separation. [7,8]

Expansion appliances can be classified as rapid or slow expander. Rapid maxillary expansion (RME) is an expansion of maxilla accomplished through heavy forces that are capable of separating the midpalatal suture at the rate of 0.2 to 0.5 mm per day, while the slow maxillary expansion is an expansion of maxilla accomplished through light forces that are capable of separating the midpalatal suture at the rate of 0.5 to 1.0 mm per week.

Rapid maxillary expansion produces large forces at the sutural site over a short period of time. [6] These high magnitude forces maximize skeletal separation of midpalatal suture by overwhelming the suture before any dental movement or physiological sutural adjustment can occur. [2, 9, 10] In this technique, the doctor will make/used a custom appliance for the patient which is fixed to the upper molars. Generally the patient/parent will turn this appliance every day for a proscribed number of days as directed by the doctor. The appliance is usually activated on a daily basis by having the patient turn the active part of the screw or spring a prescribed amount.

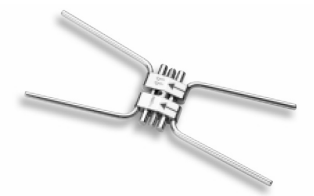

Fig. 1 Butterfly RME appliance

This procedure can be done rapidly or slowly depending upon the patient s age and treatment plan. RME appliances are generally activated 0.2 to 0.5 mm per day with active expansion time usually less than a month. Isaacson and Ingram,[6] using a Haas rapid expander, reported that single activations of the jackscrew (0.2mm) produce forces ranging from 3 to 10 pounds and that multiple daily activation can produce forces up to 20 pounds.

After turning is stopped, the appliance may be kept in place for a number of weeks to allow the widening of the jaw to become permanent, the appliance is then removed.

II. Background of the design problem.

The current devices being used all have limitations, including restricted movement, on-universal application and inefficiency. Current devices are inefficiency because it requires many clinical visits to manipulate the orthopedics or to replace jackscrews as shown in Fig.2. Current expanders turned by placing a pin in a tiny hole (capstan) and pushing that hole with the pin inserted to the rear of the expander. Some of the difficulties using the pin driven

F. Ibrahim, N.A. Abu Osman, J. Usman and N.A. Kadri (Eds.): Biomed 06, IFMBE Proceedings 15, pp. 182-184, 2007
www.springerlink.com ' Springer-Verlag Berlin Heidelberg 2007

expanders are that the expander gets stuck midway because the parent/patient does not push far enough back or the hole gets clogged with food and the patient/parent cannot get the pin in to push or turn it.

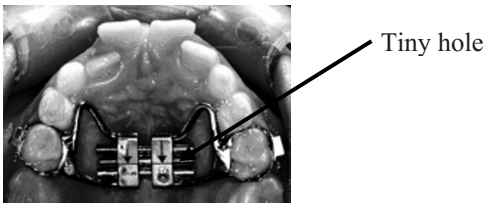

Fig. 2 Butterfly RME appliance fixed to the upper molars

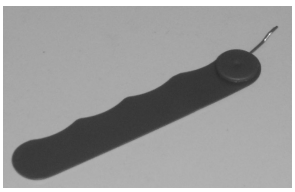

Fig. 3 Butterfly RME pin

Current orthopedics devices share these common features that can be considered as disadvantage to the patient:

- Need to activate manually
  Current devices need the patient/parent to manually activate the screw which is difficult for the parent to use and have been swallowed or inhaled by patients.
- Need to keep track of the number of activations.
  Current practice is to ask parents/patient to keep track of the number of activation. Appliances are usually activated daily. This places the responsibility on the parent to remember both to perform the activation and to record the activation.
- Unknown the force magnitude

All these difficulties and disadvantage will course disruptive to the orthodontics result. Based on this consideration, it is very important to design and develop the new automated appliance that eliminates the conventional tiny pin and will activating automatically and does not require the regular replacement of screw or other mechanism.

III. Appliances construction and design

To overcome the limitations of conventional expansion appliances, the automated RME appliance was designed and developed using a combination of butterfly expander, micro gear and micro motor and also the microcontroller to produce light, continuous pressure on the midpalatal suture as shown in Fig. 4. This appliance is self-activated by micro motor under the control of a microcontroller, which means it can automatically expand the expander to the desired of amount. In this way patient errors such as missed, over-zealous or reversed screw-turns are eliminated, and the visit to the dental heath care provider is reduce to an optimized level.

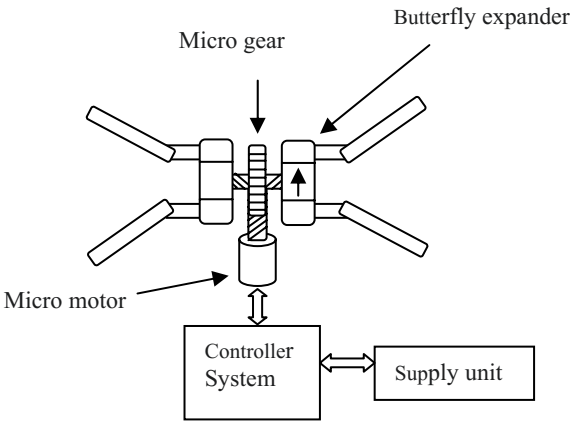

Fig. 4 Schematic diagram of Automated RME appliance

The design and construction of automated RME can be divided into several phases. First phase consists of preliminary design of automated RME system. This includes how to move the expander without using RME pin. Also it is important to decide what type of gear, motor and microcontroller that will be used in this system.

The second phase is mechanical modification of the butterfly expander. Modification is made by replace the tiny hole section of expander screw with the micro gear. The purpose of this micro gear is to interface with micro motor, and when the micro motor spins it will turn this micro gear to a desired position.

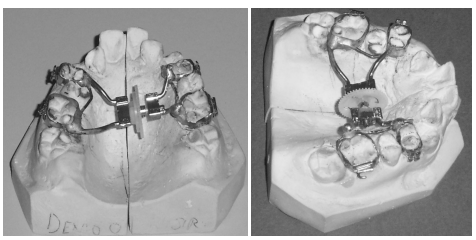

(a) Top View (b) Side view

Fig. 5 Modified Butterfly expander with micro gear

F. Ibrahim, N.A. Abu Osman, J. Usman and N.A. Kadri (Eds.): Biomed 06, IFMBE Proceedings 15, pp. 182-184, 2007
www.springerlink.com ' Springer-Verlag Berlin Heidelberg 2007

The third phase is microcontroller system design. Microcontroller circuit drawing has been done using PCB circuit design. Testing is made to the circuit by writing testing program using assembly language.

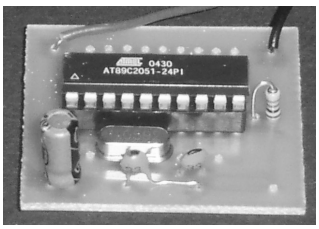

Fig. 6 Microcontroller circuit

Fourth phase is system integration. In this phase, all subsystem consists of microcontroller system, micro motor and modified butterfly expander will be integrated. Assembly language will be used as programming code to control the movement of micro motor.

The fifth phase is testing and clinical trial. In this phase, testing of the new automated RME appliance will be done consists of testing the repeatancy of dental arch movement, measuring the force applied to the RME and also running a preliminary clinical trial

IV. Conclusion

This appliance appears to have a number of advantages over the traditional appliance, the main one being that it can reduce the patient co-operation in RME treatment.

The construction of automated RME is now in phase 4 i.e. system integration. After that the work will continue with phase 5 to determine if the design is feasible and will perform the function intended in the design. From this test, more modification can be made, if needed, to make the appliance perform as required.

References

1. Ladner PT, Muhl ZF. (1995) Changes concurrent with orthodontic treatment when maxillary expansion is a primary goal. Am J Orthod Dentofac Orthop; 108:184-93.
2. Cotton LA. (1978) Slow maxillary expansion: Skelatal versus dental response to low magnitude force in macaca mulatta. Am J Orthod; 73:1-22.
3. Hicks EP. (1978)Slow maxillary expansion. A clinical study of the skeletal versus dental response to low-magnitude force. Am J Orthod: 73:121-41.
4. Krebs AA. (1958) Expansion of the midpalatal suture studied by means of metallic implants. Trans Eur Orthod Soc; 34:163-71.
5. Haas AJ. (1961)Rapid expansion of the maxillary dental arch and nasal cavity by opening the mid-palatal suture. Angle Orthod; 31:73-90.
6. Issacson RJ, Ingram AH. (1964) Forces produced by rapid maxillary expansion. II. Forces present during treatment. Angle Orthod; 34:261-70.
7. Storey E. (1973) Tissue response to the movement of bones. Am J Orthod; 64: 229-47.
8. Ohshima O. (1972) Effect of lateral expansion force on the maxillary structure in cynomolgus monkey. Osaka Dent univ;6:11-50.
9. Haas AJ. (1970) Palatal expansion: Just the beginning of dentofacial orthopedics. Am J Orthod; 57:219-55.
10. Wertz RA. (1970) Skeletal and dental changes accompanying rapid midpalatal suture opening. Am J Orthod;58:41-66.

Address of the corresponding author:

Author: A. A. Sharizli
Institute: Department of Biomedical Engineering, Faculty of Engineering, University of Malaya
City: Kuala Lumpur
Country: Malaysia

F. Ibrahim, N.A. Abu Osman, J. Usman and N.A. Kadri (Eds.): Biomed 06, IFMBE Proceedings 15, pp. 182-184, 2007
www.springerlink.com ' Springer-Verlag Berlin Heidelberg 2007

Effect of Stress Relaxation on Layer Thickness of Articular Cartilage due to Dynamic Loadings

B. Punantapong[1] and M.J. Fagan[2]

[1] Faculty of Applied Science, King Mongkut s Institute of Technology North Bangkok, Bangkok, Thailand
[2] Centre for Medical Engineering and Technology, University of Hull, Hull, UK

Abstract — **Articular cartilage is the bearing material of diarthrodial joints as hydrated soft material such as knee, hip, shoulder, and etc. Then articular cartilage has exceptional lubricating properties and low coefficient of friction that greatly assist its function in synovial joints. Some studies of cartilage lubrication have hypothesized that pressurization of the interstitial fluid may contribute predominantly to reducing the friction coefficient at the contact interface of articular layers. In this paper, we present the response of interstitial fluid pressurization within hydrated soft material of cartilage, which accounts for the cartilage defects. For the computation model, we have chosen an axisymmetric model with two uniformly thick cartilage layers and solved by using finite element method. This model demonstrates that a simultaneous prediction of compression experiments of articular cartilage were under stress relaxation and dynamic loading. For the experimental results, we found that the increased fluid concentration of the tissue's solution can be achieved the minimum friction coefficient. Furthermore, it is observed that the friction coefficient does not remain constant under various loads or fluid concentration and correlation analyses that the equilibrium value depends in part on the compressive strain in the cartilage.**

Keywords — **Stress relaxation, Articular cartilage**

I. Introduction

The function of articular cartilage is to serve as the bearing material of diarthrodial joints. This tissue generally remains viable over a lifetime of loading, maintaining a low friction coefficient even under high stresses. Therefore, it has been the focus of many researchers to investigate the friction and lubrication properties of articular cartilage and to understand its normal and pathological behaviors. However, articular cartilage exhibit markedly different material properties in tension and compression. Then its nonlinearity in the tissue response is dictated by the collagen content and its microstructural architecture, which govern primarily the tissue s tensile properties, and the proteoglycan content and its molecular organization as well as water content, which govern its compressive properties.

In recent studies [1,2,13,14], They have been shown that the incorporation of tension-compression nonlinearity in biphasic constitutive models of articular cartilage can considerably improve the prediction of the tissue s response to unconfined compression. The intrinsic viscoelasticity of the solid matrix of cartilage has also been shown to improve the prediction of experimental response in unconfined compression [3,8]. These models were more comprehensive for describing a variety of articular cartilage mechanical behavior. At the same time, the experimental measurement of cartilage interstitial fluid pressure have verified the mechanism of fluid load support and demonstrated good agreement between theoretical predictions and experimental measurement [11,13]. Thus the objective of this study was to test the axisymmetric model with two uniformly thick cartilage layers against experimental data from unconfined compression tests under stress-relaxation at slow and fast strain rates as well as dynamic loading.

II. Materials and methods

Since contact studies of articular cartilage have provided valuable insight on the state of stress in tissues modeled as solid-fluid mixtures or poroelastic materials [1,10]. These studies have assumed a linear, isotropic model for cartilage, and although there is agreement between predicted regions of high stress and experimental evidence of tissue damage, some observed failure modes have yet to be predicted by such tissue models [16]. Some studies of acute articular loading of joints also suggest that fissures are observed at the surface of cartilage immediately after loading [12,15], failure at these sites has not been predicted by isotropic biphasic models of cartilage. So the contact boundary conditions for interfaces between dissimilar biphasic materials developed by researchers [4,6,7]. However, the numerical solution of a contact problem was intrinsically nonlinear, since the contact area is unknown in advance.

However, the finding of this study is that the observed transient response of the friction coefficient of cartilage, as represented by μ_{eff} / μ_{eq} which can be predicted the frictional force results primarily from solid-to-solid interactions at the contact interface. Assuming smooth surfaces, the fraction of contact area over which the opposing solid phases are in contact with each other, therefore the area fraction over which the fluid pressure is

F. Ibrahim, N.A. Abu Osman, J. Usman and N.A. Kadri (Eds.): Biomed 06, IFMBE Proceedings 15, pp. 185-188, 2007
www.springerlink.com ' Springer-Verlag Berlin Heidelberg 2007

actually supporting load [1]. According to this model, the solid-to-solid contact force, W^{ss} is equal to the total normal load minus the portion of the normal load supported by fluid-to-fluid or fluid-to-solid interactions. So the load transmitted across solid to-solid contact at the interface is given by [13].

$$W^{ss} = W - (1 - \phi^{s_0}\phi^{s_1})W^{p} \qquad (1)$$

where W^{p} is the fluid load at the ambient pressure and W is the total normal load.

Therefore, the measured (effective) friction coefficient at the contact interface is given by $\mu_{eff} = F/W$, where F is the friction force. Since most of the friction is presumed to occur at the solid-to-solid interface, the model postulates that the friction force is proportional to the solid-to-solid normal contact force, $F = \mu_{eq} W^{ss}$, where μ_{eq} is the equilibrium friction coefficient achieved when fluid pressure has subsided, $W^{p} = 0$. Then

$$\mu_{eff} = \mu_{eq}\left[1 - (1 - \phi^{s_0}\phi^{s_1})\frac{W^{p}}{W}\right] \qquad (2)$$

At the same time, these model properly are reduced to Coulomb s law when $\phi^{s0} = \phi^{s1} = 1$ (i.e., for non porous media); whereas it predicts negligible friction in the absence of a solid phase on either side of the interface ($\phi^{s0} = 0$ and $W^{p} = W - conditions$ which subsume fluid film lubrication). Then the ratio W^{p}/W is time dependent under most loading conditions, this model produces a transient friction coefficient, as typically observed experimentally.

In this experiment, we have chosen an axisymmetric model with two uniformly thick cartilage layers, to study the effects of transverse isotropy and tissue curvature under dynamic loading (Fig. 1). These models do not represent specific diarthrodial joints, but are representative axisymmetric appropriations to three-dimensional contact geometries found in the knee, hip, or shoulder. So the finite element meshes for each model had over 28,000 elements with 8 nodes and analyzed by using ANSYS code. These meshes are graded toward the contact surfaces with the mesh density based on findings in validation studied of the numerical procedure. For the indentation tests, the specimen was compressed between two impermeable flat smooth platens. For each experiment, a tare load of 0.65 N was first applied on the specimen and maintained until equilibrium was achieved (approx. 30 min) ; We choose this value of load to ensure that results are valid for the linear form of the biphasic theory [10]. After that, the load and unload were changed between 0.65-800 N at a fast ramp displacement rate of 1 mm/s with over a period of at least 10 min.

III. Results and discussion

The axisymmetric model was constructed using all of the measured geometric data reported above. For the indentation tests, we were applied identical force magnitude and directions as used in the experiments. Fig. 1 shows two identical cylindrical biphasic layers boned to impermeable rigid subchondral bone substrates are subjected to the step load intensity, W. Each layer has a radius of curvature, R, and cartilage thickness, b_i , which R is varied from 5-120 mm and b_i is fixed 0.8 mm respectively. The lower bone is held fixed, the left edge of the model is the axis of rotation, and the uniform traction is applied to the upper bone. In addition, if the curvature increased, the contact radius will be decreased and hence the contact stress is increased at the tissue surface. Since the contact radius does not change significantly in the short time, contact tractions also do not vary significant, but at very long times after the load is applied (e.g. $t >>$ 20 min.) all of the load is supported by the solid phase. Thus more highly curved models had smaller contact areas and larger contact stresses than corresponding isotropic or flat models. Then the surface curvature is decreased, the stress at the surface will be increased as shown in Fig. 2.

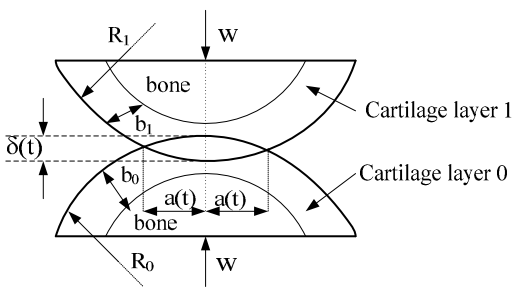

Fig. 1 Axisymmetric geometry for the case analyzed.

F. Ibrahim, N.A. Abu Osman, J. Usman and N.A. Kadri (Eds.): Biomed 06, IFMBE Proceedings 15, pp. 185-188, 2007
www.springerlink.com ' Springer-Verlag Berlin Heidelberg 2007

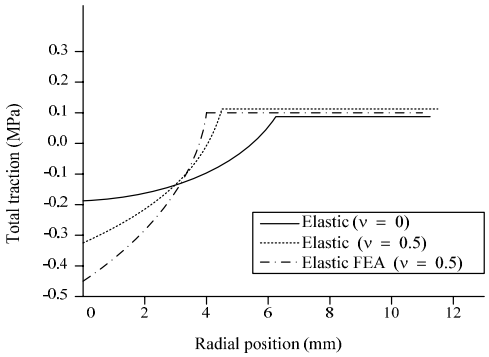

Fig. 2 Total contact traction, calculated as arc-length along the contact surface at time response(t = 0.5 sec.)

Next, we were tested the traction of load supported by fluid pressurization. So the tests were simulated the movement of indenter in a function of time and radius of curvature as shown the result in Fig. 3. It shows that greater joint congruence promotes greater interstitial fluid load support. These results demonstrate that the interstitial fluid pressure supports the majority of the applied load immediately after load application. From Fig. 3, the fluid pressurization then decreases with increasing time, eventually dropping to zero at equilibrium, because the applied load intensity remains constant, the effective solid traction can be seen to increase with increasing time. Therefore, fluid pressurization is maintained longer with increased congruence. It is the fact that the fraction of fluid load support becomes greater as the applied load increases.

According to Eqn. (2), the effective friction coefficient, μ_{eff} achieves its smallest value when W^p/W is greatest; this occurs at the instantaneous response. The experimental result, we found that μ_{eff}/μ_{eq} is observed to follow opposite trends when increasing osmotic pressure by these two alternate mechanisms. With concentration-induced

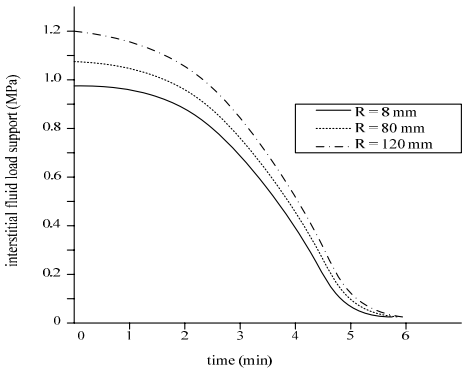

Fig. 3 The load supported by fluid pressurization, as a function of time and radius of curvature.

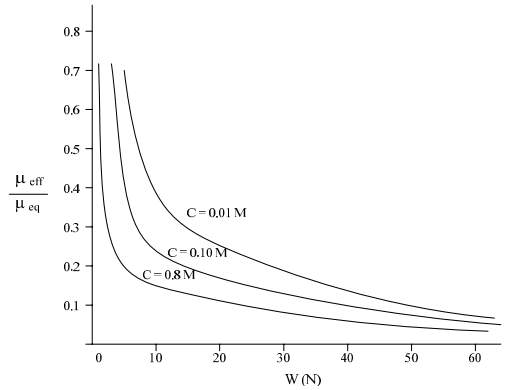

Fig. 4 Ratio of the friction coefficient, μ_{eff}/μ_{eq} as predicted when using the instantaneous fluid load support, assuming a radius of curvature, r = 1 mm and various the fluid concentration rate.

increases in osmotic pressure μ_{eff}/μ_{eq} is increased, but with load-induced increases in osmotic pressure this ratio decreased. This higher fluid load support produces a ratio μ_{eff}/μ_{eq} which decreases with increasing the fluid concentration, C and increasing, W, as demonstrate in Fig. 4 and Fig. 5. These finding on μ_{eff} and μ_{eff}/μ_{eq} will be effective on the failure of cartilage, especially the qualitative agreement with the prediction of the thickness water contend, and unconfined compression modulus of cartilage as a function of solution concentration of fluid and applied load on the articular cartilage.

In Fig. 6 shows the comparison of the experiment data of the dynamic modulus as measured from the dynamic compression tests [5,9] and the data were obtained from the indentation by dynamic loading on the model. Then they tested on the sinusoidal displacement amplitude of 6 μm and frequency between 0.001 Hz to 1 Hz (10 cycles each). For the conversion of the experiment data, it converted from the time domain to the frequency domain using the procedure outlined in [5]. From Fig. 6, we found that the

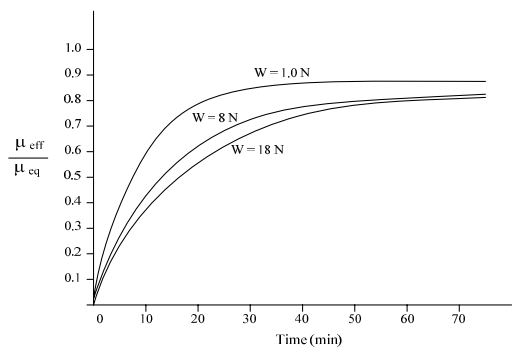

Fig. 5 Average experimental friction response of the friction coefficient, μ_{eff}/μ_{eq} versus time.

F. Ibrahim, N.A. Abu Osman, J. Usman and N.A. Kadri (Eds.): Biomed 06, IFMBE Proceedings 15, pp. 185-188, 2007
www.springerlink.com ' Springer-Verlag Berlin Heidelberg 2007

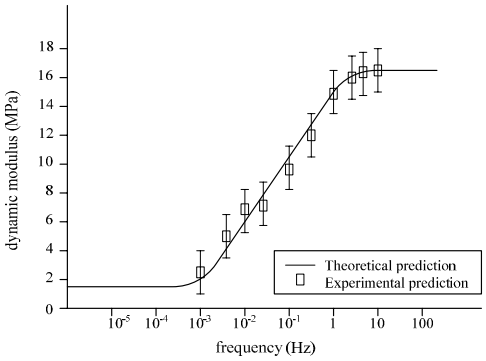

Fig. 6 Comparison of the experiment data of the dynamic modulus as measured from the indentation tests and theoretical prediction [5,9].

peak dynamic unconfined compression modulus measured from the tests averages 16 MPa at the frequency of 1 Hz, while the previous studies reported at 12-20 MPa [5,9].

IV. Conclusions

This experimental study was to use finite element method to investigate the influence of cartilage anisotropy and curvature on the prediction of indentation in coated articular cartilage under stress relaxation and dynamic loading. The results demonstrate that the friction coefficient of cartilage can be as good as agreement with other reports in the literature. Then we have maintained that this remarkably low friction coefficient should be attributed to a boundary lubricant present in the cartilage or synovial fluid.

References

[1] Ateshian G.A., Wang H. and Lai W.M. (1998) The role of interstitial fluid pressurization and surface porosities on the boundary friction of articular cartilage. J. Tribol. 120: 241-251.

[2] Basser P.J., Schneidermann R., Bank, R.A., Wachtel E.and Maroudas A. (1998) Mechanical properties of the collagen network in human articular cartilage as measured by osmotic stress technique. Arch. Biochem. Biophys. 15(351): 207-219.

[3] Donzelli P.S. and Spilker R.L. (1998) A contact finite element formulation for biological soft hydrated tissues. Comp. in Meth. in Appl. Mech. Eng. 153: 63-79.

[4] Farguhar T., Dawson P.R.and Torzilli P.A. (1990) A microstructural model for the anisotropic drained stiffness of articular cartilage. J. Biomech. Eng. 112: 414-425.

[5] Fortin M., Soulhat J., Shirazi-Adl A., Hunziker E.B. and Buschmann M.D. (2000) Unconfined compression of articular cartilage: nonlinear behavior and comparison with a fibri-reinforced biphasic model. J. Biomech. Eng. 122: 189-195.

[6] Hale J.E., Rudert M.J. and Brown T.D. (1993) Indentation assessment of biphasic mechanical property deficits in size-dependent osteochondral defect repair. J. Biomech. 26: 1319-1325.

[7] Holmes, M.H. and Mow V.C. (1990) The nonlinear characteristics of soft eels and hydrated connective tissues in ultrafiltration. J. Biomech. 23: 1145-1156.

[8] Huyghe J.M. and Janssen J.D. (1997) Quadriphasic mechanics of swelling incompressible porous media. Inst. J. Eng. Sci. 35: 793-802.

[9] Kim Y.J., Bonassar L.J. and Grodzinsky A.J. (1995) The role of cartilage streaming potential, fluid flow and pressure in the stimulation of chondrocyte biosynthesis during dynamic compression. J. Biomech. 28: 1055-1066.

[10] Mow V.C., Kuei S.C., Lai W.M. and Armstrong C.G.(1980) Biphasic creep and stress relaxation of articular cartilage in compression: Theory and experiments. J. Biomech. Eng. 102: 73-84.

[11] Narmoneva D.A., Wang J.Y. and Setton L.A. (1999) Nonuniform swelling-induced residual strains in articular cartilage. J. Biomech. 32: 401-408.

[12] Newberry W.N., Zukosky D.K. and Haut R.C. (1997) Sunfracture insult to a knee joint causes alterations in the bone and in the functional stiffness of overlying cartilage. J. Ortho. Res. 15: 450-455.

[13] Soltz M.A. and Ateshian G.A. (2000) Interstitial fluid pressurization during confined compression cyclical loading of articular cartilage. Ann. Biomed. Eng. 28: 150-159.

[14] Suh J.K. and Bai S. (1997) Biphasic poroviscoelastic behavior of articular cartilage in creep indentation test. Trans. Ann. Meet.-Orthop. Res. Soc. 22: 823.

[15] Thompson R. and Oegema T., Lewis J. and Wallace L. (1991) Osteoarthritic changes after acute transarticular load. J. Bone and Joint Surg. 73A: 990-1001.

[16] Woo, S., L.-Y. Simon, B.R., Kuei, S.C. and Akeson W.H. (1980) Quasi-linear viscoelastic properties of normal articular cartilage. J. Biomech. Eng. 102: 85-90.

Corresponding author:

Author: Assoc.Prof. Boonyong Punantapong
Institute: King Mongkut s Institute of Technology North Bangkok
Street: Piboolsongkram Rd., Bangsue
City: Bangkok 10800
Country: Thailand
E-mail: bpp@kmitnb.ac.th

F. Ibrahim, N.A. Abu Osman, J. Usman and N.A. Kadri (Eds.): Biomed 06, IFMBE Proceedings 15, pp. 185-188, 2007
www.springerlink.com ' Springer-Verlag Berlin Heidelberg 2007

Effects of Targets on Reaching Performance and Postural Balance during Standing in Persons with Left Cerebral Vascular Accidents

Ching-yi Wu[1], Tzu-hui Wei[1], Hsieh-ching Chen[2], and Keh-Chung Lin[3]

[1] Department of Occupational Therapy & Graduate Institute of Clinical Behavioral Science, Chang Gung University, Taoyuan, Taiwan
[2] Department of Industrial Engineering and Management, Chaoyang University of Technology, Wufong, Taiwan
[3] School of Occupational Therapy, College of Medicine, National Taiwan University, Taipei, Taiwan

Abstract—**Purpose: The aim of this study is to investigate the effects of concrete vs. abstract tasks on reaching and postural performance during standing.—Methods: Twenty subjects with left cerebral vascular accidents (LCVA) and 15 age-matched healthy subjects performed the tasks under the target present vs. the target absent conditions with their less affected arm during standing. The condition of target present required the patients to push the glass forward as far as possible whereas the object absent condition involved reaching forward along the track as far as possible. The reaching performance was measured by forward reaching distance, and the postural control by derivatives of center of pressure (CoP) including forward displacement (FD), medial-lateral (M-L) shift, and average velocity (AV) of CoP.—Results: The LCVA group showed significant effects on reaching distance and AV of CoP. The control group demonstrated significant effects on AV of CoP.—Conclusion: The findings of this study partially support the notion that target present task optimized task performance. Beneficial effects were found on reaching distance and AV of CoP in healthy adults and on AV of CoP in LCVA patients, indicating LCVA patients demonstrated deficits in response to task target. These finding have implications for postural trainings in patients with stroke.**

Keywords-- **cerebrovascular accident, reaching, postural balance, kinematics, kinetics.**

I. Introduction

A self-initiated movement such as stand reaching movement is more important for daily function and more essential for practical standing balance than the movement arising from external perturbation.[1] In the stand reaching task, the central nervous system may program movement and posture together to ensure the smooth transition from one posture/movement to another one.[1] The trajectory of reaching movement can be constrained by postural change and characterized by reaching distance. The standing balance can be maintained by a combination of coordinated joint rotations that may involve movement of the center of pressure (CoP).[2]

CoP indicates the location where the resultant ground reaction force has its origin and is directed towards the body. The CoP distance in the forward direction indicates the extent to which the upper extremity and the trunk move forward without balance loss. The CoP distance in the medial-lateral (M-L) direction indicates the instability of trunk during task performance because the M-L shift of CoP has been suggested to be associated with fall incidents.[3] The average velocity (AV) of change in CoP refers to the rate of change in sway path which may indicate the extent of postural sway.[2] Patients with better balance control may have slower AV of change in CoP.[4]

Reaching and postural responses during stand reaching are reliant on many factors such as environmental context.One line of research showed that the seated tasks with target present produced better reaching performance than those without targets present.[1] There was only one study investigating the influence of a stand reaching task with concrete targets on reaching performance in older adults. Another line of research[1,5] modulated the task targets (e.g., target distance or picking up an object off the floor) to be reached, grasped to observe the changes of postural response. There is a lack of research on evaluating the effects of the presence or absence of objects under the stand reaching task.

Converging these two lines of research, this study examined the performance of reaching and postural response by contrasting a task with concrete target (i.e., a target-present task) during standing with a task excluding a concrete target (i.e., a task-absent task) in patients with LCVA and healthy adults. We hypothesized that a target-present task would elicit better performance than a target-absent task in both the LCVA and the control groups. Better performance was reflected by a farther reaching distance, and farther FD and less M-L shift of CoP.

II. Methods

A. Subjects

Twenty patients with LBD (12 men, 8 women, aged 46 to 79 years, mean age 61 yrs) and 15 patients with RBD (9 men, 6 women, aged 41 to 68 years, mean age 60 yrs) volunteered for this study. All participants were enrolled after having given their informed consent and were right-handed. The duration post onset of stroke ranged from 9 to 21 months.

F. Ibrahim, N.A. Abu Osman, J. Usman and N.A. Kadri (Eds.): Biomed 06, IFMBE Proceedings 15, pp. 189-191, 2007
www.springerlink.com ' Springer-Verlag Berlin Heidelberg 2007

B. Materials and instrumentation

A glass with 14.5 cm in height and 6.5 cm in diameter was used as the target object for the condition of target present.

A 6-camera motion analysis system (VICON 370 3-D, Oxford Metrics Inc), 2 force plates 510 * 460 mm in size (AMTI, Advanced Mechanical Technology Incorporation, Model Or 6-5-1000), and an IBM-compatible personal computer were connected to record kinematic and kinetic data. The motion analysis system, which sampled at a rate of 60 Hz, was used to capture the upper extremity movements of infrared markers during standed reaching tasks (see Fig.1). The force plates were mounted side by side, sampling at a rate of 60 Hz to obtain CoP displacement.

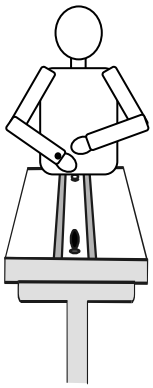

Fig. 1. Experimental set-up.

A hand switch, connected to the analog input of the VICON system, was used to indicate the time when the hand started to move. The end of the movement was obtained when the least distance between the marker attached on the glass and another marker located on the table occurred.

C. Procedures

The experimental set-up was shown in Fig. 1. The subjects received two experimental conditions. Under the condition of target present, the subject was instructed to push the glass forward as far as possible. For the condition of target absent, the patient was required to reach forward along the track as far as possible.

D. Research design

A counterbalanced repeated-measures design was used.

E. Data reduction

The 3-D data obtained from the marker on the head of ulna were processed by a customer written program to obtain reaching distance.

The force plate raw data were reduced to obtain CoP displacement including the variables of FD, M-L shift, and AV of CoP. The variables of M-L shift of CoP were normalized to correct for differences in reaching distance.

F. Data analysis

The 2*2 mixed (i.e., one between-factor and one repeated-factor) analyses of variance (ANOVA) were conducted to test the a priori hypotheses. The between-factor was the sequence and the repeated-factor (or the within-factor) was the order. The effects of target presence/absence were embedded in the sequence by order interaction.

III. Results

The LCVA group showed significant effects on reaching distance and AV of CoP. The control group demonstrated significant effects on AV of CoP. No significant effects on FD and M-L shift in the LCVA group, and on reaching distance, FD and M-L shift in the control group were found.

IV. Discussion

The findings of this study partially support out hypotheses that target present task optimized task performance, in comparison with target absent task. There is no difference in FD and L-M shift of CoP between two conditions in two groups, indicating FD and L-M might not be sensitive to detect the changes in task targets in this study.

The findings in the healthy adults suggested that task target has an impact on programming movement and posture together. These findings are consistent with those of previous studies.[6] Better reaching performance and balance control reflected by AV of CoP, in the target presence task suggested that the target object might induce better organization of reaching and postural coordination in certain aspect. The central nervous system programmed reaching and posture in accordance with task demands and, in comparison with the target absent task, the target presence provided concrete visual target to help better organization of reaching and postural control in terms of reaching distance and the certain aspect of CoP displacement.

F. Ibrahim, N.A. Abu Osman, J. Usman and N.A. Kadri (Eds.): Biomed 06, IFMBE Proceedings 15, pp. 189-191, 2007
www.springerlink.com ' Springer-Verlag Berlin Heidelberg 2007

Different from the results of the healthy adults, LCVA patients only showed better balance control (AV of CoP), not reaching performance, in the target presence task, suggesting that the target object might only induce better organization of postural coordination. The target present task did not elicit farther reaching distance than the target absent task in the LCVA group. The possible reason for the finding is that the former task involved reaching and grasping components during the whole task performance whereas the latter task only required reaching forward one. The former task demanded more attention on coordination of reaching and grasping to move the cup forward without knocking it down than the latter one. Since stroke patients preserved deficits in movement coordination, they compromised the goal of reaching forward as far as possible to secure the posture balance.

The implication for practice is that the training programs for postural control may use functional reaching task with target presence during standing to decrease the postural instability or sway. To accumulate more evidence about the efficacy of task target on movement control, future research may also provide tasks with more challenges to postural control such as giving obstacles during stand reaching.

V. Conclusion

This study is one of few studies showing functional utilization of objects during stand reaching task could decrease postural sway in patients with LCVA. These finding have implications for postural trainings in patients with stroke and for further research on validating the therapeutic efficacy of task demands utilizing objects during stand reaching on postural control.

Acknowldegement

The National Health Research Institute in Taiwan (NHRI-EX94-9103EC).

References

1. Stapley P, Pozzo T, Grishin A. The role of anticipatory postural adjustments during whole body forward reaching movements. *Neuroreport.* 1999;9:395-401
2. Jonsson E, Henriksson M, Hirschfeld H. Does the functional reach test reflect stability limits in elderly people? *J Rehabil Med*. 2002;35:26-30.
3. Wernick-Robinson M, Krebs DE, Giorgetti MM. Functional reach: does it really measure dynamic balance? *Arch Phys Med Rehabil*. 1999;80:262-269.
4. Berg KO, Maki BE, Williams J, Holliday P, Wood-Dauphinee SL. Clinical and laboratory measures of postural balance in an elderly population. *Arch Phys Med Rehabil*. 1992;73:1073-1080.
5. Kaminski TR, Simpkins S. The effects of stance configuration and target distance on reaching: I. movement preparation. *Exp Brain Res.* 2001;136, 439-446.
6. Trombly CA, Wu C. Effect of rehabilitation tasks on organization of movement post stroke. *Am J Occup Ther* .1999;53:333-344.

Address of the corresponding author:

Author: Ching-yi Wu
Institute: Department of Occupational Therapy & Graduate Institute of Clinical Behavioral Science, Chang Gung University
Street: 259 Wen-hwa 1st Road, Kwei-shan,
City: Taoyuan
Country: Taiwan
Email: cywu@mail.cgu.edu.tw

F. Ibrahim, N.A. Abu Osman, J. Usman and N.A. Kadri (Eds.): Biomed 06, IFMBE Proceedings 15, pp. 189-191, 2007
www.springerlink.com ' Springer-Verlag Berlin Heidelberg 2007

Human Kicking Motion Using Efficient Forward Dynamics Simulation and Optimization

M. Stelzer and O. von Stryk

Technische Universität Darmstadt, Simulation and Systems Optimization Group, Darmstadt, Germany

Abstract— **The problem of finding and predicting muscle activations for free goal oriented or measured human motion is one of the basic problems in biomechanics. While currently inverse dynamics approaches are most commonly used for their computational efficiency, they can not handle the problem in its most general form. We here present computational methods that increase the computational efficiency of the forward dynamics approach by two orders of magnitude. Results are presented for a time optimal kicking motion and the analysis of a measured kicking motion. Current work includes investigation of a jumping motion and finding optimal walking motions for a robot that is driven by artificial muscles.**

Keywords— **human kicking motion, efficient forward dynamics simulation and optimization, direct collocation, goal oriented motions, analysis of measured motion**

I. Introduction

Biomechanical systems are very complex due to the absence of a unique assignment of actuation and resulting motion: one joint is driven by more than one muscle and there are muscles that span and influence more than one joint. Furthermore, a certain motion goal like reaching a certain position may be realized by an infinite number of joint motions. The subject of this paper is how to overcome these two redundancy problems and calculate muscle activations for measured or free (goal oriented) human motions efficiently using general biodynamical human models, where the latter in fact means prediction of human motion.

II. Biomechanical multibody systems

The human body is modeled as multibody system in two or three dimensions including mass, center of mass and inertia of all limbs, position and orientation of the joints and boundary constraints for the joint angle range. The dynamic behavior of the multibody system is described by the well known differential equations of second order:

$$\mathbf{M}\ddot{\mathbf{q}} = \boldsymbol{\tau} - C(\mathbf{q},\dot{\mathbf{q}}) - G(\mathbf{q}) + \mathbf{J}_c^T\mathbf{f}_c,$$

where $\mathbf{q}$ are the joint angles, τ are the total torques, $\mathbf{M}$ is the mass matrix, $C(\mathbf{q},\dot{\mathbf{q}})$ are the Coriolis and centrifugal forces, $G(\mathbf{q})$ are the gravitational forces, and $\mathbf{J}_c^T\mathbf{f}_c$ are the contact forces. The equation is solved for $\ddot{\mathbf{q}}$ by the Articulated Body Algorithm, cf. Section IV.A.

The muscles are modeled in a Hill-type way[12]; force-velocity-(FV) and tension-length-(TL)-relations describe the functional capabilities of the muscles. Muscle paths are modeled to get the right working range of the FV- and TL-relation and to get the right line of action and point of actuation of the muscles. The muscles may not exert their forces instantaneously but the force generation follows certain chemical processes: muscle activation leads to an increased concentration of calcium ions which then results in the force generation. To include the muscle activation dynamics into our model, we use the following differential equation:

$$\dot{\gamma} = c_1(c_2 u - \gamma),$$

where u is the muscle activation (which will be a control of the optimal control problem) and γ is the calcium ion concentration (which will be a state in the optimal control problem). Properties of tendons and ligaments are taken into account by passive torques.

Several general merit functions for distribution of the total joint torque to the muscle forces are of interest, e.g. minimization of the sum of all muscle forces, where each of the forces may be scaled by diameter of the muscle or by the torque to be applied to the joint.

With our approach all general merit functions may be investigated. The models are validated by comparing the optimization results with data of real human data such as EMG measurements or joint angle trajectories. Once having validated the model and having found which merit function applies in human motion, it is possible to predict motions.

III. Forward vs. inverse dynamics simulation

The problem to be solved may be stated as: minimize a suitable merit subject to the multibody system and muscle activation system of differential equations and nonlinear and boundary constraints. Two generally different approaches exist for solving it: inverse and forward dynamics calculations. While inverse dynamics calculation directly concludes from the joint motion to the muscle activations by some specific assumptions on the model only [6], forward dynamics approaches solve the optimization problem of adjusting the muscle activations so that the resulting

F. Ibrahim, N.A. Abu Osman, J. Usman and N.A. Kadri (Eds.): Biomed 06, IFMBE Proceedings 15, pp. 192-196, 2007
www.springerlink.com ' Springer-Verlag Berlin Heidelberg 2007

motion (here the forward dynamics calculations are involved) best fit the given (measured) motion.

Inverse dynamics approaches currently are the most efficient numerical methods but they have the drawback that they are directly applicable only to the problem of analyzing a given motion; forward dynamics approaches also can handle the problem of optimizing goal oriented motions (i.e. predicting human motion) for validated models. The assumption of specific merit functions in inverse dynamics approaches does not allow considering general merit function of interest as it is the case with forward dynamics.

Currently, forward dynamics approaches are based on control parameterization where only the controls are discretized; the states are obtained by numerical integration of the differential equations of motion[5]. Repeated evaluations are needed to obtain gradients for optimization which leads to high computational effort. Our approach is based on discretizing both the controls and the states and thus solving the differential equations of motion simultaneously to the optimization [8], which is more efficient.

IV. Dynamics Algorithms and Optimal Control Techniques

The two main numerical tasks with the forward dynamics approach are computing of the forward dynamics of the underlying multibody system and solving the optimal control problem to overcome the redundancies.

A. Efficient dynamics algorithm: Articulated body algorithm

For only few degrees of freedom, the systems of differential equations of motion may be stated in closed form. For larger systems, numerical methods are used. We use the Articulated Body Algorithm [1], which is a recursive algorithm of linear order w.r.t. the number of joints and is highly modular for different components of the model which allows an efficient object oriented implementation [3].

B. Numerical optimal control techniques

To be able to treat the problem of finding muscle activations for free or given human motions, it is necessary to consider the most general form of optimal control problems involving box constraints, boundary conditions and nonlinear inequality constraints. More precisely, the target is to find control vectors $\mathbf{u}(t)$ (and thus also state vectors $\mathbf{x}(t)$) that minimize some objective function

$$J=\varphi(\mathbf{x}(t_f),\mathbf{x},t_f)+\int_0^{t_f} L(\mathbf{x}(t),\mathbf{u}(t),t)dt$$

which consists of a scalar part (which may involve the state at final time t_f, all states and the final time) and an integral part (which may involve all states and controls). This objective function is minimized subject to constraint, which may consist of a system of nonlinear ordinary differential equations

$$\dot{\mathbf{x}}(t)=\mathbf{f}(\mathbf{x}(t),\mathbf{u}(t),t),$$

initial and final values

$$\mathbf{r}(\mathbf{x}(0),\mathbf{x}(t_f),t_f)=\mathbf{0},$$

and nonlinear state and control constraints

$$\mathbf{g}(\mathbf{x}(t),\mathbf{u}(t),t)=\mathbf{0},$$

where a special case of the latter are box constraints (simple lower and upper bounds for the states and controls).

The optimal control problem is solved using the direct collocation method DIRCOL [8]. Note that the differential equations of motion are of second order, while currently the optimal control technique used only treats differential equations of first order. Therefore the second order differential equations of motion are transformed into a set of differential equations of first order but double size.

Both the controls and the states are discretized by piecewise polynomials and thus the optimal control problem is transformed into a nonlinear constrained optimization problem (NLP). The NLP is solved using efficient SQP method SNOPT [2]. By this descretization of both the states and the controls, the system of differential equations is solved simultaneously to the optimization. SNOPT exploits the special structure of the discretization which results in an extremely efficient numerical method.

V. Applications

A. Time optimal kicking motion

As a first application of the method, the kicking motion from [9] was chosen. The task is to find a kicking motion, i.e. the motion of the leg from a given initial posture to a final posture in minimum time. The objective function is thus chosen to be:

$$J=t_f.$$

The planar leg model consists of two joints and five muscle groups, cf. Fig. 1. The resulting optimal control problem comprises two states for each of the joint angles, two states for the joint angle velocities and five states for the calcium ion concentration in the muscles. The muscle activations of the five muscle groups are the controls. The complete state vector is thus given by:

F. Ibrahim, N.A. Abu Osman, J. Usman and N.A. Kadri (Eds.): Biomed 06, IFMBE Proceedings 15, pp. 192-196, 2007
www.springerlink.com ' Springer-Verlag Berlin Heidelberg 2007

$$x = \begin{pmatrix} q_1 \\ q_2 \\ \dot{q}_1 \\ \dot{q}_2 \\ \gamma_1 \\ \vdots \\ \gamma_5 \end{pmatrix} = \begin{pmatrix} \text{hip angle} \\ \text{knee angle} \\ \text{hip velocity} \\ \text{knee velocity} \\ \text{ca ion concentration muscle 1} \\ \vdots \\ \text{ca ion concentration muscle 5} \end{pmatrix}$$

and the control vector is given by

$$u = \begin{pmatrix} u_1 \\ u_2 \\ u_3 \\ u_4 \\ u_5 \end{pmatrix} = \begin{pmatrix} \text{activation of muscle 1} \\ \text{activation of muscle 2} \\ \text{activation of muscle 3} \\ \text{activation of muscle 4} \\ \text{activation of muscle 5} \end{pmatrix}.$$

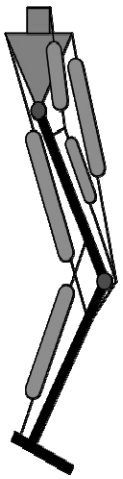

Fig. 1 Kinematic structure of the leg.

To make the model perform a kicking motion, the initial and the final value of the hip and knee angles are enforced as boundary conditions for the starting time t_0

$$\begin{aligned} q_1(t_0) &= 0.1, \\ q_2(t_0) &= 0.15 \\ \dot{q}_1(t_0) &= \dot{q}_2(t_0) = 0 \\ \gamma_1(t_0) &= \ldots = \gamma_5(t_0) = 0 \end{aligned}$$

and for final time t_f

$$\begin{aligned} q_1(t_f) &= 0.8 \\ q_2(t_f) &= -0.05 \\ \dot{q}_2(t_f) &= 0. \end{aligned}$$

Inequality constraints are imposed to the states and controls to model geometric constraints and the box constraints on the activation rates and calcium ion concentrations:

$$\begin{aligned} 0 \le q_1 \le 1.5 \\ -0.05 \le q_2 \le 1.5 \\ 0 \le u_i, \gamma_i \le 1, i = 1, \cdots, 5. \end{aligned}$$

As a starting solution, linear interpolation of initial and final value are used if known and 0 otherwise. More details may be found in [7,10].

Discretization of the states and controls on a grid of 60 grid points leads to a NLP with 531 variables and 829 nonlinear constraints which is solved in about 6 sec on a 1700 MHz+ Athlon computer, which is two orders of magnitudes faster than current methods for forward dynamics optimization for exactly the same problem [11]. Computation times and details on the size of the resulting nonlinear optimization problem are shown in Table 1. The resulting joint motions match those observed in real human kicking very well (cf. Fig. 2). The activations may be found in Fig. 3.

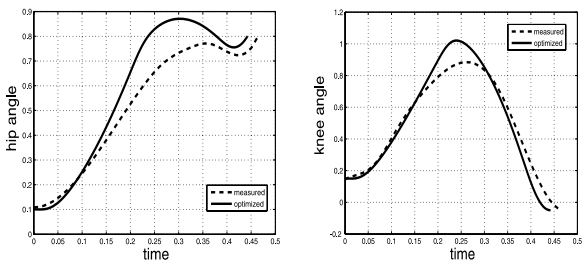

Fig. 2 Joint motion of the hip (left) and the knee (right). Solid line is obtained from optimization, dashed line a measurement of real human kicking.

Table 1 Details about the size and calculation times for time optimal kicking motion

Grid points	10	60
Nonlinear constraints	81	829
Nonlinear variables	129	531
Computing time (1700 MHz+)	1.2 s	6.3 s

F. Ibrahim, N.A. Abu Osman, J. Usman and N.A. Kadri (Eds.): Biomed 06, IFMBE Proceedings 15, pp. 192-196, 2007
www.springerlink.com © Springer-Verlag Berlin Heidelberg 2007

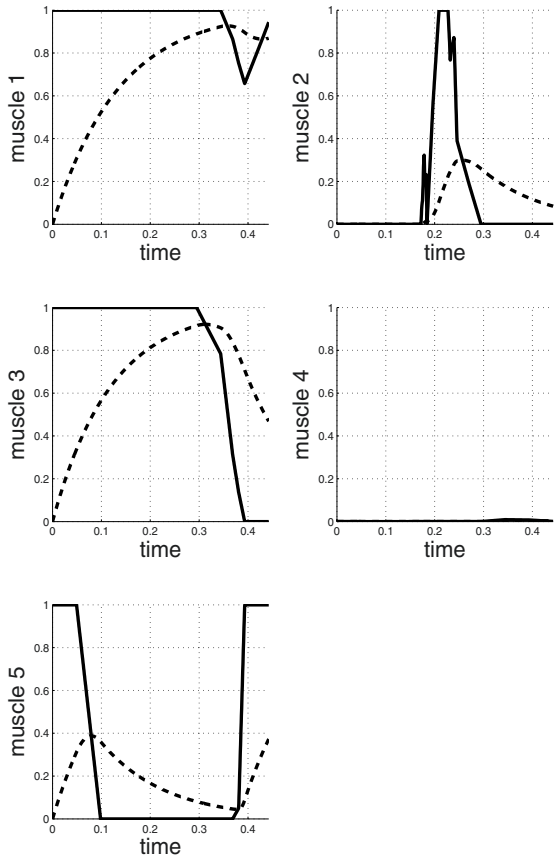

Fig. 3 Computed muscle activations (solid line) and calcium ion concentrations (dashed line) for the five muscle groups (time optimal kicking)

B. Analysis of measured kicking motion

If not a free, goal oriented motion, shall be predicted and optimized but a measured motion is to be analyzed, the forward dynamics approach may be used in a similar way. The only difference lies in the objective function. Let φ_{hip} and φ_{knee} be the measured hip and knee angle trajectories. Then, to calculate the muscle activations that lead to the measured motion and take into account human motion control which is supposed to minimize the activation effort, the objective function is chosen to be

$$J=\int_0^{t_f} (x_1-\varphi_{hip})^2+(x_2-\varphi_{knee})^2+c\mathbf{u}^T\mathbf{u}dt,$$

where c is a weight factor for taking into account human motion control. Note that by minimizing the differences of measured and calculated joint angle trajectories, the optimization result must not exactly match the measured motion like it is the case when applying the inverse dynamics approach. Thus, measurement errors may be implicitly compensated for which avoids that small measurement errors lead to large errors in the computation results like with inverse dynamics simulation and optimization.

The calculated and measured joint angle trajectories now of course better match (cf. Fig. 4). The results for the activations are given in Fig. 5. Computation times are about only 20% of that of the free goal oriented motion from the previous section. The reason for this is that as a starting solution for the joint states, the measured motion may be taken as it is known and involved in the objective function.

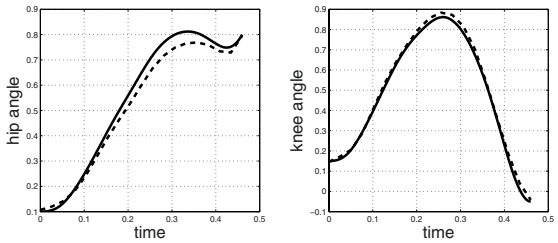

Fig. 4 Joint motion of the hip (left) and the knee (right). Solid line is obtained from analysis, dashed line a measurement of real human kicking.

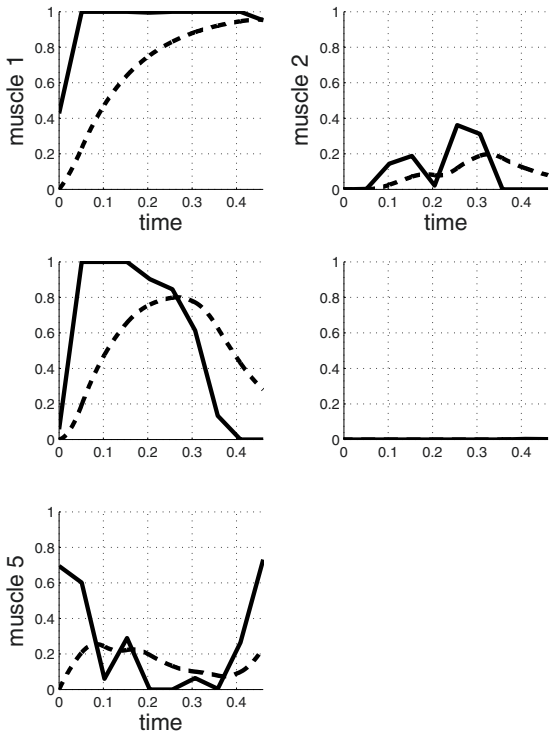

Fig. 5 Computed controls (analysis of measured kicking motion)

F. Ibrahim, N.A. Abu Osman, J. Usman and N.A. Kadri (Eds.): Biomed 06, IFMBE Proceedings 15, pp. 192-196, 2007
www.springerlink.com ' Springer-Verlag Berlin Heidelberg 2007

VI. Conclusions and outlook

Our approach for forward dynamics simulation and optimization reduces the computational effort by two orders of magnitude. We verified our approach and validated the model by a simple example for both optimization of a free, goal oriented motion (i.e. prediction of the kicking motion) as well as analysis of a measured motion. This gives rise to the hope that forward dynamics simulation and optimization can be used for actual problems in biomechanics.

Current work includes computation of the analyzing of human kicking on refined grids, the extension to more complex models such as for jumping, where contacts of the feet and the ground must be considered, and to motions where the upper body and wobbling masses must be considered. Furthermore, the method shall be applied to a humanoid robot driven by artificial muscles [4], where similar problems arise when a computational model of the robot shall be optimized for walking speed or energy consumption.

Acknowledgment

This paper has been funded by the German Research Foundation (DFG) under grant STR 533/3-1.

References

1. Featherstone R (1983): ·The calculation of robot dynamics using articulated-body inertias·, The International Journal of Robotics Research, 2(1), pp. 13 30
2. Gill P E, Murray W , Saunders M A (2002): SNOPT: An SQP algorithm for large-scale constrained optimization·, SIAM Journal on Optimization, 12, pp. 979 1006
3. Höpler R, Stelzer M, von Stryk O (2005): ·Object-oriented dynamics modeling for simulation, optimization and control of walking robots·, Proc. 18th Symposium on Simulation Technique, ASIM, Erlangen, September 12-15, 2005, pp. 588-593
4. Kratz R, Stelzer M, von Stryk O (2006): ·Macroscopic SMA Wire Bundle Actuator/ Sensor System: Design, Measurement, Control Approach , 4th IFAC-Symposium on Mechatronic Systems, Heidelberg, Germany, Sept. 12-14, 2006, to appear.
5. Pandy M G, Anderson F C, and Hull D G (1992): ·A parameter optimization approach for the optimal control of large-scale musculoskeletal systems·, J. of Biomech. Eng., 114, pp. 450 460
6. Rasmussen J, Damsgaard M, and Voigt M (2001): ·Muscle recruitment by the min/max criterion? A comparative numerical study . Journal of Biomechanics, 34(3), pp. 409 415
7. Stelzer M, von Stryk O (2005): ·Efficient forward dynamics simulation and optimization of locomotion: from legged robots to biomechanical systems·, Proc. 3rd Intl. Symposium on Adaptive Motion in Animals and Machines (AMAM), September 25-30, 2005
8. von Stryk O (2001): ·User s guide for DIRCOL version 2.1: A direct collocation method for the numerical solution of optimal control problems·, Technical report, Simulation and Systems Optimization Group, Technische Universität Darmstadt, 2001, http://www.sim.tu-darmstadt.de/sw/dircol
9. Spägele T (1998): ·Modellierung, Simulation und Optimierung menschlicher Bewegungen·, PhD thesis, Universität Stuttgart
10. Stelzer M, von Stryk O (2006): ·Efficient Forward Dynamics Simulation and Optimization of Human Body Dynamics·, ZAMM, to appear
11. Spägele T (2005), personal communication.
12. Nigg B M, Herzog W (1999): ·Biomechanics of the Musculo-skeletal System·, John Wiley & Sons, Chichester

Address of the corresponding author:

Author: M. Stelzer
Institute: TU Darmstadt, Simulation and Systems Optimization Group
Street: Hochschulstrasse 10
City: 64289 Darmstadt
Country: Germany
Email: stelzer@sim.tu-darmstadt.de

F. Ibrahim, N.A. Abu Osman, J. Usman and N.A. Kadri (Eds.): Biomed 06, IFMBE Proceedings 15, pp. 192-196, 2007
www.springerlink.com ' Springer-Verlag Berlin Heidelberg 2007

Instrumented Shoes for Measuring Ground-Reaction Force of Persons with Stroke in Level Walking, Stair Ascending and Descending

Hsieh-Ching Chen[1,2], Chia-Ling Chen[2], Yu-Ming Chen[3], Alice M. Wong[2], Jye Lee[3]

[1] Department of Industrial Engineering and Management, Chaoyang University of Technology, Taiwan
[2] Department of Physical Medicine and Rehabilitation, Chang Gung Memorial and Children Hospital, Taiwan
[3] Graduate Institutes of Medical Mechatronics, Chang Gung University, Taiwan

Abstract— **Analysis of foot-floor reactions during one's locomotion can be helpful for clinical diagnosis of his dynamic stability, walking ability, and balancing performance. The objective of this study is to design a pair of instrumented shoes to measure ground-reaction forces of persons with stroke in their level walking, stair ascending and descending. This study integrates a pair of instrumented shoes and a microprocessor-controlled data logger to build a portable system for measuring vertical foot-floor reaction forces. The instrumented shoes consist of 14 load cells, adjustable shoe modules, and signal conditioning circuits. The system is capable of synchronizing with a video recorder and continuously acquiring data up to 2h under a 100 Hz sampling rate. Plantar forces of 5 healthy adults and 6 persons with stroke were measured in their level walking, stair ascending and descending up to 10min. Their temporal and spatial gait parameters were calculated using analysis software programmed by LabVIEW. The instrumented shoes have 0.08 % and 1.72 % averaged static error and dynamic error, respectively, and were proved to equip with portability, high resolutions, and long operation time. Significant group differences were found in force waveforms, COP loci and bilateral symmetry of temporal and spatial gait parameters. Furthermore, the force waveforms and COP loci seems to accordingly reflect the severity of participants with stroke. Experiment results show the system is capable of acquiring foot-floor reaction forces for both normal and pathological gaits and can derive adequate parameters for clinical diagnosis.**

Keywords—**Stroke, gait analysis, stair climbing, foot-floor reaction**

I. Introduction

Walking ability is one of the most important ability in one s daily living. Gait performance may differ among individuals with disabilities. How to quantitatively and qualitatively assess and improve their walking ability is an important issue in the rehabilitation medicine. Analyzing foot-ground reactions of people with disability during locomotion can be helpful for a doctor to diagnosis his walking ability, stability, and balancing performance.

The foot-floor reactions during locomotion are wildly applied in areas such as shoemaking, clinical diagnosis, sports medicine, rehabilitation engineering, orthopedics and biomechanics research, and so on. In 1988, Zhu et al. developed a portable system to evaluate the plantar forces of ulcerated diabetics feet. Though the acquired data was limited to metatarsal head and hallux area, test results showed that the system was reliable [1]. In 1991, Harris et al. designed a portable foot-pressure system to locate the ulcerated area where diabetic nerves have no function [2]. Abu-Faraj and colleagues applied a portable foot pressure system to measure the gait of children with cerebal palsy [3]. Wervey et al. described the foot pressure pattern of 7 healthy adults while walking upstairs or downstairs [4]. MacWilliams and Armstrong reported the acquired information of foot-pressure was able to determine walking stability [5]. In 2001, Smith applied a plantar pressure measurement system to assess the foot pressure of kids with a clubfoot [6].

Despite many studies have reported gait of the disabled persons, we are not aware of any study focused on stair ascending and descending of persons with stroke. The objective of this study is thus to develop an instrumented shoes system for measuring plantar forces of persons with stroke while walking upstairs and downstairs.

II. Material and Method

A. Instrumented shoes

The instrumented shoe consists of a forefoot part and a rearfoot part. Each part comprises a surface and a base segment of 15mm-thick composite material. This material is lightweight whereas firm enough to be stepped on. Between the segments, 4 and 3 load cells were sandwiched in between segments of forefoot and rearfoot part, respectively (Fig. 1). Each load cell is 9.5mm height, 20mm diameter, 20g weight, and is sank in a circular cavity of 5mm depth on the surface segment. Meanwhile, each load cell also withstands a 1.5mm-thick steel coin which sank in a circular cavity of 5mm depth on the base segment, on its tip point (Fig. 1). This design assures the overall reaction force exerted on the face segments will be transmitted only onto the load cells. All load cells can withstand 50kgw (LM-50K,

F. Ibrahim, N.A. Abu Osman, J. Usman and N.A. Kadri (Eds.): Biomed 06, IFMBE Proceedings 15, pp. 197-200, 2007
www.springerlink.com ' Springer-Verlag Berlin Heidelberg 2007

Kyowa Inc, Japan) alone and the one located at heel position can withstand 100kgw (LM-100KA, Kyowa Inc, Japan). Load cells were placed to cover a region of hallux, medial metatarsal, lateral metatarsal, medial midfoot, lateral midfoot, and calcaneus. A total of 14 load cells were used for a pair of instrumented shoes. Fishing wire was used to stitch the surface and base segments together. A spring steel plate, adjustable in length, was used to fix forefoot and rearfoot parts of a shoe so as to allow flexion between these parts. The shoes look similar to a pair of sandals and the design of a shoe is shown in Fig. 2.

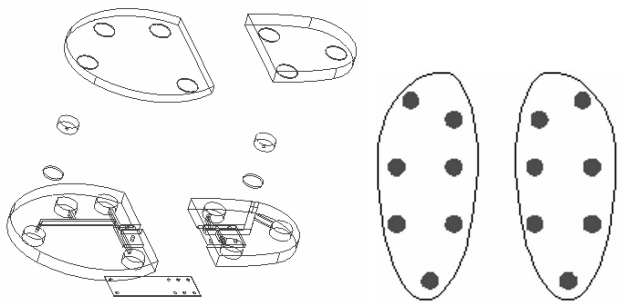

Fig. 1 Structural view and sensor locations of the instrumented shoe

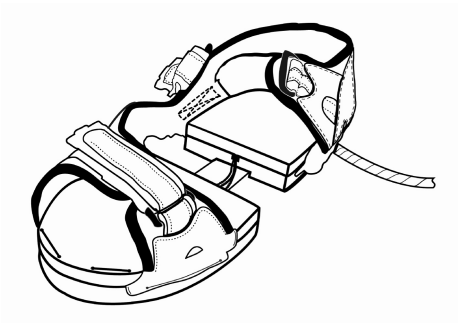

Fig. 2 Outward appearance of the instrumented shoe

Since the output signal of each load cell was only few mV, pre-amplification of the signal was needed before conducting analog to digital (A/D) conversion. Two 7-channel signal conditioning circuit boards, one for each shoe, were built by instrumentation amplifiers (INA122, Burr-Brown Inc., UAS) to entail the work. The gain of the amplifier was set to 553 by using 365Ω external resistors.

B. Data logger

A 720g logger which had dimensions 170mm × 160mm × 5.5mm, a battery and a CF memory card was used together with the instrumented shoes to register plantar forces. The data logger, powered by a 7.2V rechargeable Li-ion battery, comprises circuit boards of signal acquisition and digital control modules. An 8-bit microprocessor (C8051F020, Silicon Laboratories, USA) was employed to operate the logger.

The signal acquisition module was powered by –5V by a positive low dropout regulator (LT1117-5, Linear Technology Corp., USA) converted directly from the 7.2V Li-ion rechargeable battery. This module converted pre-amplified load cell signals of each shoe via a separate A/D converter. Each A/D converter (ADS8344N, Texas Instruments Inc., USA) had an 8-channel multiplexer, 16-bit resolution, and a sampling rate of 100 Hz.

The digital control module was powered by +3.3V, provided by a LT1117-3 regulator, and by +5V, provided by a LT1117-5 regulator, from the 7.2V Li-ion rechargeable battery. This module consists of digital I/O circuitries for controlling data storage, LCD module, and RF synchronization. A CompactFlash memory card (CF card) with storage capacity of 512 Mbytes was used. A set of 315MHz RF receiver module and decoder IC (PT2272, Princeton Technology, Taiwan) was used to register externally triggered events and synchronize the logger and video camcorder.

A 128×64 dot graphic LCD module (LMG-SSC12A64, SDEC Technology Corp., Taiwan) was adopted to display the information of operation modes. With the information displayed on the LCD module, users can control the logger, check signal quality, and manage the data files stored on the CF card manually via the control buttons.

C. System calibration

Both static and dynamic calibrations were conducted. Static calibration was conducted to assure no significant cross talk exists between load cells. A 20-pound counterweight was applied directly above each load cell on the surface segment of instrumented shoe.

Dynamic calibration was conducted to determine a set of scaling parameters that converts corresponding voltage signal of load cells into engineering unit of force (N). Dynamic calibration was conducted by an experimenter while wearing the instrumented shoes and walking on a force plate system (BP2436, ATMI Inc., USA). Data was collected simultaneously by the shoes system and the force plate system with an external synchronizing signal. Since the relationship between force and voltage signal of a load cell was linear, the relationship between the overall plantar force and signals of load cells can be represented as:

$$F_{total} = \sum_{i=1}^{14} F_i = \sum_{i=1}^{14} s_i V_i \quad (1)$$

F. Ibrahim, N.A. Abu Osman, J. Usman and N.A. Kadri (Eds.): Biomed 06, IFMBE Proceedings 15, pp. 197-200, 2007
www.springerlink.com ' Springer-Verlag Berlin Heidelberg 2007

where F_i, s_i, Vi denotes the load cell force, scaling parameter, and voltage signal of the *i*th load cell, respectively. Since the total plantar force and voltage signals of the 14 load cells were measured over time, the best set of scaling parameters can be derived by minimizing the overall square errors:

$$\min \sum_{t=1}^{n} \varepsilon_t^2 = \sum_{t=1}^{n} \left(\tilde{F}_t - \sum_{i=1}^{14} s_i V_{i,t} \right)^2 \quad (2)$$

where ε_t denotes error and $\tilde{F}_t$ denotes resultant force measured by the force plate system at time *t*.

Dynamic calibration was conducted repeatedly over 2 weeks to ensure consistent system performance, and the derived scaling parameters were saved for further application.

D. Subjects and experiment protocol

Five participants with stroke, aged 21 - 75 yrs, were recruited from the rehabilitation department of Cheng Gung Memorial Hospital to joint this study. A medical doctor was responsible for screening and conforming all participants with stroke equipped were capable of stair ascending and descending independently in their daily living. Another five healthy university graduate students, aged 25 - 27 yrs, were recruited as control group of this study.

All participants wore the pair of instrumented shoes and carried the logger in a small knapsack. They were instructed to walk on level surface for 25m and then climb up stairs of 18.5cm-height and 27.5cm-depth at their own pace. The participants with stroke could choose to stop climbing at their comfort after they have climbed more than 12 stairs, while the control group had to climb more than 60 stairs. After a short break, participants were instructed to walk down stairs and returned to the starting position of the task. Each task took about 10 to 20 minutes from the time the participant started to walk on level surface. Each participant was video-taped during the task period and a laser pointer with wireless transmitter was used to synchronize the video and the logger.

III. Results

A. System accuracy

The averaged static calibration errors was 0.08 % and the averaged dynamic calibration errors was 1.72 %. The calibration results showed the instrumented shoes system was accurate and reliable over a long period of time.

A. Gait of the controls

All gait parameters and force waveforms of the controls were bilaterally symmetric (Table 1). Significant peak force was found in stair descending (160 %bw) and ascending (138 %bw) compare to level walking. According to COP loci, forefoot was the main weight bearing area of the foot during stair ascending and descending.

Table 1 Averaged Gait Parameters of Control Group

Movement / Parameter	Level-1	Ascending	Descending	Level-2
Cycle (sec)	1.42	1.48	1.45	1.39
Double support (%cycle)	20.5	21.2	19.3	21.5
Single support (%cycle)	(L) 29.1 (R) 30.0	28.9 28.7	31.7 30.0	28.2 29.1
Speed (cm/s)	66.0	71.0	70.9	66.0
Peak (%bw)	(L) 109.8 (R) 110.3	138.7 138.5	162.1 161.5	108.0 108.0
Force waveform				
COP loci				

Table 2 Averaged Gait Parameters of Level Walking

Subject	Participants with stroke					Control group
Parameter	A	B	C	D	E	
Cycle (sec)	1.25	2.29	1.67	1.88	1.35	1.42
Double support (%cycle)	28.0	35.8	30.6	30.4	25.2	20.5
Sound support (%cycle)	26.3	21.5	24.0	25.2	33.9	29.1
Affect support (%cycle)	17.8	7.0	14.7	14.1	15.8	30.0
Speed (cm/s)	60.8	11.6	35.0	24.8	32.4	66.0
Sound (Affected) peak force (%bw)	109.4 (107.9)	108.5 (102.9)	109.7 (105.5)	109.0 (108.7)	110.7 (107.5)	110.3 (109.8)
Force waveform (sound)						
Force waveform (affected)						
COP loci						

F. Ibrahim, N.A. Abu Osman, J. Usman and N.A. Kadri (Eds.): Biomed 06, IFMBE Proceedings 15, pp. 197-200, 2007
www.springerlink.com ' Springer-Verlag Berlin Heidelberg 2007

B. Gait of participants with stroke

During level walking, the participants with stroke walk slower and exhibited a significantly longer period of double support than the controls (Table 2). They adopt a longer single support period and larger plantar support at their sound side than the affected side, especially at stair ascending and descending (Table 3). Their COP loci and force waveforms were not bilaterally symmetric in all locomotion. The areas enclosed by COP loci were significantly smaller in the participants with stroke than the controls. Moreover, the force waveforms of the stroke were more irregular in their stair ascending than in their level walking.

Table 3 Averaged Gait Parameters of Stair ascending (Top) and Stair descending (Bottom)

Subject	Participants with stroke					Control
Parameter	A	B	C	D	E	group
No. of Stairs	156	12	60	36	72	66
Stair ascending						
Cycle (sec)	3.01	5.45	2.86	3.57	3.43	1.48
Double support (%cycle)	19.3	30.8	29.1	25.5	27.2	21.2
Sound support (%cycle)	46.5	27.6	29.0	37.9	31.3	28.9
Affect support (%cycle)	14.8	10.8	12.9	11.1	14.4	28.7
Sound (Affected) peak force (%bw)	121.2 (108.3)	117.6 (106.)	122.9 (118.6)	117.6 (111.2)	115.6 (114. 2)	138.5 (138.7)
Force waveform (sound)						
Force waveform (affected)						
COP loci						
Stair descending						
Cycle (sec)	2.96	3.97	1.71	2.71	2.54	1.45
Double support (%cycle)	29.3	17.3	27.0	22.9	29.2	19.3
Sound support (%cycle)	26.9	58.7	34.6	44.2	22.0	31.7
Affect support (%cycle)	14.5	6.6	11.4	10.1	19.6	30.0
Sound (Affected) peak force (%bw)	117.0 (109.1)	120.4 (108.9)	116.8 (109.2)	120.0 (116.2)	117.7 (108.6)	161.5 (162.1)
Force waveform (sound)						
Force waveform (affected)						
COP loci						

IV. Discussions

Experimental results showed that the difference between the controls and the participants with stroke can be easily recognized. The analytical results revealed positive correlation between stroke participants walking speed and the number of stairs they were able to climb. With this developed shoes system, walking ability of the persons with stroke can be documented via various analysis outcomes such as temporal gait parameters, bilateral symmetry of plantar force waveforms and COP loci, peak weight-bearing, etc. Since symmetry and consistency of gait are also important factors of one s mobility, an assessment tool with portability and capacity of long-period data collection is required to achieve this goal. The developed portable shoes system can overcome environmental restrictions and measure gait besides level walking for an extended-period.

Accuracy and reliability of the shoes system were checked by calibration procedure. Despite the small number of subjects, the results of this feasibility study showed that the shoes system was promising for assessment of pathological gait and can provide an alternative solution for evaluating gait performance of some people with disabilities.

References

1. Zhu H, Maalej N, Webster J, et al. (1988) A microprocessor-based data-acquisition system for measuring pressures between the foot and shoe, Proc. vol. 10, Annu Conf IEEE Eng Med Biol Soc., 1988, pp 1599 1600
2. Harris G, Acharya K, Bachschmidt R (1996) Investigation of spectral content from discrete plantar areas during adult gait: an expansion of rehabilitation technology. IEEE Trans Biomed Eng 4:360 374
3. Abu-Faraj Z, Harris G, Abler J, et al. (1996) A Holter-type microprocessor-based rehabilitation instrument for acquisition and storage of plantar pressure data in children with cerebral palsy. IEEE Trans Rehabil Eng 4:33 38
4. Wervey R, Harris G, Wertsch J (1997) Plantar pressure characteristics during stair climbing and descent. Proc. vol. 4, 19th Int Conf IEEE Eng Med Biol Soc, Chicago, USA, 1997, pp 1746 1748
5. MacWilliams B, Armstrong P (2000) Clinical applications of plantar pressure measurement in pediatric orthopedics. Pediatric Gait: A new millennium in Clinical Care and Motion Analysis Technology , 22 July 2000 pp 143 150
6. Smith P, Abu-Faraj A, Harris G (2001) Surgical rehabilitation of the planovalgus foot in cerebral palsy. IEEE Trans Rehabil Eng 9:202 214

Address of the corresponding author:

Author: Hsieh-Ching Chen
Institute: Department of Industrial Engineering and Management, Chaoyang University of Technology
Street: No. 168 Jifong E. Rd.
City: Wufong Township, Taichung County 41349
Country: Taiwan
Email: hcchen@cyut.edu.tw

F. Ibrahim, N.A. Abu Osman, J. Usman and N.A. Kadri (Eds.): Biomed 06, IFMBE Proceedings 15, pp. 197-200, 2007
www.springerlink.com ' Springer-Verlag Berlin Heidelberg 2007

Kinematic Analysis of Speech Motor Control in Children with Cerebral Palsy

Wei Hsien Hong[1], Chia Ling Chen[2], Liang Yi Yang[2], Hsieh Ching Chen[3]

[1]School of Sports Medicine, China Medical University, Taiwan
[2] Departments of Physical Medicine and Rehabilitation, Chang Gung Memorial Hospital and Chang Gung University, Taiwan
[3] Industrial Engineering and Management, Chaoyang University of Technology, Taiwan

Abstract—**the aim of this study is to use kinematic analysis to investigate the speech motor control in children with CP. We collected 10 children with CP having spastic quadriplegia. Another 10 children with normal development (ND) were selected as control group. A motor analysis system (Vicon 370) and a mobile video were synchronized to collect kinematic data and video images during speaking. Each subject received /pa/, /pi/, /pu/, /po/ mono-syllable tasks. Kinematic parameters included the spatiotemporal indexes (STIs), duration, peak velocity of jaw, and peak displacement of lower lip during speaking. Statistical significance was set as *p* less than .05. The results showed CP with spastic quadriplegia had greater STIs in /pa/, /pi/, /pu/, and /po/ tasks ($p<0.05$), and larger peak velocity of lip in /pi/, /pi/, and /po/ tasks than children with ND ($p<0.05$). Children with CP non-progressive brain damage may cause impairment in cognition, language, and motor speech functions. Therefore, CP children had greater STIs and peak velocity of lip. Kinematic data of motor speech control provided in this study may allow clinicians to understand the motor speech control with children with CP.**

Keywords— **Speech motor control, Kinematics, Cerebral Palsy**

I. Introduction

Speech is perhaps the ultimate exemplar of complex motor skill (Lashley, 1951). The speech production for communication is often affected in cerebral palsy (CP) (Surveillance, 2002). Both receptive and expressive language deficits are common. Articulation disorders and impaired speech are present in 38% children with CP (Sankar & Mundkur, 2005). To treat motor speech dysfunction, it is based on the understanding the mechanism of speech motor control in children with CP. Previous studies had established the speech motor control pattern in children with normal development by lip and jaw kinematic analysis (Smith & Goffman, 1998; Green et al., 2000), Previous study found that the developmental sequence of pronounce began in plosive bilabials (e.g. /b/, /p/) for the ND children (Sharkey & Folkin, 1985 ; McClean & Clay, 1995). Because the product of sound was bilabial motor by upper-lower lip contact, and bilabial is earliest complete development in language. The combined syllables by bilabial and vowel may be used to clearly observe the movement process of lip and jaw during speaking. Some pathological studies were focused subjects in stutter and specific language impairment by acoustic and kinematic analysis (McClean et al., 1990 ; Kleinow & Smith, 2000; Story et al., 1996). However, no study, insofar as we could determine, attempted to investigate speech motor control of children with CP. Therefore, the purpose of this study is to use kinematic analysis to investigate the speech motor control in children with CP.

II. Methods

We collected 10 children with CP having spastic quadriplegia, age was 8.2±1.6 years, body height 120.5±10.1 cm, and body weight 23.5±5.4 kg. Another 10 children with normal development (ND) were selected as control group, age was 8.1±1.8, body height 122.5±11.0 cm, and body weight 26.5±9.0 kg. The ND children were no learning disabilities, speech/language impairment, or neurological problems.

A motion analysis system (Vicon 370, Vicon Motion System, Oxford Metrics Inc, UK) with 6 infrared cameras and a mobile video were synchronized to collect kinematic data and video images by a 60 Hz sample rate during utterance task. Eight reflective markers were attached on the mask, including the fore head, bilateral pre-auricular area, and nose, to establish a rigid body and defined the vertical (z), anterio-posterior (y), and horizontal (x) directions as the reference coordination system (Fig 1). For oral-movement tracking, markers were attached on the bilateral mouth corners, the upper and lower lips at midline.

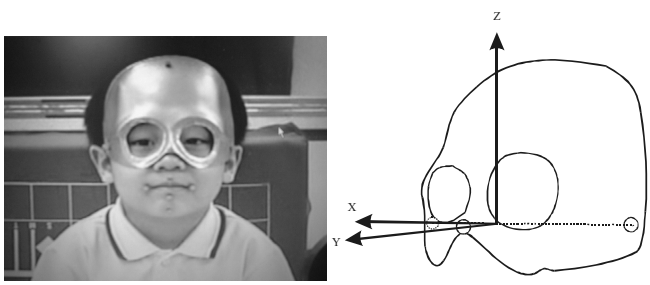

Fig 1 The marker positions and definition of coordination system.

F. Ibrahim, N.A. Abu Osman, J. Usman and N.A. Kadri (Eds.): Biomed 06, IFMBE Proceedings 15, pp. 201-203, 2007
www.springerlink.com ' Springer-Verlag Berlin Heidelberg 2007

Table 1 The comparisons of STI, duration, and peak velocity of lower lip between groups during utterance tasks

Parameters	groups	/pa/	/pi/	/pu/	/pæ/	/po/
STI	CP	5.0±1.2	4.6±0.7	5.0±1.1	4.6±1.3	4.8±1.8
	Normal	3.2±1.1	2.8±0.7	2.4±0.9	2.8±1.4	2.7±1.2
P value		0.003**	0.042*	0.038*	0.229	0.025*
Duration (sec)	CP	10.3±1.6	9.6±1.0	10.2±1.5	10.3±1.9	9.7±1.5
	Normal	9.6±0.7	9.8±0.9	9.9±0.7	9.8±0.9	9.5±0.8
P value		0.307	0.823	0.641	0.506	0.677
Peak velocity of	CP	86.7±30.0	75.4±35.3	54.2±16.3	70.3±24.5	66.0±24.0
lip (mm/s)	Normal	78.7±28.4	52.5±30.0	32.8±15.5	58.2±22.5	42.3±20.5
P value		0.578	0.038*	0.045*	0.229	0.029*

*, p<0.05; **, p<0.01

Table 2. The comparisons of peak displacement lower lip between groups during utterance tasks

Parameters	groups	/pa/	/pi/	/pu/	/pæ/	/po/
vertical displacement	CP	17.2±3.2	14.9±2.5	14.2±2.1	16.2±3.1	15.3±2.7
(mm)	Normal	16.0±1.6	15.0±2.1	14.2±2.0	15.0±1.4	14.9±1.2
P value		0.270	0.954	0.980	0.255	0.679
anterioposterior	CP	20.2±7.8	16.7±4.8	20.0±10.5	17.0±9.4	18.2±7.2
displacement (mm)	Normal	20.7±6.4	20.9±8.0	21.6±11.2	20.7±10.3	18.7±5.1
P value		0.880	0.170	0.717	0.0.423	0.860
Horizontal	CP	11.0±1.0	11.2±0.7	11.3±1.3	12.5±5.0	12.4±5.0
displacement (mm)	Normal	10.6±0.7	10.8±0.5	10.4±0.7	10.5±0.8	10.4±0.6
P value		0.278	0.276	0.053	0.237	0.232

*, p<0.05; **, p<0.01

Subjects were comfortably seated in view of cameras system and received the different mono-syllable tasks randomly (/pa, pi, pu, pæ, po/) at their normal rate and loudness. Each mono-syllable repeated ten times in a trail and trials were continued until at 10 good exemplars had been obtained.

The kinematics data were analyzed using the Lab View processing program. The measured parameters included the spatiotemporal indexes (STIs), duration, peak velocity of jaw, and peak displacement of lower lip during utterance tasks. Displacement waveforms were extracted for analysis as the interval between the peak velocity of the first and lasting opening movements for each mono-syllable task. The duration of the speech movement was computed in real time as the interval between the first and lasting velocity peaks. For the sets of 10 time- and amplitude-normalized displacement waveforms for each individual, a standard deviation was computed across the 10 samples at one point in relative time. The standard deviations were computed successively at 2% intervals. These 50 standard deviations were summed, and the result, which reflects the overall STI (Fig 2). A student t test was used to compare the differences between groups in kinematics variables. Statistical significance was set as *p* less than.05.

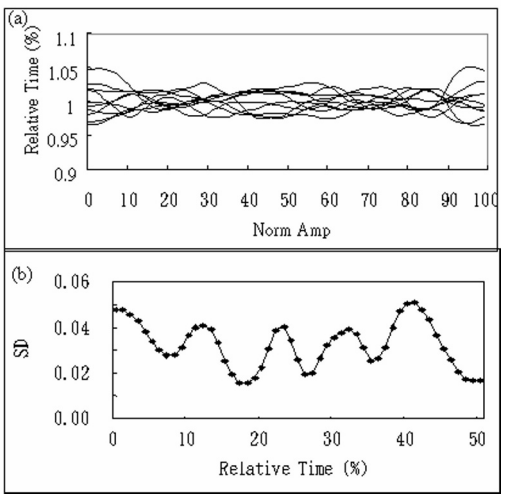

Fig 2 Sample data for on subject for a mono-syllable task (a) the waveforms after amplitude- and time normalization from law data; (b) the standard deviation computed at 2% intervals in relative time. The STI is the sum of these 50 standard deviations.

III. Results

CP with spastic quadriplegia had greater STIs in four mono-syllable tasks (/pa/, /pi/, /pu/, and /po/) (p<0.05), and

F. Ibrahim, N.A. Abu Osman, J. Usman and N.A. Kadri (Eds.): Biomed 06, IFMBE Proceedings 15, pp. 201-203, 2007
www.springerlink.com ' Springer-Verlag Berlin Heidelberg 2007

larger peak velocity of lower lip in /pi/, /pu/, and /po/ tasks than children with ND ($p<0.05$) (Table 1). There was no significant difference in duration and displacements of lower lip during all utterance tasks (Table 2).

IV. Discussion

The STI values reflected the degree to which repeated the performance of a task produces movement trajectories that converge on a single pattern. Mecham et al. (1960) pointed out that speech characteristics are highly variable, both within the groups and within the individual CP from one time to another. In this study, CP with quadriplegia produced less stable movement trajectories, as reflected in higher values on the STI. The production of speech may be due to cognitive deficits, or oromotor dysfunction leading to dysarthria (Newman, 1985).

Children with CP have large peak velocity of lip in speech. The velocity movement style may reflect different underlying control processes. Previous study pointed out the peak velocity of lip represented the muscle impulse. A larger velocity of lip, and larger muscle strength was induced (Fasoli et al., 2002). Children with CP have poor motor control and were affected in speech performance, thereby leaded to more and more velocity in speech.

In normal speech, for instance, the vowel /u/ is found more commonly in the word final position (Singer, 1976). In the speech of CP and normal children, this vowel is rather reduced in its speed in that position. The rounding of the lips required in the production of this vowel /u/ probably requires an additional effort; this might have resulted in the lesser speed in /pu/ task.

The duration and displacement were not significant differences between children with CP and ND. It is probable due to the mono-syllable task is short and simple to utter for children with CP in this study. Previous studies found increased multiple syllable or word did not change the fundamental nature of CP speech as characterized by single word utterances. In almost all the cases, children with CP did not go beyond the single word utterances (Lencione, 1968). The present work was a small step toward understanding of speech motor control in CP children by mono-syllable utterance. The multiple syllable or words utterance tests were not addressed, which could be part of future investigations.

V. Conclusion

In children with CP non-progressive brain damage may cause impairment in cognition, language, and motor speech functions. Therefore, CP children had greater STIs and peak velocity of lip during utterance tasks. Kinematics data of motor speech control provided in this study may allow clinicians to understand the motor speech control with children with CP.

References

1. Green JR, Moore CA, Ruark JL, Rodda PR, Morvee W, VanWitzenburg M. Development of Chewing in Children from 12 to 48 Months: a longitudinal study of EMG patterns. *J Neurophysiology* 1997; 77:2704-16.
2. Kleinow J, Smith A. Influences of length and syntactic complexity on the speech motor stability of the fluent speech of adults who stutter. J Speech Lang Hear Res 2000;43:548-59
3. Lashley KS. The problem of serial order in behavior. In L Jeffress (Ed.), Cerebral mechanisms in behavior (pp. 506-28), New York: Wiley.
4. Lencione R. A Rationale for Speech and Language Evaluation of Cerebral Palsy. Br J Disord Commun 1968; 3:161-70.
5. McClean MD, Kroll RM, Loftus NS. Kinematics analysis of lip closure in stutterers' fluent speech. J Speech Lang Hear Res 1990; 33:755-60.
6. Mecham MJ, Berko MJ, Berko FG. Speech therapy in cerebral palsy. Thomas, Springfield, Il, 1960.
7. Newman JM. Insight from recent reading and writing research and their implications for developing whole language curriculum. In J.M. Newman (Ed.), Whole language: Theory in use. (pp. 17-36). Portsmouth, NH: Heinemann, 1985.
8. Sankar C, Mundkur N. Cerebral palsy-definition, classification, etiology and early diagnosis. Indian J Pediatr 2005; 72:865-8.
9. Singer L.Grammatical Development in Normal and in Cerebral Palsy Children." In Raffler-Engel W.V. and Lebron, Y. (eds.) Baby Talk and Infant Speech. Neurolinguistics 5, 1976.
10. Smith A, Goffman L. Stability and patterning of speech movement sequences in children and adults. J Speech Lang Hear Res 1998; 41:18-30.
11. Story B, Titze I, Hoffman E. Vocal tract area functions from magnetic resonance imaging. J Acoust Soc Am 1996; 100:537 54.
12. Surveillance of cerebral palsy in Europe. Prevalence and characteristics of children with cerebral palsy in Europe. Dev Med Child Neurol 2002; 44: 633-42.

Address of the corresponding author:

Author: Wei Hsien Hong
Institute: School of Sports Medicine, China Medical University
Street: 91 Hsueh-Shih Road, Taichung 40402.
City: Taichung
Country: Taiwan
Email: whhong@mail.cmu.edu.tw

F. Ibrahim, N.A. Abu Osman, J. Usman and N.A. Kadri (Eds.): Biomed 06, IFMBE Proceedings 15, pp. 201-203, 2007
www.springerlink.com ' Springer-Verlag Berlin Heidelberg 2007

Modeling and Simulation of Sit-to-Stand Exercise

M.A. Rahim[1], M.O. Tokhi[2] and N.F. Mohd. Nasir[3]

[1] Mechatronic Engineering, School of Mechatronic, Northern Malaysia University College of Engineering, Kangar, Malaysia
[2] Departments of Automatic and Control Systems, Sheffield University, United Kingdom
[3] Biomedical Electronics Engineering, School of Mechatronic, Northern Malaysia University College of Engineering, Kangar, Malaysia

Abstract— **Sit-to-stand, (SiSt) exercise is an exercise which is simple and easy to be implemented. A seesaw is an example of basic mechanism which is able to assist a person, especially paraplegic to perform the exercise. Understanding the dynamics of motion would beneficial to rehabilitation engineering field which is a study to improve the quality life of disability people. This study presents a dynamic simulation of humanoid model performing sit-to-stand (SiSt) exercise. The main goals of this project are; the development of humanoid model with seesaw exercise machine, and the development of controller for controlled movement of the system. To achieve this, a humanoid model with seesaw mechanism have been designed in Visual Nastran software, while a closed loop system with PD, (proportional-plus-derivative) controllers that track desired reference input have been implemented by Matlab/Simulink. Here, both software packages (Visual Nastran and Matlab/Simulink) have been integrated in order to produce the simulation of humanoid motion. The simulation result of humanoid model performing SiSt mode with seesaw mechanism proved the developed models and the designed controller are able to perform and function as desired before will be implemented into FES application.**

Keywords— **FES, humanoid model, PID Controller**

I. Introduction

Paraplegia is a condition where the lower half of patient s body is paralyzed and cannot move due to spinal cord injury. The paraplegics will experience lack of motor control and sensation in the lower extremities and are unable to provide the lower extremity force and motions (plantar/dorsiflexion1, knee/hip extension, and knee/hip flexion) [1]. The effects of functional degeneration are vast and greatly reduce the overall health of paraplegics, particularly within the musculoskeletal and cardiovascular systems, thereby increasing their risk for cardiovascular disease. Currently, Functional Electrical Stimulation, (FES) has been widely used to facilitate various exercises for paraplegics, such as cycling, rowing and sit-to-stand. This is achieved by placing an electrode on the skin, over the paralyzed muscle that need to produce contraction. Through this method, an electrical current will propagates along the nerves after passing through the electrode on the skin and indirectly will trigger muscle to contract under minor control.

The main focus on this project is about sit-to-stand (SiSt) exercise. This exercise is encourage by medical expert, in order to prevent lower limb contractures and able to reduce the risk of bone fractures by minimizing the development of osteoporosis. Furthermore, the motion also can improve blood circulation and as an aid in the psychological rehabilitation of the patient. There were plenty of SiSt and StSi studies have been done in the past few years [1]-[5]. In the study, a subject-centered approach for standing-up and sitting down using seesaw mechanism was developed on the basis of patient model [2]. This strategy is called patient-driven motion reinforcement (PDMR), which is based on an inverse dynamic model (IDM) that predicts the stimulation pattern required to maintain the movement as its initiated by the patient s voluntary effort. The results showed that the patients were able to influence the stimulator output and to control the movement by their voluntary effort.

II. Materials and Methods

Basically, this study consists of two main tasks; the first task is the development of dynamics of humanoid model in SiSt mode using seesaw exercise machine. The second task is the development of controller of the system movement. To achieve this, a humanoid model which is based on existing anthropometrical data with seesaw exercise machine is developed in Visual Nastran software. Here, the dynamics of SiSt movement is studied and analyzed in order to design controller for the movement. In this work, Simulink tool in Matlab software is used for controller design process. Initially, the desired SiSt trajectory is established. Then, a PD (proportional-plus-derivative) knee controller has been developed for the mode. At this stage, the controller has been tested and verified to follow their desired mode. Trial-and-error method has been applied in determining the P, (proportional) and D, (derivative) term. The simulation of humanoid is produced by the integration of Matlab/Simulink and Visual Nastran software package. From the acquired simulation, the torque profile of each active joint is investigated and analyzed.

F. Ibrahim, N.A. Abu Osman, J. Usman and N.A. Kadri (Eds.): Biomed 06, IFMBE Proceedings 15, pp. 204-207, 2007
www.springerlink.com ' Springer-Verlag Berlin Heidelberg 2007

A. Humanoid Model

*Determining body segment parameters:*The main function of humanoid model is to present dynamics and real physical human body in term of length and weight. The parameter of each body segment was based on anthropometrical data provided by Winter [10]. Winter formularized the length of each body segment is a result of the fraction of total human height, while the fraction of total human body weight, determined the weight of each body segment. Figure 1 illustrates the length of each body segment of a complete human body. The body segment length is expressed as a fraction of total body height, H.

Basically, the humanoid model consists of 15 body segments: 1 head, 1 neck, 1 trunk, 2 arms, 2 lower arms, 2 hands, 2 thighs, 2 shanks and 2 feet. The total height of the designed humanoid model is set to 175cm, while its total weight is chose to be 70kg. These values are very practical as a normal healthy male with 22.9kg/m2 of Body Mass Index. The length and weight of each body segment is presented in Table 1 and Table 2 respectively.

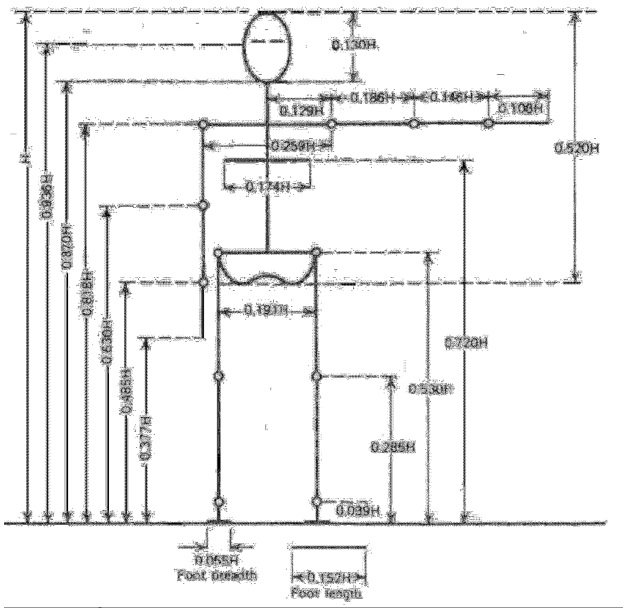

Fig. 1 Body Segment Parameter

Modeling body segments: In the modeling process, approximation and simplification of shape for each humanoid model body segment is made in order to meet the basic shape of human body. For example, sphere shape is used to model humanoid s head, while box shape is used to design feet. Other part such as neck and lower arm, cylindrical shape is applied. For the hand dimension, polygon shape is used to model it. However, in modeling several complex shapes such as trunk, upper arm, shank and thigh, the shapes were imported from stunt man model in Visual Nastran demo file. All the parameters of each body segment are according to the calculated values in Table 1 and Table 2.

Table 1 Length of humanoid model s body segment H=total body height

Segment	Segment Length (Fraction•H)	Calculated Segment Length [cm]
Hand	0.108H	18.9
Lower arm	0.146H	25.55
Arm	0.186H	32.55
Foot height	0.039H	6.825
Foot breath	0.055H	9.625
Foot length	0.152H	26.6
Shank	0.246H	43.05
Thigh	0.245H	42.875
Neck	0.052H	9.1
Head	0.13H	22.75
Trunk	0.288H	50.4

Table 2 Weight of humanoid model s body segment M=total body weight

Segment	Segment Length (Fraction•M)	Calculated Segment Weight [kg]
Hand	0.006M	0.42
Lower arm	0.016M	1.12
Arm	0.028M	1.96
Foot	0.0145M	1.015
Shank	0.0465M	3.255
Thigh	0.1M	7
Head and Neck	0.083M	5.81
Trunk	0.497M	34.79

Connecting body segments: Each of body segments is connected by passive joint in order to form a complete humanoid model. In this design, 13 joints have been used: 1 neck, 2 shoulders, 2 elbows, 2 wrists, 2 hips, 2 knees, and 2 ankles. There were two types of joint which was rigid joint and revolute joint have been applied. Rigid joint is a joint that rigidly joint two bodies, where no movement is allowed in between the bodies. On the other hand, revolute joint is a joint that allows one degree of freedom movement between the two connected bodies.

In SiSt movement, the major joints involve are hip, knee and ankle. Since both of the motions are only to be considered in sagittal plane and trunk is required to stay in vertical position, the movements of other upper bodies are neglected. Thus, the rigid joints are used on upper half body such as on neck, shoulders, elbows and wrists. In contrast, for lower part body, revolute joints are used on hips, knees and ankles. Figure 2 illustrates the joints on completed humanoid model.

F. Ibrahim, N.A. Abu Osman, J. Usman and N.A. Kadri (Eds.): Biomed 06, IFMBE Proceedings 15, pp. 204-207, 2007
www.springerlink.com ' Springer-Verlag Berlin Heidelberg 2007

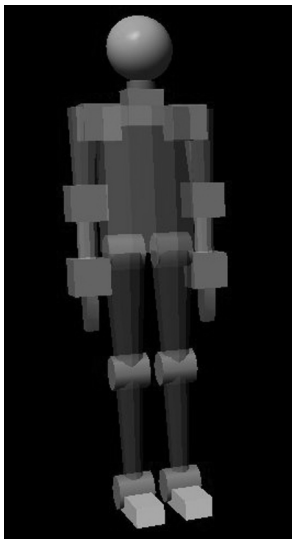

Fig. 2 Humanoid Model Joints

B. Seesaw Model

Seesaw Description: A seesaw is a long, narrow board suspended in the middle so that, as one end goes up, the other goes down. Basically, the mechanism of seesaw is an example of a Class 1 lever application. A lever is a rigid bar free to rotate about fixed point called the fulcrum. The position of the fulcrum is fixed so that it is not free to move with the respect of the bar. The function of seesaw in this project is to support humanoid model in the process of standing up for SiSt exercise. In addition, it acts as mechanical construction that constrains the position of the pelvis in such way that it moves in the sagittal plane on a circular path about the seesaw axis [5]. In someway, trajectory of SiSt can be obtained by the seesaw motion, and the acquired trajectory will be utilized as an indication of desired reference input in designing controller.

Constructing the Seesaw: Two major components of a seesaw are; a bar and a hinge joint. In this seesaw construction, the bar dimension is designed as 0.2x0.2x3m, while the hinge joint is pivoted at the centre of the bar. The seesaw model is illustrated in Figure 3. The finished humanoid model with seesaw in sitting position is shown in Figure 4.

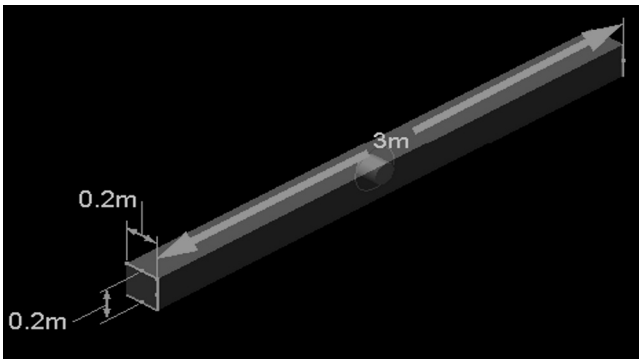

Fig. 3 Seesaw Model

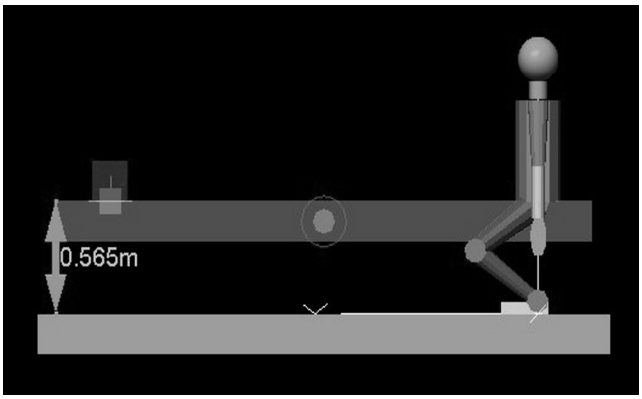

Fig. 4 Humanoid model with seesaw

III. Results

The dynamics of humanoid model in SiSt mode with seesaw exercise machine has been developed successfully. The most crucial part in this study is to design closed loop feedback controller that follows the desired SiSt reference trajectory as shown in Figure 5. After applying PD controller on the humanoid knee, the controller was enabled to follow closely to the desired SiSt trajectory which has been developed. The result is shown in Figure 6. While, the knee torque profiles during SiSt is illustrated in Figure 7.

F. Ibrahim, N.A. Abu Osman, J. Usman and N.A. Kadri (Eds.): Biomed 06, IFMBE Proceedings 15, pp. 204-207, 2007
www.springerlink.com ' Springer-Verlag Berlin Heidelberg 2007

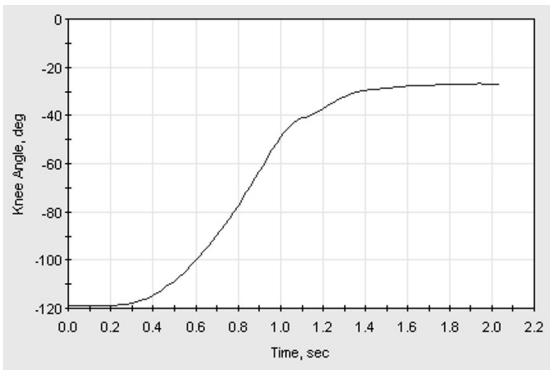

Fig. 5 SiSt desired trajectory

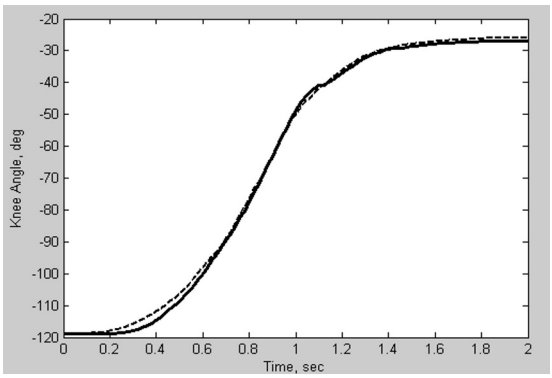

Fig. 6 SiSt trajectory with PD Controller

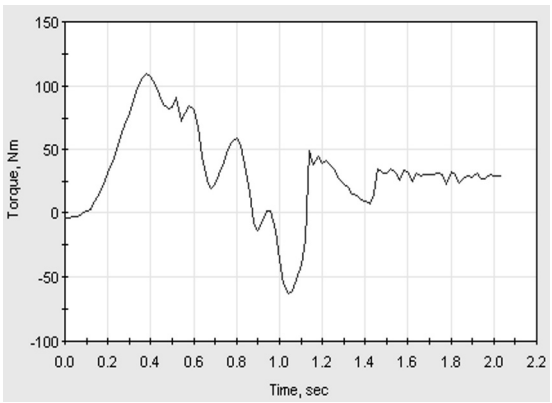

Fig. 7 SiSt Knee Torque Profile

IV. Discussion

The results indicated that knee torque profile had response variably during the phase of desired trajectory given. The value of knee torque used to lift a load by using the seesaw also increased as the load increases. The simulation results proved the measured knee torque profile as expected.

However, throughout this work the trunk position is being simplified to stay in vertical position by using sliding joint. As a recommendation, hip controller should be introduced to control trunk movement during motion both of modes. A part of that, ground reaction force has been ignored in the design process, where the feet have been set to fix on the ground. Hence, in future work the feet should not being fixed on the ground, where ground reaction force can be measured. Therefore, future study should consider friction between feet and the ground, without ignoring the balance and stability of the humanoid model during motion. Moreover, the scope of this project just focus only on knee joint, while other active joints such as ankle and toe are assumed to be passive joint and neglected. In addition, the orientation of upper body joints such as shoulder, elbow and head also has been ignored. Thus in future work, the interrelation between other active joints should be considered. The more advance advanced control strategies such as fuzzy logic should be implemented in order to control multiple input multiple output, (MIMO) system.

Abbreviations

FES Functional Electrical Stimulation
PD Proportional and Differential
SiSt Sit-to-Stand

References

1. Gaekel EM, McFarland JW, Shellabarger M, Thompson C (2002) Rowing Machine for an Individual with Paraplegia, NSF Engineering Senior Design Projects to Aid Persons with Disabilities.
2. Riener R, Ferrarin M, Pavan EE, Frigo CA (2000) Patient-driven control of FES-supported standing up and sitting down: experimental results. Rehab. Eng. IEEE Trans. 8: 523-529
3. Dolan MJ, Andrews BJ, Veltink P (1998) Switching curve controller for FESassisted standing up and sitting down. Rehab. Eng. IEEE Trans. 6: 167-171
4. Donaldson N, Yu CH (1998) A strategy used by paraplegics to stand up using FES. Rehab. Eng. IEEE Trans. 6:162 167
5. Kamnik R, Bajd T (2002) Human voluntary activity integration into the control of standing-up rehabilitation robot.Adv. Mot. Cont., 7th International Workshop 2002, pp 402 407

Address of the corresponding author:

Author: Muhajir Ab. Rahim
Institute: Northern Malaysia University College of Engineering
Street: Jalan Kangar-Arau
City: Kangar
Country: Malaysia
Email: muhajir@kukum.edu.my

F. Ibrahim, N.A. Abu Osman, J. Usman and N.A. Kadri (Eds.): Biomed 06, IFMBE Proceedings 15, pp. 204-207, 2007
www.springerlink.com ' Springer-Verlag Berlin Heidelberg 2007

Motion Analysis in Dual-task on Patients with Mild Dementias

[1]Jing-Jung Chen, Alice-MK Wong, MD, [2]Jin-Jang Wong

[1]From the Graduate Institute of Rehabilitation Sciences, Chang Gung University
[2] Department of Neurology, Chang Gung Memorial Hospital, Taipei, Taiwan

Abstract—**Background: Most factors cause motor and gait impairment in patients with dementias are related to lesion of different areas and lobes. However, patients with different types of dementias may have distinct motor impairment features because of different neuropsychological dysfunction that may resulted in different motor features.**

Objective: To compared patients with mild Alzheimer's disease (AD) and patients with mild vascular dementia (VaD) in motion analysis of gait and hand function.

Participants: The subjects were recruited into three groups: Group I .healthy elderly (HE) ,n=10; Group II. Mild possible Alzheimer's disease (AD) ,n=10; Group III. Mild possible vascular dementia (VaD) ,n=10. This study was used Clinical Dementia Rating Scale(CDR) to diagnosis the dementia severity. The including criteria for dementia patient was CDR scale below 2 which means mild dementia.

Design: In this study, motion analysis was used to evaluate the kinematic parameters to compare gait performance, hand function was measured by a new designed computer board. In gait aspect, there were three motor tasks: (1) comfortable walking;(2) comfortable walking combined dual-task;(3) comfortable walking combined dual-task (memory). In hand function evaluation, there were three motor task: (1) sequence task;(2) sequence task combined dual-task;(3) random sequence task. Dual-task in this study was asked subjects performance secondary task at the same time which invert three numbers experimenter recited. The data were been analysis through two-way mixed ANOVA to compare within and between groups .

Result: There was no different motor ability in gait and hand function of AD group compared with VaD group in single-tasks. However, they were significant different represent in dual-task. Besides, AD group had more variation than VaD group in dual-task. Among them, the change of hand function seems more sensitive than gait in biomechanical analysis in dual-task.

Conclusion: Patients with AD present poor motor strategies than VaD in dual-task of gait and hand function. Among them, the change of hand function seems more sensitive than gait in biomechanical analysis in dual-task.

Keywords— **Motion, Dementia, Dual-task, Gait**

I. Introduction

Dementia is defined as an important of memory plus impairment in at least one other cognitive function (eg, aphasia, apraxia, agnosia and disturbance in executive function), representing a decline and leading to the impairment of social and/or occupational function [1]. However, even this definition is becoming inadequate, as researchers and clinicians become aware of specific early patterns of cognitive impairment in the different types of dementia. For instance, in the early Alzheimer s disease, there may be isolated memory impairment for many years before other features become apparent [2].

The lesions of medical temporal lobe and hippocampal usually apparent in early stage of Alzheimer s disease, cause the patient's cognitive function to have very great influence. Executive function refers to a variety of higher cognitive processes that modulate and use information from the posterior cortical sensory systems to produce behavior [3-6]. That include initiation or intention of action, planning, working, memory, and attention. Patients of Alzheimer s disease were proved poor ability in dual-task that was combined with attentions and motor tasks at the same time [7-8].

The purpose of the present study were therefore to compared patients with mild Alzheimer s disease ***(AD)*** and patients with mild vascular dementia ***(VaD)*** in motion analysis of gait and hand function. Therefore, with a focus on measures of automaticity and rhythmicity, we studied the motor features of different types of dementia.

II. Method

All participants in this study were recruited from the Department of Neurology, Chang Gung Memorial Hospital, Taipei, Taiwan. There are three groups in this study : *Group I* .healthy elderly **(*HE*)** ,n=10; *Group II.* Mild possible Alzheimer s disease ***(AD)*** ,n=10; *Group III.* Mild possible vascular dementia **(*VaD*)** ,n=10. This study was used Clinical Dementia Rating Scale***(CDR)*** to diagnosis the dementia severity. The including criteria for dementia patient was CDR scale below 2 which means mild dementia.

In this study, motion analysis system was used to evaluate the kinematic parameters to compare gait performance, hand function was measured by a new designed computer board [Fig.1]. In gait aspect, there were three motor tasks [Table.1]: **(1)** comfortable walking; **(2)** comfortable walking combined dual-task; **(3)** comfortable walking combined dual-task (memory).In hand function evaluation, subjects were required to connect randomly arranged circles into an

F. Ibrahim, N.A. Abu Osman, J. Usman and N.A. Kadri (Eds.): Biomed 06, IFMBE Proceedings 15, pp. 208-210, 2007
www.springerlink.com ' Springer-Verlag Berlin Heidelberg 2007

ascending numeric sequence as quickly as possible, there were three motor task: **(1)** sequence task; **(2)** sequence task combined dual-task; **(3)** random sequence task. Dual-task in this study was asked subjects performance secondary task at the same time which invert three numbers experimenter recited. The data were been analysis through two-way mixed ANOVA to compare within and between groups.

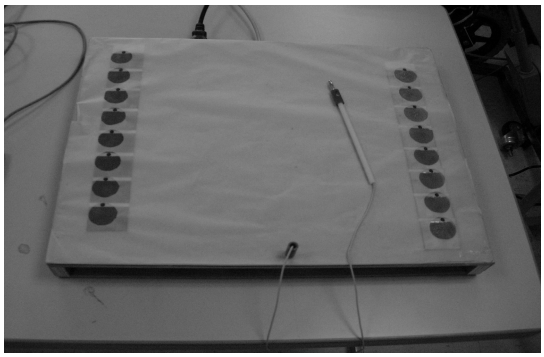

Fig.1

Table1

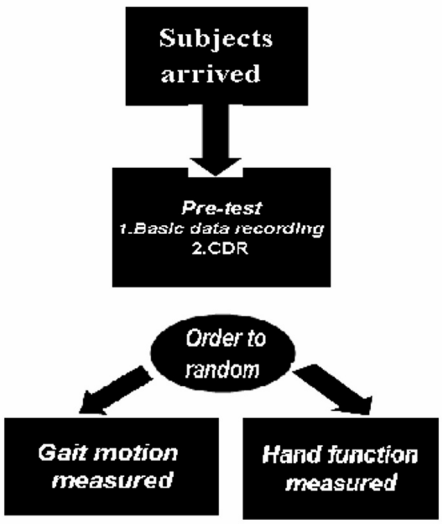

III. Results

Among the groups were similar with respect to age, gender, height, weight, and years of education. As expected, the subjects with dementia scored higher (worse) on the CDR scales ($p<0.05$). In the gait aspect, there was no different in the single-task of cadence (steps/min), stride length (m), and stride time (s) among the three groups ($p<0.05$). Compared with HE and subjects with dementia, HE had higher walking speed (m/s) .Compared with AD and VaD, there was no different in cadence (steps/min), stride length (m), walking speed (m/s) and stride time (s). In the trunk movement while gait, three groups had no significant different ($p>0.05$). In the dual-task of gait, there was significant decreased in AD on walking speed, cadence, and stride length ($p<0.05$); and significant increased in stride time, and trunk movement degree (both trunk and shoulder, $p<0.05$).In the stride length and stride time gait variation (CV, 100%×SD/mean), HE and VaD had no significant different between single-task and dual-task. In the AD group, there was significant different between single and dual-task [Fig.2]. In the hand function measured results, HE and VaD had no significant different in single and dual-task. In the AD groups, there had significant different between single and dual-task. In the random sequence task, three groups had significant different [Fig.3].

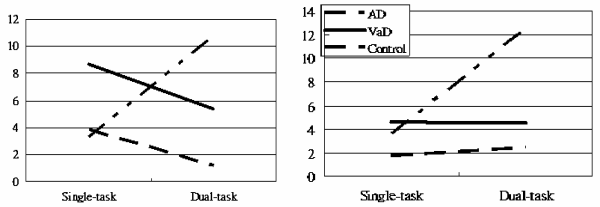

Fig.2

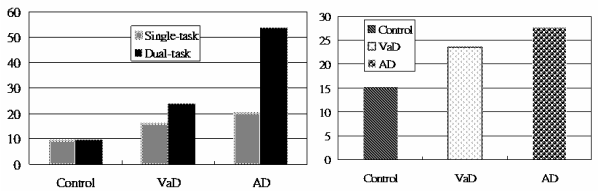

Fig.3

IV. Conclusions

Patients with AD present poor motor strategies than VaD in dual-task of gait and hand function. Among them, the change of hand function seems more sensitive than gait in biomechanical analysis in dual-task.

Acknowledgment

We thank the staff and patients of the, Department of Neurology, Chang Gung Memorial Hospital, Taipei, Taiwan, for there time and assistance.

F. Ibrahim, N.A. Abu Osman, J. Usman and N.A. Kadri (Eds.): Biomed 06, IFMBE Proceedings 15, pp. 208-210, 2007
www.springerlink.com ' Springer-Verlag Berlin Heidelberg 2007

REFERENCES

1. Henry Brodaty. (2001) Overview of dementia. Essentials of Dementia,1-15.
2. Linn RT, Wolf PA, Bachman DL et al.(1995) The preclinical phase of probable Alzheimer s disease. Arch Neurol;52:485-490.
3. Jahanshahi M, Frith CD.(1998) Willed action and its impairments. Cog. Neuropsychol;15:483-533.
4. Shallice T, Burgess P.(1996) The domain of supervisory processes and temporal organization of behavior. Philos Train R Soc Lond B Biol Sci;351:1405-1411.
5. Adams RL, Parsons OA, Culbertson JL et al..(1996) Neuropsychology for Clinical Practice: Etiology, Assessment, and Treatment of Common Neurologic Disorders. Washington, DC: American Psychological Association.
6. Spreen O, Strauss E.(1998) A Compendium of Neuropsychological Tests: Administration, Norms and Commentary, 2nd ed. New York: Oxford University Press.
7. Alexander N, Mollo J, Giordani B.(1995) Maintenance of balance, gait pattern, and obstacle clearance in Alzheimer s disease. Neurology; 45:908-914.
8. P. Manckoundia, F. Mourey, P. Pfitzenmeyer, C. Papaxanthis.(2006) Comparison of motor strategies in sit-to-stand and back-to-sit motions between healthy and Alzheimer s disease elderly subjects. Neuroscience;137(2):385-92.

Address of the corresponding author:

Author: Jing-Jung Chen
Institute: Graduate Institute of Rehabilitation Sciences, Chang Gung University
City: Taipei
Country: Taiwan

F. Ibrahim, N.A. Abu Osman, J. Usman and N.A. Kadri (Eds.): Biomed 06, IFMBE Proceedings 15, pp. 208-210, 2007
www.springerlink.com ' Springer-Verlag Berlin Heidelberg 2007

Muscles activity of the Back and Hamstring during Trunk Flexion and Extension Task in Healthy and Low Back Pain Women

S.H. Othman[1], N.F. Muhammad[1], F. Ibrahim[1], S.Z. Omar[2]

[1]Department of Biomedical Engineering, Faculty of Engineering, University of Malaya, 50603 Kuala Lumpur, Malaysia.
[2]Department of Obstetric and Gynecology, Faculty of Medicine, University of Malaya, 50603 Kuala Lumpur, Malaysia.

Abstract **This paper describes the investigation of Surface Electromyography (sEMG) signals of back muscles and hamstring muscles during forward flexion and extension in healthy and low back pain (LBP) women. There were two groups of Malaysian females aged between 20 to 55 years old voluntary participated in this study. Group 1 consisted of 10 healthy females while group 2 consisted of 6 females suffered with low back pain. Every subject was trained to perform two types of forward flexion; maximum forward flexion (bowing as far as they can) and 90^o forward flexion with hands on the knees. The electromyogram (EMG) and the motion signals were recorded during forward flexion of the trunk at the back and hamstring muscles. The findings indicated that the flexion relaxation phenomenon (FRP) was found only at the back muscles in healthy subjects during full flexion of the trunk, however it was absent at the hamstring muscles. For low back pain patients, the FRP was absent in both muscles. Mann-Whitney test showed a statistically significant differences in flexion relaxation ratio (FRR) between two groups during maximum forward flexion ($p<0.05$) and 90^o forward flexion ($p<0.001$).**

Keywords— **Flexion relaxation phenomenon, low back pain, back muscles, hamstring muscles**

I. Introduction

In 1948, Allen [1] was the first researcher to describe that electrical activity in the erector spine can suddenly decrease after a certain amount of trunk flexion. Later, it has been recognized as flexion relaxation phenomenon (FRP) in 1955 by Floyd and Silver [2]. The flexion relaxation phenomenon (FRP) was found to occur at 40° to 70° of body flexion [3, 4] with the knees straight [5]. Previous study [3, 4, 6] showed during forward flexion in normal subjects without low back pain (LBP), the muscles were initially active as the muscles contract to lower the trunk, but as the motion nears its end range position, the muscles became electromyographically silent. When the subject straightened up, the muscles contract and causes an increase electrical output. However, in the subject with back pain, FRP is frequently absent. Due to that, FRP is then becomes a recognized indicator for low back dysfunction [2-4, 6-8].

A number of physiologic mechanisms have been proposed to explain the etiology of the FRP in the back muscles. Stretch receptors have been suggested in the ligamentum flavum and other ligaments at the back of the body. When these ligaments are stretched, the stretch receptors will be stimulated and sending afferent impulses to cause reflex inhibition of the erector spinae [2, 7, 8]. However, Gupta has found that the FRP in the back muscles in healthy subject can be made to appear earlier or later in the vertebral flexion. Thus, it goes against the theory of stretch receptors in the ligaments causing reflex inhibition of the erector spinae [9]. He suggested that FRP occurs as a result of the passive equilibrium between the gravity-induced tensile torque and the extensor torque provided by the stretched posterior vertebral ligaments. Others etiology have been suggested are muscle lengthening reaction [10] and the flexion-limiting role of the erector spinae [11]. The persistent activity in erector spinae in patient with LBP is suggested to provide stability to help protect the diseased passive spinal structure from movements that may cause pain [12].

Sihvonen pioneered in proving that the hamstring muscles relax during forward flexion with different time compared to back muscles [3]. The relaxation of hamstring was found in normal and LBP subjects. He also found that the hamstring muscles active first and followed by back muscles during the initial of the extension. However, McGorry *et al* [13] and Gupta [9] found inconsistence of FRP occurred around the hamstring.

Several studies [4, 14] have come out with calculation ratio of muscle activity between full flexion and partial flexion to compare between LBP and healthy subjects. This ratio involved by dividing the maximum root mean square (RMS) EMG signal values during partial flexion by the RMS of EMG signal during full flexion. Study by Watson *et al* showed that the flexion relaxation ratio (FRR) of the LBP patients is lower than the healthy control subjects, it was demonstrated a highly significance differences between groups [4]. Geisser *et al* [15] preferred to use a similar method as Shirado *et al* [16] to calculate FRR. The FRR value was computed by employing normalization of the EMG values. Normalization of EMG was done by dividing the maximum EMG during flexion and average EMG in full flexion by the average EMG during standing. Then, the FRR value was acquired by dividing the normalized maximum EMG by the normalized average EMG in full flexion [15].

F. Ibrahim, N.A. Abu Osman, J. Usman and N.A. Kadri (Eds.): Biomed 06, IFMBE Proceedings 15, pp. 211-214, 2007
www.springerlink.com ' Springer-Verlag Berlin Heidelberg 2007

The objective of this study is to investigate the surface electromyography (sEMG) signals of the back and hamstring muscles during forward flexion and extension in healthy and LBP women.

II. Subjects and methods

A. Subjects

Two groups of voluntary females, aged between 20 to 55 years old were recruited in this study and consent form was obtained from every subject. The subjects were divided into two groups. Group 1 consisted of 10 healthy women (mean age 24–1.49) while Group 2 consisted of 6 women with LBP (mean age 35.67–12.56) at least for 12 weeks. In this study, LBP patients were defined as one who had not suffered from back pain due to the non-musculoskeletal disorder. Pregnant women were excluded in this study.

B. Apparatus

Ag-AgCl surface electrodes (3cm diameter) were used to collect the electromyography (EMG) muscle activity of the sampled muscles. The EMG activity was recorded by using 8-channel Noraxon Telemyo2400T Gen 2 Telemetric Real time which connected to a notebook. The EMG bandwidth was 10-500Hz at sampling rate 1500Hz without notch filter at 50Hz. The information was observed constantly on a monitor and stored digitally in raw form for further analysis using MATLAB 7.0 software at 1500Hz sampling rate.

C. Experimental procedure

The subjects were briefed on the study protocol which involved two types of forward flexion and extension with knee straight; maximum forward flexion (bowing as far as they can) (Fig.2) and 90^o forward flexion with hands on the knees (Fig.1) and return to the upright position three times.

The skin over the fourth lumbar (L4), fifth lumbar (L5) and the middle of the hamstring muscles were cleaned thoroughly with an alcohol abrade. The spinal process of the L4 vertebra was identified and the Ag-AgCl surface electrodes were attached bilaterally about 2 cm laterals from spinous processes at L4 and L5. At the 5cm distal from the gluteal fold in the middle of the hamstring muscles, the surface electrodes were placed too for both legs. The surface electrodes were attached to the skin while the subject was in midflexion to avoid electrodes from loosens during the bending cycle as suggested by Sihvonen [3]. The sEMG and motion signals were recorded during flexion and extension with knees straight and the feet about 15 cm apart. They were then required to practice the movements (i.e. maximum forward flexion and 90^o forward flexion with return to upright position) prior to testing to ensure that they could perform those movements. During the recordings of EMG, each movement was repeated three times. Basically the forward bending was divided into four phases which were phase 1: standing (10 seconds), phase 2: forward flexion (2 s), phase 3: full flexion (5 s), and phase 4: extension (3 s). The whole cycle of forward flexion and extension took about 20 seconds.

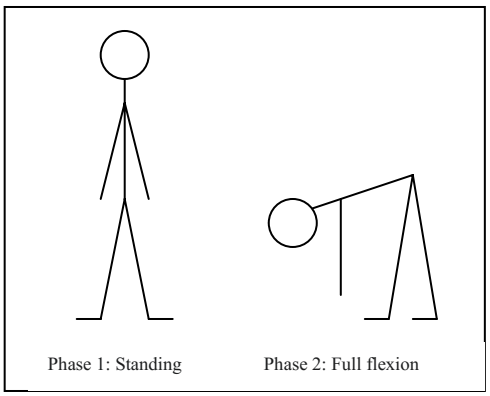

Fig. 1 Posture of maximum forward flexion

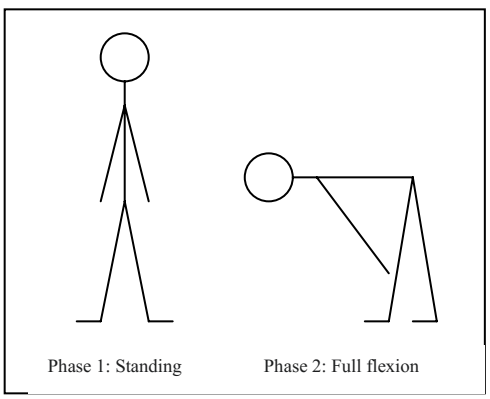

Fig. 2 Posture of 90^o forward flexion

D. Measurement of Flexion Relaxation Ratio

The data obtained from each subject were divided into four phases as mentioned above. Since this is the preliminary study, it focused and analyzed the EMG signal on the right side of the back and hamstring muscles.

F. Ibrahim, N.A. Abu Osman, J. Usman and N.A. Kadri (Eds.): Biomed 06, IFMBE Proceedings 15, pp. 211-214, 2007
www.springerlink.com ' Springer-Verlag Berlin Heidelberg 2007

Table 1 Mean and median of FRR at the back muscles during maximum and 90° forward flexion

Posture	Healthy Group (n=10)			LBP Group (n=6)			p
	Mean	Median	SD	Mean	Median	SD	
Maximum forward flexion	0.23	0.16	0.12	0.13	0.12	0.07	0.042
90° forward flexion	0.33	0.34	0.13	0.06	0.06	0.01	0.000

The maximum (MAX) EMG during flexion was calculated by dividing the MAX EMG in Phase 2 by the average EMG from Phase 1. The average (AVE) EMG in full flexion was calculated by dividing the AVE EMG during Phase 3 by the AVE EMG in Phase 1. Finally, the MAX EMG in extension was calculated by dividing the MAX EMG in Phase 4 by the AVE EMG in Phase 1. The FRR was computed by dividing the maximum EMG during flexion by the average EMG in full flexion. A similar method was reported by Geisser *et al* [15] and Shirado *et al* [16].

E. Statistical Analysis

The statistical analysis was performed using SPSS statistical package version 12.0 for Windows. Data were expressed as median. Mann-Whitney Test was applied for comparison between the median in healthy groups and LBP groups. A probability level of $p<0.05$ was taken as significant.

III. Results

The experimental result of the EMG signals of all the healthy subjects during maximum and 90° forward flexion showed that the FRP exist in the back muscles while it was absent in the hamstring muscles. The EMG signal of a healthy subject is shown in the Fig. 3.

However, in LBP patients the FRP was absent at the back and hamstring muscles during maximum forward flexion (Fig. 4 (a) to 4 (d)) and 90° forward flexion.

Table 1 shows the mean and median of FRR at the back muscles during maximum and 90° forward flexion. The result shows that all the healthy subjects experience higher FRR as compared to the LBP patients. Mann-Whitney test indicates a statistically significant differences in FRR during performing maximum forward flexion ($p<0.05$) and 90° forward flexion ($p<0.001$).

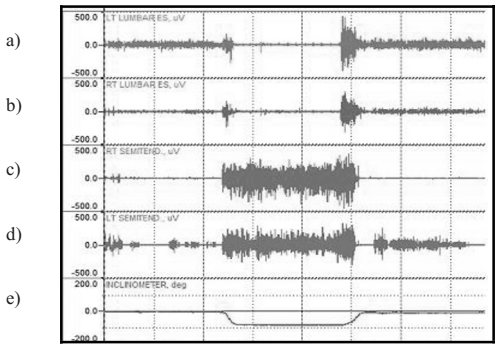

Fig. 3 The EMG and inclinometer signals (e) of a healthy subject during maximum body flexion recorded at the back muscles [(a) and (b)] and hamstring muscles [(c) and (d)].

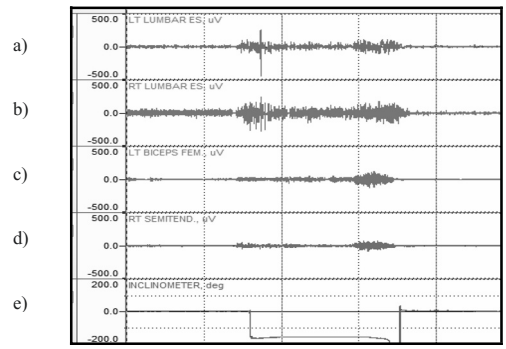

Fig. 4 The EMG and inclinometer (e) signals of a LBP patient during maximum forward flexion recorded at back muscles [(a) and (b)] and hamstring muscles [(c) and (d)].

IV. Discussions

The experiment findings indicate that FRP occurred at the back muscles (L4-L5) in healthy subjects. A highly significant differences in the FRR between healthy and LBP subjects was found for maximum forward flexion ($p<0.05$) and 90° forward flexion ($p<0.001$). Thus, the result of FRR can be use to discriminate between healthy and LBP subjects which is also in agreement with other studies [4, 17].

FRP in hamstring muscles was neither found in LBP group nor healthy group. The inconsistence of FRP occurred around the hamstring also reported by McGorry *et al* [13] and Gupta [9]. However, study by Sihvonen demonstrated that the hamstring muscles ceased when nearly

F. Ibrahim, N.A. Abu Osman, J. Usman and N.A. Kadri (Eds.): Biomed 06, IFMBE Proceedings 15, pp. 211-214, 2007
www.springerlink.com ' Springer-Verlag Berlin Heidelberg 2007

reached the full lumbar flexion (95%). The reason of inconsistency activity at the hamstring site is still unclear.

During the trunk extension in standing postures, the hamstring muscle activated first and followed by back muscle. This result is consistent with reports of kinematics with findings indicating that hip motion leads trunk motion during extension in standing postures [18-20]. Other investigators also have documented this phenomenon by using electromyography method [3, 13]. The need for proximal stabilization could explain the earlier activation of hamstring [13].

Watson [4] found that discriminant validity for the FRR for all four sites (L1/2 and L4/5) resulted in 93% sensitivity and 75% specificity. Therefore, it appears to be stable enough to be used to assess the return to normal of the surface EMG pattern following treatment and would be sensitive to the effect of treatment on the restoration of the normal pattern of muscle activity. Current research is under way to investigate the utility of the FRR in assessing a treatment outcome and the role of physical and psychological factors in the development and resolution of guarded maneuvers in low back pain.

V. Conclusions

In conclusion, during full flexion of healthy subjects, FRP appeared only in the back muscle but it was absent in the hamstring muscles. However, in the LBP patients, FRP was absent in both muscles. FRR for back muscles was significantly higher ($p<0.05$) in the healthy subjects than the LBP patients. This study demonstrated that FRR can be used as one of the indicator for identifying healthy and LBP patients.

References

1. Allen CEL (1948) Muscle action potential used in the study of dynamic anatomy. Br J Phys Med 11: 66-73
2. Floyd WF and Silver PHS (1955) The function of the erector spinae muscles in certain movements and postures in man. J Physiol. 129: 133-143
3. Sihvonen, T. (1997) Flexion relaxation of the hamstring muscles during lumbar-pelvic rhythm. Arch Phys Med Rehabil. 78: 486-490.
4. Watson PJ, Booker CK, Main CJ, Chen CAN (1997) Surface electromyography in the identification of chronic low back pain patients: the development of the flexion relaxation ratio. Clinical Biomechanics; 12 (3): 165-171.
5. Shin G, Shu Y, Li Z, Jiang Z, Mirka G (2004) Influence of knee angle and individual flexibility on the flexion-relaxation response of the low back musculature. J Electromyogr Kinesiol. 14(4): 485-494.
6. Kuriyama N, Ito H (2005) Electromyographic functional analysis of the lumbar spinal muscles with low back pain. J Nippon Med Sch. 72: 165-173.
7. Kippers V, Parker AW (1984) Posture related to myoelectric silence of erector spinae during trunk flexion. Spine 9:740-745
8. Schultz AB, Hadespeck-Grib K, Sinkora G, Warwick DN (1985) Quantitative studies of flexion-relaxation phenomenon in the back muscles. J Orthop Res. 3(2):189-197.
9. Gupta A (2001) Analyses of myo-electrical silence of erectors spinae. J Biomech. 34 (4): 491-496.
10. Portnoy H, Morin F (1956) Electromyographic study of postural muscles in various positions and movements. Am J Physiol. 186(1):122-6
11. Taylor J, Towmey L (1980) Sagittal and horizontal plane movement of the human lumbar vertebral column in cadavers and in living. Rheumatol Rehabil.19(4):223-32
12. Kaigle AM, Wessberg P, Hansson TH (1998) Muscular and kinematic behavior of lumbar spine during flexion-extension. J Spinal Disord. 11(2):163-74
13. McGorry RW, Hsiang SM, Fathallah FA, Clancy EA (2001) Timing of activation of the erector spinae and hamstrings during a trunk flexion and extension task. Spine. 26(4) :418-425
14. Ahern DK, Follick MJ, Council JR, Laser-Wolston N, Litchman H (1988) Comparison of lumbar paravertebral EMG patterns in chronic low back pain patients and non-pain controls. Pain 34: 153-160.
15. Geisser ME, Haig AJ, Wallbom AS, Wiggert EA (2004) Pain-related fear, lumbar flexion, and dynamic EMG among persons with chronic musculoskeletal low back pain. Clin J Pain. 20(2): 61-69
16. Shirado O, Ito T, Kaneda K et al (1995) Flexion-relaxation phenomenon in the back muscles: a comparative study between healthy subjects and patients with chronic low back pain. Am J Phys Med Rehabil. 74:139-144
17. Geisser ME, Ranavaya M, Haig AJ, Roth RS, Zucker R, Ambroz C, Caruso M (2005) A Meta-analytic review of surface electromyography among persons with low back pain and normal, healthy controls. J Pain. 6(11):711-726
18. McClure PW, Esola M, Schreier R, Siegler S (1997) Kinematic analysis of lumbar and hip motion while rising from a forward, flexed position in patients with and without a history of low back pain. Spine 22(5): 552-558
19. Nelson JM, Walmsley RP, Stevenson JM (1995) Relative lumbar and pelvic motion during loaded spinal flexion/extension. Spine.20(2):199-204.
20. Paquet N, Malouin F, Richards CL (1995) Hip-spine movement interaction and muscle activation patterns during sagittal trunk movements in low back pain patients. Spine. 19:569-603

Address of the corresponding author:

Author: Siti Hajar Othman
Institute: Biomedical Engineering, Faculty of Engineering, UM
Street: 50603
City: Kuala Lumpur
Country: Malaysia
Email: ct_ jaja5@yahoo.com

F. Ibrahim, N.A. Abu Osman, J. Usman and N.A. Kadri (Eds.): Biomed 06, IFMBE Proceedings 15, pp. 211-214, 2007
www.springerlink.com ' Springer-Verlag Berlin Heidelberg 2007

Music therapy effect of music pillow for sleep – preliminary study

Yu Yi Chen[1], Alice M.K. Wong, MD[2]

[1,2]Graduate Institute of Rehabilitation Science, Chang Gung University, Taipei Taiwan

Abstract—**Background and Purpose: Sleep, a vital ingredient in life, is an active and complex rhythmic state that may affected the health of people. Based on theory, sedative music may induce relaxation and distraction responses. Music also has the effect on the change of muscular energy, heart rate and respiratory rates, blood pressure, and psychological distress. Choice the good pillow and environment could enhance good sleep in quality. The purpose of this study was use music pillow for good sleep.**

Methods: The test on effect of music pillow for sleep promotion includes two conditions, music pillow or non-music pillow. Six people aged 20-30 years in normal state of sleep will be included into this study. Participants listen to sedative piano music with or without block sound one hours in the naptime for four days. Polysomnography was used for recording of sleep and physiology variation.

Preliminary results: From the result of sleep promotion, people sleep with music pillow had shorter period of latency to fall asleep than without music. Slow down of heart rate was also found. Music can promote the rapid onset of sleep in young people , block sound might enhance the effect of music for the onset of sleep in young people.

Conclusion: People sleep on pillow with music could promote sleep. Block sound might enhance the effect of music for the onset of sleep in young people.

Keywords— **Music therapy, music, pillow, sleep**

I. Introduction

Sleep, a vital ingredient in life, is an active and complex rhythmic state that may be affected by the aging process. that may affected the health of people. These changes in sleep patterns are reflected in the common sleep-related complaints of young adults, such as taking longer to fall asleep, awakening more often, and being sleepy in the daytime. Sleep disorders can result in tiredness, fatigue, depression, greater anxiety, irritability, pain sensitivity, muscle tremors, immunosuppression, and lack of daytime alertness (Pandi- Perumal et al. 2002). Although there is much research about sleep, few studies have focused on the effects of music in improving sleep quality, particularly in young adults. One method to improve sleep is to take medication Hypnotics are taken regularly by 15 19% of older adults (Clapin-French 1986, Morgan et al. 1988, Englert & Linden) But that is not the only way to improve sleep quality.

Only three investigators have studied the use of music to promote sleep. Each found that music had beneficial effects (Mornhinweg & Voignier 1995, Zimmerman et al. 1996, Levin 1998), but there were methodological problems of mixed age groups, small sample size, lack of randomization, unbalanced groups, and lack of rationale for the choice of music intervention. Further, none considered confounding factors of anxiety and depression, and none studied the effects of music on sleep in older people and that not in young adults.

Based on a psychophysiological theory synthesized from the literature, sedative music induces relaxation and distraction responses (Good et al. 2001), which reduce activity in the neuroendocrine and sympathetic nervous systems, resulting in decreased anxiety, heart rate, respiratory rate, blood pressure (Standley 1986, Zimmerman et al. 1988, Good et al. 1999) and sleep (Johnson 1991). Music has been found to reduce circulating noradrenaline (Mockel et al. 1994, Gerra et al. 1998), which is associated with sleep onset (Irwin et al. 1999). Thus, a sedative music intervention was expected to improve sleep quality.

The purpose of this study is to use a self composed music by our music therapist to test its effect on young people for promotion of sleep.

II. Methods

2.1 Participant

Six volunteer subjects (three males and three females, mean_SD age=24.8_2.42 year) participated in the present study. Written informed consent was obtained from all participants before the experiment. All subjects were screened for health status with a structured medical interview. Medical illness, psychiatric/psychological disturbance, sleep disorders, substance abuse, and/or neurological disorders were criteria for exclusion. Subjects were instructed to maintain a normal sleep-wake schedule and refrain from alcohol, caffeine, medication, and/or drug consumption during 48 h prior to each experimental session. Sleep logs indicated no variations in the length of sleep time in the naps preceding the baseline and experimental sessions.

F. Ibrahim, N.A. Abu Osman, J. Usman and N.A. Kadri (Eds.): Biomed 06, IFMBE Proceedings 15, pp. 215-218, 2007
www.springerlink.com ' Springer-Verlag Berlin Heidelberg 2007

2.2 Experimental

A randomized controlled trial design was used. Permuted block randomization, with sealed envelopes stratified on gender, was used to assign participants to four groups. The envelopes were prepared by a different person so that the investigator (first author) was blind to block size and order of assignment. Because sleep onset has been found to take about 13 35 minutes in adults (Hayter 1983, Gislason et al. 1993), we decided to use one hours of music as therapy every naps at bedtime to guard against music ending earlier than sleep onset.

Participants were visited in the Chang Gung Memorial Hospital by the investigator at the start of the study to screen for eligibility, collect baseline data, allocate them to the study groups, and teach the experimental group to use the music intervention at bedtime each naps.

Participants were also join the study period at a week to the protocol (Fig. 1).

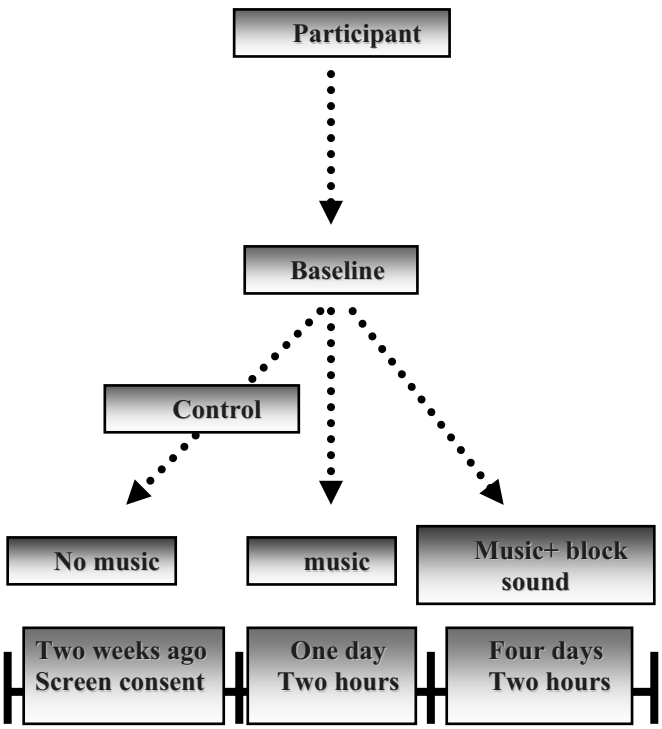

Fig. 1 study design

2.3 Experimental intervention

A self composed music for music therapist sedative music played for one hours at naptime. The tempo of the sedative music was 60 80 beats/minute. In this study we choice the 60 beats/minutes.

2.4 Measures

The PSQI (Buysse et al. 1989) is a questionnaire that measures self-reported sleep habits during the previous week. It is a global measure with seven components: perceived sleep quality, sleep latency, sleep duration, sleep efficiency, sleep disturbance, use of sleep medication, and daytime dysfunction. The score for each component ranges from 0 to 3, and the sum is a global score that ranges from 0 to 21. Higher scores indicated poorer sleep quality. Both the global PSQI and the component subscale scores were analysed so that effects of music on individual elements of sleep could be determined.

Polysomnographic recordings were carried out in an acoustically shielded room from 12:00 (lights-off) to 14:00 h (lights-on). The EEG was continuously recorded from 6 scalp locations (C3, C4, T3, T4, O1, and O2), and referenced to a linkedmastoid derivation. Standard EOG and EMG electrode placements were also used. Electrophysiological measurements were recorded using silver silver chloride disk electrodes filled with electrode cream and attached with either surgical tape or collodion (scalp placements). Impedance of electrode-skin was kept below 5000 ohms. The same recording protocol was used in all experimental sessions. Each recording was randomly scored by two independent technicians for consecutive 30 s epochs. Scorers were not informed of the purpose of the investigation. All scorers were from the same laboratory and had received the same training, although the length of their experience differed. Disputed epochs were blind-scored one-by-one by a third technician strictly according to standard rules for human sleep stages scoring

2.5 Data collection

Screening for eligibility occurred at the first home visit and included testing for sleep quality (PSQI). The scores were immediately calculated, and participants were told whether or not they were eligible.

They were then randomly assigned either to the treatment or control group, while controlling for gender.

2.6 Statistical analysis

The following sleep parameters were measured in the baseline nap and those naps preceded by the bilateral auditory stimulation: (1) sleep onset latency (time elapsed from the lights-off to the onset of stage 1 sleep); (2)efficiency to the first SWS period. Sleep and wakefulness parameters obtained from baseline and experimental naps were compared using a repeated measure ANOVA When a significant main effect was found, post hoc Bonferroni correction comparisons were performed between naps.

F. Ibrahim, N.A. Abu Osman, J. Usman and N.A. Kadri (Eds.): Biomed 06, IFMBE Proceedings 15, pp. 215-218, 2007
www.springerlink.com ' Springer-Verlag Berlin Heidelberg 2007

III. Preliminary Results

3.1. Sleep onset time (latency)

The Fig. 2 shows the sleep onset time of all participants. We can find the music+block sound and music decreased the sleep onset time rather than no music.

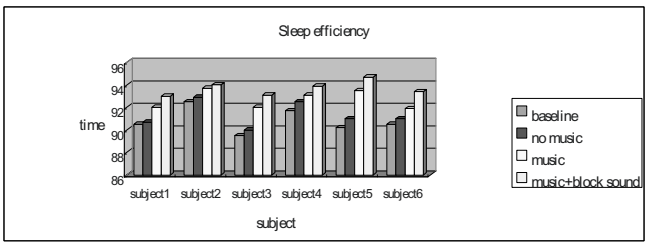

Fig. 2 sleep onset time

The Fig. 3 shows the sleep efficiency of all participants. We can find the music+block sound and music decreased the sleep onset time rather than no music.

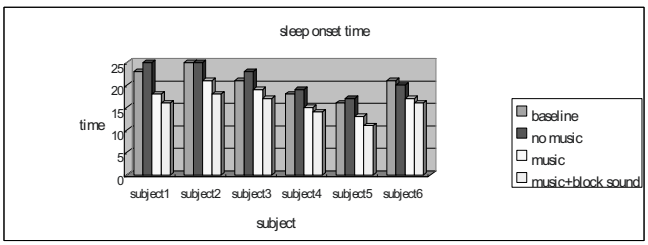

Fig. 3 sleep efficiency

From the result of sleep promotion, people sleep with music pillow had shorter period of latency to fall asleep than without music. Slow down of heart rate was also found. Music can promote the rapid onset of sleep in young people, block sound might enhance the effect of music for the onset of sleep in young people.

IV. Conclusions

Our findings to knowledge about the effectiveness of soft slow music used as therapy on sleep quality in young people. Music is pleasant and safe and can be used therapeutically for young people. The intervention is quick and easy to learn, is low cost.

People sleep on pillow with music could promote sleep. Block sound might enhance the effect of music for the onset of sleep in young people

References

1. Buysse, D. J., Reynolds, C. F. III, Monk, T. H., Berman, S. R., & Kupfer, D. J. (1989). The Pittsburgh Sleep Quality Index: A new instrument for psychiatric practice and research. *Psychiatry Research, 28, 193—213.*
2. Chlan LL (2000) Music therapy as a nursing intervention for patient supported by mechanical ventilation. *American Association of Critical Care Nurse 11, 128–138.*
3. Chlan LL (1998) Effectiveness of a music therapy intervention on relaxation and anxiety for patients receiving ventilatory assistance. *Heart & Lung 27, 169–176.*
4. Clair AA (1996) *Therapeutic Use of Music with Older Adults.* Health Professions Press, Baltimore, MD.
5. Gaston E.T. (1968) Man and music. *In Music in Therapy. (E.T. Gaston, ed.) Macmillan, New York, pp. 7–29.*
6. Gaston E.T. (1951) Dynamic music factors in mood changes. *Music Educators Journal 37, 42–44.*
7. Gerra G., Zaimovic A., Franchini D., Palladino M., Giucastro G., Reali N., Maestri D., Caccavari R., Delsignore R. & Brambilla F. (1998) Neuroendocrine responses of healthy volunteers to technomusic : relationships with personality traits and emotional state. *International Journal of Psychophysiology 28(1), 99–111.*
8. Good M., Stanton-Hicks M., Grass J.A., Anderson G.C., Lai H.L., Roykulcharoen V., et al. (2001) Relaxation and music reduce postsurgical pain across activities and days. *Journal of Advanced Nursing 33(2), 208–215.*
9. Irwin M., Thompson J., Miller C., Gillin J.C. & Ziegler M. (1999) Effects of sleep and sleep deprivation on catecholamine and interleukin-2 levels in humans: clinical implications. *Journal of Clinical Endocrinology and Metabolism 84(6), 1979–1985.*
10. Johnson J. (2003) The use of music to promote sleep in older women. *Journal of Community Health Nursing 20(1), 27-35*
11. Kaempf G & Amodei ME (1989) The effect of music on anxiety. *AORN Journal 50, 112–118.*
12. Kollef MH, Levy NT, Ahren TS, Schaiff R, Prentice D & Sherman G (1998) The use of continuous IV sedation is associated with prolongation of mechanical ventilation. *Chest 114, 541–548.*
13. Lai H., Good M. (2004) Music improves sleep quality in older adults. *Journal of Advanced Nursing, 49(3),234-244*
14. Lee O. , Chung Y., Chan M., Chan W.(2004) Music and its effect on the physiological responses and anxiety levels of patients receiving mechanical ventilation: a pilot study. *Journal of Clinical Nursing, 14, 609–620*.
15. Maestri D., Caccavari R., Delsignore R. & Brambilla F. (1998) Neuroendocrine responses of healthy volunteers to technomusic : relationships with personality traits and emotional state. *International Journal of Psychophysiology 28(1), 99–111.*
16. McClellan R (1991) *The Healing Forces of Music: History, Theory and Practice.* Element Inc., MA, USA.
17. Mockel M., Rocker L., Stork T., Vollert J., Danne O., Eichstadt H., Muller R. & Hochrein H. (1994) Immediate physiological responses of healthy volunteers to different types of music: cardiovascular, hormonal and mental changes. *European Journal of Applied Physiology and Occupational Physiology 68(6), 451–459.*
18. Munro S & Mount B (1978) Music therapy in palliative care. *Canadian Medical Association Journal 119, 1029–1034.*
19. Pandi-Perumal S.R., Seils L.K., Kayumov L., Ralph M.R., Lowe A., Moller H. & Swaab D.F. (2002) Senescence, sleep, and circadian rhythms. *Ageing Research Reviews 1(3), 559–604.*
20. Priestley M (1975) *Music Therapy in Action*. Constable, London.
21. Sejnowski T., Destexhe A.(2000) Why do we sleep? *Brain Research 886 (2000) 208–223.*

F. Ibrahim, N.A. Abu Osman, J. Usman and N.A. Kadri (Eds.): Biomed 06, IFMBE Proceedings 15, pp. 215-218, 2007
www.springerlink.com ' Springer-Verlag Berlin Heidelberg 2007

22. Standley J.M. (1986) Music research in medical/dental treatment: meta-analysis and clinical applications. *Journal of Music Therapy 23(2), 56–122.*
23. Tan L. (2004) The effects of background music on quality of sleep in elementary school children. *Journal of Music Therapy, XLI(2), 128-150.*

Address of the corresponding author:
Author: Yu Yi Chen
Institute: Graduate Institute of Rehabilitation Sciences, Chang Gung Uiversity
City: Taipei
Country: Taiwan

F. Ibrahim, N.A. Abu Osman, J. Usman and N.A. Kadri (Eds.): Biomed 06, IFMBE Proceedings 15, pp. 215-218, 2007
www.springerlink.com ' Springer-Verlag Berlin Heidelberg 2007

Pneumatic Artificial Muscle in Biomedical Applications

Ramesh Ramasamy[1], Mohamed Rizon Juhari[2], Masanori Sugisaka[3,4] and Noor Azuan Osman[5]

[1]DAG Technology (M) Sdn. Bhd. Lot 2-7 Innovation House, Technology Park Malaysia,
Lebuhraya Puchong-Sg.Besi, 57000 Kuala Lumpur, Malaysia.
[2]School of Mechatronic Engineering, Northern Malaysia University College of Engineering, 01000 Kangar, Perlis, Malaysia.
[3]Advanced Research Institute for Science and Engineering, Waseda University, 3-4-1 Okubo, Shinjuku, Tokyo, 169-8555 Japan
[4]Department of Electrical and Electronics Engineering, Faculty of Engineering, Oita University, 700 Dannoharu, Oita-shi, 870-1192 Japan
[5]Deparment of Biomedical Engineering, University of Malaya, 50603 Kuala Lumpur, Malaysia

Abstract— **The intention of this article is to introduce and overview Pneumatic Artificial Muscles (PAMs). The construction of PAMS mainly consist of flexible, inflatable membranes, having orthotropic material behaviour. The main properties shaping the PAMs will be explained in terms of their load-carrying capacity and low weight in assembly. Discussion on their designs and capacity to function as locomotion device in robotics applications will be laid out, followed by viewpoint on the materials and strength models, concluded by some future directions in this research work.**

Keywords— **artificial muscle, pneumatic artificial muscle, fluid actuators, McKibben muscles**

I. Introduction

Recently, pneumatic actuators have found their way into factory floor automation, and have been widely used in robotics equipments. These actuators are usually cylindrical in shape, and have since their advancement over the years, become a more attractive source of locomotion device in robotics. One of the desirable properties for pneumatic actuators is the relatively low weight in assembly, as compared to their electric and hydraulics counterparts. This enables an easy control over the end-effectors attached to these actuators, whereby delicate and fragile objects can be handled accordingly by controlling the air pressure, hence generating a soft-touch . Various types of pneumatic actuators used currently in the field are cylinders, bellows, pneumatic engines and pneumatic stepper motors. A lesser-known type in this category is the Pneumatic Artificial Muscles (PAMs). PAMs operate opposite to bellows, i.e., they contract when pressurized, generating a load-carrying capacity during this contraction. They are extremely light-weight due to simple core construction materials consisting of inflatable and flexible membranes, more desirable to be assembled into mobile robotics equipments. Throughout literature, various names have been employed to identify a PAM, namely, Pneumatic Muscle Actuators [1], Fluid Actuator [2], Fluid-Driven Tension Actuator [3], Axially Contractible Actuator [4] and Tension Actuator [5]. PAM operates via overpressure, whereby gas pressure is charged into the membranes to move loads, instead of discharging gas pressure out of the membranes, as in the case of underpressure operated bellows. Overpressure is usually easier to achieve than underpressure with gas compressors,noting that ambient pressure in the vicinity of 101.3 kPa.

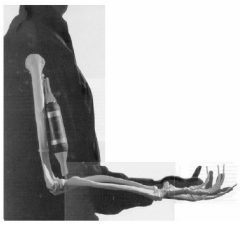

Fig. 1 Artist impression of PAM use

II. Characteristics of PAMs

As described previously, PAMs are operated by gas pressure and are contractile in nature upon inflation. Their construction materials simply consist of a flexible inflatable membrane, reinforced with fibrous filament, and fitted with gas closure fittings for mechanical load-carrying at its ends. As the membrane is pressurized, it bulges outwards in the radial direction, whilst contracting in length along is axial direction. It is during this axial contraction where PAM exerts a pulling force on its end-effectors. This force generated from contraction and the subsequent motion on the loads moved are unidirectional. This distinguishes the PAMs from other pneumatic devices like the bellows, which extends in length when pressurized. PAMs source of energy comes from pressurized gas, usually air, which is forced into the membranes. This pressurization creates a gauge pressure or differential pressure, which simply means the difference between the air pressure inside the membrane and that of the ambient atmospheric pressure outside the membrane. So, a PAM is in fact powered by gauge pressure or differential pressure to carry loads. To understand the characteristics of PAMs, two simple experiments can be reviewed [6,7,8].

F. Ibrahim, N.A. Abu Osman, J. Usman and N.A. Kadri (Eds.): Biomed 06, IFMBE Proceedings 15, pp. 219-221, 2007
www.springerlink.com ' Springer-Verlag Berlin Heidelberg 2007

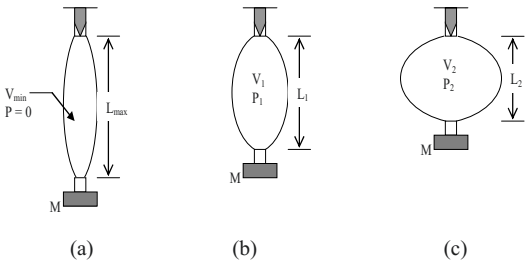

Fig. 2 PAM with constant load

Consider a mass M hanging at one end on a PAM which is fixed on the other end as shown in Fig. 2. The gauge pressure is increased from an initial value of zero. At zero gauge pressure shown in Fig. 2 (a), the enclosed volume is V_{min}, and its length is full, L_{max}. As the gauge pressure in the muscle is increased to a value P_1 in Fig. 2 (b), the enclosed volume is now V_1, bulging radially, as the overall lengths begins contracting, generating a pulling force on the mass M, lifting it upwards until force equilibrium achieved, i.e., when the generated pulling force reaces the value of Mg (g = gravitational constant, 9.81 m/s^2). A further increase in pressure to P_2 in Fig. 2(c), increases the enclosed volume to V_2, lifting the mass M further upwards by newly generated pulling force. From this test, two characteristics of PAMs are obvious: First, PAM shortens in length by increasing its enclosed volume and secondly, it will contract against a constant load as pneumatic pressure is gradually increased.

A second experiment setup [6,7,8] will now be reviewed to see other characteristics of PAM as shown in Fig. 3 below. This time the gauge pressure is kept at a constant value, while the mass will be reduced from an initial value of 2M, as seen in Fig. 3 (a). As mass is reduced to value of M in Fig. 2 (b), the PAM shortens, while increasing its enclosed volume. As all mass is completely removed as depicted in Fig. 3 (c), the bulging goes to its full extent, PAM shortens to a minimal length L_{min} and the pulling force will drop to zero. At this point, there is no more contraction is possible on the PAM. Further deductions can be added to the existing PAM characteristics: Firstly, PAM contracts in length under constant pressure as loading is reduced, and secondly, it reaches an optimal point at which no more contraction is possible and the pulling force subsequently falls to zero, under maximum enclosed volume. Based on both the experiments carried out and the four characteristics observed about the PAM, a fifth characteristics can thus be derived: For each configuration of applied pressure and attached pulled load, there exists an equilibrium length on the PAM, exhibiting a spring-like behaviour.

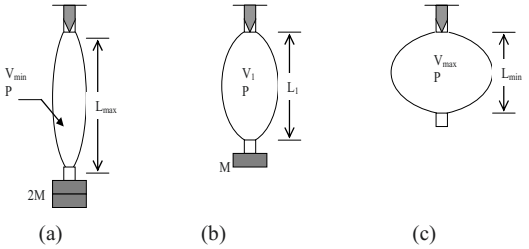

Fig. 3 PAM with constant pressure

III. Design of PAMs

PAMs were introduced into practice in the 1930 s by a Russian inventor named S. Garasiev [6]. This original design, however, is just a simple fluid-driven muscle-like actuator and due to limited material technology at the time, was limited in use. Since then, several other designs have emerged with improved materials technology, leading to a more practical applicability of PAMs in the industry, particularly robotics. The braided muscle [9], composed of gas-tight elastic bladder, surrounded by braided sleeves as shown in Fig. 3, seems like a practical construction, consisting of a flexible membrane, enclosed by braid fibres running helically (at angles of +θ and -θ) about the muscle s longitudinal axis.

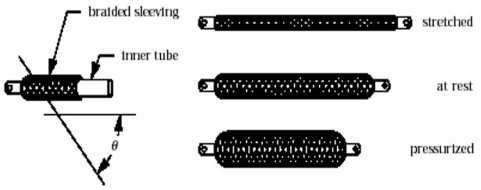

Fig. 4 Typical Braided Muscle Concept

When pressurized, the membranes will bulge out laterally against the braid fibres, achieving equilibrium by balancing internal pressure with tension in fibres. The fibres are locked at the PAM ends to balance external loads. The membranes will impose a pressing contact against the fibres, causing the fibres to curve outwards, shortening the overall PAM in the process, hence generating pulling force at ends. This concept was originally introduced by J.L McKibben [10] as an orthotic actuator in late 1950 s due to its similarity in contractile skeletal muscles. Typical materials used for the membranes constructions are latex and silicone rubber, whilst nylon is normally used in the fibres. Looking at Fig. 4, and denoting L_s as length of each fibre strand with N numbers of turns over the entire PAM, the

F. Ibrahim, N.A. Abu Osman, J. Usman and N.A. Kadri (Eds.): Biomed 06, IFMBE Proceedings 15, pp. 219-221, 2007
www.springerlink.com ' Springer-Verlag Berlin Heidelberg 2007

enclosed volume of the membrane with fibre pitch angle θ, can be found to be:

$$V = \frac{L_s^3}{4\pi N^2} \sin^2\theta \cos\theta \quad (1)$$

Thus, maximum enclosed volume may be achieved with a braiding angle of 54.7°. The force-carrying capacity of the PAM can also be deduced from work-energy theorem [9]. Consider work done in expanding a PAM by ***dV*** by charging it with pressure ***P***, amounting in net work of ***PdV***, this work is then used to move a payload with generated force ***F*** over distance of ***dL***, resulting work done by external force of ***FdL***. Neglecting hysterisis and any loss of energy due to friction, the following terms can be expressed for the generated force, ***F***:

$$F = -P\, dV / dL \quad (2)$$

Based on equations (1) and (2), one can ideally predict the performance of a PAM in terms of force generated, contraction lengths and enclosed volume changes, without considering the losses due to friction, material hysterisis and membrane deformation. Substituting (1) into (2) would yield Material stress-strain fields can also be derived from equilibrium state of internal and external forces on the membranes and fibres for a complete strength characteristics of the PAM design. Further advanced analyses can be carried out using a more robust Finite Element Method. A continuation of this work shall look at a more in-depth membrane materials strength formulation, considering effects of residuals due to hysterisis and friction.

IV. Conclusion

Since their conception, PAMs have evolved into practical device, though not widely used in a large scale in field applications. Their low assembly weight, and high power-to-weight ratio are most desirable for PAMs to be considered for use in mobile robotics, such as those conceived in [11]. A future direction in this research here will consider a more in-depth analysis into materials of construction for PAMs and testing in terms of actual functional performance as well as a localized strength envelope characteristics under operational conditions. A possible functional setup to be setup may be in terms of a suitable mechanism, similar to that listed in [11], and shall be a development o look forward to.

References

[1] D.G Caldwell, G.A Medrano-Cerda and M.J. Goodwin, Braided pneumatic actuator control of multi-jointed manipulator , Proceedings of the IEEE International Conference on Systems, Man and Cybernatics, pp.423-428, Le Touquet, 1993.

[2] J.M Yarlott, Fluid actuator , US Patent No.3 645 173, 1972.

[3] H.M. Paynter, Hyperboloid of revolution fluid-driven tension actuators and methods of making , US Patent No. 4 733 603, 1989.

[4] F. Daerden and D. Lefeber, Pneumatic artificial muscles: actuators for robotics and automation , European Journal of Mechanical and Environmental Engineering, 47(1)10 21, 2002.

[5] F. Daerden and D. Lefeber, The concept and design of pleated pneumatic artificial muscles , International Journal of Fluid Power, 2(3)41 50, 2001.

[6] B. Verrelst, F. Daerden, D. Lefeber, R. Van Ham and D. Verrelst, Pleated pneumatic artificial muscles: compliant robotic actuators , 2001 IEEE/RSJ International Conference on Intelligent Robots and Systems, Maui, Hawaii, October November 2001, pp. 1958 1963.

[7] B. Verrelst, F. Daerden, D. Lefeber and R. Van Ham, Pleated pneumatic artificial muscles: actuators for automation and robotics , 2001 IEEE/ASME International Conference on Advanced Intelligent Mechatronics, Como, July 2001, pp. 738 743.

[8] G.K Klute and B. Hannaford, Accounting for elastic energy storage in McKibben artificial muscle actuators , ASME Journal of Dynamic Systems, Measurement and Control, 122(2):386-388, 2000.

[9] Chou, C.P., B. Hannaford, Measurement and Modeling of McKibben Pneumatic Artificial Muscles , IEEE Transactions on Robotics and Automation, Vol. 12, No. 1, pp. 90-102, Feb 1996.

[10] G.K Klute and B. Hannaford, Fatigue characteristics of McKibben artificial muscle actuators , Dept. Of Electrical Engineering, University of Washington.

[11] B. Verrelst, J. Vermeulen , B. Vanderborght and R. Van Ham, Motion Generation And Control For The Pneumatic Biped LUCY , Available Source Listed at URL www.clawar.com .

Address of the corresponding author:

Author: Ramesh Ramasamy
Institute: DAG Technology (M) Sdn. Bhd.
City: Kuala Lumpur
Country: Malaysia
Email: ramesh@dagtech.com.my

F. Ibrahim, N.A. Abu Osman, J. Usman and N.A. Kadri (Eds.): Biomed 06, IFMBE Proceedings 15, pp. 219-221, 2007
www.springerlink.com ' Springer-Verlag Berlin Heidelberg 2007

Prediction of Optimal Pillow Height by Anthropometric Parameters

Pei-Te Huang [1], Alice M.K. [2]

[1] Graduate Institute of Rehabilitation Sciecence, Chang Gung University, Taipei, Taiwan

Abstract—**To find out the optimal height of pillow fit for comfortable sleep, we used manual measure, 3D body scanning system, and FSA Pressure Mapping (pressure imaging) System to establish an anthropometric database for the adult populations.**

Keywords— **pillows, neck support, Anthropometric**

I. Introduction

Almost one third of our life is spent on sleep. Sleep is an essential biological need. Besides of rest and relaxation, it is necessary in order to maintain good physical and mental health. In recently years, people change lifestyle because of too many activities, sleep time is compress to lesser and lesser. How to improve the quality of sleep in such a limited duration of sleep will be very important issue. It depends on on more research to obtain better knowledge help people sleep better and faster.

The quality of sleep is influenced by many factors. Good pillow is an essential factor. There are a wide variety of pillows available on the market today in various materials and shapes and sizes. They are always emphasize to be a better product in benefic to sleep than others. However, there is not enough scientific evidence to prove it. The purpose of our study will be focus on the viewpoint of pillows optimal height for good sleep.

II. Materials and method

Participants

Forty participants who were healthy adults without any known organic pathology within or neck pain were invited to join this study. Participants were recruited from Chang Gung University.

Pittsburg Sleep Quality Index and was applied for assessment of sleep quality. Ten male and 10 female with good sleep quality and poor sleep quality were included. Manual anthropometric measure meat from shoulder, head and neck were recorded. 3D scanning body measurement was also applied for comparison with manual measure. The FSA pressure mapping system was also used for imaging the pressure distribution during supine and side lying sleep with memory form pillow in individual height adjustment for comfortable sleep.

Instruments

7-Day Daily Sleep Log

The 7-day Daily Sleep Log is a sleep diary that collects information on total time spent in bed (TTSIB), sleep onset latency (SOL), total sleep time (TST), and frequency of awakenings. Sleep efficiency (SE) can be calculated using the formula: SE= TST/TTSIB. Participants were asked to fill out the sleep log as soon as they get out of the bed each morning for a consecutive 7-day period. Questions in the 7-day Daily Sleep Log include:

1. Last night, I went to bed at: (clock time)
2. Last night, I fell asleep in: (minutes)
3. I got out of bed this morning at: (clock time)
4. Last night I slept a total of: (hours and minutes)
5. I woke up during the night: (times)

Sleep Quality Visual Analogue Scale

The Sleep Quality Visual Analogue Scale (SQVAS) assesses an individual's subjective feelings of overall sleep quality with a possible score ranging from 0 to 10; the greater the SQ-VAS score the better the sleep quality. The SQ-VAS contains a 10-cm line with numerals '0' on one side and '10' on the other, indicating 'very poor' sleep quality and 'very good' sleep quality, respectively. Participants were given an example of how to respond and asked to draw a vertical line to indicate their subjective sleep quality.

Pillows

Participants were studied using pillow, which consists of a urethane foam foundation, an overlying memory foam supporting the head and neck, a stretch terry-cloth cover, and a cotton pillowcase. The pillow was fitted to each subject by three simple measurements of the neck, shoulder, and cervical curvature.

Whole Body 3D Laser Scanner

The Chang Gung Whole Body 3D Laser Scanner scans a cylindrical volume 1.9 meters high and 1.0 meter in diameter. These dimensions accommodate the vast majority of human subjects. A platform structure supports the subject and provides alignment for the towers. The system is built to withstand shipping and repeated use without alignment or adjustment. The standard scanning apparel for both men and women included light gray cotton biker shorts, and a gray sports bra for women.

F. Ibrahim, N.A. Abu Osman, J. Usman and N.A. Kadri (Eds.): Biomed 06, IFMBE Proceedings 15, pp. 222-223, 2007
www.springerlink.com ' Springer-Verlag Berlin Heidelberg 2007

Latex caps were used to cover the hair on subjects heads. Each subject was measured in three different scanning postures. Automatic landmark recognition (ALR) technology was used to automatically extract anatomical landmarks from the 3D body scan data. The landmarks were then placed on the subject.

The FSA pressure mapping system

The FSA Pressure Mapping (pressure imaging) System is a tool aiding clinicians and others by imaging the pressure distribution and helping with pressure reduction solutions where pressure is leading to physiological complications. FSA Pressure Mapping systems are available to address physiological interface pressure imaging when the participants beds on the mattress. It provides the pressure image, necessary information to calculate.

III. Results and disscusion

Statistical Analysis

Regression analyses were used to estimate relationships among all measured parameters. The following data were established: (1) mean and standard deviation of anthorpomrtric data from whole body parameters, and (2) regression models for the independent variables with the dependent variables (pillow height).

Results: Cases with definite without any known organic pathology within or neck pain were excluded.Delicate calculations of anthropometric parameters were acquired. In addition, we also established regression models for pillow height relationships among separated parts. Results also showed that adults had higher values for body weight, head girth, half shoulder length, external occipital protuberance to cervical seven length.(table 1)

Table 1: Body anthropometric higher values with pillow height.

Coefficients[a]

Model		Unstandardized Coefficients		Standardized Coefficients		
		B	Std. Error	Beta	t	Sig.
1	(Constar	13.485	.000		.	.
	weight	-.110	.000	-.844	.	.
	head	.090	.000	.084	.	.
	half sh	-.285	.000	-.158	.	.
	eop	.142	.000	.248	.	.

a. Dependent Variable: pillow

The linear comprehensive equation for pillow height is

Pillow height = 13.485-0.11(weight)+0.09(head girth)-0.285(half shoulder length)+0.142(EOP-C7 length)

The presumed positive effects of the pillow height may be due to anthropometric parameters. This study we established a model for measuring optimal pillow height. In addition, relationships among body were also predicted. The relation ship of anthropometric parameters to optimal pillow height will be discussed.

References

1. ACNielsen. (2004,2005). Sleepless in Asia: 40% of Asia Pacific Consumers Aren't in Bed Until After Midnight.
2. Addison, R. G., Thorpy, M.J., Roth, T. (1986). A survey of the United States public concerning the quality of sleep. Sleep Res, 16, 244.
3. Buysse DJ, R. C. r., Monk TH, Berman SR, Kupfer DJ. (1989). The Pittsburgh Sleep Quality Index: a new instrument for psychiatric practice and research. Psychiatry Res., 28(2), 193-213.
4. Clete A. Kushida, S. R., Christian Guilleminault , Sylvie Giraudo, Janie Hsieh, Pamela Hyde and William C. Dement. (1999). Cervical positional effects on snoring and apneas., 2(1), 7-10.
5. Cohen D, E. C., Prinz P, Breen A, Davis M, Gadsby A. (1983). Sleep disturbances in the institutionalized aged. J Am Geriatr Soc, 31(2), 79-82.
6. Erfanian P, H. C., Guerriero R. (1998a). Pilot study: An investigation on the relationship between external cervical measurements and the preference of cervical pillow thickness. JCCA, 42(2), 83 89.
7. Erfanian P, H. C., Guerriero R. (1998b). A preliminary study assessing adverse effects of a semi-customized cervical pillow on asymptomatic adults. JCCA, 42(3), 156 162.
8. Fletcher.DJ. (1986). Coping with insomnia. Helping patients manage sleeplessness without drugs. Postgrad Med, 79(2), 265-274.
9. Hagino C, B. J., Dover L, Letendre R, Wicks M. (1998). Before/after study to determine the effectiveness of the Aligh-Right cylindrical pillow in reducing chronic neck pain severity. JMPT, 21(2), 89-93.
10. Hyland.JK. (1999). Cervical support pillows: useless or helpful? Canadian Chiropractic, 2(3), 54 56.
11. Lavin RA, P. M., Kuhlemeier KV. (1997). Cervical pain: a comparison of three pillows. Arch Phys Med Rehabil., 78(2), 193-198.
12. MF, O. M. V. (2005). Normative sleep data, cognitive function and daily living activities in older adults in the community. SLEEP, 28(8), 981-989.
13. Parham Erfanian, S. T., Rocco C Guerriero. (2004). Assessing effects of a semi-customized experimental cervical pillow on symptomatic adults with chronic neck pain with and without headache. J Can Chiropr Assoc 48(1), 22-28.
14. Persson L, M. U. (1998). Neck support pillows: A comparative study. J Manipulative Physiol Ther, 21(4), 237-240.
15. SMYTHE, H. A. (1994). The C6-7 syndrome--clinical features and treatment response. J Rheumatol, 21(8), 1520-1526.
16. Tanahashi, H., Shibuya, A. (1999). The relationship between the height of the pillow on which a person's head rests and the head pressure distribution. Journal of the Japan Research Association for Textile End-Uses 40(2), 56-63.
17. 棚橋,ひとみ; 渋谷,惇夫; 長,澄人; 工藤,翔二. (1999). 枕の高さ変化が呼吸機能に及ぼす影響. 日本生理人類学会誌, 4(1), 35-40.

Address of the corresponding author:

Author: Pei-Te Huang
Institute: Graduate Institute of Rehabilitation Sciecence, Chang Gung University
City: Taipei
Country: Taiwan
Email: hpat.tw@gmail.com

F. Ibrahim, N.A. Abu Osman, J. Usman and N.A. Kadri (Eds.): Biomed 06, IFMBE Proceedings 15, pp. 222-223, 2007
www.springerlink.com ' Springer-Verlag Berlin Heidelberg 2007

Stress and Strain Analysis of Anterior Cruciate Ligament for Arthroscopy Knee Reconstruction

K. Sundaraj and S. Yaacob [1]

[1]Northern Malaysia University College of Engineering, School of Mechatronics Engineering, Kompleks Pusat Pengajian KUKUM Jalan Kangar Arau, 02600 Jejawi Perlis, Malaysia

Abstract — **The replacement of an injured anterior cruciate ligament (ACL) using minimum invasive techniques is called an arthroscopy knee reconstruction (AKR). A strong biologic substitute is necessary to restore this primary stabilizing structure of the knee. To perform this, a natural graft is first harvested, then two bone tunnels are drilled in the tibia and the femur. Finally, the graft is inserted inside these tunnels and fixed using screws. A wrong positioning of one or both tunnels can easily lead to a failure of the graft. As the ACL graft geometry does not fit the original ACL shape, the goal, when placing the graft, is to obtain an isometric behavior for it during knee flexion. However, because only a small area of the graft section is isometric, even in the best case, the graft is subjected to stress during flexion, and may fail if this stress is above its failure threshold. Within this context, we investigate the use of an online physical model to virtually simulate the stress and strain conditions of the ACL graft *before* the tunnels are drilled. This information can help surgeons make a better decision when positioning the graft.**

Keywords — **Surgical Simulation, Medical Robots, Virtual Reality, Finite Elements.**

I. Introduction

The replacement of an injured ACL using minimum invasive techniques is called an AKR procedure. The ACL (see Figure 1) is the primary stabilizer of the knee joint which is frequently injured by a twisting or pivoting movement. Left untreated, an ACL injury can allow a process of deterioration and dysfunction of the knee to occur. The replacement of the damaged ACL with a strong biologic substitute is necessary to restore this primary stabilizing structure of the knee. To perform this, a natural graft is first harvested, then two bone tunnels are drilled in the tibia and the femur. Finally, the graft is inserted inside these tunnels and fixed using interference screws (see Figure 2). A wrong positioning of one or both tunnels can easily lead to a failure of the graft. As the ACL graft geometry does not fit the original ACL shape, the goal, when placing the graft, is to obtain an isometric behavior for it during knee flexion.

However, because only a small area of the graft section is isometric, even in the best case, the graft is subjected to stress during flexion, and may fail if this stress is above its failure threshold. To provide a solution, we have developed an application which has the goal of automatically generate, intra-operatively, a virtual model of the graft in order to be able to predict failure in case of too high stress during flexion **before** the tunnels are drilled. This application considers the ACL graft to consist mainly of blood and elastic fibers. During surgery, a virtual physical model of the ACL is generated by the surgeon. Then, the application simulates the stress and strain in the virtual ACL graft for the entire knee flexion by considering the position and orientation of the graft. Elongation and friction are the main factors that contribute to stress and strain in the graft.

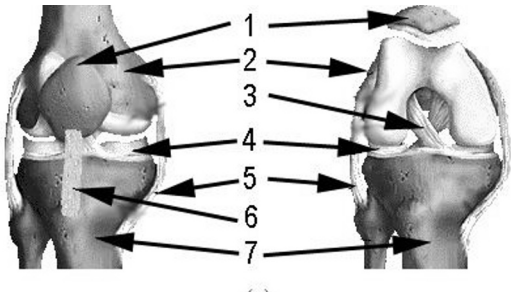

Fig. 1 The knee joint anatomy with extension on the left and flexion on the right, 1 Patella 2 Femur 3 ACL 4 Meniscus 5 Collateral Ligament 6 Patella Tendon 7 Tibia

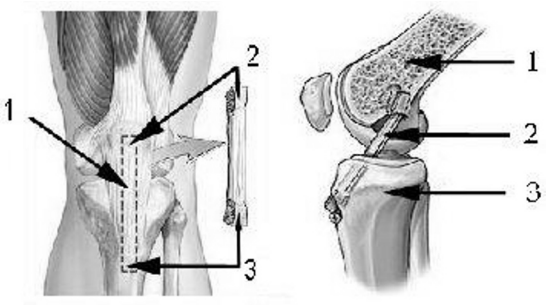

Fig. 2 Bone Tendon Bone ACL graft harvesting, 1 Patella Tendon 2 Patella 3 Tibial Tubercule (LEFT). ACL graft insertion and fixation using screws, 1 Femur 2 ACL Graft 3 Tibia (RIGHT)

F. Ibrahim, N.A. Abu Osman, J. Usman and N.A. Kadri (Eds.): Biomed 06, IFMBE Proceedings 15, pp. 224-227, 2007
www.springerlink.com ' Springer-Verlag Berlin Heidelberg 2007

II. VIRTUAL MODEL of ACL

A. Geometry & Physic

The geometrical model of the virtual ACL graft comes from the patient. During the ACL reconstruction procedure, the surgeon begins by an arthroscopic inspection of the knee joint. This examination allows the surgeon to practice, if necessary, meniscus resection and to remove the damaged remaining pieces of the torn ACL (on tibia and femur sides). Then, the graft is harvested. The graft may be compounded by a piece of bone, taken from the patella, a piece of the patella tendon and a piece of bone taken on the tibia (see Figure 2). Other types of grafts can be used, according to the choice of the surgeon. Once the graft has been harvested, it's measurements can be determined. We note that this step is **per operation**. The harvested graft is generally a beam shape deformable object. This object is then discretized into finite elements according to the surgeon's choice using the developed application (see Figure 3). Given the planned orientation of the graft with respect to the patient's knee bones, the two ends of the graft are modified to reflect the positioning with respect to the patient s femur and tibia bones (see Figure 4). This is done by tapering off both the ends of the graft according to the surgeon's choice. A tapered virtual ACL graft is shown below. A suitable mathematical model known as the Volume Distributed Method (VDM) [1] is used as the physical model for the ACL graft. This physical model is mapped directly onto the geometrical model of the virtual ACL graft.

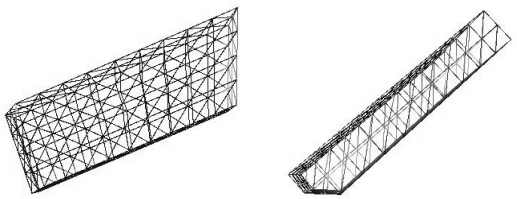

Fig. 3 The virtual ACL graft from 2 views

B. Parameter Estimation

This is the most difficult part of our work. The parameters of the VDM model namely the bulk modulus and the connectivity bulk modulus need to be estimated so that we can have reasonable accuracy in our results. Since we do not have any means and expertise to really conduct experiments to determine these values on the operated patients, we had to resort to data available in the literature. We considered that the ACL graft is full of blood (incompressible) and contains mainly elastic fibers. A problem here is that we had to match physical parameters that were only available for finite element models of high complexity to our VDM model. We used [2] and [3] as sources. The parameters are given in Table 1.

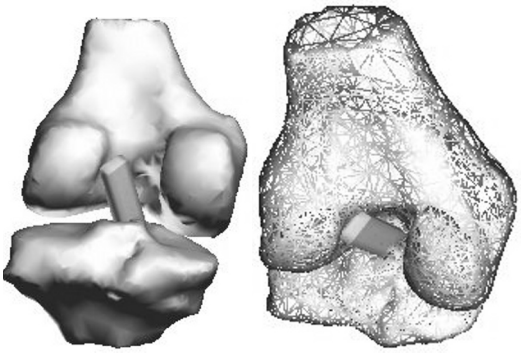

Fig. 4 Positioning and orienting the virtual ACL graft with respect to the patient s knee.

Table 1 Physical parameters of the virtual ACL graft

Height (H)	5 mm
Width (W)	10 mm
Cross-section Area (A)	50 mm^2
Length (L)	25 mm
Surface Area (S)	850 mm^2
Volume (V)	1250 mm^3
Resolution (Q)	138 elements
Density of Blood (ρ)	1055 kgm^{-3}
Bulk Modulus of Ligament (B_1)	0.3 x 10^6 Nm^{-2}
Connectivity Bulk Modulus of Fiber (B_2)	4.0 x 10^3 Nm^{-2}
Angle of Flexion (θ)	0° 90°

C. System Resolution

Using the VDM formulation, the virtual ACL graft is modelled by the following matrix system:

$$K \cdot \Delta L = R \quad (1)$$

where K is the sparse state matrix of the virtual ACL graft, L is the displacement vector of the nodes and R is the exter

F. Ibrahim, N.A. Abu Osman, J. Usman and N.A. Kadri (Eds.): Biomed 06, IFMBE Proceedings 15, pp. 224-227, 2007
www.springerlink.com ' Springer-Verlag Berlin Heidelberg 2007

nal load vector. Due to the nature of the simulated environment, the two ends (fixture points) of the virtual ACL graft is subjected to constraints. The end which is in contact with the femur is fixed while the other end is subjected to the displacement of the tibia bone. These nodes can be constrained by modifying their respective nodal equations. In the developed application, a nonlinear analysis using the Bi-Conjugate Gradient (BCG) method is used to solve the system.

III. Intra Operative SURGERY

A. Data Acquisition

The first step in using the system is getting the dimensions of the virtual ACL graft. This is obtained from the harvested graft taken off the patella tendon of the patient. These dimensions are fed into the simulator to generate a virtual geometrical mesh of the ACL graft (as shown in Figure 3). Then the VDM physical model is mapped onto the geometrical model.

B. Knee Kinematics

To simulate the stress and strain conditions in the ACL graft, the kinematics of the fixture points (end points) of the graft has to be known for the entire knee flexion. Several surgical navigation systems exist for this purpose. In this procedure, firstly, specific landmarks are acquired by the surgeon [4][5]. To each of these landmarks, a marker is attached. Each marker is a set of diodes, fixed to the bone using a screw. As the marker s position is surgeon dependent, it not possible to know their placement *a priori*. Each marker's position and orientation can be read using the infra-red camera. With this set-up, as the knee is flexed from 0° to 90°, a set of spatial transformations at 1.5° intervals is obtained. This set of spatial transformations (4×4 matrices) will define the kinematics of the knee.

C. Online Diagnostic

Diagnostic is done in real-time by checking the state of the virtual ACL graft for the entire knee flexion using the graphical user interface of the AKR stress and strain simulator (as shown in Figure 5). Given the kinematics of the knee, the position and orientation of the fixture points of the ACL graft, will be known for the entire knee flexion. With this information the VDM model will be able to compute the stress and strain at each interval. These results will be displayed to the surgeon.

The AKR stress and strain simulator consists of two views; one for the graphical view of deformation and another for the surgeon to manipulate the position and orientation of the ACL graft. If the surgeon is not happy with the results of the stress state of the virtual ACL graft for a particular angle of flexion, the navigation system can be inquired for another suitable position and orientation of the ACL graft. The new data is fed into the AKR simulator and the process is repeated until the surgeon finds an optimal configuration.

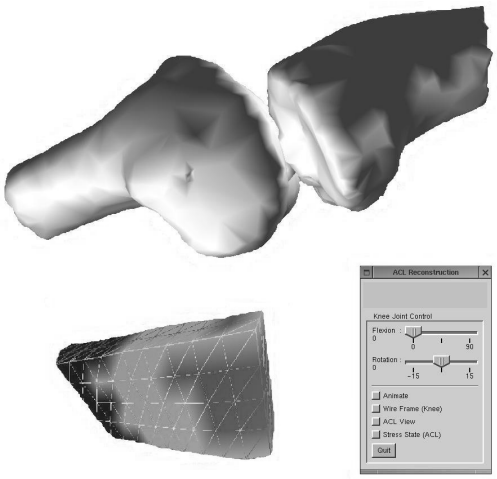

Fig. 5 The AKR stress and strain simulator

IV. Simulation results

To test our model, the virtual ACL graft with its ends fixed at the femoral and tibial tunnels outlets, was subjected to a sample set of transformations obtained from one of the surgical navigation system s database. The retrieved leg kinematics is used as position boundary conditions for the physical model. We assumed that only the tibia moves with respect to the femur during flexion.

A. Stress and Strain

In Figure 6 we show the results given by our stress and strain simulator. We would like to note that the bones of the knee joint are **not** acquired by the system because this is a CT-Free procedure. The system only generates the ACL graft mesh. We included these bones to show the site of the virtual ACL graft with respect to a patient's knee. To better visualize the simulation, we have found that it is better to include a generic mesh of the femur and tibia. At each transformation of angle 1.5°, the strain and stress state of the ACL was calculated and analyzed to know if the failure threshold has been reached. Thus it is possible to know where and for which angle of flexion the graft will fail.

F. Ibrahim, N.A. Abu Osman, J. Usman and N.A. Kadri (Eds.): Biomed 06, IFMBE Proceedings 15, pp. 224-227, 2007
www.springerlink.com ' Springer-Verlag Berlin Heidelberg 2007

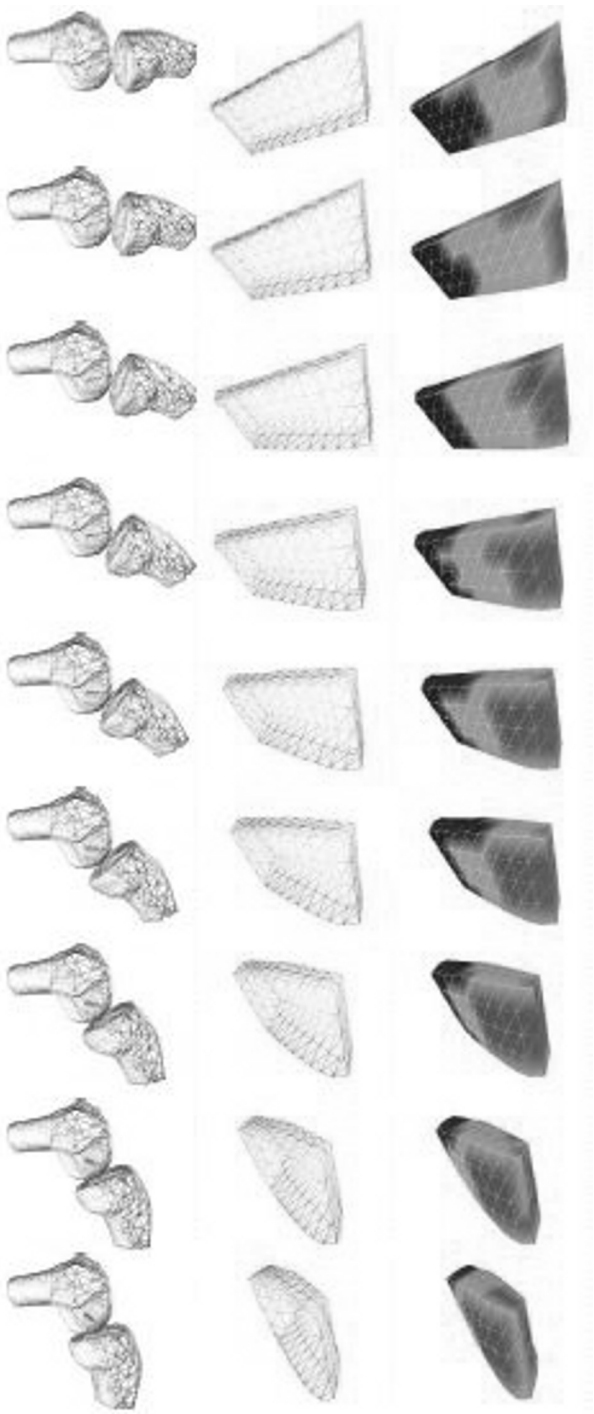

Fig. 6 Strain and stress at intervals of 10° from 0° to 90°

Conclusions

From the mesh configuration and stress state in Figure 6, we can deduce that the graft is stressed at the tibia and femur end the most. This was found to be correct by comparing results from [2] and from discussions with surgeons. But [2] used a simplified geometrical model of the real ACL ligament constructed from femoral and tibial insertion sites. We on the other hand are interested in the ACL graft, whose dimensions are known for each patient. A point to note is that since the graft is bigger than the real ligament, more areas are subjected to stress. This is because of the difference between the real isometric area and the area occupied by the graft. Furthermore, the difference in size causes the graft to be more in contact with the knee bones and the surroundings during flexion. This contact also causes stress. We also find that the deformation of the ACL graft seems consistent with the predicted results whereby there is very little change in the length of the ACL graft.

Acknowledgment

The authors wish to thank Francois Boux-de-Casson of Aesculap-BBraun in Grenoble-France for the help in providing data from the OrthoPilot® surgical navigation system.

References

1. Sundaraj K (2004) Real-time dynamic simulation and 3D interaction of biological tissue: Application to medical simulators. PhD Thesis, Institute Nationale Polytechnique de Grenoble, France.
2. Pioletti D (1998) Viscoelastic Properties Of Soft Tissues: Application to Knee Ligaments and Tendons. PhD Thesis, Ecole Polytecnique Federale de Lausanne, Switzerland.
3. Tumer S, Engin A (1993) Three Body Segment Dynamic Model of the Human Knee. J Biomech. Eng.
4. Eichhorn J (2002) Navigation und Robotik in der Gelenk und Wirbelsäulenchirurgie. Konermann, Germany.
5. Saragaglia D. et al (2003) OrthoPilot® Assisted Anterior Cruciate Ligament Reconstruction Analysis of Tunnel Positioning in 12 Cases. Proc. of Int. Conf. on Computer Assisted Orthopaedic Surgery.

Address of the corresponding author:

Author: Kenneth Sundaraj
Institute: Kolej Universiti Kejuruteraan Utara Malaysia (KUKUM)
Street: Jalan Kangar Arau
City: 02600 Jejawi Perlis
Country: Malaysia
Email: kenneth@kukum.edu.my

F. Ibrahim, N.A. Abu Osman, J. Usman and N.A. Kadri (Eds.): Biomed 06, IFMBE Proceedings 15, pp. 224-227, 2007
www.springerlink.com ' Springer-Verlag Berlin Heidelberg 2007

Biomedical Engineering Education and Training In Hong Kong: Recent Developments

Min Wang

Department of Mechanical Engineering, The University of Hong Kong,
Pokfulam Road, Hong Kong

Abstract— **Since our last report on biomedical engineering (BME) education and training in Hong Kong which was presented at the 6th Asian-Pacific Conference on Medical and Biological Engineering (APCMBE 2005) more than one and half years ago, there have been significant developments in this field in Hong Kong. This paper gives an update of the status of BME education and training in Hong Kong. It also looks into some critical issues in a wider context. The experience gained and lessons learnt with regard to BME education and training in Hong Kong may prove to be useful for BME developments in other parts of the world.**

I. Introduction

Just like the industrialized nations in Europe and North America, Asian countries are having a rapidly aging population. Currently, about 12% of people in Hong Kong are over 65 years old. The Hong Kong Government has predicted that by year 2033, over 27% of Hong Kong residents will be elderly citizens [1]. With an increase on such a scale in Hong Kong and perhaps also in other parts of Asia, the provision of good-quality healthcare for their citizens (old as well as young) is obviously the top priority of governments in Asia. The demand for well-educated biomedical engineers will surely steadily increase in the next few decades in the Asian-Pacific region. Realizing potential changes and demands of the society, it is probably no surprise that governments in places such as Singapore and Hong Kong started in the 1990s to widen up biomedical engineering (BME) education and training in these territories.

As described in our previous report [2], Hong Kong has a unique environment for BME education and training. Hong Kong benefits from learning BME education and training programmes from both Europe and North America because (1) a certain percentage of practicing engineers in Hong Kong are graduates of various BME educational programmes in Western Europe and North America, and (2) teaching staff in BME programmes in local tertiary institutions have experiences with BME programmes in the West (some of them are also graduates of these programmes) and are open-minded in adopting the best practices in BME education and training. In the previous report [2], the BME education and training in Hong Kong was analyzed at the levels of Bachelor-degree, taught postgraduate programmes, and postgraduate research, as well as post-university training, not on an individual-university basis. This paper, however, will deal with each university s BME programmes and then provide some thoughts on BME education and training in Hong Kong as a whole.

In Hong Kong, currently there are eight University Grants Committee (UGC) [3] supported tertiary institutions. They are The University of Hong Kong (HKU), The Chinese University of Hong Kong (CUHK), The Hong Kong University of Science and Technology (HKUST), The Hong Kong Polytechnic University (PolyU), City University of Hong Kong (CityU), Hong Kong Baptist University (HKBU), Lingnan University (LU), and Hong Kong Institute of Education (HKIEd). These eight tertiary institutions, together with The Open University of Hong Kong [4], adopt the Joint University Programmes Admissions System (JUPAS) [5] for their yearly admission of students to various undergraduate programmes in these institutions. The BME educational programmes (at the undergraduate and postgraduate levels) are now offered in HKU, CUHK, HKUST and PolyU. Research-led educational programmes (MPhil and PhD) in BME can be found in these four universities plus CityU. This paper only focuses on taught programmes in BME in Hong Kong.

A. BME Programmes in The Hong Kong Polytechnic University

PolyU is still the only university in Hong Kong that has a BME-related academic department. The newly established Department of Health Technology and Informatics (HTI) [6], which was inaugurated on September 1, 2005, in the Faculty of Health and Social Sciences evolved from the Jockey Club Rehabilitation Engineering Center (REC) of the same faculty, taking in units of Medical Laboratory Science and Radiography of the Faculty during its formation. The HTI department currently offers three Bachelor-degree programmes in biomedical engineering, medical laboratory science, and radiography.

F. Ibrahim, N.A. Abu Osman, J. Usman and N.A. Kadri (Eds.): Biomed 06, IFMBE Proceedings 15, pp. 228-231, 2007
www.springerlink.com ' Springer-Verlag Berlin Heidelberg 2007

With the formation of HTI department, the original Bioengineering concentration (one of the three concentrations, the other two being Orthotics and Prothetics) in the BSc in Health Technology Programme provided by the REC [2] became a fully fledged BSc in Biomedical Engineering Programme. And this BSc in Biomedical Engineering at PolyU has gained full accreditation from the Hong Kong Institution of Engineers (HKIE), which is one of the signatory to the Washington Accord. This programme also offers the options of study pathways that lead to double degrees. The double-degree programme aims to equip students with interdisciplinary expertise in both biomedical engineering and biotechnology to meet the growing demand both locally and internationally.

PolyU's BME-related educational programmes (at both undergraduate and postgraduate levels) have the longest histories among all BME educational programmes in the territory. The HTI department continues to offer MSc / Postgraduate Diploma (PgD) in Health Care (Health Technology) that its predecessor REC offered. Students of the part-time MSc programme, i.e., the taught Master's, should finish it within three years earning 30 credit units, while the PgD only requirs 18 credit units.

B. BME Programme in The University of Hong Kong

As described in our previous report [2], relying on its two strong faculties, Engineering and Medicine, HKU launched its BEng in Medical Engineering programme in 2002, which is an inter-faculty programme and hosted by the Faculty of Engineering [7]. This BME programme gained its provisional accreditation from HKIE in early 2006 and will apply for full accreditation soon. The Programme still has the strong support from the two participating faculties in HKU. The current annual student intake of the programme is maintained at around 30. With HKU s increased activities in its designated strategic areas, with BME being one of them, it can be expected that the programme may grow bigger in the next few years. The programme had its first batch of graduates in the summer of 2005. Currently, graduates of the programme are studying for a research degree in local and overseas universities, working in government departments, or working in local or multinational companies such as SIEMENS.

After running the programme for three years, the BEng in Medical Engineering programme at HKU has its first major curriculum review in the spring of 2006. Taking into consideration of the Programme External Examiner s advice and suggestions and adjusting the programme s positioning, a number of new BME courses have been added to the new curriculum, the syllabuses of some existing courses have been modified, and a significant number of courses offered by the participating departments have been included as elective courses in the new curriculum. Another big change in the programme is the offer of two tracks for the final-year students of the programme: (1) biomechanics, biomaterials, and tissue engineering, and (2) medical electronics and biomedical imaging. Students can choose one of the tracks to specialize in and select the elective courses accordingly for the specific track.

HKU currently does not offer taught Master s programme in BME. But courses in the BME area such as Biomaterials and Magnetic Resonance Imaging (MRI) Technology and Applications are offered in existing MSc programmes (e.g., MSc in Materials Science and MSc in Electrical Engineering) in the Faculties of Science and Engineering.

C. BME Programmes in The Hong Kong University of Science and Technology

As described previously [2], HKUST operates an integrated BME programme for MSc, MPhil and PhD degrees [8]. At the postgraduate level, HKUST still maintains four streams in BME: (1) Biological Information Engineering; (2) Bioprocessing and BioProduct Design; (3) BioMEMS and Biomaterials; and (4) Pharmaceutical Engineering.

The recent development in BME education in HKUST is at the undergraduate level: it launched a Minor in Bioengineering Program in July 2006. Any undergraduate students at HKUST with a minimum CGA of C+ or above may enroll in the Bioengineering Minor Program. The Bioengineering Minor Program has three areas of concentration, which are: (1) bioporcessing, (2) biological informatics and data processing, and (3) applied bioscience. The Bioengineering Minor Program requires a minimum of 18 credits to be taken from the following courses:

(1) 6 credits must be taken from the compulsory courses, of which one course is from the School of Science (Cell Biology , Introduction to Biochemistry , and Nature of Biochemistry and Biotechnology) and one from School of Engineering (Biotechnology and its Business Opportunities , Bioproducts and Processing , and Introduction to Biomicrosystem);
(2) 12 credits are need to be taken from fourteen groups of elective courses (some groups have only one course). The curriculum requires that (a) at least one elective course must be from a 300-level course (i.e., a final-year level undergraduate course), and (b) no more than one course within the same course group can be counted toward the elective requirements of this minor.

F. Ibrahim, N.A. Abu Osman, J. Usman and N.A. Kadri (Eds.): Biomed 06, IFMBE Proceedings 15, pp. 228-231, 2007
www.springerlink.com ' Springer-Verlag Berlin Heidelberg 2007

The elective courses are clearly catagorized into the respective areas of concentration mentioned above.

Students can transfer a maximum total of 6 credits to the minor program and courses accepted for transfer credits must normally be at a level equivalent to HKUST courses of 100-level or above. To graduate with a minor in Bioengineering, the students must be enrolled in the minor program and complete all of its requirements, as well as the requirements of the major program of study. They must attain an average of at least C+ in course taken within the minor program.

HKUST s move to offer a Bioengineering Minor Program in 2006 can be viewed as an initiation of having a Bachelor-degree BME programme in HKUST.

D. BME Programme in The Chinese University of Hong Kong

CUHK did not have a BME educational program till 2006 even though staff at CUHK have been maintaining BME research activities for years. In March 2006, CUHK formed a virtual Division of Biomedical Engineering and launched the MSc in Biomedical Engineering Program. This MSc programme is a joint programme of CUHK s Faculties of Engineering and Medicine [9]. It is a part-time MSc programme and students should finish it within two years (the maximum study period is four years). For student admission, the Programme requires that (1) the applicant must fulfil the General Qualifications for Admission and the English Language Proficiency Requirement prescribed by the Graduate School of CUHK, and (2) the applicant have a Bachelor's degree in a relevant Engineering, Science, or Medical discipline from a recognized university or an approved institution. The total number of credit units required for graduation is 24. The students must earn 9 credit units by completing the three Required Courses: Introduction to Biomedical Engineering , Basic Biomedical Science , and M.Sc. Project . The other 15 credit units should be earned by successfully completing courses from a group of Elective Courses (all these courses are 3 credit unit courses): Medical Devices and Sensor Networks , E-medicine Technologies , Medical Robotics , BioMEMS and Bio-Nanotechnology , Smart Materials for Medical Applications , Bioinformatics , Prosthetics and Artificial Organs , Virtual Medicine and Computer Aided Surgery , and Medical Imaging .

On the basis of a successful MSc programme, CUHK can build up an undergraduate BME programme that can be offered in a few years time.

E. Formation of the Biomedical Discipline in the Hong Kong Institution of Engineers and Activities of the Biomedical Division

The Hong Kong Institution of Engineers (HKIE) [10] is the professional body representing engineers in Hong Kong. Admission into HKIE was through one of its seventeen disciplines: (1) building, (2) building services, (3) chemical, (4) civil, (5) control, automation & instrumentation, (6) electrical, (7) electronics, (8) environmental, (9) fire, (10) gas, (11) geotechnical, (12) information, (13) manufacturing & industrial, (14) marine & naval architecture, (15) materials, (16) mechanical, and (17) structural. Engineers admitted into HKIE can join one of its sixteen divisions, the Biomedical Division being one of them. Current members of the Biomedical Division have joined HKIE through the aforementioned seventeen divisions. Through their hard work over the years, members (past and present) of the Biomedical Division had been trying to convince the Council of HKIE of the needs to form the Biomedical Discipline within HKIE. The Council finally approved the formation of this discipline in HKIE in September 2004 (therefore, there are now eighteen disciplines in HKIE) and graduates of local BME programmes can now join HKIE through this discipline. The formation of the Biomedical Discipline in HKIE is a milestone of the development of BME education and training in Hong Kong and is of great importance to the biomedical engineering profession in Hong Kong.

The Biomedical Division has successfully applied to the the Commerce, Industry and Technology Bureau (CITB) of the Hong Kong SAR Government for the Professional Services Development Assistance Scheme (PSDAS) project in order to upport the arrangement of seminars and activities which the Biomedical Division organises. Examples of such activities include Biomedical Engineering Conferences held in 2004 and 2006 (BME 2004 and BME 2006) which provide a forum for local researchers to present their findings and to interact among themselves and with invited overseas speakers.

Technical visits to hospitals in Hong Kong and factories (which manufacture medical devices for the domestic market and the US and European markets) in the Pearl River Delta (PRD) area of mainland China which were organised by the Biomedical Division have proven to be very attractive to undergraduates of BME programmes in HKU and PolyU. Regular technical seminars organised by the Biomedical Division are well attended by members from both academia and the industry.

F. Ibrahim, N.A. Abu Osman, J. Usman and N.A. Kadri (Eds.): Biomed 06, IFMBE Proceedings 15, pp. 228-231, 2007
www.springerlink.com ' Springer-Verlag Berlin Heidelberg 2007

The Biomedical Division also arranges activities in Hong Kong for visiting delegations or student groups. One example is the arrangement of a recent visit to various BME-related places in Hong Kong by a group of 28 Biomedical Engineering students and Technical Medicine students and 3 academic supervisor from the University of Twente, The Netherlands, during their Pushing the Limits study tour in Asia.

The Biomedical Division, representing Hong Kong s BME profession, participated in the IFMBE Asia-Pacific Traveling Fellowships Programme (APTF) and arranged technical visits of the fellows from Singapore, Hong Kong, Japan, Taiwan and Korea to BME-related facilities in Hong Kong in August 2006.

F. Strength, Weakness, and the Future

Various BME educational programmes at the undergraduate and postgraduate levels offered by universities in Hong Kong differ from each other greatly. These universities strength of research in respective BME areas is certainly reflected by the courses they offer in their programmes and the emphasis of individual BME programmes. Compared to BME programmes in the US and Europe, BME educational programmes in Hong Kong are still at a young age and it may be still too early to judge their special features and characteristics. But in a highly competitive environment, these programmes ought to develop their prominent characters very quickly in order to attract the students.

There are two universities in Hong Kong that have their own Medical Faculty: HKU and CUHK. Both have BME educational programmes now, at either the undergraduate or postgraduate level. These two universities can provide BME education and training from the undergraduate level all the way to PhD (and post-doctoral) training.

For a university without a medical faculty, there can be difficulties for developing BME educational programmes. However, PolyU s efforts in BME education have shown that these difficulties can be overcome if sufficient support is provided by the university and sources outside the university. With PolyU as an example and precedent, it will not be a surprise if next year or in a few years time, HKUST offers a Bachelor-degree BME programme, thus completing a BME education package of all levels at HKUST. Another university in Hong Kong that may be able to provide a BME educational programme is CityU. It should not be a surprise either when CityU announces, at any time, its offer of a BME educational programme.

Hong Kong currently has a population of ~7 million. If all capable universities in the territory offer BME educational programmes of some sort, the competition for each programme to attract students will be fierce. Another issue is how many BME graduates the Hong Kong job market can accommodate each year. These are serious issues for the universities concerned to consider.

Overall, the BME education and training in Hong Kong has been advancing at a steady pace. More BME programmes may appear in the next few years. The next stage of development for BME educational programmes in Hong Kong should be the development of each programme s characteristic features.

SPECIAL NOTE

The author of this paper is currently serving in the Biomedical Division Committee of the Hong Kong Institution of Engineers (HKIE) and is a key faculty member of the undergraduate Medical Engineering Programme of The University of Hong Kong (HKU). However, views and opinions expressed in this paper do not represent those of the Biomedical Division of HKIE, HKIE itself, the Medical Engineering Programme of HKU, or HKU itself.

ACKNOWLEDGMENT

The author thanks his colleagues in the Biomedical Division Committee of the Hong Kong Institute of Engineers for useful information and discussions. He also wishes to thank his former colleagues in The Hong Kong Polytechnic University and current colleagues in The University of Hong Kong for sharing their thoughts with him on matters related to biomedical engineering when he was / is working with them.

REFERENCES

1. Hong Kong Commercial Daily, August 17, 2005
2. M.Wang, A.F.T.Mak, A.W.H.Sit, "Biomedical Engineering Education in Hong Kong: Current Status and Future Development", *CD-ROM Proceedings of the 6th Asian-Pacific Conference on Medical and Biological Engineering*, Tsukuba, Japan, 2005, Paper #VI-5
3. http://www.ugc.edu.hk
4. http://www.ouhk.edu.hk
5. http://www.jupas.edu.hk
6. http://www.polyu.edu.hk/hti/
7. http://engg.hku.hk/MedE/
8. http://bien.ust.hk/
9. http://www2.acae.cuhk.edu.hk/~bme/
10. http://www.hkie.org.hk/

Address of the corresponding author:

Author: Min Wang
Institute: Department of Mechanical Engineering, The University of Hong Kong
Street: Pokfulam Road
Country: Hong Kong
Email: memwang@hku.hk

F. Ibrahim, N.A. Abu Osman, J. Usman and N.A. Kadri (Eds.): Biomed 06, IFMBE Proceedings 15, pp. 228-231, 2007
www.springerlink.com ' Springer-Verlag Berlin Heidelberg 2007

A quantitative study of post-biopsy radiofrequency cauterization

C.A. Azlan[1], N.F. Mohd. Nasir[2], N.A. Kadri[3], A.A. Saifizul[4], K.H. Ng[1], B.J.J. Abdullah[1]

[1] Department of Biomedical Imaging, University of Malaya, Kuala Lumpur, Malaysia
[2] School of Mechatronics Engineering, Kolej Universiti Kejuruteraan Utara Malaysia, Perlis, Malaysia
[3] Department of Biomedical Engineering, University of Malaya, Kuala Lumpur, Malaysia
[4] Department of Mechanical Engineering, University of Malaya, Kuala Lumpur, Malaysia

Abstract— **Percutaneous image-guided needle biopsy is typically performed in highly vascular organs or in tumors with rich macroscopic and microscopic blood supply. The main risks related to this procedure are bleeding and implantation of tumor cells in the needle tract. From numerous conducted studies, it was found that heating the needle tract using a radiofrequency (RF) ablation system has a potential to minimize these effects. However, this solution requires the use of specially designed RF needles which would make the procedure relatively expensive and complicated. Thus, in order to solve this problem, we propose a simple solution by using readily available biopsy needles connected to an RF generator. In order to do so, we have designed and developed an adapter to interface between these two devices. A bovine liver has been used as a sample tissue for the experimental procedure. The delivery of the RF was varied by varying the values for delivered power, power delivery duration, and insertion depth. The results showed that the size of the coagulation necrosis region is affected by all of the parameters tested. In general, the size of the region is enlarged with higher delivery of RF power, longer duration of power delivery, and shallower needle insertion.**

Keywords— **RF ablation, biopsy needle interface**

I. Introduction

Biopsy is a medical diagnostic test used to determine the structure and composition of tissue or cells. The procedure involves sampling cells or tissue from an organ or other part of the body using a specialized needle. Examination of the tissue sample is then performed using a microscope in order for a diagnosis to be made. The outcome of this procedure is a definitive method to test for the presence of a malignant tumor (cancerous) or to confirm if an abnormality is benign (not cancerous). Another important use of this procedure is to determine the causes of infections or inflammations that cannot be diagnosed with routine testing methods.

The main risks related to this procedure are hemorrhage (bleeding) and implantation of tumor cells in the needle tract after the needle is withdrawn. Patients with cirrhosis or hepatic tumors are at greater risk of hemorrhagic complications after biopsy, as are patients with uncorrected coagulopathy [1-2]. Hemorrhage has been reported to be one of the main concerns in biopsy procedures, occurring in up to 90% of patients following a percutaneous renal biopsy [3], which may require blood transfusion or other types of intervention. This risk may go undetected unless the patient undergoes subsequent imaging procedures or develops alterations in hemodynamic status as a result of blood loss. In order to minimize these problems, several approaches have been used and reported in the literature. These include transneedle placement of steel coils [4], injection of fibrin [5], injection of gelatin particles and thrombin [6], and injection of fibrinogen and thrombin [7].

From the various studies conducted, it was found that RF cauterization of the needle tract using a coaxial system has a great potential [7-8] in safely minimizing these risks. The use of coaxial needle eliminated the risk of specimen injury, because RF ablation is routinely performed using an introducer needle. This makes RF ablation as one of the therapeutic option of choice, since it reduces bleeding during the procedure.

Pritchard *et al*. [9] have developed a coaxial needle biopsy system that uses RF energy to cauterize the needle track following a biopsy, and found that the technique effectively reduced bleeding (Figure 1). The main limitation of the technique used is that it is proprietary in nature, and requires the use of specially designed RF needles, which would make the procedure relatively expensive and complicated. In order to solve this particular problem we have designed and developed a low cost and simple adapter to interface between the RF generator and the biopsy needle.

II. Materials and Methods

A. Device

We developed an adapter to interface between the available RF generator and a commercial biopsy needle. The device allows the flow of alternating current (AC) with RF frequencies from RF generator to the biopsy needle and later to a large dispersive pad that acts as a grounding electrode. Current in RF frequency range passing through these two electrodes leads to ion agitation, which is then converted by into heat caused by the tissue impedance. This

F. Ibrahim, N.A. Abu Osman, J. Usman and N.A. Kadri (Eds.): Biomed 06, IFMBE Proceedings 15, pp. 232-235, 2007
www.springerlink.com ' Springer-Verlag Berlin Heidelberg 2007

heating process induces almost an immediate and irreparable cellular damage, which leads to coagulation necrosis. Because tissue heating is greatest in areas with the highest current density located around the active electrode, necrosis is therefore limited to a relatively small volume of tissue surrounding the electrode.

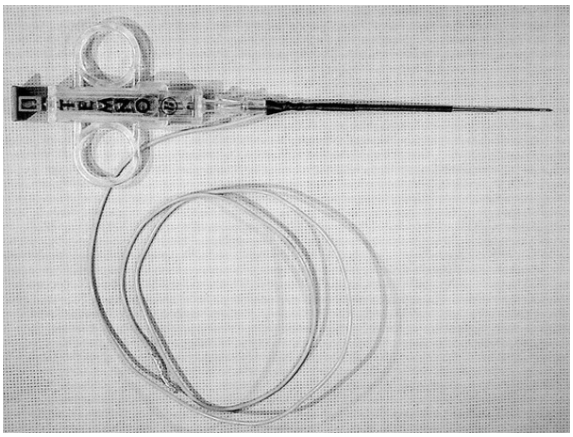

Fig. 1 A prototype of coaxial RF cauterization system developed by Pritchard et al. [9]. The needle is electrically connected to the RF generator by a copper wire with one end enclosed in a shrink-wrapped plastic.

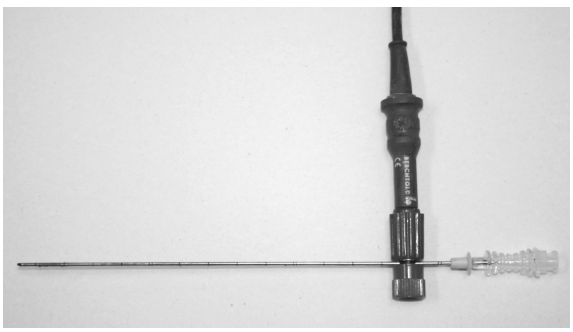

Fig. 2 The complete set up of the adapter prototype, with the biopsy needle interfaced to an active electrode of the RF generator.

In order to use the device, the adapter s slot is placed onto the outer part of the biopsy needle. By turning the bolt to the needle s slot direction, the biopsy needle is thus fixed at its place. The RF generator s active electrode will then be inserted into the female slot of the adapter (Figure 2). Once the set up is completed, the RF power may be switched on for the delivery of AC.

B. Ex-vivo experiment

An experiment has been performed on a bovine liver to study how the size of the coagulation necrosis regions varied with different settings of delivered power, power delivery duration, and insertion depth. Prior to the procedure, the liver sample was placed on a metal bowl that was attached to the neutral electrodes of the Electrotom 106 RF generator (Berchtold, Tuttlingen, Germany) (Figure 3). The biopsy needle was inserted at the depth of 1.5 cm. The adapter was then connected to the RF generator and attached to the outer part of a semiautomatic spring loaded biopsy needle with 18G detachable cannula co-axial needle (Medax Sci Carni, Italy) using the unipolar co-axial system setting. The RF generator power was set to 10 W and it was left on for 30 seconds, after which the needle was slowly withdrawn. To measure the necrosis region, the sample was sliced at about 3 mm from the surface and the size was measured using a ruler (–1 mm). These procedures was repeated for different power settings (20 W, 30 W, 40 W, 50 W and 60 W for 30 s duration and 2 cm insertion depth), depth of needle insertion (2.5 cm, 3.5 cm, 4.5 cm and 5.5 cm for 30 s duration and 30 W power), and duration of ablation (10 min, 20 min, 40 min and 50 min at 30 W power and 1.5 cm insertion depth). Five measurements were done for each parameter setting.

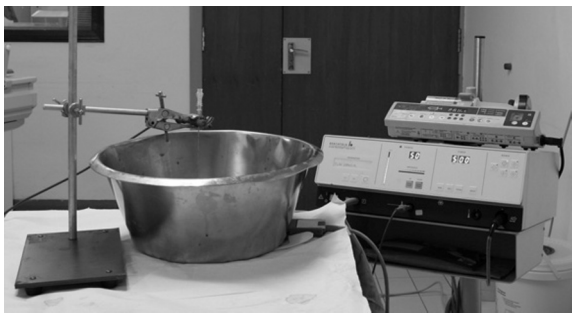

Fig. 3 The experiment setup showing how the biopsy needle is connected to the RF generator using the adapter developed.

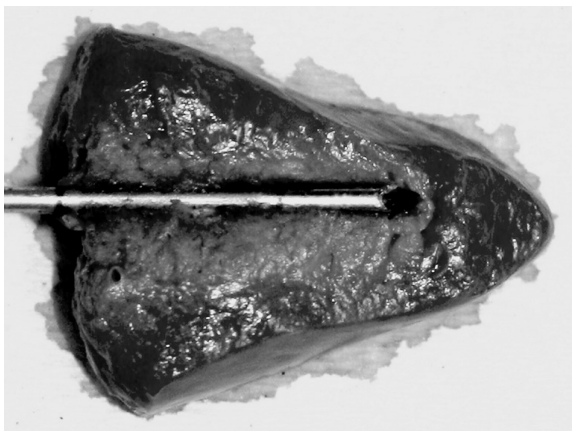

Fig. 4 A typical necrosis region on a bovine liver sample after an RF AC current (30 W) was delivered for 30 seconds. The needle was inserted at a depth of 1.5 cm.

F. Ibrahim, N.A. Abu Osman, J. Usman and N.A. Kadri (Eds.): Biomed 06, IFMBE Proceedings 15, pp. 232-235, 2007
www.springerlink.com ' Springer-Verlag Berlin Heidelberg 2007

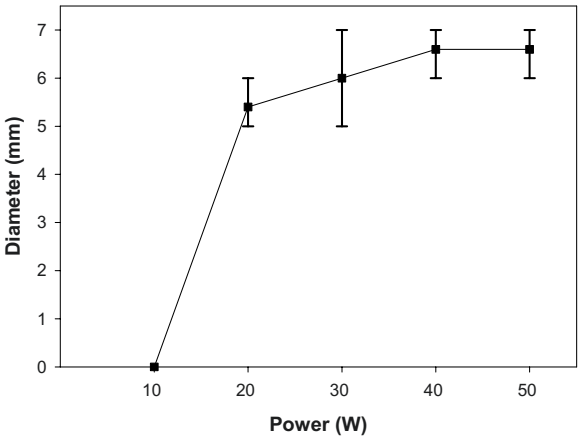

Fig. 5 Relationship between the necrosis size and the RF power (30s power delivery duration and 1.5 cm depth of needle insertion).

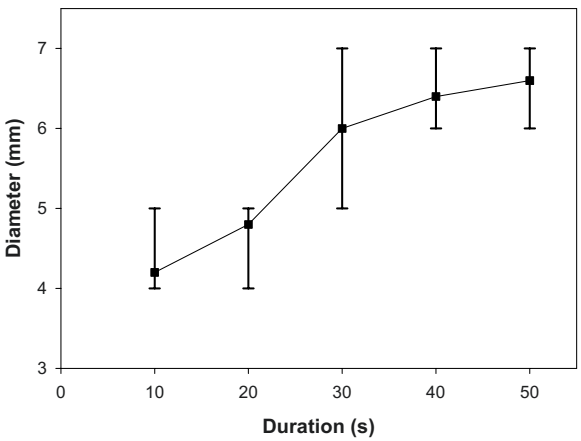

Fig. 6 Relationship between the necrosis size and the power delivery duration (30 W power and 1.5 cm depth of needle insertion).

III. Results and discussion

Figure 4 shows the necrosis area caused by heating generated by AC current from the RF generator. It can be clearly observed that the area is homogenous up to a certain width in the surroundings of the biopsy needle insertion. It was also found that the three identified parameters, namely delivered power, power delivery duration, and insertion depth; all have an effect on the final size of the coagulation necrosis region. In general, the size of the region is enlarged with higher delivery of RF power, longer duration of power delivery, and shallower needle insertion. The size however, becomes relatively constant once the power, duration, and depth reached a certain value. This phenomenon may be attributed to the relatively high deposition of energy per volume of liver tissue at the beginning of the delivery; followed by desiccation and carbonization of liver tissues that produced a constant necrotic tissue size. The sizes of necrosis area caused by varying RF power, power delivery duration and depth are shown in Figures 5, 6, and 7, respectively. The diameters plotted in these figures are the mean values from five measurements and the minimum and maximum values of the error bars denote the smallest and largest sizes.

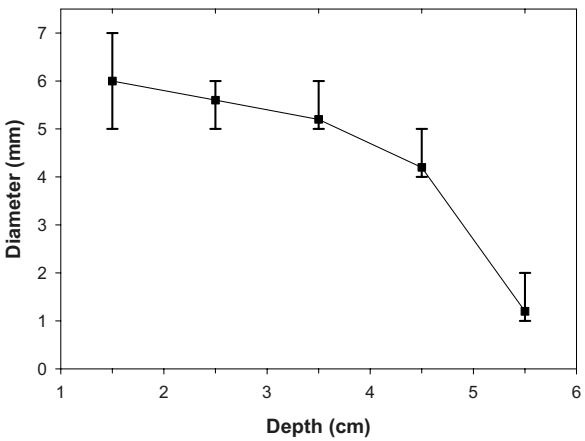

Fig. 7 Relationship between the necrosis size and the needle insertion depth (30W RF power and 30s power delivery).

IV. Conclusion

We have developed an adapter to interface between RF generator and biopsy introducer needle to serve as an RF ablation electrode following a core biopsy procedure. From the ex vivo experiments conducted on a bovine liver, it was found that the device provides a practical and reusable solution in minimizing bleeding and implantation of tumour cells in the needle tract during the biopsy procedure. There are numerous advantages of our adapter, namely its compatibility with almost all biopsy needle types available in the market, lightweight low cost, and it also provides a safe and fit interfacing. Further studies including in vivo investigations however, are needed in order to determine the optimum settings for this post-biopsy procedure to be applied in a real clinical environment.

References

1. Piccinino F, Sagnelli E, Pasquale G, Giusti G. Complications following percutaneous liver biopsy: a multicentre retrospective study on 68,276 biopsies. J Hepatol 1986; 2:165-173
2. Sugano S, Sumino Y, Hatori T, Mizugami H, Kawafune T, Abei T. Incidence of ultrasound-detected intrahepatic hematomas due to Trucut needle liver biopsy. Dig Dis Sci 1991; 36:1229-1233

F. Ibrahim, N.A. Abu Osman, J. Usman and N.A. Kadri (Eds.): Biomed 06, IFMBE Proceedings 15, pp. 232-235, 2007
www.springerlink.com ' Springer-Verlag Berlin Heidelberg 2007

3. Ralls PW, Barakos JA, Kaptein EM, Friedman PE, Fouladian G, Boswe WD, Halls J, Massry SG. Renal biopsy related hemorrhage: Frequency and comparison of CT and sonography. J Comput Assist Technol 1987; 11:1031-1034
4. Allison DJ, Adam A. Percutaneous liver biopsy and track embolization with steel coils. Radiology 1988; 169:261-263
5. Chisholm RA, Jones SN, Lees WR. Fibrin sealant as a plug for the post liver biopsy needle track. Clin Radiol 1989;40:627-628
6. Zins M, Vilgrain V, Gayno S, *et al*. US-guided percutaneous liver biopsy with plugging of the needle track: a prospective study in 72 high-risk patients. Radiology 1992; 184:841-843.
7. Paulson EK, Stephenson GR, Neal MC, Rossin V, Lawson JH. Use of fibrin sealant as a hemostatic agent after liver biopsy in swine. J Vasc Interv Radiol 2000; 11:905-911
8. Dromi SA, Lockin J, Wood BJ. Radiofrequency cauterization: an alternative to reduce post-biopsy hemorrhage. Cardiovasc Intervent Radiol 2005; 28(5):681-682
9. Pritchard WF, Wray-Cahen D, Karanian JW, Hilbert S and Wood BJ. Radiofrequency cauterization with biopsy introducer needle. J Vasc Interv Radiol 2004; 15:183-187

Address of the corresponding author:

Author: Azlan Che Ahmad
Institute: Department of Biomedical Imaging, University of Malaya
City: Kuala Lumpur
Country: Malaysia
Email: azlanbme@um.edu.my

F. Ibrahim, N.A. Abu Osman, J. Usman and N.A. Kadri (Eds.): Biomed 06, IFMBE Proceedings 15, pp. 232-235, 2007
www.springerlink.com ' Springer-Verlag Berlin Heidelberg 2007

A Study of Nodule Detection Using Opaque Object Filter

L.P. Wong, H.T. Ewe

Multimedia University, Cyberjaya, Selangor, Malaysia

Abstract— **This paper describes a study of Opaque Object Filter to extract region with nodule from chest x-ray image. A gray level chest x-ray image is preprocessed using Euler number algorithm to extract lung region. Defined Euler number algorithm is a statistical extraction of data obtained from Euler numbers for binary image. Suitable threshold value is computed based on minimum and maximum of the correlated gray scale value. After lung region was extracted, we applied our defined Opaque Object Filter to extract nodules image window. We use defined filter to perform heuristic search through the chest x-ray image. Defined Opaque Object Filter utilized radius and spatial axis vector analysis to extract nodules image window. Noise filter is defined to eliminate the border of lung area effects. A flow chart for the search is introduced. Initial result shows the filter is able to extract nodules image window within chest x-ray image**

Keywords— **Euler Number, Opaque Object Filter, Noise Filter, Nodule Detection, Chest X-ray.**

I. Introduction

Chest x-ray is easily available for health screening purpose. Screening lung cancer with chest x-rays can detect early lung cancer but also can produce many false positive test results and cause needless extra tests [1]. Computer aided detection (CAD) system for lung cancer on chest x-ray is able to complement radiologists in the detection of nodule. When CAD is used together with manual x-ray reading, the radiologists are able to detect additional cases of cancer [2]. Also in [3], it is mentioned that multiple false positive detections made by the CAD system depend on whether radiologists unaided interpretation is a true positive or a false negative and whether the machine result is a true positive or negative. These findings encourage further exploration in algorithm to extract nodules area from chest x-ray for lung cancer detection.

From literatures, we learn the evolution of cancer nodule detection techniques over a decade. Lo et al proposes subtracting a nodule suppressed from a nodule enhanced image using 2-D FFT and background correction. Subtracted image is then used to train neural networks using back propagation method to segment the image types [4]. Further evaluation using double matching and convolution neural networks for cancer nodule detection yields improvement [5]. Another approach using sector geometry and multiple circular path neural networks is reported to have improvement for the segmentation of cancer nodule from chest x-ray [6]. However, these approaches still yield high false positive.

Other interesting approach for cancer nodule segmentation includes wavelet-based snake model for distinction between nodules and false positives [7]. Convergence index filter (Coin filter) and adaptive coin filter (Iris filter) are proposed to detect rounded opacities on x-ray images [8] [9]. Optimal feature set approach, which utilizes geometric, contrast, first and second order statistics in segmentation of chest x-ray has been presented too [10]. These approaches yield encouraging results.

We perform analysis of opaque objects in our study. It is found that there are correlation of radius and spatial axis vector with an opaque object. We could extract the nodules image window by the radius and spatial axis vector characteristics. Therefore, we design a filter named Opaque Object Filter to extract nodules image windows from chest x-ray image. Heuristic search by Opaque Object Filter through the pre-processed chest x-ray has been done. It is found that the filter could extract nodules region from chest x-ray image.

II. Opaque object filter

A perfect opaque object shall have unified radius correlates with the angle, θ through the centric; so for the spatial axis vector. Figure 1 shows the perfect opaque object together with its radius and spatial vector. However, nodules within a chest x-ray shall have different shapes and sizes. In order to calculate the radius and spatial axis vector of the radius with respect to θ, we convert the gray level image window to binary image. Calculation of radius and spatial axis vector could be done based on the pixel value, where number of binary high value pixel represents length of the line. Spatial vector can be obtained by using:

$$\text{Horizontal axis vector, } \underline{\mathbf{X}} = r \times \cos\theta \quad (1)$$

$$\text{Verctial axis vector, } \underline{\mathbf{Y}} = r \times \sin\theta \quad (2)$$

Where r = radius, which is obtained from pixel count from the center of the given image window. θ = angle of rotation from the nominal position.

F. Ibrahim, N.A. Abu Osman, J. Usman and N.A. Kadri (Eds.): Biomed 06, IFMBE Proceedings 15, pp. 236-240, 2007
www.springerlink.com ' Springer-Verlag Berlin Heidelberg 2007

We rotate the image window through 360° by interval of 30°. Radius, $r_{\theta i}$ is defined as the number of pixels with binary high value at horizontal axis line across 0° from the centric. For nodule object, we have $r_{\theta i}$ with different values due to the nature of the nodule object and also the quality of the nodule extraction methods from the given image.

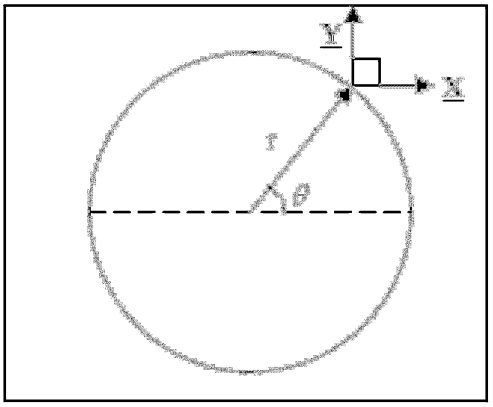

Figure 1: Perfect Opaque Object. r = radius, θ = angle, $\underline{\mathbf{Y}}$ =Vertical Axis Vector, $\underline{\mathbf{X}}$ = Horizontal Axis Vector

There are a few methods to convert gray level image to binary image. One of the popular methods is by Otsu threshold [11]. Otsu threshold utilizes global property of the histogram to determine suitable threshold level for gray scale images. We have tested Otsu threshold with nodules image windows preprocessed with histogram equalization to ensure homogeneous of the raw data. However, binary image obtained from Otsu threshold is unable to extract the nodule object. Therefore, we apply our algorithm from our previous works [12], named Euler number algorithm to extract nodule object within the given image window. It is found that by using gray scale level to correlate with minimum and maximum Euler number obtained from binary image through threshold search, nodule object within a given image window can be extracted. Figure 2 shows the comparison between Otsu threshold and Euler number algorithm in extracting nodule object from nodules image window.

Opaque object filter is defined as threshold of radius and spatial vector on (3) and (6).

$$R_{threshold} = \sqrt{\frac{\max(r_{\theta i})^2 + \min(r_{\theta i})^2}{2}} \tag{3}$$

where $r_{\theta i}$ = radius obtained from the rotation of θ angle from the nominal position.

$$\underline{\mathbf{X}}_{threshold} = \sqrt{\frac{\max(X_{\theta i})^2 + \min(X_{\theta i})^2}{2}} \tag{4}$$

$$\underline{\mathbf{Y}}_{threshold} = \sqrt{\frac{\max(Y_{\theta i})^2 + \min(Y_{\theta i})^2}{2}} \tag{5}$$

Where $\underline{\mathbf{X}}_{\theta i}$ = Horizontal Axis Vector obtained from the rotation of θ angle from the nominal position. $\underline{\mathbf{Y}}_{\theta i}$ = Vertical Axis Vector obtained from the rotation of θ angle from the nominal position.

We defined Spatial Axis Vector threshold as the absolute difference between Vertical Axis Vector and Horizontal Axis Vector. It can be written as:

$$\underline{\mathbf{V}}_{threshold} = |\underline{\mathbf{X}}_{threshold}| - |\underline{\mathbf{Y}}_{threshold}| \tag{6}$$

By substituting (4) and (5) into (6) will give us spatial vector threshold, $\mathbf{V}_{threshold}$.

The threshold value for radius and spatial vector are set based on our best knowledge of characteristic for binary nodules image which is obtained from the Euler number algorithm. This values are different due to the intensity histogram and contrast of the chest x-ray image simply because there are variation from machine to machine as well as human factors involved. Also, noise could be another factor to be considered in choosing the suitable threshold value.

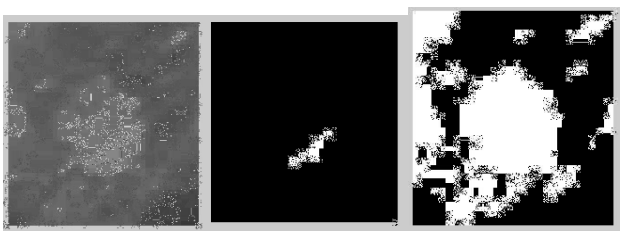

Figure 2: Comparison of Otsu threshold and Euler number algorithm in extracting nodule object from nodules image window. Left to right: original nodules image after histogram equalization, binary image obtained from Otsu threshold, binary image obtained from Euler number algorithm.

F. Ibrahim, N.A. Abu Osman, J. Usman and N.A. Kadri (Eds.): Biomed 06, IFMBE Proceedings 15, pp. 236-240, 2007
www.springerlink.com ' Springer-Verlag Berlin Heidelberg 2007

III. Result

Opaque object filter was used to perform heuristic search through the chest x-ray to extract nodules image window. Gray level chest x-ray image was preprocessed to extract lung region. There are a few ways to extract lung region from chest x-ray image [13]. In this work, we use algorithm which is defined from our previous works [12]. Our works use the Euler number obtained from the binary image. The value of the optimum threshold gray level in extracting lung region is the correlation between minimum and maximum of Euler number obtained from the binary image. This part is similar to what we have discussed above, except the input image is the whole chest x-ray image. The chest x-ray image is histogram-equalized to ensure homogeneous of the raw data from the chest x-ray.

The image window is chosen as 50x50 pixels. To speed up the computation of the heuristic search, interval of 10 pixels is used. However, this interval is important and it affects the efficiency of the search. This is because the Opaque Object Filter is simply based on the rotation of the image window to obtain the radius and spatial vector. Due to the randomization occurrence of nodules image, the interval between the image windows will affect the result too.

Since we perform heuristic search through the chest x-ray image, it is difficult to avoid the border of lung area having the value within our threshold radius and spatial vector. To deal with this problem, we carefully select the threshold value in our noise filter. The purpose of this noise filter is to reduce the false positive and eliminates the border effects. Threshold of our noise filter is defined as the average value of the raw image window. It can be represented as:

$$\chi_{threshold} = \frac{\sum_{i=0}^{\#Column} \sum_{j=0}^{\#Row} Intensity}{\#Column \times \#Row} \quad (7)$$

Where $\chi_{threshold}$ = Threshold for noise filter, *#Column* = number of column in term of pixels, *#Row* = number of row in term of pixels.

Figure 3 shows the flow chart of our application of the Opaque Object Filter. The chest x-ray images with known nodule area are obtained from internet [14]. Initial result shows our algorithm is able to extract nodules image with 2 false negative spots out of 10 nodules spots. This is due to constrain of fixed image window size and contrast problem which affect the Euler number algorithm. There were 2 false positive spots due to the border of lung effect which can be identified and ignored easily. Figure 4 shows the original chest x-ray image and chest x-ray image with nodules image window extracted.

Result obtained can be improved through improvement of the nodule extraction technique and better noise filter to eliminate the border of lung area effect. Also, characterization of suitable threshold value for radius and spatial vector can help to improve the result too.

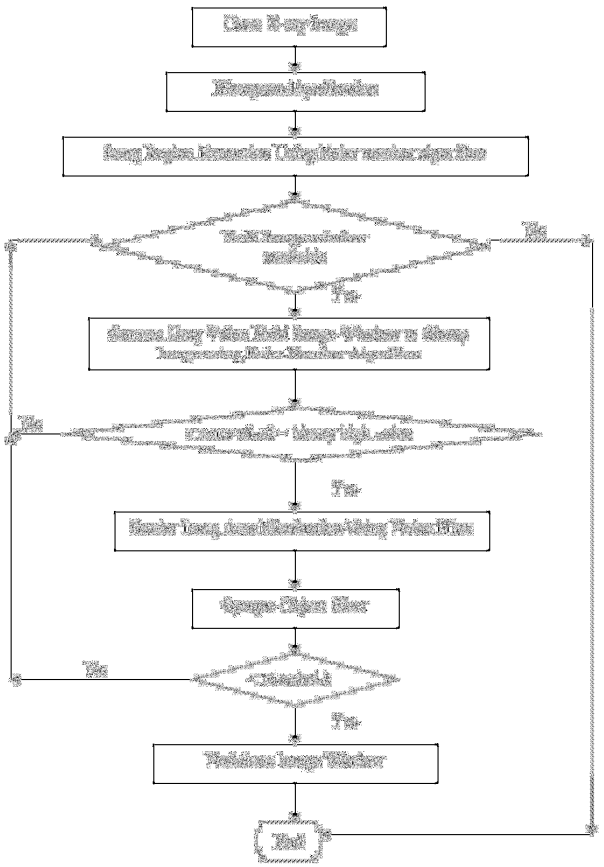

Figure 3: Flow chart for Nodules Image Window Extraction from chest x-ray image

F. Ibrahim, N.A. Abu Osman, J. Usman and N.A. Kadri (Eds.): Biomed 06, IFMBE Proceedings 15, pp. 236-240, 2007
www.springerlink.com ' Springer-Verlag Berlin Heidelberg 2007

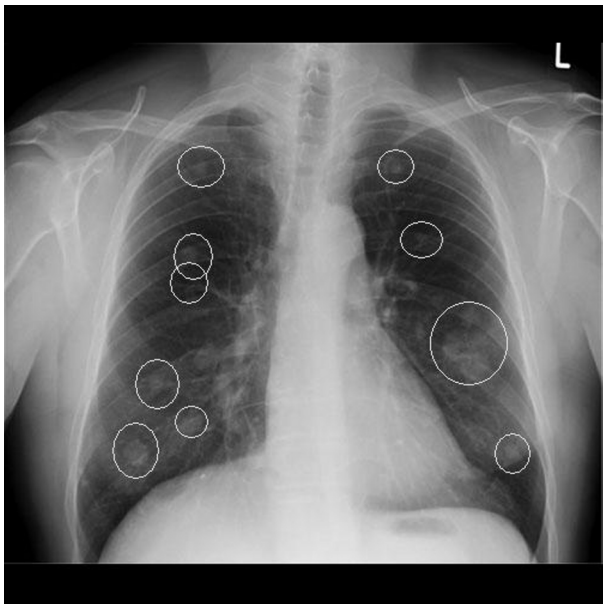

Output with Nodulous Image Windows Detection (vector<20, r<25, 50x50 pixels, 10 pixels interval, Noise>80 Pixels)

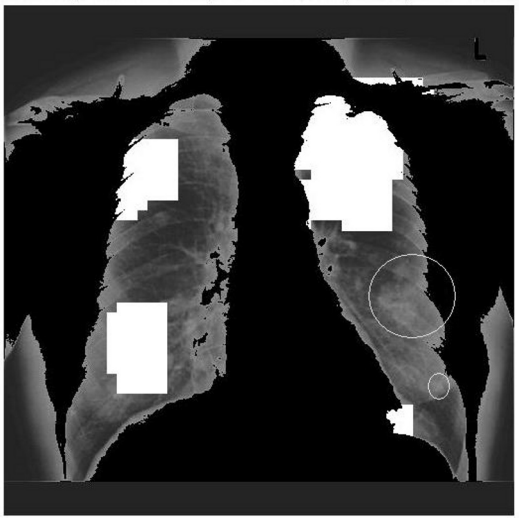

Figure 4: Above Original chest x-ray image,
Below Chest x-ray with nodules image windows extracted. Note that there are 2 false negative spots out of 10 nodules spots. Also, there are 2 false positive spots due to the border of lung area effect. It could be identified and ignored easily.

IV. Conclusion

Opaque Object Filter had been defined and applied to extract nodules image window from chest x-ray. Besides, we also define an algorithm to extract the nodules image window. Initial result is encouraging. This method can be used as a second reader for radiologists to perform the initial health screening by using chest x-ray image. Due to the nature of the chest x-ray, where nodule object could be easily mistaken or hidden from another anatomy. So, by using simple Opaque Object Filter can help to improve the detection of nodule object within chest x-ray.

Acknowledgement

Authors would like to express gratitude to GE Medical Inc. for the usage of chest x-ray image posted at their website.

References

1. Oken MM, Marcus PM, Hu P, Beck TM, Hocking W, Kvale PA, Cordes J, Riley TL, Winslow SD, Peace S, Levin DL, Prorok PC, Gohagan JK. Baseline chest radiograph for lung cancer detection in the randomized prostate, lung, colorectal and ovarian cancer screening trial. JNCI, Dec. 21, 2005. Vol. 97, No. 24.
2. Matthew Freedman, Shih-Chung Benedict Lo, Fleming Lure, Xin-Wei Xu, Jesse Lin, Hui Zhao, Teresa Osicka, Ron Zhang. Computer Aided Detection of Lung Cancer on Chest Radiographs. Algorithm Performance vs Radiologists' Performance by Size of Cancer. Visualization, Display, and Image-Guided Procedures. Proceedings of SPIE Vol. 4319 (2001).
3. Matthew T. Freedman, Shih-Chung Benedict Lo, Teresa Osicka, Fleming Lure, Xin-Wei Xu, Jesse Lin, Hui Zhao, Ron Zhang. Computer aided detection of lung cancer on chest radiographs: Effect of machine CAD false positive locations on radiologists' behavior. Medical Imaging 2002: Image Processing, Proceedings of SPIE Vol. 4684 (2002).
4. Shih-Chung B. Lo, Matthew T. Freedman, Jyh-Shyan Lin, Brian H. Krasner, and Seong K. Mun. Computer-Assisted Diagnosis for Lung Nodule Detection Using A Neural Network Technique. SPIE Vol. 1652 Medical Imaging VI: Image Processing 1992.
5. Shih-Chung B. Lo, Shyh-Liang A. Lou, Jyh-Shyan Lin, Matthew T. Freedman, Minze V. Chien, and Seong K. Mun. Artificial Convolution Neural Network Techniques and Applications for Lung Nodule Detection. IEEE Transactions On Medical Imaging, Vol. 14, No. 4, December 1995.
6. Shih-Chung B. Lo, Matthew T. Freedman, Jyh-Shyan Lin, and Xin-Wei Xu, and Andrzej Delegacz. Feature Analysis of Lung Nodules using Sector Geometry and Multiple Circular Path Neural Network. SPIE Conference on Image Processing, San Diego, California. February 1999. SPIE Vol. 3661.
7. Hiroyuki Yoshida, Bilgin Keserci, Kunio Doi. Computer-Aided Diagnosis of Pulmonary Nodules in Chest Radiographs: A Wavelet-Based Snake Approach. Proceedings Computer-Based Medical Systems, 1998. 11th IEEE Symposium on 12-14 June 1998.
8. Hidefumi Kobatake and Shigeru Hashimoto. Convergence Index Filter for Vector Fields. IEEE Transactions on Image Processing, Vol. 8, No. 8, August 1999.
9. Jun Wei, Yoshihiro Hagihara and Hidefumi Kobatake. Detection of Rounded Opacities on Chest Radiographs using Convergence Index Filter. International Conference on Image Analysis and Processing, 1999, Proceedings.
10. Jun Wei, Yoshihiro Hagihara, Akinobu Shimizu, Hidefumi Kobatake. Optimal image feature set for detecting lung nodules on chest X-ray images. 4th International Workshop on Computer-Aided Diagnosis, Computer Assisted Radiology and Surgery International Conference. June 26-29, 2002 Palais des Congr s, Paris, France

F. Ibrahim, N.A. Abu Osman, J. Usman and N.A. Kadri (Eds.): Biomed 06, IFMBE Proceedings 15, pp. 236-240, 2007
www.springerlink.com ' Springer-Verlag Berlin Heidelberg 2007

11. Nobuyuki Otsu, A threshold selection method from gray-level histogram, IEEE Transactions on Systems, Man, and Cybernetics, Vol. 9, No. 1, 1979, pp. 62-66.
12. Lip-Pang Wong, Hong-Tat Ewe. A Study of Euler Number Based Lung Region Detection in Chest X-ray Image. International Conference on Robotics, Visions, Information and Signal Processing. ROVISP 2006, Penang, Malaysia. 20-22 July 2005.
13. L.P.Wong and H.T. Ewe, A Study of Lung Cancer Detection using Chest X-Ray Images, Proceedings of 3rd APT Telemedicine Workshop, Kuala Lumpur, 27-28, January, 2005, pp. 210-214.
14. Available at http://www.gehealthcare.com/usen/xr/radio/products/digital_xray/adv_apps/case1.html

Address of the corresponding author:

Author: L.P. Wong
Institute: Multimedia University
Street: Jalan Multimedia,
City: Cyberjaya
Country: Malaysia
Email: lippang@yahoo.com

F. Ibrahim, N.A. Abu Osman, J. Usman and N.A. Kadri (Eds.): Biomed 06, IFMBE Proceedings 15, pp. 236-240, 2007
www.springerlink.com ' Springer-Verlag Berlin Heidelberg 2007

An Automatic Cell Counting Method for a Microscopic Tissue Image from Breast Cancer

P. Phukpattaranont[1] and P. Boonyaphiphat [2]

[1] Department of Electrical Engineering, Prince of Songkla University, Songkhla, Thailand
[2] Department of Pathology, Prince of Songkla University, Songkhla, Thailand

Abstract— **This paper presents an automatic cell counting method for a microscopic tissue image from breast cancer. We perform color space changing from RGB to CIELab and anisotropic diffusion filtering for noise removal in the preprocessing stage. Subsequently, the segmentation algorithm based on local adaptive thresholding, morphological operations, and cell size considerations is performed. In order to obtain the more correct counting number of cancer cells, we further process the image containing attached cancer cells with marker-controlled watershed segmentation. Results from our automatic counting approach show a promising solution to the traditional manual analysis. That is, the counting number of cancer cells from the automatic approach is comparable to that from a specialist.**

Keywords— **Quantitative immunohistopathology, Image segmentation, Cancer cell images**

I. Introduction

Immunohistochemistry is a technique that allows cellular protein products to be detected in tissue components *in situ* by the use of the antibody, i.e., antigen reaction. Analysis of cancer cell images from immunohistopathological tissue sections to make diagnostic decisions is performed on the basis of their appearance such as sizes, shapes, textures, and colors. Pathologists carry out this analysis by visual inspection of the image. However, the task is time consuming, costly, and tedious. In addition, visual inspection yields only subjective results. In order to overcome these problems, an automation of medical image analysis that previously requires manual operations is performed on the basis of the developments in computer capabilities and image processing algorithms [1-4].

There are a number of benefits that result from an automated analysis. These include an acceleration of time and a reduction in cost for image analysis as well as a decrement in a false inspection due to fatigue. Additionally, the automated analysis provides a quantitative description of each particular cell in the image. Based on this quantitative measurement, the analysis result is objective. The quantitative description can be used as a concise representation of the image for efficient storage and quick retrieval. Furthermore, the correlation of the quantitative categorization of tissue diseases with patient symptoms may allow for an automated diagnostic system [5, 6]. However, it is not expected that automated image analysis will replace the pathologist's inspection of the tissue. The automated method is only an aid to the pathologist for the majority of routine descriptive analyzes and yields quantitative results which complement and enhance interpretations of pathologists. Visual examination by the pathologist is still required where unusual or abnormal cells that the method is not trained to deal with are encountered.

The objective of our work is to develop an automatic image processing algorithm for partitioning and characterizing microscopic structures on immunohistological stained slides from breast cancer tissue. This staining procedure is employed to demonstrate the existing of estrogen or progesterone receptors in the breast cancer cells. We have recently presented the use of local adaptive thresholding and morphological operators for segmenting cancer cells microscopically [7, 8]. Good segmentation results of detached cancer cells are demonstrated. However, in order to obtain more accurate segmentation results, in this paper we further process the attached cancer cells with marker-controlled watershed segmentation for separating touching cells. Details and results of the proposed algorithm are given below.

II. Algorithm for cancer cell segmentation

An algorithm for segmenting cancer cells is described in this section. As shown in Fig. 1, the procedure for the approach is composed of two stages, i.e. the image preprocessing and image segmentation. While the image preprocessing stage consists of color space transformation and anisotropic diffusion, the segmentation stage comprises local adaptive thresholding, mathematical morphology, and marker-controlled watershed segmentation. Details of each stage are as follows.

F. Ibrahim, N.A. Abu Osman, J. Usman and N.A. Kadri (Eds.): Biomed 06, IFMBE Proceedings 15, pp. 241-244, 2007
www.springerlink.com ' Springer-Verlag Berlin Heidelberg 2007

A. Image preprocessing

Two processes are performed in the preprocessing stage.

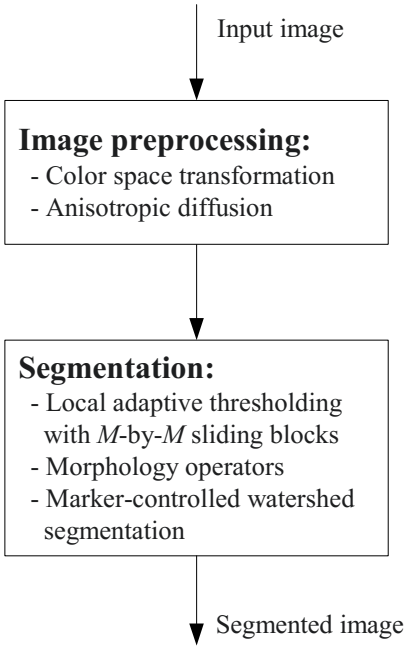

Fig. 1 Algorithm for an automatic cell counting method.

Firstly, we transform the red-green-blue (RGB) color space to CIELab space. The CIELab space is chosen due to the close correlation between its Euclidean distances and human perception of colors. The CIELab space can be defined by

$$L^* = 116\left(\frac{Y}{Y_n}\right)^{\frac{1}{3}} - 16$$
$$a^* = 500\left[\left(\frac{X}{X_n}\right)^{\frac{1}{3}} - \left(\frac{Y}{Y_n}\right)^{\frac{1}{3}}\right] \quad (1)$$
$$b^* = 200\left[\left(\frac{Y}{Y_n}\right)^{\frac{1}{3}} - \left(\frac{Z}{Z_n}\right)^{\frac{1}{3}}\right]$$

for X/X_n, Y/Y_n, $Z/Z_n > 0.01$. The values X_n, Y_n, Z_n are the CIE (Commission Internationale de l'eclairage) tristimulus values of the reference white under the reference illumination, and X, Y, Z are the tristimulus values, which are mapped to the CIE color space. While the L^* component represents intensity, the a^* and b^* components are proportional to red-green and yellow-blue color contents, respectively.

Secondly, we apply the anisotropic diffusion to the L^* component from the first step. The objective of this operation is to smooth regions inside cancer cells while still preserve the edge and contrast at sharp intensity gradients. The image resulting from this step significantly facilitates the segmentation algorithm in the next stage. The anisotropic diffusion equation can be expressed as [10]

$$I_t = div(c(x,y,t)\nabla I), \quad (2)$$

where *div* is the divergence operator, $c(x,y,t)$ is the diffusion coefficient, and ∇I is the gradient operator. In order to smooth the area within an object of interest and simultaneously preserve high gradient boundaries, the diffusion coefficient is given by

$$c(x,y,t) = g(||\nabla I(x,y,t))||) = e^{-(||\nabla I(x,y,t))||/\kappa)^2}, \quad (3)$$

where κ is a constant that controls conduction. We implement the numerical solution of Equation (2) using the algorithm provided in [10], which is given by

$$I_{i,j}^{t+1} = I_{i,j}^{t} + \lambda[c_N \cdot \nabla_N I + c_S \cdot \nabla_S I + c_E \cdot \nabla_E I + c_W \cdot \nabla_W I], \quad (4)$$

where $0 \le \lambda \le 1/4$ for the numerical scheme to be stable. Please see [10] for more details.

B. Segmentation

We use the combination of local adaptive thresholding, morphological operations, and cell prior knowledge in our segmentation algorithm. For local adaptive thresholding, we apply *M*-by-*M* sliding blocks with the output image from the anisotropic diffusion. The threshold of each local block is determined using Otsu's method [11]. After finishing adaptive thresholding for all local blocks, we process the black and white image using morphological opening in combination with a cell size consideration. These two operations are successively used to eliminate spike noise and fill holes.

In order to separate the attached cancer cells into individual objects, we further process the result from last step with marker-controlled watershed segmentation. The watershed algorithm is shown to be a powerful tool for dividing attached objects [12]. The marker computation is used as an additional processing because the direct use of watershed transform usually yields the over-segmented result. The computational procedures for marker-controlled watershed segmentation are as follows:

F. Ibrahim, N.A. Abu Osman, J. Usman and N.A. Kadri (Eds.): Biomed 06, IFMBE Proceedings 15, pp. 241-244, 2007
www.springerlink.com ' Springer-Verlag Berlin Heidelberg 2007

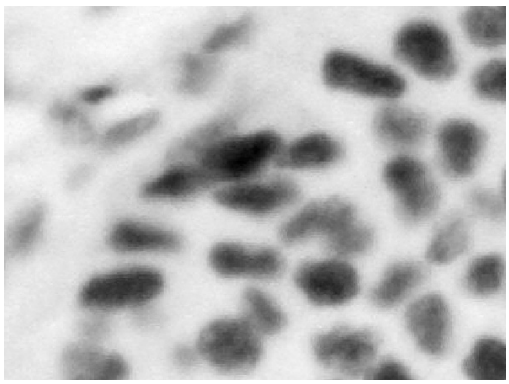

Fig. 2 Intensity image, i.e. the L^* component of CIELab color space, of a stained cancer cell image.

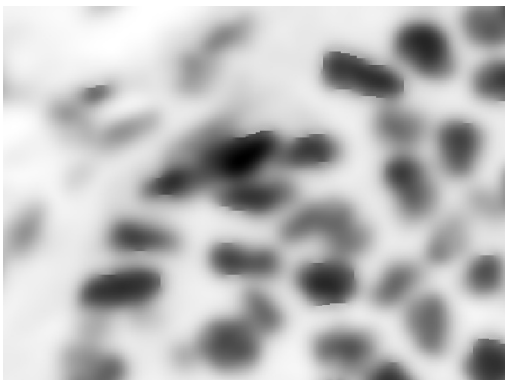

Fig. 3 Output image from the anisotropic diffusion filtering with conduction coefficient $\kappa = 20$ and speed of diffusion $\lambda = 0.2$.

(1) Use the Sobel edge marks to compute the gradient magnitude and use it as the segmentation function, (2) Compute foreground markers, which are connected blobs of pixels inside each of the foreground objects, (3) Compute background markers, i.e., pixels that are not part of any object, (4) Modify the segmentation function so that it only has minima at the foreground and background marker locations, and (5) Compute the watershed transform of the modified segmentation function.

III. Acquisition of the Images

The images used in this paper were obtained from the tissue sections containing breast cancer which had been stained. The tissue sections were observed by a microscope with a magnifying factor of 20. The contrast and intensity of staining were manually corrected in such a way that the digitized image became visually acceptable for further manual classification by a specialist. The cell images were acquired in color using the Eclipse 80i advanced research microscope (Nikon Instech Co., Ltd., Japan). The digital image was saved as an 8-bit gray-level 2560 × 3200 JPEG files for processing.

IV. Results and Discussion

Fig. 2 shows an intensity image, i.e. the L^* component of CIELab color space, of a sample slide containing stained cancer cells after the change of color space from RGB to CIELab. One can see the mixture of attached and detached cancer cells in the image. This image is used as the input of anisotropic diffusion processing and the output image is shown in Fig. 3. Parameters used for the numerical solution of anisotropic diffusion in this paper are as follows: speed of diffusion (λ) = 0.2, conduction coefficient (κ) = 20, and number of iterations = 50. It can be seen from the image that the anisotropic diffusion filtering successfully removes undesirable noise while still preserving sharp edges of cancer cells.

A segmented image from the algorithm described in Section IIB before the application of marker-controlled watershed segmentation is shown in Fig. 4. For this result, the 11-by-11 sliding block is used for local adaptive thresholding. Analysis of appropriate parameter selections for anisotropic diffusion and block size for local adaptive thresholding are addressed in [8]. In order to eliminate spike noise, the binary image is processed using morphological opening with the disk-shaped structuring element. The algorithm based on morphological reconstruction is subsequently used to fill holes in the image. Additionally, the size of cancer cells under consideration must be greater than 140. We can clearly see that the boundaries of segmented cancer cells are in agreement with those of their original images shown in Fig. 2. The total number of cancer cells is 32. However, there are attached cancer cells, i.e. cancer cell number 9, 12, and 13. These cells must be separated into individual objects so that the meaningful features for each cell can be extracted.

Fig. 5 shows a segmented image after the application of marker-controlled watershed segmentation. We can see that the attached cancer cells are appropriately separated. That is, cancer cell number 9 in Fig. 4 is separated into cancer cell number 9, 15, and 19 in Fig. 5. In addition, cancer cell number 12 and 13 in Fig. 4 are correctly divided into cancer cell number (12, 13) and (14, 18) in Fig. 5, respectively.

F. Ibrahim, N.A. Abu Osman, J. Usman and N.A. Kadri (Eds.): Biomed 06, IFMBE Proceedings 15, pp. 241-244, 2007
www.springerlink.com ' Springer-Verlag Berlin Heidelberg 2007

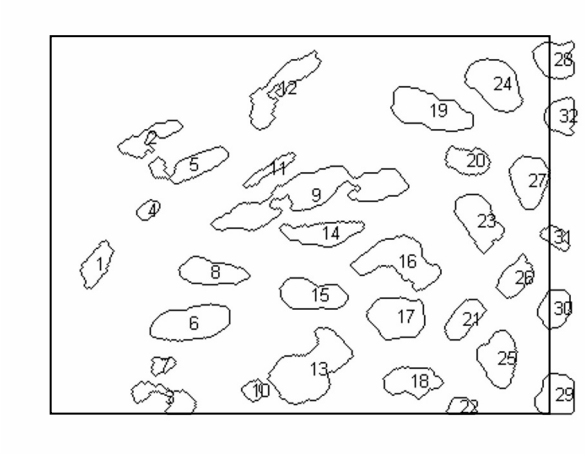

Fig. 4 Segmented image before the application of marker-controlled watershed segmentation. The total number of cancer cells in the image is 32.

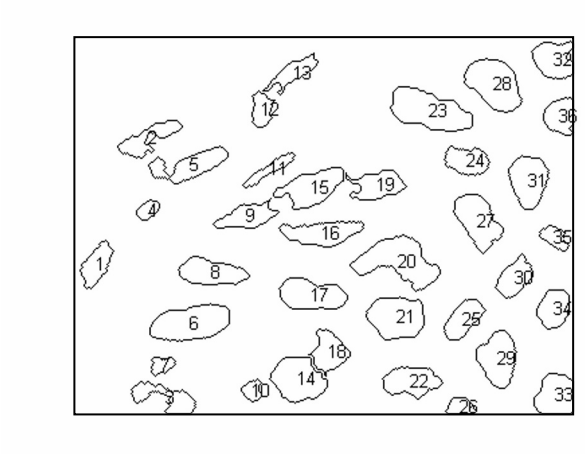

Fig. 5 Segmented image after the application of marker-controlled watershed segmentation. The total number of cancer cells in the image is 36.

Consequently, the more accurate total number of cancer cells in the image is counted to be 36.

V. Conclusions

We present an approach for automatic counting of cancer cells in a microscopic tissue image from breast cancer. Color space changing and anisotropic diffusion filtering for noise removal are performed in the preprocessing stage. Subsequently, the preprocessing result is segmented using local adaptive thresholding, morphological operations, and cell size considerations. Then, the imaging result is further processed with marker-controlled watershed segmentation in order to separate the attached cancer cells. Results show that cancer cells are successfully separated with the proposed algorithm.

References

1. Thiran J, Macq B (1996) Morphological feature extraction for the classification of digital images of cancerous tissues. IEEE Transactions on biomedical engineering 43(10):1011 1020
2. Fang B, Hsu W, Lee M (2003) On the accurate counting of tumor cells. IEEE Transactions on nanobioscience 2(2): 94 103
3. Zhao P, Mao K, Koh T, Tan P (2003) Automatic cell analysis for P53 immunohistochemistry in bladder inverted papilloma. IEEE EMBS Asian-Pacific Conference on Biomedical Engineering, 2003, pp 168 169.
4. Petushi S, Katsinis C, Coward C et al (2004) Automated identification of microstructures on histology slides, IEEE International Symposium on Biomedical Imaging: Macro to Nano vol. 1, 2004, pp 424 427.
5. O Gorman L, Sanderson A, Preston K Jr (1985) A system for automated liver tissue image analysis: Methods and results. IEEE Transactions on biomedical engineering 32(9):696 706
6. Wu K, Gauthier D, Levine M (1995) Live cell image segmentation. IEEE Transactions on biomedical engineering 42(1):1 12
7. Phukpattaranont P, Boonyaphiphat P (2006) Automatic classification of cancer cells in microscopic images: Preliminary results, The 2006 ITC-CSCC International Conference vol. 1, Chiang Mai, Thailand, 2006, pp 113-116
8. Phukpattaranont P, Boonyaphiphat P et al (2006) Segmentation of cancerous cell image using local adaptive thresholding and morphological operators, The 2nd Regional Conference on Artificial Life and Robotics, Songkhla, Thailand, 2006, pp 68-71
9. Trussell H, Saber E, Vrhel M (2005) Color image processing (basics and special issue overview). IEEE signal processing magazine 22(1): 14 22
10. Perona P and Malik J (1990) Scale-space and edge detection using anisotropic diffusion. IEEE Transactions on pattern analysis and machine intelligence 12(7):629 639
11. Otsu N (1979) A threshold selection method from graylevel histograms. IEEE Transactions on Systems, Man, and Cybernetics 9(1):62 66
12. Vincent L (1993) Morphological grayscale reconstruction in image analysis: applications and efficient algorithms. IEEE Transactions on Image Processing 2(2):176 201

Address of the corresponding author:

Author: Pornchai Phukpattaranont, Pleumjit Boonyaphiphat
Institute: Prince of Songkla University
Street: 15 Kanjanavanit Road, Hat-Yai
City: Songkhla
Country: Thailand
Email: pornchai.p@psu.ac.th, pleamjit.b@psu.ac.th

F. Ibrahim, N.A. Abu Osman, J. Usman and N.A. Kadri (Eds.): Biomed 06, IFMBE Proceedings 15, pp. 241-244, 2007
www.springerlink.com ' Springer-Verlag Berlin Heidelberg 2007

Automatic Retrieval of Microscopic Blood Cells Images

N. Selvanathan[1], Lee Shi Yun[1], Mangalam Sankupellay[1], V. Purushothaman[2], S. Jameelah[2]

[1]University of Malaya, Kuala Lumpur Malaysia
[2]General Hospital Kuala Lumpur, Malaysia

Abstract - **The research explores various methods to retrieve microscopic blood cell image on the basis of features automatically extracted from the image. The query image is selected from a large collection of blood cell image. After the region of interest is selected from the image, Query by Image Content (QBIC) catalog is used to measure the low level attributed of the query image such as average color, histogram color, positional color and texture. The low level attributes are used to find matching image in the DB2 (DataBase 2 by IBM) database. The most accurate and relevant blood cell images are retrieved along with the description of the blood disorder.**

Keywords - **Content Based Image Retrieval, Blood Cell Images**

I. Introduction

The term content-based image retrieval (CBIR) is used most early in the literature seems to have been by [1], who described his experiments into automatic retrieval of images from a database by colour and shape feature. The term has since been widely used to describe the process of retrieving desired images from a large collection on the basis of features (such as colour, texture and shape) that can be automatically extracted from the images themselves. The features used for retrieval can be either primitive or semantic, but the extraction process must be predominantly automatic. Retrieval of images by manually-assigned keywords is definitely not CBIR as the term is generally understood even if the keywords describe image content. In general "content based image retrieval" is the possibility to make queries on image databases based upon visual characteristics. This means that there are normally no text tags at the images that can be searched. The queries should be made with visual characteristics like the distribution of colors, textures in the image or based on object in the images. Most available systems use a couple of features of all these areas.

CBIR differs from classical information retrieval in that image databases are essentially unstructured, since digitized images consist purely of arrays of pixel intensities, with no inherent meaning. One of the key issues with any kind of image processing is the need to extract useful information from the raw data (such as recognizing the presence of particular shapes or textures) before any kind of reasoning about the image s contents is possible. Image databases thus differ fundamentally from text databases, where the raw material (words stored as ASCII character strings) has already been logically structured by the author [2].

CBIR draws many of its methods from the field of image processing and computer vision, and is regarded by some as a subset of that field. While there are grey areas (such as object recognition by feature analysis), the distinction between mainstream image analysis and CBIR is usually fairly clear-cut. An example may make this clear. Many police forces now use automatic face recognition systems. Such systems may be used in one of two ways. Firstly, the image in front of the camera may be compared with a single individual s database record to verify his or her identity. In this case, only two images are matched, a process few observers would call CBIR. Secondly, the entire database may be searched to find the most closely matching images. This is a genuine example of CBIR.

A. The Need For Content Based Medical Image Retrieval

In the radiology department of the University Hospital of Geneva (HUG), the number of image produced per day in 2002 was 12,000, and it is still rising [11]. Video and images produced in cardiology are equally multiplying. The management and access of these large image repositories become increasingly complex. Most accesses to these systems are based on patient identification as it is defined in the DICOM (Digital Imaging and Communications in Medicine) standard [11].

The goals of medical information systems have been defined to deliver the needed information at the right time, the right place to the right person in order to improve the quality and efficiency of care processes [11]. In clinical decision making process it may be beneficial and important to find other images of the same modality, the same anatomic region of the same disease [11]. Clinical decision support techniques such as case based reasoning [9], or evidence based medical [10] produce a stronger need to retrieve images that area valuable for supporting certain diagnostics. Image based reasoning (IBR) is imagined as a new disciple for diagnostic aid [11].

In principle, all image-producing departments can profit from content-based technologies, but there are some departments and some sort of images that seem to stand out are textures and colors as color and texture features play an

F. Ibrahim, N.A. Abu Osman, J. Usman and N.A. Kadri (Eds.): Biomed 06, IFMBE Proceedings 15, pp. 245-249, 2007
www.springerlink.com ' Springer-Verlag Berlin Heidelberg 2007

important role for diagnosis [11]. This includes pathology, dermatology and radiology. In pathology, microscopic images are analyzed and the clinical decision-making depends on the color changes and texture within the mages [11]. Dermatology has classification application for potential melanoma cases. In radiology, large number of people profit from the methods to retrieve similar cases for a number of applications, often without realizing that the results come from content based image retrieval engine [11].

Besides diagnostics, teaching and research especially are expected to improve through the use of visual access methods as visually interesting images can be chosen and can actually be found in the existing large repositories. Visual features do not only allow the retrieval of cases with patients having similar diagnoses but also cases with visual similarity but different diagnoses [11].

Researches can also benefit from visual retrieval methods. Researchers have more option for the choice of cases to into research and studies by allowing text-based and visual access. New correlation between the visual nature of a case and its diagnosis can be found. Visual data can also be mined to find changes which can lead to discovery of new knowledge.

II. Retrieval technique

Every CBIR application is characterized by a typical set of possible queries reflecting a specific semantic content.

This section classifies several important CBIR applications based on their semantic requirements. There are three main partition levels [3].

A. Low Level (Level 1)

This level comprises retrieval by *primitive* features such as colour, texture, shape or the spatial location of image elements. In this level,the commonest features used are mathematical measures of colour, texture or shape; hence virtually all current CBIR systems, whether commercial or experimental, operate at low level. Some of the more commonly used types of feature used for image retrieval are described below.

1. Color Retrieval

Several methods for retrieving images on the basis of colour similarity have been described in the literature, but most are variations on the same basic idea. Each image added to the collection is analysed to compute a *colour histogram* which shows the proportion of pixels of each colour within the image [3]. The colour histogram for each image is then stored in the database. At search time, the user can either specify the desired proportion of each colour (75% olive green and 25% red, for example), or submit an example image from which a colour histogram is calculated. Either way, the matching process then retrieves those images whose colour histograms match those of the query most closely. The matching technique most commonly used, histogram intersection, was first developed by [4].

Positional color is used to search for images that have a predominant color in a general location in the image. For example, an image with a purple musical note in the top right corner has a positional color of purple.

2. Texture Retrieval

Texture refers to visual patterns with properties of homogeneity that do not result from the presence of only a single color or intensity [5]. Tree barks, clouds, water, bricks, and fabric are examples of textures. Typical textural features include contrast, uniformity, coarseness, roughness, frequency, density and directionality. Texture always contains the structural arrangement of surfaces and their relationship to the surrounding environment [6]. There are two basic classes of texture descriptors: statistical model based and transform based.

3. Shape Retrieval

The ability to retrieve by shape is perhaps the most obvious requirement at the primitive level. Unlike texture, shape is a fairly well-defined concept and there is considerable evidence that natural objects are primarily recognized by their shape [7]. A number of features characteristic of object shape (but independent of size or orientation) are computed for every object identified within each stored image. Queries are then answered by computing the same set of features for the query image, and retrieving those stored images whose features most closely match those of the query. Two main types of shape feature are commonly used *global* features such as aspect ratio, circularity and moment invariants and *local* features such as sets of consecutive boundary segments. Alternative methods proposed for shape matching have included elastic deformation of templates, comparison of directional histograms of edges extracted from the image, and *shocks*, skeletal representations of object shape that can be compared using graph matching techniques. Queries to shape retrieval systems are formulated either by identifying an example image to act as the query, or as a user-drawn sketch [3].

4. Spatial Layout

The use of global color or texture features for the retrieval of images tends to be misleading, especially in homogeneous image collections. To overcome this, the use of spatial layout is often used. For example, for the color feature, the use of color layout was proposed; this method

F. Ibrahim, N.A. Abu Osman, J. Usman and N.A. Kadri (Eds.): Biomed 06, IFMBE Proceedings 15, pp. 245-249, 2007
www.springerlink.com ' Springer-Verlag Berlin Heidelberg 2007

consists in combining both the color feature and the spatial relations. A natural approach to do this is to divide the whole image into sub-blocks and extract color feature from each of these sub-blocks. A variation of this approach is the quad-tree based color layout, where the entire image was split into quad-tree structure and each tree branch had its own histogram to describe its color content. In order to achieve computational and storage constraints, a more elaborated approach is to segment the image into salient color features by Color Set Back-projection [8], and then store the position and Color Set feature of each region. This last method has shown accurate, but the problem is again to define a reliable segmentation of the image. Spatial layout useful if it can capture a semantically meaningful division of scene.

B. Intermediate Level (Level 2)

This level comprises retrieval by *derived* (sometimes known as *logical*) features, involving some degree of logical inference about the identity of the objects depicted in the image. This level is characterized by a deeper involvement of users with visual content. This involvement is peculiarly emotional and is difficult to express in rational and textural terms. Examples of visual content with a strong emotional component can be derived from the visual arts (painting, photography). From the view point of intermediate level content, visual art domain are characterized by presence of either figurative elements such as people, manufactured objects and so on. Specifically, the shape of single objects dominates over color both in artistic photography and in figurative art [3].

C. High Level (Level 3)

This level comprises retrieval by *abstract* attributes, involving a significant amount of high-level reasoning about the meaning and purpose of the objects or scenes depicted. Again, this level of retrieval can usefully be subdivided into:

1. retrieval of named events or types of activity (e.g. find pictures of Scottish folk dancing);
2. retrieval of pictures with emotional or religious significance (find a picture depicting suffering).

Success in answering queries at this level can require some sophistication on the part of the searcher. Complex reasoning, and often subjective judgments, can be required to make the link between image content and the abstract concepts it is required to illustrate. Queries at this level, though perhaps less common than level 2, are often encountered in both newspaper and art libraries.

III. IBM DB2 AIV (Audio, Image and Video) EXTENDER

The DB2 AIV(Audio, Image and Video) Extender gives lot flexibilities to application in searching for information. Application can search for objects that are associated with traditional types of data that are stored in database. With DB2 AIV Extender s Query by Image Content (QBIC) capability, users can create applications that search for images in this visual way.

Average color - The sum of color values for all pixels in the image divided by number of pixel in the image. QBIC uses this value to search for image that has a predominant color.

Histogram color - Histogram color feature measures the distribution of color in an image against a spectrum of 64 colors. The histogram is used to search for images that have a variety of colors.

Positional color - The average color value for the pixel in a specified area in an image is obtained. This is used to search for image that has a predominant color in particular area.

Texture - Texture is used to search for image that has a particular pattern. It measures the coarseness, contrast, and directionality of an image. Coarseness indicates the size of repeating item. Contrast identifies the brightness variations in an image. Directionality indicates whether a direction predominates.

IV. RESULT

The retrieval blood images based on different features, average color, histogram color, positional color and texture are compared to find the best fit method to retrieve the erythrocytes blood samples. The selection area of Region of Interest (ROI) also affects the retrieval results. In this project, the correctness of the results is very important to user for further study on erythrocytes.

Comparison On Average Color, Histogram Color, Positional Color And Texture

The series of result of retrieval images are shown as in Table 1. The four highest ranked images are retrieved by the system. Table 1 indicates the rank of the retrieved images.

The same query image with the same selection area will give different retrieval results with different feature selected by user (average color, histogram color, positional color and texture). Average color feature is calculating the total pixel of certain colors divided by the sum of pixels. For example, an image that has 50% red pixels, 50% blue pixels the average color is purple value. While, histogram color

F. Ibrahim, N.A. Abu Osman, J. Usman and N.A. Kadri (Eds.): Biomed 06, IFMBE Proceedings 15, pp. 245-249, 2007
www.springerlink.com ' Springer-Verlag Berlin Heidelberg 2007

feature measure an image against a spectrum of 64 colors. Texture feature will find the coarseness, contrast and pattern of the image.

Table 1 – Results of Retrieval using different features

Query Image / Retrieval Feature	Histogram Color	Average Color	Positional Color	Texture
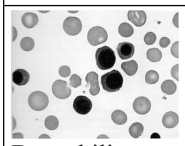 Basophilic and polychromatic erythroblasts	First Result	First Result	First Result	First Result
Query Image / Retrieval Feature	**Histogram Color**	**Average Color**	**Positional Color**	**Texture**
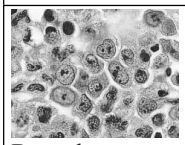 Round macrocytes	First Result	First Result	First Result	No Result
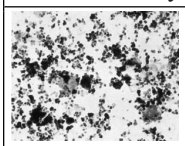 Clostridal sepsis	First Result	First Result	First Result	First Result
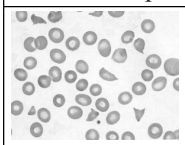 HELLP syndrome	First Result	First Result	No Result	Fourth Result
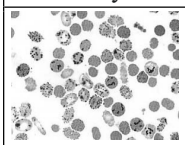 HbH disease	First Result	First Result	First Result	No Result
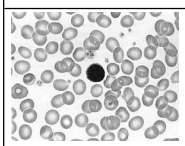 a-Thalassaemia trait	First Result	Second Result	First Result	First Result

From the sample queries above, the histogram color feature retrieves the most accurate and most relevant image. When the average color feature was used for retrieval, the retrieval was accurate most of the time. However, the most accurate results are not presented as the first result sometimes. Positional color feature retrieves the most accurate image most of the time. On the other hand, when the retrieval fails for some queries, the results presented are not relevant at all to the query. The texture feature seldom provides the accurate result or the results are not relevant at all.

V. Conclusion

In general, it is difficult to compare any two retrieval systems in image retrieval domain [11]. For medical image retrieval system, the evaluation issue almost non-existent in most the paper. We have used the ranking of the result to compare the effectives of the different features used in retrieval.

Based on the comparison of the result, the accuracy of the retrieval features can be ranked as following:-

1. Histogram Color
2. Average Color
3. Positional Color
4. Texture

Future work in this area would concentrate on exploring new retrieval techniques that are more accurate. The retrieval techniques would also focus on analysis of blood cell features to produce a more accurate and reliable retrieval method.

A more accurate retrieval system would help clinician for faster and more accurate diagnosis of blood disorder. This would help patients receive the appropriate treatment in time.

Reference

[1] Hirata K. and T. Kato. 1992. Query by visual example. Lecture notes in computer science. In *Advances in database technology,* vol. 580, ed. A. Pirotte et al. Berlin: Springer-Verlag

[2] Ying Li, C.-C. Jay Kuo, and X. Wan Introduction to Content-Based Image Retrieval Overview of Key Techniques In Image Databases: Search and Retrieval of Digital Imagery edited by Vittorio Castelli, 261-275, John Wiley & Sons, Inc. 2002.

[3] P.E.John, E.G.Margaret, *Content-based Image Retrieval: Report to the JISC Technology Applications Programme*. January, 1999. <http://www.unn.ac.uk/iidr/report.html>(August 10, 2004)

[4] Swain, M.J., Ballard, D.H. (1991). Color Indexing . International Journal of Computer Vision. 7(1). pp. 11-31.

[5] J.R. Smith and S.-F. Chang, Automated binary texture feature sets for image retrieval, *Proc. ICASSP-96*, Atlanta, GA, 4, 2241-2246 (1996).

F. Ibrahim, N.A. Abu Osman, J. Usman and N.A. Kadri (Eds.): Biomed 06, IFMBE Proceedings 15, pp. 245-249, 2007
www.springerlink.com ' Springer-Verlag Berlin Heidelberg 2007

[6] R.M. Haralick, K. Shanmugam, and I. Dinstein, Texture features for image classification*, IEEE Trans. Sys. Man. Cyb.* SMC-3(6), 1345-1350 (1973).

[7] Biederman, I (1987) Recognition-by-components: a theory of human image understanding *Psychological Review* 94(2), 115-147

[8] J. R. Smith, S.-F. Chang, Tools and Techniques for Color Image Retrieval, *Proc. IS&T/SPIE Storage & Retrieval for Still Image and Video Databases IV*, San Jose, CA, Feb., 1996, pp. 426-437.

[9] Daniel M. Krainak, L. Rodney Long, George R. Thoma, Method of content-based image retrieval for a spinal x-ray image database, Medical Imaging 2002: PACS and Integrated Medical Information Systems: Design and Evaluation, SPIE Proceedings Vol. 4685, pp.108-116

[10] IBM DB2 UDB AIV Extender <http://www-306.ibm.com/software/data/db2/extenders/aiv/index.html>August 24, 2004

[11] Henning Müller, Nicolas Michoux, David Bandon, Antoine Geissbuhler, *A review of content-based image retrieval systems in medical applications—clinical benefits and future directions*, International Journal of Medical Informatics (2004) 73, 1 23

Address of the corresponding author:

Author: angalam Sankupellay
Institute: ac. of Comp. Sc. & IT
Street: University of Malaya
City: Kuala Lumpur
Country: Malaysia
Email: angalam@um.edu.my

F. Ibrahim, N.A. Abu Osman, J. Usman and N.A. Kadri (Eds.): Biomed 06, IFMBE Proceedings 15, pp. 245-249, 2007
www.springerlink.com ' Springer-Verlag Berlin Heidelberg 2007

Boundary Enhancement For Echocardiogram Using Local Image Characteristics And Ratio Of Averages

S. Chan and G. Sainarayanan

School of Engineering and Information Technology, Universiti Malaysia Sabah, Kota Kinabalu, Malaysia

Abstract—**A method for echocardiogram boundary enhancement using local image characteristics and Ratio-of-Averages (RoA) is proposed in this paper. Local image characteristics, namely "steepness" and "symmetry", are used along side with RoA to determine "edgeness" of the image. The task is achieved by employing a fuzzy inference system where fuzzy sets and rules are derived heuristically to define "edgeness". All results obtained are compared to a standard edge detector and a similar method without RoA for quantitative and qualitative performance evaluation.**

Keywords— **Boundary Enhancement, Echocardiogram, Local Image Characteristic, Ratio-of-Averages, and Fuzzy Inference System**

I. Introduction

Ultrasound is a technology that uses high frequency sound waves which are reflected by tissue in the body. It is emerging as the preferred tool particularly in cardiac performance investigation. For example, rapid estimates of ventricular filling, ejection fraction, and the degree of wall motion abnormality derived from transesophageal images would be valuable for patient management but currently require laborious manual identification of the endocardial borders. Consequently, an automated or semi-automated method of border identification would have wide application in real-time patient monitoring, a well as in cardiology [1].

Ultrasound images are formed as a combination of interference patterns (speckle) and reflections at tissue transitions. Different tissues are mostly not distinguishable by their intensity values or texture. Moreover, many imaging artifacts occur, resulting in the loss of anatomical information: significant amounts of noise, dropouts (for structures parallel to the ultrasound beam), shadowing (behind acoustically dense structures), side lobes, reverberations, and limited echo windows [2].

Therefore, many researchers have worked using various approaches to enhance or detect the boundaries in ultrasound images [3]-[5]. However, in the proposed method, fuzzy application is preferred to avoid the need for initial manual definition and reduce trade-off between edge detection and noise suppression caused by subjective ad hoc parameters. The proposed method offers an alternative to the many available fuzzy methods [6]-[7] to enhance echocardiogram boundary.

The next section explains the application of Ratio-of-Averages (RoA) in the proposed method and is ensued by the section defining local image characteristics and RoA. The section after that provides a description on the fuzzy inference system and edge extraction procedures implemented in the proposed system. The results obtained are compared with other methods in the section that follows subsequently. Finally, a proposal for future work is included in conclusion.

II. Application of Ratio-of-Averages

In [8], the RoA edge detector is used together with the Laplacian of Gaussian (LoG) edge detector to detect edges in speckle imagery. By taking the intersection of the LoG edge map (i.e. the zero-crossings) with the RoA edge map, the resulting edge map is able to extract edges from synthetic aperture radar applications. However, the method in [8] is not appropriate for use in ultrasound images because the character of the edges is fundamentally different [9]. Since ultrasound images are generated from acoustic waves reflected from tissue discontinuities, the edges in a typical image often appears as lines in an apparently constant-intensity background, rather than as boundaries between different regions in an image corrupted with simple additive noise [9].

In [9], speckle noise is described as a chaotic phenomenon caused when a coherent imaging system such as ultrasound is used to image a surface which is rough on the scale of the wavelength used. The surface produces many reflections in each resolution cell which add coherently to produce the speckle pattern. The speckle noise is often modeled as being at least weakly multiplicative, since the intensity of the speckle pattern at each point is directly related to the intensity of the reflection at that point. As a result, the performance of an edge detector searching simply for a large derivative magnitude will depend on the image intensity at each point, and will vary from location to location [9].

Consequently, steepness applied in [10] is not effective per se, but will vary with the underlying image intensity if the noise is multiplicative [8]. The steepness in [10] is approximated by computing the root mean square (rms) value

F. Ibrahim, N.A. Abu Osman, J. Usman and N.A. Kadri (Eds.): Biomed 06, IFMBE Proceedings 15, pp. 250-254, 2007
www.springerlink.com ' Springer-Verlag Berlin Heidelberg 2007

of the difference of neighborhood averages taken along the horizontal and vertical directions. To overcome this problem, steepness is applied together with symmetry in a fuzzy system in [10], thus providing an intuitive approach to determine the gradient magnitude. Furthermore, SRAD introduced in [11], is applied initially to reduce the speckle noise efficiently without over blurring the edges in [10]. SRAD is an edge sensitive diffusion method that uses the strengths of the partial differential equation (PDE) approach to produce edge-sensitive speckle reduction. SRAD uses the instantaneous coefficient of variation (ICOV), which combines a normalized gradient magnitude operator and a normalized Laplacian operator to act like an edge detector for speckle imagery. In overall, the method in [10] has produced favorable results by using rule-based fuzzy reasoning on local image characteristics.

Hence, the proposed method is an effort to improve the method in [10] by introducing the RoA to work along with the local image characteristics, i.e. steepness and symmetry, to define gradient magnitude in the image. Unlike steepness, the statistics of the overall RoA magnitude estimate do not depend on the underlying image intensity [8]. Therefore, the inclusion of RoA in the fuzzy system offers good potential for improvement, although the combined application of RoA and LoG edge detectors in [8] on echocardiogram does not yield satisfactory results. From observation, noise can be detected in ultrasound images where there is occurrence of very low steepness and high RoA. Therefore, steepness is retained in the proposed method as a check for false edge triggered by high RoA in the images.

III. Definition of Local Image Characteristics and RoA

The local image characteristics in the proposed method and the system in [10] are adapted from [12]. Similar to the gradient notion used in [12], the gradient magnitude of the pixel concern, i.e. the pixel (x,y) in the center of the 3X3 window in Figure 1, is determined by the characteristics of two neighboring regions on both sides of edge direction crossing the center pixel (x,y).

Steepness is measured by two components at orthogonal directions. Pixels that lie directly on the crossing of each steepness component are ignored to disregard noise effect as much as possible. For example, in Figure 1, pixels (x,y+1) and (x,y-1) are ignored when calculating the horizontal component of steepness for pixel (x,y). Likewise, pixels (x-1,y) and (x+1,y) are ignored when calculating the vertical component of steepness.

(x-1,y+1)	(x,y+1)	(x+1,y+1)
(x-1,y)	(x,y)	(x+1,y)
(x-1,y-1)	(x,y-1)	(x+1,y-1)

Fig. 1 A 3X3 window for steepness and symmetry evaluation

Thus, the horizontal component of steepness takes the absolute difference given as

$$S_h(x,y) = \left| R(x,y) - L(x,y) \right| \tag{1}$$

where *R(x,y)* and *L(x,y)* are the average intensity values of neighborhoods immediately to the right and left of pixel (x,y) respectively. The value of steepness used for fuzzy reasoning is estimated by computing the rms value of its components according to Equation (2).

$$S(x,y) = \left[S_h^2(x,y) + S_v^2(x,y) \right]^{1/2} \tag{2}$$

where S_y is the corresponding vertical component of steepness *S(x,y)*.

Symmetry is measured by horizontal and vertical components likewise. In a 3X3 window, there are only two pairs of pixels to be compared for each component. For example, along the horizontal steepness track, the corresponding symmetry component compares pixel (x-1,y+1) and (x-1,y-1) in one pair and pixels (x+1,y+1) and (x+1,y-1) in the other. The symmetry component is thus the sum of absolute differences of both pairs. To make the sum a positive value which increases with symmetry, it is subtracted from the largest possible value as in Equation (3).

$$M_h(x,y) = M_{\max} - \sum_{i=1}^{2} P_i(x,y) \tag{3}$$

where $M_h(x,y)$ is the horizontal symmetry component and *P(x,y)* is the absolute difference of a pixel pair in comparison.

Similar to computing steepness, the function to estimate the horizontal component of the overall RoA is

$$A_h(x,y) = \max\{ R(x,y)/L(x,y), L(x,y)/R(x,y) \} \tag{4}$$

F. Ibrahim, N.A. Abu Osman, J. Usman and N.A. Kadri (Eds.): Biomed 06, IFMBE Proceedings 15, pp. 250-254, 2007
www.springerlink.com ' Springer-Verlag Berlin Heidelberg 2007

The overall estimate value of symmetry and RoA taken for fuzzy reasoning is the rms values of their respective horizontal and vertical approximations.

IV. Fuzzy inference system and edge extraction

The proposed method aims to improve the boundary enhancement system in [10] by extending the fuzzy rules on local image characteristic and RoA. The fuzzy approach is adopted to handle ambiguous edge definition in noisy echocardiogram. Two Gaussian membership functions are assigned for each fuzzy input. The antecedents are linked using fuzzy operator *And* which applies the minimum function. The output of the fuzzy system is obtained via centroid defuzzication. The fuzzy rules applied are shown in Table 1.

The edge extraction procedures applied in this experiment is the same as in [10]. The procedures for edge extraction follow the sequence of contrast adjustment, hysteresis thresholding, and morphological edge extraction. All operations and the values of thresholds are determined empirically.

Table 1 Input/output of the fuzzy inference system

Input 1	**Input 2**	**Input 3**	**Output**
Steepness	**Symmetry**	**RoA**	**Gradient**
small	low	small	low
small	low	large	low
small	high	small	low
small	high	large	medium
large	low	small	low
large	low	large	medium
large	high	small	medium
large	high	large	high

V. Comparison of results

The output of the proposed system is compared to the results obtained in [10] and the Canny edge detector. Four sets of test data are used for the proposed method where each set is comprised of 5 sequential frames of a particular video. The results are compared quantitatively using Pratt s Figure of Merit (FOM) [11]. FOM ranges between 0 and 1, with unity for ideal edge detection. FOM is taken from the average reading of 5 sequential images for each data set.

Figure 2 shows the output of each method used for comparison. The results are compared to the desired edge images outlined manually from the raw echocardiograms. The parameter values chosen for Canny edge images are purely subjective and based on the best output with good representation.

Analysis via visual observation or quantitative measure shows that the proposed method is as good as the method in [10] compared to the Canny edge detector. As shown in Figure 2, the frame in test set 1 of the proposed method produced more accurate representation and the frame in test set 4 less noise. However, the proposed method show some loss of information in the frame of test set 2. In general, the proposed method offers no significant improvement to the method in [10].

Table 2 tabulates the FOM readings to give a quantitative comparison. The slight difference in the FOM readings is insignificant considering that they are compared to desired edge images outlined manually which are subject to observer variability.

Table 2 Average FOM for quantitative comparison

Test Data (5 in each set)	Canny Edge Detector	Method in [10] without RoA	Proposed method
Test set 1	0.67481	0.71022	0.71177
Test set 2	0.64588	0.72258	0.72544
Test set 3	0.52740	0.73537	0.73512
Test set 4	0.46935	0.54342	0.54677

VI. Conclusions

The flexibility of the fuzzy system used in [10] for echocardiogram boundary enhancement allows the proposed method to implement RoA and fine-tune the system in search for improvement. Indefinite edge definition in noisy echocardiogram caused by speckle and artifacts makes the fuzzy approach appropriate for the proposed method.

From the results obtained, the performance of the proposed method does not meet the expectation to produce significant improvement to the method in [10]. Therefore, for future work, the rule-based fuzzy inference system using steepness and symmetry in [10] is proposed to be optimized using Adaptive Neuro-Fuzzy Inference System (ANFIS) [13]. To save computation time and reduce complexity, RoA need not be included since it does not contribute any significant improvement in the proposed method.

F. Ibrahim, N.A. Abu Osman, J. Usman and N.A. Kadri (Eds.): Biomed 06, IFMBE Proceedings 15, pp. 250-254, 2007
www.springerlink.com ' Springer-Verlag Berlin Heidelberg 2007

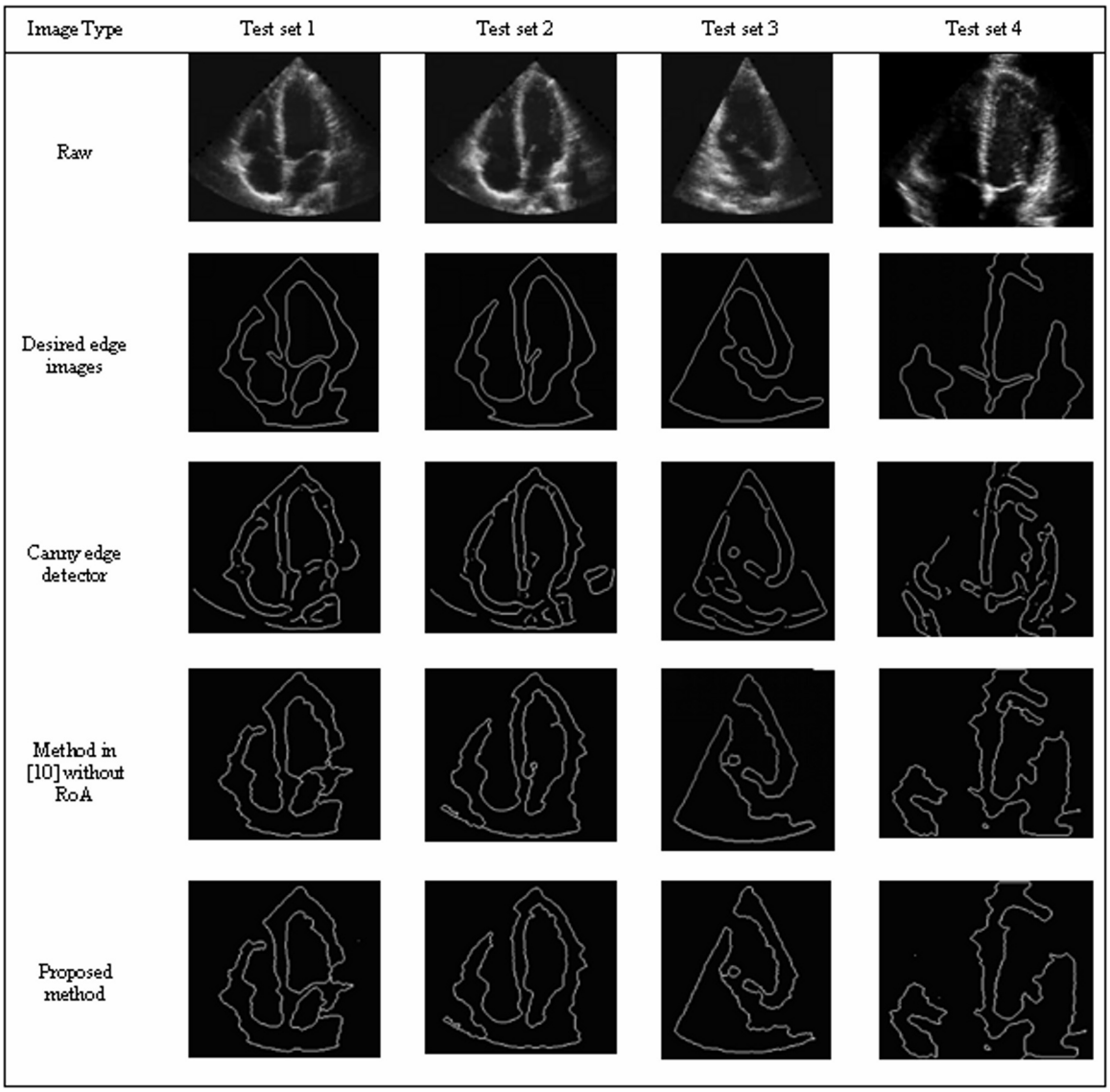

Fig. 2 Comparison of results

References

1. Detmer P R, Bashein G, Martin R W (1990) Matched filter identification for left-ventricular endocardial borders in transesophageal echocardiograms. IEEE Trans. Medical Imaging: 396-404.
2. Bosch, J G, Mitchell S C, Lelieveldt B P F et al. (2002) Automatic segmentation of echocardiographic sequences by active appearance motion models. IEEE Trans. Medical Imaging: 1374-1383.
3. Chu C H, Delp E J, Buda A J (1988) Detecting left ventricular endocardial and epicardial boundaries by digital two-dimensional echocardiography. IEEE Trans. Medical Imaging: 81 90.
4. Chalana V, Linker D T, Haynor D R et al. (1996) A multiple active contour model for cardiac boundary detection on echocardiographic sequences. IEEE Trans. Medical Imaging: 290-298.
5. Czerwinski R N, Jones D L, O Brien, W D Jr (1999) Detection of lines and boundaries in speckle images Application to medical ultrasound. IEEE Trans. Medical Imaging: 126 136.
6. Manivannan J, Reddy M R, Thanikachalam S et al. (2003) Endocardial edge detection by fuzzy inference system. IEEE TENCON 2003, Conference on Convergent Technologies for the Asia-Pacific Region, Bangalore, India, 2003, pp 3 5.
7. Chan S, Sainarayanan G, Ramachandran R (2006) Echocardiogram boundary enhancement using fuzzy inference system on multiscale derivative images, Int. Conference on Man-Machine Systems (ICOMMS), Kangar, Malaysia, 2006. In press.
8. Bovik A C (1998) On detecting edges in speckle imagery. IEEE Trans. On Acoustic, Speech, and Signal Processing:1618-1627.
9. Czerwinski R N, Jones D L, O Brien, W D Jr (1993) An approach to boundary detection in ultrasound imaging. IEEE Ultrasonics Symp., Baltimore, MD, 1993, pp 951-955.

F. Ibrahim, N.A. Abu Osman, J. Usman and N.A. Kadri (Eds.): Biomed 06, IFMBE Proceedings 15, pp. 250-254, 2007
www.springerlink.com ' Springer-Verlag Berlin Heidelberg 2007

10. Chan S, Sainarayanan G (2006) Echocardiogram boundary enhancement using rule-based fuzzy inference system on local image characteristics, Int. Conference on Man-Machine Systems (ICOMMS), Kangar, Malaysia, 2006. In Press.
11. Yu Y, Acton S T (2002) Speckle Reducing Anisotropic Diffusion,.IEEE Trans. Image Processing: 1260 1270.
12. Law T, Itoh H, Seki H (1996) Image filtering, edge detection, and edge tracing using fuzzy reasoning. IEEE Trans. Pattern Analysis and Machine Intelligence: 481-491.
13. Jang J-S R (1993) ANFIS Adaptive-Network-Based fuzzy inference system. IEEE Trans. Systems, Man, and Cybernetics: 665 685.

Address of the corresponding author:

Author: Sheila Chan Oi Yip
Institute: Universiti Malaysia Sabah
Street: Jalan UMS
City: Kota Kinabalu
Country: Malaysia
Email: sheilachan_oiyip@yahoo.com

F. Ibrahim, N.A. Abu Osman, J. Usman and N.A. Kadri (Eds.): Biomed 06, IFMBE Proceedings 15, pp. 250-254, 2007
www.springerlink.com ' Springer-Verlag Berlin Heidelberg 2007

Contrast Enhancement of MRI Images

A. Al-Manea and A. El-Zaart

Department of Computer Science, College of Computer and Information Sciences, King Saud University, Riyadh, Saudi Arabia

Abstract— **The technique of modification of the histogram of an image can be applied to the problem of image enhancement. Global histogram equalization and local area histogram equalization are two well-known techniques for the same purpose. In this paper new method is proposed to enhance the contrast of bimodal MRI images using histogram specification with Gamma distribution. The method is aimed to read the original image and calculate its histogram original histogram then apply the Maximum Likelihood Gamma Distribution (MLGD) method to get an accurate statistical information of the original histogram as the means and *prior* probabilities of the two modes, then we separate the two modes by shift the first mode left or shift the second mode right or perform both shifts. After that we will generate a new histogram called "Desired Histogram" using the new data. By applying a histogram specification method, a high contrast image will be produced. The new method of contrast enhancement of MRI image using histogram specification with Gamma distribution has been tested and showed good results.**

Keywords— **Contrast image enhancement, Histogram specification, Desired histogram, Gamma distribution**

I. Introduction

Magnetic resonance imaging (MRI) is an imaging technique used primarily in medical settings to produce high quality images of the inside of the human body. It is very necessary to enhance the contrast of such images before further processing or analysis can be conducted [8]. Image enhancement is a major area of image processing. Its principal objective is to process an image so that the result is more suitable than the original image for a specific application. There are several techniques to enhance an image [1]. Histogram equalization and specification have been widely used to enhance information in a gray scale image. The histogram specification technique has the advantage of allowing the output histogram to be specified as compared to histogram equalization, which attempts to produce an output histogram that is almost uniform. The problem of histogram specification method is to generate a desired histogram in order to construct the new improved image based on the desired histogram. In this paper, we used Gamma distribution in order to generate the desired histogram. Gamma distribution is more general than the Gaussian. It showed a good result in the case of radar images [4,10,11]. The idea of our method is to estimate the statistical parameters of the histogram using maximum likelihood with Gamma then we separate the two modes by shift the first mode left or shift the second mode right or perform both shifts. After that we will generate a new histogram called Desired Histogram using the new data. By applying a histogram specification method, a high contrast image will be produced. In section 2, we explain the feature of Gamma distribution. Section 3, presents the new method in details. Section 4 presents the results of the new method applied on MRI images. Finally, we conclude in section 5.

II. Gamma distribution

In probability theory and statistics, the Gamma distribution is a continuous probability distribution. The probability density function of the Gamma distribution in homogeneous area is known to [4, 10, 11]:

$$f(x,\mu,N)=\frac{2q}{\mu}\frac{N^N}{\Gamma(N)}\left(\frac{qx}{\mu}\right)^{2N-1}e^{-N(qx/\mu)^2}$$

where $q=\dfrac{\Gamma(N+0.5)}{\Gamma(N)\sqrt{N}}$, and x is the intensity of the pixel, μ is the mean value of the distribution and N represents the parameter shape of the distribution. The shape of the Gamma distribution could be symmetry or skewed to the right. Gamma Distribution is better than Gaussian because Gaussian works only with symmetric histograms but in the case of Gamma distribution, if we want a symmetric histogram, we set N to a high value. By using Gamma distribution we can get a histogram skewed to the right by setting N to a small value. Fig. 1 represents three shapes of Gamma distribution.

In this paper, we used Gamma maximum likelihood technique (MLGD) to approximate the original histogram. In the next section we will explain the basic idea of the new method of desired histogram generation using Gamma distribution in details.

F. Ibrahim, N.A. Abu Osman, J. Usman and N.A. Kadri (Eds.): Biomed 06, IFMBE Proceedings 15, pp. 255-258, 2007
www.springerlink.com ' Springer-Verlag Berlin Heidelberg 2007

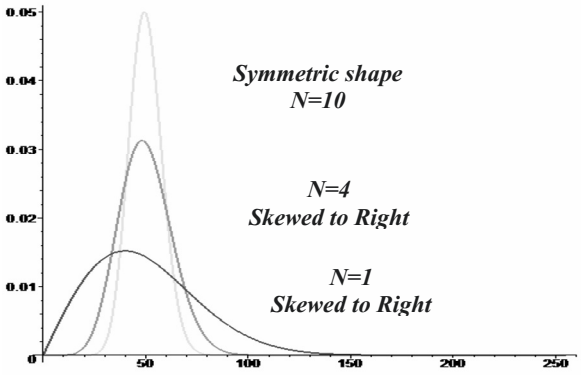

Fig. 1 Three Gamma distributions with different values of N

III. New desired histogram method using gamma distribution

In this paper, we work on the contrast enhancement of bimodal histogram. The main idea of our new method is to estimate the statistical parameters of the histogram using MLGD technique in order to obtain the shape of the original histogram. After that we can derive a desired histogram that must be a parent or close to the original histogram but with mode separations. This separation is done by shifting one or more than one mode in order to have a reasonable separation (high contrast).

We consider an original bimodal image *I(x,y)*. Let *h(x)* be its histogram. This histogram can be written as a combination of two Gamma distributions.

$$h(x) = \sum_{i=1}^{2} p_i f(x, \mu_i, N)$$
$$= p_1 f(x, \mu_1, N) + p_2 f(x, \mu_2, N)$$

Where (p_i, μ_i) are the statistical parameters of the i^{th} mode of the histogram, p_i and μ_i represents respectively the *prior* probability and the mean of that mode. The low contrast in image is caused by close values between μ_1 and μ_2 i.e. the difference value is small. There is no effect of *prior* probabilities p_1 and p_2 on the contrast level. For that, our method concentrates on the mean values. We have to make change on contrast from low to high by setting the difference values between means to a high value. Fig. 2 shows two cases of low contrast or overlap between two modes where the dotted curve is the original (overlapped) histogram and continues curve is the desired histogram. In fig. 2(a) the original histogram is formed by (μ_1=50, p_1=0.75, μ_2=80, p_2=0.25 and N=8).

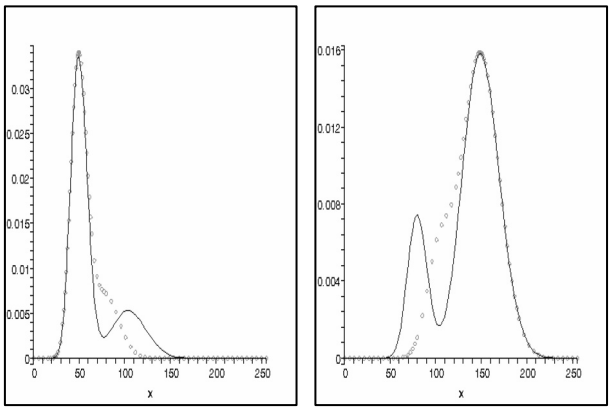

(a) (b)

Fig. 2 (a) Shift to right and (b) Shift to left

To generate a desired histogram for this case, we can only shift the value of μ_2 to right. For example, we can add 25 to μ_2. The new desired histogram is formed by (μ_1=50, p_1=0.75, μ_2=105, p_2=0.25 and N=8). The second overlap histogram in fig. 2(b) is formed by (μ_1=105, p_1=0.2, μ_2=150, p_2=0.8 and N=8). In this case of low contrast, we can only shift the value of μ_1 to left. For example, we can subtract 25 from μ_1. The new desired histogram is formed by (μ_1=80, p_1=0.2, μ_2=150, p_2=0.8 and N=8).

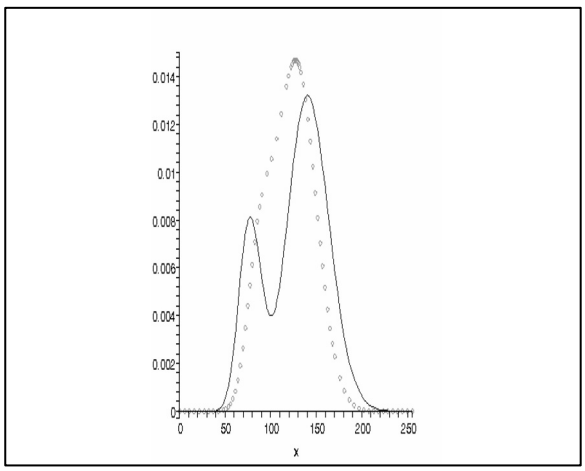

Fig. 3 Shift to right and left

The third overlap original histogram is presented in fig. 3. It is formed by (μ_1=90, p_1=0.25, μ_2=130, p_2=0.75 and N=10). In this case of low contrast, we can shift the value of μ_2 to right and the value of μ_1 to left. For example, we can add 12 to μ_2 and subtract 12 from μ_1. The new desired histogram is formed by (μ_1=78, p_1=0.25, μ_2=142, p_2=0.75 and N=10).

F. Ibrahim, N.A. Abu Osman, J. Usman and N.A. Kadri (Eds.): Biomed 06, IFMBE Proceedings 15, pp. 255-258, 2007
www.springerlink.com ' Springer-Verlag Berlin Heidelberg 2007

In Fig. 2 and 3, we separated between two modes by adding or subtracting some values from the means manually but in our method this is happens *automatically* by using the following equations: We find the range or interval of the histogram [*min*, *max*], where *max* is the maximum grey level in the original image and *min* is the minimum grey in the original image. After estimating the statistical parameters of the original histogram (p_i, μ_i) by MLGT technique, we do the following tasks:

1 - We can shift the first mode to left by updating the value of μ_1 as: $\mu_1 = \mu_1 - value1$

2 - We can shift the second mode to right by updating only the value of μ_2 as: $\mu_2 = \mu_2 + value2$

3 - We can also make both shifts left and right as:

1- *Read* the low contrast image.

2- *Compute* the original histogram.

3- *Apply* the MLGD on the original histogram to get precise of statistical information (p_i, μ_i) for each mode.

4- *Separate* the modes by shifting right or left or both.

5- *Construct* the desired histogram using data in the previous two steps.

6- *Map* the original histogram to match the desired histogram [1].

7- *Display* the enhanced image.

$\mu_1 = \mu_1 - value1$ *and* $\mu_2 = \mu_2 + value2$

Where *Value1=Min/2* and *Value2=(255-max)/2*

After modifying the value of μ_1 and/or μ_2 we then generate the desired histogram from the updated values of histogram and after that construct the output image. In the following, we will cite the algorithm of our method:

IV. Experimental results

In this paper images are enhanced based on histogram specification using Gamma distribution. We have tested our method on various MRI images. In this section, however, we only show several examples of MRI images and demonstrate the enhanced results then a comparison is made between the original image and the enhanced images.

Fig. 4 (a) shows the input image before enhancement, (b) shows the original histogram of the input image, (c) displays the output image from our method by using shift right and shift left to separate between modes (d) shows the desired histogram after applying shift right and shift left to separate between modes.

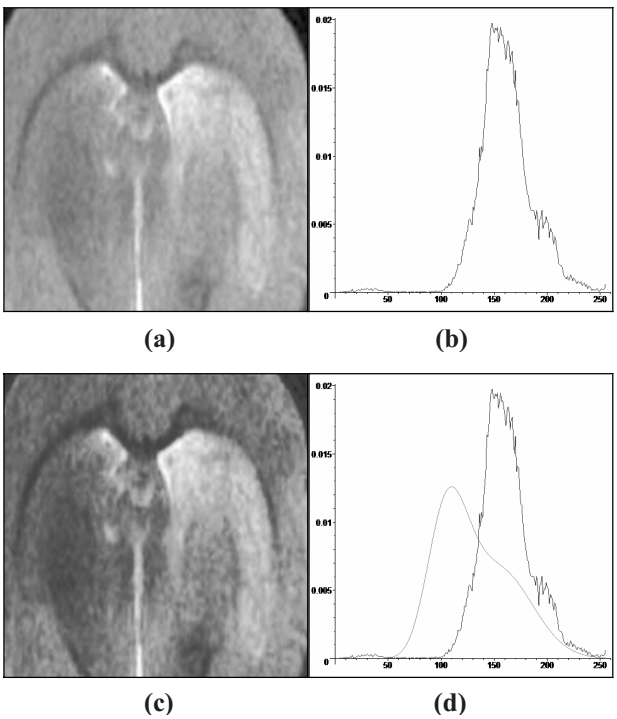

Fig. 4 (a) original image, (b) Its histogram, (c) enhanced image using desired histogram presented in (d), (d) original and desired histogram

Fig. 5 (a) shows the input image before enhancement. (b) shows the original histogram of the input image, (c) displays the output image from our method by using shift right only and, (d) shows the desired histogram after applying shift right only to separate between modes. Fig. 6, (a) shows the input image before enhancement. (b) shows the original histogram of the input image, (c) displays the output image from our method by using shift right only and, (d) shows the desired histogram after applying shift right only to separate between modes.

The same procedure for the result presented in fig. 6. As comparison between original and enhanced images, we can remark that there is an enhancement in the contrast.

F. Ibrahim, N.A. Abu Osman, J. Usman and N.A. Kadri (Eds.): Biomed 06, IFMBE Proceedings 15, pp. 255-258, 2007
www.springerlink.com ' Springer-Verlag Berlin Heidelberg 2007

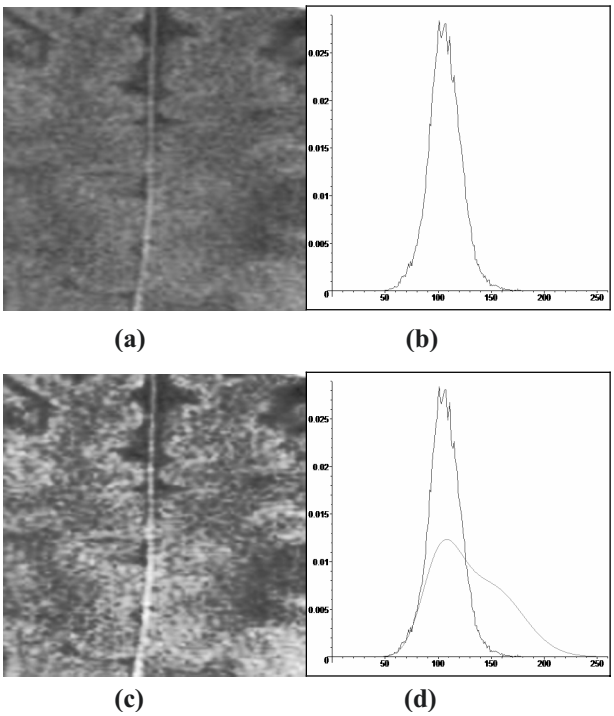

Fig. 5 (a) original image, (b) Its histogram, (c) enhanced image using desired histogram presented in (d), (d) original and desired histogram

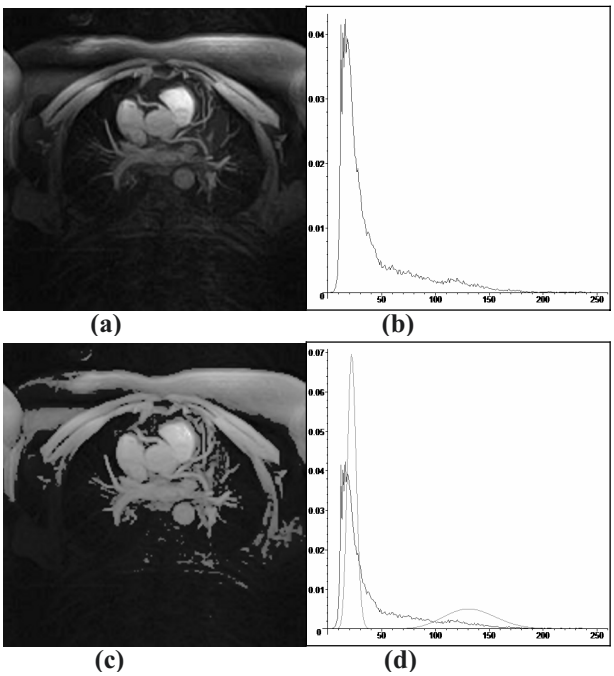

Fig. 6 (a) original image, (b) Its histogram, (c) enhanced image using desired histogram presented in (d), (d) original and desired histograms.

V. Conclusions and Future Work

In this paper, we present a fast approach for MRI images contrast enhancement by using histogram specification with Gamma distribution. The algorithm first, estimates the statistical parameters of the histogram in order to have the shape of the original histogram. Second, the desired histogram can be obtained by shifting one or two modes of the original histogram. The algorithm proposed in this paper can enhance MRI images effectively. It has advantages over histogram equalization. Experimental results show that the quality of enhanced images is good. Our method presented in this paper works only for bi-modal histograms, as future work, we will generalize this method to separate M modes and test it on different type of MRI images.

References

1. R. C. Conzalez and R. E. Woods, *Digial Image Processing*. New Jersey: Prentice-Hall, Inc., 2001.
2. Yang Xue-Dong, Qinghan Xio, Hazem Raafat, Direct Mapping Between Histograms: An Improved Interactive Image Enhancement Method , IEEE,19991.
3. American College of Radiology (ACR) and the Radiological Society of North America (RSNA), Magnetic Resonance Imaging (MRI) - Body , Radiological Society of North America, Inc. ,April 2003.
4. Ali El Zaart, Ali Al-Mejrad and Ali Saad, *Segmentation of Mammography Images for Breast Cancer Detection* , Proceedings of the Kuala Lumpur International Conference, On Biomedical Engineering 2004, pp. 225-228. September 2-4, 2004, Kuala Lumpur, Malaysia
5. S. D. Chen and A. R. Ramli, Contrast enhancement using recursive mean-separate histogram equalization for scalable brightness preservation, *IEEE Trans. Consumer Electron.*, vol. 49, no. 4, pp. 1301 1309, Nov. 2003.
6. Sun Chi-Chia, Shanq J. Ruan, Mon C. Shie, TunW. Pai, Dynamic Contrast Enhancement based on Histogram Specification , IEEE Transactions on Consumer Electronics, 51(4), Nov. 2005.
7. Chen Bor-Tow, Yung S. Chen, Wen H. Hsu, Automatic Histogram Specification Based on Fuzzy Set Operations for Image Enhancement , IEEE SIGNAL PROCESSING LETTERS, 2(2), Feb. 1995.
8. Yu Zeyun, Chandrajit Bajaj, A Fast and Adaptive Method For Image Contrast Enhancement . International Concefrence on Image Processing, pp. 1001-1004, 2004
9. Jian Wang Bing, Liu S. qian, Li Qing, Zhou H. xin, A real-time contrast enhancement algorithm for infrared images based on plateau histogram , Infrared Physics & Technology, 2005.
10. Ali El Zaart, Djemel Ziou, Shangrui Wang and Qingshan Jiang, *Segmentation of SAR images.* Pattern Recognition Journal, Vol. 35, No. 3, pp. 713-724, March 2002.
11. Ali El Zaart and Djemel Ziou, Mixture Modelling Using Minimum Message Length. 13th Conference in Pattern Recognition and Artificial Intelligent (RIFIA), pp. 509-518, 2002, Conference, Angres, France, January 2002.

Address of the corresponding author:

Author: A. Al-Manea
Institute: Department of Computer Science, College of Computer and Information Sciences, King Saud University
City: Riyadh
Country: Saudi Arabia

F. Ibrahim, N.A. Abu Osman, J. Usman and N.A. Kadri (Eds.): Biomed 06, IFMBE Proceedings 15, pp. 255-258, 2007
www.springerlink.com ' Springer-Verlag Berlin Heidelberg 2007

Converting Data from the Lunar DPX-IQ Bone Densitometer for Interoperability

L.K. Tan[1,2], K.H. Ng[1,2], S. Shaharuddin[2] and B.J.J. Abdullah[1]

[1] Department of Biomedical Imaging
[2] Medical Physics Unit, Faculty of Medicine, University of Malaya, Kuala Lumpur, Malaysia

Abstract— **The Lunar DPX-IQ is a bone densitometer from the Lunar Corporation (now part of GE Healthcare), and was released around the year 1997. The main control system is built upon the MS-DOS operating system, and stores its data in a proprietary database and format. The system is not DICOM compatible, has no built-in computer networking functionality, and does not have any functionality to export its images or data to any standard format. With the ongoing consolidation and centralization of modality data, the Lunar DPX-IQ risks being prematurely retired from service due to its inoperability with other systems.**

This paper describes an early effort to extract a digital copy of the scan data in a standard format from the DPX-IQ. We have made no attempt to implement DICOM compatibility or other advanced functionality, though our effort may be seen as a first step towards a more comprehensive solution. Our method revolves around redirecting and capturing the printer data stream via port redirection, followed by a PCL to PDF conversion resulting in a digital copy of the scan report ready for archiving. Future improvements to the project will focus on a parser to extract patient and study metadata from the captured PCL file. Complete DICOM-ization of the data may continue from there.

Keywords— **File Formats, Lunar DPX-IQ, Data Conversion, Image Conversion**

I. Introduction

A bone densitometer is a medical imaging device that uses x-ray beams to measure the bone mineral density (BMD) of a patient. The usual output result is a projection image of the scanned portion of the skeleton, as well as the calculated BMD index and other reference data [1,2].

The Lunar DPX-IQ is a bone densitometer from the Lunar Corporation (now part of GE Healthcare), and was released around the year 1997. The main control system is built upon the MS-DOS operating system; data storage is via a proprietary database and format. The system is not DICOM compatible, has no built-in computer networking functionality, and does not have any functionality to export its images or data to any standard format. With the ongoing consolidation and centralization of modality data, the Lunar DPX-IQ risks being prematurely retired from service due to its inoperability with external data management systems.

This paper describes an early effort to extract a digital copy of the scan data into a standard format from the DPX-IQ. We have made no attempt to implement DICOM compatibility or other advanced functionality, though the effort may be seen as a first step towards a more comprehensive solution. Successful implementation would allow such a legacy system to be integrated into modern healthcare management, enabling continued use. The method revolves around redirecting and capturing the printer data stream via port redirection, followed by a PCL to PDF conversion resulting in a digital copy of the scan report ready for archiving.

II. Methodology

A. Initial Attempts

Initial efforts revolved around two possibilities: screen capturing and printer output capture via Windows print redirection, i.e., running the DPX-IQ control software within a DOS-box in Windows.

Screen captures were attempted using a pure DOS program (Screenthief; Villa Software [3]) and a Windows program capable of capturing DOS windows (SnagIt; TechSmith Corporation [4]). However, the captured images turned out severely distorted or corrupted. A possible reason for this may be due to the DPX-IQ control software utilizing custom DOS memory extenders and non-VESA video modes.

Windows print redirection also failed to work, due to the DPX-IQ control software utilizing custom built-in printer drivers rather than through direct DOS printing. This also meant that the choice of compatible printers is very limited.

B. DOS LPT Redirection

We eventually settled on software redirection of the DOS LPT port, i.e., a virtual data dump of the printer port. It turned out that DOS LPT port redirection software was once relatively common, but their usage has understandably phased out. Upon investigation, we noted that most of the existing redirection software (PRN2FILE; Tom Kihlken. LPT2DSK; George G Bouche [5]) were designed for plain text printing, and subsequently failed with buffer full errors

F. Ibrahim, N.A. Abu Osman, J. Usman and N.A. Kadri (Eds.): Biomed 06, IFMBE Proceedings 15, pp. 259-261, 2007
www.springerlink.com ' Springer-Verlag Berlin Heidelberg 2007

when fed with graphical output from the DPX-IQ control software.

A suitable program was eventually found (PRINDIR; JM Allen Creations [5]), a DOS terminate-stay-resident (TSR) program with configurable buffer sizes. It successfully captured all graphical printouts from the DPX-IQ control software to a specified file.

C. PCL Conversion

We initially assumed the captured printer output would be in Postscript (PS) format, from which conversion to other formats would a straightforward process. However, it turned out that the majority of printers supported by the DPX-IQ control software were Hewlett Packard (HP) models, thus the captured output turned out to be in Printer Command Language 5 (PCL5) [6].

The second step thus involves conversion of the captured print output from PCL5 to a standard archive format, in this case Portable Document Format (PDF) (Fig. 1). There are numerous programs offering this capability, although the conversion quality varies widely. We settled on PCLWorks by Page Technology Marketing, Inc [7].

In summary, the process of capturing and transforming data from the Lunar DPX-IQ involves two steps: redirection and capture of printer output, and conversion of the capture output to PDF (Fig. 2).

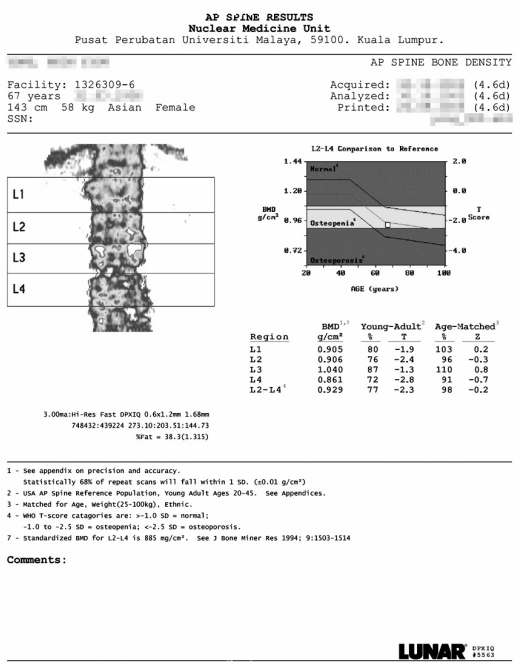
AP SPINE RESULTS
Nuclear Medicine Unit
Pusat Perubatan Universiti Malaya, 59100. Kuala Lumpur.

AP SPINE BONE DENSITY

Facility: 1326309-6
67 years
143 cm 58 kg Asian Female
SSN:

Acquired: (4.6d)
Analyzed: (4.6d)
Printed: (4.6d)

L1
L2
L3
L4

L2-L4 Comparison to Reference

Region	BMD[1,7] g/cm²	Young-Adult[2] %	Young-Adult[2] T	Age-Matched[3] %	Age-Matched[3] Z
L1	0.905	80	-1.9	103	0.2
L2	0.906	76	-2.4	96	-0.3
L3	1.040	87	-1.3	110	0.8
L4	0.861	72	-2.8	91	-0.7
L2-L4[4]	0.929	77	-2.3	98	-0.2

3.00ma:Hi-Res Fast DPXIQ 0.6x1.2mm 1.68mm
748432:439224 273.10:203.51:144.73
%Fat = 38.3(1.315)

1 - See appendix on precision and accuracy.
Statistically 68% of repeat scans will fall within 1 SD. (±0.01 g/cm²)
2 - USA AP Spine Reference Population, Young Adult Ages 20-45. See Appendices.
3 - Matched for Age, Weight(25-100kg), Ethnic.
4 - WHO T-score catagories are: >-1.0 SD = normal;
-1.0 to -2.5 SD = osteopenia; <-2.5 SD = osteoporosis.
7 - Standardized BMD for L2-L4 is 885 mg/cm². See J Bone Miner Res 1994; 9:1503-1514

Comments:

LUNAR DPXIQ #8563

Fig. 1 Sample captured output from the Lunar DPX-IQ in PDF format

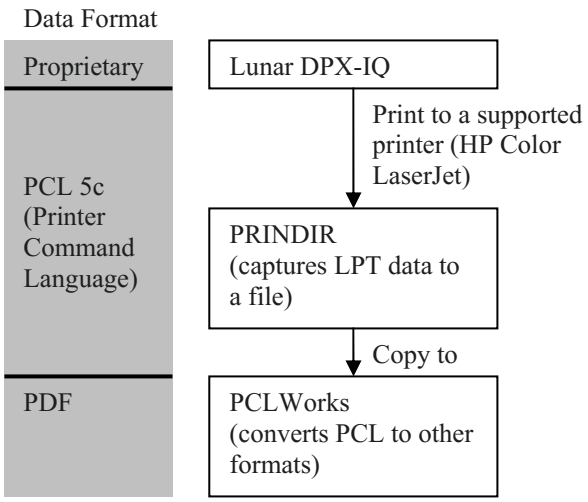

Fig. 2 Overview of data capture process from the Lunar DPX-IQ bone densitometer

III. Discussion

The stated goal of this project was to obtain a full-quality digital capture of the scan results and output. By these criteria we may deem the methodology a success. However, if the captured images are to be reliably indexed, certain core metadata such as patient name and study date are still missing.

The Lunar DPX-IQ appears to be using ASCII as its PCL output format. It is thus highly likely that such useful metadata may be extracted from the captured PCL file itself. Preliminary trials proved quite productive; we were able to take advantage of positional and formatting information in the standard output format of the DPX-IQ report sheet to identify extractable data.

For example, the patient name was found to be reliably preceded by hex codes 0x1b 0x2a 0x70 0x39 0x30 0x78 0x32 0x30 0x30 0x59, which we deemed to be PCL positioning code (Fig. 3). Study date was even more straightforward; a simple ASCII search of the term Acquired: proved a reliable marker of its location. There is little doubt that further effort would produce a reliable parser for much of the useful metadata.

F. Ibrahim, N.A. Abu Osman, J. Usman and N.A. Kadri (Eds.): Biomed 06, IFMBE Proceedings 15, pp. 259-261, 2007
www.springerlink.com ' Springer-Verlag Berlin Heidelberg 2007

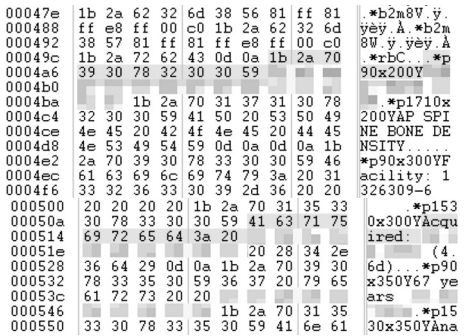

Fig. 3 Hex / ASCII dumps of the captured PCL data. Highlighted addresses indicate possible parse points for data extraction, including positional data (top) and text matching (bottom).

IV. Conclusion

A method has been described to extract and convert the scan output and results of the Lunar DPX-IQ bone densitometer into a standard format (PDF), enabling interoperability with modern data management systems, thus extending the useful lifespan of a legacy device. Ongoing improvements promise reliable extraction of patient and study metadata in the future.

References

1. Banks L M. Dual energy X-ray absorptiometry (DXA). In: Grainger & Allison's Diagnostic Radiology: A Textbook of Medical Imaging, eds. Granger R G and Allison D. New York: Churchill Livingstone, (1997)
2. Webber C E. (2006) Photon absorptiometry, bone densitometry and the challenge of osteoporosis. Phys Med Biol 51:R169-R185
3. Bone Densitometry at http://www.radiologyinfo.org
4. Villa Software at http://www.villa.nildram.co.uk (closed)
5. TechSmith Corporation at http://www.techsmith.com
6. MSDOS Printing at http://www.bookcase.com/library/software
7. Hewlett-Packard Co. (1999) PCL 5 Printer Language Technical Quick Reference Guide.
8. Page Technology Marketing Inc. at http://www.pagetech.com

F. Ibrahim, N.A. Abu Osman, J. Usman and N.A. Kadri (Eds.): Biomed 06, IFMBE Proceedings 15, pp. 259-261, 2007
www.springerlink.com ' Springer-Verlag Berlin Heidelberg 2007

Evaluation of Texture Analysis Techniques for Characterization of Multimode-Based Liver Images Using SGLCM and FOS

S. H. Chung and R. Logeswaran

Faculty of Engineering, Multimedia University, Cyberjaya, Malaysia

Abstract—**This paper is a study of using Spatial Grey-Level Co-occurrence Matrix (SGLCM) and First-Order Statistics (FOS), for characterization of liver tissue. SGLCM and FOS are applied on three modalities of liver images, consisting of Magnetic Resonance Imaging (MRI), Ultrasound and Computed Tomography (CT), for the diagnosis of liver diseases. The results indicate that the proposed texture analysis methodology is able to characterize cyst, fatty liver and healthy liver in clinical test images with high success rates. The study indicates viable use of SGLCM and FOS in multimode image analysis and development of a texture-based multimode computer-aided diagnostic (CAD) system for liver diseases.**

Keywords— **Texture analysis, Spatial Grey-Level Co-occurrence Matrix (SGLCM), First-Order Statistics (FOS), MRI, Ultrasound, Computed Tomography (CT)**

I. Introduction

Computer-assisted liver tissue characterization can be defined as the characterization of liver tissue made by a physician who takes into consideration the results from a computer-based image analysis system [1]. Texture analysis for tissue characterization can provide useful information that may not be obtained through visual interpretation. For the diagnosis of liver diseases, many researchers have developed texture-based computer aided systems [2], but the tissue structure and attenuation in medical images cannot be represented by just a single parameter extracted from one diagnostic imaging modal as this can reduce certainty in diagnosis. Several studies have shown that the characterization accuracy of liver diseases using just simple visual interpretation was estimated to be only around 70% [3]. As such, a study on texture analysis techniques on multimode-based liver images is proposed in this paper. The Modalities Magnetic Resonance Imaging (MRI) produces images of the insides of the body using a magnetic field that makes the body s cells vibrate [4]. The vibrations give off electrical signals which are interpreted and turned into very detailed images of slices of the body. MRI may be used to make images of every part of the body, including the bones, joints, blood vessels, nerves, muscles and organs. Different types of tissue show up in different grey-scale intensities on a computer-generated image. Ultrasound uses high-frequency sound waves. It is one of the safest methods used in imaging human organs or their functions [5]. Ultrasound images can also show movement of internal tissues. CT-scans, on the other hand, employ radiology and is a method that provides two-dimensional slices of a designated target area in the patient s body [6]. CT-scans use X-ray taken from different angle and processed with a workstation to become a 3-D image called a tomogram [6]. Examples of healthy liver in MRI, CT and Ultrasound images are shown in Figure 1.

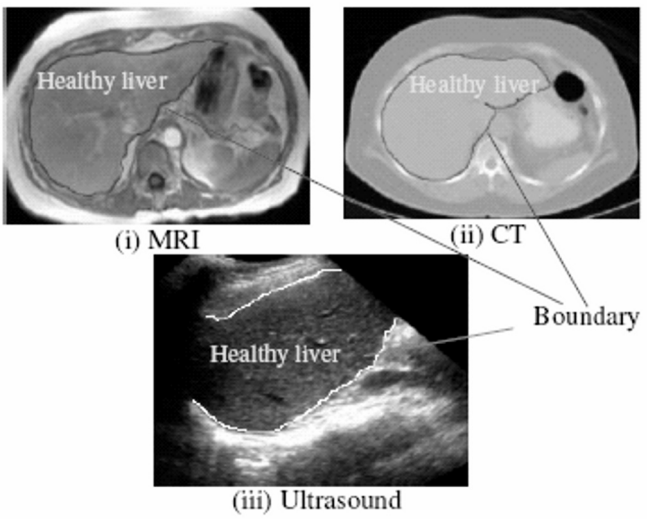

Fig. 1: Healthy liver images

II. Liver diseases

Liver diseases can be divided into two main categories, focal liver diseases and diffused liver diseases. A focal liver disease is where the pathology is concentrated in a small area, while the rest of the liver volume remains normal. A diffused liver disease is where the pathology is distributed over the liver volume. An example of a focal liver disease is liver cyst, a closed sac having a distinct membrane and developing abnormally in a liver [4]. Cysts may often be dangerous as they may have negative effects (e.g. constriction) on the nearby tissue. They may contain air, fluids, or semi-solid material, thus a cyst may be identified as an abnormal fluid-filled sac-like structure [4]. In the liver pa-

F. Ibrahim, N.A. Abu Osman, J. Usman and N.A. Kadri (Eds.): Biomed 06, IFMBE Proceedings 15, pp. 262-266, 2007
www.springerlink.com ' Springer-Verlag Berlin Heidelberg 2007

renchyma, a cyst is a thin-walled bubble or cavity that may be empty or contain fluid [4]. Figure 2 depicts the liver cysts in MRI, CT and Ultrasound images.

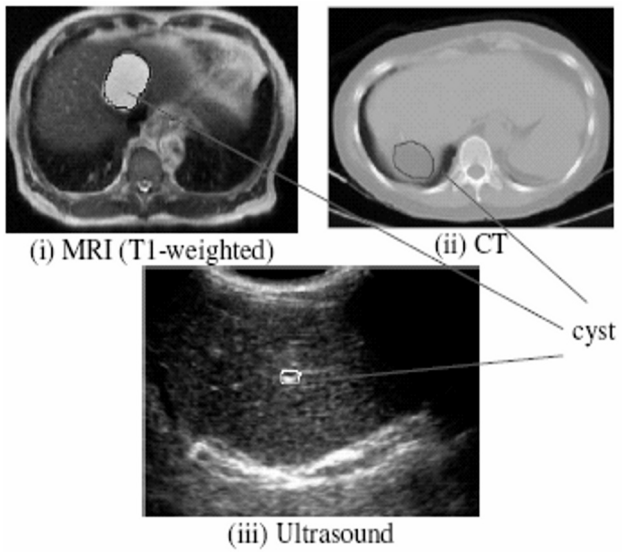

Fig. 2 Liver cyst images

An example of diffused liver disease is fatty liver, also known as Non-Alcoholic Fatty Liver Disease (NAFLD). It is the excessive accumulation of a type of fat, triglyceride, inside the liver cells, causing liver enlargement, tenderness, and abnormal liver function [7]. Fatty liver will progress to advance scarring of the liver, fibrosis and cirrhosis, which is referred to as nonalcoholic steatohepatitis (NASH) [8]. Figure 3 shows fatty liver disease in MRI, CT and Ultrasound images.

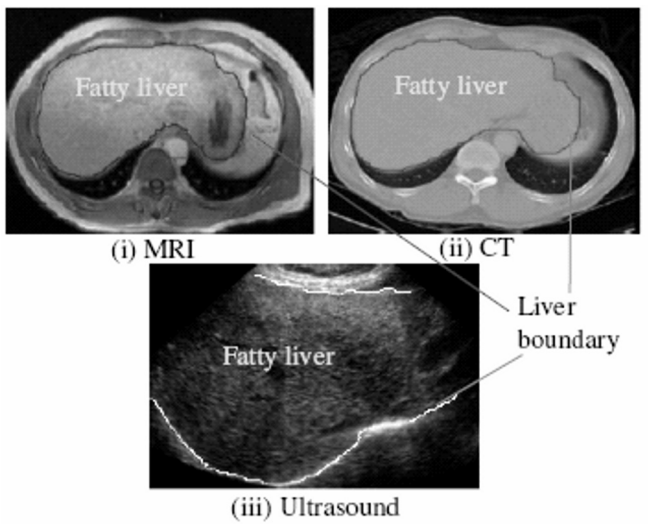

Fig. 3 Fatty liver images

III. Texture Analysis Overview

There is a considerable number of texture analysis algorithms used to characterize image texture over the years [2]. The most well known are Spatial Grey-Level Co-Occurrence Matrix (SGLCM), Fourier Power Spectrum (FPS), Grey Level Different Statistics (GLDS) and Laws Texture Energy Measures [9]. In this paper, two different analysis techniques are used to differentiate the liver tissues, namely SGLCM and First-Order Statistics (FOS). Regions of interest (ROI) from cysts, fatty liver and healthy liver images are used as input for the FOS and SGLCM calculations.

A. First-Order Statistics (FOS)

FOS describes the grey-level distribution without considering spatial independence. As a result FOS can only describe echogenity of texture and the diffuse variation characteristics within the ROI [10]. In this approach, the parameters derived from the grey-level histogram are average grey-level, standard deviation, entropy, skewness, kurtosis and coefficient of variance. These features algorithms are described by the following equations (1)-(6) where G is the total grey-level in the image and *i* H represents the pixel intensity at grey-level *i*.

$$\text{Average grey-level,} \quad \mu = \sum_{i=0}^{G-1} iH_i \tag{1}$$

$$\text{Standard deviation,} \quad \sigma = \left(\sum_{i=0}^{G-1} (i-\mu)^2 H_i \right)^{\frac{1}{2}} \tag{2}$$

where σ measures the global contrast in the image and μ is the average pixel intensity.

$$\text{Entropy,} \quad s = -\sum_{1=0}^{G-1} H_i \log H_i \tag{3}$$

where *s* measures the uniformity of the histogram. This quantity is widely used in image compression.

$$\text{Skewness,} \quad \gamma_1 = \frac{1}{\sigma^3} \sum_{i=0}^{G-1} (i-\mu)^3 H_i \tag{4}$$

where γ_1 measures the extent to which outliers favor one side of the distribution. Skewness is invariant under a linear grey-scale transformation.

$$\text{Kurtosis,} \quad \gamma_2 = \frac{1}{\sigma^4} \sum_{i=0}^{G-1} (i-\mu)^4 H_i - 3 \tag{5}$$

F. Ibrahim, N.A. Abu Osman, J. Usman and N.A. Kadri (Eds.): Biomed 06, IFMBE Proceedings 15, pp. 262-266, 2007
www.springerlink.com ' Springer-Verlag Berlin Heidelberg 2007

where γ_2 measures the peakedness or tail prominence of the distribution. It is 0.0 for the Gaussian distribution and is invariant under a linear grey-scale transformation.

$$\text{Coefficient of variance,} \quad cv = \frac{\sigma}{\mu} \tag{6}$$

where cv is invariant under a change of scale. Thus, if the intensity scale has a natural zero, then the cv will be a scale invariant measure of global contrast.

IV. SGLCM

The SGLCM algorithm is based on the assumption that texture properties of an image are contained in the overall or average spatial relationship between the grey-levels [11]. SGLCM is based on the estimation of the second-order conditional probability density function (7) [12].

$$f(i, j \mid d, \theta) \tag{7}$$

where $\theta = 0°, 45°, 90°, 135°, 180°, 225°, 270°$ and $315°$

Each $f(i,j|d,\theta)$ represents the probability of going from grey-level i to grey-level j, given that the inter-sample spacing is d and the direction is given by the angle θ. The features derived from SGLCM are entropy, contrast, homogeneity and correlation, as given by (8)-(11) where $S_\theta(i, j, d)$ represents the SGLCM matrix.

$$\text{Entropy, } H(S_\theta(d)) = \sum_{i=0}^{NG-1} \sum_{j=0}^{NG-1} S_\theta(i,j,d) \log S_\theta(i,j,d) \tag{8}$$

where $S_\theta(i, j, d)$ is the (i, j)th entry in a co-occurrence matrix, NG is the number of grey levels in the image from which the SGLCM matrices are extracted.

Contrast,

$$Con(S_\theta(d)) = \sum_{i=0}^{NG-1} \sum_{j=0}^{NG-1} (i-j)^2 S_\theta(i,j,d,\theta) \tag{9}$$

Homogeneity,

$$L(S_\theta(d)) = \sum_{i=0}^{NG-1} \sum_{j=0}^{NG-1} \frac{1}{1+(i-j)^2} S_\theta(i,j,d) \tag{10}$$

Contrast,

$$C(S_\theta(d)) = \frac{\sum_{i=0}^{NG-1} \sum_{j=0}^{NG-1} (i-\mu_i)(j-\mu_j) S_\theta(i,j,d,\theta)}{\mu_i \mu_j} \tag{11}$$

where μ_i and μ_j refer to the mean intensity values of the image in the x and y directions, respectively.

V. RESULTS AND ANALYSIS

Using the three modalities of liver images, FOS and SGLCM texture analysis techniques are applied to evaluate the ability of first-order and second-order statistical measurements in characterizing the liver tissue. For all images, 4 x 4 pixels image blocks were selected on various parts of the liver and used in the evaluation. As observed in Table 1, SGLCM analysis shows that entropy and correlation are useful for characterizing liver cyst, fatty liver and healthy liver in MRI images. For liver cysts, entropy is in the range of 5.174-7.911 and correlation in the range of 5.962-6.997. As for fatty liver classification, entropy is in the range of 2.487-3.862 with correlation in the range of 2.300- 4.932. Finally for healthy liver classification, entropy is in the range of 0.054-1.954 and correlation within the range of 0.071-1.500.

Table 1 Classification of liver cyst, fatty liver and healthy liver using entropy and correlation of SGLCM for MRI images.

MRI	Entropy		Correlation	
Liver Tissue	Min	Max	Min	Max
Liver Cyst	5.174	7.911	5.962	6.997
Fatty Liver	2.487	3.862	2.300	4.932
Healthy Liver	0.054	1.954	0.071	1.500

From the SGLCM results obtained for the Ultrasound modality, only contrast is selected for classification of liver cyst, fatty liver and healthy liver. The contrast values for liver cyst is (3.012-4.571), fatty liver (1.450- 2.699) and healthy liver (0.103-1.109), as shown in Table 2.

Table 2 Classification of liver cyst, fatty liver and healthy liver using contrast of SGLCM for Ultrasound images.

Ultrasound	Contrast	
Liver Tissue	Min	Max
Liver Cyst	3.012	4.571
Fatty Liver	1.450	2.699
Healthy Liver	0.103	1.109

For CT liver images, only correlation is selected for classification of liver cyst, fatty liver and healthy liver. The optimum correlation feature range selected based on the results are listed in Table 3.

F. Ibrahim, N.A. Abu Osman, J. Usman and N.A. Kadri (Eds.): Biomed 06, IFMBE Proceedings 15, pp. 262-266, 2007
www.springerlink.com ' Springer-Verlag Berlin Heidelberg 2007

Table 3 Classification of liver cyst, fatty liver and healthy liver using correlation of SGLCM for CT images.

CT	Correlation	
Liver Tissue	**Min**	**Max**
Liver Cyst	4.230	4.950
Fatty Liver	3.170	3.900
Healthy Liver	2.160	2.850

For the FOS experiments and evaluation, average grey-level of MRI and CT liver images, as shown in Table 4, is useful for characterizing the three liver classes. None of the FOS measures were successful at characterizing the liver tissues in the Ultrasound images.

Table 4 Classification of liver classes using average grey-level based on FOS for MRI and CT images.

	Average grey-level			
Modalities	**MRI**		**CT**	
Liver Tissue	**Min**	**Max**	**Min**	**Max**
Liver Cyst	92	146	91	143
Fatty Liver	41	64	38	63
Healthy Liver	5	23	10	25

The overall evaluation results of the two texture analysis techniques are shown in Table 5. The results represent the success rate achieved by each texture analysis technique in correctly identifying the liver tissue in diagnosing the liver condition. The results are for experimentation on 462 clinical images in total, comprising of 162 MRI (62 cyst, 47 fatty liver, 53 healthy liver), 148 CT (49 cyst, 52 fatty liver, 47 healthy liver) and 152 Ultrasound (41 cyst, 52 fatty liver, 59 healthy liver) as shown in Table 6.

Table 5 Comparison of classification performance for each texture analysis algorithm.

Liver Cases	**FOS**	**SGLCM**
Liver Cyst	79.6%	81.5%
Fatty Liver	75.8%	85.2%
Healthy Liver	72.1%	89.2%
Overall Accuracy	75.8%	85.3%

The results show that FOS achieved 75.8% overall accuracy for characterizing liver tissues in MRI and CT images, and failed to characterize the Ultrasound images. SGLCM achieved 85.3% overall accuracy for characterizing all three liver classes for MRI, Ultrasound and CT images.

Table 6 MRI, CT-scans and Ultrasound images used in FOS and SGLCM.

Liver Tissue	**MRI**	**CT**	**Ultrasound**	**Total**
Liver Cyst	62	49	41	152
Fatty Liver	47	52	52	151
Healthy Liver	53	47	59	159
Total	162	148	152	462

VI. Conclusions

In this paper, the evaluation of multimodality texture analysis has been presented, aiming to discriminate three different liver classes, namely, liver cyst, fatty liver and healthy liver from MRI, CT and Ultrasound images. The research indicates successful classification of the three liver classes in clinical test images, using SGLCM and FOS, achieving high success rates. The paper details the specific FOS (i.e. average grey-level) and SGLCM (i.e. entropy, correlation and contrast) for possible use in liver tissue identification in CAD systems.

References

1. KIM, S.I., CHOI, K.C. and LEE, D.S. (1991): Texture classification using run difference matrix , Proceedings of Ultrasonics Symposium. 2(10), pp. 1097-1100
2. VALANIS, I., MOUGIAKAKOU, S.G., NIKITA, K.S. and NIKITA, A. (2004): Computer-aided Diagnosis of CT Liver Lesions by an Ensemble of Neural Network and Statistical Classifiers , Proceedings of IEEE International Joint Conference on Neural Networks, 3, pp. 1929-1934
3. CHEN, E.L., CHUNG, P.C., CHEN, C.L., TSAI, H.M. and CHANG, C.L. (1996): An automatic diagnostic system for CT liver image classification , IEEE Transactions on Biomedical Engineering, 45(6), pp. 783-794
4. KIM, S.I., CHOI, K.C. and LEE, D.S. (1991): Texture classification using run difference matrix , Proceedings of Ultrasonics Symposium. 2(10), pp. 1097-1100
5. A.H. MIR, M. HANMANDLU and S.N. TANDUN (1993): Texture Analysis of CT Images , IEEE Transactions on Computers, 42(4), pp. 501-507
6. A. CARRILLO, J.L. DUERK, J.S. LEWIN, D.L. WILSON (2000): Semiautomatic 3-D image registration as applied to interventional MRI liver cancer treatment , IEEE Transactions on Information Technology in Biomedicine, 19, pp. 175-185
7. M. GLETSOS, S.G. MOUGIAKAKOU, G.K. MATSOPOULUS, K.S. NIKITA, A.S. NIKITA and D. KELEKIS, A Computer-aided Diagnostic System to Characterize CT Focal Liver Lesions: Design and Optimization of a Neural Network Classifier , IEEE Transactions on Information, 42, pp.35-41
8. S. KITAGUCHI, S. WESTLAND and M.R. LUO (2005): Suitability of Texture Analysis Methods for Perceptual Texture , Proceedingsof the 10th Congress of the International Colour Association, 10, pp. 923-926
9. M. MICHEL (2005): Fatty liver: Nonalcoholic Fatty Liver Disease (NAFLD) and Nonalcoholic Steatohepatitis (NASH) , MedicineNet, pp. 1-14

F. Ibrahim, N.A. Abu Osman, J. Usman and N.A. Kadri (Eds.): Biomed 06, IFMBE Proceedings 15, pp. 262-266, 2007
www.springerlink.com ' Springer-Verlag Berlin Heidelberg 2007

10. B. JULESZ, Experiments in the Visual Perception of Texture , Scientific American, 232(4), pp. 34-43
11. D. GOLDBERG (1989): Genetic Algorithms in Search, Optimization and Machine Learning, Addison-Wesley, pp. 192-203
12. A. MATERKA and M. STRZELECKI (1998): Texture Analysis Method-A Review , COSTB11 Report, pp. 1-33
13. R. HARALICK (1979): Statistical and Structural Approaches to Texture , Proceedings of IEEE, 67(5), pp. 786-804
14. G.D. KENDALL and T.J. HALL (2002): Performing fundamental image processing operations using quantized neural networks , International Conference on Image Processing and its Applications. 4(1), pp. 226-229

Address of the corresponding author:

Author: Sheng Hung, Chung
Institute: Faculty of Engineering, Multimedia University
Street: Jalan Multimedia
City: Cyberjaya
Country: Malaysia
Email: shchung@mmu.edu.my

F. Ibrahim, N.A. Abu Osman, J. Usman and N.A. Kadri (Eds.): Biomed 06, IFMBE Proceedings 15, pp. 262-266, 2007
www.springerlink.com ' Springer-Verlag Berlin Heidelberg 2007

Feature extraction in Medical Ultrasonic Image

Somkait Udomhunsakul and Pichet Wongsita

Faculty of Engineering, Department of Information Engineering, King Mongkut s Institute of Technology Ladkrabang
Charongkrung Road, Ladkrabang, Bangkok, 10520 Thailand

Abstract— **This paper presents a method for speckle noise reduction as well as feature extraction in medical ultrasonic images to effectively reduce the speckle noise and extract the object in ultrasonic images. In noise reduction process, the logarithm transform of the ultrasonic image is analyzed into wavelet domain by using 2D stationary wavelet transform (SWT). Next, the Weiner filter is used to apply over areas in each subband (HH, HL, LH and LL). Finally, the inverse wavelet transform is computed and applying the exponential. In feature extraction process, first the denoised image is enhanced by histogram equalization technique. Haar filter is used to extract the object. Moreover, nonmaxima suppression technique is adopted to get the edge localization. Finally, the adaptive hysteresis thresholding is applied to get the final result. The experiments show that the proposed algorithm can be detected well-localized and thin edges.**

Keywords— **Feature extraction, Stationary Wavelet Transform, Speckle noise reduction, Nonmaxima suppression**

I. Introduction

Ultrasonic images suffer from a special kind of noise called speckle. Speckle is a term used for a kind of multiplicative noise. It significantly degrades the image quality and increases the difficulty in discriminating fine details in mages during diagnostic examinations [1]. There are several techniques for speckle suppression such as wiener filtering, median filtering, homomorphic wiener filtering and soon. They can effectively suppress speckle but it fail to preserve many useful detail, being merely a lowpass filter. Recently, there has been considerably interest in using the wavelet transform as a powerful tool for recovering signal from noisy data. This method is generally referred to as wavelet shrinkage techniques. In 1995, Donoho presented a soft thresholding method for denoising in 1-D signal [2]. However, thresholding method have two main drawbacks: 1) the choice of the threshold, and 2) the specific distributions of the signal and noise may not be well matched at different scales [3].

In this paper, we present a method for speckle reduction and feature extraction in ultrasonic images. First, the 2D wavelet transform is applied to the logarithm image in order to convert the multiplicative noise into the additive noise case. Then, the Weiner filter is used to apply over areas in each wavelet domain subband (HH, HL, LH and LL). Finally, the inverse wavelet transform is computed and applying the inverse logarithm. In feature extraction process, first the denoised image is enhanced by histogram equalization technique. Harr filter is used to extract the object. Moreover, nonmaxima suppression technique is adopted to get the edge localization. Finally, the adaptive hysteresis thresholding is applied to get the final result in the binary format.

In the next sections, we review the principal of stationary wavelet transform. In section III, we show the method for ultrasonic speckle suppression in wavelet domain. Section IV, we briefly discuss the method for feature extractrction. Section V contains some experimental results. Finally, the conclusion is provided in the last section.

II. Stationary wavelet transform

The 2D stationary wavelet transform (SWT) is based on the idea of no decimation. It applies the discret wavelet transform (DWT) and omits both down-sampling in the forward and up-sampling in the inverse transform. More precisely, it applies the transform at each point of the image and saves the detail coefficients and uses the low-frequency information at each level. This property is good for noise removeal because the noise is usually spread over small number of neighboring pixels.

III. Speckle noise reduction

A. Approximate speckle noise model

The speckle noise of ultrasonic images is usually modeled as purely multiplicative noise process of the from given $g = f * n$ [4]. The pixel values return by the ultrasonic process (g) of the true values f and the speckle noise n. In order to change the multiplicative nature of the noise to additive one, we apply a logarithmic transformation to the ultrasonic image data.

F. Ibrahim, N.A. Abu Osman, J. Usman and N.A. Kadri (Eds.): Biomed 06, IFMBE Proceedings 15, pp. 267-270, 2007
www.springerlink.com ' Springer-Verlag Berlin Heidelberg 2007

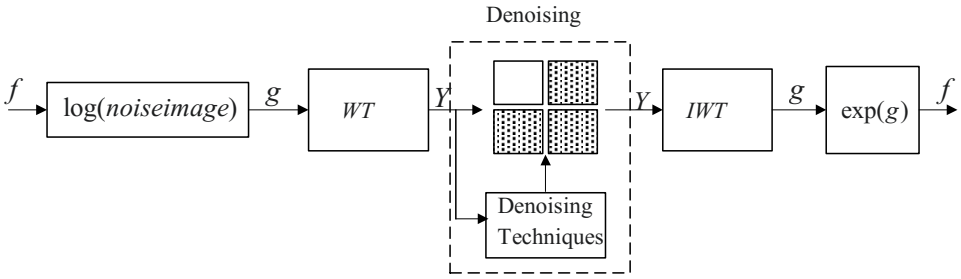

Fig. 1 Block diagram for speckle noise reduction in wavelet domain

B. Proposed method

In figure 1**,** 2D stationary wavelet transform is applied to the logarithm image (*f*) in order to convert the multiplicative noise into the additive noise case. Let *g* and $\hat{g}$ denote the 2D stationary wavelet transform (SWT) matrix and its inverse respectively. *Y* represents the matrix of wavelet coefficients having four subbands (LL, LH, HL and HH). The subbands $\mathbf{HH_k}$,$\mathbf{HL_k}$,$\mathbf{LH_k}$ are called detail, where k is the scale varying from 1 to 2. Then, the weiner filter is used to apply over areas in detail subband (HH, HL and LH) with mask 7x7 and subband LL filtered with mask 3x3. The wiener uses a neighborhood of window sizes to estimate the noise power from the local image mean and standard deviation [5].

$$\mu = \frac{1}{MN} \sum_{x_i, y_j \hat{I} \eta} Y(x_i, y_j) \tag{1}$$

$$\sigma^2 = \frac{1}{MN} \sum_{x_i, y_j \in \eta} Y^2(x_i, y_j) - \mu^2 \tag{2}$$

where μ, σ^2 and *Y* represent the local mean, variance and subband images, respectively. Wiener filter has output defined by

$$Y(x_i, y_j) = \mu + \frac{\sigma^2 - v^2}{\sigma^2}(Y(x_i, y_j) - \mu) . \tag{3}$$

Finally, the inverse wavelet transfrom is computed and applying the inverse logarithm (f).

IV. Feature extraction

Figure 2 shows the feature extraction process. First, the denoised image is enhanced by histogram equalization technique where the accumulative histogram of the image is linear [6]. The goal of this method is to make structure within the image more visible to human observers. Next, Harr filter is used to extract the object from denoised images in the vertical and horizontal direction separately and modulus sum is used to get the edge detection result. Then, nonmaxima suppression technique is adopted to get the edge localization. Finally, the adaptive hysteresis thresholding is applied to get the final result in the binary format. In a binary image, each pixel value is represented by a single binary format. In this paper, the upper and lower threshold values can be obtained from,

$$\mathrm{T_{upper}} = \frac{1}{2}\left[\max(Y(x)) - \frac{1}{\sqrt{2}}\left(\mathrm{var}\left|Y(x)\right| \right) \right] \tag{4}$$

$$\mathrm{T_{lower}} = \sqrt{2}(std\left|Y(x)\right|) \tag{5}$$

where Y is a gradient image;
max is the gradient maximum value;
var is variance;
std is standard deviation.

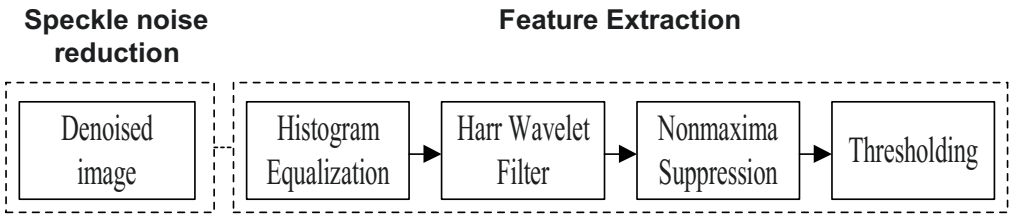

Fig. 2 Block diagram for feature extraction

F. Ibrahim, N.A. Abu Osman, J. Usman and N.A. Kadri (Eds.): Biomed 06, IFMBE Proceedings 15, pp. 267-270, 2007
www.springerlink.com ' Springer-Verlag Berlin Heidelberg 2007

V. Experiments

In this section, we show simulation results obtained by two ultrasonic images of size 256x256. The original images are shown in figure 3(a) and 4(a). Figure 3(b), 4(b) show the denoised image using our proposed approach. We used Duabechies8 stationary wavelet series with two levels of decomposition and denoising with the mask of wiener filters.

The enhanced image using histogram equalization is shown in figure 3(c) and 4(c). In the feature extraction process, we used Haar wavelet filter for feature extraction compared with other mother wavelets, Gabor and Daubechies wavelets, to extract the object from the ultrasonic images. In fact, gray level is important information for diagnosis. Haar wavelet is seemed to be able to preserve original gray level after edge detection. The result is pointed out by an ultrasonographer. Thin edge detected image with preserved gray level is important information for diagnosis because gray level expresses power of reflected signal. So, we can know the ratio of sound velocity at tissue-tissue-interface from the gray level, which may mean elasticity of tissue. Figure 3(d,e,f) and 4(d,e,f) performed by applying Sobel operator, Canny operator and proposed method respectively to generate the edge feature. From the experiment results, we found that the proposed method leads to an effective method for ultrasonic speckle denoising and yield the best possible edge of the object in ultrasonic images.

VI. Conclusions

In this paper, we presented a noise reduction in wavelet domain for speckle reduction. The approach adopts the denoising using SWT and wiener filters. It has effectively to reduce the speckle noise while preserving the resolvable details. In the feature extraction result reveals that the proposed approach compared with Sobel operator and Canny operator can be detected well-localized and thin edges. Therefore, our approach leads to a practical method for speckle reduction and feature extraction in ultrasonic images.

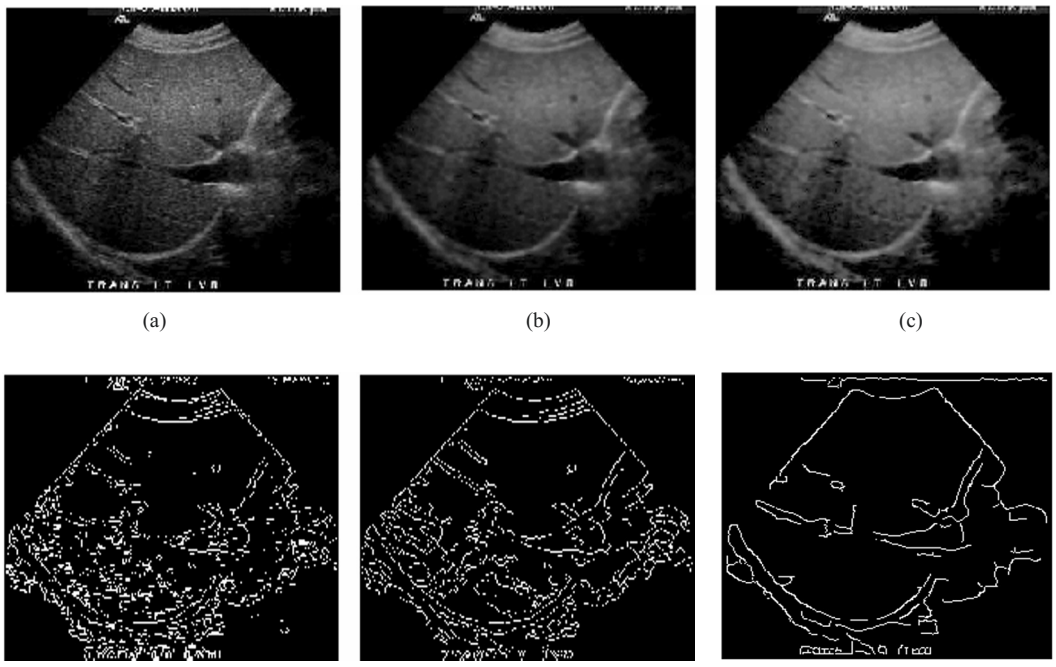

(a) (b) (c)

(d) (e) (f)

Fig. 3 (a) Liver image (b) Denoised image (c) Enhanced image (d) Sobel operator (e) Canny operator (f) Proposed method

F. Ibrahim, N.A. Abu Osman, J. Usman and N.A. Kadri (Eds.): Biomed 06, IFMBE Proceedings 15, pp. 267-270, 2007
www.springerlink.com ' Springer-Verlag Berlin Heidelberg 2007

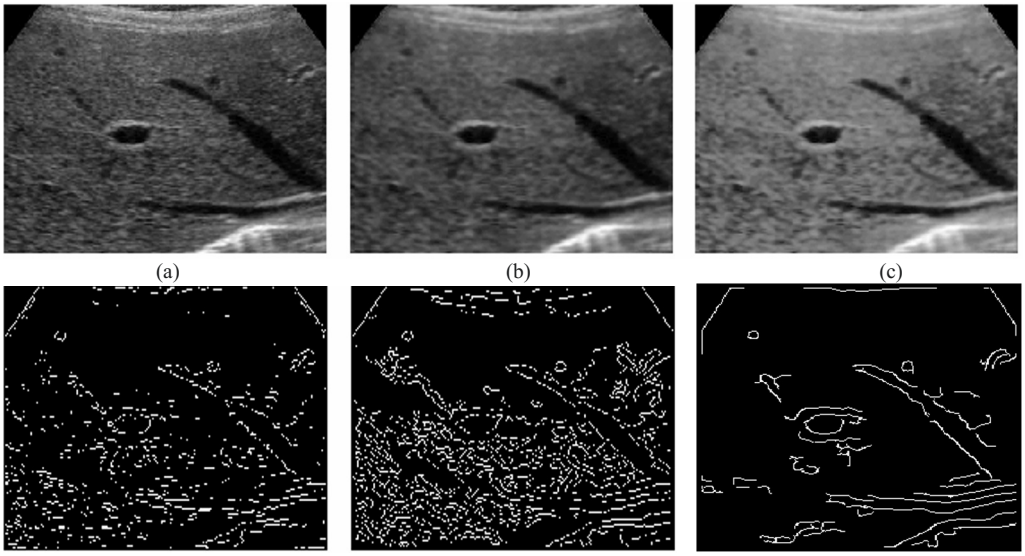

(a) (b) (c)

(d) (e) (f)

Fig. 4 (a) Vein image (b) Denoised image (c) Enhanced image (d) Sobel operator (e) Canny Operator (f) Proposed method

Acknowledgment

The authors would like to thank Ms. Kawakami, an ultrasonographer from Tokai University Hachioji Hospital, for her very helpful suggestion of this research study.

References

1. S.Gupta, L.Kaur, R.C. Chauhan and S.C. Saxena, (2003) A Wavelet based Statistical Approach for speckle Reduction in Medical Ultrasound Images. IEEE Trans. Med. Imag. Vol.2: 534-537
2. Donoho, D.L. (1995) Denoising by soft-Thresholding. IEEE Trans. Inform. Theory. vol. 41: 613-627
3. R.N. Strickland, He Il Hahn. (1997) Wavelet transform methods for object detection and recovery. IEEE Transactions on Image Processing. Vol. 6: 724 73.
4. A. Achim, A. Bezerianos and P. Tsakalides. (2001) Novel Bayesian multiscale method for speckle removal in medical ultrasound images. IEEE Trans. Med. Imag. Vol. 20 no. 8: 772-783
5. Lim, Jae S (1990) Two-Dimensional Signal and Image Processing, Prentice Hall
6. Alasdair McAndrew (2004) Introduction to Digital Image Processing with MATLAB, Thomson Course Technology

Address of the corresponding author:

Author: Somkait Udomhunsakul
Institute: Faculty of Engineering, Department of Information Engineering, King Mongkut s Institute of Technology Ladkrabang Charongkrung Road
City: Bangkok
Country: Thailand

F. Ibrahim, N.A. Abu Osman, J. Usman and N.A. Kadri (Eds.): Biomed 06, IFMBE Proceedings 15, pp. 267-270, 2007
www.springerlink.com ' Springer-Verlag Berlin Heidelberg 2007

High Resolution Imaging of TGFβ3 Treated Human Keratinocyte via a Newly Developed Widefield Surface Plasmon Resonance Microscope

M. Mahadi Abdul Jamil [1, 2, 4], M. Youseffi [2], S.T. Britland [3], S. Liu [5], C.W. See [5], M.G. Somekh [5] and M.C.T. Denyer [3, 4]

[1] Tun Hussein Onn College University of Technology: Faculty of Electrical & Electronic Engineering, Department of Electronic Engineering, Batu Pahat 86400, Johor, Malaysia
[2] University of Bradford: School of Engineering, Design & Technology, Bradford BD7 1DP, UK
[3] University of Bradford: School of Pharmacy, Bradford BD7 1DP, UK
[4] University of Bradford: Institute of Pharmaceutical Innovation, Bradford BD7 1DP, UK
[5] University of Nottingham: School of Electrical and Electronic Engineering, Nottingham NG7 2RD, UK

Abstract— **In this study high resolution imaging of human adult (HaCaTs) Keratinocytes cells using the newly developed Widefield Surface Plasmon Resonance (WSPR) system will be discussed. Surface Plasmon Resonance (SPR) occurs at the interface between a dielectric and a thin conducting layer when p-polarized light strikes at a specific angle thus excites free electrons and generates surface plasmon electromagnetic wave. The SPR excitation angle can be changed by the binding of bio-molecular species to the metallised layer, and is directly proportional to the refractive index and thickness of that molecular species. Our WSPR system provide high lateral resolution imaging close to 500 nanometers [1] and was used to investigate cell surface interactions under two different culture conditions: HaCaTs cultured on SPR substrate with Transforming Growth Factor β3 (TGFβ3) *(50ng/ml)* [2] and without TGFβ3. In less than 24 hours, HaCaTs cultured in the presence of TGFβ3 showed enhanced division and motility along with decreased cell attachment as compared with cells maintained in TGFβ3 free media. It is to be noted that cellular signaling by TGFβ3 is very important for enhancing tissue development in wound repair and that this study for the first time enabled optical interrogation of cell surface interface without the need for Immunostaining.**

Keywords— **Surface plasmons, TGFβ3, HaCaTs, Cell attachments, High resolution imaging .**

I. Introduction

Surface Plasmons (SPs) resonance based imaging is a relatively new field [3] that has a potentially broad range of applications in biological imaging. The pioneering work of E. Kretschmann and H. Raether in 1960s indicated that attenuated total reflectance (ATR) prism based on SPs excitation could be induced in a configuration known as the Kretschmann configuration [4]. In this configuration *p*-polarized light striking the metallic coated surface from a region of high refractive index at a specific angle θ_p will resonantly excite the electrons in the metallic film [5]. This resonance will propagate along the conductor, giving rise to a surface plasmon wave. The SPR angle θ_p is changed when bio-molecular species binds to the coated metal layer and this change in angle enables the thickness of that molecular species to be determined [6]. Surface plasmon microscopes have a wide range of uses, such as chemical sensors, biomolecule and biological binding/attachment sensors, and in any areas where sensitivity to minute changes in the properties of an interface is required. Standard Kretschmann based SP techniques are extremely powerful, but they lack the spatial resolution required to image highly localized regions at micron to submicron scales [3]. We have developed a new WSPR microscope capable of high lateral resolution imaging close to one micron. This system uses a high numerical aperture 1.45, oil immersion objective lens, which allows *p*-polarized light to be applied to a metallised glass slide at an angle capable of exciting surface plasmons [7, 8]. In this system we combined widefield phase confocal microscopy [9] with high resolution scanning SPR microscopy [7] where the imaging in the WSPR microscope is achieved by disruption of coherence using a rotating diffuser conjugated with the back focal plane [3, 8]. When stationary the diffuser illuminates the sample with a speckled pattern, but on rotation this speckled pattern is averaged enabling the generation of a wide field image. At present, various system are available as means for investigating the cell surface interface, such as Atomic Force Microscope (AFM) [10], Quartz Crystal Microbalance, Scanning Force Microscopy, Scanning Nearfield Optical Microsope (SNOM), Field-Emission Secondary Electron Microscopy (FESEM), and various immunostaining methods combined with confocal microscopy [11]. Each of these systems enables high resolution imaging, but do not readily enable the imaging of interfacial interactions. Thus we aim to demonstrate that the new WSPR can be used to image the cell surface interface and interrogate changes at the interface induced by the potent cytokine TGFβ3. TGF-β, is a chemotactic stimulant in fibroblasts where it enhances fibroplasias and the production of extracellular matrix (ECM) components such as collagen and elastin whilst suppressing the ECM breakdown. Thus, TGF-β is an important component in the process of wound healing and is produced naturally by cells such as platelets, macrophages and endothelial cells. There are various iso-

F. Ibrahim, N.A. Abu Osman, J. Usman and N.A. Kadri (Eds.): Biomed 06, IFMBE Proceedings 15, pp. 271-274, 2007
www.springerlink.com ' Springer-Verlag Berlin Heidelberg 2007

forms of TGF-β, (TGF-β1, TGF-β2, TGF-β3, TGF-β4 and TGF-β5) and these induce different cellular responses via the same suite of membrane receptors.

II. Materials and methods

Cell Culture: HaCaTs cell lines were cultured in small standard Plug seal cap 25cm^2 culture flask with ratio 1:5 ml cell suspension in Rosewell Park Memorial Institute media (RPMI, SIGMA). Cells were incubated at 37℃ and were split upon reaching confluence, usually every 4-5 days.

SPR Substrate Preparation: Two glass cover slips (0.18mm thick), coated with 50 nm Gold/1 nm Chromium were plated with HaCaTs cells for 24 hours in two conditions i.e. HaCaTs cultured on SPR substrate with TGFβ3 *(50ng/ml)* and without TGFβ3. After 24 hours, the cells were then fixed with 0.1% Glutaraldehyde solution in Hank s Balanced Salt Solution (HBSS, SIGMA) for 5 minutes and dehydrated in serial alcohol. The SPR substrate were imaged with a Ziess Axioplan 2 microscope using a long working distance 40x objective under Differential Interference Contrast (DIC) imaging conditions. The substrates were then mounted in the sample holder of the WSPR microscope and imaged further.

Trypsinisation Process: To verify the effects of TGFβ3 on HaCaTs cell attachment to the surface, HaCaTs cells were cultured in two conditions, with TGFβ3 at 50ng/ml and without TGFβ3 for 6 days in small standard Plug seal cap 25cm^2 culture flask and trypsinised (1ml of 0.25% Trypsin/EDTA were applied to cover the whole surface area of the 25cm^2 culture flask) from the surface upon reaching confluence. The degree of cell attachment was then determined by measuring via time lapse microscopy (1 frame every 20 seconds for 7 minutes) the time required for trypsinisation to induce the cells to take on a rounded phase bright morphology.

III. Results and discussion

In this experiment we imaged human keratinocytes. These cells attach strongly to one another and also to the culture substrate. Imaging with the WSPR system showed that HaCaTs cells attach to the surface via concentrically arranged, high contrast band like structure, with the highest contrast band like components being localized at the cell perimeter and in the lamellapodia (Figs 1e, 1f). However, when HaCaTs cells treated with TGFβ3 were imaged with WSPR system, significant differences in cell morphology were seen at the cell surface interface (Figs 1g, 1h). After treatment with TGFβ3, the band like accumulation of focal contacts disappeared and focal contacts became more diffusely arranged. This was accompanied by the TGFβ3 cells acquiring a more spread morphology. These results strongly indicate that TGFβ3 decreases the degree of cell attachment and promotes increased motility. This is in good agreement with the morphological changes observed using DIC microscopy, in which treatment with TGFβ3 resulted in cells acquiring a spread diameter up to a 3 fold that of untreated cells (Figs 1c, 1d). Our results not only show that TGFβ3 promoted increased spreading, but also show that TGFβ3 promoted an increase in cell replication rate after 24 and 48 hours (Fig 2). To further verify this finding, trypsinisation experiments were carried out to quantify TGFβ3 related changes in cell attachment.

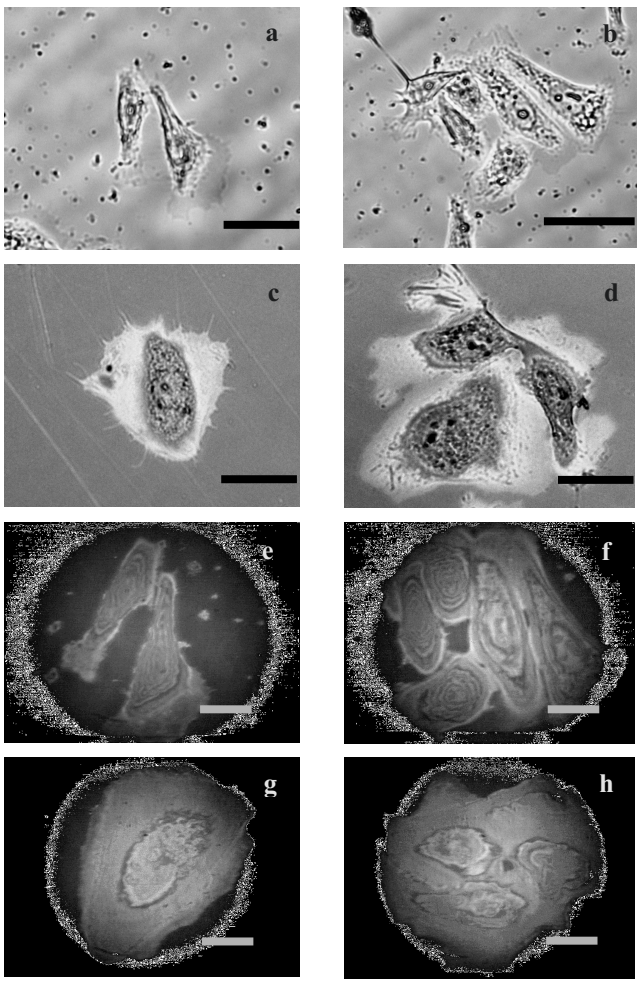

Fig. 1 (a) Image of individual and (b) group of fixed HaCaTs cells cultured without TGFβ3 on SPR gold coated substrate; (c) Image of individual and (d) group of fixed HaCaTs cells cultured with TGFβ3; Image taken with DIC microscope, objective x40 (*scale bar 35μm*); (e) the same individual cell as in (a) imaged with WSPR system; f) the same group of cell as in (b) imaged with WSPR system; (g) TGFβ3 treated single HaCaTs cell imaged with WSPR system; (h) TGFβ3 treated group of HaCaTs cell imaged with WSPR system (*scale bar 25μm*).

F. Ibrahim, N.A. Abu Osman, J. Usman and N.A. Kadri (Eds.): Biomed 06, IFMBE Proceedings 15, pp. 271-274, 2007
www.springerlink.com ' Springer-Verlag Berlin Heidelberg 2007

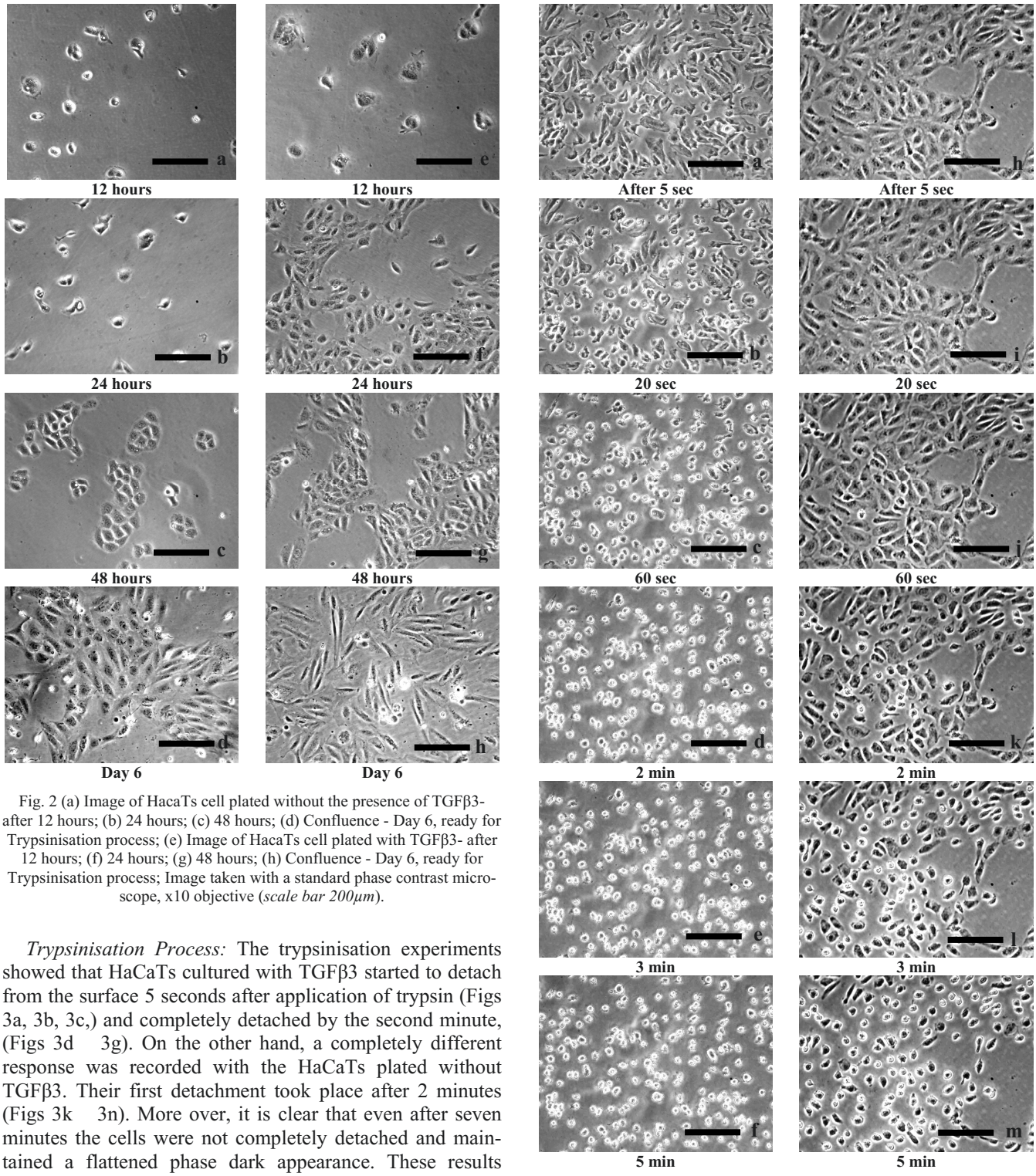

Fig. 2 (a) Image of HacaTs cell plated without the presence of TGFβ3- after 12 hours; (b) 24 hours; (c) 48 hours; (d) Confluence - Day 6, ready for Trypsinisation process; (e) Image of HacaTs cell plated with TGFβ3- after 12 hours; (f) 24 hours; (g) 48 hours; (h) Confluence - Day 6, ready for Trypsinisation process; Image taken with a standard phase contrast microscope, x10 objective (*scale bar 200μm*).

Trypsinisation Process: The trypsinisation experiments showed that HaCaTs cultured with TGFβ3 started to detach from the surface 5 seconds after application of trypsin (Figs 3a, 3b, 3c,) and completely detached by the second minute, (Figs 3d 3g). On the other hand, a completely different response was recorded with the HaCaTs plated without TGFβ3. Their first detachment took place after 2 minutes (Figs 3k 3n). More over, it is clear that even after seven minutes the cells were not completely detached and maintained a flattened phase dark appearance. These results confirm that application of TGFβ3 at 50ng/ml decreases the degree of cell surface attachment (Fig 3).

F. Ibrahim, N.A. Abu Osman, J. Usman and N.A. Kadri (Eds.): Biomed 06, IFMBE Proceedings 15, pp. 271-274, 2007
www.springerlink.com ' Springer-Verlag Berlin Heidelberg 2007

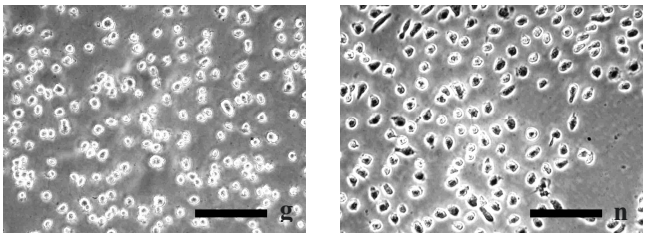

Fig. 3 Shows the sequence of images with time lapse captured for the trypsinisation process of HaCaTs cells plated with TGFβ3 (a, b, c, d, e, f, g) and without TGFβ3 (h, i, j, k, l, m, n) to show the detachment of HaCaTs cell from the culture flask. Image taken with a standard phase contrast microscope, x10 objective (*scale bar 200μm*).

IV. Conclusions

Traditionally cell surface contacts are investigated using immunostaining techniques, all of which require various step of staining and cell fixation. In this study we demonstrated that the new WSPR system can be used for studying cytokine induced changes in cell surface coupling/interactions at a high lateral resolution of less then a micron without the need for traditional immunostaining process. This finding represents a significant enhancement in cell imaging and will enable interrogation of cell surface interfacial interactions at a level that was previously unimaginable. This in turn will have significant implications in determining the functional characteristics of novel surface chemistries developed for use in wound healing systems.

Acknowledgment

The authors wish to acknowledge the financial support of the Engineering and Physical Sciences Research Council (EPSRC). We would also like to thank the Public Service Department of Malaysia for funding Mr. M. Mahadi Abdul Jamil for his MPhil/PhD at University of Bradford.

References

1. A. J. M. Mahadi, M. C. T. Denyer, M. Youseffi, S. T. Britland, S. Liu, C. W. See, M. G. Somekh, and S. Marlafeka, "Monitoring immunostaining process of proteins by using a widefield surface plasmon microscope," at Winter Meeting: Conf. on Craniofacial develp, St Anne's College, Oxford, Conf. Proc: Journal of Anatomy vol. 206, pp. 515, 2005.
2. D. P. P. Vooijs, X. F. Walboomers, J. A. T. C. Parker, J. W. V. d. Hoff, and J. A. Jansen, "Transforming growth factor-β3-loaded microtextured membranes for skin regeneration in dermal wounds," *Journal of Biomedical Materials Research Part A*, vol. 70A, pp. 402-411, 2004.
3. M. G. Somekh, *Surface plasmon and surface wave microscopy, Optical Imaging and Microscopy*, vol. 87. Berlin Heidelberg, 2003.
4. E. Kretschmann and H. Raether, "Radiative decay of non-radiative surface plasmons excited by light," *Zeitschrift Fur Naturforschung*, vol. 23A, pp. 2135-2136, 1968.
5. H. Kano and W. Knoll, "Locally excited surface-plasmon-polaritons for thickness measurement of LBK films," *Optics Communications*, vol. 153, pp. 235-239, 1998.
6. A. J. M. Mahadi, M. Youseffi, S. T. Britland, S. Liu, C. W. See, M. G. Somekh, and M. C. T. Denyer, "Applications of a novel high resolution widefield surface plasmon microscope in cell imaging and development of new binding assays," Microscience 2006: ExCel, London, Conf. Proceedings: "High resolution live cell imaging" pp. 60, 2006.
7. G. Stabler, M. G. Somekh, and C. W. See, "High-resolution wide-field surface plasmon microscopy," *Journal of Microscopy*, vol. 214, pp. 328-333, 2004.
8. S. Marlefeka, S. T. Britland, S. Liu, P. C. Twigg, C. W. See, M. G. Somekh, and M. C. T. Denyer, "Imaging biomolecular nanofilms at micrometer lateral resolutions using widefield surface plasmon microscopy," Conf. Proceedings: 3B2-03, Singapore, 2005.
9. M. G. Somekh, C. W. See, and J. Goh, "Wide field amplitude and phase confocal microscope with speckle illumination," *Optics Communications*, vol. 174, pp. 75-80, 2000.
10. E. Nagao and J. A. Dvorak, "An integrated approach to the study of living cells by atomic force microscopy," *Journal of Microscopy*, vol. 191, pp. 8-19, 1998.
11. H. Andersson, T. Baechi, M. Hoechl, and C. Richter, "Autofluorescence of living cells," *Journal of Microscopy*, vol. 191, pp. 1-7, 1998.

Address of the corresponding author:

Author: M. Mahadi Abdul Jamil
Institute: SoEDT 4, University of Bradford
Street: Richmond Rd
City: Bradford, West Yorkshire
Country: United Kingdom
Email: M.M.Abduljamil@bradford.ac.uk

F. Ibrahim, N.A. Abu Osman, J. Usman and N.A. Kadri (Eds.): Biomed 06, IFMBE Proceedings 15, pp. 271-274, 2007
www.springerlink.com ' Springer-Verlag Berlin Heidelberg 2007

Microwave Holographic Imaging Technique for Tumour Detection

M. Jayanthy[1], N. Selvanathan[2], M. Abu-Bakar[3], D. Smith[4], H.M. Elgabroun[3], P.M. Yeong[2], S. Senthil Kumar[5]

[1] Sunway University College/School of Computer Technology, Selangor, Malaysia
[2] University Malaya/Faculty of Computer Science, Kuala Lumpur, Malaysia
[3] University Malaya/Faculty of Engineering, Kuala Lumpur, Malaysia
[4]Northumbria University/School of Engineering and Technology, Newcastle upon Tyne, UK
[5]Dept. of Neurosurgery/ University of Manchester, Manchester, UK

Abstract— **Early, accurate and efficient screening of tumour will go a long way to improve the life expectancy and quality of life. Microwave holographic technique uses non-ionising radiation which has the potential to screen patients for tumour at low cost. It offers high contrast between healthy and malignant tissues and assists in forming image of the location and the extent of the malignant tissue. This technique exploits the advantages of holography without requiring the direct measurement which uses an expensive network analyser.**

This paper will investigate the use of an alternative microwave imaging technique using indirect holographic method. The use of continuous wave signal for imaging avoids the problems associated with pulsed systems. The use of two stage holographic technique requires recording of a holographic interference pattern as stage one and reconstruction of original image of the object as stage two. As a preliminary study, the transmitted microwave signal is bombarded on a suitable phantom and the scattered signals are measured. The significance of this technique is that it offers real time imaging possibility which can be used as intra operative imaging tool during the surgery to remove tumour.

Keywords— **Microwave, Tumour, Imaging, Indirect Holographic method**

I. Introduction

Microwaves can penetrate materials with different dielectric properties and can be used for imaging objects beneath the surface**.** Microwave imaging with near field focusing is essential to obtain images of adequate quality which explains the contrast in dielectric properties of normal and malignant tissues. Microwave imaging system avoids ionising radiation which poses risk to patients health. In addition, it is less expensive and more comfortable imaging method then Magnetic Resonance Imaging (MRI) and nuclear medicine [1].

Recent advances in the usage of direct microwave holographic technique to diagnose tumours are encouraging. However, this method which measures the complex field of antenna over selected aperture in near field using vector network analyzer [2] to reconstruct image of tumour is slow and expensive [5]. In this work, the use of indirect holographic technique as an alternative to detect tumours is investigated.

II. Method and materials

A. Indirect holographic technique

Indirect holographic method uses the application of Fourier transform, frequency domain filtering and direct back transformation onto the measured interference pattern. This method is used at optical frequencies and does not measure complex fields directly. It consists of two stages. Stage one is the recording of a holographic intensity pattern, I(x,y), by combining the signal scattered from the object, E(x,y), with a phase coherent reference plane wave signal, R(x,y). Stage two is the image reconstruction using Fourier transformation from the 2D holographic intensity pattern produced [5]. Fig. 1 shows the holographic intensity pattern recorded.

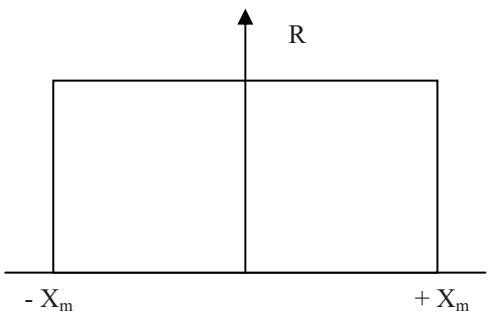

Fig. 1 Intensity pattern (I) of transmitted antenna

The mathematical equation to measure intensity pattern is given in equation (1) [5].

$$I(x,y) = |E(x,y) + R(x,y)|^2 = |E(x,y)|^2 + |R(x,y)|^2 + E(x,y)\,R^*(x,y) + E^*(x,y)\,R(x,y) \quad (1)$$

F. Ibrahim, N.A. Abu Osman, J. Usman and N.A. Kadri (Eds.): Biomed 06, IFMBE Proceedings 15, pp. 275-277, 2007
www.springerlink.com ' Springer-Verlag Berlin Heidelberg 2007

Fourier transform of the intensity pattern I(x.y) which forms the terms as shown in the Fig. 2 is derived through equation 2 below [5],[6].

$$F\{I(x,y)\}=F\{|E(x,y)|^2\}+F\{|R(x,y)|^2\} + F\{E(x,y)\}\otimes F\{R^*(x,y)\} + F\{E^*(x,y)\}\otimes F\{R(x,y)\} \quad (2)$$

In equation 2 the first zero components are the spectral intensity of two waves, which is centered at the origin (Fig. 2). The second two components are offset from the origin of the spectrum and contain the scattered object waves. It is important that the two components are sufficiently offset so that the object field can be obtained by suitably filtering the plane wave spectrum.

In optical holography a reference wave is required to recover the object wave and it s conjugate. Here, in microwave holography a reference wave is not required to recover the object wave. Intensity measurements are taken over a planar grid of points of sample spacing of ~ λ/2. At each of the measured points, the reading recorded consists of a linear combination of the reference and scattered wave. The phase and amplitude of the reference wave is by the phase shifters and attenuators to a predetermined value, enabling a wave with a linear phase gradient to be recorded over the planar of grid points.

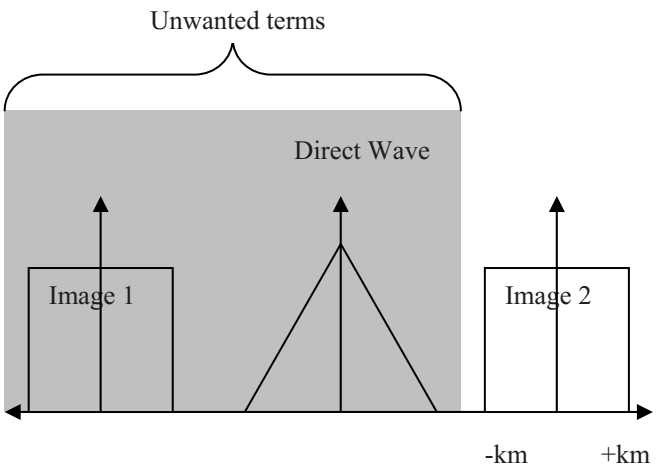

Fig. 2 Fourier Transform of Intensity Pattern

The intensity pattern recorded is filtered (Fig. 2) so as to obtain the spectra at the extreme right and is then centered at the origin. Then the Inverse Fourier Transform can be applied to obtain the intensity field (2 dimension or alternatively can back propagate the phase to the field of the object so as to obtain the 3 dimension shape of the object). Here, an algorithmic technique was used to extract the field information and to obtain the phase of the field unlike in optical holography where a reference beam is required for reproduction of the object.

The required term is obtained by filtering the unwanted terms as depicted in Fig. 2. Inverse Fourier transform is done to refocus the image to its original position as shown in Fig. 3 [6].

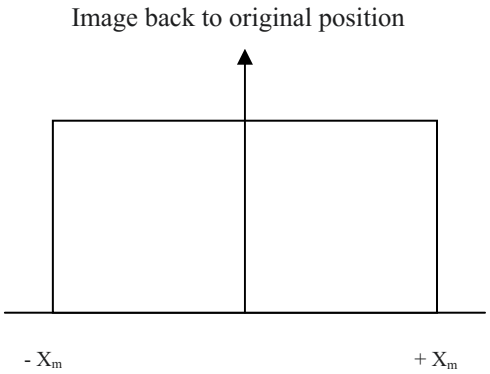

Fig. 3 Inverse Fourier transform of required term

B. Experimental setup

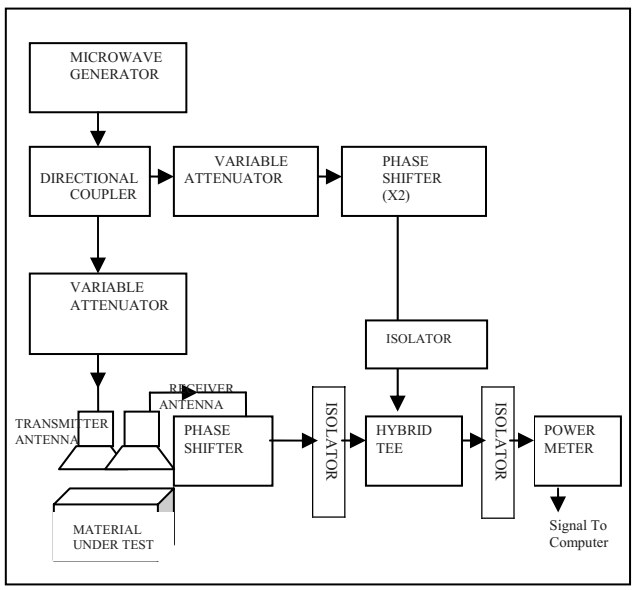

Fig. 4 Microwave holographic imaging experimental setup

The experimental setup for this work is as depicted in Fig. 4. The microwave generator transmits microwave signal through the directional coupler. The coupler splits the signal to an object and reference beam. The reference beam pass through the variable attenuator and phase shifter which adjusts the intensity and phase of the splitted reference

F. Ibrahim, N.A. Abu Osman, J. Usman and N.A. Kadri (Eds.): Biomed 06, IFMBE Proceedings 15, pp. 275-277, 2007
www.springerlink.com ' Springer-Verlag Berlin Heidelberg 2007

wave (R) to the hybrid tee. The phase angle setting is important to obtain the necessary offset angle to ensure separation of terms as shown in Fig. 2.

At the same time, the object beam is illuminated through the transmitter antenna onto a suitable material (phantom).The phantom reflects scattered wave which is received by the receiver antenna and forwarded to the hybrid tee. Particular care has to be taken to avoid system reflection. This can be achieved by placing isolators around hybrid tee. The mixing of the reference wave and scattered wave forms interference pattern. The intensity I(x,y) is sensed by the diode detector and measured by the power meter. The reading is automated by interfacing the meter to the computer. Fourier Transformation, filtering, refocusing and recentering are performed using computer software so as to recover the original image.

III. Tumour

A. *Phantom*

Varying water content causes the variation in the dielectric properties of human tissue. Skin, bone and fat have low water content therefore are low in permittivity. Where else, muscle, blood, liver and gut have high water content and are high in permittivity [3]. Tumour tissues were found to have at least 10 to 20% high permittivity than healthy tissues due to higher water content [1].

In the past corn syrup [4], saline and glycerine [1] have been used as phantom for microwave breast imaging studies. For this study, suitable phantoms will be selected based on the dielectric properties as medium of imaging for detection of various tumors.

B. *Imaging*

Mammogram techniques are at present the gold standard for detection of breast tumours and uses X rays. Breast compression is required to reduce image blurring and to create uniform tissue density, and this causes discomfort and pain for the patients. Also, X rays detect tumours by discriminating the density of tumours and healthy tissues. A relatively high false negative rate (4% - 34%) [7] and high false positive rate (70%)[8] have been detected, particularly with patients having dense breast tissue [9].

In this study, indirect microwave holographic imaging technique is used. Microwaves are transmitted through phantoms with similar dielectric properties to normal and tumour tissues and the scattered incident waves are measured. The differences in the dielectric properties of normal and tumour tissues are detected at the receiver and transmitter antennas as shown in Fig. 4. Image of the tumor contained in the normal tissue is reconstructed through the two stage process of indirect holographic technique as described above.

IV. Conclusions

Microwaves are non-ionising radiation which can be suitably employed as an effective and safe screening procedure for tumours. Microwave imaging techniques show a significant contrast in dielectric properties at microwave frequency of normal and tumour tissues and hold promise of a more accurate and painless detection of tumours. Microwave imaging can also be utilised for real time intra operative imaging for removal of tumours at a low cost.

References

1. E.C. Fear, P.M. Meaney, M.A. Stuchly (2003) Microwaves for breast detection? IEEE potentials, DOI 0278-6648/03
2. Y. Rahmat-Samii, L.I. Williams, R.G. Yaccarino (Dec 1995) The UCLA Bi-polar Planar Near-Field Antenna Measurement and Diagnostic Range. IEEE Antennas and Propogation Mag., vol. 37, No. 6, pp 16-35
3. A.W. Preece, J.L. Green, N. Pothecary and R.H. Johnson (1994) Microwave Imaging For Tumour Detection. The Institution of Electrical Engineers, IEE, Savoy Place, London WC2R OBL, UK.
4. G. Bindu, A. Lonappan, V. Thomas, C.K. Aanandan, and K.T. Mattew (2006) Dielectric studies of Corn Syrup for Applications in Microwave Breast Imaging. Progress in Electromagnetic Research, PIER 59, 175-186.
5. D.Smith, M. Leach, A.J. Sambell (Sept. 2003) Microwave Indirect Holographic Imaging using an Adaptation of Optical Techniques. IEEE Microwave and Wireless Components Letters, Vol. 13, No. 9, pp 379-381.
6. D. Smith, M. Leach (Sept. 2003) 3D Imaging of Antenna Fields and Metal Objects using New Indirect Holographic Technique. Int. Conf. On Electromagnetics for Advance applications, ICEAA-03, Torino, Italy, pp 711- 714.
7. P.T. Huynh et al , The false negative mammogram, Radiograph vol 18, no 5, pp 1137-1154, 1998
8. J.G Elmore et al, Ten year risk of false positive screening mammograms and clinical breast examinations, New Eng. J. Med, vol. 338, no. 16, pp. 1089-1096, 1998
9. V.P Jackson et al, Imaging of a radiographically dense breast, radiology vol. 188, pp 297-301, Aug 1993.

Address of the corresponding author:

Author: Jayanthy Maniam
Institute: Sunway University College
Street: 5, Jalan Kolej, Bandar Sunway
City: Petaling Jaya
Country: Malaysia
Email: jmaniam@academic.sunway.edu.my

F. Ibrahim, N.A. Abu Osman, J. Usman and N.A. Kadri (Eds.): Biomed 06, IFMBE Proceedings 15, pp. 275-277, 2007
www.springerlink.com ' Springer-Verlag Berlin Heidelberg 2007

One-dimensional evaluation of a least-square polynomial fitting approach to estimate the pressure domain from velocity data obtained from medical images

A. Pashaee, G. Ataee, M. Rezazadeh and N. Fatouraee

Biomedical Engineering Faculty, Amirkabir University of Technology (Tehran Polytechnic), Tehran, Iran

Abstract— **Common methods for deriving pressure value from velocity images, use Computational Fluid Dynamics (CFD) techniques. One of the major restrictions is that these images are prone to noise and they have low resolution. In this study we developed a domain approximation approach using least-square fitting methods to overcome these problems. In this regard in this first challenge a one-dimensional mathematical flow phantom is approximated by a polynomial function. The results obtained from the proposed technique are compared by the CFD approach. The effect of accumulation of noise and the effectiveness of this technique in estimation of pressure domain is also evaluated.**

Keywords— **Blood Flow Imaging, Pressure Estimation, Least-square polynomial fitting, CFD.**

I. Introduction

Among flow characteristics, the pressure gradient is a sensitive marker for ischemia. It is also shown that pressure maps have clinical value in vessel stenosis and restricted value orifice studies. Recent developments on medical imaging techniques provide some information on blood flow inside the cardiovascular system. Commonly used noninvasive techniques are restricted to recording the deformation and velocity components in the imaging domain. Therefore noninvasive measurement of pressure distribution is now limited to calculation of these data from the velocity field. A technique for estimation of the pressure wave from aortic wall compliance was originally developed by Urchuk et al [1]. Accurate algorithms for pressure estimation from velocity data use the Navier-Stokes equations which also include the viscose effect of flow. Song et al [2] presented a technique using Pressure-Poisson Equations (PPE) in deriving pressure maps from ultra fast CT cardiac images. Ebbers et al [3] developed a technique to integrate pressure gradients along specific flow streamlines computed from PC-MRI. Tasu et al [4] proposed a pressure domain estimation method based on MR acceleration measurement.

At all these studies, the estimation of pressure distribution from velocity domain is based on CFD methods [5]. On the other hand they adopt the discrete data obtained from the acquired images as a computational grid data. Generally the velocity data obtained from medical imaging techniques are prone to noise accumulation. Also imaging techniques commonly suffer from resolution restrictions. Considering these constraints, in this work we propose another approach which makes use of an approximation technique and fits a function to the velocity data. With the use of this function and the pressure-velocity correlation one, we can estimate the pressure field and other useful flow characteristics.

In this paper at first the type of fitted function and approximation method is discussed. Then a one-dimensional mathematical phantom for evaluation of the proposed method is considered. A comparison between the results obtained from the proposed technique and a conventional CFD method are compared. Finally the effectiveness of applying this pressure estimation method on a noise contaminated velocity domain is evaluated.

II. Materials and Methods

Here an appropriate approximation method for flow velocity domain reconstruction is discussed. Also the proper function type for this aim is recommended. The method to estimate the pressure distribution from the velocity functions is then presented.

A. Approximation Function

As mentioned before, the velocity data obtained from medical imaging techniques are noisy and suffer from resolution restrictions. Because of these two sources of error in the velocity data, we must decrease the estimation dependency to all data and their magnitudes. Using the least-squares approximation method a description of velocity at whole domain will be obtained. Also by this technique the root-mean-square error at velocity data will be minimized and the resulted function has not to satisfy all velocity data.

The principle of least-squares fitting method is to minimize the norm of data error vector, so it will eliminate the data noise and will smooth the resulted velocity field. Using least-squares method for approximation of data function y with function f, the following relation will be minimized:

$$\|y - f\|^2 \tag{1}$$

F. Ibrahim, N.A. Abu Osman, J. Usman and N.A. Kadri (Eds.): Biomed 06, IFMBE Proceedings 15, pp. 278-281, 2007
www.springerlink.com ' Springer-Verlag Berlin Heidelberg 2007

Because polynomials can be readily manipulated, fitting such functions to data that do not plot linearly is common. Also its non-pulsating behavior and ease of parametric differentiation and integration makes it suitable for this pressure estimation method. So we offered these types of functions in fitting of the velocity data.

In development of this technique, we use n as the degree of the polynomial and N as the number of data pairs. It is obvious that, if $N=n+1$, then the polynomial will pass precisely through each point. Suppose we have a table of data with N pairs of (x_i,y_i). Here x_i presents the position of data. By minimizing the sum of squares (1), the following matrix form equation will be obtained:

$$AA^T a = Ay \tag{2}$$

which design matrix A, coefficient matrix a and y are,

$$A=\begin{bmatrix} 1 & 1 & 1 & \cdots & 1 \\ x_1 & x_2 & x_3 & \cdots & x_N \\ x_1^2 & x_2^2 & x_3^2 & \cdots & x_N^2 \\ \vdots & & & & \vdots \\ x_1^n & x_2^n & x_3^n & \cdots & x_N^n \end{bmatrix}, a=\begin{bmatrix} a_0 \\ a_1 \\ a_2 \\ \vdots \\ a_n \end{bmatrix}, y=\begin{bmatrix} \sum y_i \\ \sum x_i y_i \\ \sum x_i^2 y_i \\ \vdots \\ \sum x_i^n y_i \end{bmatrix} \tag{3}$$

Details on the numerical solution of this equation are presented at reference 6. Solving this set of linear equations obtains the approximating polynomial coefficients.

B. Pressure Approximation

By fitting three functions to the three spatial velocity components obtained from the velocity images, **u** as a function of **x** (the spatial position vector) will be obtained. In order to calculate the pressure function from the estimated velocity functions, the Pressure Poisson Equation (PPE) is used here. The resulted velocity function can be directly used in PPE to calculate the pressure as below:

$$\nabla^2 p = \nabla.\mathbf{b} \tag{4}$$

here p is pressure and **b** is defined as below,

$$\mathbf{b} = \frac{\mu}{\rho}\nabla^2\mathbf{u} - \mathbf{u}.\nabla\mathbf{u} \tag{5}$$

Also μ and ρ are the viscosity and density of the fluid, respectively. Substituting $\mathbf{b} = \nabla p$ in (5) results in the steady Navier-Stokes equations without the body force term.

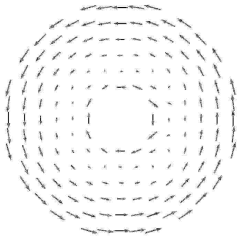

Fig. 1 Couette flow fields with a resolution of six points per radial field.

III. Results

A. Couette Flow System

Here the quantitative performance of the proposed method is evaluated on a numerically generated divergence free velocity data. The result of this method will be compared with the pressure calculated from the CFD approach. The Couette flow system consists of two concentric cylinders with fluid filled in the annular region. The fluid flow is generated by the relative rotation of two cylinders. The Navier-Stokes equation for this particular geometry can be solved in cylindrical coordinates 7. It can be shown that the velocity and the pressure field of fluid are as below,

$$v = c_1 r + c_2 / r \tag{6}$$

$$p = \rho(c_1^2 r^2 - c_2^2 / r^2 + 4c_1 c_2 \ln r) + c_3 \tag{7}$$

considering c_1 and c_2 to be constant and dependent on radii and angular velocity of the two cylinders. c_3 denotes the integration constant. Now we are equipped with a nontrivial divergence free velocity field with a known pressure distribution. Because of the symmetry, using (6) the discrete velocity field is generated along the r direction to construct a one-dimensional axisymmetric flow domain. The distance between the cylinders is discredited by six equally spaced velocity data nodes to simulate a low resolution image data. Fig. 1 shows the Couette flow field for such velocity image.

This six point velocity data is used to approximate a function to fit a least-squares polynomial. The obtained velocity domain is applied in calculation of the pressure domain using (4). **b** was computed as dictated by (5).

Fig. 2 presents the estimated (dashed line) and the real pressure distribution (solid line) obtained from (7). $n = 4$ is used in calculation of the polynomial coefficients. This figure shows a good approximation from this method over only six points. Further experiments show that using higher degree polynomials and more data points in velocity domain will improve the coincidence of the approximation curve.

F. Ibrahim, N.A. Abu Osman, J. Usman and N.A. Kadri (Eds.): Biomed 06, IFMBE Proceedings 15, pp. 278-281, 2007
www.springerlink.com ' Springer-Verlag Berlin Heidelberg 2007

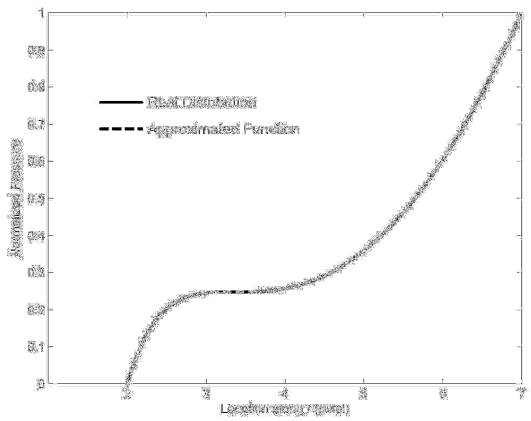

Fig. 2 The results from fitting a 4 degree polynomial in the Couette flow system on six points (dashed line) and the real distribution (solid line).

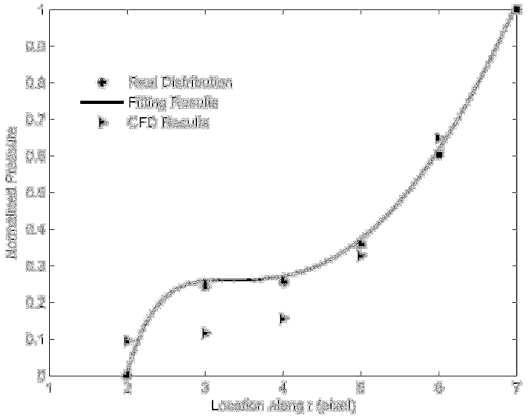

Fig. 3 Pressure distribution from fitting a 4 degree polynomial in Couette flow system (Solid line), CFD results (triangle symbols) and their comparison with the real pressure (circular symbols).

B. CFD Results

In order to compare this approach with the conventional CFD methods, a commonly used CFD technique for the calculation of pressure map from velocity data is considered. In this technique, the Pressure-Poisson Equation (4) together with the Neumann boundary condition which is the most appropriate boundary condition for PPE is considered. Details of this technique could be found in reference 2. The Neumann boundary condition is presented as below,

$$\nabla p.\mathbf{n} = \mathbf{b}.\mathbf{n} \tag{8}$$

PPE is a second order elliptic PDE. For this equation the pressure at a given point must be simultaneously solved with the pressure at all other points. For construction of **b** the radial components of the Navier-Stokes equations must be considered in cylindrical coordinates as below,

$$b_x = \mu\left(\frac{\partial^2 u}{\partial r^2} + \frac{1}{r}\frac{\partial u}{\partial r} - \frac{u}{r^2}\right) - \rho\left(u\frac{\partial u}{\partial r} - \frac{v^2}{r}\right) \tag{9}$$

The axial and angular derivations of the velocity components are ignored because of the planar flow and symmetry conditions. Also the velocity component along the z axis is ignored. It should be mentioned that with zero radial velocity component u, the differentiated terms of (9) will not account in the resulted pressure. Obviously taking the effects of these derivatives will improve the results of the estimated pressure field.

In this study we applied a Finite Difference method to calculate the pressure domain from the velocity data. Explicit discretization of PPE for one-dimensional axisymmetric flow domain is generally obtained from a two point central approximation method as below:

$$\frac{p_{i+1} - 2p_i + p_{i-1}}{\Delta x^2} = \frac{\partial b_x}{\partial x} \tag{10}$$

b_x is calculated from the velocity data. Staggered computational grid is used in the arrangement of velocity and pressure data in the domain 8. The stability of this iterative method is guaranteed when it does not diverge.

By applying an iterative Jacobi method in solving these set of equations, the pressure field is estimated as presented in Fig. 3. The solid line presents the result of the least-squares fitting method, circular symbols present the real data and triangle symbols demonstrate the result of the CFD algorithm. Standard deviation from the real pressure distribution by the least-squares and CFD algorithms are 0.1638 and 2.4207, respectively. Again $n = 4$ is used in calculation of polynomial coefficients. This figure shows a good coincidence between the line and the real pressure distribution.

C. Couette Flow Experiment with Noise

Velocity field data will generally be contaminated by noise. Also the operation of mapping the velocity fields to the pressure distributions is not linear. Therefore, it is difficult to predict the behaviour of the PPE on a given noisy velocity field. Here we will present the experiments which illustrate the influence of the approximation and the CFD techniques in prediction of the pressure distribution from a noisy velocity map. White Gaussian noise of SNR = 10 were added to the Couette flow field. The SNR was defined as the ratio of the maximum speed and the square root of the noise variance. The resulted velocity field with the same six point resolution image is presented at Fig. 4.

F. Ibrahim, N.A. Abu Osman, J. Usman and N.A. Kadri (Eds.): Biomed 06, IFMBE Proceedings 15, pp. 278-281, 2007
www.springerlink.com ' Springer-Verlag Berlin Heidelberg 2007

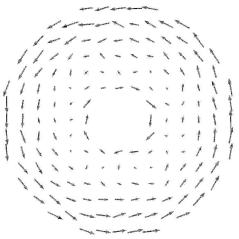

Fig. 4 Couette flow contaminated by a SNR = 10 white Gaussian noise.

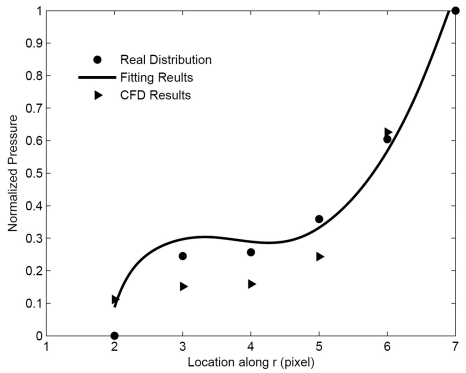

Fig. 5 Pressure estimation from the approximation of a 4 degree polynomial on a noisy Couette flow (Solid line), CFD results (triangle symbols) and their comparison with real pressure (circular symbols).

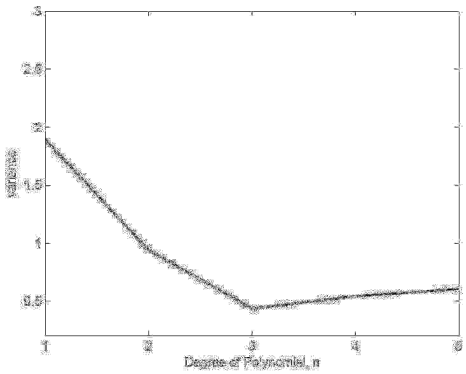

Fig. 6 Variance as a function of polynomial degree in a noisy flow domain.

Using these velocity data, the approximation and CFD algorithms provide a pressure distribution as presented in Fig. 5. Again $n = 4$ is used in pressure domain estimation. Standard deviation 0.9694 and 2.8664 is obtained from the approximation and CFD methods, respectively.

D. On Degree of Polynomial

In general, we may wonder what degree of polynomial should be used in estimation of velocity data. In order to determine the optimum degree of polynomial the variance below is calculated for each degree of approximation:

$$\sigma^2 = \frac{\sum e_i^2}{N - n - 1} \tag{11}$$

e_i is the error for each data set. Fig. 6 presents this variance as a function of the polynomial degree. The results show an optimum degree of 3 for this approximation.

IV. Conclusion

The Least-squares polynomial fitting method for approximation of a function on a set of one-dimensional low resolution and noisy velocity data obtains relatively accurate pressure estimation. A primary study of this technique on a standard mathematical couette flow system shows precision of approximately 3 folds regard to the conventional methods. We predict this method will obtain a precise estimation in two and three dimensional velocity maps relative to the conventional CFD techniques.

References

1. S. N. Urchuk, S. E. Fremes, D. B. Plewes, In vivo validation of mr pulse pressure measurement in an aortic flow model: preliminary results, *Magnetic Resonance in Medicine*, vol. 38, pp. 215-223, 1997.
2. S. M. Song, R. M. Leahy, D. P. Boyd, B. H. Brundage, and S. Napel, Determining cardiac velocity fields and intraventricular pressure distribution from a sequence of Ultrafast CT cardiac images, *IEEE Trans. Med. Imaging*, vol. 13, no. 2, pp. 386-397, 1994.
3. T. Ebbers, L. Wigstrom, A. Bolger, J. Engvall, and M. Karlsson, estimation of relative cardiovascular pressures using time-resolved three-dimensional phase-contrast MRI, *Magnetic Resonance Imaging*, vol. 45, pp. 872-879, 2001.
4. J. P. Tasu, E. Mousseaux, A. Delouche, C. Oddou, O. Jolivet, and J. Bittoun, Estimation of pressure gradients in pulsatile flow from magnetic resonance acceleration measurement, *Magnetic Resonance in Medicine*, vol. 44, pp. 66-72, 2000.
5. J. H. Ferziger, and M. Peric, *Computational methods for fluid dynamics*. 3rd ed., New York: Springer-Verlag, 2002.
6. C. F. Gerald, and P. O. Wheatley, *Applied Numerical Analysis.* 6th ed., Addison Wesley Longman, Inc., 1999.
7. L. D. Landau, and E. M. Lifshitz, *Fluid Mechanics.* 2nd ed., Pergamon Press plc, 1987.
8. A. Pashaee, P. Shooshrai, N. Fatouraee, Measurement of Intravascular Pressure Distributions Using Velocity Images, International Conference on Biomedical Engineering (ICBME 2005), Singapore, 2005.

Address of the corresponding author:

Author:	Nasser Fatouraee
Institute:	The Biological Fluid Mechanics Research Laboratory, Bio medical Eng. Faculty, Amirkabir University of Technology
Street:	Hafez Avenue
City:	Tehran
Country:	Iran
Email:	Nasser@aut.ac.ir

F. Ibrahim, N.A. Abu Osman, J. Usman and N.A. Kadri (Eds.): Biomed 06, IFMBE Proceedings 15, pp. 278-281, 2007
www.springerlink.com ' Springer-Verlag Berlin Heidelberg 2007

Quantification of Collagen Orientation in 3D Engineered Tissue

F. Daniels[1], B.M. ter Haar Romeny[1], M. Rubbens[2] and H. van Assen[1]

Eindhoven University of Technology - Department of Biomedical Engineering, Eindhoven, the Netherlands
[1] Biomedical Image Analysis
[2]Soft Tissue Biomechanics & Engineering

Abstract— **Tissue engineered heart valves are a promising alternative for current heart valve replacements. However, the mechanical properties of these valves are insufficient for implantation at the aortic position [1]. Collagen orientation is important to improve the mechanical properties of tissue engineered valves. Two-photon laser-scanning microscopy allows us to study the influence of strain on collagen orientation in 3D. A method based on the 2nd order derivative of the 3D image structure was used to determine the general orientation of the collagen fibers with automatic scale selection of the operator. We studied the effect of strain on collagen orientation. Alignment in the direction of the applied strain is seen. Histograms show that the distribution of orientations becomes smaller for increased strain. This indicates that the collagen fibers align more.**

Keywords— **Collagen, orientation, tissue engineering, heart valve, computer vision**

I. Introduction

The most common treatment for valvular heart valve diseases is the replacement of the valve. Classical heart valve substitutes are mechanical prosthetic valves with components manufactured of non-biologic material (e.g. polymer, metal, carbon) and biological valves (figure 1a, b) which are constructed, at least in part, of either human (homografts) or animal tissue (xenografts). The mayor drawback of the mechanical valves is that they contain foreign materials, which increases the risk of infections and tromboembolic complications. To prevent thromboembolism, the patient needs to take medication that prevents or slows down the clotting of blood (anticoagulation medication) for the rest of its life. Biological prostheses do not require such medication, because of higher immunological competence. However they show a limited durability (10-15 years) because of structural dysfunction due to tissue deterioration [2]. To overcome these shortcomings another type of heart valve replacement has to be developed and preferably one that has the ability to grow, repair and remodel. One approach that has been used to make such a valve is tissue engineering. Autologous cells are seeded on a pre-shaped biodegradable scaffold and cultured in a bioreactor under conditions that mimic the physiological environment of the tissue. To date, tissue engineered heart valve replacements (Figure 1c) show promising results when implanted at the pulmonary position in animal studies [3]. However these valves lack the mechanical integrity to withstand the pressures at the aortic side. A tissue engineered aortic heart valve with mechanical properties similar to the native aortic valve would be the ideal prosthesis.

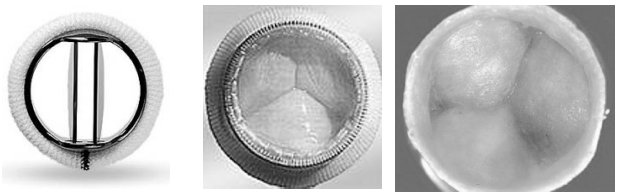

Fig. 1 Examples of heart valve protheses. a) Mechanical heart valve (Medtronic). b) Biological heart valve of non living fixed tissue (Hancock). c) Living tissue engineered tri-leaflet heart valve based on human marrow stromal cells [3].

The protein primary responsible for the load-bearing properties of heart valves is collagen. The strength collagen provides to these tissues depends on collagen fiber content, thickness, length, and orientation. A promising way of improving the mechanical integrity of tissue engineered valves is to optimize collagen remodeling (i.e. changes in fiber content, thickness, length, cross-links and orientation) via mechanical conditioning strategies. Collagen remodeling is a balance between collagen synthesis and degradation. The way remodeling takes place is strongly influenced by mechanical straining. In a study by Mol [4] the influence of different strain levels on the strength of tissue engineered constructs is shown. The Young s modulus increases with applied strain.

Previous research by Billiar [5] has shown that collagen orientation rather then collagen content determines the mechanical properties in aortic valve cusps. Determining the relationship between mechanical straining and collagen orientation may be helpful to improve the strength of tissue engineered aortic heart valves. The focus of this paper is to investigate this relationship.

We investigate the orientation of collagen fibers by using tissue engineered constructs and visualizing collagen with a two-photon laser-scanning microscope (TPLSM).

F. Ibrahim, N.A. Abu Osman, J. Usman and N.A. Kadri (Eds.): Biomed 06, IFMBE Proceedings 15, pp. 282-286, 2007
www.springerlink.com ' Springer-Verlag Berlin Heidelberg 2007

A new fluorescent probe, CNA35 [6], is used to specifically mark collagen. This probe has a high affinity for collagen type-I. The probe consists of a collagen binding domain (bacterial collagen receptor) and a fluorescent dye, which is conjugated to the binding domain.

TPLSM produces large 3D datasets and the complexity of the 3D fibrous networks makes observation and extraction of quantitative information from these datasets very difficult. We provide an automatic method for extraction of orientation information which is a faster, more objective and more accurate way to analyze the data compared to analysis by hand. TPLSM shows collagen fibers that are curved and vary in thickness, i.e. the notion of scale is an important parameter for our analysis.

II. Algorithm for orientation analysis

We propose to estimate the local orientation in the images by determining principal curvature directions from the Hessian matrix, followed by scale selection and spatial context enhancement. To enhance the collagen fibers, a preprocessing step is performed by coherence enhancing diffusion [11].

A. Principal curvature directions in 3D

Curvature is a local feature, which can be determined at any point on a curve and a surface. The general definition for curvature in mathematics is the rate of change of the angle (at a point) between a curve and a tangent to the curve [7]. In the case of a line in 2D there is only one direction along the curve for which curvature is defined. On a surface the maximum and minimum curvatures are the principal curvatures and the directions in which these occur are the principal directions. At a point on an object (3D image) three principal curvatures and principal directions can be defined (Figure 2). The minimal curvature direction is oriented along the general orientation of the object. This method therefore may be used for determining the local orientation of a tubular structure.

$$\nabla^2 L(\mathbf{x},\sigma) = \begin{pmatrix} L_{xx} & L_{xy} & L_{xz} \\ L_{yx} & L_{yy} & L_{yz} \\ L_{zx} & L_{zy} & L_{zz} \end{pmatrix}$$

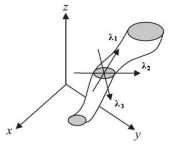

Fig. 2 The eigenvalues of the second order Hessian matrix (left) are the principal curvatures of the 3D structure (right).

The eigenvalues and the eigenvectors of the Hessian matrix correspond to the principal curvatures and principal directions of the image [7]. The principal directions are in 3D commonly represented by an ellipsoid which is scaled by the eigenvalues (Figure 3).

When the scale of the Gaussian derivatives in the Hessian matrix matches the scale of the collagen fiber the Gaussian will give an optimal response. The eigenvalues are ordered from small to large $|\lambda_1| \le |\lambda_2| \le |\lambda_3|$.

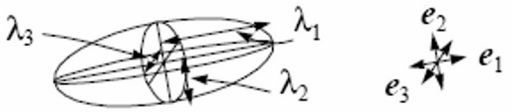

Fig. 3 Graphical representation of principal direction by a 3-dimensional ellipsoid with its eigensystem.

The relations between the eigenvalues determine the local shape (see Table 1).

Table 1: Possible structure types depending on theeigenvalues.

Structure type	Polarity	Eigenvalues
blob	bright	$\lambda_1<<0, \lambda_2<<0, \lambda_3<<0$
blob	dark	$\lambda_1>>0, \lambda_2>>0, \lambda_3>>0$
tubular	bright	$\lambda_1\approx 0, \lambda_2<<0, \lambda_3<< 0$
tubular	dark	$\lambda_1\approx 0, \lambda_2>>0, \lambda_3>>0$
plane	bright	$\lambda_1\approx 0, \lambda_2\approx 0, \lambda_3<<0$
plane	dark	$\lambda_1\approx 0, \lambda_2\approx 0, \lambda_3>> 0$

A *confidence measure* can be associated to a certain orientation [8] to measure whether the orientation has a high enough confidence to be included in the final result. The confidence measure is defined as

$$C(\lambda,\sigma) = \begin{cases} 0 \\ 1 - e^{\frac{(\lambda_\Delta)^2}{2c^2}} \end{cases} \qquad (1)$$

with $\lambda_\Delta{}^2 = \left(|\lambda_1| - |\lambda_2|\right)^2 + \left(|\lambda_2| - |\lambda_3|\right)^2 + \left(|\lambda_3| - |\lambda_1|\right)^2$,
$|\lambda_1| \le |\lambda_2| \le |\lambda_3|$ and c a predefined threshold.

The value of c is chosen to be 0.25, because the intensities in the image range from 0 to 1 and we assume that voxels with a values larger than 0.25 belong to a fiber. The measure becomes 0 for regions with no preferred orientation and has a maximum of 1 for regions with a high preference for one orientation.

F. Ibrahim, N.A. Abu Osman, J. Usman and N.A. Kadri (Eds.): Biomed 06, IFMBE Proceedings 15, pp. 282-286, 2007
www.springerlink.com ' Springer-Verlag Berlin Heidelberg 2007

B. Vesselness measure

The vesselness measure defined by Frangi et al., [9] is mainly used to enhance blood vessels.

The measure consists of three components. The first component is a ratio that expresses how much a structure deviates from a blob but cannot distinguish between a line- and a plate-like structure:

$$R_B = \frac{Volume/(4\pi/3))}{(Largest\ Cross\ Section\ Area/\pi)^{3/2}} = \frac{|\lambda_1|}{\sqrt{|\lambda_2\lambda_3|}} \quad (2)$$

This ratio has a maximum for blob-like structures and is zero when $\lambda_1 \approx 0$ or λ_2 and λ_3 tend to zero.

The second component refers to the largest area cross section of the ellipsoid. It distinguishes between plate-like and line-like structures because only in the latter case it will be zero:

$$R_A = \frac{(Largest\ Cross\ Section\ Area)/\pi}{(Largest\ Axis\ Semi-length)^2} = \frac{|\lambda_2|}{|\lambda_3|} \quad (3)$$

These two ratios are invariant under intensity scaling. When all eigenvalues have a small magnitude the pixel belongs to the background. The Frobenius matrix norm gives the third component of second order structureness

$$S = \|H\|_F = \sqrt{\sum_{j\le m} \lambda_j^2} \quad (4)$$

where *m* is the dimension of the image. This results in the final vesselness measure

$$V(\lambda,\sigma) = \begin{cases} 0 \\ \left(1-\exp\left(-\frac{R_A^2}{2\alpha^2}\right)\right)\exp\left(-\frac{R_B^2}{2\beta^2}\right)\left(1-\exp\left(-\frac{S^2}{2c^2}\right)\right) \end{cases} \quad (5)$$

where α, β and c are thresholds which control the sensitivity of the line filter to the three components R_A, R_B and S. For α and β a default value of 0.5 is chosen corresponding to the default values in Frangi [10]. For c a value of max(im)/4 is chosen.

C. Coherence Enhancing Diffusion

It would be desirable to improve the quality of structures in the image without destroying, e.g. the boundaries between the fibers. With coherence-enhancing diffusion (CED) smoothing occurs along but not perpendicular to the preferred orientation of the structures in the image. With CED the process of filtering is steered by a diffusion tensor instead of a scalar-valued diffusivity. This enables direction-dependent diffusion and not only adapts diffusion to the location. Weickert [11] uses the structure tensor $D = \nabla u.\nabla u^T$ to describe the orientation of the structures in image *u*. The basic equation which governs nonlinear diffusion filtering is $\partial_t u = div(D \cdot \nabla u)$ on $\partial\Omega \times (0,\infty)$. We solved the PDE with a Additive Operator Splitting (AOS) scheme, introduced by Weickert et al, [12]. When applying CED in 3D to the TPLSM collagen images (Figure 4) the images appear less noisy and the fibers are enhanced. The methods described were implemented in *Mathematica* [13]. Images were corrected for the exponential decrease of intensity with depth.

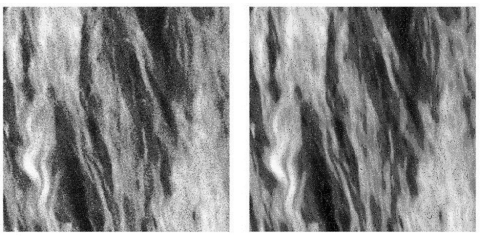

Fig. 4 Left: Original slice of a TPLSM image of the native heart valve. Right: Image after CED with α = 0.001, C=1, σ = 2, ρ = 8 and t = 4.

III. Experiments

The model system consists of a flexercell FX-4000T straining system, on which four 6 well plates with flexible membrane bottoms are mounted. The scaffolds, which serve as a cell carrier, were made by cutting polyglycolic acid (PGA) strips in a rectangular shape of 25 x 4 x 1 mm^3. These samples were coated with a solution of 1% of Poly-4-hydroxybutyrate (P4HB) and attached to the flexible membrane of the flexercell FX-4000T straining system. The samples were cultured for one week in a static condition at 37°C.

After 1 week of static culture, the samples were divided into three groups to study the effect of different straining protocols on the collagen orientation. One group of static constructs (A, static) was not strained by external load. The second and third group were strained uniaxially by 4% (B) or 8% (C) at a physiologically relevant frequency of 1 Hz. The control group consisted of floating samples (E, unattached). After three additional weeks the samples were sacrificed and imaged the same day by TPLSM. The microscope setup consisted of a BioRad Radiance 2100MP in combination with a Spectra Physics Tsunami Ti: Sapphire laser and a Nikon E600FN microscope.

F. Ibrahim, N.A. Abu Osman, J. Usman and N.A. Kadri (Eds.): Biomed 06, IFMBE Proceedings 15, pp. 282-286, 2007
www.springerlink.com ' Springer-Verlag Berlin Heidelberg 2007

IV. Results

Selected image slices from the TPLSM data are shown for two constructs (Figure 5):, one attached construct of 0% strain (A, static) and one with 4% strain (B, dynamic). The constructs were strained horizontally. Note how the collagen fibers appear more aligned in the direction of the strain for the 4% strained construct then in the static construct.

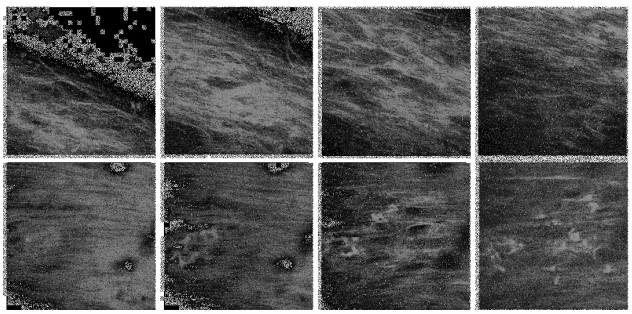

Fig. 5. Selected image slices (206 x 206 μm) from the TPLSM data. one attached construct of 0% strain (A, static) and one of 4% strain (B, dynamic).

In Figure 6 the histograms of both angles are given for unattached, static and dynamically strained samples. The distribution of orientations becomes smaller when the constructs are strained compared to the unattached construct. An even smaller peak in φ can be seen when the strain is increased.

The mean orientation was calculated to determine the general orientation of the collagen fibers. The mean orientation is the orientation with the maximum response in the histogram. The variance in orientation from this mean is used as a measure for alignment.

The variance in θ decreases when 4% and 8% strain is applied compared to the unattached sample and 0% strain sample. The variance in φ decreases when strain is applied.

Changes in collagen orientation can be observed in the TPLSM images such as shown in Figure 5. The fibers of the constructs that were only attached but not strained show a more random collagen orientation then the constructs that were strained. Figure 6 shows that the peak in the histogram is smaller for the tissue engineered constructs that are strained compared to the unattached constructs. This indicates that strain results in more aligned collagen fibers.

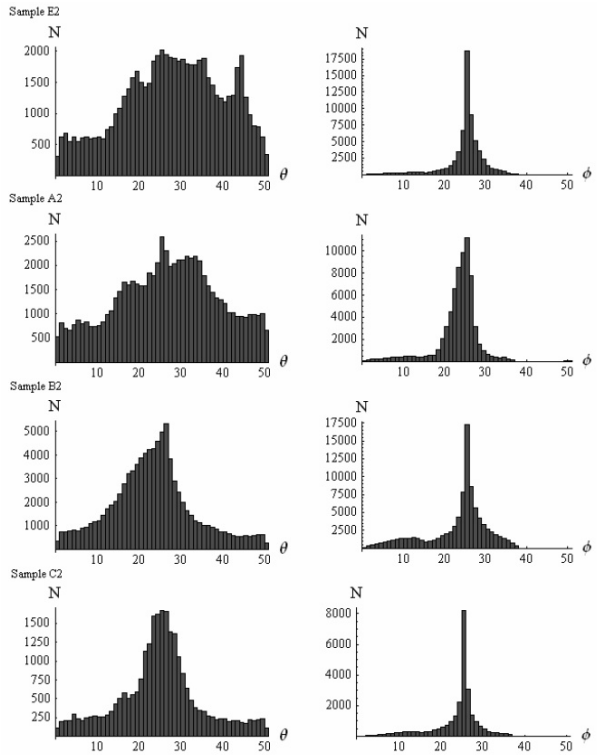

Fig. 6 Orientation analysis results of attached construct A (static), B (4%, dynamic), C (8%, dynamic) and E (unattached control). Histograms of the orientation are given for every angle with both angles (left φ, right θ) divided into 50 bins each bin representing 0.02 π. N is the number of counts. The histograms are shifted so that the maximum response is centered.

V. Conclusions

This work contains a multi-scale analysis method which can be used to obtain robust 3D orientation information. The method determines the minimal principal curvature directions from the Hessian matrix. Three possible methods were described to improve the orientations found by the principal curvature analysis by taking into account the context of the structures in the image. The algorithm was used to study collagen orientation in 3D engineered tissue. The conclusions are summarized below.

- 3D principal curvature directions are an effective way to determine local orientation of tubular structures.
- CED can be used to enhance collagen fibers in TPLSM images.

F. Ibrahim, N.A. Abu Osman, J. Usman and N.A. Kadri (Eds.): Biomed 06, IFMBE Proceedings 15, pp. 282-286, 2007
www.springerlink.com ' Springer-Verlag Berlin Heidelberg 2007

- TPLSM makes it possible to study collagen orientation in 3D tissue engineered constructs.
- This study indicates that there is an increase in collagen alignment with increased strain magnitude based on the orientation histograms.

REFERENCES

[1] Neuenschwander S., Hoerstrup S.P. Heart valve tissue engineering. *Transplant Immunology*, 12: 359-365, 2004.
[2] Schoen F.J., Levy R.J. Tissue Heart Valves: Current Challenges and Future Research Perspectives. *J. Biomed. Mater. Res*., 47: 439-465, 1999.
[3] Hoerstrup S.P., Kadner A., Milnitchouk S., Trojan A., Eid K., Tracy J., Sodian R., Visjager R., Kolb S.S., Grunenfelder J., Zund G. Turina M.I. Tissue Engineering of functional Trileaflet Heart Valves From Human Marrow Stromal Cells. *Circulation*, 106: 134-150. 2002.
[4] Mol A., Functional tissue engineering of human heart valve leaflets, 2005, ISBN 90-386-2956-7.
[5] Billiar K.L., Sacks M.S. Biaxial Mechanical Properties of the Native and Glutaraldehyde-Treated Aortic Valve Cusp: Part II-A Structural Constitutive Model. *J.Biomed. Eng*.,122:137-335, 2000.
[6] Nash-Krahn K., Bouten C.V.C., van Tuijl S., van Zandvoort M.A.M.J., Merkx M. Fluorescently labeled collagen binding proteins allow specific visualization of collagen in tissue and live cell culture. *Analytical Biochem*., 350: 177-185, 2006.
[7] http://wordnet.princeton.edu/perl/webwn?s=curvature
[8] ter Haar Romeny B.M.. Front-End Vision and Multiscale Image Analysis. Springer Verlag, 2002.
[9] Niessen W.J., Lopez A.M., Van Enk W.J., van Roermund P. M., ter Haar Romeny B.M., and Viergever M.A., In vivo analysis of trabecular bone architecture, *in Proc.Information Processing in Medical Imaging*, 1230 (Lecture Notes in Computer Science): 435-440, 1997.
[10] A.F. Frangi, W.J. Niessen, K.L. Vincken, and M.A. Viergever. Multiscale Vessel Enhancement Filtering. MICCAI 98, LNCS 1496, pp. 130 137, 1998.
[11] Weickert J. Coherence-Enhancing Diffusion Filtering. *Int. J. Comp. Vision*, 31: 111-127, 1999.
[12] Weickert J., ter Haar Romeny B.M., Viergever M.A. Efficient and Reliable Schemes for Nonlinear Diffusion Filering. *IEEE Trans. Image Proc*., 17: 398-410, 1998.
[13] Wolfram Research, Inc., *Mathematica*, Version 5.2, Champaign, IL 61820 USA, 2005. URL: www.wolfram.com.

Address of the corresponding author:

Author: Bart M. ter Haar Romeny
Institute: Eindhoven University of Technology
Street: Den Dolech 2 WH2.108
City: NL-5600 MB Eindhoven
Country: the Netherlands
Email: B.M.terHaarRomeny@tue.nl

F. Ibrahim, N.A. Abu Osman, J. Usman and N.A. Kadri (Eds.): Biomed 06, IFMBE Proceedings 15, pp. 282-286, 2007
www.springerlink.com ' Springer-Verlag Berlin Heidelberg 2007

Scale Space Texture Classification Using Combined Classifiers with Application to Ultrasound Tissue Characterization

M.J. Gangeh[1, 2], R.P.W. Duin[3], C. Eswaran[1] and B.M. ter Haar Romeny[2]

[1] Multimedia University, Faculty of Engineering, Cyberjaya, Malaysia
[2] Eindhoven University of Technology, Department of Biomedical Engineering, Biomedical Image Analysis, Eindhoven, the Netherlands
[3] Delft University of Technology, Faculty of Electrical Engineering, Mathematics and Computer Science, Information and Communication Theory Group, Delft, the Netherlands

Abstract—**Texture is often considered as a repetitive pattern and the constructing structure is known as texel. The granularity of a texture, i.e. the size of a texel, is different from one texture to another and hence inspiring us applying scale space techniques to texture classification. In this paper Gaussian kernels with different variances (σ^2) are convolved with the textures from Brodatz album to generate the textures in different scales. After some preprocessing and feature extraction using principal component analysis (PCA), the features are fed to a combined classifier for classification. The learning curves are used to evaluate the performance of the texture classifier system designed. The results of classification show that the scale space texture classification approach used can significantly improve the performance of the classification especially for small training set size. This is very important in applications where the training set data is limited. The application of this method to ultrasound liver tissue characterization for discrimination of normal liver from cirrhosis yields promising results.**

Keywords— **Scale space, texture classification, combined classifiers, tissue characterization, liver**

I. Introduction

Liver disease is one of the most prevalent diseases in the world and an early diagnosis helps to prevent changing the state of the disease to a developed stage. Liver diseases are of two types: focal and diffused. In the former, only part of the liver is affected by a tumor while in the latter, the whole liver or at least one lobe is completely affected. In diffused liver diseases like cirrhosis, the texture of liver in ultrasound B-scan images is affected by the kind of pathology that makes it distinguishable from normal liver. However, the accuracy of the diagnosis by the sonologist based on qualitative criteria, i.e. visual inspection of the ultrasound images is low. Thus, computer aided texture classification systems can help to improve the diagnosis. In this paper we develop one algorithm for texture classification, which is proved to be efficient especially when just a small number of data samples is available for training and testing.

There is a vast literature on texture analysis, as can be judged from the innumerable applications the texture analysis has in various fields [1, 2].

Texture analysis techniques are classified basically into four types of approaches: statistical [3], structural, transform-based [4, 5] and model-based [1, 6, 7].

In recent years, scale space theory has been recognized as the vital tool for texture analysis [8]. This is because texture displays a multi-scale property. Whatever may be the representation, it is applicable in different scales.

In this paper scale space theory is used to produce multi-scale texture images. The patches are extracted from these textures and after feature extraction using principal component analysis (PCA), the features are applied to some basic classifiers. The outputs of these basic classifiers are then combined using a fixed combination rule to classify the textures. The performance of the whole system is evaluated using learning curves for different learning set sizes. Finally the application of the method and its effectiveness to liver ultrasound tissue characterization is shown.

II. Scale space texture classification

A texture classification system is typically consisting of several stages including preprocessing, feature extraction and classification [9]. Each stage is explained below in the context of scale space texture classification.

A. Scale space analysis

Texture is usually considered as a repetitive pattern and this constructing repetitive structure is of varying size in different textures. This inspires us to apply multi-scale techniques in texture analysis. Here, scale space theory, which is biologically motivated based on the model of front end vision, is used for multi-scale texture classification. In scale space image analysis, 2-D Gaussian kernels as given in (1), with different variances (σ^2) are convolved with the image to generate the image in different scales. This generates multi-scale images and each image emphasizes on

F. Ibrahim, N.A. Abu Osman, J. Usman and N.A. Kadri (Eds.): Biomed 06, IFMBE Proceedings 15, pp. 287-290, 2007
www.springerlink.com ' Springer-Verlag Berlin Heidelberg 2007

details in the corresponding scale. The larger the Gaussian kernel variance (σ^2), the more emphasis on coarser structures.

$$G_{2D}(x,y;\sigma) = \frac{1}{2\pi\sigma^2} e^{-\frac{x^2+y^2}{2\sigma^2}} \quad (1)$$

This is shown in Fig. 1 where a texture from Brodatz album is convolved with Gaussian kernel of varying variance.

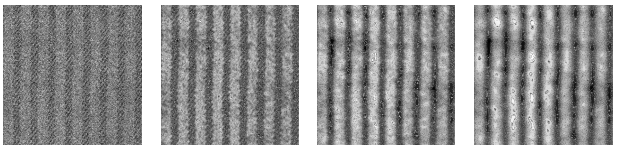

Fig. 1 Texture D11 of Brodatz album in 4 different scales.

To discriminate two or more textures, we use the additional information provided in different scales to achieve a better performance (comparing to single scale). To this end, the patches are extracted from the textures in the original and other scale space. The size of the patch is an important factor that depends on the sizes of the texel and the applied Gaussian kernel. It also affects the dimensionality of the feature space as larger patches generate more features. This may impose problems with respect to the computation speed as well as to the necessary training set size. This is further explained in relation to feature extraction and classification.

B. Feature extraction

Working in high dimensional feature space usually imposes problems as we need more data samples for training. This phenomenon is called the curse of dimensionality. It may cause the peaking phenomena in classifier design [2]. There are two solutions to this problem. First, to increase the training set size and second to reduce the feature space dimension using feature selection/extraction techniques. Many feature selection/extraction techniques are addressed in the literature among which Principal Component Analysis (PCA) is one of the most prevalent ones.

In PCA, we consider a population of random vectors of the form:

$$\mathbf{x} = \begin{bmatrix} x_1 & x_2 & \cdots & x_n \end{bmatrix}^T \quad (2)$$

The mean vector and covariance matrix of this random population can be calculated as follows:

$$\mathbf{m}_\mathbf{x} = E\{\mathbf{x}\} \quad (3)$$

$$\mathbf{C}_\mathbf{x} = E\{(\mathbf{x}-\mathbf{m}_\mathbf{x})(\mathbf{x}-\mathbf{m}_\mathbf{x})^T\} \quad (4)$$

In PCA, the eigenvectors of the covariance matrix C_x are used to define a transform matrix A, the rows of which are made up of the eigenvectors weighted by decreasing magnitude of corresponding eigenvalue. Rotation of the input vectors to the eigenvectors yields an uncorrelated data set, i.e., its covariance matrix is a diagonal matrix.

Feature extraction for the purpose of dimension reduction using PCA can be achieved by selection of only first few components (eigenvectors) corresponding to the largest eigenvalues. This preserves up to specified fraction of the variance in the original data set [9]. The main question is how many components are needed to guarantee that thereby sufficient information of the original data set is preserved in the transformed (uncorrelated) space. We answer this question here in our multi-scale context of texture classification. By going to higher scales, i.e. convolving the image with the Gaussian kernel of larger variances, we lose the details and therefore we expect that fewer components are needed to preserve the information in the original random vector. This is shown in Fig. 2 by drawing the cumulative fraction of the eigenvalues, which also represent the fraction of the variance of the original data, in two scales for texture D11 from Brodatz album. It is clear that as we go to higher scales, fewer components are required to preserve the same amount of variance of the original data.

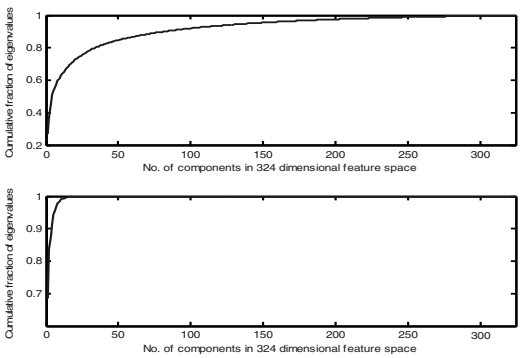

Fig. 2 Cumulative fraction of eigenvalues (i.e., preserved variance) for texture D11 in the original space (top graph) and after convolving the texture with a Gaussian kernel of variance 9 (bottom graph).

C. Classifier

The next issue to address in this texture classification system is the classifier. We have so far produced the data in different scales and reduced the dimensionality of the feature space using PCA. As explained in the previous section, the feature space dimension will be different after applying PCA when we go from one scale to another.

Based on this, parallel combined classifiers seem natural as they can be used for combining different feature spaces. Combined classifiers are used in multiple classifier source

F. Ibrahim, N.A. Abu Osman, J. Usman and N.A. Kadri (Eds.): Biomed 06, IFMBE Proceedings 15, pp. 287-290, 2007
www.springerlink.com ' Springer-Verlag Berlin Heidelberg 2007

applications like different feature spaces, different training sets, different classifiers applied for example to the same feature space, and different parameter values for the classifiers for example k in k nearest neighbor (k-NN) classifier. The block diagram of the parallel combined classifier used in this paper is shown in Fig. 3. There are two parameters to be selected in this combined classifier, i.e. the type of the basic classifier and the combination rule. The selection of these two options is discussed in section IV.

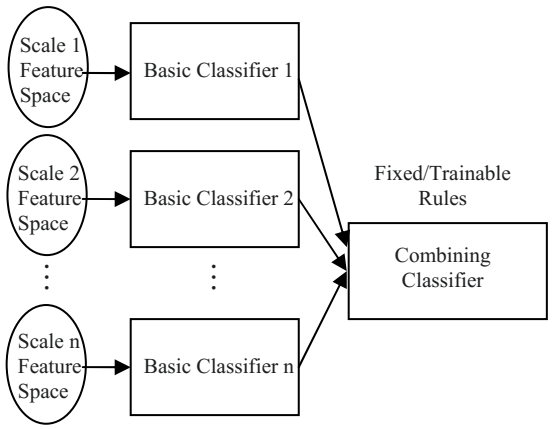

Fig. 3 Block diagram of the combined classifier used in this paper.

III. Experiments

To verify the effectiveness of the proposed method, experiments were performed on a supervised classification of some test images. The test images are from Brodatz album and some normal and cirrhosis B-scan ultrasound liver images shown in Fig. 4 and Fig. 5 respectively. The experiments performed are explained separately for textures from Brodatz album and liver images.

A. Experiments on textures from Brodatz Album

Preprocessing: The textures are convolved with 2D Gaussian kernels in 5 different scales. The scales ($\sigma^2/2$) of the Gaussian kernels used in the convolution are 1.5, 3, 4.5, 6 and 7.5. We add the original texture to this scale space to get a scale space texture of 6 scales.

To make sure that for all textures the full dynamic range of the gray level is used contrast stretching is performed on all textures in different scales. Also, to make the textures indiscriminable to mean or variance of the gray level, DC cancellation and variance normalization are performed.

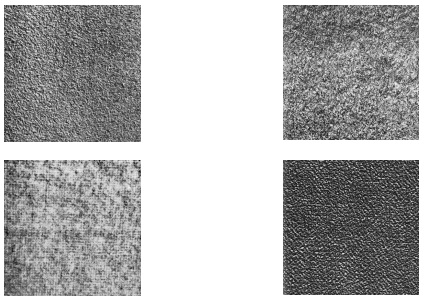

Fig. 4 Textures D4, D9, D19 and D57 from Brodatz album used in the experiments.

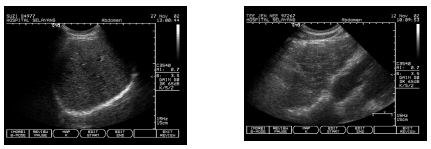

Fig. 5 A typical normal liver (left) and cirrhosis (right) B-scan image used in the experiments.

Feature extraction: 1800 patches with size 18×18 are extracted from the textures in different scales. Then, PCA is used for the purpose of feature extraction. The number of components used for dimension reduction is chosen to preserve 90% of the original variance in the transformed (reduced) space. This is between about 3 and 50 components in the highest and lowest scales.

Combined classifier: A variety of basic classifiers and combining rules are tested to find the best one. Among the basic classifiers tested are some normal-based density classifiers like quadratic discriminant classifier (qdc), linear discriminant classifier (ldc), and nearest mean classifier (nmc). The Parzen classifier was also tested as a representative of non-parametric based density classifier. Six basic classifiers one for each scale are used. The mean, product and voting fixed combination rules as well as the nearest mean trainable combination rule are tested for comparison.

Evaluation: The performance of the texture classification system is evaluated by drawing the learning curve for a variety of training set sizes. For each training set size, the remaining of the patches are used to test the system and hence the training and testing data are separate. The error is measured 10 times for each training set size and the results are averaged.

B. Experiments on B-scan ultrasound liver images

Normal liver and liver affected by cirrhosis are used in the experiments. The region of interest (ROI) is taken from the center of the image where the image is the most focused. The size of the ROI is 32×32. Here, only three different

F. Ibrahim, N.A. Abu Osman, J. Usman and N.A. Kadri (Eds.): Biomed 06, IFMBE Proceedings 15, pp. 287-290, 2007
www.springerlink.com ' Springer-Verlag Berlin Heidelberg 2007

scales in addition to the original image are used and since the granularity of the texture is lower, lower scale values are used for the Gaussian kernel, i.e. 1, 2 and 3. The patches have the size of 6×6. 1000 patches are extracted from the liver images in different scales. Based on the results of texture classification on Brodatz album, the quadratic classifier (qdc)is used as base classifier and the mean fixed combination rule as combined. Evaluation is performed in the same way as for the experiments on Brodatz album.

IV. Results

A variety of tests are performed using different parameters as explained in the previous section. Among tested basic classifiers explained in the previous section, qdc performed the best. This can be justified based on the feature extraction method used as PCA is a linear dimension reduction that performs integration in the feature space. Consequently, the features tend to be normally distributed based on the central limit theorem. On the other hand, among tested combination rules, mean fixed rule performs the best.

Fig. 6 displays the learning curves in single and multiple scales for the textures from Brodatz album. The peak of the curve is a result of peaking phenomena as explained in Subsection II-B. It is important to notice that multi-scale texture classification improves the performance of the classification significantly especially in low training set sizes which is very important in applications where training data set is limited like ultrasound liver tissue characterization.

Fig. 7 displays the learning curves in single and multiple scales for liver images. Although the size of the training set is quite limited here, the performance is still remarkable that shows the effectiveness of the approach.

V. Discussion and conclusion

Scale space theory, PCA and combined classifiers are integrated into a texture classification system. The system is very efficient especially in low training set size that the system can significantly improve the performance of the system comparing to single scale based on the information provided in multiple scales.

Since in liver tissue characterization one major problem is limitation in image acquisition as the images should be standardized, this method can be very effective in this application. Promising results obtained from applying the method to discriminate normal liver from cirrhosis.

In this paper we only used intensity scale space for texture classification. As future work, we will also consider gradient scale space, i.e. derivatives of Gaussian kernel in different scales for generation of multi-scale texture.

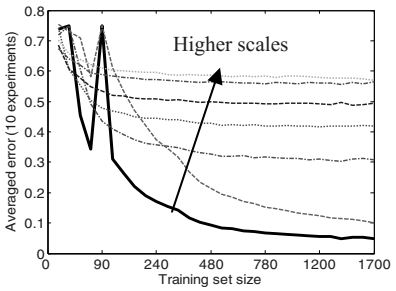

Fig. 6 Learning curves for the classification of 4 textures from Brodatz album in single (thin curves) and multiple (thick curve) scales.

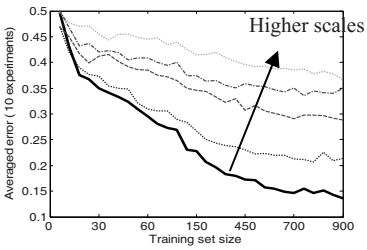

Fig. 7 Learning curves for the classification of normal liver and cirrhosis in single (thin curves) and multiple (thick curve) scales.

References

1. Materka A and Strzelecki M (1998) Texture analysis methods-A review, Technical University of Lodz, Institute of Electronics, COSTB 11 report, Brussels.
2. Jain AJ, Duin RPW and Mao J (2000) Statistical pattern recognition: a review, IEEE Trans. on PAMI, 22 (1): 4-37.
3. Baraldi A and Parmiggiani F (1995) An investigation of texture characteristics associated with gray level co-occurrence matrix structural parameters, IEEE Trans. on Geoscience and Remote Sensing, 33 (2): 293-304.
4. Randen T and Husoy JH (1999) Filtering for texture classification: a comparative study, IEEE Trans. on PAMI, 21 (4): 291-310.
5. Jain AK and Farrokhnia F (1991) Unsupervised texture segmentation using Gabor filters, Pattern Recognition, 24 (12): 1167-1186.
6. Reed TR and Hans du Buf JM (1993) A review of recent texture segmentation and feature extraction techniques, VGIP: Image Understanding, 57 (3): 359-372.
7. Krishnamachari S and Chellappa R (1997) Multi-resolution Gauss-Markov random field models for texture segmentation, IEEE Trans. on Image Processing, 6 (2): 251-267.
8. ter Haar Romeny BM (2003) Front-end vision and multiscale image analysis, Kluwer Academic Publishers, Dordrecht, the Netherlands.
9. Webb A (2002) Statistical pattern recognition, 2nd Ed., John Wiley and Sons, West Sussex, England.

Address of the corresponding author:

Author: Mehrdad J. Gangeh
Institute: Multimedia University
Street: Jalan Multimedia
City: Cyberjaya
Country: Malaysia
Email: mehrdad@mmu.edu.my/M.Gangeh@tue.nl

F. Ibrahim, N.A. Abu Osman, J. Usman and N.A. Kadri (Eds.): Biomed 06, IFMBE Proceedings 15, pp. 287-290, 2007
www.springerlink.com ' Springer-Verlag Berlin Heidelberg 2007

Spinal Curvature Determination from an X-Ray Image Using a Deformable Model

T.A. Sardjono[1], M.H.F. Wilkinson[2], P.M.A. van Ooijen[3], A.G. Veldhuizen[4], K.E. Purnama[1], G.J. Verkerke[1, 5]

[1]Department of Biomedical Engineering, University Medical Center Groningen, University of Groningen,Netherland
[2]Institute for Mathematics and Computing Science, University of Groningen, Netherland
[3]Department of Radiology, University Medical Center Groningen, University of Groningen , Netherland
[4] Department of Orthopaedic Surgery, University Medical Center Groningen, University of Groningen
[5]Department of Biomechanical Engineering, University of Twente, Netherland

Abstract- **This paper presents a spinal curvature determination from frontal X-ray images of scoliotic patients. A new deformable model, Modified CPM (Charged Particles Model), has been developed and used to determine the spinal curvature. The Modified CPM is a new approach of a deformable model based on CPM, which was introduced in 2004. The X-ray image is charged negatively according to the edge-map or gradient-magnitude image. The particles are attracted towards the contour of the object of interest, because this contour is very dark, thus charged very negatively. We modified the CPM by putting springs between the particles to prevent the particles from moving away and keep the movement of the particles in the appropriate distance without reducing the flexibility to follow the curvature. The results of the implementation show the effectiveness of the modified charged-particle model for spinal curvature determination on X-ray images.**

I. Introduction

Scoliosis is a three-dimensional deformity of the spinal column. It is generally characterized by a lateral deviation of the spine, accompanied with an axial rotation of the vertebrae. The standard radiology evaluation of adolescent idiophatic scoliosis consists of standing antero-posterior and lateral radiograph of the full spine. The Cobb method is used to measure the curvature of spinal column on the AP (antero-posterior) film and determines the severity of the scoliosis. Usually the physician calculates the Cobb angle manually on the AP film or by drawing 2 lines from the digital image using mouse and computer will calculate the angle between those lines.

The radiographic measurements by putting six landmarks manually per vertebra on each AP radiograph were done by Wever *et. al*. [2]. These landmarks were scanned and saved as Cartesian coordinates in a computer file. He calculated the midpoint of the vertebral bodies and the lateral tilt of the upper and lower end plates of each vertebra by a computer algorithm. The Cobb angle consisted of the angle between the upper endplate of the upper, most tilted vertebra and the lower endplate of the lowest, most tilted vertebra in the scoliotic curve.

A comparison of manual versus computer-assisted radiographic measurement of Cobb angle (performed on digitized images using a computer mouse) was done by Shea *et. al.* [3] in 1998. By using these computer technique sources of intrinsic error, e.g., the variability introduced by using different manual protractors, the inaccuracy of standard protractors, and the use of wide-diameter radiographic markers, were avoided. However, determining the upper and lower vertebra still has to be done manually and can cause an intrinsic error.

To further automate curvature determination will be a great contribution for this problem. We propose the use of deformable models, more specifically a tailored version of the Charged-Particles Model to determine the curvature automatically.

Deformable models were first introduced by Terzopoulous *et al.* [4] in 1998. A survey of deformable models in medical image analysis has been performed by McInerney *et al.* [5]. Deformable models are curves, surfaces or particles defined within an image domain that can move under the influence of *internal forces* and *external forces*. Internal forces are defined within the curve, surface or particle and external forces are computed based on the image data.

A different approach of the deformable model is based on the use of charged-particles. The Charged-Particle Model (CPM) was first introduced by Jalba *et al.* [1]. This model is inspired by classical electrodynamics and is based on a simulation of charged particles moving in an electric field. The particles have a positive charge and move freely in an external electrostatic field $\bar{E}$, generated by fixed, negative charges, placed at each pixel position of the input image, with a charge magnitude proportional to the edge-map of the input image.

The important characteristics of the CPM are lower sensitivity to initialization, better capture range and convergence into boundary concavity [1]. However, the

F. Ibrahim, N.A. Abu Osman, J. Usman and N.A. Kadri (Eds.): Biomed 06, IFMBE Proceedings 15, pp. 291-295, 2007
www.springerlink.com ' Springer-Verlag Berlin Heidelberg 2007

particles can move apart if the inter-particle force is too high or the distance is too small. Other disadvantages of CPM are the difficulty to maintain any structure in the distribution of the particles, or defining some shape prior. These problems become severe in the presence of many cluttered features, as in the case of our X-rays.

In this paper we introduce a new method based on the inclusion of springs in the CPM. The charges are attracted toward the contour of the object of interest by a negative electric field. The springs prevent the particles from moving apart and keep the movement of the particles at appropriate distances without reducing the flexibility to follow the curvature.

This paper will describe the feasibility of a modified charged-particle model to determine the spinal curvature from an X-ray image.

II. Materials and Methods

1. Frontal X-ray images

50 Frontal X-ray images of scoliotic patients were used, both single and double curved. The acquisition of a series images was done on a Philips Multidiagnost Radiofluoroscopy system and the reconstruction process which combines the different parts of the spine was done by the Philips Easy Vision system, Radiology Department, University Medical Center Groningen, The Netherlands.

2. Image Pre-processing

Six groups of morphological image pre-processing methods, namely top-hat filtering (TH) and five modified top-hat filtering (ModTH-1 ModTH-5) methods were studied to improve the quality of the X-ray images, especially to eliminate an uneven background, which usually appears on X-ray images and to boost the thoracic part which is less visible due to over projection of the sternum. The modified top-hat filtering method is based on eq.1.

$$f_{ModTH} = \frac{(f \bullet b_n) - f}{f \bullet b_n} \gamma \qquad (1)$$

where f_{ModTH} is modified dark top-hat filtering, $\bullet$ is closing of morphological operator, b_n is a structural element and γ is an attenuation factor. For every modified top-hat filtering method, five different sizes of structural element (disk1-disk5) and five different attenuation factors were used to evaluate 50 frontal images. The positions of the particles of 31 images for every frontal image, before and after preprocessing, are evaluated visually. This resulted in the evaluation of more than 1500 images. For each image we recorded whether the particles fit the curvature or not.

3. Curvature determination

The curvature determination was done by Modified CPM. This method simulates the behaviour of positively charged particles moving in a simulated electric field derived from the grey level image. This electric field has a charge magnitude proportional to the edge-map of the input image.

The modified CPM is formulated based on (2), so the resulting force $\vec{F}$ acting on every particle is:

$$\vec{F}(\vec{r}_i) = \vec{F}_c(\vec{r}_i) + \vec{F}_l(\vec{r}_i) + \vec{F}_s(\vec{r}_i) - \beta\vec{v}_i \qquad (2)$$

where $\vec{F}_c$, $\vec{F}_l$, $\vec{F}_s$ and $\beta\vec{v}_i$ are the Coulomb force, Lorentz force, Spring force and damping or viscous factor. The particles that are charged positively, are attracted towards the curvature of the image, because this contour is very dark, thus charged very negatively.

The Coulomb force $\vec{F}_c$ acting on a particle p_i with charge q_i is the sum of all Coulomb forces generated by all other free particles and given by:

$$\vec{F}_c(\vec{r}_i) = q_i \sum_{j \neq i}^{N} \frac{q_j}{4\pi\varepsilon_o} \frac{\vec{r}_i - \vec{r}_j}{|\vec{r}_i - \vec{r}_j|^3} \qquad (3)$$

The Lorentz force $\vec{F}_l$ acting on particle p_i with charge q_i is given by

$$\vec{F}_l(\vec{r}_i) = q_i\left(\vec{E}(\vec{r}_i) + \frac{\vec{v}_i}{c} \times \vec{B}(\vec{r}_i)\right) \qquad (4)$$

where v_i, c, $\vec{E}(\vec{r}_i)$ and $\vec{B}(\vec{r}_i)$ are the speed of the particle, the speed of light, electric field and the magnetic field. Since a magnetic field is absent ($\vec{B}$ = 0), and the Lorentz force becomes

$$\vec{F}_l(\vec{r}_i) = q_i\vec{E}(\vec{r}_i) \qquad (5)$$

with a direction parallel to that of the electric field $\vec{E}$. The magnetic field generated by the moving particles is ignored.

A spring is put between two particles and the spring force is calculated in every particle. A spring is characterized by Hooke's law.

$$\vec{F} = -kd\vec{X} \qquad (6)$$

where k is the spring stiffness and $d\vec{X}$ is the spring deflection from the undeflected position, caused by a force $\vec{F}$.

F. Ibrahim, N.A. Abu Osman, J. Usman and N.A. Kadri (Eds.): Biomed 06, IFMBE Proceedings 15, pp. 291-295, 2007
www.springerlink.com ' Springer-Verlag Berlin Heidelberg 2007

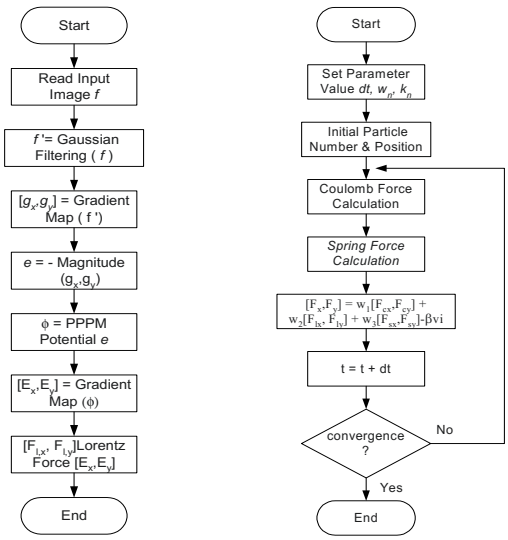

Fig.1 Flowchart for the external field (Lorentz Force) and movement of particles

The springs prevent the particles from moving away and restrict the movement of the particles without reducing the flexibility to follow the curvature

The algorithm of this method consists of two parts, the calculation of the electric field from a postero-anterior X-ray image and the computation of the particle dynamics. Fig. 1 shows the flowchart of modified CPM algorithms.

The algorithm is based on the CPM algorithm [1], but we insert the spring force calculation in the total force calculation of the particle dynamics for every particle. First step in the computation of the external force, Lorentz force, is image filtering using Gaussian filtering. The gradient map from the result of Gaussian filtering and the magnitude of the gradient map are computed and passed as input to the Particle-particle particle mesh (PPPM) method from molecular dynamics [9]. Finally, the external field or Lorentz force is created from the gradient map [E_x, E_y]. The second part of the algorithm concerns the movement of particles based on the Coulomb and spring force, shown as flowchart in Fig. 1 (right). We define the number and the initial position of the particles. Then, the Coulomb force and spring force are calculated and the particles will move until convergence.

III. Results

1. Image pre-processing

50 Frontal images of scoliotic patients have been improved by pre-processing using top-hat filtering or a modified top-hat filtering method. Fig. 2 shows the results of curvature detection after the different types of filters were applied. The filters are modified top-hat filters using different size of structural elements and different attenuation factors (group 2 group 6, left bar). The type of the structural elements is disk .

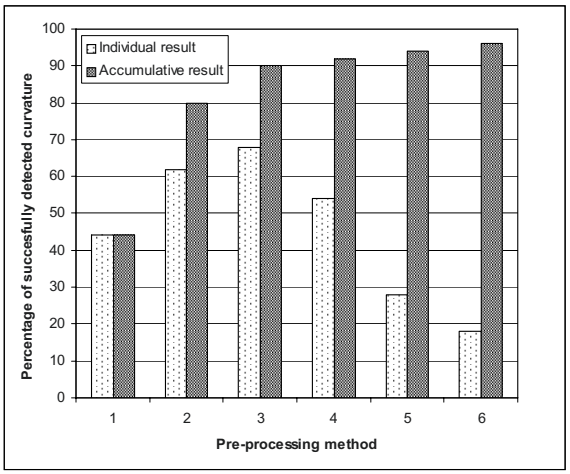

Fig. 2 The result of curvature detection using 6 different groups of image pre-processing, left bar: the individual result- right bar: accumulative result. (1) Without pre-processing, (2) Top-hat filtering, (2-6) Modified top-hat with different structural disc element and different attenuator factor.

Fig. 3 shows an example of an original image and the resulting image after enhancement using the modified top hat filtering method with 3 different attenuator factors.

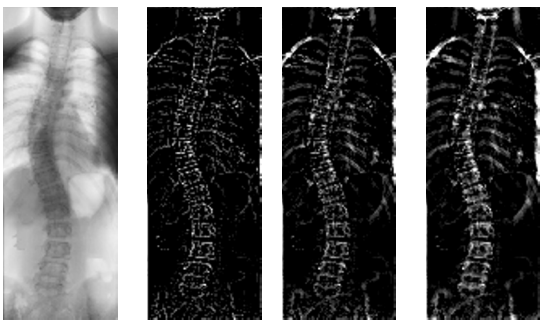

Fig. 3 (a) The original image and (b), (c), (d) the images after the enhancement result by using modified top-hat filtering with 3 different attenuator factors.

2. Curvature determination using modified CPM

The modified CPM is applied to determine the spinal curvature from an X-ray. 2 reference points were placed at top and bottom. For several images which have more complicated curvature, 3 or 4 reference points are needed. Only the first and last reference points will be fixed on that position.

F. Ibrahim, N.A. Abu Osman, J. Usman and N.A. Kadri (Eds.): Biomed 06, IFMBE Proceedings 15, pp. 291-295, 2007
www.springerlink.com ' Springer-Verlag Berlin Heidelberg 2007

The curvature of 22 frontal original images (44%) was detected without image pre-processing. By applying different image pre-processing method 96% of the spinal curvature can be determined.

By using this method, the physician must accept or reject the result. If the result is rejected, then he/she can continue using the image pre-processing to get better result. Fig. 4 shows the result of the modified CPM on an X-ray image of a scoliotic patient.

Fig. 5 shows the failed result of the implementation of modified CPM on X-ray image curvature determination caused by unclear vertebra structure or the spinal curvature too close to the boundary of image. Some cluttered features, such as ribs, also cause the particles to move from the spinal curvature. This problem can be solved by putting fixed reference points in certain places, so the particles will be in the proper position.

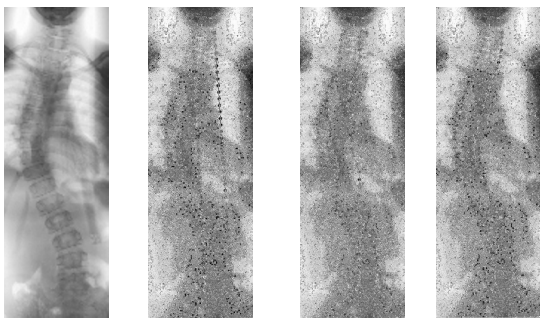

(a) (b) (c) (d)

Fig.4 The modified CPM applied on an X-ray image of a scoliotic patient. (a) Original Image, (b) Initial particles position, (c) Particles attached the curvature, (d) Final particles position

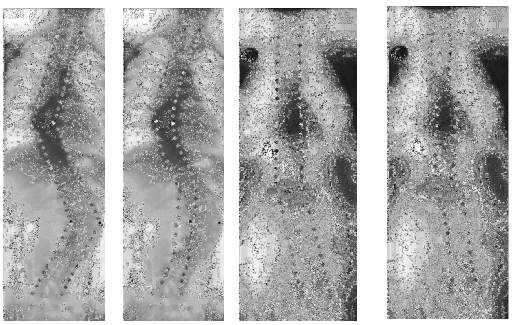

(a) (b) (c) (d)

Fig. 5 Failed result of the implementation of modified CPM on X-ray image curvature determination. (a) (b) Initial position and final result of frontal 4, (c) (d) Initial position and final result of frontal 18

IV. Discussion

The determination of the spinal shape is very important for the orthopaedic surgeon to evaluate curve progression especially for severe cases of scoliosis (Cobb angle greater than 45 degrees). Spinal curvature determination and Cobb angle measurement is the most important step before we can determine the spinal shape. For this purpose, modified CPM could give a contribution to determine the curvature and Cobb angle measurement.

The result of detecting the spinal curvature on an X-ray image with an artifact in the thoracic area shows that the combination of spring and CPM can detect the spinal curvature very well. A more detailed investigation shows that a technical improvement of spring forces in the CPM method with different configuration (closed spring curve and its combinations) can be adapted for general applications and specific applications by using appropriate spring-particle configuration.

Detecting the spinal curvature only failed totally in two of the fifty images because the position of some vertebrae was very close to the image boundary. To overcome this problem, a marker is needed to be given in a certain area to increase the negative field. The other frontal X-ray images of scoliotic patients can be detected when one of the proposed image pre-processing methods is applied.

V. Conclusions

With the modified CPM the global curve of a spinal X-ray image of a scoliotic patient can be determined, even though there are many cluttered features. The modified CPM can also be used to determine both open curves and closed curves without collapse. Other shape priors could also be generated. The modified top-hat filtering gives very good results based on the number of detected curvatures.

References

[1]. Jalba A.C., M. H. F. Wilkinson, Jos B. T.M. Roerdrink (2004): CPM: A Deformable Model for Shape Recovery and Segmentation Based on Charged Particles , *IEEE Trans Pattern Analysis and Machine Intelligence,* 26 (10), pp. 1320-1335

[2]. Wever D.J., Tonseth K.A., Veldhuizen A.G., Cool J.C., Horn J.R. (2000): Curve Progression and Spinal Growth in Brace Treated Idiopathic Scoliosis , *Clinical Orthopaedics and Related Research*, **377**, pp. 169-179

F. Ibrahim, N.A. Abu Osman, J. Usman and N.A. Kadri (Eds.): Biomed 06, IFMBE Proceedings 15, pp. 291-295, 2007
www.springerlink.com ' Springer-Verlag Berlin Heidelberg 2007

[3]. SHEA, KEVIN G., STEVENS, PETER M., NELSON, MARK, SMITH, JOHN T., MASTERS, KEVIN S., YANDOW, SUZANNE M.D. (1998): Comparison of Manual Versus Computer-Assisted Radiographic Measurement: Intraobserver Measurement Variability for Cobb Angles , *Spine*. **23(5)**, pp. 551-555

[4]. TERZOPOULOS D., FLEISCHER K. (1998): Deformable models . *The Visual Computer,* **4(6)**, pp 306-331

[5]. MCINERNEY T., TERZOPOULOS T. (1996): Deformable models in medical image analysis: a survey , *Medical Image Analysis*, **1(2)**, pp. 91-108

Address of the corresponding author:

Author: T.A. Sardjono
Institute: Department of Biomedical Engineering, University Medical Center Groningen, University of Groningen
Country: Netherland
Email: t.a.sardjono@med.umcg.nl

F. Ibrahim, N.A. Abu Osman, J. Usman and N.A. Kadri (Eds.): Biomed 06, IFMBE Proceedings 15, pp. 291-295, 2007
www.springerlink.com ' Springer-Verlag Berlin Heidelberg 2007

Thresholding of Medical Images Using Minimum Cross Entropy

R. Al-Attas and A. El-Zaart

Department of Computer Science, College of Computer and Information Sciences, King Saud University, Riyadh, Saudi Arabia

Abstract— **In industrial application, image thresholding has been widely used due to the simplicity of implementation and time execution. Many entropy algorithms have been developed for image thresholding. Gamma distribution showed good result in the modeling of data in images. Gamma distribution has a general shape than the Gaussian distribution. In this paper, we developed a fast iterative method from minimum cross entropy thresholding using Gamma distribution. Experimental results showed that the use of Gamma distribution produced good results.**

Keywords— **Thresholding, entropy, Gamma Distribution.**

I. Introduction

Medical imaging is the process by which physicians evaluate an area of the subject's body that is not externally visible. Modern imaging technology includes radiography (x-ray), fluoroscopy, tomography (CT scan), magnetic resonance imaging (MRI) and ultrasound. Medical imaging is the most important method for diagnosis. It also plays an increasingly important role in treatment through use of image-guided intervention procedures, minimally invasive surgery, and individual monitoring of response to drug treatment. Image segmentation is considered as the fundamental step in medical image processing due to its ability of extracting objects of interest. Thresholding provides an easy and convenient way to perform segmentation on the basis of the different intensities in the foreground and background regions of an image. The key parameter in thresholding is obviously the choice of the threshold. Several different methods for choosing a threshold exist. Sankur and Sezgin (2004) categorized the thresholding methods in six groups according to the information they are exploiting [1]. One of these categories uses entropy as thresholding criteria. Entropy serves as a measure of separation that separates the information into two regions, above and below an intensity threshold. Entropy-based methods result in algorithms that use the entropy of the foreground and background regions, the cross-entropy between the original and binarized image and etc [1]. These methods can be subdivided into: entropic thresholding, cross-entropic thresholding, and fuzzy entropic thresholding. Entropic thresholding considers the image foreground and background as two different signal sources, so that when the sum of the two class entropies reaches its maximum, the image is said to be optimally thresholded. Fuzzy entropic thresholding considers the fuzzy memberships as an indication of how strongly a grey value belongs to the background or to the foreground. Cross-entropic thresholding formulates the thresholding as the minimization of an information theoretic distance [1]. In this work we will use the cross-entropy thresholding to segment medical images. The threshold can be selected to minimize the cross-entropy. Some entropy thresholding methods use Gaussian distribution as an ideal reference histogram for the images to be thresholded. Clearly, it is doubtful that any natural images would generate a histogram with such a distribution. In this paper, a new thresholding method using Gamma distribution is proposed, since it is more general than other distributions. This method is useful in extracting objects of interest in images especially medical ones. The remainder of this paper is structured as follows: section 2 discusses Gamma distribution. Section 3 explains the new method. Finally, section 4 shows the results of applying the new method on different images and compares this method with Gaussian entropy thresholding method.

II. Gamma distribution

In probability theory and statistics, the Gamma distribution is a continuous probability distribution. The probability density function of the Gamma distribution in homogeneous area is known to [5,6,7]:

$$f(x,\mu,N)=\frac{2q}{\mu}\frac{N^N}{\Gamma(N)}\left(\frac{qx}{\mu}\right)^{2N-1}e^{-N(qx/\mu)^2}$$

Where $q=\dfrac{\Gamma(N+0.5)}{\Gamma(N)\sqrt{N}}$, and x is the intensity of the pixel, μ is the mean value of the distribution and N represents the parameter shape of the distribution. The shape of the Gamma distribution could be symmetry or skewed to the right. Gamma Distribution is better than Gaussian because Gaussian it works only with symmetric histograms but in the case of Gamma distribution if we want a symmetric histogram, we set N to a high value. By using Gamma distribution we can get a histogram skewed to the right by setting N to a small value.

F. Ibrahim, N.A. Abu Osman, J. Usman and N.A. Kadri (Eds.): Biomed 06, IFMBE Proceedings 15, pp. 296-299, 2007
www.springerlink.com ' Springer-Verlag Berlin Heidelberg 2007

III. Minimum cross entropy using gamma distribution

In this section, a new method is derived from improving Li .et al. methods [2,3]. They obtained threshold using minimum cross entropy with Gaussian distribution. Gamma distribution showed good result in the modeling of data in images and it is more general than Gaussian distribution [5,6,7]. Our method presented in this paper, obtains the optimal threshold that minimizes the minimum cross entropy using Gamma distribution.

For a histogram *h(i)* defined on the grey level range *[1, L]*. The estimation of mean values for background and object using Gamma distribution is defined as follow [5,6,7] :

$$\mu_B^2(t) = \frac{\sum_{i=0}^{t-1} h(i).i^2q^2}{\sum_{i=0}^{t-1} h(i)} \text{ and } \mu_O^2(t) = \frac{\sum_{i=t}^{L} h(i).i^2q^2}{\sum_{i=t}^{L} h(i)}$$

We can write the mean formulas as follow:

$$\mu_B(t) = \frac{m_{1B}(t)}{m_{0B}(t)}, \qquad \mu_O(t) = \frac{m_{1O}(t)}{m_{0O}(t)}.$$

where

$$m_{1B}(t) = \sqrt{\sum_{i=0}^{t-1} h(i).i^2q^2} \text{ and } m_{0B}(t) = \sqrt{\sum_{i=0}^{t-1} h(i)}$$

and the same is for $m_{1O}(t)$ and $m_{0O}(t)$

$$m_{1O}(t) = \sqrt{\sum_{i=t}^{L} h(i).i^2q^2} \text{ and } m_{0O}(t) = \sqrt{\sum_{i=t}^{L} h(i)}$$

The criterion function of threshold selection which minimizes the cross entropy of the image is found to be [3]:

$$\eta(t) = -m_{1B}(t)\log(\mu_B(t)) - m_{1O}(t)\log(\mu_O(t))$$

By replacing the $m_{1B}(t)$, $m_{1O}(t)$, $\mu_B(t)$, and $\mu_O(t)$ of Gamma distribution in the above expression, we can find the optimal threshold t_{opt} which minimizes $\eta(t)$.

$$t_{opt} = \arg\min_t(\eta(t))$$

The optimal value of the threshold can be estimated by tow methods: (i) we can calculate the value of $\eta(t)$ by using all the possible value of *t* and then we select the value of t_{opt} which minimizes the $\eta(t)$ and (ii) the computation of the first method can be reduced if we can estimate the optimal threshold by setting the derivative of $\eta(t)$ to zero. The optimal threshold t_{opt} is estimated by solving the following equation:

$$\frac{\partial \eta(t)}{\partial t} = 0.$$

The solution of the above equation is:

$$t_{n+1} = \sqrt{\frac{\frac{\mu_B(t_n)}{m_{0B}(t_n)} - \frac{\mu_O(t_n)}{m_{0O}(t_n)}}{\frac{q^2}{m_{1B}(t_n)}\left[\log(\mu_B(t_n)+1)\right] - \frac{q^2}{m_{1O}(t_n)}\left[\log(\mu_O(t_n)+1)\right]}},$$

where $n \geq 0$, with an initial threshold equals to the average of the image to be thresholded until the iteration converges. The convergence is the condition where $t_{n+1} = t_n$. The existence of a solution the above equation can be proved by noting the general theorem on solutions of the one-point iteration method by Atkinson (1988) [4]. A solution exists within the interval [1, L] where the histogram is defined if the following is satisfied

$$1 \leq \sqrt{\frac{\frac{\mu_a(t_n)}{m_{0a}(t_n)} - \frac{\mu_O(t_n)}{m_{0O}(t_n)}}{\frac{q^2}{m_{1a}(t_n)}\left[\log(\mu_a(t_n)+1)\right] - \frac{q^2}{m_{1O}(t_n)}\left[\log(\mu_O(t_n)+1)\right]}} \leq L$$

in next section, we will use this formula to estimate the optimal threshold and then segment the image.

IV. Experimental results

The Gamma entropy thresholding method is tested on artificial images and applied on real images.

A. Artificial Images.

We tested Gamma entropy thresholding on four noisy images affected by a noise model: Gaussian, Raleigh, Gamma, and Exponential noise. The original images and the results are shown on table 1.

F. Ibrahim, N.A. Abu Osman, J. Usman and N.A. Kadri (Eds.): Biomed 06, IFMBE Proceedings 15, pp. 296-299, 2007
www.springerlink.com ' Springer-Verlag Berlin Heidelberg 2007

Table 1 Artificial Noisy Images.

Noise Model	Original Image	Threshold	Result Image
Gaussian Noise	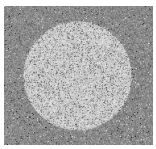	166	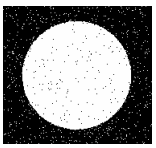
Rayliegh Noise	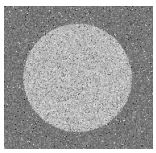	145	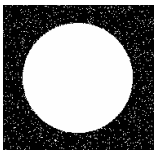
Gamma Noise	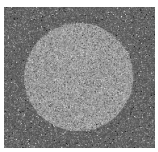	123	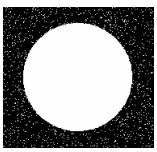
Exponential Noise	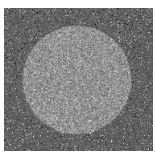	116	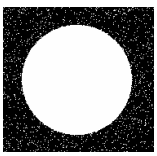

B. Real Medical Images.

We applied Gamma entropy thresholding on medical images.

1- we applied the method on MRI image that has a histogram with overlapped modes. The histogram of the image is non symmetric and it has two overlapped modes which makes its shape similar to the shape of Gamma probability density function. The image and the result are shown in table 2.

Table 2 Images Having Overlapped Modes

Original Image	Threshold	Segmented Image
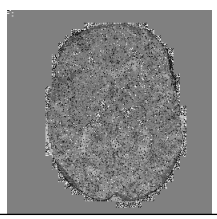	128	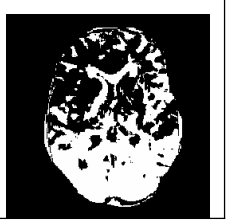

2- The Gamma entropy thresholding was applied on two medical images. In each case it was successful in isolating areas of interest as shown in table 3.

Table 3 Two medical images Thresholding

Original Image	Threshold	Result Image
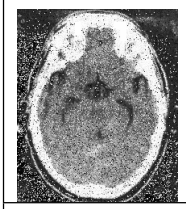	123	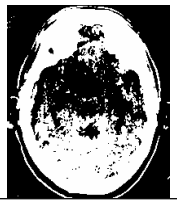
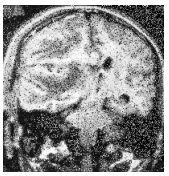	132	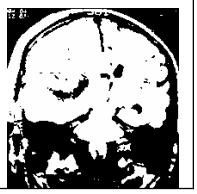

3- we compared our method with the minimum cross entropy with Gaussian method [2] on the medical image where the contrast is low or there is an overlap between modes. Gamma entropy thresholding extracted the object of interest (i.e. brain) and showed its details in a clear way. Gaussian entropy thresholding extracted only the contour of the brain, which is an unacceptable result. Both results along with the original image are shown again in table 4 for convenience. We conclude from the experimental results, that our method works better than its mother method (Gaussian entropy thresholding); since it works properly with all image types.

Table 4 Gamma Vs. Gaussian Entropy Thresholding

Original Image	Gaussian T. Result	Gamma T. Result
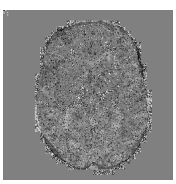	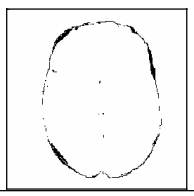	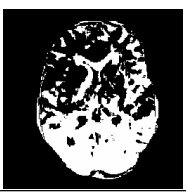

V. Conclusions

In this paper, we developed a minimum cross entropy thresholding method based on the Gamma distribution. The estimation of threshold is iterative and fast. Due the symmetric and non-symmetric of Gamma distribution, this method is more general than the method based on Gaussian

F. Ibrahim, N.A. Abu Osman, J. Usman and N.A. Kadri (Eds.): Biomed 06, IFMBE Proceedings 15, pp. 296-299, 2007
www.springerlink.com ' Springer-Verlag Berlin Heidelberg 2007

distribution. Experimental results showed that good results in thresholding. This method work only on bi-modal images that have only two classes of pixels, as future work, we will generalize the method on multi-modal images and test it on several medical images.

References

1. Sezgin, M. and Sankur , B., 2004. Survey over image thresholding techniques and quantitative performance evaluation. Journal of Electronic Imaging.
2. Li, C.H. and Tam, P.K.S., 1998. An Iterative Algorithm for Minimum Cross Entropy Thresholding. Elsevier - Pattern Recognition.
3. Li, C.H. and Lee, C.K., 1993. Minimum cross entropy thresholding. Elsevier - Pattern Recognition.
4. Atkinson, K.E., 1988. An Introduction to Numerical Analysis, Wiley, New York.
5. Ali El Zaart, Djemel Ziou, Shangrui Wang and Qingshan Jiang, *Segmentation of SAR images.* Pattern Recognition Journal, Vol. 35, No. 3, pp. 713-724, March 2002.
6. Ali El Zaart and Djemel Ziou, Mixture Modelling Using Minimum Message Length. 13th Conference in Pattern Recognition and Artificial Intelligent (RIFIA), pp. 509-518, 2002, Conference, Angres, France, January 2002.
7. Ali El Zaart, Ali Al-Mejrad and Ali Saad, *Segmentation of Mammography Images for Breast Cancer Detection* , Proceedings of the Kuala Lumpur International Conference, On Biomedical Engineering 2004, pp. 225-228. September 2-4, 2004, Kuala Lumpur, Malaysia

Address of the corresponding author:

Author: R. Al-Attas
Institute: Department of Computer Science, College of Computer and Information Sciences, King Saud University
City: Riyadh
Country: Saudi Arabia

F. Ibrahim, N.A. Abu Osman, J. Usman and N.A. Kadri (Eds.): Biomed 06, IFMBE Proceedings 15, pp. 296-299, 2007
www.springerlink.com ' Springer-Verlag Berlin Heidelberg 2007

Ultrasound monitoring of temperature change during interstitial laser thermotherapy of liver: an in vitro study

T. Gorji-Ara[1], M. Mokhtari-Dizaji, H. Ghanaeati[2]

[1]Medical Physics Department, Tarbiat Modares University, Tehran, Iran
[2]Radiology Department, Imam Khomeini Hospital, Tehran Medical Sciences University, Tehran, Iran

Abstract— **Laser interstitial thermotherapy (LITT) is an internal ablation therapy consists of the percutaneous or intraoperative insertion of laser fibers directly into the liver tumor with maximum diameter of 5 cm. It is very important to control temperature increasing non invasively, because on high temperatures, tissue carbonization occurs and it can damage normal tissues. In this research, pixel shift changes on ultrasound B-mode images with temperature were measured. LITT in vitro was performed on 11 freshly sheep liver tissues using a Nd:YAG laser with a bare-tip optical fiber. Invasive temperature monitoring was performed during heating and cooling down by fixing micro thermocouples on tissue. At the same time, noninvasive temperature monitoring was performed with ultrasound B-mode images. The speed of sound variations with the temperature changes are create virtual shifts in scattering positions and time shifts into the received echo signals. It can locally cause pixel shifts on B-mode images. These pixel shifts were measured by echo tracking algorithm. Linear and nonlinear regression analysis between independent variable (temperature changes) and dependent variable (pixel shift on images) were performed. It was shown that with correlation coefficient of 0.892, cubic function was suitable. In this method, because of bubbles formation and tissue carbonization, monitoring of more than 100ºC, was difficult. This method could be used for noninvasive temperature monitoring for a large number of patient, during LITT.**

Keywords— **LITT, Ultrasound, Imaging, Temperature, Pixel shift.**

I. Introduction

Hepatocellular carcinoma is one of the most common solid organ malignancies worldwide, with an annual incidence of at least 1 million new patients and virtually any other cancer can metastasize to the liver [1]. Metastases from colorectal primaries account for approximately half of all hepatic metastases. Optimal therapy of both primary and metastatic liver disease is complete resection with negative margins. If this disease was untreated, the survival rates of both these diseases are dismal [2-4]. This high risk, coupled with the low number of resection candidates, has increased the interest in minimally invasive treatments, such as focal ablation therapies for both primary and secondary liver tumors. The use of laser as a heat source to destroy liver tumors was first reported by Bown in 1983 [5, 6]. The Nd:YAG laser has the higher tissue penetration and produces the greater volume of tissue destruction. It is the preferred laser unit for LITT, despite being larger and less portable than diode devices. It is very important to control temperature increasing for having efficient tumor treatment plan, because on low temperatures there is any irreversible thermal lesion and on high temperatures, tissue carbonization, charring, and smoking occur and it can damage normal tissues [7]. There are invasive; with use of thermocouple or thermister; and non-invasive; imaging technique like MR, CT and US; methods for monitoring of tissue temperature [5, 8, 9]. The LITT procedure generally carries out under ultrasound (US) guidance. This is the most commonly used modality because it provides real time visualization of probe placement, and is portable, costs little and can target and guide ablation therapy [1, 3]. However, standard B-mode images are less than optimal for visualizing the response to heating because it is difficult to detect the extent to which the tissue is being heated, and it is nearly impossible to delineate the treated tissue margins with conventional US [5]. Although conventional US does not provide clear delineation of treated regions by LITT, information in the raw US signals may prove useful. Several ultrasonic methods was been proposed to estimate temperature changes in tissue. These methods are related different temperature-induced changes in the tissue, including changes in the frequency-dependent attenuation, backscattered power, speed of sound, thermal expansion or a combination of the last two effects.

In this paper, LITT in vitro was performed on freshly sheep liver tissue using a bare tip optical fiber from a Nd:Yag laser. Invasive temperature monitoring performed during heating and cooling down by fixing micro thermocouples on tissue. At the same time, noninvasive temperature monitoring performed with Ultrasound B-mode images. Temperature changes can cause changes and pixel shift on B-mode images that these changes are measured.

F. Ibrahim, N.A. Abu Osman, J. Usman and N.A. Kadri (Eds.): Biomed 06, IFMBE Proceedings 15, pp. 300-303, 2007
www.springerlink.com ' Springer-Verlag Berlin Heidelberg 2007

II. Materials and methods

LITT performed on 11 slices of freshly excised sheep liver tissues having approximate dimensions of 50 mm by 60 mm and 60 mm thickness, in vitro. An aluminum plate was placed in chamber s floor as a reference in US images. US imaging to guide the laser s fiber and thermocouples placement and to monitor the temperature in tissue was non-invasively performed using a real time scanner (Logiq 500 GE, GE Inc., Germany, with a 6-9MHz linear array transducer). Tissue temperature invasively was monitored by K-type wiry thermocouples (TP-01, Lutron Electronic Enterprise Co., Taiwan) that were inserted into the tissue through holes drilled along the length of the chamber in the height of 25 mm. Thermocouple s data were recorded every second as a Doc s file by a digital thermometer (Multiligger Thermometer CHY502A, Taiwan). Thermometers were connected to computer by RS-232 port.

A Nd:Yag laser model Hercules 5060 (Heraeus Surgical, Inc. Germany, P<60W with 1064 nanometer continues wavelength) was used for in vitro ablation. The bare-tip optical fiber, 600 □m diameters (Heraeus Lasersonic Inc. Germany) was used for laser s energy transmission to the liver. The fiber was inserted into the liver by one hole was drilled in width of chamber in height of 25 mm. US imaging was performed in a direction perpendicular.

For invasively temperature monitoring of different points of liver tissue during LITT, thermocouples were inserted in distances of 2.5, 5.0, 7.0, 10.0 and 15.0 mm (–1.0 mm) in front of laser fiber and 1.0, 3.0 and 5.0 mm (–1.0 mm) in the back of laser fiber, under US guide. LITT was performed in 1Watt power setting at 700 seconds exposure time (2477 J/mm2). At the same time, noninvasive temperature monitoring was performed with Ultrasound B-mode images. These images were saved on computer by Video Blaster hardware and software, for each 5℃ temperature increasing from 25℃ to 100℃. Ultrasound images were saved at 25℃ and used as reference and were compared with ultrasound images at 30, 35, 40, , 100℃ with temperature steps of 5℃, then pixel shifts that occur through every 5℃ temperature increasing were measured by echo-tracking algorithm. All of the observations and procedures were performed by the same investigator under same standard conditions. Statistical analysis was performed with SPSS V. 11.5 software (SPSS/PC Inc.; Chicago, II). The invasive temperature profile in different distances in the front and the back of optical fiber are reported. Maximum of temperature in every distance are measured in 700 seconds irradiation time. Mean and standard deviation of thermal ablation area was calculated. Correlation analysis between maximum temperature of liver tissue and thermal ablation area are evaluated. With images processing, pixel shift due to 5°C temperature changes were extracted and non linear regression analysis with higher correlation coefficient between independent variable of temperature changes and dependent variable of pixel shift due to speed of sound changes were calculated.

III. Results

Fig. 2 shows dependence of pixel shift on ultrasound B-mode images as a function of temperature changes. Non-linear (cubic) regression analysis between independent variable (temperature changes) and dependent variable (position shift on image) were performed. Regression function and correlation coefficient were showed on Table 1.

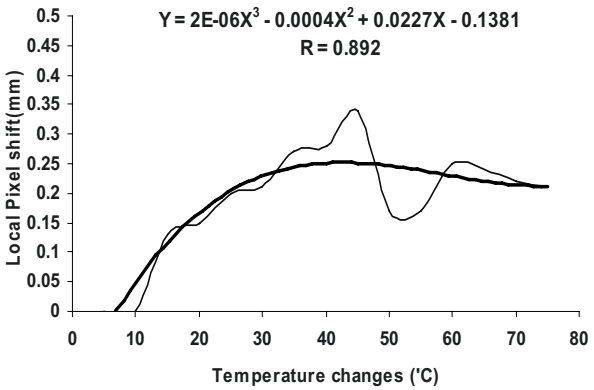

Fig. 1 dependence of pixel shift on ultrasound B-mode images as a function of temperature changes

Table 1. Non-linear regression function for independent variable of temperature changes and dependent variable of pixel shift on images and their correlation coefficient. P-value of less than 0.01 was significant.

	Regression Function	R
Cubic	$\Delta X=-0.1381+0.0227\Delta T-0.0004\Delta T^2+2\times10\text{-}6\Delta T^3$	0.9

Fig. 1 shows cubic regression function between pixel shifts on US B-mode images due to speed of sound changes as a function of temperature changes. In this function, correlation coefficient is maximal related to other regression function. It is considerable, when temperature increased, pixel shift occur in ultrasound images. Maximum pixel shift is observed between 60 to 70℃ (temperature changes (ΔT) of 35℃-45℃). After 70℃, local pixel shift due to speed of sound change in liver tissue has an irregular decreasing.

Fig. 2a and b show invasive temperature profile at thermocouple positions in different distances in the front and the back of optical fiber, respectively.

F. Ibrahim, N.A. Abu Osman, J. Usman and N.A. Kadri (Eds.): Biomed 06, IFMBE Proceedings 15, pp. 300-303, 2007
www.springerlink.com ' Springer-Verlag Berlin Heidelberg 2007

Maximum temperatures and cooling down profile in every distance are also shown. With these temperatures, necrosis could be occurred at distances of less than 7 mm in the front of the optic fiber and less than 3 mm at the back of the optic fiber. At the distances less than 1 mm, temperature is near 100℃ that it could be occurred carbonization.

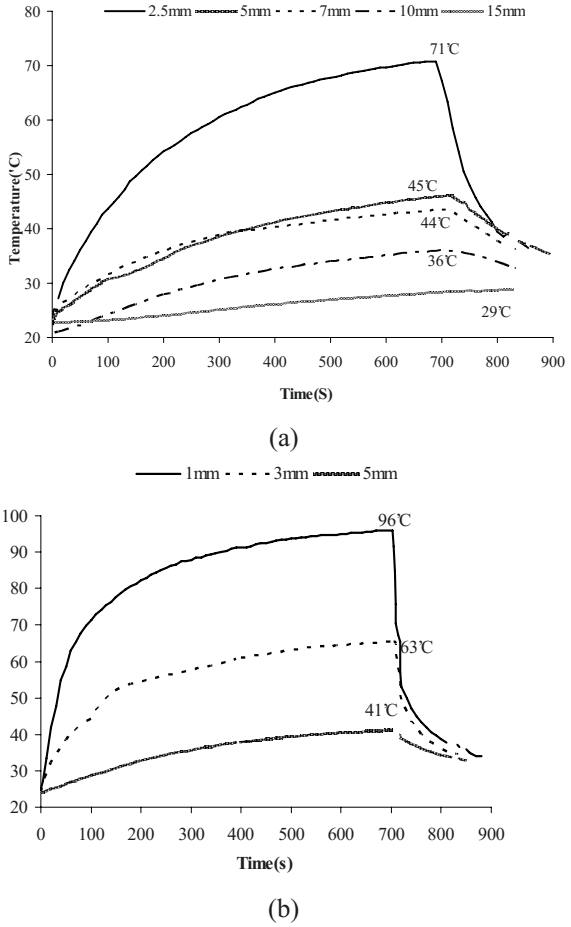

Fig.2 Temperature profiles at thermocouple positions, a) 2.5, 5, 7, 10 and 15 mm in front of fiber, b) 1, 3 and 5 mm at the back of fiber. The final temperature reached at each location before cool-down is also shown.

IV. Conclusions

In the most of in vitro researches, investigators studied effects of temperature changes on ultrasonic properties of tissue so that used a water bath for increasing the temperature of whole tissue [11-15]. In this method, control and monitor of tissue s temperature with imaging methods is easier because every point of tissue has same temperature, thus, change in speed of sound and ultrasonic attenuation coefficient are same in liver tissue, but this method couldn t used in vivo, because it s impossible to rise the temperature of whole liver tissue in an alive existence.

In a few study, (radiofrequency ablation by Varghese et al 2002 and microwave ablation by Sherar and Bevan 2000) examinations of changes in ultrasound properties of liver tissue by local radiation were qualitatively reported usage temperature mapping based on time shift in RF signals and log envelope slope attenuation [1,16].

In this paper, liver tissue were heated locally by laser bare-tip fiber and tried to do stages of this procedure like in vivo LITT. This method could use in clinical study. There is limitation for monitoring of local thermotherapy with ultrasound because changes in ultrasound properties just create in a small part of tissue.

Most of published paper, investigators examined changes of ultrasound properties in less than 40℃, just a few studies, ultrasonic properties changes were evaluated up to 80℃ [11-13, 16, 17]. There is just one report, by Varghese et al [1], about monitoring of temperature changes up to 100℃.

In present paper, we examined the temperature s range from 25℃ (room s temperature) to 100℃ because in temperature higher than 100℃, bubble information increased and quality of ultrasound B-mode images changed very much. In the other side, on high temperatures, carbonization occurred too, hence, ultrasound absorption increased that it could change the quality of ultrasound B-mode images. Of course, physicians believe that ideal temperature is temperatures that do not occurred carbonization.

On most of available publishing, RF signals were used for monitoring of temperature [1, 16] but in this study, pixel shifts that occurred through temperature increasing in ultrasound B-mode images were evaluated, because B-mode images are most common ultrasound data and are available easier than signal data.

Fig.2 show that, through 10℃ temperature increasing from 25℃ to 35℃, there isn t any observable pixel shifts. After that, through every 5℃ temperature increasing, pixel shifts have an ascending trend. Maximum pixel shift were observed from 60℃ to 75℃ and after that when temperature increased, pixel shifts were decreased in irregular way.

According to Mass-Moreno and Damianou study (1996), time shift occurred by changes in speed of sound through temperature increasing, and Worthington et al (2001 and 2002) note that in pig s liver and human s prostate gland, maximum speed of sound sequentially are at 50℃ and 55℃ [1, 11, 12]. In a study (1998) by Sun and Ying [18], temperature distribution in heated tissue was estimated by computer simulation, and they find a relation between speed of sound (C: m/s) and temperature changes (T: ℃) in water; major component of biological tissue according to this formula:

$$C(T)=0.000126T^3-0.046645T^2+4.807092T+1453.430000 \quad (1)$$

F. Ibrahim, N.A. Abu Osman, J. Usman and N.A. Kadri (Eds.): Biomed 06, IFMBE Proceedings 15, pp. 300-303, 2007
www.springerlink.com ' Springer-Verlag Berlin Heidelberg 2007

Equation 2 shows relationship between pixel shifts and temperature changes that was estimated in present paper:

$$\Delta X=-0.1381+0.0227\Delta T-0.0004\Delta T^2+2\times10\text{-}6\Delta T^3 \quad (2)$$

According to Equation 2, maximum pixel shifts observe in range of 35℃ to 50℃ temperature changes (temperature range of 60-75℃). Equation 1 shows that maximum speed of sound changes are in temperatures between 65℃ to 75℃. These kinds of changes in speed of sound could create time shift in RF signals and pixel shift in B-mode images. In higher temperatures, physical shift in position of scatterer was introduced by thermal expansion of medium and it affect on B-mode images. In the other side, bubble information, vaporization and carbonization affect on quality of images near and upper than 100℃, thus, it create difficulty for measurement of pixel shift with this method in these temperatures. Therefore it could be one of the limitations of this method. Actually physician s aim from hyperthermia and thermal therapy is creating necrosis not carbonization, hence, this imaging and monitoring method could help them in a good way.

References

1. Varghese T, Zagzebski J A, Chen Q, Techavipoo U. Ultrasound monitoring of temperature change during radiofrequency ablation: Preliminary In-vivo Results. Ultrasound Med Biol 2002; 28: 321-329.
2. Moroz P, Jones A K, Gray B N. Status of hyperthermia in the treatment of advance liver cancer. J Surg Oncol 2001; 77: 259-269.
3. http:// www.Mayoclinic.com
4. Geoghegan J G and Scheele J. Treatment of colorectal liver metastases. Br J Surg 1999; 86: 158-169.
5. Nikfarjam M and Christophi C. Interstitial laser thermotherapy for liver tumors. Br J Surg 2003; 90: 1033-1047.
6. Muralidharan V and Christophi C. Interstitial laser thermotherapy in the treatment of colorectal liver metastases. J Surg Oncol 2001; 76: 73-81.
7. Solbiati L. New applications of ultrasonography: interventional ultrasound. Euro J Radiol 1998; 28: 200-206.
8. Ishikawa T, Zeniya M, Hokari A, Kawabe T, Suziki K, Fujise K and Toda G. An experimental study on Nd-YAG laser induced thermotherapy it possible application of the laser irradiation for therapy of hepatocellular carcinoma. Hepato Res 2002; 23: 25-30.
9. Volg T J, Eichler K, Straub R, Engelmann K, Zangos S, Woitaschek D, Bottger M and Mack M G. Laser-induce thermotherapy of malignant liver tumors: general principle, equipment, procedure-side effects, complications and results. Euro J Ultrasound 2001; 13: 117-127.
10. Lizzi F L, Muratore R, Deng C X, Ketterling J A, Alam S K, Mikaelian S and Kalisz A. Radiation-force technique to monitor lesions during ultrasonic therapy. Ultrasound Med Biol 2003; 29: 1593-1605.
11. Worthington A E and Sherar M D. Changes in ultrasound properties of porcine kidney tissue during heating. Ultrasound Med Biol 2001; 5: 673-682.
12. Worthington A E, Trachtenberg J and Sherar M D. Ultrasound properties of human prostate tissue during heating. Ultrasound Med Biol 2002; 10: 1311-1318.
13. Clarke R L, Bush N L, Ter Haar G R. The changes in acoustic attenuation due to in vitro heating. Ultrasound Med Biol 2002; 29: 127-135.
14. Guiot C, Cavalli R, Gaglioti P, Danelon D, Musacchio C, Trotta M and Todros T. Temperature monitoring using ultrasound contrast agents: in vitro investigation on thermal stability. Ultrasonics 2004; 42: 927-930.
15. Gertner M R, Worthington A E, Wilson B C and Sherar M D. Ultrasound imaging of thermal therapy in in vitro liver. Ultrasound Med Biol 1998; 24: 1023-1032.
16. Bevan P D and Sherar M D. B-scan ultrasound imaging of thermal coagulation in bovine liver: log envelope slope attenuation mapping. Ultrasound Med Biol 2000; 3: 379-387.
17. Bamber J C and Hill C R. Ultrasonic attenuation and propagation speed in mammalian tissue as a function of temperature. Ultrasound Med Biol 1979; 5: 149-157.
18. Sun Z, Ying H. A multi-gate time of flight technique for estimation of temperature distribution in heated tissue: theory and computer simulation. Ultrasonics 1999; 37: 107-122.

Address of the corresponding author:

Author: T. Gorji-Ara
Institute: Medical Physics Department, Tarbiat Modares University
City: Tehran
Country: Iran

F. Ibrahim, N.A. Abu Osman, J. Usman and N.A. Kadri (Eds.): Biomed 06, IFMBE Proceedings 15, pp. 300-303, 2007
www.springerlink.com ' Springer-Verlag Berlin Heidelberg 2007

Unsupervised Learning Technique for Skin Images Segmentation Using a Mixture of Beta Distributions

A. Al-Saleh and A. El-Zaart

Department of Computer Science, College of Computer and Information Sciences, King Saud University, Riyadh, Saudi Arabia

Abstract— **Image segmentation, i.e., identification of homogeneous regions in the image, has been the subject of considerable research activity over the last three decades. Segmentation of images is a major task of image processing. There is no general segmentation procedure that can deal with all sorts of images, and the correct solution will always depend to a certain degree on subjectivity. Many algorithms have been elaborated for gray scale images. Those algorithms are based on different methods including: classification-based methods, edge-based methods, region-based methods, and hybrid methods. Iterative Self-Organizing Data Analysis Technique (ISODATA) is one of the classification-based methods in image segmentation. It is an unsupervised learning Technique. Statistical approach is wieldy used in image processing in order to model the data of image. Gaussian and Gamma distributions have been used in this technique. Gaussian can only approximate a symmetric shape of histogram. Gamma distribution can only approximate a symmetric and a skewed to right shapes of the histogram. However, Beta distribution is more general than Gaussian and Gamma, and it can approximate any shape of histogram as skewed to left, skewed to right, and symmetric. The algorithm developed here is based on the technique of unsupervised learning using a mixture of Beta distributions. Experimental results are presented to show good performance on segmentation of skin images.**

Keywords—**Image Segmentation, Beta Distribution, Skin Images, ISODATA.**

I. Introduction

In artificial vision, the performance of the pattern recognition step is based directly on the segmentation step. Image segmentation is a fundamental step in many applications of image processing. In medical images as example, segmentation of tissues in Magnetic Resonance Images (MRI) is essential especially for a radiologist to be able to identify a disease, tumors, or any tissue [8]. In mammography images, the segmentation is used to detect the region of the breast cancer [5, 6]. In radar images, for oil slicks detection, the segmentation is the main step for detecting the oil slick and defining its boundary [7]. In skin images, the segmentation can detect the cancer regions. In this paper, we will work on the segmentation of skin image in order to define the boundary of the skin regions. Many techniques exist for image segmentation based on different methods. There are four broad classes of segmentation methods, which are: classification-based methods, edge-based methods, region-based methods and, hybrid methods [1]. The principal approach of segmentation is based on thresholding that is related to the problem of the thresholds estimation. Iterative Self-Organizing Data Analysis Technique (ISODATA) is one of the thresholding methods in image segmentation. It is an unsupervised learning Technique. Statistical approach is wieldy used in image processing in order to model the data of image. Gaussian and Gamma distributions have been used in this technique. Gaussian can only approximate a symmetric shape of histogram. Gamma distribution can only approximate a symmetric shape and a skewed to right shapes of the histogram. However, the Beta distribution is more general than Gaussian and Gamma, and it can approximate any shape of histogram as skewed to left, skewed to right, and symmetric. The algorithm developed here based on the technique of unsupervised learning using a mixture of Beta distributions. In section 2 we give a definition of the Beta distribution. Section 3 explains, the algorithm of the developed method. Section 4 includes experimental results of applying our method. We conclude in section 5.

II. Beta distribution

The Beta distribution is a continuous probability distribution with the probability density function defined on the interval [0, 1]:

$$f(x, \alpha, \beta) = \frac{\Gamma(\alpha + \beta)}{\Gamma(\alpha)\,\Gamma(\beta)} \; x^{\alpha-1} \; (1 - x)^{\beta-1}$$

where α and β are the shape parameters of the distribution and must be greater than zero, x is the intensity of the pixel and it must be between 0 and 1. Γ is the gamma function. The Beta distribution can take different shapes depending on the values of the two parameters (see figure 1):

F. Ibrahim, N.A. Abu Osman, J. Usman and N.A. Kadri (Eds.): Biomed 06, IFMBE Proceedings 15, pp. 304-307, 2007
www.springerlink.com ' Springer-Verlag Berlin Heidelberg 2007

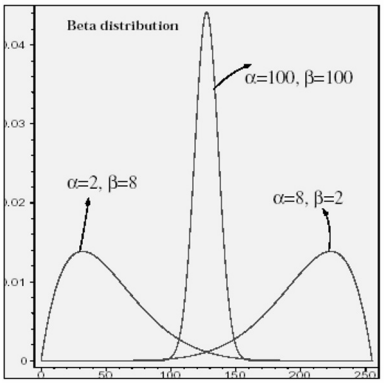

Fig. 1 Three Beta distributions with their parameters [3].

If α = β then the Beta distribution is symmetric, see figure 1 for α = β =100. If α < β then the Beta distribution is skewed to right, see figure 1 for α = 2 and β=8. If α > β then the Beta distribution is skewed to the left, see figure 1 for α = 8 and β=2. The moment-based estimators for α and β and are given by [2,4]:

$$\alpha = m_1 (m_1 - m_2)/((m_2 - m_1^2))$$
$$\beta = \frac{(m_1 - 1)(m_2 - m_1)}{(m_2 - m_1^2)} \quad \text{(eq.1)}$$

Where the rth sample moment of a homogenous region (R_k) is given by: $\hat{m}_r = (\sum_{i \in R_K} h(x_i)\ x_i^r) / \sum_{i \in R_K} h(x_i)$

We assume that an histogram skin images is formed by a mixture of Beta distributions:

$$h(x_j) = \sum_{i=1}^{M} f(x_j, \alpha_i, \beta_i) p_i$$

Where M is the number of modes (classes) of the skin image histogram (skin image), (α_i, β_i, p_i) is the statistical parameter of the i^{th} mode of the skin image histogram. In this paper, the objective is to estimate statistical parameters of a mixture of Beta distributions. In next section, we will explain the algorithm of the new method.

III. Algorithm

The unsupervised learning technique algorithm using a mixture of Beta distribution subdivides an image into a set of disjoint regions. Regions are then merged if either the number of members (pixel) in a region is less than a certain threshold (minimum class members input from user) or if the distance between the centers of two regions is less than a certain threshold (minimum class mean distance also input from the user). The following is the algorithm for the proposed method:

1- Input skin image.
2- Select a homogeneous test (standard deviation).
3- Calculate the image histogram.
4- Calculate the statistical parameters of Beta distributions and then estimate threshold value.
5- Split the image. This is an iterative process that splits any non-homogenous region until all regions are homogenous.
6- Merge any two homogeneous regions if merging criteria holds.
7- Output segmented image.

Next, we will explain the 5th and 6th steps.

Split Image: For each class, apply a homogeneous test on it; if it is not homogeneous then split it by repeating the following steps from1 to 6. The steps for splitting are:

1. Calculate initial threshold $T^{0.}$
   T^0 = Average gray level value of the class to be spitted.
2. Split the class into two classes C_1 and C_2 according to T^0.
3. Calculate values of α and β for each class (C_1 and C_2) using equation (1).
4. Calculate *prior* probabilities P_1 for C_1 and P_2 for C_2. Let n_1 and n_2 be the number of pixels in class C_1 and C_2 respectively.

   $$n_1 = \sum_{i \in C_1} h(x_i) \quad \text{and} \quad n_2 = \sum_{i \in C_2} h(x_i)$$

   Thus: $p_1 = n_1/(n_1 + n_2)$ and $p_2 = n_2/(n_1 + n_2)$
5. Calculate the new threshold T by using statistics of both classes C_1 (α_1, β_1, P_1) and C_2 (α_2, β_2, P_2) [3].

   $$T^{new} = 1 - e^{(A + B \log(T^{old} - 1)/C)}$$

   Where: $A = \log((p_1 K_1)/(p_2 K_2))$, $B = \alpha_1 - \alpha_2$,

   and $C = \beta_1 - \beta_2$ Where $K_r = \frac{\Gamma(\alpha_r + \beta_r)}{\Gamma(\alpha_r)\ \Gamma(\beta_r)}$

   In this step, estimation of threshold is an iterative process. The initial value

   $$T^{old} = (\mu_1 + \mu_2)/2 \text{ where } \mu_r = \alpha_r/(\alpha_r + \beta_r)$$
6. If $|T^0 - T^{new}| > 1$ then $T^0 = T^{new}$ and repeat step 2 until step 5. else record T^{new} in thresholds list and record

F. Ibrahim, N.A. Abu Osman, J. Usman and N.A. Kadri (Eds.): Biomed 06, IFMBE Proceedings 15, pp. 304-307, 2007
www.springerlink.com ' Springer-Verlag Berlin Heidelberg 2007

two classes C1 and C2 where pixels in C1 are less than or equal to T^{new} and pixels in C2 are greater than T^{new} .

Merge Regions/Classes The steps for merging: (1) if number of pixels in class is less than minimum class pixels then merge this class with the nearest class to it i.e. the class who has the closest mean. (2) if the distance between the mean of a class and the mean of another class is less than a certain threshold then, the two classes are merged (3) the result new mean will be the average of the two merged classes. (4) the threshold between these two classes will be removed from the list of thresholds. Both of the minimum class members and minimum class are input by the user.

IV. Experimental results

In this section, we will apply the proposed method on real skin images. We consider a skin cancer image presented in figure 2. Figure 2.a represents the original image.

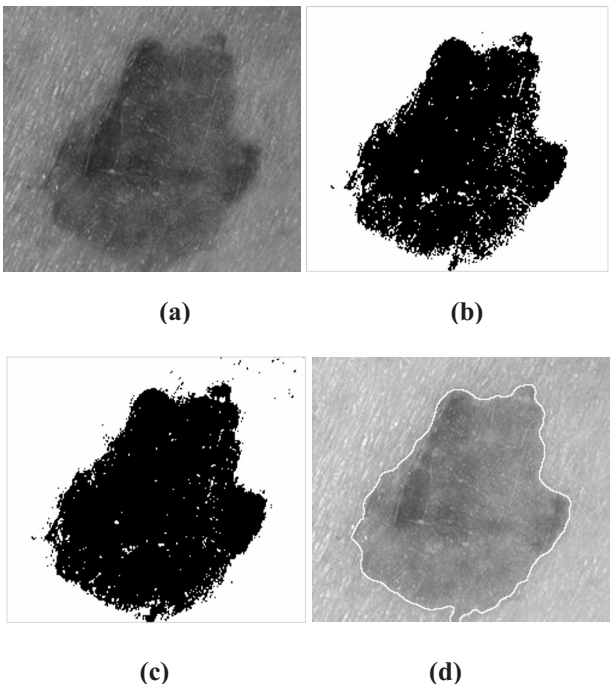

Fig. 2 (a) original Image, (b) segmented image with Gamma [9], (c) segmented with Beta (our method), (d) skin caner region defined by boundaries.

Figure2.b represents the segmented image using the unsupervised learning technique with Gamma distribution [9]. Figure 3.c, represents the segmented image using the unsupervised learning technique with Beta distribution (proposed method), see Table 1 for numerical result of our method. Figure 2.d represents the original image with the interested object, which is the skin cancer region. By doing a comparison for this result, we can find that the method used Beta is better that the method used Gamma.

Table 1 Numerical Results for image presented in figure 2.a

Threshold=85 and M =2 Estimated parameters	P	α	β
First mode (class)	0.41	22.75	68.81
Second modes (class)	0.59	47.37	62.97

We consider a second skin cancer image presented in figure 3. Figure 3.a represents the original image. Figure3.b represents the segmented image using the unsupervised learning technique with Gamma distribution [9]. Figure 3.c, represents the segmented image using the unsupervised learning technique with beta distribution (proposed method).

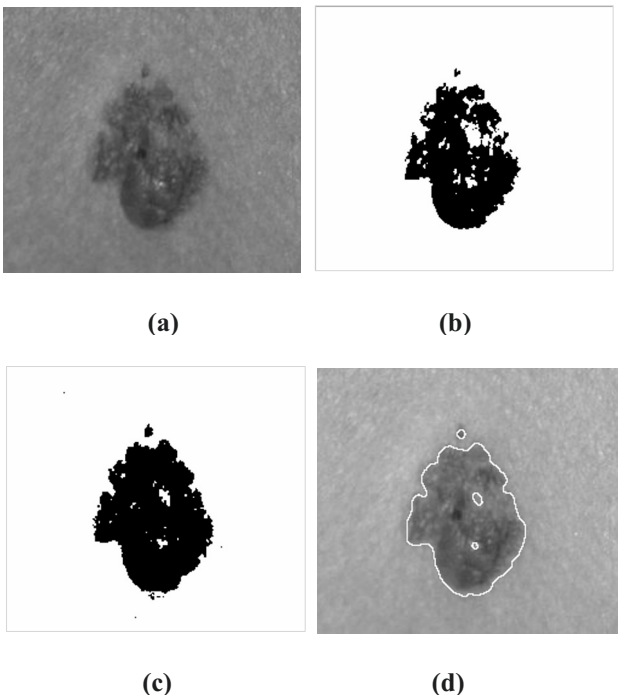

Fig. 3 (a) original Image, (b) segmented image with Gamma [9], (c) segmented with Beta (our method), (d) skin caner region defined by boundaries.

See table 2 for numerical result of our method. Figure 3.d represents the original image with the interested object, which is the skin cancer region. By doing a comparison for this result, we can find that the method used Beta is better that the method used Gamma.

F. Ibrahim, N.A. Abu Osman, J. Usman and N.A. Kadri (Eds.): Biomed 06, IFMBE Proceedings 15, pp. 304-307, 2007
www.springerlink.com ' Springer-Verlag Berlin Heidelberg 2007

Table 2 Numerical Results for image presented in figure 3.a

Threshold=86 and M =2 Estimated parameters	P	α	β
First mode (class)	0.15	21.69	67.43
Second modes (class)	0.85	110.7	152.2

We consider a third skin cancer image presented in figure 4. Figure 4.a represents the original image. Figure4.b represents the segmented image using the unsupervised learning technique with Gamma distribution [9]. Figure 4.c, represents the segmented image using the unsupervised learning technique with beta distribution (proposed method).

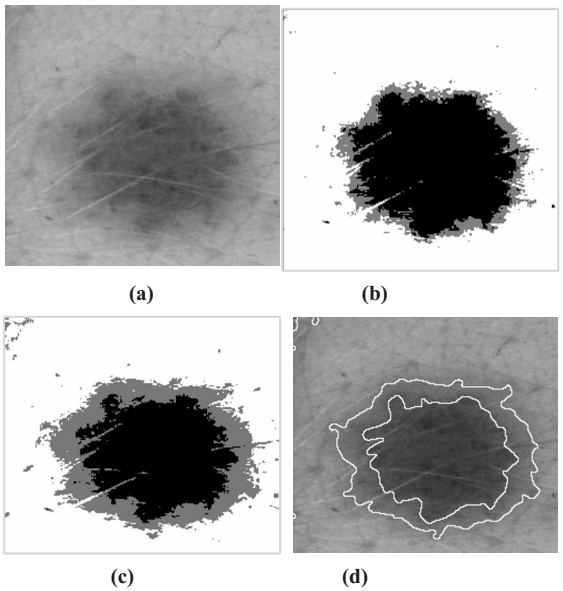

Fig. 4 (a) original Image, (b) segmented image with Gamma [9] (c) segmented with Beta (our method), (d) skin caner region defined by boundaries.

See table 3 for numerical result of our method. Figure 4.d represents the original image with the interested object, which is the skin cancer region. By doing a comparison for this result, we can find that the method used Beta is better that the method used Gamma.

Table 3 Numerical Results for image presented in figure 4.a

T1=87, T2=121 and M =3 Estimated parameters	P	α	β
First mode (class)	0.21	46.38	123.2
Second modes (class)	0.18	63.76	62.97
Third mode (class)	0.61	68.89	51.31

V. Conclusions and Future Work

Image segmentation is a major task of image processing. It is an important technique used to identify related objects in an image. Many methods exist for image segmentation that attempts to segment an image into homogenous regions. Among those methods are classification-based methods that were used in this project. As the technique for applying classification based methods, ISODATA was the one followed for segmenting images. In this project, we proposed a new method that uses the ISODATA algorithm. Because of its ability to represent almost any shape of an image histogram, the Beta distribution was chosen for parameter estimation in the proposed method. Experimental results showed good segmentation of skin images. As future work, we will test the developed method on several skin images.

References

1. R. C. Gonzalez and R. E. Woods, *Digital Image Processing*. New Jersey: Prentice-Hall, Inc., 2001.
2. Evans, M.; Hastings, N.; and Peacock, B. "Beta Distribution." Ch. 5 in *Statistical Distributions, 3rd ed.* New York: Wiley, pp. 34-42, 2000.
3. A. El Zaart and D. Ziou. Statistical Modeling of Heterogeneous Multimodal Image Histogram Using Parametric Distribution . Accepted in International Journal of Remote Sensing, 2006.
4. Jambunathan, M. V. "Some Properties of Beta and Gamma Distributions." *Ann. Math. Stat.* **25**, 401-405, 1954.
5. A. El Zaart, A. Al-Mejrad and A. Saad, *Segmentation of Mammography Images for Breast Cancer Detection* , in the Proceedings of the Kuala Lumpur International Conference on Biomedical Engineering 2004 , pp. 225-228. September 2-4, 2004,
6. Ferrari R.J., Rangayyan R.M., Borges R.A, frere A.F. (2004): *Segmentation of the fibro-glandular disc in mammograms using Gaussian mixture modeling'*, *Med. Biol. Eng. Comput*., **42**, pp. 378-87
7. A. El Zaart, D. Ziou, Shengrui Wang, Qingshan Jiang: Segmentation of SAR images . Pattern Recognition 35(3): 713-724 (2002).
8. P.D..Mitsias, MA Jacobs, R Hammond , M Pasnoor , S Santhakumar, NI Papamitsakis, et al. Multiparametric MRI ISODATA ischemic lesion analysis: correlation with the clinical neurological deficit and single-parameter MRI techniques*"*. Stroke 2002;33: pp. 2839 44.
9. Ali El-Zaart, Unsupervised Learning Technique for Image Segmentation , Proceedings of First National Information Technology Symposium, February 6-7, 2006, Riyadh, Saudi Arabia.

Address of the corresponding author:

Author: A.Al-Saleh
Institute: Department of Computer Science, College of Computer and Information Sciences, King Saud University
Country: Riyadh, Saudi Arabia
http://www.ifmbe.org/

F. Ibrahim, N.A. Abu Osman, J. Usman and N.A. Kadri (Eds.): Biomed 06, IFMBE Proceedings 15, pp. 304-307, 2007
www.springerlink.com ' Springer-Verlag Berlin Heidelberg 2007

A Fiber Optic Immunosensor for Rapid Bacteria Determination

M. Taniguchi[1], E. Akai[2], T. Koshida[3], K. Hibi[4], H. Kudo[5], K. Otsuka[5], H. Saito[5], K. Yano[3], H. Endo[4] and K. Mitsubayashi[1,5]

[1] School of Biomedical Science, Biomedical Science PhD Program, Tokyo Medical and Dental University, Tokyo, Japan
[2] School of Information Technology and Electronics, Tokai University, Kanagawa, Japan
[3] School of Bionics, Tokyo University of Technology, Tokyo, Japan
[4] Tokyo University of Marine Science and Technology, Tokyo, Japan
[5] Institute of Biomaterials and Bioengineering, Tokyo Medical and Dental University, Tokyo, Japan

Abstract— **Attention is currently focused on fiber optic immunosensor as sensitive and nearly real time protein detector. This kind of sensor is expected to detect bacteria in foods directly by dipping the thin optical fiber dominant area into foods. In the study, an antibody based fiber optic immunosensor to detect *Escherichia coli* O157:H7 (*E.coli* O157:H7) was constructed. The principle of the sensor was a sandwich immunoassay on the optical fiber surface. A goat polyclonal antibody was first immobilized on polystyrene optical fiber. *E.coli* O157:H7 and a cyanine 5 (Cy5) -labeled goat polyclonal antibody were used to generate a specific fluorescent signal. An excitation light (λ = 635 nm) was illuminated into the optical fiber, and the Cy5 florescent molecules near the optical fiber (approximately 100 nm) were excited by evanescent wave emitted from the optical fiber. The fluorescent light (λ = 670 nm) collected by the optical fiber was measured using a photodiode. The measurement range for *E.coli* O157:H7 diluted with phosphate buffer (PB) was from 1×10^2 to 1×10^7 cells/ml. This method could also detect *E.coli* O157:H7 in milk artificially inoculated with 1×10^2 to 1×10^7 cells/ml. This immunosensor was specific for *E.coli* O157:H7 and showed significantly higher signal strength than for nonpathogenic *E.coli* or other bacteria, including *Listeria monocytogenes* and *Vibrio s.p.*, in pure or in mixed-culture setup. The results could be obtained within about 15 min of sampling.**

Keywords—**optical fiber, evanescent wave, biosensor, antigen-antibody complex reaction, *Escherichia coli O157:H7***

I. Introduction

Detection of bacteria is very important in the field of clinical assay, food industry and environmental measurement. Conventional methods for determining the cell counts of bacteria employ selective culture, biochemical and serological characterization. Although these achieve sensitive and selective bacteria detection, they are typically restricted by prolonged assay times (at least 2 days), requiring initial enrichment for detection of pathogens that are initially present in low number [1]. Not only sensitive and specific, but also more rapid and simple methods for bacteria detection are desired to response promptly to bacterial contamination.

Immunological assays with antibodies are suggested as the methods provide specific, reproducible, and reliable detection of bacteria, viruses, or toxins [2,3]. Commonly used direct assays are radioimmunoassay (RIA) and enzyme-linked immunosorbent assay (ELISA). In both RIA and ELISA, a radioisotope or an enzyme is covalently linked to the pure antigen or antibody. The unlabeled component, which most often is the antigen, is attached to the surface of a plastic well. The labeled antibody is allowed to bind to the unlabeled antigen. Antibody binding is measured as the amount of radioactivity retained by the coated wells in RIA or as fluorescence emitted by the product of an enzymatic reaction in the case of ELISA. Even though these methods may reduce the assay time compared to traditional culture techniques, RIA needs particular facilities, ELISA requires cumbersome procedures, and they still lack the ability to detect bacteria in real time [4].

Recently, fluorescent immunoassay (FLIA), using fluorescence dye for the labeling antigen or antibody, has gotten attention as it doesn t require things like particular facilities or times to react enzyme [5]. And again, biosensors use some combination of biological receptors and physical or chemical transducers, which represent a new and unique technology with great potential to meet the need for the rapid detection of low levels of biomolecules [6,7]. A fiber optic immunosensor is a biosensor using FLIA principle. The sensor exploit the measurement of fluorescent light excited by an evanescent wave generated by a laser to quantitatively detect biomolecules immobilized on the optical fiber surface. This kind of sensor is expected to detect bacteria in foods directly by dipping the thin optical fiber dominant area into foods and expected as promising bacteria detector that realizes almost real time measurement [8].

In this study, we applied the fiber optic immunosensor to detect *E.coli* O157:H7. *E.coli* O157:H7 is one of hundreds of strains of bacterium *Escherichia coli*. This strain produces a powerful toxin and can cause severe illness in spite of low number [9]. A sensor to detect *E.coli O157:H7* more rapidly, easily is needed.

F. Ibrahim, N.A. Abu Osman, J. Usman and N.A. Kadri (Eds.): Biomed 06, IFMBE Proceedings 15, pp. 308-311, 2007
www.springerlink.com ' Springer-Verlag Berlin Heidelberg 2007

II. Materials and methods

A. Optical Fiber Pretreatment

The polystyrene optical fibers (4 cm in length and 0.78 mm in diameter) (Canon Inc.) were incubated for 15 h at 4 °C with 100 µl of capture antibody (40 µg/ml). A commercial polyclonal antibody was used for a capture antibody (*Anti-E.coli* O157:H7*, Goat-Poly*, catalog No.01-95-90, size:1.0 mg, Kirkegaard & Perry Laboratories Inc.). The Optical fiber was rinsed with phosphate-buffer (PB) (pH7.4) and then incubated with 100 µl of PB containing 1 % of bovine serum albumin (BSA) (Lot No.401-041, size:10 g, Itoham foods Inc.) to minimize the nonspecific reaction.

B. Antibody Labeling

An antibody labeling kit (Cy5-Ab labeling kit, product code: PA35000, Amersham Biosciences UK Limited) was used for labeling antibody. The antibody was same as capture antibody (*Anti-E.coli* O157:H7*, Goat-Poly*, catalog No.01-95-90, size:1.0 mg, Kirkegaard & Perry Laboratories Inc.). First, 1ml of antibody (1mg/ml) was added to a dye vial wrapped with aluminum foil and incubated at room temperature for 30 min with mixing approximately every 10 min. Then, free dye was removed by a gel filtration column provided by the labeling kit. The labeled antibody was diluted with PB containing 1 % BSA and 0.1 % Triton X-100. The final concentration of the labeled antibody was estimated to be 2.5 mg/ml and stored at 4 °C until used.

C. Bacteria

Serial dilution of pure culture of *E.coli* O157:H7 (ATCC43894 killed microbe) from 1×10^0 to 1×10^7 cells/ml were prepared in PB with 0.1 % Triton X-100 (PBT) or commercial milk. Nonpathogenic *E.coli* (IAM12119), *Listeria monocytogenes* (ATCC15313 killed microbe), *Vibrio s.p.,* was diluted with PBT to 1×10^5 cells/ml to test the specificity of the sensor.

D. The Assay Principle of the Immunosensor Measurement

The assay principle is based on a sandwich immunoassay, using a capture antibody, immobilized onto the optical fibers, and a Cy5-labeled antibody for detection. An excitation light ($\lambda = 635$nm) was illuminated into the proximal end of optical fiber, and the Cy5 florescent molecules within several hundred nanometers of the optical fiber were excited by an evanescent wave. The fluorescent light ($\lambda = 670$nm) collected by the optical fiber was measured using photodiode [10].

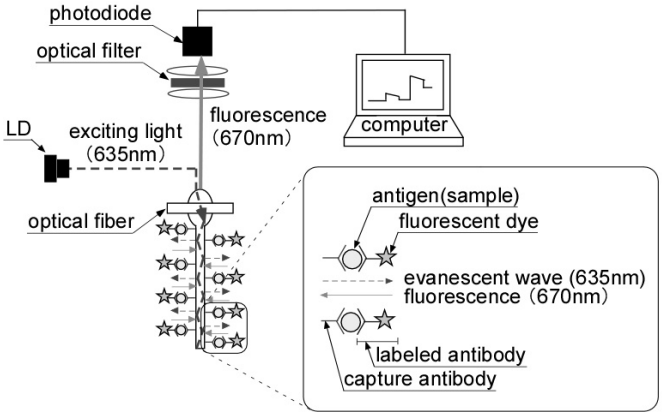

Fig.1 Fluorescent immunoassay using optical fiber

E. Process of the bacteria measurement

First, the optical fiber with capture-antibody was rinsed with PB (initial value). Then, the optical fiber was dipped into Cy5-labeled antibody for 5 min (check nonspecific reaction). The fiber was dipped into sample for 5 min (primary antigen-antibody reaction). Finally, the optical fiber was dipped into Cy5-labeled antibody for 5 min again (secondary antigen-antibody reaction).

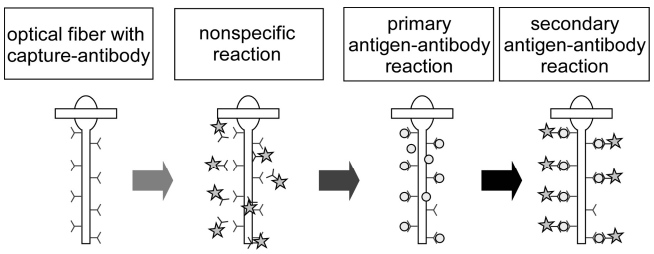

Fig.2 Process of the bacteria measurement

The fiber was set to the fiber holder after each reaction and rinsed by PBT. After that, the fiber holder was injected with 350 µl of PBT. Then the proximal end of optical fiber connected to a 635 nm laser light source and the final reading was taken at a wavelength of 670 nm. This reading value, recorded in picoamperes (pA).

III. Resultes

A. Sensor behavior of the optical fiber immunosensor

Signal differences between primary and secondary antigen-antibody reactions were taken as output value. *E.coli* O-157:H7 concentration of 1×10^7 cells/ml gave the strongest signal enhancement (6000 pA) after secondary antigen-

F. Ibrahim, N.A. Abu Osman, J. Usman and N.A. Kadri (Eds.): Biomed 06, IFMBE Proceedings 15, pp. 308-311, 2007
www.springerlink.com ' Springer-Verlag Berlin Heidelberg 2007

antibody reaction and the signal strength decreased when the cell concentration decreased. The lowest cell concentration that gave a positive signal (30 pA) compared to a control (no bacteria) was 1×10^2 cells/ml and was considered to be the detection limit for this sensor. There was almost no signal of nonspecific reaction.

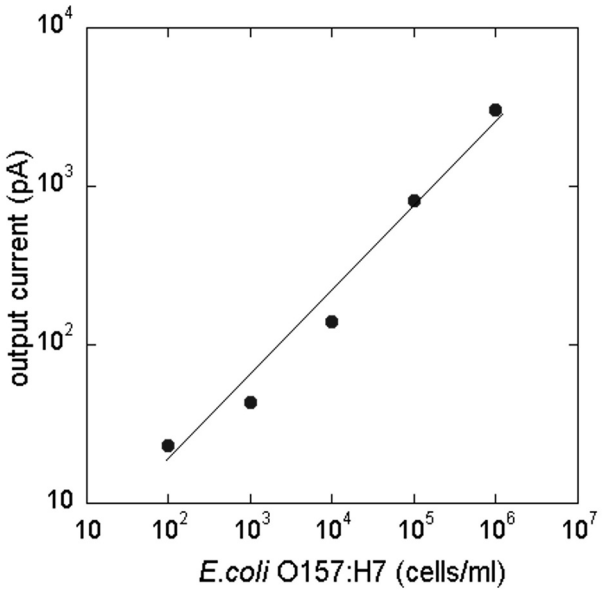

Fig.3 Calibration curve for E. coli O157:H7 solution

B. Selectivity of the optical fiber immunosensor

Evaluation of the sensor with other bacteria indicated that *E.coli* O157:H7 (1×10^5 cells/ml) generated a signal of 810pA, which was significantly stronger than that of equivalent concentration of nonpathogenic *E.coli* (10 pA), *Listeria monocytogenes* (11 pA), *Vibrio s.p.* (19 pA).

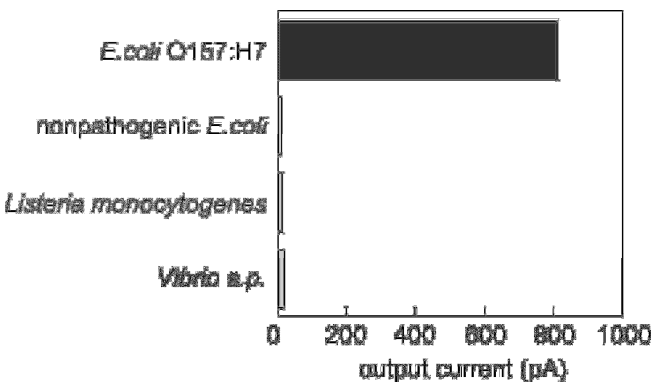

Fig.4 Bacteria selectivity of the immunosensor

C. Measurement of food sample (milk)

Signal difference primary and secondary antigen-antibody reaction was taken as output value. Artificially contaminated milk with *E.coli* O-157:H7 at concentration of 1×10^7 cells/ml gave the strongest signal enhancement after secondary antigen-antibody reaction (7700 pA) and the signal strength decreased when the cell concentration decreased. The lowest cell concentration that gave a positive signal (30 pA) compared to a control (no bacteria) was 1×10^2 cells/ml and was considered to be the detection limit for this sensor. There was almost no signal of nonspecific reaction.

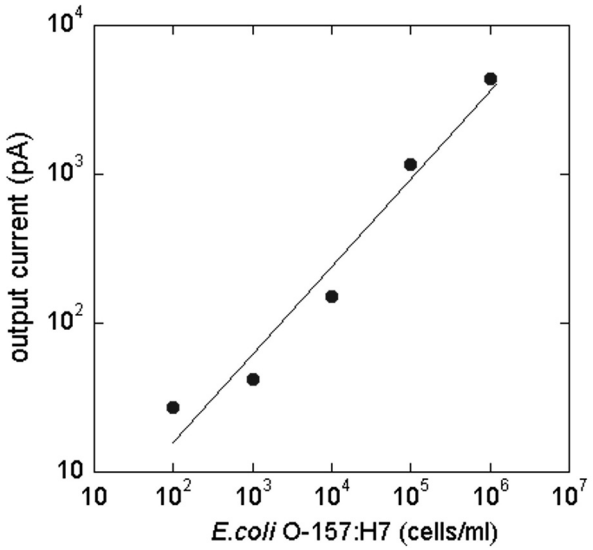

Fig.5 Calibration of *E.coli O157:H7* measurement in milk. The concentration of *E.coli O157:H7* was controlled.

IV. Discussion

E.coli O157:H7 is one of hundreds of strains of bacterium *Escherichia coli*. This strain can cause severe illness in spite of low number. Therefore, rapid and sensitive methods are required to detect this pathogen. Conventional methods are time consuming. Several rapid methods, such as PCR, RIA and ELISA are sensitive and specific but often expensive and sophisticated. Furthermore, the efficacy of those methods to detect pathogens from food samples without culture microbe has not been thoroughly investigated.

In this study, we constructed a fiber optic immunosensor for *E.coli* O-157:H7. Commercial polyclonal antibodies were used as a capture antibody and a Cy5-labeled antibody. Preparation for the sensor avoided to use expensive materials, and avoided to do cumbersome procedures.

F. Ibrahim, N.A. Abu Osman, J. Usman and N.A. Kadri (Eds.): Biomed 06, IFMBE Proceedings 15, pp. 308-311, 2007
www.springerlink.com ' Springer-Verlag Berlin Heidelberg 2007

The measurement range for *E.coli* O157:H7 diluted with phosphate buffer (PB) was from 1×10^2 to 1×10^7 cells/ml. The results could be obtained within about 15 min of sampling. As the detection limit for *E.coli* O-157:H7 by ELISA method could vary from 1×10^3 to 1×10^5 cells/ml [11], and the time to get results could require from 1 to 2 hours, this fiber optic immunosensor could be one of the best methods to meet the need for rapid, sensitive, and simple microbial detection system. This method could also detect *E.coli* O157:H7 in milk artificially inoculated with 1×10^2 to 1×10^7 cells/ml. The calibration curve was largely similar to the curve obtained from *E.coli O157:H7* in PB. Fat globule and protein in milk are difficult to filter and these components are known to become inactivators for pathogens detection. To detect *E.coli O157:H7* by dipping the thin optical fiber dominant area into milk means that this method could apply for the direct detection of pathogen in various food samples. Also, this immunosensor was specific for *E.coli* O157:H7 and showed higher signal strength than for nonpathogenic *E.coli* or other bacteria, including *Listeria monocytogenes* and *Vibrio s.p.*

V. Conclusions

A fiber optic immunosensor for *E.coli* O-157:H7 was constructed. The measurement range for *E.coli O157:H7* diluted with PB was from 1×10^2 to 1×10^7 cells/ml. This method could also detect *E.coli O157:H7* in commercial milk artificially inoculated with 1×10^2 to 1×10^7 cells/ml. The calibration curve was largely similar to the curve obtained from *E.coli O157:H7* in PB. This indicates that immunosensor can detect *E.coli O157:H7* from food sample without pretreatment. Optical fiber results could be obtained within about 15 min of sampling. The method has been proved to be much faster than that of conventional one.

Acknowledgment

This study was supported in part by CANON INC. and JSPS (Japan Society for Promotion of Science) Grants-in-Aid for Science Research System.

References

1. Azuma M, Oguma K (2000) Conicise Text of Microbiology. Nankodo, Tokyo
2. Miyasaka N, Karasuyama H, Asakawa H, Tozawa H (2001) Clinical immunology. Kodansha, Tokyo
3. Jeffrey F, Joan S (1999) Monoclonal Antibodies Directed Against the Flagellar Antigens of *Listeria* Species and Their Potential in EIA-Based Methods, Vol.50, No.6:479-480
4. Book Rags at http://www.bookrags.com/
5. Urayama S (2003) Clinical chemistry. Ishiyaku Publishers, Tokyo
6. Karube I (2002) Biosensor. CMC Publishers, Tokyo
7. Ivnitski D, Abdel-Hamid I, Atanasov P, Wilkins E (1999) Biosensors for detection of pathogenic bacteria. Biosens. Bioelecron.14:599-624
8. Tao G, Mark M, Arun B (2004) Detection of Low Level of *Listeria monocytogenes* Cells by Using a Fiber-Optic immunosensor. Appl. Environ. Microbiol, vol.70,10: 6138-6146
9. Masumoto K, Nishimoto Y, Taguchi T, Tsutsumi Y, Kanemitsu S, Hara T and Suita (2005) Colonic stricture secondary to hemolytic uremic syndrome caused by *Escherichia coli O-157*. Pediatr Nephrol, vol.20: 1496-1499
10. Anderson P, Breslin K, Ligler F (1996) Assay development for a portable fiberoptic biosensor. ASAIO J.42 :942-946
11. SCAN NEWS 2005-2 at http://www.scas.co.jp/company/news/22/frontier1_22.pdf

Address of the corresponding author:

Author: Kohji Mitsubayashi
Institute: Department of Biomedical Devices and Instrumentation, Institute of Biomaterials and Bioengineering, Tokyo Medical and Dental University
Street: 2-3-10 Kanda-Surugadai
City: Chiyoda-ku, Tokyo
Country: Japan
Email: m.bdi@tmd.ac.jp

F. Ibrahim, N.A. Abu Osman, J. Usman and N.A. Kadri (Eds.): Biomed 06, IFMBE Proceedings 15, pp. 308-311, 2007
www.springerlink.com ' Springer-Verlag Berlin Heidelberg 2007

A review of MEMS drug delivery in medical application

S. Karman[1], F. Ibrahim[1] and N. Soin[2]

[1]Department of Biomedical Engineering , Engineering Faculty , Malaya University, Malaysia
[2]Department of Electrical Engineering, Engineering fakulty, Malaya University, Malaysia

Abstract—**This paper overviews various components of MEMS drug delivery devices in medical application such as micropumps, microvalves, microactuator and microneedles, using biocompatible material such as silicon. The review will focus on micropumps structures in different actuators. The electrostatic actuated micropumps and circular bossed membrane were found out to be the most suitable device for medical application and offer better linearity pumping rate respectively.**

Keywords—**MEMS, drug delivery, micropump, microneedles**

I. Introduction

Microelectromechanical systems (MEMS) are an advanced technology to develop a high performance and low cost medical devices. It is a very small system which involves both electronic and non-electronic elements and performs functions that include sensing, processing, actuation, display and control with high functionality, precision and performance [1]. In the past 10 to 15 years, many of Biological Micro-Electro-Mechanical System (BioMEMS) currently being developed are for *in-vitro/ex-vivo* application which major in analytical application; such as biomolecular recognition and affinity sensors and etc [2]. In contrast to the conventional drug delivery practice such as oral tablets consumption or injections using syringe, MEMS drug delivery system offer better drug therapy which allow accurate dosing with more efficient and effective [3]. The applied of MEMS for drug delivery through biocapsules, microneedles, micropumps and microresevoirs offer a less invasive therapeutic and improve the quality of life in diabetic patients [4]. External and implantable micropumps are being used clinically for the treatment of diabetes that offer better insulin therapeutic [5]. This paper overviews the structure of MEMS micropump, microvalve and microactuator for silicon based MEMS drug delivery development. The details of the components and mechanisms will be described in this paper.

II. Mems drug delivery system

MEMS drug delivery system offer better drug therapy which allow accurate dosing with more efficient and effective and less invasive therapeutic especially for better hospitality to the diabetic patients. There are two types of device application, external device such as microneedles or patch and implantable device, commonly utilize a micropump. Sometimes, external device can be a combination of an array of microneedles and micropumps. The micropump structures, microneedles and the recent studies of micropumps will be discussed in this paper.

A Component of MEMS drug delivery system

A.1 Micropump

Micropump is a major component of the MEMS drug delivery system where it involved diaphragm membrane, microvalve, microchamber, microchannel, microactuator, inlet and outlet in its structure. The diaphragm membrane (usually silicon) is a critical part where it can be deflected in actuated state [6]. The reciprocating displacement of this diaphragm membrane was elaborated completely by Laser DJ *et. al*.[7]. There are two major pumps categories (fig.1): (1) displacement pumps , which exert pressure forces on the working fluid through one or more moving boundaries and (2)dynamic pumps, which continuously add energy to the working fluid in a manner that increases either its momentum. This review will focus on displacement micropump studies.

A.2 Microvalve

Microvalves are devices to control the fluid motion. There are two types of valves, passive check valves and active valves [8][9]. Passive check valves utilize an energy from the flow such as cantilever valve, while the active valves need external energy from actuator (electrostatic, piezoelectric, thermal bimetallic, thermal expansion, electrochemical, electromagnetic, thermo viscous, pneumatic, thermopneumatic and shape memory alloy) to function. In stable state (not in actuated state), the active valves can be split into two groups: normally closed (NC) and normally open (NO) valve type. The ideal valves have characteristics like zero leakage, zero power consumption, zero dead volume, infinite differential pressure capability, zero response time, insensitivity to particulate contamination and able to operate

F. Ibrahim, N.A. Abu Osman, J. Usman and N.A. Kadri (Eds.): Biomed 06, IFMBE Proceedings 15, pp. 312-315, 2007
www.springerlink.com ' Springer-Verlag Berlin Heidelberg 2007

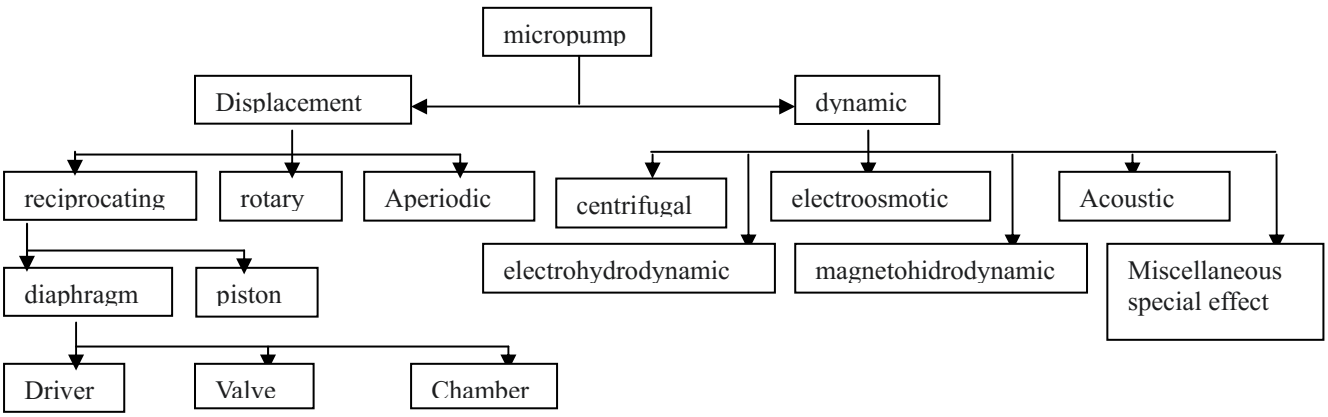

Fig.1 Classification of pumps and micropumps; after Krutzch and Cooper. (Laser DJ *et. al* [6].)

with any fluid. Henning A [8] reported that electrostatic, piezoelectric and electromagnetic actuated valves have a response time less than 10msec.

A.3 Microactuator

Micropumps can be actuated by various mechanisms such as piezoelectric, electrostatic, thermopneumatic, pneumatic, shape memory alloy, bimetallic, and electromagnetic actuation [10]. Each actuation principle has its advantages and disadvantages. Both electrostatic and piezoelectric actuation principles provide very good reliability and energy efficiency [11]. In comparison with the other type especially piezoelectric counterpart, electrostatic actuators have an advantage in reducing size to achieves a small size micropump [12].

A.4 Microneedles

Transdermal drug delivery is a convenient for therapeutic agent delivery and can be a valuable alternative to oral administration by avoiding the gastrointestinal tract [13]. It take place of hypodermic needle to make a minimal invasive which could less pain [14]. To allow this minimal invasive become efficient, drug infuse into the viable epidermis, 60-130µm thick below the stratum corneum (the 10-20 µm thick outer layer of the skin, which forms the main barrier for transport of drugs across the skin) [15]. The studies of transdermal drug delivery including solid microneedles (*i.e.* i. poke with patch [16][17] ii) coat and poke iii) dip and scrape), hollow microneedle, and etc. Solid microneedle have been shown can increase skin permeability to a broad range of molecules in vitro [18] while hollow microneedles offer the possibility of transporting drugs by diffusion or, for more rapid rates of delivery, by pressure-driven flow. Han J.G.E Gardeniers *et al* [19] presented the design of an array of out-plane silicon hollow microneedles. Aggarwal P *et al* [20] proposed the design of in-plane silicon microneedles for sensing the resistive force offered by human skin. Takaya Miyano *et al* [21] designed and fabricated an array of sugar microneedles which molded out of maltose mixed with pharmaceutical material. Yu Xie *et al* [13] explored a novel approach to enhancing transdermal drug delivery using an array of microneedles loaded with dry drug film (drug compounds dispersed in chitosan films).

A.5 microreservoir

Shawgo *et al* [4] has developed an array of reservoir etched on a silicon substrate. Each reservoir contains a single dose of drug and is covered with a gold membrane which will be converted to soluble gold chloride upon the application of an anodic potential to the device in a medium with a physiological concentration of saline.

B. Recent research of MEMS drug delivery micropump

B.1 Electrostatic actuator devices

There are many papers reported on MEMS electrostatic device for variety of medical applications; e.g. microsgyroscope [22], microgripper for blood vessel [23], low frequency micropower generator [24], optical coherence tomography[25]. MEMS micropump is one of the electrostatic device that mostly use for drug delivery system [26]. Zengerle R [27] presented an electrostatic actuated bulk micromachined membrane pump with outer dimensions of 7x7x2 mm^2. This single chamber micropump consists of two passive check valves, a pump membrane and a counter electrode for electrostatic actuation.
Zengerle R *et. al.* [28] extended their study to a bidirectional silicon electrostatic actuated micropump, which dif-

F. Ibrahim, N.A. Abu Osman, J. Usman and N.A. Kadri (Eds.): Biomed 06, IFMBE Proceedings 15, pp. 312-315, 2007
www.springerlink.com ' Springer-Verlag Berlin Heidelberg 2007

ferent in the layout of the valves. Tachung C Yih *et. al.* [10] discovered a single chamber electrostatic actuated micropump with circular bossed membrane which could generate larger drawing and pumping forces , better than other flat membrane . The boss will stabilize the membrane vibration under high driving frequency. Mir Majid Teymoori *et al* [12] designed and simulated a novel of electrostatic actuated micropump based on peristaltic motion. The valve-less electrostatic micropump optimization has been studied by Dan S.Popescu *et al* [29]. Implantable electrostatic actuation micropump studies being widely because of its inherent low power comsumption, which compatible to medical application[30], such as reported by B.Wagner *et al*. which presented an implantable electrostatic micropump using bistable silicon microvalves [31].

B.2 Piezoelectric actuation devices

Li Cao *et al* [11] designed and simulated an implantable drug delivery system with multiple piezoelectric actuated micropump in peristaltic motion .The design includes inlet, three pump chambers, three silicon membranes, three normally closed active valves, three bulk piezoelectric actuators (lead zirconate titanate), three actuation reservoirs, flow microchannels , and outlet . H.Q.Li *et.al* [32] presented the fabrication and testing of a high performance piezoelectrically driven fluidic silicon micropump with passive valves. The non-invasive drug delivery system presented by Songmei Yuan, was a MEMS-based piezoelectric array microjet[33].The device consists of a fluid chamber, which is formed by a piezoelectric transducer bonded to a silicon wafer with nozzles.

B.3 Pneumatical and thermoneupmatical Actuated device

Pneumatical actuated micropump that designed by Chih-Hao *et. al* [34] featured a serpentine-shape(S-shape) microchannel. The micropump fabricated in polydimethylsiloxane (PDMS) is controlled using a single electromagnetic valve (EMV) switch, which improved the pumping rate, achieved maximum pumping rate 7.43µl/min. The recent study of thermopneumatic micropump fabrication reported by Ok Chan Jeong *et. al* [35] which consists of a heater, an air chamber , a corrugated silicon diaphragm , and a pair of cantilever-type aluminium flap valves. The novel single-stroke, pipette-like thermopneumatic micropump fabrication is presented by W.H.Song *et .al* [36]. This design is capable of delivering discrete amounts of liquid in the microliter range in free of pulsations.

B.4 Magnetically actuated devices

Anson Hatch *et. al* [18] present a novel of magnetically ferrofluid valveless micropump . A ferrofluid contains nanosize ferromagnetic particles that actuate the motion of the ferrofluid. The maximum flow rate achieved with minimal backpressure was 45.8 µl/min.

B.5 Shape memory alloy devices

Benard W.L *et al*. reported [37] the shape memory alloy devices using alloy titanium nickel [38] , have an advantage of capable of both high force and high strains for high pressure head and large volume pumped per cycle respectively.

III. Summary

This review shows that MEMS drug delivery devices is designed in order to improve the drug delivery for more accurate dosing , efficient and effective and also provide less invasive into patient s skin. Micropump is a major component of MEMS drug delivery system and diaphragm membrane is a most critical part in micropump s structure. The electrostatic actuated micropumps have been shown to be suitable for medical application because of its small size and low voltage, while circular bossed membrane of micropumps membrane offer the better linearity for pumping rate of electrostatic micropumps. However, this bossed membrane utilization caused less sensitivity of membrane which necessary for medical application.

References

[1] Stephen D. Senturia, Microsystem Design, Kluwer Academic Publisher, p3-13
[2] (Electronic MEMS for triggered delivery Amy C.Richard Grayson et.al Advanced Drug Delivery Reviews 56 (2004) 173-184+-)
[3] Mark R. Prausnitz , Microneedles for transdermal drug delivery , Advanced Drug Delivery reviews 56 , 2004 , 581-587
[4] Rebecca S.Shawgo , Amy C Richard Grayson , Yawen Li , Biomems for drug delivery , Current Opinion in Solid State and Material Science 6 , 2002 , 329-334
[5] my C.Richard Grayson et.al , Electronic MEMS for triggered delivery, An Advanced Drug Delivery Reviews 56 (2004) 173-184+-
[6 Olivier Francais, Isabelle Dufour, Emmanuel Sarraute, Analytical static modeling and optimization of electrostatic micropumps, J.Micromech.Microeng. 7(1997) 183-185]
[7] DJ Laser and JG Santiago , A review of micropumps, J Micromech.Microeng 14(2004) R35-R64]
[8] Albert K Henning et.al , Physics, technology, applications, and reliability of microvalves, AFRL Microfluidic Workshop May 2003
[9]. Edwin Oosterbroek , Modeling, design and realization of microfluidic components,p89-121
[10] Tachung C. Yih , Chiming Wei , Bashar Hammad, Modelling and characteristic of a nanoliter drug delivery MEMS micropumps with circular bossed membrane ,nanomedicine: Nanotechnology Biology and medicine , 2005 , 164-175

F. Ibrahim, N.A. Abu Osman, J. Usman and N.A. Kadri (Eds.): Biomed 06, IFMBE Proceedings 15, pp. 312-315, 2007
www.springerlink.com ' Springer-Verlag Berlin Heidelberg 2007

[11] Li Cao et. al, Design and simulation of an implantable medical drug delivery system using microelectromechanical systems technology, Sensors and Actuators A 94 (2001) 117-125
[12] Mir Majid Teymoori , Ebrahim Abbaspouc Sani , Design and simulation of a novel electrostatic peristaltic micromachined pump for drug delivery applications , Sensor and Actuators A 117 , 2005, 222-229
[13] Yu Xie et.al, Controlled transdermal delivery of model drug compounds by MEMS microneedle array, Nanomedicine: Nanotechnology, biology, and medicine 1(2005) 184-190
[14] Mark R. Prausnitz , Microneedles for transdermal drug delivery , Advanced Drug Delivery reviews 56 , 2004 , 581-587
[15] Meghan F. Wilkosz et.al, Transdermal drug delivery, U.S Pharmacist , http://www.pharmacist.com/
[16] Wei Qi Lin et.al, Transdermal delivery of Antisense Oligonucleotides with Microprojection Patch Technology , Pharmaceutical Research , vol. 18, no. 12 (2001)
[17] Wijaya Martanto et.al, Transdermal delivery of insulin Using Microneedles in vivo, Pharmaceutical Research , vol. 21, no. 6 (2004)
[18] Anson Hatch, Adrew Evan Kamholz , A Ferrofluidic Magnetic Micropump , J. Of Micromechanical Systems, vol.10, No.2 June 2001]
[19] Han J.G.E. Gardeniers et.al, Silicon micromachined hollow microneedles for transdermal liquid transport, J.MEMS vol.12, no.6 (2003)
[20] P.Aggarwal et.al, Geometrical effects in mechanical characterizing of microneedle for biomedical applications, Sensor and Actuators B102 , 2004, 226-234
[21] Takaya Miyano et.al, Sugar Microneedles as transdermic drug delivery system, biomedical microdevices 7:3, 185-188, 2005
[22] S.Rajendran, K.M.Liew, Design and simulation of an angular vibrating microsgyroscope, Sensor and Actuator A 116 (2004) 241-256
[23] R. Wierzbicki, Debski, A. Eisinberg, A. Menciassi, M.C. Carrozza and P. Dario,Design and fabrication of an electrostatically driven microgripper for blood vessel manipulation, Microelectronic Engineering Volume 83, Issues 4-9 , April-September 2006, Pages 1651-1654
[24] P. D. Mitcheson、Holmes and T. C. Green , MEMS electrostatic micropower generator for low frequency operation , Sensors and Actuators A:physical Volume 115, Issues 2-3 , 21 September 2004, Pages 523-529
[25] J. M. Zara, and S. W. Smith , Optical scanner using a MEMS actuator, Sensors and Actuators A:Physical Volume 102, Issues 1-2 , 1 December 2002, Pages 176-18
[26] Peter Woias, Micropumps-past, progress and future prospects, sensors and actuators B 105(2005) 28-38
[27] R.Zengerle et.al , A Micro Membrane pump with electrostatic actuation, Micro electromechanical systems 1992.
[28] R.Zengerle et.al , A Bidirectional silicon micropump, IEEE 1995
[29] Dan S.Popescu, Phileppi Lerch, Camelia Dunare, Dan Dascalu, Modeling and optimization for an electrostatic actuation of a valveless micropump using a silicon buckled membrane , IEEE 1997]
[30] Robert Puers, Daniel Lapadatu ,Electrostatic Forces and their effects on capacitive mechanical sensors , Sensors and Actuators A 56 (1996) 203-210]
[31] B.Wagner, H.J. Quenzer, S. Hoerschermann, T. Lisec, M. Juerss,Micromachined bistable valves for implantable drug delivery system, 18th International Conference of the IEEE Engineering, in Medicine and Biology society, Amsterdam 1996]
[32] H.Q. Li, D.C Roberts, J.L Steyn, K.T. Turner, J.A Carretero, A high frequency high flow rate piezoelectrically driven MEMS micropump Proceedings IEEE solid State Sensors and Actuators Workshop, Hilton Head , June 2000]
[33] Songmei Yuan, Zhaoying Zhou, Guohui, Wang, Changgeng Liu, MEMS-based piezoelectric array microjet, Microelectronic Engineering 66(2003)767-772
[34] Chih Hao Wang and Gwo-Bin Lee , Pneumatically driven peristaltic micropumps utilizing serpentine-shape channels , J. Micromech. Microeng.14(2006) 341-348]
[35] Ok Chan Jeong and Sang Sik Yang, Fabrication of a Thermopneumatic micropump with aluminium flap valves , J. of the the Korean Physical society , Vol.37, No.6, December 2000, pp873-877]
[36] W H Song and J Lichtenberg , Thermopneumatic , single stroke micropump, J. Micromech.Microeng.15 (2005) 1425-1432]
[37] William L. Benard et.al, Thin film shape-memory alloy actuated micropumps , J. of microelectromechanical systems, vol.7, no.2 June 1998]
[38] H Kahn, M A Huff , A.H Heuer ,The TiNi shape-memory alloy and its applications for MEMS, J. Micromech.Microeng.14(1998) 213-221]

Address of the corresponding author:

Author: S.Karman
Institute: Department of Biomedical Engineering,
Faculty of Engineering, University of Malaya
City: Kuala Lumpur
Country: Malaysia
Email: salmahkarman@gmail.com

F. Ibrahim, N.A. Abu Osman, J. Usman and N.A. Kadri (Eds.): Biomed 06, IFMBE Proceedings 15, pp. 312-315, 2007
www.springerlink.com ' Springer-Verlag Berlin Heidelberg 2007

A Review on Design Parameters of Micro-Fluidic System

M.P. Yogarajan[1] N. Soin[1] and F. Ibrahim[2]

[1]Department of Electrical Engineering, Engineering Faculty, University of Malaya, Malaysia
[2]Department of Biomedical Engineering, Engineering Faculty, University of Malaya, Malaysia

Abstract — **The area of micro fluidic system is a significant sub-component of micro-electro-mechanical systems (MEMS). Many of these MEMS applications will require components of dynamic fluids, either of Newtonian or non-Newtonian characteristics to be pumped into micro-ducts. At such small scales this is a rather gigantic challenge. Some of the early reviews on micro-channel analysis, at the very basics liken micro-channel design (device design) to a macro channel design e.g. piping design. Reasonably, conventional fluid mechanic laws govern these design analysis; laws which are often violated in the micro-environment. This paper appraises the approximation of micro-fluid engineering to macro-fluid engineering and key parameters which contradict to conventional fluid laws. Subsequently this paper also discusses the role of micro-fluid analysis in design; specifically in bio-MEMS applications.**

Keyword — **MEMS, bio-MEMS, micro-fluidic, micro-channel**

I. Introduction

One property of an intelligent micro-system is the existence of various physical domains such as microelectronics, micromechanics, micro-fluidics and micro-optics [1]. Recent advances in the fabrication of micro-electro-mechanical systems (MEMS) offer unique opportunities, specifically in the biomedical industry to create novel implantable drug delivery systems to maximize the efficacy of drug therapies [2] The multi-disciplinary task of modeling a bio-MEMS incorporating, mechanical and biochemical parameters on an electronics platform requires detailed identification of several variance existent in the system. The modeling or miniaturization process incorporating bio-compatible fluids should also, at any point of design be clinically agreeable. A comprehensive summary on theoretical analysis and experimental observation of design variables in micro-channel was discussed in [3]. In that respect, this paper reviews experimental and laboratory analysis on the most known micro-fluidic design parameters to date and discusses further on specific micro-fluidic analysis governing specific applications.

II. Characteristics of working-fluid

Different phenomena have been observed in various works indicating that the mechanisms of flow and heat transfer in micro-channels are still not understood and it seems that even problem of modeling the basic single phase straight channel case is still open [3]. A common term used on classification of working materials is either as Newtonian and Non-Newtonian fluids [3]**.** Non-Newtonian fluid effects are expected to be important for polymeric liquids and particle suspension flows. A homogeneous isothermal Newtonian fluid is characterized by a constant viscosity, which is an intrinsic material property of the fluid, confining neither to geometry nor flow conditions [4]. Contrary to conventional fluid dynamics, it is found that the viscosity is lower in the narrower channel. However another study shows that the viscosity is independent of the dimension of the flow channel for liquids such as water, silicon oil and alcohol [5].

Perhaps the next most vital design factor in modeling a micro channel is on the mode of flow generation or fluidic transport. It s most common approach; fluid can either be filled into different parts of the micro system by pressure driven and electro-osmotic driven.

Pressure-driven flow exhibits a parabolic velocity profile and average velocity is proportional to the second power of transverse channel dimension (Fig. 1). As a result, the required pressure drop could be too large and may become impractical in very small devices.

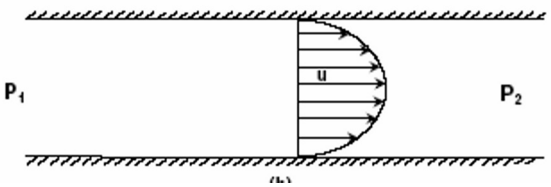

Fig.1 :Parabolic velocity of pressure driven flow

Electro-osmotic and electro-phoretic transports are developed when an electric field was applied between the ends of the channels. In almost all recent cases an electro-osmotic fluid transport is preferred to the pressure driven method as it requires less mechanically moving parts, such

F. Ibrahim, N.A. Abu Osman, J. Usman and N.A. Kadri (Eds.): Biomed 06, IFMBE Proceedings 15, pp. 316-320, 2007
www.springerlink.com ' Springer-Verlag Berlin Heidelberg 2007

as valves and pumps, which have thus far been difficult to construct and interface to microchip systems [5]. The thickness of EDL becomes significant in comparison to the cross section of the micro-channel. The presence of EDL and the flow-induced electro-kinetic field has an important effect on the flow characteristics especially of pure water and dilute aqueous solutions in small micro-channels. The initial parabolic profile is altered to a plug-like velocity profile (Fig 2).

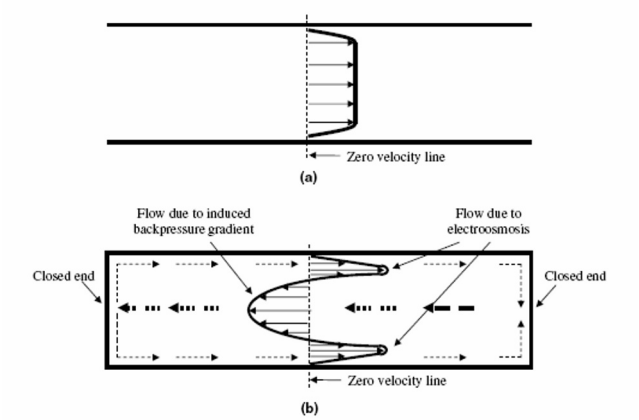

Fig.2 Plug-like velocity profile of electro-osmotic flow in (a) open and (b) closed channel

If the liquid contains a certain amount of ions (for instance, an electrolyte solution or a liquid with impurities), the electrostatic charges on the solid surface will attract the counter-ions in the liquid (Fig. 3). A condition infused by conduction of current in these moving ions is apparent in micro-channels.

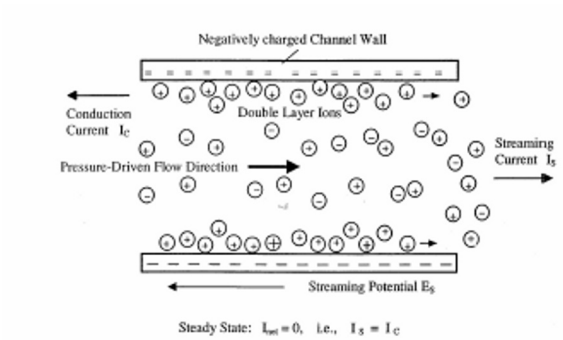

Fig.3 Illustration of the flow-induced electro-kinetic field in a micro-channel

This flow induced streaming potential is a potential difference that builds up along a micro-channel. According to the electro-kinetic theory, the higher the streaming potential, the higher the electro-viscous effect on flow. The absolute value of streaming potential was observed to increase as the Re increases [6]. This phenomenon is usually referred to as the electro-viscous effect and reduces the flow rate in comparison to flow rate prediction by conventional fluid mechanics theory [7]. Since the problem involves electrostatics, electro-migration and fluid motion, this requires coupling of several differential state equations in the simulation. Simulations show a strong dependence of $dP/dx \propto$ Re relationship on the channel size, the ionic concentration, the ionic valence and the bulk conductivity of the liquids. [6]. Moreover, it is found that the strength of applied electric field does not contribute to the flow patterns but only to the magnitude of the fluid velocity [8].

III. Theory of Miniaturization

A design scale at micron level requires system with minimum mechanical movements coupled with critical design factors. In order to optimize the final micro design [1], a macro prototype of the system will be first considered with conventional engineering tools. The million-fold increase in surface area relative to the mass of the minute device substantially affects the transport of mass, momentum and energy through the surface [9]. In the selection of appropriate material for micro-fluidic devices, material properties need to be carefully evaluated. The current trend for biomedical applications strongly points towards use of polymer-based substrates. The choice of silicon as the standard basic material for micro-systems leads to micro-channels with rectangular cross-sections. With more conventional processes such as photolithography, the cross-sections are trapezoidal, but generally remain close to rectangular sections, the depths being often very small compared to the widths.

A. Geometrical Design Parameters

In the event of low Reynolds number (≤700), design analysis should take in account Poiseuille Number (Po number) which is shown in Fig. 4.[10]. The characteristics of flow in micro-channels agree with conventional behaviors predicted by Navier-Stokes Equations; however this is applicable only for micro-channels with hydraulic diameter smaller than 30μm [11].

The unusual behavior of Nu receding with *Re* increasing in the laminar regime is explained and further. A relation of surface conductivity to the channel height in micro-channel was observed through experimental works. [6][18]. A directly proportional co-relation was documented in these papers. In almost all cases, the flow is considered fully

F. Ibrahim, N.A. Abu Osman, J. Usman and N.A. Kadri (Eds.): Biomed 06, IFMBE Proceedings 15, pp. 316-320, 2007
www.springerlink.com ' Springer-Verlag Berlin Heidelberg 2007

developed to ignore entrance effect and uniform temperature through out the duct. The micro-channel effects influencing the friction factor and ultimately the liquid flow behavior analyzed at the entrance is studied [7]. A correlation of Nusselt Number to Reynolds Number advice that theoretical value Nu_{th}, does not depend on Re, but on channel cross sectional shape and heating [13]**.** Square channels have the lowest friction factor among the rectangular channel family for a given Reynolds number.

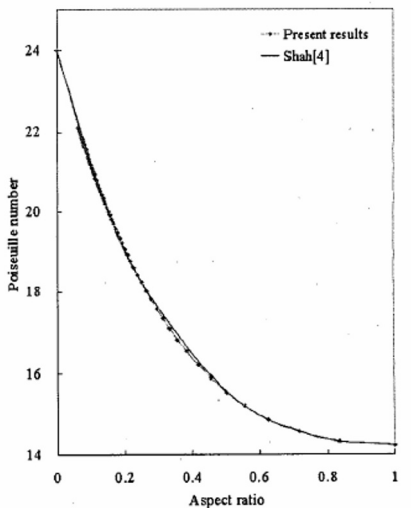

Fig.4 Appreciation of Poiseuille Number to aspect ratio of micro-channel

A visualization experiments with simultaneous measurement of the local heat transfer coefficient in micro-channels with different shaped cross-sections were carried out [9]. The heat transfer coefficient was higher for the square micro-channel compared to a circular micro-channel of a similar material. In order to have a fully developed flow in the duct, it is essential that the channel length L is high compared to D_h [6].

Due to the compact micro system design, the only possible way to increase the channel length would be through serpentine channels and turns to increase the separation distance [5]. However, bends or curves degrade the performance of separation efficiency. The basic design component is a T-channel analysis [9][10], which were approximated to circuit diagram for analysis. The channels are modeled with different types of 90 degree turns to reduce the racetrack effect**.** Accordingly, the racetrack effect is reduced in the detection area when the bend ratio is 4:1. In this manner, literature also suggested U-shaped channel is better for miniaturization [11]**,** pleated and coiled channels to minimize dispersion in micro channel turns [12]**.**

Channels need to be smooth with minimal curvature variation. Smooth channels are often the result of fabrication and material type. Literature discuses various observations e.g. fabricated by the glass drawn process, the second was fabricated by anisotropic etching on silicon. A hypothesis relying on surface roughness was made, based on which simple models were derived to predict most of the phenomena encountered in micro-channels. Simulations on roughness of different regular shapes (half circular, rectangular and triangular) in the channel were also analyzed and presented.

B. Gas Entrapment

The presence of gas bubbles in the micro-channels, a situation also commonly known as gas entrapment is a critical design parameter which plays a significant role to the overall efficiency of a micro-system. One of the earliest reviews on the quantitative criterion for gas entrapment was done by Bankoff [12].

In micro-channels, two forces dominate the filling of fluid. The capillary force sucks the fluid into the microstructure and viscous forces retard the flow. The capillary pressure was deduced from the Washbum equation in a Hagen-Poiseuille -type flow by P. Man [13].

The importance of a reliable liquid filling has been recognized in micro-fluidics. The crucial parameter is bubble encapsulation in the channels. In many cases entrapped air bubbles will drastically alter device performance and thus have to he avoided. The entrapment of air bubbles in micro-fluidic reservoirs has been examined and the importance off instable menisci in critical edges has been demonstrated [14]. Experiments were conducted to investigate the gas/ vapor entrapment process in closed-end micro-channels of various sizes agrees the micro-channel depth has the most pronounced effect on design geometry to the phenomenon. A recent experimental model by Ana V.Pesse [15] concluded the following:

- For fixed width, breadth and contact angle, the flooding time increases nonlinearly (up to two orders of magnitude) with increasing micro-channel depth
- For fixed depth and contact angle, the flooding time increases with increasing micro-channel width(w) and breadth (b)
- For fixed depth, width and breadth, the flooding time increases with increasing contact angle.

Further to this, a common design rule for a filling-friendly microstructure, taking into account the actual shape of the meniscus was derived by F. Goldschmidtboiu [14].

F. Ibrahim, N.A. Abu Osman, J. Usman and N.A. Kadri (Eds.): Biomed 06, IFMBE Proceedings 15, pp. 316-320, 2007
www.springerlink.com ' Springer-Verlag Berlin Heidelberg 2007

IV. Design methodology

A typical bottom-up design methodology used early in micro system designs was compared to a proposed top down design methodology [2][16]**.** A macro model is designed based on conventional engineering principles to validate the conceptual framework. This is followed by stepwise substitution of the macro components by the micro. In the process, deviations from conventional engineering analysis are reviewed, analyzed and modified.

Numerical simulations can predict the fluid flow and heat transfer in mechanical devices and evaluate the performance of a new micro-device before hardware fabrication. A numerical model for the simulation of three-dimensional, transient, and combined electro-osmotic and pressure driven flow in micro-systems was developed and implemented using FLOW- 3D [17].

The approximation of a typical micro-fluidic channel system to an electric circuit model is preferred in evaluation of preliminary design concepts (Fig 5). Numerical results indicate that the compact model can be several orders of magnitude faster compared to detailed numerical simulations without sacrificing too much accuracy [18].

For micro-fluidic devices that rely on electro-kinetic force for fluid flow, the electric field must be solved first. Aveek in modeling of an advanced compact micro-fluidic system presented the fluidic network by a circuit model [19].

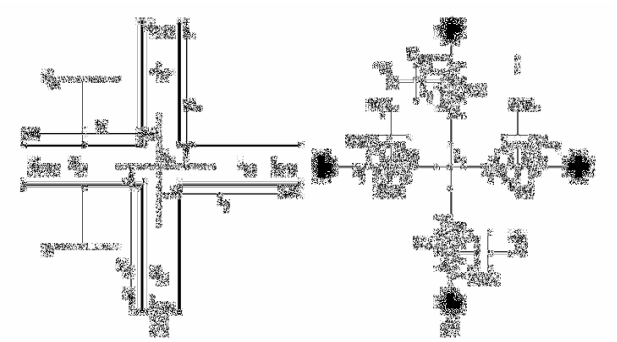

Fig.5 Typical approximation of micro-channel to a circuit diagram

Two distinctive numerical approaches have been used in previous literature for micro flow simulation. Navier Stokes equation was used in pioneering studies [4] in for micro flow simulation. Another numerical method is based on molecular path modeling e.g. Monte Carlo simulation [20] which analyses time step to that the movement and collision processes of molecular modeling involves tracking of all molecular paths requiring enormous amounts of information. It simulates a flow system by tracking the evolution of particle distributions, not single particles. A detailed description on Direct-Simulation- Monte Carlo (DSMC) application in micro-channel was presented and excellent agreement against the Navier-Stokes equation was concluded [20]. In small Mach numbers (M<0.l), the Lattice Boltzmann Method (LBM) does an excellent job of simulating the incompressible Navier-Stokes equation. T.Mautner [21] addresses numerical analysis for 2-phase flow in micro channels using the LBM simulation model and provided a reasonable temperature and flow profile.

V. Conclusions

The review identifies some of the recent discrepancies in experimental micro-fluidic modeling against earlier design principles. To some extent, the review has also identified the variable parameters through various experimental evidence indicate strong co-relation to fluid flow in micro-channels against macro-channel flow behavior but further case specific analysis is required as, laboratory observations are often inconsistent and contradictory. A further experimental analysis on a bio-fluid (Non-Newtonian) working condition is required for the scope of the proposed design work.

Acknowledgement

The author wishes to thank Associate Professor Dr. Fatimah Ibrahim and Dr. Norhayati Soin for their continuous guidance and advice in the completion process of this paper.

References

1. S. Meinzer, A. Quinte, M. Gorges-Schleuter 1996 Simulation and Design Optimization of Microsystems Based on Standard Simulators and Adaptive Search Techniques
2. Yawen Lia, Rebecca S. Shawgo 2004 In vivo release from a drug delivery MEMS device Journal of Controlled Release 100 (2004) 211 219
3. Junemo Koo and Clement Kleinstreuer 2003 Liquid flow in microchannels: experimental observations and computational analyses of microfluidics effects
4. Matthew Scott The modeling of Blood Rheology in small vessels
5. B. H. Weigl, R. L. Bardell, and C. R. Cabrera, Lab-on-a-chip for drug development, *Adv. Drug Del. Rev.*, vol. 55, pp. 349 377, 2003.
6. D. Li /Colloids and Surfaces A : Physicochem. Eng. Aspects 195 (2001) 35 57
7. R.J. Hunter, Zeta potential in colloid science, in: Principles and Applications, Academic Press, New York, 1981
8. Marcos, K.T. Ooi, C. Yang *, J.C. Chai, T.N. Wong Developing electro-osmotic flow in closed-end micro-channels
9. The Fluid Mechanics of Microdevices The Freeman Scholar Lecture

F. Ibrahim, N.A. Abu Osman, J. Usman and N.A. Kadri (Eds.): Biomed 06, IFMBE Proceedings 15, pp. 316-320, 2007
www.springerlink.com ' Springer-Verlag Berlin Heidelberg 2007

10. Modeling and Designing of Microfluidic System Using Poiseuille Number
11. http://www.dbanks.demon.co.uk/ueng/microsys.htm
12. S.B. Bankoff, Entrapment of gas in the spreading of a liquid over a rough surface, AICHE J. 4 (1958) 24 26
13. P. Man et al., Microfabricated capillaritydriven stop valve and sample injector , Proc. MEMS 98,4S-S0
14. F. Goldschmidtboiu Capillary filling of micro-reservoirs wlth various cross sections
15. A.V. Pesse et al. / International Journal of Heat and Mass Transfer 48 (2005) 5150 5165
16. K. Kundert, A Formal Top-Down Design Process for Mixed-Signal Circuits, *Advances in Analog Circuit Design*, April 2000
17. A numerical model for simulation of combined electroosmotic and pressure driven flow in microdevices
18. R. Qiao and N. R. Aluru A Compact Model for Flowrate and Pressure Computation in Micro-fluidic Devices
19. Aveek N. Chatterjee and N. R. Aluru Combined Circuit/Device Modeling and Simulation of Integrated Microfluidic Systems
20. H. Xue*, Q. Fan, C. Shu Prediction of micro-channel flows using direct simulation Monte Carlo
21. T. Mautner, Lattice Boltzmann Simulations: Flow-Through PCR

Author: Murali Prasad Yogarajan
Institute: University of Malaya
City: Kuala Lumpur
Country: Malaysia
Email: vandayars@yahoo.com

F. Ibrahim, N.A. Abu Osman, J. Usman and N.A. Kadri (Eds.): Biomed 06, IFMBE Proceedings 15, pp. 316-320, 2007
www.springerlink.com ' Springer-Verlag Berlin Heidelberg 2007

Bioelectrical Impedance Analysis: Phase Angle - An Independent Predictive Health Marker and its Clinical Applications

P. N. Goswami[1], Khan Munna[2], Moinuddin[3]

[1] Shobhit Institute of Engg & Technology, Modipuram, Meerut, India
[2] Jamia Milia Islamia, Department of Electrical Engineering, New Delhi, India
[3] National Institute of Technology, Jalandhar-144011, India

Abstract— **This article provides an overview of Bioelectrical Impedance Analysis (BIA) and its merits over other body composition methods. BIA phase angle technique is fast emerging as an independent clinical tool besides being a good and practical in-vivo method for estimation of human body composition. Body composition analysis is used in preventative, therapeutic, and research applications such as nutritional assessment, anti-aging therapy, physical performance assessment, weight management, obesity, fluid and nutritional assessment etc. Based on these developments, current and future clinical applications and directions of BIA research are discussed.**

Keywords— **Body Composition, Bioelectrical Impedance Analysis, Phase Angle**

I. Introduction

Body composition analysis is the clinical assessment of tissue and fluid compartments in the human body in terms of Fat Mass (FM), Fat-Free Mass (FFM), Body Cell Mass (BCM), Extracellular Mass (ECM), Total Body Water (TBW), Intracellular Water (ICW) and Extracellular Water (ECW). A normal distribution of tissue and fluid in the body is associated with immunity, high function, and longevity. To perform body composition analysis, the mass and fluid compartments of the body are modeled, measurements are taken, and results are analyzed. Body composition analysis is used in preventive, therapeutic, and research applications.

Bioelectrical impedance analysis (BIA) measures the impedance or opposition to the flow of an electric current through the body fluids contained mainly in the lean tissue. Impedance is low in lean tissue due to presence of intracellular fluid and electrolytes, and high in fat tissue. Impedance is thus related to total body water volume (TBW). The impedance of a biological tissue comprises two components, the resistance 'R' and the capacitive reactance 'X_c'. The conductive characteristics of body fluids provide the resistive component, whereas the cell membranes, acting as imperfect capacitors, contribute a frequency-dependent reactive component. Several electrical circuits have been used to describe the behavior of biological tissues in-vivo. One such circuit involves arranging resistance R and capacitance C in series, while some other put these in parallel. Other models are more complex arrangements of R & C. A common circuit which is used to represent biological tissues in-vivo, is one in which the 'R_e' of extracellular fluid is arranged in parallel to the second arm of the circuit which consists of capacitance 'C' of cell membranes in series with 'R_i' of intracellular fluid (fig.1).

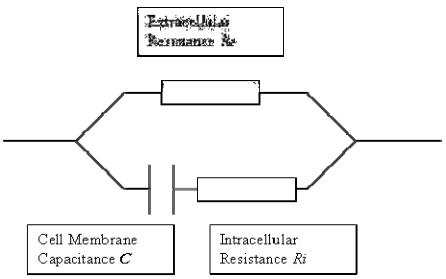

Figure.1 Biological Tissue Eqvt. Circuit

At low frequencies, the current does not penetrate the cell membrane, which acts as an insulator, and therefore the current passes through the extracellular fluid only, which is responsible for the measured R (R_0) of the body. At very high frequencies (around 1MHz) the capacitor behaves as near perfect short, and therefore the total body R (R_∞) reflects the combined effect of both intracellular and extracellular fluid (Fig.2).

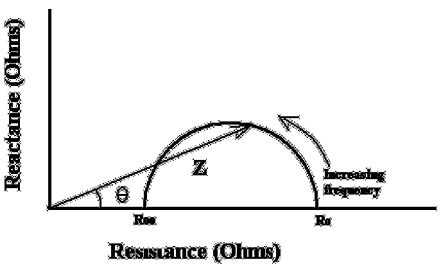

Figure.2 Cole-Cole plot

F. Ibrahim, N.A. Abu Osman, J. Usman and N.A. Kadri (Eds.): Biomed 06, IFMBE Proceedings 15, pp. 321-324, 2007
www.springerlink.com © Springer-Verlag Berlin Heidelberg 2007

Impedance measurements made over a range of low to high (5 kHz-1MHz) frequencies, therefore allow development of prediction equations which relate impedance measures at low frequencies to extracellular fluid volume and at high frequencies to total body fluid volume. This is also known as Cole-Cole plot or multi-frequency bioelectrical impedance analysis (MFBIA).

II. BIA PRINCIPLES & METHODS

BIA is based on the premise that when an electrical current is passed through the body, the voltage drop between two electrodes is linked to the body s fluid volume in that region of the body. Although measurements can be performed at any frequency, 50 kHz has become the standard for commercial instruments. The BIA measurement is performed by attaching a pair of electrodes at the right wrist and at the right ankle, so that a weak but constant alternating current (800 μA) can be passed through the body. The outer clips (black) are for injecting the current and voltage is measured across the inner clips (red) (fig.3).

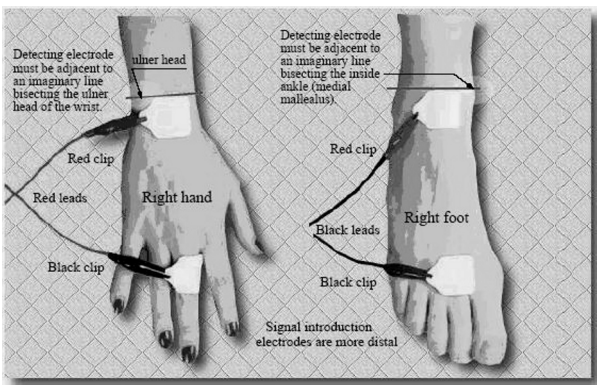

Figure.3 BIA measurement sites

From the voltage and corresponding current reading, the body resistance R is calculated. To estimate the volume of TBW, the following assumptions are used. The whole body acts like a cylindrical conductor, the conductor s length is proportional to the subject s height, and the reactance component of the voltage signal can be disregarded. Under these conditions, the impedance index (Ht^2/R) is assumed to be proportional to the volume of TBW. The water content of the FFB is ~ 73%; hence FFM can be estimated from TBW. The resistance to current flow will be greater in individuals with large amounts of body fat as the adipose tissue is a poor conductor of electrical current due to its relatively low water content[1, 2].

Commonly used whole-body BIA equations provide two-component model estimate of FFM for men and women of diverse ethnic groups for whom these equations were developed. The equations for children are based on three-component model estimates of FFM with density of the body (Db) adjusted for TBW. On average, these equations will accurately estimate FFM within –2.8 kg for women, –3.5 kg for men, and –2.1 kg for children. In order to ensure the predictive accuracy of these equations, clients must strictly follow each of the BIA testing guidelines with standardized testing procedures. Activities performed within 4 hrs before the measurement, such as moderate/vigorous exercise, consumption of excessive alcohol, excessive sweating can substantially alter these readings.

Results for FFM, BF, BCM, TBW, ECW and ICW from various studies in healthy and ill subjects are reported and compiled in ESPEN guidelines [3, 4]. BIA allows the determination of the FFM and TBW in subjects who do not have significant fluid and electrolyte abnormalities, by using appropriate population, age or pathology-specific BIA equations and established procedures.

III. BIA PHASE ANGLE

The overall opposition (bioelectric impedance) that a body presents to an alternating current has two components which are resistance R and reactance Xc . Fat-free mass in the human body is proportional to the resistance and Body cell mass is proportional to the reactance. Phase angle is a linear method of measuring the relationship between resistance and reactance in series or parallel circuits (fig.4).

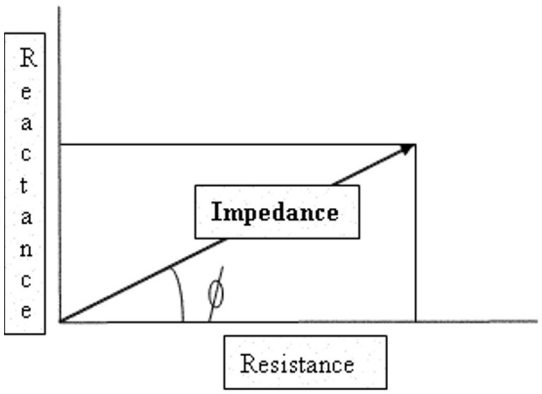

Figure.4 Body phase angle

Phase Angle = arctan (reactance/ resistance). Phase angle can range from 0 to 90 degrees; 0 degrees if the circuit is only resistive (as in a system with no cell mem-

F. Ibrahim, N.A. Abu Osman, J. Usman and N.A. Kadri (Eds.): Biomed 06, IFMBE Proceedings 15, pp. 321-324, 2007
www.springerlink.com ' Springer-Verlag Berlin Heidelberg 2007

branes) and 90 degrees if the circuit is only capacitive (all membranes with no fluid). A phase angle of 45 degrees would reflect a circuit (or body) with an equal amount of capacitive reactance and resistance at a given fixed frequency, such as in fresh vegetables. Lower phase angles appear to be consistent with low reactance and either cell death or a breakdown in the selective permeability of the cell membrane. Higher phase angles appear to be consistent with high reactance and large quantities of intact cell membranes and body cell mass. (Fig.5)

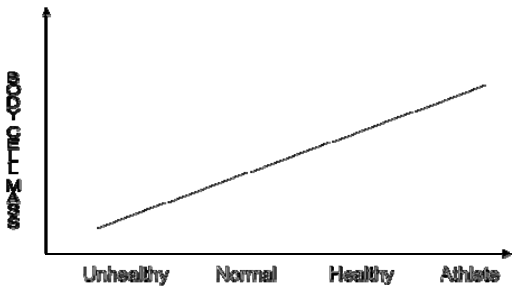

Figure.5 Cellular Health vs. Phase Angle

The average phase angle for a healthy individual is approximately 6 to 9 degrees (Table.1), depending on gender and decreases with age [5, 6]. Its positive association with physical activity suggests that it might also assess function besides evaluation of body composition.

Table.1 Normal Phase Angles

MALES Age vs. Phase Angle (º)							
15-24	25-34	35-44	45-54	55-64	65-74	75-84	≥85
7.3	7.5	7.2	7.1	6.6	6.1	5.3	4.6
FEMALES Age vs. Phase Angle (º)							
15-24	25-34	35-44	45-54	55-64	65-74	75-84	≥85
6.6	6.6	6.7	6.5	6.0	5.4	4.8	4.5

IV. BIAS CLINICAL & OTHER APPLICATIONS

BIA appears to be a better measure of FFM and percentage of body fat than weight, height, or body mass index at little extra cost or difficulty but with somewhat greater complexity. BIA may provide a more accurate measure of adiposity than do skin-fold measurements and may be more easily standardized. However, measurements of skin folds and girths may provide additional useful information on body fat patterning. Clinical use of BIA in subjects at extremes of BMI ranges or with abnormal hydration is not recommended for routine assessment of patients. Multi-frequency and segmental BIA may have advantages over single-frequency BIA in these conditions, but further validation is necessary. Further validation of BIA is necessary to understand the mechanisms for the changes observed in acute illness, altered fat/lean mass ratios, extreme heights and body shape abnormalities.

BIA has been widely used in the clinical setting for assessment of body composition for the last 20 years. Numerous investigations have demonstrated the usefulness of BIA in assessing body composition, body composition changes and body fluid distribution in a wide range of physiological and clinical conditions [7-10]. Predictions of leg-segment electrical impedance (LEI) are extremely useful for aviators when determining medical diagnosis and therapy in aerospace medicine. Khan [11] investigated a unique application of BIA in a study of blood pooling in the simulated leg segment of an aircraft pilot under G-stress. In another study, BIA was also used to simulate and measure arm blood pooling of an aircraft pilot under G-stress. The results of the studies may then lead to practical designs and develop countermeasures to reduce or remove arm pain of aircraft pilot.

BIA is useful for patients undergoing hemodialysis. One application is in the prescription and monitoring of the adequacy of dialysis for which urea kinetic modeling has become the common standard. This model requires an accurate assessment of TBW, which can be provided by BIA. BIA can also be of value in assessing volume status in the dialysis patients in order to minimize common problems related to inaccurate volume determination. Knowledge of TBW might also serve to improve interpretation of drug pharmacokinetics. According to available data and research publications, the potential uses of BIA in clinical situations have yet not been exhausted. Much work needs to be done in the validation of BIA method against a "gold standard" in different population, as well as appropriate equations to estimate body composition variables from the raw data collected. General BIA applications could be summarized as detailed below

- University medical and hospital medical research,
- Healthcare - Clinics, physicians, nurses, physiotherapists,
- Sports medicine, health & fitness clubs,
- Nutritional counseling and diet centers,
- Veterinary - research and routine monitoring,
- Meat Industry - non-invasive measure,
- Resorts and spa - Subject progress monitoring,
- Agriculture – oil content of produce and freshness of vegetables.

F. Ibrahim, N.A. Abu Osman, J. Usman and N.A. Kadri (Eds.): Biomed 06, IFMBE Proceedings 15, pp. 321-324, 2007
www.springerlink.com © Springer-Verlag Berlin Heidelberg 2007

V. BIA FUTURE APPLICATIONS

BIA started as a research tool but is currently providing clinicians with data that they have no other rapid, reliable or non-invasive way of obtaining. Studies demonstrate that BIA could be successfully used to support clinical decision-making for patients with a broad range of disease states. The development of sophisticated electronic platforms have enabled rapid algorithm calculations and processing as well as the ability to take continuous measurements providing real-time data. BIA instruments are continually breaking into new areas of medicine and are challenging many current methodologies.

Further studies are focused strongly on the significance of BIA measurement values in diseased populations. New approaches such as segmental, multi-channel and multi-frequency analysis have greatly expanded the utility of this electrical technique and eliminated the limitations of BIA in different disease states, sex and ethnic diversity. The simplicity and non-invasive nature of a bioelectrical impedance measurement is a major operational advantage of the BIA technology. Moreover the utility and efficacy of BIA can be highly appreciated in large longitudinal studies, if our understanding of the significance of changes in various electrical properties of the body, can be improved. Many studies and clinical trials are going on across the world to find new applications for BIA.

The development of BI Spectroscopy and BI Vector Analysis have enhanced the utility of BIA in clinical practice by quantifying ECW/ICW, BCM etc., even though the equations may be inaccurate for body composition analysis. The determination of changes in BCM, extra cellular ECW and ICW requires further research using a valid model that guarantees that ECW changes do not corrupt the ICW. The use of segmental-BIA, multi-frequency BIA, or bioelectrical spectroscopy in altered hydration states also requires further research. BIA and these field assessment methods need to be evaluated for their relation to clinically important risk factors such as blood pressure, lipids, and glucose tolerance. Data on the validity of BIA measurements performed in settings such as clinicians' offices and health clubs would also provide valuable information on the effective applications of this technology in non-research settings.

BIA equations and reference values need to be further developed for ethnic groups. The BIA phase angle could be considered another global marker of health, and future studies are needed to prove its utility in intervention studies. Confirmation of the relevance of low phase angle in the prediction of survival in larger populations is necessary.

ACKNOWLEDGMENT

We are thankful to Nice Society Vice Chairman Kunwar Shekhar Vijendra for encouraging and providing support to the research team to work in this niche area. We are also grateful to Prof. Mini S Thomas, Head Deptt of EE, Jamia Milia Islamia, New Delhi for allowing Laboratory and Library facilities of the Institute during odd hours for experimentation and preparation of this document.

REFERENCES

1. Kushner R.F. Bioelectrical impedance analysis: a review of principles and applications. J Am Coll. Nutr 1992; 11; 199-209.
2. De Lorenzo A, Andreoli A, Matthie J, Withers P. Predicting body cell mass with bioimpedance by using theoretical methods: a technological review. J Appl Physiol 1997; 85: 1542 58.
3. Kyle UG et al: Bioelectrical impedance analysis part II: utilization in practice: Clinical Nutrition (2004) 23, 1430 1453
4. Kyle UG et al: Bioelectrical impedance analysis part I: review of principles and methods: Clinical Nutrition (2004) 23, 1226 1243
5. Bioelectrical Impedance Analysis in Body Composition Measurement National Institutes of Health Technology Assessment Conference Statement December 12—14, 1994
6. Barbosa Silva et al. Bioelectrical Impedance Analysis: population reference values for phase angle by age and sex. Am J Clin Nutr 2005; 82:49-52.
7. D. Gupta, C. A Lammersfeld, J. L Burrows, S. L Dahlk, P. G Vashi, J. F Grutsch, S. Hoffman, and C. G Lis Bioelectrical impedance phase angle in clinical practice: implications for prognosis in advanced colorectal cancer Am. J. Clinical Nutrition, December 1, 2004; 80(6): 1634 - 1638.
8. A. C. Buchholz, C. Bartok, and D. A. Schoeller The Validity of Bioelectrical Impedance Models in Clinical Populations Nutr Clin Pract, October 1, 2004; 19(5): 433 - 446.
9. C. P. Earthman, J. R. Matthie, P. M. Reid, I. T. Harper, E. Ravussin, and W. H. Howell A comparison of bioimpedance methods for detection of body cell mass change in HIV infection J Appl Physiol, March 1, 2000; 88(3): 944 - 956.
10. S Swaraj, G Marx, G Masterson and M Leuwer. Bioelectrical impedance analysis as apredictor for survival in patients with systemic inflammatory response syndrome. Critical Care 2003, 7(suppl):P185.
11. Khan M and Guha SK. Electrical Impedance Analysis for Simulated Arm Blood Pooling of an Aircraft Pilot under G-Stress (Abstract). Aviat Space Environ Med 2003;74(4):406.

Address of the corresponding author:

Author: P.N. Goswami, Dean Acdemics
Institute: Shobhit Institute of Engg. & Technology
(Deemed University)
Street: Modipuram, Roorkee Road
City: Meerut - 250110
Country: India
Email: pngoswami@rediffmail.com; pn.goswami@nicesociety.org

F. Ibrahim, N.A. Abu Osman, J. Usman and N.A. Kadri (Eds.): Biomed 06, IFMBE Proceedings 15, pp. 321-324, 2007
www.springerlink.com ' Springer-Verlag Berlin Heidelberg 2007

Estimation of heart rate variability from peripheral pulse wave using PPG sensor

K. Srinivas[1], L. Ram Gopal Reddy[1], R. Srinivas[2]

[1]Department of Physics, National Institute of Technology, Warangal-506004, India
[2]Consultant Cardiologist, Srinivasa Heart Center, Hanamkonda-506001, India

Abstract – **Heart rate variability (HRV) analysis is gaining acceptance as a potential non-invasive means of cardiac assessment in clinical as well as research domains. Although it is a standard practice to derive HRV from the R-R peaks of electrocardiogram (ECG), there have been attempts to deduce it from peripheral pulse wave signal. HRV is measured using photoplethysmographic (PPG) pulse wave signal in this work. A versatile algorithm governed by the physiology of the cardiovascular system developed by the authors is used to derive peak intervals from the PPG signal. In addition to normal time and frequency domain techniques, sequential trend analysis (STA) is applied to analyse HRV. Out of 20 subjects monitored, the results of three, one healthy and two with known cardiac problems, are presented and discussed. In all cases monitored, the results of HRV deduced from PPG are in tune with clinical picture of the subjects. The usefulness of STA in the analysis of HRV is also discussed.**

Keywords – **Heart rate variability, Photoplethysmography, Sequential trend analysis, Vagal, Sympathetic.**

I. Introduction

Heart rate variability analysis is fast emerging as a noninvasive research and clinical tool for assessing cardiac and autonomic nervous system function [1]. Hon and Lee [2], in 1965, first noted that fetal distress was preceded by alterations in inter beat intervals. HRV analysis is based on the fact that heart beat is not absolutely regular even in healthy subjects. Heart rate and its embedded rhythm are governed basically by sinoatrial node, which is influenced by autonomic nervous system. Vagal and sympathetic nervous systems constantly act to regulate the heart and circulatory system [3].

Usually HRV is analyzed in time and frequency domains using the variations in successive R-R intervals taken from electrocardiogram (ECG). However, various workers have explored the use of photoplethysmographic signal for the study of heart rate variability. Teng and Zhang [4] found that variability of peak intervals in PPG and R-R intervals in ECG was almost same. Further, it was reported that the LF component of HRV spectra in resting position was almost same whether it was estimated using peak intervals from PPG or R-R intervals from ECG [5-7]. These studies point to the possible use of PPG signal for HRV estimation.

Reduced HRV indicates the blunted autonomic nervous system and is associated with patients having chronic heart failure. Frequency domain techniques use the power spectral distribution of HRV, which gives insight into the health of vagal and sympathetic nervous system [8]. In this background, the present work is aimed at deriving HRV from PPG instead of ECG. Further sequential trend analysis is applied to HRV along with frequency and time domain techniques.

II. Methods

A. PPG Sensor and Data Acquisition

In photoplethysmography red light using a LED (KLSL 3228 SR, 660nm) is allowed to pass through the finger and the transmitted light is detected by a photodiode. The pulsations in arterial blood modulate the transmitted light owing to the absorption of the red light by hemoglobin. When the blood in the artery is at its peak the absorption of light passing through it is also high keeping the transmitted light minimum. Between the pulsations when the blood recedes in the artery, the absorption of the light is also minimum and a peak is produced in the transmitted light. The transmitted light is detected and amplified by OPT101, which combines photodiode with a transimpedance amplifier in a single IC. The output of OPT101 is inverted to make the peaks in the signal correspond to the peaking of arterial blood due to left ventricular contraction. It is pertinent to take note of the fact that the ventricular contraction starts immediately after the R peak of ECG. This signal is acquired with a DAQ card, PCI 6014 of National Instruments, having 16-bit resolution and 200 KHz bandwidth. The signal is band limited before it is acquired by a Butterworth filter of third order with a low frequency limit of 0.4 Hz and high frequency cutoff at 5 Hz, to minimize the effect of noise and motion artifacts. The acquired signal is processed using LabVIEW7.1. The heart beat intervals, which are traditionally obtained by taking R-R peaks from ECG, are obtained here by calculating the time interval between the peaks in PPG signal. PPG signals are recorded for 2-minutes on each subject, resting comfortably in sitting posture, using index finger. The data base consisted of 20 volunteers between the age of 23 to 59 years.

F. Ibrahim, N.A. Abu Osman, J. Usman and N.A. Kadri (Eds.): Biomed 06, IFMBE Proceedings 15, pp. 325-328, 2007
www.springerlink.com ' Springer-Verlag Berlin Heidelberg 2007

B. Signal Processing and Analysis

A versatile algorithm developed by the authors based on the physiology of the cardiovascular system is used to identify the peaks and determine the intervals between them. The algorithm uses moving averages combined with multi-looping until all the dicrotic notches, ectopic pulses and peaks due to noise are eliminated. The algorithm was thoroughly tested and validated. The successive pulse intervals obtained from PPG signal are used to get tachograms where beat intervals are plotted against beat number. FFT is used to extract the power spectral density of HRV in each case. The statistical parameters such as mean and standard deviation are also computed. In addition to the above, sequential trend analysis (STA) of HRV is also carried out. In STA, the differences among successive beat intervals are plotted with Δt_n on one axis and Δt_{n+1} on the other. Δt_n gives the difference in heart beat intervals of n-1 and nth beats and Δt_{n+1} gives the difference in heart beat intervals of nth and (n+1)th beats. This plot has an advantage that it clearly segregates the moments that increase the heart rate and those which slow down it. Thus it separates the vagal tone from sympathetic activity and displays them separately in -/- and +/+ quadrants respectively. Whereas the other two quadrants -/+ and +/- show the transitions from vagal to sympathetic and vice versa. The number of points in each quadrant are calculated in absolute and percentile terms.

III. Results

Tachograms, power spectral density and STA plots of HRV along with PPG signal are given in Fig. 1, 2 and 3. Fig.1 gives the HRV of a young & healthy subject of 27 years age, while the Fig.2 pertains to a 53 year old subject with known heart problems. The HRV of a 43 year old patient with diabetic neuropathy is given in Fig.3. Table1 lists together the mean, standard deviation along with the percentile of points falling in each quadrant from STA plots, for all the three subjects.

IV. Discussion

The power spectral density of HRV from Fig. 1, 2 and 3 clearly show the two standard peaks, one in the LF (0.04 to 0.15 Hz) and the other in HF (0.15 to 0.4 Hz) regions. The LF peak in Fig.3 is much lesser signifying the reduced HRV due to diabetic neuropathy in subject 3 as against the normal LF peak of young and healthy subject in Fig.1. The conspicuous absence of LF peak in Fig.2 is reflective of the heart condition of subject 2 who is a known cardiac patient. Regarding HF peaks, it is prominent only for subject 1 and much less for subjects 2 and 3. These results are in tune with the findings of Daunping Liao et al [9] who reported the association of lower HRV among the diabetic patients developing coronary heart disease. Further, Phillippe van de Borne et al [10] identified near absence of LF component among heart failure patients. The HRV results of remaining 17 subjects are also consistent with their clinical picture.

The plots of STA exhibited distinct patterns for each of the three subjects. While it is closely clustered for subject 3 indicating lower HRV, the points are well spread in subject 1. The pattern for subject 2 is interestingly quite different from the other two and is indicative of frequent switching between vagal and sympathetic activity. The specific advantage of STA is that even if some errors crop up in the beat to beat interval data owing to noise, artifacts or ectopic beats they simply get scattered in the plot and do not affect or alter the character of the overall trend/result. Whereas in case of frequency domain analysis the presence of even one or two such errors will drastically change the power spectrum of HRV rendering it unusable.

Although ECG provide much more insight into the problems of the heart, the PPG based HRV can be used as a preliminary screening tool for large populations with increased risk of heart problems such as due to smoking, alcohol consumption, diabetes and genetic heredity. This is because PPG method is simple to use and takes much less time. Further, it does not require any electrodes. Even semi skilled workers can handle it. However, more investigations are needed to understand the influence of pulse transit time on pulse intervals of PPG.

Table 1

	Subject 1 Normal Age: 27 yrs	**Subject 2 Heart Patient Age: 53 yrs**	**Subject 3 Diabetic Age: 43 yrs**
Mean Interval	0.5848	0.5035	0.6087
Standard Deviation	0.0145	0.0084	0.0095
Percentile Fraction of points in +/+ quadrant	0.25	0.125	0.212
Percentile Fraction of points in -/+ quadrant	0.275	0.393	0.256
Percentile Fraction of points in -/- quadrant	0.193	0.081	0.262
Percentile Fraction of points in +/- quadrant	0.275	0.393	0.275

F. Ibrahim, N.A. Abu Osman, J. Usman and N.A. Kadri (Eds.): Biomed 06, IFMBE Proceedings 15, pp. 325-328, 2007
www.springerlink.com ' Springer-Verlag Berlin Heidelberg 2007

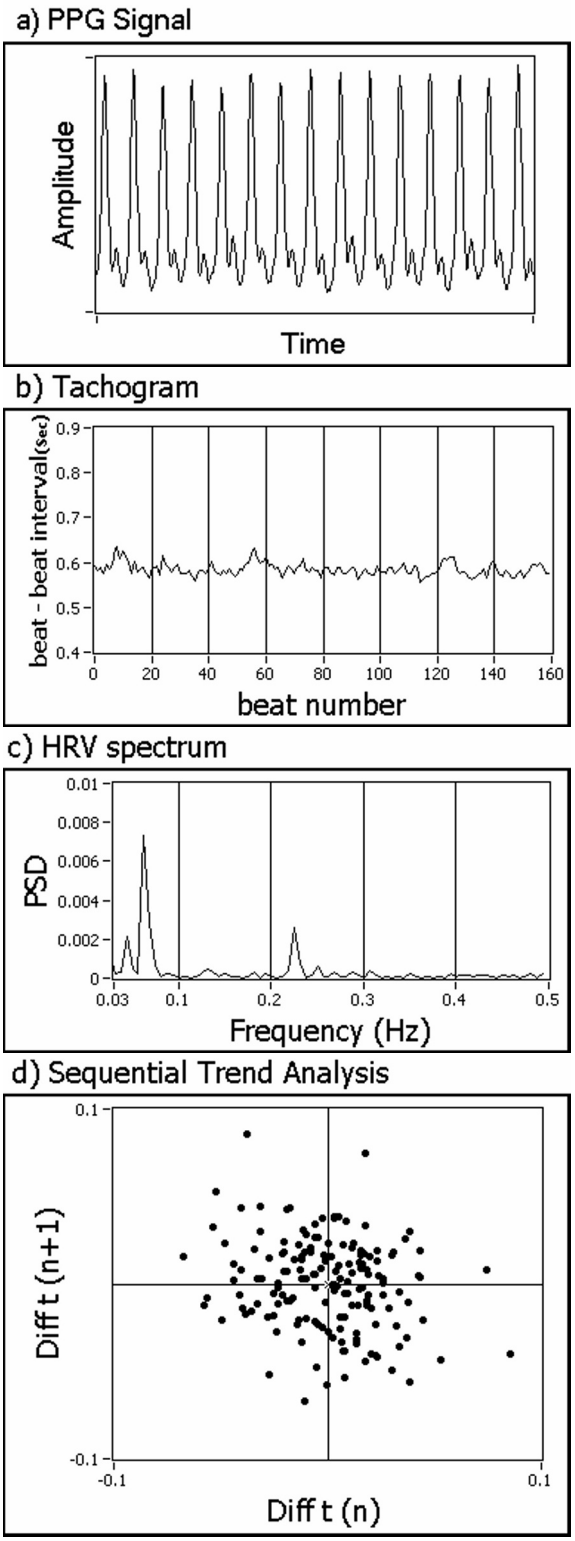

Fig.1 HRV results of normal subject
(Age: 27 years)

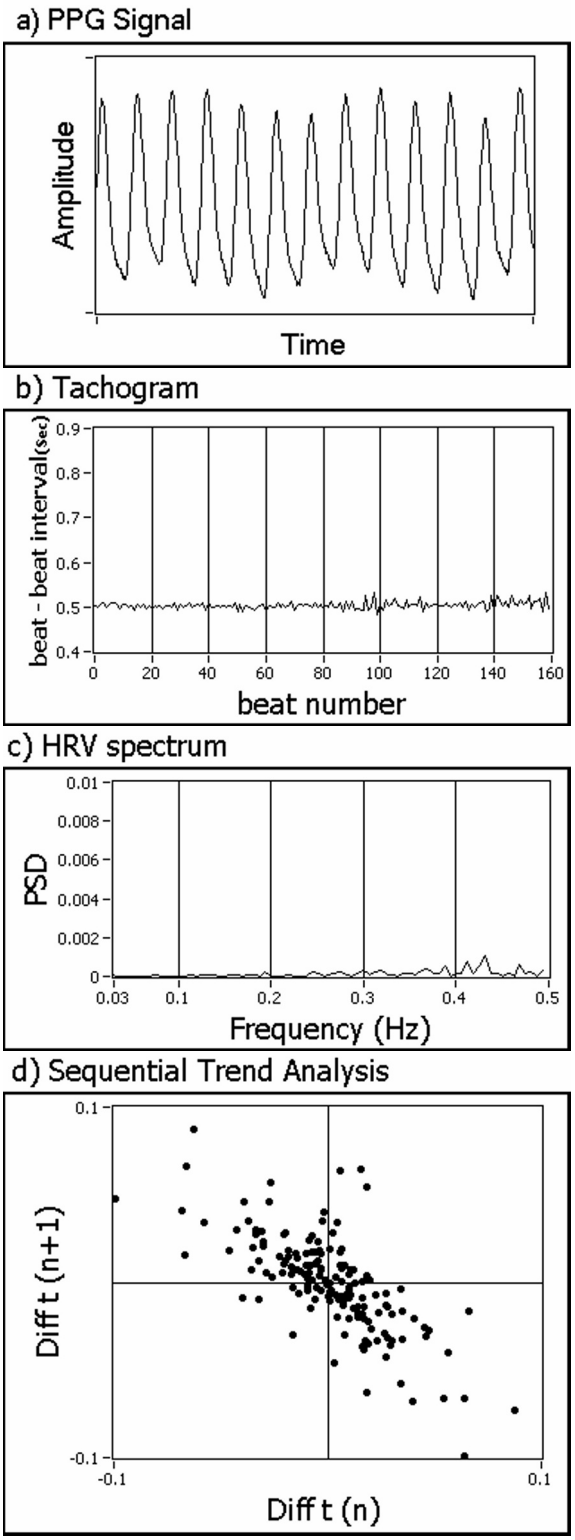

Fig. 2 HRV results of subject with heart problems
(Age: 53 years)

F. Ibrahim, N.A. Abu Osman, J. Usman and N.A. Kadri (Eds.): Biomed 06, IFMBE Proceedings 15, pp. 325-328, 2007
www.springerlink.com ' Springer-Verlag Berlin Heidelberg 2007

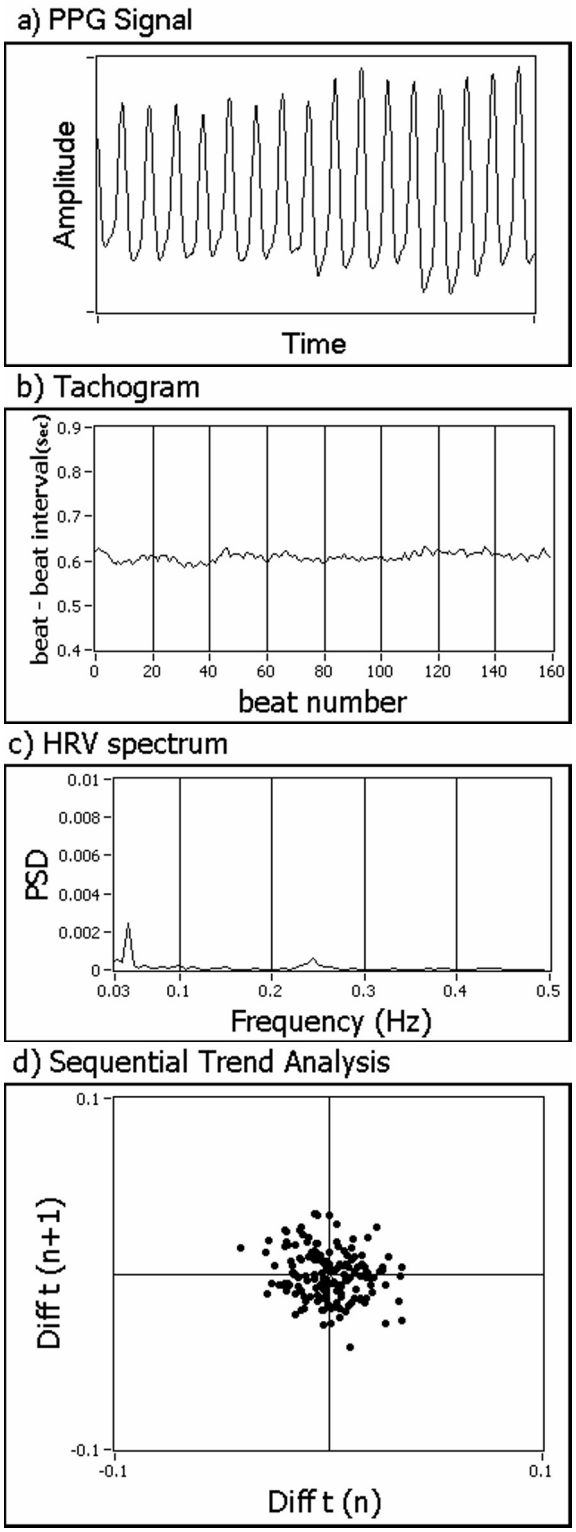

Fig. 3 HRV results of diabetic subject (Age: 43 years)

In non-medical applications such as emotion recognition by computers using HRV [11], use of PPG offers great convenience over ECG.

Acknowledgment

The authors are grateful to Prof. Y.V.Rao, director NIT, Warangal for his support and encouragement and the ministry of Human Resources Development, Government of India for extending the financial assistance.

References

1. Dreifus L.S, Agarwal J.B. et al. (1993) Heart rate variability for risk stratification of life-threatening arrhythmias. J Am Coll Cardiol. 22:948-950
2. Hon E.H, Lee S.T. (1965) Electronic evaluations of the fetal heart rate patterns preceding fetal death, further investigations. Am J Obstet Gynec. 87:814-826.
3. Arthur C. Guyton, John E. Hall. (2000) Text book of Medical Physiology. 10th ed. W.B. Saunders Company.
4. X.F Teng, Y.T. Zhang (2003) Study on the peak interval variability of photoplethysmographic signals. Proc. IEEE EMBS conf. 20-22 Oct, 2003, pp 140-141.
5. Isabelle Constant, Dominique Laude et al. (1999) Pulse rate variability is not a surrogate for heart rate variability. Clinical Science. 97:391-397.
6. M. Karrakchou, J.M vesin et al. (1992) Analysis of heart rate variability: Comparison between spectra obtained from ECG and finger blood pressure. Proc. IEEE EMBS conf. vol. 14, 1992, pp 569-560.
7. Paula S. Mckinley, Peter A. Shapiro et al. (2003) Deriving heart period variability from blood pressure waveforms. Journal of Applied Physiology. 95:1431-1438.
8. Task Force of the European Society of Cardiology and North American Society of Pacing and Electrophysiology.(1996) Heart rate variability Standards of measurements, physiological interpretation, and clinical use. Eur Heart J. 17:354-81.
9. Duanping Liao, Mercedes Carnethon et al. (2002) Lower heart rate variability is associated with the development of coronary heart disease inn individuals with diabetes. Diabetes. 51: 3524-31.
10. Phillipe van de Borne, Nicola Montano et al. (1997) Absence of low frequency variability of sympathetic nerve activity in severe heart failure. Circulation. 95:1449-54
11. Kim KH, Bang SW, Kim SR.(2004) Emotion recognition system using short-term monitoring of physiological signals. Med Biol Comput. 42:419-27.

Address of the corresponding author:

Dr. L. Ram Gopal Reddy
Asst. Professor & Chief Investigator
Department of Physics
National Institute of Technology
Warangal-506004
INDIA
Email: reddylrg@yahoo.com

F. Ibrahim, N.A. Abu Osman, J. Usman and N.A. Kadri (Eds.): Biomed 06, IFMBE Proceedings 15, pp. 325-328, 2007
www.springerlink.com ' Springer-Verlag Berlin Heidelberg 2007

Nano-porous Polysilicon Fabrication for Micro Electro Mechanical System (MEMS) Drug Delivery Device

S. Mohmad[1], C.F. Chau[2], T. Melvin[2], S. Atri[2] and C. Kaminski[2]

[1] Electrical and Electronics Department, Universiti Teknologi Petronas, Malaysia
[2] School of Electronics and Computer Science, University of Southampton, UK.

Abstract— **Porous polysilicon is a biocompatible, non-toxic and biodegradable material, thus making it a suitable material to be implanted into human body as a drug delivery device. In this study, the method of stain etching in solution consists of HF, HNO_3 and H_2O in a ratio of 1:3:5 by volume has been used to create the nano-porous structures. The etching time was less than 30 seconds on a LPCVD polysilicon with sheet resistance of ~28 Ω/sq. The topography of the surface was then investigated by Scanning Electron Microscope (SEM) and Atomic Force Microscope (AFM). The resulting porous structure also exhibits a photoluminescence (PL) peak at around 700nm. The fabricated porous polysilicon is suitable as the material for an implantable drug delivery device, which offers significant advantages such as the ability to avoid dose dumping and providing patients with the required drug dosage over an extended period of time.**

Keywords— **Porous polysilicon, drug delivery, MEMS**

I. Introduction

Attention to micro-electromechanical system (MEMS) continues to increase worldwide and has a phenomenal growth in the past few years. This is due to its wide application including medicine studies and bioengineering. As for medicine technology, much research had been carried out over the past few years in the field of controlled release of pharmaceutical agents. These are done in hopes of improving current drug deliveries methods, in order to deliver therapies that need greatest possible healing effects [1].

Silicon had always been the main material used in MEMS device fabrication. Only in recent years, studies in processing the material to obtain nano-structures (*i.e.: porous silicon*) had become popular. Porous silicon is a form of silicon that is tolerated by the body's immune system due to its biocompatibility, non-toxic and biodegradable behaviour [2]. Besides its compatibility with the human body, porous silicon also has several other properties that allowing it to be use in biomedical devices such as unique electrical properties [3], elasticity property [4] and efficient visible light emission capability [5]. Due to all these properties, porous silicon is the most suitable device to be used to implement an implantable device into the human body.

Polysilicon is the polycrystalline form of silicon, which exhibit a random grain boundary, but with similar material characteristic to silicon. Hence, it is sensible to utilize the random grain boundary of polysilicon to produce a random porous structure suitable as the material for drug delivery device. Method of stain etching by submersing the material in combination of three different chemicals (HF, HNO_3 and H_2O) is chosen for the fabrication of porous polysilicon and the resultant porous structure is characterized by Scanning Probe Microscopy (SEM), Atomic Force Microscopy (AFM) and photoluminescence (PL) measurement.

Currently, four methods to fabricate porous silicon and polysilicon can be identified. These include electrochemical etching; stain etching, reactive ion etching and one step low-pressure chemical vapor deposition (LPCVD) process. Of all these processes, stain etching is the most cost effective and most straight forward method to form a porous structure. However, compared to the other methods, stain etching lacks high reproducibility and the porous structures formed are usually non-uniform across the sample.

Electrochemical etching, also known as anodic etching, is usually carried out in an etching cell controlled by applied bias. Porous silicon results from the electrochemical dissolution of a silicon substrate in the presence of a Hydrofluoric acid (HF) electrolyte and positive charge carriers (holes) [6]. In the traditional electrochemical etching, porous polysilicon is directly formed on top of the conductive material [7]. The porosity of the porous structure formed at the pore tips is proportional to the current density through the cell at that time [8]. However, the morphology of the porous silicon matrix that remains after electrochemical etching is not only dependent on current density, but also affected by the substrate doping, HF electrolyte concentration, the duration of the etch, temperature, and ambient lighting conditions [9].

On the other hand, stain etching uses an open circuit chemical etching with hydrofluoric acid (HF), nitric acid (HNO_3) and de-ionized water (H_2O) as the electrolyte. Since no bias is applied, no electrodes are needed in the process. Instead, the silicon surface and its clusters will behave as the built in electrodes in the process. Sometimes sample is

F. Ibrahim, N.A. Abu Osman, J. Usman and N.A. Kadri (Eds.): Biomed 06, IFMBE Proceedings 15, pp. 329-333, 2007
www.springerlink.com ' Springer-Verlag Berlin Heidelberg 2007

first immersed in a mixture containing higher proportion of HNO_3 for a few seconds before the stain etching process is carried out to reduce the incubation time and improve the etching uniformity [10].

An alternative method to produce porous polysilicon films is by reactive ion etching (RIE) [11]. The cost of this method is higher than the previous methods but a native and more stable surface of micro pores can be obtained. This method does not require any additional photolithography mask or additional electrode and does not use any chemical solution, and thus making it a unique approach in porous structure fabrication.

Recently, a simple, one-step LPCVD process for porous structure fabrication without chemical solution has been reported [12]. This method allows the repeatable fabrication of polysilicon thin films containing through-pores measuring 10nm to 50nm in diameter, as deposited, with no additional processing steps required. This process is very simple and requires a very short time to complete (approximately 10 minutes) but the cost is very high.

II. Materials and Methods

The drug delivery devices have been fabricated on standard 4 <100> p-type silicon wafers. In order to isolate the active area from the substrate, a 600 nm of SiO_2 layer was grown by wet oxidation process at 1100°C.

Next, an undoped amorphous Si film of around 1 μm thick was deposited on the SiO_2 by LPCVD at 610°C. The as-deposited amorphous Si film was then doped by ion implantation of $1x10^{16}$ cm^{-2} dose of Boron at 80keV. The film was annealed in N_2 at 1150°C for 200minutes to activate the dopant and crystalline the amorphous Si. The annealed polysilicon film had a sheet resistance of ~28Ω/sq.

In order to create a reservoir where the drugs or the pharmaceutical agents will be charged, the wafers were patterned with standard photolithography technique. First, a SiO_2 layer of 300nm was deposited by LPCVD at 400°C on top of the annealed polysilicon film. A silicon nitride (Si_3N_4) of 160nm was then deposited by plasma enhanced chemical vapor deposition (PECVD) at 740°C. The SiO_2 Si_3N_4 layer served as the masking material from the subsequent stain-etching process. Shipley SPRT 510 positive photoresist was then spun to achieve a thickness of 1.1μm. The photoresist was the exposed and developed to create a circular opening of 6mm in diameter on each of the 12mm x 12mm chip. A RIE was then carried out to remove the exposed Si_3N_4 layer, and subsequently the SiO_2 layer. This revealed the polysilicon in the 6mm circular region, which then defines the reservoir where the drugs will be charged.

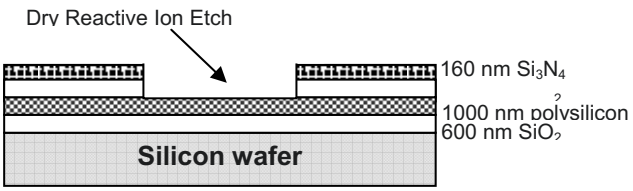

Fig 1: Layers condition after DRIE

The photoresist was then stripped from the wafers in an ash-barrel using plasma O_2 etch. Next, to form the nano-porous structures on the exposed polysilicon layer, the wafers were stain-etched in a solution containing a mixture of HF, HNO_3 and H_2O. All reagent used were standard electronic-grade 49% HF, 70% HNO_3 and de-ionized (DI) water.

Several ratios of HF, HNO_3 and H_2O etching solution and different etching time had been investigated on the samples in order to identify the best condition for the production of nano-porous structures on the polysilicon layer. Table 1 summarises the ratio of the chemicals used and the etching time for each combination.

Table 1 : Summary of the ratio of the chemicals used and the etching time for each combination.

Ratio (HF: HNO_3: H_2O)	Etching Time
1:4:4	17 minutes
1:4:2	1 minute
1:25:13	1 minute
1:3:5	1 minute
1:3:5	10, 15, 20, 25 & 30 sec

The SEM images of the porous structures formed on the polysilicon layer were acquired with LEO 1455VP electron microscope, while the topological AFM images were obtained using TopoMetrix Accurex II in contact mode. The room-temperature PL spectra were acquired with Cary Eclipse Fluorescence Spectrophotometer, with an operational wavelength range of 200-900nm, a 80Hz Xenon pulse lamp and dual R928 photomultiplier tube (PMT) detectors.

III. Results

From the experiment conducted, it was observed that etching time of 1 minute or more, regardless of the ratio of etching solution, would etch the entire polysilicon layer away, hence exposing the SiO_2 layer underneath it. Thus, shorter etching times ranging from 10s to 30s were conducted for the

F. Ibrahim, N.A. Abu Osman, J. Usman and N.A. Kadri (Eds.): Biomed 06, IFMBE Proceedings 15, pp. 329-333, 2007
www.springerlink.com ' Springer-Verlag Berlin Heidelberg 2007

experiment. Ratio of 1:3:5 (HF: HNO_3: H_2O) gives the best etching rate and consistent to that found in literature [10, 13].

SEM image depicted in Fig 2(a) shows a sample of the device etched for 10 seconds. From the image, it can be observed that a rough and slightly porous structure was formed on the polysilicon layer. In order to investigate the surface topology of the pores, an AFM was conducted. The obtained AFM image, as depicted in Fig 2(b), indicates that the average depth of the porous structures is approximately 120 nm, and this suggests a good porosity of the layer. From the AFM image too it is observable that the porous structures are not uniform, where some areas were not entirely etched, hence leaving a flat area instead of a porous structure. This might affect the efficiency of the drug delivery device, as not the whole area of the reservoir can be charged with drugs or pharmaceutical agents.

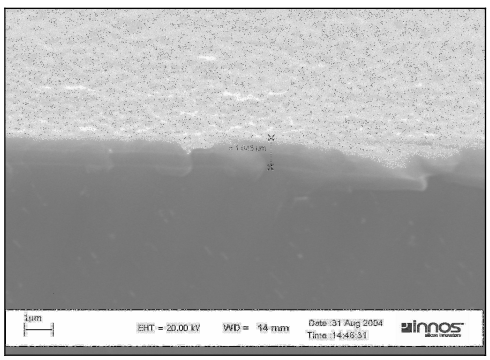

Fig 2(a): SEM image of sample etched in HF:HNO_3:H_2O (1:3:5) for 10 seconds

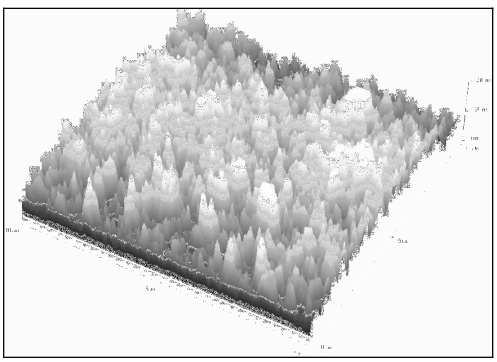

Fig 2(b): AFM image of sample etched in HF:HNO_3:H_2O (1:3:5) for 10 seconds

Sample stain-etched for 20s, as depicted in SEM image of Fig 3(a), reveals a rougher surface with more dense, uniform and greater porosity morphology than previous sample. The AFM topological image indicates that the average depth of the porous structures is approximately 75nm.

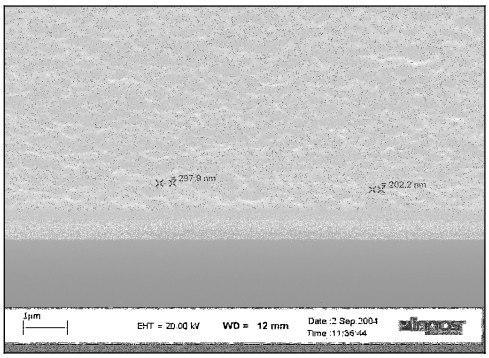

Fig 3(a): SEM image of sample etched in HF:HNO_3:H_2O (1:3:5) for 20 seconds

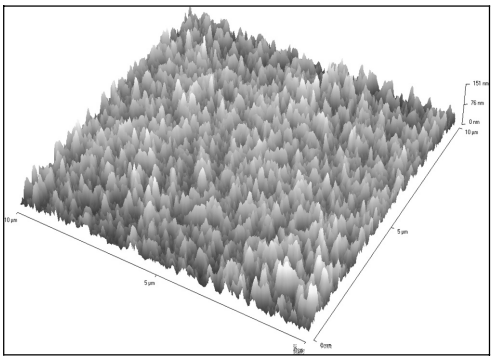

Fig 3(b): AFM image of sample etched in HF:HNO_3:H_2O (1:3:5) for 20 seconds

For sample stain-etched for 30s, it can be observed from Fig 4(a) that the polysilicon layer had started to peel off from the wafer and revealing the SiO_2 layer underneath it. As clearly shown in the AFM image in Fig 4(b), most of the polysilicon layer had already been etched leaving only small area intact. Definitely this is not suitable to be implemented as the drug delivery device since not much pharmaceutical agents can be charged on it.

F. Ibrahim, N.A. Abu Osman, J. Usman and N.A. Kadri (Eds.): Biomed 06, IFMBE Proceedings 15, pp. 329-333, 2007
www.springerlink.com ' Springer-Verlag Berlin Heidelberg 2007

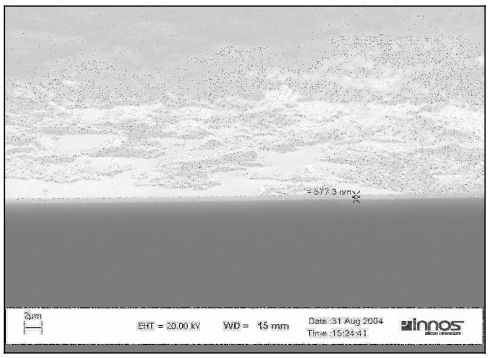

Fig 4(a): SEM image of sample etched in HF:$HN0_3$:H_20 (1:3:5) for 30 seconds

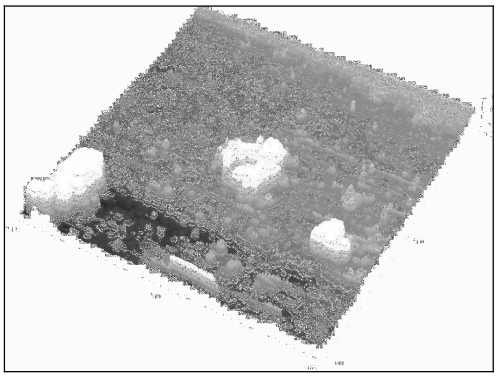

Fig. 4(b): AFM image of sample etched in HF:HNO_3:H_2O (1:3:5) for 30 seconds

IV. Discussions

From the previous observations, the most suitable ratio of HF:HNO_3:H_2O to fabricate a porous polysilicon structure using stain etching is 1:3:5 with etching time of 20 seconds. This condition gives a good porosity level and uniformity on the 1 μm thick polysilicon layer. It is believed that this kind of porous structure can serve as the reservoir for the device where drugs and pharmaceutical agents can be well charged.

To further verify the porosity of the stain-etched structures, PL spectra were acquired at room temperature. It is well established that porous silicon [5, 8, 13] and porous polysilicon [10, 11, 14] exhibit photoluminescence properties, which peak in the range of 600 700nm. From the PL graph in Fig. 5, it can be observed that the sample emits the most light at wavelength of approximately 706 nm when excited at wavelength of 478nm. This does resemble the red-light properties of porous silicon and is consistent to that reported in the literature. Thus the sample can be said to have the same properties of other porous silicon structures in term of its visible light emission capability.

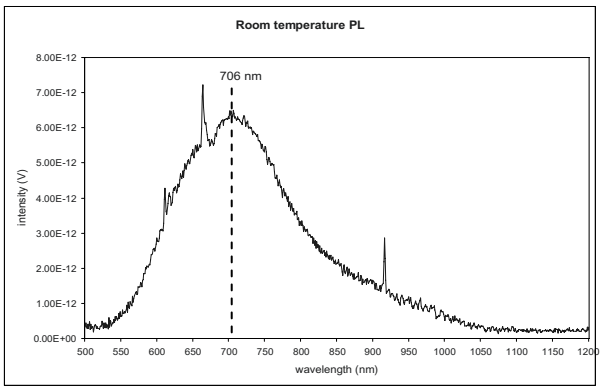

Fig. 5: Room temperature PL spectrum on sample etched in 1:3:5 for 20 seconds

V. Conclusion

A porous polysilicon structure is fabricated as part of the fabrication process for the drug delivery device. Porous structure serves as the reservoir, which is electrically addressable and capable of delivering pharmaceutical agents without the disadvantage of dose dumping.

The method of stain etching has been chosen for creating the porous structure. An etching solution containing HF: HNO_3: H_2O was proposed. A characterization of the etching effects on the polysilicon layer was carried out and ratios of 1:4:4, 1:4:2, 1:25:13, and 1:3:5 were investigated. Porous structures in polysilicon created using ratios of 1:3:5 was deemed most suitable for the application of drug delivery. A few etching time were also performed on the sample with this ratio and it was found that etching time of 20s is the most appropriate to obtain the desired porous structure.

Cross-sectional SEM and topological AFM images of sample stain-etched for 20s indicate a rough surface with average pore depth of 75nm. The PL measurement of the same sample shows a peak at around 700nm, consistent to that discovered by other groups.

Acknowledgement

The author would like to thank people at ECS, University of Southampton for their help and support in completing this part of the project. Not forgetting all the support and guidance received from colleague and staff of EE Department, Universiti Teknologi PETRONAS.

F. Ibrahim, N.A. Abu Osman, J. Usman and N.A. Kadri (Eds.): Biomed 06, IFMBE Proceedings 15, pp. 329-333, 2007
www.springerlink.com ' Springer-Verlag Berlin Heidelberg 2007

References

1. Santini, J. T., Cima, M. J. and Langer, R. (1999) A controlled-release microchip. Nature 397:335 338
2. Canham, L. and Aston, R. (2001) Will a chip everyday keep the doctor away? Physics World @ physicsweb.org, July 2001
3. Balagurov, L. A., Bayliss, S. C., Orlov, A. F., Petrova, E. A., Unal, B. and Yarkin, D. G. (2001) Electrical properties of metal/porous silicon/p-Si structures with thin porous silicon layer. J. Appl. Phys. 90:4148 4190
4. Matthai, C. C., Gavartin, J. L. and Cafolla, A. A. (1995) Structural and elastic properties of porous silicon. Thin Solid Films 225:174 176
5. Cullis, A. G., Canham, L. T. and Calcott, P. D. J. (1997) The structural and luminescence properties of porous silicon. J. Appl. Phys. 82(3):910 956
6. Turner, D. R. (1958) Electropolishing silicon in Hydrofluoric acid solutions. J. Electrochem. Soc. 105:402 408
7. He, R., Fan, L., Wu, M. C. and Kim, C. J. (2004) Porous polysilicon shell formed by electrochemical etching for on-chip vacuum encapsulation. Solid-state sensor, Actuator and Microsystem Workshop: 322 335
8. Chan, S. and Fauchet, P. M. (1999) Tunable, narrow and directional luminescence from porous silicon light emitting devices. Appl. Phys. Lett. 75(2):274 276
9. Fauchet, P. M. Porous polycrystalline silicon thin film solar cells Final Report, University of Rochester, New York
10. Huang, W. H., Tong, K. Y. and Chan, P. W. (1997): Photoluminescence in porous sputtered polysilicon films formed by chemical etching. Semicond. Sci. Tech.12:228 233
11. Han, G., Wong, H. Chan, A. H. P. and Poon, M. C. (2002) A novel approach for fabricating light emitting porous polysilicon films. Microelectronics Reliability 42:929 933
12. Dougherty, G. M., Sands, T. D. and Pisano, A. P. (2003): Microfabrication using one-step LPCVD porous polysilicon films. J. Microelectrochem. Syst. 12(4):418 424
13. Steckl, A. J., Xu, J. and Mogul, H. C. (1993) Photoluminescence from stain-etched polycrystalline Si thin films. Appl. Phys. Lett. 62 (17):2111 2113
14. Xu, Z. Y., Gal, M. and Gross, M. (1992) Photoluminescence studies on porous silicon. Appl. Phys. Lett. 60:1375 1377

Address of the corresponding author:

Author: Salina bt Mohmad
Institute: Universiti Teknologi PETRONAS (UTP)
City: Bandar Sri Iskandar, Perak
Country: MALAYSIA
Email: salinamohmad@petronas.com.my

F. Ibrahim, N.A. Abu Osman, J. Usman and N.A. Kadri (Eds.): Biomed 06, IFMBE Proceedings 15, pp. 329-333, 2007
www.springerlink.com ' Springer-Verlag Berlin Heidelberg 2007

Widefield Surface Plasmon Resonance Microscope: A Novel Biosensor Study of Cell Attachment to Micropatterned Substrates

M. Mahadi Abdul Jamil[1, 2, 4], M. Youseffi,[2], S.T. Britland[3], S. Liu[5], C.W. See[5], M.G. Somekh,[5] and M.C.T. Denyer,[4, 5]

[1] Tun Hussein Onn College University of Technology: Faculty of Electrical & Electronic Engineering, Department of Electronic Engineering, Batu Pahat 86400, Johor, Malaysia
[2] University of Bradford: School of Engineering, Design & Technology, Bradford BD7 1DP, UK
[3] University of Bradford: School of Pharmacy, Bradford BD7 1DP, UK
[4] University of Bradford: Institute of Pharmaceutical Innovation, Bradford BD7 1DP, UK
[5] University of Nottingham: School of Electrical and Electronic Engineering, Nottingham NG7 2RD, UK

Abstract— **In this study, Human adult, low Ca2+, high Temperature (HaCaTs) Keratinocytes were cultured on micro-contact printed fibronectin repeat gratings of 1.8, 3.8, 5, 12.5 and 25µm for 24 hours. The cells were then fixed with 0.1% Glutaraldehyde and dehydrated in serial alcohol [1]. The alignment of the cells were then measured, where 0º represents 100% alignment to the pattern, in order to identify those features that promoted the highest degree of cell alignment. From the quantitative analysis it became clear that HaCaTs cells align most readily to the 12.5µm pattern. A 12.5µm stamp was therefore used to stamp pattern fibronectin on to prefabricated Au/Cr/glass surface plasmon substrates. HaCaTs cells were cultured on the substrates for 24 hours and imaged with the "Widefield Surface Plasmon Resonance" (WSPR) microscope [1]. The WSPR system enables the examination of nanometric interfacial interactions of HaCaTs on patterned and un-patterned surface at lateral resolution down to 500nm. Our preliminary results demonstrate that the WSPR microscope is capable of imaging the cell surface interface and as such will prove to be a very useful tool in understanding the processes involved in cell guidance and wound repair.**

Keywords— **surface plasmons, HaCaTs, micro-contact printing, cell guidance, cell alignment, high resolution imaging**

I. Introduction

Surface Plasmons (SPs) resonance is a collective oscillation of free electrons which occurs between a dielectric and conductor interface when *p*-polarized light at a specific angle strikes the conductor interface [2]. Deposition of biomolecular species at the metallised surface changes the SPs excitation angle and this change is directly proportional to the refractive index and thickness of that particular molecular species [1]. Present standard SPs system are mostly based around the Kretschmann configuration [3] which are extremely powerful, but they lack the spatial resolution for imaging highly localized region at micron to submicron scales [2]. We have now developed a new WSPR microscope capable of high lateral resolution imaging close to 500nm [4, 5] . In this system we use a high numerical aperture 1.45, oil immersed objective lens, allowing p-polarized light to be applied at a gold fabricated glass slide at an angle capable of exciting SPs [4, 5] . Our preliminary results demonstrated that this new WSPR system is exploitable as immunosensor for monitoring series of protein binding study [1], and in any areas where sensitivity to minute changes in the properties of an interface is required. In this study we will demonstrate that the WSPR system can be used for high resolution imaging of nanometric interfacial interactions associated with HaCaT cell guidance on micro-contact printed cell culture substrates. There are various methods of controlling wound repair [6] and cell behaviour using a mixture of topographic guidance and topographic/adhesive guidance cues such as those generated by Micro-Contact Printing (MCP) techniques [7]. In this study we will examine HaCaT cell guidance induced by micro-contact printed patterns of fibronectin [8]. Extracellular Matrix (ECM) protein such as Fibronectin [9] and Laminin [10] have been used extensively to mediate cell responses. Briefly, the formation of this ECM protein repeat gratings promotes cell alignment and directed migration. However, different cell types respond to guidance cues of different dimensions in different ways. Thus, we aim to determine the optimal MCP dimensions required to induce HaCaT cell guidance and then examine interfacial changes induced by the MCP patterns using the new WSPR microscope.

II. Materials and Methods

Cell Culture: HaCaTs cell lines were cultured in small standard Plug seal cap 25 cm^2 culture flask with ratio 1:5 ml cell suspension in Rosewell Park Memorial Institute media (RPMI, SIGMA). Cells were incubated at 37℃ and were split upon reaching confluence, usually every 4-5 days.

Stamp Fabrication: Glass templates consisting of 1.8, 3.8, 5, 12.5 and 25 µm wide repeat gratings were micro-

F. Ibrahim, N.A. Abu Osman, J. Usman and N.A. Kadri (Eds.): Biomed 06, IFMBE Proceedings 15, pp. 334-337, 2007
www.springerlink.com ' Springer-Verlag Berlin Heidelberg 2007

fabricated in the clean rooms at the Department of Electronics and Electrical Engineering, University of Glasgow. Sylgard elastomer gel (Polydimethylsiloxane from BDH Laboratory Suplies) stamps were then produced at University of Bradford from these templates by firstly coating the templates with 2% Dimethylchlorosilane mixed with 98% Trichloroethylene. Next, 30ml of (Sylgard) elastomer gel and a curing agent was poured onto the templates and allowed to cure overnight. After curing, the Sylgard gel was removed from the template enabling sylgard stamps exhibiting a negative relief of the template to be produced. These stamps were then used to functionalise plain glass slides and gold coated test substrates with Fibronectin.

MCP Technique: The overall stamping processes were carried out in sterile condition. Plain glass cover slips, were micro-contact printed with Fibronectin (220-240 KDa) via the following method: stamps were inked by dipping in Bovine fibronectin [SIGMA] dissolved in water at a concentration of 0.1mg/ml. The stamp was then removed from the fibronectin solution, air-dried for 30 seconds and stamped on to the glass cover slips for 50 seconds. The same procedure applies for each stamping process, i.e. 1.8, 3.8, 5, 12.5 and 25μm stamp including the SPs substrate.

Plating of cells: The glass slides micro-contact printed with 5 different gratings were then plated with HaCaTs cell (0.1ml of a 60,000 cells/ml cell suspension in 2ml media) for 24 hours. After 24 hours, cells were then fixed with 0.1% Glutaraldehyde diluted in Hank s Balanced Salt Solution (HBSS, SIGMA) for 5 minutes and imaged with standard phase contrast microscope. This same procedure for plating cells applies for the SPs substrate. Cells alignment to the pattern was measured by measuring the angle of the long axes of the cells in relation to the stamp pattern, such that an angle of 0" represents 100% alignment to the pattern. The pattern giving the best cell alignment was then selected and used to stamp pattern SPs substrate.

SPs substrate preparation: A prefabricated glass slide (0.18 mm thick), coated with 48 nm Gold/1 nm Chromium were stamp patterned with Fibronectin protein by using a 12.5 μm stamp. The substrate was then plated with HaCaTs cells as described earlier. After fixing the cell, the substrate were dehydrated in serial alcohol and were imaged with a Ziess Axioplan 2 microscope using a long working distance 40x objective under Differential Interference Contrast (DIC) imaging conditions. The substrates were then mounted in the sample holder of the WSPR microscope and imaged further.

III. Results and discussion

Stamp Fabrication: In this experiment we fabricated PDMS stamps successfully (Figs 1a-e) for MCP process in order to mediate HaCaTs cell migrations.

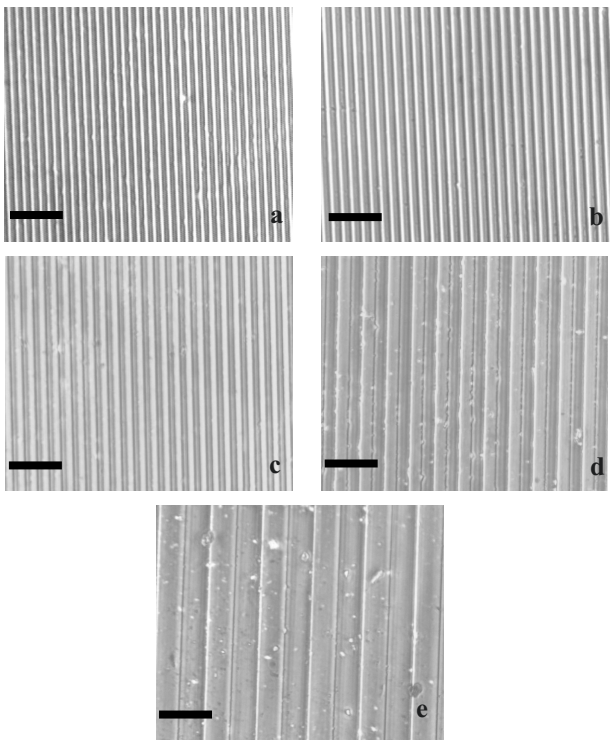

Fig. 1: Various gratings size of stamp fabricated for MCP work: (a) 1.8 μm, (b) 3.8 μm; (c) 5 μm; (d) 12.5 μm; and (e) 25 μm; Image taken with standard phase contrast microscope under bright field imaging condition, objective x10 (*scale bar 50μm*).

MCP Technique: MCP of fibronectin on to the culture substrates resulted in the substrates being successfully patterned with 1.8, 3.8, 5, 12.5 and 25 μm wide repeat gratings (Figs 2a-e). By scoring the alignment of HaCaT cells to different micro-contact printed patterns it became clear that the cells responded very differently to different gratings. The 1.8 μm wide pattern induced a poor alignment of (23.4^o – 1.65), as did the 3.8, 5 and 25μm wide patterns (23.9^o – 1.80, 17^o – 1.55, 17^o – 1.77 respectively), but in comparison the 12.5μm wide grating induced a good alignment of 7.9^o – 1.38 (Figs 2f-j). In all cases negative control cells showed an angle of alignment of 55^o indicating random cell orientation.

F. Ibrahim, N.A. Abu Osman, J. Usman and N.A. Kadri (Eds.): Biomed 06, IFMBE Proceedings 15, pp. 334-337, 2007
www.springerlink.com ' Springer-Verlag Berlin Heidelberg 2007

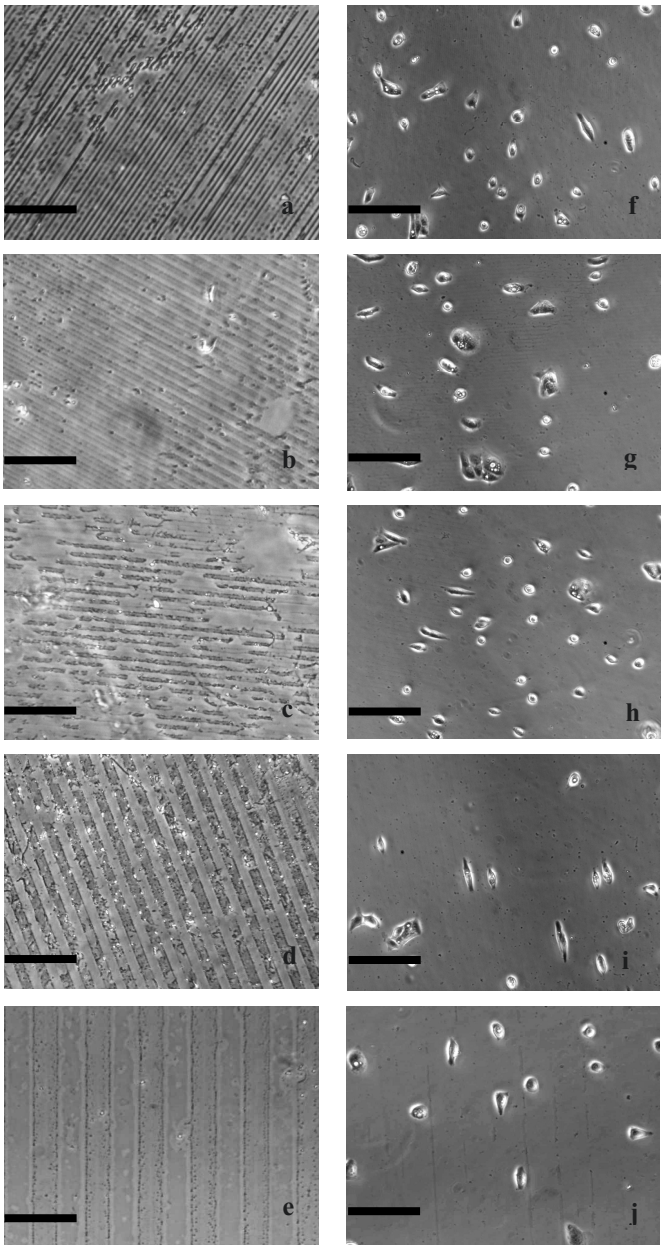

Fig. 2: (a - e) Image of Fibronectin micro-patterned glass cover slips; (f - i) The same micro-patterned surface 24 hours after plated with HaCaTs; (a) 1.8 µm; (b) 3.8 µm; (c) 5 µm; (d) 12.5 µm; and (e) 25 µm; Image taken with standard phase contrast microscope, objective x10 (*scale bar 70µm*).

SPs substrate preparation: SPs substrate patterned with Fibronectin using a 12.5µm stamp were initially imaged with a DIC microscope to verify the findings achieved via the newly developed WSPR system (Fig 3).

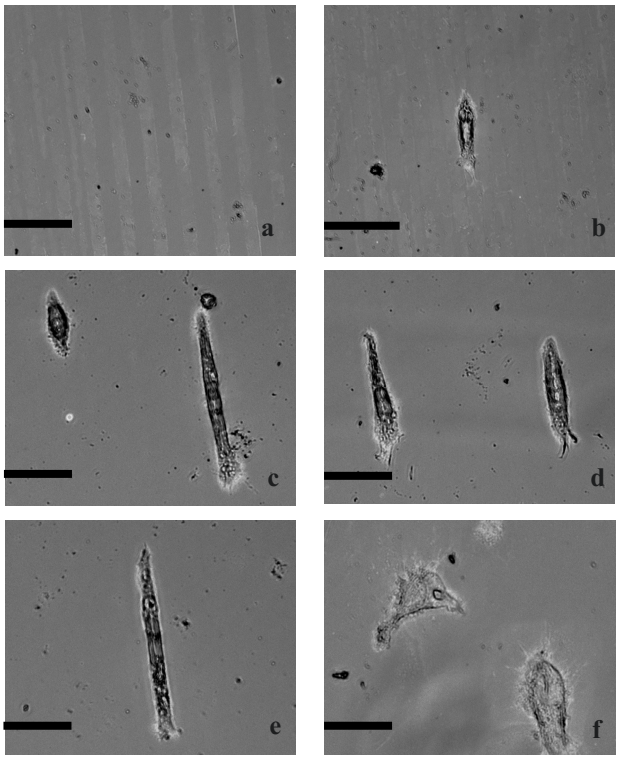

Fig. 3: (a) Image of Fibronectin gratings on SPs substrate achieved via MCP technique; (b - e) Image of fixed HaCaTs cells cultured on the 12.5 µm fibronectin patterned SPs substrate following the pattern direction; (f) control HaCaTs growing outside the patterned surface, Image taken with DIC microscope, objective x40 (*scale bar 100µm*).

Imaging with the WSPR system revealed that HaCaTs cells attach to the un-patterned surface via concentrically arranged high contrast band like concentrations of focal contacts, with the highest contrast band like components being localized at the cell periphery. The un-patterned cells had lengths ranging between 30 to 40 µm (Figs 4e, 4f). However, guided HaCaTs cells had a very different peripheral structure. The WSPR system showed that the patterned cells acquiring the high contrast band like structure at boarder of the elongated features along with less concentrically formed band like structure across the cell body. This enabled the cells to extend between 40 to 70 µm (Figs 4a-d). This significant differences in cell morphology, clearly indicates that the cell/pattern interaction induces significant changes in cell signaling, resulting in upregulation of proteins associated with the changes in morphology associated with the cells acquiring a more migratory phenotype. The capability of the WSPR system imaging these changes may help us towards understanding the unresolved question about the role of integrin/ECM interactions and gene product upregulation in induced cell migration during wound repair.

F. Ibrahim, N.A. Abu Osman, J. Usman and N.A. Kadri (Eds.): Biomed 06, IFMBE Proceedings 15, pp. 334-337, 2007
www.springerlink.com ' Springer-Verlag Berlin Heidelberg 2007

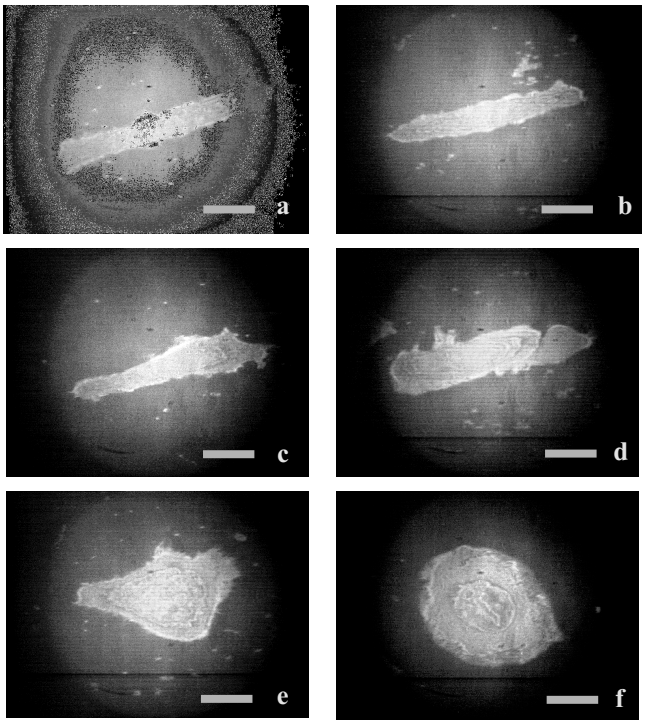

Fig. 4: (a - d) WSPR Image of HacaTs cell 100% aligned to the 12.5 µm Fibronectin pattern; (e and f) WSPR image of control HaCaTs outside the patterned area (*scale bar 25µm*).

IV. Conclusions

The patterned substrates promoted a significant elongation of HaCaT cells and associated with this a change in the formation of the band like accumulation of focal contacts as seen from the WSPR images. Although in this study we imaged fixed dehydrated cells using this new system, we are in the process of modifying the WSPR to enable real-time imaging in fluid. This combined with the ability to image focal contacts without Immunostaining presents a tremendous opportunity, that of imaging cell surface coupling in real time. This will allow us to, for the first time, to examine the cell signaling pathways associated with cell migration and cell guidance in real time. The implications of this in tissue and cell engineering cannot be understated.

Acknowledgment

The authors wish to acknowledge the financial support of the Engineering and Physical Sciences Research Council (EPSRC) for a research grant in the Metrology in life sciences programme . We would also like to thank the Public Service Department of Malaysia for funding Mr. M. Mahadi Abdul Jamil for his MPhil/PhD at University of Bradford.

References

[1] A. J. M. Mahadi, M. Youseffi, S. Marlafeka, S. T. Britland, S. Liu, C. W. See, M. G. Somekh, and M. C. T. Denyer, "Advanced biological applications of the novel widefield surface plasmon microscope," at Winter Meeting: The Anatomy of Tissue Engineering, St Anne's College, Oxford, 2005 (**In Press**).

[2] M. G. Somekh, *Surface plasmon and surface wave microscopy, Optical Imaging and Microscopy*, vol. 87. Berlin Heidelberg, 2003.

[3] E. Kretschmann and H. Raether, "Radiative decay of non-radiative surface plasmons excited by light," *Zeitschrift Fur Naturforschung*, vol. 23A, pp. 2135-2136, 1968.

[4] G. Stabler, M. G. Somekh, and C. W. See, "High-resolution wide-field surface plasmon microscopy," *Journal of Microscopy*, vol. 214, pp. 328-333, 2004.

[5] S. Marlefeka, S. T. Britland, S. Liu, P. C. Twigg, C. W. See, M. G. Somekh, and M. C. T. Denyer, "Imaging biomolecular nanofilms at micrometer lateral resolutions using widefield surface plasmon microscopy," Conf. Proceedings: 3B2-03, Singapore, 2005.

[6] A. Curtis and M. Riehle, "Tissue engineering: the biophysical background," *Physics in Medicine and Biology*, vol. 46, pp. R47-R65, 2001.

[7] A. Folch and M. Toner, "Microengineering of Cellular Interactions," *Annual Review Biomedical Engineering*, vol. 2, pp. 227-256, 2000.

[8] M. Matsuzawa, P. Liesi, and W. Knoll, "Chemically modifying glass surfaces to study substratum-guided neurite outgrowth in culture," *Journal of Neuroscience Methods*, vol. 69, pp. 189-196, 1996.

[9] S. Yamamoto, M. Tanaka, H. Sunami, K. Arai, A. Takayama, S. Yamashita, Y. Morita, and M. Shimomura, "Relationship between adsorbed fibronectin and cell adhesion on a honeycomb-patterned film," *Surface Science*, vol. In Press, Corrected Proof.

[10] L. Lauer, C. Klein, and A. Offenhausser, "Spot compliant neuronal networks by structure optimized micro-contact printing," *Biomaterials*, vol. 22, pp. 1925-1932, 2001.

Address of the corresponding author:

Author: M. Mahadi Abdul Jamil
Institute: SoEDT 4, University of Bradford
Street: Richmond Rd
City: Bradford, West Yorkshire
Country: United Kingdom
Email: M.M.Abduljamil@bradford.ac.uk

F. Ibrahim, N.A. Abu Osman, J. Usman and N.A. Kadri (Eds.): Biomed 06, IFMBE Proceedings 15, pp. 334-337, 2007
www.springerlink.com ' Springer-Verlag Berlin Heidelberg 2007

A Generic Algorithm for Detecting Obstructive Sleep Apnea Hyponea Events based on Oxygen Saturation

Y.K. Lee[1], M. Bister[2], Y.M. Salleh[1]

[1] Faculty of Electrical Engineering, Universiti Teknologi MARA, Malaysia
[2] School of Electrical and Electronic Engineering and CS & IT, University of Nottingham, UK & Malaysia Campus

Abstract—**Generic aspect in the automated detection of obstructive sleep apnea hypopnea (OSAH) events based on only oxygen saturation (Sp02) is investigated. The objective is to develop and verify an algorithm (GTA) capable of generalizing three auto detection algorithms (ADA, DDA, MNA) which represent the classical threshold algorithms based on clinical definitions for desaturation. This is the first attempt a generic algorithm is developed for the classical threshold algorithms for automated detection of desaturation. This makes efficient the benchmarking of new automated algorithms for the detection of OSAH events based on the analysis of Sp02 alone, in terms of time, cost and resources. GTA is the consequence of recognizing a common pattern in the response characteristics of ADA, DDA, MNA and generalizing them. The most significant contribution is the reduction from three different auto detection procedures to two rules for event extraction and another two for event authentication. This has been verified against detection outcomes and operating characteristics. Full agreement is found between GTA and ADA, DDA, MNA with minimal rounding error. The credibility of assessment is founded on a standard comparison basis for all algorithms, which includes database, optimal performance criteria and evaluation method.**

Keywords—**apnea hypopnea events, oxygen saturation, automated detection, generic algorithm**

I. Introduction

Obstructive Sleep Apnea Hypopnea (OSAH) Syndrome is the most common syndrome of Sleep Breathing Disorder (SBD) [1]. Polysomnography (PSG) is the golden standard for its diagnosis. It involves multi-channel measurements of eight or more signals, including oronasal flow, oxygen saturation and heart rate. This makes the subsequent analysis expensive, resource intensive and time consuming. Furthermore, the manual scoring process is also susceptible to intra- and inter-scorer discrepancy.

The OSAH events are usually found to be accompanied by characteristic variation in oxygen saturation (Sp02). In fact, Sp02 is one of the conditions listed by the America Academy of Sleep Medicine Task Force to characterize the OSAH events [1]. If OSAH events can be detected using Sp02 alone, one of the many PSG variables, it could then be possible to automate the screening or diagnosis of OSAHS inexpensively. Early diagnosis and treatment of the disease will clearly benefit the health of patients.

Attempts with different techniques have been made, ranging from classical threshold algorithms [2-8] to contemporary wavelet [9] and spectral [10] algorithms. Results from these studies support the automated detection of moderate and severe OSAH events for purpose of auto-scoring, screening or diagnosis from analysis of Sp02 alone [2-4, 11-12].

To detect desaturation, some of the classical threshold algorithm make use of the positive and negative deviation from baseline alone [4-5, 8]; some combine it with duration [2-3]; some include the rate of change of desaturation [2]; some adopt the rate of change of desaturation or/and resaturation [11-12]; some threshold the actual amplitude [13-14] or combine it with duration [7].

Despite differences in the choice of event markers, it is found that these algorithms can be classified into three auto detection algorithms based on the clinical definitions adopted. Further analysis on the detection outcomes and operating characteristics of these algorithms revealed a generalized response. This leads to the hypothesis that these algorithms can be generalized. This is the first attempt to generalize the classical threshold algorithms for detecting desaturation which can be associated to OSAH events.

Our work investigates the generic aspect in the automated detection of OSAH events based on only Sp02. The objective is to develop and verify an algorithm capable of generalizing the three auto detection algorithms, representing the classical threshold algorithms. This makes the benchmarking of new automated algorithms for the detection of OSAH events based on Sp02 alone efficient, in terms of time, cost and resources.

II. Methodology

A. Data

Data from the Apnea ECG Challenge of Physionet [15] were chosen for their annotation of golden standard. They total at a study time of 47.4 hours or 17,064,000 samples, at a sampling frequency of 100 Hz, with a fair distribution of subjects with different frequencies of OSAH events.

F. Ibrahim, N.A. Abu Osman, J. Usman and N.A. Kadri (Eds.): Biomed 06, IFMBE Proceedings 15, pp. 338-341, 2007
www.springerlink.com ' Springer-Verlag Berlin Heidelberg 2007

B. Algorithm

Three auto detection algorithms were first developed and then generalized through *one* generic algorithm.

The **Amplitude Duration Algorithm** (ADA) flags signal with amplitude and duration < the predefined desaturation amplitude and desaturation period. It is interpreted from a clinical definition for OSAH [7], *Clinically significant oxygen desaturation events were defined as any decrease in Sp02 < 90% for ≥ 1 second*. These criteria values are substantiated by finding from [16] that the mean of the lowest oxygen saturation of healthy subjects is 90.4%.

In concept, the **Drop Duration Algorithm** (DDA) is similar to the above algorithm. The difference being the use of drop in Sp02 over a 5-minute window (drop gap) instead of a fix amplitude threshold. It is derived from a clinical definition [6], *Blood oxygen saturation falls during apnea, … reaches a clinical significance, if the blood oxygen saturation < 95% of saturation level before the episode of apnea and lasts >10 seconds.*

The **Modified Nervus Algorithm** (MNA) defines different levels of drop for desaturation (drop gap) and resaturation (return gap). The clinical definition comes from [8], *Desaturation starts as soon as the oxygen level < baseline by a specified amount, and continues until the signal recovers to a level < baseline by 25% of the specified amount*.

The **Generic Threshold Algorithm (GTA)** generalizes the above algorithms. The ADA works on a rigid threshold on the depth and width of an event. The DDA with single threshold and MNA with double threshold operate on the cyclic pattern of events, limiting their depth and length. The generic procedure to extract events is explained in Fig. 1. The upStartIndex and dropStartIndex arrays are used to store the probable start and stop indices of events.

```
while data in baseline window is not exhausted do
        Find start and stop of deviation below baseline    drop gap)
        such as point d1, d2 in Fig. 3
        Add to dropStartIndex and dropStopIndex array

        Find start and stop of deviation above (baseline    return
         gap) such as point u1, u2 in Fig. 2
        Add to upStartIndex and upStopIndex array Read next data
end-while
```

Fig. 1 Pseudo code for the generic event extraction method of GTA

The generic intelligence to filter the *actual* start and stop of events is contained in just two conditions with synchronisation. The first condition filters data qualified for the eventStart array (see Fig. 2). It requires for current dropStartIndex element (d2) > previous upStartIndex element (u1), to be authenticated as the actual start of an event. The dropStartIndex element (d3) is disqualified from the eventStart array because it precedes upStartIndex element (u2). If the baseline window starts with an event data or if the event overflows to the next baseline window, this condition also prohibits them to be accepted by the eventStart array.

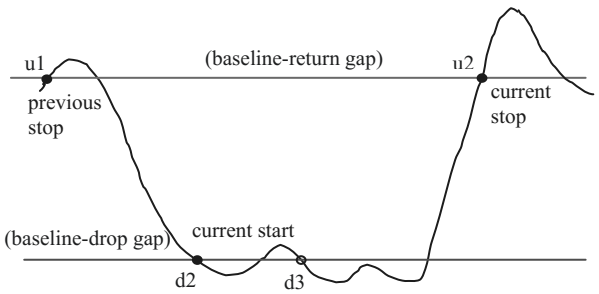

Fig. 2 Condition to filter data as actual start of event

The second condition filters data qualified for the eventStop array (see Fig. 3). It ensures that current upStartIndex element (u1 or u2) is ≥ current dropStartIndex element (d1 or d2) before it can be recognized as the end of an event. The upStartIndex element (u3) is skipped because it precedes dropStartIndex element (d2). If the first data in the recording or the first data of the baseline window is a non-event data, this condition will exclude it from eventStop array, provided there is no dropStartIndex element before it.

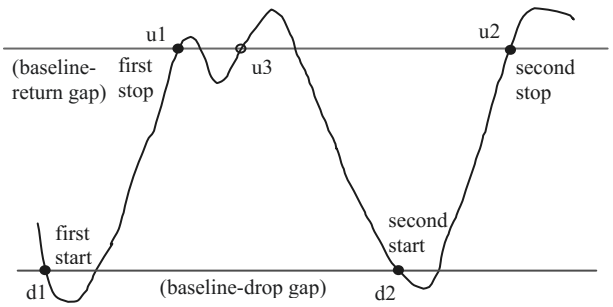

Fig. 3 Condition to filter data as actual stop of event

C. Performance Measurement Method

Tests were conducted on the four algorithms to verify that GTA is sufficient to replicate ADA, DDA and MNA. The verification is evaluated by measuring the agreement in performance output between them, over the same finest tuned event marker [17], baseline computation method and database. The performance measurement parameters for assessing the agreement are true positive (TP), true negative

F. Ibrahim, N.A. Abu Osman, J. Usman and N.A. Kadri (Eds.): Biomed 06, IFMBE Proceedings 15, pp. 338-341, 2007
www.springerlink.com ' Springer-Verlag Berlin Heidelberg 2007

(TN), false positive (FP), false negative (FN), sensitivity (Se), specificity (Sp) and score (Sc) [18-19].

III. Results

Table 1 summarizes setting to the event markers of GTA and the rest for a uniform assessment.

Table 1 Setting for event markers of ADA, DDA, MNA and GTA

	GTA (ADA)	GTA (DDA)	GTA (MNA)
desaturation amplitude (%)	40-100		
desaturation period (s)	1		
baseline window (min)		5	5
drop gap (%)		1-20	1-80
minimum duration (s)		10	

Fig. 4, Fig. 5 and Fig. 6 show the variation in the performance measurement parameters against event markers of the different algorithms, desaturation amplitude for ADA while drop gap for both DDA and MNA. It is found that the graphs produced by GTA coincide with those by ADA, DDA and MNA with minimal rounding error.

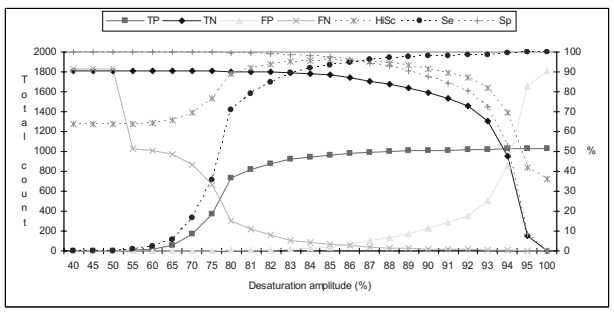

Fig. 4 Variation in TP, TN, FP, FN, Sc, Se, Sp against desaturation amplitude for GTA and ADA

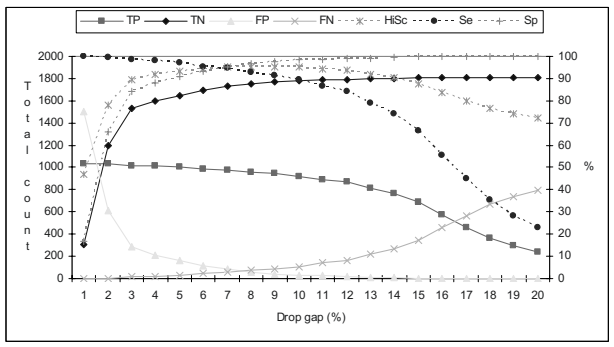

Fig. 5 Variation in TP, TN, FP, FN, Sc, Se, Sp against drop gap for GTA and DDA

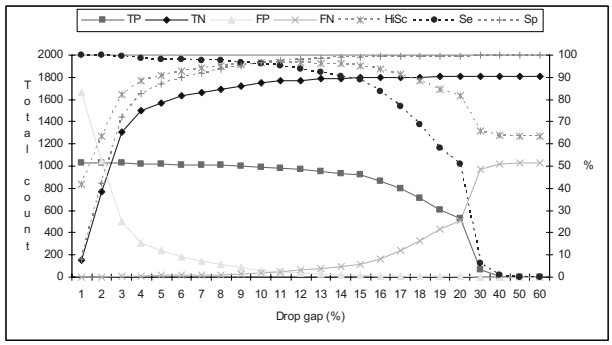

Fig. 6 Variation in TP, TN, FP, FN, Sc, Se, Sp against drop gap for GTA and MNA

IV. Discussion

The capability of GTA to generalize the classical algorithms for automated detection of OSAH events is proven with full agreement between graphs of variation in performance measurement parameters against event markers from ADA, DDA, MNA and GTA (see Fig. 4, Fig. 5 and Fig. 6). The agreement is assessed with consideration from all aspects of event detection. The performance measurement parameters, TP, TN, FP, FN, provide a measure of the detection outcomes while Se, Sp, Sc, a measure of the accuracy and operating characteristics of the detection algorithms. The assessment is conducted with similar databases, optimal performance criteria and evaluation methods for a more credible appraisal, also cited as future challenges to communicate merits of new algorithm [20].

The event markers in Table 1 are chosen in preference to the others in the clinical criteria for they have been proven to be the most valid for the detection of OSAH events [9]. They produce full ROC graph (which shows trade off between Se and Sp) within reasonable range of event markers. The other event markers such as duration or desaturation period produces ROC graphs of short span but high Sp; baseline window leads to insignificant changes in Se and Sp [17], hence are not considered here.

GTA is founded on a generalization drawn on the variation patterns of performance measurement parameters for ADA, DDA and MNA for detection of desaturation events in the Sp02, regardless of the clinical criteria, as event markers vary (see Fig. 4, Fig. 5 and Fig.6). Deeper threshold on amplitude or change in amplitude, expressed differently in the algorithms, imposes more stringent condition to qualify as an event. Hence, lesser events are admitted. As a result, TP and FP decreases while TN and FN increases. Detection becomes less sensitive but more specific. The score rises to a maxima point and declines as detection changes from totally inclusive with majority of TP and FP,

F. Ibrahim, N.A. Abu Osman, J. Usman and N.A. Kadri (Eds.): Biomed 06, IFMBE Proceedings 15, pp. 338-341, 2007
www.springerlink.com ' Springer-Verlag Berlin Heidelberg 2007

to totally exclusive with majority of TN and FN. If the threshold is very low, the algorithms will succeed in detecting almost all events at the expense of a large number of FP. For ADA, the deeper amplitude threshold is equivalent to lower desaturation amplitude. For DDA and MNA, the deeper amplitude threshold represents higher drop gap. This explains the reversal in the response characteristics between ADA and DDA (see Fig. 4 and Fig. 5). It is this generalization that leads to the novel development of a generic algorithm for event detection, GTA. In fact, GTA is able to detect any event defined as a deviation in width and depth from a slowly varying background, of which, desaturation events in Sp02 signal is only an example.

V. Conclusion

Generic Threshold Algorithm is the consequence of recognizing a common pattern in the response of ADA, DDA, MNA, which represent the classical threshold algorithms for detecting OSAH events based on Sp02, to variation in event markers and generalizing them. The most significant contribution is the reduction from three different auto detection procedures to two rules for event extraction and another two for event authentication. This has been verified against detection outcomes and operating characteristics, with full agreement between GTA and ADA, DDA, MNA. This makes efficient the benchmarking of new automated algorithms for the detection of OSAH events based on the analysis of Sp02 alone, in terms of time, cost and resources.

Acknowledgment

The authors thank Dr. George C F and Dr. Penzel T for their advices and free use of their database.

References

1. American Academy of Sleep Medicine Task Force, Sleep related breathing disorder in adults: recommendation for syndrome definition and measurement techniques in clinical research, *Sleep*, vol. 22, pp. 667-689, 1999.
2. George C F, Millar T W, Kryger M H (1988) Identification and quantification of apneas by computer based analysis of oxygen saturation, America Review Respiratory, vol. 137, pp. 1238-1240.
3. Oeverland B, Skatvedt O, Kvarner K J, Akre H (2002) Pulse oximetry: sufficient to diagnose severe sleep apnea, Sleep Medicine, vol. 3, pp. 133-138.
4. Vazquez J C, Tsai W H, Flemons W W, Masuda A, Brant R, Hajduk E, Whitelaw W A, Remmers (2000) Automated analysis of digital oximetry in the diagnosis of obstructive sleep apnea, Thorax 2000, vol. 55, pp. 302-307
5. Epstein L J, Dorlac G R (1998) Cost effectiveness analysis of nocturnal oximetry as a method of screening for sleep apnea-hypopnea syndrome, Chest, vol. 113, pp. 97-103
6. Varady P, Micsik T, Benedek S, Benyo Z (2002) A novel method for detection of apnea and hypopnea event in respiration signal, IEEE Trans. Biomed. Eng., vol. 49, no. 9, pp. 936-942
7. Thoyre S M, Carlson J (2003) Occurrence of oxygen desaturation event during preterm infant bottle feeding near discharge, Early Human Development, vol. 72, pp. 25-36
8. Nervus (2002) Nervus 2.3 Service Pack 6 new sleep algorithm at:http://www.nervus.is/support/SP6/sp6_new_sleep_algorithms.htm
9. Lee Y K, Bister M, Blanchfield P, Salleh Y M (2004) Automated detection of obstructive apnea and hypopnea events from oxygen saturation signal, 26th Annual International Conference of the IEEE Engineering in Medicine and Biology Society, pp. 321-324
10. Zamarron C, Romero P V, Rodriguez J R (1999) Oximetry spectral analysis in the diagnosis of obstructive sleep apnea, Clinical Science, vol. 97, pp. 467-473
11. Taha B H, Dempsey J A, Weber S M, Badr M S, Skatrud J B, Young T B, Jacquesj A J, Seow K C (1997) Automated detection and classification of sleep disordered breathing from conventional polysomnography data, Sleep, vol. 20 (11), pp. 991-1001
12. Rauscher H, Popp W, Zwick H (1991) Computerised detection of respiratory events during sleep from rapid increases in oxyhaemoglobin saturation, Lung, vol. 169 (6), pp. 335-342
13. Oniki T A, Gardner R M (1994) Computerised detection of arterial oxygen desaturation in an Intensive Care Unit, Annual Symposium Computer Application Medical Care, pp. 356-360
14. Varady P, Nagy L, Szilagyi L (2000) On-line detection of sleep apnea during critical care monitoring, 22nd Annual IEEE EMBS International Conference, pp. 1299-1301
15. Penzel T, McNames J, Chazal P, Raymond B, Murray A, Moody G (2000) Systematic comparison of different algorithms for apnoea detection based on electrocardiogram recording, Medical & Biological & Computing, vol. 40, pp. 402-407
16. Netzer N, Eliasson A H, Netzer C, Kristo D A (2001) Overnight pulse oximetry for sleep disordered breathing in adults, Chest, vol. 120 (2), pp. 625-633
17. Lee Y K (2006) Analysis, Compression and Remote Display of Long-Term Biomedical Signals with Infrequent Short Duration Events, Ph.D. dissertation, Department of Electrical and Electronic Engineering, University of Nottingham, UK, chapter 4
18. Kraulis P, Uppsala University (2001, January) Molecular Bioinformatics 2001: Lecture 22: Sensitivity and specificity at http://www.sbc.su.se/~per/molbioinfo2001
19. Canadian Association of Medical Education (2002) Screening and Diagnosis at http://www.dante.med.utoronto.ca/doch/Year3/pdfs/ doch3-3.pdf
20. Giger M L, Karssemeijer N, Armato S G (2001) Guest Editorial Computer Aided Diagnosis in Medical Imaging, IEEE Transactions on Medical Imaging, vol. 20 (12), pp. 1205-1208

Address of the corresponding author:

Author: LEE Yoot Khuan
Institute: Universiti Teknologi MARA
Street: Faculty of Electrical Engineering
City: 40450 Shah Alam. Selangor Darul Ehsan.
Country: Malaysia
Email: leeyootkhuan@salam.uitm.edu.my

F. Ibrahim, N.A. Abu Osman, J. Usman and N.A. Kadri (Eds.): Biomed 06, IFMBE Proceedings 15, pp. 338-341, 2007
www.springerlink.com ' Springer-Verlag Berlin Heidelberg 2007

A Measuring System for Coronary Pulse Wave Velocity

Taewoo Nam[1], Jongman Cho[1], Soohong Kim[1], Jaehong Lim[1] and Wookhyun Cho[2]

[1] Department of Biomedical Engineering, Inje University, Gimahe, 621-749, Korea
[2] Department of Internal Medicine, Inje University Seoul Paik Hospital, Seoul, Korea

Abstract— **Pulse wave velocity (PWV) is a basic parameter in the dynamics of pressure and flow wave traveling in arteries. But it is difficult to measure the pulse wave transmission time between coronary arterial proximal and distal point by manual method using the graph on which pulse wave and ECG are recoded. The system that can measure PWV was developed and the experiment was carried out for one patient to validate the accuracy of the measured coronary arterial PWV. The average value of the measured coronary arterial PWV was 936.571±105.161 cm/sec.**

Keywords— **Coronary arterial PWV (Pulse Wave Velocity), Invasive PWV measurement**

I. Introduction

In clinical diagnosis, several factors are used in assessing arterial stiffness, and PWV is one of them. Several studies have highlighted the importance of PWV in parameters of pathophysiology, prognosis, and therapy and shown close correlations between PWV and atherosclerosis [1][2].

Nowadays, aorta PWV can be measured using variety of invasive and non-invasive methods. However, coronary arterial PWV actually has many important information of cardiovascular disease.

Generally, PWV is defined as the ratio of pulse wave transmission distance ($\Delta dist$) and pulse wave transmission time (Δt) as shown in Eq. (1).

$$PWV = \Delta dist / \Delta t \quad (1)$$

As shown in Figure 1, $\Delta dist$ is a distance between point 1 and point 2 in the coronary angiograph, and Δt denotes a time difference of point T1 and point T2 in pulse wave-ECG graph.

As a result of measurement coronary arterial PWV using an invasive method during coronary angiography, distance of two points (point 1 and point 2), which are coronary arterial proximal and distal point, is measured accurately using the length of infusion catheter. But it was difficult to measure the pulse wave transmission time between coronary arterial proximal and distal point by manual method using the graph on which pulse wave and ECG were recorded. The aim of this study is to develop a PWV calculation system that can acquire the pulse wave and ECG signal over the 10,000 samples per second, measure the accurate transmission time, and calculate the accurate coronary arterial PWV automatically.

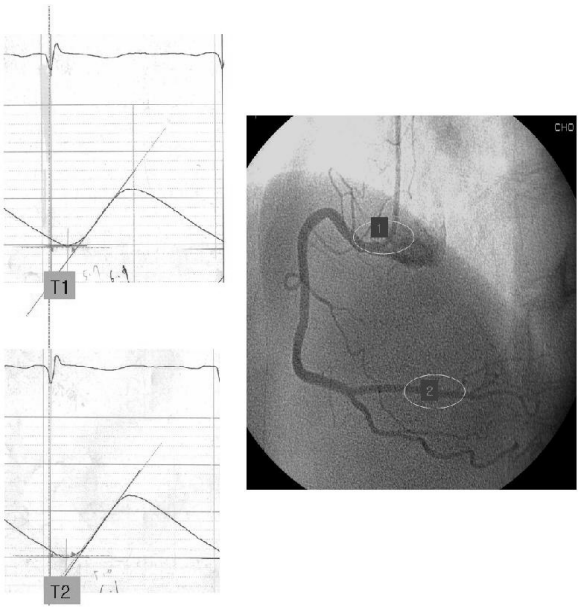

Fig. 1 The graph which shows recorded pulse wave and ECG, and the coronary angiograph

II. Methodology

A. System modeling

We must know the patient s pulse wave and ECG to calculate coronary arterial PWV. Accordingly, the system is made up of a pressure transducer which measures the patient s pulse wave, an amplifier to amplify the signals from the pressure transducer and ECG electrodes, a filter circuit to remove noises, an analog-to-digital converter to convert the source signals into digital forms, and a computer to process the acquire signal and calculate the PWV.

B. Experimental equipment

The system was developed to measure patient s pulse wave and ECG, and to calculate coronary arterial PWV.

F. Ibrahim, N.A. Abu Osman, J. Usman and N.A. Kadri (Eds.): Biomed 06, IFMBE Proceedings 15, pp. 342-344, 2007
www.springerlink.com ' Springer-Verlag Berlin Heidelberg 2007

We used a pressure transducer (PX260, Edwards Lifesciences) which is widely used at intensive care units (ICUs) and operation rooms to measure pulse wave. An ECG module was designed to measure ECG, and the source signal from a blood pressure (BP) transducer is amplified 1,000 times by an amplifier (AD524, Analog Devices Inc.). The noise signal in the amplified BP signal is removed using a filter (LM244N, Motorola Inc.) and the filtered BP signal and output signal from ECG module are converted to digital forms by DAQ board (USB-9215, National Instrument Inc.), and transmitted to the notebook computer via a Universal Serial Bus (USB). Figure 2 shows the experimental setup.

C. Data acquisition

The patient s coronary arterial pulse wave is measured using an invasive method during coronary angiography, and ECG is also measured simultaneously. Sampling rate was 10,000 samples per second. Figure 3 shows the apparatus of the developed system to measurement the ECG and pulse wave and Figure 4 shows the developed software which shows blood pressure, ECG, and PWV calculation.

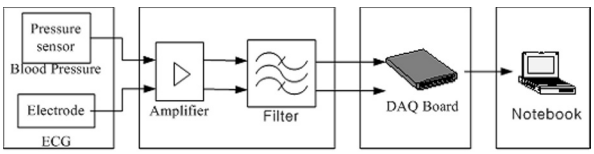

Fig. 2 Experimental setup

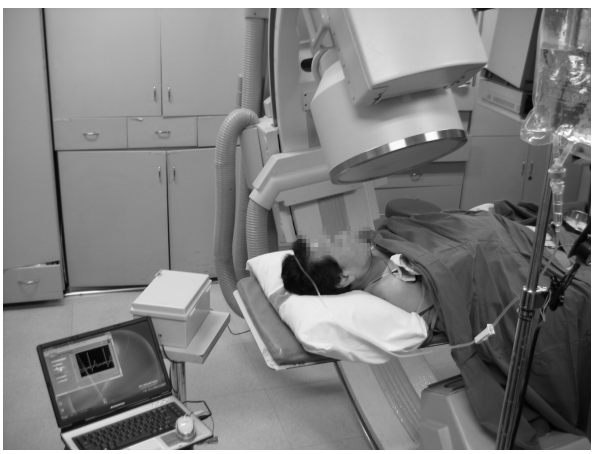

Fig. 3 Apparatus of system for measurement of ECG and pulse wave

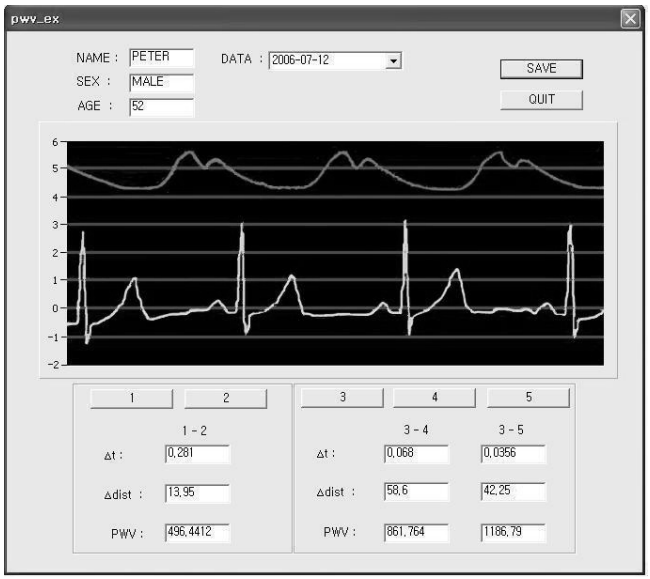

Fig. 4 The developed software showing blood pressure, ECG, and PWV calculation

III. Results and Discussions

The system could record a patient s pulse wave signal and ECG signal in real time, and measure the time difference between R-peak of the ECG signal and a specific point of pulse wave within a cycle. This calculated time difference for each cycle is averaged for 10 cycles. At the same time, the distance between point 1 and point 2 in the coronary angiograph in Figure 4 (*Δdist*) is inputted by manual way with the length of infusion catheter. Finally, the system calculates the coronary arterial PWV automatically.

One patient was studied three times. As shown in table 1, the average value of coronary arterial PWV is 936.571–105.161 cm/sec.

Table 1 Reproducibility test of the system

Experimental ID	*Δdist* (cm)	*Δt* (sec)	PWV(cm/sec)
1	13.5	0.0148	912.162
2	13.95	0.0163	855.82
3	13.23	0.0127	1041.732

F. Ibrahim, N.A. Abu Osman, J. Usman and N.A. Kadri (Eds.): Biomed 06, IFMBE Proceedings 15, pp. 342-344, 2007
www.springerlink.com ' Springer-Verlag Berlin Heidelberg 2007

IV. Conclusions

A system is developed and applied to measure coronary arterial PWV through this study and we make certain that our system can calculate coronary arterial PWV automatically. Further clinical validation is required through more experiments. In addition, the developed system can provide more accurate measurement tool in coronary arterial studies.

Acknowledgment

This work was supported by a grant No. Sanhak 5 from the Korean Society of Circulation.

References

1. Asmar R. (1999) Arterial Stiffness and Pulse Wave Velocity: clinical applications. Elsevier
2. Asmar R. (2001:1) Effect of Antihypertensive Agents on Arterial Stiffness as evaluated by Pulse Wave Velocity Clinical Implications. Am. J. Cardiovasc. Drugs vol.5 387-397
3. Walter J. Rogers, Yong-Lin Hu, Douglas Coast, etc. (2001) Age Associated Changes in Regional Aortic Pulse Wave Velocity, Journal of American College of Cardiology, Vol 38 No. 4

Address of the corresponding author:

Author: Taewoo Nam
Institute: Department of Biomedical Engineering, Inje University
Street: 607, Obang-dong,
City: Gimhae
Country: Korea, South
Email: ntw99@bse.inje.ac.kr

F. Ibrahim, N.A. Abu Osman, J. Usman and N.A. Kadri (Eds.): Biomed 06, IFMBE Proceedings 15, pp. 342-344, 2007
www.springerlink.com ' Springer-Verlag Berlin Heidelberg 2007

A Simple Histogram Based Approach for Detection of Baseline and QRS of ECG

S.Mitra[1] and M.Mitra[1]

[1]Department of Applied Physics, Faculty of Technology, University of Calcutta, Kolkata, India

Abstract— **An efficient, very simple and new approach for detection of both base line and QRS complexes from the horizontal and vertical histogram of ECG data is described in this paper. The vertical and horizontal histograms are generated from the number of ordinates for a particular abscissa at the vertical and horizontal direction respectively. The base line is determined at the maxima of the horizontal histogram whereas QRS or R peaks are determined from the local maximas of the maximum area zone of vertical histograms. A very high accuracy level is achieved for both the cases (99.5% for QRS and 92% for base line). The method is advantageous because both QRS and base lines can be determined directly from ECG data without computation of complex mathematical models even when ECGs are tilted due to respiration and in the presence of power line oscillation.**

Keywords— **ECG, Histogram, QRS, Baseline**

I. Introduction

Baseline and QRS complex detection are essential tasks in ECG analysis for extraction of different time domain features. Most methods for base line or isoelectric line detection are based upon the assumption that the isoelectric level of the signal lies on the area ~80 ms left of the R-peak, where the first derivative becomes equal to zero for at least 10 ms or in the flattest 20 ms segment [10].

A great research effort has been devoted in the development and evaluation of automated QRS detectors [1]. Two types of QRS detectors have been developed. There are two parts in these detectors one is the processor and the other is the decision rule[2]. The processor performed linear filtering and non-linear transformation. It produces a noise suppressed signal in which the QRS complexes are enhanced. The decision rule detects or classifies whether the enhanced parts are QRS complexes or not.

Hidden Markov models[3] and pattern recognition are also used for detection of QRS complexes [4, 5]. In another scheme simple morphological operator is used for detection of QRS complexes[6]. In this approach the operator (openings and closings) works as peak-valley extractor. Different wavelet functions are also used for QRS complex detection in ECG. It has been noted that wavelet functions that support symmetry and compactness provide better results[7]. In another scheme a QRS complex detector based on the dyadic wavelet transform (Dy WT) which is robust to time varying QRS complex morphology and to noise has also been developed [8]. Another approach for QRS detection is an adaptive matched filtering algorithm based upon an artificial neural network (ANN). An ANN adaptive whitening filter is used to model the lower frequencies of the ECG signals which are inherently non linear and non-stationary. The residual signal which contained mostly high frequency QRS complex energy was then passed through a linear matched filter to detect the location of the QRS complex [9].

All the approaches described above for QRS or baseline detection are based on computation of complex mathematical models. But in the present approach a new and comparatively simple (with no such mathematical and computational complexities) method is described for both baseline and QRS detection of ECG signals from the horizontal and vertical histogram of every ECG data. We achieved a very high level of accuracy in detection of QRS and base line by this method even in the presence of noises like baseline drift due to respiration and power line oscillation (up to 15%).

II. Methodology

In the present work we consider the ECG plot appearing on computer screen that may be considered as a two-dimensional picture consisting of elements, organized in rows and columns, with values 0 (corresponds to points having no ordinate) and 1 (corresponds to points having ordinate).

A. Determination of Baseline from Horizontal Histogram

For a particular row the number of 1 is being computed for plotting of the horizontal histogram of ECG data. Since the baseline regions contain few almost straight line portions, then searching the maxima of this horizontal histogram, the baseline region can be obtained. Figure 1 and 2 show the baseline region of the plotted ECG signals.

B. Determination of QRS complex from vertical histogram

Similarly, the vertical histogram of an ECG data is being plotted after considering the number of 1 for a particular column. Each vertical histogram contains only high positive peaks of small width at the QRS complex region. A small window of considerable length (say W) is taken to detect

F. Ibrahim, N.A. Abu Osman, J. Usman and N.A. Kadri (Eds.): Biomed 06, IFMBE Proceedings 15, pp. 345-347, 2007
www.springerlink.com ' Springer-Verlag Berlin Heidelberg 2007

the area of this curve and we obtained maximum area at those peak regions (fig. 1 and 2). So extracting the local maxima of the maximum area zone for no. of peaks times the R waves of each ECG signals can be detected. Two consecutive R waves and hence the total samples and a distance between them are also computed. So, the sampling period can easily be calculated for each signal. The accuracy of detection of QRS complex very much depends on W. Very high or very low values of W will decrease the accuracy. Hence an optimum value of W is required. An experiment is being done for choosing the appropriate value of W with the considerable number of test samples of signals to achieve the maximum accuracy in detection of QRS.

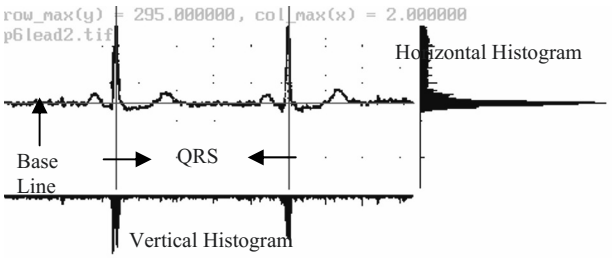

Fig. 1 QRS and baseline detection from vertical and horizontal histogram

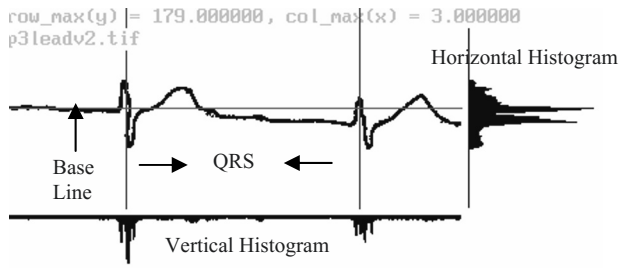

Fig. 2 QRS and baseline detection from vertical and horizontal histogram

III. Result

For this observation a database of 12 lead ECG signals of 130 subjects (60 normal and 70 abnormal) was generated [11]. The abnormal subjects have mostly myocardial infarction and ischemia. So, the algorithm was tested by 36 types of ECG waves. The system also tested for both noise free and noisy signals. The levels of both type of noises are increased from 0% to 15% and still we achieved 99.5% accuracy in an average in detection of QRS complexes and 92% for detection of baseline. The result obtained in different noise levels are given in table 1 and 2. A testing has been made for checking the accuracy in the detection of QRS. After detection of QRS complexes the heart rate of every signal is computed and is checked with the values given on paper ECG records.

Table 1 QRS Detection Accuracy in Two Different Noise Levels

Noise Level (Power line Interference)	QRS Detection Accuracy	Noise Level (Base line shift)	QRS Detection Accuracy
0%	100%	0%	100%
5%	100%	5%	100%
10%	99.3%	10%	100%
15%	97.75%	15%	98.8%
Average	99.26%	Average	99.70%

Table 2 Baseline Detection Accuracy in Two Different Noise Levels

Noise Level (Power line Interference)	QRS Detection Accuracy	Noise Level (Base line shift)	QRS Detection Accuracy
0%	94.50%	0%	94.50%
5%	93.80%	5%	93.20%
10%	91.20%	10%	90%
15%	90.15%	15%	89.20%
Average	92.41%	Average	91.73%

IV. Conclusions

A very simple vertical and horizontal histogram based approach for detection of QRS complex and baseline of ECG signal is described in this paper. Problem arises to make a diagnostic decision from time plane ECG waves when they are corrupted by different noises. Different types of filters have been used to reduce those noises but that may result the loss of clinically significant data. The performance of the developed QRS and baseline detector is satisfactory especially in noisy environment and still we obtained a 99.5% and 92% accuracy in an average in detection these.

References

1. G.M. Friensen, T.C. Jannett, M.A. Jadallah, S.L. Yates, S.R. Quint and H.T. Nagle, A comparison of the noise sensitivity of nine QRS detection algorithms , IEEE Trans. Biomed. Eng., vol. BME-37, pp 85-89, 1990.
2. O.Pahlm, L. Sommo, Software QRS detection in ambulatory monitoring A review, Med. Biomed. Eng. Comput., Vol. 22, pp. 289-297, 1984.
3. D.A. Coast, R.M. Stem, G.G. Cano, S.A. Briller, An approach to cardiac arrhythmia analysis using hidden Markov models, IEEE Trans. Biomed. Eng., vol. BME-37, pp. 826-836, 1990.

F. Ibrahim, N.A. Abu Osman, J. Usman and N.A. Kadri (Eds.): Biomed 06, IFMBE Proceedings 15, pp. 345-347, 2007
www.springerlink.com ' Springer-Verlag Berlin Heidelberg 2007

4. P.E. Trahanias, E. Skordalakis, Bottom-up approach to ECG pattern recognition problem, Med. Biomed. Eng. Comput., vol. 27, pp. 221-229,1989.
5. P.E. Trahanias, E. Skordalakis, Syntactic pattern recognition of the ECG, IEEE Trans. Pattern Anal. Mach. Intell., vol. PAMI-12, pp.648-657, 1990.
6. P.E. Trahanias, An approach to QRS complex detection using mathematical morphology, IEEE Trans. Biomed. Eng., vol. BME-40, pp. 201-205,1993.
7. Dinh H A, Kumar D K, Pah N D, Burton P. Wavelets for QRS detection, Australas Phys Eng Sci Med.;vol. 24, pp.207-211, 2001.
8. Kadamb S, Murray R, Boudreaux-Bartels GF. Wavelet transform-based QRS complex detector .IEEE Trans Biomed Eng. ;vol. 46 ,pp.838-48, 1999.
9. Yu X, Xu X, QRS detection based on neural-network , Journal of Biomed. Eng, ..;vol. 17, pp.59-62, 2000.
10. N. Maglaveras, T. Stamkopoulos, C. Pappas, M. Strintzis, An adaptive back-propagation neural network for real-time ischemia episodes detection. Development and performance analysis using the European ST-T database, IEEE Trans. Biomed. Eng., vol. 45, no 7, pp. 805 813, 1998.
11. Sucharita Mitra, M. Mitra , An Automated Data Extraction System From 12 Lead ECG Images , Computer Methods and Programs in Biomedicine, vol. 71(1), pp. 33-38, May(2003).

Address of the corresponding author:

Author: S.Mitra
Institute: Department of Applied Physics, University of Calcutta
Street: 92 APC Road
City: Kolkata
Country: India
Email: susa68@hotmail.com

F. Ibrahim, N.A. Abu Osman, J. Usman and N.A. Kadri (Eds.): Biomed 06, IFMBE Proceedings 15, pp. 345-347, 2007
www.springerlink.com ' Springer-Verlag Berlin Heidelberg 2007

A Software Based Approach for Detection of QRS Vector of ECG Signal

M.Mitra[1] and S.Mitra[1]

[1]Department of Applied Physics, Faculty of Technology, University of Calcutta, Kolkata, India

Abstract— **A software based approach for determination of the frontal plane QRS vector is described in this paper. For this purpose, a module is developed for determination of R-R interval of each ECG wave of six limb leads (Leads I, II, III, AVR, AVL and AVF) by using square derivative curve technique. Baseline or isoelectric level of every ECG signal is also determined for accurate computation of net QRS deflection (NQD) at all the six above-mentioned leads. Depending on the rules of cardiac axis determination by searching the minimum NQD, an algorithm is developed for computation of the angle, amplitude and direction of the frontal plane QRS vector for both normal and diseased subjects to find out the clinical significance of this vector in disease identification. In the present work, the PTB diagnostic ECG database is used for computation of the QRS vector and interesting result is achieved.**

Keywords— **ECG, software, QRS vector, NQD, baseline**

I. Introduction

The most widely used bio-signal in clinical practice is Electrocardiogram (ECG), the electrical views of the heart. Electrocardiography is an effective non-invasive diagnostic technique, which generates the ECG by placing electrodes on the patient s body. It is important to realize that two components are important in determining the appearance of the QRS complex in any given lead: the direction of electrical forces relative to the lead, and the magnitude of forces. A large positive deflection will be produced in any lead when the electrical forces are moving in parallel with the lead, while minimal deflections will be formed when the electrical forces are moving perpendicular to the lead. The direction of deflection, positive or negative (upward or downward) in any lead is determined by the direction in which the electrical forces are moving in relation to the lead. The appearance of QRS vector is important for getting the QRS axis as well as the cardiac vector.

Cardiac vector is used for identifying myocardial ischaemia during carotid endarterectomy[3] and also to locate major anatomical position of the injured region in the heart ventricles for various localizations of the lesion[4].

On the other hand detection of R-R interval is essential for the task of ECG analysis. A great research effort has been devoted in the development and evaluation of automated QRS detectors [5]. Two types of QRS detectors have been developed. There are two parts in these detectors one is the processor and the other is the decision rule[6]. The processor performed linear filtering and non-linear transformation. It produces a noise suppressed signal in which the QRS complexes are enhanced. The decision rule detects or classifies whether the enhanced parts are QRS complexes or not.

Hidden Markov models [7] and pattern recognition are also used for detection of QRS complexes [8, 9]. In another scheme simple morphological operator is used for detection of QRS complexes[10]. In this approach the operator (openings and closings) works as peak-valley extractor. Different wavelet functions are also used for QRS complex detection in ECG. It has been noted that wavelet functions that support symmetry and compactness provide better results[11]. In another scheme a QRS complex detector based on the dyadic wavelet transform (Dy WT), which is robust to time varying QRS complex morphology and to noise, has also been developed [12]. Another approach for QRS detection is an adaptive matched filtering algorithm based upon an artificial neural network (ANN). An ANN adaptive whitening filter is used to model the lower frequencies of the ECG signals which are inherently non linear and non-stationary. The residual signal which contained mostly high frequency QRS complex energy was then passed through a linear matched filter to detect the location of the QRS complex [13].

In the present work, a software-based approach for detection of frontal plane QRS vector for both normal and pathological subjects is proposed. Some interesting clinical properties are observed which are stated here.

II. Methodology

For computation of frontal plane cardiac axis the following steps are involved:

A. Determination of R-R interval of ECG wave

Proper detection of the R-R interval between two consecutive ECG waves is very important for various application of its analysis. In the present work, differentiation technique is used to get second order derivative of ECG wave by using 5-point Lagrangian interpolation formulae for differentiation [1]. The formulae is given below:

F. Ibrahim, N.A. Abu Osman, J. Usman and N.A. Kadri (Eds.): Biomed 06, IFMBE Proceedings 15, pp. 348-351, 2007
www.springerlink.com ' Springer-Verlag Berlin Heidelberg 2007

$$f_0' = \frac{1}{12h}(f_{-2} - 8f_{-1} + 8f_1 - f_2) + \frac{h^4}{30} f^{v}(\xi) \quad (1)$$

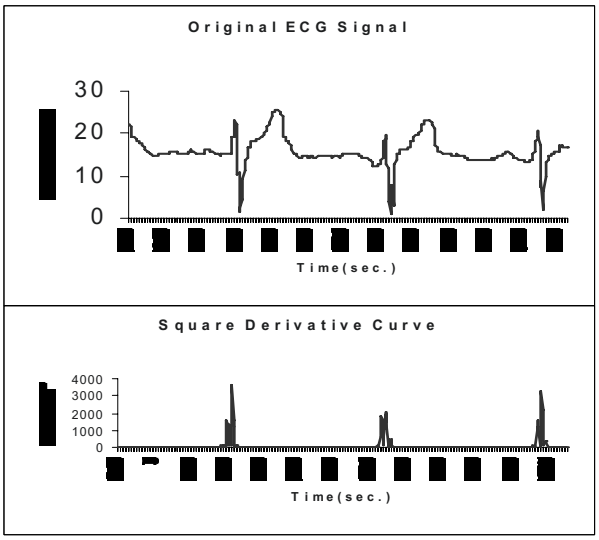

Fig. 1 R-R interval detection

Here ξ lies between the extreme values of the abscissas involved in the formula. After squaring the values of second order derivative, a square-derivative curve having only high positive peaks of small width at the QRS complex region can be obtained (fig. 1). A small window of length (say W) was taken to detect the area of this curve and we obtained maximum area at those peak regions. The local maxima of these peak regions are considered as R-peak. For this experiment W is set as ~0.07 sec. The system was tested for both noise free and noisy signals. The levels of all types of noise were increased from 0% to 30% and still we achieved 99.4% accuracy in the detection of QRS complexes.

B. Detection of base line or isoline

In order to accurately detect the net QRS deflection, isoelectric line must be correctly identified. Most methods are based upon the assumption that the isoelectric level of the signal lies in the region ~80 ms left of the R-peak, where the first derivative becomes equal.

In particular, let $y_1, y_2, ..., y_n$ be the samples of a beat, $y_1', y_2', ..., y_n'_{-1}$ be their first differences and y_r the sample where the R-peak occurs. The isoelectric level samples y_b are then defined if either of the two following criteria is satisfied:

$$|y'_{r-j-int(0.08f)}| = 0, j=1,2,....,0.01f \quad \text{or} \quad (2)$$

$$|y'_{r-j-int(0.08f)}| \le |y'_{r-i-int(0.08f)}|, \; i, j = 1,2,....,0.02f$$

[For positive slope j<i, for negative slope j>i]

where f is the sampling frequency. After the isoelectric level is found, and after comparing the current beat with the previous corrected one (y^{p}_{bp}), it is easy to align the current beat with the previous one, using the declination of the line connecting the isoelectric levels of the two beats. If we define,

$$\gamma = \frac{y_b - y^{p}_{b_p}}{n_b}$$

where n_b is the number of samples between the two baseline points, the alignment procedure becomes:

$$y_t \rightarrow \gamma\, y_t \quad (3)$$

Other baseline correction techniques rely on adaptive filtering of the ECG beat and provide reliable results as well, however the QRS wave shape is corrupted by the use of such techniques [2].

C. Computation of net QRS deflection (NQD) in a lead

After detection of baseline, the location of Q wave is determined by searching the first transition from positive to negative or vice versa from the R point. After getting q point the net QRS deflection can be computed from the following equation:

$$NQD = (Qpt\text{-}avg\text{-}bpt) + (Rpt \quad avg\text{-}bpt) \quad (4)$$

Where, Qpt = Q point, Rpt = R point, avg-bpt = Average baseline point

D. Detection of frontal plane cardiac axis

An algorithm is developed for detection of cardiac axis on the basis of the following rules

(1) Look for a limb lead with NQD close to zero. This could be either a lead with very little recognizable deflection in either direction, or equally large positive and negative deflections, such that the sum of positive and negative deflections is close to zero. The mean electrical axis will then be either perpendicular or 270^0 out of phase to this lead depending on the sign (+ve or ve) of NQD at that lead. For example, if lead I has close to zero net amplitude, the axis would be either +90° or -90° (fig. 2). Then, look at any of the inferior leads: II, III, or aVF. If these leads register a

F. Ibrahim, N.A. Abu Osman, J. Usman and N.A. Kadri (Eds.): Biomed 06, IFMBE Proceedings 15, pp. 348-351, 2007
www.springerlink.com ' Springer-Verlag Berlin Heidelberg 2007

Table 1 A portion of detected NQD and angle of QRS vector

Patient No.	Net QRS Deflection (NQD)						Angle tan $^{-1}(B/A)$
	L1	L2	L3	AVR	AVL	AVF	
N292l	0.562167	1.1315	0.404462	-0.84936	0.132091	0.8495	36.89824385
N301l	0.326333	0.835	0.469818	-0.62623	0.021833	0.6524	38.0011292
N302l	0.366182	0.635909	0.173231	-0.50309	0.16	0.420462	38.34881734
N303l	0.344111	0.627909	0.232182	-0.50162	0.08	0.434364	38.62043848
M140l	0.206	0.68	0.473444	-0.42857	-0.10239	0.577	40.31558466
M141l	0.1856	0.55425	0.542615	-0.3536	-0.08978	0.482727	41.05440987
M145l	0.1526	0.55212	0.44256	-0.3626	-0.09925	0.482322	41.1398722

predominantly positive deflection, the QRS axis will be closer to +90°. If the inferior leads (II, III, aVF) are predominantly negative, the axis is closer to -90°.

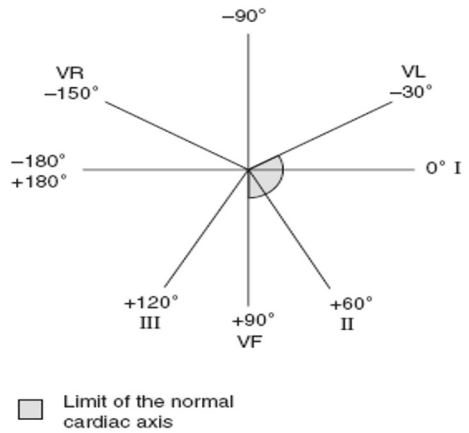

Fig.2 Angle of different limb leads from the frontal plane

(2) Sometimes, no ECG lead can be identified which appears to have zero net amplitude i.e, NQD ≠0 in every lead. In this case, decide which lead(s) have the largest positive or negative deflections. The QRS axis will be close to the direction of this lead.

Let, NQD = A in the lead having maximum deflection and in a neighboring lead NQD = B which is near to maxima , then the frontal plane cardiac axis will be inclined at the angle $\tan^{-1}(B/A)$ from the lead having maximum deflection. The amplitude of the axis will be $\sqrt{B^2 + A^2}$.

III. Result

Still the observation is being done on 20 normal and 20 diseased subjects having myocardial infraction (MI) of PTB diagnostic ECG database available in physionet. The net QRS height along with the angle of direction of QRS vector for all the six limb leads is given in table 1. An interesting property is being observed that in the majority cases (~80%) the angle of QRS axis lies in distinct regions for normal and MI subjects though there is no axis deviation i.e., the angle lies within the normal range.

IV. Conclusion

A software based approach for detection of QRS vector of ECG signals is described in this paper. For this purpose the accurate detection of both baseline and NQD is necessary. Hence, modules for computation of those are been developed. Finally, depending on the rules of cardiac axis determination by searching the minimum NQD, an algorithm is developed for computation of the angle, amplitude and direction of the frontal plane QRS vector for both normal and diseased subjects to find out the clinical significance of this vector in disease identification. Still we achieved interesting result and also expect that the resultant cardiac vector of frontal and horizontal plane axis will play significant role in disease identification.

References

1. F.B. Hildebrand, Introduction To Numerical Analysis , T M H edn., Tata Mcgraw-Hill Publishing Company Ltd., pp. 82-84.
2. N Maglaveras, T Stamkopoulos, K Diamantaras, ,C Pappas, M Strintzis, ECG pattern recognition and classification using non-linear transformations and neural networks: a review , *International Journal of Medical Informatics*, vol. 82, pp. 191-208, 1998.

F. Ibrahim, N.A. Abu Osman, J. Usman and N.A. Kadri (Eds.): Biomed 06, IFMBE Proceedings 15, pp. 348-351, 2007
www.springerlink.com ' Springer-Verlag Berlin Heidelberg 2007

3. S. Kawahito, H. Kitahata, K. Tanaka, J. Nozaki and S. Oshita, Dynamic QRS-complex and ST-segment monitoring by continuous vectorcardiography during carotid endarterectomy British Journal of Anaesthesia, vol. 90 (2), pp. 142-147, 2003.
4. E.A.I. Aidu, V.G. Trunov, L.I. Titomir, V. Szathmary, M. Ty ler, Noninvasive Location of Acute Ischemic Lesion in the Heart Ventricles Using a Few-lead System: Study on a Realistic Mathematical Model , Measurement Science Rreview, Vol.3 (2), , pp. 33-36, 2003
5. G.M. Friensen, T.C. Jannett, M.A. Jadallah, S.L. Yates, S.R. Quint and H.T. Nagle, A comparison of the noise sensitivity of nine QRS detection algorithms , IEEE Trans. Biomed. Eng., vol. BME-37, pp 85-89, 1990.
6. O.Pahlm, L. Sommo, Software QRS detection in ambulatory monitoring A review, Med. Biomed. Eng. Comput., Vol. 22, pp. 289-297, 1984.
7. D.A. Coast, R.M. Stem, G.G. Cano, S.A. Briller, An approach to cardiac arrhythmia analysis using hidden Markov models, IEEE Trans. Biomed. Eng., vol. BME-37, pp. 826-836, 1990.
8. P.E. Trahanias, E. Skordalakis, Bottom-up approach to ECG pattern recognition problem, Med. Biomed. Eng. Comput., vol. 27, pp. 221-229,1989.
9. P.E. Trahanias, E. Skordalakis, Syntactic pattern recognition of the ECG, IEEE Trans. Pattern Anal. Mach. Intell., vol. PAMI-12, pp.648-657, 1990.
10. P.E. Trahanias, An approach to QRS complex detection using mathematical morphology, IEEE Trans. Biomed. Eng., vol. BME-40, pp. 201-205,1993.
11. Dinh H A, Kumar D K, Pah N D, Burton P. Wavelets for QRS detection, Australas Phys Eng Sci Med.;vol. 24, pp.207-211, 2001.
12. Kadamb S, Murray R, Boudreaux-Bartels GF. Wavelet transform-based QRS complex detector .IEEE Trans Biomed Eng.: vol. 46 ,pp.838-48, 1999.
13. Yu X, Xu X, QRS detection based on neural-network , Journal of Biomed. Eng, ..;vol. 17, pp.59-62, 2000.

Address of the corresponding author:

Author: S.Mitra
Institute: Department of Applied Physics, University of Calcutta
Street: 92 APC Road
City: Kolkata
Country: India
Email: susa68@hotmail.com

F. Ibrahim, N.A. Abu Osman, J. Usman and N.A. Kadri (Eds.): Biomed 06, IFMBE Proceedings 15, pp. 348-351, 2007
www.springerlink.com ' Springer-Verlag Berlin Heidelberg 2007

Assessment of Steady-State Visual Evoked Potential for Brain Computer Communication

R. S. Leow[1], F. Ibrahim[1] and M. Moghavvemi[2]

[1] Department of Biomedical Engineering, University of Malaya, Malaysia
[2] Department of Electrical Engineering, University of Malaya, Malaysia

Abstract—**This paper describes the investigation of the steady-state visual evoked potential (SSVEP) response elicited by a flickering visual stimulus. Preliminary results from five subjects have shown that SSVEP have certain characteristics including good signal to noise ratio (SNR), minimal user training and number of electrodes, despite constraints such as the need for a visual stimulating apparatus and possible induced of visual fatigue. Based on these promising results, SSVEP can be used as a tool for controlling signal for future brain computer interface (BCI) application.**

Keywords—**brain computer interface (BCI), electroencephalography (EEG), steady-state visual evoked potential (SSVEP)**

I. Introduction

A brain-computer interface (BCI) is a device that allows human to communicate with a computer by using brain signals. For individuals who have severe neuromuscular disorders, BCI can serve as an alternative method of communication or control so that the communication process does not have to depend on the brain s normal output pathways of peripheral nerves and muscles [1].

The input to the BCI system can be obtained via invasive or non-invasive methods. The non-invasive electroencephalographic (EEG) signals acquired from human scalp are the more favorable method nowadays due to its simple and safer approach, although its signal to noise ratio (SNR) is less prominent [2]. By measuring and analyzing the EEG signals, specific features of brain activity can be translated into desired control commands.

There are several types of EEG activities that can be utilized as input features for BCI systems, e.g. slow cortical potentials [3], oscillatory EEG activity [4], P300 potential [5] and visual evoked potential [6]. The input feature is usually selected based on their effect on information transfer rate and reliability of the BCI system, besides considering other factors such as its applicability for majority individuals and training period required.

Steady-state visual evoked potential (SSVEP) is a periodic response elicited in the brain by visual spatial attention on flickering stimulus at frequency of 6Hz and above [7]. SSVEPs have the same fundamental frequency as the stimulating frequency, but they also include higher and / or subharmonic frequencies under some situation [8]. SSVEPs are usually recorded from the occipital region of the scalp. Compared to other types of EEG features, SSVEP has better SNR. It is phase-locked to the triggering source. Therefore, simple frequency domain algorithms can be used to extract SSVEP signals [9].

For SSVEP-based BCI system, a flickering apparatus is needed to provide visual stimulus to the subject. Therefore, many of the applications are for subjects who have the ability to control their eye movement but not by those with severe ocular motor impairment [7].

In this study, SSVEP is being investigated as an approach for future BCI applications. The results are very promising.

II. Subjects and methods

A. Subjects

A total of five voluntary healthy subjects consisted of three females and two males, aged between 22 and 24 were recruited in the study. All of them have normal or corrected-to-normal vision. Subjects were briefed about the overall procedure of the experiment, and required to sign a consent form.

B. Experimental Procedure

Subject was seated comfortably on a chair. The visual stimulus was placed 1.5 m in front of the subject, at about the same height as the subject s eyes. The visual stimulus was composed of a 2cm diameter red color light emitting diode (LED), with the flickering frequency controlled by a programmable microcontroller. Frequencies ranging from 7Hz to 35Hz were tested.

Before the experiment, few minutes of spontaneous EEG data with subjects closing their eyes were recorded to collect some brain alpha activity. After that, subject was given a few minutes time to adapt to the flickering stimulus before the experiment started. During the experiment, subjects were required to maintain their gaze on the stimulus device. In each session of the experiment, the subject concentrated

F. Ibrahim, N.A. Abu Osman, J. Usman and N.A. Kadri (Eds.): Biomed 06, IFMBE Proceedings 15, pp. 352-354, 2007
www.springerlink.com ' Springer-Verlag Berlin Heidelberg 2007

on the testing of a particular frequency which consisted of at least 10 trials. For each trial, the LED stimulus is programmed to blink for 6 seconds at the preset frequency and OFF for 10 seconds. This short intermittent resting time allows the subject to rest their eyes and helps to reduce visual fatigue.

EEG signals were recorded from positions O1and O2 according to the international 10-20 system and referred to the left and right mastoid respectively. All the electrodes were referenced to an electrode placed on the forehead of the subject. The ground electrode was placed on the location Cz. Electrooculographic (EOG) signals were recorded by placing two electrodes beside and below either eye to allow offline artifact study to be done. Gold-plated electrodes were used. The signals were acquired using a commercial EEG machine at a sampling rate of 256 Hz.

C. Signal Processing

The recorded data was converted into ASCII form and processed offline using Matlab. Fast Fourier Transform (FFT) was used to process the data in frequency domain. The EEG data of one second was zero padded to 2560 points to produce a frequency resolution of 0.1 Hz. The amplitude of the SSVEP power spectrum was plotted to examine the response of the SSVEP signals triggered by the stimulating frequency. Linear Discriminant Analysis (LDA) was used to classify the computed features.

III. Results and Discussion

The results of the stimulation frequency which gave the best performance and the number of correct trials were presented in Table 1. Three of the subjects have very good SSVEP response to 7 Hz stimulation frequency, while the other two subjects vary at 14 Hz and 22 Hz.

Table 1 Offline analysis results for all five subjects.

Subject	Frequency (Hz)	Correct/Total Trials
S1	7	15/15
S2	7	15/15
S3	22	10/12
S4	14	11/12
S5	7	10/14

Figure 1 shows a single-trial SSVEP power spectrum of subject S1. The amplitude of the SSVEP induced by the 7 Hz driving stimulus was obviously larger compared to other frequencies. Besides, a smaller second harmonic response was also obvious. Figure 2 shows the amplitude spectrum of the 7 Hz frequency component of the same subject throughout an experimental session which consisted of 15 trials.

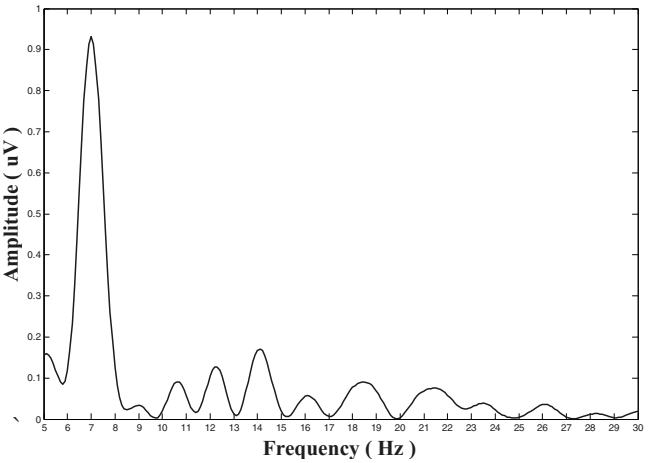

Fig. 1 Single trial SSVEP spectrum of subject S1 induced by 7 Hz stimulation frequency.

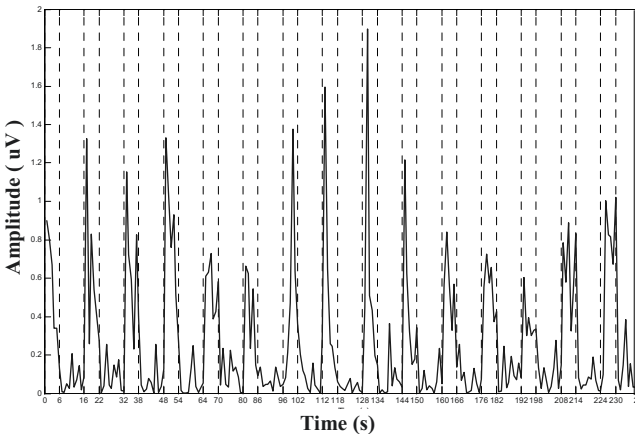

Fig. 2 Amplitude of the 7Hz frequency spectrum of subject S1 participating in a 15 trials experiment induced by 7 Hz stimulation frequency.

The preliminary research finding indicates that SSVEP response can be obtained when the subject is in full concentration attending to the visual stimulus during the experiment. Some of the subjects have shown enormous adaptability to the SSVEP experiments by producing very promising results during their first time participation in the experiment with less training involved [10].

The result shows that each individual subject has different SSVEP responses to various stimulation frequencies. Therefore, the stimulation frequencies need to be optimized for each individual subject [11].

F. Ibrahim, N.A. Abu Osman, J. Usman and N.A. Kadri (Eds.): Biomed 06, IFMBE Proceedings 15, pp. 352-354, 2007
www.springerlink.com ' Springer-Verlag Berlin Heidelberg 2007

IV. Conclusion and future work

SSVEP is suitable to be used as input feature for BCI system, having good characteristics such as noninvasiveness, minimum number of electrodes, less or no training required, wide applicability, etc. Future studies will emphasize on developing of online SSVEP-based BCI application system, besides optimizing other parameters such as electrode positions and stimulation frequencies for each subject individually.

References

1. J. R. Wolpaw *et al.* (2000) Brain-computer interface technology: a review of the first international meeting. *IEEE Trans. Rehab. Eng.* 8:164 173
2. T.M. Vaughan *et al.* (2003) Guest editorial brain-computer interface technology: a review of the second international meeting. *IEEE Trans. Neural Syst. Rehabil. Eng.* 11(2): 94-109
3. N. Birbaumer *et al.* (2000) The thought translation device (TTD) for completely paralyzed patients. *IEEE Trans. Rehab. Eng.* 8:190 193
4. G. Pfurtscheller *et al*. (2000) Current trends in Graz brain computer interface (BCI) research. *IEEE Trans. Rehab. Eng*. 8:216 219
5. E. Donchin *et al.* (2000) The mental prosthesis: Assessing the speed of a P300-based brain computer interface. *IEEE Trans. Rehab. Eng.* 8:174 179
6. E. E. Sutter (1992) The brain response interface: Communication through visually-induced electrical brain responses. *J. Microcomput. Appl.* 15:31 45
7. M. Cheng *et al.* (2002) Design and implementation of a brain computer interface with high transfer rates. *IEEE Trans. Biomed. Eng.* 49:1181 1186
8. C. S. Herrmann (2001) Human EEG responses to 1 100 Hz flicker: resonance phenomena in visual cortex and their potential correlation to cognitive phenomena. *Exp. Brain Res.* 137:346 353
9. S. T. Morgan *et al.* (1996) Selective attention to stimulus location modulates the steady state visual evoked potential. *Proc. Natl. Acad. Sci.* 93:4770 4774
10. R. Wahnoun *et al.* (2002) A real-time brain-computer interface based on steady-state visual evoked potentials. *IFESS*
11. S. P. Kelly *et al.* (2005) Visual Spatial Attention Tracking Using High-Density SSVEP Data for independent brain-computer communication. *IEEE Trans. Neural Syst. Rehabil. Eng.* 13(2):172-178

Author: Leow Ruen Shan
Institute: Department of Biomedical Engineering,
Faculty of Engineering, University of Malaya.
Country: Malaysia
Email: ruen_shan@yahoo.com

F. Ibrahim, N.A. Abu Osman, J. Usman and N.A. Kadri (Eds.): Biomed 06, IFMBE Proceedings 15, pp. 352-354, 2007
www.springerlink.com ' Springer-Verlag Berlin Heidelberg 2007

Characterizing EOG signal from the Chaotic Point of View

S. Farshad Hendi, Aini Hussain, Salina Abdul Samad, Badariah Bais

Dept. of Electrical, Electronic & Systems Engineering, Faculty of Engineering, 43600 UKM Bangi Malaysia

Abstract- ***E*lectrooculogram (EOG) signal is the physiological signal that represents the eye ball movements. In this paper, the behavior of EOG signal is studied from the nonlinear and chaotic viewpoint using Hurst exponent, Iterated Function System (IFS) plot, average mutual information and Lyapunov exponent. Our findings indicate that the EOG signal has deterministic chaotic characteristics and therefore can be used in prediction and/or detection purposes.**

Keywords- **Electrooculogram, Chaos, phase plot, Hurst Exponent, Iterated Function System (IFS), Lyapunov Exponent**

I. INTRODUCTION

The Electrooculogram signals or simply EOG represent the eye balls movements. The waveform contains useful information about the movement of the eye balls and generally it may also represent the overall condition of the human subject such as the state of drowsiness of the subject. The EOG signal when extracted and analyzed using computers, are highly useful in detecting changes in the states of the subject and could be useful in applications such as wake-sleep detection and human-computer interface (HCI) [1,2]. Such application can be further enhanced if some form of prediction is available. The time plot of the EOG signal as shown in Fig. 1 depicts somewhat random characteristic. Randomness in data structure does not allow any form of time series prediction. Therefore, in this paper, we intend to prove that the EOG data structure is not random but instead it is chaotic. Consequently, we will consider the use of nonlinear tools to exhibit the chaotic behavior of the EOG signals. Such chaotic nature would make the data valid for prediction purpose.

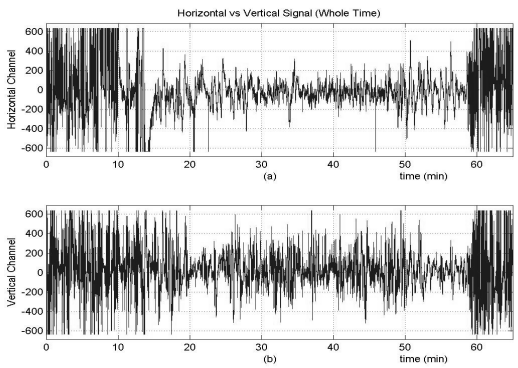

Fig.1. A typical EOG signals: horizontal (top) and vertical (bottom) channels

II. EOG SIGNAL

EOG is the recording of the standing corneal retinal potential arising from hyperpolarizations and depolarizations existing between the cornea and the retina. This potential can be considered as a steady electrical dipole with a negative pole at the fundus and a positive pole at the cornea. This standing potential in the eye can thus be estimated by measuring the voltage induced across a system of electrodes placed around the eyes as the eye gaze changes. EOG signal varies from 50 to 3500 V in magnitude with a frequency range of about dc-100 Hz. Its behavior is practically linear for gaze angles of – 30°. It should be pointed out that the variables measured in the human body (any biopotential) are rarely deterministic. Its magnitude varies with time, even when all possible variables are controlled.

Most of these biopotentials vary widely even under similar measuring conditions which means that the EOG readings variability are due to many factors that are difficult to determine. Perturbations may be due to other biopotentials such as EEG, electromyogram (EMG) and those of the acquisition system devices. Additional causes include positioning of electrodes, skin-electrode contacts, lighting conditions, head movements, blinking etc. [3]. Various studies were made of the accuracy and precision of the EOG in tracking the eye gaze [4]. The EOG signals, by nature, are corrupted by a variety of noises that continually vary due to temporal changes in their sources.

III. CHAOTIC INDICATOR

Three schemes are considered to explore the nature of EOG signals. The schemes are the Hurst exponents, Iterative Function System (IFS) plots and Largest Lyapunov Exponent. The quantitative schemes involves Hurst Exponent and Lyapunov Exponent calculations where as the qualitative scheme involves IFS computation. A brief explanation of Hurst Exponent is given first followed by explanation on IFS and Largest Lyapunov Exponent.

F. Ibrahim, N.A. Abu Osman, J. Usman and N.A. Kadri (Eds.): Biomed 06, IFMBE Proceedings 15, pp. 355-359, 2007
www.springerlink.com ' Springer-Verlag Berlin Heidelberg 2007

A. Hurst Exponent

The Hurst exponent, proposed by H.E. Hurst exponent is a measure for long-term memory and fractional Gaussian process (fractal) of a time series. It is based on the rescaled range analysis (R/S analysis) and the Hurst exponent, H, is defined as:

$$H = \frac{\log(R/S)}{\log(T)} \quad (1)$$

where T is the duration of the sample of data and R/S is the corresponding value of rescaled range [5]. Hurst exponent usage in fractal analysis has been applied to many research fields. Since it is robust, with few assumptions about the underlying system, it has broad applicability for time series analysis. The value of the Hurst exponent ranges between 0 and 1. A time series can be classified into three categories based on the Hurst exponent value H, that is,

- when H=0.5, it indicates a random series.
- when 0<H<0.5, it indicates an anti-persistent series.
- when 0.5<H<1 indicates a persistent series.

An anti-persistent series has a characteristic of mean reverting , meaning an upward value is very likely to be followed by a downward value and vice versa. The strength of mean reverting increases as H approaches zero. On the other hand, as H approaches 0.5, the series is getting more and more random in nature. Additionally, a persistent series is trend reinforcing, which means the direction of the next value is more likely the same as current value. For example, if the current direction is upward, it is very likely that the next will also have the upward trend. The strength of trend increases as H approaches 1.0.

B. Iterative Function System (IFS)

The IFS is the qualitative scheme to characterize chaos. IFS, short for Iterative Function System, is quite new in which, the structure of time series is visualized and derived from the return map of the fractal structure. Modern ideas about nonlinear dynamics are often presented in geometric term or pictures [6]. One way to visualize contradiction between chaotic signal and random walk signal is through IFS. The IFS plot of a chaotic signal shows a structured format where as a random signal tends to be scattered and does not show any structured format. The algorithm to calculate IFS can be found in [7].

C. Largest Lyapunov Exponent

Lyapunov exponents determine the initial rate of divergence or convergence of nearby trajectories in phase space[8]. In general, an m-dimensional system has m different Lyapunov exponents λ_i , where $i = 1, 2, \ldots, m$. They can be ordered from the largest to the smallest, thereby forming the Lyapunov exponents spectrum (λ_1, λ_2, , λ_m). It has been shown that the sign of each Lyapunov exponent uniquely determines the system attractor. Specifically, negative exponent indicates the presence of a fixed point, zero largest Lyapunov exponent indicates a limit cycle and positive largest Lyapunov exponent shows chaotic attractor. But, the most important observation is that the largest Lyapunov exponent λ_{max}, can uniquely determines whether the system is chaotic or not. If $\lambda_{max} > 0$, it implies that there are two initial nearby trajectories of the attractor that diverge exponentially fast as time progresses. This behavior constitutes the extreme sensitivity to changes in initial conditions, which is the hallmark of chaos. In this work, an algorithm developed by [9], which implements the theory in a simple and direct way, is presented. The first step of the algorithm engages in finding the nearest neighbor of the initial point

$$P(0) = (x_0, x_{0+\tau}, x_{0+2\tau}, \ldots, x_{0+m\tau}) \quad (2)$$

Let L_0 denotes the Euclidean distance between two points. Then, both points have to be iterated forward for a fixed evolution time t, which should be of the same order of magnitude as the embedding delay τ. Let the final distance between the evolved points be known as L_{evolv}. Typically, if the attractor is chaotic, L_{evolv} will be larger than L_0, whereas in the case of periodicity $L_{evolv} \approx L_0$. In practice, however, this is true only if t is chosen small enough (usually $\leq m\tau$) so that the initial length element L_0 is propagated only through the small-scale structure of the attractor. To be exact, if t is too large, there is a possibility that the two trajectories defining L_0 will pass through a folding region of the attractor causing, $L_{evolv} < L_0$, and eventually leads to an underestimation of the largest Lyapunov exponent λ_{max}. After each t, a replacement step is executed to search for a new point in the embedding space whose distance to the evolved initial point is as small as possible, under the constraint that the angular separation between the evolved and replacement element is also small. This procedure is repeated until the initial point $P(0)$ reaches the end of the time series. Finally, λ_{max} is calculated according to equation (3) shown below;

$$\lambda_{\max} = \frac{1}{Mt}\sum_{i=0}^{M} \ln \frac{L^{(i)}{}_{evolv}}{L_0^{(i)}} \quad (3)$$

where M is the total number of replacement steps.

F. Ibrahim, N.A. Abu Osman, J. Usman and N.A. Kadri (Eds.): Biomed 06, IFMBE Proceedings 15, pp. 355-359, 2007
www.springerlink.com ' Springer-Verlag Berlin Heidelberg 2007

IV. RECONSTRUCTION OF PHASE SPACE

In using Lyapunov exponent as an indicator to determine chaos, an important procedure of reconstruction of phase space needs to be considered. The key idea is to view the underlying dynamic structure of the EOG signal. Such dynamic takes place in a space of vectors $y(t)$ of larger dimension and to view it, one must project it down on the axis of the observed variable. As an example, the horizontal EOG signal is used in this study, which has the time sequence of the form $\{x_0, x_1, x_2, ., x_i, ., x_n\}$, where x_i denotes the signal at time i. Accordingly, one can identify a space formally equivalent to the original space of variables using coordinates made out of the observed variables and its time delayed copies [10]. The reconstructed attractor of the original system is given by the vector sequence as shown in equation (4);

$$y(t) = [x(t), x(t+\tau), x(t+2\tau), ...x(t+(m-1)\tau)] \qquad (4)$$

where τ and m are the embedding delay and the embedding dimension, respectively. The famous theorem by Takens states that for a large enough m, this procedure, known as delay coordinate embedding provides a one-to-one image of the original system [10]. As such, the mathematical properties (e.g. its dimension, Lyapunov exponents etc) of the constructed attractor are the same as the original system. Although the delay coordinate embedding concept may seem somewhat mystic, in particular the fact that one can reconstruct the whole phase space of a system from a single scalar measurement, there exist a rather intuitive explanation of why the reconstruction can be made.

According to [11], all variables in a nonlinear process are generically connected, i.e. they influence one another. Thus, every subsequent point of a given measurement x_i is the result of an entangled combination of influences from all other system variables. Consequently, $x(t + \tau)$ may be viewed as a substitute second system variable, which carries information about the influences of all other variables during time τ. With the same reasoning, one can introduce the 3rd, 4th, ..., m^{th} substitute variables of $x(t+2\tau)$, $x(t+3\tau), ..., x(t+(m-1)\tau)$, respectively, and thus obtained the whole m-dimensional phase space where the substitute variables incorporate all influences of the original system variables, provided that m in equation (3) is large enough.

To successfully reconstruct the attractor using equation (1), appropriate values for τ and m have to be determined. For estimation of τ, two criteria are important. First, τ has to be large enough so that the information we get from measuring the value of x at time $i + \tau$ is significantly different from the information we already have by knowing the value of x at time i. Only then will it be possible to gather enough information about all other system variables that influence the value of x to reconstruct the whole attractor. Second, τ should not be larger than the typical time in which the system loses memory of its initial state. This is particularly important for chaotic systems, which are intrinsically unpredictable and hence lose memory of the initial state as time progresses.

Following this reasoning, Fraser and Swinney [12] introduced the mutual information (MI) between $x(t)$ and $x(t+\tau)$ as a suitable quantity for determining τ. The MI between $x(t)$ and $x(t+\tau)$ quantifies the amount of information we have about the state $x(t+\tau)$ presuming that we know the state $x(t)$. Given a time series of the form $\{x_0, x_1, x_2, ., x_i, ., x_n\}$, one has to find the minimum x_{min} and the maximum x_{max} of the sequence. Then, the absolute value of their difference $|x_{max} - x_{min}|$ has to be partitioned into j equally sized intervals, where j is a large enough integer. Finally, one calculates the expression

$$I(\tau) = -\sum_{h=1}^{j}\sum_{k=1}^{j} p_{h,k}(\tau) \ln \frac{p_{h,k}(\tau)}{P_h P_k} \qquad (5)$$

where P_h and P_k denote the probabilities that the variable assumes a value inside the h^{th} and k^{th} bins, respectively, and $P_{h,k}(\tau)$ is the joint probability that x(t) is in bin h and $x(t+\tau)$ is in bin k. To have better understanding of equation (2), let us consider a limit example. In the case of chaotic behavior $I(\tau) \rightarrow 0$ as $\tau \rightarrow \infty$, since x(t) and $x(t+\tau)$ are then no longer correlated, and thus $P_{h,k}(\tau)$ factorizes to $P_h P_k$ yielding zero in equation (5). In general, we are interested in minima of $I(\tau)$. At the first minimum of $I(\tau)$, $x(t+\tau)$ adds the largest amount of information to the information we already have by knowing x(t), without completely losing the correlation between them [13]. Hence, the first minimum of $I(\tau)$ marks the optimal choice for the embedding delay. The first minimum of $I(\tau)$ for the horizontal EOG signal of Fig. 1, is located at $\tau = 4$.

To determine the proper embedding dimension m, we use the FNN method. The method relies on the assumption that an attractor of a deterministic system folds and unfolds smoothly with no sudden irregularities in its structure. Therefore, points that are close in the reconstructed embedding space have to stay sufficiently close also during forward iteration. If this criterion is met, then under some sufficiently short forward iteration the distance between two points $P(i)$ and $P(j)$ of the reconstructed attractor, which are initially only a small ε apart, cannot grow further as $R_{tr}\,\varepsilon$, where R_{tr} is a given constant.

However, if an i^{th} point has a close neighbor that does not fulfill this criterion, then this i^{th} point is marked as having a false nearest neighbors (FNN). We have to minimize the fraction of points having a FNN by choosing a sufficiently large m. If m is too small, two points of the attractor may

F. Ibrahim, N.A. Abu Osman, J. Usman and N.A. Kadri (Eds.): Biomed 06, IFMBE Proceedings 15, pp. 355-359, 2007
www.springerlink.com ' Springer-Verlag Berlin Heidelberg 2007

solely appear to be close, whereas under forward iteration they are mapped randomly due to projection effects. The random mapping occurs because the whole attractor is projected onto a hyperplane that has a smaller dimensionality than the actual phase space and so the distances between points became distorted. To calculate the fraction of FNN, the following algorithm is used.

Given a point $p(i)$ in the m-dimensional embedding space, first, one has to find a neighbor $p(i)$, so that $\|p(i) - p(j)\| < \varepsilon$, where $\|..\|$ is the square norm and ε is a small constant usually not larger than the standard deviation of data. We then calculate the normalized distance between the $(m+1)^{th}$ embedding coordinate of points $p(i)$ and $p(j)$ according to equation (6); if this amount is larger than a given threshold R_{tr}, then, $p(i)$ is marked as having a FNN.

$$\frac{\left|x_i(t+m\tau) - x_j(t+m\tau)\right|}{\|p(i) - p(j)\|} > R_{tr} \qquad (6)$$

Equation (5) has to be applied for the whole time series and for various m = 1,2,... until the FNN amounts asymptotically approach zero. According to [14], R_{tr}= 10 has proven to be a good choice for most data sets. The results obtained with the FNN method could be well shown that the fraction of FNN approach to zero for m = 9.

V. RESULTS & DISCUSSION

The Hurst exponent of the EOG signals were computed using the algorithm described earlier. Both horizontal and vertical channels of the raw EOG signals are analyzed and their Hurst exponents computed. The Hurst Exponents of the raw EOG signals are 0.8894 and 0.9371 for the horizontal and vertical channel, respectively. Next, the EOG data was scrambled and the Hurst exponent calculation repeated. After scrambling, the Hurst exponents are found to be 0.5595 for the horizontal EOG and 0.5398 for the vertical EOG. These results showed that scrambling changes the EOG signals from a structured data type to a random type. Next, the IFS plot is generated using four bins. There are a variety of methods to perform bin selection. In this work, we have used the equal size bin. Fig. 2(a) depicts the IFS plot of the original horizontal EOG signal where as Fig. 2(b) shows the IFS plot of its scrambled signal. Fig. 2(c) on the other hand depicts the IFS plot of a random signal. The results using IFS agree with the results using Hurst exponent. It is easily seen that after scrambling, its IFS plot is very similar to the IFS of a random signal; however before scrambling a structure could be distinguished in its IFS plot.

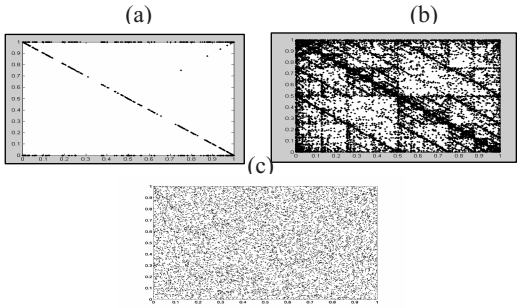

Fig. 2. The IFS plots of (a) raw horizontal EOG signal, (b) scrambled horizontal EOG signal & (c) a randomly generated signal.

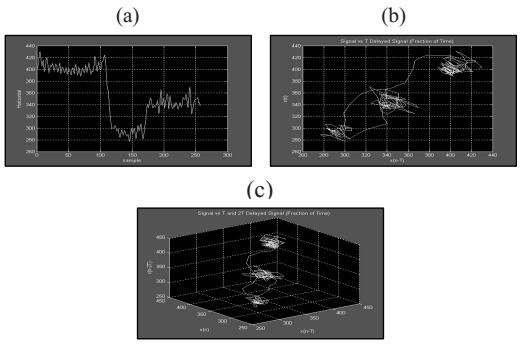

Fig. 3. Plots of 1 sec duration of (a) horizontal EOG signal (b) its 2D reconstructed Phase Space & (c) its 3D reconstructed Phase Space

Using equation (5) shown previously, the largest Lyapunov exponent for the reconstructed attractor of horizontal EOG is calculated. The largest Lyapunov exponent converges to λ_{max} = 0.04. This is a firm proof for the chaotic behavior of the studied signal. As aforementioned, the value of the largest (positive) Lyapunov exponent represents the extent to which initially nearby trajectories diverge from each other. Having calculated the optimal embedding delay and embedding dimension as explained in section 4, we are able to successfully reconstruct the attractor. The reconstruction results of the horizontal EOG channel in 2-D and 3-D phase space plots are shown in Fig. 3 (b) and (c), respectively. Fig. 3(a), on the other hand, illustrates the horizontal EOG signal. The correct reconstruction of the attractor is a key step towards establishing whether the experimentally observed behavior originated from a deterministic chaotic system, since it enables us to calculate the largest Lyapunov exponent.

F. Ibrahim, N.A. Abu Osman, J. Usman and N.A. Kadri (Eds.): Biomed 06, IFMBE Proceedings 15, pp. 355-359, 2007
www.springerlink.com ' Springer-Verlag Berlin Heidelberg 2007

VI. CONCLUSION

In this work, we have systematically analyzed the EOG signal using basic methods of nonlinear time series approach. We found that short, densely sampled EOG recordings possess properties that are typical of deterministic chaotic systems. In conclusion, we believe that the methods described in this paper represent an excellent starting point for more advanced studies, such as wavelet analysis to determine different states using the bio physiological signals or applications of nonlinear state-space projections to extract information from EOG.

REFERENCES

1. Dinesh Kumar, Eric Poole, Classification of EOG for Human Computer Interface ; Proceedings of second joint EMBS/BMES Conference Houston, TX, USA.
2. Robert J.K. Jacob. "Eye Movement-Based Human-Computer interaction Techniques: Toward Non-Command Interfaces". Human-Computer Interaction Lab. Naval Research Laboratory. Washington, D.C.
3. A. W. North, Accuracy and precision of electrooculographic recording , Invest. Ophthalmol., vol. 4, pp. 343 348, 1965.
4. Rafael Barea, Luciano Boquete, Manuel Mazo, and Elena López ; System for Assisted Mobility Using Eye Movements Based on Electrooculography ; IEEE Transactions on Neural Systems and Rehabilitation Engineering, Vol. 10 No. 4, December 2002; pp. 209-218.
5. Carbone, A., Castelli, G., and Stanley, H.E., Time dependent Hurst exponent in financial time series Physica A journal, 344, 2004.
6. Francis C. Moon; Chaotic Vibration; Wiley; 2004. p19.
7. Michael Barnsley, eds. 1988, Fractal everywhere , Academic Press Professional.
8. Ott, E. 1993. Chaos in Dynamical Systems (Cambridge: Cambridge University Press)
9. Wolf, A., Swift, J. B., Swinney, H. L. and Vastano, J. A. 1985. Determining Lyapunov exponents from a time series. Physica D 16: pp 285 317
10. Takens, F. 1981. Detecting Strange Attractor in Turbulence (Lecture Notes in Mathematics vol. (898) eds. D A. Rand and L. S. Young (Berlin: Springer) p. 366
11. Abarbanel, H. D. I. 1996 Analysis of Observed Chaotic Data (New York: Springer)
12. Fraser, A. M. and Swinney, H. L. 1986 Independent coordinates for strange attractors from mutual information Phys. Rev. A 33: pp 1134 40
13. Kaplan, D. T. and Glass, L. 1992. Direct test for determinism in a time series. Phys. Rev. Lett. 68: 427 30.
14. Kennel, M. B., Brown, R. and Abarbanel, H. D. I 1992. Determining embedding dimension for phase space reconstruction using a geometrical construction. Phys. Rev. A (45): pp 3403 11.

Address of the corresponding author:

Author: S. Farshad Hendi
Institute: Dept. of Electrical, Electronic & Systems Engineering,
Faculty of Engineering,
Universiti Kebangsaan Malaysia
City: Bangi, Selangor
Country: Malaysia.

F. Ibrahim, N.A. Abu Osman, J. Usman and N.A. Kadri (Eds.): Biomed 06, IFMBE Proceedings 15, pp. 355-359, 2007
www.springerlink.com ' Springer-Verlag Berlin Heidelberg 2007

Classification of Electrocardiogram Signal using Multiresolution Wavelet Transform and Neural Network

M.F.M. Elias, H. Arof

Department of Electrical Engineering, Faculty of Engineering, University of Malaya, Malaysia

Abstract—**This paper discusses on the classification of electrocardiogram (ECG) signal using multiresolution wavelet transform and neural network. Multiresolution wavelet transform is used as a method of feature extraction of ECG signal since it has the ability to analyze the signal both in time and frequency domain. Neural network is used because of its ability to learn and perform classification on ECG signal. In this paper, four type of ECG signal has been chosen for classification. Based on the data obtained from MIT-BIH Arrhythmia Database the classification rate is found to be 95.08%.**

Keywords—**Electrocardiogram, multiresolution, wavelet transform, neural network, classification.**

I. Introduction

In the present world of medicine, digital signal processing has been increasingly popular for assisting doctors in making decision for particular problems. In the case of detecting heart disease for example, this can be done by applying digital signal processing on ECG signal. ECG signal is the recording of electrical activity generated by the cells of the heart that reaches the body surface. The signal can be obtained by placing recording electrodes at certain body points. With digital signal processing, automatic classification or interpretation of ECG signal is possible. To date, researchers are still looking for the best algorithms that can gives the best classification with as high classification rate as possible. Many classification methods can be used such as template matching, Hidden Markov models, Fourier transform, neural network and so on. In this paper, classification method using wavelet transform and neural network will be discussed.

II. Wavelet theory

A. Discrete Wavelet Transform

In general, any signal or function g(t) $\in L^2$ can be represented by using scaling function and wavelet function as given by the following equation.

$$g(t) = \sum_{k=-\infty}^{\infty} c(k)\varphi_k(t) + \sum_{j=0}^{\infty}\sum_{k=-\infty}^{\infty} d_j(k)\psi_{j,k}(t) \qquad (1.1)$$

where $\varphi_k(t)$ is the scaling function at scale j=0 and $\psi_{j,k}(t)$ is the wavelet function at various j and k scales. $c(k)$ and $d_j(k)$ are called discrete wavelet transform (DWT) coefficients. Scaling function and wavelet function are required to be orthogonal such that

$$<\varphi_{j,k}(t), \psi_{j,k}(t)> = \int \varphi_{j,k}(t)\psi_{j,k}(t)dt = 0 \quad j,k \in Z \qquad (1.2)$$

This enables the DWT coefficients to be calculated by taking its inner product.

$$c(k) = <g(t), \varphi_k(t)> = \int g(t)\varphi_k(t)dt \qquad (1.3)$$

$$d_j(k) = <g(t), \psi_{j,k}(t)> = \int g(t)\psi_{j,k}(t)dt \qquad (1.4)$$

Deriving from the mother wavelet, the scaling function is defined as

$$\varphi(t) = \sum_n h(n)\sqrt{2}\varphi(2t-n) \qquad (1.5)$$

where $h(n)$ is the scaling function coefficient.
Since both functions are required to be orthogonal, this leads the wavelet function to be defined as

$$\psi(t) = \sum_n h_1(n)\sqrt{2}\varphi(2t-n) \qquad (1.6)$$

where $h_1(n)$ is the wavelet function coefficient.

The relationship between $h(n)$ and $h_1(n)$ is given by

$$h_1(n) = (-1)^n h(N-1-n) \qquad (1.7)$$

for even length-N $h(n)$. In most practical application, scaling function and wavelet function have never been used explicitly. Instead, only their function coefficients are used. It is noted that different type of wavelet will have different type of coefficients, $h(n)$ and $h_1(n)$. This coefficients can be obtained by solving the minimum properties on the $h(n)$ comprising normalization, double shift orthogonality and K-regular scaling filter requirements [1] .

F. Ibrahim, N.A. Abu Osman, J. Usman and N.A. Kadri (Eds.): Biomed 06, IFMBE Proceedings 15, pp. 360-364, 2007
www.springerlink.com ' Springer-Verlag Berlin Heidelberg 2007

B. Multiresolution Wavelet Transform

Multiresolution wavelet transform is designed to decompose a signal into finer and finer details at several levels. At each level, applying a signal with discrete wavelet transform decomposes the signal into two parts containing high frequency and low frequency components. High frequency component is represented by coefficient $d(k)$ whereas the low frequency component is represented by $c(k)$. This is obtained by using (1.8) and (1.9) which is derived from (1.3) and (1.4) [1].

$$c_{j-1}(k) = \sum_m h(m-2k)c_j(m) \quad (1.8)$$

$$d_{j-1}(k) = \sum_m h_1(m-2k)c_j(m) \quad (1.9)$$

$c_j(k)$ and $c_{j-1}(k)$ are the coefficients at higher and lower scales respectively. It is noted that the DWT coefficients at different levels of scale can be obtained by convolving the coefficients $c(k)$ at scale j by the time reversed recursion $h(-n)$ and $h_1(-n)$ then down sampling to give the DWT coefficients at the lower level of j-1. Figure below shows two-level signal decomposition using multiresolution wavelet transform for instance.

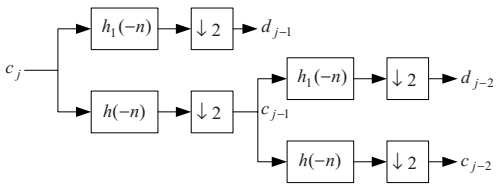

Fig. 1 Two-level signal decomposition using multiresolution wavelet transform

Basically, a signal is decomposed into several level to find the important information it contained. The number of decomposition level depends on the length of the original signal. Further decomposition is using the low frequency content, $c(k)$ of a signal.

III. Neural Network

A. Multi-layer Perceptron

Multi-layer perceptron (MLP) neural network are the configurations of simple perceptron in a hierarchical structure. The structure basically has three layers which are input layer, hidden layer and output layer. Figure 2 shows three-layer MLP.

B. Back-propagation Learning Algorithm

Back-propagation (BP) is a general purpose learning algorithm for training MLP neural network. Two major learning parameters are used to control the training process of a back propagation network. The learning rate, η/μ is used to specify whether the neural network is going to make major adjustments after each learning trial or if it is only going to make minor adjustments. Momentum, α/β is used to control possible oscillations in the weights, which could be caused by alternately signed error signals. A summary of back propagation algorithm is as follows [2].

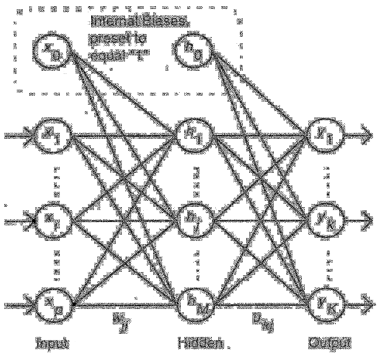

$$h_j = f_j\left(\sum_{i=0}^{p} w_{ji}x_i\right) \quad (2.0)$$

for $j = 1, 2, ..., M$

$$y_k = f_k\left(\sum_{j=0}^{M} u_{kj}h_j\right) \quad (2.1)$$

for $k = 1, 2, ..., K$

$$f(z) = \frac{1}{1+e^{-z}} \quad (2.2)$$

Fig. 2 Three-layer MLP

Weight updates for each new training vector pair:

$$u_{kj}(t+1) = u_{kj}(t) - \eta\delta y_k h_j + \beta[u_{kj}(t) - u_{kj}(t-1)]$$

for $k = 1, ..., K$, and $j = 0, ..., M$ (2.4)

$$w_{ji}(t+1) = w_{ji}(t) - \mu\delta h_j x_i + \alpha[w_{ji}(t) - w_{ji}(t-1)]$$

for $j = 1, ..., M$, and $i = 0, ..., p$ (2.5)

where

$$\delta y_k = (y_k - d_k)y_k(1-y_k) \quad (2.4)$$

$$\delta h_j = \sum_{a=1}^{K}[\delta y_a u_{aj}]h_j(1-h_j)] \quad (2.5)$$

IV. Methodology

A. Data Pre-processing

The ECG data used in this study was obtained from MIT-BIH Arrhythmia Database which is the standard material used for research purpose in ECG signal. There are four types of ECG signal has been chosen for classification. They are denoted by N, V, R and L. N indicates normal signal pattern, V indicates ventricular premature beat, R and L indicate right bundle branch block and left bundle branch block respectively. These signals were obtained from ECG Lead II sam-

F. Ibrahim, N.A. Abu Osman, J. Usman and N.A. Kadri (Eds.): Biomed 06, IFMBE Proceedings 15, pp. 360-364, 2007
www.springerlink.com ' Springer-Verlag Berlin Heidelberg 2007

pled at 360Hz. All these signals are different in their shape, even in each type as well. In this study, the signal will be classified mainly based on the QRS complex morphology. Therefore, this type of data must be extracted from the recording signal for each signal type. QRS complex is defined at 100ms before and 150ms after R peak of ECG signal. The data for each signal type is randomly selected from the database which will be used for neural network training. Table 1 below shows the number of data associated with the ECG signals and the recording number where they were obtained.

Table 1 ECG data

ECG Signal	Total Data	Recording Number
N	65	100, 105, 106, 116, 212
V	75	105, 106, 109, 116, 118, 214
R	45	118, 124, 212
L	35	109, 214

ECG signal basically varying in nature, therefore it must be normalized first before the important information is extracted from it. Normalization sets the signal to have the mean and standard deviation equal to 0 and 1 respectively. The extracted ECG signal N, V, R and L after normalization is shown in Figure 3.

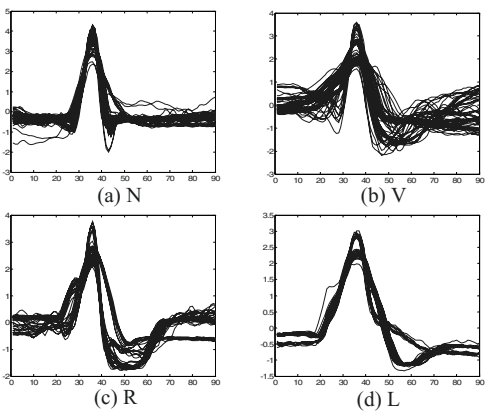

Fig. 3 Normalized QRS complex

B. Feature Extraction

In this study, ECG signal is decomposed into five-level by using DWT. Four types of wavelet are tested to find the best wavelet for decomposition. They are Haar, Daubechies, db2, db3 and db4 wavelets. The selection of wavelet is incorporated with the neural network architecture.

In this study, all DWT coefficients, $c(k)$ and $d(k)$ at particular decomposition level are tested as the neural network input. The neural network training performance in terms of the number of epochs as well as mean square error is compared between coefficients set at different level. The coefficients set that give the best tradeoff will be chosen for feature extraction. In this study, the number of perceptron used in the hidden layer is 20 and the number of output is 4, which is the same as the number of ECG signal to classify.

C. Testing and Classification

The best wavelet selected is used for feature extraction of ECG signal. The coefficients set that give the best tradeoff is fed to the neural network input. The number of neural network input will be the same as the number of coefficients set chosen. The number of perceptron in the hidden layer and the output layer will remain the same. The neural network parameters will be using the same parameters used during training with coefficients set selected. The neural network is not only tested with the training data but also with the actual ECG data recorded from MIT-BIH Arrhythmia Database. This is possible because the classification for each ECG beat is provided for comparison purpose.

V. Result and Discussion

The result obtained is based on the following parameters used for configuring the neural network.

Learning algorithm: Adaptive learning rate with momentum
Learning rate: 0.05
Learning rate increment: 1.05
Learning rate decrement: 0.7
Momentum coefficient: 0.9
Maximum epochs: 50000
Mean square error goal: 0.01

F. Ibrahim, N.A. Abu Osman, J. Usman and N.A. Kadri (Eds.): Biomed 06, IFMBE Proceedings 15, pp. 360-364, 2007
www.springerlink.com ' Springer-Verlag Berlin Heidelberg 2007

Table 2 Performance comparison of different wavelets

	Haar			Db2			Db3			Db4		
	Num. of Coef	Epoch	MSE	Num. of Coef	Epoch	MSE	Num. of Coef	Epoch	MSE	Num. of Coef	Epoch	MSE
Level1	92	1738	0.01	90	4390	0.01	94	1287	0.01	96	1082	0.01
Level2	48	4860	0.01	46	9649	0.01	52	5109	0.01	54	7210	0.01
Level3	26	28373	0.01	24	43093	0.01	30	11277	0.01	34	16231	0.01
Level4	16	50000	0.0197	12	50000	0.0362	20	50000	0.0111	24	50000	0.0197
Level5	10	50000	0.0777	6	50000	0.185	14	50000	0.0618	18	50000	0.0777

Table 3 Classification results

	Number of Misclassification								
Recording Number Period	100	105	106	109	116	118	124	212	214
0s 180s	1	1	14	7	0	0	20	3	33
180s 360s	0	13	1	23	0	2	45	10	18
360s 540s	0	0	2	8	3	27	12	25	11
540s 720s	0	26	2	3	1	0	29	25	13
720s 900s	0	15	24	12	1	17	18	1	8
Total Misclassification	1	55	43	53	5	46	124	64	83
Total Beat	1141	1283	1046	1272	1185	1157	798	1405	1157
Misclassification Rate (%)	0.088	4.287	4.111	4.167	0.422	3.976	15.539	4.555	7.134
Misclassification Average (%)	4.924								

Based on the results obtained in Table 2, it is found that Daubechies, Db3 wavelet gives the smallest number of epochs or mean square error. This implies that it differentiate the ECG signals best. The DWT coefficients selected for neural network input is obtained at level 4 because it gives very small mean square error that is close to the goal value even though the number of epochs reached the maximum value. At decomposition level 4, the number of coefficients is 20. Even though level 5 has smaller number of coefficients, it has higher mean square error value. In the case of level 1, 2 and 3, they have considerably high number of coefficients while having mean square error the same as the goal value. Higher number of coefficients causes the neural network architecture becomes more complex and hence requires longer computation time. The classification result in Table 3 is obtained by testing the trained neural network with the first 15 minutes or 900s data of all recording data used to acquire the ECG learning data. Based on the results obtained, the overall classification rate is found to be 95.08% which is comparable to the result reported in [4] with different type of recognition system as shown in Table 4.

The lowest misclassification rate is 0.088% for recording data 100 whereas the highest misclassification rate is 15.539% for recording data 124. The classification rate can be increased further if more number of learning data is used.

Table 4 Comparison of different ECG classification methods

Method	**Arrhythmia types**	**Classification rate (%)**
Discrete Wavelet Transform Neural Network	13	96.79
Unsupervised Soft Competitive Learning	5	98.02
Mixture of Experts	4	94.00
Fuzzy Hybrid Neural Network	7	96.06
Fourier Transform Neural Network	3	98.00
Discrete Fourier Transform	10	89.40
Discrete Wavelet Transform	10	97.00
* Multiresolution Wavelet Transform Neural Network	4	95.08

In this study, the number of learning data is only 2.11% of the total number of beats, which is considerably very small. It is noted that the classification based on the QRS pattern depends on the number of learning data used. This means that the learning data should have almost all patterns that represent a particular heart beat condition. The larger the number of learning data, the higher the classification rate will be. But, this will cause more complex neural network architecture to be used and hence takes a longer time for the classification process.

F. Ibrahim, N.A. Abu Osman, J. Usman and N.A. Kadri (Eds.): Biomed 06, IFMBE Proceedings 15, pp. 360-364, 2007
www.springerlink.com ' Springer-Verlag Berlin Heidelberg 2007

VI. Conclusions

In this study, the classification and recognition of ECG signals using multiresolution wavelet transform and neural network has been presented. The ECG signal interpretation is based on the QRS complex pattern obtained from ECG lead II. There are 4 types of ECG signals chosen for classification which are N, V, R and L. The ECG data used in this study has been obtained from MIT-BIH Arrhythmia Database. From the result obtained, the classification rate is equal to 95.08% which is based on signal decomposition using Daubechies, Db3 wavelet and taking coefficients at level 4 decomposition as inputs to the neural network. This is comparable with the classification results reported.

References

1. Primer A, (1998) Introduction to Wavelets and Wavelet Transform, Prentice Hall Inc.
2. Zaknich A, (2003) Neural Networks for Intelligent Signal Processing, World Scientific Publishing.
3. Wagner G.S, (2001) Marriot s Practical Electrocardiography, 10th Edition, Lippincott Williams & Wilkins.
4. Prasad G.K, Sahambi J.S, Classification of ECG Arrhythmias using Multiresolution Analysis and Neural Networks, Conference on Convergent Technologies for Asia-Pacific Region, Vol.. 1 (2003).

Address of the corresponding author:

Author: M.F.M. Elias
Institute: Department of Electrical Engineering, Faculty of Engineering, University of Malaya
City: Kuala Lumpur
Country: Malaysia

F. Ibrahim, N.A. Abu Osman, J. Usman and N.A. Kadri (Eds.): Biomed 06, IFMBE Proceedings 15, pp. 360-364, 2007
www.springerlink.com ' Springer-Verlag Berlin Heidelberg 2007

Comparison of different Montages on to EEG classification

S.C. Ng[1] and P. Raveendran[2]

[1] Department of Biomedical Engineering, University of Malaya, Kuala Lumpur, Malaysia
[2] Department of Electrical Engineering, University of Malaya, Kuala Lumpur, Malaysia

Abstract— **This study is to investigate the effects of different montaging methods on the classification rate. The EEG signal is recorded from the motor cortex region when the subjects tap the keyboard using the left or right index finger. In this experiment, One subject's data is downloaded from the BCI 2003 competition and two other right handed subjects participated in a similar experiment. In this preliminary experimental study, we found that the surface laplacian method outperforms other types of montaging.**

Keywords— **EEG, Classification, Montaging.**

I. Introduction

The classification of intentions base on Electroencephalogram (EEG) brain signals have captured the attention of researchers all over the world. The Brain Computer Interface (BCI) 2005 competition managed to attract 49 research laboratories all over the world to participate [1]. It is interesting to point out that most of the classification methods used in the competition is linear.

In this current study, two different linear classification methods to find threshold will be applied on to different montages of the EEG signal. The purpose is to compare the effects of different montages on to the classification rate of the EEG signal.

II. Distribution separability

Fig. 1 shows the distribution of one feature for 2 classes of data. Both the classes have normal distribution with the first class having a mean of 500 and the second class having a mean of 800. Based on Bayes' Theorem, the optimum discrimination is obtained using the threshold of 650 (shown by the arrow). If an unknown data has a value of less than 650, it should belong to the first class and if its value is more than 650, it belongs to the second class.

A simple way to find this threshold value is by using the Fischer's method. The Fischer's method first finds the mean (mean class 1, m_1 and mean class 2, m_2) and standard deviation (standard deviation class 1, σ_1 and standard deviation class 2, σ_2) of both classes. Thus the threshold value will be

$$thres = m_1 + \frac{|m_2 - m_1|}{\sigma_1 + \sigma_2}$$

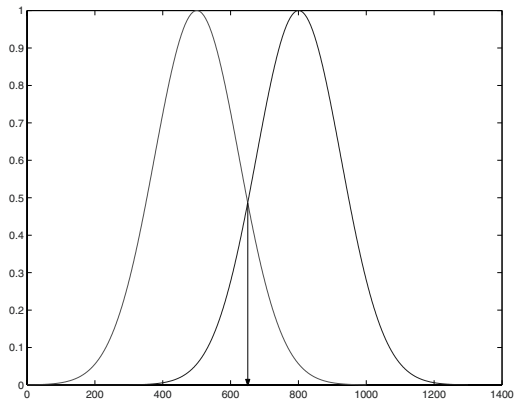

Fig. 1 Probability Density Function of 2 classes of data

Another method of finding the threshold is by sorting the data. Fig. 2 shows the values for 10,000 raw data. It can be seen that the extremely messy data from fig. 2 looks to be a rather smooth curve fig. 3 after being sorted. The curve is a rather straight line for about 80 percent of the time. The distribution acted nonlinearly at the first and last 10 percent of the data.

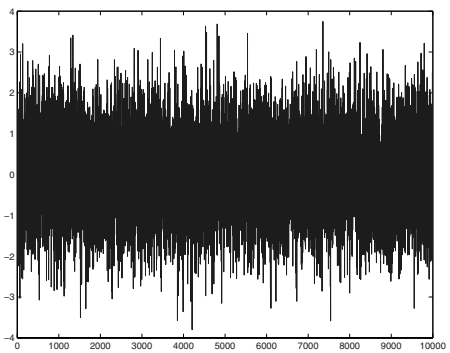

Fig. 2 Raw data

Fig. 4 shows 2 classes of data that are distributed normally. The first class has a mean value of 0 and is sorted from the smallest value to the biggest value for that class. The second class has a mean value of 1 and is sorted from the biggest value to the smallest value for that class. Both graphs intersect at 0.5 for the y-axis and 70 for the x-axis.

F. Ibrahim, N.A. Abu Osman, J. Usman and N.A. Kadri (Eds.): Biomed 06, IFMBE Proceedings 15, pp. 365-368, 2007
www.springerlink.com ' Springer-Verlag Berlin Heidelberg 2007

The optimum threshold value is actually 0.5 and it will give and accuracy of 70 percent. The Fischer's method would have given the same optimum threshold value with the same performance in its accuracy.

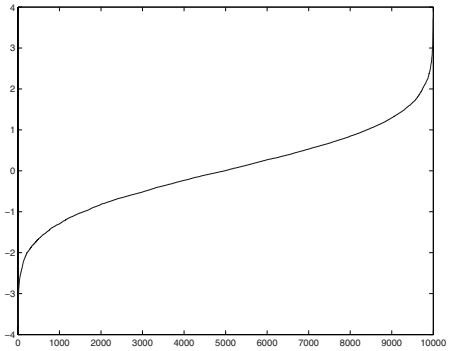

Fig. 3 Sorted Raw data

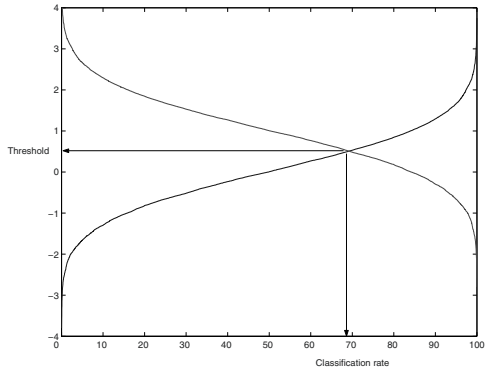

Fig. 4 Sorted data for 2 classses

However, the Fischer's method is based on the assumption that the distribution of the data for both classes is normal. If the set of data has outliers, the value for mean and variance may change significantly and thus produce unstable results. Furthermore, if the data is skewered, the Fisher's method will also not be optimum.

The method of sorting on the other hand does not make any assumption of the distribution. Outliers also do not pose any significant effect on to this method. For this method of sorting to work, the following assumptions must be met.

- The 2 different data sets are discriminable.
- The training data set has a distribution similar to the testing data set.

The strength of this method compared with Fischer's method are:

1. Algorithm very simple to understand
2. Stable to outliers
3. The normal distribution need not be assumed. Most small datasets is not normally distributed.
4. Works equally well for skewered data.

The main weakness of this method compared to Fischer's method is that the computational load involved is higher. However, with more powerful processors, this may not be an issue.

III. Experimental protocol

A. Data Collection

The experimental protocol used here is similar to Blankertz et al.[2]. Their experimental protocol is preferred because it is very easy to set up as well as no human training is required. Data from 3 subjects are used here. The first subject's data is downloaded from the BCI 2003 competition data set IV. The data set for the second and third subject is collected using our own EEG data acquisition machine.

There are some minor differences in the set up of the experiment for subject 2 and 3 as compared to the data of subject 1. The subject is seated on a chair. Both hands are placed on the keyboard where the index finger of both hands is required to tap the keyboard approximately once every 2 seconds. The experiment consists of 3 or 4 sessions of 5 to 6 minutes each. There is a break of 1 minute in between each session.

The electrocap according to the international 10-10 system is used to acquire data. The sampling rate used is 256. In order for the data of subject 2 and subject 3 be make equivalent to the data downloaded for subject 1, only the channels over the motor cortex region is considered. Each epoch of data is obtained from 630ms to 130ms before the finger tap.

Table 1 Differences in the data

Subject	S1	S2	S3
Epoch	416	302	451
Sampling Rate	100	256	256

B. Montaging

Montages are used as a spatial filtering method to enhance relevant signals and suppress noise. Eight different montages have been tested.

1. Common Reference: No remontaging is done
2. Surface Laplacian (4 adjacent): The mean of the 4 adjacent electrodes is removed from the central electrode. E.g. $C3_{SL4}$=C3-(FC3+C1+C5+CP3)/4
3. Surface Laplacian (8 adjacent): The weighted mean (depends on the distance) of the 8 surrounding electrodes is removed from the central electrode. E.g. $C3_{SL8}$= C3-[(FC3+C1+C5+CP3)+0.7(FC5+FC1+CP5+CP1)] /1.7x4)

F. Ibrahim, N.A. Abu Osman, J. Usman and N.A. Kadri (Eds.): Biomed 06, IFMBE Proceedings 15, pp. 365-368, 2007
www.springerlink.com ' Springer-Verlag Berlin Heidelberg 2007

4. Common average reference: The mean of all the electrodes is removed for all the electrodes. E.g. $C3_{CAR}$=C3-(F3+F1+Fz+ +CP2+CP4+CP6)/26
5. Bipolar (front to back): The difference of an electrode with the one behind it. E.g. $C3_{BFB}$= C3-CP3
6. Bipolar (front to back skip 1): The difference of 2 electrodes that lies in front and also behind that electrode. E.g. $C3_{BS1}$= FC3-CP3
7. Bipolar (Symmetrical): The difference of 2 electrodes that is symmetrical to one another. E.g. $C3_{SYM}$= C3-C4
8. Bipolar (left to right): The difference of an electrode with the one right to it. E.g. $C3_{LR}$= C3-C1

IV. Signal processing

The EEG signals are processed using the following steps:

Step 1: The original raw data will be remontage as stated using 1 of the 8 methods stated above. This is the only step that is different for the results obtain. The other steps are the same for all the different remontage data.

Step 2: The raw data will be process for each channel individually. The data will be windowed using a triangle window to reduce spectral leakage. Each data will be padded with 50 zeros (128 zeros for S2 and S3) to increase its frequency resolution from 2Hz to 1Hz. The Fourier Transform will be applied to the data and the Power Spectral Density will be obtained as a feature.

Step 3: Obtain the optimum location, frequency range and threshold value. Since the number of choices is rather limited, an exhaustive search method is used. The optimum value is obtained based on the discriminative accuracy for the distribution of the training data set. The main steps are:

1) Find the discriminative accuracy of each individual frequency for each channel.

2) Sum the adjacent frequency and repeat step 1.

3) Check for the location and frequency range that gives the highest discriminative accuracy. For the current study, the maximum allowable range is a 10Hz band to prevent over training.

Step 4: Find the actual classification rate. Use the optimum values obtain from step 3 to find the classification rate for each type of montage.

The sorting method as well as the Fischer's method is tested and compared with one another.

V. Results and discussion

Based on the result, we can see that Common Reference, Common Average Reference and Bipolar (symmetrical) methods of referencing produce unacceptable classification rate for all the 3 subjects using the 8 different montages (assume that 60 percent is the minimum acceptable classification rate).

Table 2 Classification Rate for S1 (Sorting Method)

Montage	Location	Frequency	Percentage
Common Reference	C4	15-19	58
Surface Laplacian (4 adjacent)	C4	20-28	78
Surface Laplacian (8 adjacent)	C4	21-27	74
Common Average Reference	CP4	1	51
Bipolar (Front to Back)	FC3-C3	12-21	64
Bipolar (Front to Back skip 1)	F4-C4	15-24	68
Bipolar (Symmetrical)	CP3-CP4	1	58
Bipolar (Side to Side)	C2-C4	14-21	65

Table 3 Classification Rate for S2 (Sorting Method)

Montage	Location	Frequency	Percentage
Common Reference	FC1	26-29	57
Surface Laplacian (4 adjacent)	C3	11-12	65
Surface Laplacian (8 adjacent)	C4	23-24	65
Common Average Reference	FC1	3	54
Bipolar (Front to Back)	FC4-C4	11-20	67
Bipolar (Front to Back skip 1)	FC3-CP3	11-12	62
Bipolar (Symmetrical)	CP1-CP2	11	57
Bipolar (Side to Side)	CPz-CP2	11-13	68

Table 4 Classification Rate for S3 (Sorting Method)

Montage	Location	Frequency	Percentage
Common Reference	CP5	12-13	63
Surface Laplacian (4 adjacent)	C4	12-15	70
Surface Laplacian (8 adjacent)	C4	11-18	72
Common Average Reference	C4	47-48	56
Bipolar (Front to Back)	C4-CP4	12-14	72
Bipolar (Front to Back skip 1)	FC4-CP4	12-13	74
Bipolar (Symmetrical)	C1-C2	17	51
Bipolar (Side to Side)	C1-C3	13-22	70

It is obvious that Common Reference will not produce high classification rate as certain noise factor may contaminate the data. Common Average Reference does not work well here also although certain studies claim that CAR is a very good method [3]. It should be noted that the proper method of applying CAR requires data from all over the scalp. In this case, the data is only within the motor cortex region. Furthermore, removing the average of the data within the motor cortex region may have removed the key discriminative features along with the noise factor. Bipolar (symmetrical) is a very effective method of removing EOG artifacts. However, the current classification method uses the ERS/ERD of the brain signals in the different hemi-

F. Ibrahim, N.A. Abu Osman, J. Usman and N.A. Kadri (Eds.): Biomed 06, IFMBE Proceedings 15, pp. 365-368, 2007
www.springerlink.com ' Springer-Verlag Berlin Heidelberg 2007

sphere. By montaging them symmetrically, the differences of the ERS/ERD would have been eliminated.

Table 5 Classification Rate for S1 (Fischer s Method)

Montage	Location	Frequency	Percentage
Common Reference	C4	16-25	59
Surface Laplacian (4 adjacent)	C3	20-29	71
Surface Laplacian (8 adjacent)	C3	20-29	74
Common Average Reference	C1	31-40	51
Bipolar (Front to Back)	FC3-C3	22-31	62
Bipolar (Front to Back skip 1)	FC3-CP3	23-32	64
Bipolar (Symmetrical)	CP3-CP4	1-10	59
Bipolar (Side to Side)	C1-C3	18-27	65

Table 6 Classification Rate for S2 (Fischer s Method)

Montage	Location	Frequency	Percentage
Common Reference	FC5	1-10	56
Surface Laplacian (4 adjacent)	C4	21-30	61
Surface Laplacian (8 adjacent)	C4	11-20	57
Common Average Reference	FC5	3-12	45
Bipolar (Front to Back)	C2-CP2	11-20	65
Bipolar (Front to Back skip 1)	FC4-CP4	11-20	63
Bipolar (Symmetrical)	CP1-CP2	10-19	55
Bipolar (Side to Side)	CPz-CP2	11-20	63

Table 7 Classification Rate for S3 (Fischer s Method)

Montage	Location	Frequency	Percentage
Common Reference	CP3	10-19	57
Surface Laplacian (4 adjacent)	C3	7-16	60
Surface Laplacian (8 adjacent)	C3	7-16	61
Common Average Reference	C6	7-16	50
Bipolar (Front to Back)	C4-CP4	12-21	68
Bipolar (Front to Back skip 1)	F3-C3	7-16	58
Bipolar (Symmetrical)	C3-C4	5-14	59
Bipolar (Side to Side)	CP1-CP3	13-22	70

It can be seen that the usage of different montage is suitable for different subjects. The EEG signal of S1 classifies very well when Surface Laplacian is used. The EEG signal of S2 on the other hand does not seem to have much difference for the bipolar methods as well as the surface Laplacian methods. Those methods all give classification in the range of 60 to 70 percent. The same thing can be said about the EEG signal for S3. However, the classification rate for S3 is in the range of 70 to 75 percent.

Different subjects also have different optimum discriminative frequencies. S1 modulates the higher beta frequency (20-28 Hz) to perform the different finger tapping motion. S2 on the other hand show changes in the μ rhythm (11-13Hz) when performing the same motion. Although the μ rhythm of S3 also changes, the optimum frequency is from 12-13 Hz.

The comparison of the sorting method as compared to the Fischer's method indicates that the sorting method generally performs better.

VI. Conclusion

Base on this study, we can see that surface laplacian method outperform the other methods if the discrimination feature used is the ERD/ERS of the brain signals in the different hemisphere.

Acknowledgment

The authors would like to acknowledge the Fraunhofer FIRST, Intelligent Data Analysis Group and CharitØ University Medicine Berlin, Campus Benjamin Franklin, Department of Neurology, Neurophysics Group for S1 data.

References

1. Blankertz, B.; Muller, K.-R.; Krusienski, D.J.; Schalk, G.; Wolpaw, J.R.; Schlogl, A.; Pfurtscheller, G.; Millan, Jd.R.; Schroder, M.; Birbaumer, N. (2006) The BCI competition III: validating alternative approaches to actual BCI problems, IEEE Transactions On Neural Systems And Rehabilitation Engineering, Vol. 14, No. 2, June 2006, pp 153- 159
2. B. Blankertz, G. Curio and Klaus-Robert Mller, Classifying Single Trial EEG: Towards Brain Computer Interfacing, In: T. G. Diettrich and S. Becker and Z. Ghahramani (eds.), Advances in Neural Inf. Proc. Systems 14 (NIPS 01), 2002.
3. Dennis J. McFarland, Lynn M. McCane, Stephen V. David and Jonathan R. Wolpaw (1997), Spatial filter selection for EEG-based communication, EEG Clin. Neurophysiol., Volume 103, Issue 3, pp 386-394

Address of the corresponding author:

Author: Ng Siew Cheok
Institute: Dept. of Biomedical Engineering, University of Malaya
City: Kuala Lumpur
Country: Malaysia
Email: siewcng@um.edu.my

F. Ibrahim, N.A. Abu Osman, J. Usman and N.A. Kadri (Eds.): Biomed 06, IFMBE Proceedings 15, pp. 365-368, 2007
www.springerlink.com ' Springer-Verlag Berlin Heidelberg 2007

Complexity Analysis of Heart Beat Time series by Threshold based Symbolic Entropy

W. Aziz[1,2] and M. Arif[1]

[1] Department of Computer and Information Sciences PIEAS (Nilore) Islamabad Pakistan
[2] Department of Computer and Information Technology AJK University Muzaffarabad (A.K) Pakistan

Abstract—**Complex variations have been observed in heart rate. Analysis of these variations, i.e., heart rate variability (HRV) analysis has become an important non-invasive technique to study the sympathovagal interactions in physiological and pathological conditions. Increasing efforts were made in the development of HRV measures for quantifying heart rate variations in order to make clinically useful assessments of patient welfare. Heart is not a periodic oscillator under normal physiologic conditions and standard linear HRV measures may not be able to detect subtle, but important changes in heart rate time series, whereas, most of nonlinear measures suffer from the curse of dimensionality. To overcome these difficulties, several complexity measures, especially from symbolic dynamics have been proposed. Recently, we have used threshold dependent symbolic entropy to study the dynamics of stride interval time series of control (healthy) and neurodegenerative diseased subjects. Normalized corrected Shannon entropy (NCSE) was used to quantify these dynamics. In this paper, using this technique, we have compared the complexity of normal sinus rhythm (NSR), congestive heart failure (CHF) and atrial fibrillation (AF) subjects. We investigated that the dynamics of healthy (NSR) subjects are more complex than diseased (AF and CHF) subjects within the short range of thresholds.**

Keywords—**HRV analysis, physiological Signals, symbolic entropy, Complexity Analysis,**

I. Introduction

Variability analysis tracks the patterns of change in an individual parameter over time in order to evaluate the state of a complex system, which may be physiological or pathological [1]. One such parameter is heart rate. Heart rate variability (HRV) analysis has become a widely used tool for assessing autonomic neural regulation of heart [2]. The clinical importance of HRV analysis gained popularity in the late 1980 s, when it was confirmed that it is a strong and independent predictor of mortality after an acute myocardic infarction [2].

In 1996, task force of European Society of Cardiology (ESC) and North American Society of Pacing Electrophysiology (NASPE) published standards in HRV analysis proposing several time and frequency domain parameters [2]. Time domain analysis, measures changes in heart rate over time or the intervals between successive normal cardiac cycle [2,3], whereas, frequency domain analysis describes periodic oscillations of the heart rate signal decomposed at different frequencies and amplitudes [2,4]. Heart is not a periodic oscillator under normal physiologic conditions [5] and standard HRV measures may not be able to detect subtle, but important changes in heart rate time series. Nowadays, indices for characterization of the dynamics and complexity of heart rate variability have arisen with promising results [6,7,8]. These indices are robust in the presence of artifacts and are easy for the physicians to understand. Several nonlinear measures have been developed to quantify the dynamics of heart rate fluctuations, but most of these measures suffer from the curse of dimensionality. To overcome these problems several complexity measures have been proposed [10,11,12]. However, there is no straightforward correspondence between entropy and complexity. In traditional entropy based algorithms, entropy increases with the degree of disorder and attains a maximum value for a completely random system. An increase in entropy may not always be associated with the increase in the complexity of the system. For example, a randomized time series has higher entropy than the original time series, although the process of generating surrogate data destroys the correlations and degrades the information content of the original signal [13].

Recently Costa et al proposed a new method termed multiscale entropy (MSE) [13,14] to calculate entropy over multiple scales. They used sample entropy [11], a refinement of the approximate entropy family of parameters [10] introduced by Pincus to quantify regularity of the finite length time series. They employed MSE method to cardiac inter beat interval time series of healthy subjects and pathological subjects (congestive heart failure and atrial fibrillation) and observed that dynamics of healthy subjects are more complex than diseased subjects. To calculate sample entropy, one has to fix the value of the similarity criterion that depends on the standard deviation of the time series. Therefore, results may significantly be affected by non-stationarities, outliers and artifacts.

Recently we have used symbolic measure normalized corrected Shannon entropy (NCSE) was used to study the dynamics of stride interval time series of health control

F. Ibrahim, N.A. Abu Osman, J. Usman and N.A. Kadri (Eds.): Biomed 06, IFMBE Proceedings 15, pp. 369-373, 2007
www.springerlink.com ' Springer-Verlag Berlin Heidelberg 2007

subjects and neurodegenerative disease subjects at different threshold values [9]. The results showed that mean value of NCSE of healthy subjects was greater than that of diseased subjects (ALS, Hunt and Parkinson) and demonstrated that the dynamics of healthy subjects are more complex than pathological subjects at short threshold values. Decrease in NCSE with advanced disease was also observed and study revealed that loss of complexity is generic feature of disease. We have also investigated that physiological signals are more complex than random noisy data at short threshold values [9]. In this paper we have used NCSE to calculate the dynamics of heart beat time series of healthy (NSR) and diseased subjects (CHF and AF) subjects. The results revealed that healthy dynamics are complex at short range of threshold. Student s t-test was used to find the significant difference between the groups and area under receiver operator curve was used to quantify the degree of separation between the groups [15].

II. Materials and methods

A. Symbolic Measure of Complexity

Symbolic dynamics is based on coarse graining of the signal and results depend on how coarse graining is performed. Some microscopic detail of the dynamics may be lost but the coarse dynamics behavior remains and can be analyzed.

Given a RR-interval time series x={x_i, i=1, ,N}. The time series is transformed into symbol sequence x={x_i, i=1, ,N} having fixed number of ξ values labeled from zero to ξ-1. Quantization level 2 (symbols 0 and 1) and following criterion for symbolization is used

$$x^{\xi} = \begin{cases} 1 & |\, x_{n+1} - x_n \,| \geq T \\ 0 & |\, x_{n+1} - x_n \,| < T \end{cases} \quad (1)$$

where T is the threshold. The symbol sequence is then divided to make word sequence of length L of three or more symbols. The number of all possible words is ξ^L. We have used the probability distribution of length 5 words (word consisting of 5 symbols) and thus obtained 32 different types of words (bins). Symbols sequences have been quantified by using Normalized Corrected Shannon entropy (NCSE). Shannon entropy of order L is defined as

$$SE(L,\xi) = -\sum p(x_L^{\xi}).\log_2 p(x_L^{\xi}) \quad (2)$$

Where $p(x_L^{\xi})$ is the probability of x_L^{ξ} being the pattern. The estimate is affected by random error in numbers and also by a systematic error or bias. Eguia et al (2000) report the leading correction for the entropy [16]. The Corrected Shannon Entropy (CSE) can be obtained as

$$CSE(L,\xi) = SE(L,\xi) + \frac{C_R - 1}{2M \ln 2} \quad (3)$$

Where M is the total number of words and C_R is the number of occurring words among the possible words. The value of CSE is maximum for a certain word length L and quantization level ξ, when all M words occurs and they occurs with uniform distribution in a data series. Hence it will be,

$$CSE^{\max}(L,\xi) = -\log_2\left(\frac{1}{M}\right) + \left(\frac{M-1}{2M \ln 2}\right) \quad (4)$$

From the above equation it is clear that the maximum value of CSE will not be same for two different word lengths and as word length L increases, number of words M increases, and hence the maximum value of CSE also increases. Therefore, it is not possible to compare two values of CSE for two different word lengths at same threshold level. To overcome this problem, we propose normalized corrected Shannon entropy (NCSE). The normalizing factor in NCSE will be CSE^{max}, which is the maximum value of CSE for a certain word length L and quantization levelξ. NCSE is defined as

$$NCSE(L,\xi) = \frac{CSE(L,\xi)}{CSE^{\max}(L,\xi)} \quad (5)$$

$$NCSE(L,\xi) = \frac{CSE(L,\xi)}{\left(-\log_2\left(\frac{1}{M}\right) + \left(\frac{M-1}{2M \ln 2}\right)\right)} \quad (6)$$

The value of NCSE will vary from 0 to 1 for any word length and quantization level.

B. Data Sets

All the data sets for the analysis were taken from Physionet database [17]. The data for normal sinus rhythm (NSR) subjects was taken from 24 hour holter monitor recordings of 72 healthy subjects (54 from RR-interval normal sinus rhythm database and 18 from MIT BIH normal sinus rhythm database) [17]. The measured group consists of 35 men and 37 women, aged 54.6–16.2 years (mean–SD) and range of 20-78 years. ECG data was sampled at 128 Hz.

The data for congestive heart failure (CHF) group was taken from 24 hour holter monitor recordings of 44 subjects

F. Ibrahim, N.A. Abu Osman, J. Usman and N.A. Kadri (Eds.): Biomed 06, IFMBE Proceedings 15, pp. 369-373, 2007
www.springerlink.com ' Springer-Verlag Berlin Heidelberg 2007

(29 from RR interval congestive heart failure database and 15 from MIT-BIH Bidmic congestive heart failure database) [17]. CHF group consists of 29 men and 15 women aged 55.5–11.4 (mean–SD), range 22-78 years. Fifteen recording were sampled at 250 Hz and 29 recordings were sampled at 128 Hz. Atrial Fibrillation (AF) group data was taken from MIT BIH atrial fibrillation database [17]. The individual recordings are of 10 hour duration. The originals analog recordings were made using ambulatory ECG recorders with a typical recording bandwidth of approximately 0.1-40 Hz.

III. Results and discussions

We have calculated the complexity of symbolic sequences of healthy subjects (NSR) and diseased subjects (CHF and AF). We have used quantization level 2 (symbols 0 or 1) and word length of 5. Student s t-test was used to find significant difference between the groups. The degree of separation between groups at different threshold values was quantified by obtaining the area under the receiver operator curve (ROC) [15]. The ROC is a graphical presentation of sensitivity versus 1-specificity , where sensitivity shows that how good is the test at picking the patients and specificity is the ability of the test to pick the normal subjects. The area under the ROC (AUC) serves as a well-established index of diagnostic accuracy. The maximum value of AUC is 1 corresponding to the perfect separation of two classes and a value of 0.5 means picking a class by a pure chance.

Fig. 1 (a-c), shows the mean NCSE distribution for NSR Vs CHF, NSR Vs AF and CHF Vs AF subjects respectively. Symbols represent mean for each group and bars represent the standard error (standard error=SD/sqrt(n), where n is the number of subjects and SD is the standard deviation). For healthy (NSR) subjects at smaller threshold values, NCSE increased with the increase in the threshold value and reached a maximum value at a threshold of 10 ms. The value of NCSE also increased for diseased subjects at smaller threshold values and reached a maximum value at a threshold of 8 ms for CHF subjects, at 12 ms for AF subjects. The maximal entropy of NSR subjects was higher than that of both CHF and AF subjects. At short threshold values less than 10 ms and large threshold values greater than 70 ms, the value of NCSE for CHF subjects was higher than that of NSR subjects, whereas, for threshold values in the range 10-70 ms, a gradual decrease in the value of NCSE for CHF subjects was observed. On comparing AF subjects with NSR and CHF subjects, we observed that NCSE of AF subjects was less than both NSR and CHF subjects for shorter threshold values. NCSE of NSR subjects at threshold values greater than 30 ms and NCSE of CHF subjects at threshold values greater than 14 ms decreased rapidly far below the value of AF subjects.

In table 1, mean – standard error of NSR, CHF and AF subjects and their corresponding p-values are given at threshold values. We have found significant separation between NSR and CHF for short thresholds greater than 4 ms. The most significant difference between NSR and CHF subjects was obtained at threshold value of 16 ms (0.9085–0.010, 0.7595–0.033, p-value 4.68×10^{-08} and AUC 0.78), at 2 ms for NSR Vs AF (0.7107–0.012, 0.4590–0.030, p-value 2.15×10^{-14} and AUC 0.95) and for CHF Vs AF subjects at 2 ms (0.7477–0.018, 0.4590–0.030, p-value 4.19×10^{-12} and AUC 0.92).

The results showed that at short threshold values greater than 8 ms and less than 20 ms, the distribution of patterns in NSR subjects is more uniform than diseased subjects (CHF and AF) subjects, which leads to large values of NCSE in NSR subjects. At large threshold values, the pattern of diseased subjects becomes more uniform than healthy subjects and consequently leads to high complexity. Although NCSE showed significant difference between healthy and diseased subjects at wide range of threshold (short as well as large), but findings showed that the results at short threshold are important. The reason for this is that under pathological conditions the dynamical route to disease is either associ-

Table 1 Values of NCSE mean – standard Error of healthy and diseased subjects and p-values

T(ms)	NSR	CHF	AF	NSR Vs CHF	NSR Vs AF	CHF Vs AF
2	0.7107–0.012	0.7477–0.018	0.4590–0.030	ns	2.15×10^{-14}	4.19×10^{-12}
4	0.7113–0.012	0.7517–0.017	0.4720–0.030	4.85×10^{-02}	1.95×10^{-13}	8.15×10^{-12}
6	0.7151–0.012	0.8335–0.017	0.7344–0.034	6.37×10^{-08}	ns	4.76×10^{-03}
8	0.8228–0.011	0.8868–0.012	0.7422–0.034	2.37×10^{-04}	4.26×10^{-03}	4.38×10^{-06}
10	0.9433–0.006	0.8653–0.020	0.8062–0.029	1.23×10^{-05}	3.21×10^{-04}	ns
12	0.9430–0.006	0.8624–0.020	0.8094–0.029	1.05×10^{-05}	4.12×10^{-04}	ns
14	0.9413–0.006	0.8102–0.029	0.8040–0.026	1.35×10^{-07}	6.55×10^{-04}	ns
16	0.9085–0.010	0.7595–0.033	0.8030–0.025	4.68×10^{-08}	7.28×10^{-02}	ns
18	0.8082–0.018	0.6257–0.033	0.7746–0.027	6.94×10^{-07}	ns	ns
20	0.8076–0.018	0.6225–0.033	0.7717–0.027	5.66×10^{-07}	ns	ns

F. Ibrahim, N.A. Abu Osman, J. Usman and N.A. Kadri (Eds.): Biomed 06, IFMBE Proceedings 15, pp. 369-373, 2007
www.springerlink.com ' Springer-Verlag Berlin Heidelberg 2007

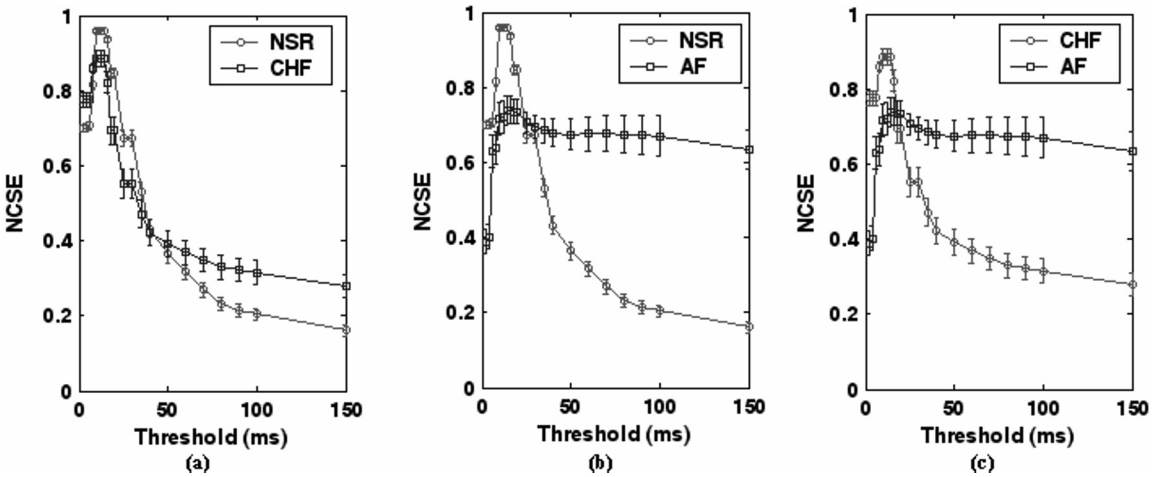

Fig. 1 Mean NCSE at different threshold values (a) NSR Vs CHF, (b) NSR Vs AF (c) CHF and AF

ated with loss of variability (in CHF subjects) and emergence of more regular patterns or with more random types of outputs (in AF subjects) [16]. Thus loss of complexity may be a generic feature of pathological dynamics [16]. Our results revealed that the dynamics of healthy subjects are more complex than pathological subjects within the short range of thresholds, whereas, traditional entropy based measures [10,11] does not provide this information.

IV. Conclusions

In this paper, we have used symbolic entropy at different threshold values to study the dynamics of heart rate time series. We have used NCSE to quantify these dynamics. We calculated NCSE of healthy (NSR) and diseased (CHF and AF) subjects. NCSE showed significant differences between healthy and diseased groups as well as within the diseased groups at wide range of thresholds (short as well as large). It was observed that healthy (NSR subjects) dynamics are more complex than either both of CHF and AF subjects at short range of thresholds. These results verify that the loss of complexity is a generic feature of pathological dynamics.

Acknowledgment

This work is financially supported by the higher education Commission (HEC) of Pakistan. We are thankful to the organizers and contributors of Physionet (the research resource for complex physiological signals) for providing data.

References

1. Seely AJE, Macklem PT (2004) Complex systems and the technology of variability analysis. Critical Care 8:R367-384.
2. Malik M (1996) Task force of the European society of cardiology and north American society of pacing electrophysiology: Heart rate variability: standards of measurement, physiological interpretation and clinical use. Circulation 93:1043-1065.
3. Kleiger RE, Stein PK, Bosner MS et al. (1992) Time domain measures of heart rate variability. Amb Electrocardol 10:487-98.
4. Malliani A, Pagani M, Lombardi F et al (1991) Cardiovascular neural regulation explored in the frequency domain. Circulation 84:428-92.
5. Makikallio T (1998) Analysis of heart rate dynamics by methods derived from nonlinear mathematics clinical applicability and prognostic significance. PhD thesis University of Oulu.
6. Garcia-Gonzalez MA, Rames-Castro J, and Fernandez-Chimeno M (2003) A new index for the analysis of heart rate variability dynamics: characterization and application. Physiological Measurement 24:819-32.
7. Aziz W, Abbas R, Arif M (2004) Threshold Based Acceleration Change Index (TACI) for Heart Rate Variability Analysis. IEEE proceedings 8th international multitopic conference National University of Computer and Emerging Sciences Lahore Pakistan.
8. Aziz W, Arif M (2005) Application of threshold based acceleration change index (TACI) in heart rate variability analysis. Physiological Measurement, 26:653-665 (doi:10.1088/0967-3334/26/5/007).
9. Aziz W and Arif, M (2006) Complexity analysis of stride interval time series by threshold dependent symbolic entropy. European Journal of Applied Physiolog (online doi: 10.1007/s00421-006-0226-5)
10. Pincus SM (1991) Approximate Entropy as a Measure of System Complexity. Proceedings of National Academy of Sciences 2297-2301.
11. Richman JS, and Moorman JR (2000) Physiological time series analysis using approximate entropy and sample entropy. American journal of physiology H2039- H3049.
12. Wessel N, Voss A, Kurths J, Witt A and Osterziel KJ (1995) 24 hour heart rate variability analysis based on new methods of non-linear dynamics. Comput Cardiol 22: 693-696.

F. Ibrahim, N.A. Abu Osman, J. Usman and N.A. Kadri (Eds.): Biomed 06, IFMBE Proceedings 15, pp. 369-373, 2007
www.springerlink.com ' Springer-Verlag Berlin Heidelberg 2007

13. Costa M, Goldberger AL, Peng CK (2002) Multiscale Entropy Analysis of Physiologic Time Series. Physical Review Letters, The Americam Physiological Society 89: 068102 (1-4).
14. Costa M, Goldberger AL, Peng CK (2005) Multiscale Entropy Analysis of biological signals. Physical Rev E, The Americam Physiological Society 71: 021906 (1-18).
15. McNeil BJ and Hanley JA (1984) Statistical approach to the analysis of receiver operating characteristic (ROC) curves. Med. Decis. Making 4 137 50.
16. Eguia MC, Rabinovich MI and Abarbanel HDI (2000) Information transmission and recovery in neural communication channels. Physical review E 62: 7111-22.
17. Goldberger AL, Namaral LA, Glass L, et al. (2000) PhysioBank, PhysioToolkit, and PhysioNet: Components of a new research resource for complex physiologic signals. *Circulation* 101: 215 20.

Address of the corresponding author:

Author:	WAJID AZIZ LOUN
Institute:	Pakistan Institute of Engineering and applied Sciences (PIEAS) Nilore.
Department:	Computer and Information Sciences
City:	Islamabad
Country:	Pakistan
Email:	Kh_wajid@yahoo.com

F. Ibrahim, N.A. Abu Osman, J. Usman and N.A. Kadri (Eds.): Biomed 06, IFMBE Proceedings 15, pp. 369-373, 2007
www.springerlink.com ' Springer-Verlag Berlin Heidelberg 2007

Computer-based System to Assess Efficacy of Stuttering Therapy Techniques

Ooi Chia Ai[1], Jasmy Yunus[2]

[1] Universiti Teknologi Malaysia/Department of Electronic Engineering, Faculty of Electrical Engineering, Skudai, Malaysia
[2] Universiti Teknologi Malaysia/Department of Electronic Engineering, Faculty of Electrical Engineering, Skudai, Malaysia

Abstract— **This paper presents a computer-based system tool used to assess efficacy of stuttering therapy techniques. The software assists Speech-Language Pathologist (SLP) in determining suitable techniques for each client .The project implements Digital Signal Processing (DSP) techniques to analyze speech signals and incorporates standard speech fluency shaping techniques that can be used as part of fluency rehabilitation regimen. The software provides real-time visual and audio feedbacks for clients to be aware of their speech patterns. It provides self training aid for clients that motivates them to practice at home. The software runs under Windows XP on a computer equipped with multimedia capabilities. Real-time visual and audio displays enable the clients to compare their average magnitude profiles (AMPs) with clinician's and alter their speech to match clinician's AMP. The start and end alignment, maximum magnitude and duration of two AMPs are compared. A score is assigned to each category. The software is developed using Microsoft Visual C++ 6.0. Software is designed as graphic user interface (GUI), which makes therapy user friendly. Three techniques that are implemented in the project have been decided through the discussion with SLP in Hospital Sultanah Aminah (HSA). The techniques are Shadowing, using a Metronome (Taping) and Delayed Auditory Feedback (DAF). This project is done in collaboration with HSA where the hospital assists in the clinical trial.**

Keywords— **Stuttering, speech therapy, fluency shaping, therapy techniques, digital signal processing**

I. Introduction

Stuttering [1] is a disorder of fluency characterized by excessive amounts of dysfluencies, excessive durations of dysfluencies, and unusual amount of muscular effort in speaking. It is a disorder in the rhythm of speech in which the individual knows precisely what he wishes to say but at the time is unable to say because of an involuntary repetition, prolongation, or cessation of a sound.

The most commonly utilized techniques of facilitating fluency are fluency shaping and stuttering modification. Both techniques were considered by Person Who Stutters (PWS) to be better than those strategies that were intuitive on the part of the speaker such as forcing out the speech or avoidance [2]. Stuttering can be treated by fluency-shaping therapies [3] which effectively and durably replace the chronic stuttered speech pattern with a newly learned prolonged and rhythmic fluent speech. Stuttering Modification therapies [4] focus on changing individual moments of stuttering to make them smoother, shorter, less tense, and less penalizing.

The use of computer technology in speech therapy and assessment is still new in Malaysia. There are many clinical approaches to treat individuals who stutter, however, the treatment process may take months of repeated procedures that are costly and overly generalized. Normally, 2 to 3 months are required to determine suitable technique for each client. The maximum magnitudes of the clients and the clinicians, corresponding to the average magnitude profiles (AMPs), are determined and compared in our software. The maximum magnitude is determined where a total of 15 neighboring samples are summed to obtain a maximum value. Our hypothesis is by doing comparison between client s and clinician s AMPs for three therapy techniques (Shadowing, Metronome and Delayed Auditory Feedback), the computer analysis can help SLP to assess the efficacy of each technique, thus determining suitable technique for each client in faster and more accurate manner.

II. Stuttering treatment framework design

A. Problem Formulation

Speech therapy does not cure stuttering. Typically, clinical treatment for stuttering involves visiting a Speech-Language Pathologist (SLP) for a series of therapy sessions. Initially, the visits are once or twice a week, and between visits the PWS do various activities, exercises, and practice routines that will ultimately provide relief from stuttering. PWS can learn to control their speech fluency by shaping the tempo, loudness, effort or duration of their utterances. However, speech fluency treatment should not be limited to clinical sessions. Speech assessments should be obtained under multiple conditions and on various occasions [5]. This may not be feasible if particular equipment can be used only in laboratory settings or if parents are not able to bring a child to the clinic, necessitating clinicians to visit a child at home.

Stutterers must continue their practices at home so that it becomes their daily routines. The major problem [6] with practicing outside the clinic is that clinicians cannot ensure that clients are practicing correctly and/or consistently.

F. Ibrahim, N.A. Abu Osman, J. Usman and N.A. Kadri (Eds.): Biomed 06, IFMBE Proceedings 15, pp. 374-377, 2007
www.springerlink.com ' Springer-Verlag Berlin Heidelberg 2007

Clients may practice utterances at home regularly, but if they practice incorrectly, they will not see any progress in their rehabilitation. Lack of progress causes clients to practice less frequently, resulting in a cycle of poor practice where no improvement is achieved. The training process could be enhanced if clients have a surrogate clinician to assist them during daily home treatment sessions. In this system, the surrogate clinician will be a software package that clients use at homes. The software implements standard fluency shaping technique by providing immediate visual feedback to clients to let them know if they are practicing correctly. This motivates clients to practice at home and at the same time allows clinicians to assess the progress.

Studies [7] indicated that treatment was eventually helpful in reaching goals of successful management for PWS. Interestingly, however, there was no pattern regarding the approach or techniques that participants found helpful. Participants had difficulty identifying specific approaches or techniques to which they could attribute their success. Findings [8] suggest that a system that can identify suitable techniques is important because any rational and empirically informed procedure that enables the client to self-assess and systematically modify speech behaviors and the associated cognitive features may be likely to successfully facilitate fluency.

B. Underlying Design Principles

The research evidence [9] showed that changes in stuttering treatment based on prolonged speech were needed and, as a result, corrective action is important and self-correction is the sine qua non of a scientific approach. Self-measurement serves as the basis for determining the clinical significance of a treatment change from the client s perspective. Our software is designed based on the facts that clients must be involved directly in the treatment process. Software provides real-time visual and audio bio-feedbacks where client's AMP is displayed as it is spoken and it is superimposed on the clinician s AMP. The display of AMP is intended to convey to the client those locations where the client's utterance differed from the clinician s in the aspect of start and end alignment, magnitude and duration. AMP of the spoken utterance is the primary source used to gauge the fluency and performance of the client.

Camperdown program outcomes [10] supported our project where it demonstrated that PWS could develop natural-sounding, nearly stutter-free speech without specific clinician instructions with regard to speech modifications although they do require consistent and reliable feedback concerning stuttering severity and speech naturalness. The success of the Lidcombe [11] and the Camperdown programs appear to suggest that many PWS are able to produce nearly stutter-free and natural-sounding speech by (1) developing a cognitive set to speak without stutters and (2) monitoring their speech, initially with the help of clinicians or family members, to verify that this goal is achieved. This inference has strong empirical foundation.

Many of the clinical therapy techniques require a conscious effort on the part of the clients [12]. Therefore, the element of motivation must be integrated into stuttering therapy. It is essential that the child enjoys the treatment and finds it to be a positive experience. Computer-based therapy displays speech waveforms and amplitude curve in graphical representation which can motivate and encourage child to practice their therapy for longer periods.

Rewards are important to motivate the clients. Research [12] supported that both tangible forms of rewards and verbal rewards were effective in reducing stuttering. Both forms of reward appeared to be successful, but their unique contributions could not be measured because treatment involved a number of therapy procedures. Therefore, in our software, we implemented rewards for the client whenever he or she manages to obtain scores of 80 and above.

Research [13] indicated that basically five steps are required in implementing clinical treatment system as follows.

1. Convert a clinical need into an answerable question.
2. Search for the best evidence to answer the question.
3. Critically evaluate the evidence for validity and applicability.
4. Apply the results to clinical practice.
5. Evaluate and audit performance

By performing the above tasks, the surrogate clinician helps minimize the problems associated with practice outside of clinic. This software tool enhances the treatment process by providing clients with the feedback necessary to identify speech properties while still allowing the clinician to have control of the treatment process. This combination of feedback, progress records, and customizable practice phrases would be a valuable asset to current treatment techniques. The clients themselves modify their speech in subtle and variable ways to gain control over stuttering and, in that, they appear to be similar to a well-known experimental technique for suppressing stutters known as response contingent stimulation.

Prolonged speech based stuttering treatment typically involves shaping speech systematically by requiring participants to meet specific criteria for rate and an assortment of related speech modifications such as gentle voice onset, continuous vocalization, and soft articulatory contact in small, incremental steps [14]. Thus, our project required significantly fewer clinician contacts compared to the traditional behavior therapies used in the past.

F. Ibrahim, N.A. Abu Osman, J. Usman and N.A. Kadri (Eds.): Biomed 06, IFMBE Proceedings 15, pp. 374-377, 2007
www.springerlink.com ' Springer-Verlag Berlin Heidelberg 2007

III. System design

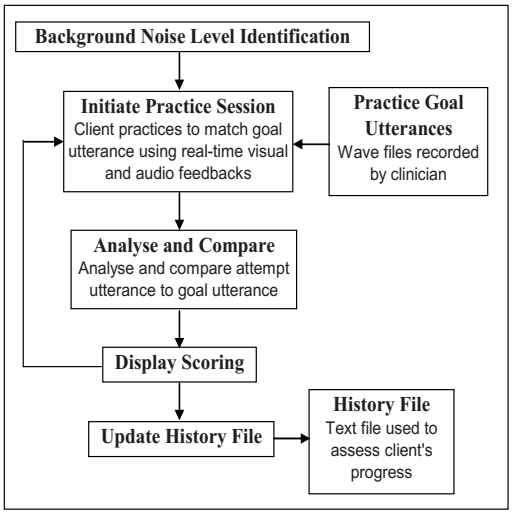

Fig. 1 System Design

Fig. 1 shows system design. Sound recording of 5 goal utterances is implemented where the software incorporates functions record, playback, open, close and save of standard WAVE file. In the speech pathology clinic, after the clinician has identified client s stuttering problem, the clinician verbally records 5 speech utterances, which the clients will later on practice at home. The 5 goal utterances are customized by the clinician for each client depending on the age and language level. Goal utterances are chosen based on their phonetic characteristics. Each goal utterance is stored in a separate WAVE file, which can be individually selected for practice. The duration for each target utterances is six seconds.

The software is able to calculate and display the AMP of the client as it is spoken as shown in Fig. 2. The speech processing is done in real-time. This provides immediate feedbacks to the client, which give clients the opportunity to alter their speech. A text history file is generated after completing a treatment session as shown in. A separate history file is created for each client. The history file summarizes the client attempts. Clinician can use this information to assess or monitor client progress and observe how much time client spends to practice. This information can be used as reference for clinician to determine suitable techniques for each client.

The selection of scoring parameters is important because the parameters will influence in our clinically significant outcome for behavioral treatments for stuttering within an evidence-based framework [15]. Moreover, it is important to make sure that a framework might lead towards outcomes that are meaningful for the clinician or clinical researcher, the client and relevant others such as parents of a child who stutters. The stuttering measures also enable the SLP and the parent to communicate effectively about the severity of the child s stuttering throughout the treatment process. Any departure from the criterion speech performance, as specified with the stuttering measures above, results in more frequent clinic visits and possibly an increase in parental contingencies. Client s AMP is compared with clinician s AMP in four categories. They are start location identification, end location identification, maximum magnitude comparison and duration comparison.

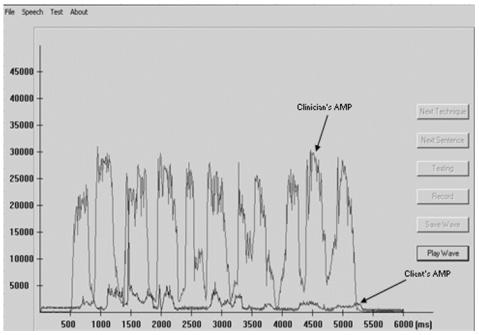

Fig. 2 Average Magnitude Profiles of Clinician and Client

IV. Results and discussions

Test subjects were selected from 6 primary schools located in Skudai, Malaysia. A total of 11 subjects participated, 10 males and 1 female. 10 of the test subjects had been diagnosed by a SLP as having stuttering and had been stuttering for at least six months. One of whom have been omitted from analysis because the subject in question was identified to be not a stuttering client. The age span was between 8 and 12 years old. They were not familiar with speech technology in any way. The participants were tested in a quiet setting in one session which required approximately 5 10 minutes.

The data collection process began by engaging each participant in a short conversation regarding their favorite sports or interests to obtain data on participants language level so that the author knows precisely which set of sentences to be used for that subject s oral-reading task. The test was presented on a computer monitor positioned at a comfortable reading level for each participant. At the beginning of the recording session, participants were given a short practice for each sentence before the actual recording.

Each subject carried out three tasks. Of the data collected, a total of 281 subject utterances have been analyzed in the present work. In time, this amounts to 1686 seconds or 28.1 minutes of speech. The speech sample was pre-

F. Ibrahim, N.A. Abu Osman, J. Usman and N.A. Kadri (Eds.): Biomed 06, IFMBE Proceedings 15, pp. 374-377, 2007
www.springerlink.com ' Springer-Verlag Berlin Heidelberg 2007

sented to the SLP in both the audiovisual and audio-only mode. SLP judged each sample individually.

Measures of %SS (Percent Stuttered Syllables) for three techniques were made by SLP from HSA as shown in Table 1. From Table 1, it was certified that two subjects (Subjects G and H) were identified as having mild stuttering, two subjects (Subjects C and E) were identified as having mild-to-moderate stuttering, three subjects (Subjects B, D, and F) as moderate, two subjects (Subject A and I) as moderate-to-severe, and one subject (Subject J) was identified as having severe stuttering. Out of ten subjects, only one subject had a history of receiving traditional speech therapy for remediation of dysfluency through their school systems. The measure of %SS provides additional references for determining suitable therapy techniques for each client other than the scoring generated by the software.

Table 1 %SS for Each Technique

Test Subject	Percentage of Stuttered Syllables (%SS)		
	Technique 1	Technique 2	Technique 3
A	15.23	20.97	9.62
B	11.11	13.46	14.86
C	5.77	5.77	11.54
D	16.00	7.84	7.14
E	8.62	4.76	11.90
F	17.46	7.69	13.51
G	5.77	5.77	3.85
H	7.69	9.62	11.54
I	22.41	16.42	12.77
J	20.24	23.08	35.87

V. Conclusions

Currently, we implemented three stuttering therapy techniques in our software. The project can be extended by implementing more stuttering therapy techniques in order to increase the accuracy. We hope that the current outcomes will be re-examined with larger and diverse samples and that the proposed topics will be investigated through innovative methodologies in efforts to inform treatment directions in stuttering. Due to the well-documented variability of stuttering within subjects, speech samples should ideally be obtained under multiple conditions and on multiple occasions. This can be particularly important for young children, as stuttering has been reported to fluctuate greatly over time and sometimes cease entirely. Our current software aimed at determining suitable therapy techniques for each client by looking at the scoring generated automatically by the software and the %SS measured from speech samples. This personal computer-based system is intuitive to use, cost-effective, and easily integrated into current speech rehabilitation regimens. We believe our software tool will improve the effectiveness and availability of stuttering treatment.

Acknowledgment

Thanks to Ministry of Science, Technology and Innovation of Malaysia for funding this project.

References

1. M.N. Hedge (1998) PocketGuide to treatment in speech-language pathology. Singular, London
2. Crichton-Smith, I. (2002) Communicating in the real world: Accounts from people who stammer. Journal of Fluency Disorders, 27: 333-352
3. Katrin Neumann et al. (2005) Cortical plasticity associated with stuttering therapy. Journal of Fluency Disorders, 30: 23-39
4. Walter H. Manning (2001) Clinical decision-making in fluency disorder. 2nd Edition, Singular, Canada
5. Carys Thomas, Peter Howell (2001) Assessing efficacy of stuttering treatments. Journal of Fluency Disorders, 26: 311-333
6. Harold B. Starbuck (1992) Therapy for stutterers. Stuttering Foundation of America, Memphis, Tennessee
7. Laura P. et al. (2005) A phenomenological understanding of successful stuttering management. Journal of Fluency Disorders, 30: 1-22
8. Anderson, T. K., Felsenfeld, S. (2003) A thermatic analysis of late recovery from stuttering. American Journal of Speech-Language Pathology, 12: 243-253
9. Patrick Finn (2003) Evidence-based treatment of stuttering: II. Clinical significance of behavioral stuttering treatments. Journal of Fluency Disorders, 28: 209-218
10. O Brian et al. (2003) The Camperdown program: Outcomes of a new prolonged-speech treatment model. Journal of Speech, Language, and Hearing Research, 46: 933-946
11. Onslow et al. (2002) Speech timing in children after the Lidcombe program of early stuttering intervention. Clinical Linguistics & Phonetics, 16: 21-33
12. Franklin H. Silverman (1996) Stuttering and other fluency disorders. Allyn & Bacon, Needham Heights
13. Sackett et al. (2000) Evidence-based medicine: How to practice and teach EBM. Edinburgh, Churchill Livingstone
14. Onslow et al. (1996) Speech outcomes of a prolonged-speech treatment for stuttering. Journal of Speech and Hearing Research, 39: 734-749
15. Garen Sparks et al. (2002) The effect of fast speech rate on stuttering frequency during delayed auditory feedback. Journal of Fluency Disorders, 27: 187-201

Address of the corresponding author:

Author: OOI CHIA AI
Institute: Universiti Teknologi Malaysia (UTM)
Street: 2662, Lrg Tun Syed Sheh Shahabudin 6/1, Taman Lumba Kuda
City: 05250 Alor Star, Kedah Darul Aman.
Country: Malaysia
Email: OoiChiaAi@yahoo.com

F. Ibrahim, N.A. Abu Osman, J. Usman and N.A. Kadri (Eds.): Biomed 06, IFMBE Proceedings 15, pp. 374-377, 2007
www.springerlink.com ' Springer-Verlag Berlin Heidelberg 2007

Development of an EEG amplifier for Brain-Computer-Interface

Y.Q.Tan[1], F. Ibrahim[1], M. Moghavvemi[2] and J. Ibrahim[3]

[1] Department of Biomedical Engineering, Faculty of Engineering, University of Malaya, Kuala Lumpur, Malaysia.
[2] Department of Electrical Engineering, Faculty of Engineering, University of Malaya, Kuala Lumpur, Malaysia.
[3]Power Engineering Society, IEEE Malaysia Chapter

Abstract— **This paper describes the development of a bi-polar EEG amplifier designed specifically for use in a brain-computer-interface (BCI). AC coupling is performed in the input stage to prevent electrode offset voltages from saturating the amplifier when high gain is used. The amplifier is easily modified to amplify other biopotential signals. The circuit described is suitable for low power consumption, battery power application. The low power requirement of the amplifier allows it to be powered through the USB connection and thus suitable for portable applications.**

Keywords— **EEG, differential amplifier, pre-amplifier, ac-coupled.**

I. Introduction

A brain-computer-interface (BCI) is a communication system that does not depend on the brain s normal output pathways of peripheral nerves and muscles. BCI employs either EEG activity recorded from the scalp, or the activity of individual cortical neurons recorded from implanted electrodes [1]. BCI has been introduced to record the EEG signals from subject and process the recorded signals for further application.

The EEG or electroencephalograms represents the electrical activity of the brain. EEG records the electrical potentials generated due to excitatory and inhibitory post-synaptic potentials developed by cell bodies and dendrites of pyramidal neurons [2].

EEG signal, as one of the biological signals, are recorded at very low level of voltage ranging between 1μV and 100mV. These signals have to be amplified to make compatible with other devices such as display, recorders or A/C converters for computerized equipment. A specific high gain amplifier (gain of 10,000 - 1,000,000) is required to boost signal strength up to an acceptable level required, as an input to recording devices.

However, the typical BCI system is designed specifically for one particular BCI method and is, therefore, not suited to the systematic studies that are essential for continued progress for new BCI method and further signal processing [3].

Thus, to condition the EEG signal for further processing and applications for an EEG based BCI system, a low frequency, high gain EEG amplifier, is preferable.

Over the decades, various biopotential amplifiers had been designed by researchers to record the biopotential signals [4-12]. These proposed designs used the differential amplifier as the main core for the modules. Most of these designs are relying on three op-amp instrumentation-amplifier (IA), to differentiate and amplify the signal [4-7] [11-12].

Integrated Circuit (IC) chips had been used as the differential amplifier for the designs [4-12]. However, the commercial IC chips had had specific value of gain, which had been preset initially, and do not meet with the biopotential signal requirements. To adapt these amplifiers to the applications, the circuits require some modifications such as the addition of passive component such as resistors and capacitors, in order to control the amplification.

Due to this problem, it is necessary to design and develop an EEG amplifier using the discrete components such as transistor, resistor and capacitor, instead of IC chips. By using the transistors, the amplifier characteristic can be easily designed and set to the desired values with the help of resistors and capacitors. Thus, the amplifier can be perfectly matched to the biopotential signal applications requirements.

II. The Proposed Designed Circuit

As illustrated in Figure 1, the proposed circuit consists of 3 main parts: pre-amplifier, differential amplifier, and filter. The collector output signal is captured through a data acquisition card (DAQ) for further processing on a computer.

The proposed design circuit is as shown in Figure 2.

Fig. 1 Overall block diagram of the BCI system.

F. Ibrahim, N.A. Abu Osman, J. Usman and N.A. Kadri (Eds.): Biomed 06, IFMBE Proceedings 15, pp. 378-382, 2007
www.springerlink.com ' Springer-Verlag Berlin Heidelberg 2007

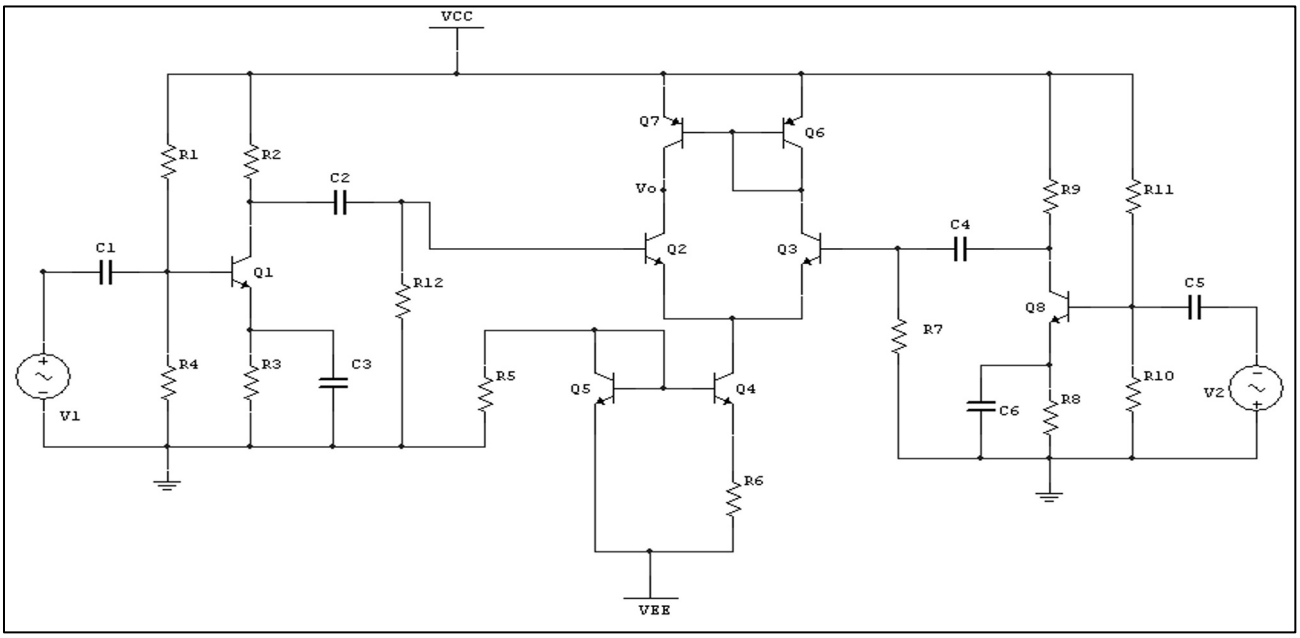

Fig. 2 Circuit schematic

A. Pre-amplifier

A pre-amplifier (preamp) is an electronic amplifier which precedes another amplifier to prepare an electronic signal for further amplification or processing.

Normally, the biopotential signal generated by human body ranges between μV (EEG) and mV (ECG), and this signal is too weak in order to activate the differential transistor. Therefore, a preamp is required to boost the strength of the signal and at the same time, provided a stable current to drive the next stage differential amplifier.

There are few approaches to get the good performance of the electrical characteristics with the present of pre-amplifier circuits [4-5].

There are 3 types of amplifier configuration commonly being used: Common-Base (CB), Common-Collector (CC) and Common-Emitter (CE) amplifiers.

Based on the requirement of the biopotential amplifier, CE amplifier is the most suitable configuration used to provide moderate input impedance and voltage gain.

The output of this preamp will act as the input for the next stage, the differential amplifier, in order to increase the voltage gain of the signal.

B. AC coupling

Electrodes and the electrolyte paste convert ionic currents in the body to electronic currents that can be measured by the amplifier. Oxidation and reduction reactions occurring at the electrode-electrolyte interface forms a layer of charge at the interface, causing an electrode potential to develop across the interface. The difference in electrode potential between two electrodes is a dc voltage called the electrode offset potential [13].

As for the proposed circuit, coupling capacitors and bypass capacitors (C1 C6) had been located in preamp circuit to block the dc offset voltage and increase the gain value.

However, capacitor is a frequency response element and this will affect the amplification gain of the amplifier in low frequency. As frequency increases, the gain will continuously increases until the frequency reaches the cutoff point, where the gain remains constant at a certain value.

Therefore, the cutoff point should be designed lower than the desired frequency, which is the EEG band.

For an ideal situation, the value of capacitors should be increase to a very large value, i.e. 1 Farad, to decrease the cutoff frequency towards zero Hertz [14]. However, in practical sense, increasing the value of capacitor will also increase the size of the component, which in turn will increase the total size of amplifier module. Trade off between the size of component and break point frequency should always been considered in the design.

C. Differential amplifier

Most operational amplifier consists of a series of transistors, resistors and capacitors forming a complete system on a single chip [14]. Commercially available op-amp chips

F. Ibrahim, N.A. Abu Osman, J. Usman and N.A. Kadri (Eds.): Biomed 06, IFMBE Proceedings 15, pp. 378-382, 2007
www.springerlink.com ' Springer-Verlag Berlin Heidelberg 2007

come with a set of predetermined gain value. Thus, some modification should be carried out to reset the gain to the desired value, as what was done by other researchers [4-12].

The proposed designed circuit, however, was directly constructed using the conventional transistors, resistors and capacitors, instead of using op-amp chips. As such, the desired gain is achieved by design rather than through gain modification on an op-amp.

Differential amplifier was used to amplify the difference of signals, collected from two electrodes.

A basic differential amplifier is composed of two emitter-coupled common-emitter dc amplifiers with two inputs, v_1 and v_2 and outputs v_{o1} and v_{o2}, as shown in figure 3 [15]:

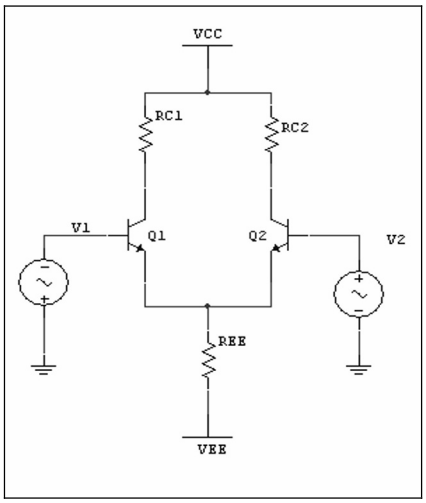

Fig. 3 Basic differential amplifier.

To achieve a high gain, a current source had been used to replace R_C as an active load. Usually, current mirror acted as an active load as a way to accomplish high gain (Q6 and Q7, refer to figure 2).

Because of the high gain requirement, the bias current must be small, and this can be achieved by replaced R_{EE} with a constant current source, such as Widlar current source (Q4, Q5, R5 and R6, figure 2). In addition, the current source can be designed to provide small current, which is not limited by the early voltage of the transistor [14].

The voltage gain produce by this differential amplifier with active load was always being constant. The equation of the gain as shown following [14]:

$$A = \frac{v_o}{v_i}$$

$$= \frac{r_m r_o}{2} \qquad (1)$$

$$r_m r_o = g_m r_o = \frac{V_A}{V_T}$$

Where early voltage, V_A is a preset value by transistor, which is 100V, and threshold voltage, V_T is a constant value, 26mV. Thus:

$$g_m r_o \approx 4000$$

$$A = \frac{4000}{2}$$

$$= 2000$$

The total gain of the amplifier is the product of preamplifier gain and differential amplifier gain. The differential amplifier gain was fixed to a value of 2000. Therefore, the total gain of the proposed amplifier can be adjusted by changing the value of gain at preamplifier.

As for the requirement of an EEG amplifier, the total gain is required to be in the range of 50,000 - 100,000, in order to amplify the input signal of μV to the output signal of around 2V.

D. Filter

The amplified signal was then run through a filtering system to filter out any undesired noise, such as 50-Hz noise, white noise, and other biopotential signals. Biopotential signals, such as the movement of the eyes, which is electro-oculargram (EOG) signal, act as artifacts and affect the EEG signal collection.

High pass and low pass filters may be added based on the requirement of different applications.

E. Discussion

The biopotential amplifier specific for EEG signal amplification has been designed and simulated using Multisim 7 software. After the appropriate resistors and capacitors values have been identified, a bipolar EEG amplifier was constructed using conventional *npn* and *pnp* transistor, resistors and capacitors.

To test the performance of the design circuit, the testing is first been carried out using cleaned signal, without any artifacts or noises. A 40 Hz, 10mVpp sine wave signal generated by function generator, had been used to test the circuit performance.

Because of the limitation of oscilloscope, the minimum signal that can be measured is in range of mV. Therefore, to avoid the saturation of signal, the amplifier had been tested stage by stage.

For the pre-amplifier, with the power supply of – 5V and an input signals of 10mVpp, an output signal of about 500mVpp been achieved. Thus the resultant amplification of about 50 is achieved. However, in comparison with the simulated output result of 600mVpp, there is a minimal

F. Ibrahim, N.A. Abu Osman, J. Usman and N.A. Kadri (Eds.): Biomed 06, IFMBE Proceedings 15, pp. 378-382, 2007
www.springerlink.com ' Springer-Verlag Berlin Heidelberg 2007

deviation. The deviation from the simulation output value may be due to the resistance of measuring probe and the limitation of the oscilloscope.

To check the stability of gain provided by pre-amplifier, the circuit had been tested with fix amplitude (10mVpp) sine wave input signal, and various frequencies. The result shown as below:

Table 1 Amplification gain of various frequencies input

Frequency (Hz)	Gain
1	57
5	58
10	60
20	60
30	60
40	60
50	60
100	61
500	60
1000	60

For the differential amplifier, the resulted gain is 2000, in concurrence with the simulated result.

Multisim 7 had simulated the complete circuit; the result is as shown in Figure 4. Two input signals of 5μVpp (upper trace), with different polarity, producing an output signal of 2Vpp (lower trace).

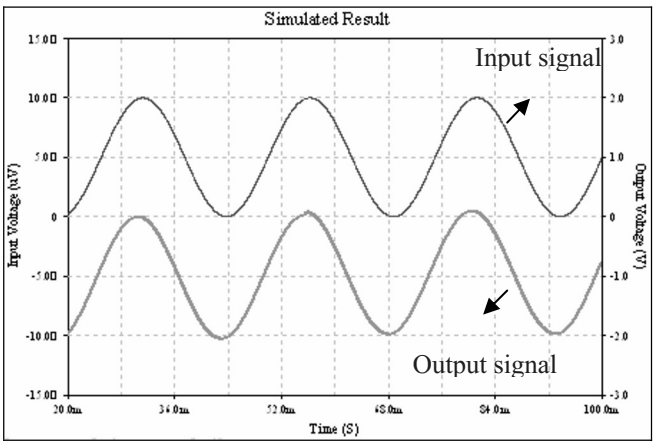

Figure 4 Simulated result

This result shows that this biopotential amplifier has achieved an overall total gain of about 100,000. Furthermore, changing the gain of the pre-amplifier can easily modify the gain.

To increase the usability and robustness of the designed circuit for clinical testing, the amplifier with a multi channel had been fabrication onto printed circuit board (PCB).

III. Conclusions and future works

A novel design of simple bipolar EEG amplifier has been designed using basic electronic components such as transistors, resistors and capacitors. The circuit is suitable to operate on normal dry cell batteries.

The design had satisfied the requirement of low power consumption, high gain and low frequency response.

The gain and bandwidth can be easily modified and tuned to amplify other biopotential signals such as electromyogram (EMG) or electrocardiogram (ECG), by simply change the value of resistors and/or capacitors.

For future works, the performance of the amplifier will be evaluated by collecting some clinical sample data such as the real-time EEG or EMG signal data.

Many other factors will determined the performance of an amplifier, such as white noise signal, 50-Hz noise from power supply, time reliability, temperature, connection of electrodes and output connection to DAQ system. Therefore, future improvement and testing is required to prove the performance and reliability of this proposed design. For further improvement, the designed circuit can be fabricated onto an integrated circuit (IC) chips.

References

1. Wolpaw J R, Birbaumer N, McFarland D J, Pfurtscheller G, Vaughan T M (2002) Brain-computer interfaces for communication and control. Clin. Neurophysiol. 113:767 791
2. Rangayyan R M (2001) Biomedical Signal Analysis. Wiley-Interscience, New York
3. Schalk G, McFarland D J, Hinterberger T, Birbaumer N, Wolpaw J R (2004) BCI2000: A general-Purpose Brain-Computer Interface (BCI) System. IEEE Transaction on Biomedical Engineering, 51:1034-1043
4. Metting van Rijn A C et al (1999) The isolation mode rejection ratio in bioelectric amplifiers. IEEE trans. On BME. 38(11):1154-1157
5. Metting van Rijn A C et al (1991) High quality recording of bioelectric events Part2. Med. & Biol. Eng. & Comput. 29:433-440
6. Spinelli E M, Martinez N H, Mayosky M A (2001) A single supply biopotential amplifier. Medical Engingeering & Physics. 23:235-238
7. Metting van Rijn A C, Peper A, Grimbergen C A (1994) Instrumentation amplifiers for bioelectric events: a design with a minimal number of parts. Med. & Biol. Eng. & Comput. 32:305-310
8. Badillo L, Ponomaryov V, Ramos E, Igartua L (2003) Low noise multichannel amplifier for portable EEG biomedical applications. Proceedings of the 25th Annual International Conference of the IEEE EMBS, Cancun, Mexico, 2003, pp3309-3312
9. EDN at http://www.edn.com
10. Dobrev D (2004) Two-electrode low supply voltage electrrocardiogram signal amplifier. Med. & Biol. Eng. & Comput. 42:272-276
11. Spinelli E M, Mayosky M A (2000) AC coupled three op-amp biopotential amplifier with active DC suppression. IEEE Transaction on Biomedical Engineering. 47(12):1616-1619
12. Spinelli E M, Pallas-Areny R, Mayosky M A (2003) AC-coupled front-end for biopotential measurements. IEEE Transaction on Biomedical Engineering. 5(3):391-395
13. Cromwell, L., Weibell, F.J. and Pfeiffer, E.A. (1999) Biomedical Instrumentation and Measurements, 2nd edn. New Delhi: Prentice-Hall, New Jersey

F. Ibrahim, N.A. Abu Osman, J. Usman and N.A. Kadri (Eds.): Biomed 06, IFMBE Proceedings 15, pp. 378-382, 2007
www.springerlink.com ' Springer-Verlag Berlin Heidelberg 2007

14. Savant C J Jr, Roden M S, Carpenter G L (1991) Electronic Design Circuits and Systems. Addison-Wesley Publishing Company, California
15. Boylestad R L, Nashelsky L (1999) Electronic Devices and Circuit Theory, 7th edn. Prentice-Hall, New Jersey

Address of the corresponding author:

Author: Tan Yin Qing
Institute: Department of Biomedical Engineering, Faculty of Engneering, University of Malaya
City: Kuala Lumpur
Country: Malaysia
Email: yq_nicole@yahoo.com

F. Ibrahim, N.A. Abu Osman, J. Usman and N.A. Kadri (Eds.): Biomed 06, IFMBE Proceedings 15, pp. 378-382, 2007
www.springerlink.com ' Springer-Verlag Berlin Heidelberg 2007

Enhancement of Epileptic Seizure in EEG Signals using Novelty Filtering based on Neural Networks

A. Erfani[1], M. Farjadi Nasab[2]

[1] Dept. of Physics, Faculty of Physics, I. Azad University, Karaj , Iran
[2] Dept. of Electrical Engineering, Faculty of Electrical Engineering, I. Azad University, Karaj , Iran

Abstract—**Preprocessing and signal enhancement methods can be applied to improve quality of signal detection in the presence of background noise. This article concerns the novel preprocessing techniques for enhancement of EEG signals and background noise suppression during epileptic seizure by using Independent Component Analysis (ICA) and Novelty Filtering which employs an artificial neural network performing autoassociative task. ICA is used for removing biological artifacts and noise from EEG signals and stabilizing its probabilistic behavior. At the next stage Novelty Filtering technique has been used to suppress background EEG activities and improvement of signal-to-noise ratio for the detection and identification of epileptic seizure. A novelty filter consist of neural networks of retinotopic topology having a one-to-one correspondence between input and output units to perform autoassociative mappings. Filtering effect is obtained by subtracting the network output from the input vectors. The results show that novelty filtering combined with ICA is a powerful preprocessing tool for the detection and enhancement of epileptic seizure activity in the nonstationary EEG signals.**

Keywords—**Novelty Filtering, Autoassociative Neural Networks, Independent Component analysis, Epileptic Seizure, EEG Signals.**

I. Introduction

Epilepsy is a neurological disorder that affects nearly 1% of the world population. Epilepsy is characterized by the spontaneous and unforeseeable occurrence of seizures, during which the perception or behavior of patients is disturbed. Epilepsy involves uncontrolled neuron firings, including sustained rhythmic activity (seizures), brief transient discharges (spikes), or combinations (spike-wave discharges). There are more than 30 distinct classes of seizure [1]. The Electroencephalogram (EEG) is the most used tool for the evaluation of such patients in a non-invasive manner. Currently the detection of abnormal electrographic patterns, such as epileptic seizures is done by manually reviewing the EEG recordings. However, with the introduction of digital systems in the analysis of EEG signals, quantitative methods have been developed. The major goal of these methods is to detect and classify such electrographic patterns being supplement to the wide range of all recently developed detection techniques [2, 3].

In the field of automatic signal detection or recognition, strong signals relative to surrounding noise generally make easier the task of extracting the features for recognition and classification [10]. Novel introduced preprocessing techniques such as Independent Component Analysis (ICA) and Novelty Filtering can be applied for this purpose. This paper is directed at the exploitation of neural networks as a preprocessor tool for Novelty Filtering and signal enhancement. Since the novelty filter is highly sensitive to statistical properties of signal, ICA is used for removing noise, artifacts from signal and stabilization of it s statistical behavior, prior to perform the novelty filtering.

This paper is organized as follows. We first briefly introduce the concepts of ICA and it s application to removing noise and biological artifacts from EEG signal. The novelty filtering and it s behavior are then presented. Results of applying mentioned methods for the purpose of EEG signal enhancement and detection of epileptic seizure activity are given in the next section followed by conclusions.

II. Noise and artifact rejection

EEG signals usually are contaminated by artifacts and noise. Artifacts includes eye blinks, movements and activation of muscles. These artifacts may seriously obscure the analysis quality and interpretation. So for designing a robust recognition system, it is it essential to remove noise and artifacts from EEG signal.

A. Independent Component Analysis

Recently ICA has been applied for analysis of brain signals [6,7, 8]. Also This method can be used to detect and remove a wide variety of artifacts and noise from spontaneous EEG data [5].

ICA is a statistical technique that aims at finding linear projections of the data that maximize their mutual independence. Its main applications are in feature extraction, classification and blind source separation (BSS) [4], with special emphasis to physiological data analysis. The separation principle in these methods relies on the statistical independence of the reconstructed sources [6].

F. Ibrahim, N.A. Abu Osman, J. Usman and N.A. Kadri (Eds.): Biomed 06, IFMBE Proceedings 15, pp. 383-386, 2007
www.springerlink.com ' Springer-Verlag Berlin Heidelberg 2007

In the blind source separation, The problem setting of ICA is as follows: Assume that there is an N-dimensional zero-mean non-gaussian source vector $s(t) = [s_1(t),...,s_N(t)]^T$ such that the components $s_i(t)$ s are mutually independent and an observed data vector $x(t) = [x_1(t),...,x_N(t)]^T$ is composed of linear combinations of sources $s_i(t)$ at each time point t such that

$$x(t) = A.s(t) \quad (1)$$

where A is a full rank matrix. ICA tries to solve an inverse problem and it s goal is to find a linear mapping W such that each component of an estimate *u* of the source vector

$$u(t) = W.x(t) = WA.s(t) \quad (2)$$

Several algorithms have been developed to find such a linear transformation. In this work, we used the online version of FastICA algorithm [9]. We have decided to concentrate on concepts and example results in this paper. Whilst the mathematical details of the theory are of importance, they are fully covered elsewhere [4].

B. EEG signals and Artifact Rejection

Twelves channels of EEG from a patient were recorded by Ag/AgCl scalp electrodes placed according to the International 10-20 system. The signals were band-pass filtered between 1-30 Hz, sampled at 128 Hz and digitized to 12 bits. Figs. 1(a) and (b) show a subset of 12 EEG signals and their independent components. No seizure events contained for the presented interval. As shown in Figs.1(b) several artifact structures are evident, such as eye and muscle activity and noise. IC1 and IC8 are clearly eye blinks and eye movements, respectively. Artifacts related to muscle activity are separated in IC12, whereas IC10 belongs to the noise. Artifact and noise-free EEG signals, can be obtained by mixing and projecting back onto the scalp channels selected non-artifactual ICA components by multiplying the selected activation waveforms, by the inverse mixing matrix.

III. NOVELTY FILTERING

Weak signals present a difficult challenge to the methods tasked to extract robust features for classification and recognition. Therefore, improvement of signal to noise ratio increases the performance of an automatic signal detection

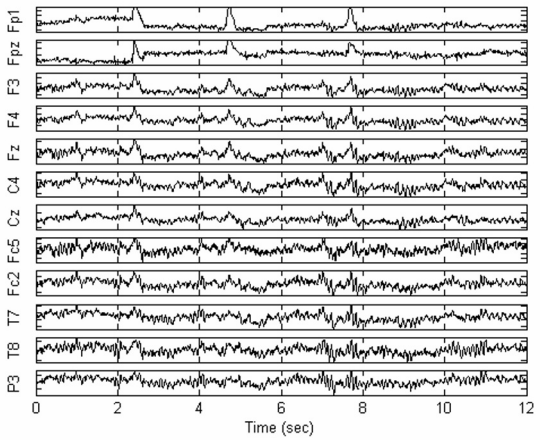

(a)

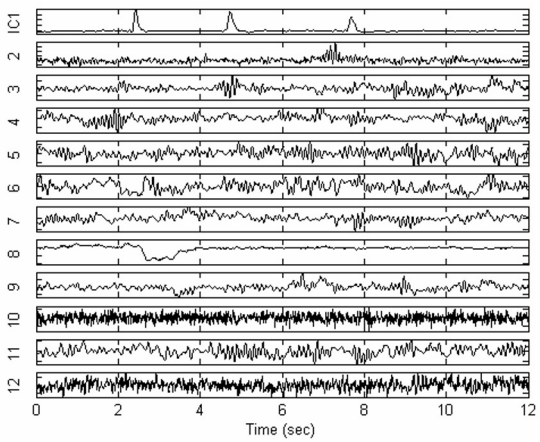

(b)

Fig. 1(a): a subset of twelve channels of EEG signals, (b): independent components of EEG signals

and recognition algorithm. A neural network based preprocessor that learns to selectively filter out the background activity without significantly affecting the interested signal will be highly useful in solving these practical signal enhancement problems [11]. This work aims to apply such an idea for the operation of neural network based novelty filters which enhance the signal detectability in the presence of interference and noise background. In this setting, the output of the novelty filter, that is less noisy than the input, is to be passed through a signal detector or feature extraction stage.

Such filter is formed from a simple retinotopic perceptron network with sigmoidal output units performing auto-association for novelty filtering. Networks of retinotopic topology having a one-to-one correspondence between input and output units can be readily trained using the delta learn-

F. Ibrahim, N.A. Abu Osman, J. Usman and N.A. Kadri (Eds.): Biomed 06, IFMBE Proceedings 15, pp. 383-386, 2007
www.springerlink.com ' Springer-Verlag Berlin Heidelberg 2007

ing rule, to perform auto-associative mappings. A novelty filter is obtained by subtracting the network output from the input vector. Then the presentation of a familiar pattern tends to evoke a null response, but any anomalous component is enhanced. Such a behavior exhibits a promising feature for enhancement of weak signals in additive noise.

The other key factor is the presence of a so-called bottleneck that occurs in at least one of the hidden layers of the neural network. The size of the bottleneck, while very application-specific, must be of a dimension smaller than the input layer. All neural networks discussed herein were trained using standard error-backpropagation methods, and all networks were fully connected [13, 14].

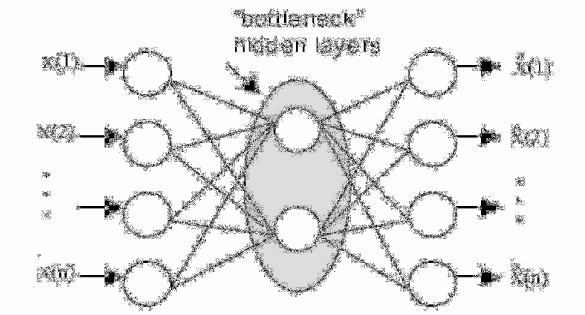

Fig. 2: Retinotopic feed-forward network with single hidden layer, can be trained to perform auto-associative mapping[13].

Fig 3. shows the idea of signal enhancement. The perfect novelty filter trains on the background until its output approaches zero. When a weak transient is added to the background, the adaptive network ignores it. The output of the regular novelty filter then reproduces the added transient with negligible distortion [12].

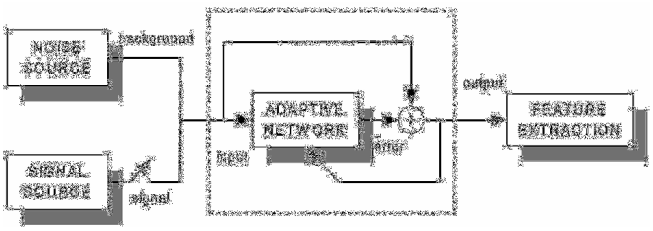

Fig. 3: Ideal novelty filtering process[12]

TRAINING: input = EEG background (normal EEG)
output = input-{ EEG background} ==> 0

TESTING: input = EEG background + signal (epileptic seizure)
output = input-{EEG background} = EEG background +
signal-{EEG background} ==> signal (epileptic seizure)

In Fig. 3, during training phase the key is open and the network trains by intervals of patient s normal EEG. After training, filter output has minimum response to the background EEG activities. During the test phase, the key is closed and EEG with epileptic seizure activities is fed to filter. Filter detects the epileptic seizure activities and interprets them as novelties.

IV. Results

Fig 4. shows 13 seconds interval of channel T7 patient s EEG signal. Note that the artifacts and noise are rejected by ICA from EEG. epileptiform activity commences around sixth second and the changes in signal structure are clearly evident.

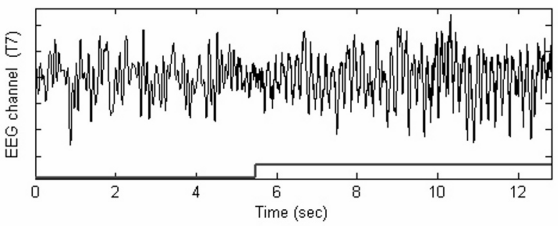

Fig. 4 a segment of channel T7 EEG signal, epileptiform activity begins around sixth second.

In this work best performance is obtained by a neural network of 20-14-20 structure (20 inputs/outputs, and a single hidden layer). Activation function for hidden layers was set to binary function. Approximately 15,000 training patterns were generated in the form of sliding running window of 20 data points from ICA-refined raw EEG data, containing no epileptiform activity, and they are used as training patterns. During the training, the patterns were randomly selected and then fed into the network. The learning process is stopped when it is apparent that the generalization performance has peaked.

Training patterns were not used for the validation procedure. For testing procedure of the novelty detector a new sequence of patterns, which include epileptic seizure activities, again was created from ICA-refined raw EEG data, in the same manner as generating of training patterns. This sequence was run through the novelty detector using the same method used in training. If correctly working, the novelty filter should filter out the EEG background or normal EEG activities while the epileptic seizure is brought out prominently.

Fig. 5(up) shows 35 seconds interval of patient s EEG signal (channel T7). epileptic seizure onset is occurred around seventeenth moment. Output of filter and it s variance are shown in the middle and at the bottom of the Fig. 5, respectively. Fearing that the detector can works simply as a thresholding mechanism. In the Fig. 5 original signal (channel T7) and enhanced signal (filter output) both are shown for comparison.

F. Ibrahim, N.A. Abu Osman, J. Usman and N.A. Kadri (Eds.): Biomed 06, IFMBE Proceedings 15, pp. 383-386, 2007
www.springerlink.com ' Springer-Verlag Berlin Heidelberg 2007

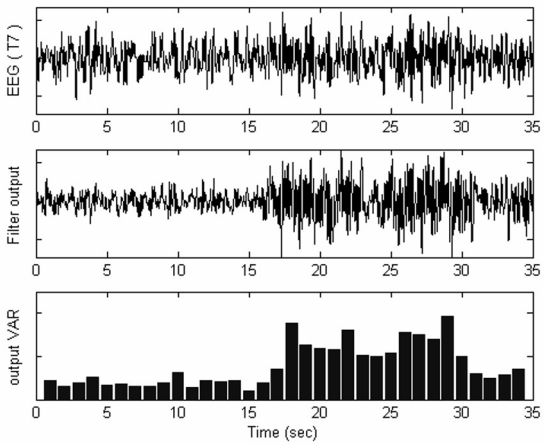

Fig. 5 (up): 35 seconds of patient s EEG signal (channel T7), epileptic seizure onset is occurred around seventeenth second, (middle): enhanced signal (filter output), (bottom): variance of enhanced signal.

V. Conclusions

In this work, we showed that the novelty filtering technique combined with ICA is a powerful preprocessing tool for the detection and enhancement of epileptic seizure activity in the nonstationary EEG signals. We also showed that a neural network with retinotopic structure can learn underlying statistical behavior of EEG signals in the implicit manner.

References

1. Kandel E R, Schwartz J H, Jessel T M, (1991) Principles of Neural Science, New Jersey: Prentice-Hall
2. Esteller R, (2000) Detection of Seizure Onset in Epileptic Patients from Intracranial EEG Signals, in ECE. Atlanta: Georgia Institute of Technology
3. Gotman J, (1985) Seizure recognition and analysis, Electroencephalogr Clin Neurophysiol Suppl, vol. 37, pp. 133-45.
4. Hyvarinen A, Karhunen J and Oja E, (2001) Independent ComponentAnalysis. John Wiley & Sons.
5. Vigario R, Sarela J, Jousmaki V, Hamalainen M, Oja E, (2000) Independent Component Approach to the Analysis of EEG and MEG Recording, IEEE Trans. Biomed. Eng. vol. 47, no. 5
6. Jung T,makeig S, Westerfield M, Townsend J, Courchesne E, Sejnowski T, (2001) Analysis and visualizion of single-trial event-related potentials, Human Brain Mapping, vol. 14, pp. 166-185
7. Erfanian A, Erfani A, (2004) ICA-Based Classification Scheme for EEG-based Brain- Computer Interface: The Role of Mental Practice and Concentration Skills, Proc. of the 26th IEEE EMBS
8. Erfani A, Erfanian A, (2004) The Effects of Mental practice and Concentration Skills on EEG Brain Dynamics During Motor Imagery Using Independent Component Analysis, Proc. of the 26th IEEE EMBS
9. Elsabrouty M, Bouchard M, Aboulnasr T, (2003) A new on-line negentropy-based algorithm for blind source separation, Proc. of 46th IEEE International Midwest Symposium on Circuits and Systems
10. Hanseok Ko, Arazulla M., (2000) Background Noise Suppression for Signal Enhancement by Novelty Filtering, IEEE Transactions on Aerospace and Electronic Systems., vol. 36 no. 1, pp 102-113
11. Arozullah M, Hanseok Ko, (2000) Background noise suppression for signal enhancement by novelty filtering, IEEE Transactions on Aerospace and Electronic Systems, vol. 3, no.6
12. Hanseok Ko, Jacyna M, (1999) Dynamical Behavior of Autoassociative Memory Performing Novelty Filtering for Signal Enhancement, IEEE Transaciotn on Neural Networks, vol.11, no. 5
13. Benjamin B Thompson , Robert J Marks II , Jai J Choi, Mohamed A El-Sharkawi, (2002) Implicit Learning in Autoencoder Novelty Assessment, Proc. of the 2002 International Joint Conference on Neural Networks, pp. 2878-2883
14. Benjamin B Thompson , Robert J Marks II , Jai J Choi, Mohamed A El-Sharkawi, (2005) Implicit Parameter Resonance in Autoassociative Neural Network Encoders, IEEE Transactions on Neural Networks, submitted

Address of the corresponding author:

Author: Ali Erfani
Institute: Department of Physics, Karaj Branch, I. Azad University
Street: Moazen Blvd
City: Karaj
Country: Iran
Email: a.erfani@yahoo.com

F. Ibrahim, N.A. Abu Osman, J. Usman and N.A. Kadri (Eds.): Biomed 06, IFMBE Proceedings 15, pp. 383-386, 2007
www.springerlink.com ' Springer-Verlag Berlin Heidelberg 2007

Feasibility of Fetal Photoplethysmography Signal Extraction using Adaptive Noise Cancelling

K.B. Gan[1], E. Zahedi[1] and M.A.Mohd Ali[1]

[1]Department of Electrical, Electronic & Systems Engineering, Faculty of Engineering, UKM, Bangi, Malaysia

Abstract—**In this paper, an approach based on adaptive noise cancellation (ANC) is evaluated to extract the fetal heart-rate using photoplethysmographic (PPG) signals from the maternal abdomen. Results of simulations using semi-synthetic PPG signals are presented which show the feasibility of the proposed technique. Then a mixture of PPG signal is produced by recording the PPG from overlapping fingers from two different subjects in-lieu of the mother and fetus. Results show that a recursive least-squares algorithm is capable to extract the peaks of the desired PPG signal, hence the heart-rate, even at a SNR of -34 dB.**

Keywords—**Photoplethysmography, Adaptive signal processing**

I. Introduction

Photoplethysmography (PPG) is an optoelectronic method for measuring and recording changes in the volume of body parts such as finger and ear lobes [1,2]. PPG is a non-invasive monitoring technique widely used for the estimation of blood oxygenation and heart rate.

In [3], optical methods have been proposed for fetal cerebral blood oxygenation measurement where four 20 W halogen lamps and a pair of 0.575 W tungsten lamps act as light sources and detection is done by a photomultiplier. These techniques require a high optical power, an expensive detection system (photomultiplier) and are difficult to implement from a practical point of view due to the sheer size of the components.

Further work [4] has been directed towards trans-abdominal monitoring of fetal arterial blood oxygenation using pulse-oximetry and by the same means fetal heart rate (FHR) [4]. Selection of the wavelengths (675-700 nm and 850-900 nm regions) results in reduced saturation errors and a large source-detector separation leads to less measurement error caused by optical shunting [4].

In this research, a low-power optical technique based on the photoplethysmogram (PPG) is proposed. This is to ensure that the amount of injected light do not affect the fetal growth especially fetal optic system. Lowering the input power of the incident radiation clearly leads to a lower SNR due to the presence of ambient light and especially the interference by the larger magnitude maternal signal. Thus, appropriate signal processing techniques are needed in order to extract the fetal PPG.

II. Adaptive noise cancelling

This technique is widely used in signal processing where the source of the contamination is accessible [5]. The desired signal *d(n)* (Fig. 1) is contaminated by an uncorrelated noise signal $v_0(n)$, where n is the running time index. The result $d(n) + v_0(n)$ is the primary measurement signal *s(n)*. The reference input, $v_1(n)$, is only correlated with $v_0(n)$ and fed to an adaptive FIR filter. The output of the FIR adaptive filter *(y(n))* is subtracted from the primary input *s(n)* to produce the error signal *e(n)*:

$$e(n) = d(n) + v_0(n) - y(n) \tag{1}$$

The adaptive filter uses *e(n)* to adjust its own impulse response to produce an output *y(n)* as close a replica as possible to $v_0(n)$. Squaring and applying the expectation operator to both sides of Equation (1):

$$E\{e^2(n)\} = E\{d^2(n)\} + E\{(v_0(n) - y(n))^2\} - 2E\{d(n)(v_0(n) - y(n))\} \tag{2}$$

As *d(n)* is uncorrelated with v_0(n) and v_1(n), $E\{d(n)(v_0(n)-y(n))\} = 0$ and therefore Equation 2 can be simplified:

$$E\{e^2(n)\} = E\{d^2(n)\} + E\{(v_0(n) - y(n))^2\} \tag{3}$$

An iterative procedure minimizes $E\{e^2(n)\}$, which will occur when $y(n) = v_0(n)$ (ideal situation) producing $e(n) = d(n)$.

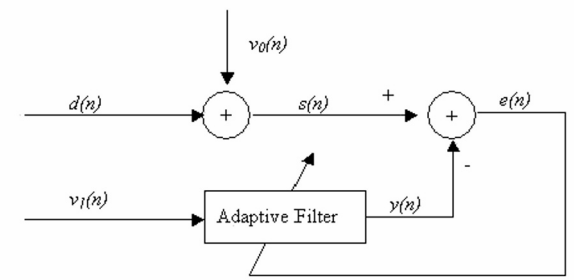

Fig. 1 Adaptive noise cancelling system

F. Ibrahim, N.A. Abu Osman, J. Usman and N.A. Kadri (Eds.): Biomed 06, IFMBE Proceedings 15, pp. 387-390, 2007
www.springerlink.com ' Springer-Verlag Berlin Heidelberg 2007

III. METHODS

A. Data acquisition and pre-processing

PPG signals are acquired from the index finger of two healthy subjects A (right index finger) and B (right and left) by using PPG recording systems (Dolphin Medical, Inc.) at a rate of 275Hz and at 16-bit resolution. All signal processing is done using Matlab (The Mathworks, Inc.).

After removing any linear trend in the signals, the low and high frequency components are filtered with a 0.6-15Hz bandpass filter. These cut-off frequencies are selected in such a way that the respiration signal that occurs at 0.1-0.55Hz and high frequency noise are rejected [6,7]. The last pre-processing step consists of scaling the acquired signal to 1 to +1.

B. Signal emulation

There are four signals, PPG_{M_1}, PPG_{M_2}, PPG_F and the primary PPG signal, to be emulated in this study (Fig. 2). To emulate PPG_F, the right index finger s PPG of subject A is down sampled by a factor of two (resulting in a heart rate twice as the original signal) and its amplitude is reduced by a variable factor *k*. The mother abdomen signal PPG_{M_1} is emulated from the right index finger of subject B s PPG. Then, the primary PPG signal (PPG_{M_1} + PPG_F) that contained both maternal and fetal PPG signal is emulated.

The reference signal PPG_{M_2} is created from the left index finger of subject B s PPG. Thus, PPG_{M_2} is not identical to PPG_{M_1} but is correlated with it [8]. All signals are pre-processed according to the description given in section A.

C. Adaptive Noise Cancelling (ANC) Simulation

ANC using the Recursive Least Square (RLS) algorithm was implemented in Matlab by using emulated signals (section B). By varying the PPG_F amplitude, the minimum (signal to noise ratio) SNR where PPG_F is still detectable is investigated. The ANC model applied to fetal PPG extraction is shown in Fig. 2 where the primary PPG signal (PPG_{M_1} + PPG_F) is the input to the RLS algorithm and PPG_{M_2} is the reference signal.

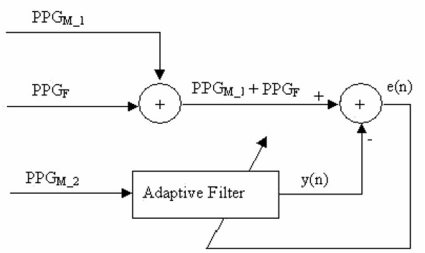

Fig. 2 Adaptive Noise Cancelling model applied to fetal PPG extraction

The FIR filter order was fixed to 100 after trying orders from 30 to 200. The δ value, a small positive value in RLS algorithm, is set using $\delta = P_x$ where $P_x = E\left[v_1^2(n)\right]$ is the average power of $v_1(n)$.

Haykin [9] has shown that $\mu = 1 - \lambda$ plays a role similar to the step size in the LMS method. After trying λ values from 0.99 to 0.9999, λ is fixed to 0.9999. Therefore, λ should be close to unity to keep μ small.

D. " Two-Finger" Experiment

In order to evaluate the RLS algorithm under realistic conditions, an experiment is realized by overlapping the left index finger from one subject (LS1) with right index finger from a second subject (RS2). A reference PPG signal is acquired from the right index finger of subject one (RS1) so that RS1 is not identical to the LS1 but is correlated with it. Then the RS2 is estimated using RLS algorithm (Fig. 3).

The pre-processing procedures and signal extraction are as described in sections III-A and III-C.

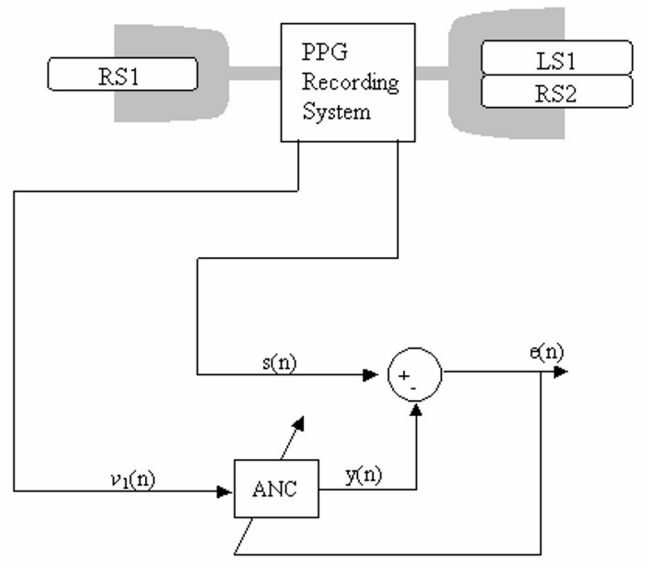

Fig. 3 Schematic of the two-finger experiment setup and ANC

IV. RESULTS

A. Adaptive Noise Cancelling (ANC) Simulation

Sample traces of PPG_{M_1} + PPG_F and PPG_{M_2} are shown in Fig. 4. The desired signal PPG_F and the estimated PPG_F signal, *e(n)* are shown in Fig. 5. The normalized PSD of the estimated PPG_F is shown in Fig. 6. The PSD plot shown is smoothened by a delay compensated 4th order

F. Ibrahim, N.A. Abu Osman, J. Usman and N.A. Kadri (Eds.): Biomed 06, IFMBE Proceedings 15, pp. 387-390, 2007
www.springerlink.com ' Springer-Verlag Berlin Heidelberg 2007

moving average filter. The simulated maternal heart rate is 60 BPM while the simulated fetal heart rate is 162 BPM.

The performance of the RLS algorithm is evaluated by computing the signal to noise ratio:

$$SNR = 10\log\left(\frac{\sum_{n=1}^{m}\left(PPG_F(n)\right)^2}{\sum_{n=1}^{m}\left(PPG_{M\_1}(n)\right)^2}\right) \quad (4)$$

where m is the record length.

The simulation shows that the minimum SNR where PPG_F is still detectable is 34.6 dB.

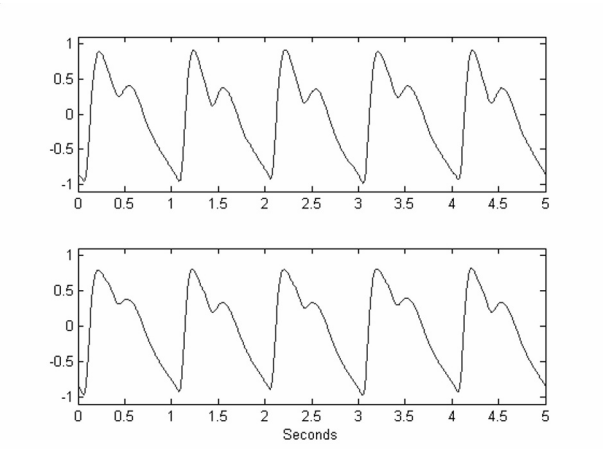

Fig. 4 PPG_{M_1} + PPG_F (top) and PPG_{M_2} (bottom) SNR = – 34.6 dB

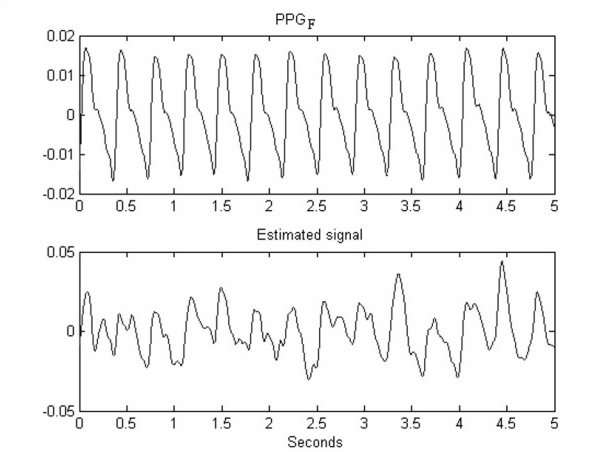

Fig. 5 PPG_F (top) and the output of RLS filter signal (bottom), input signals, Fig. 4 (SNR = −34.6 dB)

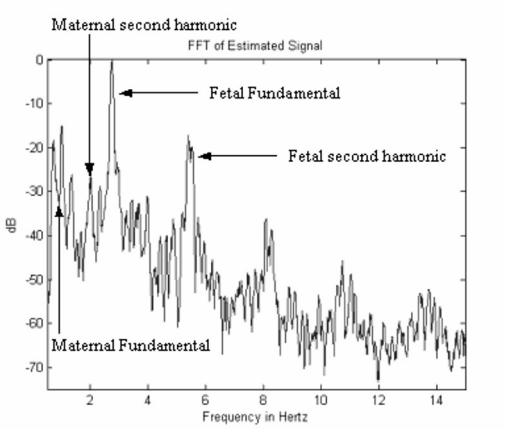

Fig. 6 Normalized PSD of the estimated PPG_F (input SNR = – 34.6 dB)

B. "Two-Finger" Experiment

Sample traces of RS1 ($v_1(n)$), mixed signal ($s(n)$) where LS1 overlapped with RS2 and finally the estimated RS2 ($e(n)$) are shown in Fig. 7.

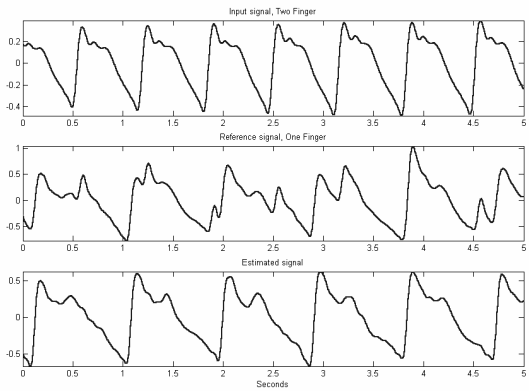

Fig. 7 RS1 ($v_1(n)$) (top), mixed signal where LS1 overlapped with RS2 ($s(n)$) (middle) and filter order = 50 estimated RS2 ($e(n)$) (bottom).

V. Conclusions

The simulation results show that adaptive noise cancelling using RLS algorithm is able to extract the PPG_F from the primary PPG signal (PPG_{M_1} + PPG_F) and the minimum SNR where PPG_F is still detectable is 34.6 dB. Moreover, it is possible to estimate a PPG signal from a mixture produced by overlapping two fingers from different subjects using the proposed algorithm.

The main limitations of this technique are the presence of motion artifacts and probe placement. Any motion artifact affecting PPG_F will not be filtered by ANC, as the ref-

F. Ibrahim, N.A. Abu Osman, J. Usman and N.A. Kadri (Eds.): Biomed 06, IFMBE Proceedings 15, pp. 387-390, 2007
www.springerlink.com ' Springer-Verlag Berlin Heidelberg 2007

erence signal does not contain any correlated component to this signal.

Currently, work is under progress toward realization of an optical model, a physical phantom and eventually clinical test for the optical extraction of the FHR.

Acknowledgment

This work has been partially supported by an Intensive Research Priority Areas grant (IRPA-09-02-02-0106-EA258) from the Ministry of Science and Technology, Malaysia.

References

1. Bronzino JD (2000) The Biomedical Engineering Handbook. Boca Raton.
2. Bhattacharya PP, Kanjilal, Muralidhar (2001) Analysis and characterization of photoplethysmographic signal. IEEE Transaction. Biomedical Engineering 48:5-11.
3. Ramanujam N, Vishnoi G, et. al. (2000) Photon migration through the fetal head in utero using continuous wave, near infrared spectroscopy: clinical and experimental model studies. Journal of Biomedical Optics 163-172.
4. Zourabian A, Chance B, et. al. (2005) Trans-abdominal monitoring of fetal arterial blood oxygenation using pulse oximetry. Journal of Biomedical Optics 391-405.
5. Widrow B, Glover JR, et. al. (1975) Adaptive noise cancelling: principles and applicatio ns, Proceedings of the IEEE, 63:1692-1716.
6. Nakajima K, Tamura T and Miike H (1996) Monitoring of heart and respiratory rates by photoplethysmography using a digital filtering technique, Medical Engineering & Physics 18 (5):365-372.
7. Barschdorff D and Zhang W (1994) Respiratory rhythm detection with photoplethysmographic methods, Engineering in Medicine and Biology Society, Engineering Advances: New Opportunities for Biomedical Engineers. Proceedings of the 16th Annual International Conference of the IEEE 912 913.
8. Allen J and Murray A (2000) Variability of Photoplethysmography Peripheral Pulse Measurements at the Ears, Thumbs and Toes, IEEE Proceeding Science and Technology 147 (6):403-407.
9. S. Haykin (2002) Adaptive filter theory, Prentice Hall.

Address of the corresponding author:

Author: Gan Kok Beng
Institute: Universiti Kebangsaan Malaysia
Street: 43600 UKM
City: Bangi, Selangor,
Country: Malaysia
Email: kok_beng_gan@yahoo.com

F. Ibrahim, N.A. Abu Osman, J. Usman and N.A. Kadri (Eds.): Biomed 06, IFMBE Proceedings 15, pp. 387-390, 2007
www.springerlink.com ' Springer-Verlag Berlin Heidelberg 2007

Feasibility of Photoplethymographic Signal for Assessment of Autonomic Response using Heart Rate Variability Analysis

Nandakumar Selvaraj[1], Jayashree Santhosh[2] and Sneh Anand[1]

[1] Centre for Biomedical Engineering, Indian Institute of Technology-Delhi, New Delhi, India.
[2] Computer Services Centre, Indian Institute of Technology-Delhi, New Delhi, India.

Abstract—**Heart rate variability (HRV) represents one of the most promising quantitative markers of autonomic nervous system activity. It is commonly derived from RR interval of electrocardiographic (ECG) signal to evaluate the balance of sympathetic and parasympathetic responses due to the change in heart rhythm. However, in this present study, peak-to-peak interval variability of photoplethysmographic (PPG) signal has been used for the estimation of HRV. Further, to demonstrate the accuracy and feasibility of HRV extraction from PPG signal, finger-tip PPG and standard lead II ECG signals were simultaneously acquired under normal and deep breathing conditions. A comparative analysis of time- and frequency-domain measures of HRV was carried out. The correlation analysis of tachograms of ECG and PPG (Pearson linear correlation coefficient 0.9698 and 0.7389 under normal and deep respiration respectively) and error analysis of HRV parameters suggest that PPG can be considered as a simpler and reliable alternative for the HRV analysis and estimation of autonomic regulation.**

Keywords—**Heart rate variability, Photoplethysmograph, Spectral analysis, Autonomic nervous system and Respiratory rate.**

I. Introduction

The autonomic nervous system (ANS) functions automatically at the reflex and subconscious levels to maintain the equilibrium of basic parameters such as heart rate, respiratory rate, blood pressure and body temperature, through sympathetic and parasympathetic responses. It plays a major role in the physiological interaction of respiration and circulation, known as the respiratory sinus arrhythmia (RSA) by which the R-R interval of electrocardiogram (ECG), sequences of successive inter-beat interval, is shortened during inspiration and prolonged during expiration [1]**.** Heart rate variability (HRV) is generally determined directly from R-R interval of ECG signal. From the spectral analysis of HRV signal, low frequency (LF) band is related to sympathetic activity and the high frequency (HF) band is related to parasympathetic activity. The LF/HF ratio and absolute power contained in these bands are good indicators for the assessment of alterations in the nervous system behavior [2]. The photoplethysmographic (PPG) signal has also proved its potential for evaluation of ANS response [3]**.**

Photoplethysmography is a noninvasive optical technique where peripheral blood volume changes in living tissue due to the pulse radiating through heart beat are monitored. The HRV time series can also be obtained from the PPG waveform instead of traditional ECG signal. It is quite possible to analyze the HRV using PPG signal when subjects are in stationary cardiovascular condition [4]. Thus, PPG has been reported as an alternative diagnostic tool to study the cardiovascular system viz HRV [5].

In this study, ECG and PPG signals were simultaneously acquired under normal and deep breathing conditions and the HRV signal was derived from both of them. A comparative analysis of time- and frequency-domain parameters of HRV signal and also the correlation analysis of instantaneous heart rate were carried out to prove the feasibility of PPG signal for HRV extraction. Further, the alteration in ANS response due to the induced respiratory variation was quantified.

II. Materials and methods

Subjects with no history of cardiovascular disease and hypertension were included in this exploratory study. Each subject was placed comfortably in sitting posture under controlled room temperature with a resting period of 5 to 10 minutes prior to the study. The data was recorded for about 5 minutes each under normal and deep breathing conditions from every subject.

A. Experimental set-up

The photoplethysmograph transducer (TSD200), primarily designed for finger attachment, consists of a matched infrared emitter of wavelength 860 nm and a photo diode, which transmits variation in infrared reflectance resulting from blood flow variation. This transducer was strapped on to the right middle finger of the subject and connected to the PPG amplifier (PPG100C) through a shielded cable to record the blood volume pulse (BVP) waveform with gain 100 and cut-off frequencies 0.05 and 10 Hz. Disposable Ag

F. Ibrahim, N.A. Abu Osman, J. Usman and N.A. Kadri (Eds.): Biomed 06, IFMBE Proceedings 15, pp. 391-395, 2007
www.springerlink.com ' Springer-Verlag Berlin Heidelberg 2007

AgCl electrodes (EL503) were used to record standard lead II ECG signal. An ECG amplifier (ECG100C) was used to amplify the ECG signal with a gain of 1000 and cut-off frequencies 0.05 and 35 Hz. The MP 150 (BIOPAC Systems Inc., USA), a computer-based data acquisition system with software AcqKnowledge 3.8.2, was used to acquire the PPG and ECG data simultaneously at a sampling rate of 1 KHz. The signal processing techniques were implemented offline with Matlab 7.0.

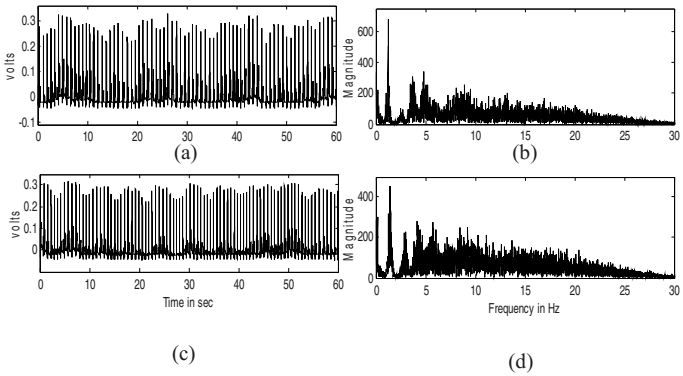

Fig. 1 ECG signal and its magnitude spectrum under normal (a & b) and deep breathing (c & d) conditions.

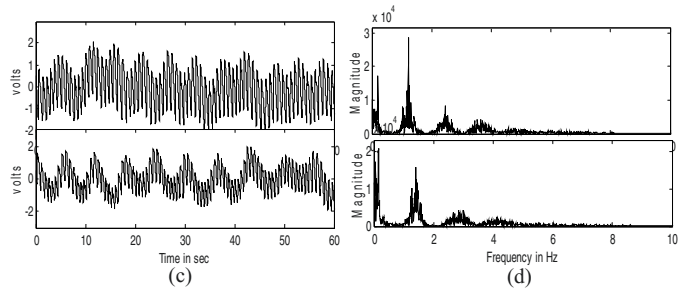

Fig. 2 PPG signal and its magnitude spectrum under normal (a & b) and deep breathing (c & d) conditions.

B. Data preprocessing

A typical data of a subject RP (25 years) has been presented under normal and deep breathing conditions. After eliminating DC component or the baseline signal, ECG and PPG data were filtered with moving average window to eliminate HF as well as the interference noise. Fast Fourier Transformation (FFT) spectral analysis was performed on preprocessed ECG and PPG to determine their frequency components. The preprocessed ECG, and PPG signal, their magnitude spectrum are shown in Fig. 1 & 2 respectively. As the frequency band from 0.15 to 0.4 Hz has been linked with respiration, the respiratory signal (Fig. 3) was derived from the processed PPG signal to estimate the respiratory rate [6, 7].

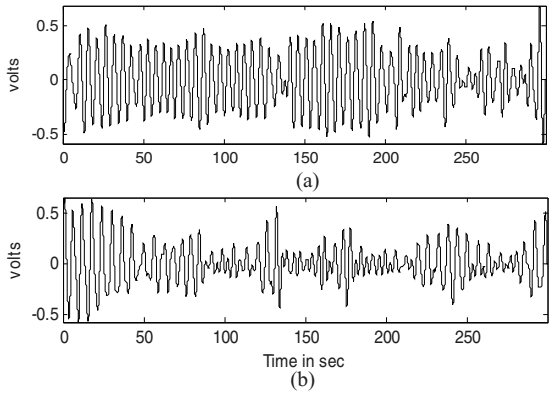

Fig. 3 The respiratory derived from PPG signal under normal (a) and deep breathing (b) conditions.

C. Spectral analysis of HRV signal

The spectral analysis of the HRV signal enables to understand the sympathetic and parasympathetic activities of the autonomic nervous system in controlling the cardiovascular system. HRV signal is conventionally extracted from RR interval of ECG data. As RR interval samples are not uniform and spaced according to the heart beat intervals, some preprocessing is required to obtain RR intervals evenly spaced in time [2]. The series of RR interval was interpolated by cubic spline and re-sampled at a higher and uniform rate of 4 Hz. The interpolated RR interval and PP interval series are shown in Fig. 4.

The DC component of the HRV signal was removed and finally power spectral density was obtained using FFT and 15^{th} order Burg auto-regressive (AR) model. The HRV power spectrum was divided into three bands: Very Low Frequency (VLF) (0.01 to 0.04 Hz), Low Frequency (LF): (0.04 to 0.15 Hz) and High Frequency (HF): (0.15 to 0.4 Hz). Their absolute band power and the LF/HF ratio were calculated.

Time domain variables-mean Normal-to-Normal (NN) interval, mean HR and the variance of NN interval and statistical time domain measures-standard deviation of NN interval (SDNN), the square root of the mean squared differences of successive NN intervals (RMSSD), standard deviation of differences between adjacent NN interval (SDSD), the number of interval differences of successive NN intervals greater than 50 ms (NN50) and the proportion derived by dividing NN50 by the total number of NN intervals (pNN50) were calculated from interpolated RR interval [8]. Further, frequency domain measures such as power in VLF, LF and HF, total power and the LF/HF ratio were also calculated from the HRV power spectrum.

F. Ibrahim, N.A. Abu Osman, J. Usman and N.A. Kadri (Eds.): Biomed 06, IFMBE Proceedings 15, pp. 391-395, 2007
www.springerlink.com ' Springer-Verlag Berlin Heidelberg 2007

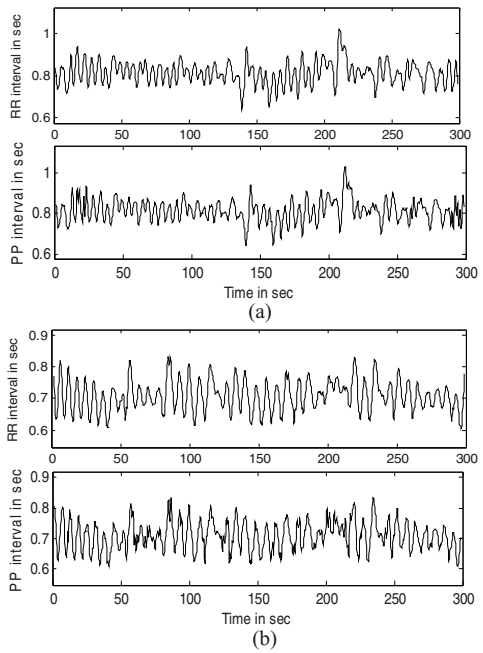

Fig. 4 The Tachograms derived from ECG and PPG signal under normal (a) and deep breathing (b) conditions.

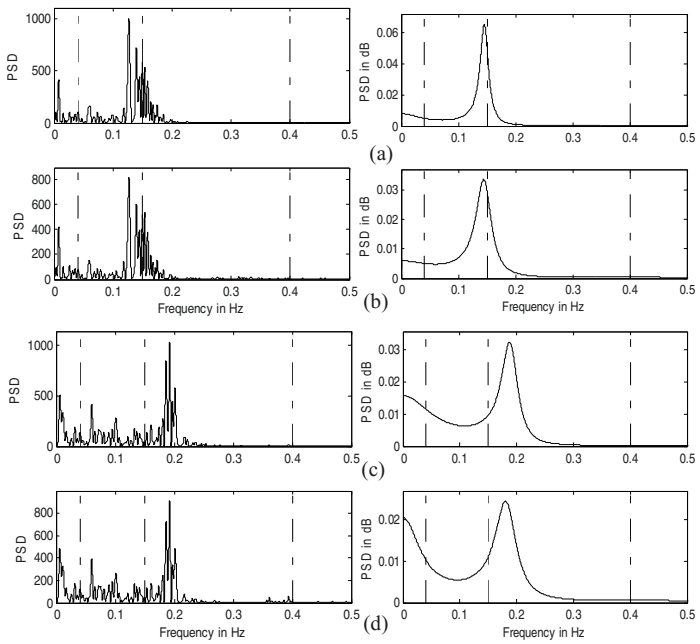

Fig. 5 FFT and Burg-AR model HRV power spectrum of normal (a-ECG & b-PPG) and deep breathing (c-ECG & d-PPG) conditions.

The peak-to-peak intervals obtained from PPG peaks were also employed to derive the HRV signal instead of RR signal of ECG. The entire time-, statistical time- and frequency-domain parameters were also obtained with the above mentioned procedures used for ECG-HRV analysis. The error was estimated in percentage for all the HRV parameters as the ratio of difference in each parameter derived from PPG and ECG to the parameter derived from ECG [4]. The HRV power spectrum obtained from ECG and PPG signals under normal and deep respiration using FFT and Burg-AR model are shown in Fig. 5.

E. Correlation Analysis

To correlate the heart rate derived from ECG and PPG measurements, the instantaneous values of heart rate were estimated separately from RR interval and PP interval series [10] and the Pearson linear correlation coefficient was determined as shown in Fig. 6.

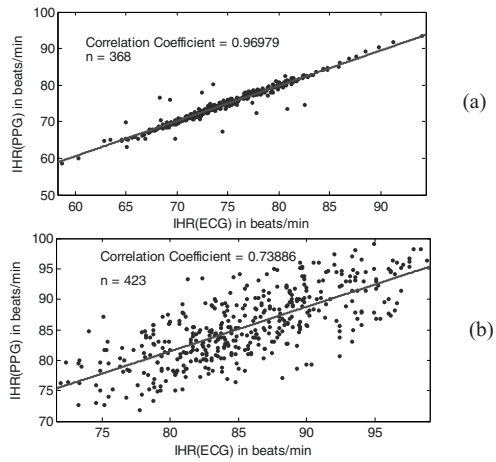

Fig. 6 Linear correlation analysis of Instantaneous HR of PPG and ECG under normal (a) and deep breathing (b) conditions.

III. Results

The induced variation in respiration rate alters especially the base line variability of PPG signal which is inversely related to the tissue blood volume (Fig. 2c). The mean respiration rate under normal and deep breathing conditions was found to be 11.8 and 9.9 respectively. The similarity in variation of RR interval of ECG and peak-to-peak interval of PPG for each beat-to-beat was observed in Fig. 4. The HRV spectrum (Fig. 5) obtained from the tachogram signals of ECG and PPG illustrated the dominance of parasympa-

F. Ibrahim, N.A. Abu Osman, J. Usman and N.A. Kadri (Eds.): Biomed 06, IFMBE Proceedings 15, pp. 391-395, 2007
www.springerlink.com ' Springer-Verlag Berlin Heidelberg 2007

thetic and sympathetic activities during normal and deep respiration respectively. Further, the time- and frequency-domain HRV parameters were calculated (Table 1). The increase in heart rate due to induced reduction in respiration rate was faithfully quantified by PPG signal with zero error; where as the ANS response (LF/HF ratio) was obtained with 4.5 and ~20 % error under normal and deep breathing conditions respectively. The correlation analysis of instantaneous heart rate estimated from ECG and PPG signals showed a significant linear correlation with Pearson correlation coefficient 0.9698 and 0.7389 under normal and deep breathing conditions respectively.

Table 1 Heart Rate Variability parameters

Parameter		Normal respiration		Error (%)	Deep respiration		Error (%)
		ECG	PPG		ECG	PPG	
Time domain	Mean (NN)	0.8136	0.8136	0	0.7084	0.7084	0
	SD (NN)	0.0540	0.0533	-1.30	0.0476	0.0466	-2.10
	Var. (NN)	0.3824	0.3871	1.23	0.2267	0.2290	1.01
	Mean (HR)	74.073	74.062	-0.01	85.078	85.059	-0.02
Statistical time domain	RMS SD	28.163	28.127	-0.13	24.503	24.502	-0.01
	SDSD	0.0131	0.0147	12.2	0.0108	0.0130	20.4
	NN50	2.0000	1.0000	-50.0	0	0	0
	pNN50 (%)	0.1676	0.0840	-49.9	0	0	0
Frequency domain	Total power	909790	886640	-2.54	707670	677990	-4.2
	VLF	46970	45300	-3.55	19020	19760	3.89
	LF	148840	145030	-2.56	216630	184960	14.6
	HF	218810	204040	-6.75	90330	96480	6.81
	LF/HF	0.6802	0.7108	4.5	2.3982	1.9171	-20.1

IV. Discussion

As the respiratory signal extracted from PPG signal showed good correspondence with the respiratory thermistor signal and had a sufficient time resolution [11], the respiratory rhythm was extracted from PPG measurements alone. The fluctuation in PPG base line is mediated mainly by the sympathetic activity of ANS [12]. The variation in sympathetic and parasympathetic activities due to the induced respiratory changes reported in this present study confirms the above. It is in agreement with the results of earlier reports which demonstrated the presence or absence of sympathetic pacing of heart with HRV spectrum of normal and cardiovascular patients [5]. Further, the estimation of variation in time-and frequency-domain HRV parameters ascertain the feasibility of PPG signal for the assessment of ANS response. However, the components of HRV provide measurements of the degree of autonomic modulations rather than the level of autonomic tone [8].

From our study, it is evident from the correlation and error analysis that the HRV parameters derived from PPG very closely resemble to HR measures derived from traditional ECG recordings. Therefore, the simplicity and user friendliness of PPG transducer can be considered as an alternative diagnostic tool to extract multiple physiological variables such as respiration, HRV and arterial stiffness even for combat and trauma medicine.

To completely understand the respiratory modulation of autonomic activity, the study has to be continued to probe HRV in synchrony with respiration cycle to cycle and with more cross-sectional data. Further, the monitoring and assessment of ANS regulation of cardiovascular functions can be effectively carried out for different ailments using photoplethysmography.

Acknowledgment

The authors would like to thank Dr. K. K. Deepak and Dr. Ashok Jariayal, Department of Physiology, All India Institute of Medical Sciences, New Delhi and the technical staff of Rehabilitation Laboratory, IIT-Delhi for their help in data collection.

References

1. Fumihiko Yasuma and Jun-ichiro Hayano (2004) Respiratory sinus arrthymia-Why does the heart beat synchronize with respiratory rhythm? Chest 125(2): 683-690.
2. J. L. A. Carvalho, A. F. Rocha et al (2003) A tool for time-frequency analysis of heart rate variability. Proc. of the 25th Annual International Conf. of the IEEE EMBS, Cancun, Mexico, 2003, pp 2574-2577.
3. Meir Nitzan, Anatoly Babchenko et al (1998) The variability of the photoplethysmographic signal-a potential method for the evaluation of the autonomic nervous system. Physiol. Meas. 19: 93-102.
4. X. F. Teng and Y. T. Zhang (2003) Study on the peak interval variability of photoplethysmographic signals. IEEE EMBS Asian-Pacific Conference on Biomedical Engineering, 2003, pp 140-141.
5. V. S. Murthy, S. Ramamoorthy et al (2001) Analysis of photoplethysmographic signals of cardiovascular patients. Proceedings of the 23rd Annual EMBS International conference, 2001, pp 2204-2207.
6. L. Zhao, S. Reisman and T. Findley (1994) Derivation of respiration from electrocardiogram during heart rate variability studies. Computers in Cardiology. 53-56.
7. L. G. Lindberg, H. Ugnell and P. A. Oberg (1992) Monitoring of respiratory and heart rates using a fibre-optic sensor. Med. & Biol. Eng. & Comput. 30: 533-537.
8. Heart rate variability-Standards of measurement, physiological interpretation and clinical use-Task Force of the European Society of Cardiology and The North American Society of Pacing and Electrophysiology (1996). European Heart Journal 17: 354-381.

F. Ibrahim, N.A. Abu Osman, J. Usman and N.A. Kadri (Eds.): Biomed 06, IFMBE Proceedings 15, pp. 391-395, 2007
www.springerlink.com ' Springer-Verlag Berlin Heidelberg 2007

9. John L. Semmlow (2004), Biosignal and biomedical image processing MATLAB-based applications, Marcel Dekker, Inc., New York.
10. W. Johnston and Y. Mendelson (2005) Extracting heart rate variability from a wearable reflectance pulse oximeter. Proceedings of the IEEE 31st Annual Northeast, 2005, pp 157-158.
11. Dieter Barschdorff and Wei Zhang (1994) Respiratory rhythm detection with photoplethysmographic methods. Proceedings of the 16th Annual International Conference of the IEEE, 1994, pp 912-913.
12. Bar Gal-on, Ian Brown and Andrew Nunn (2005) Monitoring and assessment of cardiovascular regulation in spinal cord injured patients. Proceedings of the IEEE Engineering in Medicine and Biology 27th Annual conference, 2005, pp 6859-6862.

Address of the corresponding author:

Author: Nandakumar Selvaraj
Institute: Centre for Biomedical Engineering, Indian Institute of Technology-Delhi
City: New Delhi
Country: India

F. Ibrahim, N.A. Abu Osman, J. Usman and N.A. Kadri (Eds.): Biomed 06, IFMBE Proceedings 15, pp. 391-395, 2007
www.springerlink.com ' Springer-Verlag Berlin Heidelberg 2007

FPGA Accelerator For Medical Image Compression System

K. A. Mohamed Junaid[1] and Dr.G.Ravindrann[2]

[1] RMK Engineering College / Electronics & Instrumentation Engg., Professor & Head, Kavaraipettai - 601206, India
[2] Anna University / Information & communication Engineering, Chairman, Chennai, India

Abstract— **This Project describes the benefits of using an FPGA as a Co-processor for Digital Signal Processor, for increasing speed and reducing the power consumption. This approach uses the advantage of fine grain parallel operation of FPGA. An ASIC implementation of a filter algorithm might have numerous MACs so that, all the taps can be processed in parallel. Likewise, FPGA has a flexible architecture that can be used for all MAC operations in parallel. Programmable logic combines the flexibility of a general-purpose DSP and ASIC. In this project the Spartan 2E FPGA has been interfaced with TMS320C6711 DS Processor. The speed is improved 453.52 times than the conventional DSP processor implementation.**

Keywords— **FPGA, DSP, ASIC, Image Compression**

I. Introduction

Traditionally, digital signal processing (DSP) algorithms are implemented using general-purpose (programmable) DSP chips for low-rate applications, or special-purpose (fixed function) DSP chip-sets and ASICs for higher rates [5]. Advancements in FPGAs provide new options for DSP design. The FPGA maintains the advantages of custom functionality like an ASIC and adds design flexibility and adaptability with optimal device utilization while conserving both board space and system power, which is often not the case with DSP chips

Compression is the process of reducing the size of the data sent and bandwidth required for the digital representation of a signal. Compression technology can result in reduced transmission time due to less data being transmitted [6]. It also decreases the storage requirements because there is less data. However, signal quality, implementation complexity, and the introduction of communication delay are potential negative factors that should be considered when choosing compression technology. Video and audio signals can be compressed because of the spatial, spectral, and temporal correlation inherent in these signals. Spatial correlation is the correlation between neighboring samples in an image frame. Temporal refers to correlation between samples in different frames but in the same pixel position. Spectral correlation is the correlation between samples of the same source from multiple sensors. There are two categories of compression are lossy and lossless [1]. In medical system applications, image losses can translate into costly medical mistakes; therefore, lossless compression methods are used. Fortunately, the majority of video and image processing applications do not require the reconstructed data to be identical to the original data [6]. In such applications, lossy compression schemes can be used to achieve higher compression ratios.

II. Fpga co-processor

A. Block Diagram

The block diagram shows the connection of Xilinx FPGAs to a Digital Signal Processor (DSP) platform using the available External Memory Interface (EMIF). The External Memory Interface (EMIF) in the TMS DSP platform is used as the interface to the FPGA. Normally, the EMIF connects to different types of memory devices (SRAM, Flash RAM, etc.).The EMIF connects to the FPGA, making the FPGA perform as a coprocessor, high-speed data processor, or high-speed data transfer interface.

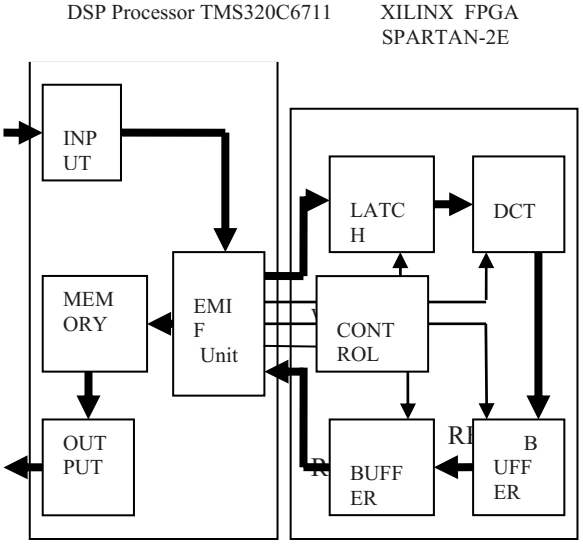

Fig. 1 Block diagram of FPGA based Image Compression

F. Ibrahim, N.A. Abu Osman, J. Usman and N.A. Kadri (Eds.): Biomed 06, IFMBE Proceedings 15, pp. 396-399, 2007
www.springerlink.com ' Springer-Verlag Berlin Heidelberg 2007

B. FPGA Based DSP Accelerator

General-purpose DSP devices have been the enabling technology for most mid to high-end electronic systems. Although high-volume applications favor ASIC implementations, the general-purpose DSP devices are used to drive the technology forward [10]. The engine in the DSP system is typically a specialized time-multiplexed sequential computer system that performs a continuous mathematical process, attempted in real-time .While the DSP processor may perform multiple instructions per clock cycle. This process is Adequate for independent sequential algorithms. The DSP processor becomes less efficient when an algorithm is dependent on two or more of the past, present, and/or future state conditions. This is primarily due to the feedback or parallel structure of the data flow being processed sequential with additional wait-states in a DSP. System performance requirements continue to increase.

The figure shows the interfacing between DSP and FPGA [6, 16].

The DSP processor the connector no is J1. The combined functionality of the FPGA and the general-purpose DSP can support several magnitudes higher data throughput than two or more parallel DSP devices. The FPGA/DSP implementation is more flexible and proves to be more cost effective than multiple DSPs or an ASIC. The FPGA design cycle requires less hardware-specific knowledge than most DSP chips or ASIC design solutions. Smaller design groups, with less experienced engineers, can design larger, more complex DSP systems in less time than larger design groups with more experienced engineers who are required to know device specific programming languages [10]. The FPGA-based DSP System-level design team can design, test, verify, and ready a complex DSP system for production in weeks.

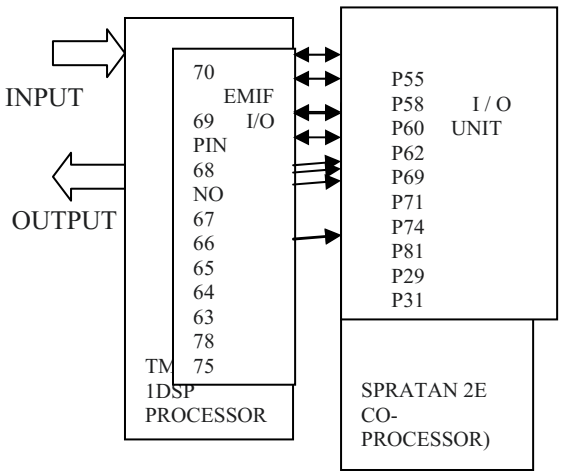

Fig. 2 Main Diagram

FPGAs also replace ASICs in DSP systems. Designers chose ASIC in the past for two reasons: Either they required DSP processing power beyond the capabilities of a general purpose DSP, or the system had sufficiently high production volumes to justify a semi custom solution. Cache Logic FPGAs are now available for use as a reconfigurable DSP (or other processor) coprocessor. These FPGAs consist of a fine grain architecture, meaning that there are thousands of logic cells, each cell can be individually reprogrammed in system without loss of its register content, and portions of the FPGA can be reconfigured without disruption of the remainder of the array. This enables compute-intensive or specialized tasks of a processor to be off-loaded and executed in a dynamically reconfigurable FPGA. By using the thousands of registers and in-system reconfigurability of these FPGAs, new algorithms and coefficients can be downloaded into the FPGA, and high speed can be achieved by utilizing pipelining techniques similar to those found in DSPs. The result is a 2-chip embedded DSP solution, achieving higher performance designs, using less power and less board area.

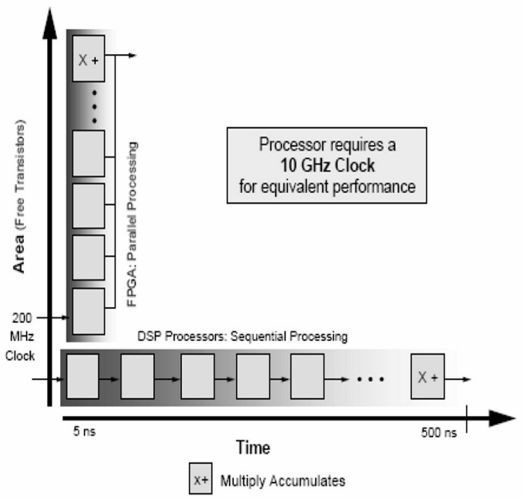

Fig. 3 FPGA vs. DSP for multiply and Accumulate Implementation

The SRAM-based FPGA is well suited for arithmetic, including Multiply & Accumulate (MAC) intensive DSP functions [7]. A wide range of arithmetic functions (such as Fast Fourier Transform s (FFT s), convolutions, and other filtering algorithms) can be integrated with surrounding peripheral circuitry. The FPGA can also be reconfigured on-the-fly to perform one of many system level functions. When building a DSP system in an FPGA, the design can take advantage of parallel structures and arithmetic algorithms to minimize resources and exceed the performance of single or multiple general-purpose DSP devices. Distributed

F. Ibrahim, N.A. Abu Osman, J. Usman and N.A. Kadri (Eds.): Biomed 06, IFMBE Proceedings 15, pp. 396-399, 2007
www.springerlink.com ' Springer-Verlag Berlin Heidelberg 2007

Arithmetic for array multiplication in an FPGA is one way to increase data bandwidth and throughput by several order of magnitudes over off-the-shelf DSP solutions. The FIR design supports more than 8 million samples per second. This can also be implemented using multiple bits, until a Fully Parallel Distributed Arithmetic algorithm is obtained for higher sample rates (i.e., 55.89 million samples per second). An In-System Programmable (ISP) FPGA can also be reconfigured on the board during system operation. Taking advantage of the reconfigurability feature means a minimal chip solution can be transformed to perform multiple functions.

The Fig. 3 shows the FPGA vs. DSP for multiply and Accumulate Implementation [2].For example, an FPGA could be the basis for a system that performs one of several DSP functions. Suppose, for instance, one function is to compress a data stream in transmit mode and another function is to decompress the data in receive mode. The FPGA can be reconfigured on-the-fly to switch, or toggle, from one function to another. This capability of the FPGA adds functionality and processing power to a minimum-chip DSP system controlled with an internal or an external controller [10]. This Reconfigurable Computing technique is beginning to impact design methodologies.

The advancement in performance for DSP devices is lagging behind this growth. Because of this imbalance the DSP designer is forced to use a systolic array of DSP processors to boost the overall performance. The software code for a DSP algorithm of this type is not efficiently implemented in a general purpose DSP. Typically, about 10-30% of the DSP code utilizes 60-80% of the processors power. Analyzing the DSP algorithm and breaking out any parallel structures or repetitive loops into multiple data paths, one can enhance the overall performance of the algorithm [10]. The multi-path parallel data structures can be processed either through parallel DSP devices or in a single FPGA-based DSP hardware accelerator with or without the assistance of a DSP device. The FPGA is well suited for many DSP algorithms and functional routines. The FPGA can be programmed to perform any number of parallel paths. The FPGA can also be partially or completely reconfigured in the system for a modified or completely different algorithm. The primary concept is to unload the compute-intensive functions requiring multiple DSP clock cycles into the FPGA and allow the DSP processor to concentrate on Optimized single-clock functions. DSP architecture directly affects system performance. Because most DSP functions are multiply/accumulate-based, the performance of the MAC is crucial. For the write and read operations shown in above fig 4.4 and 4.5 respectively. The write enable is active after the chip enable is active. The write enable state changes after every rising edge of clock. The write operation the read enable in high state. The one data transfers within one cycle of write enable. After 8th clock of write enable, the DCT operation will be performed. During the read operation the read enable signal active after the chip enable and output enable active. Each data will read every falling edge of read enable signal.

The FPGA-based DSP accelerator is conceptually similar to a Coprocessor for the Microprocessor Units (MPUs) in the computer market. Initially, the MPU required a Math-Coprocessor to accelerate computational algorithms. The functionality of the Coprocessor became so frequently used that it is now an integrated part of the latest processor families. Some DSPs have been optimized to do some dedicated functions much faster than a MPU (Von Neumann architecture). For example, some DSPs can multiply and Accumulate (MAC) in one clock cycle (DSP @66 MHz = 15 n sec per MAC) compared to eleven clock cycles (P5@100 MHz = 110 n sec per MAC) in the Pentium ^{tm}. processor [10]. Design debugging, system verification, and initial production are done with FPGAs. Once verified, the Hard Wire gate arrays provide a low risk migration path to a high-volume, low-cost solution. The combined functionality of the FPGA and the general-purpose DSP can support several magnitudes higher data throughput than two or more parallel DSP devices. The FPGA/DSP implementation is more flexible and proves to be more cost effective than multiple DSPs or an ASIC.

III. Results and Conclusions

Implementation Results

Spartan-2E 2s300epq208-6 Device Utilization for 8-Tap FIR Filter

Number of External GCLKIOBs	1	out of	4
Number of SLICEs	1143	out of	3072
Number of GCLKs	1	out of	4
Number of TBUFs	8	out of	3200

Minimum period: 3.876ns (Maximum Frequency: 257.998MHz)

Maximum output required time after clock: 29.286ns

Maximum combinational path delay: 8.802ns

Vertex v1000fg680-4 Device Utilization for 1D-DCT

Number of occupied Slices:	7,788	out of	12,288
Number of Slice Flip Flops:	754	out of	24576
Number of 4 input LUTs:	14,558	out of	24,576
Number of bonded IOBs:	96	out of	516
Number of GCLKs:	1	out of	4

Minimum period: 5.657ns (Maximum Frequency: 176.772MHz)

F. Ibrahim, N.A. Abu Osman, J. Usman and N.A. Kadri (Eds.): Biomed 06, IFMBE Proceedings 15, pp. 396-399, 2007
www.springerlink.com ' Springer-Verlag Berlin Heidelberg 2007

Minimum input arrival time before clock: 5.274ns

Maximum output required time after clock: 35.160ns

FIR filter is implemented using FPGA Co-processor method, the 8-point ID-DCT has been implemented using FIR filter. The DS Processor operates at 150 MHz. Therefore single clock cycle is 6.6667 ns. The FPGA was interfaced with TMS320C6711 DSP through EMIF.

The DSP and FPGA combination gives better performance than conventional DSP implementation. The Digital Signal Processor needs 320.16 ns for to implement 8 Tap FIR Filter and 2560.0128 ns for 1D-DCT. But the proposed method requires, 3.876ns for 8 tap FIR filter and 5.657ns for 1D-DCT operation. The speed is improved 453.52 times than the conventional DS Processor implementation.

In future it can be extended for 2D-DCT for processing the motion pictures.

References

1. Ahmed N., Natarajan T. and Rao K.R. (1974) Discrete cosine transform IEEE Trans. Comput., vol. 23, pp. 90 93.
2. Antolin.Agatep (2000), Xilinx Spartan-II FIR filter solution xilinx, Inc Literature Number: WP116 (V1.0).
3. Emmanuel C.Ifeachor and Barrie W.Jervis, (1996), Digital Signal Processing - A Practical Approach , Addison-Wesley publishing Company.
4. Gregory Ray Goslin (1995), A Guide to Using Field Programmable Gate Arrays (FPGAs) for Application-Specific Digital Signal Processing Performance Xilinx, Inc.
5. John G.Proakis and Dimitris G. Manolakis (2002), Digital signal Processing- Principles, Algorithms and Applications , Prentice-Hall of India private limited.
6. Marc Defossez (2004), FPGA Interface to the TMSC6000 DSP Platform Using EMIF , Xilinx, Inc, Literature Number: XAPP753.
7. www.xilinx.com

Address of the corresponding author:

Author: Prof. K.A.Mohamed Junaid
Institute: RMK Engineering College
Street: RSM Nagar
City: Kavaraipettai - 601206
Gummidipoondi
Thiruvallur District
Country: India
Email: mohamedjunaid@yahoo.com

F. Ibrahim, N.A. Abu Osman, J. Usman and N.A. Kadri (Eds.): Biomed 06, IFMBE Proceedings 15, pp. 396-399, 2007
www.springerlink.com ' Springer-Verlag Berlin Heidelberg 2007

Frequency Modulation in EEG Signals

V. Vijayakumar[1], Rahimi Yusoff[1] and C. Eswaranr[2]

[1] FOSEE, Multimedia University, 75450 Melaka, Malaysia
[2]Faculty of Information Technology, Multimedia University, Cyberjaya

Abstract—**In this paper we first explain how EEG signals can be described using Lommel functions. When the Lommel functions are allowed to time-evolve and analysed using the method of instantaneous frequency, we obtain a frequency modulated harmonic spectrum. This perspective allows new insights in interpreting the nonlinear behavior of EEG signals such as chaos.**

Keywords—**EEG, Chaos, Lommel. Instantaneous frequency, Frequency Modulation.**

I. Introduction

Lommel functions arise from Fresnel or near field diffraction of circular apertures[1][2][3]. The special property of these functions enable analysis of signals that allows for the preservation of time and frequency components of signals which are important in biomedical signals. These functions can be further designed to encode dynamic evolution of harmonics of a given signal leading to a unique analytical method suitable for real-time biomedical signals.

In this paper we will first describe the nature and property of Lommel functions. We then show how a sampling of the steady state portion of a given EEG spectrum can be synthesized using Lommel functions. We will then show the ease with which the spectrum can be made to evolve dynamically[4][5]. We will then compare the synthesized spectrum with real time dynamic EEG spectra. We will the discuss how this model can lead to new directions towards interpreting EEG signals.

II. Lommel functions

A. Let $X_s(f)$ denote the complex value of the amplitude of a wave of frequency f with model parameters, ξ and η. $X_s(f)$ has a single value for each input frequency f which is given by[1]:

$$X_s(f) = \cos(\xi\eta f) + V_0(\xi,\eta)\cos(\eta f/2\xi)\ V_1(\xi,\eta)\sin(\eta f/2\xi) + j\sin(\xi\eta f) + j\ V_0(\xi,\eta)\sin(\eta f/2\xi) - j\ V_1(\xi,\eta)\cos(\eta f/2\xi) \quad \ldots \quad (1)$$

and

$$V_0(u,v) = [\ J_0(\eta f) \quad \xi^2 J_2(\eta f) + \xi^4 J_4(\eta f) \quad]$$
$$V_1(u,v) = [\xi J_1(\eta f) \quad \xi^3 J_3(\eta f) + \xi^5 J_5(\eta f) \quad]$$

where

(i) J_i represents a Bessel function of i-th order, ξ and η are constants, and f is the frequency of the wave.

B. Spectral characteristics

The frequency spectra obtained by Eqn. 1, for different values of parameters ξ and η are shown in Figs. 1a-c for a continuous range of frequencies from 0Hz to 5000Hz.

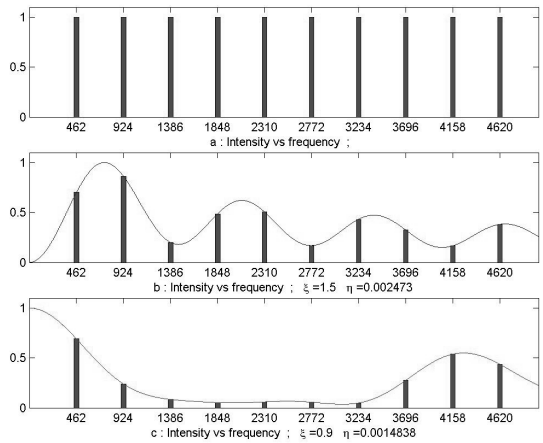

III. Methodology for analysis and synthesis of EEG spectra

To test the proposed model, we use sample EEG spectrum and optimization programs written in MATLAB to find suitable values of ξ and η, so that the synthesized spectrum matches the chosen steady state region of the EEG spectrum. We then modulate η gradually to obtain the dynamic spectrum. The method chosen to modulate η is dependant on the original signal. In this paper we will only suggest how this

F. Ibrahim, N.A. Abu Osman, J. Usman and N.A. Kadri (Eds.): Biomed 06, IFMBE Proceedings 15, pp. 400-401, 2007
www.springerlink.com ' Springer-Verlag Berlin Heidelberg 2007

procedure works. Future plans include the use of the Empirical Mode Decomposition method using Hilbert-Huang transforms to relate the modes with the frequency modulated harmonics in EEG signals. This will provide us an insight into the choice for the scheme to modulate η. The Lommel functions so obtained are analysed using the instantaneous frequency method. We will then see how harmonic frequencies present in EEG signals are frequency modulated. The slow shifts in frequencies are the unique feature of this method of analysis. We can the see chaos in EEG signals will come about due to FM modulation.

IV. Conclusion

In this paper we proposed the use of Lommel functions to describe EEG signals that will enable us to better describe dynamic biomedical signals which are not easily understood using traditional Fourier techniques with sinusoidal kernals..

References

1. Klaus D. Mielenz, Algorithms for Fresnel diffraction at Rectangular and Circular Apertures , Journal of the National Institute of Standards and Technology, vol.103, No. 5 (1998).
2. J. Durnin, Exact Solutions for nondiffracting beams. The scaler theory Journal of the Optica society of America A, vol. 4, no. 4 , April 1987, pp: 651-654
3. Eugene Hecht, Optics , 4th Edition, Addison Wesley pp: 467-470
4. V. Vijayakumar, C. Eswaran, Nonlinear behavior of interacting harmonics in audio spectra , Journal of the Acoustical Society of America, Vol.119, No.5, May 2006 pg.3274
5. C. Eswaran, V. Vijayakumar , Synthesis and dynamic behavior of diffracted audio spectra Journal of the Acoustical Society of America, Vol.119, No.5, May 2006 pg.3441

Address of the corresponding author:

Author: V Vijayakumar
Institute: Multimedia University
Street: Jalan Air Keroh Lama
City: Melaka
Country: Malaysia
Email: vijaya@mmu.edu.my

F. Ibrahim, N.A. Abu Osman, J. Usman and N.A. Kadri (Eds.): Biomed 06, IFMBE Proceedings 15, pp. 400-401, 2007
www.springerlink.com ' Springer-Verlag Berlin Heidelberg 2007

Heart Sound Analysis Using MFCC and Time Frequency Distribution

I. Kamarulafizam[1], Sh-Hussain. Salleh[1], J.M. Najeb[1], A.K. Ariff[1] and A. Chowdhury[1]

[1]Centre for Biomedical Engineering (CBE), Faculty of Electrical Engineering, Universiti Teknologi Malaysia, Johor Bahru, Malaysia

Abstract—**This paper presents heart sound analysis method based on Time-Frequency Distribution (TFD) analysis and Mel Frequency Cepstrum Coefficient (MFCC). TFD represents the heart sound in term of time and frequency simultaneously which while the MFCC defines a signal in term of frequency coefficient corresponding to the Mel filter scale. There are 100 normal data and 100 data with disease obtained from the hospital which consists of various kinds of problems including mitral regurgitation and stenosis, tricuspid regurgitation and stenosis, ventricular septal defect and other structural related disease. B-Distribution is chosen from a number of time-frequency analysis methods due its capability to represent the signal in the most efficient way in term of noise and cross term reduction. The advantage of MFCC is that it is good in error reduction and able to produce a robust feature when the signal is affected by noise. SVD/PCA technique is used to extract the important features out of the B-Distribution representation. The coefficient obtained from SVD-PCA and MFCC is later used for classification Artificial Neural Network. The results show that the system is able to produce the accuracy up to 90.0% using the TFD and 80.0% using the MFCC.**

Keywords—**Heart Sound, Time Frequency Analysis, Mel-Frequency Cepstrum Coefficient, Singular Value Decomposition, Principle Component Analysis, and Artificial Neural Network.**

I. Introduction

Auscultation, the act of listening to the sounds of internal organs, is a valuable medical diagnostic tool. Auscultation methods provide the information about a vast variety of internal body sounds originated from the heart, lungs, bowel and vascular disorders. The information acquired by a traditional stethoscope is, however, subjective and qualitative in nature since the differentiation of signals picked up by the sensor during manual interpretation is limited by human perception abilities and varies with personal aptitude and training. This may result in inaccurate or insufficient information due to the inability of the user to discern certain complex, low-level, short duration or rarely encountered abnormal sounds. It is, thus, desirable to enhance the diagnostic ability by processing the auscultation signals electronically and providing a visual display and automatic analysis to the physician for a better comparative study. During the last decade, efforts have been made in this direction and electronic stethoscopes are now available commercially with phono-cardiograph display. The usage of such devices, however, is less common due to the involvement of cumbersome instrumentation and complex/additional skills. Our research at CBE, UTM encompasses a more user friendly and quantitative approach together with automatic signal analysis using intelligent algorithms.

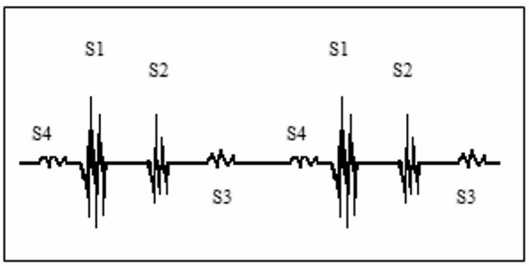

Fig. 1 Heart sound

II. Background

A. Time Frequency Analysis

Time Frequency Signal Processing is a method and technique developed for representation, analysis and processing of non-stationary signals, which time and frequency are interrelated. Time representation, *s(t)*, and frequency representation, *S(f)*, are related via the Fourier Transform.

$$s(t) = \int_{-\infty}^{\infty} S(f) e^{j2\pi ft} df \quad {}_t \overset{FT}{\leftrightarrow}_f \quad S(f) = \int_{-\infty}^{\infty} S(t) e^{j2\pi ft} .dt \qquad (1)$$

Time-frequency representation represent signals in time and frequency which all signals information is accessible and provides a distribution of signal energy versus *t* and *f* simultaneously which called time frequency distribution (TFD). TFD reveals the number of signal components, the time variation of frequency content of the components and order of appearance in time of the different frequencies present.

The B-Distribution is a Quadratic or bilinear Time frequency Distribution algorithm which capable to minimizing cross term [6] and it defined as:

$$B(t,f) = \iint (|\tau| / \cosh^2(u-\tau))^{\beta} z(u+\tau/2) z^*(u-\tau/2) e^{-j2\pi f\tau} du d\tau \qquad (2)$$

F. Ibrahim, N.A. Abu Osman, J. Usman and N.A. Kadri (Eds.): Biomed 06, IFMBE Proceedings 15, pp. 402-405, 2007
www.springerlink.com ' Springer-Verlag Berlin Heidelberg 2007

B. Mel Frequency Cepstrum Coefficient-MFCC

A representation of heart sounds using Mel-Frequency Cepstrum Coefficient (MFCC) would be provided by a set of cepstrum coefficients. These coefficients are the results of a cosine transform of the real logarithm of the short-term energy spectrum expressed on a mel-frequency scale. The MFCC are also an efficient method to extract any kind of features [12]. The number of resulting mel-frequency cepstrum coefficients is practically chosen relatively low, in the order of 12 to 20 coefficients. However, in many cases of MFCC analysis, the 0th coefficient of the 7 MFCC cepstrum is ignored because of its unreliability [13]. In fact, the 0^{th} coefficient can be regarded as a collection of average energies of each frequency bands in the signal that is being analyzed. The energy of heart sound signal is also a very important feature for pattern recognition. Many experiments have shown that the performance can be improved when the energy information is added as another model feature in addition to cepstrums [10]. Mel Frequency Cepstrum Coefficients (MFCC) is also used as a method that analyzes how the Fourier transform extracts frequency components of a signal in the time-domain. In addition, it is a representation defined as the real cepstrum of a windowed short-time signal derived from the Discrete Fourier Transform (DFT) of that signal. The difference from the real cepstrum is that a non-linear frequency, a mel-scale is used. The mapping from linear frequency to Mel frequency is done using an equation as follows

$$\text{Mel (f)} = 2595 \log10 (1 + f/700) \quad (3)$$

C. Singular Value Decomposition-SVD

The singular value decomposition (SVD) has become an important tool in statistical data analysis and signal processing. The existence of SVD was established by the Italian geometer Beltrami in 1873 which was only 20 years after the conception of a matrix as a multiple quantity by Cayley. SVD based technique is introduced to reduce the effect of noise from TFD which deal with singular matrices, or once which are very close to being singular. They are an extension of eigen decomposition to suit non-square matrices. Any matrix may be decomposed into a set of characteristic eigenvector pairs called the component factors, and their associated eigenvalues called the singular value.

In order to extract data dynamically which decompose the X, TF distribution matrix of the power disturbance signals, which $m \times n$ (*time x frequency*) into a set of characteristic. A singular value decomposition of an $m \times n$ matrix X is any factorization of the form:

$$X = U\Sigma V^T \quad (4)$$

where U is an $m \times m$ orthogonal matrix; i.e. has orthonormal columns, V is an $n \times n$ orthogonal matrix and Σ is $m \times n$ an diagonal matrix of singular values with components $\sigma_{ij}=0$ if and $i \neq j$; (for convenience we refer to the *i-th* singular value $\sigma_i=\sigma_{ii}$). Furthermore it can be shown that there exist non-unique matrices U and V such that singular values $\sigma_1 \geq \sigma_2 \geq \ldots \geq \sigma_n \geq 0$. The columns of the orthogonal matrices U and V are called the left and right singular vectors respectively; an important property of U and V is that they mutually orthogonal [4].

D. Principle Component Analysis-PCA

PCA is generally used when the research purpose is data reduction (to reduce the information in many measured variables into a smaller set of components) and it can minimize the reconstruction error in the sense of least square error then find out the most representative feature. PCA seeks a linear combination of variables such that maximum variance is extracted from the variables. It then removes this variance and seeks a second linear combination which explains the maximum proportion of the remaining variance, and so on. This is called the principle axis method and results in orthogonal (uncorrelated) factors. PCA analyzes total (common and unique) variance. We can see that the SVD is in fact closely related to the PCA. In fact the matrix product $U\Sigma$ is analogous to the matrix Y defined for PCA as:

$$Y = XV = U\Sigma \quad (5)$$

Because both the singular vectors defined for an SVD are square and have orthonormal columns their inverses are given by their transposes. Now the relation in Equation 4 can be expressed $X=U\Sigma V^T$ which is the definition of an SVD. The pairs of eigenvectors are the row in U and the column in V [14].

III. METHODOLOGY

The heart sound is segmented into a small duration of a complete one (1) cycle of heart beat. This is an important procedure which needs to be carefully handled because a poorly handled segmentation process may affect the performance of the feature extractor and the classifier.

In this experiment, the heart sound samples are processed using two (2) methods which are TFD-SVD-PCA and MFCC. In the first procedure, the heart sound sample is transformed using TFD utilizing B-Distribution as a transformation kernel. This will result a time and frequency representation with the

F. Ibrahim, N.A. Abu Osman, J. Usman and N.A. Kadri (Eds.): Biomed 06, IFMBE Proceedings 15, pp. 402-405, 2007
www.springerlink.com ' Springer-Verlag Berlin Heidelberg 2007

high resolution plane (*data length x dft points*). At this stage the features can be observed clearly by looking at the energy at the most dominant frequency with the respect of the time scale. However, selecting the best features is not easy when dealing with a very high dimension of data.

In addition to an appropriate process, it is often essential that dimensionality reduction be performed on the TFD, so that the information is sufficiently compact for presentation to a classifier such as ANN. The main goal of SVD technique is to ensure that as much relevant information as possible is preserved in as few dimensions as possible.

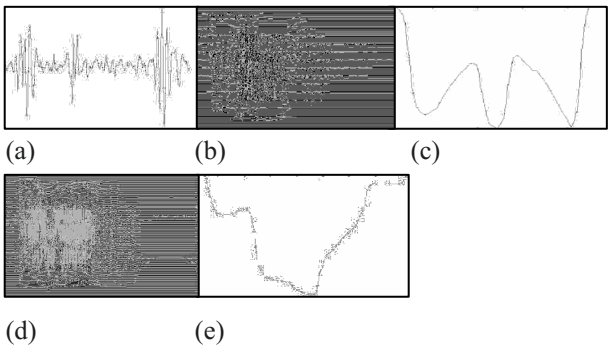

Fig. 2 (a) Time domain heart sound signal, (b) Time-frequency representation of a normal heart sound, (c) SVD-PCA representation of a normal heart sound signal. (d) Time-frequency representation of an abnormal heart sound. (e) SVD-PCA representation of an abnormal heart sound signal

As for the second method, the segmented heart sound sample is transformed using MFCC. This experiment is carried out based on the initial parameter of 12 coefficients with 240 samples for each frame and with 80 samples overlap between each frame. MFCC has a property where the transformation scale is linear for the frequency below 1 kHz and expand logarithmically above 1 kHz. This property works well for speech processing as it suit the human auditory spectral band. However for the heart sound analysis, the higher filter bank scale will not affect much as most of the heart sound component exist below 1 kHz [15]. This experiment is carried out to verify the property of MFCC in terms of filter bank analysis and transformation,

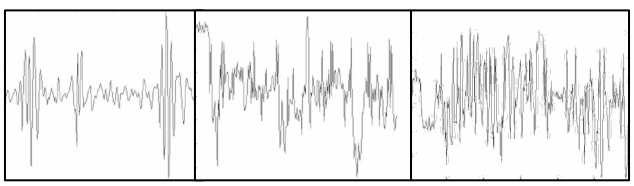

Fig. 3 (a) Time domain heart sound signal, (b) MFCC coefficient of a normal heart sound. (c) MFCC coefficient of an abnormal heart sound

IV. Results

The output features of both methods are fed to Multi Layer Back Propagation Artificial Neural Network for performance comparison.

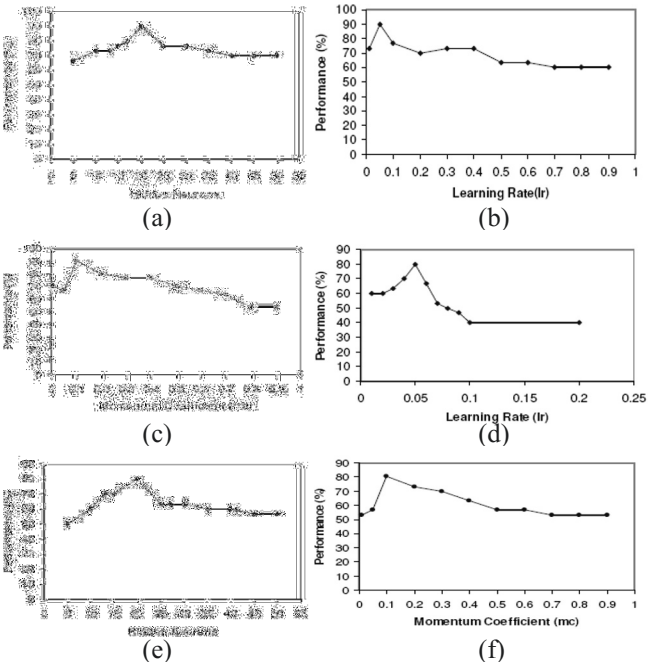

Fig. 4 (a) Verification on hidden node for TFD, (b) Verification on learning rate for TFD. (c) Verification on momentum term for TFD. (d) Verification on hidden node for MFCC. (e) Verification on learning rate for MFCC. (f) Verification on momentum term for MFCC.

Fig. 4(a) 4(c) shows the results of verification technique using TFD. They showed that the highest performance they can achieved is up to 90% at hidden nodes = 20, learning rate = 0.05 and momentum coefficient = 0.1. Fig. 4(d) 4(f) shows the results of verification technique using MFCC. They showed that the highest performance they can achieved is only up to 80% at hidden nodes = 20, learning rate = 0.05 and momentum coefficient = 0.1.

Table 1 Result analysis using TFD and MFCC

Item	TFD,SVD/PCA	MFCC
Feature Dimension	256	170
Training Data	50	50
Testing Data	50	50
Hidden Layer	20	20
Learning Rate	0.05	0.05
Momentum Term	0.1	0.1
Accuracy	90%	80%

F. Ibrahim, N.A. Abu Osman, J. Usman and N.A. Kadri (Eds.): Biomed 06, IFMBE Proceedings 15, pp. 402-405, 2007
www.springerlink.com ' Springer-Verlag Berlin Heidelberg 2007

Table 1 shows the result obtained by the analysis using TFD and MFCC. It is obvious that analysis using TFD gives a better performance based on ANN. This is due to the ability of TFD to represent the heart sound in various frequencies as a non-stationary signal. Transformation using MFCC maps the time domain signal into frequency domain according to the Mel filter scale. Although MFCC offers a detail analysis of a short duration of the heart sound with the overlapping property, it is still unable to represent the signal as good as the time frequency.

V. Conclusions

This paper presents the most widely used signal analysis methods which are time frequency analysis and Mel-Frequency Cepstrum Coefficient with the application to heart sound analysis. The proposed method is able to discriminate the normal heart sound from the abnormal heart sound. The result shows that the time frequency analysis performs better compared to the MFCC in term of providing the best resolution in frequency domain representation. The analysis using TFD preserved the uniqueness of the input signal in term of time and frequency. It enhanced the signal information while suppressing the unnecessary noise and interference.

References

1. J.Y.Lee,T.J Won, Jeong And S.W.Nam, Classification Of Power Disturbances Using Feature Extraction In Time Frequency Plane , 2002.
2. Z. Chen, Senior Member, Ieee, And P Urwin, Power Quality Detection & Classification Using Digital Filter, Ieee, 2001.
3. Y.J Shin, Antony C.Parsons, Edward J.Powers, W.M. Gardy, Time-Frequency Analysis of Power System Disturbance Signals for Power Quality , pp 402-407,1999
4. Michael E.Wall, Andreas Rechtsheiner, Luis M. Rocha, Singular Value Decomposition and Principal Component Analysis , 2003
5. Boashash, B. (1992). Time Frequency Signal Analysis: Methods andApplications. Melbourne, Australia: Longman Cheshire.
6. Boashash, B. and Sucic, V. (2000). A Resolution Performance Measure for Quadratic Time-Frequency Distributions. Proceedings of the Tenth IEEE Workshop on Statistical Signal and Array Processing. August 14 -16. 584 -588.
7. Barkat B. and Boashash B. (2001). A High-Resolution Quadratic Time Frequency Distribution for Multicomponent Signals Analysis. IEEE Transactions on Signal Processing. 49(10). October 2001. 2232-2239
8. Cohen L. (1989). Time-Frequency Distributions: A Review. Proceedings of the IEEE. 77(7). July 1989. 941-981.
9. Daliman, S. and Sha ameri, A. Z. (2003). Time-Frequency Analysis of Heart Sounds using Windowed and Smooth Windowed Wigner-Ville Distribution. Proceedings Seventh International Symposium on Signal Processing and its Application. 2. July 1-4. 625-626.
10. Molau, S., Pitz, M., Schluter, R. and Ney, H. (2001). Computing Mel- Frequency Cepstral Coefficients on the Power Spectrum. Proceedings ICASSP 01) 2001 IEEE International Conference on Acoustics, Speech and Signal Processing. May 7-11. 73-76.
11. Sucic, V., Barkat B. and Boashash, B. (1999). Performance Evaluation of the B-Distribution. Fifth International Symposium on Signal Processing and its Applications. August 22-25. Brisbane, Australia: IEEE, 267-270.
12. Davis, S. B. and Mermelstein, P. (1980) Comparison of Parametric Representations for Monosyllabic Word Recognition in Continuously Spoken Sentences. IEEE Transactions on Acoustics, Speech and Signal Processing. 28(4). August 1980. 357-366.
13. Picone, J. W. (1993). Signal Modeling Techniques in Speech Recognition. Proceedings of the IEEE. 81(9). September 1993. 1215-1247.
14. Wall, M. E., Rechtsteiner, A. and Rocha, L. M. (2003). Singular Value Decomposition and Principal Component Analysis. in D. P. Berrar, W. Dubitzky, and M. Granzow, A Practical Approach to Microarray DataAnalysis, Kluwer: Norwell. 91-109.
15. Jozef Wartak, M.D. (1972). Phonocardiology: Integrated Study of Heart Sound and Murmurs, Harper and Row Publisher.
16. Hotelling, H. (1933), "Analysis of a Complex of Statistical Variables into Principal Components," Journal of Educational Psychology, 24, 417-441, 498-520.

Address of the corresponding author:

Author: I.Kamarulafizam
Institute: Centre for Biomedical Engineering, Universiti Teknologi Malaysia
City: Johor Bahru
Country: Malaysia
Email: mr_fizam@yahoo.com

F. Ibrahim, N.A. Abu Osman, J. Usman and N.A. Kadri (Eds.): Biomed 06, IFMBE Proceedings 15, pp. 402-405, 2007
www.springerlink.com ' Springer-Verlag Berlin Heidelberg 2007

Limb Cardiovasculature System Identification Using Adaptive Filtering

C.M. Chew[1] and E. Zahedi[1]

[1]Department of Electrical, Electronic and Systems Engineering, Faculty of Engineering, Universiti Kebangsaan Malaysia, Bangi, Malaysia

Abstract—**An approach is proposed to determine the transfer function of the human heart-to-finger upper-limb vascular segment. The instant of occurrence of the left ventricular blood pressure was estimated using simultaneous electrocardiography and photoplethysmography (PPG). A well-established, generic shape is assumed for the left-ventricular pressure. The weights of an adaptive finite impulse response filter were tuned using a least mean-square algorithm so that the output of the model fitted measured peripheral volume change pulses. Results show that the above iterative system identification scheme eventually converges to a set of filter coefficients representing the subject's vascular segment. A potential application of this technique is to gain more insight into the mechanical properties of the arterial wall, namely compliance.**

Keywords—**Adaptive System Identification, Circulatory Parameter, Left-Ventricular Pressure, Photoplethysmography, Electrocardiography**

I. Introduction

Human cardiovasculature system identification and modeling has long been the great interest topic of theoretical and experimental researches in engineering and medical field [1-3]. Yet, the underlying physiological mechanisms have not been completely understood due to the complex nature of the system itself [4], expensive and safety concerns in invasive measurements [5,6]. Past researches indicated that age, certain disease states and response to drugs, also individual lifestyle are associated with an increase in cardiovascular events that alter the physical characteristics of blood vessel walls and impair the pulsatile function of arteries [6].

Hence, experimental and physiological studies of the inter-relationships among haemodynamic properties between blood pressure and volume using appropriate non-invasive identification techniques are important. The aim is to provide otherwise difficult-to-get information about the patient circulatory systems. This study intends to 1) develop an appropriate approach to estimate the left-ventricular pressure input utilizing information obtained from electrocardiograms (ECG) and photoplethysmograms (PPG), and 2) propose a model that describes the dynamic relationship between estimated left-ventricular pressure (eLVP) and PPG signals. Fig. 1 shows the representation of human upper limb cardiovasculature system (heart-to-finger) to be modeled with corresponding input-output interfaces.

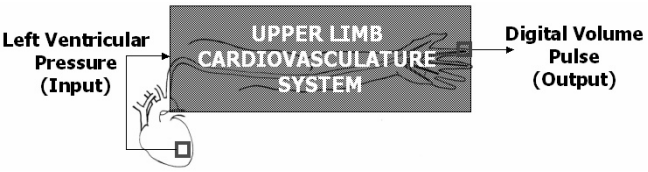

Fig. 1 Human upper limb cardiovasculature system

II. Materials and Methods

A. Data acquisition

The electrical activity of the heart (ECG) and peripheral volume pulses (PPG) were obtained from seven subjects with no risk factors for cardiovascular disease (5 males; 2 females; mean age 32.6 ± 6.0 years) volunteered for this experiment. All measurements were performed in the laboratory. Subjects were asked to abstain from having food, caffeinated drinks, alcohol and cigarettes for 4 hours prior to the study to minimize the effect of external factors on the vascular systems. Each subject was asked to rest comfortably in a supine position for at least 10 minutes (ambient temperature of around 25 ^{o}C) to allow cardiovascular stabilization. A three lead ECG was recorded using ECG100A module (BIOPAC systems, Inc.), while PPG signals were acquired through a stationary transmission-type photoelectric probe attached to the left index finger connected to the serial port of a pulse oximetry module (OEM-601^{TM} from Dolphin Medical, Inc.). Both signals were digitized at a sampling rate of 275 Hz. The devices were directly connected to the communication port of two PCs and running software provided by their respective manufacturer. Fig. 2 shows the schematic of experimental setup. The length of each recording was 200 seconds (55,000 samples). Recorded ECG and PPG were then stored under the condensed format and subsequently exported to ASCII files.

F. Ibrahim, N.A. Abu Osman, J. Usman and N.A. Kadri (Eds.): Biomed 06, IFMBE Proceedings 15, pp. 406-409, 2007
www.springerlink.com ' Springer-Verlag Berlin Heidelberg 2007

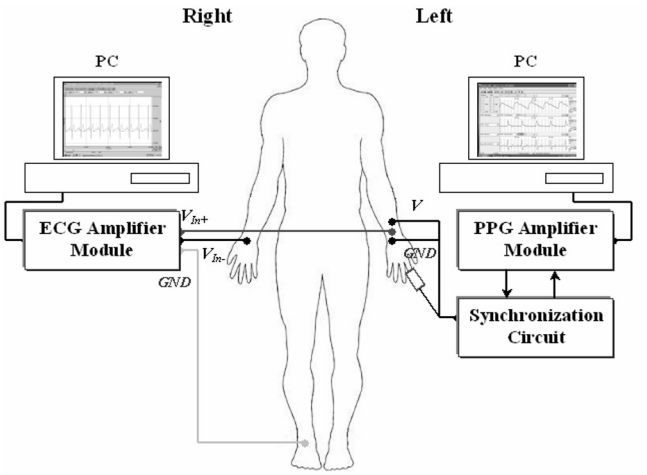

Fig. 2 Schematic of experimental setup

B. Pre-processing

The waveforms were analyzed off-line using MATLAB (The MathWorks, Inc.). Pulses without significant movement artefact were manually selected for analysis. The following pre-processing were done on the raw data:

1. Linear trend removal.
2. ECG and PPG synchronization.
3. Band-pass filtering,
   - PPG (0.6 15 Hz)
   - ECG (1 40 Hz)
4. Amplitude normalization to unity.
5. Segment selection, approximate by 16,500 samples (60 seconds).

It is known that the PPG signal consists of two main signals: an AC signal and a quasi-DC signal that corresponds to the absorption due to venous blood, skin, bone and tissues [7]. The quasi-DC signal was removed and the signal was detrended before being subjected to analysis. Besides, ECG and PPG signals were digital band-pass filtered to remove high-frequency noise caused by ambient light and low-frequency noise due to subject s respiration rate or artifact.

C. Estimated LVP signal generation

The half-sinusoidal waveform was selected for the generation of eLVP because it assumed the shape of the left-ventricular pressure in human. It is common and relatively simple to generate as human ventricular ejection [8]. The authors tried two different inputs (triangular waveform and half-sinusoidal waveform) in their study and found the latter a more realistic approximation of ventricular ejection. Finally the 3rd power of a half-sinusoidal waveform was selected in this study due to the sharper inclination of the waveform that best expressed the actual LVP waveform.

The following procedures were done on the pre-processed signals:

1. PPG local maximums and minimums detection.
2. ECG R-waves detection.
3. 70 pulses with approximate 60 seconds of eLVP generation from 3rd power half-sinusoidal waveform,
   - Each eLVP pulse frequency has the same pulsatile frequency to the respective ECG cycle with T_{sys} equal 45 % of respective pulse period [9].
   - Start each eLVP pulse at detected PPG global minimum point.
   - Each eLVP pulse peak-to-peak value was adjusted to match respective PPG peak-to-peak value and global minimum point as shown in Fig. 3.
4. Append all single pulses into series according to respective ECG R-wave starting timing as shown in Fig. 4.

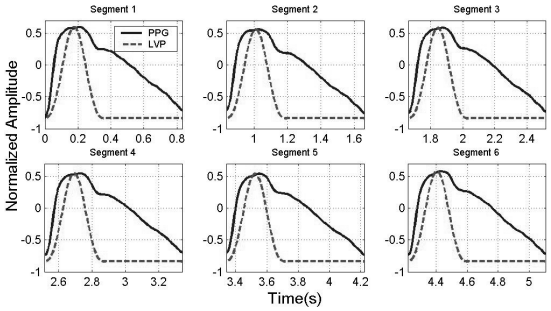

Fig. 3 First six pulses of PPG (solid) and eLVP (dashed) signals

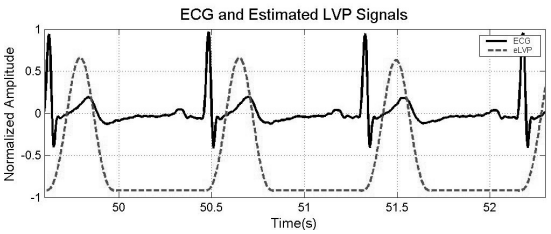

Fig. 4 ECG (solid) and eLVP (dashed) signals

D. Adaptive system identification

An adaptive filter is used to model human upper limb cardiovasculature system to provide a linear model that best fit the actual system based on reference or desired response from the system output. This identification approach distinguished itself by the characteristic of having a noise-free

F. Ibrahim, N.A. Abu Osman, J. Usman and N.A. Kadri (Eds.): Biomed 06, IFMBE Proceedings 15, pp. 406-409, 2007
www.springerlink.com ' Springer-Verlag Berlin Heidelberg 2007

input in contrast to the desired response that is corrupted by additive noise uncorrelated with the input signal [10]. Fig. 5 shows the typical adaptive system identification interfaces scheme. The procedures are described as follows:

1. Make eLVP and PPG samelength to allow point-to-point identification process between two signals.
2. Add white Gaussian noise (AWGN) to PPG with signal-to-noise ratio as 30 dB to simulate the signal with instrumentation noise.
3. System interfaces setting as shown in Fig. 5,
   - eLVP as the system input, *x* and,
   - PPG with AWGN as the system desired signal, *d*.
4. Model order, *N* selection using step-size 1 for fastest convergence,
   - Order set as 41, which give the lowest residual sum-of-square (best fit between measured and estimated PPG) as shown in Fig 6.
5. Applying FIR adaptive system identification using normalized LMS algorithm based on steepest descent gradient method. The general behavioral representation of the FIR model for input $x(n)$ and output $y(n)$ is:

$$\text{Filter output, } y(n) = \sum_{k=0}^{N-1} w_k x(n-k) \qquad (1)$$

where, w_k is the array of filter coefficients (k = 0, 1, 2, , N- 1), N is filter order.

6. Compute the root-mean-square (RMS) residual,

$$e\_RMS = \sqrt{\frac{\sum_{i=1}^{n} e^2}{n}} \qquad (2)$$

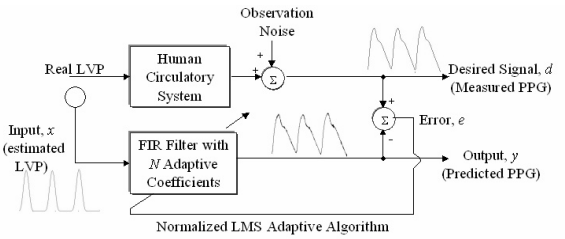

Fig. 5 Adaptive system identification interfaces scheme

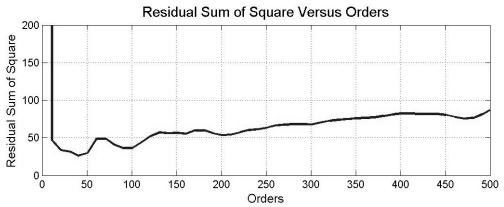

Fig. 6 Model order selection using step-size 1

III. Results

Results from one of the subjects are shown below. Original, estimated and error signals are shown in Fig. 7 and Fig. 8. The cumulative residual sum-of-square between filter output and PPG signal is shown in Fig. 9. The magnitude and phase of the FIR frequency responses are shown in Fig. 10.

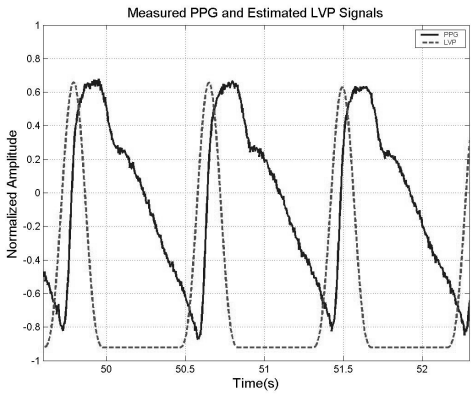

Fig. 7 PPG desired signal (solid) and eLVP input signal (dashed)

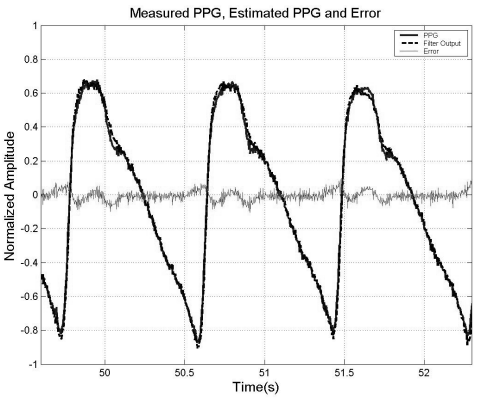

Fig. 8 Measured PPG (solid) superimposed with estimated PPG (dashed), and error/residual signal (middle) after adaptation

F. Ibrahim, N.A. Abu Osman, J. Usman and N.A. Kadri (Eds.): Biomed 06, IFMBE Proceedings 15, pp. 406-409, 2007
www.springerlink.com ' Springer-Verlag Berlin Heidelberg 2007

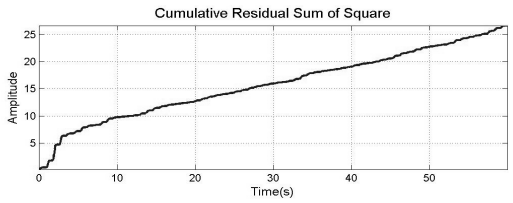

Fig. 9 Cumulative residual sum-of-square between measured and estimated PPG signals

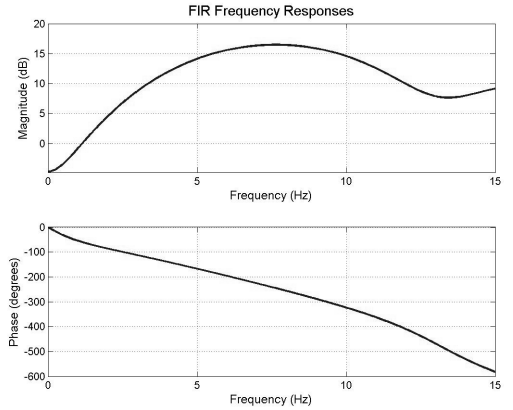

Fig. 10 FIR filter frequency response: magnitude (top) and phase (bottom)

IV. Discussion

The resulting filter output shows a close fit to the actual recording with minimal RMS residual of 0.0398. Meanwhile, the cumulative residual sum-of-square in Fig. 9 shows a constantly linearly increasing at around 3 seconds (825 samples) from the beginning of the signal, this fact indicates that the normalized LMS optimization algorithm used in this identification had achieved accurate determination of the signal with fast convergence. In fact, the FIR coefficients could potentially represent the actual subject s upper limb cardiovasculature system. Likewise, the magnitude and phase of the FIR transfer function versus frequency of the subject could be used to provide great insight to interpret the subject s overall cardiovasculature dynamics.

V. Conclusions

A propagation model for human upper limb cardiovasculature system was proposed to describe the underlying dynamics of the physiological mechanisms. The study showed that the proposed approach is capable to produce a close fit to the varying PPG waveform shape with minimal RMS residual by the relatively simple source of adjusted 3rd power half-sinusoidal input. This non-invasive and simple approach could be clinically useful to identify abnormalities in the subject s cardiovasculature system in association with age or pathological risk factors. Further work with different input sources and age groups are now in progress.

Acknowledgment

This work was partially supported by an Intensive Research Priority Areas grant (IRPA-02-02-0106-EA258) from the Ministry of Science, Technology and Innovation, Malaysia.

References

1. Snyder MF, Rideout VC, Hillestad RJ (1968) Computer modeling of the human systemic arterial tree. Journal of Biomechanics 1:341-353
2. Westerhof N, Bosman F, De Vries CJ et al (1969) Analog studies of the human systemic arterial tree. Journal of Biomechanics 1:121-143
3. Allen J, Murray A (1999) Modelling the relationship between peripheral blood pressure and blood volume pulses using linear and neural network system identification techniques. Physiol. Meas. 20:287-301
4. Li KJJ (2004) Dynamics of vascular system. World Scientific Publishing, Singapore
5. Connors AF Jr, Speroff T, Dawson NV et al (1996) The effectiveness of right heart catheterization in the initial care of critically ill patients. Journal of the American Medical Association 276(11):889-897
6. McVeigh GE, Hamilton PK, Morgan DR (2002) Evaluation of mechanical arterial properties: clinical, experimental and therapeutic aspects. Clinical Science 102:51-67
7. Echiadis A, Crabtree VP, Smith PR (2005) VENOX technology implementation. http://www.lboro.ac.uk/departments/el/research/conferences/esc2005/aggelos_echiadis.pdf
8. Shirouzu S, Shirouzu E, Tsuda Y et al (1998) Circulatory parameter extraction from digital plethysmogram I: waveform analysis of digital plethysmogram. Proc. IEEE Eng. Med. Biol. Soc. 20th Int. Conf. 20(6):3087-3089
9. Guarini M, Urz a J, Cipriano A et al (1998) Estimation of cardiac function from computer analysis of the arterial pressure waveform. IEEE Transaction on Biomedical Engineering, 45(12):1420-1428
10. Manolakis DG, Ingle VK, Kogon SM (2000) Statistical and adaptive signal processing: spectral estimation, signal modeling, adaptive filtering and array processing. McGraw-Hill

Address of the corresponding author:

Author: Chew Choon Min
Institute: Universiti Kebangsaan Malaysia
City: Bangi, Selangor
Country: Malaysia
Email: wes_chew81@yahoo.com

F. Ibrahim, N.A. Abu Osman, J. Usman and N.A. Kadri (Eds.): Biomed 06, IFMBE Proceedings 15, pp. 406-409, 2007
www.springerlink.com ' Springer-Verlag Berlin Heidelberg 2007

Modifying the Classic Template Matching Technique Using a Fuzzy Multi Agent to Have an Accurate P300 Detection

G.R. Salimi Khorshidi[1], Ali M. Nasrabadi[2], M.R. Hashemi Golpayegani[1]

[1]Department of Biomedical Engineering Amirkabir University of Technology (Tehran Polytechnic), Tehran, Iran
[2] Group of Biomedical Engineering, Faculty of Engineering, Shahed University, Tehran, Iran

Abstract-**EEG-based brain computer interface (BCI) provides a new communication channel between human brain and computer. The classification of EEG data is an important task in EEG-based BCI. In this paper we present a new modification on classic "Template Matching" to make a better detection for a specific pattern in EEG. The new method shows a significant improvement in P300 detection which is a common approach in BCI systems. The proposed model uses more than one scalp electrodes and combines the outputs with a fuzzy technique, to detect P300 cognitive component.**

Keywords-**EEG, ERP, BCI, Template Matching (TM), Fuzzy Membership Functions**

I. Introduction

One of the most interesting fields of current researches is to develop a machine that can communicate with brain, directly. Many methods for discrimination between different mental and cognitive activities have been developed so far, like; many feature extraction, feature selection and classification techniques. Each of these methods has their own benefits and drawbacks that make their use totally case-dependent. BCI systems use different methods to communicate with human brain. One of the most common communication techniques is to find a specific pattern in scalp-recorded EEG; like P300, N400, and N170 or generally ERP components. Different methods have been proposed to find a specific pattern in EEG, some like template matching and peak picking are classical ones while other methods like using a feature extraction block in combination with a classifier are modern ones. The aim of this study is to show that a modification in a classical method (template matching), can yield good results for P300 detection. This modification is using a simple fuzzy multi-agent to vote for a final decision based on decisions made by some template matching blocks for some scalp electrodes (Fig.1). So, this paper is organized as follows. After this introduction, in part 2, the EEG data will be introduced. Then in part 3, a brief overview over Template Matching will show its efficiency for P300 detection. In part 4, the proposed model for the classifier will be introduced and used to show the benefit with new model. Finally in part 5, the conclusion will be made.

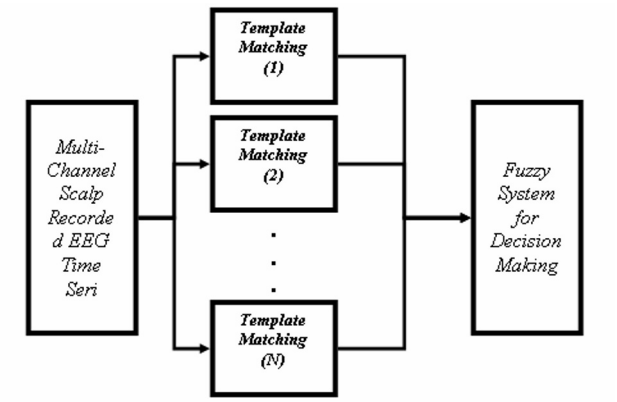

Fig.1 Block diagram of the proposed classifier which comprises N template matching (TM) block and a fuzzy decision making system, (representing a typical multi-agent classifier)

II. EEG data

In the present article, the EEG data is BCI Competetion2003 EEG dataset recorded from 64 scalp positions with P300 speller paradigm in which the subject was supposed to distinguish between two classes of stimulus; one class which contains P300 cognitive component and the other one which lacks this component.
The aim of this competition is to detect the P300 component in scalp recorded EEG; which seems identical to our aim in P300 detection in this study. After data acquisition, there will be a 64 electrodes EEG data. Processing all these channels will be a time consuming task. So two important issues most be considered; 1) the efficiency in processing and 2) the classification accuracy. The first step to have an efficient classification is to know the scalp active regions during P300 speller paradigm. In Fig.2, the average waveform for EEG data for a subject is shown for two classes of stimuli; with P300 (the upper panel, dashed line) and without P300 (the upper panel, solid line) for Cz electrode. The lower panel in Fig.2 shows the *r* value for

F. Ibrahim, N.A. Abu Osman, J. Usman and N.A. Kadri (Eds.): Biomed 06, IFMBE Proceedings 15, pp. 410-414, 2007
www.springerlink.com ' Springer-Verlag Berlin Heidelberg 2007

these two classes of data. The *r* value (Eq.1) represents the difference between two classes of data with respect to time in which *i* is time sample, *j* is the trial, *s* is the EEG with P300, *n* is the EEG without P300.

$$r_{i,j} = s_{i,j} - n_{i,j} \quad (1)$$

The r value shows that the major difference between two classes, happens around 300ms which is actually the time associated with P300 occurrence in the literature. Using plots in Fig.3 and 4, the major active regions during P300 occurrence can be estimated. In these plots, Fig.3 shows a contour plot of the average for a subject over time (*x-axis*) and electrode (*y-axis*) and Fig.4 shows a head plot at 300ms after stimulus onset for one subject using all 64 scalp electrodes. Using these plots, it is easier to decide which electrodes to choose the most efficient electrodes for P300 detection.

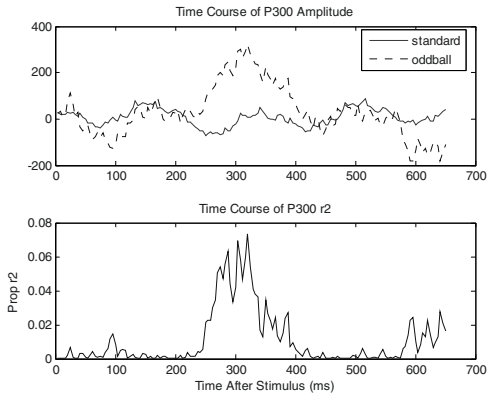

Fig.2 (Upper panel) average EEG for two classes of stimulus for Cz channel that shows a significant difference in about 300ms. (Lower panel) in this figure, the squared difference value (*r*) for each sample is plotted. This plot confirms that importance of 300ms in cross-class discrimination.

III. Using Template Matching for P300 Detection

As the name indicates, the aim of template matching (TM) technique is to detect a specific pattern based on its matching to a prespecified template. So the first step to have TM machine is to have a template. The best template to show an ERP (even-related potential) is the waveform resulting from averaging. Performing averaging over some EEG trials, the ERP which seems to be more stationary and deterministic will remain and the ongoing EEG and other noises will be cancelled. Having the ERP waveform, the next step is to compare a single trial with this template using a correlation measure (Eq.2) which shows the similarity between the single trial and the template with respect to different latencies in one of them.

$$R_{xy}(m) = \sum_{n=-\infty}^{+\infty} x[n] * y[n-m] \quad (2)$$

By Eq.2, the more the similar two signals *x* and *y* at $t=t_0$, the bigger the R_{xy} value at $t=t_0$. So if a trial contains P300, its corresponding *R* value will show a maximum around $m=0$ (Eq.2). So after calculating the cross correlation for different lag values, using a threshold for the *R* value around the zero lag, can determine existence of P300 (Fig.5).

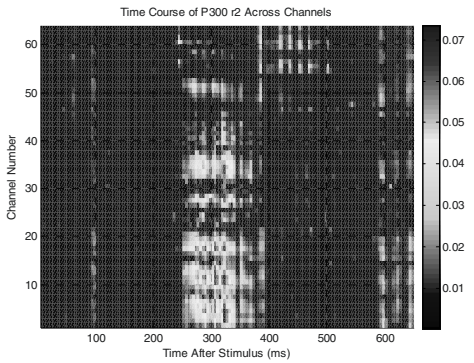

Fig.3 The contour plot of the *r* value with respect to time (*x-axis*) and electrode number (*y-axis*) which indicates the time and place of activity during a P300 occurrence.

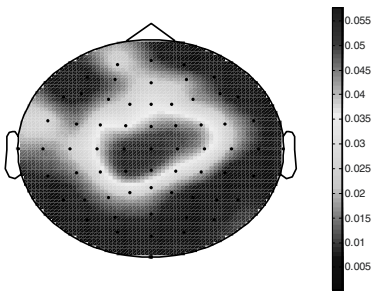

Fig.4 The head plot for r value at 300ms after stimulus which can represent the activity at this time in head surface.

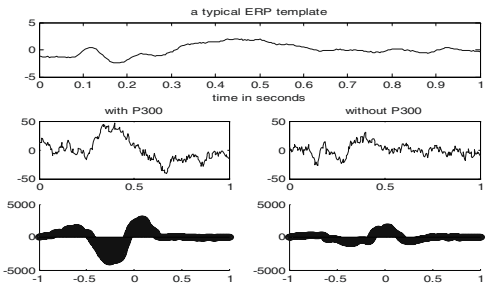

Fig.5 (Upper panel) an ERP template, (Middle panel) two trials with (left side) and without P300 (right side) and their corresponding correlation with respect to lag values.

F. Ibrahim, N.A. Abu Osman, J. Usman and N.A. Kadri (Eds.): Biomed 06, IFMBE Proceedings 15, pp. 410-414, 2007
www.springerlink.com ' Springer-Verlag Berlin Heidelberg 2007

Before using the TM technique, data was preprocessed using a filtering (0.5-30Hz) and normalization (to the interval of [-1, 1]). Using this technique on Fz, Cz, Pz, Oz, F3, F4, C3, C4, P3 and P4 electrodes (templates shown in Fig.6), the results (Table1) shows that the accuracy for this technique is not acceptable (comparing with the results of new researches using modern techniques). The P300 detection process in a pseudo code step by step form is as follows;

i. Select a trial from EEG dataset.
ii. Filter this trial with band-pass filter (0.5-30Hz) to cancel the high frequency content of the trial.
iii. Use Eq.2 to calculate filtered trial's correlation with corresponding template in different lag values.
iv. Select the correlation values for lags -10 to +10
v. Calculate the average of these 21 correlation values.
vi. If the resulting value is bigger than a specific threshold, the trial contains P300 and if not, then the trial doesn't contain this component.
vii. Calculate the "Target Accuracy" and "Non-target Accuracy" and "Total Accuracy" for each electrode.

According to percentage in columns 2 and 3 of Table1, it seems obvious that, for a specific trial, different channels can show different labels. This means that using a combination of the outputs, based on a previous knowledge of the classifier, can make the results better. In the next section, using a fuzzy multi agent for this combination will be discussed.

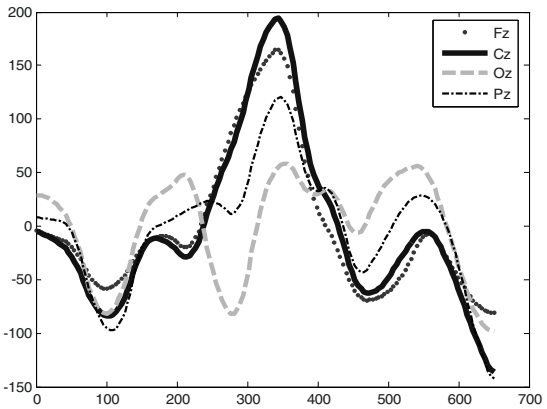

Fig.6 The averaged waveform over electrodes Fz, Cz, Oz, and Pz after a band-pass filtering that shows a bigger peak in Cz.

Table1. The accuracy for P300 detection using the classic TM technique over some scalp electrodes (in percent) over 2000 trials (1000; target and 1000; nontarget).

Electrode	Target Accuracy	Nontarget Accuracy	Total Accuracy
Fz	66.5	68.5	67.5
Cz	71.3	78.1	74.4
Oz	51.6	46.8	49.2
Pz	58.2	61.5	59.85
F3	64.6	65.7	65.15
F4	67.3	63.5	65.4
C3	72.3	75.2	73.75
C4	78.9	73.7	**76.3**
P3	54.6	58.1	56.35
P4	66.4	58.2	62.3

IV. Modifying the Classic Template Matching for P300 Detection

The spreading use of fuzzy logic shows its power in different task; specially inference and decision making. As shown in previous sections, a specific trial, can obtain different labels after going through each TM block in Fig.1. This means that for each trial, some of TM blocks can have accurate P300 detection while some others cannot. In this section, we are going to modify TM technique for better and more accurate detection by simultaneous using it over some electrodes and voting over outputs to have a final label which will be better than a single TM block.

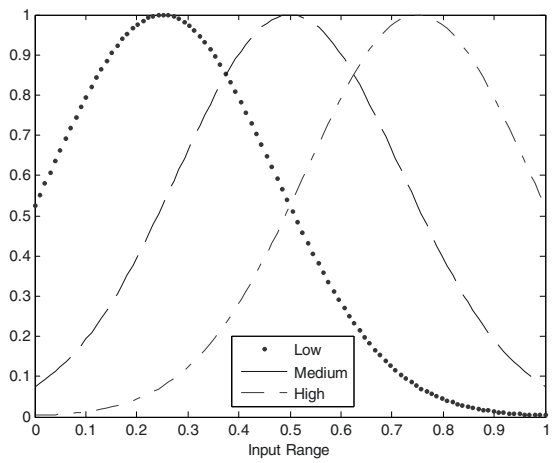

Fig.7 Three Gaussian membership functions used to assign the outputs with a label; High, Low or Medium

F. Ibrahim, N.A. Abu Osman, J. Usman and N.A. Kadri (Eds.): Biomed 06, IFMBE Proceedings 15, pp. 410-414, 2007
www.springerlink.com ' Springer-Verlag Berlin Heidelberg 2007

For this reason, we used a fuzzy block as a voter or mixing block at the output to have all the TM blocks' outputs as input to make the final output. As shown in Fig.5, the correlation over all lag values can have a maximum value and a minimum value. After calculating the correlation values for each trials (10*2000 vectors) the maximum of maximums (grand maximum) and The minimum of minimum (grand minimum) for each electrode will be calculated and normalized between 0.05 and 0.95 using Eq.3 in which the *C* and *Val* represent the correlation vector and the new value to be normalized, respectively.

$$Min = \min(\min)_{electrode},\ \ Max = \max(\max)_{electrode}$$
$$NormVal = [\frac{(0.95)-(0.05)}{Max - Min} * (Val - Min)] + Min \quad (3)$$

After doing all these operations, each correlation average (step5 of previous section) value will be a member of three rules in Fig.7 with a specific membership. Having membership values for each trial over each electrode and the rules in Table2, the final label for the input trial will be determined. Because of poor accuracy of Oz, Pz, P3 and P4 electrodes, they will not be taken into consideration. Using this technique, for the same input trials as what used for section2, the accuracy result is shown in Table3. As can be seen, the results are really better than the previous ones.
Rules in Table2 are extracted based on some experimental and trial and error procedure. This table shows a reduced set of rules that were the most effective and accurate ones.

Table2. Fuzzy rules used to determine the final label of an input trial based on the TM output of it in electrodes Cz, C3, C4, Fz, F3, and F4.

Rule#	If	Then
01	Sum (High)>Sum(Low)	Label=High
02	Sum(Low)>Sum(High)	Label=Low
03	Sum(Low)=Sum(High) C3=C4=Cz=Medium	Label=Low
04	Sum(Low)=Sum(High) C3=C4≠Medium	Label=Label(C3)
05	Sum(Low)=Sum(High) C3=Cz≠Medium	Label=Label(C3)
06	Sum(Low)=Sum(High) Cz=C4≠Medium	Label=Label(Cz)
07	Sum(Low)=Sum(High) C3=C4≠Medium	Label=Label(C3)
08	Sum(Low)=Sum(High) C3=C4=Medium Cz≠Medium	Label=Label(Cz)
09	Sum(Low)=Sum(High) Cz=C3=Medium C4≠Medium	Label=Label(C4)
10	Sum(Low)=Sum(High) C4=Cz=Medium C3≠Medium	Label=Label(C3)

Table 3. Accuracy values for final system (Fig.1) over 2000 trials (1000 target and 1000 nontarget).

System	Target Accuracy	Nontarget Accuracy	Total Accuracy
TMs+ Fuzzy Voter	86.6	81.8	84.2

V. A REVIEW OF THE METHOD FOR AN EXAMPLE TRIAL

Now that everything is described for this method, in this part we will evaluate a sample trial to detect whether it contains the P300 or not. The following step will be done till the final output (label) gets determined:

i. A trial must be selected for a particular stimulus for electrodes Cz, C3, C4, Fz, F3 and F4.
ii. All six trials from previous step must get filtered for a noise cancellation (0.5-30Hz band-pass filter).
iii. The correlation vector with respect to different lag values must be calculated.
iv. For lag values between -10 to +10, the correlation values must be averaged to yield a single value.
v. This single value must go through a normalization process.
vi. The output of step5 must go for membership functions in Fig.7 to determine its membership for three rules.
vii. It will yield six memberships for six electrodes that will determine the final label based on rules in Table2.

All these steps for a sample trial are shown in Fig.8. The only important point left is the *Min* and *Max* for Eq.3. At the training part, we will find a *Min* and *Max* which will be a system parameter. Then for a new trial, if the maximum and minimum are not bigger than these values, they will get normalized with respect to these values and if not, *Max* and *Min* values will be replaced with new ones.

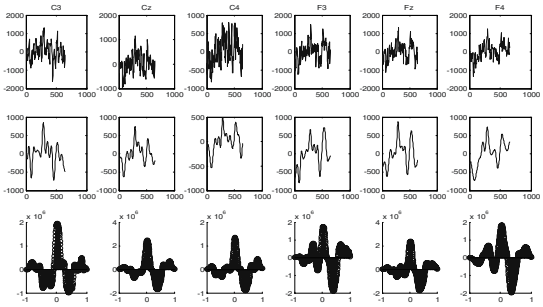

Fig.8 Six trials for six electrodes before filtering (upper panel), after filtering (middle panel) and their correlation with corresponding templates (lower panel). Here all six channels show a High value for memberships so the final output is high.

F. Ibrahim, N.A. Abu Osman, J. Usman and N.A. Kadri (Eds.): Biomed 06, IFMBE Proceedings 15, pp. 410-414, 2007
www.springerlink.com ' Springer-Verlag Berlin Heidelberg 2007

VI. Conclusion and discussion

In this study, we used a new technique to modify a simple classification technique like Template Matching. As shown in results, the poor TM results got much better by a simple combination based on a fuzzy rule set. This idea can be used for better accuracy by combining some more accurate classifiers; like SVM, LDA, ANN, etc. The main advantage of this method that caused such good results was to combine information from different scalp places for a better classification.

References

[1] B. Blankertz, K.-R. Müller, G. Curio, T. M. Vaughan, G. Schalk, J. R. Wolpaw, A. Schlögl, C. Neuper, G. Pfurtscheller, T. Hinterberger, M. Schröder, and N. Birbaumer, The BCI Competition 2003: Progress and perspectives in detection and discrimination of EEG single trials, in *IEEE Trans. Biomed. Eng.*, vol. 51, pp. 1044 1051, June 2004.

[2] *Handbook of Electroencephalographic Clinical Neurophysiology*, vol. 3, Endogenous Event-Related Potentials, T. W. Picton and S. A. Hillyard, Eds., Elsevier, Amsterdam, The Netherlands, 1988, pp. 361 426.

[3] N. Birbaumer, N. Ghanayim, T. Hinterberger, I. Iversen, B. Kotchoubey, A. Kübler, J. Perelmouter, E. Taub, and H. Flor, A spelling device for the paralyzed, *Nature*, vol. 398, pp. 297 298, 1999.

[4] Piotr Jaskowski, Rolf Verleger, An evaluation of methods for single trial estimation of P300 latency, Psychophysiology, vol.37, 2000, pp.153-162

[5] *Fuzzy Expert Systems and Fuzzy Reasoning*, William Siler, James J. Buckley, Wiley Interscience, 2006.

Address of the corresponding author:

Author: G. R. Salimi Khorshidi
Institute: Department of Biomedical Engineering Amirkabir University of Technology (Tehran Polytechnic)
City: Tehran
Country: Iran

F. Ibrahim, N.A. Abu Osman, J. Usman and N.A. Kadri (Eds.): Biomed 06, IFMBE Proceedings 15, pp. 410-414, 2007
www.springerlink.com ' Springer-Verlag Berlin Heidelberg 2007

Multi-resolution Analysis of Near Infrared Spectroscopic Data for Calibration and Prediction of Active Substances in Phosphate Buffer Solution

C.S. Soh and P. Raveendran

Department of Electrical Engineering, Faculty of Engineering, University of Malaya, Kuala Lumpur, Malaysia.

Abstract— **Discrete wavelet transform is performed on near infrared spectroscopic data as a preprocessing step in calibration and prediction of active substance concentrations in phosphate buffer solutions. Wavelet coefficients from different scales are used as predictor variables to build regression model via partial least squares. The prediction results are compared with calibration model developed from raw spectroscopic data (without wavelet transform). The wavelet scale, which gives the best-improved prediction accuracy, is selected to form prediction model.**

Keywords—**near infrared spectroscopy, discrete wavelet transform, partial least squares, multivariate regression.**

I. Introduction

Near infrared (NIR) spectroscopy is a useful measurement method for nondestructive and noninvasive analysis of various biomedical [1], food [2], agricultural [3], and pharmaceutical industry [4,5]. A typical near infrared spectrum consists of absorbance values recorded at large number of wavelengths or wavenumbers. Thus, NIR spectroscopic data set usually has large amount of data size with hundreds or thousands of variables recorded for each sample.

An important characteristic of NIR spectroscopic data is the high multi-colinearity between adjacent variables or wavelengths. This effect can be easily observed from broad peaks in the NIR spectra. Due to the overlapping peaks present in NIR spectra, a large amount of wavelength regions are redundant or do not yield useful information for substance contents prediction. For this reason, NIR spectra are highly compressible, that is, instead of storing the spectra in their large number of original variables or wavelengths, the spectra can be processed and stored in reduced number of variables. This reduces the dimension of the data set for easy storage and post processing with negligible loss of information.

Wavelet transform is a popular method used in signal processing to achieve high compression ratio. In addition to that, it is also capable of noise and baseline removal of NIR spectra [6]. Thus, wavelet transform is a useful method to perform preprocessing of NIR spectra.

Due to broad and overlapping peaks in NIR spectrum, information on the contents of solution under study is not contained is any specific single wavelength. A range of wavelengths is used to analyze the chemical content of solution. Only certain wavelength regions of the NIR spectrum contain information on the compound concentration. These regions of interest are useful for the prediction of concentration of substance. Predictive information in these regions could be ideally captured in a few variables.

Wavelet transform has the advantage of performing multi-resolution analysis on signal at different scales and time. In NIR spectra, wavelength corresponds to time analysis used in other temporal signals. Absorbance values of a range of adjacent wavelengths can be reduced to a single wavelet coefficient using wavelet transform. In fact, a single wavelet coefficient can carry information of several original variables to produce a more parsimonious model [7]. The ability of wavelet transform to analyze signal at different scales is useful in NIR spectral analysis to enhance or highlight predictive information in regions that correlate with concentration of substance.

Multivariate data analysis via partial least squares can be performed using the wavelet coefficients to build calibration model to predict the concentration of substance. The information on substance of interest is present in different scales of wavelet coefficients. The scale that gives the best improvement in the prediction accuracy of calibration model is selected as the final prediction model.

II. Methods

A. Discrete Wavelet Transform

Discrete wavelet transform (DWT), as its name implies, refers to wavelet transform applies to discrete time signal. As in our case, it is applied to spectroscopic data, consisting of spectra with absorbance values at discrete wavenumbers or wavelengths.

A DWT is a linear transformation whereby a function f(t) is decomposed into a weighted sum of basis function $\psi_{j,k}(t)$ as follows:

F. Ibrahim, N.A. Abu Osman, J. Usman and N.A. Kadri (Eds.): Biomed 06, IFMBE Proceedings 15, pp. 415-418, 2007
www.springerlink.com ' Springer-Verlag Berlin Heidelberg 2007

$$f(t) = \sum_j \sum_k c_{jk} \psi_{j,k}(t) \quad (1)$$

where j and k are integers and $\psi_{j,k}(t)$ is a wavelet basis function generated from a single mother wavelet $\psi(t)$ by dyadic dilation and translation, as follows:

$$\psi_{j,k}(t) = 2^{-\frac{j}{2}} \psi(2^{-j} t - k) \quad (2)$$

where j is the dilation scale index and k is the translation index.

Wavelet coefficient c_{jk} in equation (1) is calculated by projecting the function $f(t)$ onto the wavelet basis set $\psi_{j,k}(t)$. The wavelet coefficient c_{jk} can be considered as the measure of similarity between the function $f(t)$ and basis $\psi_{j,k}(t)$.

$$c_{jk} = \langle f(t), \psi_{j,k}(t) \rangle = \int_{-\infty}^{\infty} f(t) \psi_{j,k}(t) dt \quad (3)$$

Multi-resolution analysis (MRA), which is a basic idea of wavelet analysis, decomposes the near-infrared (NIR) data such that the data appears on multiple scales. Mallat presented a fast wavelet transform algorithm for multi-resolution analysis [8].

In multi-resolution analysis, the raw spectral data is decomposed into approximation coefficients and details coefficients. Approximation coefficients capture the slow variation in the raw data while the details coefficients keep the fast varying changes in the raw data. Thus, approximation coefficients and details coefficients can be considered as the result of low pass and high pass filtering respectively.

Approximation coefficients from the current scale can undergo another round of decomposition into yet another approximation and details coefficients at the next higher scale. The process of subjecting approximation coefficients of each scale to further decomposition to yield approximation and details coefficients at the next scale can be repeated until there is only a single remaining approximation coefficient. If the raw spectral data is of length 2^n, the raw data can be resolved into n scales. For spectrum length not equals to 2^n, it can be easily extended to length 2^n by padding the spectral data. See Fig. 1 for graphical illustration of MRA process.

Details coefficients from each scale are used as predictor variables for multivariate regression using partial least squares. One calibration model is built from details coefficients from each scale and the prediction accuracy of each model is compared with one another and also with that of the model using original raw NIR spectral data (without wavelet transformation). The prediction accuracy is compared quantitatively using standard error of prediction (SEP) calculated with the following equation:

$$SEP = \sqrt{\frac{1}{M-1} \sum_{i=1}^{M} (y_i - y_i)^2} \quad (4)$$

where M is the number of samples in the validation set, y_i is the actual substance concentration of i-th sample from the validation set and y_i is the predicted substance concentration of i-th sample from the validation set.

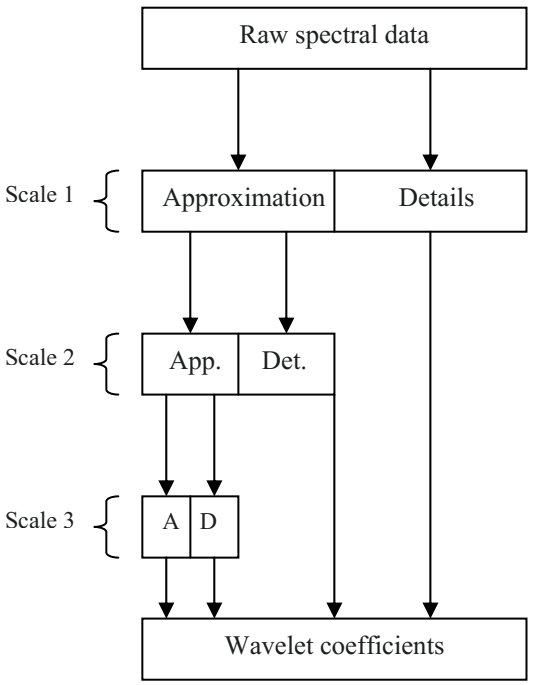

Fig. 1 Multi-resolution analysis of spectral data

B. Data set

The data set used in this study was provided by S. Kasemsumran *et al*. and had been used in their work [9,10]. There are three components of active substances:- human serum albumin (HSA), γ-globulin and glucose in phosphate buffer solutions. There are five different concentration values for each substance. HSA concentration varies with values of 3.2, 3.9, 4.6, 5.3 and 6.0 g/dl, γ-globulin with concentrations of 2.2, 2.65, 3.1, 3.55 and 4.0 g/dl whereas glucose with concentration values of 0.288, 0.716, 1.144, 1.572 and 2.000 g/dl.

This data set has 125 samples or observation for different combination of concentrations for three substances. The predictor variables are absorbance values at different wavelengths.

F. Ibrahim, N.A. Abu Osman, J. Usman and N.A. Kadri (Eds.): Biomed 06, IFMBE Proceedings 15, pp. 415-418, 2007
www.springerlink.com ' Springer-Verlag Berlin Heidelberg 2007

Each NIR spectrum is defined by absorbance values at 2048 wavenumbers, ranging from 8000cm^{-1} to 4000cm^{-1}. Therefore, the predictor matrix **X** has the size of 125×2048. Since each spectrum is generated by spectroscopic measurement of solution of three substances, there are three concentration values (human serum albumin (HSA), γ-globulin and glucose) associated with it. The response matrix **Y** has the size of 125×3. The data set is divided into two sets: the calibration set with 95 samples and the testing set or validation set with 30 samples. The calibration set is used for developing the calibration model via partial least squares (PLS) regression, while the independent testing set is to validate the accuracy of the calibration model.

III. Result

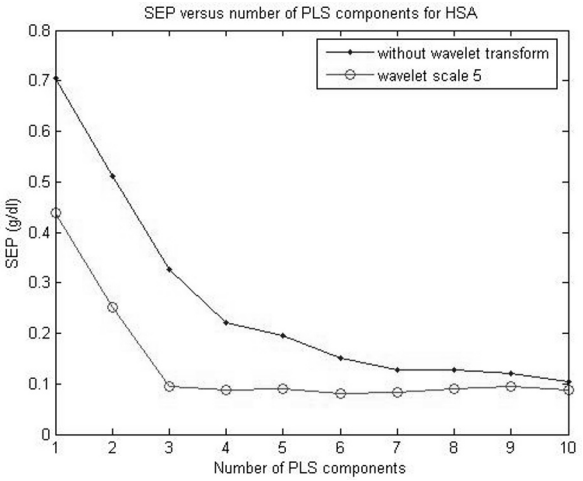

Fig 2. SEP versus number of PLS components for HSA.

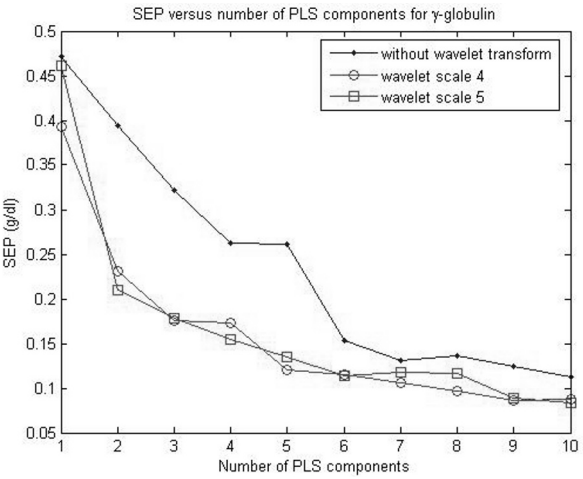

Fig 3. SEP versus number of PLS components for γ-globulin.

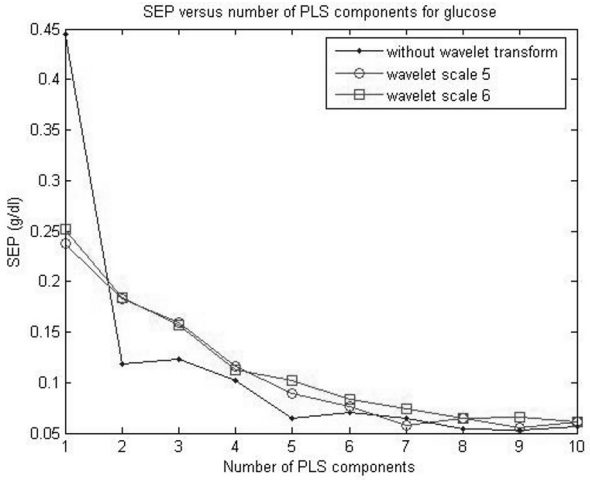

Fig 4. SEP versus number of PLS components for glucose.

Fig. 2, 3, and 4 illustrates the variation of SEP values with number of PLS components for HSA, γ-globulin and glucose respectively from various regression models with and without wavelet transformation. Note that only SEP values from wavelet coefficient regression models that give significant improvement or closely approximate the SEP values of the regression model without wavelet transform are shown in the figures. For example, in Fig. 2, wavelet coefficient regression model using scale 5 is shown in comparison with the model without wavelet transformation since scale 5 gives the best improvement in SEP values compared to other scales. This is similar for γ-globulin results where scale 4 and scale 5 are selected for comparison.

However, for glucose in Fig. 4, no wavelet coefficient regression model gives a general improvement in SEP. Therefore, we selected scale 5 and scale 6 which closely follow the SEP trend of model without wavelet transform as comparison with regression model without wavelet transform.

IV. Discussion

Results from HSA shows that wavelet coefficients from scale 5 yields the best improvement in SEP values in comparison to model without wavelet transforms. The graph is Fig. 2 clearly shows all SEP values for scale 5 model are less than that of the model without wavelet transform. Three PLS components is sufficient for building regression model using scale 5 wavelet coefficients, which gives SEP=0.0952 g/dl, since additional PLS components do not give much significant in reduction in SEP. Regression model without wavelet transform needs 7 PLS factors with corresponding SEP=0.1264 g/dl. Thus, scale 5 wavelet coefficients regression model not only resulted in lower prediction error

F. Ibrahim, N.A. Abu Osman, J. Usman and N.A. Kadri (Eds.): Biomed 06, IFMBE Proceedings 15, pp. 415-418, 2007
www.springerlink.com ' Springer-Verlag Berlin Heidelberg 2007

but also requires less PLS factors to predict HSA concentration with acceptable accuracy.

Results from γ-globulin shows that scale 4 and 5 of wavelet coefficients give the most significant improvement in SEP values. SEP values for scale 4 and 5 wavelet coefficient regression are generally lower than that of regression model without wavelet transform. Number of PLS factors sufficient to predict the concentration of γ-globulin is 5 PLS factor (SEP=0.1209 g/dl) at scale 4 and 6 (SEP=0.1141 g/dl) at scale 5. For PLS model without wavelet, 7 PLS components are required (SEP=0.1310 g/dl). The same conclusion as that of HSA can be derived for PLS factors is sufficient to predict the concentration of γ-globulin, that is, regression models with wavelet coefficients produce the least prediction error and also require the least PLS factor in comparison with regression model without wavelet coefficients.

Result for glucose, however, differs from that of HSA and γ-globulin. Generally, model without wavelet coefficients produces lower SEP values for all number of PLS factors except at 7 PLS factors, where scale 5 regression model performs better. PLS regression model without wavelet coefficients uses 5 PLS factors at SEP=0.0645 g/dl to predict glucose concentration with sufficient accuracy. Scale 5 regression model requires 7 PLS components with SEP=0.0571 g/dl while scale 6 model requires 8 PLS factors with SEP=0.0641 g/dl.

From the above analysis, we can conclude that wavelet coefficient regression could only improve the prediction accuracy of HSA and γ-globulin. Glucose concentration prediction meanwhile yields poorer prediction accuracy compared with the regression model using original raw variables (without wavelet coefficients). The only explanation for this discrepancy is that HSA and γ-globulin are major substances in the solution, which varies from 3.2 g/dl to 6.0 g/dl and 2.2 g/dl to 4.0 g/dl, respectively. Therefore, significant variation in the NIR spectra describes these major substances very well. On the other hand, glucose as minor substance, with concentration varies from 0.288 g/dl to 2.000g/dl, contributes only slightly to the variation in the NIR spectral data.

V. Conclusion

We have investigated the calibration and prediction of three compounds in phosphate buffer solution (HSA, γ-globulin, glucose) using wavelet coefficients at different scales. Wavelet coefficient regression model could only improve prediction accuracy of major compounds, which present in a significant amount in the solution, as revealed in the result from HSA and γ-globulin. For minor compound, the prediction accuracy is worse than that without wavelet transform. However, considering that not all wavelet coefficients are useful in the prediction of active substances, the accuracy could be improved if variable selection is performed prior to calibration using PLS. Our future work will focus on using variable selection and wavelet transform in multivariate calibration of NIR spectra.

Acknowledgment

We would like to thank Prof. Yukihiro Ozaki and his researchers from the Department of Chemistry and Research Center for Near-Infrared Spectroscopy, School of Science and Technology, Kwansei-Gakuin University, Japan for providing the data set used in this study.

References

1. Gributs C.E.W., Burns D.H. (2006) Parsimonious calibration for near-infrared spectroscopy using wavelets and scaling functions. Chemometr. Intell. Lab. Syst. 83: 44-53.
2. Chen B., Fu X., Lu D. (2002) Improvement of predicting of oil content in instant noodles by using wavelet transforms to treat near-infrared spectroscopy. Journal of Food Engineering 53: 373-376.
3. Odlare M., Svensson K., Pell M. (2005) Near infrared reflectance spectroscopy for assessment of spatial soil variation in an agricultural field. Geoderma 126: 193-202.
4. Eustaquio A., Blanco M., Jee R.D. Moffat A.C. (1999) Determination of paracetamol in intact tablets by use of near infrared transmittance spectroscopy. Anal. Chim. Acta 383: 283-290.
5. Blanco M., Coello J., Eustaquio A., Iturriaga H., Maspoch S. (1999) Analytical control of pharmaceutical production steps by near infrared reflectance spectroscopy. Anal. Chim. Acta 392: 237-246.
6. Chen D., Shao X., Hu B., Su Q. (2004) A background and noise elimination method for quantitative calibration of near infrared spectra. Anal. Chim. Acta 511: 37-45.
7. Coelho C.J., Galvao R.K.H., Araujo M.C.U., Pimentel M.F., da Silva E.C. (2003) A solution to the wavelet transform optimization problem in multicomponent analysis. Chemometr. Intell. Lab. Syst. 66: 205-217.
8. Mallat S. (1989) A theory for multiresolution signal decomposition: the wavelet representation. IEEE Trans. Pattern Anal. Machine Intell. 11(7): 674-693.
9. Kasemsumran S, Y. ping Du, Murayama K, Huehne M, Ozaki Y. (2003) Simultaneous determination of human serum albumin, gamma-globulin and glucose in a phosphate buffer solution by near-infrared spectroscopy with moving window partial least squares regression. The Analyst 128:1471-1477.
10. Kasemsumran S, Y. ping Du, Murayama K, Huehne M, Ozaki Y. (2004) Near-infrared spectroscopic determination of human serum albumin, gamma globulin and glucose in a control serum solution with searching combination moving window partial least squares. Anal. Chim. Acta 512:223-230.

Address of the corresponding author:

Author: .S. Soh
Institute: University of Malaya
Street: Lembah Pantai
City: Kuala Lumpur
Country: Malaysia
Email: itsiang@perdana.um.edu.my

F. Ibrahim, N.A. Abu Osman, J. Usman and N.A. Kadri (Eds.): Biomed 06, IFMBE Proceedings 15, pp. 415-418, 2007
www.springerlink.com ' Springer-Verlag Berlin Heidelberg 2007

Performance Evaluation of Coifman Wavelet for ECG Signal Denoising

H.G.Rodney Tan[1], K.M.Lum[2] and V.H.Mok[1]

[1] Centre for R&D Commercialization, UCSI, Kuala Lumpur, Malaysia
[2] School of Engineering, UCSI, Kuala Lumpur, Malaysia

Abstract—**The performance evaluation of Coifman wavelet for ECG signal denoising is presented in this paper. The Coifman wavelet family was use to evaluation its performance on the denoising of ECG signal. The denoising technique was performed by forward discrete wavelet transform up to decomposition of 5 levels, soft thresholding on the wavelet coefficients and inverse discrete wavelet transform. The Signal to Noise Ratio (SNR) in dB is used as a numerical measurement of denoised signal quality. The ECG Signal was obtained from MIT-BIH Arrhythmia reference database. White gaussian noise was added to the clean reference ECG signal to produce the noisy ECG signal with 3 noise levels of initial SNR of 6.5dB, 16.1dB and 20.5dB for denoise evaluation. The evaluation results shows that Coifman *N* = 5 wavelet achieves the best overall denoise performance at all 3 noise levels for ECG signal with the SNR improvement of up to 6.3dB. The evaluation results presented in this paper provide a basic reference for Coifman wavelet family selection for ECG signal denoising applications.**

Keywords—**Coifman Wavelet, ECG, Denoising, Discrete wavelet transform.**

I. Introduction

Electrocardiogram (ECG) is a noninvasive body surface measurement of biopotential signal that is generated by the heart muscle contraction and pumping activity. ECG signal is useful in diagnosing the heart condition by detection and identification of the PQRST waves and segments, time duration, amplitude, cardiac rhythms and conduction patterns. During ECG measurement and recording the ECG signal, it is usually contaminated by power line interference noise, electrode contact noise, motion artifacts noise, muscle contraction noise cause by superimpose of Electromyography (EMG) signal, base line drift, instrumentation noise generated by electronic devices and electrosurgical noise. Noises that require attention and need to be taken care of during ECG measurement and recording are electrode contact noise and muscle contraction noise, these noises are very subjective and it is superimpose into the ECG signal. Based on visual observation an ECG signal with SNR that is less than 10dB are not only fetal to automatic ECG diagnosis and analysis system, as well as human observer such as cardiologist.

Denoising is a process to remove noise that is present in the signal of interest. Many denoising technique based on filter has been developed to remove the noise from the ECG signal. Filtering techniques are well established and effective in removing power line interference noise and base line drift, however it is not very effective on EMG and electrode contact noise that actually superimpose and overlapping in the ECG signal. Wavelet transform has been proven as a useful tool for ECG [1] signal analysis and it is widely used in biomedical signal processing and denoising applications [2][3][4]. But most wavelet based denoise papers are emphasize toward the denoise methodology rather than the wavelet function itself. Hence does not provide performance evaluation on the particular wavelet function on the ECG signal denoising applications. This paper present a comprehensive performance evaluation of Coifman wavelet functions in ECG signal denoise using soft thresholding technique proposed by Donoho [5][6].

II. Approach

The wavelet transform approach of signal denoising is shown in Fig 1. The discrete wavelet transform can be represented in equation (1) where $s(n)$ is the signal, $C(a,b)$ are dyadic wavelet coefficients, a is dilation or scale, $a = 2^j$, b is translation, $b = k2^j$, $j \in N$, $k \in Z$ and $g_{j,k}(n)$ is the wavelet function.

$$C(a,b) = \sum_{n \in Z} s(n) g_{j,k}(n) \tag{1}$$

The forward discrete wavelet transform is used to decompose the noisy signal into difference levels of approximation and details in wavelet domain. The Soft Thresholding is shows in equation (2) where S_t is the thresholded signal, s is the signal and th is the threshold value.

$$S_t = \begin{cases} |s| - th & |s| > th \\ 0 & |s| \le th \end{cases} \tag{2}$$

F. Ibrahim, N.A. Abu Osman, J. Usman and N.A. Kadri (Eds.): Biomed 06, IFMBE Proceedings 15, pp. 419-422, 2007
www.springerlink.com ' Springer-Verlag Berlin Heidelberg 2007

The threshold estimator is compute by equation (3) where σ is the standard deviation and *n* is the number of signal samples.

$$th = \sigma\sqrt{2\log(n)} \tag{3}$$

The inverse discrete transform is used to transform the thresholded wavelet coefficients back to time domain which is the denoised signal.

Fig. 1 Wavelet Transform Denoising Approach

The Coifman wavelet was built by Ingrid Daubechies [7] at the request from Ronald Coifman. The Coifman wavelet family has the properties of *N* up to 5 orders, compact support, filter length of 6*N*, ψ wavelet function of 2*N* vanishing moment, θ scaling function of 2*N* -1 vanishing moment and near symmetry. The Coifman wavelet was chosen to evaluation the denoise performance of the ECG signal because of it properties of near symmetry and θ scaling function that resemble closely with the ECG signal and ψ wavelet function resemble the noise within the ECG signal.

III. Evaluation parameters

The ECG signal from MIT-BIH Arrhythmia Database [8] was chosen to evaluate the performance of Coiflet wavelet denoising ability. The MIT-BIH Arrhythmia Database is a Class 1 reference database with lead II configuration containing 48 30 minutes excerpts of two-channel ambulatory ECG recordings, obtained from 47 subjects studied by the BIH Arrhythmia Laboratory. The recordings were digitized at 360 samples per second per channel with 11-bit resolution over a 10 mV range. The first 1024 samples of ECG signal were extracted from the 30 minutes length of recording for offline denoising evaluation. Gaussian white noise was added to artificially contaminate the clean reference ECG signal as shown in equation (4) where *y* is the noisy signal, *x* is the signal, σ is the standard deviation and *e* is the gaussian white noise *N*(0,1). The Gaussian white noise was chosen as it closely resembles the electrode contact and EMG noise.

$$y(n) = f(n) + \sigma e(n)\ ,\ 0 \le n \le N\text{-}1 \tag{4}$$

Noisy ECG signals with initial SNR of 20.5dB, 16.1dB and 6.5dB were produce for denoise evaluation. The ECG signal for denoise evaluation is shown in Fig 2. At initial SNR of 6.5dB the ECG P wave, QRS complex and T wave was completely corrupted by the noise except the R peak.

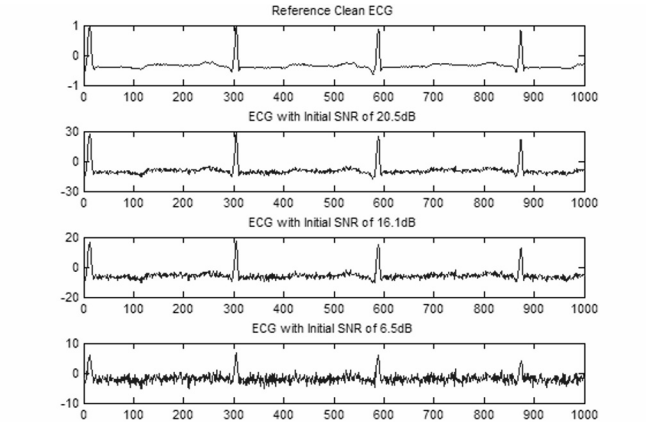

Fig. 2 ECG Signal for Denoise Evaluation

The evaluation was performed offline through all order of Coifman wavelets family from *N* = 1 to 5 and transform up to 5 levels of decomposition for each Coifman wavelet order with soft threshold estimation proposed by Donoho.

IV. Results

The result of denoising using Coifman wavelet on the ECG signal with initial SNR of 6.5dB is shows in Fig 3. The denoise result shows that Coifman *N* = 5 produces the best SNR of 12.8dB with an improvement of 6.3dB. Coifman 1 has the least performance at level 1 and 2 of decomposition but out perform Coifman *N* = 2 and Coifman *N* = 4 at level 3 of decomposition onward up to 0.9dB. The least denoise performance is Coilman *N* = 4 with SNR of 10.9dB at decomposition level 5 but it is still 3.8dB higher than the initial SNR.

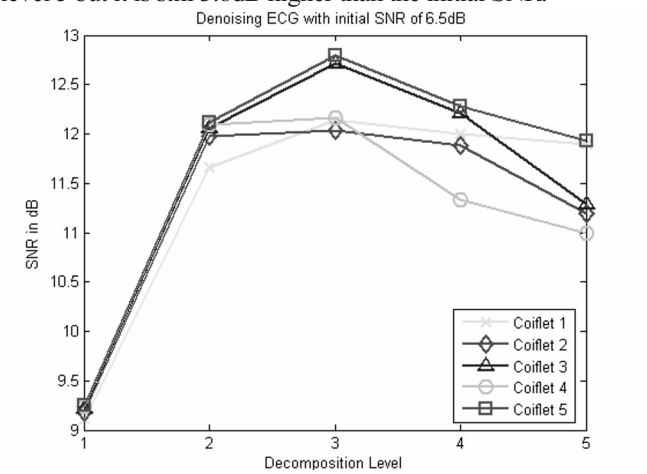

Fig. 3 Denoising ECG with initial SNR of 6.5dB

F. Ibrahim, N.A. Abu Osman, J. Usman and N.A. Kadri (Eds.): Biomed 06, IFMBE Proceedings 15, pp. 419-422, 2007
www.springerlink.com ' Springer-Verlag Berlin Heidelberg 2007

The result of denoising using Coifman wavelet on the ECG signal with initial SNR of 16.1dB is shows in Fig 4. The denoise result shows that Coifman $N = 5$ produces the best SNR of 19.9dB with an improvement of 3.8dB. Coifman $N = 1$ has the least performance at level 1 and 2 of decomposition but out perform all other Coifmans at level 5 of decomposition onward up to 0.7dB. The least denoise performance is Coilman $N = 4$ with SNR of 17.2dB at decomposition level 5 but it is still 1.1dB higher than the initial SNR.

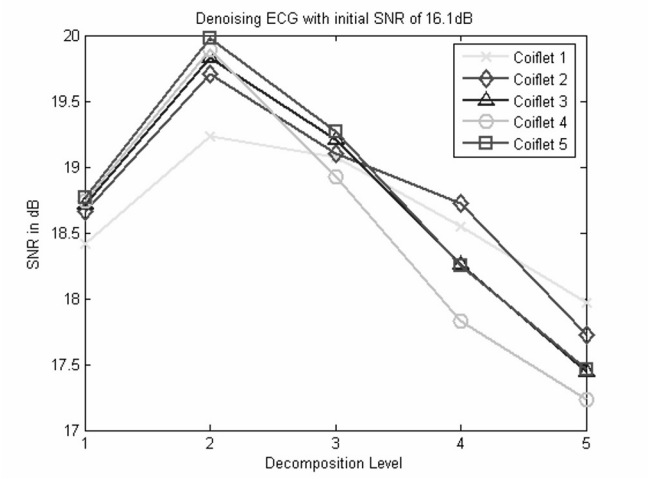

Fig. 4 Denoising ECG with initial SNR of 16.1dB

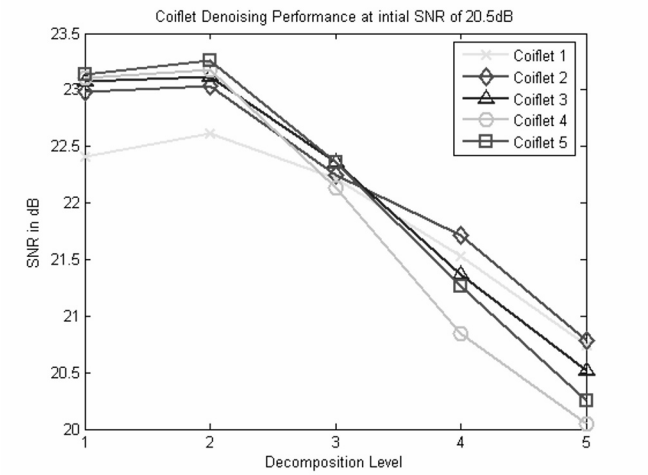

Fig. 5 Denoising ECG with initial SNR of 20.5dB

The result of denoising using Coifman wavelet on the ECG signal with initial SNR of 20.5dB is shows in Fig 5. The denoise result again shows that Coifman $N = 5$ produces the best SNR of 23.3dB with an improvement of 2.8dB. Coifman $N = 1$ has the least performance at level 1 and 2 of decomposition but

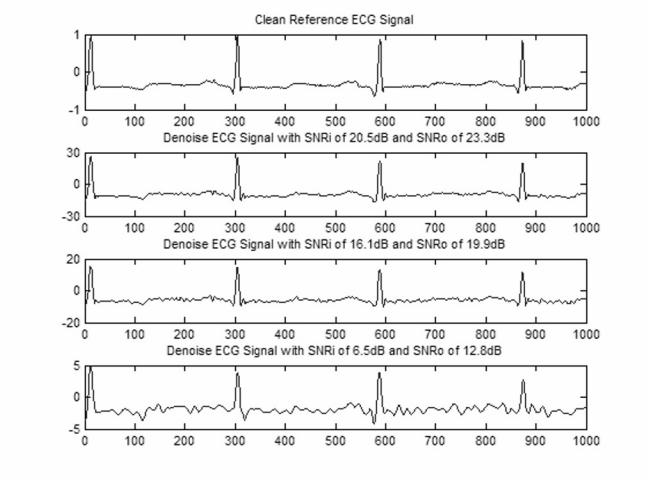

Fig. 6 Denoising ECG Signal for Visual Assessment

out perform all other Coifmans again at level 5 of decomposition onward up to 0.5dB. The least denoise performance again is Coilman $N = 4$ with SNR of 20dB at decomposition level 5 and it is 0.5dB lower than the initial SNR.

For the purpose of visual assessment for the denoise performance of Coifman wavelet, the best denoise output SNR for each noise level is shown in Fig 6. It can be observe that the higher the initial SNR the better it resembles the clean reference ECG Signal which means better recovery of signal from noise.

V. Discussion

Based on the denoise results obtained from the evaluation it was observe that for overall best denoise performance the Coifman $N = 5$ wavelet produces the highest SNR for all noise levels. For ECG signal with initial SNR that is less than 10dB the wavelet transform decomposition levels have to be decomposed up to level 3 in order to achieve the highest SNR, this is because the noisy ECG signal need to decomposed into the higher level in order to effectively extract the high amplitude noise for threshold shrinkage, but for visual assessment it is unlikely to recover the signal from these noise level completely. However, for SNR that is greater than 15dB the wavelet transform decomposition levels only have to decompose up to level 2 to achieve the highest SNR. For visual assessment the denoise ECG Signal have better signal recovery as compare to the clean reference ECG Signal. The Coifman $N = 4$ wavelet has the least overall denoise performance after 3 level of decomposition and Coifman $N = 1$ wavelet has the best denoise performance at decomposition level 5 for all noise level. From the evaluation results it was also observe that Coifman wavelet

F. Ibrahim, N.A. Abu Osman, J. Usman and N.A. Kadri (Eds.): Biomed 06, IFMBE Proceedings 15, pp. 419-422, 2007
www.springerlink.com ' Springer-Verlag Berlin Heidelberg 2007

have the trend of the higher the noise level the higher the SNR improvement as well as the higher the level needed for the wavelet transform to decompose in order to achieve the highest SNR and vice versa.

VI. Conclusion

The performance of Coifman wavelet family was evaluated on the denoise for ECG Signal with 3 level of white Gaussian noises having initial SNR of 6.5dB, 16.1dB and 20.5dB. It was found the Coifman $N = 5$ achieve the best denoise performance in term of highest SNR for all noise levels. As for visual assessments only noise level with initial SNR that is greater than 15dB are require for better ECG characteristics and signal recovery. The evaluation results provide a basic reference for Coifman wavelet family selection for ECG signal denoising as well as contribution to the global wavelet family basis selection for biomedical signal denoise applications.

Acknowledgment

The author would like to express his deepest gratitude and appreciation to those who contribute to made this paper publication possible. UCSI for the financial support and my wife for her support and understanding.

References

1. Paul S Addison (2005), Wavelet Transforms and the ECG: a review Physiological Measurement, pp.155-199.
2. Daniel Novak, David Cuesta Frau, Vladimir Eck, Juan C. Perez-Cortes, Gabriela Andreu-Garcia (2000), Denoising Electrocardiogram Signal using Adaptive Wavelets Euroconference Biosignal 2000.
3. A.Emad, M.B.Shamsollahi (2005), ECG Denoising using M Band Wavelet Transform 12th International Conference on Biomedical Engineering.
4. Hamid Krim, Dewey Tucker, Stephane Mallat, David Donoho (1999), On Denoising and Best Signal Representation IEEE Trans. On Inf. Theory, 45, 7.
5. Donoho, D.L. (1995), "De-noising by soft-thresholding," IEEE Trans. on Inf. Theory, 41, 3, pp. 613-627.
6. Donoho, D.L., I.M. Johnstone (1994), "Ideal spatial adaptation by wavelet shrinkage," Biometrika, vol 81, pp. 425-455.
7. Daubechies, I. (1992), Ten lectures on wavelets, SIAM.
8. MIT-BIH Arrhythmia Database at http://www.physionet.org

Address of the corresponding author:

Author: H.G. Rodney Tan
Institute: UCSI
Street: No:1, Jalan Menara Gading, UCSI Heights, 56000
City: Kuala Lumpur
Country: Malaysia
Email: rodneyt@ucsi.edu.my

F. Ibrahim, N.A. Abu Osman, J. Usman and N.A. Kadri (Eds.): Biomed 06, IFMBE Proceedings 15, pp. 419-422, 2007
www.springerlink.com ' Springer-Verlag Berlin Heidelberg 2007

Photoplethysmographic Pulse Amplitude Response to Flow Mediated Dilation

R. Jaafar[1], E. Zahedi[1], M.A. Mohd Ali[1], A.L. Mohamed[2] and O. Maskon[3]

[1] Department of Electrical, Electronics & Systems Engineering, Universiti Kebangsaan Malaysia, Bangi, Malaysia
[2] Faculty of Medicine, Cyberjaya University College of Medical Sciences, Cyberjaya, Malaysia
[3] Department of Medicine, Faculty of Medicine, Universiti Kebangsaan Malaysia, Bandar Tun Razak, Malaysia

Abstract—**In this paper, the photoplethysmographic (PPG) pulse amplitude response to flow-mediated dilation (FMD) is investigated. Vessel dilation is induced in the right-arm brachial artery (BA) in response to a shear force due to the sudden opening of the BA following supra-systolic blockage of blood supply for 4 minutes. The diameter of the BA is recorded through ultrasound imaging measurement before and after blockage. Concurrently, PPG of the left and right index fingers are recorded before blood occlusion (baseline) and after release. Results on ten human subjects (age 49.7 $\pm$ 10.4 years, range 34-64 years) show that the PPG pulse amplitude measured at the finger of the stimulated arm shows a very distinctive pattern associated to the FMD in the conducting artery. A potential application for the proposed technique is the evaluation of the vascular endothelial function, using a significantly lower-cost and less operator-dependent alternative to conventional ultrasound-FMD.**

Keywords—**Endothelium, flow-mediated dilation, reactive hyperemia, photoplethysmography**

I. Introduction

In order to maintain homeostasis, the human vascular system, which is a complex organ, changes its lumen size in response to different physiological stimulus [1]. Under normal conditions, the vascular endothelium responds to short term increases in shear force (often due to increase of flow) by releasing endothelium-derived relaxing factors that dilate the arteries; this process is known as endothelial function [2]. Endothelial dysfunction, on the other hand, has been recognized as an early marker for cardiovascular disease [3]. Flow-mediated dilation (FMD) is commonly studied non-invasively in the brachial artery (BA) through ultrasound imaging during reactive hyperemia.

It is known that endothelial dysfunction is a systemic disorder [4] and impairment in large arteries is similar to its impairment in small resistance arteries [5]. In quest of endothelial dysfunction assessment, we decided to study the possibility of using photoplethysmography (PPG). This technique utilizes an optical transducer, which produces a signal associated with changes in the volume of red blood cells in the peripheral circulation modified by the heart pumping actions. Next to being non-invasive in nature, the PPG technique is advantageous because of its non-complex instrumentation system, ease of probe attachment, and convenient to both the operator and patient. We expected that PPG signals acquired at the finger circulation, which is downstream to that of the BA, will produce corresponding response to FMD of the BA.

II. Materials and Methods

A. Experimental protocols

The study has been granted approval by the Research & Ethics Committee of Hospital Universiti Kebangsaan Malaysia. Ten subjects were entered in the study and all subjects gave their informed written consent. The subjects (6 females and 4 males) were healthy non-smokers and they had no known cardiovascular disease risk factors.

The study implemented the standard procedures for FMD measurement in the BA [6]. In all subjects, the pressurized cuff was applied to the right arm at 50 mmHg above the subject s systolic blood pressure to stop the flow of blood for approximately 4 minutes. Then the cuff was suddenly released which induced shear stress that caused FMD. Measurements were done while subjects were in supine position.

Two PPG systems, each comprised of the sensor, software and hardware from a commercial PPG recording system (Dolphin Medical Inc.) were incorporated to obtain the PPG signals from the right and left index fingers, RA and LA, respectively. Each finger pulse oximeter probe system was pre-installed to a personal computer for ease of data acquisition, restoration and analysis. Since the PPG systems are independent of each other, a separate module [7] was implemented for synchronization making the acquired finger PPG signals simultaneous. PPG signals were recorded continuously from 3 minutes prior to the start of blockage (to obtain the PPG signals at baseline condition), during the blockage (4 minutes), and for the following 5 minutes (to investigate reactive hyperemia) after release of blockage.

F. Ibrahim, N.A. Abu Osman, J. Usman and N.A. Kadri (Eds.): Biomed 06, IFMBE Proceedings 15, pp. 423-426, 2007
www.springerlink.com ' Springer-Verlag Berlin Heidelberg 2007

B. Signal Analysis

PPG signals contain two major components [8]:

- low frequency component resulting from the slow moving baselines of the signals, related to the relative vascularization and influenced by breathing and brain control; this is referred to as the DC values
- high frequency component resulting from the fast changes in pulse amplitude, related to local blood volume change and corresponding to the beating of the heart; this is referred to as the AC values

Typical PPG pulses are illustrated in Fig. 1 with values of DC, AC, and peaks of the pulses identified. The DC value is represented by the PPG baseline and the AC value is represented by the difference between two adjacent maximum and minimum. In this study, we investigated the response of pulse amplitude (AC) changes as a consequence of anticipated FMD. Signal analysis was performed off-line by MATLAB (The Mathworks, Inc.). The extraction of AC values from the raw PPG data was successfully obtained using a peak detection algorithm. The instantaneous AC values of the RA before blockage ($AC_{Rb}(t)$) and after release of blockage ($AC_{Ra}(t)$) were normalized to that of the mean value at baseline condition, $AC_{mean,Rb}$:

$$AC_{Rb,\text{norm}}(t) = \frac{AC_{Rb}(t) - AC_{mean,Rb}}{AC_{mean,Rb}} x100 \quad (1)$$

$$AC_{Ra,\text{norm}}(t) = \frac{AC_{Ra}(t) - AC_{mean,Rb}}{AC_{mean,Rb}} x100 \quad (2)$$

Similarly, the unblocked arm PPG signals were normalized. These signals were used as control signals. Statistical data analysis was conducted to evaluate significant trends. Baseline and hyperemic conditions were reported as the mean peak AC values (± SD). The difference between baseline and hyperemic condition was calculated using paired samples *t* test. P value < 0.05 was considered significant. Statistical analysis was performed using SPSS application software (SPSS Inc.)

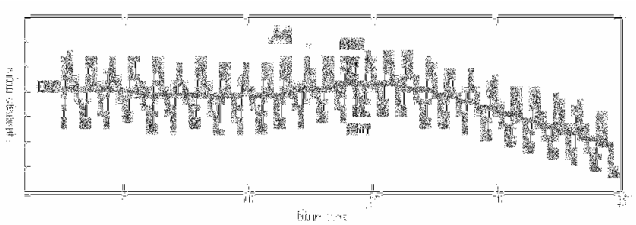

Fig. 1: Typical PPG signals

III. Results

The characteristics of ten healthy subjects (6 females, 4 males) are presented in Table 1. Fig. 2 shows the raw PPG signals recorded from one of the subject (S11) during (a) baseline condition and (b) after release of blockage. The corresponding AC values obtained through a peak detection algorithm for both situations are shown in Fig. 3.

Table 1: Characteristics of the subjects

Parameters	Mean value	Standard Deviation
Age, years	49.7	± 10.4
BP (Systolic/Diastolic), mmHg	125.6 / 76.1	± 11.4/ 7.7
Pulse rate, BPM	73.6	± 7.8

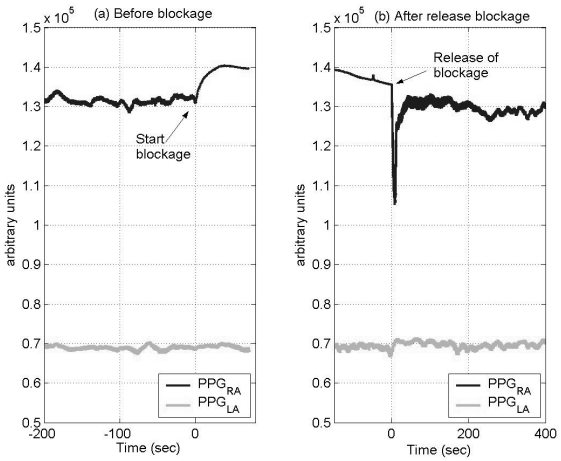

Fig. 2: Raw PPG signals for one subject (S11)

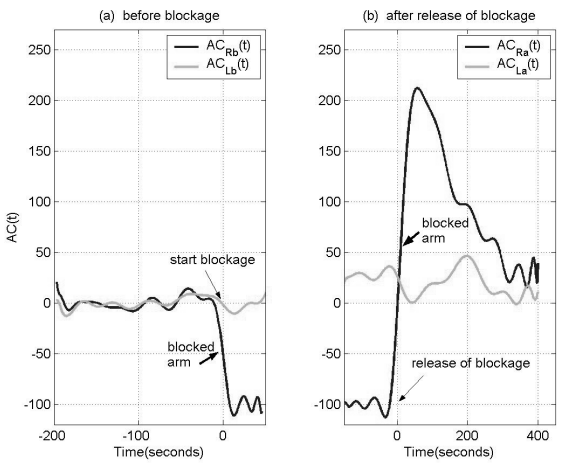

Fig. 3: AC(t) for one subject (S11)

F. Ibrahim, N.A. Abu Osman, J. Usman and N.A. Kadri (Eds.): Biomed 06, IFMBE Proceedings 15, pp. 423-426, 2007
www.springerlink.com ' Springer-Verlag Berlin Heidelberg 2007

During baseline condition (before start of blockage), $AC_{Rb}(t)$ fluctuates around zero. The reactive hyperemia condition (after release of blockage) shows that $AC_{Ra}(t)$ goes through a significant cycle, increasing abruptly following cuff release followed by slower decrease that approaches the baseline condition. The shape of $AC_{Ra}(t)$ curve resembles the typical shape of change of BA size obtained through ultrasound FMD measurement [6]. The shape of the $AC_{Ra}(t)$ curves for all subjects (Fig 4) follow a similar trend with variations in the slope during rising, falling, and the peak value from one subject to another.

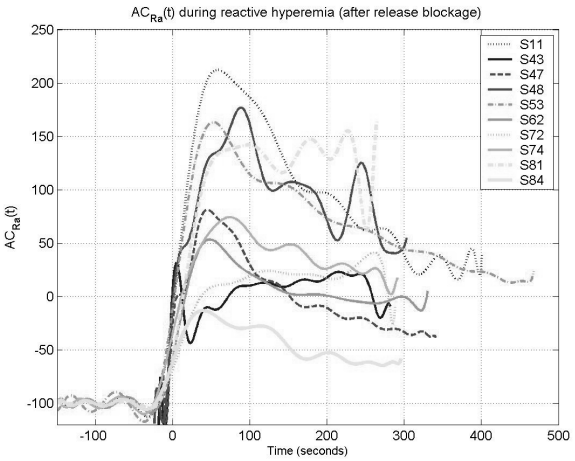

Fig.4: $AC_{Ra}(t)$ curves for all subjects

Fig. 5 shows the 95 % confidence interval and standard deviations of the mean peak AC values of the blocked arm for all subjects during before blockage and after release of blockage, with quantitative results shown in Table 2.

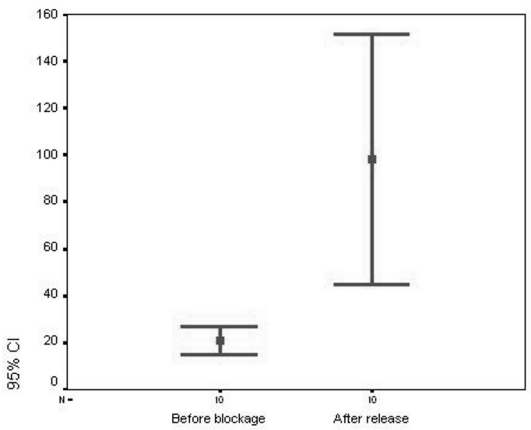

Fig. 5: 95 % confidence interval and SD of peak AC values before blockage and after release

Table 2: Peak AC before blockage and after release

Parameters	Mean value	Standard Deviation
Peak $AC_{Rb,norm}(t)$	20.86	$\pm$ 8.49
Peak $AC_{Ra,norm}(t)$	98.16	$\pm$ 74.80

In all subjects during reactive hyperemia, the pulse amplitude of RA significantly differs from that of during baseline condition. The observed increase in the PPG pulse amplitude of the blocked arm is significant (paired samples *t* test peak $AC_{Rb}(t)$ vs peak $AC_{Ra}(t)$, P=0.0109).

IV. Discussion

The introduction of flow stimulus in the conduit artery has resulted in a significant increase in PPG pulse amplitude of the blocked arm after release of blockage. This implies that significant pulsatile volume increase in the peripheral arteries under the PPG probe occur as a result of the incident flow stimulus in the right BA, which is upstream to the right index finger. The PPG pulse amplitude rise in the finger arteries is an indication of related FMD response being present in the peripheral circulation. As such, it is implied that temporary flow blockage in the BA has induced related FMD in the downstream vessels.

The change of PPG pulse amplitude in relation to FMD in all subjects has a common trend of rising and falling phase with variations in different subjects. The values of both rising and falling slopes as well as the peak of the PPG pulse amplitude curve of the blocked arm after release of blockage may characterize individual subject's vascular properties, which affect FMD. The observed variations in the PPG pulse amplitude curves might indicate variations of vascular properties among the subjects.

Although this study does not reveal the exact amount of FMD which may have taken place in the BA and it does not specify quantitatively the underlying related FMD response in the finger vasculature among the subjects, it has shown that there is significant change in PPG pulse amplitude in response to FMD. This study was mainly powered to detect changes in the PPG signals because there was no information available at the moment regarding its relationship with FMD. Another constraint of the study is that it was based on a small population. The outcome of the study will be enhanced if more subjects were involved. Nevertheless, this study reveals that PPG has the potential capacity to detect the peripheral arterial volume change resulting from the FMD initiated in the conducting artery.

F. Ibrahim, N.A. Abu Osman, J. Usman and N.A. Kadri (Eds.): Biomed 06, IFMBE Proceedings 15, pp. 423-426, 2007
www.springerlink.com ' Springer-Verlag Berlin Heidelberg 2007

V. Conclusions

Results of the current study showed that the evaluation of PPG pulse amplitude responses measured at the fingers is capable of detecting peripheral blood volume changes resulting from flow-mediated dilation, indicative of its potential vascular endothelial function assessment. Further studies are required to advance the current PPG technique in its evaluation of related FMD. The next step of the study is to quantify for the amount of vessel dilation. This will require cross reference to an establish method of FMD measurement such as the ultrasound FMD measurement of BA.

Acknowledgment

This work has been partially supported by an Intensive Research in Priority Areas grant (IRPA-02-02-0106-EA258) from the Ministry of Science, Technology and Innovation, Malaysia. We would like to thank Hartini Mohtar for her kind assistance in subjects' recruitment and data collection.

References

1. Vanhoutte PM (1989) Endothelium and control of vascular function: State of the Art lecture, *Hypertension* 13:658-667
2. Cai H, Harrison DG (2000) Endothelial dysfunction in cardiovascular diseases: The role of oxidant stress, Circulation Research 87:840-844
3. Kinlay S, Creager MA, Fukumoto M et al (2001) Endothelium-Derived Nitric Oxide Regulates Arterial Elasticity in Human Arteries In Vivo. Hypertension 38:1049-1053
4. Bonetti PO, Lerman LO, Lerman A et al (2003) Endothelial Dysfunction: A Marker of Atherosclerotic Risk. Arteriosc Thromb Vasc Biol 23:168-175
5. Iiyama K, Nagano M, Yo Y et al (1996) Impaired endothelial function with essential hypertension assessed by ultrasonography. Am Heart Jour 132: 779-82
6. Corretti MC, Anderson TJ, Benjamin EJ et al (2002) Guidelines for the ultrasound assessment of endothelial-dependent flow-mediated vasodilation of the brachial artery: A report of the International Brachial Artery Reactivity Task Force. J Am Coll Cardiol 39(2):257-265
7. Zahedi E, Mohd Ali MA (2004) Synchronization of Independent Photo-plethysmography Channels. IFMBE Proc. vol.7, Int. Conf. on Biomed. Eng., Kuala Lumpur, Malaysia, 2004, pp 295-296
8. Lindberg LG, Öberg PÅ (1991) Photoplethysmography Part 2: Influence of light source wavelength. Med Biol Eng Comp 29:48-54

Address of the corresponding author:

Author: Rosmina Jaafar
Institute: University Kebangsaan Malaysia
Street: 43600 UKM
City: Bangi, Selangor
Country: Malaysia
Email: rosmina@vlsi.eng.ukm.my

F. Ibrahim, N.A. Abu Osman, J. Usman and N.A. Kadri (Eds.): Biomed 06, IFMBE Proceedings 15, pp. 423-426, 2007
www.springerlink.com ' Springer-Verlag Berlin Heidelberg 2007

Reduction of Movement Artifacts in Photoplethysmograph Using SFLC (scaled Fourier linear combiner)

S.C. Kim[1], E.J. Hwang[1], D.W. Kim[2]

[1]Graduate School of Environmental Biotechnology and Information Technology, Hankyong National University, Anseong, Korea
[2]Department of Medical Engineering, Yonsei University College of Medicine, Seoul, Korea

Abstract— **Wearable computer is new trend and it will make healthcare service/system changed in the future. Photoplethysmograph (PPG) is very useful to measure indirectly heart rate, blood oxygen saturation (SpO_2) with a little constraint. Therefore, many researchers in the field of ubiquitous healthcare and pervasive computer are using the PPG, one of vital signals related to human physiological information, to monitor human health condition. However, the signal is weak and sensitive to motion artifacts. In this study, we applied the scaled Fourier linear combiner (SFLC) to remove effectively the motion artifacts as well as background noise. The proposed method would be useful to reduce the movements and background noise which are non-periodic signal as well as asynchronous signal with heart rate.**

Keywords—**Fourier linear combiner, Noise canceller, Photoplethysmograph, Motion artifacts**

I. Introduction

Heart rate and SpO_2(or SaO_2) can be measured non-invasively and easily by photoplethysmograph (PPG). This method is widely used in clinics and researches since blood flow change obtained from PPG is one of the vital signals related to human physiological information[1-4]. There is a growing need for monitoring or measuring the bio-signal continuously from the subject without any constraint in company with increasing interest in wearable computer, home/ubiquitous health care, pervasive computer [2, 4].

However, it is not easy to obtain the stable bio-signal during free movements, because the signal to noise ratio (SNR) is not enough when the bio-signal is compared with the human movements. Especially, the finger or hand movements cause the PPG signal a lot of noise.

There are many researches to solve this problem in the last decade. One of representative researches is to use accelerometers [5]. The signal from accelerometer is uncorrelated signal with bio-signal, but it highly depends on movements. The movement artifacts from PPG signal can be removed by using accelerometers but it causes an additional cost. The other methods are that based on linear or non-linear, or digital or analog fixed filters, or independent component analysis [6]. However, there are still problems for reducing movement artifacts. Fixed digital/analog filters, or independent component analysis does not perform well in the case of changing the frequency characteristics of signals. That of PPG can be varied by individual heart rate and the conditions.

In this study, we proposed the adaptive scaled Fourier linear combiner (SFLC) to reduce the effect of movement without using any additional sensor from PPG signal and compared the adaptive filter using accelerometer signals and digital filter.

II. Methods

A. Scaled Fourier Linear Combiner (SFLC)s

The periodic signal can be represented by the fundamental frequency and its harmonics. SFLC can be implemented as the structure in Fig. 1 even if the fundamental frequency of input signal changes [7, 8]. The structure is similar to adaptive filter. The signal can be reconstructed from reference signal (X) and its harmonics from equation (1). d_k is composed of the signal of s_k contaminated by an uncorrelated noise n_k. We assumed that s_k is the pure signal without noise, n_k is noise signal by background and movement artifacts. Weight vectors, W, control the amplitude of reference signal, X, in the direction of reducing the error, e_k. We used the least mean square, LMS method in Equation (2) and (3) to update the weight vectors W. The output y_k is obtained by product of X_k and W_k.

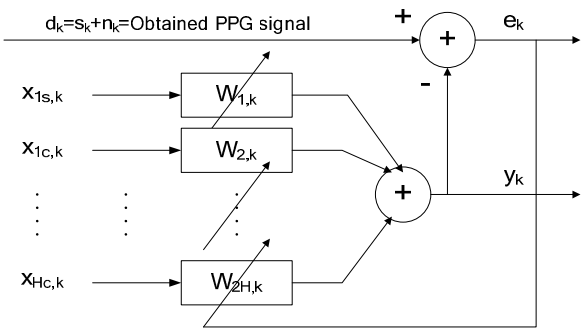

Fig. 1 Block diagram of the adaptive noise canceller using SFLC

F. Ibrahim, N.A. Abu Osman, J. Usman and N.A. Kadri (Eds.): Biomed 06, IFMBE Proceedings 15, pp. 427-430, 2007
www.springerlink.com ' Springer-Verlag Berlin Heidelberg 2007

$$x_{1s,k(m,l)} = \frac{1}{\sqrt{H}} \sin\left(2\pi \frac{il}{L_m}\right) \quad i = 1,2,3,\cdots,H$$
$$x_{1c,k(m,l)} = \frac{1}{\sqrt{H}} \cos\left(2\pi \frac{il}{L_m}\right) \quad i = 1,2,3,\cdots,H \tag{1}$$

$$e_k = E\left[(d_k - y_k)^2\right] \tag{2}$$

$$W_{k+1} = W_k - 2\mu(d_k - y_k)X_k \tag{3}$$

Reference input vector:

$$X_k = [x_{1,k}, x_{2,k}, \cdots, x_{2H,k}]^T \tag{4}$$

Weight vector:

$$W_k = [w_{1,k}, w_{2,k}, \cdots, w_{2H,k}]^T \tag{5}$$

H: the number of harmonics required to reconstruct the signal

L_m: the number of sample at mth beat

m: beat (R-R interval) number index (1, 2, 3, …, *N*)

l: index of sample within beat (1, 2, 3, …, L_m)

k: iteration number

To implement this algorithm on line, we should know the R-R interval, but we can t apply this algorithm within the current ECG because we don t know the current R-R interval period on the current QRS complex signal. Therefore, we just used the previous R-R interval. The peaks was detected using the piece-wise local maxima within the set window.

B. Data acquisition

We made PPG system and the signal was digitized by PCI-6221 (National Instruments Inc., USA) with 200Hz sampling rate. The algorithm was evaluated by Matlab (Mathworks, USA) and LabVIEW (National Instruments Inc., USA). Two accelerometers (ADXL 150, Analog Devices Inc., USA) are attached on the photo sensor (DS-100, Nellcor, USA) to get simultaneously the horizontal and vertical movements.

C. Experiments

To test the SFLC algorithm, we made artificial signal as follows. The simulated signal is triangular waveform whose fundamental frequency is changed from 0.9~1.7Hz. The noise was superimposed using a simulated respiratory artifact, a simulated movement artifact, and a random noise with Gaussian distribution. The respiratory signals are composed of a fundamental frequency 0.2Hz and its harmonics. The movement artifacts are also 1.8Hz and its harmonics.

Figure 2 shows the simulation results of SFLC algorithm using simulated signals by off-line. Figure 3 is the power spectrum of the simulated data as shown in Figure 2. The uncorrelated signals with the fundamental frequency signal and its harmonics were almost removed. The adaptation speed, μ was 0.05, the number of harmonics was 30, and sampling rate was 200Hz.

Figure 4 shows the real data obtained for 110 seconds from PPG system with 200Hz sampling rates. The photo sensor was put into left index finger. We made movement artifacts as moving a left hand in direction of left-right, up-down, and rotation. PPG signal is at the top in the figure, the horizontal movements are at the middle, and vertical movements are at the bottom.

Figure 5 shows the filtered signal by the SFLC under the condition of μ and H were set to 0.05 and 30, respectively. At the start point the amplitude of the signal is small, because the initial weight vector, *W* is zero. The short vertical lines are R-R intervals which are calculated automatically with 0.5sec window. The lower of figure 5 shows magnified data between 15sec and 30sec to observe clearly the filtered signal by SFLC and FIR filter from raw signals. The specifications of FIR filter by Equiripple method are as follows. The filter order is 156th, the pass band is between 1 and 9 Hz. FIR filter is not effective, because the frequencies of signal and movements noise are overlapped, and it has large time delay by the high order, either.

Figure 6 shows that the power spectra of the raw signal and the filtered signal by SFLC. The uncorrelated signals with heart rate such as movement artifacts, respiratory, and background noise, especially low frequency signal were almost removed. The fundamental frequency in this signal is about 1.5Hz and the spectrum by motion artifacts is between 0 and 1 Hz.

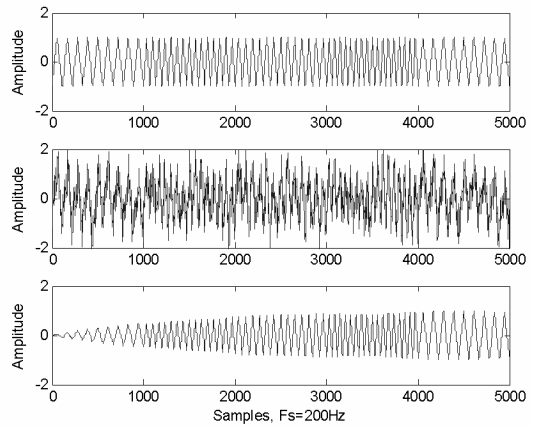

Fig. 2 Simulation of SFLC algorithm using triangular waves

F. Ibrahim, N.A. Abu Osman, J. Usman and N.A. Kadri (Eds.): Biomed 06, IFMBE Proceedings 15, pp. 427-430, 2007
www.springerlink.com ' Springer-Verlag Berlin Heidelberg 2007

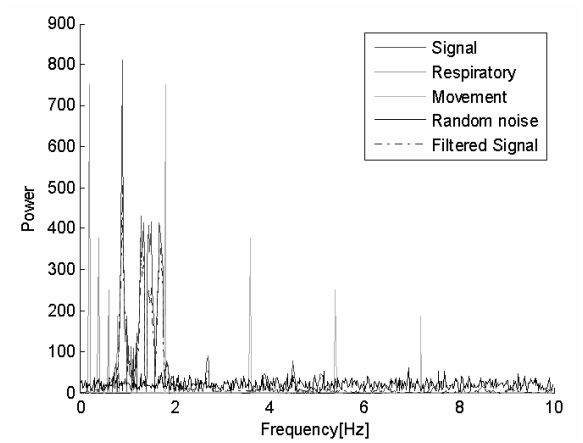

Fig. 3 Power spectrum of the simulated data

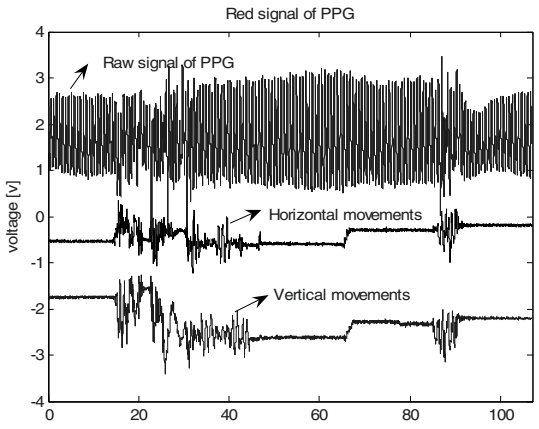

Fig. 4 PPG and movement signals obtained from Photo sensor and two accelerometers, respectively

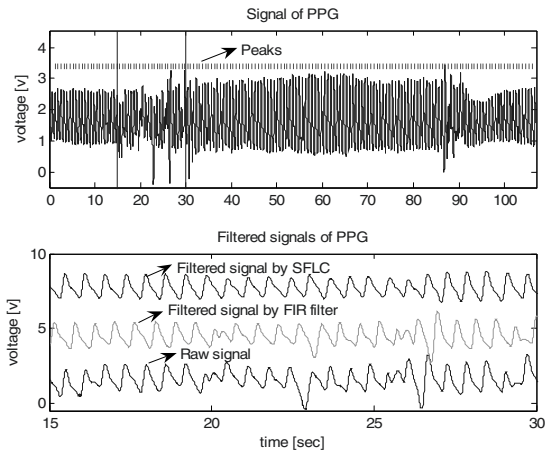

Fig. 5 Comparison among filtered data by SFLC and FIR

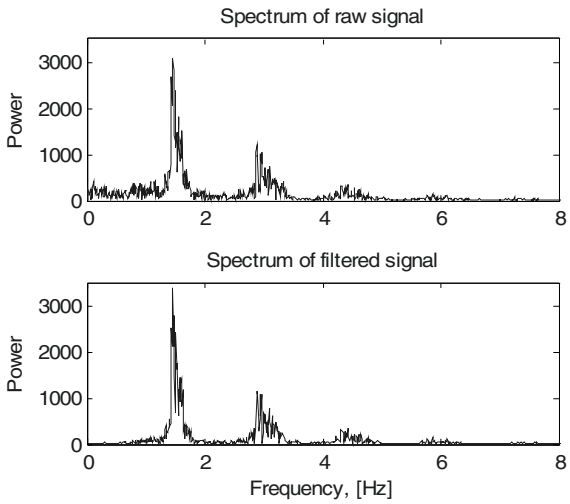

Fig. 6 Power spectrum comparison between raw and filtered signals

III. Conclusions

Medical devices and equipment as well as electronics devices are being miniaturized by progress of wireless and semiconductor technology. In the near future, some devices are involved the pervasive and ubiquitous computers to monitor vital signals any time and everywhere. However, the bio-signals are very sensitive to movements as well as that is very weak.

SFLC is based on the simple theory, as it is called, Fourier series. Therefore it is not new method, but this method is very effective to remove signals uncorrelated with heart beats except the bio-signals such as ECG, blood pulse, and cardiac output. In addition to, this method is not required the additional process and hardware to get R-R interval because the intervals is also need to calculate heart rate or SpO_2. However, the wrong R-R intervals, that is, the wrong peak detection results make some serial signal distortion. The fundamental periods exert a powerful influence on this algorithm. To solve this problem, we should use or develop the stable peak detector from PPG signal.

Acknowledgment

The research was supported by the Driving Force Project for the Next Generation of Gyeonggi Provinci.

This work was supported by Brain Korea 21 program for Environment-Friendly Bio-Fusion Technology, Hankyong National University.

F. Ibrahim, N.A. Abu Osman, J. Usman and N.A. Kadri (Eds.): Biomed 06, IFMBE Proceedings 15, pp. 427-430, 2007
www.springerlink.com ' Springer-Verlag Berlin Heidelberg 2007

References

1. Budinger, T.F., Biomonitoring with wireless communications. Annu Rev Biomed Eng, 2003. 5: p. 383-412.
2. Asada, H.H., et al., Mobile monitoring with wearable photoplethysmographic biosensors. IEEE Eng Med Biol Mag, 2003. 22(3): p. 28-40.
3. Hayes, M.J. and P.R. Smith, A new method for pulse oximetry possessing inherent insensitivity to artifact. IEEE Trans Biomed Eng, 2001. 48(4): p. 452-61.
4. Jovanov, E., et al., Stress Monitoring Using a Distributed Wireless Intelligent Sensor System, in IEEE Engineering in Medicine and Biology Magazine. 2003. p. 49-55.
5. Shaltis, P., Wood, L., Reisner, A., Asada, H. Novel Design for a Wearable, Rapidly-Deployable, Wireless Noninvasive Triage Sensor. in 27th Annual International Conference of the IEEE/EMBS. 2005. Shanghai, China.
6. Barros, A.K., M. Yoshizawa, and Y. Yasuda, Filtering noncorrelated noise in impedance cardiography. IEEE Trans Biomed Eng, 1995. 42(3): p. 324-7.
7. Laguna, P., et al., Adaptive filter for event-related bioelectric signals using an impulse correlated reference input: comparison with signal averaging techniques. IEEE Trans Biomed Eng, 1992. 39(10): p. 1032-44.
8. Bentt, L.R., et al., Accuracy and utility of pulse oximetry in the surgical intensive care unit. Curr Surg, 1990. 47(4): p. 267-8.

Address of the corresponding author:

Author: Soochan Kim
Institute: Gaduate School of Environmental Biotechnology and Information Technology, Hankyong National University
Street: eokjung-dong 67
City: nseong
Country: outh Korea
Email: irmware@hknu.ac.kr

F. Ibrahim, N.A. Abu Osman, J. Usman and N.A. Kadri (Eds.): Biomed 06, IFMBE Proceedings 15, pp. 427-430, 2007
www.springerlink.com ' Springer-Verlag Berlin Heidelberg 2007

Two-dimensional representation of spatial structure changes in brain bioelectric potential field

Dr. Riad Taha Al-kasasbeh

Faculty of Engineering Technology, Electrical Engineering Department, Al-Balqa Applied University, Amman, Jordan

Abstract—**A new method for visualization of EEG-process is developed, using factorial analysis. This method permits data compression and visualization in form adequate for human to trace continuous change patterns, compare data from brain hemispheres and delete appearing artifacts using combined man-computer mode for achieving additional reliability. Accordingly, this method is realized in software which allows an operator to select various modes of representation of results and speed of visualization.**

Keywords—**EEG, factorial analysis, automation, visualization, dynamic representation, man-machine system, reliability.**

I. Introduction

The analysis of time-continuously relations of fluctuations in biopotential concurrently in many points of a brain provides a great volume of the computing operations connected to the correlation or coherent analysis of EEG-signals. This next led to development of both hardware and software systems for research automation. An effective methodical example for similarity analysis of EEG-signals appeared representation of correlation matrix EEG in three-dimensional factorial space [1,2]. However static representation of results of factorial analysis EEG limits opportunities of the analysis and ordering of the observable dynamic phenomena accompanying because of fast reorganization of structure of a biopotential field of a brain which by itself suggests dynamic representation.

In the following work we develop an appropriate program and adequate means for visualization of results of factorial analysis EEG which allow the researcher to visually trace dynamics of system bioelectric processes of a brain in real time and in convenient forms, thus partially solving the problem.

II. Methods and results

First we provide the basic theoretical preconditions and concepts of multivariate statistics which are used in particular, in the analysis of multiple channel EEG signals. An effective way of a compression of the information contained in correlation matrixes EEG, it is a factorial analysis (FA) of the initial data [3,4]. Evidently, that the visual analysis of positional relationship of dozens vectors in multivariate space is to the utmost inconvenient. These vectors, if statistically dependent, can be approximately transformed into space of some dimension **m,** with **m** possibly considerably less than number of parameters **n**. Coordinate axles of such reduced space are some general factors F_m and initial parameters x_i can be linearly expressed through them:

Equation:

$$\times_i = a_{i1}F_1 + a_{i2}F_2 + \ldots + a_{im}F_m + d_iU_i \quad (1)$$

(i=1, 2, 3... n)

It is the basic model of the classical FA. Here xi and F_m are random variables, as well as the characteristic factor U_i. The classical model of the factorial analysis, in our case, gets the following form:

Equation:

$$\begin{aligned}
&\times_1(t) = a_{11}F_1(t) + a_{12}F_2(t) + \ldots + a_{1j}F_j(t) + \ldots + a_{1m}F_m(t) + d_1U_1(t)\\
&\times_2(t) = a_{21}F_1(t) + a_{22}F_2(t) + \ldots + a_{2j}F_j(t) + \ldots + a_{2m}F_m(t) + d_2U_2(t)\\
&\ldots\ldots\ldots\ldots\ldots\ldots\ldots\ldots\ldots\ldots\ldots\ldots\ldots\ldots\ldots\ldots\ldots\ldots\\
&\times_i(t) = a_{i1}F_1(t) + a_{i2}F_2(t) + \ldots + a_{ij}F_j(t) + \ldots + a_{im}F_m(t) + d_iU_i(t)\\
&\ldots\ldots\ldots\ldots\ldots\ldots\ldots\ldots\ldots\ldots\ldots\ldots\ldots\ldots\ldots\ldots\ldots\ldots\\
&\times_n(t) = a_{n1}F_1(t) + a_{n2}F_2(t) + \ldots + a_{nj}F_j(t) \ldots + a_{nm}F_m(t) + d_nU_n(t).\\
&(m \ll n)
\end{aligned} \quad (2)$$

Here ***n*** of EEG processes are linearly connected with ***m,*** the common for all constituent factors $F_j(t)$ which in this model represent mutually orthogonal processes. Number ***m*** by adequately chosen algorithm of FA is usually significantly less then number ***n*** of outputs of EEG. Each of EEG processes also linearly depends on one local, not interconnected statistically with other processes, the so-called characteristic factor $U_i(t)$. Its value determines the contribution of local component EEG in the given lead.

During EEG representation in separate brain on the CRT screen by radiuses - vectors as projections on the plane from multivariate factorial space it was found that angles between vectors are inversely proportional to correlation between corresponding EEG leads [5]. Thus, the closer

F. Ibrahim, N.A. Abu Osman, J. Usman and N.A. Kadri (Eds.): Biomed 06, IFMBE Proceedings 15, pp. 431-434, 2007
www.springerlink.com ' Springer-Verlag Berlin Heidelberg 2007

are vectors in factorial space EEG, above correlation between these processes is larger. And inverse, at angles approaching to 90 degrees, correlation coefficients are close to zero.

In consecutive periods of EEG analysis (duration of each of 4 seconds), after their transformation to the digital form, degree of statistical affinity of signals between each pair of the leads (1-2, 1-3, 1-4 ... 1-n, 2-3, 2-4, 2-5 ... 2-n, 3-4, 3-5, 3-6, ... n-n) is calculated. On the basis of these calculations correlation matrixes is created. After FA EEG is carried out by centroid method, the weight of first 3 factors contains usually more than 80 % of the information about structure of a correlation matrix [3,4].

In result, FA values of 3 factors for all EEG leads (from 12 up to 20) and consecutive periods of analysis EEG turn out. The received data can be displayed on the screen as radiuses-vectors and are used for the visual analysis. However such approach does not provide an opportunity of animation that can be essentially important if necessary investigate dynamics of process. For the solution of this problem it is expedient to keep results FA in a databank from which one can take them in a sequence and next it will be possible to take compares and analyze.

EEG is most commonly recorded according to the international 10-20 electrode placement system shown on following figure:

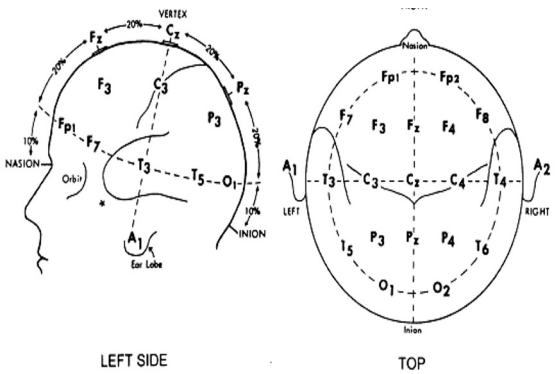

Fig 1. Placement of Electrodes

The 10-20 system [12] was developed to standardize the collection of EEG and facilitate the comparison of studies performed at different laboratories. When only a few channels of EEG are collected the electrodes are placed at a subset of the sites. The recorded signal is obtained by subtracting a signal measured below the eye from one measured above the eye.

III. Discussions

At the further data processing (for example for studying dynamics of factors values changes) it is possible to use specialized software developed by us. It is written in Microsoft Visual Studio 6.0 [6,7]. It allows the operator to choose for research: a plane of factors, a period of the analysis, a dynamic or static mode of display, various modes of representation of results and speed of visualization.

Let's stop more in detail on algorithm of the program which allows to carry out the following operations in particular:

1. Display of factorial analysis EEG results in static (traditional) and dynamic mode of displaying: Depending on desire it is possible to use various modes of display. For realization of animation the value of factors on an interval between the next period for both displayed factors and for all leads are calculated by consecutive approach of value of the factor from last by the subsequent period of the analysis. These values of factors on all periods of the analysis are known from a file with the data of FA.

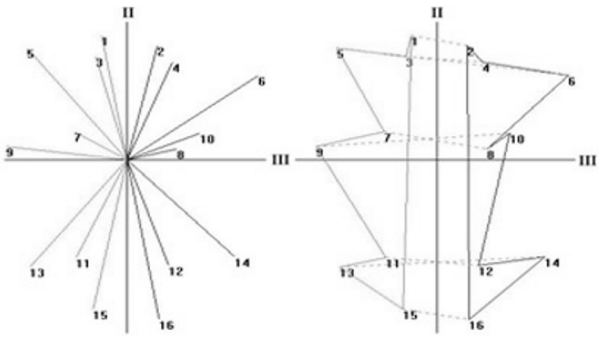

Fig. 2 Representation of results FA EEG in a plane formed by axes 2-nd and 3-rd Factors for 16 leads. a - traditional form of representation, b - the mode offered by us.

At the analysis of the data it is convenient to use the accelerated viewing as it is possible to find out easily and quickly sharp changes, in particular biological and technical artifacts which frequently deform the EEG-SIGNAL.

2. Display of the processes occurring in bilateral symmetric areas of the left and right hemisphere of a brain: Display lead number i in factorial space is designated by one of figures 1-16 which corresponds to number of an electrode - for the left hemisphere - even, for right - odd figures (fig. a and, б).

At a traditional mode of display the center of coordinates of factorial space incorporates to display of each lead in factorial space. Thus color of lines of the connection going to display of electrodes located on left hemisphere, gets out

F. Ibrahim, N.A. Abu Osman, J. Usman and N.A. Kadri (Eds.): Biomed 06, IFMBE Proceedings 15, pp. 431-434, 2007
www.springerlink.com ' Springer-Verlag Berlin Heidelberg 2007

green, and color of the lines going to display of electrodes located on right hemisphere - blue.

At a mode offered by us the display of leads located above different hemispheres are united in factorial space in two groups. Displays of electrodes of the left hemisphere incorporate the order of increase 1-15, display of last electrode 15 (that corresponds to occipital lead) incorporates to display 1 (frontal lead). The similar picture is under construction for the right hemisphere.

In a case when on axes are chosen II-d and III-rd factors additional shaped lines are drawn: they connect displays of symmetric electrodes located in different hemispheres.

3. Viewing autocorrelation function: Value of the factor on an axis of x-coordinate remains same, as well as at traditional representation of results FA EEG, and value on an axis of ordinates will correspond to value of the factor for a period of the analysis earlier. Autocorrelation function allows to fix occurrence of changes of results FA effectively.

4. Display of the contribution of value of each factor in color of the image of brains contours. The structure of a biopotential field of a brain can be submitted as a color ellipse (corresponding to a brain contour) in which color of pixel is calculated under the normal law depending on size of each of three factors and distance from pixel to display of corresponding lead EEG. Thus red color corresponds to the I-st factor, green color to the II-nd , blue color to the III-d . A combination of factors (i.e. different combinations of intensities of red, green and blue colors) determine color of pixel.

Thus, the algorithm developed by us allows carries out dynamic display of results of the factorial analysis the fluctuations of brain bioelectric activity. For researcher most information is provided by changes in mutual disposition of vectors, by changes in weights of orthogonal 1,2,3 factors and also by appearance or strengthening of 4,5,6 factors.

Table 1 The result of using software of factorial analysis

Diseases	Number of Realization	Result of analysis	
		coincidence with expert	false alarm
Schizophrenia	36	89.1%	10.9%
Brain stress	33	91%	9%
Brain damage	29	90.2%	9.8%

For practical implementation of developed method we chose three types of diseases: schizophrenia, brain stress and brain damage. For classification of diseases EEGs of 98 patients were used. The result of classification with using specialized software developed by us represented in table 1:

To compare with others classical methods of EEG analysis such as Spectral Analysis [16-17,19], Coherence Analysis [18, 23-24], Neural network applications [21,25], Fractal series analysis [22] we used the results of publications review represented in table 2.

Table 2 The results of diseases classification with using conventional methods of EEG analysis

Methods of EEG classifications	Schizophrenia		Brain Stress	
	coincidence with expert	false alarm	coincidence with expert	false alarm
SA	72.1%	27.9%	64.5%	14.5%
CA	82%	18%	-	-
NNA	87%	13%	-	-
FSA	84%	16%	-	-

The methods in the table are SA- is spectral methods of EEG analysis, CA - Coherence Analysis, NNA - methods based on Neural network, FSA - Fractal series analysis. Unfortunately, the data about brain stress and brain damage for conventional methods not published.

The results represented in Table 1 and 2 shows that proposed method of factorial analysis greatly sensitive in the field of schizophrenia and brain stress diagnosis to compare with traditional methods. As we can see, measurement of 98 patients records shows approximately a 90% of successful diagnosis. Also very favorable results were acquired by applications of the algorithm to diagnostics of brain stress and brain damage by newly born children.

It can be easily seen, that this algorithm is to be especially effective when there are not local, but system damage to the brain. Algorithm provides essential advantages in comparison with a traditional way of static representation of results, additional opportunities to use potential advantages of system "man - machine" are created. Due to mobility of the image the researcher can estimate a condition of the examinee not only on displays of leads in factorial space, but also on dynamics of their moving. As the spatial arrangement of radius-vectors with a high degree of affinity reflects an arrangement of electrodes in a surface of a head, the opportunity to estimate dynamics of brain processes is created, and it has paramount value for studying laws of neurological-and- mental activity.

The accelerated animation provides more effective search of rough changes EEG, i.e. allocation of artifacts that allows approaching to the decision important, actual and stilling far from the decision the problem of automatic exclusion of artifacts on EEG.

Autocorrelation function is expedient for using for revealing those electrodes, the potential under which changes

F. Ibrahim, N.A. Abu Osman, J. Usman and N.A. Kadri (Eds.): Biomed 06, IFMBE Proceedings 15, pp. 431-434, 2007
www.springerlink.com ' Springer-Verlag Berlin Heidelberg 2007

to the greatest degree and as when change of values only one of factors takes place.

Usage of the mode of display of results FA for division of electrodes of different hemispheres allows to present more evidently functional interaction of symmetric departments of the left and right hemisphere (for example 1-2,3-4). Especially it is appreciable, when on factorial axes are chosen II-nd and III-d factors as in this mode additional shaped lines which connect displays of symmetric electrodes are drawn. Parallelism of these straight lines concerning an axis of II factor is shown as far as similar the organization of processes in a right and left hemisphere.

It is necessary to note, that the described program can be used not only for analysis EEG, but also for the analysis of any other types of three factorial data for which the average size of values of factors differs less than on the order.

Here we should mention that formidable task of finding and deleting artifacts in EEG and similar biomedical data is now proceeding with attempts to use different methods. There are, for example, attempts to use neural network systems for finding and deleting artifacts (see Clochon et al., 1992 [8]; Durka et al., 1996 [9]; Bogacz et al., 1999 [10]). Gibson and James [11] use independent constraind analysis for seizure onset analysis of EEG. Al-Kasasbeh, Al-Kasasbeh and Lvov [13, 14, 15] also used factor analysis wavelet and fractal analysis technologies for finding artifacts. However, as one could have expected, this approaches are in experiment phases and do not provide general solutions.

We expect that visualization ideas from our software can be also for such methods, different from FA. Also combined methods can be effective.

References

1. Tsitseroshin M.N. Analysis of statistical interrelation of fluctuations of brain biopotentials in three-dimensional factorial space // Autometria. 1986. N6. P. 89.
2. Tsitseroshin M.N., A.A.Pogosjan, E.I.Galperina, A.N.Shepovalnikov System interaction cortical fields at realization verbal - memory activity Human physiology. 2000, that 26, №6, pp. 20-30.
3. Blagush P. Faktornyj analysis with features M.: the Finance and statistics, 1989.248pp.
4. Ajvazjan S.A., Buhshtaber V.M., Enjukov I.S., Meshalkin L. D. Applied statistics: Classification and decrease of dimension // M.: Finance and statistics, 1989.607 pp.
5. Tsitseroshin M.N., Pogosjan A.A. About display of activity integrative mechanisms of a brain and its bioelectric activity // Biophysics. 1993. T. 38. Edit..2. P. 341.
6. Bob Swart. Borland C++ Builder 2005 Migration to .NET using VCL for NET ISBN 1-57268-059-4.
7. Holzner Z. Visual C ++ 6: a training course // SPb: Peter, 2000. - 576 pp.
8. Clochon P., Perchey G., Couque C., Rebeyrolle H., Bloyet D., Etevenon P., automatized classification by neural networks of EEG signals with artefact rejection. Proc 14th Ann Int Conf IEEE Eng Med & BiolSoc, Lyon, France: Satellite Symosium on Neuroscience and Technology, 1992. pp. 51 55.
9. Durka P., Kiezyk R., Blinowska K., Neural networks and wavelet analysis in EG artifact recognition. II Konferencia Siec Neuronowe CH Zastosowanie szczyrk 301V4 V 1996 pp.6 (htpp://brain.fuw.edu.pi/~durka/pd_paper.html
10. Bogacz R., Markowska-Kaczma U., Kozlik A. Blinking artifact recognition in EEG signal using neural network. Proc 4th conference neural networks and Applications. Poland Zakopane 1999 p.6.
11. Gibson O., James C., Constraind ICA for seizure onset analysis in the EEG. Biomedical Information Engineering Research Group, Aston University, Birmingham, UK.
12. H.H. Jasper. The ten-twenty electrode system of the international federation. Electroencephalography and Clinical Neurophysiology, 10:371{373, 1958}.
13. R. T. Al-Kasasbeh. 2004. Wavelet-based method for EEG artifacts classification. IFMBE Proceedings, pp.157 159, Kuala Lumpur, Malaysia, 2-4.09
14. B.V. Lvov, Riad Al-Kasasbeh. 2005. Classification of EEG signals with artifacts, on fractal dimension analysis, wavelet transform and neural network, Dirasat Journal, v.32. p. 78-90.
15. R. T. Al-Kasasbeh , B.V. Lvov. 2006. Detection of Eye Movement and Muscle Artifact in EEG of Normal Subjects by Classification of Fractal Dimension Dynamics. Dirasat Journal, v.33 (in print)
16. Kirsch P, Besthorn C, Klein S, Rindfleisch J, Olbrich R. The dimensional complexity of the EEG during cognitive tasks reflects the impaired information processing in schizophrenic patients. Int J Psychophysiol. 2000 Jun;36(3):237-46. Related Articles, Links
17. Schellenberg R, Schwarz A. EEG- and EP-mapping--possible indicators for disturbed information processing in schizophrenia Prog Neuropsychopharmacol Biol Psychiatry. 1993 Jul;17(4):595-607. Related Articles, Links
18. Koukkou M. EEG correlates of information processing in acute and remittent schizophrenic patients. Schweiz Arch Neurol Psychiatr. 1985;136(1):37-43.
19. Sigl JC, Chamoun NG. An introduction to bispectral analysis for the electroencephalogram. J Clin Monit. 1994 Nov;10(6):392-404.
20. Freeman FG, Mikulka PJ, Prinzel LJ, Scerbo MW. Evaluation of an adaptive automation system using three EEG indices with a visual tracking task. Biol Psychol. 1999 May;50(1):61-76.
21. W.Szelenberger, W. Androsiuk, Neural Networks with Wavelet Preprocessing in EEG Artifact Recognition. Laboratory of Medical Physics, Institute of Experimental Physics, Warsaw University, 2004.
22. Kulish V, Sourin A, Sourina O. Human electroencephalograms seen as fractal time series: mathematical analysis and visualization. Comput Biol Med. 2006 Mar;36(3):291-302.
23. Caviness JN, Liss JM, Adler C, Evidente V. Analysis of high-frequency electroencephalographic-electromyographic coherence. J Speech Lang Hear Res. 2005 Apr;49(2):424-38
24. Yeragani VK, Cashmere D, Miewald J, Tancer M, Keshavan MS. Decreased coherence in higher frequency ranges (beta and gamma) between central and frontal EEG in patients with schizophrenia: A preliminary report. Psychiatry Res. 2006 Jan 30;141(1):53-60.
25. Nigam VP, Graupe D. Related Articles, Links A neural-network-based detection of schizophrenia. Neurol Res. 2004 Jan;26(1):55-60.

Address of the corresponding author:

Author: Dr.Riad Taha Al-kasasbeh
Institute: Faculty of Engineering Technology,
Electrical Engineering Department,
Al-Balqa Applied University
City: Amman
Country: Jordan
Email: rjordanjodanjo@yahoo.co.uk

F. Ibrahim, N.A. Abu Osman, J. Usman and N.A. Kadri (Eds.): Biomed 06, IFMBE Proceedings 15, pp. 431-434, 2007
www.springerlink.com ' Springer-Verlag Berlin Heidelberg 2007

Using Simple MLPs in Modular Architecture to Improve the P300 Detection Accuracy

G.R. Salimi Khorshidi[1], Ali M. Nasrabadi[2], M.R Hashemi Golpayegani[1]

[1]Department of Biomedical Engineering Amirkabir University of Technology (Tehran Polytechnic), Tehran, Iran
[2] Group of Biomedical Engineering, Faculty of Engineering, Shahed University, Tehran, Iran

Abstract- **One of the most important aspects of new researches in both engineering and medical sciences is to extract useful information from biomedical signals and find a reliable method for machine to learn it which makes the BCI a common field of interest for researches from both groups. Developing a reliable machine learning method plays a very crucial role in this issue. For a typical problem in BCI, ERP detection task, the major method is to classify the input EEG time series into two classes; with a desired ERP/Cognitive Component and without that desired ERP/Cognitive Component. Any powerful feature extraction or classifier block that can do this task accurately, can be of a great help. In this study, a new classifier based on modular learning strategy and a new wavelet for feature extraction, will be introduced and compared with some other classifiers in two states; with GA and without GA, which shows a an improvement in classification accuracy.**

Keywords- **EEG, ERP, BCI, MLP, Genetic Algorithm (GA), DWT, Modular Learning Strategy**

I. Introduction

Event-related brains potentials (ERPs) are psychophysiological correlates of neurocognitive functioning that reflect the responses of the brain to changes (events) in the external or internal environment of the organism. Besides their wide usage for clinical-diagnostic and research purposes, they have also been used in brain computer interfaces (BCI), which allow completely paralyzed people to communicate with the world solely by means of their brain waves [1]. The smallest unit of information (one bit) is transferred from the brain to the computer by the discrimination between two different ERPs. This process includes feature extraction from the raw signals of the electroencephalogram (EEG). The features that distinguish the ERPs may be extracted in the time, frequency, or time-frequency domain. In a standard BCI paradigm there are two data sets; the training data set and the test data set. Each data set contains two groups of ERP trials, reflecting two different brain responses to certain stimuli. Each trial comprises the EEG signals acquired from one or more scalp positions (channels). In the training data set, the two groups of trials are known; each trial carries the label of the group, to which it belongs. The trials in the test data set are not labeled and have to be separated into groups according to the pattern that discriminates between the groups of the training set. The success of the classification generally depends on two factors. The first factor is how well the distinguishing pattern is represented by the features extracted from the test data. The second factor is the power of the classification method. Powerful classifiers like Artificial Neural Networks (ANN) or support vector machines (SVM) may yield very good results using simple and redundant features. The present study shows that, modifying both feature extraction block and classifier block will result in a good classification for EEG.

II. EEG data

The present article focuses of BCI Competetion2003 EEG dataset recorded from 64 scalp positions with P300 speller paradigm in which the subject was supposed to distinguish between two classes of stimulus. Based of different stimuli, different cognitive patterns will occur in recorded EEG that is supposed to be discriminated to help machine with distinguishing between classes (Fig.1). As can be seen in Fig.1, the difference in about 300ms, which

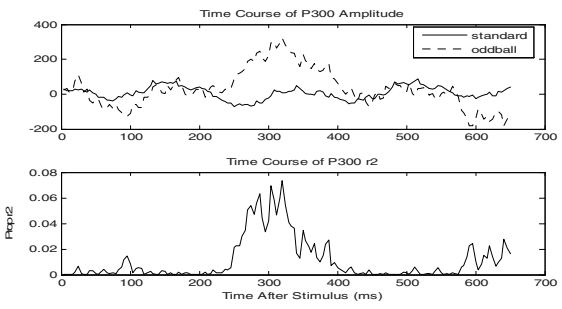

Fig.1 (Upper panel) average EEG for two classes of stimulus for Cz channel that shows a significant difference in about 300ms. (Lower panel) in this figure, the squared difference value for each sample is plotted. This plot confirms that importance of 300ms in cross-class discrimination.

F. Ibrahim, N.A. Abu Osman, J. Usman and N.A. Kadri (Eds.): Biomed 06, IFMBE Proceedings 15, pp. 435-439, 2007
www.springerlink.com ' Springer-Verlag Berlin Heidelberg 2007

indicates the existence of P300 cognitive component elicited by an oddball stimulus, can be a useful hint to make a BCI which can determine the classes with detecting the existence/lack of this component. So the rest of this study will try to develop a process to detect P300 cognitive component.

III. Designing the BCI System

Now that the BCI system is supposed to classify between two classes, as a typical pattern recognition machine it will need a feature extraction, feature selection and feature classification cooperating with each other to detect this component. Each of these parts will be as follows.

A. Feature extraction

To have a better classification over the input EEG time series, it is important to have the most important characteristics of the signal as input for the classifier. For some time traces, the time samples can be good inputs, but for the EEG which is completely nondeterministic with many noise mixtures and ongoing activities, using the time samples can not be a good way of discrimination. The solution here is to use features extracted from EEG that can map the input to another space in which the classification is simpler. To date, different feature extraction techniques have been developed for EEG time series; like time domain, Frequency domain, Time-frequency, Chaotic and many other features among which, the time frequency features are the most used ones for many reasons; 1) good simultaneous time and frequency resolution that makes it better than solely time or frequency features, 2) no sample limitation like what is an important issue in chaotic analysis of a signal, 3) the tuning capability of the mother wavelet that makes it useful for many applications, and so forth. Consequently, in this study, the discrete wavelet transform will be used to extract the time-frequency features from EEG.

The main issue in selecting a wavelet foe such feature extractions, is its mother function's waveform which must match a desired pattern in the recorded signal (P300 component in the EEG). There are many choices for a mother function that makes the selection process totally case-dependent, so in this study, four wavelets will be used; Biorthogonal (W1), Daubechies (W2), Manually tuned wavelet used by Quiroga[6] *et al* (W3) and a new wavelet based on neuronal basis of ERP generation (W4) developed by Glassman [7]. the W4 is based on single neuron action potential that comes from the brain to the scalp and affected by the volume conductor's characteristics, makes the scalp recorded ERP.

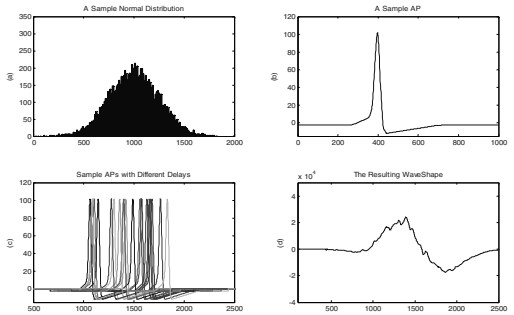

Fig.2 (a)the normal distribution to model the number of neurons (b) a simple neuron AP, (c) some delayed APs which will be superposed to generate the new wavelet's waveform, (d) the final waveform that will reconstruct the new wavelet

As Fig.2 shows, a typical normal distribution of neurons is assumed to generate ERP after a stimulus. The firing latencies will generate some APs with relative delays which will be superposed to generate the final ERP. To extract features from EEG using DWT, fist, signal will be decomposed into its frequency sub-bands using multi-resolution analysis (MRA). Then, the signal is decomposed into details and one final approximation. In this study we used 5-scale decomposition, thus obtaining coefficients in the following frequency bands: 62 125Hz, 31 62Hz (gamma), 16 31Hz (beta), 8 16Hz (alpha), 4 8Hz (theta) and the last approximation giving the activity in the 0.5 4Hz band (delta). The wavelet coefficients from this process will be used as features. Using all these wavelets, time-frequency features from each trial for all 64 channels were extracted and a statistical discrimination test were performed on it based on (1) in which the μ is average and σ^2 is the variance of a feature's value over a class[13]. The D value extracted here can represent cross-

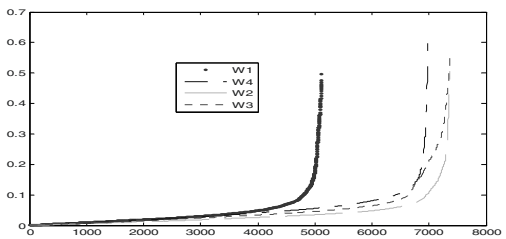

Fig.3 In this figure a plot of D Values for all features extracted from all 64 scalp channels which shows the bigger D values for W4 and W3 which are customized wavelets especially developed for EEG-ERP applications.

F. Ibrahim, N.A. Abu Osman, J. Usman and N.A. Kadri (Eds.): Biomed 06, IFMBE Proceedings 15, pp. 435-439, 2007
www.springerlink.com ' Springer-Verlag Berlin Heidelberg 2007

class discriminablity for a typical feature. Fig.3 shows a plot of D values for each of four wavelets over the number of features.

$$D= (\mu_1-\mu_2)/ (\sigma_1^2+\sigma_2^2)^{0.5} \quad (1)$$

So, features extracted from the EEG using W4 will be used as the input to the classifier. Having a good feature extraction process will not solely solve the problem. The other challenging prerequisite for an accurate classification is to have the non-redundant feature vector with maximum information content possible, which implies the importance of a feature selection or dimensionality reduction process.

B. Feature selection

One important issue in a classification process is to have the optimum architecture for the classifier. The optimum architecture is the simplest architecture that performs the best. An important issue to simplify a classifier is to reduce the input vector's dimensionality. To date, many different methods have been developed this reason; some based on rejecting the redundancy by rotating the data space to space with a fewer dimensions (PCA), some based on an intelligent search in the input space to find the most fitted features (GA) and some based on statistical criteria (D value test). Here all these three methods will be used to yield the best classification accuracy in system's overall architecture. Here, three major methods will be adopted to reduce the number of features extracted from each trial of scalp recorded EEG; 1) selecting top 150 features based on their D value (feature-set1), 2) using PCA to reduce the feature vector's dimension to 25 (feature-set2) and 3) using GA to have a reduced number of features (no matter how many) to have a better or at least the same classification accuracy (feature-set3).

C. Classifiers

The aim of this part of current study is to introduce the Modular ANN (MANN) as a powerful classifier, but to show its power, it seems necessary to compare it with some other classifiers; like MLP, LDA and SVM with RBF kernel [9].

In an artificial neural network with modular learning strategy, there are some simple ANN modules that cooperate to make a better model for a complex system. In the current study, the MANN will comprise three simple MLPs, as can be seen in Fig.4, which have two parallel MLP (MLP1 and MLP2) and one that plays a vigilance role (MLP3). The basic idea here is that the scalp recorded EEG comprises two components; 1) the stationary ERP and which is assumed to be the target signal (the one to be detected) and 2) the non-stationary ongoing EEG that is assumed to be the interference signal. Two parallel channels (the target channel/1 and interference channel/2), are actually trying to learn one of aforementioned components. As shown in Fig.4, two PCA blocks are actually providing the network with this characteristic. The PCA^1 is trained by representing it with the feature vectors of input data known to have the target component, once the training is complete; the free parameters of PCA^1 are fixed thereafter. So we may speak of PCA^1 as adaptively matched to target components. The similar criteria will be done for PCA^2 for interference component, so we may speak of PCA^2 as adaptively matched to interference components. Now the feature vector comes to PCA blocks and two feature sets will be extracted, as far as the simple MLP is supposed to be able to construct the arbitrary decision boundaries between two classes, two outputs of MLP networks will be combined (MLP^3) to have the final digital output as the label for an unknown input trial.

In this study, this modular strategy will be used in three major architecture; 1) offline training of MLP^1 and MLP^2, using MLP^3 as a new classifier with two other MLPs' output as its input (MANN1), 2) training all three MLPs together with errors back-propagating from MLP^3 to both MLP^1 and MLP^2 (MANN2) and 3) using a fuzzy lookup table (Table2) instead of MLP^3 to vote to each classifier's output to determine the final output (MANN3).

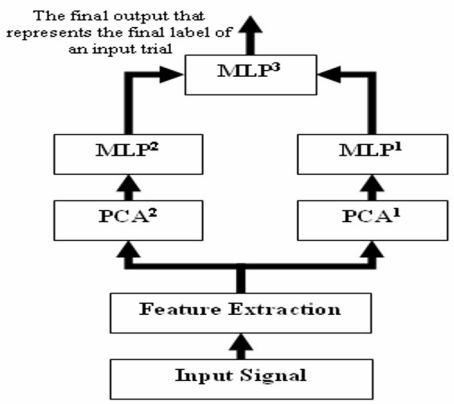

Fig.4 Block diagram of a typical ANN with modular learning strategy. Two channels (1 and 2) are representing two groups of input data for each the PCAs will be trained and then their parameters will be fixed for test data [12].

F. Ibrahim, N.A. Abu Osman, J. Usman and N.A. Kadri (Eds.): Biomed 06, IFMBE Proceedings 15, pp. 435-439, 2007
www.springerlink.com ' Springer-Verlag Berlin Heidelberg 2007

For the fuzzy systems used here, three types of rules will be defined; Low, High and Medium with Gaussian membership functions centered on 0.25, 0.5 and 0.75 respectively. After an offline training for PCA-MLP block for two parallel channels (1 and 2), the results were as shown in Table1 which shows useful information to define the rules for an accurate final decision. As Table1 implies, the target channel's results for class +1 are more likely to be correct than its results for class -1. So such weaknesses can be compensated using the power of non-target channel on determining the class-1. Using an expert to define the rules, we will have the Table2 which is trying to use information in Table1 for a better accuracy.

Table1 Two MLPs' results for testing after an offline train for 500 samples containing 283 with-P300 and 217 without-P300 trials.

MANN Channel	Overall Accuracy		Target Accuracy		Nontarget Accuracy	
	Number	Percent	Number	Percent	Number	Percent
MLP^1+PCA^1	384	76.8%	243	85.8%	141	64.9%
MLP^2+PCA^2	365	73%	212	74.9%	153	70.5%

Table2 Fuzzy rules used to define the final output based on the membership value of each channel's output in three rules. The Class+1 represent trials with P300 and Class-1 represents trials without P300 which are two labels for an input trial

PCA^1+MLP^1	PCA^2+MLP^2	Final Decision
High	High	High (class+1)
High	Medium	High (class+1)
High	Low	High (class+1)
Medium	High	High (class+1)
Medium	Medium	High (class+1)
Medium	Low	Low (class-1)
Low	High	High (class+1)
Low	Medium	Low (class-1)
Low	Low	Low (class-1)

This classifier will be compared to three other classifiers; MLP, LDA and SVM that are used in a variety of classification tasks.

IV. Results

Now that all blocks required for a simple classification task are described for this particular classification, it's time to test the system for the BCI Competition2003 dataset for three types of feature selection (3.2). Results for all of these classifiers, on the same input data are as shown in Table1. For classification task on BCI Competition2003 data, 3000 trials were used for classifiers' train and test (2500 for train and 500 for test) among which 1500 trials were associated with oddball and 1500 trials were associated with standard stimuli. The best architecture for a classifier was determined using a 10-fold cross validation.

Table3 The classification results for first feature selection method (feature-set1). Average accuracies are in percent.

Classifier	Accuracy on Train Dataset		Accuracy on Test Dataset	
	Average	Variance	Average	Variance
MLP	65.9	9.2	61.6	6.8
SVM[1]	80.2	5.1	82.1	3.8
LDA	75	6.9	77.3	7.2
MANN1	73.2	12.1	78.2	9.3
MANN2	81.2	6.9	83	4.8
MANN3	79.5	4.8	81.2	5.7

Table4 The classification results for second feature selection method (feature-set2). Average accuracies are in percent.

Classifier	Accuracy on Train Dataset		Accuracy on Test Dataset	
	Average	Variance	Average	Variance
MLP	69.3	5.3	71	4.9
SVM	79.7	2.9	76.7	5.1
LDA	80.3	9.2	76.5	3.5
MANN1	67	5.3	62.9	8.2
MANN2	68	11.3	59.8	7.2
MANN3	71.3	5.9	67.8	4.4

Table5 The classification results for third feature selection method (feature-set3). Average accuracies are in percent.

Classifier	Accuracy on Train Dataset		Accuracy on Test Dataset	
	Average	Variance	Average	Variance
MLP	75.1	11.2	75	5.9
SVM	89.5	4.8	86.1	6.2
LDA	86.6	5.7	87.4	4.7
MANN1	69.3	5.3	66.5	6.7
MANN2	83.6	3.8	78.2	6.4
MANN3	79.8	7.2	76.9	9.1

[1] SVM in these tables uses an RBF kernel and is tuned with a uniform search for σ and C from 1 to 100 for both, with a step of 0.5 ().

F. Ibrahim, N.A. Abu Osman, J. Usman and N.A. Kadri (Eds.): Biomed 06, IFMBE Proceedings 15, pp. 435-439, 2007
www.springerlink.com ' Springer-Verlag Berlin Heidelberg 2007

V. Discussion and conclusion

Having three MLPs in modular architecture, can improve the classification accuracy up to 10% that seems to be a step forward in classification due a more parallel processing technique. As the results imply, the complexity added to a simple MLP in architecture and learning, cannot solve all the problems with it, although makes it much better. The simple MLP has the weakest results in classification over all three feature selection methods, while MANN is near to the top accurate classifiers under all feature selection methods but GA. Using GA as a feature selection compartment, LDA and SVM show a good improvement that shows the power of this technique, but the MLP based techniques (MLP and MANN) cannot show this improvement. It was predictable to some extent because of a major drawback with a simple MLP. Running a simple MLP on a specific dataset for *n* times, it is possible to have *n* different discriminant hyperplanes while in classifiers like LDA or SVM, there is only and only *one* discriminant hyperplane that separates the data for all the running times (the optimum hyperplane). So the GA has less uncertainty in its fitness value when combined with LDA or SVM, because it learns to find the best hyperplane which is a better search target over all possible selections from feature pool.

References

[1] N. Birbaumer, N. Ghanayim, T. Hinterberger, I. Iversen, B. Kotchoubey, A. Kübler, J. Perelmouter, E. Taub, and H. Flor, A spelling device for the paralyzed, *Nature*, vol. 398, pp. 297 298, 1999.

[2] A. C. Rencher, *Multivariate Statistical Inference and Applications*. New York: Wiley, 1998.

[3] L. A. Farwell and E. Donchin, Talking off the top of your head: Toward a mental prosthesis utilizing event-related brain potentials, *Electroencephalogr.Clin. Neurophysiol*, vol. 70, pp. 510 523, 1988.

[4] V. J. Samar, A. Bopardikar, R. Rao, and K. Swartz, Wavelet analysis of neuroelectric waveforms: A conceptual tutorial, *Brain Lang.*, vol. 66, pp. 7 60, 1999.

[5] T. Demiralp, J. Yordanova, V. Kolev, A. Ademoglu, M. Devrim, and V. J. Samar, Time-frequency analysis of single-sweep event-related potentials by means of fast wavelet transform, *Brain. Lang.*, vol. 66, pp. 129 145, 1999.

[6] R. Quian Quiroga , O.W. Sakowitz , E. Basar , M. Schurmann Wavelet Transform in the analysis of the frequency composition of Evoked potentials Brain Research Protocols vol.8, pp.16 24, 2001.

[7] Elena L. Glassman, A Wavelet-Like Filter Based on Neuron Action Potentials for Analysis of Human Scalp Electroencephalographs , IEEE TRANSACTIONS ON BIOMEDICAL ENGINEERING, VOL. 52, pp.1851-1862, 2005

[8] S. Mallat, A theory for multiresolution signal decomposition: the wavelet representation, IEEE Trans. Pattern Anal. Machine Intell. 2 (1989) 674 693.

[9] E. R. Kandel, J. H. Schwartz, and T. M. Jessell, *Principles of Neural Science*, 3rd ed. New York: Elsevier, 1991, pp. 27, 98, 778 779, 784, 785.

[10] F. H. Duffy, V. G. Iyer, andW.W. Surwillo, *Clinical Electroencephalography and Topographic Brain Mapping*. New York: Springer-Verlag, 1989, pp. 73, 74, 84 86.

[11] M. F. Bear, B.W. Connors, and M. A. Paradiso, *Neuroscience: Exploring the Brain*, 2nd ed. Baltimore, MD: Lippincott, Williams, & Wilkins, 2001, pp. 119 123.

[12] Simon Haykin, Tarun Kumar, "Modular learning strategy for signal detection in a nonstationary environment", IEEE transaction on signal processing, vol 45, pp.1619-1637, 1997

[13] R. O. Duda, P. E. Hart, and D. G. Stork, *Pattern Classification*, 2nd ed. New York: Wiley, 2001, pp. 48 49.

Address of the corresponding author:

Author: G. R. Salimi Khorshidi
Institute: Department of Biomedical Engineering Amirkabir University of Technology (Tehran Polytechnic)
City: Tehran
Country: Iran

F. Ibrahim, N.A. Abu Osman, J. Usman and N.A. Kadri (Eds.): Biomed 06, IFMBE Proceedings 15, pp. 435-439, 2007
www.springerlink.com ' Springer-Verlag Berlin Heidelberg 2007

Wavelet based compression technique of Electro-oculogram signals

Ayush Bhandari[1], Vijay Khare[1], Jayashree Santhosh[2], Sneh Anand[3]

[1] Dept. of Electronics and communication Engineering, Jaypee Institute of Information Technology, Noida, India
[2] Computer service Centre, Indian Institute of Technology, Delhi India
[3] Centre for Biomedical Engineering, Indian Institutes of Technology, Delhi India

Abstract—**In this paper, we present a compression technique for the acquired Electro-oculogram (EOG) signals. Researchers in the past have mainly focused on the EOG signals while dealing with Electroencephalogram signals for the removal of Ocular Artifacts. From a new perspective, a scheme pivoted on multi-resolution analysis and the Wavelet Transform theory was used essentially to process and enhance non-stationary and time-varying EOG Signals. Coiflet wavelets were used for the compression of EOG signals by thresholding of wavelet coefficients.**

Keywords—**Electro-oculogram, Wavelet Transform, Thresholding, Compression and Coiflet Wavelets.**

I. Introduction

Electro-oculogram (EOG) signals are a subset of Bio-signals. Bio-signal Processing is an inter-disciplinary field by which it is not difficult to observe the divergence and paradigm shifts caused in multiple areas such as intelligent device assistance [1−4], removal of ocular artifacts from EEG signals, study of EOG signals to monitor human responses and alertness and the development of EOG biopotential amplifiers [5]. Innovation in this field has mainly been illustrated in the form of human - computer interface developments [6, 7] and these continue to evolve as better techniques are being searched to exploit EOG signals. A typical EOG signal acquired from the vertical channel is shown in figure 1. The EOG signals which are essentially time varying and non stationary can be analyzed using wavelets. The ability of wavelets to precisely resolve the signals such as EOG in to specific time and frequency components [8] leads to several analysis based applications and one amongst them is compression [9].

The EOG signals are band limited (1 Hz to 50 Hz) due to the fact that there is a limit to which the speed of eye movements is restrained. For a signal, the amplitude peaks obtained from intentional eye blinks or eye motion are prominent and can be clearly differentiated from the unwanted ripples in any form which can be removed as they don t provide any information.

A large class of EOG signals has decaying spectrum and this means that the sub−bands also follow the trend of decreasing energy (Figure 2). Moreover, most of the energy in the EOG signals is concentrated in lower frequencies or higher scales. In this investigation, it was observed that the band of frequencies 1-12Hz contained almost 90 % of the signal energy. The human eye contains an electric dipole formed by a positive cornea and a negative cornea. Thus a potential difference in range 10 to 100 nV exists between these two opposite charges. The blinking or motion of eyes produces a large electrical potential around the eyes. This potential difference and the rotation of the eye are the basis for a signal measured at a pair of surface electrodes. This is known as EOG. The strength of raw EOG signals is too feeble and thus it s required that these signals are adequately amplified.

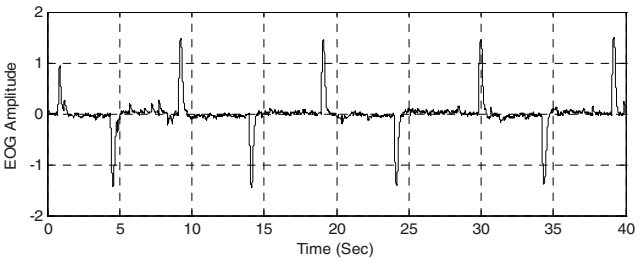

Fig. 1. Voltage waveform of an EOG Signal

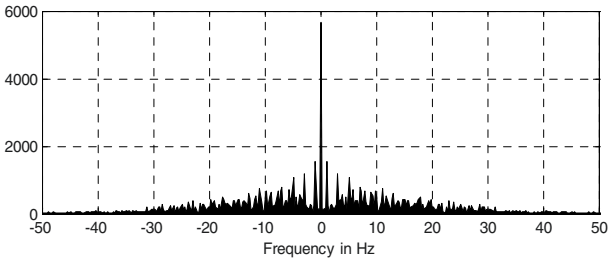

Fig. 2. Frequency spectrum of an EOG Signal

II. Materials and methods

A. Generation of EOG biopotentials

The human eye contains an electric dipole formed by a positive cornea and a negative cornea. Thus a potential difference of about a 100mV exists between these two op-

F. Ibrahim, N.A. Abu Osman, J. Usman and N.A. Kadri (Eds.): Biomed 06, IFMBE Proceedings 15, pp. 440-443, 2007
www.springerlink.com ' Springer-Verlag Berlin Heidelberg 2007

posite charges. The blinking or motion of eyes produces a large electrical potential around the eyes and this is known as Electro-oculogram. The voltage waveforms of EOG depend mainly on the direction of the eye movements and blinks. Intentional eye blinks have a larger output voltage than unintentional eye blinks. Eye movements, vertical, horizontal or round produce a somewhat square shaped waveforms. The type of eye gesture considered in this paper is due to the eye-blinks which is mainly due to the periorbital muscles. The eye is controlled by three sets of muscles. The Superior Rectus and Inferior Oblique are used for upward motion and for down-gazing, respectively. The Superior and Lateral Oblique rotate the eye. The *lateral* and *medial Rectus* moves the eyes from side to side. Electro-oculography (EOG) measures the potential difference at the skin s surface caused by muscle movement. The electrodes are placed on the inner and outer corners of the eye to record the side to side activity of the Lateral and Medial Rectus muscles. The electrodes are placed above the eyebrow and below the eye to record the up and down motion of the *superior* and *inferior Rectus,* respectively. Because the muscles governing the vertical motion of the eyes are the same in both eyes, the electrodes can be placed to record activity in either the right or the left eye. This provides reciprocity for electrode placement

B. Data source

The signal used for investigation in this paper was acquired from the vertical channel of the Medlec profile reader (EEG machine) available at the All India Institute of Medical Sciences. The Sampling frequency for this signal was 500 Hz. The electrodes are placed above the eyebrow and below the eye to record the up and down motion of the *superior* and *inferior Rectus,* respectively.

C. Wavelet compression of the EOG Signals

Data compression is achieved by reducing redundancy [12] and the redundancy in this investigation is the unwanted ripple. Signal components which are unwanted and can be removed. The denoised signal, $\tilde{s} = \mathcal{W}^{-1}\eta_{\lambda}(\mathbf{Y})$ can be considered to be made up of low-frequency, high energy signals which form the main part of $\tilde{s}$ and high-frequency, low energy signals which attributes to the ripples in the signal. Let, $\tilde{s}(t) = \sum_{k=1}^{m} \alpha_k u_k(t)$ which represents $\tilde{s}$ as a linear combination of the Coiflet 3 basis functions $\{u_k, k = 1,....m\}$ and the coefficients α_k . For compressing the signal, we need a method which searches for an equivalent of $\tilde{s}$ with a fewer basis functions. Quantitatively, this can be shown by equation 1 while allowing some error tolerance

$$\xi \geq \left\| \tilde{s}(t) - \sum_{k=1}^{\hat{m}} \hat{\alpha}_k \hat{u}_k(t) \right\| \geq 0 \,.$$

$$\tilde{s}_{\Delta}(t) = \sum_{k=1}^{\hat{m}} \hat{\alpha}_k \hat{u}_k(t) \,, \hat{m} < m \qquad (1)$$

This strategy corresponds to the lossy compression. The problem here is to identify the first $\hat{m}$ elements that give the best approximation when measured in the L_2 norm. This means that the space of $\tilde{s}$ is denoted by L_2 – the Hilbert Space that corresponds to the inner product,

$$\langle f, g \rangle_{L_2} = \int_{-\infty}^{\infty} f(x) g(x) dx$$

The process of approximation would automatically nullify details or the low-scale information that constitutes ripples in the signal $\tilde{s}$. We now aim at minimizing the error in approximation. Let $\pi(k)$ be a permutation – arrangement in all possible ways of $\{1,....m\}$ and $\sum_{k=1}^{\hat{m}} \hat{\alpha}_k \hat{u}_k(t)$ be the function that uses first $\hat{m}$ numbers of the arrangements. Taking into account all the possible arrangements,

$$\tilde{s}_{\Delta}(t) = \sum_{k=1}^{\hat{m}} \hat{\alpha}_{\pi(k)} \hat{u}_{\pi(k)}(t)$$

Using the pair wise orthogonality of Coiflet 3 wavelet, $\langle u_k, u_l \rangle = \delta_{kl}$, we get,

$$\begin{aligned} \left\| \tilde{s} - \tilde{s}_{\Delta} \right\|_2^2 &= \left\langle \tilde{s} - \tilde{s}_{\Delta}, \tilde{s} - \tilde{s}_{\Delta} \right\rangle_{L_2} \\ &= \left\langle \sum_{k=\hat{m}+1}^{m} \alpha_{\pi(k)} u_{\pi(k)}, \sum_{k=\hat{m}+1}^{m} \alpha_{\pi(k)} u_{\pi(k)} \right\rangle_{L_2} \\ &= \sum_{k=\hat{m}+1}^{m} \alpha_{\pi(k)}^2 \end{aligned} \qquad (2)$$

The above equation shows that in order to get the ordering,

$$\left\| \tilde{s} - \tilde{s}_{\Delta} \right\|_2^2 = \alpha_{\pi(m)}^2 + \alpha_{\pi(m-1)}^2 + ... + \alpha_{\pi(\hat{m}+1)}^2 \qquad (3)$$

where the error in approximation is minimized for a given number $\hat{m}$ of basis functions, we should sort the coefficients by their absolute amplitudes so as

$$\left|\alpha_{\pi(1)}\right| \geq \left|\alpha_{\pi(2)}\right| \geq ..... \geq \left|\alpha_{\pi(m)}\right| .$$

We can t afford to discard coefficients with larger amplitude as it directly affects the error in reconstruction of the signal from its coefficients. The idea is to cut-down the size of $\tilde{\mathbf{S}}$ $(= \mathcal{W}\tilde{s})$ from m to $\hat{m}$. This chopping off of the coefficient vector $\tilde{\mathbf{S}}$ will result in some approximation error equivalent to $\sum_{k=\hat{m}+1}^{m} \alpha^2{}_{\pi(k)}$, where $\tilde{S} = \{\alpha_1, \alpha_2, ...\alpha_{\hat{m}}\}$. In case of denoising the signal, our aim was to retain minimum number of coefficients which contained maximum possible energy and thus decomposing the signal to five levels was a good decision. Once we are assured that the denoised signal is a good estimate of the original EOG signal, we can de-

F. Ibrahim, N.A. Abu Osman, J. Usman and N.A. Kadri (Eds.): Biomed 06, IFMBE Proceedings 15, pp. 440-443, 2007
www.springerlink.com ' Springer-Verlag Berlin Heidelberg 2007

compose the estimated signal into higher levels. The motif now is − feature extraction i.e. to attenuate very low-scale or high frequency components to suppress ripples and at the same time keep the peaks of the eye blinks intact.

Table 1 Thresholding Strategies for Signal Compression

Method	Thresholding Scheme
Remove Near 0	$\lambda = \text{median}(\lvert c\rvert)$, where c denotes the detail coefficients at level 1 obtained from the decomposition of the signal be compressed, using db1 and $\max(\lvert c\rvert)/20$ if $\text{median}(\lvert c\rvert) = 0$
Balance Sparsity Norm	With the details coefficients, the L_2 recovery in percentage and the relative sparsity in percentage (obtained from the compressed signal by setting to 0 the coefficients less than λ in absolute value) are equated to select the threshold.
BirgØMassart	The strategy leads to select the highest coefficients in absolute value at each level; the numbers of kept coefficients grow scarcely with $L-j$. For a given level, $n_j = M/(L+2-j)^{\gamma}$ coefficients are kept. There are three different ways of selecting M. Scarce high ($M=\ell$), Scarce low ($M=2\ell$) and Scarce medium ($M=1.5\ell$).

Threshold criterion can always be applied to the coefficients for feature extraction. There are two basic threshold based strategies for signal compression: level-dependent thresholding and global thresholding (figure 3). Both methods deploy hard thresholding. The level dependent strategy uses the BirgØMassart method and antithesis to this, the global thresholding method uses Balance sparsity−norm (figure 4) and remove near 0 techniques. The BirgØMassart method is based on an approximation result from BirgØand Massart [13]. This method is characterized by three important parameters − L (level of decomposition), M (length of coarsest approximation coefficients) and the sparsity parameter γ with condition $\gamma > 1$ [14-15]. The procedure for thresholding is as follows. For the level L, the approximation coefficients are kept intact and for a level $j \in [1, L)$ n_j largest coefficients are retained so as, $n_j = M/(L+2-j)^{\gamma}$.For the purpose of compression the sparsity parameter γ is set to 1.50. For ι , the length of the coarsest approximation coefficients, there are three different choices for selecting M. These are summarized in Table 1. The compression score assessment is done by screening two observations. The compression ratio,

$$\kappa = \frac{\text{No. of zeros of current coefficients}}{\text{Length of the signal}} \tag{4}$$

and the retained energy in the compressed signal,

$$\varepsilon = 100\left(\sum \lvert \tilde{s}_{\Delta} \rvert^2 / \sum \lvert \tilde{s} \rvert^2\right) \tag{5}$$

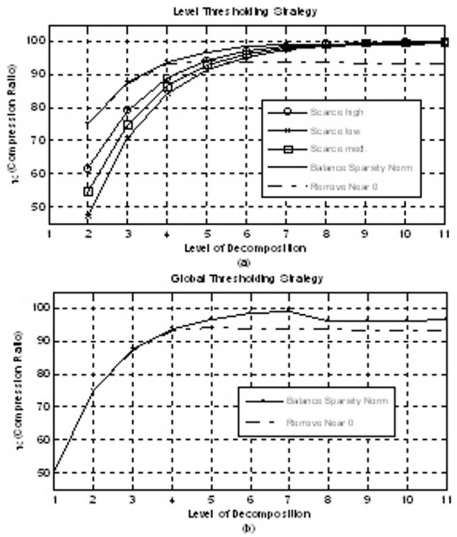

Fig. 3 (a) & (b) the compression ratio against the level of decomposition for the level and global thresholding strategy respectively.

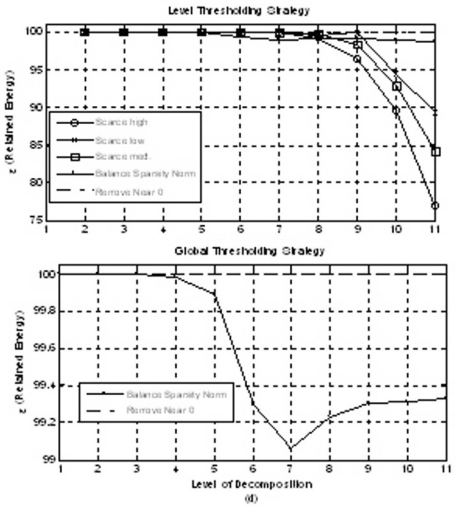

Fig. 3 (c) & (d) the energy retained in the signal for the level and global thresholding strategy respectively

D. Comments on compression

without loss of generality the compression ratio ┌ improve with an increment in the level of decomposition .which is in fruitful synergy ,however the relative improvement is not very significant .when the signal is decomposed beyond the level of seven.

F. Ibrahim, N.A. Abu Osman, J. Usman and N.A. Kadri (Eds.): Biomed 06, IFMBE Proceedings 15, pp. 440-443, 2007
www.springerlink.com ' Springer-Verlag Berlin Heidelberg 2007

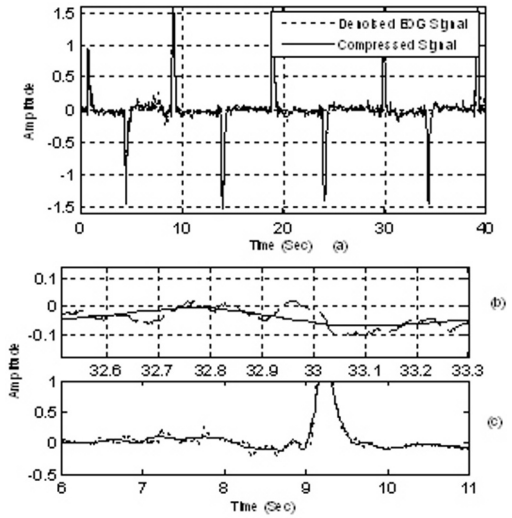

Fig. 4 (a) voltage waveform of compressed EOG signal decomposition to 7 level was used with the global thresholding & balance sparsity norm as the threshold criteria (b) & (c) show the detail view compression has efficient surpassed high frequency ripple

There are two predominant disadvantage of decomposition signal into the higher level (1) the computational complexity increase dramatically and (2) the signal loses the important information (note that this compression is lossy)

For the level dependent thresholding and global thresholding methodology, the performance of the balance sparsity norm techniques is better than the contemporary strategies the evaluation parameter being ┌ and E .where as the remove near zero strategy retain 100% energy at all this time. its capability to compress the signal saturate near around 93%.balance sparity norm method provide a good trade-off with the maximum compression of 99.04%with the least 99.06% retained energy (for the global thresholding strategy) .

III. Conclusions

Much recent wok has examined the Electro-oculogram signal primarily to subdue its effect in EEG signal in this research we suggested a scheme to enhance these signals .this research show that the balance sparsity norm strategy offer better compression ratio than the other contemporary method for the both global and level thresholding

This paper enhance the quality of the noisy EOG signal to an extent that the signal can be store for future purpose (with the best compression)or can be used for the direct application on relating to the human computer interfacing design etc.

Acknowledgment

The author would like to thank Mathworks for providing wavelet toolbox of the matlab.

References

1. D Kumar, Eric Poole Classification of EOG for Human Computer Interface, Proceedings of the Second Joint EMBS/BMES Conference Houston. TX. USA .October 23-26.2C02
2. S. Venkataramanan, Pranay Prabhat, Shubhodeep Roy Choudhury, Harshd B. Nemade, J.S. Sahambi Biomedical Instrumentation based on Electrooculogram (EOG) Signal Processing and Application to a Hospital Alarm System
3. Kuno Y, Yagi T, Uchikawa Y: Development of eye pointer with free head-motion. Proceedingsof the 21Ybnnual International Conference of the IEEE Engineering in Medicine and biologySociety, Vol20, no4 1998
4. Kwon S H, Kim H C, EOG-Based Glasses-Type Wireless Mouse for the Disabled Proceedings of the First Joint BMES/EMBS Conference Serving Hzirnaniq, Advancing Technology, Oct 13-16,99, Atlanta, GA, USA IEEE
5. Norris G, Wilson E , The eye mouse, An Eye Communication Device, IEEE Tr SMC, 1997,pp 66-67.
6. Qiuping Ding, Kaiyu Tong, and Guang L Dvelopment of an EOG (Electro-Oculography) Based Human-Computer Interface Proceedings of the 2005 IEEE Engineering in Medicine and Biology 27th Annual ConferenceShanghai, China, September 1-4, 2005
7. Strang, G. & Nguyen, T. (1996). Wavelets and Filter Banks, Wellesley-Cambridge Press, Wellesley, MA.
8. Tatjana Zikov, StØphane Bibian, Guy A. Dumont, Mihai Huzmezan A Wavelet based de-noising technique for ocular artifact correction of the Electroencephalogram
9. Martin Vetterli , Wavelets, Approximation,and Compression IEEE Signal processing magazine September 2001 pages 59-73
10. S. Mallat, A theory for multiresolution signal decomposition: The wavelet representation, IEEE Trans. Pattern Recognition Machine Intell., vol. 11,pp. 674-693, July 1989.
11. S. Mallat, A Wavelet Tour of Signal Processing. San Diego, CA: Academic,1998.
12. David Salomon , 3rd Ed. Data Compression - The Complete Reference ,; Springer Publications
13. BirgØ L.; P. Massart (1997), "From model selection to adaptive estimation," in D. Pollard (ed), Festchrift for L. Le Cam, Springer, pp. 55-88.
14. Estimation of the Mean of a Multivariate Normal Distribution Charles M. SteinThe Annals of Statistics, Vol. 9, No. 6. (Nov., 1981), pp. 1135-1 151.
15. Haar. Zur theorie der orthogonalen funktionensysteme. Mathematische Annalen,pages 331 371, 1910.

Author: Ayush Bhandari
Institute: Dept. of Electronics and communication Engineering,
Jaypee Institute of Information Technology
City: Noida
Country: India

F. Ibrahim, N.A. Abu Osman, J. Usman and N.A. Kadri (Eds.): Biomed 06, IFMBE Proceedings 15, pp. 440-443, 2007
www.springerlink.com ' Springer-Verlag Berlin Heidelberg 2007

Wireless Real-time Brain Mapping

Parmida Moradi Birgani and Meghdad Ashtiyani

1 University of Islamic Azad /BME Dpt, Tehran, Iran
[2] University of Imam Hossein / Communication M.S Dpt., Tehran, Iran

Abstract— **As we know different brain regions have specific functions. And also before performing any surgery on the brain, including surgery for the treatment of epilepsy, the surgeon seeks to understand the functions of the areas affected by the seizures or of the lesion. The attempt to specify in as much detail as possible the location of function in the human brain is called Brain mapping. In this paper we produced Brain mapping from digitized EEG data recordings. And we developed our software to obtain continuous movie map and spect slide. And also we made it possible to be real-time and wireless for getting the best results.**

Keywords— **EEG, Brain mapping, Classification, Wireless**

I. Introduction

The recording and use of electroencephalograms (EEG) to visualize what the brain is doing has been practiced since 1928 when Hans Berger first attached two electrodes to a scalp surface and recorded the first EEG on a cathode ray tube. The evolution of EEG technology has since improved substantially, including multi-channel recording, but the basic use of the EEG systems remain the same: to record changes in potential between various locations on the scalp surface.

As we know different brain regions have specific functions. And also before performing any surgery on the brain, including surgery for the treatment of epilepsy, the surgeon seeks to understand the functions of the areas affected by the seizures or of the lesion. All of the surgical planning is done to preserve important functions such as speech, comprehension, sight, movement, or sensation, and to lessen the risk of loss of function from the surgery.

While recognizing the vital role EEG plays in clinical diagnoses, it must be emphasized that the output of multi-page row waveforms is rather difficult to interpret, especially for someone without long experience in EEG.
The task of identifying the function of different regions of the brain is called brain mapping [4]. The first aim of this project is to generate a brain map from digitized EEG recordings and the development of its software to obtain continuous movie map (animation movie) and spect slides. Which help the physicians to seek the area more carefully and compare the slides to find out what the brain exactly done. And our second aim is making it real time. So that it is more possible to study how electrical activity evolves and changes over time in a manner that is clear to even the casual observer. And our last aim is preparing a system for wireless electrical brain mapping.

The greatest advantage of this wireless system is practically unlimited movement of the patients. The users can carry such EEG devices not only in their house, but also while working or sleeping. Also the computer system allows the selection of the number of the electrodes, the interpolation method, the display mode, and also the number of spects slides and the exact interval of EEG.

II. Elecrical recordings from the brain

The EEG is a recording of the brain s electrical activity, in most cases made from electrodes over the surface of the scalp. It may also be made from electrodes places over the surface of the brain or from needle electrodes inserted into the brain. The recordings are the summation of volume conductor fields produced by millions of interconnecting neurons. The architecture of the brain is not uniform but varies with different locations. Thus the EEG can vary depending on the location of the recording electrodes. Recordings made from an electrode on the surface of the scalp, using a distance reference electrode, are the resultant field potential at the boundary of a large volume conductor containing many neurons. Action potentials in axons contribute little to scalp surface records as they are asynchronous and the axons run in many different directions. Surface records are the net effect of local postsynaptic potentials of cortical cells.

III. Brain waves classification

For obtaining basic brain patterns of individuals, subjects are instructed to close their eyes and relax. Brain patterns from wave shapes that are commonly sinusoidal. Usually, they are measured from peak to peak and normally range from 0.5 to 100 μV in amplitude, which is about 100 times lower than EEG signals. By means of Fourier transform power spectrum from the row EEG signal is derived. In Power spectrum contribution of sine waves with different frequencies are visible. Although the spectrum is

F. Ibrahim, N.A. Abu Osman, J. Usman and N.A. Kadri (Eds.): Biomed 06, IFMBE Proceedings 15, pp. 444-446, 2007
www.springerlink.com ' Springer-Verlag Berlin Heidelberg 2007

continuous, ranging from 0 Hz up to one half of sampling frequency, the brain state of the individual may make certain frequencies more dominate. Brain waves have been categorized into four basic groups (Figure1):

- Beta (>13 Hz),
- Alpha (8-13 Hz),
- Theta (4-8 Hz),
- Delta (0.5-4 Hz).

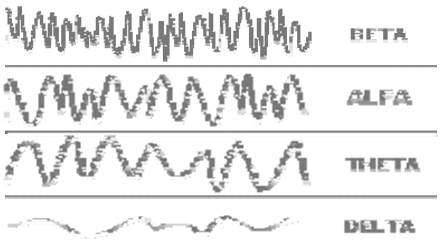

Figure1

IV. EEG LEAD SYSTEM

The internationally standardized 10-20 system is usually employed to record the spontaneous EEG. In this system 21 electrodes are located on the surface of the scalp, as shown in Figure 2. The positions are determined as follows: Reference points are nasion, which is the delve at the top of the nose, level with the eyes; and inion, which is the bony lump at the base of the skull on the midline at the back of the head. From these points, the skull perimeters are measured in the transverse and median planes. Electrode locations are determined by dividing these perimeters into 10% and 20% intervals. Three other electrodes are placed on each side equidistant from the neighboring points.

V. SIGNAL TRANSMITTING

The advances in sensor technologies have made it possible to construct highly functional "smart" sensors and also to connect a large number of sensors for distributed measurement and control applications. The networking of many smart sensors enables high quality Detection/measurement networks with low cost and easy deployment, and it provides new monitoring and control

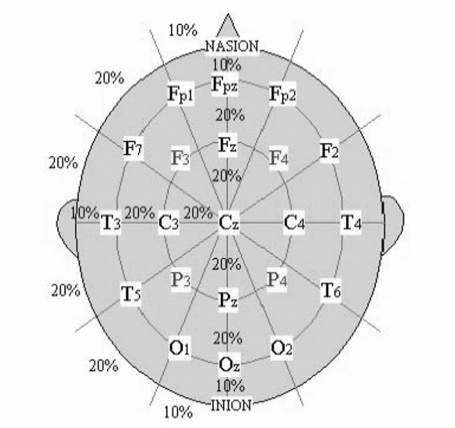

Figure2

capability for a wide range of applications, such as medical process monitoring, health care. For data transferring we apply a Sensor Bus Standard. A sensor usually imposes very moderate requirements on the communication rate and hardware complexity. A serial bus structure is the most efficient realization among different bus structures. It can provide the minimum number of interconnects in the sensor network and also achieve low cost and high reliability.

VI. CREAT 2D BRAIN MAPPING

In order to use the superior power and flexibility of the computer to store and to analyze the EEG and other biosignals, an invention was of fundamental importance: the so-called analog-digital converter. Sampling is preformed at a high speed (100 to 200 time per second), and the resulting numbers are stored in computers disk (Figure 3). Each channel of EEG has its own separate DAC process, in parallel with the others, and this proceeds in real time [3]. The format of EEG recordings which we had to use was unknown, so the first step was rereading of these data. next step was interpolation. For this step the cubic spline interpolation is applied [5]. However, one of our software's options is choosing the interpolation method. And the points for interpolation are chosen from the standard 10-20-electrode placement. The final generated brain map is shown in Figure 4. Using Matlab Software does all the process. And finally by using Matlab GUI, we've produced the spect slides and animation movie and also made it real-time. The number of slides and also the special time period of EEG can be chosen by the operator or neurologists (Figures 5,6).

F. Ibrahim, N.A. Abu Osman, J. Usman and N.A. Kadri (Eds.): Biomed 06, IFMBE Proceedings 15, pp. 444-446, 2007
www.springerlink.com © Springer-Verlag Berlin Heidelberg 2007

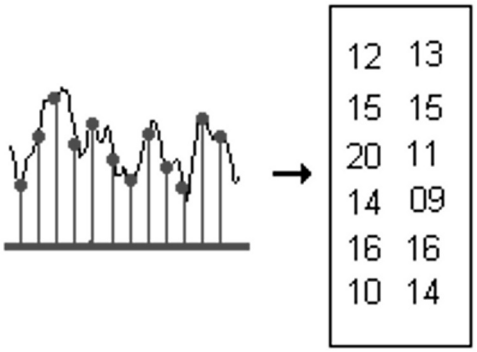

Figure 3

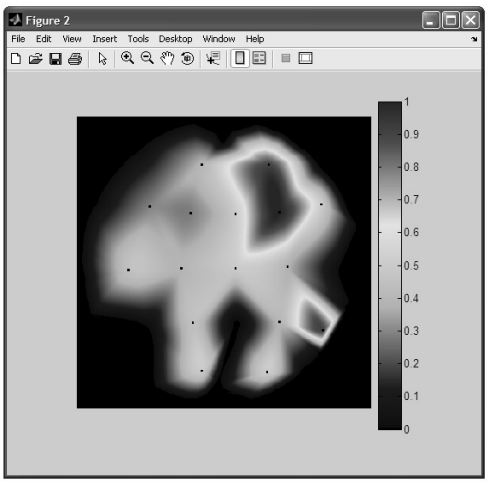

Figure 4

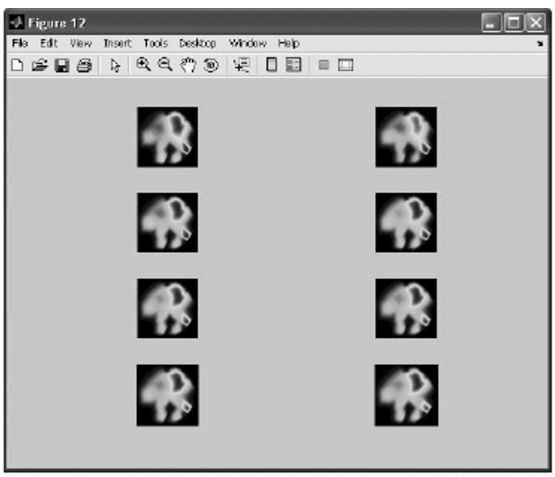

Figure 5

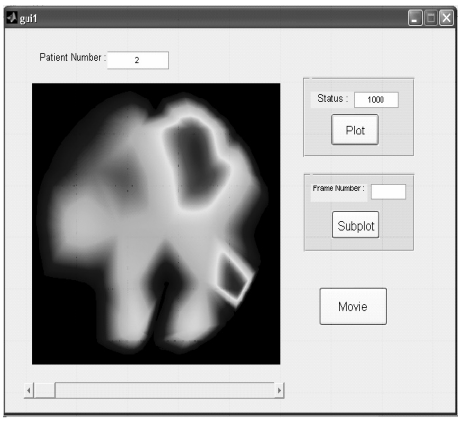

Figure 6

VII. Conclusions

Topographical mapping of brain electrical activity presents temporal and spatial information From EEGs in direct and cleaner manner. Presenting these maps in a manner that we described in this paper help physicians to find out the functions of the area affected by seizures or of the lesion more carefully.

Acknowledgment

The authors would like to thank Dr. F. Farrokhi for his fruitful advices. And also the authors are grateful to Islamic Azad University and Imam Hossein University.

References

1. S.K. Law, P.L. Nunez, A.F. Westdrop, A.V.Nelson, K.L. Pilgreen. Topographic Brain Electrical Activity, IEEE Visualization 1991, PP.194-201.
2. I. Gonzalez, A. Eblen-Zajjur. Tridimensional animated brain mapping from conventional paper-ink EEG recordings. Computer in Biology and Medicine 34 (2004)
3. Renato M.E. Sabbatini. Mapping the Brain.
4. Howard L. Review of Brain Mapping
5. Sky McKinley and Megan Levine. Cubic Spline Interpolation.

Address of the corresponding author:

Author:	Parmida Moradi Birgani	Meghdad Ashtiyani
Institute:	Iran Azad University	Imam Hossein University
City:	Tehran	Tehran
Country:	Iran	Iran
Email:	pmb_81@yahoo.com	m.ash.80@gmail.com

F. Ibrahim, N.A. Abu Osman, J. Usman and N.A. Kadri (Eds.): Biomed 06, IFMBE Proceedings 15, pp. 444-446, 2007
www.springerlink.com ' Springer-Verlag Berlin Heidelberg 2007

Aromatherapy: It's Effect on Brain Signal, Math Computation, Blood Pressure and Heart Rate

S.F. Khyasudeen, and M. Abu Bakar

Department of Biomedical Engineering, University of Malaya, Kuala Lumpur, Malaysia

Abstract— **The effect of aromatherapy on the brain signal is investigated to find the correlation with the heart rate, blood pressure and mathematical computation. First the experiment is conducted to find the effect of aromatherapy on heart rate, blood pressure and mathematical computation and the result is then been correlated to brain signal obtained. Thus the study of effect of aromatherapy covers the physiology and psychologically effects which are important to be identified to know the significant effect of aromatherapy to physiology and psychological as well as to determine the correlation between physiology and psychological of the human body. In this study, Rose has been chosen as the aroma for the study of the effect of aromatherapy.**

Keywords—**aromatherapy, brain signal, signal processing**

I. Introduction

Aromatherapy can be defined as therapy using the aroma. To be more precise, aromatherapy is the entire branch of botanical medicine using volatile aromatic plants compounds that believe can be as a treatment of various conditions. The aromatherapy use essential oil as the main components. Essential oil is making from a concentrated volatile aromatic compound that is produced by plants. Each plant species originates in certain countries of the world because particular country has particular environment conditions and neighboring fauna and flora. Essential oil can be extracted from oil 'sacs' in flower, leaves, stems, roots, seeds, wood and bark.There are plenty of essential oils that are believed can give certain effects to the person who inhaled it. Rose for instance is believed to give effects of various sensations basically for promoting relaxing state. The scientific name for Rose is *Rosa Damascena*.

The Olfactory System is basically the body's system of smell as illustrated in Figure 1. Tiny molecules of aroma are inhaled by the nose. These aroma molecules are trapped in the nose by hair like nerve endings that pass the aroma on to receptors that then carry the molecules to the Olfactory Bulb. From the Olfactory Bulb, the aroma molecules are transported to the limbic system in the brain. Amygdala plays a very important role in storing emotional trauma and that odor triggers a profound effect from the gland. The Olfactory nerves react as other nerves in the body do, responding to electrical signals and impulses and dispatching information to the rest of the body. An odor is perceived through thousands of olfactory nerves in the nostrils, which contain bundles of highly sensitive nerve cells. Unlike other nerve cells, these cells regenerate every 30 to 40 days. Specific aromatic molecules of essential oils react with specific nerve receptors, which in turn trigger electrochemical impulses that are conducted directly into the brain. Aromas are transmitted to the limbic system, a part of the brain which perceives and responds to memory, pleasure and emotions. Odor triggers the limbic system to release brain-affecting chemicals known as neurochemicals. Encephalin reduces pain and creates a feeling of well-being. Because the olfactory nerves are a direct extension of the brain's limbic system, recognition of smell is relayed immediately, whereas recognition of taste, sound and touch is not as immediate.

Alpha is one of the four basic brain waves [Delta, Theta, Alpha, and Beta], which make up the electroencephalogram signal (EEG). These are all oscillating electrical voltages in the brain, but they are very tiny voltages, just a few millionths of a volt. The Alpha waves oscillate about 10 times per second, and the range is 8-13 cycles per second. Alpha appears and disappears. It is not always present. For example, in deep sleep there is no Alpha, and if someone is very highly aroused as in fear or anger, again there is virtually no Alpha. Delta is seen only in the deepest stages of sleep (Stages 3 and 4). Theta is seen in light sleep and drowsiness (sleep stages 1 and 2). Alpha is seen in wakefulness where there is a relaxed and effortless alertness. Beta is seen in

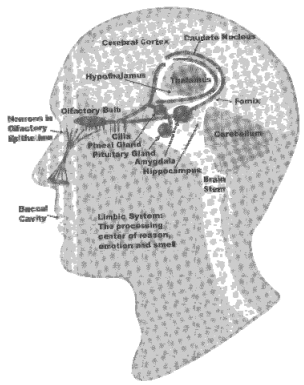

Fig. 1 The Olfactory System

F. Ibrahim, N.A. Abu Osman, J. Usman and N.A. Kadri (Eds.): Biomed 06, IFMBE Proceedings 15, pp. 447-450, 2007
www.springerlink.com © Springer-Verlag Berlin Heidelberg 2007

highly stressful situations, and where there is difficult mental concentration and focus [4].

Delta waves are the slowest oscillating waves (0-4 cycles per second). Theta waves oscillate somewhat faster (4-7 cycles per second). Alpha waves oscillate 8-13 times per second. Beta waves oscillate still faster (13-40 cycles per second). There are many other kinds of electrical activity in the brain, especially the short-lived evoked potentials that occur when the brain responds to sensory input (like a sound, or a touch, or a flash of light). However, the four basic EEG waves of Delta, Theta, Alpha, and Beta constitute the standard lineup of EEG activity.

Each of the four basic EEG waves is linked to a different state of consciousness. Each of the four types of waves is good for something different [4].

II. Methods

The method consists of two parts; the first part involved the collection of data from 30 subjects; 15 males and 15 females. For each of the subject, three different readings have been taken which are the heart rate, blood pressure and time taken to complete five basics mathematical questions. The data is recorded during pre and post exposure to Rose. So, for each and every subject, six different readings were recorded namely heart rate, blood pressure and time taken to solve mathematical questions for pre and post exposure. The second part involved the collection of brain signal from the same subjects and were recorded for both pre and post exposure to Rose as well.

First Part: For measuring the heart rate and blood pressure, digital non-invasive blood pressure is used. When the subject arrived to the lab, he or she will be asked to take a rest for about 15 minutes in order to ensure they are in resting condition. Then, blood pressure and heart rate of the subject is taken. Subsequently, the subject is given five different mathematical questions and told to finish the question as fast as they can while time is recorded. After completed the questions, subjects is asked to sniff dental swap contained three drops of diluted Rose for the duration of three minutes continuously. Immediately after that, the heart rate and blood pressure of the subject is taken again. Similarly, five mathematical questions are given and time taken to complete the questions is recorded. The procedure is repeated for each and every subject to ensure the consistency of the date obtained. All the data obtained from the experiment conducted is plotted using the SPSS V13.The type of data presentation that is used to analyze and interpret the data is the simple error bar graph.

Second Part: For recording and acquiring the EEG signal, BIOPAC MP150 is used. The montage used is the standard montage of 10-20 system and the technique of placing the electrodes is bipolar technique. Bipolar technique refers to the technique of measuring the impedance between two active electrodes and it is chosen as BIOPAC MP 150 is only compatible with the bipolar technique. In this study only the frontal part of the brain is been focused as it is most associated to the sense of smell. The signal is acquired from six channels comprised of Fp1-Fp2, F3-F4 and F7-F8. Before placing the electrode, the gel is spread onto the scalp in order to reduce the impedance exists in the scalp surface. The impedance is waited to reach al least 3kOhms before the recording of the brain signal is started. The flow of the steps taken can be seen from Figure 2 below.

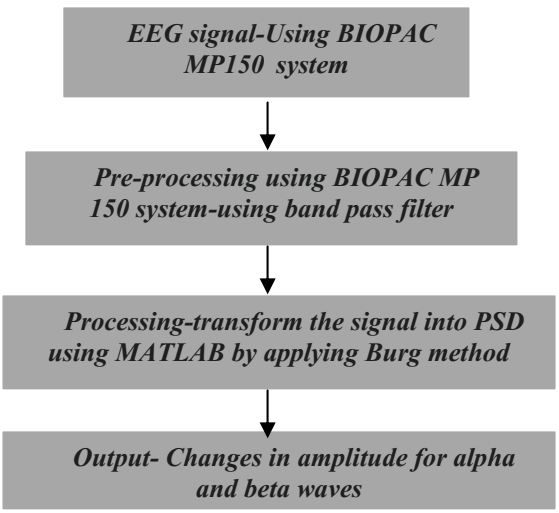

Fig 2 Summaries of the Steps Taken to Process Brain Signal.

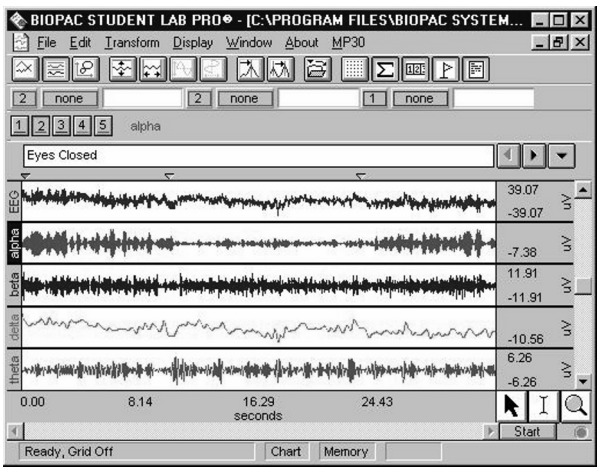

Fig 3 User Interface of Hardware BIOPAC MP 150. Example of Signal Acquired. [*www.biopac.com*, 06/05/2006]

F. Ibrahim, N.A. Abu Osman, J. Usman and N.A. Kadri (Eds.): Biomed 06, IFMBE Proceedings 15, pp. 447-450, 2007
www.springerlink.com ' Springer-Verlag Berlin Heidelberg 2007

III. Results and discussion

A. Effect of Rose on Heart Rate, Blood Pressure and Time Taken to Solve Mathematical Questions

For all the figures presented below, 0 represents before exposure and 1 represents after exposure and the sample subject taken is within the 95% confidence interval for both pre exposure and post exposure.

From Figure 4, there is slight difference between pre and post exposure for the heart rate in which the mean heart rate is dropped about 2.5 percent. Figure 5 shows a significant drop in the blood pressure which is about five percent after the exposure to the Rose. From Figure 6, it shows that subjects take 35 percent less time to complete the mathematical questions after exposing to the aroma.

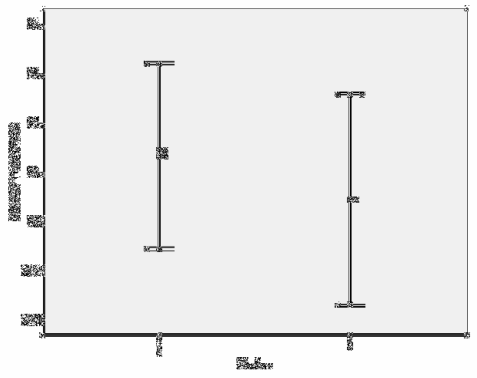

Fig 4 Effect of Rose on Heart Rate

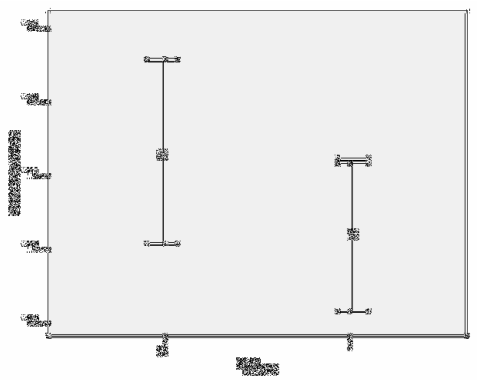

Fig 5 Effect of Rose on Blood Pressure

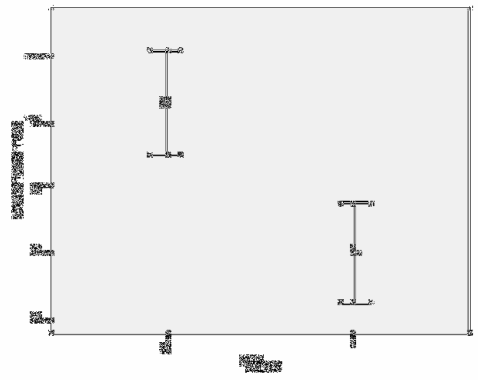

Fig 6 Effect of Rose on Time Taken on Solving Mathematical Questions

B. EEG Signal Obtained After Exposing to Rose

For all the Power Spectral Density (PSD) graphs shown (Fig 7 and Fig 8), blue represents before and red represents after exposure.

From the Table 1 it shows that there are subjects who recorded to have higher magnitude of alpha power and also subjects shows lower magnitude of alpha power. About 29 percent of the subjects show an increase of alpha power and the rest shows the decrease of alpha power. About 43 percent of the subjects show an increase in beta power and the rest, which is about 57 percent show the decrease in beta power. Hypotheses make is that Rose makes subject feel more relax and drowsy [4]. Increase in alpha magnitude indicates that the subject feels more relaxed after the exposure whereby the decrease of alpha magnitude shows that

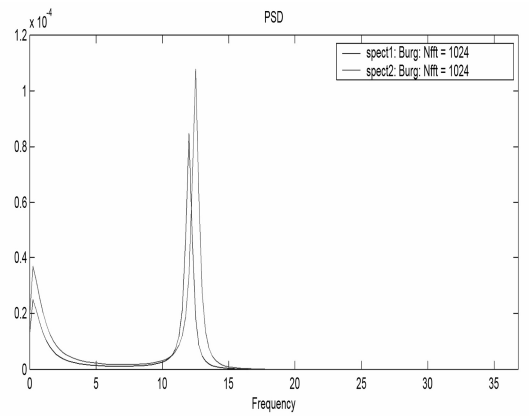

Fig 7 PSD obtained for Alpha Wave for Subject 1

F. Ibrahim, N.A. Abu Osman, J. Usman and N.A. Kadri (Eds.): Biomed 06, IFMBE Proceedings 15, pp. 447-450, 2007
www.springerlink.com ' Springer-Verlag Berlin Heidelberg 2007

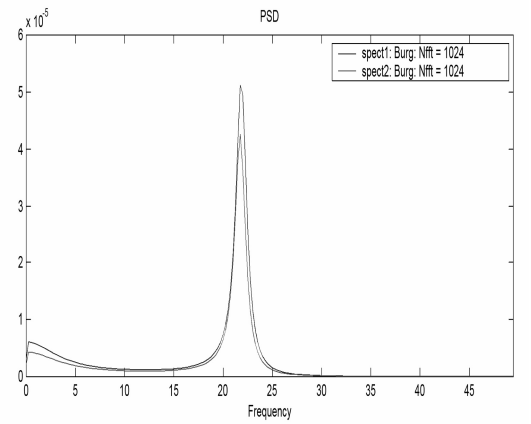

Figure 8 PSD Obtained for Beta Wave for Subject 1

Table 1 Comparison of Alpha and Beta Waves for Pre and Post Exposure for Six Subjects Respectively.

subject becomes tense or less relaxed [1]. Increase in beta magnitude indicates that subject feels more alert after the exposure and decrease of beta magnitude indicate that subject feels drowsy or less alert [*7*]. The result does not support the hypothesis that alpha makes subject feel relaxed.

Nevertheless the founding that more half of the subjects feel drowsy after the exposure likely supports the hypothesis. However the results from the first part is found to be a bit contradict from the second part as the first part of the experiments shows that Rose makes most the subjects to experienced lower heart rate after the exposure. Relaxed state will decrease the heart rate (or at least the heart rate is not changed) and vice versa [*7*]. This shows that most of the subjects feel relaxed after been exposed to the Rose which is contradict from the result of the brain signals obtained which shows minority of the subjects experienced relaxing state indicated by the increase in alpha power.

IV. Conclusion

Rose affects subject in various way. There are subjects who feel relaxed after the exposure and so did subjects feel tense after the inhalation. Rose does not make all the subjects feel drowsy or less alert because there are subjects feel alert after the inhalation. However there is subject who said that he likes the aroma but the brain signals show that he feels tense after exposure. The best thing to conclude is that psychological effect sometimes does not indicate the physiological effect. One might said he feels relaxed after the exposure but the brain signal shows that he feel tense indeed.

References

1. T.Hirai, Electroencephalogram Study of Zen Meditation, Psychiatrist Neurologist, Japanese, 62, pp 76-105 (1960)
2. http://members.aol.com/networktcp/research/freq.htm
3. www.biopac.com
4. http://vava.essortment.com/aromatherapyoil_rtds.htm
5. http://www.madison_avenue.com/storefront/Aromatherapy/oils/Rose.asp
6. www. biocybernaut.com
7. www.drwardbond.com

Address of the corresponding author:

Author: S.F. Khyasudeen
Institute: Department of Biomedical Engineering, University Malaya
Street: Lembah Pantai, 50603
City: Kuala Lumpur
Country: Malaysia

F. Ibrahim, N.A. Abu Osman, J. Usman and N.A. Kadri (Eds.): Biomed 06, IFMBE Proceedings 15, pp. 447-450, 2007
www.springerlink.com ' Springer-Verlag Berlin Heidelberg 2007

On the Linearity/Non-linearity of Mental Activity EEG for Brain-Computer Interface Design

T. Balli[1], R. Palaniappan[1] and D.P. Mandic[2]

[1]Department of Computer Science, University of Essex, Colchester, United Kingdom
[2] Department of Electrical and Electronic Engineering, Imperial College, London, United Kingdom

Abstract— **In this study, we investigated the linearity/non-linearity of mental activity electroencephalogram (EEG) signals for Brain-Computer Interface (BCI) designs using the recent but well established Delay Vector Variance (DVV) method. EEG data recorded from seven subjects while they were performing five different mental activities were used in the experimental study. Through the use of DVV, it was investigated whether EEG signals would become linear or non-linear when segmented into smaller parts. Concluding, the results of the studies showed that a large percentage of the EEG signals exhibited non-linear behaviour. This is an important result as it shows that the currently used linear modelling methods are mostly unsuitable.**

Keywords— **Brain-Computer Interface, Delay Vector Variance, Electroencephalogram, Non-linearity analysis, Surrogate data**

I. Introduction

Electroencephalogram (EEG) is a representative signal that contains information about the electrical condition of the brain. These signals can be used to assess brain damage, epilepsy and other disorders. In recent years, there have been many developments in utilising EEG for Brain-Computer Interface (BCI) design as an alternative communication tool between disabled people and their environment [1], [2], [3]. These studies used EEG signals recorded during mental activities and focused on designing BCI systems that can discriminate between these different mental activities.

While designing these BCI systems, it is important to verify the presence of linearity or non-linearity in the corresponding signals so that appropriate modelling methods can be used. However, the previous studies assumed that the EEG signals were linear and used linear modelling methods like autoregressive. The use of linear methods simplifies the implementation but it is likely to give erroneous results when the signal is in fact non-linear.

In this study, the aim is to investigate on the linearity (or non-linearity) of the mental activity EEG signals using Delay Vector Variance (DVV) method. DVV is a recently proposed method for assessing the non-linearity [4]. This method works by testing the local unpredictability of the signal. It is hoped that the DVV method would yield a reliable characterisation of the EEG signals, which will move future BCI system design towards minimising the classification error of different mental activities.

II. Eeg data and pre-processing

A. Data

The EEG data used in this study were obtained from http://www.cs.colostate.edu/eeg/. These data were recorded from seven subjects. Subjects performed five trials on each day. Subjects 2 and 7 performed only one five-trial session, while subject 5 performed three five-trial sessions and the rest of the subjects performed two five-trial sessions. The EEG data were recorded from six positions (channels) C3, C4, P3, P4, O1, and O2. There was an additional EOG channel (for reducing eye blink contamination).

Signals were recorded for 10s during each activity and each activity was repeated for several sessions (subjects 2 and 7 performed only one session). The sampling rate of the signals was 250 Hz, so the length of EEG signals were 2500 sampled points for each channel.

In this study, the EEG signal for each mental activity was segmented into 20 parts with length 0.5s i.e. 125 data points in length. We studied EEG with this segmentation length as it has been used in the previous studies [2, 3].

EEG signals from five different mental activities performed by each subject were used. These mental activities were:

1. Baseline activity: The subjects were asked to relax and think of nothing in particular. This activity was used as a control and baseline measure of the EEG signals.

2. Math activity: The subjects were given a multiplication activity and were asked to perform it without vocalising or making any other physical movements. The numbers were selected such that none of the subjects could complete the activity before the end of 10s recording session.

3. Mental letter composing activity: The subjects were asked to mentally compose a letter to a relative or friend without vocalising. Since the activity was repeated several times, the subjects were told to continue where they left off in the previous activity.

F. Ibrahim, N.A. Abu Osman, J. Usman and N.A. Kadri (Eds.): Biomed 06, IFMBE Proceedings 15, pp. 451-454, 2007
www.springerlink.com ' Springer-Verlag Berlin Heidelberg 2007

4. Geometric figure rotation activity: The subjects were given 30s study the drawing of a complex 3D object. After that, they were asked to visualise the object being rotated about an axis. The EEG was recorded during the mental rotation.

5. Visual counting activity: The subjects were asked to imagine a blackboard and to visualise the numbers being written on the blackboard sequentially with the previous number being erased before the next number was written. The subjects were asked not to verbally read the numbers but to visualise them and they were told to continue counting where they left off in the previous activity rather than starting again.

Keirn and Aunon [1] specifically chose these mental activities since they involve hemispheric brainwave asymmetry.

B. Pre-processing

The eye blinks occur naturally during the EEG recording process and they cause contamination to the recorded EEG data. In this paper, the original EEG was recovered by subtracting separately recorded EOG (with appropriate weights) from EEG data. The weights were 0.1 for C3 and C4, 0.05 for P3 and P4, and 0.025 for O1 and O2.

Next, EEG signals were high pass filtered to reduce baseline noise. A forward and reverse Elliptic digital filter with cut off frequency at 1 Hz and minimum 20 dB attenuation in stop band below 1 Hz were used. The ripples in the pass band were kept below 0.1 dB.

A further pre-processing step was to low pass filter the signals to remove 60 Hz powerline interference. For low pass filtering, the same specifications were used but with cut-off at 59 Hz and minimum 20 dB attenuation beyond 60 Hz.

III. Data analysis

In this section, surrogate data and DVV methods will be introduced. Besides these the concept of null hypothesis will be covered briefly.

A. Null Hypothesis

In this study the aim is to test the non-linearity of EEG data. In order to test the non-linearity, a hypothesis is generated that the time series is linear. As it is not possible to test the properties of non-linearity directly, this null hypothesis of linearity is generated. The main idea is to compare the test statistics of original time series against surrogate time series. Surrogate time series are the realisation of null hypothesis. The test statistics of time series will be obtained by DVV method, which will be introduced later in this section.

B. Surrogate Time Series

The surrogate time series are artificially generated time series that retain some statistical properties of original time series (such as mean, variance and Fourier magnitude spectra) in order to have the same linear properties with original data set. They are used for testing non-linearity [5].

There are several methods for generating surrogate time series. In this paper iterative Amplitude Adjusted Fourier Transform (iAAFT) [6] is used for generating surrogate time series, which is an improvement of Amplitude Adjusted Fourier Transform Method (AAFT).

The iAAFT algorithm produces surrogate time series that follow the same distribution and have identical magnitude spectra with the original time series [6].

In order to produce iAAFT based surrogate time series, the following steps must be followed:

- Initially, we have original time series x(t) in which t=1...N;
- Next, apply Fast Fourier Transform to original time series and save the magnitudes in α;
- In the iterative process, we have two time series; r(t) which have the same distribution with original time series and s(t) which have same magnitude spectrum with original time series;
- r(0) is the shuffled sequence of original time series.

- In every iteration:

1. Compute the phase spectrum of r(t-1) and save it to Ø;
2. Calculate the Inverse Fourier Transform of (|α| exp(i Ø)) and save the results to s(t);
3. r(t) is obtained by rank ordering of s(t) so as to match the sorted version of original time series.

C. Delay Vector Variance Method

For obtaining the test statistics of the original and surrogate time series, many methods have been proposed in the literature [7]. In this paper, a relatively recent method for obtaining test statistics will be used. This method is the DVV method [7]. The idea behind DVV is testing the local predictability of time series. Using this method the target variances are computed, σ^{*2}, which are the inverse measure of local predictability of time series for a given embedding dimension, m.

The DVV method is based on time delay embedding method, in which original time series X={x(k) | k=1 N}

F. Ibrahim, N.A. Abu Osman, J. Usman and N.A. Kadri (Eds.): Biomed 06, IFMBE Proceedings 15, pp. 451-454, 2007
www.springerlink.com ' Springer-Verlag Berlin Heidelberg 2007

will be represented by a set of delay vectors where each delay vector contains *m* consecutive time samples, denoted by $x(k)=[x_{k-m\tau}, \ldots, x_{k-\tau}]$. Every delay vector has a corresponding target, namely next sample x_k. Note that τ is time lag which is set to unity for all of the simulations here.

In order to represent time series in phase space accurately and get the best predictability, the optimal embedding dimension must be determined before performing DVV analysis. The optimal embedding dimension can be determined by trial and error method, in which a number of DVV analyses are performed for different values of *m*. The *m* value which yields the lowest target variance, σ^{*2}, will be selected. For the simulations performed for this paper, the target variances were computed for *m* values between 2 and 40.

Using the selected optimal embedding dimension *m*, the DVV method can be performed as follows:

- Initially, we have original time series x(t) in which t=1...N;

1. Generate the target vector depending on the embedding dimension *m*, in which the target vector is Y={ x(k) | k=m...N};
2. Calculate the variance of the target vector, σ^2_x;
3. Determine delay vectors using the number of delay vectors parameter, Nn, such that Nn delay vectors are obtained from original time series;
4. Calculate the Euclidean distance between Nn delay vectors and N-m delay vectors that is generated from original time series (i.e: DV(1)=x(1)..x(m), DV(2)=x(2)..x(m+1),...,DV(N-m)=x(N-m)..x(m));
5. Calculate mean, μ_d, and standard deviation, σ_d, of all pairwise distances obtained in step 4;
6. Generate the sets $\Omega_k(r_d)$ by grouping DVs that are closer to x(k) than a certain distance r_d such that; $\Omega_k(r_d)=\{x(i)| \, \| x(k)-x(i) \| < r_d \}$.

- The $r_d(n)$ is computed as:

$$r_d(n) = (\mu_d - n_d * \sigma_d) + \frac{2 * n_d * \sigma_d * n}{N_{tv} - 1}, \; n = 1 \ldots N_{tv}, \tag{1}$$

where n_d is the maximal span parameter which is used to determine the range of standardized distances to consider and N_{tv} is the number of evaluation points for which the target variances are computed such that $N_{tv} = 25 * n_d$;

7. For every set, $\Omega_k(r_d)$, compute the variance of corresponding targets, $\sigma_k^2(r_d)$;
8. Normalise the averages of variances by the variance of target vector, σ^2_x, that yields the target variance, σ^{*2}, which is the inverse measure of predictability of the time series,

$$\sigma^{*2} = \sum \frac{\frac{1}{N}\sum_{k=1}^{N} \sigma_k^2}{\sigma_x^2}. \tag{2}$$

- Its worthy to note that the variance estimates will be reliable only if the $\Omega_k(r_d)$ set contains at least 30 delay vectors [7].

The $r_d(n)$ distances are normalised to have zero mean and unit variance. Plotting normalised distances versus target variance, σ^{*2}, will result in DVV plots.

The DVV plots of original and surrogate time series can be combined in a scatter diagram. The target variances are averaged for surrogate time series and are plotted against those of original time series for corresponding normalised distances. This can be obtained by calculating the root mean square error (RMSE) between the degree of unpredictability of original time series and average degree of nonlinearity of surrogate time series. This degree of unpredictability can be computed as

$$t^{DVV} = \sqrt{\left\langle \left(\sigma^{*2}(r_d) - \frac{\sum_{i=1}^{Ns} \sigma_{s,i}^{*2}(r_d)}{N_s} \right)^2 \right\rangle_{,valid \; r_d}}. \tag{3}$$

IV. Results

Figure 1 shows the non-linearity percentages of each channel for different mental activities. The channels stand for positions C3, C4, P3, P4, O1, and O2 respectively defined by 10-20 system. These results were obtained by averaging the non-linearity percentages of seven subjects for each channel. From Figure 1, the highest percentage of non-linearity was detected in channel P4 whereas the lowest percentage of non-linearity was detected in channel O1. It is also obvious that the percentage of non-linearity did not vary significantly for different channels.

F. Ibrahim, N.A. Abu Osman, J. Usman and N.A. Kadri (Eds.): Biomed 06, IFMBE Proceedings 15, pp. 451-454, 2007
www.springerlink.com ' Springer-Verlag Berlin Heidelberg 2007

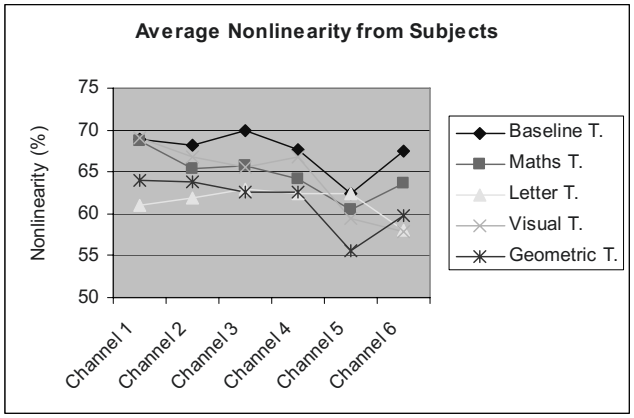

Fig. 1 The average nonlinearity from subjects

Figure 2 shows the non-linearity percentage of each mental activity. These results were obtained by averaging the percentage of non-linearity from six channels for every mental activity. From Figure 2, the highest percentage of non-linearity (68%) was obtained from baseline activity whereas the lowest was obtained from letter composing activity and geometric figure rotation activity.

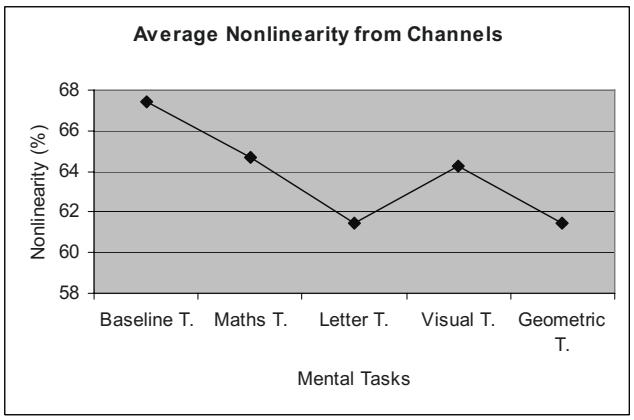

Fig. 2 The average nonlinearity from channels

The overall results show that when the EEG signals were segmented into smaller parts, approximately 65% of them were non-linear. However, changing the length of segments would require a re-analysis of the non-linearity.

V. Conclusion

In this paper, the non-linearity of mental activity EEG signals for BCI designs has been investigated. The EEG data recorded from seven subjects while they were performing mental activities were used in this study. The results indicated that approximately 65% of the segments were non-linear. Accordingly, we conclude that it is more appropriate to use non-linear modelling methods for mental activity based EEG.

Acknowledgment

The author would like to acknowledge the assistance of Dr. C. Anderson of Colorado State University, USA for giving permission to use EEG data.

References

1. Keirn Z A, Aunon J I (1990) A new mode of communication between man and his surroundings. IEEE Transactions on Biomedical Engineering 47:1209-1214
2. Palaniappan R (2006) Utilizing gamma band spectral power to improve mental task based brain computer interface design. IEEE Transactions on Neural Systems and Rehabilitation Engineering 14 (3): 1-6
3. Palaniappan R, Paramesran R, Nishida S, Saiwaki N (2002) A new brain-computer interface design using fuzzy ARTMAP. IEEE Transactions on Neural Systems and Rehabilitation Engineering 10:140-148
4. Gautama T, Van Hulle M M, Mandic D P (2003) Indications of nonlinear structures in brain electrical activity. Physical Review E 67 046204
5. Theiler J, Eubank S, Longtin A, Galdrikian B, Farmer J D (1992) Testing for nonlinearity in time series: The method of surrogate data. Physica D 58:77-94
6. Schreiber T, Schmitz A (1996) Improved surrogate data for nonlinearity tests. Phys. Rev. Lett. 77:635-638
7. Gautama T, Van Hulle M M, Mandic D P (2004) On the characterization of the deterministic/stochastic and linear/nonlinear nature of time Series. Technical Report DPM-04-05, Imperial College, London.

Address of the corresponding author:

Author: Tugce Balli
Institute: Computer Science Dept., University of Essex
Street: Wivenhoe Park
City: Colchester, CO4 3SQ
Country: United Kingdom
Email: tballi@essex.ac.uk

F. Ibrahim, N.A. Abu Osman, J. Usman and N.A. Kadri (Eds.): Biomed 06, IFMBE Proceedings 15, pp. 451-454, 2007
www.springerlink.com ' Springer-Verlag Berlin Heidelberg 2007

Heart Rate Variability Characterization Using a Time-Frequency Based Instantaneous Frequency Estimation Technique

MB Malarvili [1], L. Rankine [1,] M. Mesbah [1], P. B. Colditz [1] and B. Boashash [1, 2]

[1] Perinatal Research Centre, University of Queensland, Herston, Australia
[2] University of Sharjah, UAE

Abstract— **In this paper, a new method for characterizing the newborn heart rate variability (HRV) is proposed. The central of the method is the newly proposed technique for instantaneous frequency (IF) estimation specifically designed for nonstationary multicomponen signals such as HRV. The new method attempts to characterize the newborn HRV using features extracted from the time–frequency (TF) domain of the signal. These features comprise the IF, the instantaneous bandwidth (IB) and instantaneous energy (IE) of the different TF components of the HRV. Applied to the HRV of both normal and seizuresuffering newborns, this method clearly reveals the locations of the spectral peaks and their time-varying nature. The total energy of HRV components, ET and ratio of energy concentrated in the low-frequency (LF) to that in high-frequency (HF) components have been shown to be significant features in identifying the HRV of newborn with seizures.**

Keywords— **Heart rate variability, time-frequency distribution, component linking, instantaneous frequency.**

I. Introduction

Analysis of HRV has become a major non-invasive tool for assessing the disturbance in autonomic nervous system (ANS) regulation. The ANS has two branches; the sympathetic and parasympathetic. The separate rhythmic contributions from sympathetic and parasympathetic activities modulate the heart rate, and thus the RR intervals in the ECG, at distinct frequencies. In newborns, sympathetic and parasympathetic activities manifest themselves in the low frequency (LF) and the high frequency (HF) components of the HRV respectively. The mid frequency (MF) component is known to be both parasympathetically and sympathetically mediated [1].

The components of HRV, traditionally estimated using spectral analysis techniques [2], commonly exhibit 3 prominent peaks located in the LF, MF and HF bands of the spectrum. This spectrum is usually obtained from a short term recordings of newborn HRV. The locations of these frequency bands vary depending on the researchers. Currently, the most commonly recommended ones for newborns are [0.01 0.05] Hz for LF, [0.05 0.2] Hz for MF, and [0.2 1] Hz for HF [1]. Since the traditional spectral analysis methods depend on the assumption of stationarity, they can only provide averaged information about the signal frequency content. Information related the time evolution of the spectral components is obscured. HRV, as most biological signals, is a non-stationary signal. This means that the location of the spectral peaks (frequency) and the spread of these peaks (bandwidth) may vary with time. To overcome the limitations of the stationary techniques, non-stationary methods such as time-frequency distribution (TFD) are required [3].

The TFD of a signal represents its energy density in the joint time-frequency domain where the most valuable information is encoded in the IF of the different TF components. These IFs not only show the TF regions where the signal energy is concentrated but also how these regions are changing with time. TF-based techniques have been used in [4, 5, 6] to estimate the instantaneous parameters of HRV in the process of identifying cardiac abnormalities. However, the existing methods require *a priori* selection of the frequency bands of interest in order to decompose the HRV into band-limited monocomponent signals. This requirement is dictated by the fact that a single IF is only meaningful for monocomponent signals. These are the signals with only one time-varying continuous spectral concentration [7]. In the case of HRV, which is multicomponent [8], the signal s energy is locally distributed at and around two or more frequency peaks. *A priori* selection of the frequency bands is subjective and usually inaccurate since these bands are patient-dependent and can be strongly affected by the ANS state (healthy vs. diseased), age and physiologic conditions (body position, breathing frequency, etc) [9].

Recently, a new IF estimation method specifically designed for multi-component signals was proposed [10]. This method uses image processing techniques to estimate the number of TF components and extract their individual IFs. This IF estimation method has the advantage that it does not require a priori information about the number of frequency bands of interest and their locations. This characteristic makes it very suitable for the analysis of HRV. In this paper, we propose using this new approach to accurately extract the components of HRV. Applied to the HRV of normal newborns and newborns with seizure, this technique clearly reveals the locations of the time-varying spectral peaks. The extracted HRV components are further characterized by their

F. Ibrahim, N.A. Abu Osman, J. Usman and N.A. Kadri (Eds.): Biomed 06, IFMBE Proceedings 15, pp. 455-459, 2007
www.springerlink.com ' Springer-Verlag Berlin Heidelberg 2007

IE and IB. The purpose of this HRV characterization is to determine the parameters capable of distinguishing normal newborns from those having seizure. Qualitative changes in ANS during neonatal seizure have been reported in the literature [11, 13]. The goal of this paper is to try to quantify the HRV changes during seizure to be used as features in our planned automated newborn seizure detection.

II. METHODS

A. IF Estimation Technique based on TFD

The process of extracting the IFs from the HRV is composed of the following stages:

Preprocessing: The smoothed nonlinear energy operator (SNEO) is used to localize and extract the R points (the maximum point of thr R wave) from the newborn ECG [8]. The RR interval time series is obtained as the time difference between consecutive R points. The RR interval series is transformed into an evenly sampled signal using Berger's algorithm [12] and then resampled at 2 Hz. It was shown that this technique outperforms other existing techniques in terms of the reduction of energy of harmonics and artifacts [12]. The inverse of the equidistantly sampled RR time series is called the instantaneous heart rate (IHR). The IHR is taken as a measure of the heart rate variability in our present study.

TF Mapping: There are a large number of TFDs that can be used to map a signal from the time domain to the time-frequency domain. The choice of a suitable TFD depends on both the characteristic of the signal under analysis and on the application [3]. In this study we restrict ourselves to the class of quadratic TFDs represented by the following general expression [3]:

$$\rho_Z(t,f) = \iiint e^{j2\pi(\nu t-\nu u-f\tau)} g(\nu,\tau) z(u+\frac{\tau}{2}) z^*(u-\frac{\tau}{2}) d\nu du d\tau \quad (1)$$

where $z(t)$ is the analytic associate of the real signal $s(t)$ [3]. The function $g(\nu,\tau)$ defined in Doppler-lag (ν,τ) domain is known as the TFD kernel and determines the characteristics of the TFD.

In a previous study [8], a number of TFDs was used to represent the HRV signals. It was found that modified-B distribution (MBD) realizes the best compromise in terms of cross-term reduction and TF resolution and as a consequence has been used in our analysis. The kernel for MBD is given by

$$\left|\Gamma(\beta + j\pi\nu)\right|^2 \Big/ \Gamma^2(\beta) \quad (2)$$

where $\Gamma(.)$ stands for the gamma function and β is a real, positive number that controls the trade off between components resolution and cross-terms suppression [3]. The optimal value of β was found to be around 0.01.

TFD Local Peaks Extraction: At this stage, the TFD is treated as a 2D image whose local maxima (peaks) are extracted using the first and second order partial derivatives, with respect to frequency. A binary image, $B(t,f)$, is then obtained by assigning the value one to the *(t,f)* locations which represent a maxima as well as meet the threshold criterion around $\rho_z(t,f) > \delta = 0.1 \times \max(\rho_z(t,f))$. All other (t,f) locations are assigned the value zero.

Component Linking: A linked component in $B(t,f)$ is a continuous function $f(t)$ of local maxima. In other words, a linked component is an approximation of the IF of a local TF component. The linked component is detected using connectivity analysis and thresholding. The connectivity analysis checks the relationship between each pixel of $B(t,f)$ and its neighbors in order to decide whether the pixels belong to the same IF. The size of neighboring set to be used for this purpose is carefully chosen to avoid the issue of false component linking [10]. A 12-connected neighboring set is used in this paper. A threshold is used to only account for linked components (or IFs) whose durations are larger than a predefined value. In this paper, this value is chosen as the minimum time duration of the IF, α. We found that α = 30s was optimal for our database.

B. Application

The proposed method is tested on HRV obtained from the ECG recordings of newborns admitted to the Royal Brisbane and Women Hospital, Brisbane, Australia. The one channel newborn ECG was recorded simultaneously along with 20 channels of Electoencephalogram (EEG). The EEG seizure were identified and annotated by a neurologist. In the present study, we analyzed 39 seizure and 12 non-seizure epochs of 64 seconds each from 8 newborns. The ECG was sampled at 256 Hz.

Figure 1 and 2 show the result of applying the proposed method to HRV related to non-seizure and seizure epochs respectively. Figures 1(a) and 2(a) represents the time series (left plots), the joint TFDs (centre plots), and the spectra (bottom plots) of the HRV related to non-seizure and seizure newborns respectively. It is clear from these plots that that the TF representation is much more infromative then the time or frequency domain plots. Figures 1(b) and 2(b) show the three extracted IFs from the TFDs along with their means and ranges. The number and locations of IFs obtained using the prposed method give a more accurate

F. Ibrahim, N.A. Abu Osman, J. Usman and N.A. Kadri (Eds.): Biomed 06, IFMBE Proceedings 15, pp. 455-459, 2007
www.springerlink.com ' Springer-Verlag Berlin Heidelberg 2007

characterization of the different HRV components than that provided by the spectrum. The different frequency bands (LF, MF and HF) are clearly separated and their time-varying nature clearly exhibited.

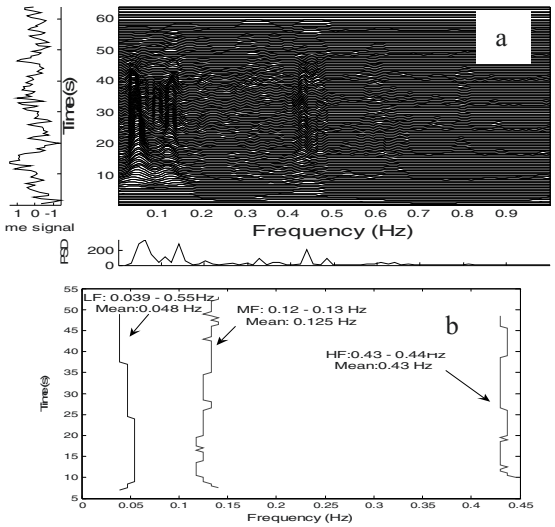

Fig 1: (a) TFD of HRV related to non-seizure, (b) Extracted IFs with its means and frequency ranges.

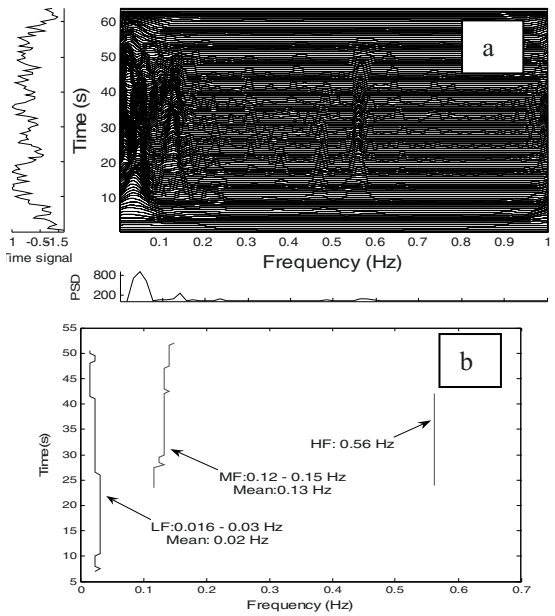

Fig 2: (a) TFD of HRV related to seizure, (b) Extracted IFs with its means and frequency ranges.

From these figures, it is evident that the HRV related to seizure has higher energy in LF compared to non-seizure while it is significantly lower in HF. This indicates that the newborn seizure manifest itself in both the LF (sympathetic activity) and the HF (parasympathetic activity) of the HRV. Furthermore, we have found that 61.54% of seizure epochs have 3 distinct components and 38.46% of them have only 2 components. However, 100% of the non-seizure epochs have one distinct component at each frequency band. Figure 3(a) and (b) show an example of the HRV related to seizure which has 2 components.

The energy in LF is significantly high. Absence of the HF component has two possible interpretations. It may indicate that the respiration rate for the newborn with seizure tends to shift to a lower rate causing reasonably high energy magnitude in MF. This is supported by the facts that the HF is attributed to the respiration rate and the MF is both parasympathetically and sympathetically mediated. Decreased respiration rate is a well-documented symptom of newborn during seizures [11]. The second interpretation is the presence of apnea. Apnea during neonatal seizures has been reported in [13]. The reduction in complexity of HRV as illustrated by the reduction in the number of TF components and their shorter time durations observed during seizure is supported by results in [14] which reported that the complexity of HRV is reduced in infants with brain injuries compared to the healthy ones.

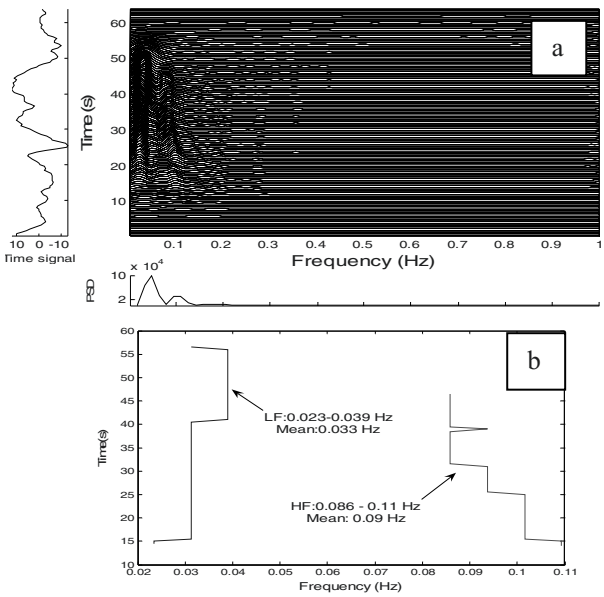

Fig 3: (a) TFD of HRV related to seizure, (b) Extracted 2 IFs with its means and frequency ranges.

F. Ibrahim, N.A. Abu Osman, J. Usman and N.A. Kadri (Eds.): Biomed 06, IFMBE Proceedings 15, pp. 455-459, 2007
www.springerlink.com ' Springer-Verlag Berlin Heidelberg 2007

C. Estimation of the Instantaneous TF Parameters.

The characteristics of each HRV components are further studied by means of IE and IB. The IE is measured as the instantaneous amplitude of a component, extracted from the TFD. The spread of each HRV component is measured by means of the IB or the standard deviation from IF. Here, the IB refers to bandwidth of instantaneous spectrum at every time instants when the energy of the respective component drops by half (the 3 dB energy). Figure 4 shows IB for an instantaneous spectrum at t = 30s for the LF component in Figure 1.

For each HRV component, we explore the mean IF, mean IB, mean ET and the mean ratio of IE concentrated in the LF to HF peaks (LF/HF) during non-seizure and seizure. All the features were normalized for easy comparison.

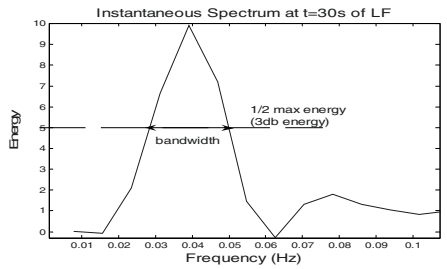

Fig 4: IB for instantaneous spectrum of the LF at t = 20s in Figure 1.

III. Results and Discussion

A receiver operating characteristics (ROC) is used to acquire appropriate sensitivity (Sn), specificity (Sp), statistical significance (p-value), the area under the ROC curve (AUC) and the 95% confidence interval (CI) of AUC for all the parameters mentioned to identify the best features that can be used to distinguish the seizures from the non-seizure newborns. The results are shown in Table 1. A p-value < *0.05* is considered statistically significant. If the lower limit of the CI for the AUC is >0.5, the feature tested is considered to have discriminatory potential. ROC is also used to determine the best cut-off value to differentiate the non-seizure and seizure.

From the table, we can see that mean IF and IB for LF and HF could not reliably discriminate between newborn with and without seizure. For this analysis only 24 epochs of seizure related HRV were used (61.54% of which had 3 HRV components). The table shows that there is no considerable difference in the location of the spectral peak in LF and HF for newborn with seizure and non-seizure. The remaining 38.46% of seizure related HRV epochs had only 2 components which is a significant feature to differentiate the seizure and non-seizure newborns. Thus, mean IF and IB were not found in our study to be efficient features for the classification of seizure and non-seizure.

The HRV related to seizures can best be discriminated from the ones related to non-seizure using the mean ET (92.31% of Sn and 91.67% of Sp) and mean of LF/HF ratio (94.87% of Sn and 91.67% of Sp). The optimal threshold was found to be 0.05257 and 0.3028 respectively. These result show that the newborn seizure corresponds to a greater total energy concentration in HRV compared to the non-seizure ones. The LF/HF ratio tends to increase in HRV related to seizure and decreases in the non-seizure ones. This is due to the decreased IE in the HF and significantly increased IE in the LF for the case of seizure.

IV. Conclusions

Accurate components of HRV were extracted using a recently developed TF-based multicomponent IF estimation technique. The components are clearly separated and their time-varying nature clearly exhibited. We also explored the discriminating capability of IF, IB, ET and LF/HF ratio. The results obtained so far showed that ET and LF/HF ratio are potentially good features to discriminate between seizure and non-seizure. Incorporating these features in one of our previously developed EEG-based newborn seizure detector is expected to enhance its overall robustness.

Table 1 Analysis of TF Parameters using ROC

Features	*Sn (%)*	*Sp (%)*	*AUC(CI)*	*p*
MeanIF(LF)	84.62	33.33	0.5556(0.3653-0.7458)	<0.5637
MeanIF(HF)	41.03	83.33	0.5876(0.4047- 0.7706)	<0.3626
MeanIB(LF)	56.41	58.33	0.5470(0.3557- 0.7383)	<0.6252
MeanIB(HF)	71.76	50.00	0.6389(0.4763- 0.8015	<0.1490
Mean ET	**92.31**	**91.67**	**0.8889(0.7642- 1.014)**	**<0.0001**
MeanLF/HF	**94.87**	**91.67**	**0.9690(0.9195- 1.019)**	**<0.0001**

References

1. E. Longin, T. Schaible, T. Lenz, S. Konig, (2005). Short term heart rate variability in healthy neonates: normative data and physiological observations , *Early Human Development, 81, pp.663-71.*
2. Task Force of the Euro. Soc. of Cardiol., the North Amer. Soc. of Pacing and Electrophysiol., (1996). Heart rate variability: standards of measurement, physiological interpretation and clinical use", *Circulation, 93, pp. 1043-65.*
3. B. Boashash, (2003) *Time-Frequency Signal Analysis and Processing: A Comprehensive Reference*, Elsevier, Oxford.
4. J. Villa, F. Palacios, J. Presedo, M. Fernandez-Deigado, P. Felix, S. Barro. (1997): Time-frequency analysis of heart-rate variability: an improved method for monitoring and diagnosing myocardial ischemia , *IEEE Eng. in Med. and Biol.*, pp.119-126.

F. Ibrahim, N.A. Abu Osman, J. Usman and N.A. Kadri (Eds.): Biomed 06, IFMBE Proceedings 15, pp. 455-459, 2007
www.springerlink.com ' Springer-Verlag Berlin Heidelberg 2007

5. H. G van Steenis, W. L. J. Matens, J. H. M. Tulen. (2002). Time-frequency parameters of heart rate variability: using instantaneous amplitude and frequency to unravel the dynamics of cardiovascular control process , *IEEE Eng. in Med. and Biol*., pp.46-58.
6. A. Monti, C. Medigue, L. Mangin. (2002): Instantaneous parameter estimation in cardiovascular time series by harmonic and time-frequency analysis , *IEEE Trans. on Biomed. Eng*., 49, pp. 1547-1556.
7. B. Boashash. (1992): Estimating and interpreting the instantaneous frequency of a signal - Part 1 & 2 , *Proc. of the IEEE,* 80, pp. 520-568.
8. MB Malarvili, M. Mesbah, B. Boashash (2006). Time-frequency analysis of heart rate variability for neonatal seizure detection , Phys. Eng. Sci. Med, pp. 67-72.
9. Y.Goren, L. R. Davrath, I. Pinhas, E. Toledo, S. Akselrod. (2006). Individual time-dependent spectral boundaries for improved accuracy in time-frequency analysis of heart rate variability , *IEEE Trans. on Biomed. Eng*., 53, pp. 35-42.
10. L. Rankine, M. Mesbah, B. Boashash. (2006): IF estimation for multicomponent signals using image processing techniques in the time-frequency domain , submitted to *Signal Processing.*
11. M. Rennie. (1997). Neonatal seizures , Eur J Pediatr 156, pp: 83 87.
12. H. N. Guimaraes, R. A. S. Santos. (1998): A comparative analysis of preprocessing techniques of cardiac event series for the study of heart rhythm variability using simulated signals , *Brazilian Journal of Medical and Biological Research*, 31, pp. 421-430.
13. S. L. Helmers, M. J. Weiss, G. L. Holmes, (1991). Apneic seizures with Bradycardia in a newborn , *J. Epilepsy, 44,pp.173-180.*
14. G Sugihara, W Allan, D Sobel, K D Allan. (1996). Nonlinear control of heart rate variability in human infants , *Proc Natl Acad Sci U S A., 93, pp: 2608–2613.*

Address of the corresponding author:

Email: nm.balakrishnan@uq.edu.au

F. Ibrahim, N.A. Abu Osman, J. Usman and N.A. Kadri (Eds.): Biomed 06, IFMBE Proceedings 15, pp. 455-459, 2007
www.springerlink.com ' Springer-Verlag Berlin Heidelberg 2007

Evaluation of ECG Compression via Optimal Bit Allocation on DCT Coefficients

N. Bouali, R. Zergui, D. Berkani

Laboratoire Signaux & Communications, Ecole Nationale Polytechnique, Algiers, Algeria

Abstract—**Transform compression consists to apply an orthogonal transform on a window of the signal, and then proceed to reduce the number of bits representing transform coefficients. The simplest transform compression algorithm is one which eliminate the transform coefficients under threshold fixed a priori, this kind of algorithm is known as zonal transform compression system [5]. Applying this algorithm on ECG provides us a compression ratio of three (CR=3) approximately with an error ratio of five percent (PRD=5%) [3] [6]. In this paper, we develop a DCT compression algorithm for ECG, based on optimal bits allocation. The test results show that this method improve compression performances in term of compression ratio (CR) and the error percent ratio (PRD).**

Keywords—**ECG, Transform Compression, DCT, Optimal bit allocation**

I. Introduction

The volume of *ECG* signal required to be stored and transmitted is increasing. The need for *ECG* signal compression stems from two main reasons: effective storage and effective real time transmission.

The compression of the signal is performed by removing redundancy. The redundancy exhibits itself in terms of statistical dependence between adjacent samples and the nonunifomity of the amplitude probability of the quantized signal Linear correlation between neighbouring samples may be removed, for example by various delta modulation methods or by linear prediction methods, while nonuniform amplitude probability may be handled by entropy coding. ECG compression methods have also been divided into three functional groups [4]:

1. Direct methods: where the samples of the signal are directly handled to provide the compression. Examples of the methods belonging to this group are: the turning point (TP) method, The amplitude zone time epoch coding (AZTEC) method, the coordinate reduction time encoding system (CORTES), delta code algorithms, sample skipping, and SLOPE.

2. Transformation methods: where the original samples are subjected to a linear transformation and the compression is performed in the new domain: Examples of methods belonging to this group are Fourier transformation, Fourier descriptors, K-L transformation, and Walsh transforms.

3. Parameter extraction methods: where a preprocessor is employed to extract some futures that are later used to reconstruct the signal. Examples of some method belonging to this group are peak picking, linear prediction methods, syntactic methods, and neural nets methods.

Performance criterion used to evaluate *ECG* compression algorithm must include two factors. The amount of compression and the resultant reconstruction error. The amount of compression is very often represented in terms of the compression ratio (*CR*), and is defined as the ratio between the rate of the compressed signal (in terms of bits per second) to the rate of the original signal. The compression may also be measured in terms of bits per samples. This type of representation is again not standard because it depends on the sampling frequency. The best way to represent the compressed signal is in terms of bits per second. Such representation has the advantage of directly providing the information rate of the compressed signal. In this sense it is independent of the input signal sampling frequency and quantization level.

Expressing the reconstruction error is a very difficult and challenging task. The definition of error must be made in the sense of the ability of the reconstructed signal to retain the diagnostic information. The only way to measure diagnostability is to perform a survey among a relatively large number of cardiologists who will evaluate strips of reconstructed signals and grade them. This is, of course, impractical for most cases. Most often, the error used in association with ECG compression algorithm is the percent rms difference (*PRD*) given by:

$$PRD = 100 \left[\frac{\sum (x(i) - y(i))^2}{\sum x^2(j)} \right]^{\frac{1}{2}} \quad (1)$$

The PRD don t take into account the diagnostability, it is therefore not a very good measure of the compression error.

II. Transform compression

The approach is to devide the input signal into a number of separate frequency components and encode each of these components separately. This division into frequency components removes the redundancy in the input and provides a set of uncorrelated inputs to the channel Fig.(1)

F. Ibrahim, N.A. Abu Osman, J. Usman and N.A. Kadri (Eds.): Biomed 06, IFMBE Proceedings 15, pp. 460-463, 2007
www.springerlink.com ' Springer-Verlag Berlin Heidelberg 2007

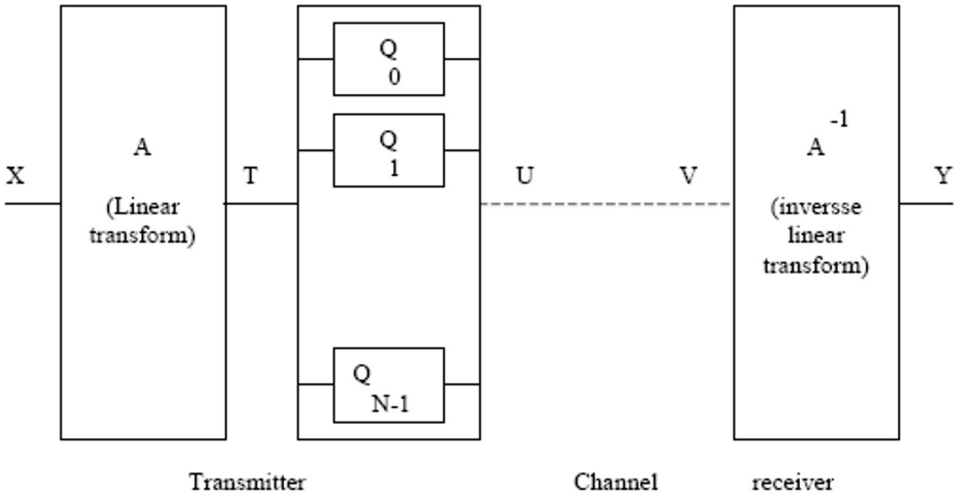

Fig. (1) Block diagram of transform compression system.

The efficiency of transform compression system will depend on the type of linear transform and the nature of bit allocation for quantizing transform coefficients. Fig.(1) is a block diagram of transform compression system. It is a waveform digitizing procedure where a block of *N* input samples *x(n)* is linearly transformed into a set of *N* transform coefficients *t(n)* (for example, a set of Fourier coefficients). The coefficients are then quantized for the transmission, and reconstruction of *x(n)* is obtained at the receiver using an inverse transform operation on quantized coefficients.

In fact, the problem of optimising a transform compression scheme can be stated as that of finding an orthogonal matrix, and then of finding a distribution (allocation) of bits R_k such the average coefficient error variance is minimised with the constraint of given average bit rate R.

$$R = \frac{1}{N}\sum_{k=0}^{N-1} R_k \tag{3}$$

The problem is to minimise, by mean of an optimum bit allocation, the reconstruction error. We arrive at an optimum bit allocation given by [1]:

$$R_k = R + \frac{1}{2}\log_2 \frac{\sigma_k^2}{\left[\prod_{j=0}^{N-1}\sigma_j^2\right]^{\frac{1}{N}}} \tag{4}$$

That depends only on the distribution of the coefficients variances $\{\sigma_k^2\}_k$. A coefficient with higher variance needs more bits than a coefficient of lower variance.

Practical quantizer for coefficient quantization have the constraint of having to use non-negative integers for the number of bits R_k obtained in the bit allocation procedure.

III. Design of compression scheme

Our work consists to develop an ECG s DCT compression algorithm based on optimal bits allocation, and to evaluate this algorithm using in laboratory ECG record sampled at 200Hz.

The optimal transform is Karhunen loeve transform (KLT). It is the transform resulting from the eigen decomposition of the auto-correlation matrix of the signal. The proposed algorithm was designed using discrete cosine transform (DCT). It is the sub optimal transform that give the best results [2].

The design is accomplished on the following steps:

- Chose the weight of analyse window, it must cover at least one pseudo-period of the signal. The pseudo period can be estimated at T=0.9 sc. That mean that the weight of the window is N>=180 samples, and we take N=184. We can obtain a matrix built of these windows. Each column is identical to a window of the signal (Fig.2).
- Apply the DCT on the signal represented by this matrix Fig.(3).
- Estimate the variance *S(k)* of each coefficient in the transform Fig. (4).
- Compute the number of bits *R(k)* given to each of transform coefficients Fig. (5).
- Estimate the maximum *Mx(k)* and minimum *Mn(k)* of each of transform coefficients.

F. Ibrahim, N.A. Abu Osman, J. Usman and N.A. Kadri (Eds.): Biomed 06, IFMBE Proceedings 15, pp. 460-463, 2007
www.springerlink.com ' Springer-Verlag Berlin Heidelberg 2007

With these parameters, we can design our algorithm:

- Calculate the resolution (Res) for each coefficient,
- Quantize each coefficients according to its resolution

```
Res = ( Max – Min ) ./ R
For each window : X
        T = [DCT] ( X )
        Q = round ( ( T – Mn ) ./ Res )
End
```

At reconstruction:

- apply the inverse DCT on the quantized coefficients.

```
Res = ( Max – Min ) ./ R
For each window : Q
        V = Res .* Q + Mn
        Y = [DCT-1] ( V )
End
```

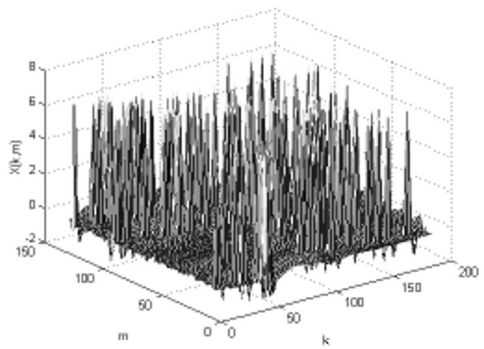

Fig. (2) ECG signal in matrix form.

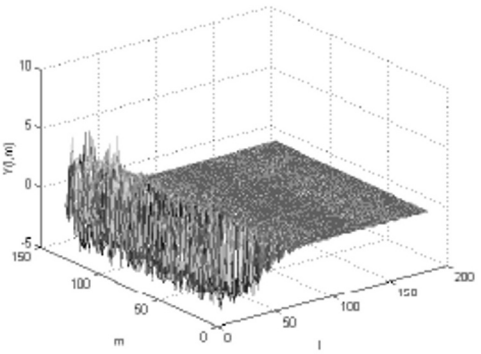

Fig. (3) DCT transform of ECG.

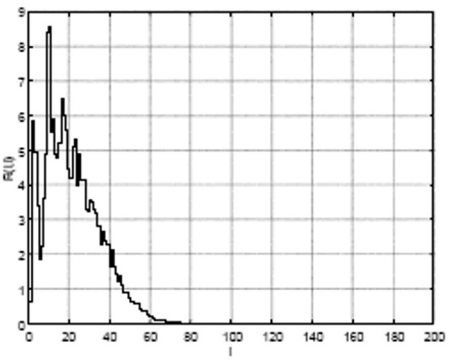

Fig. (4) Variances of DCT coefficients

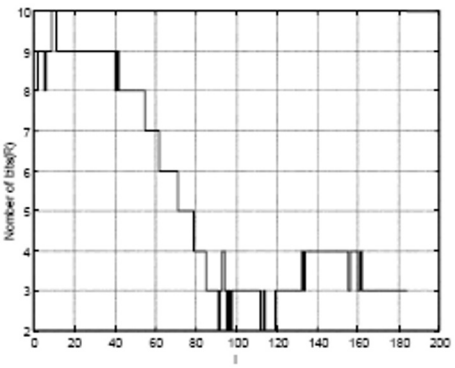

Fig. (5) Number of bits for each coefficient

IV. Results and discution

The proposed system was tested using inlaboratory record. It is an ECG record of a patient representing a normal ECG. The ECG signal was low pass filtered, sampled, and quantified at 200 Hz and 12 bits per sample Fig. (6). The performances of the algorithm are demonstrated in Fig. (7), Fig. (8) and Fig. (9).

Tests results prove that our algorithm give an interesting performances. The compression ratio is CR=4 with an error of PRD= 2%. The compression ratio can increase to CR=7 with an error of PRD=5%.

Visual quality of reconstructed signal show that this algorithm preserve the form of original signal.

When the compression ration (CR) increase upper than 8 the signal is deformed. The disadvantage of transform compression techniques face to practical implementations is the computational power which must be used in calculus of transform coefficients, even exist fast algorithms.

F. Ibrahim, N.A. Abu Osman, J. Usman and N.A. Kadri (Eds.): Biomed 06, IFMBE Proceedings 15, pp. 460-463, 2007
www.springerlink.com ' Springer-Verlag Berlin Heidelberg 2007

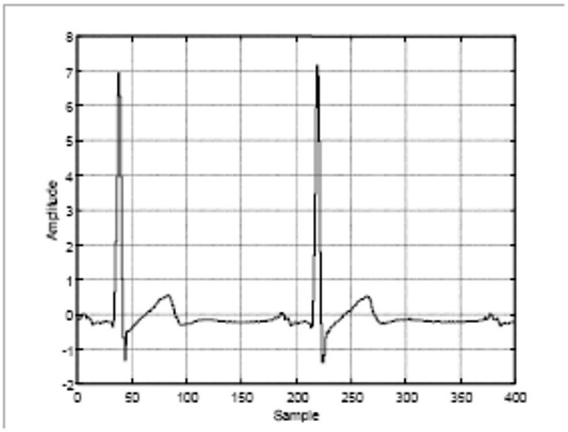

Fig. (6) Original ECG Signal.
Fs=200 Hz, Rate=2400 bits/sec

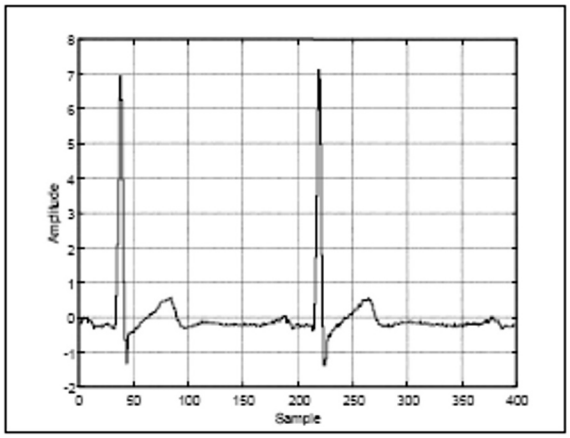

Fig. (7) Reconstructed signal
CR = 3.74, Rate = 641.30, PRD = 1.90%

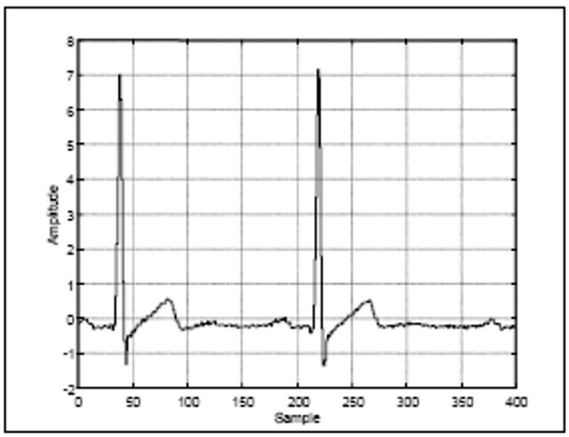

Fig. (8) Reconstructed signal
CR = 5.32, Rate = 451.09, PRD = 3.25%

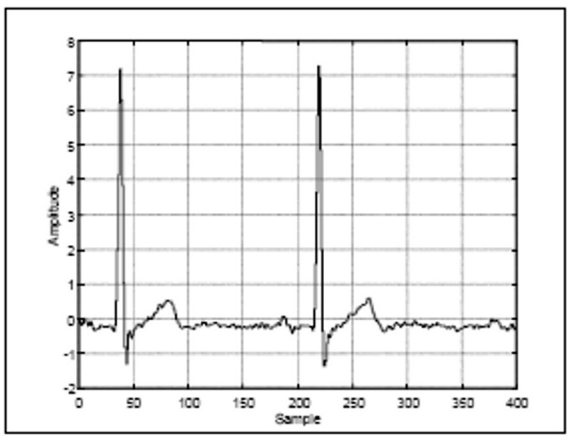

Fig. (9) Reconstructed signal
CR = 7.29, Rate = 329.35, PRD = 5.44%

V. Conclusion

Transform Compression of ECG is important to transmit or to save a lot of signals on a long time. Sub optimal transform are desired because the transform matrix is independent of the characteristics of the signal. Zonal compression limits the performance of compression. Optimal bit allocation gives good results in price of complexity of compression scheme.

References

1. N.S. Jayant & P. Nol, Digital coding of waveforms: Principles and applications to speech and video , Englewood cliffs, NJ: Prentice-Hall 1984.
2. N. Ahmed, and K. R. Rao « Discrete Cosine Transform » IEEE Trans. On Biomed. Eng.,Vol BME-22 ; Nov 1975.
3. S. Jalaleddine, « ECG data compression techniques - a unified approach » , IEEE trans. on biom. ing., vol 37, N° 4, April 1990.
4. Nave, Cohen, « ECG Compression Using Long-term Prediction » IEEE Trans. Biomed. Eng. Vol 40 , N° 9, 1993.
5. B.R.S. REDDY « ECG Data Compression Using Fourier Descriptors » IEEE Trans. Biomed. Eng. Vol.BME-33, N°4 , April1 986.
6. N. Bouali, Compression du Signal Electrocardiographique Th se de magister, ENP- Alger 1999.

F. Ibrahim, N.A. Abu Osman, J. Usman and N.A. Kadri (Eds.): Biomed 06, IFMBE Proceedings 15, pp. 460-463, 2007
www.springerlink.com ' Springer-Verlag Berlin Heidelberg 2007

Bio-Composting Process Development by SSF for Utilization Agro-Industrial Wastes

N.A. Kabbashi[1], MD.Zahangir Alam [1] and Muhammad Ainuddin[2]

[1] International Islamic University, Bioenvironmental Engineering Research Unit (BERU) Department of Biotechnology Engineering, 50728 KL, Malaysia

[2] International Islamic University, Department of Biotechnology Engineering, 50728 KL, Malaysia

Abstract **The wastes derived from oil palm industries are generated every year and becoming a great concern, consequently, an urgent development of bio-composting process has been investigated. Bio-composting is an environmental friendly bioconversion process where its products could be utilized as plant growth enhancement. In Malaysia about 50 million tons of Palm Oil Mill Effluents (POME) and about 40 million tones of Oil Palm Biomass (OPB) in forms of empty fruit bunches (EFB), oil palm trunks (OPT), and oil palm fronds (OPF) are generated from palm oil industries every year, the management practice pose significant environmental problems. This study was concerning about simple composting process using selected substrates, POME and EFB plus wheat floor as a co-substrate. The strains of P. chrysosporium, T. harzianum, A. niger (A 106, S 101), and Penicillium isolated from POME were used for effective bio-composting process. Tray bioreactor was used to evaluate the efficient composting process through solid state bioconversion. The composting time required to complete the process was two months and some parameters were determined to evaluate the compost quality. In the entire process merely, percentage of OM decreased to about 3% while total nitrogen content initially at 0.744 g/g increased to 2.96 g/g. The C/N ratio and GI achieved were 17 and 95 % respectively. The maturity of the compost could be reflected by C/N ratio, pH and GI measurement. The use of POME and EFB as mixed substrates with the induced microorganisms is a new composting trial where it has been expected to receive a good result in order to overcome a conventional composting process.**

Keywords— **Oil palm waste, microorganisms, C/N ratio, SSF, GI.**

I. Introduction

Since early 70s, palm oil industry has emerged as one of top industry in Malaysia and as a result many palm oil factories had emerged to process these fruits. The production of crude palm oil involves mechanical extraction process in which the fresh fruit bunches undergo sterilization, digestion and extraction of the oil. However, all of these processes generate palm oil mill effluent (POME) in which affecting the environment [1]. The environment had to be jeopardize in order to get highest profit. The suspended solids in POME are mainly oil-bearing lignocellulosic materials that come from fruit. Lignocellulosic is the major structural component of woody plants such as grass and represents a major source of renewable organic matter. Lignocellulosic consist of lignin, hemicellulosic, and cellulosic material. The chemical properties of the components of lignocellulose make them a substrate of enormous biotechnological value. The palm oil industry in Malaysia produces about 90 million tones of lignocellulosic biomass [2]. For instances, the oil palm biomass (OPB) produces about 40 million tonnes per year. This OPB can be categorized as a form of empty fruit bunches (EFB), oil palm trunks (OPT) and oil palm fronds (OPF) and the rest are palm oil mill effluent (POME). There are 7.0 million tones of oil palm trunks, 26.2 million tones of palm oil fronds and 23% of empty fruit bunch (EFB) per tone of fresh fruit bunch (FFB) processed in oil palm mill for re-plantation after about 20 to 25 years [3].

Much of the lignocellulosic waste is disposed by biomass burning, which is not restricted to developing countries alone, but it is considered a global phenomenon. In addition, the problem arises when all of this biomass is not being treated and left to rot in the plantations to provide some nutrient. Unfortunately, these wastes may create the environmental problems later due to high organic content accumulate on the ground. Therefore, environmental management is placing the greatest emphasis in waste minimization at source or recycling. Moreover, a growing awareness of the need not to pollute has forced this industry to look more closely at the milling operation. It is recommended to treat and manipulate the waste to produce the useful product. Therefore, bio-composting process promises a high potential on sufficiently solving the abundant wastes from agro-industries where in many cases, composting provided a viable alternative method for managing organic wastes [4].

Agro-industrial wastes are being produced or generated million tones per year such as waste from palm oil industries where it is estimated over 90 million tones were produced through out a year. The management of agro-industrial wastes should be selected with suitable techniques and technologies to minimize waste generation or re-use or recycling them to be raw materials for other productions. Wastes, if not efficiently maintained or treated, will create

F. Ibrahim, N.A. Abu Osman, J. Usman and N.A. Kadri (Eds.): Biomed 06, IFMBE Proceedings 15, pp. 464-468, 2007
www.springerlink.com ' Springer-Verlag Berlin Heidelberg 2007

mass problems that include human, living organisms, and environment.

Compost is a product produced ecologically and economically through chemical, physical and biological activities. Composting is commonly defined as a natural aerobic biochemical process in which thermophilic microorganisms transform organic materials into a stable soil-like, product. The process is well established and has been comprehensively documented in several literatures. Factors that influence microbial activity include temperature, oxygen concentration, pH, moisture content, carbon to nitrogen (C/N) ratio and particle size [5].

II. Materials and methods

Two bulk materials were used, which are palm oil mill effluent (POME) and empty fruit bunch (EFB). The equipment setup, samples, chemical and reagent, microorganisms and media composition were selected based on literature reviews. In general, sterilization is not required to fulfill this project.

Substrates and Co-substrate

Palm oil mill effluent (POME) and oil palm biomass (OPB) were obtained from a local palm oil mill manufacturer (Seri Ulu Langat Palm Oil Mill at Dengkil, Selangor, Malaysia). Co-substrate used in the experiment was wheat flour, for effective biodegradation of STP (sewage treatment plant) sludge compost using filamentous fungi [6].

Fungal Strain

Four different types of microorganisms had been used, served different function in biodegradable process. There were *Penicilium*, *Aspergillus*, *Tricorderma*, and *Phanerochaete chrysosporium*. The fungi were separated and maintained on Potato Dextrose Agar (PDA) plates for spore production and were incubated at 32°C until the entire plate is discovered by fungus. The best grow of the fungus were at seventh day.

Experimental procedures

According to the research done before, 50 L capacity of solid-state horizontal rotary drum bioreactor is the most suitable to perform this project. The period of incubation was two months where the sampling will be taken from 0, 10, 20, 30, 40, 50 and 60 day. Fermentation was done inside the solid-state horizontal rotary drum bioreactor. The process conditions set up for the process were maintained, included the pH which is in the range 5-7, temperature was at the ambient temperature (30 ± 2 °C), the moisture condition at 60-70%, the agitation was 10 minutes per day, and the aeration was 1 hour per day. The inoculum used was cultured inoculum about 5-10%.

III. Results and discussions

The experiment was carried out in the horizontal rotary drum bioreactor with the substrate and co-substrate which undergoes composting process for 60 days. Several fungi were inoculated inside the bioreactor that affects the result of compost. The mixing of the compost was done by rotating the bioreactor at 10 rpm for 10 minutes once a week through agitation. Whereby, the aeration was accomplished by means of an air compressor in which the air is sterilized by bubbling through sulphuric acid (2%) everyday.

pH of the water extract

From Fig.1, pH of the compost initially was 5.71. Within the composting period, the pH did not change very much and in the range of 5-6. This result may be described by [7] as the effect of the production of organic acids inside the bioreactor. As the next 20 days the pH is almost same, then it start to increase gradually at days 40 as the pH showed 6.4. The increasing phase of pH in alkaline was attributed to ammonification and mineralization of organic nitrogen through microbial activities. As the pH reached the highest point, it started to decrease to 5.6 at day 50 and 60.

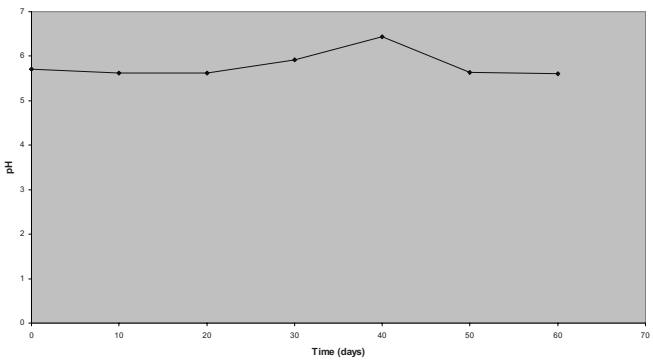

Fig. 1 Changes in pH as time increased

Color intensity/optical density of the water extract

Color intensity or optical density (OD) measurement is recognized as the most reliable parameter and more or less free from conceptual deficiencies compared to other estimation of the rate of biodegradation or compost maturity [8]. The OD of the water extract of compost at fixed wavelength could be appropriate test for compost biomaturity.

F. Ibrahim, N.A. Abu Osman, J. Usman and N.A. Kadri (Eds.): Biomed 06, IFMBE Proceedings 15, pp. 464-468, 2007
www.springerlink.com ' Springer-Verlag Berlin Heidelberg 2007

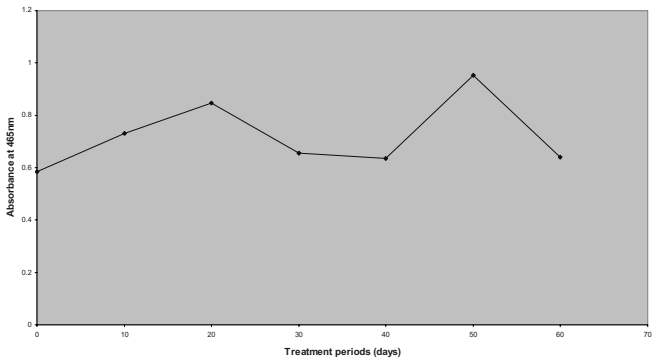

Fig. 2 Color intensity/OD profile

As in Fig. 2, the OD increase from 0.5 to 0.7 for the first 10 days and then increase to 0.8 for the next 10 days. From the figure, it can be seen that the OD is fluctuate within the composting days where the value start to decrease after day 20 and increase back at day 50. This fluctuation value can be described as the non-homogeneous product was taken during sampling time. The color of the water extract was changing to be darker as means of the presence of biomass and biochemical. The color was changed according to the growth of the fungal cells and spores. In composting process, different polymers, phenols, and organic acids are metabolized to secondary products and mineralize into simpler stable product [8]. Thus, [6] notified that the water extract of compost may have those organic constituents along with microbial cells and spores.

Protein assay

Protein assay is used as an indication of fungal biomass production which is positively correlated to soluble protein production in solid state bioconversion [9]. For this analysis, the protein assay was done in two distinctly experiment using the water extract and the solids material of the compost as seen in Fig. 3.

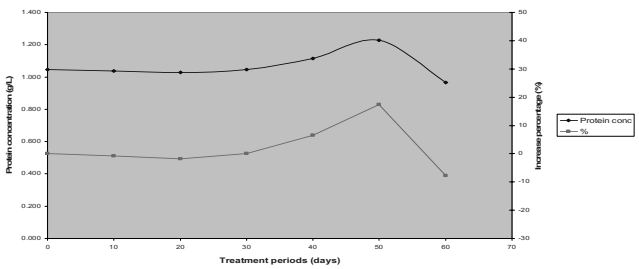

Fig. 3 Protein assay using water extract

Glucosamine assay

From Fig. 4, the glucose increased at the initial phase (day 10 and day 20) before it started to decrease between days 20 to 40 of composting time. The glucose concentration was increased at day 50 before started to decrease at day 60. This can be related due to the reduction of nutrients for the growth of fungi.

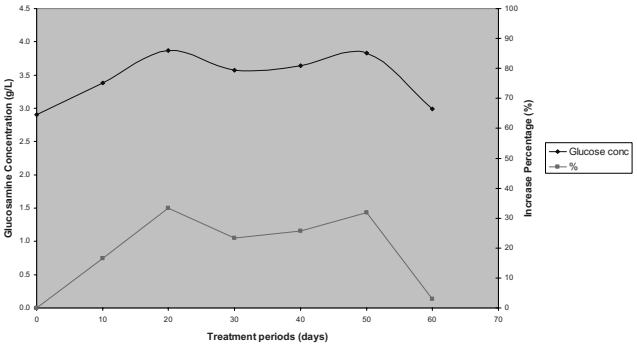

Fig. 4 Glucosamine assay as biomass indicator

It was a good compound to estimate the produced biomass from microorganism s growth. [6] described that glucosamine can be considered as a good parameter for estimation of the mycelia growth in solid substrate. Where, glucosamine is an essential component in chitin of mycelia cell wall, is a water soluble sugar and stable component. The accuracy of the glucosamine method in determining the fungal biomass depends on establishing a reliable conversion factor relating glucosamine to mycelia dry weight [4].

Organic Matter

Organic matter (OM) profile from Fig. 5 below showed that the OM content gradually decreased as the biodegradation time increased. The degradation of OM was related to the growth of microorganisms where [6] recorded in the bioconversion or composting process, the organic substrates were degraded into stabilized product. Hence, it also reduced the weight of the substrates.

F. Ibrahim, N.A. Abu Osman, J. Usman and N.A. Kadri (Eds.): Biomed 06, IFMBE Proceedings 15, pp. 464-468, 2007
www.springerlink.com ' Springer-Verlag Berlin Heidelberg 2007

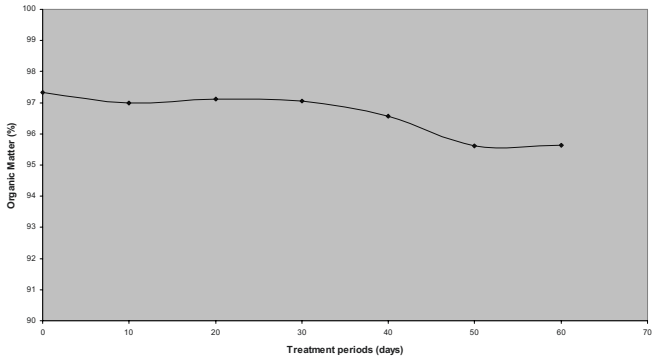

Fig. 5 Organic matter during composting of POME and EFB

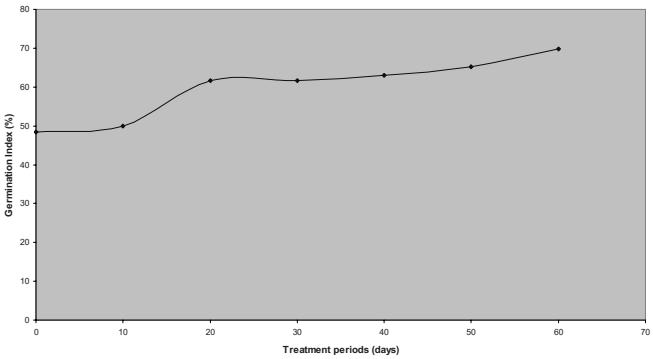

Fig. 7 Germination Index

C/N ratio

[10] described that the C/N ratio is an index traditionally used to evaluate the maturation of the end product (compost) of bioconversion, but the value cannot be used as an absolute indicator of compost maturation. The maturity of the compost is the important parameter in compost production process and its application. One of the practical ways is using C/N ratio evaluation, the C/N ratio is also widely used as an indicator of compost maturation and should become stable with time.

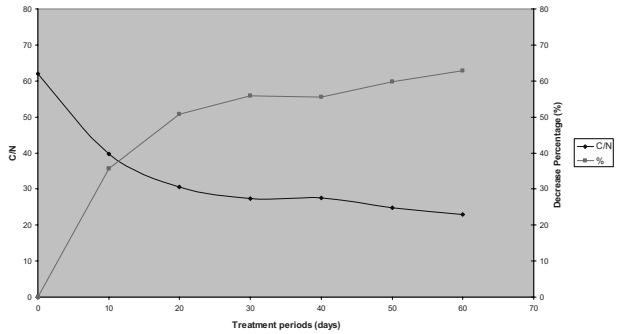

Fig. 6 Changes in C/N ratio profile of composting process

Germination Index (GI)

Germination index (GI) is the most sensitive parameter used to determine the level of toxicity of composts to seedlings and it is to test if the compost is mature [11] and [12]. In Fig. 7, the GI was at 48% in the zero days and slightly increased to 50% at day 10 of composting. By the inoculation of *Penicillium* at day 45, the GI was slightly increased to 60% and continuously increased within the treatment period. A GI value of 50 % has been used as an indication of phytotoxic-free compost [11], and a GI of more than 80 % is considered mature compost [13]. From this result, it can be concluded that the compost product is phytotoxic-free but yet is immature.

Temperature profile

For this study, there were no much differences in temperature during treatment period. The temperature was 27.5 at 0 day and increase to 27.8 at day 10 before decreasing to 27.4 at day 20. The stable value in temperature can be describe as high humidity, very closed and confined vessel. The temperature increase indicate the growth of microorganism inside the bioreactor generate heat during composting period.

IV. Conclusions and Recommendations

The study of the bio-composting process by solid-state bioconversion utilizing palm oil mill effluent (POME) and empty fruit bunch (EFB) were studied in lab scale (70 Litre Fermenter). From the research it is found that horizontal rotary drum bioreactor was the most suitable to run this study. Moreover, the batch process was conducted to run the experiment under unsterilized conditions. To make this solid-state bioconversion using composting technique become effective, several parameters were controlled instead of optimizing the process condition. pH, temperature, the moisturization, agitation and aeration. The inoculum used was cultured inoculum.

The study was carried out by utilizing POME and EFB as main substrates, wheat flour as a co-substrate, and undergoes composting process for 60 days inside horizontal rotary drum bioreactor. In addition, the inoculation of microorganisms likes *Phanerochaete chrysosporium, Trichoderma harzianum, Aspergillus niger, Penicillium sp* help to achieve good compost. The end product can be considered as good compost when several parameters like the C/N ratio, GI and glucosamine assay met their standard. The C/N ratio range from 25 to 30, the GI is up to 70% which is phyto toxic free and merely become mature compost. In this study, 4 different microorganisms were used,

F. Ibrahim, N.A. Abu Osman, J. Usman and N.A. Kadri (Eds.): Biomed 06, IFMBE Proceedings 15, pp. 464-468, 2007
www.springerlink.com ' Springer-Verlag Berlin Heidelberg 2007

and only *Trichoderma harzianum* were isolated from the POME. Other microorganisms like *Phaneochareate chrysosporium*, *Penicillium sp* and *Aspergillus niger* were cultured from single strain. The study can be improved by using the mixed culture, which can give a good degradation of cellulose and hemicellulose by producing cellulolytic enzyme. The study can be improved also by optimizing process condition to enhance the bio-composting process by solid state bioconversion

Acknowledgment

The authors wish to express their sincere thanks to IIUM, Kulliyyah Engineering, and department of Biotechnology engineering for sponsoring the project and helping during running the experiments.

References

1. MA, A.N., S.A. Cheah and M.C. Chow. (1993) Current status of palm oil processing waste management. In: Waste Managaement in Malaysia: Current Status and Prospects for Bioremediation . B.G. Yeoh et al. (Eds.), 111-136
2. Malaysian Palm Oil Board(MPOB). Malaysia. (2003)
3. SIRIM, Malaysia. (2003)
4. Sharma, P.D, Fisher, P.J and Webster, J. (1997) Critique of the chitin assay technique for the estimation of fungal biomass. Transactions of British Mycological Society. 69 479-483
5. Miller, F.C (1993) Composting as a Process Based on the Control of Ecologically selective *Factors in Soil Microbial Ecology* (Metting, F.B, ed.) Marcel Dekker
6. Molla A. B., Fakrul l-razi A. Alam M. Z. (2004) Evaluation of solid-state bioconversion of domestic wastewater sludge as a promising environmental-friendly disposal technique. Water research 338 4143-4152
7. Charest M. H., Beauchamp C. J (2001) Composting of de-inking paper sludge with poultry manure at three nitrogen levels using mechanical turning: behavior of physico-chemical parameters, Department de Phytologie, Faculti des Science de l Agricultire et de l Alimentation, Universite Laval, sainte-Foy, Que, Canada GIK 7P4
8. Mathur, S. P., Owen, G., Dinel, H. and Schnitzer, M. (1993) Determination of compost biomaturity. I. Literature review. Biological agriculture and horticulture. 10 65-85
9. Zheng, Z. and Shetty K. (1998) Cranberry processing waste for solid state fungal inoculant production. Process biochem 33 (3) 323-328
10. Fang, M., Wong, J. W. C. (1999) Effects of lime amendment on availability of heavy metals and maturation in sewage sludge composting. Environmental Pollution 106:83-89
11. Zucconi, F, Pera, A. and Fote, M. (1981) Evaluation of Toxicity of Immature Compost. BioCycle 3&4 54-57
12. Wong, J. W. C., Mak, K. F., Chan, N. W., Lam, A., Fang, M., Zhou, L. X., Wu, Q. T. and Liao, X. D. (2001) Co-composting of soybean residues and leaves in Hong Kong. Bioresources Technology 76:99-106
13. Wei, Y. S., Fan, Y. B., Wang, M. J. and Wang, J. S. (2000) Composting and compost application in China. Resource, Conservation and Recycling 30 277-300

Address of the corresponding author:

Author: Nassereldeen Ahmed kabashi
Institute: IIUM, Malaysia
Street: Jalan Gombak
City: KL
Country: Malaysia
Email: nasreldin@iiu.edu.my

F. Ibrahim, N.A. Abu Osman, J. Usman and N.A. Kadri (Eds.): Biomed 06, IFMBE Proceedings 15, pp. 464-468, 2007
www.springerlink.com ' Springer-Verlag Berlin Heidelberg 2007

Biodegradation of 2-methoxyethanol under aerobic conditions by bacterial isolate *Pseudomonas* sp. strain VB

Ekhaise Frederick Osaro

Department of Microbiology, University of Benin, P. M. B 1154, Benin City, Nigeria

Abstract— **Four bacterial isolates from four different environmental samples (agricultural soil, compost soil and sewage sludge- anaerobic and aerobic wastewaters) were screened for their ability to mineralize 2-methoxyethanol under aerobic conditions. Isolate from anaerobic sewage wastewater was most efficient with an average of 48.6mmol/day mineralisation capacity. Morphological, physiological, biochemical and molecular characterization of the isolate showed that the strain, designated VB is of the genus *Pseudomonas*. 16S rRNA sequence analysis showed that the organism is related to *Pseudomonas putida* at 99.9% and *Pseudomonas plecoglossicida* at 99.8% similarity level. It is related to members of the genus *Pseudomomas* belonging to the rRNA group 1 within the gamma (γ) *Proteobacteria*. The G+C content 64.5±0.8mol% is within the range characteristic of the genus *Pseudomonas.* In a time course experiment *Pseudomonas* sp. strain VB was grown in 2-methoxyethanol, ethylene glycol, glycollate, glyoxylate, oxalate and methanol. Strain VB was able to utilize all proposed intermediates except methanol. Comparable growth characteristics of *Pseudomonas* sp. strain VB grown in 2-methoxyethanol and proposed intermediates showed significant molar growth yields. These results indicate that ethylene glycol, glycollate, glyoxylate and oxalate might be intermediates in the degradation pathway of 2-methoxyethanol. Thus a reaction sequence: 2-methoxyethanol → ethylene glycol → glycollate → glyoxylate → oxalate is been proposed in this study.**

Keywords— **2-methoxyethanol, environmental samples, degradation, 16S rRNA and *Pseudomonas* sp. strain VB.**

I. Introduction

Glycols are compounds composed of one to four of ethylene oxide attached together by ether linkage and terminated with a hydroxyl group. Their extremely high solubility in water accounts for their universal applications [1]. The ether linkage is the most common and unifying structural feature, which confers to both biological and xenobiotic compounds a high degree of resistance to biological mineralisation [2]. 2-methoxyethanol ($C_3H_8O_2$) is a colourless substance that is highly soluble in water and acetone. It is used in nail polishes and wood staining techniques. It is as well used as a good extracting agent for a mixture of compounds of polychloroethylene, benzene, toluene and xylene aromatics [3]. 2-methoxyethanol is poisonous when ingested orally. It has a lethal concentration of 1500ppm for mice in air [4, 5]. It impairs fertility and cause harm to the unborn child when pregnant women are exposed to it. Marty and Lock-Caruso [6] reported that 2-methoxyethanol prolonged the gestation period in rodents due to its inhibition of the gap junctional communication.

2-methoxyethanol is a member of the organic compounds called glycols, which comprise one unit of ethylene oxide with a -C-O-C- ether linkage terminating with an hydroxyl bond (-OH) at one end [1]. The metabolism of 2- methoxyethanol under anaerobic conditions has been extensively investigated and detailed information has been presented on degradation rates and metabolic pathway [7, 8]. However, the degradation of 2- methoxyethanol under aerobic condition has hardly been previously investigated. A bacterium *Pseudomonas* sp. strain VB isolated from anaerobic sludge was found to degrade 2- methoxyethanol under aerobic conditions [9]. The aim of this study is to investigate the probable degradative pathway of 2- methoxyethanol by *Pseudomonas* sp. strain VB under aerobic conditions.

II. Materials and methods

Chemical: All the chemicals used were of analytical grade (99.9% pure). All of the water used was ultrapure double-distilled water. 2-methoxyethanol, ethylene glycol, glycollate, glyoxylate, methanol and oxalate were obtained from Fluka (Buchs, Switzerland).

Sampling and treatment of environmental samples in relation to the mineralisation of 2-methoxyethanol: Wastewater samples were collected from two disposal basins, the aerobic digester basin (Belüftungensbecken, BB) and the anaerobic digester basin (Vorklarbecken VB), while soil samples were collected from agricultural land (Ackerlandboden, AKB) and compost dump (Kompostboden, KB). The wastewater samples were first centrifuged at 8,000xg at 40C/10min and the suspensions discarded. The pellets were washed twice with mineral salt medium to remove any endogenous mineral or carbon source. The washed pellets were resuspended in fresh mineral salt medium. To 10ml of mineral salt medium was added 5.0g or 5.0ml of soil and wastewater samples in a 100ml flask. The culture was supplemented with 2-methoxyethanol (126.7mmol) and incubated on a rotatory shaker (200rpm) at 300C in the dark to discourage the growth of photosynthetic microorganisms.

F. Ibrahim, N.A. Abu Osman, J. Usman and N.A. Kadri (Eds.): Biomed 06, IFMBE Proceedings 15, pp. 469-475, 2007
www.springerlink.com ' Springer-Verlag Berlin Heidelberg 2007

As a control a fifth flask was performed with 1% (w/v) sodium azide (Na3N). Cultures showing growth were picked for enrichment cultures.

Enrichment and isolation of 2-methoxyethanol utilizing bacteria: To isolate a bacterial strain able to biodegrade 2-methoxyethanol, the microbial consortium from each of the four environmental samples were used for direct inoculation of 100ml mineral salt medium in 300ml Erlenmeyer flask. The medium was supplemented with 2-methoxyethanol (126.7mmol) as sole source of carbon and energy. Cultures were grown aerobically on a rotatory shaker (200rpm) at 300C for 24hr. Cultures that showed growth were transferred to fresh medium, and after 3-5 successive transfers, the enrichment cultures were plated onto solidified medium containing 1.5% (w/v) Agar and 0.5% (w/v) each of nutrient broth and yeast extract. Cultures were incubated in incubator pot containing 2-methoxyethanol in the surrounding space. After 2-3days of incubation, the plates were examined for growth. Single colonies were picked and streaked for purity. The pure isolates obtained from the environmental samples were investigated in the liquid medium supplemented with 2-methoxyethanol as sole carbon and energy sources. The isolate with the highest 2-methoxyethanol degrading capacity was picked for further experimentation [9].

Determination of cell wall type by L alanine aminopeptidase: Pure cultures of strain VB were used to determine the type of cell wall using L alanine aminopeptidase. L alanine aminopeptidase is localized only in the cell envelope of Gram negative microorganisms [10]. A test strip containing L alanine 4 nitroanilide in a reaction zone was dipped into cell suspension in a test tube such that the reaction zone was completely immersed in the bacterial suspension. The test tube was then incubated in water bath at 300C for 10 30min. The development of a yellow coloration indicated the presence of L alanine aminopeptidase which cleaved L alanine from the L alanine 4 nitroanilide in the reaction zone to form yellow coloration of 4 nitroaniline.

Determination of the cytological properties of strain VB: The specific morphological details, which play role in the characterization of microorganisms, were determined by light and electron microscopy [11].

Isolation of genomic DNA and determination of DNA base composition: Cells harvested at the exponential growth phase were washed twice with 50mM phosphate buffer (pH 7.2). DNA was isolated and purified by NaOH method [12]. The guanosine + cytosine content (mol % G+C) of the genomic DNA was determined by HPLC. The nonmethylated Lambda DNA with G+C content 49.858mol% was used as reference.16S rRNA sequence determination and phylogenetic analysis: The sequence analysis of 16S rRNA of strain VB was determined as described by Rainey *et al*. [13]. The 16S rRNA sequence manually aligned with reference 16S rRNA from representative microrganism of the γ - subclass of the Proteobacteria, obtained from the EMB Datenbank or Ribosomal Datenbank Project (RDP) [14]. The evolutionary distance was calculated by the method of Jukes and Cantor [15]. The phylogenetic dendrograms were constructed by using treeing algorithms contained in PHYLIP Package [16] and the neighbour joining method of Saitou and Nei [17].

Biodegradation of 2-methoxyethanol and proposed intermediates: An overnight culture of Pseudomonas sp. strain VB was used to inoculate 10 liter of mineral salt medium containing 2-methoxyethanol (126.7mmol). The culture was incubated at 300C under aerobic conditions. Other cultures in which 2-methoxyethanol was replaced by ethylene glycol, glycollate, glyoxylate, oxalate, methanol, formaldehyde and formate as sole source of carbon and energy were similarly treated and observed for growth. Growth in these compounds was regarded as ability of Pseudomonas sp. strain VB to degrade these compounds. The rate of degradation of 2-methoxyethanol, ethylene glycol and methanol was monitored by gas chromatography (Model 430 Packard, Netherlands) equipped with a flame ionization detector (FID), using a type Packard column Hayesap 80-100mesh, 2m long, inner diameter 2mm (model 430 from Packard, Netherlands) operated isothermally 1800C (oven) and 2000C (injector port and detector). The rate of degradation of glycollate, glyoxylate, oxalate, formaldehyde and formate was monitored colorimetrically by a spectrophotometer (LKB Biochrom, Ultrospec 4050 Cambridge, England) at 530nm, 430nm, 600nm, 500nm and 540nm respectively[18] .

Determination of cell dry weight of bacteria: Dry weight of Pseudomonas sp. strain VB was determined by method described by Gerhadt *et al.* [10].

Measurement of oxygen uptake and substrate oxidation kinetics: The determination of oxygen uptake rate was performed polarographically at room temperature using a Clarke-type oxygen electrode (Model 10 Ranke Brothers, Birmingham, Great Britain). An overnight culture of Pseudomonas sp. strain VB was centrifuged, washed twice and re-suspended in 1ml of fresh phosphate buffer (50mM, pH 7.2). From this cell suspension, 100µl was added to 3ml of saturated Oxygen - phosphate buffer. After 10mins, the oxygen consumption by the intact cells was measured and this constituted the endogenous respiratory rate. The following limiting concentrations of 2-methoxyethanol 42.2nmol, 84.5nmol and 105.5nmol were added to the cultures respectively and after 10mins, oxygen consumption rate was measured. This is the exogenous respiratory rate. The oxygen consumption rate at the expense of the substrate was determined by subtracting the value for endogenous respiratory rate from exogenous respiratory rate.

F. Ibrahim, N.A. Abu Osman, J. Usman and N.A. Kadri (Eds.): Biomed 06, IFMBE Proceedings 15, pp. 469-475, 2007
www.springerlink.com ' Springer-Verlag Berlin Heidelberg 2007

III. Results

The environmental samples (AKB, KB, BB and VB) were screened in relation to their elimination capacity of 2-methoxyethanol. The capacity and velocity of 2-methoxyethanol degradation observed with the four environmental samples (Table 1) showed various degree of elimination, with the highest degree of elimination recorded for soil samples from compost soil. Samples treated with Na_3N showed no loss of 2-methoxyethanol. Sodium azide acts as an inhibitor of protein synthesis and microbial activity, which infers that the elimination of 2-methoxyethanol is a biological process.

Table 1: Microbial elimination of 2-methoxyethanol in environmental samples

Environmental Sample	Elimination activity
Agricultural soil	0.0685 mmol/ml wastewater/day
Compost soil	0.1036 mmol/ml wastewater/day
Aerobic Sewage water	0.0665 mmol/ml wastewater/day
Anaerobic sewage water	0.0699mmol/ml wastewater/day

Enrichment and isolate capability to mineralize 2-methoxyethanol: Bacterial isolates from each of the environmental samples were screened for the ability to degrade 2-methoxyethanol. The isolate that had the highest degrading ability was picked from each of the samples for further experimentation.

The isolate from the anaerobic sewage sludge was capable of utilizing and degrading 2-methoxyethanol at a faster rate compared to isolate from the aerobic sewage sludge and the soil samples. The utilization capacity of 2-methoxyethanol was most efficient with the isolate from the anaerobic sewage sludge, with an average of 48.6 mmol/day elimination capacity compared to 4.8mol/day, 3.2mmol/day and 2.8mmol/day elimination capacity of the isolates from aerobic sewage sludge, compost soil and agricultural soil respectively. The isolate from the anaerobic sewage sludge designated strain VB, which possess the highest 2-methoxyethanol degrading capacity was selected for further experimentation.

Characteristics of Pseudomonas sp. that placed strain VB in the genus Pseudomonas: Strain VB forms small colonies with an entire margin of size 2mm in diameter. It is Gram-negative, non-spore forming straight rod measuring 0.968+0.03μm width and 2.48+0.7μm length (Table 2). It is not pigmented, motile with polar lophotrichous flagella. It possesses oxidase and catalase activity and lacks the urease activity.

Table 2: Cultural, morphological and physiological properties of isolate VB

Characteristic	Result
Gram	-
Flagella[1]	Polar lophotrichous
Cell width (μm)[2]	0.968±0.03
Cell length (μm)[2]	2.48±0.7
Colony colour	Brown
Cell form	Rod
Cell capsule	+
Spore formation	-
Oxidation Fermentation test	Strict oxidative metabolism
Urease activity	negative
Presence of oxidase	positive
Presence of catalase	positive
Pyocyanin formation	negative
Fluorescent	negative
Indole formation	negative
Presence of lysine decarboxylase	positive
Voges Proskauer reaction	positive
Methyl red reaction	negative
Arginine hydrolysis	positive
Phenylalanine hydrolysis	negative
Casein hydrolysis	negative

[1]Determined by electron microscopy
[2]Determined by light microscopy

16S rRNA sequence analysis: Strain VB is a strict aerobe, which possess the chemoorganotrophic mode of nutrient utilization requiring no growth factor and a G+C content of 64.5±0.8mol%. The sequence pattern of 16S rRNA of strain VB was compared with those of species of the genus Pseudomonas (Table 5). This was because other morphological, physiological and biochemical characterization indicated strain VB belong to the genus Pseudomonas. Table 5 and Fig. 2 show that strain VB is most closely related to Pseudomonas putida K23 1, Pseudomonas sp. Strain R1 and Pseudomonas plecoglossicida at 99.9%, 99.9% and 99.85 similarity levels respectively.

Aerobic transformation of 2-methoxyethanol and hypothetical pathway intermediates: A typical time course of 2-methoxyethanol and proposed intermediates utilization by Pseudomonas sp. strain VB is shown in Fig. 1. Fig. 3 shows the putative microbial degradation of 2-methoxyethanol in Pseudomonas sp. strain VB under aerobic conditions. Only ethylene glycol, glycollate, glyoxylate and oxalate supported growth of the organism. Growth was not observed with methanol, formaldehyde and formate. The utilization of 2-methoxyethanol was slow decreasing in concentration from 126.7mmol to 39.8mmol after 57h, glycollate decreased rapidly in the first nine hours (9h), reaching a minimum of 43.76mmol after 33h and glyoxylate degradation followed the same pattern. Oxalate decreased in the first 33h from126.7mmol to 42,50mmol. Ethylene glycol was degraded uniformly from 126.7mmolmmol to 42.6mmol at the end of 48h.

F. Ibrahim, N.A. Abu Osman, J. Usman and N.A. Kadri (Eds.): Biomed 06, IFMBE Proceedings 15, pp. 469-475, 2007
www.springerlink.com ' Springer-Verlag Berlin Heidelberg 2007

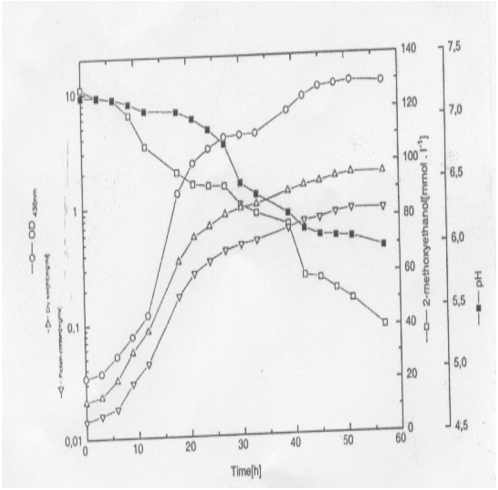

Fig.1 Growth of isolate VB with 2-methoxyethanol as sole source of carbon and energy

Growth characteristics: Growth (cell density) was highest with 2-methoxyethanol (Fig. 1) followed by glycollate and glyoxylate. However, growth was poor with ethylene glycol and oxalate. Growth peaked at 10h with glycollate and glyoxylate (Table 3), which agreed with the high degradation rate noted earlier. Doubling time of 1.739h, 1.937h, 1.198h, 1.408h and 9.231h were observed for 2-methoxyethanol, ethylene glycol, glycollate, glyoxylate and oxalate respectively. The growth yields with 2-methoxyethanol, ethylene glycol, glycollate, glyoxylate and oxalate were 13.728, 1.704, 3.511, 2.454 and 0.308g (cell dry weight/mol substrate) respectively (Table 3). The low growth yield observed with oxalate was probably due to the highly oxidized form of oxalate, which therefore produced an inhibitory effect on the growth [19].

Stoichiometry of 2-methoxyethanol with Pseudomonas sp. strain VB: The stoichiometry of 2-methoxyethanol with Pseudomonas sp. strain VB as shown in Table 4 was calculated to be in the ratio of 1:1 ratio. Pseudomonas sp. strain VB utilizes 1mol oxygen per 1mol 2-methoxyethanol as compared to the theoretically predicted ratio of 4mol oxygen per 1mol 2-methoxyethanol for the complete oxidation of 2-methoxyethanol under aerobic conditions.

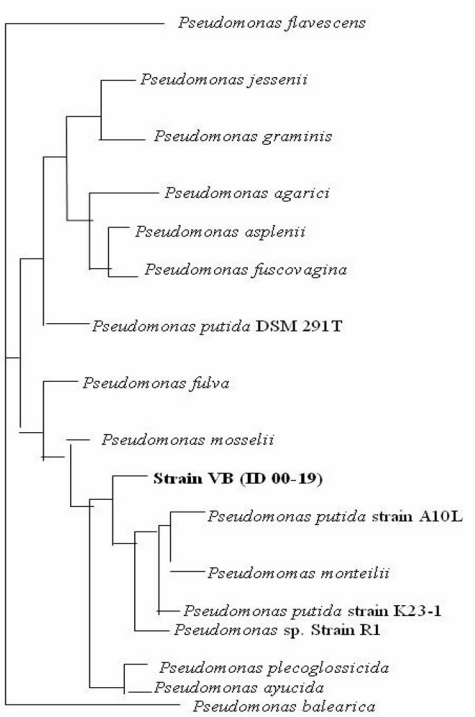

Fig. 2: Phylogenetic tree based on 16S rRNA gene sequence of strain VB showing the position of strain VB on the dendogram. (DSMZ, Braunschweig, Germany). The hierarchic taxonomic tree or dendogram was prepared from the similarity level (Table 3) for strain VB and 16 other species of the genus Pseudomonas.

Table 3: Growth yield of *Pseudomonas* sp. strain VB

Substrate	Molar growth yield (cell dry weight/mol. Substrate)	Growth rate (Generation time in hr)
2-methoxyethanol	13.728	1.739
Ethylene glycol	1.704	1.937
Glycollate	3.511	1.198
Glyoxylate	2.454	1.408
Oxalate	0.308	9.231

F. Ibrahim, N.A. Abu Osman, J. Usman and N.A. Kadri (Eds.): Biomed 06, IFMBE Proceedings 15, pp. 469-475, 2007
www.springerlink.com ' Springer-Verlag Berlin Heidelberg 2007

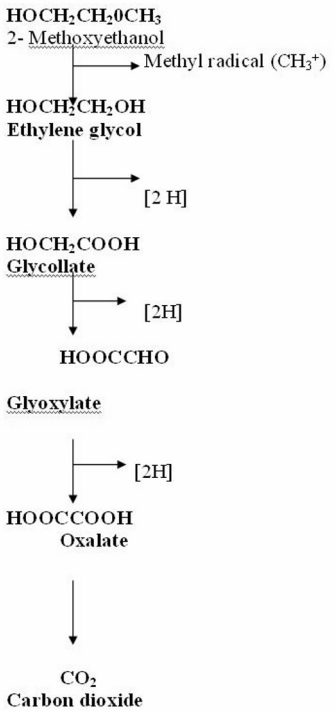

Fig 3 Reaction pathway in the degradation of 2-methoxyethanol by *Pseudomonas* sp. strain VB

Table 4: Oxygen consumption rate with limiting 2-methoxyethanol concentration

No. of analysis	2-ME nmol.ml^{-1}	O_2 uptake nmol. ml^{-1}	nmolO_2/nmol 2-ME	nmol2-ME /nmolO_2
1	Control^{-1}	143.3	-	-
2	42.2	35.5	0.84/1	1.2/1
3	84.5	80.2	1.0/1	1.0/1
4	105.5	95.4	0.9/1	1.1/1

[1]Control was determined under endogenous rate without substrate.

Equation:

$$C3H802 + 402 \rightarrow 4H2O + 3CO2 \quad (1)$$

(Total oxidation of 2-methoxyethanol)

IV. Discussions

The critical role of microorganisms in the biodegradation of organic pollutant in the environment has been well investigated [20]. The focus of glycols research in recent years on the biodegradation of 2-methoxyethanol has resulted in the isolation of a number of microorganisms that can mineralize and utilize 2-methoxyethanol as the sole source of carbon and energy [7, 8]. These isolates have been used to elucidate metabolic pathways in the mineralisation of 2-methoxyethanol [8]. However, information on the microbial degradation of 2-methoxyethanol under aerobic conditions is lacking. In this study it was revealed that, the natural microbial flora of certain soil and wastewater samples under aerobic conditions could as well mineralize 2-methoxyethanol known to be biodegraded under aerobic conditions. In this study, the highest elimination activity of 2-methoxyethanol was observed in compost soil (0.1036mmol/g wet soil day). The elimination of 2-methoxyethanol was observed to be due to biological processes since samples treated with sodium azide (Na_3N) showed no loss of 2-methyoxyethanol. The compost soil by its nature is well aerated, and this contains more aerobic microorganisms. This also gave an indication that aerobic microorganisms could also degrade 2- methoxyethanol.

Screening of these various environmental samples indicated that anaerobic sewage harboured the best degrading microorganisms unlike aerobic samples (Fig. 3). The mineralization of 2-methoxyethanol in compost soil of all the soil samples where the highest degree of mineralisation was recorded could be as a result of the effect of cometabolism and synergism, since the best degrading 2-methoxyethanol strains was isolated from the anaerobic sewage wastewater. In the proposed reaction pathway (Fig. 1, the degradation of 2-methoxyethanol was initiated by oxidative decarboxylation with methanol as a by-product. Pseudomonas sp. strain VB was however unable to utilize methanol. This may be because it ends up as a methyl radical -CH3+.The ethylene glycol resulting from above decarboxylation is converted to oxalate through glycollate, glyoxylate by oxidative dehydrogenation. Finally oxalate is converted to carbon and water. All these intermediates were actively degraded by Pseudomonas sp. strain VB. The higher rate of degradation of the ethylene glycol, glycollate, glyoxylate and oxalate compared to 2-methoxyethanol appears to support the proposal that they are intermediates in the reaction pathway. However, the high growth yield for glycollate and glyoxlate (compared to ethylene glycol) seems to show that there might be an alternative pathway which may involve a reduction reaction. This theory is supported by the report of Clarke and Ornston [21], who found that glyoxylate formed from a number of alternative pathways by species of Pseudomonas when grown on glycollate, glycine and oxalate. The utilization of glycollate and glyoxylate as substrates by Escherichia coli K-12 involves a series of similar reactions. The glycollate and glyoxylate are interconverted by distinct enzymes, glycollate oxidase and glyoxylate reductase [22].The GC analysis showed only the peak of 2-methoxyethanol during the period of degradation.

F. Ibrahim, N.A. Abu Osman, J. Usman and N.A. Kadri (Eds.): Biomed 06, IFMBE Proceedings 15, pp. 469-475, 2007
www.springerlink.com ' Springer-Verlag Berlin Heidelberg 2007

Table 5 % 16S rRNA gene sequence similarity for strain VB and the related taxa
(level of the nucleotide similarities based on the 16S rRNA gene sequence of strain VB and the related taxa)

Strain	1.	2.	3.	4.	5.	6.	7.	8.	9.	10.	11.	12.	13.	14.	15.	16.	17.
1. Strain VB (ID 00-19)	-																
2. *Pseudomonas* monsselii	99.2	-															
3. *Pseodomonas jessenii*	98.3	97.8	-														
4. *Pseudomonsa agarici*	97.5	97.1	98.0	-													
5. *Pseudomonas asplenii*	98.3	98.1	97.8	98.3	-												
6. *Pseudomonas putida* DSM 291T	99.1	98.5	97.8	97.6	98.9	-											
7. *Pseudomonas putida* strain A10L	99.8	99.4	98.1	97.5	98.5	98.9	-										
8. *Pseudomonas putida* strain K23-1	**99.9**	99.2	98.4	97.5	98.3	99.0	98.8	-									
9. *Pseudomonas fulva*	98.9	98.3	98.0	96.9	97.7	98.5	98.8	98.8	-								
10. *Pseudomonas monteilii*	99.8	99.3	98.2	97.5	98.5	98.8	99.9	99.8	98.7	-							
11. *Pseudomonas* sp. Strain R1	99.9	99.2	98.4	97.5	98.3	99.0	99.8	100	98.8	99.8	-						
12. *Pseudomonas plecoglossicida*	99.8	99.3	98.1	97.5	98.5	99.0	99.9	99.7	98.7	99.8	99.7	-					
13. *Pseudomonas flavescens*	98.1	97.4	96.8	96.5	96.9	97.5	98.0	98.1	97.1	97.9	98.1	98.1	-				
14. *Pseudomonas fuscovagina*	98.1	97.8	97.6	98.1	99.6	98.7	98.2	98.1	97.5	98.2	98.1	98.3	96.7	-			
15. *Pseudomonas ayucida*	99.8	99.3	98.1	97.5	98.5	99.0	99.9	99.7	98.7	99.8	99.7	100	98.1	98.3	-		
16. *Pseudomonas graminis*	98.0	97.5	98.0	97.8	97.6	97.6	97.8	97.9	97.2	97.8	97.9	97.9	96.9	97.4	97.9	-	
17. *Pseudomonas balearica*	95.5	95.1	95.0	94.4	95.1	95.1	95.5	95.5	94.7	95.4	95.5	95.4	94.8	94.8	95.4	94.8	-

In the anaerobic degradation of 2-methoxyethanol by Acetobacterium malicum, ethylene glycol was suggested as one of the intermediates but could not be detected by GC [7], indicating the transcient nature of these intermediates. Further work to confirm the reaction pathway involving the isolation of enzymes involved in the degradation pathway, the application of nuclear magnetic resonance(NMR), gas chromatography(GC) and mass spectrometry are currently being investigated.

Strain VB is a strict aerobe; Gram-negative, non sporing and rod shaped and possess the chemoorganotrophic mode of nutrient utilization. It is motile with polar lophotrichous flagella. It possess a G+C of 64.5±0.8mol% which falls within the range of 58 70 mol% characteristics of the genus Pseudomonas. These characteristic features would put strain VB in the genus Pseudomonas [23, 24]. It also shares with other members of Pseudomonas the ability to utilize a number of carbohydrates as carbon source and possess oxidase and catalase activities.

The phylogenetic analysis of 16S rRNA sequence also shows that strain VB is closely related to members of the genus Pseudomonas belong to the rRNA group 1 of the γ-Proteobacteria (Table 3) [24]. However, strain VB differs from other members of the genus Pseudomonas in not possessing fluorescent pigment and its inability to utilize naphthalene, trytophan, anthranilate and acetate, while it utilizes ethylene glycol, glycollate, malate, threonine, nicotinic acid and xylose which other members of the genus Pseudomonas cannot utilize. Strain VB was therefore proposed to be a representative of a new species of the genus Pseudomonas.

Acknowledgement

This study was supported by grant from DAAD, Bonn Germany as part of Ph.D research programme.

References

1. Cox, P. D, 1978. The biodegradation of polyethylene glycol. Ann. Rev. Microbiol. 23:173 194.
2. Tidswell, C. E., Russell, J. W. and White, F. G, 1996. Ether bond scission in the biodegradation of alcohol ethoxylates nonionic surfactants by Pseudomonas sp. strain SC25A. Microbiology. 142:1123-1131.
3. Brau Stromeyer, A. S and Meyer O, 1995.Verhalten von LCKW und BTEX aromaten in Terranox und Schlam aus der Hochdruck Bodeninjektion saulen. Tatigkeitsbereicht. Universitat Bayreuth, Bayreuth, Germany. 12pp.
4. ABC Chemie, Elulitz C-M, 1965. (eds.). Band 1: A-K Harri Deutsch. Frankfurt am Main 766pp.
5. Merck Index, 1998. An Encyclopedia of Chemicals, Drugs and Biologicals. Budavari, S. (eds). 11th edn. Merck and Co. Inc. New Jersey. 1010pp.
6. Marty M. S. and Loch Caruso, R, 1998. 2 methoxyethanol inhibits gap junctional communication in rats myometrial myocyts. Cell. Biol. Toxicol. 14:199 210.
7. Tanaka, K., Mikami, E. and Suzuki, T, 1986. Methane fermentation of 2 methoxyethanol by mesophilic digesting sludge. J. Ferment. Technol. 64:305-39.
8. Tanaka, and Pfennig, N, 1988. Fermentation of 2- methoxyethanol by Acetobaterium malicum sp. nov and Pelobacter venetianus. Arch. Microbiol 149:181-187.
9. Ekhaise F. O, 2002. Aerobic degradation of methyl collosolve - isolation, characterization and identification of methyl cellosolve degrading bacterium under aerobic conditions. Ph.D Thesis. University of Benin, Benin City, Nigeria.158pp.
10. Gerhardt. P., Murray, E. G. R. and Krieg, R. N. 1994. Methods for General and Molecular Bacteriology. ASM Press. Washington, DC. 791pp.

F. Ibrahim, N.A. Abu Osman, J. Usman and N.A. Kadri (Eds.): Biomed 06, IFMBE Proceedings 15, pp. 469-475, 2007
www.springerlink.com ' Springer-Verlag Berlin Heidelberg 2007

11. Ekhaise, F. O. and Aluyi, H. S. A. (2003). The morphology and ultrstructure of a new 2 methoxyethanol utilizing Pseudomonas sp.Benin Science Digest. Vol.1. 25 - 30.
12. Mesbah, M., Premachandran, U. and Whitman, W, 1989. Precise measurement of the G+C content of deoxyribonucleic acid by high performance liquid chromatography. Int. J. Syst. Bacteriol. 39: 159 169.
13. Rainey, F. A., Ward Rainey, N., Kroppenstadt, R. M. and Stackebrandt, E., 1996. The genus Nocardiopsis represent a phylogenetically cohrent taxon and a distinct actinomycetes linkage: Proposal of Nocardiopsaceae. Fam. Nov. Int. J. Syst. Bacteriol. 46: 1088 1092.
14. Maidak, B. L. and 16 other authors, 1999. A new version of the RDP (Ribosomal Datenbank Project) Nucl. Acids Res.. 27: 171 173.
15. Jukes, T. H. and Cantor, C. R, 1969.Evolution of protein molecules. P. 21 132. In Munro, N. H. (eds). Mammalian Protein Metabolism. Academic Press. New York.
16. Felsentein, J, 1993. PHYLIP. (Phylogeny Inference Package) Version 2. 5. 1. Seattle. Department Of Genetics. University of Washington.
17. Saitou, N. and Nei, M, 1987. The neighbour joining methods. A new method for reconstructing phylogenetic trees. Mol. Biol. Evol. 4: 406 425.
18. Kakac, B. and Vejedelek, J. Z. 1974. Handbuch der photometrisch Analyse Organische Verbindurgen. Band 1. Chemie GmbH, Weimherm. 718pp.
19. Harder, W. 1973. Microbial metabolism of C_1 and C_2 compounds. Antonie von Leeuwemhoek. 39: 650-652.
20. Head M. I, 1998. Bioremediation: Towards a credible technology. Microbiology. 144:599-608.
21. Clarke, H. P. and Ornston, N. L. 1975. Metabolic pathways and regulation 1, p. 191- 261. In Clark, H. P. and Richmond, H. M. (eds.). Genetic and Biochemistry of Pseudomonas. John Wiley and Sons. London.
22. Ornston, N. L. and Ornston, L. M. 1969. Regulation of glyoxylate metabolism in E. coli K12. J. Bacteriol. 98: 1098 1108.
23. Stainer, Y. R., Adelberg, A. E. and Ingraham, I. J, 1985. General Microbiology. 4th edn. Macmillan Press. London. 871pp
24. Palleroni, J. N, 1992. Introduction to the family of Pseudomonacea. p. 3071 3085. In Balows, A., Truper, G. H., Dworkin, M., Harder, W. and Schleifer, K-H. (eds.). The Prokaryotes. Vol. 3. 2nd edn. Springer Verlag. New York.

Author: Ekhaise Frederick Osaro
Institute: Deparment of Microbiology, University of Benin
Street: P.M. B 1154
City: Benin City
Country: Nigeria
Email: fredfldyn@yahoo.com

F. Ibrahim, N.A. Abu Osman, J. Usman and N.A. Kadri (Eds.): Biomed 06, IFMBE Proceedings 15, pp. 469-475, 2007
www.springerlink.com ' Springer-Verlag Berlin Heidelberg 2007

Human pi class glutathione *S*-transferase: anticancer material and functional study

Hyun-Young Cho, Jong-Uk Koh, Young-Bin Kwon and Kwang-Hoon Kong

The Department of Chemistry, College of Natural Sciences, Chung-Ang University, Seoul 156-756, Republic of Korea

Abstract— **Glutathione *S*-transferase are a family of Phase II detoxification enzymes that catalyse the conjugation of glutathione to a wide variety of xenobiotics. To gain further insight into the relationship between structure and function of glutathione *S*-transferase, the four cystein mutants and the three Tyr108 mutants of hGSTP1-1 were expressed in *E. coli* and purified to electrophoretic homogeneity by affinity chromatography on immobilized GSH. The mutants were characterized that kinetic analysis and inhibition effects. The all cystein residues are not needed for the steroid isomerase activity of hGSTP1-1. The effect of substitutions on kinetic parameters suggests that Tyr108 in hGSTP1-1 contribute to the binding of the electrophilic substrate and a major determinant in the binding of CDNB in the aromatic ring of Tyr108, not its hydroxyl group. In order to search for bioactive natural products exerting inhibitory activity toward glutathione *S*-transferase, twenty natural products extracts were screened for inhibition or activation of hGSTP1-1. As results, we found significant inhibition of GST by methanolic extracts of *Vucia unijuga*, *Sedum sarmentosum* and *Petasites japonicus* BUNGE.**

Keywords— **human glutathione *S*-transferase; inhibition effect; anticancer material; anti-tolerance; hGSTP1-1**

I. Introduction

A primary cause of cancer treatment failure and patient relapse in an acquired or intrinsic resistance to anticancer therapies. Acquisition of drug resistance can be attributed to various factors that include avoidance of apoptotic cell death, altered expression of glutathione *S*-transferase (GSTs). GSTs are a family of phase II detoxification enzyme that catalyses the conjugation of nonpolar compounds that contain an electrophilic carbon, nitrogen or sulfur atom to reduced glutathione(GSH). In this way, GSTs contribute to the metabolism of drug, pesticides and other xenobiotics [1-3]. Chemotherapeutic-resistant tumor cell lines have been shown to overexpress GST isozyme [4]. This over expression leads to an accelerated detoxification of drug substrates and thus an acquired resistance. Among various GSTs, the human pi-class (hGST P1-1) is overexpressed in a wide variety of tumors including ovarian, NSCLC, breast, colon, pancreas and lymphoma [5]. Moreover, the hGSTP1-1 has been implicated in the development of resistance of tumors towards various anticancer drugs in resistant tumor cells. Thus, the design of highly potent selective inhibitors toward hGST P1-1 may be useful in increasing the therapeutic index of commonly used anticancer agents. Therefore, in this study, we studied the roles of Cys (at position 14, 47, 101 and 109) and Tyr108 residues in hGST P1-1 by site directed mutagenesis. In order to search for bioactive natural products exerting inhibitory activity toward glutathione *S*-transferase, we also evaluated for inhibition effect of hGSTP1-1 from natural products of 20 kinds.

II. Materials and methods

Materials: GSH and 1-Chloro-2,4-dinitrobenzene were purchased from Kohjin Co. and Wako pure Chem. Ind. (Osaka, Japan), respectively. Ethacrynic acid, *S*-hexylGSH, 1,2-dichloro-4-nitrobenzene, Cumene hydroperoxide, 1,2-epoxy-3-(*p*-nitrophenoxy)propane and *S*-metylGSH were obtained from Sigma (St.Louis, USA). Glutathione Sepharose was purchased from Pharmacia Biotech (Uppsala, Sweden). All other reagents used were of the highest grade commercially available.

Preparation of hGSTP1-1 and mutant enzyme: Wild-type hGSTP1-1 was obtained by expression of a cloned cDNA in *E. coli* [6] as described in the previous paper [7]. The oligonucleotide primers were synthesized for site-directed mutagenesis experiments. Mutagenesis was performed according to the procedure of Kunkel using a Mutant^{TM}-Super Express Km kit (Takara Shuzo Co.). The mutant enzymes were expressed in *E. coli* under the control of the *tac* promoter. Cultured cells were lysed, followed by centrifugation. The crude extract was loaded GSH-Sepharose affinity chromatography that had been previously equilibrated with 20 mM potassium phosphate buffer (pH 7.0). After charge, the column washed 20 mM potassium phosphate (pH 7.0) containing 50 mM potassium chloride. The enzyme was eluted from the column with 50 mM tris-HCl buffer (pH 8.5) containing 10 mM GSH and dialyzed. The dialyzed purified enzyme was uned for next experiment.

Kinetic studies: Kinetic studies with GSH and electrophilic substrate were carried out at 30˚C as described Chen *et al* [8]. Kinetic parameter K_m values were determined first order conditions at low substrate concentration with respect to the varied substrate: for GSH with a fixed concentration of 1mM CDNB, and for CDNB with a fixed concentration of 1mM GSH. The k_{cat} values were calculated on the basis of mol dimeric enzyme using a Mr of 45,000.

F. Ibrahim, N.A. Abu Osman, J. Usman and N.A. Kadri (Eds.): Biomed 06, IFMBE Proceedings 15, pp. 476-478, 2007
www.springerlink.com ' Springer-Verlag Berlin Heidelberg 2007

Inhibition studies - The inhibitory effects on the activity of the enzyme were measured by preincubating the enzyme with 1mM GSH and the inhibitor for 2min and initiating the reaction by addition of 1mM CDNB.

III. Results and Discussions

Human GST P1-1 has been extensively studied because of the clinical interest in it as a marker during chemical carcinogenesis and its potential role in the mechanism of cellular multidrug resistance against a number of antineoplastic agents. The chemical modification and X-ray crystallographic studies have suggested that Cys and Tyr 108 residues in hGSTP1-1 were presented at or near the active site of GSTs and located at or close to the substrate-binding site of the enzyme, respectively. The analysis of the kinetic parameter of C14S, C47S and C169S resulted in 15- 25% decrease in k_{cat} and a little increase in K_m^{GSH} (except for Cys 47). On the other hand, C101S increased a little in k_{cat} and K_m^{GSH}. Cys14 seems to participate in the catalytic reaction of GST by stabilizing the conformation of the active-site loop, but no in the GSH binding directly. The substitution of Cys 47 with serine significantly reduced the affinity of GSH binding, although it dose not prevent GSH binding. On the other hand, the substitution of Cys101 with serine appears to change the binding affinity of electrophilic substrate by inducing a conformational change of the α-helix D. Cys169 seems to be important for maintaining the stable conformation of the enzyme. The substitutions of Tyr108 significantly affected K_m^{CDNB} and K_m^{ETA}, whereas scarcely affected K_m^{GSH}. K_m^{CDNB} and K_m^{ETA} values of Y108A were approximately 2-3 fold larger that those the wild type, but the K_m^{CDNB} of Y108W was half-fold smaller than that of the wild type. The substitution of Tyr108 with phenylalanine significantly affected k_{cat} and K_m^{CDNB}, whereas scarcely affected K_m^{GSH}. These results suggest that Tyr108 in hGSTP1-1 contributes to the binding of the electrophilic substrate. As shown by kinetic parameter results, K_m^{CDNB} values decreased as the size of side chain of the mutated amino acid increased (Ala<Phe<Trp), whereas K_m^{GSH} values were similar to that of the wild type. These results suggest that a major determinant in the biding of CDNB is the aromatic ring of Tyr108, not hydroxyl group. In order to search for bioactive natural products exerting inhibitory activity toward glutathione S-transferase, twenty natural products extracts were screened for inhibition or activation of hGSTP1-1. The methanolic extracts of *Vucia unijuga*, *Sedum sarmentosum* and *Petasites japonicus* BUNGE approximately more 50% decreased the conjugation reaction of GSH and 1-chloro-2,4-dinitrobenzene. These experiment results of hGSTP1-1 will be of great value in designing new inhibitors that may prove useful in chemotherapy and new enzymes having different substrate specificity.

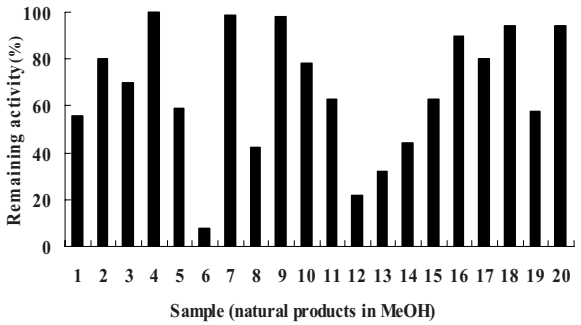

Fig. 1 Inhibition effect of natural products extracts on GSH-[1-Chloro-2,4-dinitrobenzene] conjugation
1, Cucumis sativus var. sativus; 2, Broussonetia kazinoki Siebold; 3, Poria cocas Wolf; 4, Hovenia dulcis var. koreana NAKAI; 5, Saururus chinensis BAILL; 6. Vucia unijuga; 7, Allium sativum var. sativium; 8, Morus alba L.; 9, Capsicum baccatum var. baccatum; 10, Paeonia japonica Miyabe et Takeda; 11, Prunus Africana (Hook. f.) Kalkman; 12, Sedum sarmentosum BUNGE; 13, Petasites japonicus Maxim; 14, Allium glaciale Vved; 15, Aralia elata; 16, Herba Capsellae; 17, Allium cepa var. cepa; 18, Rosa shipovnic; 19, Acanthopanaxx Senticosus; 20, Vigna radiate var. radiate.

IV. Conclusion

We studied the roles of Cys14, Cys 47, Cys101, Cys169 and Tyr108 residues in hGSTP1-1 by site directed mutagenesis. The hGSTP1-1 significant decreased the specific activity 1-chloro-2,4-dinitrobenzene for GSH conjugation reaction by methanol fraction of *Vucia unijuga*, *Sedum sarmentosum* and *Petasites japonicus* BUNGE extracts. These results offer information on the precise enzyme-substrate interactions responsible for the catalytic properties of hGSTP1-1, and it is of great value in designing new inhibitors that may prove useful in chemotherapy.

References

1. Hayes J, Flanagan J, Jowsey I (2005) Glutathione transferase. Annu Rev Pharmacol Toxicol 45: 51-88
2. Keen J, Jakoby W (1978) Glutathione transferases. Catalysis of nucleophilic reactions of glutathione. J Biol Chem 253: 5654-5657
3. Armstrong R (1997) Structure, catalytic mechanism, and evolution of the glutathione transferase. Chem Res Toxiclo 10: 2-18
4. Mcllwain C, Townsend D, Tew K (2006) Glutathione S-transferase polymorphisms: cancer incidence and therapy. Oncogene 25: 1639-1648
5. Tew K (1994) Glutathione-associated enzymes in anticancer drug resistance. Cancer Res 54: 4313-4320

F. Ibrahim, N.A. Abu Osman, J. Usman and N.A. Kadri (Eds.): Biomed 06, IFMBE Proceedings 15, pp. 476-478, 2007
www.springerlink.com ' Springer-Verlag Berlin Heidelberg 2007

6. Kano T, Sakai M, Muramatsu M (1987) Structure and expression of a human class π glutathione *S*-transferase messenger RNA. Cancer Res 47 : 5626-5630
7. Kong K-H, Inoue H, Takahashi K (1991) Non-essentiality of cyctein and histidine residues for the activity of human class Pi glutathione *S*-transferase. Biochem Biophys Res Commun 181: 748-755
8. Chen W, Hsieh J, Hong J-L, Tsai S, Tam M (1992) Site-directed mutagenesis and chemical modification of cysteine residues of rat glutathione *S*-transferase 3-3. Biochem J 286: 205-210

Address of the corresponding author:

Author: Kwnag-Hoon Kong
Institute: The Department of Chemistry,College of Natural Sciences, Chung-Ang University
City: Seoul
Country: Korea
Email: khkong@cau.ac.kr

F. Ibrahim, N.A. Abu Osman, J. Usman and N.A. Kadri (Eds.): Biomed 06, IFMBE Proceedings 15, pp. 476-478, 2007
www.springerlink.com ' Springer-Verlag Berlin Heidelberg 2007

Liquid State Bioconversion of Domestic Wastewater Sludge for Bioethanol Production

M.Z. Alam, N.A. Kabbashi, A.A. Razak

Bioenvironmental Engineering Research Unit (BERU), Department of Biotechnology Engineering, Faculty of Engineering, International Islamic University Malaysia (IIUM), Jalan Gombak, 50728 Kuala Lumpur, Malaysia

Abstract— **The production of bioethanol was conducted by utilizing domestic wastewater sludge as major substrate using the yeast, *Saccharomyces cerevisiae* in liquid state bioconversion method (submerged fermentation). The optimum media and process conditions obtained from previous studies by using central composite design were applied in this study to evaluate the bioconversion process through ethanol production. The results presented in this study showed that 9.8% ethanol was produced utilizing sludge as substrate by *Saccharomyces cerevisiae* within 48 hours of fermentation while the COD, copper and chromium (heavy metals) removal were found to be 62%, 68% and 45% respectively in treated sludge after 72 hours of fermentation period. The total suspended solids (TSS) as biosolids (microbial growth) was observed to evaluate the microbial performance in bioconversion process. The observed yield and productivity were determined as well.**

Keywords— **Domestic wastewater sludge, bioethanol, *Saccharomyces cerevisiae,* liquid state bioconversion, sludge management**

I. Introduction

About 210 million tons of sewage sludge is being produced in United States every year [1] and more than 50 million meter cube of sewage sludge is generated annually in Japan [2]. In Japan, most of it is disposed of by landfill or burning and only a small part of the sewage sludge is used to produce compost. Consequently, the valuable energy contained in organic sludge is lost without utilization in the energy cycle [2]. In Nordmaling, Sweden; there are seven different sewage treatment plants, of different sizes [3]. Together they produce about 1500 ton sludge (20% solid waste) per year [3]. In Malaysia, STP sludge is the largest contributor of organic pollution to water resources and environment. Its contribution is top listed (64.4%), followed by animal husbandry wastes (32.2%), agrobased (1.7%) and industrial effluent (1.3%) in terms of BOD load [4]. Approximately 4.2 million cubic meters of sewage sludge is produced by Indah Water Konsortium (IWK) annually in Malaysia and the total cost of managing was estimated as RM 1 billion. This sludge volume is expected to rise to 7 million cubic meters by the year 2020 [5].

Now a day, an alternative way to treat wastewater sludge is through bioconversion. Bioconversion refers to biological conversion of waste which involves the conversion of organic material into a source of energy, using biological processes or microorganisms mostly by bacteria and fungi [6]. Certain strains of bacteria and fungi have the ability to break down or transform the organic materials present in waste sludge which accelerate the biodegradability of wastewater sludge besides producing value added products [7]. Therefore bioethanol is a renewable energy could be produced from organic residues with effective and efficient bioconversion.

Bioethanol is the most potential substitute to the existing fossil fuels. Unlike fossil fuels, ethanol is a renewable energy source produced through fermentation of sugars [8]. Combustion of bioethanol provides O_2, which in turn emit low level of non-combusted hydrocarbon, CO, nitrogen oxides and exhaust volatile compound [9]. Mixing ethanol and gasoline has several advantages such that it increases octane number thus reduce toxicity and it is more efficient than gasoline in spark-ignition engines [10].

Bioethanol can be produced from starch and sugar-based crops as well as lignocellulosic biomass which include agricultural residues, herbaceous crops, forestry wastes, wastepaper and other wastes [9]. Due to the increasing costs of substrates such as molasses, sweet sorghum, maize starch, sugarcane, sugar beet, tapioca, wheat starch etc. which are human food and increasing demand for fuel ethanol, there is a need to search for cheaper and abundant substrate and to develop an efficient and less expensive technology so that product can be made available more cheaply [11]. Domestic wastewater sludge as the abundant, accessible, and cheaper (even though negative cost) was used as raw material for production of bioethanol using optimum process conditions.

II. Materials and Methods

A. Sample collection

Domestic wastewater sludge (DWS) sample was collected from secondary clarifier at Indah Water Konsortium (IWK) Sewage Treatment Plant, Damansara, Kuala Lum-

F. Ibrahim, N.A. Abu Osman, J. Usman and N.A. Kadri (Eds.): Biomed 06, IFMBE Proceedings 15, pp. 479-482, 2007
www.springerlink.com ' Springer-Verlag Berlin Heidelberg 2007

pur, Malaysia. The total suspended solids (TSS) and initial pH observed were 0.5 to 1.0% (w/w) and 6.3-6.8 respectively. The sample was stored at 4°C in cold room for further use.

B. Culture of microbial strain

Saccharomyces cerevisiae was obtained from MARDI, Serdang, Malaysia. Using quadrant-streaking method *S. cerevisiae* was cultured on PDA plate at 30°C for 1-3 days. Subculture was done once a month and stored at 4°C in refrigerator.

C. Preparation of inoculum

Using a sterilize technique, successful colonies of *S. cerevisiae* were taken from PDA plate and were inoculated into 100mL shake flask containing 50 mL of YM media (2% w/v). The flasks were incubated at 30^0C for 24 hours with 150 rpm. After incubation, the flasks were examined through the color of the cultures should be murky indicating that the matured cell was grown in the culture media. The cells from the culture media were count ($2/10^6$ cfu/ml) for further experiment of bioethanol production. The flasks containing live culture of *S. cerevisiae* can be kept in refrigerator for future used.

D. Experimental procedures

The experiment for bioethanol production utilizing sludge as media was carried out using optimum parameters obtained from media and process conditions from previous study [12,13]. A 500 ml Erlenmeyer flask containing 100 ml of sludge according the optimum media compositions was taken. The yeast (*S. cerevisiae*) was inoculated and incubated in an incubator shaker with the process conditions obtained before. Sample was collected and analyzed for every 12 hours for 3 days for bioethanol production, COD, heavy metals and total suspended solids to evaluate the production and treatment performance.

E. Analytical analysis

The parameter bioethanol was determined according to the dichromate methods [14]. The chemical oxygen demand (COD) and heavy metals measurement were followed to the method described by the HACH [15]. Total suspended solids (TSS) of treated samples were observed using APHA standard methods [16] and pH were observed using pH meters. Data were the average of three replicates.

III. Results and discussion

The media and process optimizations from previous study were applied in this study to achieve maximum production of ethanol and reduction of chemical oxygen demand (COD), heavy metals such as cadmium, chromium and copper. Fig. 1 shows the ethanol production with the function of time. As fermentation time increases, the ethanol percent yield started to increase as well until it reaches a maximum value of 9.8% after 48 hour fermentation. As reported by Srinivas et al. (1995), the fermentation duration of the optimization of single-stage direct bioconversion of cellulosic materials to ethanol are varied up to 72 hours. However, it was observed that the product level was higher at 48 h of fermentation [17]. The results also indicated that the production followed the microbial growth curve. As *S. cerevisiae* growth increased, the ethanol also increased until *S. cerevisiae* reaches its stationary phase. The ethanol therefore reached its maximum production and it started to decrease when the biomass approached its death phase. After 72 hours fermentation, the ethanol percent yield was decreased to 5.4%.

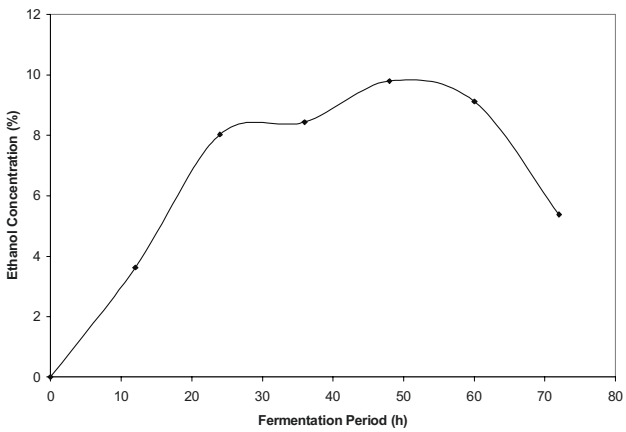

Fig. 1 Production of ethanol from wastewater sludge as substrate with variation of fermentation time.

F. Ibrahim, N.A. Abu Osman, J. Usman and N.A. Kadri (Eds.): Biomed 06, IFMBE Proceedings 15, pp. 479-482, 2007
www.springerlink.com ' Springer-Verlag Berlin Heidelberg 2007

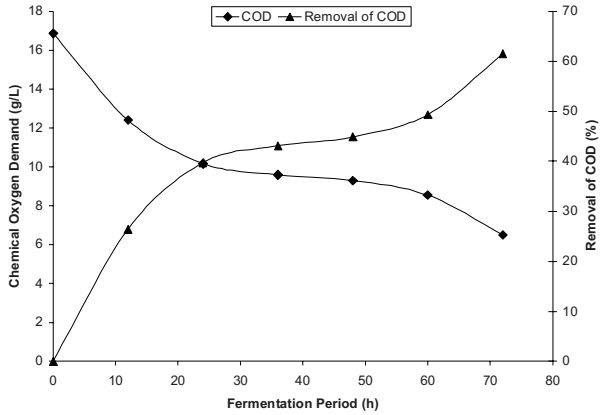

Fig. 2 Removal of COD in treated sludge using liquid state bioconversion.

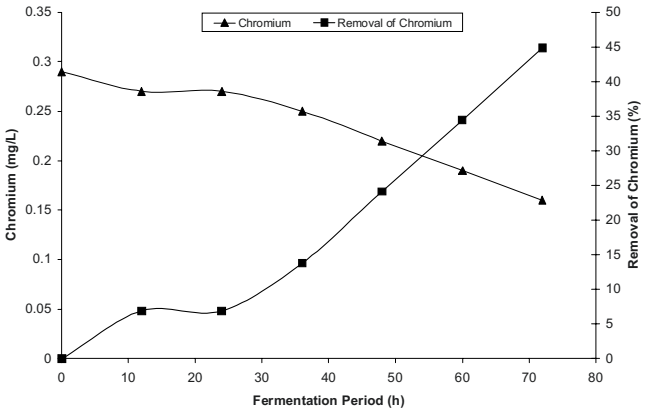

Fig. 4 Content of chromium and its removal percentage in treated sludge besides the production of ethanol.

The study of removal of COD and other heavy metals does not play a significant role in the optimization of bioethanol production from STP sludge. It is merely to prove that the production of ethanol from STP sludge may concurrently treat the sludge as the function of removal of COD and heavy metals which evaluate the bioconversion process. As can be observed in Fig. 2, the COD concentration at 0 hour is initially 16.9 g/L. As time increases, the COD concentration begins to decrease until it reaches 6.50 g/L concentration at 72 hour. Thus, 61.5% COD is removed from STP sludge after 3 days of fermentation. In a study conducted by Alam et. al. (2002), 94.2% removal of COD by microbial mixed culture of *P. corylophilum* and *A. niger* is recorded after 6 days of the wastewater sludge treatment [18]. The reduction rate of COD is highly influenced by the immobilized microbial treatment of wastewater sludge [7].

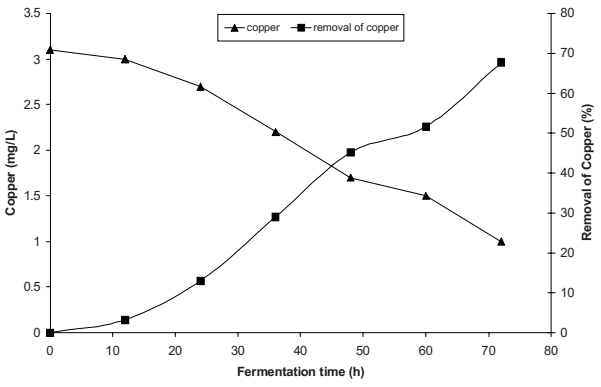

Fig. 3 Content of copper and its removal percentage in treated sludge besides the production of ethanol.

Fig. 3-4 show the removal of copper and chromium respectively as fermentation period increases. The results showed that copper was decreased from 3.1 mg/L to 1.0 mg/L concentration within 72 hour of fermentation which means 67.74% of copper is successfully removed from the sludge after 3 days fermentation. The chromium was decreased from 0.29 mg/L to 0.16 mg/L after 72 hour of treatment resulted in a total of 44.8% removal of chromium. The heavy metals removal percentages were increased with the increased production of biomass as biomass has very good adsorption capacity in different applications. Removal of cadmium from STP sludge was not represented in this study since the cadmium concentration was recorded zero throughout the fermentation period.

Observed yield of product from substrate can be calculated from plot of product versus substrate where substrate can be represented by COD with the function of time (Figure not shown). The slope of the straight line gives the ethanol observed yield, Y ps of 12.1 $g_p\ g_s^{\ 1}$. In the literature, ethanol production from wheat straw hemicellulose hydrolysate by *Pichia stipitis* has a maximum yield of 0.41 – 0.01 $g_p\ g_s^{\ 1}$, equivalent to 80.4 – 0.55% theoretical conversion efficiency [19]. With respect to ethanol yield, the best result is 0.48 $g_p g_s^{-1}$ using a wood hydrolyzate-adapted strain *Candida shehatae* ATCC 22984 [20].

The productivity then can be determined by plotting the observed yield, Y ps against time is shown in Fig. 5. The slope of the straight line represented the productivity of ethanol. By using STP sludge as substrate, the productivity is 0.3218 $g_p g_s^{-1} h^{-1}$. This means 0.3218 g of ethanol can be produced by 1g of COD utilized per hour. For the continuous ethanol production from pineapple cannery waste, the maximum ethanol productivity was found to be 0.98 $g_p\ g_x^{\ 1}$ h^{-1} [21].

F. Ibrahim, N.A. Abu Osman, J. Usman and N.A. Kadri (Eds.): Biomed 06, IFMBE Proceedings 15, pp. 479-482, 2007
www.springerlink.com ' Springer-Verlag Berlin Heidelberg 2007

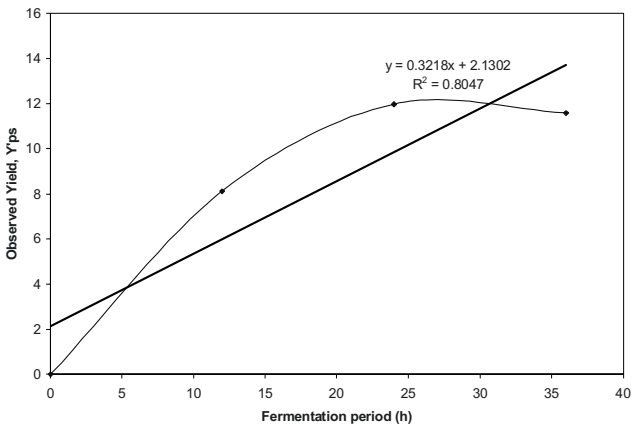

Fig. 5 Productivity of ethanol produced from sludge as substrate.

IV. Conclusions

The optimum media and process conditions from previous study enhanced the bioconversion process for bioethanol production from sludge as the major media. The results revealed that the production of bioethanol with developed process achieved was 9.8% (v/v) at 48h of fermentation period. The maximum observed yield, Y ps of 12.147 g_p g_s ^{1} and productivity of 0.3218 g_p g_s^{-1} h^{-1} in the bioconversion process were determined. The production of ethanol from wastewater sludge also leads to a total of 61.5% reduction of COD along with 67.7% and 44.8% removal of heavy metals such as copper and chromium, respectively after 72 hours fermentation period. Bioethanol production in liquid state bioconversion using sludge as substrate offers beneficial alternative for better management of waste (sludge) to provide a much lived environment.

References

1. Maryland (2004) Sewage Sludge Utilization in Maryland at http://www.mde.state.md.us
2. Inoije S, Sawayama S, Ogi T et al. (1996) Organic Composition of Liquidized Sewage Sludge. Biomass and Bioenergy 10:37-40
3. Wallman J (2000) Handling of Sludge from Sewage Treatment Plant in the Municipality of Nordmaling. Department of Studies in Biology and Environmental Sciences, Umeå University, Sweden
4. DOE (1996) Environmental Quality Reports. Department of Environment, Ministry of Science, Technology and Environmental, Kuala Lumpur, Malaysia
5. Alam M Z, Fakhru l-Razi A, Molla A H et al. (2001) Treatment of Wastewater Sludge by Liquid State Bioconversion Process. J Environ Sci Health A36 (7):1237-1243
6. Microsoft Encarta Reference Library (2003) Microsoft Corporation-(1993-2002)
7. Alam M Z, Fakhru l-Razi A, Molla A H (2003) Biosolids accumulation and Biodegradation of Domestic Wastewater Treatment Plant Sludge by Developed Liquid State Bioconversion Process using a Batch Fermenter. Water Research 37: 3569-3578
8. Sun Y, Cheng J (2001) Hydrolysis of Lignocellulosic Materials for Ethanol Production: A Review. Bioresource Technology 83:1-11
9. Wyman C E (1996) Ethanol production from lignocellulosic biomass: Overview. Taylor and Francis, Washington, DC 1-18
10. Galbe M, Zacchi G (2002) A Review of the Production of Ethanol from Softwood. Appl Microbial Biotechnol 59:618-628
11. Mamma D, Koullas D, Fountoukids G et al. (1996) Bioethanol from Sweet Sorghum: Simultaneous Saccharification and Fermentation of Carbohydrates by a Mixed Microbial Culture. Process Biochemistry 31:377-381
12. Alam M Z, Kabbashi N A, Razak A A (2006) Direct Bioconversion of Domestic Wastewater Sludge as New Substrate for Bioethanol Production through Optimization of Media. In IWA Sustainable Sludge Management Conference, 31 May-2 June, Moscow, Russia
13. Alam M Z, Kabbashi N A, Razak A A (2006) Statistical Optimization of Process Conditions for Direct Bioconversion of Sewage Treatment Plant Sludge for Bioethanol Production. In 1st International Conference on Natural Resources Engineering and Technology 2006 (INRET2006), 24-26th July, Putrajaya, Malaysia. Accepted
14. Caputi A, Ueda J M, Brown T (1968) Spectrophotometric Determination of Chromic Complex Formed during Oxidation of Alcohol. Am J Enol Viticult 19:160-165
15. HACH (2002) Analysis Handbook. 4th edition. HACH Company, pp. 185, 355, 383, 749
16. APHA (1989) Standard Methods for the Examination of Water and Wastewater. 17th Edition, American Public Health Association, Washington, D.C
17. Srinivas D, Rao J K, Theodore K et al (1995) Direct Bioconversion of Cellulosic Material to Ethanol by the Intergeneric Fusant *Trichoderma reesei* QM 9414/*S. cerevisiae* NCIM 3288. Enzyme and Microbial Technology 17:418-423
18. Alam M Z, Fakhru'l-Razi A (2002) Effect of Agitation and Aeration on Bioconversion of Domestic Wastewater Sludge in a Batch Fermenter. J Environ Sci Health A Tox Hazard Subst Environ Eng. 37(6):1087-97
19. Nigam J N (2001) Ethanol Production from Wheat Straw Hemicellulose Hydrolysate by *Pichia stipitis*. Journal of Biotechnology 87:17-27
20. Parekh S R, Wayman M (1987) Performance of a Novel Continuous Dynamic Immobilized Cell Bioreactor in Ethanolic Fermentation. Enzyme and Microbial Technology 9:406-410
21. Nigam J N (1999) Continuous Ethanol Production from Pineapple Cannery Waste. Journal of Biotechnology 72:197-202

Author: M. Z. Alam
Institute: Bioenvironmental Engineering Research Unit (BERU), Department of Biotechnology Engineering, Faculty of Engineering, International Islamic University Malaysia (IIUM)
City: Kuala Lumpur
Country: Malaysia

F. Ibrahim, N.A. Abu Osman, J. Usman and N.A. Kadri (Eds.): Biomed 06, IFMBE Proceedings 15, pp. 479-482, 2007
www.springerlink.com ' Springer-Verlag Berlin Heidelberg 2007

Microbial Bioconversion of Palm Oil Mill Effluent to Citric Acid with Optimum Process Conditions

Parveen Jamal, Md. Zahangir Alam and Aisha Bt. Mohamad

Bioenvironmental Engineering Research Unit (BERU), Department of Biotechnology Engineering, Faculty of Engineering, International Islamic University Malaysia (IIUM), Kuala Lumpur, Malaysia.

Abstract- **Oil palm industry has an important role in contributing to the Malaysian economy. Several million tonnes of crude palm oil is produced annually and approximately, about 10 million tonnes of palm oil mill effluent (POME) (highly polluted organic effluent) is generated every year. Citric acid is a commercially valuable product widely used in many industries. More than 400,000 tonnes of citric acid is produced annually by fermentation of expensive raw materials like glucose and sucrose. Efficient and effective methods of producing citric acid from different cheaper raw materials have been of great interest to many researchers, due to its extensive use. This study is an effort to achieve the goal by introducing a new substrate POME and a potential isolated strain of *Asperillus niger*. The method used was liquid state bioconversion with optimum process conditions obtained from our previous studies using central composite design (CCD) from Minitab software. The optimized parameters were temperature, agitation rate, inoculum size and pH. Analysis has been done everyday up to seven days of fermentation. Performance of the developed process was evaluated on the basis of maximum citric acid (5.24 g/L), chemical oxygen demand removal (COD), total suspended solid (TSS) and removal of heavy metals (cadmium chromium and copper).**

Keywords- **citric acid, palm oil mill effluent, optimization, filamentous fungi, bioconversion.**

I. Introduction

Malaysia is on the way to attain a developed country status with a rapid growth of industrialization programmes. However, the problem of pollution is always linked with the development of industries. Oil palm is a very important asset in the Malaysian economy. Approximately 11.9 million tonnes of crude palm produced consumable oil worth RM 14.79 billion in the year 2002 [1]. For every metric ton of oil produced 2.5 metric tons of effluent are generated, which have an average biochemical oxygen demand (BOD) of 25,000 parts per million. In Malaysia, the BOD level must be below 100 parts per million before effluent can be legally discharged into streams. In this regard, the effluent discharges from palm oil industry can contribute to the pollution problems like oxygen depletion and other related effects to watercourses, due to high content of total solid (4-5 %), suspended organic solid (2-4 %), dissolved organic matters, chemical oxygen demand (COD), BOD and some unrecovered palm oil. Various studies have been carried out in managing of POME such as water recycling using membrane technology [2], treatment by yeast, *Yarrowia lipolytica* [3], production of biodegradable plastics [4], etc.

On the other hand, there is a great demand for citric acid because of its extensive use in various branches of economy, particularly in food, pharmaceutical, toiletries and cosmetics industries as acidulant, stabilizer, flavor enhancer, preservative, antioxidant, emulsifier, and chelating agent. The current world market estimates suggest an annual 2-3 % increase in production from current 7.0×10^5 tonnes citric acid per year. Since this commodity chemical is produced by fermentation of expensive raw materials like glucose and sucrose, the search for low cost substrates has been of great interest to many researchers such as raw starch, sugarcane molasses [5]; ram horn hydrolysate and many more[6, 7]. Microorganisms like fungus and bacteria are largely used in the fermentation biotechnology for production of valuable chemicals. The entire worldwide demand for citric acid is met by fermentation of saccharide materials using filamentous fungus *Aspergillus niger*. In this project also we preferred to use a potential strain A 103 of *Aspergillus niger* selected from ten isolated strains based on the screening results [8].

The present investigation is an effort to develop an environmentally sound and cost effective fermentation process by introducing a new substrate POME for citric acid production and to control the level of the palm oil industries effluent discharge. POME is selected as a substrate because of its rich organic contents. Biosynthesis of this secondary metabolite requires a suitable media containing carbon, nitrogen and phosphorus sources for the proper growth of the microorganism and successful fermentation process. Liquid state bioconversion of POME is proposed to achieve the target because filamentous fungi enhance the biosolids accumulation, bioseparation and biodegradation of treated supernatant [9].

F. Ibrahim, N.A. Abu Osman, J. Usman and N.A. Kadri (Eds.): Biomed 06, IFMBE Proceedings 15, pp. 483-487, 2007
www.springerlink.com ' Springer-Verlag Berlin Heidelberg 2007

II. Materials and methods

A. Sample collection

Raw material, POME was collected from Seri Ulu Langat Palm Oil Mill Sdn. Bhd of Dengkil, Malaysia and stored at 4°C in the laboratory cold room for further use.

B. Fungal strain

Strain used was A-103 of *Aspergillus niger* obtained from a series of experiments of isolation / identification, screening of ten filamentous fungi and media optimization [8]. Selection of this strain was based on its high ability to utilize organic contents of POME for maximum citric acid production, treated bio-solids and COD removal. Potential strain was cultured on PDA plate and incubated at 32℃ for 10 days. Subculture was done once a month using PDA medium in Petri dishes and stored at 32℃ in incubator.

C. Inoculum preparation

Inoculum preparation (spore suspension) was done according to method suggested [8]. Cultures grown on PDA medium in Petri dishes at 32^0C for 7 days were transferred into Erlenmeyer flask (250ml) containing 100 ml of sterile distilled water. It was shaken in a rotary shaker at150 rpm for 24 hours. The filtrate was used as inoculum after measuring its concentration (spores mL^{-1}) by Haemocytometer.

D. Experimental design and optimum process conditions

The experimental design was selected from Minitab software (Minitab Inc.) for determination of optimum process conditions. A total of 31 experiments (three replicates) were conducted with five levels of temperature, agitation , inoculum size, and pH to see their capability of influencing the response i.e., citric acid production. Temperature and pH ranges were chosen to avoid any inhibition of the microorganisms and the bioconversion process as well as substrate degradation. Inoculum size and agitation speed values were chosen for practical purposes. The optimum process conditions of temperature ($30\ ^0$C) , initial pH (3), inoculum size (3%, v/v) and agitation rate (250 rpm) were selected after statistical analysis of the model by analysis of variance (ANOVA), regression coefficient (R^2), F-test (overall model significance), t-test and P-value (each coefficient significance).

E. Analytical methods

Liquid state bioconvervision was done in 500 ml shake flasks using strain A-103 of *Aspergillus niger*. Inoculum was added after sterilization and other optimum process conditions were checked for all experimental flasks. The experimental samples were analyzed everyday for seven days. The effectiveness of the optimum process conditions were evaluated by citric acid concentration determined according to the suggested method [10], pH, chemical oxygen demand (COD) and total suspended solid (TSS) following the standard methods [11] and heavy metals-cadmium, chromium and copper concentrations.

III. Result and discussion

A. Citric acid production

Bioconversion of POME substrate (2 %) for maximum citric acid production with optimum process conditions of temperature ($30\ ^0$C), initial pH (3), inoculum size (3%) and agitation rate (250 rpm) were studied every day (three replicates) for seven days. All samples were analyzed for citric acid concentration, pH, total suspended solids, heavy metals and COD removal.

The result of citric acid production can be observed in Figure-1, which clearly shows an increase in production until sixth day of fermentation. The highest concentration obtained was 5.3 g/L on the sixth day and is very close to the expected result (5.4 g/L) of acid concentration. The production increase was more from day three (2.99 g/L) to day four (4.48 g/L), may be due to heavy metals removal from the POME which can be a resistance cause for citric acid production.

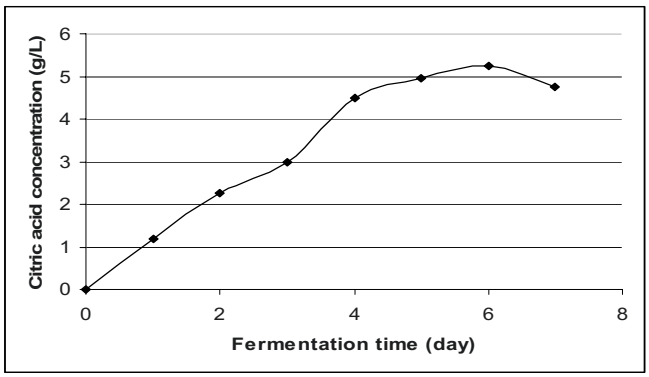

Fig. 1 Citric acid concentration varies with fermentation

F. Ibrahim, N.A. Abu Osman, J. Usman and N.A. Kadri (Eds.): Biomed 06, IFMBE Proceedings 15, pp. 483-487, 2007
www.springerlink.com ' Springer-Verlag Berlin Heidelberg 2007

Further increase in the fermentation time did not enhance the production and a decrease in the concentration was observed on the last day. It might be due to the decrease in the sugar content, available nitrogen and end of stationary phase.

B. Bio-solids

Accumulation of bio-solid (TSS) by treatment of POME with A 103 is presented in Figure-2. There was a slight increase in the biosolid from day zero (3.3g) to day three (3.4g). It increased with fermentation time and reached to maximum on the sixth day indicating that, good growth of microorganism has been obtained on sixth day. During growth phase the microorganisms increase in biomass which contributes to an increase in the mass of total suspended solid. The accumulation rate is slightly declined

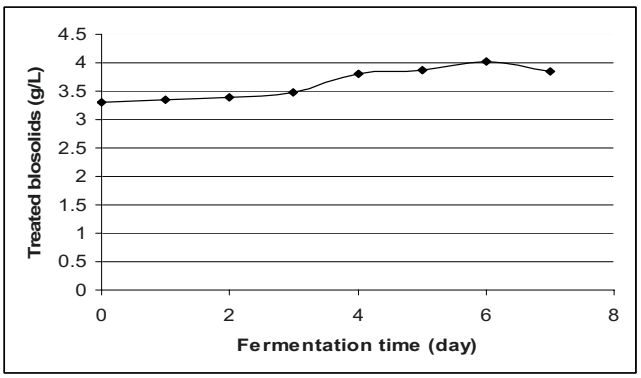

Fig. 2 Accumulation of biosolids varies with fermentation time

at final day of fermentation. It might be due to nature of the microbial growth curve in death phase. Accumulation of bio-solids can be enhanced by the low biodegradation of insoluble organic matters compared to the biosynthesis of mycelium of filamentous fungi [12].

C. pH

Figure-3 shows a decrease in the values of pH with fermentation time. The value of pH was adjusted at 3 in the beginning of fermentation in all experimental flasks having POME substrate, according to the optimum value obtained from analysis results. The curve shows a decreasing trend from day zero until last day of fermentation. The fungal growth leads to excretion of acidic metabolites and thus contributes to an increase in the acidity of the POME. It is reported that, below pH 3.00, the main fermentation product is citric acid whereas higher pH values led to substantial amount of oxalic and gluconic acid [13]. Further decrease in pH on the seventh day caused reduction in citric acid production (Figure-1), which shows that favorable pH is very essential for the successful production of citric acid.

D. Chemical oxygen demand (COD)

Chemical oxygen demand (COD) is an important factor to evaluate the concentration of soluble and insoluble organic substances present in POME. The fungi utilize these organic compounds as nutrient for their growth. Figure-4 indicates the utilization of these substances by strain A 103 and results in accelerating the reduction process of COD. The percentage removal of COD showed an increasing trend and the highest removal (61.28%) was recorded on the last day of the fermentation process. This shows that fungal growth and its secondary metabolite in this bioconversion process helped to reduce the soluble and insoluble substances in POME as well as produced a value added product citric acid. The COD reduction is reported to be more pronounced in lower solid content of waste than of higher solid content [14].

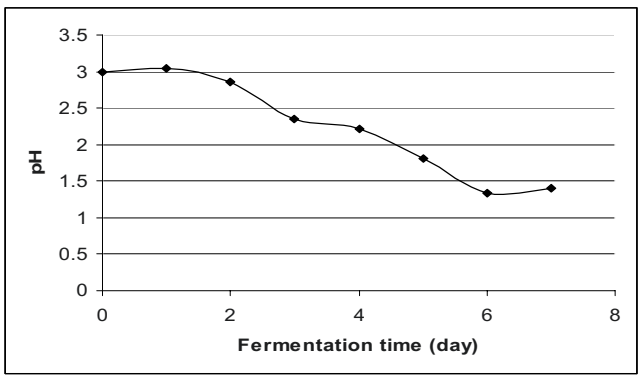

Fig. 3 pH varies with fermentation time

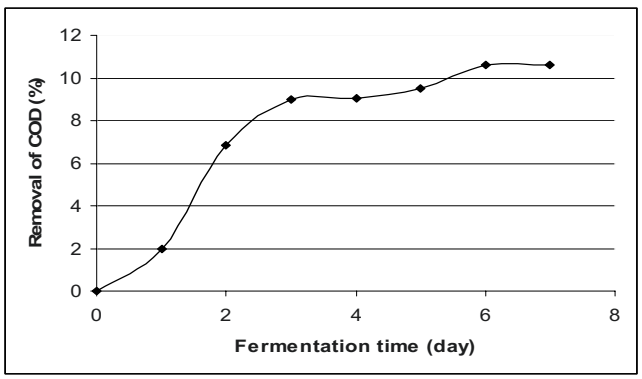

Fig. 4 COD removal varies with fermentation time

F. Ibrahim, N.A. Abu Osman, J. Usman and N.A. Kadri (Eds.): Biomed 06, IFMBE Proceedings 15, pp. 483-487, 2007
www.springerlink.com ' Springer-Verlag Berlin Heidelberg 2007

E. Heavy metals removal

Microorganisms generally accumulate metals on the cell wall and in periplasmic space. Passive metal ion adsorption by the cell wall is frequently denoted as biosorption and does not depend on cellular metabolic activity. The predominance of negatively charged free groups in several biopolymers that form the cell wall confers an anionic character on the cell surface, resulting in passive attraction of various metal cations [15, 16]. In the present study, the biosorption capacity of strain A103 of *Aspergillus niger* was also assessed for three heavy metal chromium, cadmium and copper in order to remove them from POME for safe discharge of effluent.

A continuous decrease in the concentration of chromium, cadmium and copper was observed (Figure-5) throughout the fermentation period. Concentration of chromium decreased from 12.1 mg/L to 1. 2 mg/L, cadmium from 0.85 mg/L to 0.35 mg/L and copper from 15.11 mg/L to 8. 5 mg/L. The percentage removal of chromium (90 %) was highest as compared to cadmium (56.5 %) and copper (44%). The highest percent removal of chromium was might be due to more electrostatic interaction, because the binding of metal ions to cell surface is assumed to be due to electrostatic interaction, leading, in some cases, to formation of complexes between metal cations and different functional binding groups found in carbohydrates, lipids, protein and others biopolymers of microbial cell envelop [15, 17].

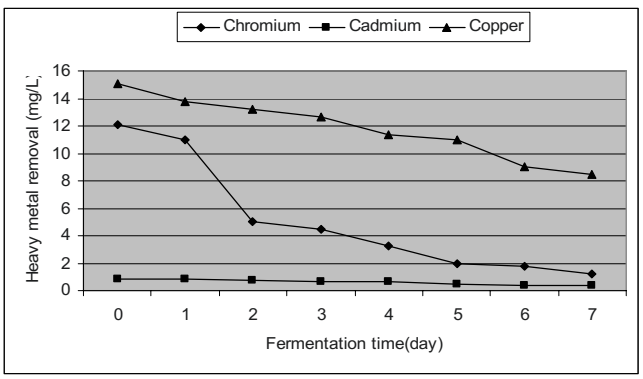

Fig. 5 Heavy metal concentration varies with fermentation

The pH of the sample solution might be another contributing factor for removal of heavy metals because it affects the surface charge of the biosorbents and the degree of ionization.According to some researchers the pH of the metal solutions affects the biosorption because it determines the availability of the metal in a soluble form for adsorption, and dictates the overall surface charge of the adsorbent [16].

IV. Conclusions

We achieved our objective to increase the production of citric acid from 1.16g/L to 5.3 g/L, when microbial bioconversion process was done with optimum process conditions, based on the model obtained. This developed bioconversion process might be a potential measure to solve the soaring environmental problem as well, because of the heavy metals removal which are toxic contaminants that must be removed from wastewaters before discharge. In addition to the removal of heavy metals copper (44 %), cadmium (56.5 %), and chromium (90 %), there was a significant decrease in COD concentration from 99.63g/l to 38.58g/l with percentage removal of 61.28% on the seventh day of fermentation. With this result, we are optimizing the process conditions in fermentor to increase the amount of citric acid. Since Malaysia is one of the major palm oil producers in the world, this method could be beneficial in providing a more effective way in managing palm industry waste, development of an environmental friendly process for the production of citric acid and contributing to the country s economy.

References

1. MPOPC. (2004) Malaysian palm oil promotion council home page. Retrieved March 21, 2004, from http://www.mpopc.org.my.
2. Ahmad A.L, Ismail S & Bhatia S (200) Water recycling from palm oil mill effluent (POME) using membrane technology. Desalination 157(1): 87-95.
3. Oswal N, Sarma P.M, Zinjarde S.S, & Pant A (2002) Palm oil mill effluent treatment by a tropical marine yeast. Bioresource Technology 85 (1):35-37.
4. Fadhil M (2002-2006) Biodegradable plastics from palm oil Mill effluent (POME). Project by University Technology of Malaysia and Delft University of Technology.
5. Ikram-Ul-Haq, Ali S, and Iqbal J (2003) Direct production of citric acid from raw starch by *Aspergillus niger*. Process Biochemistry 38(6):921-924.
6. Kurbanoglu, E.B (2004) Enhancement of citric acid production with ram horn hydrolysate by *Aspergillus Niger*. Bioresource Technology 92: 97-101
7. El-Holi, M.A & Al-Delaimy, K.S (2003) Citric acid production from whey with sugars and additives by *Aspergillus niger*. African Journal of Biotechnology 2 (10): 356- 359.
8. Jamal P, Alam M. Z, Salleh M. R. M and Nadzir M. M (2005) Screening of microorganisms for citric acid production from palm oil mill effluent. Biotechnology 4 (4): 275-278.
9. Alam M. Z, Razi A.F and Molla A.H (2003) Biosolids accumulation and biodegradation of domestic wastewater treatment plant sludge by developed bioconversion process using batch fermenter. Water research 37: 3569-3578.
10. Marier J.R, and Boulet M (1958) Direct determination of citric acid in milk with an improved pyridine- acetic anhydride method. J. Dairy Science 41:1683-92.
11. APHA eds.17th (1989) Standard Methods for the Examination of Water and Wastewater. American Public Health Association . Washington, D.C.

F. Ibrahim, N.A. Abu Osman, J. Usman and N.A. Kadri (Eds.): Biomed 06, IFMBE Proceedings 15, pp. 483-487, 2007
www.springerlink.com ' Springer-Verlag Berlin Heidelberg 2007

12. Alam M.Z, Razi A.F, and Molla A.H (2004) Evaluation of Fungal Potentially for Bioconversion of Domestic Wastewater Sludge. Journal of Environmental Sciences 16 (1):132-137
13. SIRIM Berhad. (2001) Strain improvement & scale up fermentation process by *Aspergillus niger* strain m2SG1 using glucose derived sago hydrolysate and one step membrane electrodialysis separation and purification of sodium citrate. IRPA project report, MOSTI, Malaysia.
14. Friedrich J, Cimerman A, and Perdih A (1983) The use of *Aspergillus niger* for bioconversion of apple ditillery waste. Eur. J. Appl. Microbiol. Biotechnol. 17: 243-247.
15. Gomes N.C.M, Mendonça-Hagler L.C.S, Savaidis I (1998) Metal Biorremediation by Microorganisms. Rev. Microbiol. 29:85-92.
16. Tobin J.M, White C, Gadd G.M (1994) Metal accumulation by fungi: applications in environmental biotechnology. J. Ind. Microbiol. 13:126-130.
17. Galli E, Di Mario F, Rapana P, Lorenzoni P, Angelini (2003) Copper biosorption by *Auricularia polytricha*. Let. Appl. Microbiol. 37:133-137.

Address of the corresponding author:

Author: Parveen Jamal
Institute: Bioenvironmental Engineering Research Unit (BERU), Department of Biotechnology Engineering, Faculty of Engineering, International Islamic University Malaysia (IIUM)
City: Kuala Lumpur
Country: Malaysia

F. Ibrahim, N.A. Abu Osman, J. Usman and N.A. Kadri (Eds.): Biomed 06, IFMBE Proceedings 15, pp. 483-487, 2007
www.springerlink.com ' Springer-Verlag Berlin Heidelberg 2007

Statistical Analysis in Complex-Valued Wavelet Detection of Acute Myocardial Ischemia in Rabbit

I. Provaznik[1], M. Novakova[2] and J. Bardonova[1]

[1] Department of Biomedical Engineering, Brno University of Technology, Brno, Czech Republic
[2] Department of Physiology, Masaryk University, Brno, Czech Republic

Abstract— **In this paper, an application of wavelets to basic cardiology research is described and statistically analysed. The continuous wavelet transform (CWT) is used to detect acute myocardial ischemia caused by occlusion of a coronary artery in animal experiment. The use of CWT may help to understand fundamental changes in heart electrophysiology underlying acute myocardial ischemia. Statistical analysis of wavelet transform results support hypothesed intra-QRS changes.**

Keywords— **Myocardial ischemia, continuous wavelet transform, intra-QRS changes, t-test**

I. Introduction

In the Western world, sudden cardiac death remains a leading cause of death [1]. In majority of cases, sudden death is caused by lethal arrhythmia s preceded by acute myocardial ischemia. The study of ischemic heart disease can reveal mechanisms of its genesis and its influence on the electrophysiology of the heart. Results of such a study could then contribute to a better understanding and both pre-infarction and post-infarction treatment of the disease. Further, the results could help to develop a new noninvasive method needed in cardiology diagnostics [2].

Here, wavelets are used to detect acute myocardial ischemia caused by occlusion of a coronary artery. The use of CWT may help to understand fundamental electrophysiological changes underlying myocardial ischemia. Coronary ischemia is characterized by interrelated metabolic, ionic and neurohumoral events that alter membrane properties of cardiac cells, causing electrophysiological changes. A deteriorated myocardial perfusion causes a potential difference between ischemic and normal regions during the ST segment. While ST depression is considered the most common manifestation of exercise-induced cardiac ischemia, ST elevation may be related to severe posterior, subepicardial or transmural ischemia, or to myocardial infarction. Sometimes, fixed ST elevation or depression may occur. ST changes may therefore be ambiguous and are not always able to reflect changes in myocardial perfusion [3]. Concluding, cardiac ischemia may result in changes in one or more leads of the electrocardiogram. The electrocardiographic criterion for detecting ischemia is ST-segment displacement. The value of this criterion for predicting coronary artery disease is limited and is reported between 47 and 91% for sensitivity and between 69 and 97% for specificity.

Since ischemia causes conduction changes, irregular depolarization of the myocardium may occur. This would be manifested as intra-QRS changes. There is much evidence that ischemia changes in the heart muscle may cause alterations in the QRS spectrum, as an expression of the fragmentation of ventricular depolarization. Abboud [4] detected high-frequency changes in signal-averaged QRS complexes of dogs and human patients caused by ischemia. Further, focal reduction of high-frequency components of the QRS complex under myocardial ischemia induced by percutaneous transluminal coronary angioplasty have been showed [3]. Therefore, a technique similar to the spectrotemporal analysis of late potentials [5] might prove useful in early detection of ischemic changes. This idea is further promoted in the paper by Petterson [6], where ST-segment analysis

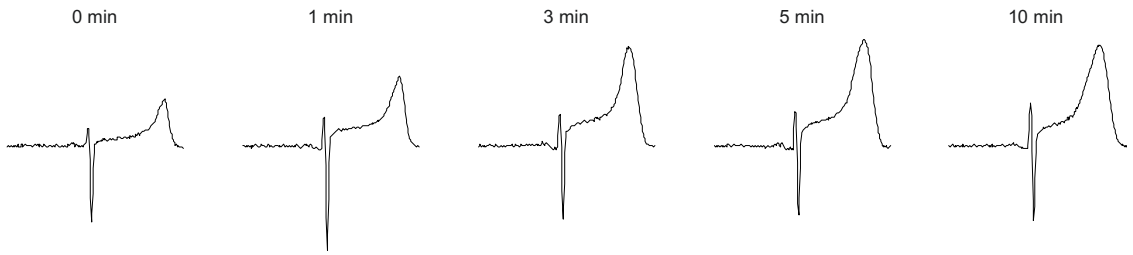

Fig. 1 Typical recordings from myocardial ischemia experiment. Legend: 0 min - control, 1 min to 10 min - acute ischemia

F. Ibrahim, N.A. Abu Osman, J. Usman and N.A. Kadri (Eds.): Biomed 06, IFMBE Proceedings 15, pp. 488-491, 2007
www.springerlink.com ' Springer-Verlag Berlin Heidelberg 2007

criteria are combined with root-mean-square values of QRS high-frequency components criteria.

II. Experiments and data colecction

A. Langendorff Experiment

The group of twelve New Zealand rabbit hearts was examined in this study. The animal was deeply anesthetized, its chest opened and the heart quickly removed. It was mounted on the Langendorff apparatus and placed in a thermostatically controlled bath filled with the solution. The hearts were perfused with Krebs-Henseleit solution (37°C – 0.1°C, 1.25 mM Ca^{2+}).

The experiment was carried out in three steps. First, each heart was allowed to stabilize for 20 minutes. Then, hearts underwent a 20 minutes episode of left anterior descending (LAD) coronary artery occlusion causing acute myocardial ischemia. Then, LAD coronary artery has been released and the heart underwent 30 minutes of reperfusion.

Six silver-silver chloride disc electrodes (4 mm in diameter) for electrogram recording were positioned in the inner surface of the bath. Electrograms were recorded from three bipolar orthogonal leads positioned around the heart. Signals were amplified and digitized at sampling rate 500 Hz. Three bipolar channel 16-bit A/D converters were used. Amplitude of recorded signals varied between 100 μV to 1 mV depending on subject.

60-second recordings of heart activity (electrograms) were taken at baseline (control recording), and 1, 3, 5, and 10 minutes after artery occlusion. Further, recordings were taken at 1, 3, 5, and 10 minutes after artery release.

B. Data Pre-Processing

The data were reduced to set null hypothesis for statistical t-test. Two recordings were chosen to generate studied sample and reference sample. Studied samples were composed of recordings after 3 minutes of ischemia, the reference samples were composed of recordings from control period. L consequent heart cycles were chosen in each recording of all n experiments. Heart cycles are physiologically of (slightly) different length. Therefore, M samples centered on a fiducial point FP were chosen. FP was set as an arithmetic center between QRS-onset and QRS-offset of each heart cycle. Thus, $n*L*2$ recordings of heart cycles were taken for the test. Overall number of signal samples for statistical analysis was $n*L*2*M$. The results in this paper are shown for n=15, L=10, M=250 (i.e. 500 msec for sampling rate of 500 Hz).

C. Wavelet Analysis

Time-frequency manifestation of myocardial ischemia should be graphically presented before some preprocessing and statistical analysis of wavelet data will be done. Such presentation should prove that statistical analysis will likely reject null hypothesis and that time-frequency image bear significant information on electrophysiological changes due to acute myocardial ischemia.

Fig. 2 shows continuous wavelet transform CWT of all recordings from Fig. 1. Time-frequency images reveal some changes within QRS complexes during ischemia (center part of particular pictures). Further, energy dissipation within QRS complex and energy accumulation in T-wave is obvious. All images are normalized in value.

It should be pointed out that QRS complex shape and duration may vary (physiological beat-to-beat variations). These variations are small but may significantly influence statistical test. Therefore, some filtering method should be applied. An efficient algorithm uses median filtering. The method computes so called median QRS complex sample-by-sample from a set of consequent (or nearby) QRS complexes. In the case, median QRS complex is computed from L recordings in both periods of each experiment.

D. Statistical Analysis of Wavelet Images

The main issue in analysis of QRS changes is to localize the abnormal time-scale components contained in each lead

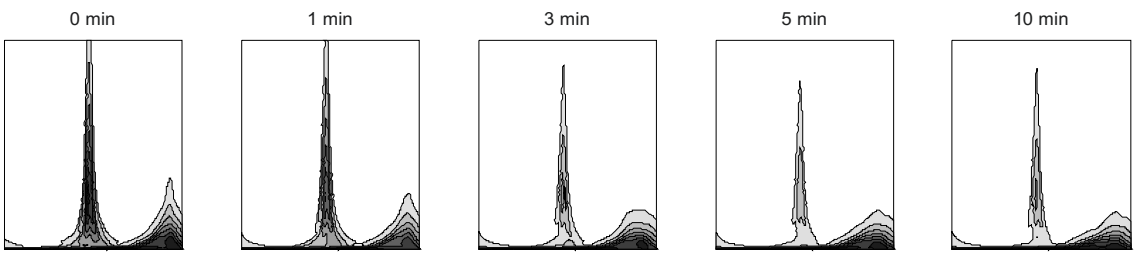

Fig. 2 Modulus of continuous wavelet transform of recordings from Fig. 1 using complex-valued Gaussian wavelet No.2. Legend: 0 min - baseline, 1 min to 10 min - acute ischemia

F. Ibrahim, N.A. Abu Osman, J. Usman and N.A. Kadri (Eds.): Biomed 06, IFMBE Proceedings 15, pp. 488-491, 2007
www.springerlink.com ' Springer-Verlag Berlin Heidelberg 2007

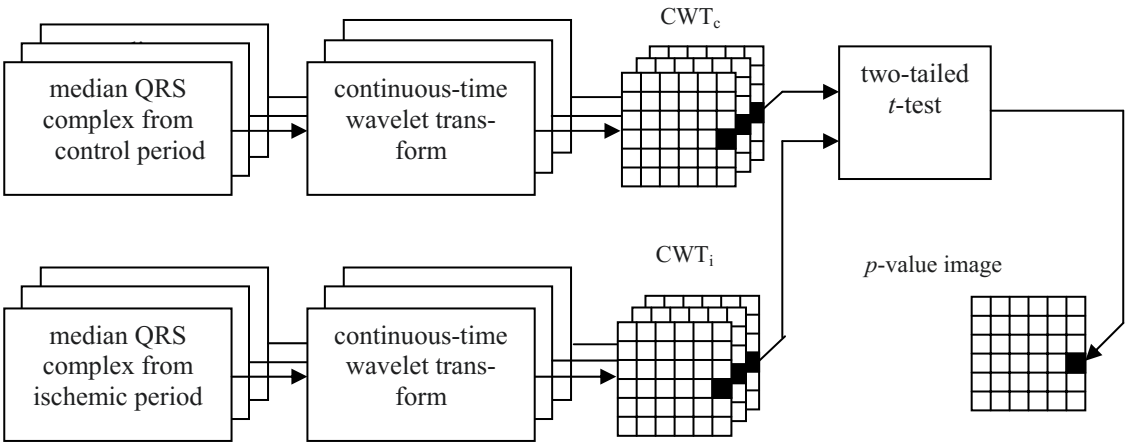

Fig. 3 Schematic representation of the time-frequency *t*-test analysis method

of the ECG signal to identify given cardiac disease. The method compares the representations of the ECGs of the studied (ischemic) sample to a reference (control) sample. The significant abnormality mapping is assessed by comparing the mean value of each of the wavelet transforms of the two studied populations by means of a two-way two-tailed *t*-test to test for the null hypothesis that means are equal.

Significant large variations in shape and duration of QRS complexes in between phases should be detected. In other words, they should serve as an ischemia marker.

Each of $n*2$ median QRS complexes was transformed using CWT. Thus, $n*2$ matrices of $M \times S$ wavelet coefficients were computed. S is a number of scales of CWT.

These matrices provided input data for two-tailed *t*-test. A schematic representation of an analysis procedure is shown in Fig. 3.

III. Results

Fig. 4 and Fig. 5 show the result of *t*-test statistical analysis of CWT modulus and CWT phase of median QRS complexes recorded from X-lead. To understand *p*-value images, one should consider gray-level bar of values below each picture. For the modulus CWT, p is shown for values from 0 to 0.01. For the phase CWT, p is shown for values from 0 to 0.1. The darker is image, the "more likely rejected" is null hypothesis. In other words, dark parts of the image represent most likely position of changes in time-frequency domain. Discussion on the *p*-value images below is concentrated to intra-QRS changes. These changes should be found within QRS complex borders marked by vertical lines in Fig. 4 and Fig. 5.

The analysis of CWT modulus resulted in compact line object at time around 43 msec where $p<0.001$ for scales $1/a=0.35$ to 1 (see Fig. 4). It confirms expected changes in this area - the null hypothesis is rejected with $p<0.001$ here. The dark strip for scales $1/a<0.1$ (at the bottom of the image) is probably generated due to very-low frequency changes remaining in the signals (baseline wandering caused by heart and electrodes movement). The analysis of CWT phase reveals several scattered spots in which the null hypothesis is rejected with $p<0.05$ (see Fig. 5). Although there is a statistical proof of changes, the spots do not compose compact objects and are unlikely an evidence of real electrophysiological changes. The changes are not expected to be sharply delimited in time or frequency.

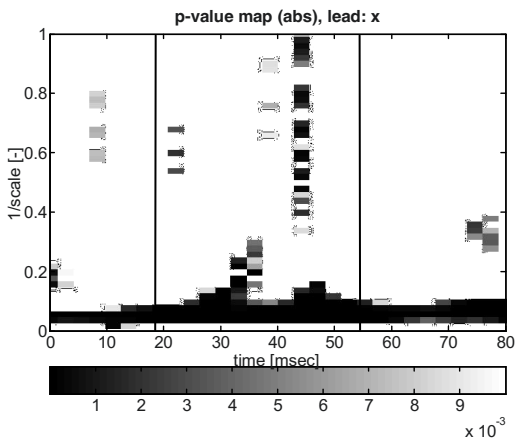

Fig. 4 *p*-value map of null hypothesis testing for modulus of wavelet transform from a set of experiments using complex Gaussian wavelet No.2

F. Ibrahim, N.A. Abu Osman, J. Usman and N.A. Kadri (Eds.): Biomed 06, IFMBE Proceedings 15, pp. 488-491, 2007
www.springerlink.com ' Springer-Verlag Berlin Heidelberg 2007

The CWT analysis discussed above using statistical results is likely a good ischemic marker. Sufficient efficiency was achieved for recordings from X-lead and in CWT modulus ($p<0.001$ for larger areas within QRS complexes in time-frequency images).

The used complex-valued Gaussian wavelet No.2 has been chosen experimentally. A number of tests with various complex wavelets have been done to find convenient solution. Definition of an optimum solution is difficult but the tests have revealed that the best results can only be reached with wavelets possessing two properties: 1. high time-frequency resolution, and 2. fast decay in time domain.

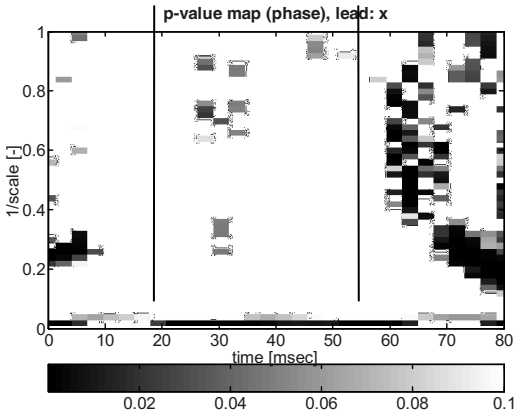

Fig. 5 *p*-value map of null hypothesis testing for phase of wavelet transform from a set of experiments using complex-valued Gaussian wavelet No.2

IV. Conclusions

Wavelets were used for detection of intra-QRS changes during acute myocardial ischemia in animal experiments. The statistical analysis of wavelet modulus and phase images revealed spots in which the given null hypothesis was rejected.

The above presented results can be used to develop an automatic on-line detector of acute myocardial ischemia. The detector would be based on comparison of a current time-frequency image to time-frequency image computed from a signal recorded at the beginning of diagnostic procedure.

Acknowledgment

The research was supported by the grants 102/04/0472 and 305/04/1385 from GACR and the Research Programme of Brno University of Technology MSM 0021630513.

References

1. Alpert A, Thygesen T (2000) Myocardial Infarction Redefined. Journal of American College of Cardiology 36(3):959-969
2. de Luna A B, Stern S (2001) Future of Noninvasive Electrocardiology. In: Zareba W, Maison-Blanche P, Locati E H. Noninvasive Electrocardiology in Clinical Practice, Futura Publishing Co., pp.475-478
3. Gramatikov B, Brinker J, Yi-chun S, Thakor N V (2000) Wavelet Analysis and Time-Frequency Distributions of the Body Surface ECG Before and After Angioplasty. Computer Methods and Programs in Biomedicine 62:87 98
4. Abboud S (1989) High Frequency ECG - A New Method to Examine Depolarization Changes Mediated by Transient Myocardial Ischemia. Proc Computers in Cardiology, 105-108
5. Lander P, Gomis P, et al (1995) Analysis of High-Resolution ECG Changes During Percutaneous Transluminal Coronary Angioplasty. Journal of Electrocardiology 28(Suppl):39-40
6. Pettersson J, Pahlm O, Carro E, Edenbrandt L, Ringborn M, Sörnmo L, Warren S G, Wagner G S (2000) Changes in High-Frequency QRS Components Are More Sensitive Than ST-segment Deviation for Detecting Acute Coronary Artery Occlusion. Journal of the American College of Cardiology 36(6):1827-1834

Address of the corresponding author:

Author:	Ivo Provaznik
Institute:	Department of Biomedical Engineering, Brno University of Technology
Street:	Kolejni 4
City:	CZ-61200 Brno
Country:	Czech Republic
Email:	ivo@ieee.org

F. Ibrahim, N.A. Abu Osman, J. Usman and N.A. Kadri (Eds.): Biomed 06, IFMBE Proceedings 15, pp. 488-491, 2007
www.springerlink.com ' Springer-Verlag Berlin Heidelberg 2007

Statistical Optimization of Process Conditions for Direct Bioconversion of Sewage Treatment Plant Sludge for Bioethanol Production

M.Z. Alam, N.A. Kabbashi, A.A. Razak

Bioenvironmental Engineering Research Unit (BERU), Department of Biotechnology Engineering, Faculty of Engineering, International Islamic University Malaysia (IIUM), Jalan Gombak, 50728 Kuala Lumpur, Malaysia

Abstract— **The production of bioethanol was conducted by utilizing domestic wastewater sludge as major substrate with the aid of yeast, *Saccharomyces cerevisiae* using liquid state bioconversion method (submerged fermentation). The optimization of process conditions such as temperature, initial pH, inoculum dosage and agitation was carried out by using the central composite design (CCD) formulated by a statistical optimization software MINITAB. Optimization of process conditions was done with different ranges of temperature, pH, inoculum sizes and agitations with fixed media compositions obtained from previous study. A polynomial regression model was developed to determine the optimum compositions. Several techniques such ANOVA, t-test, p-values were observed to evaluate the model as well as the optimization process. The maximum ethanol production (9.1% v/v) was found while model equation predicted ethanol production with 11.9% v/v using the optimum conditions: temperature of 33^0C, pH of 7, agitation of 200 rpm and inoculum of 1%. The results indicated that the temperature was highly significant ($p<0.01$) followed by the pH ($p<0.01$), inoculum ($p<0.05$) and agitation rate ($p<0.05$). The coefficient of determination (R^2) was 90.1% which satisfied the adjustment of experimental data in the model.**

Keywords— **Bioethanol, liquid state bioconversion, sewage treatment plant sludge, central composite design, optimization**

I. Introduction

The treatment and disposal of sewage sludge, which are mainly of organic origin, pose one of the most serious challenges all over the world [1]. The major problem on sludge is it contains both valuable and unwanted matter such as heavy metals and others, which create environmental and health problems despite its treatment [2]. As the rate of industrialization is accelerated the demands on advanced treatment processes for sewage and industrial wastewaters similarly increased [3]. Sewage sludge is very heterogeneous substrate where the main groups of the organic solids in the sludge are protein, carbohydrates, fats, and oils which vary with their origin, system and efficiency of the wastewater treatment plant [4, 5]. These essential nutrients offer the liquid state bioconversion by potential microbes for value added product like bioetanol beside its effective treatment.

Due to the increasing costs of substrates such as molasses, sweet sorghum, maize starch, sugarcane, sugar beet, tapioca, wheat starch etc. which are human food and increasing demand for fuel ethanol, there is a need to search for cheaper and abundant substrate and to develop an efficient and less expensive technology so that product can be made available more cheaply [6]. Ethanol can be produced from lignocellulosic biomass which includes agricultural residues, herbaceous crops, forestry wastes, wastepaper and other wastes [7-9]. In recent years it has been noted that instead of traditional feedstocks (starch crops), cellulosic biomass (cellulose and hemicellulose), such as agricultural and forestry residues, waste paper, and industrial wastes are used as an ideally inexpensive and abundantly available source of sugar for fermentation into the sustainable transportation fuel ethanol which is still under development [10,11]. Besides, it is observed that POME contains about 10% crude protein, 12% crude fiber and 54% soluble carbohydrate on the dry basis[12] which could make it suitable substrate for ethanol production. Therefore an effective solution to sludge as renewable resource was studied for higher production of bioethanol with optimum process conditions using response surface methodology.

II. Materials and methods

A. Fermentation media and culture

Sewage treatment plant (STP) sludge (0.5-1% w/w of TSS) was used as major substrate/medium with supplementary of available and cheaper nutrients for initial microbial growth in the fermentation process. The STP sludge was collected from secondary clarifier at Indah Water Konsortium (IWK) Sewage Treatment Plant, Damansara, Kuala Lumpur, Malaysia. The initial pH observed was 6.3-6.8. The sample was stored at 4°C in cold room for further use. The yeast *Saccharomyces cerevisiae* was collected from MARDI (Research Institute), Malaysia. Using quadrant-streaking method, *S. cerevisiae* was cultured on YMPG media (Yeast Extract-Malt Extract-Peptone-Glucose, Difco)

F. Ibrahim, N.A. Abu Osman, J. Usman and N.A. Kadri (Eds.): Biomed 06, IFMBE Proceedings 15, pp. 492-495, 2007
www.springerlink.com ' Springer-Verlag Berlin Heidelberg 2007

at 30^0C for 1-3 days. Subculture was done once a month and stored at 4^0C.

B. Inoculump preparation

Using a sterilize technique, one successful colony of *S. cerevisiae* were taken from PDA plate and was inoculated into 100 mL shake flask containing 50 mL of YM media. The flasks were incubated at 30^0C 24 hours for 150 rpm. After incubation, the bottles were examined. The color of the bottles should be murky indicating that the matured cell has settled with the environment of the bottle. This bottle containing the live culture of *S. cerevisiae* can be kept in refrigerator with measuring the concentration (10^7 cfu/ml) for future used.

C. Experimental design and optimization of process conditions for bioetanol production

Experimental design for optimization of process conditions was done using central composite design (CCD). Four factors were considered for optimization: initial pH, temperature, agitation and inoculum size. The different levels of their coded and actual values for CCD are shown in Table 1. Analysis of experimental results obtained by CCD design was done statistically with the aid of Minitab software. The analysis was done using these following tools; ANOVA (analysis of variance), p and t tests.

Table 1 Levels of processing conditions as factors for central composite design (CCD)

Parameters	Unit	Levels				
		-2	-1	0	1	2
Temp	°C	24	27	30	33	36
pH	-	1	3	5	7	9
Agitation	rpm	0	100	200	300	400
Inoculum	%(v/v)	1	2	3	4	5

The maximum bioethanol production was taken as the dependent variable of response (Y). A second order polynomial equation was developed using the data by multiple regression procedure. This result in empirical model that related the response measured in the independent variables to the experiment. For a four-factor system, the model equation is as follows:

$$Y = \beta_0 + \beta_1 X_1 + \beta_2 X_2 + \beta_3 X_3 + \beta_4 X_4 + \beta_{11} X_1^2 + \beta_{22} X_2^2 + \beta_{33} X_3^2 + \beta_{44} X_4^2 + \beta_{12} X_1 X_2 + \beta_{13} X_1 X_3 + \beta_{14} X_1 X_4 + \beta_{23} X_2 X_3 + \beta_{24} X_2 X_4 + \beta_{34} X_3 X_4 \quad (1)$$

where Y is bioethanol production (%), predicted response; β_0, intercept; β_1, β_2, β_3, β_4, linear coefficients; β_{11}, β_{22}, β_{33}, β_{44}, squared coefficients; β_{12}, β_{13}, β_{14}, β_{23}, β_{24}, β_{34}, interaction coefficients.

A 500 ml of Erlenmeyer flask containing 100 ml of sewage sludge with the different levels of factors (process parameters) as the experimental conditions was used to conduct the lad-scale experiment according to the experimental design shown by the MINITAB software. The optimum media was used in this study obtained from previous study [13]. Data were harvest for analysis in every day (24 hrs) until 4 days of treatment. Data were the average of three replicates.

D. Analysis of model and parameters

A second order polynomial model was developed to determine the optimum process conditions. Several techniques such as ANOVA, t-test, p-values were observed to evaluate the model as well as the optimization process. The bioethanol was determined according to the dichromate methods [14], chemical oxygen demand (COD) was measured with the method of HACH [15], total suspended solids (TSS) of treated samples were observed using APHA [16] standard methods and pH were observed using pH meters.

III. Results and discussion

Regression analysis is performed on the data obtained from the design experiments. The Minitab software was used to generate the second-order polynomial regression equation correlating the production of bioethanol with the process condition variables, X_1, X_2, X_3, and X_4 is shown in Equation 2:

$$Y \text{ (Bioethanol concentration,\%)} = -171 + 12.3 X_1 - 5.27 X_2 - 0.0743 X_3 + 8.52 X_4 - 0.215 X_1^2 - 0.0551 X_2^2 - 0.000069 X_3^2 - 0.164 X_4^2 + 0.212 X_1X_2 + 0.00244 X_1X_3 - 0.249 X_1X_4 + 0.00301 X_2X_3 - 0.295 X_2X_4 + 0.00485 X_3X_4 \quad (2)$$

Where Y is the predicted value of bioethanol, and X_1, X_2, X_3, X_4 are the independent variables, temperature (°C), pH, agitation rate (rpm) and inoculum size (%) respectively. Table 2 shows the observed (experimental) values along with the predicted values of bioethanol. The results showed that the maximum bioethanol was produced in Run 5 with production of 9.15% in given process conditions which therefore justified further optimization of conditions with maximum bioethanol production.

The R^2 value for this optimization is 90.1% signifying that the bioethanol production is highly correlated with the independent variables, namely, temperature (°C), pH, agitation rate (rpm) and inoculum size (%). The high R^2 value also signified the accuracy of the observed response to the predicted response.

F. Ibrahim, N.A. Abu Osman, J. Usman and N.A. Kadri (Eds.): Biomed 06, IFMBE Proceedings 15, pp. 492-495, 2007
www.springerlink.com ' Springer-Verlag Berlin Heidelberg 2007

Table 2 Results for observed and predicted bioethanol production obtained from regression model equation in optimization of process condition

Run	Factors								Bioethanol (%)	
	Temperature (°C)		pH		Agitation rate (rpm)		Inoculum size (%)		Observed	Predicted
	Coded	Actual (℃)	Coded	Actual	Coded	Actual (rpm)	Coded	Actual (%)		
1	0	30	0	5	0	200	0	3	7.05	8.76
2	0	30	0	5	0	200	0	3	7.05	8.76
3	0	30	2	9	0	200	0	3	7.7	8.90
4	1	33	-1	3	1	300	-1	2	2.2	4.90
5	1	33	1	7	1	300	-1	2	9.15	10.85
6	-1	27	1	7	1	300	1	4	2.5	4.55
7	0	30	0	5	0	200	0	3	6.5	8.76
8	-1	27	1	7	-1	100	-1	2	0.4	5.20
9	-1	27	-1	3	-1	100	1	4	4.7	7.57
10	1	33	-1	3	-1	100	1	4	0	3.27
11	2	36	0	5	0	200	0	3	5.53	2.22
12	0	30	0	5	0	200	-2	1	7.3	8.98
13	0	30	0	5	-2	0	0	3	8.1	5.82
14	-1	27	-1	3	1	300	1	4	0.78	6.05
15	-1	27	1	7	-1	100	1	4	1.04	3.66
16	-2	24	0	5	0	200	0	3	3.7	-0.18
17	1	33	1	7	-1	100	-1	2	6.7	8.98
18	-1	27	-1	3	1	300	-1	2	0.86	3.28
19	0	30	0	5	0	200	0	3	6.1	8.76
20	0	30	0	5	0	200	0	3	7.35	8.76
21	0	30	0	5	0	200	0	3	6.03	8.76
22	0	30	0	5	0	200	2	5	6.9	7.23
23	1	33	1	7	1	300	1	4	4.8	8.27
24	1	33	-1	3	1	300	1	4	2.9	4.68
25	0	30	0	5	0	200	0	3	7.4	8.76
26	1	33	-1	3	-1	100	-1	2	2.9	5.43
27	1	33	1	7	-1	100	1	4	2.3	4.45
28	0	30	-2	1	0	200	0	3	14.3	6.86
29	-1	27	-1	3	-1	100	-1	2	4.9	6.740
30	-1	27	1	7	1	300	-1	2	2.1	4.12
31	0	30	0	5	2	400	0	3	4.8	6.18

The Student t-distribution and the corresponding *p*-values along with the second order polynomial coefficients which are evaluated using MiniTab software are listed in Table 3. From the results, it is observed the p-values of all coefficients with the exclusion of the interaction between pH and pH and interaction between inoculum size and inoculum size are low that is less than 0.05 indicating them to be significant coefficients in this model. It was also observed that all parameters had significant contribution to the model ($p<0.01$ and $p<0.05$) for production of ethanol using sludge as substrate. According to Alam [17], the results obtained in optimum liquid state bioconversion processes indicated that wheat flour at a concentration of 1.5-2% (w/w) is a better co-substrate in sludge containing medium, with optimum initial pH of 4.5-5.5, temperature of 33-35℃ and inoculum size of 2-3% (v/w). So far, none investigation was with statistical optimization of process conditions for ethanol production using wastes as substrates.

Many studies on ethanol production have been mainly performed by *S. cerevisiae*, and most of the condition is acidic since yeast generally able to grow and efficiently ferment ethanol at pH values of 3.5 to 6.0 and at temperatures of 28°C to 35°C [18,19].

As stated before, the optimum yield of bioethanol is produced in Run 5 with a percent yield of 9.15% in process conditions. Varying the optimum factors of the said design on the basis of the regression equation generated has lead to a conclusion of a more optimum predicted bioethanol yield of 11.89% instead of 10.85% at temperature of 33°C, pH7, 200 rpm agitation rate and 1% inoculum size.

F. Ibrahim, N.A. Abu Osman, J. Usman and N.A. Kadri (Eds.): Biomed 06, IFMBE Proceedings 15, pp. 492-495, 2007
www.springerlink.com ' Springer-Verlag Berlin Heidelberg 2007

Table 3 Coefficients of linear, quadratic and interactions effects and their t- and p-values from regression analysis for central composite design

Predictor	Coefficient	SE Coefficient	T-test	P-value
Constant	-171.29	25.30	-6.77	0.000
X_1	12.258	1.481	8.28	0.000
X_2	-5.272	1.608	-3.28	0.005
X_3	-0.07431	0.03181	-2.34	0.033
X_4	8.515	3.259	2.61	0.019
X_1*X_1	-0.21550	0.02366	-9.11	0.000
X_2*X_2	-0.05505	0.05323	-1.03	0.316
X_3*X_3	-0.00006930	0.00002129	-3.25	0.005
X_4*X_4	-0.1645	0.2129	-0.77	0.451
X_1*X_2	0.21240	0.04744	4.48	0.000
X_1*X_3	0.0024396	0.0009488	2.57	0.021
X_1*X_4	-0.24896	0.09488	-2.62	0.018
X_2*X_3	0.003015	0.001423	2.12	0.050
X_2*X_4	-0.2954	0.1423	-2.08	0.054
X_3*X_4	0.004845	0.002847	1.70	0.108

IV. Conclusions

It is indicated that about 9.1% ethanol was found in the process optimization in run 5 with predicted ethanol yield of 10.9% at temperature of 33°C, pH of 7, agitation rate of 300 rpm and inoculum size of 2%. The regression model was able to increase 1% (11.9%) predicted ethanol by applying the process conditions such as 33^0C temperature 7 pH, 200 rpm agitation rate, 1% inoculum size. The observed ethanol yields for process optimization was very close to the predicted response indicating the accuracy of the results obtained. Production of bioethanol by liquid state bioconversion using STP sludge as substrate offers beneficial alternative for better management in terms of reduction of management cost and provide environmental friendly disposal of sludge.

References

1. Martin A M (1991) Biological Degradation of Wastes. Elsevier Science Publisher Ltd, Great Yarmouth, GB
2. David M L, Cornwell M L (1998) Introduction to Environmental Engineering, 3rd Ed, WCB/McGraw Hill
3. Tenenbaum D (1997) The Beauty of Biosolids. Focus, vol. 105:1 at http://ehp.niehs.nih.gov
4. McGhee T J (1991) Water Supply and Sewerage. McGraw-Hill, New York
5. Alam M Z, Fakhru l-Razi A, Molla A H (2003) Biosolids Accumulation and Biodegradation of Domestic Wastewater Treatment Plant Sludge by Developed Liquid State Bioconversion Process using a Batch Fermenter. Water Research. 37: 3569-3578
6. Mamma D, Koullas D, Fountoukids G et al (1996) Bioethanol from Sweet Sorghum: Simultaneous Saccharification and Fermentation of Carbohydrates by a Mixed Microbial Culture. Process Biochemistry 31:377-381
7. Wyman C E (1996) Ethanol Production from Lignocellulosic Biomass: Overview. Handbook on Bioethanol: Production and Utilization. Taylor and Francis, Washington, DC , pp 1-18
8. Ruanglek V, Maneewatthana D, Tripetchkul S (2006) Evaluation of Thai agro-Industrial Wastes for Bio-Ethanol Production by *Zymomonas mobilis*. Process Biochemistry 4:1432-1437
9. K d r Z, Szengyel Z, R zey K (2004) Simultaneous Saccharification and Fermentation (SSF) of Industrial Wastes for the Production of Ethanol. Industrial Crops and Products 20:103-110
10. Fujita Y, Takahashi S, Ueda M et al (2002) Direct and Efficient Production of Ethanol from Cellulosic Material with a Yeast Strain Displaying Cellulolytic Enzymes. Appl Environ Microbiol. 68(10):5136 5141
11. Kim S, Dale B E (2004) Global Potential Bioethanol Production from Wasted Crops and Crops Residues. Biomass and Bioenergy 26:361-375
12. Hutagalung R I (2005) Use of Carbohydrate Residues in Malaysia. Department of Animal Science, University Pertanian Malaysia, Malaysia
13. Alam M Z, Kabbashi N A, Razak A A (2006) Direct Bioconversion of Domestic Wastewater Sludge as New Substrate for Bioethanol Production through Optimization of Media. IWA Sustainable Sludge Management Conference, 31 May-2 June, Moscow, Russia
14. Caputi A, Ueda J M, Brown T (1968) Spectrophotometric Determination of Chromic Complex Formed During Oxidation of Alcohol. Am. J. Enol. Viticult. 19:160-165
15. HACH (2002) Analysis Handbook, 4th edition, HACH Company, pp 185, 355, 383, 749
16. APHA (1989) Standard Methods for the Examination of Water and Wastewater. 17th, American Public Health Association, Washington, DC
17. Alam M Z, Fakhru'l-Razi A, Molla A H (2003) Optimization of Liquid State Bioconversion Process for Microbial Treatment of Domestic Wastewater Sludge. J. Environ. Eng. Sci. 2 (4):299-306
18. Naim K (1996) Ethanol-Potential Source of Energy and Chemical Products. Biotechnology, vol 6, Products of primary metabolism. Rhem H.J and Reed G. (Eds), VHC Publishers, New York, pp 121-204
19. Ogunye A F, Susu A A, Digwo N N (1978) Ethanol Production from Pineapple Juice. J. Eng. Technol. 1:24-29

Address of the corresponding author:

Author: M. Z. Alam
Institute: Bioenvironmental Engineering Research Unit (BERU), Department of Biotechnology Engineering, Faculty of Engineering, International Islamic University Malaysia (IIUM)
City: Kuala Lumpur
Country: Malaysia

F. Ibrahim, N.A. Abu Osman, J. Usman and N.A. Kadri (Eds.): Biomed 06, IFMBE Proceedings 15, pp. 492-495, 2007
www.springerlink.com ' Springer-Verlag Berlin Heidelberg 2007

Study for activation of human telomerase reverse transcriptase, as major component of cancer, expressed in *E. coli*

Jong-Uk Koh, Hyun-Young Cho, Young-Bin Kwon, Kwang-Hoon Kong

The Department of Chemistry, College of Natural Sciences, Chung-Ang University, Seoul 156-756, Republic of Korea

Abstract— **Telomerase is a specialized RNA-directed DNA polymerase that extends telomeres of eukaryotic chromosomes in most human cancer. To date, little is known about how telomerase is activated and controlled in cancer, although activation is thought to be involved in cancer cell immortalization. Telomerase is composed of two main subunits, the rate-limiting catalytic subunit, human telomerase reverse transcriptase (hTERT), and the integral template of hTERT, human telomerase RNA components (hTR). Also, the hTERT are phosphor-proteins and its phosphorylation is a prerequisite for the activation of telomerase. Thus, phosphorylation of hTERT by protein kinase represents an elemental and essential step in maintenance of telomerase activity. To regulate activation of telomerase, hTERT gene amplified from FLAG-hTERT cDNA was expressed with 6xHis residues in *E. coli*. The expressed hTERT was identified using hTERT antibody and purified by His-bind resins. Also, hTR gene was amplified from genomic DNA of HeLa cell and gained hTR by *in vitro* reverse transcription methods. After the purified 6xHis-tagged hTERT and the hTR was reconstitution, the reconstituted complex was phosphorylated. Then, the activated hTERT by protein kinases was detected by PCR-based modified TRAP assay. This study will be useful for developments of drug design targeting hTERT in anticancer therapy.**

Keywords— **human telomerase reverse transcriptase, human telomerase RNA components, phosphorylation, hTERT, hTR**

I. Introduction

Telomerase is ribonucleoprotein (RNP) complex that elongates telomeres [1, 2].The telomere is a specialized structure at the ends of linear eukaryotic chromosomes that provides mechanism for maintaining chromosome length and has critical functions in maintaining chromosome stability [1, 3]. Telomeres contain distinctive repeats of guanidine-rich sequences (TTAGGG) that are replicated by DNA-dependent DNA polymerase and by telomerase-dependent synthesis of telomeric DAN from an RNA templates [4]. In a variety of organisms, the loss of telomerase activity results in telomere shortening and ultimately a period of cell death or growth arrest [5]. In human, the enzyme plays an important role in cancer. Most somatic cells lack telomerase activity and correspondingly lose telomeric DNA, thus limiting their proliferative capacity. Cancer cells can overcome this proliferative block through the illegitimate transcriptional up-regulation of the gene encoding the catalytic subunit of the enzyme [6]. It remains unclear whether these two components, hTERT and hTR are sufficient for *in vitro* telomerase reconstitution. Although hTERT and hTR are essential for telomerase activity, little is known about how telomerase is activated and maintained at the enzyme levels in human cancers. Some possible mechanism is that tertiary and quaternary structures of the large telomerase complex are modulated by protein phosphorlyation in such a way that the enzyme is activated [7, 8]. The reconstitution of hTERT, hTR and phosphorylation of hTERT is necessary to solve question for telomerase activity and to provide an experimental system in which to identify factors that are essential for or that stimulate telomerase activity *in vitro*. Here, we reported the production method of human telomerase reverse transcriptase expressed in *Escherichia coli* for anticancer therapy. Moreover, we demonstrated that the regulation of telomerase activity and subsequent maintenance of its activity required a prerequisite phosphorylation of hTERT by kinase.

II. Materials and methods

Plasmid Construction for the hTERT Expression: The plasmid for hTERT expression was made by subcloning the *Eco*R I-*Sal* I fragment of FLAG-hTERT cDNA. For construction of the expression plasmid, each hTERT fragment contained proper restriction enzyme sites were amplified by polymerase chain reaction (PCR). At Result, the hTERT gene coded $hTERT_{1\text{-}1132}$ was cloned completely and used to transform *E. coli* strain BL21 Star (DE3) contained ColE1-compatible, pACYC-based plasmid coded the *argU* and *proL* tRNA and a ColE1- and pACYC-compatible pSC101-based plasmid coded the *argU*, *ileY*, and *leuW* tRNA.

Expression and Purification of the 6xHis-taged hTERT: E. coli strain BL21 Star (DE3) harboring the constructed plasmid was grown in LB broth containing kanamycin (50 μg /ml), chloramphenicol (34 μg/ml) and streptomycin (75 μg/ml) at 37˚C until OD_{600} =0.6-0.7, and recombinant proteins were induced with 0.1mM isopropyl-1-thio-β-D-galactopyranoside. The induced cells were harvested by centrifugation at 10,000 g for 10min at 4˚C, then lysised using sonicator at 4˚C for 10 min. After centrifugation (12,000g, 30 min), a soluble fraction of the extract contain-

F. Ibrahim, N.A. Abu Osman, J. Usman and N.A. Kadri (Eds.): Biomed 06, IFMBE Proceedings 15, pp. 496-498, 2007
www.springerlink.com ' Springer-Verlag Berlin Heidelberg 2007

ing 6xHis-taged hTERT was judged by Coomassie-stained gradient sodium dodecyl sulfate-polyacrylamide gel electrophoresis (SDS-PAGE) and analyized by Western-blotting using hTERT antibody.

Preparation of hTR— The gene encoding hTR (Genebank number: U86046) was generated by PCR from HeLa genomic DNA. The resultant PCR product was digested and inserted into the plasmid vector pGEM-T easy containing the T7 RNA polymerase promoter site. The hTR was prepared with the MEGAscripts (T7) kit using pGEM-hTR digested by Ecl136II (neoschizomer of *Sac* I).

Phophorylation of the 6xHis-taged hTERT in vitro: Protein kinase Cα protein kinase were activated with the protocol provided by the manufacture. The equal concentration of Protein kinase Cα in the purified 6xHis-taged hTERT fractions were subjected to incubation in appropriate phophorylation buffer containing ATP and the reaction was allowed to proceed at 30˚C for 30min.

Telomerase activity measurement: The appropriate *in vitro* transcribed hTR and the phosphorylated 6xHis-taged hTERT were mixed together, incubated at 33˚C for 10min for reconstitution and then subjected to telomerase reaction. Telomerase activity was measured using a commercially available PCR-based according to the manufacturer s protocol.

III. Results

A, telomerase activity was measured by TRAPeze telomerase detection kit (Gel-base TRAP assay). Lane 1, as a negative control, as a negative control, telomerase reaction were performed with only telomerase storage buffer without 6xHis tagged hTERT and hTR.; Lane 2, 100ng of hTR and 100ng of non-phosphorylated 6xHis tagged hTERT were subjected to the reaction mixture for telomerase activity.; Lane 3-6, telomerase reaction were performed with 100ng of phosphorylated 6xHis tagged hTERT by protein kinase Cα and of 0, 30, 60 and 100ng of *in vitro* transcribed hTR.; Lane 7-10, 50ng *in vitro* transcribed hTR, and 0, 15, 30 or 50ng of phosphorylated 6xHis tagged hTERT by protein kinase Cα.; ***B,*** the relative telomerase activity was measursed by TRAPeze XL telomerase detection kit under varying amounts of hTR at constant amounts of phosphorylated 6xHis tagged hTERT.; ***C,*** under varying amounts of phosphorylated 6xHis tagged hTERT at constant amounts of hTR.

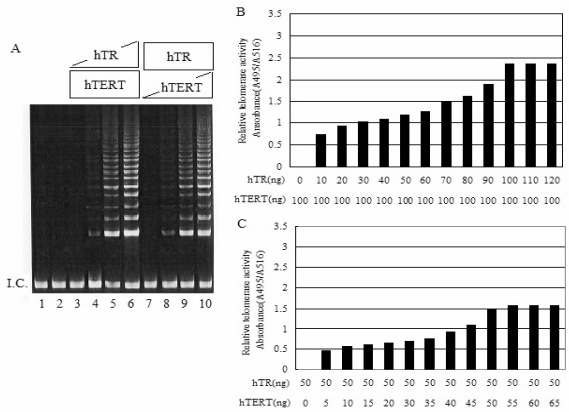

Fig. 1 Regulation of telomerase activity with activated hTERT by protein kinase Cα and hTR reconstituted *in vitro*

IV. Discussions

hTERT had not been reported expression and purification by using bacterial expression system. We thought that bacterial system used different codon usage in eukaryotic expression system was unsuited for hTERT expression problem. Therefore, the complete gene encoding $hTERT_{1\text{-}1132}$ was divided into three parts ($hTERT_{1\text{-}397}$, $hTERT_{397\text{-}676}$, $hTERT_{676\text{-}1132}$). The primers amplified each hTERT fragment were designed using *E. coli* codon usage at primers end terminals. Also, the hTERT gene coded $hTERT_{1\text{-}1132}$ used to transform *E. coli* strain BL21 Star (DE3) contained pACYC-based plasmid encoding the *argU* and *proL* tRNA and pSC101-based plasmid encoding the *argU*, *ileY*, and *leuW* tRNA. The expression level of recombinant 6xHis-taged hTERT was much higher in BL21 Star (DE3) contained pACYC-based plasmid and pSC101-based plasmid than in BL21 Star (DE3), and therefore we selected BL21 Star (DE3) contained pACYC-based plasmid and pSC101-based plasmid to express 6xHis-taged hTERT. The phosphorylation sites on hTERT have yet to be determined, protein kinase Cα in human breast cancer cells is required for the activation of telomerase activity and subsequent maintenance of its activity. We attempted phosphoylation of recombinant the 6xHis-taged hTERT using protein kinase Cα. When hTERT was not phosphorlated by protein kinase Cα, telomerase activity did not detectable. These results indicate that phosphoylation of hTERT must be required for telomerase activation. After phosphorylated 6xHis-taged hTERT and *in vitro* transcribed hTR reconstitutied *in vitro,* telomerase activity was detected qualitatively and quantitatively by using telomerase assay kits. When phosphorylated hTERT and hTR were present, telomerase activity was detected. However, phosphorylated hTERT alone did not

F. Ibrahim, N.A. Abu Osman, J. Usman and N.A. Kadri (Eds.): Biomed 06, IFMBE Proceedings 15, pp. 496-498, 2007
www.springerlink.com ' Springer-Verlag Berlin Heidelberg 2007

exhibite telomerase activity. Also, telomerase activity of the reconstituted components *in vitro* was measured quantitatively in the presence of varying molar ratios of the phosphorylated hTERT and hTR. Maximum telomerase activity was observed when phosphorylated hTERT and hTR were present at approximate equal molar ratio in the reaction mixture. Judging from the results obtained by these two methods, reconstitution of equal molar amounts of phosphorylated hTERT and hTR seemed to occur resulting in the optimal telomerase activity, suggesting efficient complex formation of the components *in vitro*.

V. Conclusion

We constructed plasmid suitable for hTERT expression using *E. coli* usage codon and expressed soluble form in *E. coli* expression system. The activated hTERT by phosphorylation and hTR are minimal components for telomerase activity *in vitro.* These expression systems, purification methods and activated methods of hTERT will be useful not only for mechanism and structural studies of telomerase but also for developments of drug design targeting hTERT in anticancer therapy.

References

1. Blackburn E.H., Szostak J.W., (1984) The molecular structure of centromeres and telomeres, Annu. Res. Biochem. 53: 163-194.
2. Greder C.W., Blackburn E.H., (1985) Identiication of specific telomere terminal transferase activity in Tetrahymena extracts, Cell 43: 405-413.
3. Nugent C.I., Lundblad V., (1998) The telomerase reverse transcriptase: Components and regulation, Genes & Dev. 12: 1073-1085.
4. Sandell L.L., Zakian V.A., (1993) Loss of telomere: arrest, recovery, and chromosome loss, Cell 75**:** 725-729.
5. Zakian V.A., (1995) Telomeres: beginning to understand the end, Science 270**:** 1601-1607.
6. Sedivy J.M., (1998) Can ends justify the means?: telomeres and the mechanisms of replicative senescence and immortalization in mammalian cells, Proc. Natl. Acad. Sci. USA 95: 9078-9081.
7. Li H., Zhao L.L., Funder J.W. et al. (1997) Protein phosphatase 2A inhibits nuclear telomerase activity in human breast cancer cells, J. Biol. Chem. 272: 16729 16732.
8. Li H., Zhao L.L., Funder J.W. et al. (1998) Telomerase is controlled by protein kinase Cα in human breast cancer cells, J. Biol. Chem. 273: 33436-33442.

Address of the corresponding author:

Author: Kwnag-Hoon Kong
Institute: The Department of Chemistry,
College of Natural Sciences, Chung-Ang University
City: Seoul
Country: Korea
Email: khkong@cau.ac.kr

F. Ibrahim, N.A. Abu Osman, J. Usman and N.A. Kadri (Eds.): Biomed 06, IFMBE Proceedings 15, pp. 496-498, 2007
www.springerlink.com ' Springer-Verlag Berlin Heidelberg 2007

Systematic Following of Telomerase during MRC5 Population Dubbling and Cell Senescence

Khosrow Aghaiypour[1], Javad Baharizadeh[1], Siavash Sadeghian[2] and Ashraf Mohammadi[1]

[1] Genomics Laboratory, Biotechnology Department, Razi Vaccine and Serum Research Institute, Karaj Tehran Iran
[2] Microbiology Department, Medical School, Hamedan Medical Sciences University, Hamedan, Iran

Abstract - **MRC5 are well-characterized human diploid fibroblast cell line approved for vaccine production. We have adapted measles, Rubella and Polio viruses for propagation in MRC5 cell lines. In this study, telomerase activity during different passages of this cell detected and traced. Stocks of MRC5 cells from passage 15 to passage 38 were monitored. Trace amount of telomerase activity detected in these cells using TRAP-PCR with gel based detection. A decreasing order of telomerase activity observed with the cell doubling number. In order to compare in more details the telomerase activity during cell passage and replicative senescence, it was reassayed with an ultra sensitive method of TRAP-PCR ELISA based method. While in gel-based method trace amount of telomerase activity decreasing with increasing passage number of cells were detected, in PCR-ELISA very lower detectable telomerase activity were observed. We think this could be because of low processivity of this enzyme.**

Keywords - **Telomerase, MCR5, TRAP-PCR**

I. Introduction

MRC-5 is a human diploid fibroblast cell line first isolated in 1966 from normal lung tissue of a 14 weeks old foetus. It has been used for about 40 years in many cellular, viral and health related studies and is a certified source as cell substrate for production of some human viral vaccines (1). Although MRC-5 cells are potentially capable of up to 46 population doublings, their limited lifespan has resulted in low passage stocks becoming increasingly difficult to source. The finite replicative lifespan of primary human fibroblasts imposes restriction on studies related these cells. Fibroblasts also change significantly as they accrue population doublings. The limited lifeapan of MRC-5 cells in culture is due to the onset of replicative or cellular senescence(2). Cells that have entered replicative senesence usually reside in G1 phase and fail to enter S phase after the addition of growth factors. The phenotype of senescent cells differs in terms of gene activation and repression, cell morphology and possibly also in their capacity to support virus replication. In fibroblasts senescence is caused by erosion of chromosomal telomeres. Telomeres protect the natural ends of linear chromosomes and are composed of arrays of (TTAGGG)n complexed with proteins such as hTRF1, hTRF2 tankyrase, hRap1, TIN2, the Mre11 complex and others arrenged into a T loop structure. Conventional DNA polymerase can not fully duplicate the terminal of a linear molecule leading to an inexorable loss of terminal DNA with repeated cell division (1,2). The lose of telomeric DNA is in the order of 50-200 bp per division in somatic cells such as fibroblasts and telomere lenth usually decreases to a threshold of about 5kb (including subtelomeric regions) in senescent cells. Certain cell types such as stem cells and those of germ line overcome the problem of telomere shortening by the action of telomerase. Mammalian telomerase synthesizes TTAGGG repeat *de novo* on to chromosome ends. For this purpose telomerase act as reverse transcriptase as the enzyme is associated with an RNA template encoding the telomeric repeat sequence. The telomerase RNA hTERC (or hTR) is expressed in most cell types. But expression of the human telomerase reverse transcriptase gene (hTERT) only occur in cell lines and only some somatic cells(3,4).

Telomerase activity is not detectable in the large majority of somatic cells whereas germinal cells, stem cells, and cancer cells present telomerase activity. According to the telomere hypothesis, this finite proliferative capacity would correlate with telomere length. MRC-5 cells support efficient replication of many viruses and used as a cell substrate for mor than forthy years. We have adapted Measles, Rubella in addition to Polio virus to propagate on this cell and for production of vaccine against them. In this study we studied telomerase activity in different MRC5 passsage with or without measles virus infection in order to find out the effect of viral genes and cellular senescence on this cell and chromosome stablising enzyme.

II. Materials and methods

MRC5 cell culture: Cells were cultured on DMEM from HiMedia in duplicate passage. After complete coverage of cells, alliquites containing 10^6 cells prepared from passage 15 to passage 38. paralel to this the second bottle of cells was transfected with measles virus and harvested when 15% CPE observed.

F. Ibrahim, N.A. Abu Osman, J. Usman and N.A. Kadri (Eds.): Biomed 06, IFMBE Proceedings 15, pp. 499-501, 2007
www.springerlink.com ' Springer-Verlag Berlin Heidelberg 2007

Whole cell extraction: Cell lysis buffer containing 10 mM Tris-HCl, 1 mM $MgCl_2$, 1 mM EGTA, 1 mM PMSF, 5 mM 2-ME, 0.5% CHAPS and 10% glycerol was used for extraction of cellular proteins (5).

Protein detemination: Bradford dye binding method used for estimation of protein concetration of cell extracts.

Detection of telomerase activity: whole cell extract used for telomerase detection using telomeric repeat amplification protocol (TRAP-PCR). TRAP-PCR performed in 0.2 ml thin wall tubes with 50 µl reaction mixture contained 20 mM Tris-HCl, pH 8.3, 1.5 mM $MgCl_2$, 63 mM KCl, 1 mM EGTA, 0.1% tween 20, 0.1 mM dNTP, 0.01 µg TS, ACX and NT primers, 0.1 amol TSR8, 0.1 amol TSNT (5).

Gel electrophoresis: of TRAP results Visualized on poly acrylamide gel electrophoresis following Ethidium bromide and Syber Green staining or with a PCR-ELISA kit from Roche company.

III. Results

Cell culture and virus propagation: MRC5 cell passage and proliferation ware successful until population doubling time of 38 but after passage number of 30 the cells were unable to support the virus propagation. There was a contineous decrease in virus yeild with increasing the passage number of cell substrate. The highest rate of cirus production was in passage number between 15- 22.

Whole cell extraction and protein concentration: Cell harvested with centrifugation of media in 2000 rpm for 5 mintes and alliquete of 10^6 cells prepared. The harvestation of virus transfected cells done, on observation of 15% CPE. After protein dteremination an increase in protein concentration observed by cell senescence.

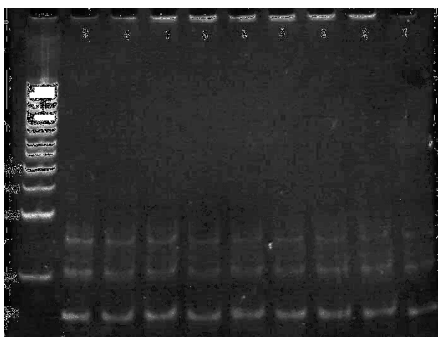

Fig. 1 Telomerase activity in different passage number of MRC5. The 50 bp bands are beside the TRAP bands from different passage numbers (PN). Lane 1: PN 32, lane 2: PN 30, lane 3: PN 26, lane 4: PN 24, Lane 5: PN 22, Lane 6: PN 20, Lane 7: PN 18, Lane 8: PN 16 and Lane 9: PN 15.

Telomerase activity detection: Determination of relative telomerase activity performed with an special RT-PCR by the name of TRAP. The results of this method visualized based on PAGE or ELISA. The results indicated some telomerase activity in a decreasing order. In cell extract from virus infected samples a trace increase in activity observed. The highest and strongest bands were for passage 18-22.

IV. Discussion

Telomerase is inactive in many somatic cells, The gratual loss of telomeric DNA with each round of replication could eventually lead to chrosomal instability which would contribute to replicative cellular senescence (1,2). This finding corroborates the observations of telomeric fusions detected in senescent fibroblasts (2). Cell senescence can be overcome in part by virus induced transformation (3). In this study we studied the telomerase activity in MRC5 cell used in our institutes for vaccine production. Our observation indicated low level of telomerase activity. This activity was in decreasing order with passage number. This could be because of the cell senescence and reduction of transcription potency. The decrease in viral particle yeild which happened with cell senescence is another indicator for cell lower protein expression systems.

Viral proteins may lead to additional mean population doublings beyond the normal cellular senescence checkpoint, which would result in an extended life-span at cellular level (3). This hypothesis was reinforced by the observation of a continued loss of telomere sequences in the transfected cells. Cells presenting critically short telomeres would cease to divide and enter crisis (5). In the other part of study we checked the telomerase activity after transfecting cells with measeles virus to see if the viral proteins have any affect on activation or induction of telomerase. After transfecting the cells with virus, slight increase in sharpness and density of bands from TRAP-PCR increased. This effect may related to interaction of one or several measles viral proteins with cellular component affecting telomerase activity.

References

1. B.P.McSharry, C.J. Joones, J.W.Skinner, D.Kipling and G.W.G. Wilkinson. (2001) Human telomerase reverse transcriptase-immortalized MRC-5 and HCA2 human fibroblasts are fully permissive for human cytomegalovirus. Journal of General Virology (2001), 82, 855-863.
2. Hay flick, L. (1965) The Limited In Vitro Life time of Human Diploid Cell Strains. Exp Cell Res 37, 614-636.

F. Ibrahim, N.A. Abu Osman, J. Usman and N.A. Kadri (Eds.): Biomed 06, IFMBE Proceedings 15, pp. 499-501, 2007
www.springerlink.com ' Springer-Verlag Berlin Heidelberg 2007

3. Counter C M, and et al (1994); Stabilization of short telomeres and telomere activity accompany immortalization of Eppstein-Barr virus Transformed human B-lymphocytes, J. Virol.;68: 3410-3414.
4. Bodnar AG and et al (1998); Extension of life-span by introduction of telomerase into normal human cells, Science 279, 349-352.
5. Kim and et al (1994), Specific association activity with immortal cell and cancer, Science.266, 2011-2015.
6. Broccoli D, young JW, de Lange T. (1995) Telomerase activity in normal and malignant hematopoietic cells. Proc Nat1 Acad Sci USA 92, 9082-9086.
7. Jiany X R and et al (1999); Telomerase expression in human somatic cells dose not induce changes associated with a transformed phenotype, Nature Genetics, 21, 111-114.

Address of corresponding author:

Khosrow Aghaiypour
Razi Vaccine and Serum Research Institute
Hesarak
Karaj
Tehran
Iran
Khosrow@rvsri.com

F. Ibrahim, N.A. Abu Osman, J. Usman and N.A. Kadri (Eds.): Biomed 06, IFMBE Proceedings 15, pp. 499-501, 2007
www.springerlink.com ' Springer-Verlag Berlin Heidelberg 2007

Analysis of Detecting the Malarial Parasite Infected Blood Images Using Statistical Based Approach

S. Raviraja[1], Gaurav Bajpai[1] and Sudhir Kumar Sharma[2]

[1]Faculty of Computer Science, Academy of Medical Sciences and Technology, Khartoum, Sudan
[2]Faculty of Biomedical Engineering, Academy of Medical Sciences and Technology, Khartoum, Sudan

Abstract – **This work introduces a blood image processing for detecting and classifying malarial parasites in images of Giemsa stained blood slides, in order to evaluate the parasitaemia of the blood. Generally blood images are made up of three different kinds of cells, red, white and blood platelets. Their dimension, shape and their color distinguish these. In malarial blood, the red corpuscles of vertebrates are infected by malarial parasites. The aim of this paper is to detect the red blood cells that are infected by malarial parasites using statistical based approach. Further evaluation of the size and shape of the nuclei of the parasite is also considered.**

Keywords – **Digital image processing, pattern recognition, shape analysis, invariant moments, malarial blood images**

I. Introduction

Malaria are protozoan parasites belonging to the subclass coccidian and this disease transmitted by the Anopheles mosquito, caused by minute parasitic protozoa of the genus Plasmodium, which infect human first in the cells of the liver and then in the red cells, and insect hosts alternatively. It probably originated in Africa and accompanied human migration to the Mediterranean shores, India and South East Asia. In the past it used to be common in the marshy areas around Rome and the name is derived from the Italian, (mal-aria) or "bad air"; it was also known as Roman fever [12]. The detection techniques, today includes manual laboratory diagnosis of blood analysis.

Generally in blood analysis, doctors look for three different kinds of cells, red, white and blood platelets. Their dimensions and their color distinguish these. In malarial blood the red corpuscles of vertebrates are infected by malaria parasites. Plasmodium, the protozoan parasite that causes malaria, exists in a variety of different forms [9], which have successfully adapted to different cellular environments, in both the vertebrate host and the mosquito vector. The parasite develops in a highly regulated manner through distinct cycles in the vertebrate host. In malarial blood we have to look for cells, red both mature and young or reticulocytes and white, and for parasites, in different stages of life, immature and mature trophozoites, schizonts and gametocytes.

The aim of this paper is to present a model to detect the parasites using a digital image or [2] color photograph of stained malarial blood from a microscope in order to evaluate the number of parasitaemia of the blood that is count number of parasites per number of red blood cells [8]. Manual analysis of slides is tiring and time-consuming so our task is to automate the process. Here we propose a method to separate automatically the parasites (trophozoites, schizonts and gametocytes) from the rest of an infected blood image using colour, shape and size information and compare the image with infected images after transformation of image by scaling, shaping to reconstruct the image. The image returned are statistically analysed and compare to generate a mathematical base. The moment s concept is put forward to criteria in a different domain.

II. Moment Theorem

The moments of a function are commonly used in probability theory. However several desirable properties that can be derived from moments are also applicable to shape analysis. Region moments representation interpret a normalized gray-level image function as a probability density of a 2-D random variable which can be described using statistical characteristic moments. Assuming that non-zero pixel values represent regions moment, a moment of the order $(j+k)$ is dependent on scaling, translation and even on gray-level transformations.

Uniqueness theorem: the set of moments of a bounded function $f(x,y)$ of two variables is defined by

$$m_{jk} = \int_{-\infty}^{\infty}\int_{-\infty}^{\infty} x^j y^k f(x,y)\,dxdy \qquad (2.1)$$

Where j and k takes on all non-negative integer values. The moments of image are widely used in probability

F. Ibrahim, N.A. Abu Osman, J. Usman and N.A. Kadri (Eds.): Biomed 06, IFMBE Proceedings 15, pp. 502-505, 2007
www.springerlink.com ' Springer-Verlag Berlin Heidelberg 2007

theory. As j and k take on all non-negative values, it generates an infinite set of moment. This set is sufficient to specify the function $f(x,y)$ completely. In other words the set $\{m_{jk}\}$ is unique for $f(x,y)$ and only $f(x,y)$ has that particular set of moments.

In digitized images we evaluate sum:

$$m_{jk} = \int_{x=-\infty}^{\infty} \int_{y=-\infty}^{\infty} x^i y^k f(x,y)\,dxdy \qquad (2.2)$$

Where x, y, j and k are the region point co-ordinates that is pixel co-ordinates in digitized image. For shape descriptive purpose, suppose $f(x,y)$ takes on the value 1 inside the object and 0 elsewhere. The silhouette function reflects only the shape of the object and ignores internal gray-level detail. Every unique shape corresponds to a unique silhouette and, to unique set of moments. The parameter $j+k$ is the order of the moment and there is only one zero-order moment.

$$m_{00} = \int_{-\infty}^{\infty} \int_{-\infty}^{\infty} f(x,y)\,dxdy \qquad (2.3)$$

It is clearly the area of the object. There are two first order moments and correspondingly more moments of higher order. We can make all first and higher moments invariant with respect to the size of the object by dividing them by m_{00}.

Central moments are the co-ordinates of the center of gravity of an object. 2.4 are central moments

$$\overline{x} = \frac{M_{10}}{M_{00}}, \overline{y} = \frac{M_{01}}{M_{00}} \qquad (2.4)$$

That are computed using the center of gravity at the origin

$$\mu_{jk} = \int_{-\infty}^{\infty} \int_{-\infty}^{\infty} (x-\overline{x})^j (y-\overline{y})^k f(x,y)\,dxdy \qquad (2.5)$$

The central moments are position invariant or in digitized image

$$\mu_{jk} = \sum_{x=-\infty}^{\infty} \sum_{y=-\infty}^{\infty} (x-x_c)^j (y-y_c)^k f(x,y) \qquad (2.6)$$

Where x_c, y_c are the co-ordinates of the regions center of gravity (centroid) which can be obtained using the following

$$x_c = \frac{M_{10}}{M_{00}}, y_c = \frac{M_{01}}{M_{00}} \qquad (2.7)$$

In the binary case m_{00} represents the region area. Scale invariant features can also be found in scaled central moments η_{jk} (scale change x=αx, y=αy)

$$\eta_{jk} = \frac{\mu_{jk}}{(\mu'_{00})}\frac{1}{\gamma}, \lambda = \frac{j+k}{2}+1 \qquad (2.8)$$

$$\mu'_{jk} = \frac{\mu_{jk}}{\alpha(j+k+2)} \qquad (2.9)$$

θ_{jk} are normalized un-scaled central moment as

$$\theta_{jk} = \frac{\mu_{jk}}{(\mu_{00})}\frac{1}{\gamma} \qquad (2.10)$$

Rotation invariance can be achieved if the co-ordinate system that is chosen such that $\mu_{11} = 0$ [4] many aspects of moment properties, normalization, descriptive power, sensitivity to noise, and computational cost [5]. A less general from invariance was given in [6] and is discussed in [3] where seven invariant moment characteristics like rotation, translation and scale are used.

$$\nu_1 = \theta_{20} + \theta_{02} \qquad (2.11)$$

$$\nu_2 = (\theta_{20} - \theta_{02})^2 + 4\theta^2_{11} \qquad (2.12)$$

$$\nu_3 = (\theta_{30} - 3\theta_{12})^2 + (3\theta_{21} - \theta_{03})^2 \qquad (2.13)$$

$$\nu_4 = (\theta_{30} - \theta_{12})^2 + (\theta_{21} - \theta_{03})^2 \qquad (2.14)$$

$$\nu_5 = (\theta_{30} - 3\theta_{12})(\theta_{30} + \theta_{12})\left[(\theta_{30} + \theta_{12})^2 - 3(\theta_{21} + \theta_{03})^2\right] + 3(\theta_{21} - \theta_{03})(\theta_{21} + \theta_{03})\left[3(\theta_{30} + \theta_{12})^2 - (\theta_{21} + \theta_{03})^2\right] \qquad (2.15)$$

$$\nu_6 = (\theta_{20} - 3\theta_{02})\left[(\theta_{30} + \theta_{12})^2 - (\theta_{21} + \theta_{03})^2\right] + 4\theta_{11}(\theta_{30} + \theta_{12})(\theta_{21} + \theta_{03}) \qquad (2.16)$$

F. Ibrahim, N.A. Abu Osman, J. Usman and N.A. Kadri (Eds.): Biomed 06, IFMBE Proceedings 15, pp. 502-505, 2007
www.springerlink.com ' Springer-Verlag Berlin Heidelberg 2007

$$v_7 = (3\theta_{21} + \theta_{03})(\theta_{30} + \theta_{12})\left[(\theta_{30} + \theta_{12})^2 - 3(\theta_{21} + \theta_{03})^2\right] - (3\theta_{30} + 3\theta_{03})(\theta_{21} + \theta_{03})\left[3(\theta_{30} + \theta_{12})^2 - (\theta_{21} + \theta_{03})^2\right] \quad (2.17)$$

Where the θ_{jk} values can be computed from 2.10.

The seven moment characteristics presented above were shown to be useful. They are only invariant to translation, rotation, and scaling.

Principal axes is the angle of rotation θ that causes the second order central moment μ_{11} to vanish and is obtained from

$$\tan 2\theta = \frac{2\mu_{11}}{\mu_{20} - \mu_{02}} \quad (2.18)$$

The co-ordinate axes x, y axes are called the principal axes of the object, the 90^0 ambiguity in 2.10 can be resolved if we specify that

$$\mu_{20} < \mu_{02}, \mu_{30} > 0$$

If the object is rotated through θ before moments are computed or if the moments are computed relative to the x, y-axes then the moment are rotation invariant.

III. Invariant Moments

The area-normalized central moments computed relative to the principle axis are invariant under magnification translation and rotation of the object only moments of third order and higher are nontrivial after such normalization. The magnitudes of these moments reflect the shape of the object and can be used in pattern recognition. Invariant moments and combinations of the shapes of printed to chromosome analysis. Invariant moments definitely have some of the properties that good shape features must have, they may or many not have all of them in any particular instances. The uniqueness of the shape of an object is spread out over an infinite set of moments. Thus a large set of features may be required to distinguish similar shapes. The resulting high dimensional classifier may become quite sensitive to noise and to infraclass variations. In some cases a few relatively low order moments may reflect the distinguishing shape characteristics of an object. Usually some experimentation will suggest which if any of the invariant moments are both reliable and discriminating features of shapes like ring form or crescent shaped.

Let $f(x, y)$ be the gray-level image of an object, rather than a binary valued silhouettes function, we can compute invariant as before. The zero order moment 2.2 becomes the integrated optical density rather than the area; however the preceding development applies in a similar manner for gray level images. The invariant moments reflects not just the shape of the object, but also the density distribution within it. As before it must be shown for each object recognition problem, that reasonably small number of invariant moments can be reliably distinguish among the different objects.

The invariance moment theorem is sensitive for noise that a result of using different types of dye in malaria diagnosis that is Gemsia, Fields and Leisman with different concentrations, which will improve the system performance by using a large image size and great color depth.

IV. Conclusion

In this paper we have presented a statistical method to analyse malarial blood images. The aim of malarial blood image processing is to detect the parasites infecting the red cells in order to evaluate the number of parasites per number of red blood cells. The proposed method automatically identifies the parasites using colour, shape and size information, extracted by a digital image operation and statistical approach. We have used the invariants moments to detect the nuclei of the parasites, according to a connectivity of a disk shaped structuring element whose radius is the greatest size of the red blood cells.

Reference

1. Rafael C. Gonzalez and Richard E. Woods (2002) *Digital Image Processing", Prentice-Hall, Inc*, 2nd edition.
2. A K Jain (1989) *Fundamentals of Digital Image Processing"*, Prentice-Hall, Englewood Cliffs, NJ.
3. W K Pratt (1991) *Digital Image Processing", John Wiley and Sons*, New York, 2nd edition.
4. Cash, G. L., and M. Hatamian (1987) *Optical character recognition by the method of moments",* Computer Vision, Graphics, and Image Processing 39 (3): 291 310.
5. M Savini. (1988) *Moments in image analysis",* Alta Frequenza, 57(2):145-152.
6. M K Hu. (1962) *Visual pattern recognition by moment invariants",* IRE Transactions Information Theory, 8(2):179-187.
7. S Maitra, (1979) *Moment invariants", Proceedings IEEE*, 67(4):697-699.
8. A. Dempster, C Di Ruerto (1999) *Morphological Processing of Malarial Slide Images* , Matlab DSP Conference 1999, Nov, 16-17, Espoo, Finland.

F. Ibrahim, N.A. Abu Osman, J. Usman and N.A. Kadri (Eds.): Biomed 06, IFMBE Proceedings 15, pp. 502-505, 2007
www.springerlink.com ' Springer-Verlag Berlin Heidelberg 2007

9. J.D. Smyth (1994) *Introduction to animal parasitology"*, Cambridge University Press, Cambridge.
10. C Di Ruberto, A Dempster, Shahid Khan, Bill Jarra (2000) "Segmentation of Blood Images Using Morphological Operators", ICPR, p. 3401, 15th International Conference on Pattern Recognition (ICPR'00) - Volume 3.
11. C Di Ruberto, A Dempster, Shahid Khan, Bill Jarra (2000) "Automatic Thresholding of Infected Blood Images Using Granulometry and Regional Extrema," ICPR, p. 3445, 15th International Conference on Pattern Recognition (ICPR'00) - Volume 3.
12. Royal Perth Hospital: Western Australia: Malaria: An on-line Resource: Website: http://rph.wa.gov.au/malaria.html.

Address of the corresponding author:

Author: Dr. Sudhir Kumar Sharma
Institute: Academy of Medical Science and Technology
Street: PO Box 12810
City: Khartoum
Country: Sudan
Email: sudhir73_2000@yahoo.com

F. Ibrahim, N.A. Abu Osman, J. Usman and N.A. Kadri (Eds.): Biomed 06, IFMBE Proceedings 15, pp. 502-505, 2007
www.springerlink.com ' Springer-Verlag Berlin Heidelberg 2007

Detecting the Vocal Disorder by Extracting the Pitch in the Phonetics of Indian Regional Marathi Language Numerical

Pramod B. Patil and V.T. Ingole

PRM Institute of Technology and Research, Badnera, Amravati(MS), India

Abstract— **The paper presents detection of the vocal disorder suffered due to the reaction of antibiotics during the course of medical treatment by extracting pitch information of the speech. Extraction of pitch of the speech is an important task due to the presence of background noise. Primarily start and end points of speech is detected and thereafter pitch boundaries are recognized using autocorrelation technique. This paper emphasized on accurate end point analysis for detection of the vocal disorder suffered due to the reaction of antibiotics during the course of treatment by extracting pitch information in the phonetics of Indian regional Marathi language numerical.**

Keywords— **Disorder, End Point, Pitch Information, and Autocorrelation**

I. Introduction

In the production of speech, there are a number of sources that generate acoustic energy in the vocal track, periodic sources include aspiration at the glottis; frication, generated further forward in the vocal track; and transient bursts produced by the rapid release of complete constrictions. The periodic source in the speech is created by vibration of the vocal folds creating periodic energy in the glottis. These sources are filtered by the vocal track to generate an output signal. [1]-[4]. Due to the reaction of the antibiotics during the course of medical treatment, patient suffers vocal disorder affecting the speech. The vocal disorder is detected by extracting pitch of the speech. The samples of the phonetics of Indian regional Marathi language numerical are used for extracting the pitch of the speech.

An important problem in speech processing is to detect the presence of speech in a background noise. [5][6] The accurate detection of words start & end points allows the subsequent processing of the desired data, which reduces the memory requirement & reduces the processing time. The start & end points detection of speech improve the detection of vocal disorder.[7][8]
The method uses two measures of the signal the zero crossing rate and the energy.

Three thresholds are computed

1. ITU Upper energy threshold.
2. ITL Lower Energy Threshold.
3. IZCT- Zero crossings rate threshold.
4. Algorithm is as follows:
5. Search from the beginning until the energy crosses ITU.
6. Back off towards the signal beginning until the first point at which the energy falls below ITL is reached results into provisional beginning N1.
7. N2 (the end point) is selected in similar way.
8. For beginning point, examine the previous 250ms of the signal s zero crossing rates.
9. If the measure exceeds the IZCT threshold, N1 is moved to the first point at which IZCT threshold is exceeded.
10. Perform similar method for the end point N2.

Fig 1 shows the flowchart for detecting start & end points of speech.

II. Methods

The phonetics of Indian regional Marathi language numerical samples for patients before and after the course of medical treatment is recorded. At every frame, the method for detecting the pitch boundaries is important, since detecting start and end point is very critical. The pitch period is estimated by autocorrelation technique by detecting the peak amplitude in the function. The second largest peak relative to the true delay of the correlation is used to determine the pitch period. The peak in the autocorrelation function tends to fall off linearly starting from the first peak [9]-[12].

The speech data is recorded at 8KHz sampling frequency with 8 bits representing each sample. Figure 2 shows block-processing model for detecting the pitch boundaries. The data is processed in frame of 200 samples and a vector of pitch is measured. The vector is obtained by pre-emphasizing speech data to flatten it using first order digital filter with coefficient a= 0.97. The signal is processed in the

F. Ibrahim, N.A. Abu Osman, J. Usman and N.A. Kadri (Eds.): Biomed 06, IFMBE Proceedings 15, pp. 506-508, 2007
www.springerlink.com ' Springer-Verlag Berlin Heidelberg 2007

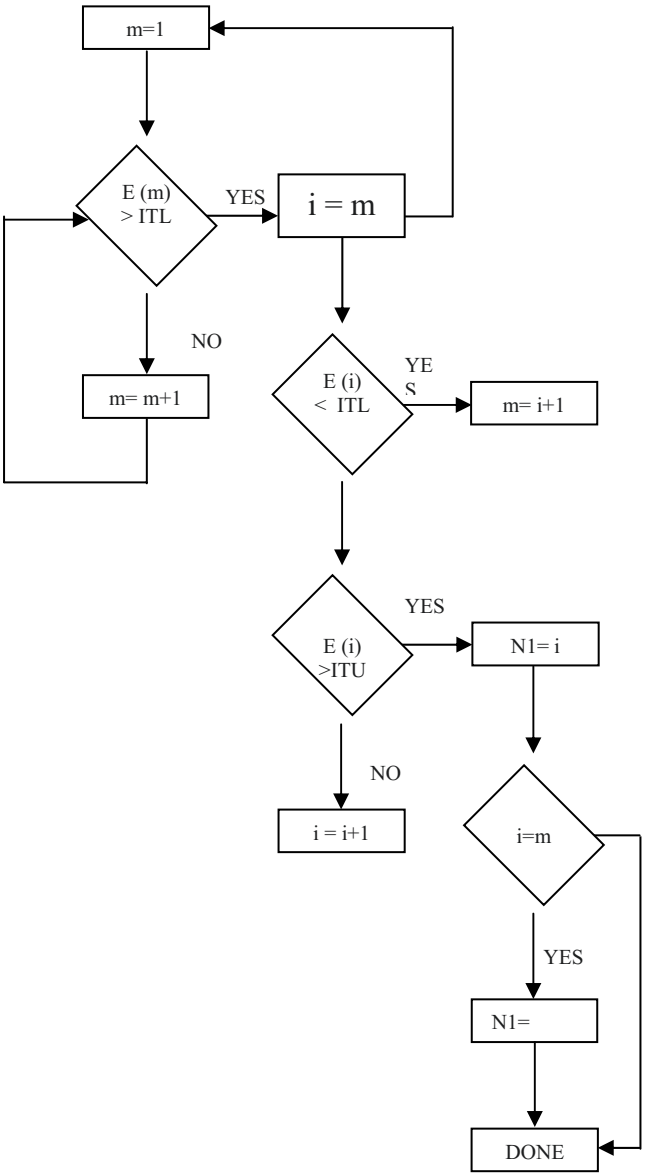

Fig. 1 Flowchart for Start & End points detection

steps of 100 samples to provide smoothing between vectors of pitch. For pitch extraction, the hamming window and autocorrelation technique with order of 10 is used. In the start & End point analysis of speech, each window samples are classified as voiced speech, unvoiced speech or silence, based entirely on measurements made on the signal during the prescribed interval [7]-[11].

III. Results

The results with the samples of the phonetics of Indian regional Marathi language numerical //ek// for patients are obtained. The autocorrelation system order selected is equal to 10 for analyzing the better performance. Fig 3,4 shows the start & end point analysis for detection of the vocal disorder by extracting pitch information using autocorrelation technique. Table 1 shows the start and end frames of spoken word ek

Table 1. Showing the Start & End frames of spoken word //ek//

Spoken Word= //ek//	Starting Frame	Ending Frame
Normal	26	50
Disorder	32	80

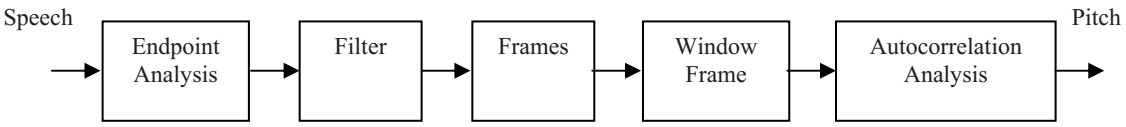

Fig. 2 Block Processing Model for Detecting Pitch Boundaries to control the Robot Activities

F. Ibrahim, N.A. Abu Osman, J. Usman and N.A. Kadri (Eds.): Biomed 06, IFMBE Proceedings 15, pp. 506-508, 2007
www.springerlink.com ' Springer-Verlag Berlin Heidelberg 2007

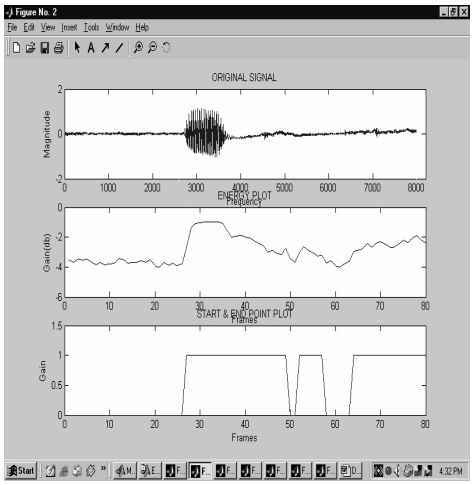

Fig. 3 Pitch for the Normal with//ek//

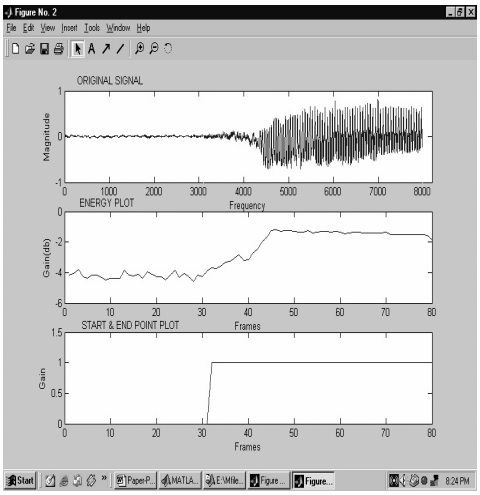

Fig. 4 Pitch for disorder detected in//ek//

IV. Conclusions

Autocorrelation method with start and end point analysis has an advantage of less computation since only a window length is used as signal component. Even though the speech waveform is not always periodic, the pitch boundaries are detected reliably and so the vocal disorder is detected.

References

1. Samad S, Hussain A, Fah L K, Pitch Detection of Speech Signals using the Cross Correlation Technique , Proceedings of IEEE on Speech, Audio and Signal Processing, pp 283 - 286,2000.
2. 2. M.J.Ross, H.L.Shaffer, A. Cohen, R. Freudberg, and H.J. Manley, Average Magnitude Difference Function Pitch Extractor , IEEE Trans. Acoustic, Speech, and Signal Processing, pp. 353-362 Oct. 1974.
3. 3. D. Takin, A Robust Algorithm for Pitch Tracking (RAPT) , Speech Coding and Synthesis, Netherlands: Elsevier Science. 1995.
4. LA. Atkinson, M. Kondoz and B.G. Evans, Time Envelop Vocoder, A New LP Based Coding Strategy for Use of Bit-Rate 2.4kb/s and Below , IEEE Journal on Selected Areas on Communications, Vol. 13, No. 2, Feb. 1995.
5. Pramod B. Patil, Dr. V.T. Ingole, Cross-Correlation Technique for the Detection and Reduction of Environmental Noise in Speech Signal , Journal of Pradushan Nirmulan, Vol 1, No2 pp 29 31, April 2004. (ISSN -0972-8902)
6. A. M. Kondoz, Digital Speech: Coding for Low Bit Rate Communications Systems, Wiley, England. 1995.
7. B.Gold and L. Rabiner, Parallel Processing Techniques for Estimating Pitch Periods of Speech in the Time Domain , Journal of Acoustics. Society, America, Vol. 46, pp. 442-448, Aug. 1969.
8. Rabiner L R, Levinson S E., Isolated and Connected Word Recognition Theory and Selected Applications , IEEE Transaction on Communications, Vol 29, No 5, 1981
9. Rabiner L R, Sambur M R, Speaker Independent Recognition Of Connected Digits , Bell System Technical Journal Vol 54, pp 202 205, 1972.
10. Rabiner L R, Schafer R W, Digital Processing of Speech Signals, Englewood Cliffs, NJ Prentice Hall, 1978.
11. Rabiner L R, A Tutorial on Hidden Markov Models and Selected Applications in Speech Recognition , Proceedings of IEEE, Vol 77, No2, pp 257-285, 1989.
12. Rabiner L R, Sambur M R, An Algorithm for Determining the Endpoints of Isolated Utterances Bell System Technical Journal, Vol 54, pp 297 315, 1975.

Address of the corresponding author:

Author: Pramod B. Patil
Institute: PRM Institute of Technology and Research
Street: Anjangaon Bari Road
City: Badnera, Amravati(MS)
Country: India
Email: pramod7568@yahoo.co.in

F. Ibrahim, N.A. Abu Osman, J. Usman and N.A. Kadri (Eds.): Biomed 06, IFMBE Proceedings 15, pp. 506-508, 2007
www.springerlink.com ' Springer-Verlag Berlin Heidelberg 2007

Importance of Performance Assurance in Medical Equipment Maintenance

W. Hemant[1] and Ir.R. Gnana Sakaran[2]

[1]Bell Comm Technologies Kuala Lumpur Malaysia
[2]Enhealth Sdn Bhd Kuala Lumpur Malaysia

Abstract- **Approach to the maintenance of Medical Equipment has changed substantially over the years. In 70s the major activity was limited to the repair of equipment whenever it failed. This is called breakdown Maintenance. It was unpredictable and hence unscheduled, tedious, also time and cost consuming. Preventive Maintenance practice slowly became prominent to overcome these difficulties. Through the years, medical electronic products are becoming increasingly reliable. Preventive Maintenance now demands beyond traditional requirements. Safety and Performance Inspection (SPI) or Performance Assurance is the present trend which meets these additional requirements. Performance Assurance is carried out with help of Performance Testers.**

Keywords- **Performance Assurance, Preventive Maintenance, Testers, Safety, Reliability.**

I. Introduction

Safety and Performance Assurance is becoming increasingly important in maintenance of medical equipment. The paper outlines its importance and benefits.

II. The paper

Over the last three decades, medical device maintenance trend has evolved from electrical safety to equipment management, from preventive maintenance to technology management, and from incident investigation to safety management. To contain risk, ensure reliable and safe operation, performance assurance measurement of medical equipment has become mandatory activity in maintenance practice.

The role of Biomedical Engineering Practitioner has expanded by many folds over the years, participating in the whole life cycle of the medical device inventory of the healthcare facility, based on the cradle to grave management philosophy. As medical technology evolves, update of maintenance procedures and methodology becomes necessary and some of the time consuming preventive maintenance (PM) tasks may not yield measurable benefit. Arising from these situations, the Medical Technology Management Providers need to design systems and tools to serve the changing needs of the healthcare facility more effectively.

To meet the changing trends in medical technology, the PM program should be built upon a foundation of safety, quality and regulatory compliance and not be a sequential series of scheduled events [1]. To prevent future failures, we need to think the entire system, i.e. the device, the environment, and the people. It may mean periodic training of the staff members in the area with high turnover, or it may mean purchasing better quality user consumables / accessories or buying equipment from different manufacturers. The goal should be to fine tune the processes to ensure the efforts are contributing to the reduction of failures.

In the traditional PDCA (Plan-Do-Check-Act) quality improvement process, maintenance providers tend to focus on Plan-Do and overlook the Check-Act. The PDCA cycle should have analysis and the development of actions based on that analysis. Those actions may change every cycle and they may not involve as many routine, periodic inspections results in reduction of equipment failures.

Medical equipment is becoming more reliable and less dependent on mechanical components; traditional maintenance requirements are decreasing [2]. Still, there is a need for providing critical equipment with the safety and performance inspection (SPI) or Performance Assurance in order to assure that no significant adverse patient outcome can be legitimately attributed to a preventable medical device failure.

Safety and performance inspection is performed after each PM and repair that affect either safety or performance. Equipment does not require PM too benefits from SPI. Determining need for SPI depends on both hidden and potential failures. Some of the SPIs may need to be performed by users other than trained technicians. Ideally, clinical users should be trained and required to verify the safety and performance of every device prior to use. Like PMs, SPI rationale, procedure, and frequency should start with the respective manufacturer s recommendations [3].

F. Ibrahim, N.A. Abu Osman, J. Usman and N.A. Kadri (Eds.): Biomed 06, IFMBE Proceedings 15, pp. 509-511, 2007
www.springerlink.com ' Springer-Verlag Berlin Heidelberg 2007

As the reliability of medical equipment has improved remarkably, the need for PM has been drastically reduced. Often there are no serviceable parts or the MTBF (mean-times-between-failure) is longer than the average useful life of equipment. PM should be considered only when there are clear, age-related failure patterns, and the tasks are both technically feasible and worth doing or cost effective [4].

The medical device regulators stringent evaluation of market clearance or approval for the devices safety, its effectiveness, and the effects of mass manufacture on the quality and consistency of the product plays a significant factor in device reliability [5].

Standards play an important role in equipment safety, performance and reliability. Medical electrical equipment standards that fall under the International Electro-technical Commission (IEC) employ a multi-tiered system [6]. A General Standard addresses requirements common to all medical electrical equipment, while Particular Standards address specific types of equipment. In addition, Collateral Standards provide information that is useful for proper application of the General Standard and Particular Standards.

The General Standard for each of the above standards is IEC 60601-1:1988, *Medical electrical equipment-Part1: General requirements for safety* with its amendments 1 (1991) and 2 (1995). It establishes a baseline of standards for the safety of all medical electrical equipment used by or under the supervision of qualified personnel in the general medical and patient environment, and also contains requirements for reliable operation to ensure safety. While the guidance of these standards is primarily directed to manufacturers of the devices, users and persons responsible for maintenance and repair will also find the information useful in implementing SPI.

Assurance of safe medical device driven by reliable software originates from the development of critical safety software originating from aviation industry [7]. Software normally does not wear out and when it fails, it is due to design or implementation defect that has always existed. Inherently safe design, preventive and corrective, mitigating measures by users enables reliable medical device operation. Improvement in safe-design practices throughout the software lifecycle by applying medical device software risk management standards and software safety activities enables reliable medical devices that do only requires minimal hardware intervention and maintenance.

There is no question that medical devices are becoming more reliable. However, we have had some difficulty finding a satisfactory method for providing persuasive documentary evidence that this improved reliability will allow us to relax our traditional planned maintenance practices without compromising patient safety [8].

All technology introduces new errors, even when its sole purpose is to prevent errors [9]. In order to prevent maintenance related errors, the maintenance provider must assist in identifying system vulnerabilities, assure that these new technologies/systems are robust and fault tolerant, and must be involved in the entire life cycle of the technology.

Examining an average PM we find that the majority of the time, the work (e.g. electrical safety test, output test, input test, alarm test, etc) goes in without question [10]. For example, in testing a defibrillator over a period of time and never found an inaccurate power output. In this case, a large history of PM data will be required to provide evidence of no value added testing.

Ideally, for maintenance strategies, inventory should be divided into multiple tiers, with life support equipment at the top of the list, asset tag items does not need maintenance at the bottom. In the middle of the list is equipment that need maintenance but won t cause life threatening situation if it fails. Other methods include reliability centered maintenance (RCM), interval based inspections, predictive maintenance and metered maintenance. RCM is based on equipment history and analysis of failure modes and affects, and revise the maintenance intervals if calibrations are always accurate.

A number of respected trend setters in the industry have, for certain devices, been using simple criterion of zero PM failures for some time to justify either extending the PM intervals or discontinuing regular PM inspection completely [8].

Today there is large amount of technology that is remotely monitored and efforts are underway to improve the ability of equipment to self diagnose, self-repair, and allow remote repair [2].

All above led to remarkable improvement in i) Hardware Reliability ii) Software Reliability iii) Risk Assessment iv) Patient Safety throughout Device Life Cycle and v) Cost Savings.

As a result the preventive maintenance activity is becoming less stringent and less periodic. As there is less

F. Ibrahim, N.A. Abu Osman, J. Usman and N.A. Kadri (Eds.): Biomed 06, IFMBE Proceedings 15, pp. 509-511, 2007
www.springerlink.com ' Springer-Verlag Berlin Heidelberg 2007

number of mechanical parts, wear and tear is less. Heat generated inside the unit is less; hence failure due to high internal temperature is less. Also force air cooling is not necessary, which eliminates possibility of air filters clogging. Internal references are provided to perform self correction. Or in some cases correction is software controlled and can be done by the user.

SPI or Performance Assurance has become major share in PM. As the equipment reliability will continue to get better and better, Performance Assurance will play bigger role in Equipment Maintenance.

Although sometime there are methods suggested by manufacture to test and verify whether the equipment is performing within specified limits or not; it can be expensive and cumbersome for individuals to assemble the test setup. That s where need was felt to develop ready to use testers to test various type of medical equipment. These Testers started showing there existence in 80 s; and new Testers are still being added.

Following is the List of Testers available today:

Electrical Safety Tester
Defibrillator Tester
Electrosurgery Unit Tester
Ventilator Tester
Infusion Pump Tester
Incubator Tester
NIBP Tester
Ultrasound Energy Tester
Pacemaker Tester
Pulse Oximeter Tester
ECG / Patient Simulator
Fetal Simulator
Oxygen Analyser
Pressure Meter
Range of Testers and Phantoms for X-Ray applications.

With the help of these testers, it possible to test and generate reports on the performance of Equipment Under Test. If the performance of the Unit Under Test of out of Manufactures specifications, due steps may be taken to adjust the parameters to bring the performance within specified limits. If it is not possible to adjust the parameters, the unit may be sent for necessary repairs.

Hence, it can be seen that Performance Assurance has already taken a major role in Biomedical Equipment maintenance activity and it will have growing importance in the coming years. Some of it s benefits are as follows:

1) Assures equipment performance within specified limits, patient safety and identifies patient risk.
2) Helps finding out Hidden problems which are not observed during normal operation.
3) Complies with regulatory requirements.
4) Leads to predictive Maintenance. From the performance analysis data collected over few years, it is possible to draw trend of the performance and predict possible failure.
5) Performance Assurance oriented maintenance can bring more cost saving, and easier to budget for.

III. Conclusions

Performance Assurance has a major role to play in Equipment Maintenance, and it will have growing importance.

References

1. PM: A look at the Big Picture, K Maddock, BIT, 167-8, March-April 2006
2. The Future of Clinical Engineering, Ted Cohen, BIT, 113-7, March-April 2003
3. Medical Equipment Management Strategies, B Wang at El, BIT 2006;40:233-237, May-June 2006
4. Is PM Still a Core Element of CE?, BIT 1997,31:408-9
5. The Critical Path to New Medical Devices, B Asher, M Barnett, D Schultz, BIT 304-306, Jul-Aug 2005
6. Revised Equipment Standards Designed to Aid Manufacturers, Users and Technicians, BIT, 240-7, May-June 2005
7. Software Safety, David A Vogel, BIT, 309-314, May-June 2005
8. Analyzing PM Inspection Data by FEMA Methodology, Malcom Ridgway, BIT 2003;37:167-179.
9. To Err is Human: Building a Safer Health System, IOM, 2000.
10. Verification Checks and PM, Geff Maxwell, BIT, 275-8, July-Aug 2005.

Address of the corresponding author:

Author: Hemant Waghdhare
Institute Bell Comm Technologies Sdn. Bhd.
Wisma KWSG, Jln Kampung Attap
City: Kuala Lumpur
Country: Malaysia
Email: hemantwaghdhare@hotmail.com

F. Ibrahim, N.A. Abu Osman, J. Usman and N.A. Kadri (Eds.): Biomed 06, IFMBE Proceedings 15, pp. 509-511, 2007
www.springerlink.com ' Springer-Verlag Berlin Heidelberg 2007

Malay Nose Tissue Measurements For Nose Reconstruction: A Preliminary Data Collection

Syarul Emy Abu Samah[1] and Arsmah Ibrahim[2]

[1,2]Fakulti Teknologi Maklumat dan Sains Kuantiatif
Universiti Teknologi MARA
40450 Shah Alam, SELANGOR

Abstract— **Reconstructing a nose in the event of an accident, birth or genetic disorder can improve the quality of human life. The biological structure of a human nose can be reconstructed based on a set of predetermined landmarks. This paper discusses the mathematics used in the reconstruction of a real human specimen extracted from the CT-scan data obtained from the Radiology Department, Universiti Hospital Kubang Kerian. Basically the triangulation technique is used in building the structural 2D and 3D outline of the nose. A recursive algorithm is then constructed to refine the triangular mesh using barycentric coordinates. The spline technique is then used to smoothen the nose outline before it is finally rendered to give a realistic effect.**

Keywords— **Nose reconstruction, tissue thickness measurement and CT Data**

I. Introduction

The nose is made up of two parts: the soft tissue and the skeleton (Gray,1985). The soft tissue is made of skin and fat. It covers the skeleton that is made of bones and cartilage. The cartilage also has two parts: the upper lateral cartilage and the lower lateral. The skin is the outer covering of the nose. It lies over a structure made of both bones and cartilage, like a painter's tarp that drapes over a piece of furniture to protect it (Gray,1985). It is this underlying structure that gives the nose its shape often referred as the *nasal scaffold.* A general diagram on the structure of the nose is illustrated in Figure 1.

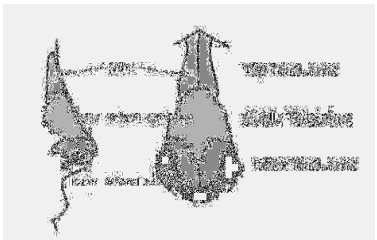

Fig. 1: Nose Structure

The skin of the nose is unique because its characteristics are quite different in different areas. In the top third area of the nose (closest to the forehead), the skin is thick and loosely attached to the nasal scaffold. In the middle third area, it becomes thinner but more tightly attached, while it is somewhat thicker but tightly adherent to the supporting structures in the lower third area (Hudson, 2002).

The upper third of the nasal scaffold is made of bone, while the lower two thirds consist of cartilage. This cartilaginous portion is made of two matched sets of cartilages: the upper and the lower cartilages. The lower cartilages are also known as the tip cartilages because they compose the scaffolding of the tip of the nose (Hudson, 2002).

Figure 2 and Figure 3 are samples of a CT scan image of a human nose. Figure 2 shows the saggital section of the nose while Figure 3 shows the axis of the nose. The technique in reading this data is based on the technique illustrated in Human Cross-Sectional Anatomy, Pocket Atlas of Body Sections and CT Images (Ellis *et al*., 1994). The flesh and bone of the nose are determined by looking at the white colour image. The white portion of the image represents the bone while the grey portion represents the flesh of the nose.

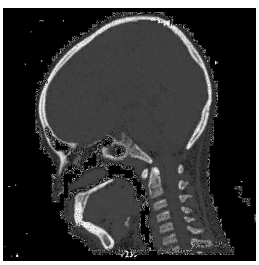

Fig. 2: Saggittal Section of Human Head

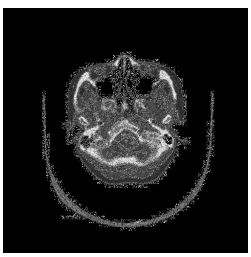

Fig. 3: Axis Section of Human Head

II. Material and methods

Before the nose model can be constructed, the landmarks for the tissue thickness must be determined. In this project,

F. Ibrahim, N.A. Abu Osman, J. Usman and N.A. Kadri (Eds.): Biomed 06, IFMBE Proceedings 15, pp. 512-515, 2007
www.springerlink.com ' Springer-Verlag Berlin Heidelberg 2007

three landmarks types for tissue thickness have been studied namely: Manchester (Attardi *et al.*, 2001), Prokopec and Ubelaker (Prokopec and Ubelaker, 2002) and Rhinoplasty (Sanchez and Balingit, 2000). Besides these three, there is another landmark technique developed by Szij tó (2000), a technique that shows the shape of the nose in computer graphic forms unlike the other three techniques.

The data collected was based on predetermined landmarks which is a hybrid of Manchester, Miroslav and Prokopec, Ubelaker and Rhinoplasty. In this hybrid, only six landmarks are used. They are *glabella*, *nasion*, *rhinion, tip-defining points, alar-sidewall* and *columella-labial angle*. These points are initially determined by considering the common points in the three techniques done by Attardi *et al.* (2001), Prokopec and Ubelaker (2002) and Sanchez and Balingit (2000). Besides these, the common critical points that represent the basic shape of the nose such as the tip and sidewall are also considered. These points are used in modeling the nose image.

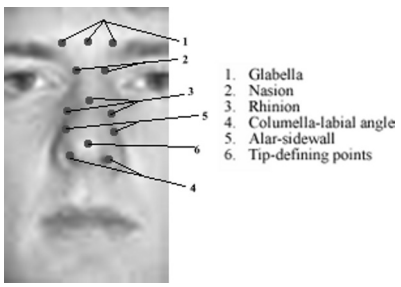

Fig. 4: The 6 Predetermined Landmark Points

In this research, only CT data were used upon recommendation by a craniomaxilla surgeon Prof Dr Rani Samsudin of HUSM. To measure the CT data, the Advantage Workstation software was used. Only CT data images on full head parts were chosen. Before the soft tissues were measured the predetermined landmarks mentioned earlier were mapped onto the image. To measure the soft tissues thicknesses, locate the surface of the bone and the surface of the skin using Advantages software at each of the six landmarks. Figure 5 and Figure 7 illustrate the location of the landmarks where the soft tissues will be measured on the image. In Figure 5, the labels A, B, C and D represent glabella, nasion, rhinion and tip-defining points respectively. In Figure 7, the labels E and F represent alar-sidewall and columella-labial angle or junction respectively. The surface of the bone is outlined in white while the surface of the skin is outlined in grey. Figure 6 and Figure 8 illustrate how the soft tissue are measured using the Advantage software.

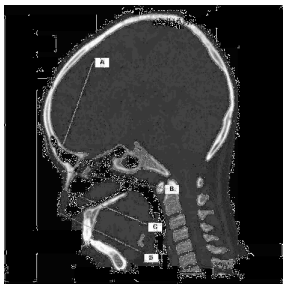

Fig. 5: Mapping landmarks on Saggital Image

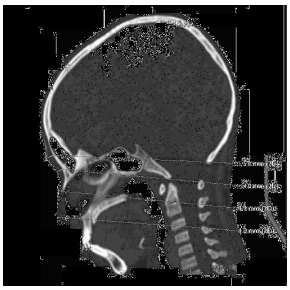

Fig. 6 : Measuring soft tissues on Saggital Image

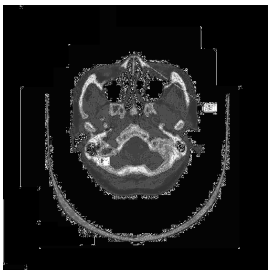

Fig.7 : Mapping landmarks on Axis Image

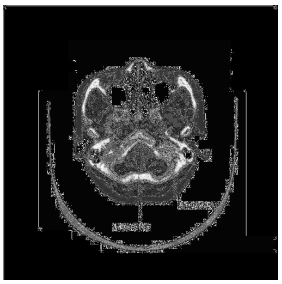

Fig. 8 : Measuring soft tissues on Axis Image

III. Result

According to the craniomaxillo surgeon, the bones in human beings in general are usually considered fully developed by the age of 13. The skin quality of human beings in the range of 13-40 years of age is usually not affected by aging. However, men are fully matured when they are in the range of 20-40 years of age, where as women are fully matured in the range of 18-40 years.

Two sets of data were obtained. The sample size of the first data set is 40, which belong to 20 men and 20 women whose ages range from 13 to 40 years old for both genders. As for the second data set, the sample size is only 20. The data belong to 10 men and 10 women whose ages range from 20 to 40 years old and 18 to 40 years old respectively. Preferably, the age range of the sample should be between 20 to 40 years old for men and between 18 to 40 years old for women. Table 1 below shows the distribution of the whole data sample managed to be collected from the Radiology Department, HUSM.

F. Ibrahim, N.A. Abu Osman, J. Usman and N.A. Kadri (Eds.): Biomed 06, IFMBE Proceedings 15, pp. 512-515, 2007
www.springerlink.com ' Springer-Verlag Berlin Heidelberg 2007

Table 1 Data Sample Distribution

Age	Men	Women	Age	Men	Women
13	3	0	27		
14	1	0	28		1
15	5	3	29		
16	4	3	30		
17	1	2	31		
18	5	3	32		
19	1	1	33		
20	2	6	34		
21	1	3	35		1
22	4	3	36		2
23	0	2	37	1	
24	1	0	38		
25	0	0	39	1	
26	0	0	40		
Total	28	26	Total	2	4

The Advantage workstation software available at the Radiology workstation was used to measure the soft tissue thicknesses required. The thickness of the soft tissue was measured from the bone surface to the outer layer of the skin (please refer to Figure 5 to Figure 7). The bone is indicated by the white region while the soft tissue is indicated by the grey-region. The measurements were done by locating the measurement tool (please refer to Figure 6 and Figure 8) at the tip surface of the bone (according to the determined landmarks) until the end of the soft tissue (that is the surface of the tissue).

The raw data must be transformed into meaningful information before they can be used in modeling the image. The mean, and standard deviation, are used. If n is the total size of data sample, and X_i is the data sample the mean is calculated as

$$\overline{X} = \frac{\sum_{i=1}^{n} X_i}{n} \qquad [1]$$

while the standard deviation is measured as

$$\sigma^2 = \frac{\sum_{i=1}^{n} | X_i - \overline{X} |}{n} \qquad [2]$$

The raw data obtained are tabulated. Table 2 illustrates the nasal soft tissue thicknesses of the males whose ages range from 13 to 40 years while Table 3 illustarates the nasal soft tissue thicknesses of the females whose ages range from 13 to 40 years too. Table 4 illustrates the nasal soft tissue thicknesses of the males whose ages range from 18 to 40 years while Table 5 illustrates the nasal soft tissue thicknesses of the males whose ages range from 18 to 40 years. These are transformed into the mean and standard deviation before they are used in modeling the image. The mean and standard deviation are used of the raw data are calculated by using Equation 1 and Equation 2 respectively. A database of the means and standard deviations for each of the six landmark points of selected age range is constructed. The database is referred when the nose is constructed.

In this research, n is a total of male/female for each data collected and X_i is the data from the patient

Table 2 Nasal Soft Tissue Thicknesses
(Male 13 40 age range)

	Nose Landmarks Name	**Mean (mm)**	***SD* (mm)**
1	Glabella	4.86	1.17
2	Nasion	4.87	1.18
3	Rhinion	2.80	1.33
4	Tip-defining points	2.42	0.99
5	Alar sidewall	1.47	0.44
6	Columella-labial angle or junction	1.29	0.33

Table 3: Nasal Soft Tissue Thicknesses
(Female 13 40 age range)

	Nose's Landmarks Name	**Mean (mm)**	***SD* (mm)**
1	Glabella	5.10	1.29
2	Nasion	5.04	1.41
3	Rhinion	2.79	1.44
4	Tip-defining points	2.04	0.59
5	Alar sidewall	1.63	0.42
6	Columella-labial angle or junction	1.49	0.43

Table 4 display results obtained for males in the age range of 20 to 40.

Table 4 Nasal Soft Tissue Thicknesses
(Male 20 40 age range)

	Nose's Landmarks Name	**Mean (mm)**	***SD* (mm)**
1	Glabella	5.4	5.8
2	Nasion	5.9	6.5
3	Rhinion	2.5	2.6
4	Tip-defining points	1.9	2.1
5	Alar sidewall	1.7	1.9
6	Columella-labial angle or junction	1.5	1.7

F. Ibrahim, N.A. Abu Osman, J. Usman and N.A. Kadri (Eds.): Biomed 06, IFMBE Proceedings 15, pp. 512-515, 2007
www.springerlink.com ' Springer-Verlag Berlin Heidelberg 2007

Table 5 display results obtained for females in the age range of 18 to 40.

Table 5 Nasal Soft Tissue Thicknesses Data (Female 18 40 age range)

	Nose's Landmarks Name	**Mean (mm)**	***SD* (mm)**
1	Glabella	5.04	5.4
2	Nasion	5.21	5.7
3	Rhinion	2.02	2.2
4	Tip-defining points	1.79	1.9
5	Alar sidewall	1.84	2.0
6	Columella-labial angle or junction	1.45	1.6

IV. Discussions

The results of this project showed the data collection and data abstraction using ready tool in order to build the nose tissue measurement table. To do this, we need to study tissue thickness measurement techniques that is available or studied before.

V. Conclusions

This paper presents pilot study for data collection for nose reconstruction that been used in this project. The generated data table was built using CT Data. These row data are abstracted using technique explained by Ellis *et al*., 1994.

References

[1] Ellis H., Logan Bari and Dixon A.(1994).Human Cross-Sectional Anatomy, Pocket Atlas of Body Sections and CT Images. Page 36-46. Reed Educational and Professional Publishing Ltd, Oxford.

[2] Gray H. (1985). Anatomy of the Human Body, 13th Edition. Page 158-225.Lea and Febiger, Philidelphia.

[3] Sanchez J.P. and Balingit J.S. (2000). Oriental Rhinoplasty: A logical and Systematic Approach. JMC Press Inc. (Journals)

[4] Attardi G.*, Betrò M.**, Forte M***, Gori R.****, Guidazzoli A****, Imboden S.*, Mallegni F.*****. (2001). 3D facial reconstruction and visualization of ancient Egyptian mummies using spiral CT data, Soft tissues reconstruction and textures application. * Dipartimento di Informatica, Università di Pisa, ** Dipartimento di Scienze Storiche del Mondo Antico - Egittologia, Università di Pisa, *** CNR (National Research Council) ITABC (Institute of Technologies Applied to Cultural Heritage), **** CINECA-VISIT (Centro Interuniversitario di Supercalcolo - Laboratorio di Visualizzazione scientifica), Casalecchio sul Reno Bologna, ***** Dipartimento di Scienze Archeologiche - Antropologia, Università di Pisa.

[5] Prokopec M.and Ubelaker D.H. (2002). Reconstructing the Shape of the Nose According to the Skull Volume 4 Number 1

[6] Szij tó G. (2000). Interactive Human Face Modeling. Budapest, Hungry. (Electronical Publications)

[7] Hudson P. (2002). Rhinoplasty: Anatomy of the Nose. http://www. phudson.com/RHINO/anatomy. html

Author: Syarul Emy Abu Samah
Institute: Fakulti Teknologi Maklumat dan Sains Kuantiatif, Universiti Teknologi MARA
City: Shah Alam, Selangor
Country: Malaysia

F. Ibrahim, N.A. Abu Osman, J. Usman and N.A. Kadri (Eds.): Biomed 06, IFMBE Proceedings 15, pp. 512-515, 2007
www.springerlink.com ' Springer-Verlag Berlin Heidelberg 2007

Quantification of Parkinsonian Rigidity: An Objective Evaluating Method

B. Sepehri[1], A. Esteki[2], G.A. Shahidi[3] and M. Moindodin[4]

[1] School of Medical Engineering, Science and Research Center of Azad University, Tehran, Iran
[2] Department of Biomedical Engineering, Shahid Beheshti University of Medical Sciences, Tehran, Iran
[3] Department of Neuroscience, Iran University of Medical Sciences, Tehran, Iran
[4] School of Medical Engineering, Science and Research Center of Azad University, Tehran, Iran

Abstract- **In this paper, a new method for quantification of rigidity in elbow joint of Parkinsonian patients is introduced. One of the most known syndromes in Parkinson's disease is increased passive stiffness in muscles, which leads to rigidity in joints. Clinical evaluation of stiffness in wrist and/or elbow, commonly used by clinicians, is based on Unified Parkinson's Disease Rating System (UPDRS). Subjective nature of this method may influence the accuracy and precision of evaluations. Hence, introducing an objective standard method based on quantitative measurements may be helpful. A test rig was designed and fabricated to measure range of motion and viscous and elastic components of passive stiffness in elbow joint. Measurements were done for 41 patients and 11 controls. Measures were extracted using Matlab-R14 software and statistic analyzes were done by Spss-13. Relation between each computed measure and the level of illness were analyzed. Results showed a better correlation between viscous component of stiffness and UPDRS score compared to the elastic component. Results of this research may help to introduce a standard objective method for evaluation of Parkinson's disease.**

Keywords- **Measurement, Stiffness, Viscous, Elastic, Parkinson**

I. Introduction

Measurement of stiffness in human joints caused by the stiffening of muscles is one of diagnostic methods to evaluate illnesses involving rigidity. In some cases, the rigidity occurs when a voluntary movement is performed. This kind of rigidity is called *active rigidity*, which is the result of activation of muscles. On the other hand, in many illnesses including Parkinson's Disease (PD), rigidity in muscle and joints exists even when there is no voluntary movement. This is called rigidity at rest or *passive rigidity*, which is the result of alteration in mechanical properties of tissues.

Parkinson's disease affects both men and women equally and usually manifests itself at a larger age, between 50 and 60 years. In this age group roughly 1 in 50 people suffer from the disease [1]. The principal symptoms of Parkinson's disease are rigidity, tremor, bradykinesia, and postural instability. Rigidity responds well to levodopa and is a main parameter monitored to evaluate the efficacy of pharmacological and surgical treatments [2]. However, there is currently no standardized objective method of measuring rigidity. At present, the clinician manipulates patient s limbs and rates the evoked stiffness according to a rating scale such as Unified Parkinson's Disease Rating System (UPDRS), which classifies the joint stiffness from zero to four in an ordinal manner. Zero indicates no rigidity and four is for the highest rigidity with limited range of motion. However the subjective nature of such scale makes it open to the interpretation of the examiner.

Efforts have been made to examine quantified measures, which verify the level of the illness. Some researchers were concentrated on the work done to move the limb [3-5], while others used stiffness index in joints [6-8]. Stiffness index, which is implemented clinically, has been the principal index in recent studies. Due to the expense, complicity and time-consuming nature of these methods, none of them have led to a standard clinical method [9].

Esteki and coworkers [10] introduced a device and measured viscous and elastic components of stiffness in passive movement of ankle joint. The aim of their work was to determine the relation between the above measures and the history of diabetes, but the method implemented was considered as a novel method for similar measurements in joints of upper extremity to find the relation among indices and the level of PD progression.

II. Materials and methods

To measure the passive torque and angular position of elbow joint in flexion-extension movement simultaneously, a test rig based on the one previously implemented in ankle joint [10], was designed and fabricated. Mechanical unit consisted of a fixed support jointed to a moving part using two bearings. Arm was placed in the horizontally fixed support and forearm was mounted on the moving part so that the axis of rotation of elbow joint was aligned with the center of bearings. The axis of rotation of elbow was considered as the line crossing the medial and lateral epicondyls of humerus [11, 12].

Both the arm and forearm were fixed using fastening belts to prevent relative motions of limbs to the device. To measure the torque, a balanced strain gage force transducer

F. Ibrahim, N.A. Abu Osman, J. Usman and N.A. Kadri (Eds.): Biomed 06, IFMBE Proceedings 15, pp. 516-519, 2007
www.springerlink.com ' Springer-Verlag Berlin Heidelberg 2007

(Fort 1000, World Precision Instruments, USA) was implemented.

The force exerted by the examiner to flex and extend the joint transmits to the force transducer through a cantilever mounted to the moving part of the device so that the torque could be measured. Angular position was measured using a 10kΩ potentiometer mounted aligned with one of the bearings. The flexion-extension cycle was performed by the operator in a relatively constant speed of 1 cycle/sec and was repeated for at least 12 cycles. Patients were trained not to exert any force during flexion-extension. Measurements were repeated if high spikes due to voluntary contraction were seen (fig 1). In some cases, surface EMG of flexor and extensor muscles was recorded.

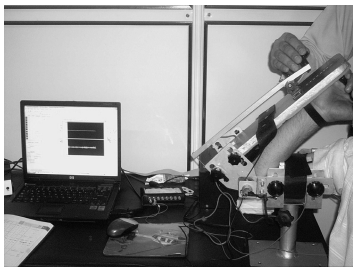

Fig. 1 Passive measurement of stiffness simultaneously with SEMG.

Data were digitized at 100 Hz and fed to a PC via a parallel port. Labview-7 software was used to monitor the real time graphs and to store data. Matlab-R14 was used to extract the measures out of the stored row data. Measures used in this research were (fig 2):

- Total Slope, TS: slope of linear fit on hysteresis loops
- Total Hysteresis, TH: surface covered by hysteresis loops
- Normalized Total Hysteresis, NTH: TH normalized to range of motion
- Range of Motion, ROM

Data for 8 cycles were averaged. Calculating indices 1-3, data corresponding to first and last 2 presents of range of motion were discarded to prevent inertial effects due to acceleration/deceleration at extremes. Data extracted using Matlab was stored in matrices grouped as Control/Patients, Men/Women, Right side/Left side, with/without Reinforcement, and according to UPDRS scores. Using Spss-13, independent samples t-test was performed to find the significance of difference in each index between paired groups and one way ANOVA test and its variance robust tests were used to do the same among UPDRS groups. Because of scarce of data in group four of UPDRS, data of this group were not accounted in ANOVA tests. Finally, Pearson test of correlation were examined to determine the relation of data in each index and UPDRS scores.

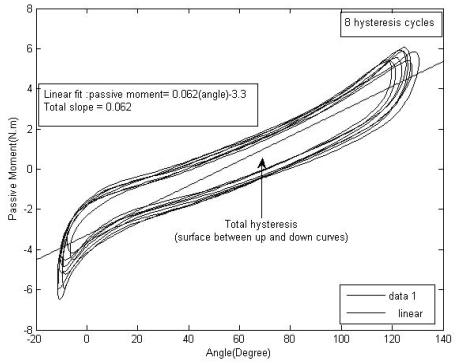

Fig. 2 A prototype of 8 hysteresis loops. Horizontal ax indicate the angular position in degree and vertical ax shows the changes in passive moment in N.m. The slope of linear fit is considered as TS, and the surface covered by the loops is used as TH.

The process was done in groups of patients and controls. The former consisted of 41 rigidity dominant patients, 35 males and 6 females, aged 36 to 75. The later covered 10 males and 1 female aged 30 to 68 with no history of neuromuscular diseases. Measurements were performed in right and left sides, with and without reinforcement. Reinforcement was considered as a mirror voluntary movement in the contralateral side to the measured joint.

Parallel to measurements done with the test rig, clinical assessments of rigidity were performed by one of the two neurologists contributing in the research. Patients elbow were flexed and extended to determine the UPDRS score.

III. Results

The differences of mean values of indices in patients/controls groups were visible. In Men/Women and Right/left sides groups, differences were not remarkable, but reinforcement makes noticeable changes. Also, mean values of visco-elastic indices in UPDRS groups were remarkably different.

Results obtained from statistical tests are shown (Table 1). Mean values were significantly different between patients and controls groups ($p<0.05$). In Men/Women and Right/left sides groups, differences were not significant. ROM index showed no significance in UPDRS groups ($p=0.258$). Except for the NTH ($p=0.013$), there is no sensitivity to sex in indices. Finally, in all indices differences between with/without reinforcement groups are significant (table 1).

F. Ibrahim, N.A. Abu Osman, J. Usman and N.A. Kadri (Eds.): Biomed 06, IFMBE Proceedings 15, pp. 516-519, 2007
www.springerlink.com ' Springer-Verlag Berlin Heidelberg 2007

Table 1. P-values of statistic tests.

	Control/Patients	Sex	Side	Reinforcement	UPDRS
Total Slope	0.000	0.508	0.390	0.000	0.000
Total hyst.	0.000	0.058	0.258	0.000	0.000
N. total hyst.	0.000	0.013	0.455	0.002	0.000
ROM	0.000	0.554	0.092	0.034	0.258

For better comparison, bar diagrams of TS and NTH in all groups are shown in figures 3 and 4.

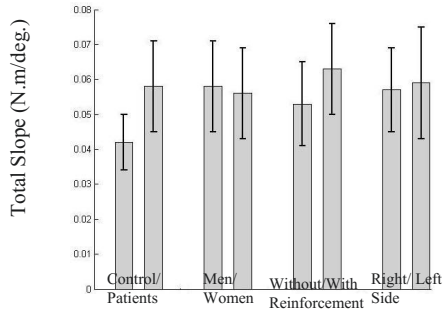

Fig 3. Bar diagrams indicating mean and Std values of total slope in pre described groups.

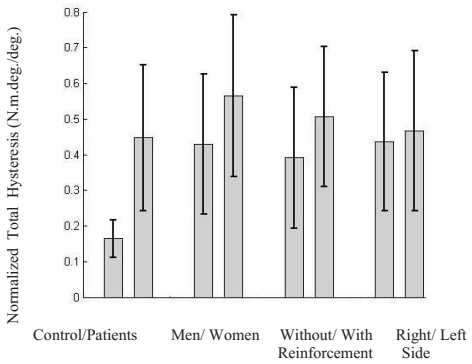

Fig 4: Bar diagrams indicating mean and Std values of normalized total hysteresis in pre described groups.

The level of correlation of the measures and UPDRS scores are shown in table 4, where age was considered as an auxiliary index and data of controls were contributed as the zero level of UPDRS score. Results showed the highest correlation between NTH and UPDRS score (r=0.860), while ROM and UPDRS have the lowest correlation (r = -0.326). Age and UPDRS have also low correlation.

Table 2. Pearson's coefficients of correlation between indices and UPDRS score.

Index	r	p
Total Slope	0.740	0.000
Total Hysteresis	0.749	0.000
Normalized Total Hysteresis	0.860	0.000
Rang of Motion	-0.326	0.000
Age	0.352	0.000

For the convenience of comparison, bar diagrams of Ts and NTH are shown in figures 5 and 6.

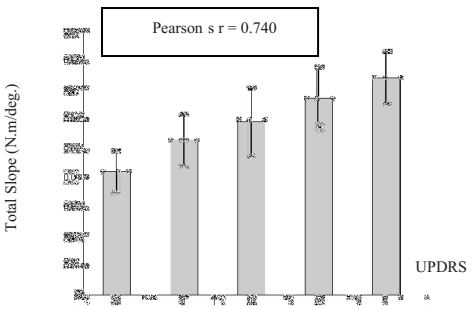

Fig. 5 Bar diagram indicating mean and std of total slope in various UPDRS levels of 0 to 4, and correlation coefficients of TS-UPDRS.

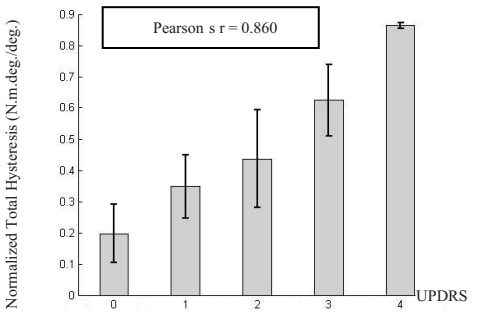

Fig. 6 Bar diagram indicating mean and std of normalized total hystersis in various UPDRS levels of 0 to 4, and correlation coefficients of NTH-UPDRS.

F. Ibrahim, N.A. Abu Osman, J. Usman and N.A. Kadri (Eds.): Biomed 06, IFMBE Proceedings 15, pp. 516-519, 2007
www.springerlink.com ' Springer-Verlag Berlin Heidelberg 2007

IV. Discussion

In this research, viscous and elastic components of passive stiffness were measured, using a custom design test rig. Some indices were extracted from these measures and the relations between each index and level of Parkinson's disease were studied.

Results showed that the test rig can be used to differentiate elastic and viscous indices well in Control/ patients groups and among the UPDRS groups. Also reinforcement increases stiffness indices, which has been proven to be a principal sign in Parkinson scoring clinically. Correlation tests indicate the highest coefficients for NTH implying that measuring the viscous properties may better score the level of the disease than elastic ones. Moreover NTH has priority to TH, because of the physiologic differences in rang of motion in people, but decrease in ROM, by itself, may not be considered as a cardinal index. Although the risk of involvement increases with aging [1], our observations showed no correlation between age and the level of illness in rigidity dominant patients.

Because of relatively big number of patients contributing in this research, the levels of significances in groups are very high which indicate the high reliability of tests. In this study the ordinal score of UPDRS for each patient was examined only by one physician. To decrease personal interpretation, in future researches it will be needed to make it possible that more than one professional physician perform clinical test on a patient at a same time. This process has been performed previously [2], but there have been other limitations: limited number of patients, using of model fitted index instead of real visco-elastic ones, and not to account for the weight of limb. Despite others [2, 8], we have accounted for the weight of the limb to calculate the net passive torque. In future studies, using sub components of visco-elastic indices (i.e. in flexion and extension ends), more precise results may be obtained.

V. Conclusion

Using results of this research, it may be possible to construct a standard objective method to score the level of PD. The method is not expensive and time consuming. To achieve a standard clinical method, more experiments and follow-ups are needed.

Acknowledgment

A. Tavakol and M. Moinodin Are acknowledged for their part in providing electronic circuits and software programming. Science and Research Center of Azad University has contributed in costs of the research.

References

1. Scenk M. and Venekamp D., Parkinson s Disease, Biomechatronics wb2432.
2. Patrick S. K., Allen A., Denington M., Gauthier G. A., Gillard D. M. and Prochazkz A., Quantification of the UPDRS Rigidity Scale, IEEE Transaction on neural systems and rehabilitation engineering,Vol.9,no1, March 2001.
3. Webster D. D.,"A method of measuring the dynamic characteristics of muscle rigidity, strength, and tremor in the upper extremity," IRE Trans. Med. Electron., pp159-164, sept. 1959.
4. Teravainen H., Tsui J. K. C., Mak E. and Calne D. B.,"Optimal indices for testing parkinsonian rigidity,' Candal. J. Neuro. Sci., vol. 16, no. 2,pp. 180-183, 1989.
5. Kirollos C., Charlett C., O neill C. J. A., Kosik R., Mozol K., Purkiss A. G., Bowes S. G. , Nicholson P. W., Hunt W. B., Weller C., Dobbos C. S. M. and Dobbos R. J., Objective measurement of activation of rigidity : diagnostic, pathogenetic and therapeutic implications in parkinsonism, British Journal of Clinical Pharmacology 1996: 41:557-564.
6. Caligigiuri M. P., "Portable device for quantifying Parkinsonian wrist rigidity." Mov. Disord., vol. 9,no. 1,pp.57-63, 1994.
7. Halpern D., Patterson R., Mackie R., Runck W. and Eyler L.,'Muscular hypertonia:Quantitative analysis," Arch. Phys. Med. Rehabil., vol. 60,no. 5,pp. 208-218, 1979.
8. Prochazka A., Bennett D. J., Stephens M. J., Patrick S. K., Sears-Duru R., Roberts T., and Jhamandas J. H., Measurement of rigidity in Parkinson s disease, Mov. Disord., vol. 12, no. 1, pp. 24 32, 1997.
9. Lang A. E. T. and Fahn S., "Assessment of Parkinson's disease,"in Quantification of Neurological Deficit, T.L.Munsat, Ed. Boston,Ma:Butterworths, 1989, pp. 285-309.
10. Hajrasouliha A. Tavakoli R. S., Esteki A., Nafisi S. and Noorolahi-Moghaddam H.,"Abnormal viscoelastic behavior of passive ankle joint movement in diabetic patients: an early or a late complication, "Diabetologia, vol. 48, pp. 1225-1228, 2005.
11. Floyed T., "Manual of structural kinesiology", McGraw-Hill.
12. Biodex System 3 Pro Manual, Biodex Medical Systems, Inc. New York 11967-0702.

Author: Behrooz Sepehri
Institute: Science and Research Center of Azad University
Street: Poonak Square, Sardar Jangal St.
City: Tehran
Country: Iran

F. Ibrahim, N.A. Abu Osman, J. Usman and N.A. Kadri (Eds.): Biomed 06, IFMBE Proceedings 15, pp. 516-519, 2007
www.springerlink.com ' Springer-Verlag Berlin Heidelberg 2007

Comparison of Different Classification Techniques Using WEKA for Breast Cancer

Mohd Fauzi bin Othman,Thomas Moh Shan Yau

Control and Instrumentation Department, Faculty of Electrical Engineering, Universiti Teknologi Malaysia, Skudai, Malaysia

Abstract— **The development of data-mining applications such as classification and clustering has shown the need for machine learning algorithms to be applied to large scale data. In this paper we present the comparison of different classification techniques using Waikato Environment for Knowledge Analysis or in short, WEKA. WEKA is an open source software which consists of a collection of machine learning algorithms for data mining tasks. The aim of this paper is to investigate the performance of different classification or clustering methods for a set of large data. The algorithm or methods tested are Bayes Network, Radial Basis Function, Pruned Tree, Single Conjunctive Rule Learner and Nearest Neighbors Algorithm. A fundamental review on the selected technique is presented for introduction purposes. The data breast cancer data with a total data of 6291 and a dimension of 699 rows and 9 columns will be used to test and justify the differences between the classification methods or algorithms. Subsequently, the classification technique that has the potential to significantly improve the common or conventional methods will be suggested for use in large scale data, bioinformatics or other general applications.**

Keywords— **Machine Learning, Data Mining, WEKA, Classification, Bioinformatics.**

I. Introduction

The aim of our work is to investigate the performance of different classification methods using WEKA for breast cancer. A major problem in bioinformatics analysis or medical science is in attaining the correct diagnosis of certain important information. For the ultimate diagnosis, normally, many tests generally involve the clustering or classification of large scale data. All of these test procedures are said to be necessary in order to reach the ultimate diagnosis. However, on the other hand, too many tests could complicate the main diagnosis process and lead to the difficulty in obtaining the end results, particularly in the case where many tests are performed. This kind of difficulty could be resolved with the aid of machine learning which could be used directly to obtain the end result with the aid of several artificial intelligent algorithms which perform the role as classifiers.

Machine learning covers such a broad range of processes that it is difficult to define precisely. A dictionary definition includes phrases such as to gain knowledge or understanding of or skill by studying the instruction or experience and modification of a behavioral tendency by experienced zoologists and psychologists study learning in animals and humans [1]. The extraction of important information from a large pile of data and its correlations is often the advantage of using machine learning.New knowledge about tasks is constantly being discovered by humans and vocabulary changes. There is a constant stream of new events in the world and continuing redesign of Artificial Intelligent systems to conform to new knowledge is impractical but machine learning methods might be able to track much of it [1].

There is a substantial amount of research with machine learning algorithm such as Bayes Network, Radial Basis Function, Decision tree and pruning, Single Conjunctive Rule Learner and Nearest Neighbors Algorithm.

II. Methods

A. Bayes Network Classifier

Bayesian networks are a powerful probabilistic representation, and their use for classification has received considerable attention. This classifier learns from training data the conditional probability of each attribute A_i given the class label C [2,3]. Classification is then done by applying Bayes rule to compute the probability of C given the particular instances of A_1 ..A_n and then predicting the class with the highest posterior probability. The goal of classification is to correctly predict the value of a designated discrete class variable given a vector of predictors or attributes [4]. In particular, the naive Bayes classifier is a Bayesian network where the class has no parents and each attribute has the class as its sole parent [3,4].

B. Radial Basis Function

Radial basis function (RBF) networks have a static Gaussian function as the nonlinearity for the hidden layer processing elements. The Gaussian function responds only to a small region of the input space where the Gaussian is centered [5]. The key to a successful implementation of these networks is to find suitable centers for the Gaussian functions [6,7]. The simulation starts with the training of an

F. Ibrahim, N.A. Abu Osman, J. Usman and N.A. Kadri (Eds.): Biomed 06, IFMBE Proceedings 15, pp. 520-523, 2007
www.springerlink.com ' Springer-Verlag Berlin Heidelberg 2007

unsupervised layer. Its function is to derive the Gaussian centers and the widths from the input data. These centers are encoded within the weights of the unsupervised layer using competitive learning [7]. During the unsupervised learning, the widths of the Gaussians are computed based on the centers of their neighbors. The output of this layer is derived from the input data weighted by a Gaussian mixture. The advantage of the radial basis function network is that it finds the input to output map using local approximators. Usually the supervised segment is simply a linear combination of the approximators. Since linear combiners have few weights, these networks train extremely fast and require fewer training samples.

C. Decision Tree and Pruning

A decision tree partitions the input space of a data set into mutually exclusive regions, each of which is assigned a label, a value or an action to characterize its data points. The decision tree mechanism is transparent and we can follow a tree structure easily to see how the decision is made [8]. A decision tree is a tree structure consisting of internal and external nodes connected by branches. An internal node is a decision making unit that evaluates a decision function to determine which child node to visit next. The external node, on the other hand, has no child nodes and is associated with a label or value that characterizes the given data that leads to its being visited. However, many decision tree construction algorithms involve a two - step process. First, a very large decision tree is grown. Then, to reduce large size and overfiting the data, in the second step, the given tree is pruned [9]. The pruned decision tree that is used for classification purposes is called the classification tree.

D. Single Conjunctive Rule Learner

Single conjunctive rule learner is one of the machine learning algorithms and is normally known as inductive learning. The goal of rule induction is generally to induce a set of rules from data that captures all generalizable knowledge within that data, and at the same time being as small as possible [10]. Classification in rule-induction classifiers is typically based on the firing of a rule on a test instance, triggered by matching feature values at the left-hand side of the rule [11]. Rules can be of various normal forms, and are typically ordered; with ordered rules, the first rule that fires determines the classification outcome and halts the classification process.

E. Nearest Neighbors Algorithm

Nearest neighbors algorithm is considered as statistical learning algorithms and it is extremely simple to implement and leaves itself open to a wide variety of variations. In brief, the training portion of nearest-neighbor does little more than store the data points presented to it. When asked to make a prediction about an unknown point, the nearest-neighbor classifier finds the closest training-point to the unknown point and predicts the category of that training-point accordingly to some distance metric [12]. The distance metric used in nearest neighbor methods for numerical attributes can be simple Euclidean distance.

F. The Data

The data used in this investigation is the breast cancer data. It has a total of 6291 data and a dimension of 699 rows and 9 columns. For the purposes of training and testing, only 75% of the overall data is used for training and the rest is used for testing the accuracy of the classification of the selected classification methods.

III. WEKA

WEKA is a data mining system developed by the University of Waikato in New Zealand that implements data mining algorithms using the JAVA language. WEKA is a state-of-the-art facility for developing machine learning (ML) techniques and their application to real-world data mining problems. It is a collection of machine learning algorithms for data mining tasks. The algorithms are applied directly to a dataset. WEKA implements algorithms for data preprocessing, classification, regression, clustering and association rules; It also includes visualization tools. The new machine learning schemes can also be developed with this package. WEKA is an open source software issued under General Public License [13].

The data file normally used by Weka is in ARFF file format, which consists of special tags to indicate different things in the data file (foremost: attribute names, attribute types, attribute values and the data). The main interface in Weka is the Explorer. It has a set of panels, each of which can be used to perform a certain task. Once a dataset has been loaded, one of the other panels in the Explorer can be used to perform further analysis.

IV. RESULT

To gauge and investigate the performance on the selected classification methods or algorithms namely Bayes Network

F. Ibrahim, N.A. Abu Osman, J. Usman and N.A. Kadri (Eds.): Biomed 06, IFMBE Proceedings 15, pp. 520-523, 2007
www.springerlink.com ' Springer-Verlag Berlin Heidelberg 2007

Classifier, Radial Basis Function, Decision Tree with pruning, Single Conjunctive Rule Learner and Nearest Neighbor, we use the same experiment procedure as suggested by WEKA. The 75% data is used for training and the remaining is for testing purposes.

In WEKA, all data is considered as instances and features in the data are known as attributes. The simulation results are partitioned into several sub items for easier analysis and evaluation. On the first part, correctly and incorrectly classified instances will be partitioned in numeric and percentage value and subsequently Kappa statistic, mean absolute error and root mean squared error will be in numeric value only. We also show the relative absolute error and root relative squared error in percentage for references and evaluation. The results of the simulation are shown in Tables 1 and 2 below. Table 1 mainly summarizes the result based on accuracy and time taken for each simulation. Meanwhile, Table 2 shows the result based on error during the simulation. Figures 1 and 2 are the graphical representations of the simulation result.

Table 1 Simulation result of each algorithm.

Algorithm (Total Instances, 175)	Correctly Classified Instances % (value)	Incorrectly Classified Instances % (Value)	Time Taken (seconds)	Kappa Statistic
Bayes Net.	89.7143 (157)	10.2857 (18)	0.19	0.7858
Radial Basis Function	87.4286 (153)	12.5710 (22)	0.53	0.7404
Decision Tree and Pruning	85.7143 (150)	14.2857 (25)	0.23	0.7019
Single Conj. Rule Learner	85.1429 (149)	14.8571 (26)	0.15	0.6893
Nearest Neighbors	84.5714 (148)	15.4286 (27)	0.81	0.6860

Table 2 Training and simulation errors

Algorithm (Total Instances, 175)	Mean Absolute Error	Root Mean Squared Error	Relative Absolute Error (%)	Root Relative Squared Error (%)
Bayes Network	0.1062	0.3217	22.2878	65.1135
Radial Basis Function	0.1999	0.3162	41.9593	63.9903
Decision Tree and Pruning	0.1871	0.3635	39.2681	73.5759
Single Conj. Rule Learner	0.2449	0.3559	51.4069	72.0207
Nearest Neighbors	0.1543	0.3928	32.3840	79.4963

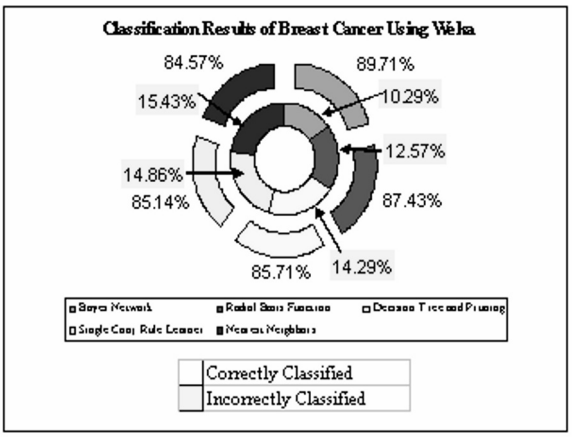

Fig. 1 Results

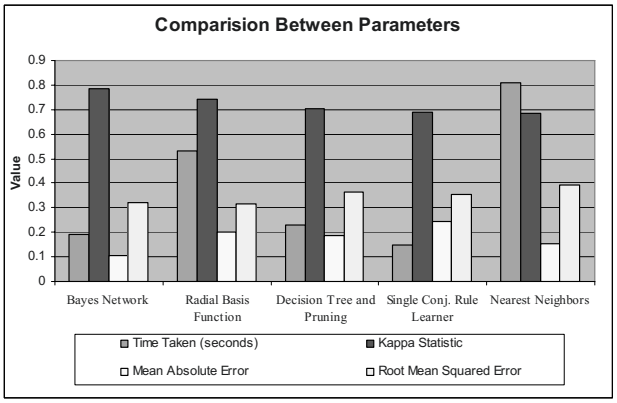

Fig. 2 Comparison between parameters

V. Disscussions

Based on the above Figures 1, 2 and Table 1, we can clearly see that the highest accuracy is 89.71% and the lowest is 84.57%. The other algorithm yields an average accuracy of around 85%. In fact, the highest accuracy belongs to the Bayes network classifier, followed by Radial basis function with a percentage of 87.43% and subsequently decision tree with pruning and single conjunctive rule learner. Nearest neighbor bottom the chart with percentage around 84%. An average of 151 instances out of total 175 instances is found to be correctly classified with highest score of 157 instances compared to 148 instances, which is the lowest score. The total time required to build the model is also a crucial parameter in comparing the classification algorithm. In this simple experiment, from Figure 2, we can say that a single conjunctive rule learner requires the shortest time which is around 0.15 seconds compared to the others. Nearest neighbor algorithm requires the longest model building

F. Ibrahim, N.A. Abu Osman, J. Usman and N.A. Kadri (Eds.): Biomed 06, IFMBE Proceedings 15, pp. 520-523, 2007
www.springerlink.com ' Springer-Verlag Berlin Heidelberg 2007

time which is around 0.81 seconds. The second on the list is Bayes network with 0.19 seconds.

Kappa statistic is used to assess the accuracy of any particular measuring cases, it is usual to distinguish between the reliability of the data collected and their validity [14]. The average Kappa score from the selected algorithm is around 0.6-0.7. Based on the Kappa Statistic criteria, the accuracy of this classification purposes is substantial [14]. From Figure 2, we can observe the differences of errors resultant from the training of the five selected algorithms. This experiment implies a very commonly used indicator which are mean of absolute errors and root mean squared errors. Alternatively, the relative errors are also used. Since, we have two readings on the errors, taking the average value will be wise. It is discovered that the highest error is found in single rule conjunctive rule learner with an average score of around 0.3 where the rest of the algorithm ranging averagely around 0.2-0.28. An algorithm which has a lower error rate will be preferred as it has more powerful classification capability and ability in terms of medical and bioinformatics fields.

VI. Conclusions

As a conclusion, we have met our objective which is to evaluate and investigate five selected classification algorithms based on Weka. The best algorithm based on the breast cancer data is Bayes network classifier with an accuracy of 89.71% and the total time taken to build the model is at 0.19 seconds. Bayes network classifier has the lowest average error at 0.2140 compared to others. These results suggest that among the machine learning algorithm tested, Bayes network classifier has the potential to significantly improve the conventional classification methods for use in medical or in general, bioinformatics field.

Acknowledgment

We would like to thank Associate Prof. Dr Naomi from the Faculty of Computer Science and Information System, Universiti Teknologi Malaysia for the data. This work is using free software from University of Waikato in New Zealand

References

1. Nils J. Nilsson (1999) Introduction to Machine Learning. California. United Stated of Americas.
2. Bouckaert, R.R. (1994). Properties of Bayesian network Learning Algorithms. In R. Lopex De Mantaras & D. Poole (Eds.), I*n Press of Proceedings of the Tenth Conference on Uncertainty in Artificial Intelligence* (pp. 102-109). San Francisco, CA.
3. Buntine, W. (1991). Theory refinement on Bayesian networks. In B. D. D Ambrosio, P. Smets, & P.P. Bonissone (Eds.), *In Press of Proceedings of the Seventh Annual Conference on Uncertainty Artificial Intelligent* (pp. 52-60). San Francisco, CA
4. Daniel Grossman and Pedro Domingos (2004). Learning Bayesian Network Classifiers by Maximizing Conditional Likelihood. *In Press of Proceedings of the 21st International Conference on Machine Learning,* Banff, Canada.
5. M. D. Buhmann (2003), Radial Basis Functions: Theory and Implementations, 12. Cambridge Monographs on Applied and Computational Mathematics, Cambridge University Press, Cambridge.
6. S. V. Chakravarthy and J. Ghosh (1994), Scale Based Clustering using Radial Basis Function Networks, *In Press of Proceeding of IEEE International Conference on Neural Networks*, Orlando, Florida. pp. 897-902.
7. Howell, A.J. and Buxton, H. (2002). RBF Network Methods for Face Detection and Attentional Frames, *Neural Processing Letters* (15), pp.197-211
8. J.S R Jang (1993). ANFIS Adaptive Network Based Fuzzy inference System. IEEE Transaction on Systems, Man and Cybernetics. Vol. 23, no3, pp 665-685
9. Mansour Y (1997). Pessimistic decision tree pruning based on tree size. *In Press of Proc. 14th International Conference on Machine Learning.* Pp.195-201.
10. Cohen, W. (1995) Fast effective rule induction. *In Press of Proceedings 12th International Conference on Machine Learning*, Morgan Kaufmann. Pp. 115 123.
11. Clark, P., Niblett, T. (1989). The CN2 rule induction algorithm. Machine Learning 3. pp. 261 284
12. T. Darrell and P. Indyk and G. Shakhnarovich (2006). Nearest Neighbor Methods in Learning and Vision: Theory and Practice. MIT Press.
13. WEKA at http://www.cs.waikato.ac.nz/~ml/weka.
14. Kappa at http://www.dmi.columbia.edu/homepages/chuangj/kappa

Address of the corresponding author:
Author: Dr Mohd Fauzi Othman
Institute: Fakulti Kejuruteraan Elektrik
Universiti Teknologi Malaysia
Street: 81300 UTM Skudai
City: Johor Bahru
Country: Malaysia
Email: fauzi@fke.utm.my

F. Ibrahim, N.A. Abu Osman, J. Usman and N.A. Kadri (Eds.): Biomed 06, IFMBE Proceedings 15, pp. 520-523, 2007
www.springerlink.com ' Springer-Verlag Berlin Heidelberg 2007

Discovery the Relationship Between Single Nucleotide Polymorphisms and Alternative Splicing Events

Fang Rong Hsu[1], Hsien Chun Lin[2], Hwan-You Chang[3]

[1] Bioinformatics Research Center, Department of Information Engineering and Computer Science, Feng Chia University, Taiwan
[2] Department of Bioinformatics, Asia University, Taichung, Taiwan
[3] Department of life science, National Tsing-Hua University, Hsinchu, Taiwan

Abstract— **Recent genome-wide analysis of alternative splicing indicate that 40–60% of human genes have alternative splice forms, suggesting that alternative splicing is one of the most significant components of the functional complexity of the human genome. Avatar (A value added transcriptome database) identified 174,546 alternative splicing events coverage of Homo sapiens through an analysis of large scale ESTs. And Single nucleotide polymorphisms (SNPs) are the most abundant form of human genetic variation. The refSNP (reference SNP) of dbSNP contained a total of 9,098,790 refSNPs information. The large volume of data produced by high-throughput sequencing projects is a rich and large source of SNPs and alternative splicing. The study of alternative splicing has long been a valuable subfield of molecular biology, can promote the proceeding of molecular biologic studies. We analyze more than 100,000 alternative splicing events from Avatar, producing 15,228 candidate SNPs that probable have relation between SNP and alternative splicing. We use Fisher's exact test to confirm the result and find 1,122 significant SNPs. Further we analyze the sequence in the area that near the alternative splicing event related SNP. We find some consensus sequences in the area, which may related to alternative splicing events.**

Keywords—**Single nucleotide polymorphisms, Bioinformatics, Alternative Splicing**

I. Introduction

The genetic polymorphism due to base substitutions is called single nucleotide polymorphism (SNP). SNPs are an increasingly important resource for understanding the structure and history of the human genome [1,2,3], because this polymorphism can cause qualitative and quantitative differences in the gene expression. A SNP is defined as a mutation involving a single DNA base substitution that is observed with a frequency of at least 1% in a given population [4]. It is estimated that SNPs occur approximately every 100 to 300 bases in the overall human population, leading to a total of several million SNPs. SNPs are expected to facilitate large-scale association genetic studies. There has recently been great interest in SNP discovery and detection [5]. The importance of SNPs in genetic studies stems from at least three different considerations. First, since most SNPs are inherited from one generation to the next, they represent a powerful tool to study the evolution of our species. Studying the frequency and distribution of SNPs in different human populations can lead to important insights on their history and mutual relationships [6,7]. SNPs can also be directly responsible for genetic diseases, since they may alter the genetic sequence of a gene or of a regulatory region, for example spinal muscular atrophy (SMA) [8,9] and inflammatory diseases [10]. Finally, SNPs can be used to build the high-density maps of the genome needed to perform association studies. Association studies try to establish a relationship between a phenotype (usually a disease) and one or more regions of the genome [4].

The study of alternative splicing has long been a valuable subfield of molecular biology. We believe that there must be some relationships between SNPs and alternative splicing events like exonic splicing enhancers (ESEs) or exonic splicing silencers (ESSs). And there are some biochemical experiments have already demonstrated that SNPs will influence the splice [11]. But to find out the relationships between SNPs and alternative splicing events by using biochemical experiments is a time-consuming and high-risk work. Using biochemical experiment sometimes takes a lot of time and might only manifest there is no obviously relationship between SNPs and alternative splicing events [12]. So we use bioiformatics approach to discover the relationship between SNPs and alternative splicing events.

II. Materials and tools

SNP Database: The National Center for Biotechnology Information has established the dbSNP database to serve as a central repository for both single base nucleotide subsitutions and short deletion and insertion polymorphisms. The refSNP (reference SNP) sequences clustered by chromo-

F. Ibrahim, N.A. Abu Osman, J. Usman and N.A. Kadri (Eds.): Biomed 06, IFMBE Proceedings 15, pp. 524-527, 2007
www.springerlink.com ' Springer-Verlag Berlin Heidelberg 2007

some (ftp://ftp.ncbi.nlm.nih.gov/snp/human/rs_fasta) and the corresponding chromosomal reports (ftp://ftp.ncbi.nlm.nih.gov/snp/human/chr_rpts) of dbSNP (Build 120 , Mar 18, 2004) [13] were downloaded from NCBI. This dataset contained a total of 9,098,790 refSNP sequences of distinct RefSNPs having the noted functional relationship to at least one mRNA in the current assembly.

Alternative splicing Database: Avatar (A value added transcriptome database) [14] mapped ESTs and mRNA sequences onto whole human genomic sequence. It identified 9,937 genes which undergo alternative splicing through an analysis of large-scale ESTs. It contains 174,645 of human alternative splicing event including 3 , 5 , cassette, retained intron and mutually exclusive alternative splicing events (http://avatar.iecs.fcu.edu.tw). The human genome draft sequence in the public domain (International Human Genome Sequencing Consortium 2001) as of July 30, 2003 (Build 34) (ftp://ftp.ncbi.nlm.nih.gov/repository/genomes/H_sapiens/) was used in Avatar.

Align ESTs to genome: We use Mugup [15] align ESTs to human genome. When aligning ESTs to genome, we also can get the detailed result include mismatch or gap position and the difference of nucleotides between ESTs and genomic sequence.

ESEfinder: Point mutations frequently cause genetic diseases by disrupting the correct pattern of pre-mRNA splicing. The effect of a point mutation within a coding sequence is traditionally attributed to the deduced change in the corresponding amino acid. However, some point mutations can have much more severe effects on the structure of the encoded protein. For example, they inactivate an exonic splicing enhancer (ESE) [16], thereby resulting in exon skipping. ESEs also appear to be especially important in exons that normally undergo alternative splicing. Different classes of ESE consensus motifs have been described, but they are not always easily identified. ESEfinder (http://exon.cshl.edu/ESE/) is a web-based resource that facilitates rapid analysis of exon sequences to identify putative ESEs responsive to the human SR proteins SF2/ASF, SC35, SRp40 and SRp55, and to predict whether exonic mutations disrupt such elements.

III. Methods

To find the relationships between SNP and alternative splicing events, we try to analyze the data in Avatar and dbSNP. There are four main steps in our method:

1. Finding exonic SNPs on the human genome.
2. Finding EST supported exonic SNPs from EST alignment result.
3. Finding alternative splicing sites where exonic SNPs nearby.
4. Confirmation of Candidate exonic SNP dependent alternative splicing events.

Finding exonic SNPs on the human genome

Based on refSNP chromosomal data (ftp://ftp.ncbi.nlm.nih.gov/snp/human/chr_rpts) in dbSNP, we query each SNP which may place on exon, using the SNP location data and Avatar exon boundary data. We cluster the exonic SNP data by chromosomes, distinguish the exonic SNPs and other SNP on intron or gap. And get more SNP detail on refSNP and Avatar including refSNP id (rs#), contig accession, and position of refSNP in contig coordinates, SNP length (some SNPs refer to over one nucleotide).

Finding EST supported exonic SNPs from EST alignment result

In Avatar project, authors used Mugup to align the entire EST set to genome. Therefore, the detailed EST alignment information was available. We query all polymorphic nucleotides positions with the refSNP data (ftp://ftp.ncbi.nlm.nih.gov/snp/human/chr_rpts) of dbSNP.

Finding alternative splicing sites where exonic SNPs nearby

We analyze the adjacent area of candidate exonic SNPs. We can use the positions (position of refSNP in contig coordinates) and exon boundary of alternative splicing events from the Avatar database to find out the SNP, which may relate to the alternative splicing event.

First, we try to find out the alternative 3 splicing site and alternative 5 splicing site events. The alternative 3 splicing site and alternative 5 splicing site events were recorded in alternative 3 splicing event and alternative 5 splicing site event tables in which contain the data of splice site and other information in Avatar. In the adjacent area, the nearest exon including downstream and upstream, of the candidate exonic SNP which we found out, we can use the positions (position of refSNP in contig coordinates) and exon boundary of alternative splicing from alternative 3

F. Ibrahim, N.A. Abu Osman, J. Usman and N.A. Kadri (Eds.): Biomed 06, IFMBE Proceedings 15, pp. 524-527, 2007
www.springerlink.com ' Springer-Verlag Berlin Heidelberg 2007

splicing event and alternative 5 splicing site event tables to find out the SNP which may relate to the alternative splicing event. We call these candidate exonic SNPs. And according to the SNP location and alternative splicing event (3 or 5), we distinguish the relationship of SNP and alternative splicing event into four determinations: 1. Upstream SNP related alternative 3 splicing site event. 2. Downstream SNP related alternative 3 splicing site event. 3. Upstream SNP related alternative 5 splicing site event. 4. Downstream SNP related alternative 5 splicing site event. Other types of alternative splicing events are processed similarly.

Confirmation of Candidate exonic SNP dependent alternative splicing events

After we find the candidate exonic SNPs in different alternative splicing events, we try to make the result more precisely. So we count the no. of EST support in different cases of related SNPs and alternative splicing events. We call it an alternative splicing-SNP pair (*A-S* pair for short). One pair affords a true condition of splicing, and the ESTs support can let we know the quantity of it that happens. Than we use Fisher s exact test on all *A-S* pairs to find significant result.

For alternative 3 splicing site and alternative 5 splicing site events, we take the form with the most ESTs support as normal form and the other as alternative splicing forms . We count the number of ESTs in four categories: a. Polymorphic nucleotide (SNP) with alternative splicing form. b. Polymorphic nucleotide (SNP) with normal splicing form. c. General nucleotide (nucleotide on EST as genome) with alternative splicing form. d. General nucleotide (nucleotide on EST as genome) with normal splicing form. Other types of alternative splicing events are processed similarly.

We run Fisher s exact test by the H0: In this SNP nucleotide type, SNP won t influence the alternative splicing frequency, and H1: In this SNP nucleotide type, SNP will influence the alternative splicing frequency. Then we will get the P value of each *A-S* pair. By two tail Fisher s exact test, we say that the P value < 0.05 might support that the SNP will influence the alternative splicing.

IV. Results

For finding exonic SNPs on the human genome we query each SNP which may place on exon, using the SNP location data and Avatar exon boundary data. Based on alternative splicing boundary data from Avatar and SNP position data from dbSNP, we find out 223,010 exonic SNPs.

After we use Mugup to align all ESTs to human genome, we find 383,554 ESTs support exonic SNPs in whole ESTs. We have found out 15,228 exonic SNPs near to alternative splicing sites. In detail, we have found out that 4,438 exonic SNPs which near to the alternative 3 splicing site or alternative 5 splicing site events, 2,686 exonic SNPs which near to retained intron alternative splicing event and 8,104 exonic SNPs which near to the cassette alternative splicing event.

After confirming the data by using Fisher s exact test, we get total 1,122 significant *A-S* pairs (P vaule < 0.05). For example, SNP rs4968215 is an alternative 3 splicing site event. It is with 40 ESTs supporting a category, 7 ESTs supporting b category, 7 ESTs supporting c category and 1,080 ESTs supporting d category. By using the Fisher s exact test, we can get the p-value 4.05E-59. In detail, we have found 311, 549, 79 and 183 SNPs which may cause alternative 3 splicing site event, alternative 5 splicing site event, retained intron alternative splicing event and cassette alternative splicing event respectively.

We use the result of alternative splicing event related SNPs that we found. We take the sequence in the area where the alternative splicing event related SNP happened, we classify them into two classes. One is the SNP which will cause the splicing incidence raise up and the other is the SNP which will decrease the splicing incidence. We try to find out if there are any splicing factors that will influence the splice. First, we get the alternative splicing event related SNPs sequence. We get the sequence 100 bp before the SNP and sequence 100 bp behind the SNP. Second, we classify the sequences into different cases by the relationship between the SNP and alternative splicing event, and the location of SNP (upstream or downstream). Third, we use ESEfinder (http://exon.cshl.edu/ESE/) to find if there is any exonic splicing enhancer changed when the amino acid at SNP position changed from genomic type to SNP type.

We have applied this approach to all *A-S* pairs which are cassette alternative splicing event and P value < 0.05. There are 126 such SNP and spread in 122 region. We have applied these 122 sequences to ESEfinder. The 72% (88/122) of these sequences have the binding site variation when the nucleotide changed. And we randomly choose 100 SNP from SNPs which are not related to alternative splicing events in our analysis. We use these sequences to run ESEfinder and find only 31% (31/100) have the binding site variation when the nucleotide changed.

F. Ibrahim, N.A. Abu Osman, J. Usman and N.A. Kadri (Eds.): Biomed 06, IFMBE Proceedings 15, pp. 524-527, 2007
www.springerlink.com ' Springer-Verlag Berlin Heidelberg 2007

V. Conclusion

The relationship between SNP and alternative splicing is an important resource and adds value to them by establishing biologically meaningful relationships among the data. We combine the data from available dbSNP and alternative splicing database Avatar to find out the relationship between SNP and alternative splicing. Based on data of ESTs, and by bioinformatics analysis, including databases and multiple sequence alignment program Mugup, we find the evidence of relationship between SNP and alternative splicing. Through our study method, we can quickly find the possible candidates related SNP and alternative splicing, and make the biologists do their studies and analysis based on more evident data to spend less time for obtaining more informative results. Human genome has 3 billion of DNA base pairs, even to analyze the 60 million SNPs with known sequence, and it is very time consuming. If we can find the possible relationship between human alternative splicing changes and SNPs rapidly, it may promote the advances of biotechnology. In our study, we not only find the relationship between one SNP and one alternative splicing event but also realize that there may have more than one SNP which may influence on the same alternative splicing event simultaneously. The accuracy of this method and the amount of alternative splicing-SNP pairs found may increase with the advancing sequencing and biological experimental data. In our result some significant relationships between SNP and alternative splicing event may have some characteristic fragments, which will influence on the splicing, like ESE. So we think the result may have value in other dimensions such as pattern finding, homologous region searching, or ESE and ESS like splicing element finding, etc.

Acknowledgment

This research was supported in part by NSC, Taiwan, grant No.: NSC92-3112-B-468-001, NSC94-2218-E-305-012, NSC94-2218-E-007-057.

References

1. G. Barker, J. Batley, H. O' Sullivan, KJ. Edwards and D. Edwards. Redundancy based detection of sequence polymorphisms in expressed sequence tag data using autoSNP. Bioinformatics. 19(3), 421-2 (2003).
2. K. Irizarry, V. Kustanovich, C. Li, N. Brown, W. Wong, S. Nelson and C. Lee. Genome-wide analysis of single nucleotide polymorphisms in human expressed sequences. Nature Genetics. 26, 233-6 (2000).
3. GT. Marth, I. Korf, MD. Yandell, RT. Yeh, Z. Gu, H. Zakeri, NO. Stitziel, L. Hillier, PY Kwok and WR. Gish. A general approach to single-nucleotide polymorphism discovery. Nature Genetics. 23, 452-6 (1999).
4. LY. Chen, SH. Lu, ES. Shih and MJ. Hwang. Single nucleotide polymorphism mapping using genome-wide unique sequences. Genome Res. 12(7), 1106-11 (2002)..
5. The International SNP Map Working Group. A map of human genome sequence variation containing 1.42 million single nucleotide polymorphisms. Nature. 409, 928 33 (2001)..
6. M. Takahashi, F. Matsuda, N. Margetic, and M. Lathrop. Automated Identification of Single Nucleotide Polymorphisms from Sequencing Data. Journal of Bioinformatics and Computational Biology. 1(2), 253-65 (2003).
7. A. Chakravarti. Single base differences between human genomes underlie differences in susceptibility to, or protection from, a host of diseases. Hence the great potential of such information in medicine. Nature. 409, 822 3 (2001).
8. H. Miyaso, M. Okumura, S. Kondo, S. Higashide, H. Miyajima and K. Imaizumi. An intronic splicing enhancer element in SMN PremRNA. J. Biol. Chem. 278(18), 15825-31 (2003).
9. SR. Lim and KJ. Hertel. Modulation of Survival Motor Neuron PremRNA Splicing by Inhibition of Alternative 3' Splice Site Pairing. J Biol Chem. 276(48), 45476-83 (2001).
10. M. Iwao, H. Morisaki and I. Morisaki. Single-nucleotide polymorphism g.1548G > A (E469K) in human ICAM-1 gene affects mRNA splicing pattern and TPA-induced apoptosis. Biochem Biophys Res Commun. 317(3), 729-35 (2004).
11. AM. Zahler, CK. Damgaard, J. Kjems and M. Caputi. SC35 and hnRNP A/B proteins bind to a juxtaposed ESE/ESS element to regulate HIV-1 tat exon 2 splicing. J Biol Chem. 279, 10077-84 (2004).
12. M. Spinola, B. Conti, F. Ravagnani, A. Fabbri, M. Incarbone, I. Cataldo, E. Pira, C. Pelucchi, C. La Vecchia and TA. Dragani. A new polymorphism (Ser362Thr) of the L-myc gene is not associated with lung adenocarcinoma risk and prognosis. Eur J Cancer Prev. 13(1), 87-9 (2004).
13. ST. Sherry, MH. Ward, M. Kholodov, J. Baker, L. Phan, EM. Smigielski and K. Sirotkin. dbSNP: the NCBI database of genetic variation. Nucleic Acid Res. 29, 308 11 (2001).
14. F. R. Hsu, Hwan-You Chang, Yaw-Lin Lin, Yin-Te Tsai, Hui-Ling Peng, Ying Tsong Chen, Chia Yang Cheng, Min Yao Shih, Chia-Hung Liu, Chin-Feng Chen, 2005, AVATAR: A database for genome-wide alternative splicing event detection using large scale ESTs and mRNAs , Bioinformation, Vol. 1, No. 1, pp. 16-18
15. F.R. Hsu and C.F. Chen. Using Multi-Layer Unique Markers to Align EST to Genome. Proc. Of the IEEE Computational Systems Bioinformatics Conference (CSB2003). 564-6 (2003).
16. L. Cartegni, J. Wang, Z. Zhu, MQ. Zhang and AR. Krainer. ESEfinder: a web resource to identify exonic splicing enhancers. Nucleic Acid Research. 31(13), 3568-71 (2003).

Address of the corresponding author:

Author: Fang Rong Hsu
Institute: Dept. of Information Engineering and Computer Science
Street: No. 100 Wenhwa Rd
City: Taichung
Country: Taiwan, R.O.C.
Email: frhsu@fcu.edu.tw

F. Ibrahim, N.A. Abu Osman, J. Usman and N.A. Kadri (Eds.): Biomed 06, IFMBE Proceedings 15, pp. 524-527, 2007
www.springerlink.com ' Springer-Verlag Berlin Heidelberg 2007

Selecting Informative Genes from Leukemia Gene Expression Data using a Hybrid Approach for Cancer Classification

Mohd Saberi Mohamad, Safaai Deris, Siti Zaiton Mohd Hashim

Laboratory of Artificial Intelligence and Bioinformatics,
Software Engineering Department, Faculty of Computer Science and Information Systems,
Universiti Teknologi Malaysia, 81310 Skudai, Johor, Malaysia

Abstract—**The development of microarray-based high-throughput gene profiling has led to the hope that this technology could provide an efficient and accurate means of diagnosing and classifying cancers. However, the large amount of data generated by microarrays requires effective selection of informative genes for cancer classification. Key issue that needs to be addressed is a selection of small number of informative genes that contribute to a disease from the thousands of genes measured on microarrays. This work deals with finding the small subset of informative genes from gene expression microarray data which maximize the classification accuracy. We introduce an improved version of hybrid of genetic algorithm and support vector machine for genes selection and classification. We show that the classification accuracy of the proposed approach is superior to a number of current state-of-the-art methods of one widely used benchmark dataset. The informative genes from the best subset are validated and verified by comparing them with the biological results produced from biology and computer scientist researchers in order to explore the biological plausibility.**

Keywords—**Gene selection; classification; genetic algorithm; support vector machine; gene expression; microarray**

I. Introduction

Due to recent advances in biotechnology, gene expression can now be quantitatively monitored on a global scale. Gene expression data is created by a process known as microarray that yields a set of floating points and absolute values [1]. These values represent the activity level of each gene within an organism at a particular point of time and a typical dataset can often consist of thousands of genes [2]. Recent studies on molecular level classification of tissue have produced remarkable results and indicated that microarray gene expression could significantly aid in the development of efficient cancer diagnosis [3,4]. However, classification based on the microarray data confronts with more challenges. One of the major challenges is the overwhelming number of genes relative to the number of training samples in the datasets [2,4,5]. Most of the genes are not relevant to the distinction between different tissue types (classes) and introduce noise in the classification process, and thus potentially drown out the contribution of the relevant ones [4].

In the gene expression domain, the gene refers to the feature. Feature selection or gene selection can be defined as a task for selecting subsets of features that maximizes the classifier ability to classify samples [6,7]. Gene selection methods can be classified into two categories. If gene selection is carried out independently from the classification procedure, the method is said to follow a filter approach. Otherwise, it is said to follow a wrapper (hybrid) approach [2,4]. Most of previous works used filter approach for selecting genes since it was computationally more efficient than the hybrid approach [4,8]. The major drawback is that an optimal selection of genes may be independent from the inductive and representational biases of the learning algorithm. Therefore, hybrid approach usually provide better accuracy but computationally more expensive than filter approach [4,9].

This research finds a small subset of informative genes from gene expression data which maximize the classification accuracy in order to make a diagnosis far more likely to be widely deployed in a clinical. In this paper, we present an improved version of hybrid of genetic algorithm (GA) and support vector machine (SVM) classifier (GASVM-II) for genes selection and classification.

In Section 2, we describe a hybrid of GA and SVM classifier (GASVM) and introduce GASVM-II. In Section 3, we analyze the experimental results followed by conclusion in Section 4.

II. A Hybrid of Genetic Algorithm and Support Vector Machine Classifier (GASVM)

The overall hybrid method consists of two main components: GA [10] and SVM [11] classifier. The GA will select subsets of features and then the SVM classifier evaluates the subsets during a classification process. The result of the classification is used for the fitness value of GA. Fig. 1 shows flow chart of GASVM.

F. Ibrahim, N.A. Abu Osman, J. Usman and N.A. Kadri (Eds.): Biomed 06, IFMBE Proceedings 15, pp. 528-532, 2007
www.springerlink.com ' Springer-Verlag Berlin Heidelberg 2007

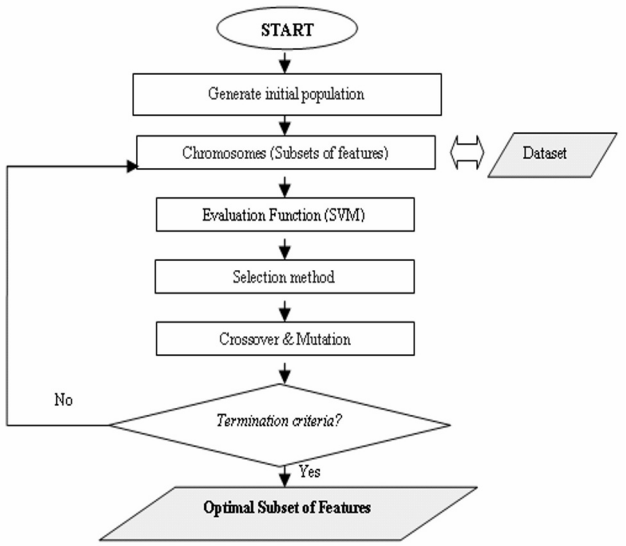

Fig. 1 A flow chart of hybrid of GA and SVM classifier (GASVM).

An individual represents a features subset (gene subset). The representation of chromosome (individual) used in GASVM appears in structural form as described in the previous works [2,9] and shown in Fig. 2.

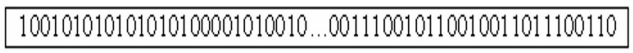

Fig. 2 A representation of chromosome in GASVM.

Let n be the total number of features available for representing the data to be classified. Hence, the chromosome is represented by binary vector of dimension n. If a bit is 1, it means that the corresponding feature is selected. A value of 0 indicates that the corresponding feature is not selected. The number of feature subsets based on the chromosome representation is calculated by using the following equation [10].

$$n_C = 2^n \tag{1}$$

where n_C is the number of feature subsets, whereas n is the number of features. A fitness function of each individual is determined by evaluating the SVM using a training set. Hence, this research has used a fitness function containing classification accuracy as mentioned below.

$$fitness(x) = accuracy(x) \tag{2}$$

where *accuracy(x)* is the *leave one out cross validation* (LOOCV) accuracy of the classifier with the features subset selection represented by x.

GA is used to maximize the fitness value in order to find the optimal features subset which has achieved the highest LOOCV accuracy. Finally, it produced the optimal subset of training set. The optimal subset from training set is used to construct SVM. Therefore, it is used to test the performance of built SVM.

A. An Improved Version of GASVM (GASVM-II)

Since the data used in this work is high dimensional data, the conventional approaches are hard to be applied. Hence, we proposed an improved chromosome representation in order to overcome the limitation. We have modified the representation of chromosome in GASVM for selecting subset of features suitable to gene expression data. The modified GASVM is called GASVM-II. This idea is based on reducing the number of feature subsets from the Equation (1) by fixing the number of selected features leading to this equation.

$$^nC_x = \frac{n!}{x!(n-x)!} \tag{3}$$

where ^nC_x is the total number of subsets of selected features x from the total of features n.

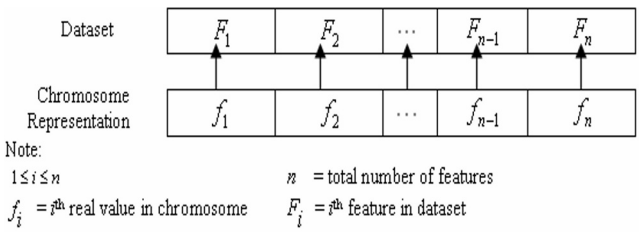

Fig. 3 An improved chromosome representation in GASVM-II

Fig. 3 shows an improved chromosome representation in GASVM-II that based on Equation (3). It includes the real value f_i in the chromosome which indicates a selected feature is the i^{th} feature among total features in dataset. For example, if $f_i = 10$, then the GASVM-II will select the 10^{th} feature in dataset in order to group it in related subset of features. The numbers of the real value f_i are equal to the numbers of selected features before evaluation process. This structure is not much affected by the total number of features and is able to represent chromosome in relatively small size. Its length can vary according to the size of the total number of features n and the number of selected features. The length of the chromosome is the same in size for each chromosome.

F. Ibrahim, N.A. Abu Osman, J. Usman and N.A. Kadri (Eds.): Biomed 06, IFMBE Proceedings 15, pp. 528-532, 2007
www.springerlink.com ' Springer-Verlag Berlin Heidelberg 2007

The improved chromosome representation is developed to support more outstanding properties in genes selection for the cancer classification. The properties are as follows:

- Reducing the number of gene subsets.
- Supporting the high dimensional data.

III. Experimental results

Several set of experiments were conducted to compare the results of the SVM, GASVM and GASVM-II. We used one gene expression dataset, i.e., leukemia cancer dataset [12]. A LOOCV procedure is employed on training data and accuracy test measurement on testing data to measure classification accuracy [9,12].

A. Results Analysis and Discussions

The experiments of GASVM-II were conducted by using 10, 20, 30, 40, 50 and 60 genes in order to choose the best subset of genes among them.

Table 1 displays all subsets of genes can achieve high LOOCV accuracy due to high correlation between samples in training set. However, results of Leukemia dataset on accuracy test are not uniform. The datasets properties, i.e., thousand of genes with less than hundred of samples in the training sets can be possibly cause the overfitting which learning a decision surface that performs well on the training data but bad on testing data. Furthermore, most of the genes are not relevant to the distinction between different tissue types (classes) and introduce noise in the classification process, and thus potentially drowning out the contribution of the relevant ones.

Table 1. Classification accuracies for different gene subsets in Leukemia Cancer dataset using GASVM-II method.

Number of Selected Gene	Accuracy for Leukemia (%)	
	LOOCV	Test
10	100	79.4118
20	100	76.4706
30	100	94.1177
40	100	97.0588
50	100	94.1177
60	100	88.2353

Note:
The best result (subset of genes) shown in shaded cells

The selection of 40 genes from Leukemia Cancer dataset has achieved the best result at 100% using LOOCV procedure while 97.0588% using accuracy test measurement. Hence, this subset will be chosen as the best subset.

Table 2. Benchmark of GASVM-II and of previous methods on Leukemia Cancer dataset.

Method / Reference	Number of Selected Genes	Accuracy (%)	
		LOOCV	Test
GASVM-II	40	100	97.0588
GASVM	3568	94.7368	85.2941
SVM	7129	94.7368	85.2941
ART-NN [13]	10	100	97.0588
LD [14]	50	100	97.0588
MN [15]	10	100	90.0
SVM [16]	49	100	100
GAWV [9]	29	94.7368	88.2353
WV [12]	50	94.7368	85.2941

Note:
Methods in boldface were experimented in this research. The best results shown in shaded cells.

GASVM : A Hybrid of GA and SVM
GASVM-II : Proposed approach
SVM : Support vector machine classifier
WV : Weight voting classifier
GAWV : A Hybrid of GA and WV
ART-NN : Adaptive resonance theory neural network
LD : Logistic discriminant
MN : Modular neural network

Based on the LOOCV and the accuracy test in Table 2, it was noted that GASVM-II performance was equal to methods produced by [13], and [14]. However, the ART-NN method proposed by [13] is the best method because it produced acceptable result with smaller number of genes (10 genes) than other methods. Despite [16] achieved 100% accuracy by using 49 selected genes, but the result is not significant in this comparison because it rejected 4 samples when the confidence level procedure was introduced. Thus, the remaining of test samples only has 30 samples. The GASVM-II and several previous methods attained 100% accuracy using LOOCV procedure, but the previous researches cannot attain the same results when using testing accuracy manner [13,14,15]. This is due to overfitting the data during the training phase when learning a decision surface in the classifiers performed well on the training data but not for testing data. GASVM-II can classify 33 out of 34 test samples correctly. Among the sample, sample 66AML was consistently misclassified as AML. This AML sample was also misclassified by first original work [12] and other previous analyses [13,14].

All the previous works except [9] used filter approach for gene selection procedure. The filter approach is generally computationally more efficient than the hybrid approach. However, it was unable to avoid the noise and overfitting of the data because it is independent on classifier and depends on probabilistic distance measures, probabilistic dependence measures or interclass distance measures. Furthermore, the learning algorithm that has been used to construct the classifier was bias. Hence, the gene selection methods based on the filter approach caused the methods to perform poorly on classification of the datasets. [9] applied the hybrid ap-

F. Ibrahim, N.A. Abu Osman, J. Usman and N.A. Kadri (Eds.): Biomed 06, IFMBE Proceedings 15, pp. 528-532, 2007
www.springerlink.com ' Springer-Verlag Berlin Heidelberg 2007

proach using GAWV. However, they required recurring experiment of the hybrid method to achieve an optimal subset. Moreover, the result is still less than others because this method was used the chromosome representation which is only supporting the data ranged from small to medium features.

As a result, when using the SVM classifier experimented in this research, the whole genes can contribute negative impact on classification performance because most of the genes in the data have many noises. GASVM method performs poorly because the chromosome representation was unable to fix the selected genes and impossible to search all feature spaces and evaluate all possible gene subsets. The GASVM is unable to evaluate all subsets due to huge number of subsets.

GASVM-II is able to avoid the noise problems because hybrid approach performs dependent on the classifier. The GASVM-II performs well in the experiment because it can fix the number of selected genes during gene selection and classification tasks. Hence, the GASVM-II reduces the complexity of search space and successfully evaluated all possible subsets of genes. It is shown that the selection of a small subset of informative genes using the GASVM-II can lead to significant improvement in classification accuracy for higher dimension data problems, i.e., gene expression data.

B. Biological Plausibility for Informative Genes in Leukemia Cancer Dataset

Biological plausibility is one of the criteria for causality in *epidemiology* [17]. It is prominent in all aspects of health risk assessments. A major goal of diagnostic research is to develop diagnostic procedures based on the least possible genes to detect diseases [2,9].

The best subset of 40 selected genes from Leukemia Cancer dataset was evaluated as the identical biological significant. These selected genes were evaluated by comparing them with the results produced from biologist and computer scientist researches.

Table 3. List of the same informative genes in Leukemia Cancer dataset produced by this research (GASVM-II) and previous works.

Previous Work	Gene Accession Number	Informative Gene Description
[18]	M13690	C1NH Complement component 1 inhibitor (angioedema, hereditary)
[3,13]	M55150	FAH Fumarylacetoacetate
[3,12,18]	M23197	CD33 antigen (differentiation antigen)
[3,18]	Y07604	Nucleoside-diphosphate kinase

Table 3 shows the lists of the similar informative genes of Leukemia Cancer dataset produced by GASVM-II and previous works. For instance, CD33 (M23197) were determined by [3,12,13], and [18]. CD33 is similarly a marker for AML, expressed in nearly all malignant *myeloblasts* [12].

From the Table 3, some of the informative genes produced by GASVM-II were validated and verified as the identical biology significance. Much time will be saved in finding and validating the genes by using the proposed approach than traditional *biopsy* procedure. A number of the genes identified by the GASVM-II in these experiments are already in use as clinical markers for cancer diagnosis. Some of the remaining genes may be excellent candidates for further clinical investigation. Thus, the GASVM-II has the ability to find out the informative genes to be used by medical and health sectors.

IV. Conclusion

We have investigated and solved the important issues of selecting a small subset of informative genes from thousands of gene measured on microarray that are inherently noisy. We have designed and developed the GASVM-II to select gene subsets for classification tasks.

Our experiments have empirically evaluated SVM, GASVM and GASVM-II using Leukemia Cancer dataset. The GASVM-II performs very well in most experiments. We are currently studying more on principle design of fitness using domain knowledge as well as mathematically well-founded tools.

Acknowledgments. This work was recognized by National Science Fellowship research program sponsored by Malaysian Ministry of Science, Technology and Environments (MOSTE).

V. References

1. Bannai, H., Inenaga, S., Shinohara, A., Takeda, M., Miyano, S.: Efficiently Finding Regulatory Elements Using Correlation with Gene Expression. J. Bioinfo. & Comput. Bio. 2 (2004) 273 288
2. Inza, I., Larranaga, P., Blanco, R., Correlaza, A.J.: Filter Versus Wrapper Gene Selection Approaches in DNA Microarray Domains. J. Art. Intel. Medic. 31 (2004) 91 103
3. Ben-Dor, A., Bruhn, L., Friedman, N., Schummer, I.M., Yakhini, Z.: Tissue Classification with Gene Expression Profiles. J. Comput. Bio. 7 (2000) 559 584
4. Wang, Y., Tetko, I.V., Hall, M.A., Frank, E., Facius, A., Mayer, K.F., Mewes, H.W. Gene Selection from Microarray Data for Cancer Classification A Machine Learning Approach. J. Comput. Bio. & Chem. 29 (2005) 37 46.

F. Ibrahim, N.A. Abu Osman, J. Usman and N.A. Kadri (Eds.): Biomed 06, IFMBE Proceedings 15, pp. 528-532, 2007
www.springerlink.com ' Springer-Verlag Berlin Heidelberg 2007

5. Soukup, M., Lee, J.K.: Developing Optimal Prediction Models for Cancer Classification using Gene Expression Data. J. Bioinfo. & Comput. Bio. 4 (2004) 681 694
6. Bins, J., Draper, B.A.: Feature Selection from Huge Feature Sets. Proc. Int. Conf. Comp. Vision. 2 (2001) 159 165
7. Zhang, P., Verma, B., Kumar, K.: Neural Vs Statistical Classifier in Conjunction with Genetic Algorithm Based Feature Selection. J. Patt. Recog Lett. 26 (2005) 909 919
8. Mohamad, M.S., Deris, S.: Feature Selection Method Using Genetic Algorithm for the Classification of Small and High Dimension Data. 1st Proc. Int. Symp. Info. Com. Tech. (2004) 13 16
9. Liu, J., Iba, H., Ishizuka, M.: Selecting Informative Genes with Parallel Genetic Algorithms in Tissue Classification. Genome Informatics. 12 (2001) 14 23
10. Michalewicz, Z.: Genetic Algorithms + Data Structures = Evolution Programs. 3rd edn. Springer-Verlag, Berlin Heidelberg New York (1996)
11. Vapnik, V.: The Nature of Statistical Learning Theory. Springer-Verlag, New York (1995)
12. Golub, T.R., Slonim, D.K., Tomayo, P., Huard, C., Gaasenbeek, M., Mesirov, J.P., Coller, H., Loh, M.L., Downing, J.R., Caligiuri, M.A., Bloofield, C.D., Lander, E. S.: Molecular Classification of Cancer: Class Discovery and Class Prediction by Gene Expression Monitoring. Sci. 286 (1999) 531 537
13. Xu, R., Anagnostopoulos, G.C., Wunsch II, D.C.: Tissue Classification Through Analysis of Gene Expression Data Using a New Family of ART Architectures, Proc. Int. Joint Conf. Neu.Netw. (2002) 300 304
14. Nguyen, D.V., Rocke, D.M.: Tumor Classification by Partial Least Squares Using Microarray Gene Expression Data. Bioinformatics. 8 (2002) 39 50
15. Su, M., Basu, M., Toure, A.: Multi-Domain Gating Network for Classification of Cancer Cells Using Gene Expression Data. Proc. Int. Joint Conf. Neu. Netw. (2002) 286 289
16. Mukherjee, S.: Application of Statistical Learning Theory to DNA Microarray Analysis. PhD Thesis. Massachusetts Institute of Technology (2001)
17. Hill, A.B.: The Environment and Disease: Association or Causation. Proc. Royal Sci. Medic. (1965) 295 300
18. Krishnapuram,B., Carin, L., Hartemink, A.J.: Joint Classifier and Feature Optimization for Comprehensive Cancer Diagnosis Using Gene Expression Data. J. Comput. Bio. 11 (2004) 27 242

Address of the corresponding author:

Author: Mohd Saberi Mohamad
Institute: Universiti Teknologi Malaysia
Street: 81310 UTM Skudai
City: Johor Bharu, Johor
Country: Malaysia
Email: saberi@fsksm.utm.my

F. Ibrahim, N.A. Abu Osman, J. Usman and N.A. Kadri (Eds.): Biomed 06, IFMBE Proceedings 15, pp. 528-532, 2007
www.springerlink.com ' Springer-Verlag Berlin Heidelberg 2007

RETRACTED CHAPTER: A High Efficiency Optical Power Transmitting System to a Rechargeable Lithium Battery for All Implantable Biomedical Devices

Naresh Kumar Pagidimarry, Vishrut Chowdary Konijeti

Department of Biomedical Engineering, J.B.Institute of Engineering & Technology, Hyderabad, India

Abstract— **A novel power supply for medical implants has been developed. Using wireless technology secondary battery of power supply for implanted devices is recharged using laser diode, which transmits power in near infrared region. Transmitted power is received by photo voltaic cell array embedded under skin and charges the secondary battery, which in turn charges primary battery providing power to the implanted device. Experiments carried out have shown that, a photo diode with surface area of 2.1 cm^2, emitting light in near infra red region at 810 nm wavelength with power density of 22 mW/cm, provides sufficient energy within 17 min to allow regular commercial cardiac pacemaker to work for 24 hrs. During continuous irradiation for 17 min on skin, temperature rise is only 1.4^{0}C which is acceptable. Thus this wireless technique can be implemented for the benefits of patient.**

Keywords— **Near Infrared, Coherent, Photo Diode Array, Power density, cardiac pacemaker.**

I. Introduction

The development of implanted medical devices relies strongly on the manner to supply them with electric power for continuous operation. Cardiac pace makers currently in use are powered with lithium primary batteries whose lifetime is in the range of 5-10 years. To date, the following two methods are used practically. One way is to equip power by radio frequency for the implanted device with a battery.

The other way is to supply electromagnetic power through skin, allowing implanted devices to be powered indefinitely. Another promising wireless power supply technique using near infra red light successfully transmitted through rat skin to photo voltaic cell powering cardiac pacemaker. It was also proposed enhancing the capability of the power supply by adding a power storage although its performance was not shown. Using light rather than RF waves, this technique has little chance of disturbing surrounding instruments that can be disturbed through electromagnetic induction; in fact, there are lot of such instruments in medical facilities. In addition, the use of near-infrared light makes this technique less invasive to tissues. In this paper, we report a modified version of the near-infrared power supply. While the previous one used a farad-order Capacitor, the present device features the use of the rechargeable lithium batteries for power storage applications. Unlike capacitors, lithium batteries provide stable output voltage during their lifetime because of their specific electrode potentials. Hence the present device does not have to be equipped with the voltage regulator, while the previous one had to. Among other rechargeable batteries, in addition rechargeable lithium batteries show excellent charge/discharge characteristics, eg., cycle life. Which can meet the requirement of operating medical implants for a long period. To our knowledge, this paper is the first to describe in detail the characteristics of a near-infrared power supply with a rechargeable battery. Experiments with a live rat have proved that the newly developed device is promising for practical use.

II. System Configuration and Components

Fig. 1 shows the schematic diagram of the power transmission system with the power supply. As shown in Fig. 1, near-infrared light from a laser diode is received and converted to electric power by a photodiode array embedded under skin. The current generated at the photodiode is supplied to a rechargeable battery and to an implanted device to which the battery is connected. The battery is charged in this way and powers the device when the photodiode array is not irradiated. The current to flow back from the battery to the photodiode array is prevented by inserting a diode between them. Fig. 2 is a photograph of the power supply.

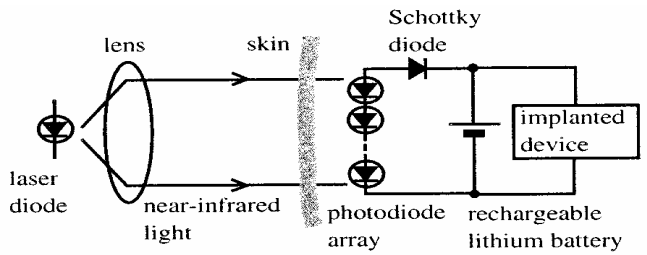

Fig.1. A schematic diagram of the near-infrared power supply system

The details of the system are as follows. The light source is a high power near-infrared laser diode (Coherent, S-81-

The original version of this chapter was revised: The plagiarized chapter was retracted. The erratum to this chapter is available at 10.1007/978-3-540-68017-8_177

F. Ibrahim, N.A. Abu Osman, J. Usman and N.A. Kadri (Eds.): Biomed 06, IFMBE Proceedings 15, pp. 533-537, 2007
www.springerlink.com ' Springer-Verlag Berlin Heidelberg 2007

1000C-100-H). The wavelength of the output beam is 810 nm. The beam is collimated with two cylindrical lenses to illuminate the photodiode array. The photodiode array consists of eight Silicon PIN photodiodes (S6775) connected in series to obtain enough voltage for the charge of battery. Among other commercially available photovoltaic cells this photodiode seems to be the best choice in terms of all over power conversion efficiency and device size. The detection area for each photodiode is 5.5-mm×4.8 mm. The Silicon chip is sealed in an epoxy package. The total size of the photodiode array, including the packages, is 28 mm×20mm×3mm. The sensitivity of the photodiode at a wavelength of 810 nm is 0.59 A/W. The series diode is a Schottky diode (Toshiba, 1SS392). Its reverse current at a reverse voltage of 3 V is of the order of 100 nA at 36^0C, a typical body temperature. The forward voltage drop for the diode is as small as 0.3 V at currents of a few mill amperes. The battery is composite dimensional manganese oxide (CDMO) lithium secondary battery (Sanyo, ML-2430, 100 mAh). The diameter and the thickness of the battery are 25.0 and 3.4 mm, respectively. The range of the output voltage, which is determined by the stored energy, is 2.0 3.1 V. This is in good agreement with the operation voltage of cardiac pacemaker. The operating temperature range of the battery is from -20^0C to $+60^0$C. The photodiode array and the battery are, at present, separated as shown in Fig. 2. It would be a good idea to contain all components in a hermetic package for their reliability. For long-term use, the package should be covered with biomaterials.

The stability of the battery voltage, an advantage of lithium batteries over capacitors, maximizes the efficiency of the power supply in the following ways. First, the present device does not require a voltage regulator. Applying a voltage regulator not only increases the device size but also gives rise to additional power consumption. Second, the photodiode array can keep the best power conversion efficiency during the battery charge because the battery regulates the voltage across the photodiode array. (The power conversion efficiency of the photodiode array changes with the voltage across it.) The improved power conversion efficiency leads to shorter charge time or reduced irradiation power, or both.

That of the rechargeable battery determines the long-term performance of the present device. Rechargeable lithium batteries show excellent charge/discharge performance. Recharging them before they are fully discharged, unlike that of rechargeable nickel cadmium or nickel metal hydride batteries do not degrade their capacity. In addition, the cycle life of rechargeable lithium batteries can be long enough to keep powering medical implants for a long period, determined by the battery capacity. In general, their cycle life is inversely proportional to the depth of discharge (the ratio of the amount of discharge to the battery capacity).

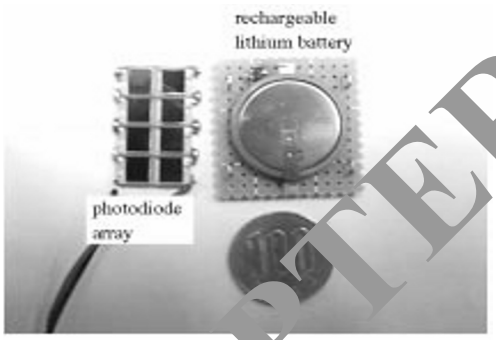

Fig.2. A photograph of the developed power supply, the photodiode array and the rechargeable lithium battery with the Schottky diode.

The maximal number of charge/discharge cycle is 8000 for 4% discharge of the battery we used. According to this, more than 60 000 times of charge/discharge cycle can be expected for 0.5% discharge, which corresponds to operation of a 20μA-consuming cardiac pacemaker for 24 h. This means that well over 100 years of continuous use of the pacemaker is possible if the battery is recharged once every day, while the lifetime of conventional pacemaker batteries (lithium primary batteries, 1 2 Ah) is within the 5 10 years range. Moreover, the battery charge does not have to be performed every day; once the battery is fully charged, it keeps its voltage above 2.4 V for about 6 months with no additional recharge, although more recharge is necessary afterwards.

III. Experiments

Before animal testing, it was examined the current voltage (I V) characteristic of the photodiode array. The photodiode array was irradiated with the laser beam mentioned above. The intensity of the laser beam was measured with another photodiode (the same type as that in the photodiode array). The uniformity of the power density was examined by scanning the beam cross section with the photodiode. The power conversion efficiency was determined from the I-V curve. Here, the power conversion efficiency is defined as the ratio of I-V, the power generated at the photodiode array, to the incident power.

Then the photodiode array was entirely embedded under a shaved abdominal skin of an anesthetized rat about 10 weeks old. (The photodiode array was covered in advance with a plastic film, whose transmittance at a wavelength of

F. Ibrahim, N.A. Abu Osman, J. Usman and N.A. Kadri (Eds.): Biomed 06, IFMBE Proceedings 15, pp. 533-537, 2007
www.springerlink.com ' Springer-Verlag Berlin Heidelberg 2007

810 nm was 92 %.) The thickness of the rat skin covering the photodiode array was 0.8 mm. In order to lead the output current to outside the body, two electric wires were connected to the photodiode array.

Before performing battery charge tests, the transmittance of the skin was measured. Measuring the Power incident on the photodiode array under the skin and then dividing the power by that measured without the skin determined the transmittance. The power incident on the photodiode array was determined by measuring its short-circuiting current, which is proportional to the incident power. For these measurements, a mask with a rectangular aperture was inserted to the beam path in order to define the beam size; with the rectangular aperture, the cross section of the beam on the skin was 30mm - 45mm, well covering the area of the photodiode array. The uniformity of the power density under the skin is unknown. Assuming that the transmittance of the skin is uniform, the power density under the skin can also be uniform despite the scattering in the skin, because the skin is thin enough compared to the beam size.

The battery charge tests were performed in the following way. First, the photodiode array, the Schottky diode, the battery, and a commercial cardiac pacemaker were connected as shown in Fig. 1. The last three were placed outside the rat for ease of testing. The pacemaker electrodes were connected to a resistor of 470Ω, a substitute for a heart. The repetition rate, pulse height, and pulse width were 65 pulses per minute, -5.0 V, and 0.4 ms, respectively. The nominal supply current for this pacemaker at an operating voltage of 2.8 V is 20 μA, a typical value for commercial pacemakers in normal settings. Irradiating the implanted photodiode array with the same optical setting as previously mentioned charged then the battery. The initial voltage of the battery was 2.74 V. The irradiation intensities were set to 11, 22, and 32 mW/cm^2. The irradiation time was 15 min for each measurement. The same battery was used throughout the experiments, although its initial voltage for each measurement changed due to successive charge. During the battery charge tests, the battery voltage and the current flowing from the photodiode array were monitored. The monitored current is almost equal to the current into the battery because it is much larger than the current into the pacemaker. In addition, the temperature of the skin was monitored with a radiation thermometer. The measured spot was about the center of the irradiated region, that is, about the center of the embedded photodiode array.

IV. Experimental results

Three I V curves obtained for the photodiode array before animal testing are shown in Fig. 3. The irradiation intensities were 5.4, 10, and 20mW/cm2. As for the uniformity of the intensity distribution, the difference between the maximum and minimum powers incident on photodiodes was less than 6% of the mean value. According to the I V curves, conversion efficiencies of 16% 21% can be obtained when the photodiode array voltage is 2.8 3.3 V, which corresponds to the battery voltage of 2.5 3.0 V for a Schottky diode voltage of 0.3 V. The maximum power conversion efficiency for 10mW/cm^2 is determined to be 20% at 3.1 V and 1.4 mA. For 5.4 and 20mW/cm^2, the maximum power conversion efficiencies are 16% and 21%, respectively. The room temperature was 29 °C during the I V measurements.

The transmittance of the rat skin was determined to be 64%. (Transmittance of the skin plus the plastic cover was 59 %.) This is a reasonable value for a transmittance of a rat skin. For this measurement and the battery charge tests, the difference between the maximum and the minimum power densities incident on the skin was about 10% of the mean value.

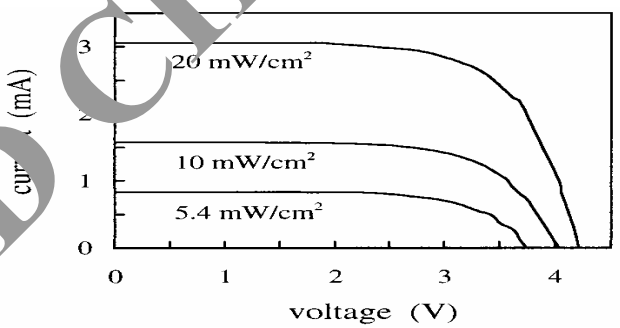

Fig.3. I V curves for the photodiode array for three different incident power densities

Embedded under the skin is assumed the same as that obtained in advance because of little difference in temperature. As shown in Table I, the power conversion efficiencies of the photodiode array were on the order of 20%. Fig. 4 shows the time-course of the battery voltage change and the skin temperature, which correspond to data in Table I. The charge current was almost constant during laser irradiation. The voltage increase during the battery charge resulted from the increase in the charge stored in the battery and from the increase in the charge stored in the battery and from its internal resistance, into which the current is injected; the latter leads to the sudden voltage

Table I Results of the Battery Charge Tests with a Live Rate for Three Different Incident Power Densities

F. Ibrahim, N.A. Abu Osman, J. Usman and N.A. Kadri (Eds.): Biomed 06, IFMBE Proceedings 15, pp. 533-537, 2007
www.springerlink.com ' Springer-Verlag Berlin Heidelberg 2007

	Power Density (mW/cm^2)		
	11	22	32
Charge Current (mA)	0.8	1.7	2.7
Initial Battery Voltage (V)	2.74	2.76	2.80
Schottky Diode Voltage (V)	0.26	0.28	0.30
Power Conversion Efficiency (%)	17	19	20
Battery Voltage Increase (V)	0.04	0.10	0.15
Temperature Rise (°C)	0.5	1.4	2.2

increase and decrease at the start and the end of the battery charge, respectively. The skin temperature seems to saturate within the period of battery charges as shown in Fig. 4(b), although, for higher power densities, it took longer time for the temperature to saturate.

V. Discussion

A. Performance of the Electronics

The time required for the battery charge to compensate the energy consumed by an implanted device is as follows. For a cardiac pacemaker consuming 20 μA, for example, the total amount of discharge for 24 h is 0.48 mAh.

This can be compensated by 17 min of charging at a charge current of 1.7mA, a value obtained in the experiment. Obviously, the charge period is inversely proportional to the charge current. The battery we use allows a charge current of up to 4.5 mA for an initial battery voltage of 2.8 V (Because of the internal resistance of the battery, excessive charge current results in excessive battery voltage, which can cause degradation of the battery.) For a charge current of 3.4 mA, for instance, the charge period will be 8.5 min. These are reasonable values for practical use of the instrument.

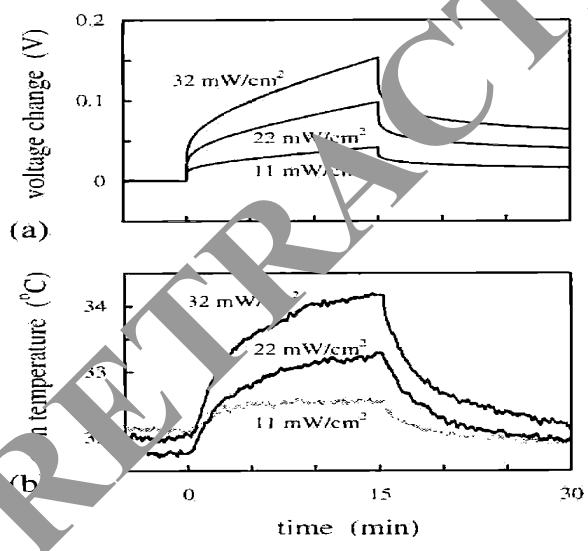

Fig 4. (a) Time-course of the battery voltage. (b) The temperature of the rat skin for three different incident power densities. The laser irradiation starts and ends at 0 and 15 min, respectively.

As shown in Table I and Fig. 4(a), the battery voltage change due to charge is sufficiently small, although it is influenced by the internal resistance of the battery. The voltage change due to the 0.48-mAh discharge is estimated to be a few tens of mill volts. These levels of battery voltage changes do not affect the operation of cardiac pacemakers. Actually, they are designed for the battery voltage which is subjected to change as the battery is discharged: the voltage of lithium primary batteries for pacemakers is 2.8 V initially and 2.0 2.2 V when the battery should be replaced.

Apart from whether the operation voltage of the cardiac pacemaker should be stable, overcharge of the battery and shortage of the stored energy should be avoided. These problems are likely to happen because the power led to the photodiode array and the power consumed by the pacemaker may vary from time to time. A good solution to them is to monitor the battery voltage from outside the body. The gradient of the voltage-discharge curve is large enough for monitoring the energy left in the battery. The monitoring can be readily performed because many pacemakers currently in use have telemetry capability. For this purpose, in addition, optical telemetry may be a good technique.

B. Limitations of Supplied Power

The current required for the battery charge determines how much power the photodiode array should receive. The power limit, determined by whether the irradiation causes any effects on the tissue, is discussed in the following.

The temperature rise at the irradiated region limits the incident power density. In our experiment, the skin temperature rise was of the order of 1^{0}C 2 ^{0}C, as shown in Table I and Fig. 4(b). A skin temperature rise of less than 2^{0}C is considered safe as for human skin, which is normally at 35.5 ^{0}C, protein desaturation does not occur at temperatures below 40^{0}C. The dominant cause of the skin temperature rise in our experiments turned out to be the photo thermal effect at the photodiode array. The heat due to light absorption by the photodiode array is much greater than that by the skin. Actually, at the same wavelength and power density, the temperature rise for the rat skin without a photodiode array was as small as 0.2 ^{0}C. (The temperature change was so small that it was not easily determined. The resolution of the radiation thermometer we used was 0.1^{0}C.) It follows from the 20% power conversion efficiency of the photodiode array that 80% of the incident power is converted to heat, assuming that the incident power is

F. Ibrahim, N.A. Abu Osman, J. Usman and N.A. Kadri (Eds.): Biomed 06, IFMBE Proceedings 15, pp. 533-537, 2007
www.springerlink.com ' Springer-Verlag Berlin Heidelberg 2007

almost entirely absorbed by the Si chips because of the anti-reflection films on them. As long as the heat generated at the photodiode array is dominant, it is likely that the power incident of the skin is limited by how much power is received by the photodiode array, but not by how much power is absorbed by the skin, which may be thick or thin.

Apart from the temperature rise at the skin, the incident power density limit can also be determined by how safe the photonic power itself is to tissues in the long run. Limits on power density of laser light, which is incident on a human, skin for longer than 10 s are 0.2, 0.5, and 1.0 W/cm^2 for wavelengths of 633, 910, and 1064 nm, respectively. The power densities of the laser beam in our experiments were much lower than these values. Repeated irradiation, however, needs long-term tests to be guaranteed safe in the long run. To some extent, the safety level can be predicted by comparing the power density of the laser beam with that of sunlight. The power density of the sunlight is about 100 and 30 mW/cm^2 on a clear and a cloudy day, respectively. The sunlight contains visible and ultraviolet rays, which are more harmful to tissue than near-infrared rays. However, exposure of skin to the sunlight for 10 20 minutes a day is not likely to cause any serious problem. Then near-infrared irradiation of the order of 20 mW/cm^2 for 10 20 minutes a day seems safer, although the penetration depth should be taken into account.

C. Application to Human Skin

The transmittance of human skin 2 mm thick 10% 20% in the near-infrared region. This is 3 6 times smaller than the transmittance of the rat skin used in our experiment. More irradiation power is accordingly required in order to obtain the same level of charge current. This can be realized by increasing the detection area of the photodiode array, rather than by increasing the incident power density. (In our experiment, the area of the photodiode array had to be small in order to embed it easily under the skin of a live rat.) A regular cardiac pacemaker of 5 cm × 4 cm ×0.7 cm, for example, would allow an area of 20 cm2 for a photodiode array. For a 10% transmittance, a photodiode array with a 10-cm^2 detection area can generate a charge current of 1.7 mA at 22mW/cm^2, a result obtained in our experiment. In addition, the 10-cm^2 photodiode area leads to a significantly reduced temperature rise, because the power density the photodiode receives is six times weaker.

Incidentally, the line width of the light source does not have to be as narrow as that of laser diodes, because the spectral bandwidth of both the skin transmittance and photodiode sensitivity are much broader. For practical use, near-infrared light-emitting diodes can be good alternative light sources. In addition, the sunlight and light from incandescent lamp can also be used, which are more common in daily life. As for the sunlight, a power of 100 mW/cm^2 is enough for the battery charge, although optical filters may be necessary in order to cut unwanted power that generates too much heat at the photodiode array.

VI. Conclusion

We have in our hands a new near-infrared power supply having a rechargeable lithium battery. The light detection area was 2.1 cm^2. For an incident power density of 22 mW/cm^2, 17 min of irradiation at an 810-nm wavelength is enough to send energy that allows a cardiac pacemaker consuming 1 μA to run for 24 h. The charge period is determined by the current the photodiode array generates. The temperature rise at the irradiated skin was 1.4^{0}C for this power density. The dominant cause of the temperature rise was the photo thermal effect at the photodiode array. The present instrument is promising for practical application for most of the implanted biomedical devices using power supply. For a human skin 2 mm thick, a photodiode array with a 10-cm^2 detection area will give the same charge performance as mentioned above with much less temperature rise.

References

[1] T. Mussiv, K. S. Holmes, A. Hum, and W. J. Keon, Transcutaneous energy transfer with voltage regulation for rotary blood pumps, *Artif. Organs*, vol. 20.
[2] Textbook of Medical Instrumentation Application & Design Concept by John.G.Webster, 3rd edition.
[3] K. Murakawa, M. Kobayashi, O. Nakamura, and S. Kawata, *"A wireless near-infrared energy system for medical implants," IEEE Eng. Med. Biol. Mag.*, vol. 18.
[4] Datasheets of ML2430, Sanyo, Osaka, Japan, 2005.
[5] Clinical datasheets of implantable pacemakers drawn from Indian Heart Journal , 2004.

Address of the corresponding author:

Author: Naresh Kumar Pagidimarry
Institute: Dept. of Biomedical Engineering,
J.B.Institute of Engineering & Technology
City: Hyderabad, Andhra Pradesh.
Country: India
Email: pagidimarry@rediffmail.com

F. Ibrahim, N.A. Abu Osman, J. Usman and N.A. Kadri (Eds.): Biomed 06, IFMBE Proceedings 15, pp. 533-537, 2007
www.springerlink.com ' Springer-Verlag Berlin Heidelberg 2007

A Portable Potentiostat for Electrochemical Sensors

Yung-Hoh Sheu[1], Chun-Yueh Huang[2]

[1]Department of Computer Science and Information Engineering, National Formosa University, Taiwan, 63208, Republic of China.
[2]Graduate Institute of Communication Engineering, National University of Tainan, Tainan, 700 Taiwan, Republic of China.

Abstract- **This paper proposes a portable and potentiostat and further exerts the potentiometric pH sensing to verify its performance. The proposed potentiostat can process the real-time measured electrochemical data can be saved temporarily to the compact flash memory card or USB disk, and then can be transferred to a PC server through USB interface. Our experimental results indicate that the proposed potentiostat has several advanced features, such as moderate accuracy, low cost, and long-term data storage capability.**

I. Introduction

Electrochemical biosensors used to detect potential or current signals have been widely utilized in many ways, such as DNA identification, protein classification, neural recording, glucose determination, pH variation detection, and drug determination of morphine. In clinical medicine, for instance, the use of electrochemical biosensors in the determination of morphine (MO) concentration of blood or urine is much more economical and convenient than high performance liquid chromatography (HPLC) or UV spectroscopy. The reason is because electrochemical sensors do not need expensive optical set-ups, such as CCD sensor and lenses, and can be realized in a portable potentiostat combining the electrochemical system with HPLC [1] or molecularly imprinted polymers (MIPs) [2]. A biosensor with higher selectivity and lower detection limit could be made.

Specifically, the potentiostat is an indispensable device in the electrochemical sensing system. Each electrochemical sensor demands a potentiostat to ensure the operational stability during sensing and to convert the sensor s output into an analog signal [3]. Additionally, many researchers devoted themselves to develop the single-chip potentiostat to reduce cost and the chip size in the past. For instance, Turner demonstrated a basic CMOS integrated potentiostat [4], Kakerow presented a monolithic potentiostat [5], Bandyopadhyay proposed a multi-channel potentiostat [6], and Frey reported an integrated potentiostat for biosensor chips [7]. In spite of their research on the integration of potentiostats and sensors, the further development of the remote signal transmission and data processing for the potentiostats was not been addressed.

This study aims to present a highly portable potentiostat for electrochemical sensor. This proposed potentiostat can be used to control and collect a large of acquired data in real-time owing to its low cost and high portability. The personal computer (PC) and wire communication devices can be eliminated while performing the electrochemical measurements. The measured electrochemical data could be saved temporarily to the USB disk, and then transferred to a PC server through USB interface. Moreover, the measurements not only can be performed outside the laboratory, but also in all kinds of environments.

II. Materials and methods

Essentially, the proposed potentiostat consists of an USB data collecting subsystem and electrochemical measuring subsystem. Figure 1 shows the block diagram of the proposed portable potentiostat. We adopt the circuit components off the shelf to design and implement a portable potentiostat system platform.

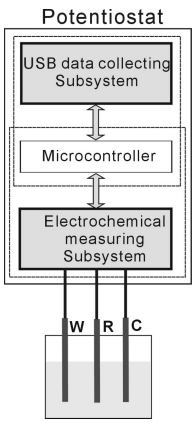

Fig.1 Block diagram of the combined portable and wireless data transmission potentiostat.

The microcontroller is used as the kernel component of the potentiostat among the two subsystems. The electrochemical measuring subsystem measures

F. Ibrahim, N.A. Abu Osman, J. Usman and N.A. Kadri (Eds.): Biomed 06, IFMBE Proceedings 15, pp. 538-542, 2007
www.springerlink.com ' Springer-Verlag Berlin Heidelberg 2007

electrochemical data, and then saves the data to the USB data collecting subsystem.

In the proposed potentiostat, the electrochemical measuring subsystem is integrated with following several features. First, the electrochemical signal is sampled at 100 Hz, and the results are transferred to the microcontroller. The acquired electrochemical data is firstly transferred to the USB disk in the USB data collecting subsystem. At 100 Hz, uncompressed electrochemical data for 24 h can be stored in a 1G Mbytes USB Disk. When the portable potentiostat connected to the host PC through USB interface, the host PC then detects it as a movable drive.

Hardware Design

As shown in the basic hardware block diagram of Fig.1, the following section presents brief descriptions of these subsystems.

A. Electrochemical measuring subsystem

Figure 2 shows the circuit diagram of an electrochemical measuring subsystem. This electrochemical measuring subsystem is compose of a microcontroller (EZ-USB FX2, CY7C68013, Cypress Semiconductor), a 12-bits D/A converter (DAC1208, National Semiconductor), two 12-bits A/D converters, ADC-1 and ADC-2 (AD574, Analog Device), a current to voltage converter, a voltage amplifier and a low-pass filter.

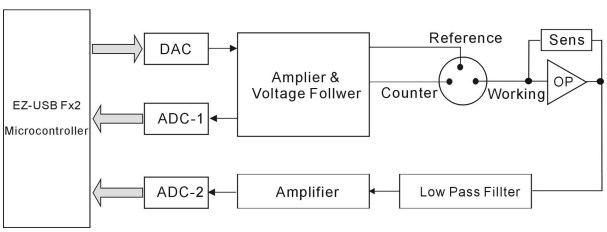

Fig.2 The circuit block diagram of the electrochemical measuring subsystem.

Basically, an electrochemical measuring subsystem is an electronic device that controls the voltage difference between a working electrode and a reference electrode. The two electrodes are basic components of an electrochemical sensor. An electrochemical measuring subsystem injects currents into the sensor via a counter electrode, which involved two processes. The subsystem first measures the potential difference between a working electrode and a reference electrode without polarizing the reference electrode, and compares the potential difference with a preset voltage (V_{WR}). Second, it injects current flowing from a counter electrode to a working electrode in order to counteract the difference between the preset voltage and the existing working electrode potential. The output of the electrochemical measuring subsystem after these two tasks completed is the current flowing from a counter electrode to a working electrode.

The controlled variable in the electrochemical measuring subsystem is the sensor s preset voltage, which is used to measure the signals in an amperometric sensor. However, the potential difference between a working electrode and a reference electrode is measured if the signals are derived from a potentiometric sensor.

The specifications of an electrochemical measuring subsystem are designed as follows: the programmable counter voltage ranges between 0 V and 5 V under the resolution 1 mV, the measured reference voltage ranges between 0 V and 5 V under the resolution 1 mV, and the measured current ranges between 1 μA and 1 mA.

In the electrochemical measuring subsystem, the control component is realized by a microcontroller, an ADC-1, and a DAC. The microcontroller is used for signal generation, data acquisition, and experimental management. The ADC-1 is used to measure the voltage differences between a reference electrode and a working electrode for re-examining whether the reference electrode reaches the preset voltage (V_{WR}) or not.

In order to avoid the loading effect caused by ADC-1 in the reference electrode, as judged by the difference between the reference electrode and ADC-1, an operational amplifier must be connected to implement a voltage follower. According to the output of ADC-1, the microprocessor will generate the corresponding control signal to DAC. In that case, DAC will produce a bias voltage to control the injecting current into the counter electrode. This feedback control procedure will continue until the voltage measured by the reference electrode is approximate to the preset voltage (V_{WR}).

In this feedback control procedure, a current-to-voltage converter is used to measure the sensing current. The sensing current is the current that flows between a counter electrode and a working electrode through a current measuring resistor. The voltage dropping across the resistor represents a corresponding current from the sensor.

Subsequently, we need an inverter amplifier to optimize the output voltage levels of the current-to-voltage converter with respect to the maximum resolution of ADC. Finally, the output voltage of the inverter amplifier, which is proportional to the electrochemical sensing current, will be

F. Ibrahim, N.A. Abu Osman, J. Usman and N.A. Kadri (Eds.): Biomed 06, IFMBE Proceedings 15, pp. 538-542, 2007
www.springerlink.com ' Springer-Verlag Berlin Heidelberg 2007

digitalized by ADC-2. The low pass filter is consists of one 10K resistor and one 10uF capacitor to reduce under 60Hz noise. The cutoff frequency is equal to $1/2\pi RC$.

B. USB data collecting subsystem

As shown in the block diagram of figure 3, the portable USB data collecting subsystem consists of a microcontroller, a USB host controller, a battery, and a power manager chip. The proposed portable potentiostat is designed as memory-mapping peripheral circuit. All components (ADC-1, ADC-2, DAC and USB host controller) are easily connected and controlled by data bus, address bus and control signals (#RD and #WR).

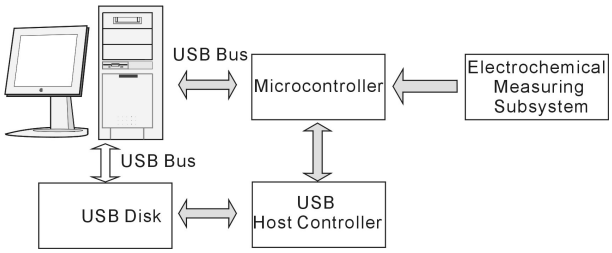

Fig.3 Block diagram of USB data collecting subsystem

A standard 1 G Mbytes USB disk provides a full 24 h of data-collecting capacity. A USB interface allows the USB data collecting subsystem device to be treated as a movable drive with Windows FAT16 file system and easily accessed via standard PC. Meanwhile, the USB disk can be unplugged and then directly plugged to PC USB port.

Accordingly, USB 2.0 technology is adopted as a communication interface because of rapid data transfer and the ability to supply power for recharging the battery in the USB data collecting subsystem.

Besides, the USB host controller (SL811HS, Cypress) is a full-featured USB embedded host controller. USB bus control is achieved by means of USB host controller, when the USB disk is plugged into the USB data collecting subsystem.

C. Fabrication of a sensor

In the present experimental setups was considered, a three-electrode electrochemical system to perform morphine sensing. A Pt electrode (0.0314 cm^2, CH Instruments) is used as the working electrode, a Pt plate (1 x 4 cm^2) as the counter electrode, and an Ag/AgCl/Sat d KCl electrode as the reference electrode [8]. The potential experiments are operated between 0 V to 0.75 V with an appropriate step potential incensement. This is done in a blank (background) electrolyte solution (0.1 M NaCl and 0.1 M NaI) and a morphine-containing solution. After each experiment procedure, the working electrode surface is washed with alcohol, polished with 0.05 μm α-alumina slurry on a micro cloth polishing pad, and wash with water and solicited for a few minutes in doubly distilled (DI) water. The net current at each operating potential is used to decide the sensing potential. After all experiments, the suitable sensing potential can be set by 0.65 V for operating potential. The sampling time is chosen as 150 sec in each experiment.

In addition, the preparation and sensing process of the pH sensor had developed and applied in the telemetric application [8]. The potentiometric pH sensing was developed relatively to verify the whole performance of the portable potentiostat.

Software Design

The components of the software for our system are composed of USB data collecting program and electrochemical signal measuring firmware.

USB data collecting program: there are two software programs written in the USB data collecting program. One was USB device microcontroller firmware, and the other was PC device driver.

The EZ-USB FX2 microcontroller used in the USB data collecting program is supplied with a template firmware program called Frame-Works (Cypress Semiconductors), which the user modifies to suit his local needs for handling USB enumeration and commands such as chip initialization, USB standard device request handling, and USB suspend power management services. In the firmware program, the 100 Hz timer interrupt requested the device to transfer A/D electrochemical values to the compact flash memory card for storages.

For the PC device driver, the EZ-USB general purpose driver (GPD) is adopted. The GPD is a general purpose device driver suitable for interfacing standard PCs with an EZ-USB-based peripheral, providing a user mode interface for common USB device requests and data transfer.

Electrochemical signal measuring firmware: the electrochemical signal is measured and acquired by the electrochemical measuring subsystem. The electrochemical signal variation of pH sensor is a voltage component.

The V_{WC} voltage value will be measured from ADC-2 and saved to the USB disk. Additionally, the V_{WC} voltage value will be transferred into ASCII codes in parallel for the further processing.

F. Ibrahim, N.A. Abu Osman, J. Usman and N.A. Kadri (Eds.): Biomed 06, IFMBE Proceedings 15, pp. 538-542, 2007
www.springerlink.com ' Springer-Verlag Berlin Heidelberg 2007

III. Results

System testing methods

One 80 MHz function/arbitrary waveform generator (Agilent, 33250A) is adopted and connected to USB data collecting subsystem. Another oscilloscope (Tektronix TD3012B) is connected in parallel with the function generator to monitor the waveform.

In addition, dual output DC power supply (Agilent, E364xA) is applied to test an electrochemical measuring subsystem. The digital DC power supply can output fixed voltage and current. Therefore, the DAC, ADC-1 and ADC-2 components can be tested and confirmed their function. These testing values are measured by a electrochemical measuring subsystem can be saved to USB disk by means of the USB data collecting subsystem.

Actual electrochemical experiment results

In order to verify the functions of the proposed portable potentiostat, we compare our experimental results with the commercial potentiostat s (Potentiostat/Gavanostat, EG&G Instruments 263A USA). First of all, a pH potentiometric sensor is used in the experimental setups. The potential between a working electrode and a reference electrode varies with the pH concentration of the solution.

In order to measure the potential of the pH sensor, we have to connect the proposed portable potentiostat with the commercial potentiostat in parallel. The output data of the proposed portable potentiostat is saved to the USB disk by means of USB data collecting subsystem.

When performing actual electrochemical experiments, the reference and the working electrodes are immersed in the standard test solution which comprised of 0.1 M HNO3, 0.001 M CH3COOH, 0.01 M H3BO3 and 0.01 M H3PO3 to enable determination to be made. The pH of the solution is changed to desired values by adding 1 M KOH or 1 M HNO3. In the meantime, a pH/mV/°C meter (CyberScan pH/Ion 510, Eutech Instruments Pte Ltd., Singapore) is employed to determine the test solution of PH.

Figure 4 shows a comparison diagram of the measured results of the proposed portable potentiostat and the commercial potentiostat. While the potential decreases along with the addition of KOH, pH value increasing from 2.05 to 10.01. From this diagram, we can observe that the results measured by the proposed portable potentiostat are almost the same as those measured by the commercial potentiostat. However, the price of proposed portable potentiostat is much cost effective than the commercial potentiostat.

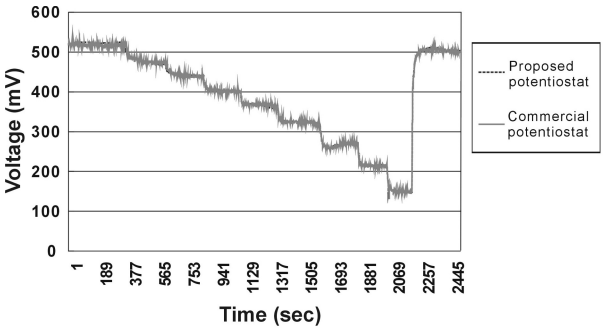

Fig.4 The pH value measurement results of the proposed potentiostat and the commercial potentiostat

IV. Discussion

The testing results of the system and actual electrochemical trials show that the portable potentiostat meets the commercial potentiostat requirement for measuring, recording, and analyzing electrochemical signal, even offering more functions. This paper proposes a high portable, long-term potentiostat and successfully demonstrates its performance by incorporating a pH sensor.

Unlike the commercial potentiostat which lacks the function of portable capability, the proposed portable potentiostat is especially suitable for processing the long-term electrochemical signal from the potentiometric sensor.

This current system tests on the potentiometric PH sensor to verify its feasibility, and will continually test on amperometric morphine sensor in the near future.

We certainly do not need heavy computers for the measurements of the electrochemical sensing. In short, the proposed portable potentiostat has the merits of moderate accuracy, low cost and high portability. In the future, we will apply this technology to a real-time and remote sensing in a home-care environment for monitoring a patient s pH levels.

Acknowledgments

This work was supported by the MOE Program for Promoting Academic Excellence of Universities, under Grant EX-93-E-FA09-5-4, and coresearched with the Department of Chemical at National Cheng Kung University.

F. Ibrahim, N.A. Abu Osman, J. Usman and N.A. Kadri (Eds.): Biomed 06, IFMBE Proceedings 15, pp. 538-542, 2007
www.springerlink.com ' Springer-Verlag Berlin Heidelberg 2007

REFERENCES

[1] Liaw W. J., Ho S. T., Wang J. J., Hu O. Y. P., Li J. H. (1998): Determination of morphine by high-performance liquid chromatography with electrochemical detection: application to human and rabbit pharmacokinetic studies, , J. Chromatogr. B, 714, pp.237

[2] Kriz D., Mosbac K. (1995): Competitive amperometric morphine sensor based on an agarose immobilized molecularly imprinted polymer, ,Anal. Chim. Acta., 300, pp.71

[3] Kissinger P. T. and Heineman W.R. (1996): Laboratory Techniques in Electroanalytical Chemistry, 2nd. Ed., Marcel-Dekker, N.Y

[4] Turner R. B. F., Harrison D. J., and Baltes H. P. (1987): A CMOS Potentiostat for amperometric chemical sensors, IEEE J. Solid-State Circuits, 22, pp.473-478

[5] Kakerow R. G., Kappert H., Spiegel E., and Manoli Y. (1995): Low power single chip CMOS potentiostat, Transducers 95, Eurosensors IX, 1, pp.142-145

[6] Bandyopadhyay, Mulliken G., Cauwenberghs G., Thakor N. (2002): VLSI potentiostat array for distributed electrochemical neural recording, Proc. of Int. IEEE Int. Symp. on Circuits and Systems, ISCAS, 2 , pp.740-743

[7] Frey, Jenkner M. et al (2003): Design of an integrated potentiostat circuit for CMOS bio sensor chips, Proc. of IEEE Int. Symp. on Circuits and Systems, ISCAS, 5, pp.9-12

[8] Liao W. Y., Lee Y. G., Huang C. Y., Lin H. Y., Weng Y. C. and Chou T. C. (2004): Telemetric electrochemical sensor, *Biosensors and Bioelectronics*, 20, pp.482-490

Author: Yung Hoh Sheu
Institute: Department of Computer Science and Information Engineering, National Formosa University
City: Taiwan
Country: Republic of China

F. Ibrahim, N.A. Abu Osman, J. Usman and N.A. Kadri (Eds.): Biomed 06, IFMBE Proceedings 15, pp. 538-542, 2007
www.springerlink.com ' Springer-Verlag Berlin Heidelberg 2007

A Preliminary Case Study of Anal Retractor Usability in Anorectal Surgery

R. Saiful Hasley[1] and N.A Abu Osman[2]

[1]Department of Industrial Design, Faculty of Design and Architecture, Universiti Putra Malaysia, 43400 UPM Serdang, Selangor Darul Ehsan, Malaysia.
[2]Department of Biomedical Engineering, Faculty of Engineering, University of Malaya, 50603, Kuala Lumpur, Malaysia

Abstract— **Surgery procedure today often relies on complete technical equipment. This will increase the important of usability as a selection criterion when hospitals purchase new equipment. In anorectal surgery, anal retractor are so important in ensure better visual field for operation, saving time and labour, with safety and reliability. Current retractors are working well but to a certain extend, it does not really offer certain ability that surgeon required. Surgery assistant especially facing a problem making a rotating movement on current retractors. With this point, an involvement of Industrial Design in the design and development process or concurrent engineering is a must.**

Keywords— **Industrial Design, concurrent engineering, anal retractor, hemorrhoidoctemy, usability.**

I. Introduction

A. Background

Anorectal surgery requires surgeons to perform good operative procedure using a standardize set of tools. The surgeons perform the operation with surgical tools and one of the important instrument is anal retractor. The anal retractor will be inserted to open anal canal at lease 35mm or more. High quality stainless steel and some by medical graded polymers normally make anal retractors. Most of these retractors have been given names after a person such as Ferguson, Parks, Sawyer and lots more. Different name are also refer to their different types and functions. Anorectal diseases such as hemorrhoids, fissure-in-ano and fistula-in-ano that require operation as the treatment, anal retractor is important to ensure successful procedures. This diseases especially hemorrhoid ia a common health problem in Malaysia. There is believed that 1 of 3 person had suffered a bleeding piles in their life time (B. Harian 2005).These diseases mostly effect and appear at the area of anus and it canal. Retractor/proctoscop is the appropriate instrument to use to retract anal canal and give a surgeon the right space to do operation. Current retractors are working well but to a certain extend, it does not really offer certain ability to ensure a good, time consuming operation. Through a preliminary interview, medical staff often have a feeling of helpessness and frustration when handling some instument. This will effect the work environment of the staff. Effectiveness and safety of medical instument depends on factors such as user compitence, safe use and appropriate application (E. Liljegren 2006). This is where the lack of total design process happened.

There is increasing understanding that human factors knowledge has a lot to offer in medical instument. Designers in other fields, e.g software design and consumer product, have been aware that their products need to be designed so that users can use the products with high usability (E. Liljegren 2005). In other word, the design process and concurrent engineering in medical equipment especially anal retractor in this research is definatly so important. In Sweden there is an increasing interest for usability evaluation of medical device, and some hospitals have started to include usability evaluation when they purchase new equipment (E. Liljegren 2005). The defininations of usability means by the ease of use of a product or service and usually refers to the detailed logic, flow and ergonomics of user interactions with the product or service. Usability yet is not the only consideration to make a good product in concurrent engineering design process. A key to the new approach is the now well-recognized importance of communication between engineering, marketing, and service functions, so too must be avenues of interaction between engineering subdisciplines- for example, design for manufacture, design recyclability, and design for safety.

Referring to a list from the book Birkhäuser Design Profile 2006/2007 , there is several design firms involved in designing medical equipment. First, we have Held + Team, a specialist in medical equipment product development base in Hamburg, Denmark. Their developed product was OES Pro 2 Resectoscop- a surgical instrument for radipathological enlarge prostate gland, sealmode forceps and needle holder for endoscopic operation.

Second, a firm called Beger Design. They have developed range of products including medical instrument. Base in Denmark, they have develop an endoscopes and new generation of emergency trolley. Here I believe that industrial design have a significant role in developing such medical equipment. A touch of industrial designer perhaps will refine the usability of medical equipment, which refers to this product research, anal retractor.

F. Ibrahim, N.A. Abu Osman, J. Usman and N.A. Kadri (Eds.): Biomed 06, IFMBE Proceedings 15, pp. 543-545, 2007
www.springerlink.com ' Springer-Verlag Berlin Heidelberg 2007

a

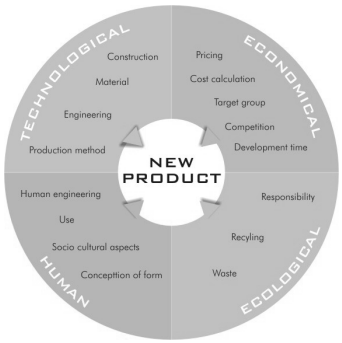

b

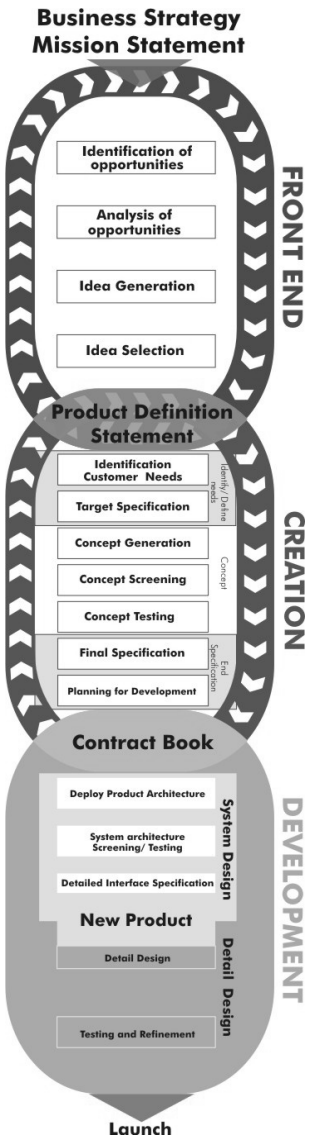

Fig 1 (a). Chart showing there is 4 main field of information should be considered in designing a product. (b) Chart showing various steps involved in designing and manufacturing a product. Depending on the complexity of the product and the type of material used.

II. The Product

A. Problem Statement

Surgeons and their assistant are still facing a problem on adjusting the retractor opening especially during procedure. Current design of anal retractors has a limited usage and suitability for every anorectal surgery. For example, when using specimen A (see picture below), assistant would have a problem in adjusting/ rotating retractor due to limited space between surgeon, patient and assistant them self. The assistant have to hold both of the wing in to prevent retractor from sliding out. Other retractor such as Ferguson Anal Retractor and Parks Anal Retractor are only suitable for static retraction. The Ferguson anal retractor have a long handle yet does not have the ability to rotate 360°. (rotating **an anal retractor is important due to nature of anal canal and operation procedure**.)

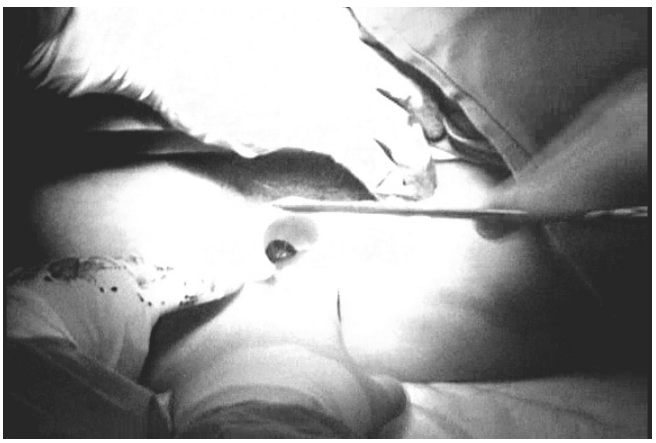

Picture 1. Surgery Assistant struggled holding the retractor. Rotating the retractor is impossible due to the limited space and assistant position. (Shown retractor is part of hemorrhiodectomy stapler set). A Video ethnography by the author on a procedure held at Kuala Lumpur Hospital.

What do the surgeons aspect from an anal retractor?

- Able to retract an anal canal wider than 35mm.
- Retractor should be able to rotate 360° manually or automatically.
- Retractor should have an opening for surgeons proceed with a procedure.
- Retractor should cover >35mm + dept of anal canal and rectum.

F. Ibrahim, N.A. Abu Osman, J. Usman and N.A. Kadri (Eds.): Biomed 06, IFMBE Proceedings 15, pp. 543-545, 2007
www.springerlink.com ' Springer-Verlag Berlin Heidelberg 2007

- LED light is an advantage for better vision. (most of current retractor have this specification.)
- Long handle for appropriate holding during procedure.
- Biocompatible material should be use for the retractor. Preferable material is medical grade stainless steel.

B. Objective

Using the preliminary finding from the previous research method in design, engineering and user centered design (video ethnography, observation), along with the result of other studies (A.E. Trejo et al., 2006, E. Liljegren, 2006, E.Liljegren et al., 2006) a proposal of new design of anal retractor was raised. The design specification will follow surgeons requirement and design wise. For initial design statement, the anal retractor should have ability to moving in a 360° circular motion in order to have a clear vision on anal canal circumferentially. Surgeons also should have clear and comfortable space to do operation and also to avoid surgery assistant to get CDT (Cumulative Trauma Disorder) problem associated with their arm. Consideration also will be take on the retractor system where should be it manually operated or automated. This will be decided after all complete study been made.

III. Conclusions

Total design process or concurrent engineering is an increasingly important aspect when medical instrument is designed. There is a significant role of industrial design in it.

The result of this preliminary study shows that how much a total design could offer to ensure a good user centered design. Anal Retractor is a good product to start with due to surgeon needs in anorectal surgery. The author hope this paper will be an open mind for designers, medical practitioners, biomedical engineers and others the importance of collaboration and communication within disciplines.

Acknowledgment

A special thanks to Dept. of Surgery, Faculty of Medicine and Health Science, Universiti Putra Malaysia (HKL Branch) for the surgery session observation and cooperation.

References

1. A.E. Trejo, K.N. Done, A.A Dimartino, D. Oleynikov, M.S. Hallbeck, 2006. Articulating vs. conventional laparoscopic grasping tool-surgeons opinion. International Journal of Industrial Ergonomics. 36 (2006) 25-35
2. Alison Black. User Centered Design. Techniques and Processes. Design Council. Website: http//designcouncil.org.uk.
3. Erik Liljegren. 2006. Usability in medical technology context assessment of method for suability evaluation of medical equipment. International Journal of Industrial Ergonomics. 36 (2006) 345-352
4. Erik Liljegren, Anna-Lisa Osvalder. 2006. Cognitive engineering methods as usability evaluation tools for medical equipment. International Journal of Industrial Ergonomic. 34 (2004) 49-62
5. Serope Kalpakjian, Steven R. Schmid, The Design Process and Concurrent engineering 2001. Manufacturing Engineering and Technology, Forth Edition.
6. Video ethnography and preliminary ethnography research at Dept. of Surgery, Faculty of Medicine and Health Science, UPM, Kuala Lumpur Hospital Branch.

Address of the corresponding author:

Author:	Saiful Hasley bin Ramli
Institute:	Dept. of Industrial Design , Faculty of Design and Architecture, Universiti Putra Malaysia
City:	40433 Serdang, Selangor Darul Ehsan
Country:	Malaysia
Email:	saifulhasley@ yahoo.com, shr@putra.upm.edu.my

F. Ibrahim, N.A. Abu Osman, J. Usman and N.A. Kadri (Eds.): Biomed 06, IFMBE Proceedings 15, pp. 543-545, 2007
www.springerlink.com ' Springer-Verlag Berlin Heidelberg 2007

Taxonomy of surrogate users for the development and evaluation of medical devices from the end users' perspective

S.G.S. Shah and I. Robinson

Centre for the Study of Health and Illness, School of Social Sciences and Law,
Brunel University, Uxbridge, Middlesex, UB8 3PH, United Kingdom

Abstract— **The development and evaluation of medical devices from users' perspectives requires the involvement of actual end users of medical devices. This kind of involvement of end users may not be always possible. A solution to this may be employing surrogates of end users. Nevertheless, this requires the identification and classification of appropriate surrogates. The study undertaken below reviewed relevant literature and suggests a taxonomy of surrogates of end users of medical devices. The taxonomy will be helpful in planning and making decisions in relation to the involvement of such surrogate users in developing and evaluating medical devices from the users' perspectives.**

Keywords— **Medical device, user, surrogate, taxonomy, user perspective.**

I. Introduction

Medical device development and evaluation (MDD&E) from users perspectives requires the involvement of actual end users of medical devices. This is important for understanding the needs and requirements of end users as well as the identification of problems related to medical devices [1]. In addition, the prevention of some of these problems, and finding solutions to others, as well as ensuring safety in the application of medical devices, are critical issues [2]. The evidence has shown that users involvement has resulted in the successful development of medical devices [3,4]. End users have therefore been involved in the development and evaluation of a variety of medical devices [5].

By the user of a medical device in this study the authors mean a professional and/or lay person that uses a medical device for or on behalf of the end-user [6]. The end user of a medical device in this study is the person who is the ultimate beneficiary of the usage of a medical device. In addition, can also be the user of the device if deploying the device for her/himself [7].

In MDD&E, the participation of end users, in particular persons with disabilities, the elderly [8] and some types of clinicians [9,10] may not be always possible. Therefore, MDD&E from users perspectives may be problematic in so far as there may be the absence of the viewpoint of end users. A possible solution to this problem can be the engagement of surrogate users instead of end users.

The aim of this study was therefore to suggest a theoretical classification of surrogates of medical device end users, which could be involved in MDD&E. The objectives were to review the published literature and to identify and classify surrogates of end users.

II. Methods

The methods included a structured review of literature published in peer reviewed journals and conference proceedings. This process was followed by the development of a novel conceptual classification model of surrogates of end users of medical devices. The literature review process was adapted from Beverley et al. [11] and Bruce and Mollison [12], which included the following:

A. Selection of bibliographic databases

The following online bibliographic databases were selected for the literature searches: ACM Digital Library; Applied Social Science Index & Abstracts; Blackwell Synergy; Cambridge Journals Online; Compendex / INSPEC; Ebscohost; Emerald; International Bibliography of the Social Sciences; IEEE/IEE Electronic Library; Ingenta; Medline; PubMed Central; ScienceDirect; SpringerLink and Web of Knowledge.

B. List of keywords

For the literature searches, a list of keywords and phrases was compiled that included key terms such as healthcare technology; medical device; proxy user; surrogate classification; user; surrogate; user classification; surrogate user.

C. Inclusion and exclusion criteria

The inclusion criteria for the selection of articles were studies about the involvement of surrogates of medical device users in MDD&E that were published in the English language from 1995 to 2005, but in any country. The exclusion criteria included studies which were not explicitly focused on medical device end users and surrogate users

F. Ibrahim, N.A. Abu Osman, J. Usman and N.A. Kadri (Eds.): Biomed 06, IFMBE Proceedings 15, pp. 546-549, 2007
www.springerlink.com ' Springer-Verlag Berlin Heidelberg 2007

within the context of MDD&E, but nonetheless referred to these issues.

D. Literature searches and record

A template was developed in-house for searching the literature, recording search hits and short-listing of articles. Literature was searched from June to September 2005. The search resulted in a large number of hits (n=26507), which were reduced by searching in addition for combinations of other relevant key words. The number of relevant articles was further consolidated by eliminating duplicate titles, abstracts and articles. This led to the identification of fifty-seven articles, which were short-listed for detailed assessment. Then a bibliographic database of articles obtained through this process was entered in a reference management software package [EndNote version 7.0.0] for quick and accurate referencing purposes.

III. Results and discussion

The literature review found the main exemplars of surrogates of different groups of medical device users which are given in table 1.

Table 1 Exemplars of surrogates of end users of medical devices

End user(s)	Surrogate user(s)	Reference(s)
Elderly people	Family members, friends and healthcare professionals (e.g. physicians)	[13,14]
Patients	Family members i.e. spouse, partner, child, parent, brother and sister as well as relatives and friends	[15-17]
	Clinicians i.e. general practitioners, nurses, physicians and surgeons, and carers	[18]
Persons with different disabilities	Physicians, nurses and therapists	[19]
Clinicians	Clinical colleagues working in the same specialty, preferably in the same healthcare facility	[9,10,20]

According to High and Turner [13], elderly people preferred family members to be their surrogates and Meeker [15] reported that the family members could also be important surrogates for terminally ill patients. High [14] suggested that healthcare professionals e.g. physicians, and friends could be chosen as surrogates of the elderly persons where there are no family members or relatives. Coppolino and Ackerson [16], suggested that the surrogates of a patient might be a spouse, partner, child, parent, brother, sister, relative or friend. This review found that in certain cases spouses were reported to be better surrogates than non-spouse surrogates [21]. Keywood [22] was of the opinion that for the persons who lacked the mental capacity to decide for themselves, carers were better surrogates than family members.

Chiu et al. [23] involved nurses and a community based technologist to carry out the usability assessment of the user interface of cardiac pacemaker programmers. Therefore, one might infer from this study that nurses and the technologist who had had experience of using the same medical device technology could act as surrogates of the end users of that technology. This review also revealed that asthma patients, general practitioners, nurses and carers were involved in the development and assessment of other devices such as an inhaler [18]. Therefore, clinicians and carers from the example above can be used as surrogates for the end users of particular medical devices.

IV. Taxonomy of surrgates of end users of medical devices

The literature review revealed that there was no existing published classification of surrogates of users of medical devices. The authors therefore suggest the following taxonomy of surrogates of end users of medical devices. The taxonomy is illustrated in figure 1.

According to this proposed taxonomy, actual users of medical devices can be divided into five groups i.e. clinicians , carers , patients , persons with special needs e.g. elderly and persons with disabilities and impairments . Clinicians and carers can be further divided in to sub-groups i.e. clinicians can be divided into surgeons, physicians, general physicians, nurses and health allied professionals; and carers can be divided into professional (formal) carers e.g. nurses, and non-professional (informal) carers e.g. family members, relatives, friends, and volunteers. A detailed classification of (actual) users of medical device technologies by the authors has already been reported elsewhere [7].

Using the definitions given earlier, patients, persons with disabilities and persons with special needs are classified as end users and the remaining categories of people are classified as users of medical devices.

The authors suggest that users i.e. clinicians and carers can act as surrogates of medical device end users for the development and evaluation of medical devices. However, there are some conditions to be able to act in a formal and appropriate way as surrogates of end users. First, surrogates should have existing clinical knowledge and substantial experience of dealing with the respective end users. Second, surrogates should have a firm understanding of the working

F. Ibrahim, N.A. Abu Osman, J. Usman and N.A. Kadri (Eds.): Biomed 06, IFMBE Proceedings 15, pp. 546-549, 2007
www.springerlink.com ' Springer-Verlag Berlin Heidelberg 2007

environment, activities and requirements of the end user(s) being represented. Based on these criteria, clinicians *could* be the most appropriate surrogates of patients because they represent patients needs based on their clinical judgment and experiences of dealing in the past, possibly with many such patients [24]. Similarly, for the same reasons clinicians *can* also be surrogates of persons with disabilities and those having special needs.

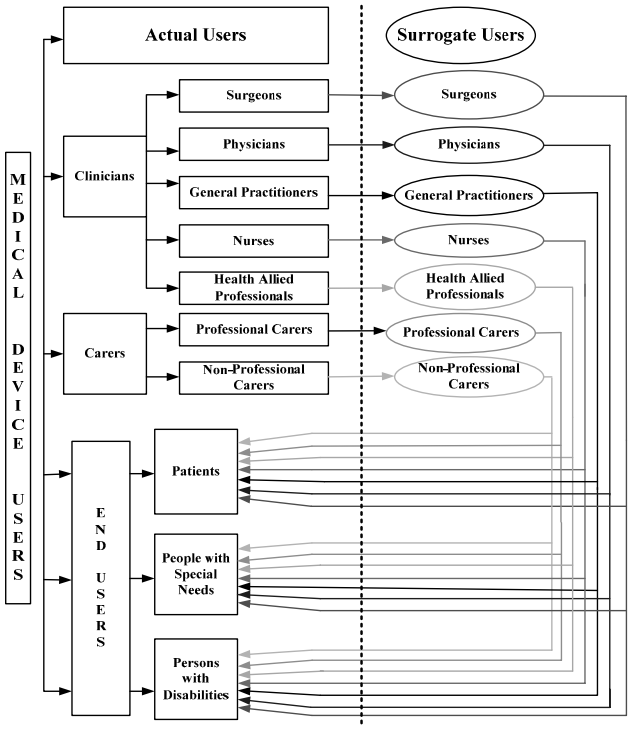

Fig. 1 Taxonomy of surrogates of end users of medical devices

In addition, selection of a surrogate will also depend on the nature of the end user and the medical device being developed and evaluated. For example, the development and evaluation of an assistive device will require the involvement of clinician(s) as well as carer(s) and the latter may include both professional and/or non-professional carers depending on the type of the end user and the medical device. Clinicians will be required for their clinical judgment and the carers required due to their knowledge about the needs, activities and surroundings of the person having special needs, disability and/or impairment. However, Coppolino and Ackerson [16] found differences between patients wishes and the decisions of their surrogates , who were informal carers, regarding patients participation in clinical trials, where there was a degree of risk involved and they found that patients would not have participated had they been able to decide for themselves. This point therefore may suggest that involvement of informal carers as surrogates may not be appropriate from the end users perspectives; hence a decision about their involvement in medical device development and evaluation may require careful consideration.

In the case of the development of a complex medical device such as a neuromagnetometer [25] and a interventricular blood pump [26], the involvement of clinicians will be required because the end-user of the device and his/her carers might know nothing about the properties of the device.

Clinicians and carers can therefore be involved as surrogate users in the development and evaluation of medical device from the end users perspective. Nevertheless, the final assessment of the device should be done by actual end users, wherever possible [27].

V. Conclusion

The development and evaluation of medical devices from users perspectives requires the incorporation of end users needs, which also requires the involvement of medical device users. Nevertheless, engagement of some types of medical device users, particularly end users may not always be possible. A solution to this problem can be the involvement of surrogates. This process however requires the identification of their appropriate surrogates. In this regard, the taxonomy of surrogates of end users of medical devices set out above may be helpful.

Acknowledgment

The authors acknowledge support of this work through the MATCH (Multidisciplinary Assessment of Technology Centre for Healthcare) Program, which is sponsored by the Engineering and Physical Sciences Research Council (EPSRC) (Grant No. GR/S29874/01), although the views expressed are entirely those of the authors.

F. Ibrahim, N.A. Abu Osman, J. Usman and N.A. Kadri (Eds.): Biomed 06, IFMBE Proceedings 15, pp. 546-549, 2007
www.springerlink.com ' Springer-Verlag Berlin Heidelberg 2007

REFERENCES

1. Tsai W-T, Mojdehbakhsh R, Rayadurgam S. (1997) Experience in capturing requirements for safety-critical medical devices in an industrial environment. In: Proceedings of second IEEE High-Assurance Systems Engineering Workshop, 11-12 Aug 1997. Washington, DC.: pp 32-36.
2. Kaye RD. (2000) Human factors (HF) in medical device use safety: how to meet the new challenges. In: Proceedings of the XIVth Triennial Congress of the International Ergonomics Association and 44th Annual Meeting of the Human Factors and Ergonomics Association, 'Ergonomics for the New Millennium', July 29-August 4, 2000. San Diego, CA, United State. pp 550-552.
3. Shaw B. (1985) The role of the interaction between the user and the manufacturer in medical equipment industry. R&D Manage. 15: 283-292.
4. Biemans WG. (1991) User and third-party involvement in developing medical equipment innovations. Technovation 11: 163-182.
5. Shah SGS, Robinson I. (2006) User involvement in healthcare technology development and assessment: Structured literature review. Int. J. Health Care Qual. Assur., 19: (Accepted, in press).
6. Robinson I, Shah SGS, Bridgelal Ram M et al. (2005) MATCH guide towards user involvement in medical device technology assessment. Multidisciplinary Assessment of Technologies Centre for Healthcare (MATCH) program. Deliverable No. 10. Available at: http://www.match.ac.uk/
7. Shah SGS, Robinson I. (2006) Medical device technologies: who is the user? Multidisciplinary Assessment of Technologies Centre for Healthcare (MATCH) program. Document No. J2304. . Available at: http://www.match.ac.uk/
8. Marshall R, Case K, Oliver R et al. (2002) A task based 'design for all' support tool. Robot Cim-Int. Manuf., 18: 297-303.
9. De P, Ferratt TW. (1998) An interorganizational information system in the health care arena: Insights gained from a hierarchical analysis. In: Proceedings of the 1998 ACM SIGCPR conference on Computer personnel research, March 26-28, (Agarwal R, ed). Boston, MA, USA. pp 214-223.
10. De P, Ferratt TW. (1998) An information system involving competing organizations. Commun. ACM 41: 90-98.
11. Beverley CA, Bath PA, Booth A. (2004) Health information needs of visually impaired people: a systematic review of the literature. Health Soc. Care Comm., 12: 1-24.
12. Bruce J, Mollison J. (2004) Reviewing the literature: adopting a systematic approach. J. Fam. Plan. Reprod. H., 30: 13-16.
13. High DM, Turner HB. (1987) Surrogate decision-making: the elderly's familial expectations. Theor. Med. Bioeth., 8: 303-320.
14. High DM. (1990) Old and alone: surrogate health care decision making for the elderly without families. J. Aging Stud., 4: 277-288.
15. Meeker MA. (2004) Family surrogate decision making at the end of life: seeing them through with care and respect. Qual. Health Res., 14: 204-225.
16. Coppolino M, Ackerson L. (2001) Do surrogate decision makers provide accurate consent for intensive care research? Chest 119: 603-612.
17. Bramstedt KA. (2003) Questioning the decision-making capacity of surrogates. Intern. Med. J., 33: 257-259.
18. Anderson GJM.(2002) Shaping the future: using voice of the customer methodology to develop inhaler design. In: Respiratory Drug Delivery VIII (Dalby RN, Byron PR, Peart J et al., eds), Vol. 1. Tucson, Arizona: Serentec Press. pp 179-188.
19. Buhler C. (1996) Approach to the analysis of user requirements in assistive technology. Int. J. Ind. Ergon., 17: 187-192.
20. Liljegren E, Osvalder A-L. (2004) Cognitive engineering methods as usability evaluation tools for medical equipment. Int. J. Ind. Ergon., 34: 49-62.
21. Debanne SM, Petot GJ, Li J et al. (2001) On the use of surrogate respondents for controls in a case-control study of Alzheimer's disease. J. Am. Geriatr. Soc., 49: 980-984.
22. Keywood K. (2003) Gatekeepers, proxies, advocates? The evolving role of carers under mental health and mental incapacity law reforms. J. Soc. Welfare Fam. Law 25: 355-368.
23. Chiu CC, Vicente KJ, Buffo-Sequeira I et al. (2004) Usability assessment of pacemaker programmers. Pacing Clin. Electrophysiol., 27: 1388-1398.
24. Hayes CM. (2003) Surrogate decision-making to end life-sustaining treatments for incapacitated adults. J. Hosp. Palliat. Nurs., 5: 91-102.
25. Miettinen R, Hasu M. (2002) Articulating user needs in collaborative design: towards an activity-theoretical approach. CSCW 11: 129-151.
26. Hummel M, van Rossum W, Omta O et al. (2001) Types and timing of inter-organizational communication in new product development. Creativ. Innovat. Manag., 10: 225-233.
27. Gotzsche PC, Liberati A, Torri V et al. (1996) Beware of surrogate outcome measures. Int. J. Tech. Assess. Health Care 12: 238-246.

Address of the corresponding author:

Author:	Syed Ghulam Sarwar Shah
Institute:	Centre for the Study of Health and Illness, School of Social Science and Law, Brunel University
Street:	Kingston Lane
City:	Uxbridge, Middlesex, UB8 3PH
Country:	United Kingdom
Email:	Sarwar.Shah@brunel.ac.uk

F. Ibrahim, N.A. Abu Osman, J. Usman and N.A. Kadri (Eds.): Biomed 06, IFMBE Proceedings 15, pp. 546-549, 2007
www.springerlink.com ' Springer-Verlag Berlin Heidelberg 2007

A Miniature Skin-Attached Hot Flash Recorder

J.G. Webster[1], D.E. Bahr[1], M.C. Shult,[1], D.G. Grady[2], J. Macer,[2]

[1]Bahr Management, Inc., Middleton WI USA
[2]University of California, San Francisco CA USA

Abstract— **We are developing an innovative miniature ambulatory hot flash recorder that is precise, accurate, reliable, affordable and aesthetically appropriate. It is a small disposable adhesive patch with two electrodes. A nondisposable, miniaturized, coated circuit board snaps onto the electrodes. The unit records the frequency, timing, and amplitude of hot flashes by measuring skin conductance, using no external wires or telemetry. The recorder contains a hot flash event marker that the subject triggers whenever she experiences a hot flash. Because hot flash skin conductance changes slowly, we measure every 10 s. We use pulsed waveforms to take the data, and sleep mode to conserve battery life. Since electrodes polarize if current always travels in a single direction, we use pulses in alternate directions. Data are downloaded directly from the patch to data acquisition software for computer display. The new recorder will be a valuable tool for researchers.**

I. Introduction

There are currently about 36 million American women between the ages of 45 and 65 years. At least two thirds of these women will experience hot flashes and approximately 20% will seek medical relief for debilitating symptoms [1]. A hot flash is the sudden onset of intense heat and flushing in the upper torso and face, often followed by profuse sweating and chills [1]. The etiology of hot flashes is thought to be related to abnormalities of thermoregulation associated with changes in hormone levels that occur at menopause (Freedman, 1998), but the mechanism is not entirely clear.

Postmenopausal hormone therapy is highly effective treatment for hot flashes [2] and 10 million women in the US are currently taking some form of estrogen, either alone or in combination with progestin [3]. However, large randomized trials have recently shown that standard-dose hormone therapy is associated with increased risk for cardiovascular disease, venous thromboembolic events, and dementia [3 6]. Given the increased risks for serious diseases and other common side effects such as uterine bleeding and breast tenderness [7], many women would like to avoid using hormone therapy for treatment of hot flashes.

As reflected in recent NIH-sponsored workshops and conferences on Menopause (http://orwh.od.nih.gov/), there is intense interest in the research community regarding the etiology of hot flashes and in finding effective and safe treatment. However, research is currently hindered by the lack of a feasible, reliable and accurate objective measure of hot flash frequency and severity. Most studies currently use a 7-day self-reported hot flash diary [8]. This measure is subjective and can be inaccurate and unreliable because participants forget or fail to enter hot flashes in the diary (especially at night when many hot flashes occur), severity is self-reported on a coarse scale (mild, moderate, severe), and the exact timing of the hot flash is not recorded [9]. In addition, keeping a daily diary is labor-intensive and inconvenient and most participants are unwilling to do this for more than about a week.

Increases in skin conductance have been shown to be a good measure of the occurrence of hot flashes [10]. Skin conductance rises sharply from baseline at the onset of a hot flash, then slowly returns to baseline as depicted in Figure 1.

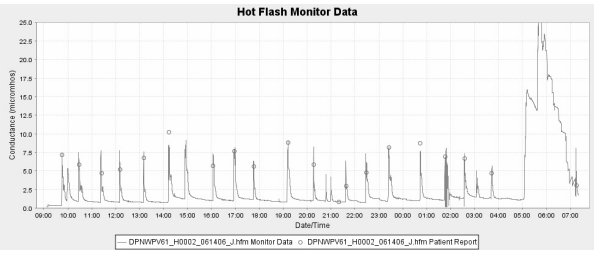

Fig. 1 Using electrodes containing gel C, baseline conductance in the participant shown is about 1.2 micromhos (μS). Typical hot flashes rise to about 7 μS and last about 2 min. The subject presses a button when she perceives a hot flash, which is recorded by the small circle shown on the 22 h record.

Ambulatory skin conductance monitors such as the BIOLOG are commercially available, but are not optimal for use in clinical research for several reasons. The device is heavy (200 g), bulky (3.3 × 7 × 13 cm), and cumbersome. Wires are used to attach the monitor, which is worn on the belt or in a case with a shoulder strap, to 2 ECG-type electrodes attached to the upper chest. The special electrode cream must be pasted into the dry electrode sponge by hand. The monitor cannot be worn under clothing or in the shower and the electrodes are awkward to attach and remove. Recording is limited to 24 h due to limited data storage

F. Ibrahim, N.A. Abu Osman, J. Usman and N.A. Kadri (Eds.): Biomed 06, IFMBE Proceedings 15, pp. 550-553, 2007
www.springerlink.com ' Springer-Verlag Berlin Heidelberg 2007

capacity and there is no measure of severity (increased skin conductance duration or amplitude or their product). Because there is marked biologic variability between individual women and from week to week in a given individual in the frequency and severity of hot flashes, longer duration of monitoring would be optimal. In addition, the BIOLOG monitors are expensive, costing $2200 each and $2000 for the associated software. At this price and with these limitations, it is impractical to use the devices in adequately powered clinical trials.

II. Methods

A. Hot flash monitor design and testing

To address these problems, we have developed a medium sized prototype skin conductance monitor which is being tested in the bioelectrical laboratory and in ambulatory participants in clinical research studies at the University of California, San Francisco. We are presently miniaturizing the monitor so it can be skin attached. It measures the frequency, timing, and amplitude of the hot flashes. See Figure 1. After miniaturization it will be a discreet, nondisposable ambulatory recorder snapped onto disposable electrodes that is easy to attach and remove, precise, inexpensive, and aesthetically acceptable. It will be self-contained with no external wires and no telemetry transmission to an external receiver.

We have completed and manufactured 9 prototype hot flash measuring devices using skin conductance measurements with appropriate electrodes, wires, and circuitry to determine skin conductance. We have tested current commercially available ECG electrodes and found that they are not suitable for conductance monitoring. We have investigated the conductance vs. time curve for different ECG electrodes and found that their high salt concentration (about 4%) results in increased skin conductance that masks the increase caused by sweating during hot flashes. Thus we investigated electrodes with low salt concentration and found that they perform very well and produce results superior to the results obtained by the BIOLOG recorder and electrode cream. We have reproduced similar conductance patterns for simulated and real hot flashes. See Figures 1 and 2.

We have developed software for measuring, storing, processing, and displaying the data. See Figure 2. We display skin conductance changes as absolute changes and also as relative changes. Software will provide the frequency of hot flashes based on conductance changes, mean and range of hot flash duration, mean severity based on fractional change from baseline or area under the curve above baseline, and a severity score, which will be the product of frequency and duration.

B. Electrode design and testing

Our philosophy is that if we use an excellent sensor, then we will be able to use signal processing software to yield optimal results. If the sensor is bad, signal processing software may not correct the problem. Thus we have performed extensive testing on electrodes.

ECG electrodes do not work because they are designed to make good skin contact. Their approximately 4% salt diffuses into the skin and deliberately increases the conductance. Then when the hot flash opens the sweat ducts, the incremental parallel-added conductance is a tiny fraction of the total and produces a negligible change.

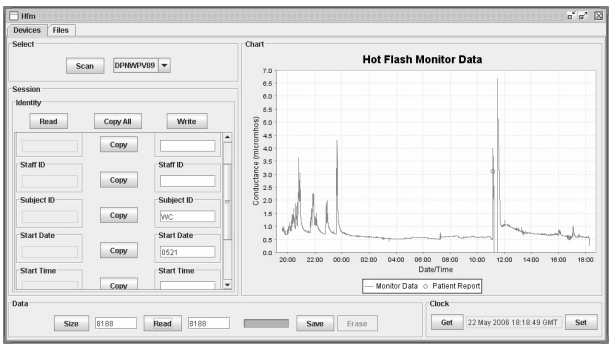

Fig. 2 Desktop computer software scans the monitor serial number, provides file labeling, downloads the data, saves them, displays them, erases the memory, and sets the clock. At the end of a 7-day test shown here, the conductive adhesive gel gives results as good as for day 2 of the same electrode (Shown below in Figure 3 bottom).

Thus we tested alternative electrodes designed with lower conductance and found excellent results with regard to low baseline and definitive increases with sweating. We also tested the cream recommended by BIOLOG and found that it yielded high baseline and erratic results.

We have tested electrodes with various adhesive tacks to ensure that the electrodes make good contact for several days, yet cause minimal irritation when removed.

We have tested solid backing materials and skin adhesives that breathe so that sweat does not accumulate in the solid gel. We have tested vinyl backing materials that do not breathe to prevent shower water from entering and accumulating within the solid gel.

Figure 3 shows a side-by-side comparison of gel A (poor results) with gel C (excellent results).

We have found gel C to be superior to gel A, BIOLOG gels, or 0.1% or 0.9% saline in hydrogels.

F. Ibrahim, N.A. Abu Osman, J. Usman and N.A. Kadri (Eds.): Biomed 06, IFMBE Proceedings 15, pp. 550-553, 2007
www.springerlink.com ' Springer-Verlag Berlin Heidelberg 2007

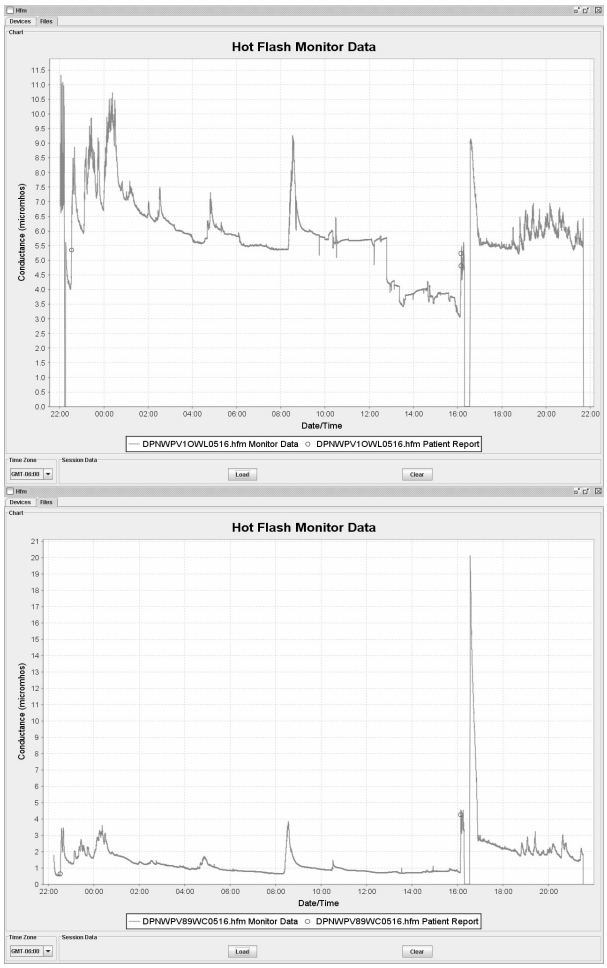

Fig. 3 Side-by-side comparison of two electrodes worn by the same subject at the same time. Top: Biolog cream causes about 6 micromho (μS) baseline conductance. Sweating caused by exercise (marked by circles) causes about 30% change. Bottom: Conductive adhesive gel causes about 0.8 μS baseline conductance and has less motion artifact. Sweat caused by exercise causes 400% change. During shower (at about 16:00 hours), the recorder was detached (0 μS). After shower, electrode was wet, recording about 20 μS and recovering in about 1 h.

Skin conductance increases with time with a standard type of electrode and electrolyte. This is likely due to the fact that electrode salts and water diffuse into the skin, hydrating it and increasing its conductance. Also, the impermeable plastic in the electrode traps sweat under the electrode which further increases hydration.

We have tested the time constant of the skin conductance to a step voltage of 0.5 V and find that the time constant is about 20 ms. We wait 20 time constants to ensure equilibrium, sample the skin conductance, then terminate the pulse after 400 ms. To save battery life we put the microprocessor to sleep and wait 10 s before taking the next sample. Hot a flash skin conductance change slowly over a period of about 2 min, therefore a measurement is only needed every 10 s. Because electrodes polarize if current always travels in a single direction, we apply pulses in alternate directions, positive and negative and electrically connect the electrodes together between pulses to discharge any residual charges. Because there is a slow drift and noise in skin conductance, we are writing computer programs to ignore slow drifts and average noise. The basic algorithm concept is to recognize hot flashes by their much higher slope. We will also use template matching. These programs will display raw data and also automatically identify and record frequency, timing, and amplitude using absolute conductances and/or their changes and/or percent changes in conductances or their changes.

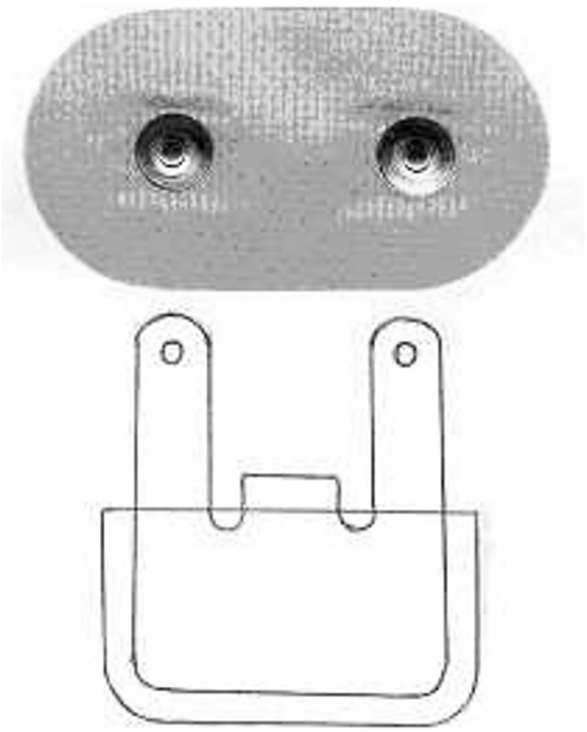

Fig. 4 Placement of the 2-electrode patch can be horizontal on the chest with hot flash miniature monitor snapped onto electrode studs by flex connections.

We have already tested modern chronic use skin adhesives in the size of a large Band-Aid similar to ScarSolution and find that the tack is too low for one-week use. We have not found an electrode tack that adheres adequately for 2 weeks and doesn t damage the skin. We tested several tacks similar to those used on ECG electrodes and find that they are satisfactory. We have found an adhesive that has improved tack, but is still well tolerated by the skin. As we move from our present Phase 1 prototype

F. Ibrahim, N.A. Abu Osman, J. Usman and N.A. Kadri (Eds.): Biomed 06, IFMBE Proceedings 15, pp. 550-553, 2007
www.springerlink.com ' Springer-Verlag Berlin Heidelberg 2007

that is the size of a cell phone to the Phase 2 miniature skin-attached model, we will use a miniature lithium watch battery to power a low power amplifier, analog-to-digital converter, microprocessor, and memory mounted on flexible polyimide or polyester. We have tested a miniature magnet on the strap of a regular wristwatch that activates a miniature magnetic reed switch so the subject can manually record the time of perceived hot flashes by pressing the wrist magnet against the monitor. A light-emitting diode (LED) will flash to acknowledge the manual subjective recording. Figure 5 shows the final miniaturized hot flash recorder. Dimensions will be about 6 L × 2 W × 1 cm T.

At the conclusion of testing, the subject will remove the instrument and return it or mail it in a supplied packet to the clinical research team for data processing. The research technician will download the data into a personal computer using a JAVA data manager that can be used on multiple platforms such as Microsoft or Apple and the data can be imported by Excel, SAS, or any data base for data analysis. We have already developed software so that the investigator can perform data processing. After each use, the lithium battery will be removed from the device for recycling and the device disposed. We anticipate that the manufactured cost of these devices should not exceed a few tens of dollars each.

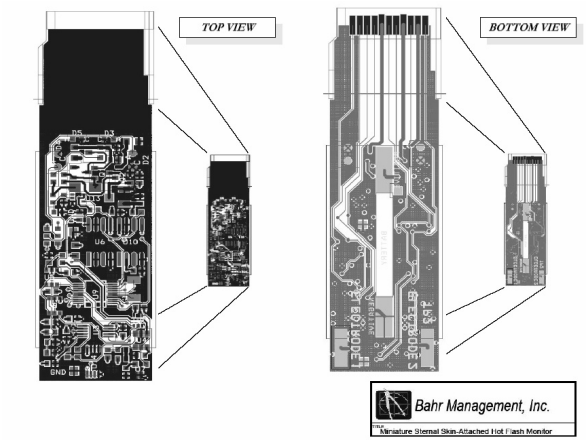

Fig. 5 We have designed a miniature skin-attached hot flash monitor that is 2 × 6 cm and will record skin conductance versus time for a week. Manufacture of 40 units begins in August 2006.

The initial medium sized prototype device 12 × 6 × 2 cm has been tested and revised by the engineers, it has been Phase 1 tested in women with frequent hot flashes at the University of California, San Francisco. The study participants are between 45 and 60 years old and have at least 10 hot flashes per day that occur both during the day and at night.

Acknowledgment

This publication was made possible by NIH Grant Number R43AT003183-01 from the National Center for Complementary and Alternative Medicine (NCCAM).

References

1. Kronenberg F. (1990): Hot flashes: epidemiology and physiology , *Ann. N. Y. Acad. Sci*. **592** 52-86
2. Maclennan A, Lester S, Moore V.(2001): Oral estrogen replacement therapy versus placebo for hot flushes: a systematic review , *Climacteric*. **4**(1) 58-74
3. Rossouw JE, Anderson GL, Prentice RL, et al. (2002): Risks and benefits of estrogen plus progestin in healthy postmenopausal women: principal results From the Women's Health Initiative randomized controlled trial , *JAMA*. Jul 17 **288**(3) 321-33
4. Shumaker SA, Legault C, Rapp SR, et al. (2003): Estrogen plus progestin and the incidence of dementia and mild cognitive impairment in postmenopausal women: the Women's Health Initiative Memory Study: a randomized controlled trial , *JAMA*. May 28 **289**(20) 2651-62
5. Anderson GL, Limacher M, Assaf AR, et al. (2004): Effects of conjugated equine estrogen in postmenopausal women with hysterectomy: the Women's Health Initiative randomized controlled trial , *JAMA*. Apr 14 **291**(14) 1701-12
6. Shumaker SA, Legault C, Kuller L, Rapp SR, et al. (2004): Conjugated equine estrogens and incidence of probable dementia and mild cognitive impairment in postmenopausal women: Women's Health Initiative Memory Study , *JAMA*. Jun 23 **291**(24) 2947-58
7. Greendale GA, Reboussin BA, Hogan P, et al. (1998): Symptom relief and side effects of postmenopausal hormones: results from the Postmenopausal Estrogen/Progestin Interventions Trial , *Obstet. Gynecol.* Dec **92**(6) 982-8
8. Sloan JA, Loprinzi CL, Novotny PJ, et al. (2001): Methodologic lessons learned from hot flash studies , *J. Clin. Oncol.* Dec 1 **19**(23) 4280-90
9. Miller, H. G., Li, R. M. (2004): Measuring hot flashes: Summary of a national institute of health workshop , *Mayo Clinic Proc*. June **79**(6) 735-7
10. Freedman, R R. (1998): Biochemical, metabolic, and vascular mechanisms in menopausal hot flashes , *Fertility and Sterility* **70** 332-7

Address of the corresponding author:

Author: J. G. Webster
Institute: Bahr Management, Inc
City: Middleton WI
Country: USA
Email: Webster@engr.wisc.edu

F. Ibrahim, N.A. Abu Osman, J. Usman and N.A. Kadri (Eds.): Biomed 06, IFMBE Proceedings 15, pp. 550-553, 2007
www.springerlink.com ' Springer-Verlag Berlin Heidelberg 2007

2D Arbitrary Lagrangian-Eulerian (ALE) Model of Blood Flow in the Left Ventricle (LV) of the Heart

Z.H. Azizul[1] and N. Selvanathan[2]

[1] Faculty of Computer Science and Information Technology, University of Malaya, 50603 Kuala Lumpur, Malaysia
[2] Faculty of Computer Science and Information Technology, University of Malaya, 50603 Kuala Lumpur, Malaysia

Abstract— **Current flow pattern simulation in the left ventricle (LV) requires method to tackle the interaction between the moving blood (fluid) and the deforming valves (structure). This fluid-structure interaction is the mechanism behind continuous cardiac activities. Capturing essence of these mechanics often involves solving complex mathematical equations which demands high computing resources. Limiting computing power has resulted in the need to optimize the degree of freedom (DOF) stemming from three-dimensional (3D) geometries. Many heart simulation projects aims to develop a 3D model for the reason that in three dimensional, the true motion of the heart muscle is better depicted. Unfortunately, higher DOF in 3D leads to difficulties in the equations modeling. For this reason, the complex equations, which in most cases derived from the differential domains; the partial differential equations (PDEs) and ordinary differential equations (ODEs), are usually modeled first on two-dimensional (2D) geometries. The focus of these prototypes is to ensure the equation modeling essentially captures the core of the fluid-structure interaction in the heart and enhancement of the prototype into 3D is usually done later to produce better graphical simulation.**

In this research, the dynamic movement of heart valves and the blood flow pattern in the LV is studied using advanced numerical-computational technique. This approach is known as the Arbitrary Lagrangian-Eulerian (ALE) and is introduced by means of a mesh movement method in a finite element environment. The ALE uses two sets of reference systems; the Eulerian reference system to track the moving blood and the Lagrangian reference system to handle the deforming valves. A working prototype of the ALE model in 2D is developed and results pertaining to the velocity pattern prior to periodicity mechanics of the valves in the LV are presented graphically in a time-step fashion.

Keywords— **Arbitrary Lagrangian-Eulerian (ALE), flow pattern simulation, fluid-structure interaction, finite element method.**

I. Introduction

Cardiovascular Diseases (CVD) is the leading cause of death in Malaysia [1]. Alarming statistics shows an increase of 14 percent death in 5 years; 96,000 cases in 1995 and 110,000 cases in 2000 [2]. An increase prevalence of CVD in the country calls for cardiologists to consider technological advancement in studying the nature of the disease; mainly the causes of rhythm disturbances leading to a heart failure.

The heart functions as the organ that generates force which circulates blood in the body. The force is generated from the dynamic interaction between the fast flowing blood and the elastic heart wall in the left ventricle (LV). In each heart beat, the blood would fill the LV and the elastic LV wall would strain and expand and the building constraint would generate high pressure enough to force the blood out from the heart and into the body. The journey of the blood into the LV and out into the body creates a profile of flow pattern.

Disturbances to the pattern of the circulating blood flow are the reason a heart fails. Changes in the flow profile generally occur due to the clogging of arteries as impact from the formation of plaque resulting in both narrowing and hardening of arteries (also known as atherosclerosis and arteriosclerosis). In consequence, the heart will not pump efficiently leading to the various CVD, examples such as coronary thrombosis, myocardial infarction, aneurysm and arrhythmia.

Information on the general pattern of the flowing blood in the left ventricle is currently retrieved using the cardiac catheterization; a technique performed on potential CVD patients requiring a small incision and sedation. Unfortunately, evaluation of patients with a potential circulatory disorder using this technique is often very difficult, long (the whole process takes up several hours) and invasive to make. Therefore, alternative methods using computational techniques capable of determining the flow pattern in the heart, non-invasively, have triggered a strong interest to clinical and physiological diagnosis.

In modern studies of the fluid-structure interactions of the heart, several researchers around the world have been identified to incorporate the ALE approach in their work.

- A group of researchers from the Eindhoven University of Technology has developed tissue engineered heart valves by analyzing how the geometry and material properties influence the movement of artery and heart valves and the flow vicinity in the heart [3].

F. Ibrahim, N.A. Abu Osman, J. Usman and N.A. Kadri (Eds.): Biomed 06, IFMBE Proceedings 15, pp. 554-557, 2007
www.springerlink.com ' Springer-Verlag Berlin Heidelberg 2007

- Simulations of valve dynamics in a simplified left ventricle flow model using the ALE method can be seen in [4].
- The ALE approach has also been used to study the fluid-structure analysis of the structural and the fluid dynamic behavior for cardiopulmonary bypass [5].
- Another work incorporating the Lagrangian-Eulerian formulation to study the incompressible viscous flow on a finite element platform can be seen in [6].
- Fluid-solid interaction of the valves leaflets motions have been investigated by means of the ALE couplings to derive two-dimensional model of the bi-leaflets valve [7] and three-dimensional model of the bi-leaflets model [8].
- Numerical analysis of fluid-solid interactions for blood flow on arterial structures is paid careful attention in some works [9] and [10]. From these experimental works, additional information pertaining to the heart s boundary positions and velocity information can be observed.

II. Methodology

A. Geometrical Modeling

A simplified surface model of the heart is needed for the purpose of preparation and acceptance of analysis in a finite element environment. Using 3D scanning, points data that represents the LV is captured and used to recreate a sensible geometrical model. Expectations of the outcome from this session are for the model to encompass parameters that contributes to proper measurements of the fundamental aspect of the LV such as the general morphology of its walls in axial direction, diameter and shape of the ventricle valves (i.e. the mitral and the aortic), and the radius angle of those working valves that positions them at such in the chamber. The generated model is tuned in a format that is recognized in a finite element setting for the 2D ALE analysis and modeling.

Framework used in the research is as follows:

- Sample LV points data from 3D scanning
- Wrap points data using computer aided design (CAD) software.
- Generate surface on the 3D geometry.
- Measure length and diameter of regions of interest.
- Design 2D geometrical model based on 3D surface model measurements.
- Perform ALE analysis on 2D model
- Mesh and solve ALE in finite element environment.

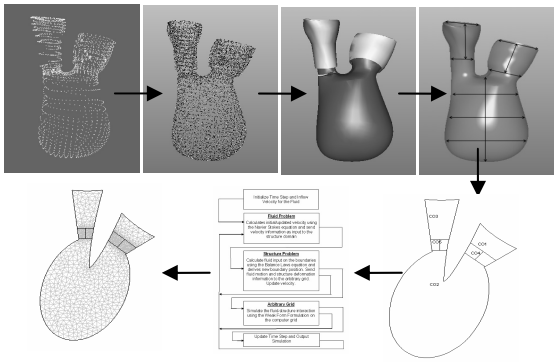

Fig 1: Framework used in the research

B. The ALE Analysis

The ALE approach is adopted in this work to solve two problems; the fluid problem (i.e. the motion of the blood) and the structure problem (i.e. the movement of the valves). The method employs the use of reference frames to represent the classical Lagrangian and Eulerian systems. The Lagrangian reference frame is used to study the structure problem and the Eulerian reference is used to study the fluid problem, respectively.

The Eulerian Reference Frame

The Eulerian reference frame studies the motion of fluid by setting its frame on the fluid mesh and allows the fluid to cross through the mesh to study the flow. Fluid has velocity and so, as the fluid flows through the mesh, the Eulerian calculation measures the differing velocity in and out of each frame section. This measurement captures velocity information of the blood at various locations in the LV geometry. Important parameters pertaining to the flow is summarized in Table 1.

Table 1 Field Variables Representing the Mesh Velocity

Mesh Velocity Field Variables	Values
Density (ρ)	1060Kg/m3
Dynamic Viscosity (π)	0.0054Pa-1s

PDE of the mesh velocity is derived based on the Navier Stokes equations and has been evaluated numerically with respect to time. The equation is presented as follows:

$$\int_{\Omega}(\tilde{u}_x(2\eta u_x - p) + \tilde{v}_y(2\eta v_y - p) + (\hat{v}_x + \hat{u}_y)\eta(v_y + u_x) + \hat{u}((u-\psi_x)u_x + (v-\psi_y)u_y) + \hat{v}((u-\psi_x)v_x + (v-\psi_y)v_y + - \hat{p}(u_x + v_y) + \rho\hat{u}\frac{du}{dt} + \rho\hat{v}\frac{dv}{dt} - \hat{u}f_x - \hat{v}f_y)d\Omega = 0 \quad (1)$$

where $\psi = (\psi_x, \psi_y)$ is the mesh velocity.

F. Ibrahim, N.A. Abu Osman, J. Usman and N.A. Kadri (Eds.): Biomed 06, IFMBE Proceedings 15, pp. 554-557, 2007
www.springerlink.com ' Springer-Verlag Berlin Heidelberg 2007

The Lagrangian Reference Frame

The Lagrangian reference frame investigates structural deformation by fixing its frame on the mesh structure then as the structure deforms the mesh deforms with it. The deformation captured by the mesh is the structural displacement of the valve leaflets. Important parameters pertaining to the mesh displacement is summarized in Table 2.

Table 2 Field Variables Representing Properties of the Mesh Displacement

Mesh Displacement Field Variables	Values
Density (ρ)	960Kg/m
Coefficient (u)	6204106 N/m
Bulk Modulus	20u
Poisson Ratio (v)	0.45
Elastic Modulus	1.017N/m

PDE for the mesh displacement is derived based on the information captured from equation (1). Poisson s equation is used to represent the displacement equation.

$$\int_{\Omega} D((\psi_{xX} I_{Xx} + \psi_{xX} I_{Xy} + \Psi_{xY} I_{Yy})\psi_{xy})d\Omega = 0 \qquad (2)$$

The Arbitrary Grid

In view of the fact that the mechanics in the heart requires simultaneous interaction between the valves movement and the blood flow, solution to the interaction is derived by setting the Lagrangian and Eulerian reference frames on an arbitrary computational grid. Coupling of both reference frames on the grid produces solution to the fluid-structure problem and a graphical simulation can be derived using visualization platforms to output the interaction. Summary of the ALE algorithm is shown in Figure 2.

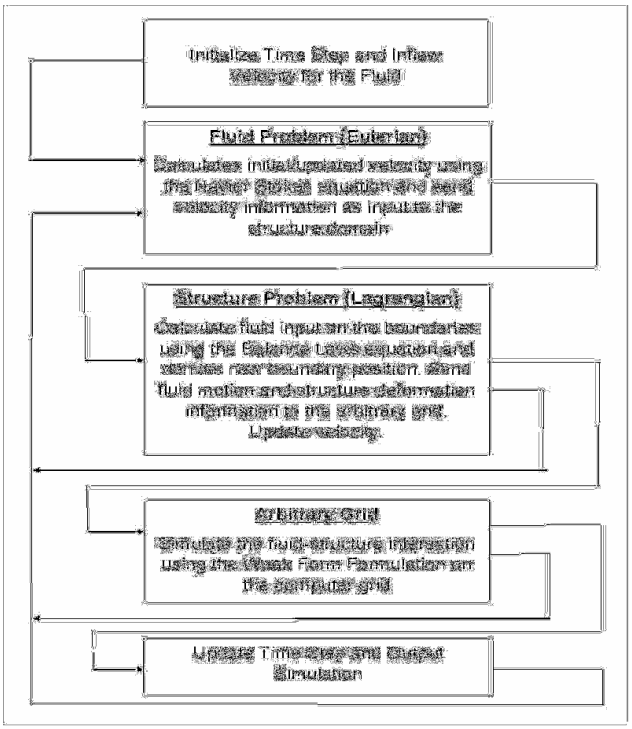

Fig 2: Summary of the ALE Algorithm

III. Results and visualization

The influence of the modulus elasticity particularly on the walls or boundaries of the working valves has posed attention to the analyzed result relating to the calculation of the Reynolds numbers; a dimensionless parameter identified from the simulation with a value of 500, which corresponds to typical values in major arteries [11] The flow dynamics analyzed in the rigid vessel of the ventricle chamber is seen to contribute to the instantaneous systolic and diastolic LV model.

The boundary layer of the mitral valve, developed during the acceleration, separates during systole and produces a small recirculating cell immediately at the downstream of the ventricle chamber. The separation phenomenon corresponds to the roll-up of the boundary layer and the formation of the vortex structure eventually traveling downstream [12].

Results of the 2D LV simulation are laid out in graphical representation in Figure 3. Using eight different plots, the velocity profile in the systolic and diastolic phase in the one second simulation time is observed with the timestep separated at approximately 0.1sec per plot. Figure 3(a) and Figure 3(b) shows the left ventricle simulation before initialization and at the first point of initialization. At this beginning, a positive separation of vorticity indicates a persistent negative shear forces in the portion of wall downstream of the enlargement. The same flow fields are reported in Figure 3(c), Figure 3(d) and Figure 3(e). It can be observed that during systole the ventricle chamber is inflated with the incoming inflow from the mitral valve, pressuring the chamber to dilate and with that the flow is seen to accelerate at a maximum velocity profile throughout the chamber.

Figure 3(f), Figure 3(g) and Figure 3(h) shows the blood flow profile during diastole. At diastole the boundary layer is thicker because of deceleration and the streamlines show about a zero net flow. The deceleration decreases the flow rate indicating vessel shrinks, not seen in the simulation but is assumed to increase the actual discharge and bulk velocity from the ventricle chamber out into the aortic. During the acceleration, the synchronous deformation of the wall

F. Ibrahim, N.A. Abu Osman, J. Usman and N.A. Kadri (Eds.): Biomed 06, IFMBE Proceedings 15, pp. 554-557, 2007
www.springerlink.com ' Springer-Verlag Berlin Heidelberg 2007

leads to a less extended separated region, while the contraction of the vessel during the deceleration phase of the imposed diastolic pulse tends to diminish the value of the negative tangential stress.

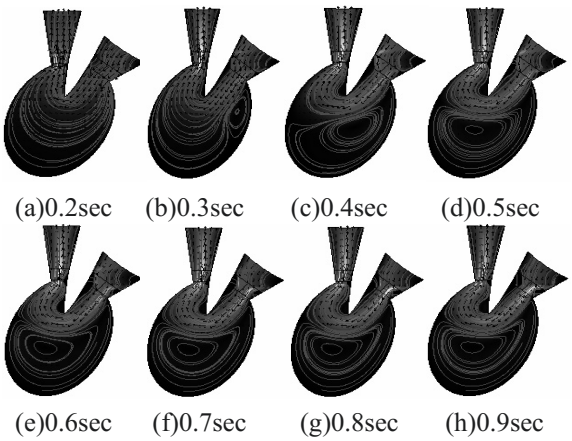

Fig 3: Velocity Profile in the Systolic and Diastolic Phase of the Left Ventricle Two Dimensional Simulation

Information gained from the velocity field is marked at each timestep to track the mean velocity at given positions in the simulation. Figure 4 shows the average velocity during (a) the mitral inflow (systole) and (b) the aortic outflow (diastole).

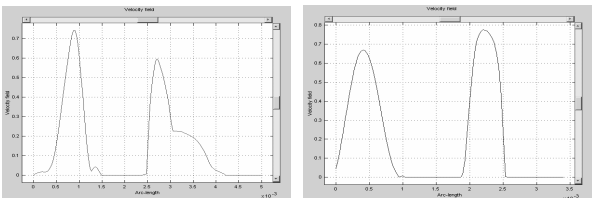

Fig 4: Mean Velocity during Systole and Diastole in each Heart Beat

IV. Conclusions

The work discussed in this paper provides a basic study on the blood flow pattern in the LV. The ALE method employed to incorporate the interaction between the blood flow and the leaflet motion has shown that simplified 2D ALE model can, within limits, predicts physiologically correct flow patterns in the LV. The model is also able to simulate forces exerted by the fluid during the mitral inflow and the aortic outflow with plausible prediction of the new displacement for the leaflet positions.

Acknowledgement

This research has been fully supported and funded by The Fellowship Scheme of University of Malaya.

References

1. Heart Foundation of Malaysia, Walk-A-Mile 2006 Press Conference
2. http://www.frost.com/prod/servlet/market-insight-top.pag?docid=18817766
3. de Hart, J., Peters, G. W. M., Schreurs, P. J. G., and Baaijens, F. P. T. (2000) A two-dimensional fluid-structure interaction model of the aortic value. Journal of Biomech., 33(9):1079 1088.
4. de Hart, J. 2002. Fluid-Structure Interaction in the Aortic Heart Valve: A Three-Dimensional Computational Analysis. Ph.D. diss., Eindhoven University of Technology.
5. Guadagni, G., Fiore, G. B., Martino, E. D., Redaelli, A., Fumero, A., Dubini, G., Inzoli, F. 2001. A fluid-structure analysis of the structural and the fluid dynamic behavior of a new disposable pulsatile pump for cardiopulmonary bypass. *Bioengineering Conference ASME volume 50.*
6. Hughes, T., Liu, W., Zimmermann, T. 1981. Lagrangian-Eulerian Finite Element Formulation for Incompressible Viscous Flows. Computer Methods in Applied Mechanics and Engineering, vol. 29, no. 3, 329-349.
7. Cheng, R., Lai, Y. G. and Chandran, K. B. 2003. Two-dimensional fluid-structure interaction simulation of bi-leaflet mechanical heart valve flow dynamics. *Heart Valve Dis.* 12:772 780.
8. Cheng, R., Lai, Y. G. and Chandran, K. B. 2004. Three-dimensional fluid-structure interaction simulation of bi-leaflet mechanical heart valve flow dynamics. *Annals of Biomedical Engineering* 32:1471-1483.
9. Hose, D. R., Lawford, P. V., Narracott, A. J., Penrose, J. M. T., Staples, C. J., Jones, I. P., Nuesser , P., Choub, L., Quinn, D. (1998) BloodSim: Coupled Solid-Fluid Simulation of Cardiovascular Systems.
10. Rutten, M. C. M. 1998. Fluid Solid Interaction in Large Arteries. Ph.D. diss., Eindhoven University of Technology.
11. Pedrizetti, G. 1998. Fluid flow in a tube with an elastic membrane insertion. *Journal of Fluid Mechanics* 375: 39-64.
12. Pedrizzetti, G. 1996. Unsteady tube flow over an expansion, *Journal of Fluid Mechanics*, 310: 89-111

Address of the corresponding author:

Author:	Zati Hakim Azizul Hasan
Institute:	Faculty of Computer Science and Information technology, University of Malaya
Street:	50603 Kuala Lumpur
City:	Kuala Lumpur
Country:	Malaysia
Email:	zati_hakim@yahoo.com

F. Ibrahim, N.A. Abu Osman, J. Usman and N.A. Kadri (Eds.): Biomed 06, IFMBE Proceedings 15, pp. 554-557, 2007
www.springerlink.com ' Springer-Verlag Berlin Heidelberg 2007

A Computer-based Surgery Planning and Simulation for the Prediction of 3D Postoperative Facial Soft Tissue using Finite Element Analysis

U.H. Obaidellah[1], N. Selvanathan[2]

[1] Department of Artificial Intelligence, Faculty of Computer Science & IT, Postgraduate Student, Kuala Lumpur, Malaysia
[2] Department of Artificial Intelligence, Faculty of Computer Science & IT, Professor, Kuala Lumpur, Malaysia

Abstract— **This paper will present our work on the planning and simulation of postoperative facial soft tissue prediction in the area of orthognathic surgery. We combine different methods of image processing, geometrical modeling and finite element analysis to predict and simulate the postoperative facial appearance of a malformed faced patient. Our approach is based on surface-based triangulation of the finite element method. The surgical planning system describes various preprocessing steps for the generation of 3D facial model and the surgery planning procedures involved. A number of procedures are highlighted during the preparation of facial model before the finite element analysis initiates. The prediction of the facial soft tissue is described based on finite element analysis through mathematical formulation by employing the linear elastic model. The surgical simulation results are shown, validated and discussed.**

Keywords— **orthognathic surgery, planning and simulation, osteotomy, soft tissue prediction, finite element method**

I. Introduction

The multi-disciplinary area of human modeling has been constantly growing including those in the field of orthognathic surgery. Before surgery, craniofacial surgeons often face problems trying to predict a patient s final appearance if a corrective surgery is deemed. Many reasons lie for a disharmony face. Among them are accidents, congenital deformities, family traits and trauma in infancy. A craniofacial surgeon is responsible for the reconstruction of the deformed face to at least a sufficiently harmony and acceptable facial appearance. Possibilities in difficulties of breathing, biting and speaking for the patient would arise if the malformed face is left untreated. Psychological consequences of an appearance that reflects to the personal development also social acceptance are other issues qualified to be considered. Therefore, under the concern of harmonious appearance, a craniofacial surgeon has to produce functional preoperative facial results under various therapeutic strategies. Due to the complexity of anatomy for individual patient, surgery planning which requires advanced surgical expertise, distinct sense of mental visualization, artistic skills and extensive communication with the patient certainly takes time. These procedures are ensured in a shorter length of time with the intervention of reliable computerized methods and appropriate tools.

This paper will present on the computerized surgery planning for the mandibular orthognathic surgery which deals with geometrical modeling and bone realignment in section II. Subsequently, in section III the facial soft tissue prediction is described. Section IV delineates the finite element approach through mathematical formulations. Finally, section V discusses the results before conclusion is illuminated in section VI.

II. Surgical Planning System

This section elucidates the general setup of our surgical planning system from the facial geometry modeling, model improvement, bone cutting and bone realignment. The surgery planning system uses commercial tools for the geometric modeling, surgical planning processes, visualization and rendering. Therefore, the handling of these processes is straightforward.

A. Geometrical Modeling

A volume data set obtained from computer tomography (CT) scanning of an actual patient suffering from bite problem is the initial procedure for the foundation of facial anatomy modeling. The facial anatomy data is distributed in slices of images where the skull and the skin layer are extracted by employing image segmentation techniques namely segmentation, region growing and triangulation. Segmentation starts with thresholding whereby the region of interest is defined on selected CT slices by specifying respective lower and upper value. Subsequently, the anatomy of interest, in this case the upper jaw, lower jaw and facial skin surface are separated from the remaining skull and head structure by performing region growing. Finally, a complete closed volume facial model is generated from the selected segmented CT slices through the Marching Cube Algorithm [1]. The process of constructing the 3D facial model which consists of triangular mesh is known as triangulation. A surface-based model composed of triangular elements surrounding the surface of the

F. Ibrahim, N.A. Abu Osman, J. Usman and N.A. Kadri (Eds.): Biomed 06, IFMBE Proceedings 15, pp. 558-562, 2007
www.springerlink.com ' Springer-Verlag Berlin Heidelberg 2007

facial model is employed instead of the volumetric model. This is because the simulation of volume-based model is time consuming and beyond the scope of the current hardware resources. The main concern of this work is to produce visually acceptable results, thus the remaining anatomy structure is of less priority. In addition, there is a need of tradeoff between the accuracy and computation time due to the size of triangular element. Fig. 1 illustrates the data used for our geometrical facial models.

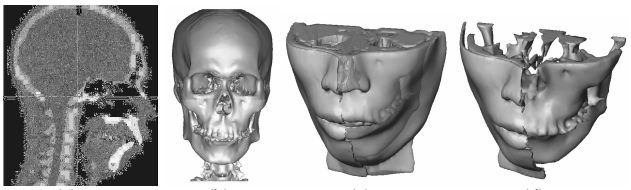

Fig. 1 Geometrical data sets. (a): Computer Tomography image slice, (b): Patient specific 3D facial model, (c): Facial model with soft tissue, (d): Facial model without soft tissue

B. Model Improvement

In order to achieve better and reliable simulation results, it is important to ensure that the model is composed of good quality elements that converge to the desired behavior. Therefore, model checks to determine the quality of mesh which include reducing the numbers of triangles without losing essential data, smoothing rough surface, removing poorly shaped elements and producing regular elements called equilateral triangles are essential prior to analysis for simulation. An optimized model is obtained on completion of these processes.

C. Osteotomy Planning

Researches in the field of orthognathic surgery systems have produced various methods for the *osteotomy* planning [2,3,4,5]. *Osteotomy* is defined as bone cutting and relocation of the sliced bone to a new position respective to the individualized treatment. In our case, the example patient suffered from *bimaxilliary protrusion, long face* and *left lateral scissors bite*, a condition where the lower jaw is rearward, thus, the lower teeth are not aligned with the upper teeth. The surgery planning is carried out with the help of craniofacial surgeons where the best location for bone cutting is defined before the bone slices is moved to a new forwarded position. Due to the reason that post surgical aesthetic is crucial, the exact replication of the real world surgery on computer is not given detailed consideration. Therefore, plates and screws were not employed in the surgery planning of this work. Fig. 2 illustrates the mandibular *osteotomy* surgery planning procedures.

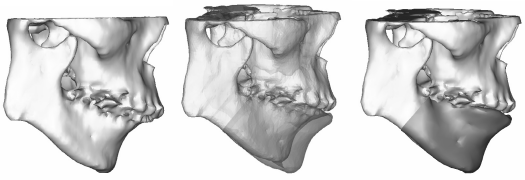

Fig. 2 Bone structure before and after osteotomy. (a): Original mandible and maxilla, (b): Repositioned mandible in new position, (c): Relocated mandible in a forward manner

III. Computational Surgery And Simulation

The work employs finite element analysis (FEA) for the prediction of post surgical facial appearance in which the numerical computation is carried out on MSC.AFEA through the MSC.Marc solver. A number of procedures involved before an analysis is permitted. They are tissue meshing, validation tests, material properties definition and boundary conditions assignment. The facial model which consists of mandible, maxilla and skin surface are further improved and simplified by reducing the numbers of triangular elements before quadrilateral meshes replaces the existing triangular mesh. Reason for this is to ensure the success of the analysis. Validation tests follows to fulfill the conditions of good quality meshing with regard to FEA. Badly shaped quadrilaterals, remaining triangular elements, unconnected or duplicated quad elements are checked for validity before the finite element analysis is accomplished. On completion of validation tests, material properties that define density, compressibility, elasticity and thickness are assigned to the tissues. The boundary condition assignment through *contact definition* available in MSC.AFEA determines the interaction between the facial soft tissue and the underlying bone structure. During *contact analysis* for our example patient, the lower jaw is simulated in a forward manner as defined in the surgery planning stage, thus changes the skin surface shape. Hence predicts the patient specific post surgical appearance.

IV. Finite Element Analysis

The FEA have been used in various orthognathic surgery and soft tissue prediction systems due to the capability of simulating exact physical behavior of human tissues [5,6,7,8,9]. The main characteristics of biological tissue are anisotropic, non-homogeneous, non-linear[10]. However, in this work we assume the facial model as isotropic, homogeneous and linear[11] properties due to limitations on mathematical formulation and hardware resources. Finite Element Analysis (FEA) is a computer based numerical procedure

F. Ibrahim, N.A. Abu Osman, J. Usman and N.A. Kadri (Eds.): Biomed 06, IFMBE Proceedings 15, pp. 558-562, 2007
www.springerlink.com ' Springer-Verlag Berlin Heidelberg 2007

used to determine an approximate solution of a problem (e.g: stress, strain, deformation etc.) for structures too complex to be solved manually or have no theoretical solution. The idea of FEA is that a structure is divided into finite numbers of simple elements such as triangles or quadrilaterals where each element is connected at a point called node. Mathematical equations are used to compute the behavior of each element. Thus, solution of the entire structure is assured for the assembly of all calculation for every element.

In this work, the quadrilateral elements are employed. Mathematical formulation known as shape function, N_i as shown in (1) is used to compute the behavior of each element.

$$N_i = \frac{1}{4}(1+\xi_o)(1+\eta_o) \tag{1}$$

where ξ_o and η_o define the coordinates of the elements.

The strain for every element is calculated by (2)

$$\varepsilon(x) = Ba \tag{2}$$

where each node is defined by a and B is the strain displacement matrix.

The stress of each element which determines the linear property of the soft tissue is computed through Hooke s law in (3)

$$\sigma(x) = E\varepsilon(x) \tag{3}$$

where Young s modulus, E is assigned as an input value.

The elasticity matrix, $[E]$ of the *homogeneous* and *isotropic* properties are defined by two *Lamé* material constants λ and μ described as

$$[E] = \begin{bmatrix} \lambda+2\mu & \lambda & \lambda & 0 & 0 & 0 \\ \lambda & \lambda+2\mu & \lambda & 0 & 0 & 0 \\ \lambda & \lambda & \lambda+2\mu & 0 & 0 & 0 \\ 0 & 0 & 0 & \mu & 0 & 0 \\ 0 & 0 & 0 & 0 & \mu & 0 \\ 0 & 0 & 0 & 0 & 0 & \mu \end{bmatrix} \tag{4}$$

through the elasticity modulus, E and *Poisson's* ratio, v

$$\lambda = \frac{vE}{(1+v)(1-2v)} \tag{5}$$

$$\mu = \frac{E}{2(1+v)} \tag{6}$$

The soft tissue for this work is represented by the constitutive equation governed by

$$\sigma_{ij} = \lambda\delta_{ij}\varepsilon_{kk} + 2\mu\varepsilon_{ij} \tag{7}$$

Finally, all elements are assembled to form the global equation system for continuity of all elements and to equilibrate the structure with its environment. This is carried out by (8)

$$Ka + f = 0 \tag{8}$$

where K defines the stiffness matrix, a is the nodal point and f defines the load at each nodal point.

Boundary conditions known as displacement given to a number of nodes of the mesh are fixed to a predetermined position and are incorporated into (8) for the solution of the linear system. On completion of the solution, the facial model which consists of the skull and skin surface is displaced to a new position and the tissue changes are visualized and simulated.

V. Results And Discussion

In the example case, the front part of the lower jaw was split and moved forward. The soft tissue appearance resulted from the forward mandibular movement based on the finite element approach is shown in Fig. 3.

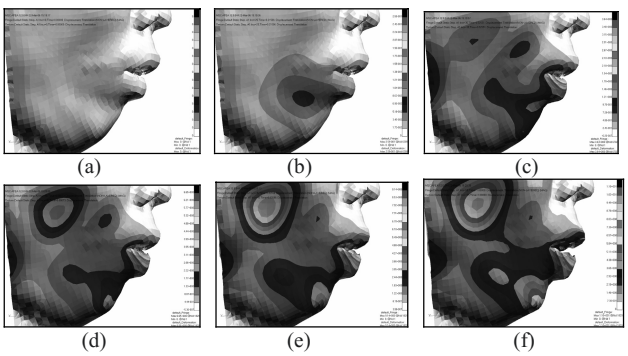

Fig. 3 The simulated appearance shown in incremental time steps at (a):0 at undeformed state, (b):25, (c): 35, (d):40, (e):45, (f):55

The predicted results are shown in Fig. 4 for enhanced visualization.

F. Ibrahim, N.A. Abu Osman, J. Usman and N.A. Kadri (Eds.): Biomed 06, IFMBE Proceedings 15, pp. 558-562, 2007
www.springerlink.com ' Springer-Verlag Berlin Heidelberg 2007

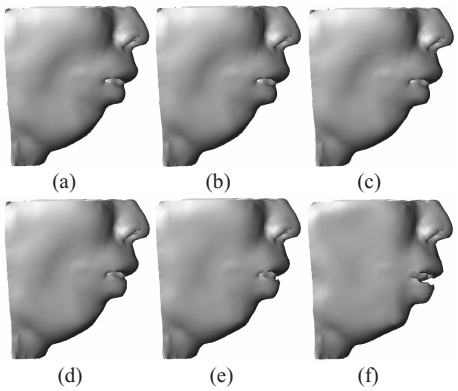

Fig. 4 Realistic facial appearance shown in incremental time steps at (a):0 at undeformed state, (b):25, (c): 35, (d):40, (e):45, (f):55

The qualitative validation of the simulated results is done by means of registration on the actual postoperative photograph as seen in Fig. 5(a). The quantitative evaluation shown in Fig. 5(b) shows the error measurement in the range of pseudo-coloring on color map which defines the distance of the facial areas influenced by the surgery. Positive values indicated by hot colors depict vital areas of facial changes whereas negative values define the contrary. The highest deviation point on the post surgical soft tissue resides in the inner side around the chin facial skin. This supports the reason that movement of the mandible affects most within the chin area of the underlying skin surface.

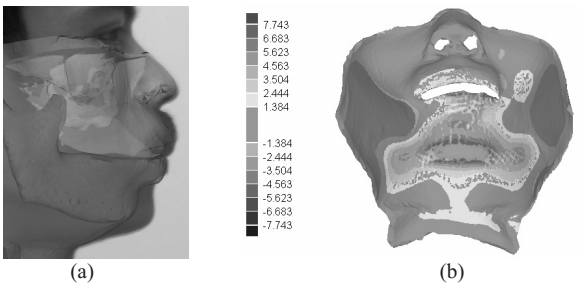

Fig. 5 (a): Qualitative validation between simulated and postoperative photograph and (b): Quantitative comparison shown by color map of pseudo-colors

VI. Conclusions

The work presented in this paper has proven that with the use of MSC.AFEA , an engineering based software package, a post-operative facial appearance prediction and simulation is possible and shown that the presented results are acceptable in this preliminary work. We consider our work as significant in the prediction of facial appearance by means of MSC.AFEA as no similar works have been reported during the research. The *contact analysis* approach is another contribution for the type of simulation employed. The finite element method provided exact mathematical description for the representation of soft tissue behavior of the facial model. Therefore, the simulation of the predicted facial appearance is possible by using this technique.

Our future research is directed towards accurate soft tissue prediction by expanding the constitutive equation for the representation of tissue properties. The current surface model would allow the incorporation of advanced anatomic features such as muscular anatomy, fat and nerves by introducing volumetric models composed of tetrahedral elements. In addition, the understanding of facial muscle anatomy allows for the simulation of dynamic facial expression of the predicted facial appearance. We intend to perform case study on patients with diverse ages, gender and ethnicity in order to achieve improved performance of the orthognathic surgery planning and facial appearance prediction system.

Acknowledgment

The work is supported by the Fellowship Scheme, University of Malaya. We would like to thank the Department of Maxillofacial Surgery, Faculty of Dentistry, University of Malaya for providing us sufficient patient data and the insights of the medical information. A special thank you is conveyed to Mr. Nor Azlan Sulaiman for the consent to work on the data.

References

1. Lorensen W E, Cline H E (1987) Marching cubes: A high resolution 3D surface construction algorithm, SIGGRAPH, ACM Computer Graphics vol. 21, 1987, pp 163-169 (in press)
2. Keeve E, Girod S, Augustin A, Binner A, Girod B (1996) Interactive craniofacial surgery simulation, Proc. 3D Image Analysis and Synthesis, Erlangen, Germany, 1996, pp 219-224 (in press)
3. Koch R M, Roth S H M, Gross M H, Zimmermann A P, Sailer H F (2002) A framework for facial surgery simulation, Proc. of the 18th Spring Conference on Computer Graphics, 2002, pp 33 42 (in press)
4. Zachow S, Gladilin E, Zeilhofer H-F, Sader R (2001) Improved 3D osteotomy planning in cranio-maxillofacial surgery, Proc of MICCAI, 2001, pp 473-481 (in press)
5. Schmidt J G, Berti G, Fingberg J, Cao J, Wollny G (2004) A finite element based tool chain for the planning and simulation of maxillofacial surgery, Proc. of European Congress on Computational Methods in Applied Sciences and Engineering (ECCOMAS), 2004, pp 1-17 (in press)
6. Gladilin E, Zachow S, Deuflhard P, Hege H-C (2001) A biomechanical model for soft tissue simulation in craniofacial surgery, Proc. of MIAR, pp 137-141 (in press)
7. Deng X Q (1988) A finite element analysis of surgery of the human facial tissue, Ph.D. diss, Columbia University
8. Keeve E, Girod S, Pfeifle S, Girod B (1996) Anatomy based facial tissue modeling using the finite element method, Proc. of IEEE Visualization, 1996, pp 1-10 (in press)

F. Ibrahim, N.A. Abu Osman, J. Usman and N.A. Kadri (Eds.): Biomed 06, IFMBE Proceedings 15, pp. 558-562, 2007
www.springerlink.com ' Springer-Verlag Berlin Heidelberg 2007

9. Koch R M, Gross M H, Bueren D F, Frankhauser G, Parish Y, Carls F R (1996) Simulating facial surgery using finite element models, SIGGRAPH, ACM Computer Graphics vol. 30, 1996, pp 421-428 (in press)
10. Fung Y C, (1993) Biomechanics: Mechanical properties of living tissues. Springer-Verlag, New York
11. Obaidellah U H, Narainasamy S (2006) 3D Computer-aided orthognathic surgery planning and simulation system, Proc. of Regional Computer Science Postgraduate Conference 2006, Penang, Malaysia (in press)

Address of the corresponding author:

Author: Unaizah Hanum Obaidellah
Institute: Department of Artificial Intelligence,
Faculty of Computer Science and Information Technology,
University of Malaya.
Street: 50603 Kuala Lumpur
City: Kuala Lumpur
Country: Malaysia.
Email: unaizah12@yahoo.com

F. Ibrahim, N.A. Abu Osman, J. Usman and N.A. Kadri (Eds.): Biomed 06, IFMBE Proceedings 15, pp. 558-562, 2007
www.springerlink.com ' Springer-Verlag Berlin Heidelberg 2007

Age-related Upper Limb Vascular System Windkessel Model using Photoplethysmography

K. Chellappan, E. Zahedi, MA. Mohd Ali

Department of Electrical, Electronics & Systems Engineering, Faculty of Engineering,
Universiti Kebangsaan Malaysia, Bangi, Malaysia

Abstract— **Arterial stiffness is known to be affected by aging, leading to changes in peripheral pulse propagation speed and shape. In this paper, the heart-finger segment of the upper-limb vascular system of six subjects in two age-groups (below 30 and above 55 years) is modeled using a modified Windkessel model. Actual left-ventricle pressure (LVP) data has been used as the input to the model. Circuit simulation results show a significantly higher amplitude for the dicrotic notch and a lower second peak in younger subjects. Among the older subjects, there was a gradual disappearance of dicrotic notch while the second peak appeared later. Comparison of the characteristics of the model output with measured peripheral pulse shows a good degree of conformity with the actual pulse signal. The parameters in the Windkessel model provide a simple, noninvasive means for studying changes in the elastic properties of the vascular system, depending on the age and potentially state of health.**

Keywords— **Windkessel, photoplethysmography, vascular system, aging**

I. Introduction

The Windkessel model is a description of the hemodynamics relationship between aortic blood flow and pressure in human vascular system [1]. It provides insight into the cardiovascular system by using a simple electrical model as in Fig. 1(a). This model has been proposed for the calculation of stroke volume. The proximal elastic arteries, such as the aorta are represented by the compliant reservoir and the output resistance models the resistance of the peripheral bed. Implicit in this model is the total simplification of the vascular system. In Fig. 1(b), blood enters from the left by ventricular contraction, and a relatively steady venous return flows out through the exit resistor R_p. In the Windkessel model, it is assumed that ventricular ejection Q(t) and intra-windkessel pressure (P) are related by the difference between inflow and outflow, assuming that volume elastic modulus E is constant. But Frank, through his observation suggested E as a pressure function not a constant. Outflow through the peripheral resistance is approximately constant, defined as the internal pressure divided by the peripheral resistance R_p assuming external pressure is zero. Both the above assumption can be developed into equation (1).

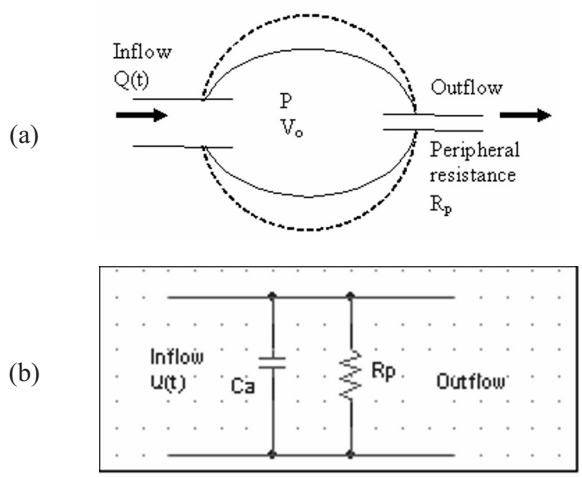

Fig. 1(a) Frank s simple Windkessel model of the arterial vascular system and (b) its equivalent electrical circuit

$$Q(t) = P/R_p = 1/E'\,(dP/dt) \qquad E' = dP/dV_0 \tag{1}$$

To improve the model, a proximal resistance is introduced in the main branch of the circuit followed by an inductor to simulate the resistance and inertia of the fluid in the hydrodynamics model as in Fig.2. Each arterial segment has been characterized by a proximal resistance (r), an inertance (L), and a capacitance (C), as in Fig. 2.

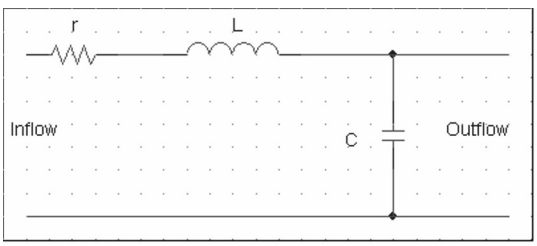

Fig. 2 Modified Windkessel model of a single segment

The inertance represent the blood viscosity, capacitance represents arterial wall compliance and resistance represents arterial diameter change. Accurate results are highly dependent on realistic parameter values being used in the

F. Ibrahim, N.A. Abu Osman, J. Usman and N.A. Kadri (Eds.): Biomed 06, IFMBE Proceedings 15, pp. 563-566, 2007
www.springerlink.com ' Springer-Verlag Berlin Heidelberg 2007

model for various estimation methods have been proposed. Estimating systemic parameters such as total peripheral resistance, total arterial compliance and inertance and characteristic impedance of the proximal aorta and this estimation generally make use of invasive techniques for measuring pulsatile aortic pressure and flow [15].

Arterial stiffness has been found to be one of the main reasons for changes in the propagation of the pulse to the periphery which has significant influence on pulse timing and shape characteristics of PPG [3]. Both the structural and functional changes have equal effect on arterial rigidity. Aging has been classified as structural effect, whereas elevated blood pressure or higher sympathetic activity are known as functional effect. Because of its significance, the origins of arterial rigidity and its dependence on the subjects age and arterial blood pressure have been extensively investigated [4, 5, and 6]. Arterial rigidity is reflected by arterial compliance, C defined by

$$C = dV/dP \tag{2}$$

which shows how much increase exits in the arterial blood volume (dV) in response to the increase in an arterial blood pressure (dP). The compliance will decrease with aging process due to progressive changes in the elastin and collagen content of the arterial wall.

In this study, we propose to utilize a more elaborate Windkessel model driven by a synthetic left-ventricle pressure to investigate the effect of age-related changes on the model parameters. To this end, photoplethysmograms (PPG) are recorded and the output of the model is compared to the real physiological signals. Windkessel models of various complexities were investigated and tested with different left ventricle pressure as input signal [10]. PPG is a non-invasive measuring method of pulsatile aortic pressure and flow. The cardiovascular pulse wave is generated by the elastic nature of the peripheral arteries excited by the quasi-periodic contraction of the heart. The pulse propagation from heart to arterial system will generate the PPG signal detected at the measuring site such as fingers or toe. This method has been adopted in similar research and found to produce acceptable results [2].

II. Materials and Methods

A. Electrical Model

The electrical design and parameter selection has been based on the human arterial system segmentation (Fig. 2. and Table 1).

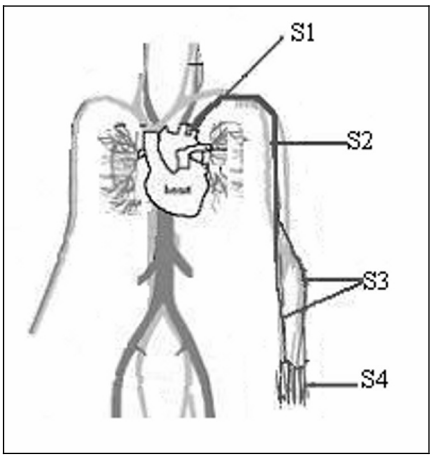

Fig. 3 Upper limb human arterial system

Table 1 Human arterial system segmentation

Arterial segment	Classification	Component
S1	Aorta	Aorta
S2	Major Artery	Subclavian, Axillary and Brachial
S3	Small Artery	Radial and Ulnar
S4	Periphery	Capillaries

In the final model retained for this study (Fig. 4) the upper limb segments are as stated in Table 1. The parameter value of the each segment for finger has been calculated based on equations and arterial segment parameters such as diameter, length and thickness from different literatures and models by previous researches [11, 12 and 13]. The diode represents the aortic valve which ensures one directional flow. The input source left-ventricular pressure (LVP) used in this study were synthesized from the details obtained from human LVP study published previously [14] and is represented in Fig 5.

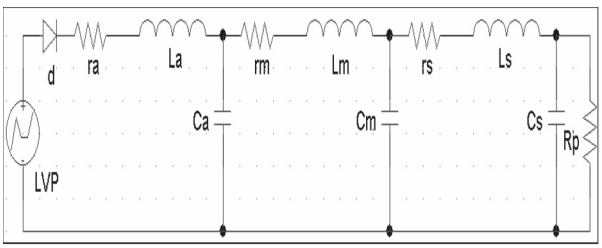

Fig. 4 Modified Windkessel model

F. Ibrahim, N.A. Abu Osman, J. Usman and N.A. Kadri (Eds.): Biomed 06, IFMBE Proceedings 15, pp. 563-566, 2007
www.springerlink.com ' Springer-Verlag Berlin Heidelberg 2007

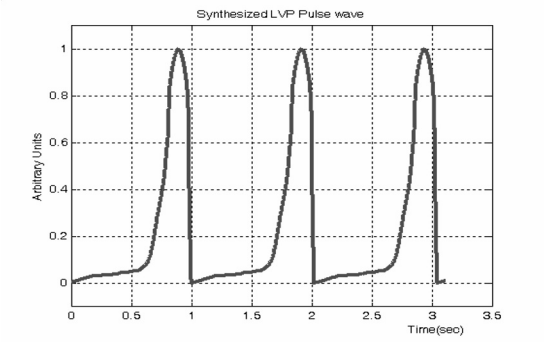

Fig. 5 Synthesized Left-ventricular pressure wave

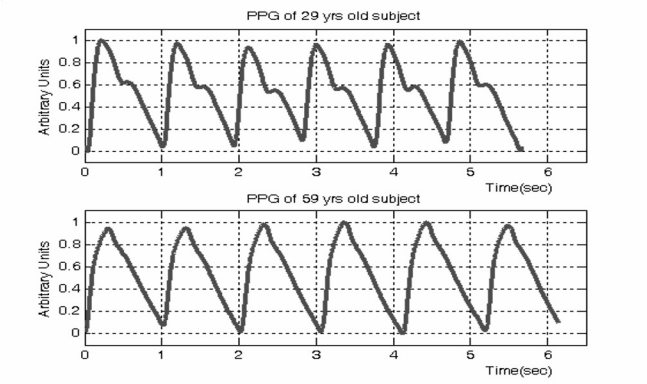

Fig. 6 Example of processed left index finger PPG of healthy (top) young and (bottom) aged subjects

B. Photoplethysmography Recordings and processing

Finger photoplethysmography (PPG) recordings were obtained from six healthy volunteers (all females), three aged below 30 and three above 55 years. The study was performed with the approval of the Hospital Universiti Kebangsaan Malaysia Ethics Committee and after the informed consent of the subjects was obtained. Noninvasive data recording using PPG systems (Dolphin Medical, Inc) were used with one connected probe to the left finger, which were in transmission mode with red light emitting diodes. Measurements were performed in lab environment in supine position while the entire hand was kept steady. Data was recorded at sampling rate of 275 in a computer and saved in ASCII format. Recording was done for a period of 90 seconds after a rest period of 20 minutes at room temperature of 25^{o}C. All the participants were asked to refrain from having beverages containing caffeine, and from smoking for at least 6 hours before the study. The recorded signals were pre-processed first off-line using MATLAB.

- Detrending: For removing outliers, drifts, offset and any movement artifacts the mean value is subtracted from the data.
- Band pass filtering: PPG signals were filtered in the frequency range of 0.6 -15 Hz for removing the effect of the respiratory rhythm and higher frequency disturbances. (The MathWorks, Inc.).

III. Results and discussion

Examples of PPG signals of healthy young female and aged female subjects are recorded and processed as stated above are shown in Fig. 6

Two different set of parameters representing the young (below 30 years) and old (above 55 years) subjects as in Table 2 have been obtained by modification of parameters from the literature [13]. The criteria for retaining the model s parameters was the degree of fitness of PPG signal of both simulated and recorded from human subject. The output of the model is reproduced in Fig.7 to be compared with the recorded traces (Fig. 6) Dataset 1 in Table 2 is captured from literature [13] and dataset 2 is adjusted based on effects. Fig. 7 demonstrates the simulated signal from the modified Windkessel model as in Fig. 4 incorporating parameter values from Table 2.

Table 2 Human arterial system segmentation

Parameter	Dataset 1	Dataset 2	Difference (%)
Aorta Resistance, R_a	1.58 Ω	1.58 Ω	0%
Aorta Inductance, L_a	15.12 H	15.12 H	0%
Aorta Capacitance, C_a	0.09698 μF	0.09698 μF	0%
Major Artery Resistance, R_m	300 Ω	1200 Ω	300%
Major Artery Inductance, L_m	45.22 H	45.22 H	0%
Major Artery Capacitance, C_m	0.2586 pF	0.2586 pF	0%
Small Artery Resistance, R_s	226.69 Ω	726.69 Ω	**!Syntaxfehler, .**
Small Artery Inductance, L_s	223.13 H	243.13 H	**!Syntaxfehler, .**
Small Artery Capacitance, C_s	0.137 μF	4.374 μF	(3093%)
Capillary Resistance, R_p	1.78 TΩ	1.78 TΩ	0%

From a parameter comparison between young and aged subjects in Table 2, the following statements can be made:

- There are no changes in aortic and major artery compliance and inductance.
- There is no change in aortic resistance.
- There are drastic increases in major and small artery resistance.
- There is a small increase in the small artery inductance.
- The capillary resistance does not change.

PPG usage in the detection of peripheral vascular age related changes in shape characteristics at individual fingers [7] and toe [8] has been established by frequency analysis,

F. Ibrahim, N.A. Abu Osman, J. Usman and N.A. Kadri (Eds.): Biomed 06, IFMBE Proceedings 15, pp. 563-566, 2007
www.springerlink.com ' Springer-Verlag Berlin Heidelberg 2007

showing that there is a general reduction in the harmonic components of the pulse in older subjects. Analysis of PPG pulse contour at the finger demonstrated that the presents of dicrotic notch disappears and the second peak position increases in older subjects [9].

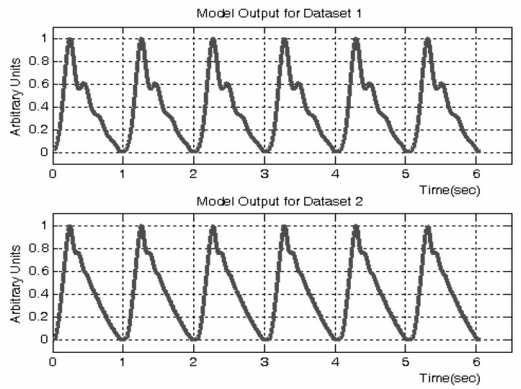

Fig. 7 Example of modified Windkessel model output for parameters in Table 2

IV. Conclusions

The above findings agree with the physiological effects of aging effect (most effects are on the peripheral arteries rather than the proximal arteries). Reduction of arterial inner diameter in both proximal and peripheral is a significant consequences of aging [1,3]. The results obtained in this study show that suitable values for arterial parameters can be obtained non-invasively from the proposed technique. Analysis of the output curve fittings suggests that a more realistic synthesized LVP waveform would probably help to improve the performance of the model. Analyzing pulse shape characteristics allows comparisons with PPG pulses from suspected vascular diseased subjects as well as age-related changes. However, a more detailed analysis of vascular diseased subjects should be carried out with comparison to a normal age-matched range.

Acknowledgment

This work was partially supported by an Intensive Research Priority Areas grant (IRPA-02-02-0106-EA258) from the Ministry of Science and Technology, Malaysia.

References

1. McDonald DA (1974) Blood Flow in Arteries. 2nd ed. Arnold, London
2. John A, Alan M. (1999) Modeling the relationship between peripheral blood pressure and blood volume pulses using linear and neural network system identification techniques. *Physiological Measurement* 20**:** 287-301
3. John A, Alan M (2003) Age-related changes in the characteristics of the photoplethysmographic pulse shape at various body sites. Physiology Measurement. Vol. 24. 297 307
4. Nichols W M, O Rourke M F (1998) McDonald s blood flow in arteries: theoretical, experimental and clinical principles. Arnold, London
5. Avolio A et *al (*1985) Noninvasive determination of aging changes in the arterial pulse. Fed. Amer. Soc. Exp. Bio. Vol. 2:No. 4: A125
6. Nichols W W et al (1990) Effects of age on ventricular vascular. Am J Cardiol. 55: 1179 - 1184
7. Sherebrin M H, Sherebrin R Z (1990) Frequency-analysis of the peripheral pulse-wave detected in the finger with photoplethysmography. IEEE Trans. Biomed. Eng. 37:313 - 317
8. Oliva I, Roztocil K (1976) Fourier analysis of the pulse wave in obliterating arteriolerosis. VASA 5: 95 100
9. Millasseau et al (2002) Determination on age-related increases in large artery stiffness by digital pulse contour analysis. Clinical. Science. 103: 371 - 329
10. K. Chellappan, Zahedi E, Ali MAM (2006) Windkessel Model Of The Arterial Vascular System Using Photoplethysmography. SPS2006, Universiti Kebangsaan Malaysia, Bangi , Malaysia, 29-30 August 2006.
11. Devasahayam, S. R. 2000. *Signals and Systems in Biomedical Engineering (Signal Processing and Physiological Systems Modeling)*. New York: Kluwer Academic/Plenium Publishers.
12. Milnor, W.R. 1992. *Hemodynamics*. Baltimore/London: Williams & Wilkins.
13. Snyder, M.F. & Rideout, V.C. 1968. Computer Modeling of The Human Systemic Arterial Tree. *Pergamon Press. Great Britain* **1**: 341-353.
14. Walter J. P et al. (1995) Paracrine Coronary Endothelial Control of Left Ventricular Function in Humans. Circulation. 92:2119-2126
15. Westerhof, N E, Van Den Bos GC. 1973. Influence of central and peripheral changes on the hydraulic input impedance of the systemic arterial tree. Med & Biology, Vol: 11: 710 723.

Address of the corresponding author:

Author : Kalaivani Chellappan
Institute : Universiti Kebangsaan Malaysia
Street : Department of Electrical, Electronics & Systems Engineering, Faculty of Engineering
City : 43600 Bangi
Country : Malaysia
Email : kckalai@unitar.edu.my

F. Ibrahim, N.A. Abu Osman, J. Usman and N.A. Kadri (Eds.): Biomed 06, IFMBE Proceedings 15, pp. 563-566, 2007
www.springerlink.com ' Springer-Verlag Berlin Heidelberg 2007

Computational Analysis of Asymmetric Arterial Stenosis with Applications of Fluid-Solid Interaction

A. Mojra, M. Tafazzoli-Shadpour and E. Y. Tafti,

Department of Biomedical Engineering, Amirkabir University of Technology, Tehran, Iran.

Abstract **Plaques have very complex structures. Real artery stenoses are rarely axisymmetric in the nature. This work is concerned with the simulation of plaque severity and eccentricity effects on arterial hemodynamic parameters in models of atherosclerotic carotid arteries with asymmetric stenoses using fluid-solid interaction (FSI). The parameters include wall shear stress, wall stress concentration and deformation. The investigation is done with the aid of finite element method for solving the structure and TDMA and SIMPLE methods in CFD for the fluid domain solution using ANSYS software. To overcome the software inconsistency in FSI mode, a new mathematical program is designed using incremental boundary iteration method. A linear elasticity approach is implemented in modeling the arterial wall and Navier-Stokes equations govern the fluid domain. Fluid separation zones, shear stress variation and fluctuation in the distal part of stenosis, minimum structural deformation, were observed under physiological and non-physiological conditions. Critical condition is determined due to severity variations which may lead to thrombus formation and possible plaque rupture. To illustrate the accuracy of proposed method, the results are compared with published experimental and numerical.**

Keywords—**Stenosis, Blood Flow, Fluid Solid Interaction, Plaque rupture, Finite Element method**

I. Introduction

One of the major causes of world mortality is related to patients with high grade of stenoses in their arteries, which alter significantly blood flow characteristics. The altered hemodynamics may further influence the development of the disease and arterial deformity, and change the regional blood reology [Smedby, 1997]. This is more significant in major arteries such as carotid and coronary arteries. High grade stenoses increase flow resistance in arteries which leading to blood pressure elevation necessary to maintain blood supply [2]. The resultant high arterial pressure causes acceleration of flow velocity when passing through the stenotic region. High shear stress and low or negative pressure at the throat are parameters affecting arterial hemodynamics. Also, at distal part, low shear stress, presence of eddies flow separation, and wall compression or even collapse, are major factors affect the pattern of the disease progress [3].

Biomechanical analysis of blood flow and arterial wall can be useful for quantification of physiological conditions under which the artery may be at risk. Evaluating deformations and stress might be of importance. Localized pattern of the structural stress is useful in predicting the endothelial cells pathology [3].

Study of the flow characters in a stenotic region has been investigated by many theoretical and experimental efforts. But, compared to the noticeable large amount of publications on flow investigations, relatively fewer publications can be found investigating both blood flow and arterial mechanics using models with fluid structure interactions (FSI). Besides, all the sets of results will be more applicable when we consider the real condition. We know that Real artery stenoses are rarely axisymmetric in the nature. They usually have very complex structures and mechanical properties. Plaque eccentricity is an important factor in the arterial wall hemodynamics which hasn t been mentioned that much in the previous published data.

Tang et al. [1,2,5] has proposed 2D and 3D and investigated the steady/pulsatile flow in elastic axisymmetric/asymmetric stenotic tubes. Also the effect of nonlinear mechanical properties of the artery wall and the plaque has been investigated taking fluid-solid interactions into account. Yamaguchi et al considered fluid structure interactions in the collapse and ablation of atheromatous plaque in coronary arteries and found that wall stress distribution has a localized pattern and that the dragging force from fluid flow has a considerable effect on wall compression.[6]. Ku et al. conducted a study of predicted and experimental wall collapse in models of highly stenotic arteries. [7]. Experimental models were constructed mainly from Poly Vinyl Alcohol (PVA) hydrogel which its mechanical properties are known to be very similar to that of bovine carotid artery. Moyarri and Zendehbodi [4] performed numerical studies where they investigated the effects of elastic property of the wall on flow characteristics through arterial stenoses. 2D axisymmetric model with pulsatile pressure waveform was introduced. Cavalcanti [8] did numerical simulation to examine the hemodynamics in a mild stenosis with consideration of pulsatile wall motion. Giddens[9] used computational methods to investigate the interaction between fluid mechanics and the artery wall. Bathe [10] introduced an axisymmetric thick-wall model

F. Ibrahim, N.A. Abu Osman, J. Usman and N.A. Kadri (Eds.): Biomed 06, IFMBE Proceedings 15, pp. 567-571, 2007
www.springerlink.com ' Springer-Verlag Berlin Heidelberg 2007

with fluid structure interactions for pulsatile blood flow through a compliant stenotic artery.

This research investigates effects of plaque severity mechanical parameters in models of human stenotic carotid arteries such as blood flows, pressure drop, wall shear stress and wall stress and consequently the progress of atherosclerosis. Also, we considered the effect of plaque eccentricity on the mentioned parameters, especially Fluid separation zones, shear stress variation in the distal part of stenosis and minimum structural deformation, and compare the results with the axisymmetric case.

II. Methodology

A typical human carotid artery is modeled using FSI technique to investigate the effects of plaque severity and eccentricity on shear and circumferential stress values for the physiological flow and pressure conditions. The arterial wall dimensions are according to previously published data [4]. Arterial wall is assumed to be elastic, homogeneous, isotropic, and nearly incompressible. Young s Modulus is E=361kPa and υ=0.49. Using the incremental linear elasticity approach let **v**, **σ**, and **ε** be the displacement, stress and strain vectors (tensors) and the superscript 0 for the values of those variables at last iteration, and ignoring inertial forces, we have the governing equations for the wall model:

$$\sigma = D(\varepsilon - \varepsilon_0) - \sigma_0 \tag{1}$$

$$\sigma^S_{ij,j} = 0 \tag{2}$$

$$\varepsilon_{ij} - \varepsilon_{ij}{}^0 = [(v_i - v^0{}_i)_j + (v_j - v^0{}_j)_i]/2 \tag{3}$$

$$d^S\,|_{innerwall} = d^f\,|_{innerwall} \tag{4}$$

$$\sigma^S_{ij}.n_j\,|_{outerwall} = 0 \tag{5}$$

$$\sigma^S_{ij}.n_j\,|_{innerwall} = \sigma^f_{ij}.n_j\,|_{innerwall} \tag{6}$$

The flow is assumed to be laminar, Newtonian, viscous and incompressible. No penetration of the fluid through the arterial wall occurs. Boundary conditions are concerned with having constant critical pressure in the inlet, and constant outlet pressure. The viscosity and density of blood are taken to be $0.0048^{Pa.sec}$ and $1035^{kg/m3}$ respectively. Reynolds number calculated at the inlet is 350 which permit to assume laminar regime [11] .The Navier-Stokes equation and conservation of mass govern the fluid flow and the vector form states as:

$$\nabla\vec{u} = 0 \tag{7}$$

$$\vec{u}\nabla\vec{u} = -\frac{1}{\rho}\nabla P + \upsilon\nabla^2\vec{u} \tag{8}$$

$$((\vec{u} - \vec{u}_g).\nabla)\vec{u} = -\frac{1}{\rho}\nabla P + \upsilon\nabla^2\vec{u} \tag{9}$$

Where **u**, P and $\mathbf{u_g}$ are the fluid velocity vector, pressure and mesh velocity vector.

The investigation is done with the aid of finite element method for solving the structure and TDMA and SIMPLE methods in CFD for the fluid domain solution using ANSYS 9.0 software. To overcome the software inconsistency due to material and geometrical complexities, a new mathematical program was designed for the fluid-solid coupling using incremental boundary iteration method. This code performs the load transfer between fluid and solid, mesh and geometry update in each iteration and convergence checking for the termination of iteration between the fluid and solid domain until a steady solution is achieved.

III. Results and discussion

Figure 1 shows effects of plaque severity in a axisymmetric stenosis, on the inlet pressure for constant outlet pressure and flow rate. The severity is elevated from 10% to 85%. Results show that to maintain constant downstream blood supply, elevation of severity leads to non-linear increase of inlet pressure with critical conditions at severity of 78% when the upstream pressure increases to about 100mmHg. Further increase of severity results in marked rise of upstream pressure which affects the systemic pressure.

Figure 2 shows effects of eccentricity for a 70% asymmetric stenosis on wall deformation along the thicker side of the arterial wall (θ=270˚). Upstream pressure is set to the critical value achieved pressure which is equal to 100mmHg. Downstream pressure is decreased to 10mmHg to observe wall deformation and collapse conditions.

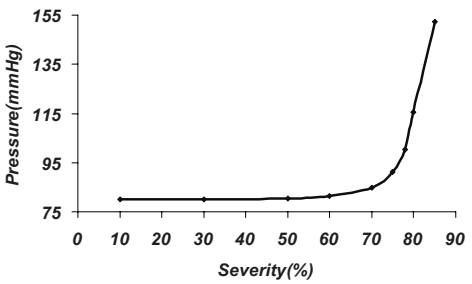

Fig. 1, Effect of plaque severity on the inlet pressure

Result shows a much lower deformation exactly in the post-stenotic region for the asymmetric plaque. It is also clearly seen that a small decrease in the downstream

F. Ibrahim, N.A. Abu Osman, J. Usman and N.A. Kadri (Eds.): Biomed 06, IFMBE Proceedings 15, pp. 567-571, 2007
www.springerlink.com ' Springer-Verlag Berlin Heidelberg 2007

pressure cause the artery collapse. This event may occur earlier as the plaque eccentricity increase.

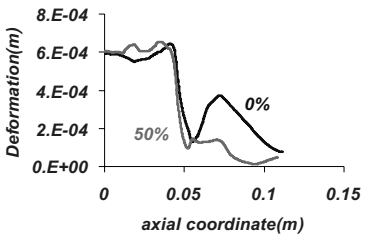

Fig. 2, Effect of eccentricity on the wall deformation along thicker side of the wall

Figure 3 shows the velocity vectors in the region near the stenotic part. Fluid separation region is clearly larger in the asymmetric model, which is along the thicker side of the wall. On the thinner side, the intensity of the vectors is much greater than the axisymmetric model.

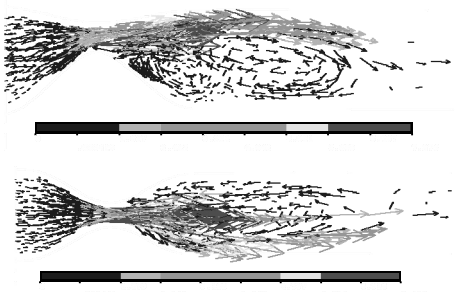

Fig. 3, Velocity vectors near the stenotic region, for 70% Stenosis along the arterial length and 50% eccentricity (left), axisymmetric stenosis (right).

Figure 4 is the pattern of shear stress on the arterial wall along the thicker and thinner side of the artery (θ=270˚, 90˚), which have marked peaks in the throat and sharp decrease (or even negative) in the distal. The results also show that the maximum of shear stress in the eccentric model along the thicker side of the arterial wall is about 12% higher than that of the axisymmetric model. But, it becomes lower about 17%, when we compare the thinner wall side with the axisymmetric stenosis. However the increase is due to the formation of eddy currents in downstream of the plaque, which causes great velocity gradients and thus high shear stress in the post-stenotic region. On the opposite side, great increase of velocity near the thinner side of the wall will decrease the gradients there.

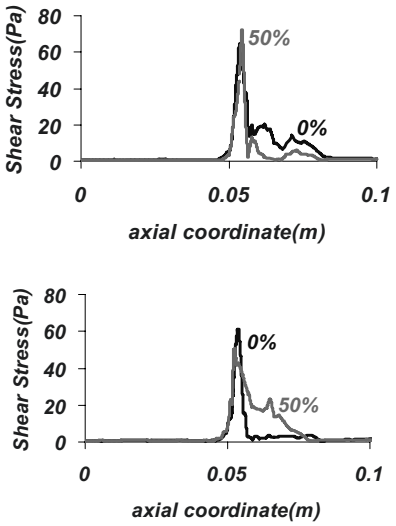

Fig. 4, Shear stress pattern for 70% Stenosis and 0,50% eccentricity along the thicker side of the arterial wall (up) and thinner side of the arterial wall (down).

circumferential stress contours is plotted in Figure 5. Maximum stress happens in the upstream of the artery. By increasing the plaque eccentricity, it moves toward the upstream of the tube. As we come around the stenotic region stress magnitude will decrease and even becomes negative. Minimum stress will go futher the plaque by increasing the tube symmetry.

The magnitude of minimum circumfreantial stress on the thinner side of the artery with asymmetric plaque is 9560.8 ^{Pa}when in non-eccentric model it is about 6368 ^{Pa} which is approximately 50% less than eccentric plaque. This higher amount pf stress may be one of the possible causes of plaque rupture.

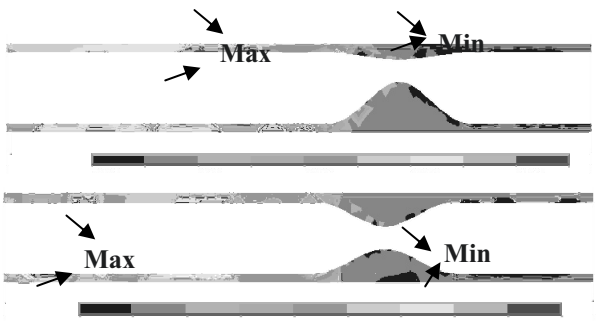

Fig. 5, Circumferential stress contours for 70% Stenosis along the arterial length (thinner and thicker side of the wall) and 50% eccentricity (up), axisymmetric stenosis (down).

F. Ibrahim, N.A. Abu Osman, J. Usman and N.A. Kadri (Eds.): Biomed 06, IFMBE Proceedings 15, pp. 567-571, 2007
www.springerlink.com © Springer-Verlag Berlin Heidelberg 2007

Figure 6 shows the pressure along axial coordinate on the arterial wall for two models with different eccentricities. Results show a marked pressure drop at throat and low level of distal pressure. Minimum pressure for 50% plaque eccentricity is -71.36^{mmHg} and for axisymmetric model is -77.46^{mmHg}, which occurs in the throat for both of them. This is mainly because of larger throat cross section in the asymmetric model compare with the axisymmetric one.

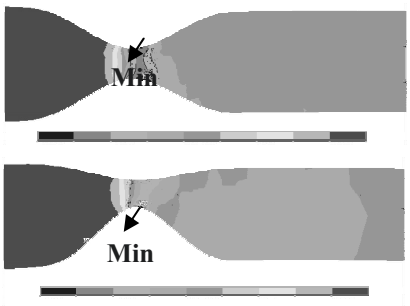

Fig. 6, Pressure contours for 70% Stenosis along the arterial length and for 50% eccentricity (up), axisymmetric stenosis (down)

Table 1 shows effects of eccentricity for a 70% stenosis. In order to make the modeled flow resemble as much as possible to the physiological flow, the idea of constant blood supply is adopted. It is assumed that a fully developed parabolic profile enters the inlet with a constant flow rate of 5.1$^{ml/sec}$ reported by Osenberg (1991) as the mean flow rate of the common carotid artery. Downstream pressure of the stenosed artery is maintained to certain level so that blood flow after passing the stenosis would be possible in downstream tissues. Therefore a uniform pressure at the outlet is specified. The value set as P_{out} is the mean downstream pressure of the common carotid artery given by Osenberg.

Table 1, comparison of minimum wall deformation and maximum shear stress for three cases, with the assumption of constant flow rate

Items compared	Case1	Case2	Case3
Severity (diameter)	70%	70%	70%
Eccentricity	0%	50%	75%
Flow rate(ml/s)	5.1	5.1	5.1
Pout(mmHg)	85	85	85
Pin(mmHg)	91.6	92.5	93
$\tau_{max}(\theta=0)$(Pa)	17.554	19.32	19.726
$\tau_{max}(\theta=180)$	17.6	17.475	15.191
$U_{min}(\theta=0)(\mu m)$	6.74	1.65	1.22
$U_{min}(\theta=180)$	6.74	15.34	19.48

As it is clear from the table, relations between different parameters for different cases are the same as previous, in which we applied constant blood pressure for the inlet and outlet. Differences are only due to the lower amounts of parameters, which are related to the much smaller pressure gradients.

IV. Conclusion

Effects of plaque severity and eccentricity in hemodynamic and mechanical parameters were studied in 3D axisymmetric and asymmetric models of atherosclerotic carotid arteries using FSI. Results showed marked influence of plaque severity and eccentricity on mechanical parameters. It can be concluded that plaque initiation and growth may be influenced by mechanical parameters. An increase of plaque severity or eccentricity may contribute to further endothelial damage due to critical stress values. This might cause plaque growth and consequently plaque rupture. To maintain blood supply in stenotic and post-stenotic regions, the systemic pressure increase in pre-stenotic region until a critical point. Increase of plaque eccentricity leads to higher wall deformation (even collapse), higher shear stress and higher circumferential stress. This might cause distal tissue damage.

References

1. D. Tang, Ch. Yang, H. Walker, Sh. Kobayashi, D.N. Ku, (2002) Simulating cyclic artery compression using a 3D unsteady model with fluid-structure interactions, Computers and Structures, 80, 1651-1665.
2. D. Tang, Ch. Yang, D.N. Ku, (1999) A 3-D thin-wall model with fluid-structure interactions for blood flow in carotid with symmetric and asymmetric stenoses , Computers and Structures, 72, 357-377.
3. Constantinides P., (1990) Plaque hemorrhages, their genesis and their role in supra-plaque thrombosis and atherogenesis. In: Pathobiology of the Human Atherosclerotic Plaque. New York: Springer-Verlag, 393-411.
4. M.S. Moayeri, G.R. Zendehbudi, (2003) Effects of elastic property of the wall on flow characteristics through arterial stenoses, Journalof Biomechanics, 36, 525-535.
5. D. Tang, Ch. Yang, D.N. Ku, A 3-D thin-wall model with fluid-structure interactions for blood flow in carotid with symmetric and asymmetric stenoses , Computers and Structures, 72, 1999, 357-377.
6. T. Yamaguchi, T. Kobayashi, and H. Liu, Fluid-wall interactions in the collapse and ablation of atheromatous plaque in coronary arteries, Proceedings of the Third,World Congress of Biomechanics, pp. 20, 1998
7. D. N. Ku, M. N. Zeigler, R. L. Binns and M. T. Stewart, A study of predicted and experimental wall collapse in models of highly stenotic arteries, Proc. 2nd Intl Symp on Biofluid Mechanics and Biorheology, D. Liepsch, ed., (1989), 409-416.
8. Cavalcanti, S., 1995. Hemodynamics of an artery with mild stenosis. Journal of Biomechanics 28, 387-399.

F. Ibrahim, N.A. Abu Osman, J. Usman and N.A. Kadri (Eds.): Biomed 06, IFMBE Proceedings 15, pp. 567-571, 2007
www.springerlink.com © Springer-Verlag Berlin Heidelberg 2007

9. Ahmed, S.A., Giddens, D.P., 1984. Pulsatile post-stenotic flow studied with laser Doppler anemometry. Journal of Biomechanics 17,695-705.
10. M. Bathe, A fluid-structure interaction finite element analysis of pulsatile blood flow through a compliant stenotic artery, B. S. Thesis, MIT, 1998
11. D. Tang, Ch. Yang, Sh. Kobayashi, J. Zheng, R.P, Vito, Effect of stenosis asymmetry on blood flow and artery compression: a three-dimensional fluid-structure interaction model, Annals of Biomedical Engineering, 31, 2003, 1182-1193.

Address of the corresponding author:

Author: Afsaneh Mojra
Institute: Amirkabir University of Technology, Department of Biomedical Engineering (15914)
Street: Hafez Avenue
City: Tehran
Country: Iran
Email: Afsaneh_Moj

F. Ibrahim, N.A. Abu Osman, J. Usman and N.A. Kadri (Eds.): Biomed 06, IFMBE Proceedings 15, pp. 567-571, 2007
www.springerlink.com ' Springer-Verlag Berlin Heidelberg 2007

Computer based quantification of the mean Achilles tendon thickness in US-images – effect of tendinosis

Sandrock, M., MD

Freiburg University Hospital, Centre for Internal Medicine, Department for Rehabilitative and Preventative Sports Medicine, D-79106 Freiburg, Germany

Abstract— ***Background and purpose:*** **B-mode measurement of the sagital diameter of the Achilles Tendon (AT) based on manual tracing (MT) procedures is partly dependent on the subjectivity of the reader. The aim of this study is to compare the tracing results of the AT boundaries with an automatic identification (AI) process, already established for the detection of the Intima-Media-Thickness (IMT), and computer-assisted MT.**

Methods and Results: **The detection of the AT boundaries was performed in 115 US images of the AT including the anterior boundary of the calcaneus bone. The measured section (starting point 4cm away from the anterior boundary of the calcaneus bone) amounted 3 cm and was divided in 3 sub segments (1 cm each). Intra- and inter-reader/ - observer variability for the mean and the maximum AT Thickness (ATT) with AI and MT were evaluated. A normal group and a group with manifest tendinosis were compared concerning mean ATT (mATT) and maximum ATT (maxATT).**

Using MT the intra- and inter-reader variability amounted 3.0 % and 6.8 %, respectively, using the AT 1.6 % and 3.9 % mm. Mean and maximum ATT were measured systematically lower by AI compared with MT in all regions by 0,4 mm. The AI procedure was most suitable in the 2nd segment. The mATT and maxATT were correctly detected in 93.9 % and 96.6 % of the images.

Conclusion: **The AI procedure detects the ATT with a high precision in all three segments. The most robust measurement was reached in the 2nd segment. It eliminates most of the inter-/intra-reader variability of the ATT measurement using MT. We suggest using the new method for new gold-standard of the ultrasound analysis of the AT.**

Keywords—**Tendinsosis, automatic analysis, Achilles tendon, pattern recognition, ultrasound**

I. Introduction

The incidence of Achilles Tendon (AT) ruptures, tendinopathia and tendinosis in the developed countries has increased during the last years [1, 2] Frequently these injuries are associated with overstress in running and ball games [1-3]. For qualitative diagnostics of these acute and chronic disorders in AT B-mode ultrasound (US) has become the gold-standard during the last years [4-7]. B-mode has more spatial and contrast resolution for superficial tendon structures than MRI does and allows a dynamic, real-time examination [2]. The main advantages of US are cost-effectiveness, little time-consuming examinations, wide accessibility and its non-invasivity [3, 7, 8]. The information get during an US investigation often render unnecessary more costly imaging examinations, such as MR imaging [7].

The ATT can be measured in US images and is an established parameter to quantify the degeneration of the AT [4, 5, 11]. However, as the main problem of the current manual examination (MA) of the ATT in US images are named the intra (IAO)- and especially the inter-observer error (IRO) due to the examiner s experience [3]. Automatic detection like it is applied for the US of the carotids [12] could reduce variability and afford a better reproducibility of the AT US. The aim of this paper was the establishment of a new contour detection program based on the algorithm for the IM Thickness (IMT) analysis for the AT US which allows to detect the maximal and mean ATT in a more objective and reproducible way.

II. Methods

Study Population: The study group consists of 59 subjects. 35 normal (NO) subjects (CS: age: 38,7–10,9) and 24 subjects (MTS: age: 45,8–11,4) with a manifest tendinosis of the Achilles tendon (TAT) took part in the examination. The excluded of the study were persons with a tendinitis, a rupture of the AT, an insertional tendinosis and a familiar hyperchoesterinaemia. None of the healthy volunteers had any signs of a TAT according to their history and the clinical examination. All examination was done by an orthopaedist. No healthy subject showed any characteristics of a TAT such as increase of thickness or hypoechogenic areals. In the MTS all patients had pain of the Achilles tendon for more than 3 months, 3 have a unilateral and 21 have a bilateral tendinosis. The CS and the MTS group were age matched in order to exclude age as a strong confounder of the Achilles tendon thickness (ATT).

Ultrasound Examination: The ultrasound examination was performed after a 15 min sitting period. A Toshiba SSA, Japan, high resolution US scanner was used with a

F. Ibrahim, N.A. Abu Osman, J. Usman and N.A. Kadri (Eds.): Biomed 06, IFMBE Proceedings 15, pp. 572-575, 2007
www.springerlink.com ' Springer-Verlag Berlin Heidelberg 2007

linear 10 MHz transducer and an aperture of 52 mm. For the examination of the Achilles tendons the ankles of the study subjects were fixed in total dorsoflexion. The transducer was positioned in a rectangle position on the tendon. The Achilles tendon was first scanned in a longitudinal image and then the transducer was rotated by 90 degree to achieve an image in the cross-sectional axis which is standard in the AT US. In this position the near and far boundaries were demonstrated. The images were intermittently stored with the cine view function of US system and directly afterwards an image was digitized on a digital disk (Sony DKR-700, Japan) to minimize the intra-beat variability of the ATT. All examinations were also videotaped in order to be able to give a further interpretation of the US images if questioned. 30/24 US images were taken by two independent sonographers in order to visualize the inter- and intra-observer variability. The readers of the images were blinded to the tendon status of the person whose images were analysed.

Manual and automatic identification process of the AT layers: The far and the near wall were defined as the two first echogenic layers across the more hypoechogenic zone inside the AT. Near and far wall were retraced automatically and manually (length 3cm). The segment was divided in 3 sub segments (each 1 cm). The starting point of the segment is the anterior boundary of the calcaneus to guarantee a better reproducibility and standardisation. Manual and automatic detection were processed by the aid of the same starting point.

In a manual analysis 115 images was performed. Far and near wall were retraced five times. The average of these five measurements was used to quantify the ATT. The maximum ATT was defined as the highest value of the ATT in the segment, the mean ATT was the arithmetic mean of 72 measurement points in each 1 cm sub segment (depending on the magnification of the image).

The AI process takes into consideration the echo gradient values and continuities of the two boundaries of the AT [14, 15]. (Fig. 1)

Table 1: Mean – SEM for the mean and maximum (max) ATT (in mm) between readers and procedures. Data are presented for all three segments of the Achilles tendon, respectively (n=70 images for each segment)

	MT		**AI**		**MT5x**
	Reader 1	**Reader 2**	**Reader 1**	**Reader 2**	**Reader 1**
1st segment					
Mean (in mm)	5,9–0,2	5,4–0,2	5,2–0,2	5,2–0,2	5,6–0,2
Max (in mm)	6,2–0,2	5,6–0,2	5,5–0,2	5,6–0,2	5,8–0,2
2nd segment					
Mean (in mm)	6,0–0,2	5,5–0,2	5,4–0,2	5,2–0,2	5,6–0,2
Max (in mm)	6,2–0,2	5,7–0,2	5,7–0,2	5,6–0,2	5,8–0,2
3rd segment					
Mean (in mm)	5,6–0,2	5,2–0,2	4,9–0,2	4,9–0,2	5,3–0,1
Max (in mm)	5,9–0,2	5,5–0,2	5,4–0,2	5,3–0,2	5,6–0,2

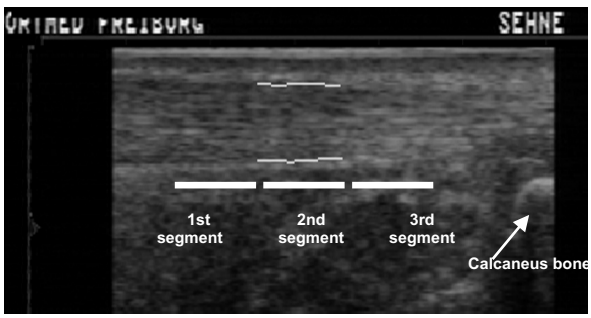

Fig. 1 Magnification of two automatic identification of the AT boundaries in the 2nd segment (starting point 4cm away from the anterior boundary of the calcaneus bone)

III. Results

Arithmetic mean and standard deviation (SEM) of the parameters are shown in (Table 1) The comparison between AI and MT5x revealed a small difference of 0,4 mm with systematically higher values for the manual tracing (Table 1, Table 2).

The Bland & Altman analysis showed a significant correlation between the two methods (MT and AI procedure).

In the ultrasound analysis TAT compared to NO had a significantly higher mATT and maxATT (Table 4).

Reproducibility of data: In 18 subjects of the NO group the examination was performed twice by the same observer and in 12 subjects twice by two different observers. Automatic and manual detection were done by two different reader in 70 images. The intra- (IAO) and inter-observer error (IRO) and Intra-(IAR) and inter-reader error (IRR) were calculated according the formula S=S.D. For the manual method IAO and IRO were 17,8 % and 20,7 % of the mean ATT. For automatic detection IAO and IRO were 5,6 % and 4,8% of the mean ATT respectively. This represents a reduction of 69 % and 77%, respectively. The IAR and IRR were 1,6% and 3,9% for the automatic detection, 3,0% and 6,8% for the manual method, respectively. The reduction amounts 45% and 43%, respectively.

F. Ibrahim, N.A. Abu Osman, J. Usman and N.A. Kadri (Eds.): Biomed 06, IFMBE Proceedings 15, pp. 572-575, 2007
www.springerlink.com ' Springer-Verlag Berlin Heidelberg 2007

Table 2: Mean – SEM for the mean and maximal (max) ATT (in mm) between readers and procedures. Data are presented for all three processed segments, respectively (n=70 images for each image)

	Reader 1		Reader 1	
	MT 1	**MT 2**	**AI 1**	**AI 2**
1st segment				
Mean (in mm)	5,9–0,2	5,4–0,2	5,2–0,2	5,2–0,2
Max (in mm)	6,2–0,2	5,8–0,2	5,5–0,2	5,4–0,2
2nd segment				
Mean (in mm)	6,0–0,2	5,4–0,2	5,4–0,2	5,5–0,2
Max (in mm)	6,2–0,2	5,7–0,2	5,7–0,2	5,7–0,2
3rd segment				
Mean (in mm)	5,6–0,2	5,1–0,2	4,9–0,2	5,0–0,2
Max (in mm)	5,9–0,2	5,5–0,2	5,4–0,2	5,3–0,2

IV. Discussions

The main findings of this paper are 1) the AI identification procedure can improve the measurement of the ATT compared to MT procedures, 2) the AI identification procedure detects the maximal sagital diameter more reliable and robust than the MT procedure and 3) TAT and NO show significant differences concerning mATT and maxATT.

In conclusion, the AI program presented provides time-saving, accurate measurements of the ATT compared with the computer-assisted MT in all three processed segments, minimizing the reader associated variability of MT. The AI process represents a clear improvement compared to the manual tracing procedures and the manual punctual measurements. The AI allows a more objective diagnostics of tendinosis which are associated which a significant increase of thickness.

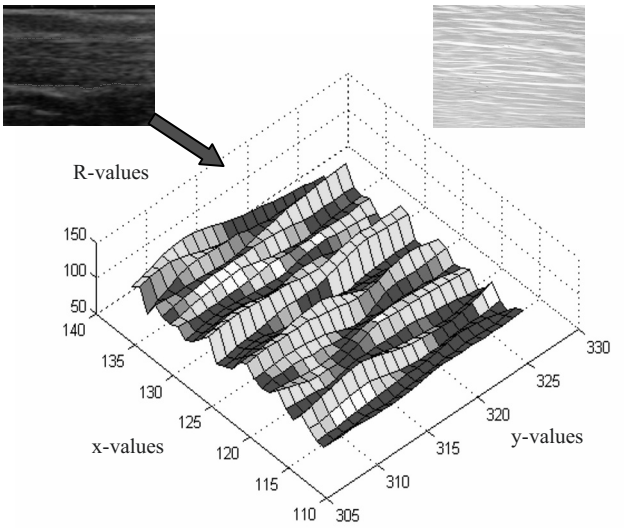

Fig. 2 The texture of the AT in an US image of a normal healthy AT. X- and y values are in pixels, the R-values represent the grey-intensity of the image. Based on this 3D-model new parameters could be designed. On left US of the AT, on the right histological images

References

1. Ulreich N, Kainberger F, Huber W et al. [Achilles tendon and sports]. Radiologe. 2002;42:811-817.
2. Gibbon WW, Cooper JR, Radcliffe GS. Distribution of sonographically detected tendon abnormalities in patients with a clinical diagnosis of chronic achilles tendinosis. J Clin Ultrasound. 2000;28:61-66.
3. Schepsis AA, Jones H, Haas AL. Achilles tendon disorders in athletes. Am J Sports Med. 2002;30:287-305.
4. Fredberg U, Bolvig L. Significance of ultrasonographically detected asymptomatic tendinosis in the patellar and achilles tendons of elite soccer players: a longitudinal study. Am J Sports Med. 2002;30:488-491.
5. Grechenig W, Clement H, Bratschitsch G et al. [Ultrasound diagnosis of the Achilles tendon]. Orthopade. 2002;31:319-325.
6. Kane D, Grassi W, Sturrock R et al. Musculoskeletal ultrasound--a state of the art review in rheumatology. Part 2: Clinical indications for musculoskeletal ultrasound in rheumatology. Rheumatology (Oxford). 2004;43:829-838.
7. Martinoli C, Bianchi S, Dahmane M et al. Ultrasound of tendons and nerves. Eur Radiol. 2002;12:44-55.
8. Grassi W, Filippucci E, Farina A et al. Sonographic imaging of tendons. Arthritis Rheum. 2000;43:969-976.
9. Astrom M, Gentz CF, Nilsson P et al. Imaging in chronic achilles tendinopathy: a comparison of ultrasonography, magnetic resonance imaging and surgical findings in 27 histologically verified cases. Skeletal Radiol. 1996;25:615-620.
10. O'Connor PJ, Grainger AJ, Morgan SR et al. Ultrasound assessment of tendons in asymptomatic volunteers: a study of reproducibility. Eur Radiol. 2004;14:1968-1973.
11. Richards PJ, Dheer AK, McCall IM. Achilles tendon (TA) size and power Doppler ultrasound (PD) changes compared to MRI: a preliminary observational study. Clin Radiol. 2001;56:843-850.

F. Ibrahim, N.A. Abu Osman, J. Usman and N.A. Kadri (Eds.): Biomed 06, IFMBE Proceedings 15, pp. 572-575, 2007
www.springerlink.com ' Springer-Verlag Berlin Heidelberg 2007

12. Schmidt-Trucksäss A, Cheng D, Sandrock M. et al. Computerized analysing system using the active contour in ultrasound measurement of carotid artery intima-media thickness. Clin Physiol. 2001;21:561-569.
13. Gustavsson T, Liang Q, Wendelhag I et al. A dynamic programming procedure for automated ultrasonic measurement of the carotid artery. Computers in cardiology. Los Alamitos, California: IEEE Computer society, 1994: 297-300.
14. Cheng D, Schmidt-Trucksäss A, Cheng K. et al. Automatic detection of the intimal and the adventitial layers of the common carotid artery wall in ultrasound B-mode images using snakes. In: Werner B, editor. International conference on image analysis and processing. Los Alamitos, California: IEEE Computer Society, 1999: 452-457.
15. Cheng D, Schmidt-Trucksäss A, Cheng K et al. Using Snakes to Detect the Intimal and Adventitial Layers of the Common Carotid Artery Wall in Sonographic Images. Computer Methods and Programs in Biomedicine. 2002;67:27-37.
16. Sandrock M, Cheng DC, Schmitz D et al. Quantification of the wall inhomogeneity in B-mode sonographic images of the carotid artery. J Ultrasound Med. 2002;21:1395-1404.
17. Kainberger FM, Engel A, Barton P et al. Injury of the Achilles tendon: diagnosis with sonography. AJR Am J Roentgenol. 1990;155:1031-1036.
18. Schmidt WA, Schmidt H, Schicke B et al. Standard reference values for musculoskeletal ultrasonography. Ann Rheum Dis. 2004;63:988-994.
19. Civeira F, Castillo JJ, Calvo C et al. [Achilles tendon size by high resolution sonography in healthy population. Relationship with lipid levels]. Med Clin (Barc). 1998;111:41-44.
20. Hartgerink P, Fessell DP, Jacobson JA et al. Full- versus partial-thickness Achilles tendon tears: sonographic accuracy and characterization in 26 cases with surgical correlation. Radiology. 2001;220:406-412.
21. Kanters SD, Algra A, van Leeuwen MS et al. Reproducibility of in vivo carotid intima-media thickness measurements: a review. [Review] [48 refs]. Stroke. 1997;28:665-671.

Author: Sandrock, M
Institute: Freiburg University Hospital, Centre for Internal Medicine, Department for Rehabilitative and Preventative Sports Medicine
Street: D-79106
City: Freiburg
Country: Germany

F. Ibrahim, N.A. Abu Osman, J. Usman and N.A. Kadri (Eds.): Biomed 06, IFMBE Proceedings 15, pp. 572-575, 2007
www.springerlink.com ' Springer-Verlag Berlin Heidelberg 2007

Finite Element Analysis of Cell-Material Interaction on Hydrated Soft Material of Cartilage

B. Punantapong[1], M.J. Fagan[2]

[1] Faculty of Applied Science, King Mongkut s Institute of Technology North Bangkok, Bangkok, Thailand
[2] Centre for Medical Engineering and Technology, University of Hull, Hull, UK

Abstract—**The role of viscoelasticity of collagen fibers in articular cartilage was examined in compression and tension, using stress relaxation measurements in axial direction (normal to the articular surface). In this study, the degree of inherent stiffness anisotropy of completely-decomposed element was evaluated using finite element method. The model accounted for elastic deformations of the nanostructure in contact and assumed laminar flow in the created voids. The stiffness parameters from the laboratory tests were utilized in analysis which the elasticity of the solid phase was investigated in the present study. The results were suggested that the dominant mechanism for stress relaxation arose from fluid pressurization, while the associated relaxation in collagen fibers mainly was resulted in an increase in radial strain. Furthermore, Young's modulus normal to the contact surface was increased from the superficial to the deep zone in articular cartilage.**

Keywords — **Finite element analysis, Soft material, Cartilage**

I. Introduction

Articular cartilage consists of three major structural constituents: collagen fibers, proteoglycan matrix and interstitial water. The function of articular cartilage serves mainly as a load-bearing medium in joints, thus the structure of cartilage is customarily designed to carry high stresses. Recent developments in mathematical modeling have improved the understanding of cartilage mechanics [1,2,3,4]. They have suggested that the proteoglycans are negatively-charged and produce a swelling pressure that depends on the saline concentration of the fluid. At equilibrium and physiological conditions, the swelling pressure is counteracted by the external load and the structural elements in the solid matrix, mainly the collagen fibers.

However, the importance of collagen fibers for the mechanical function and integrity of cartilage has been demonstrated experimentally by researchers [7,8]. At the same time, the stress relaxation and responses of articular cartilage have been observed in many testings where the viscoelasticity is attributed primarily to the collagen fibers, as have been found for other soft tissues in tension and compression [5,9].

Furthermore, The articular cartilage can be divided into three distinct morphological zones as superficial zone, middle zone and deep zone. In the superficial zone (10 20% of the total thickness), collagen fibers are oriented parallel to the articular surface. While in the middle zone (40 60% of the total thickness), there is no preferred orientation for the collagen fibers, and in the deep zone (30% of the total thickness), the collagen fibers are approximately perpendicular to the articular surface. In normal cartilage, chondrocytes change shape across the thickness [3], chondrocytes are typically flattened in the surface zone, spherical in the middle zone and arranged in columns in the deep zone. The distribution of chondrocytes in cartilage is not uniform: the average cell volumetric concentration increases from the deep zone to the surface zone by a factor of about three [6]. This study was to investigate the effects of the structural arrangement of the collagen fiber network and distribution of stress-strain on the global material behavior of articular cartilage by using finite element method.

II. Materials and Methods

Because of the great difference in material properties between proteoglycan matrix, cells and collagen fibers, cartilage is not a uniform material. In order to include these structural, non-uniform effects, cartilage has been represented using a transversely-isotropic material [1,2]. So, the global material properties have not been related to the microstucture of the tissue. Then we can be investigated theoretically the effects of the collagen fiber network on anisotropy of cartilage properties [3,8]. In their models, the effect of volumetric concentration of collagen fibers, the structure of the fiber network, and the distributed chondrocytes were not included. Since the material anisotropy of cartilage is likely caused by microstructural variations in the tissue, i.e., the distribution of cartilage fibers and chondrocytes, the description of cartilage using a uniform, transversely isotropic model is not appropriate.

However, in this study, we used axisymmetrical model to simulate the behavior of the cross-anisotropic elastic material in which the horizontal plane is isotropic, and

F. Ibrahim, N.A. Abu Osman, J. Usman and N.A. Kadri (Eds.): Biomed 06, IFMBE Proceedings 15, pp. 576-580, 2007
www.springerlink.com ' Springer-Verlag Berlin Heidelberg 2007

denoting axes *x* and *y* as the horizontal directions, and axis *z* as the vertical directions, as shown in Fig. 1 and Fig. 2. Then the effective stress-strain relationship of the element can be described. If the stress-strain behavior is governed by five independent elastic parameters: E_v, E_h, $G_{vh}(=G_{hv})$, ν_{vh}, and ν_{hh}, where E_v and E_h are the Young s moduli in the vertical and horizontal directions, respectively; $G_{vh}(=G_{hv})$ is the elastic shear modulus in any vertical plane; ν_{vh} is the Poisson s ratio for the effect of vertical strain on horizontal strain; and ν_{hh} is the Poisson s ratio for the effect of horizontal strain on the complementary horizontal strain. Then the relationship of stress-strain can be written by the following [9].

$$\begin{Bmatrix} \delta\varepsilon_{h1} \\ \delta\varepsilon_{h2} \\ \delta\varepsilon_{v} \\ \delta\gamma_{hv} \\ \delta\gamma_{vh} \\ \delta\gamma_{hh} \end{Bmatrix} \begin{bmatrix} \frac{1}{E_h} & \frac{-\nu_{hh}}{E_h} & \frac{-\nu_{vh}}{E_v} & 0 & 0 & 0 \\ \frac{-\nu_{hh}}{E_h} & \frac{1}{E_h} & \frac{-\nu_{vh}}{E_v} & 0 & 0 & 0 \\ \frac{-\nu_{vh}}{E_v} & \frac{-\nu_{vh}}{E_v} & \frac{1}{E_v} & 0 & 0 & 0 \\ 0 & 0 & 0 & \frac{1}{G_{hv}} & 0 & 0 \\ 0 & 0 & 0 & 0 & \frac{1}{G_{hv}} & 0 \\ 0 & 0 & 0 & 0 & 0 & \frac{2(1+\nu_{hh})}{E_h} \end{bmatrix} \begin{Bmatrix} \delta\sigma_{h1} \\ \delta\sigma_{h2} \\ \delta\sigma_{v} \\ \delta\tau_{hv} \\ \delta\tau_{vh} \\ \delta\tau_{hh} \end{Bmatrix} \quad (1)$$

where $G_r(t)$ $\delta\varepsilon_{h1}$ and $\delta\varepsilon_{h2}$ are the incremental horizontal strains in the h_1 and h_2 directions, respectively; $\delta\varepsilon_v$ is the incremental vertical strain; $\delta\sigma_{h1}$ and $\delta\sigma_{h2}$ are the incremental effective horizontal stresses in the h_1 and h_2 directions (*x* and *y* directions), respectively; $\delta\sigma_v$ is the incremental effective vertical stress; $\delta\gamma_{hv}$ is the incremental shear strain in the h-v plane; $\delta\gamma_{vh}$ is the incremental shear strain in the *v*-*h* plane; $\delta\gamma_{hh}$ is the incremental shear strain in the *h*-*h* plane; $\delta\tau_{hv}$ is the incremental shear stress in the *h*-*v* plane; $\delta\tau_{vh}$ is the incremental shear stress in the *v*-*h* plane; and $\delta\tau_{hh}$ is the incremental shear stress in the *h*-*h* plane.

For the model simulation, we used ANSYS finite element code for analysis under the conditions of finite deformation kinematics. The material was considered to be elastic-plastic. Isotropic linear elasticity was assumed, combined with isotropic hardening. An axisymmetric model with 9,800 eight-node elements with reduced integration was used to model a quadrant of the 3D indentation process (based on symmetry). The indenter itself is modeled using two four-node tetrahedral elements which are purely elastic with the stiffness much greater than that of the indented material. In Fig. 2, several levels of mesh refinement are used in the model to give a very fine mesh near the contact zone. In this region, the stress field can be accurately determined. The conical indenter is modeled as a rigid surface which rotated about the axis of symmetry. A convergence study was performed to ensure that the final result was not mesh dependent.

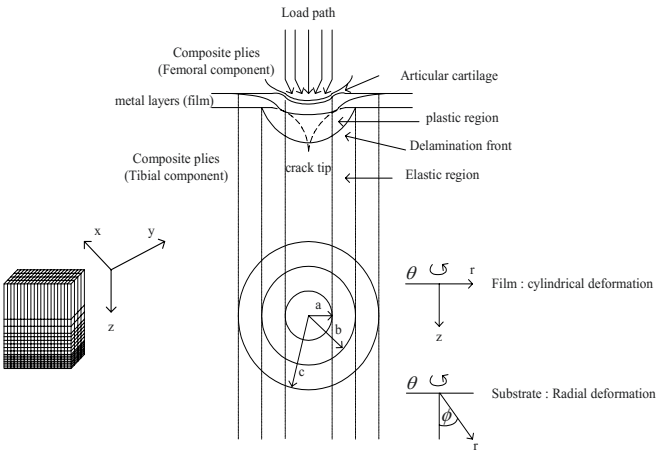

Fig. 1 Diagram of indentation model on articular cartilage

At the same time, a fibril-reinforced model was used, which consisted of a fluid-saturated elastic matrix and a collagen viscoelastic matrix [5]. Next, the properties of cartilage were defined by three strain-dependent tensile moduli of the fibrillar matrix for the coordinate directions, $E_r^f(\varepsilon_r)$, $E_\theta^f(\varepsilon_\theta)$, $E_z^f(\varepsilon_z)$ as the model tested [3]. Thus the fibers are in tension, the fibrillar stresses are determined by the hereditary integrals. For the radial (*r*) direction, we obtained

$$\sigma_r^f(t) = \sigma_r^f(0) + \int_0^t G_r(t-\tau)\, E_r^f(\varepsilon_r)\, \dot{\varepsilon}_r\, d\tau \quad (2)$$

where ε_r is the radial strain, ε_z is the axial strain, σ_r is the radial stress, σ_z is the axial stress, E_r^f is the fibrillar modulus.

F. Ibrahim, N.A. Abu Osman, J. Usman and N.A. Kadri (Eds.): Biomed 06, IFMBE Proceedings 15, pp. 576-580, 2007
www.springerlink.com ' Springer-Verlag Berlin Heidelberg 2007

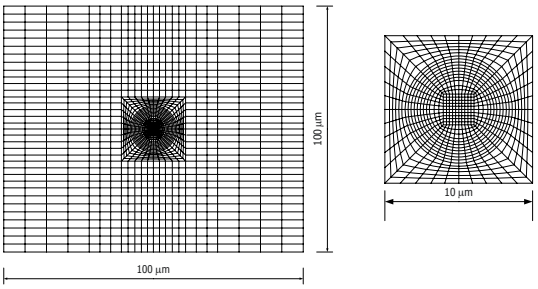

Fig. 2 The model of axisymmetric model of single cell within the articular surface.

Furthermore, The viscoelastic dissipation of the radial fibers had relatively more influence on the compressive load response in early relaxation. In late relaxation, the actual fibrillar modulus $(G_r(t)E_r^f)$ was reduced considerably, resulting in an increase in the radius strain. So, the axial and radial stresses of the proteoglycan matrix at equilibrium are

$$\sigma_z = E_m \varepsilon_z + 2\nu_m \sigma_r^m \tag{3}$$

$$\text{and } \sigma_r^m = -\frac{1}{2}\left[E_r^f(0) + E_r^f(\varepsilon_r) \right]\varepsilon_r \tag{4}$$

This formulation, to some extent, accounts for nonlinear viscoelasticity, because of the strain-dependence of the modulus (while G_r is independent on the strain and strain rate). The relaxation function is represented by a discrete spectrum approximation.

$$G_r(t) = 1 + \sum_m g_m \exp\left(\frac{-t}{\lambda_m}\right) \tag{5}$$

Here, λ_m is characteristic times for the viscoelastic dissipation and g_m is dimensionless constants.

III. Results and Discussion

For the computation, we were used axisymmetric FEA models of knee joint which the articular cartilage layers of the tibial and femoral condyles, and the bone underlying the articular cartilage of the tibia plateau were included. As in the study, we assumed that the permeability of the articular cartilage was strain-dependent. So, the model was implemented in ANSYS code, it consisted of 9,800 elements. The elements in the area under the contact surface had a characteristic length 1-15 nm. This can lead to initial mismatch between the FE model and test results at indentation depths closed to the radius magnitude.

In the test of the contact of a cartilage surface, the reaction forces predicted for the stress-relaxation tests were based on infinitesimal strain theory [1,7]. When a step load was applied to the articular cartilage and this load was increasingly different with increasing time, then the solutions approached the elastic solution and the interstitial fluid was pushed out of the cartilage tissue. Fig. 3 illustrates the reaction force predicted using ANSYS for a test with an axisymmetrical joint model, which the material properties and geometry used in the simulations were Young s modulus, E_s = 0.55 MPa, the cartilage layer thickness, b = 0.5 mm, the radius of curvature of the contacting surface, r = 25 mm, and the compression ratio, e = 3 10% . The results showed that the reaction force was varied by the compression ratio and the permeability of the cartilage which depends on the deformation state of the cartilage. Thus this analytical solutions are in good agreement for small trains (compression ratio, e is smaller than 10%) and for limited time periods.

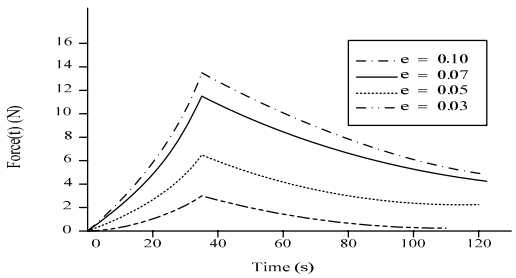

Fig. 3 The reaction force predicted using ANSYS for a test with an axisymmetrical joint model.

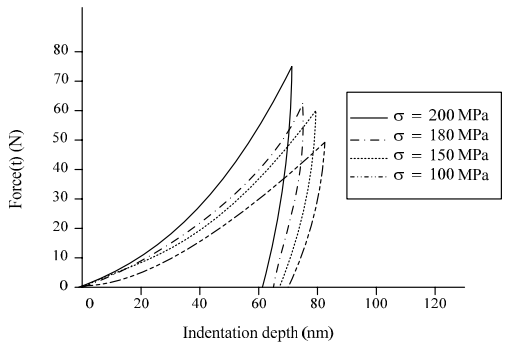

Fig. 4 The force indentation depth curve for the finite element simulation of various yield strength.

Next, we were to find the best-fit material parameters by matching the experimentally measured transient reaction force with the corresponding of Eqn. (2). Fig. 4 shows an equivalent force indentation depth curve obtained using the equivalent 2D axisymmetric model. In this test, the indentation was done to a depth between 0 100 nm with

F. Ibrahim, N.A. Abu Osman, J. Usman and N.A. Kadri (Eds.): Biomed 06, IFMBE Proceedings 15, pp. 576-580, 2007
www.springerlink.com ' Springer-Verlag Berlin Heidelberg 2007

different force 0 100 N, and various yield strength values. The results showed that peak stress-relaxation nearly matched the peak force at the end of each ramp-displacement, indicating significant interstitial fluid load support, and that stress-relaxation equilibrium occurred when the fluid pressure had subsided. Therefore, the sensitivity of the results to indenter tip sharpness was explored. So, the contact area is not only dependent on the area function of the indenter but also on the elastic-plastic response of the material.

Fig. 5 and 6 show the comparison of the effective Poisson s ratio of cartilage in axial compression and tension for one-step ramp loading with 8.0 μm at 1 μm/s followed by Eqn. (3) and (4) into ANSYS. In compression-relaxation test, the effective Poisson s ratio $(-\varepsilon_r / \varepsilon_z)$ decreased monotonically from 0.6 towards a low value of 0.1, regardless of the contact conditions. The effective Poisson s ratio was sensitive to the contact conditions in axial tension: for frictionless contact conditions, the ratio slowly changed from 0.6 towards the Poisson s ratio of the nonfibrillar matrix (0.35); for the adhesive contact conditions, it did not change monotonically. Consequently, these results agree with the sense that the ratio is normally larger for tension than for compression, and that the ratio for tension can be greater than 0.5 (Fig. 6). The results show a large influence of the contact conditions on the lateral strain of a specimen in tension. At the same time, the effective Poisson s ratio $(-\varepsilon_r / \varepsilon_z)$ deviates from the true Poisson s ratio of the tissue, depending on the length/width ratio of the specimen. The large ratio (>0.5) 6 was produced by deviations, rather than a material anisotropy (which is also the reason for large/small Poisson s ratios). Thus, the result (Fig. 6) also shows the influence of fluid pressurization on the radial strain in axial tension (for frictionless contact conditions). Then the effective Poisson s ratio was sensitive to the

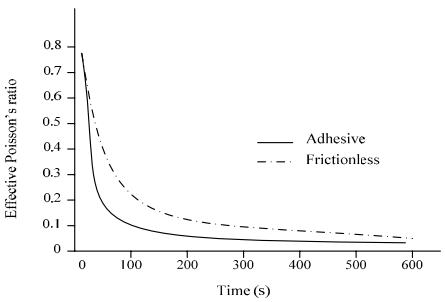

Fig. 5 Comparison of the effective Poisson s ratio ($-\varepsilon_r/\varepsilon_z$) of cartilage in axial compression for one-step ramp loading.

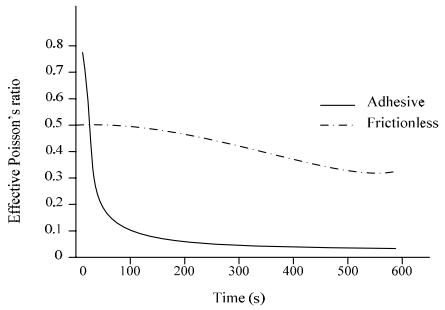

Fig. 6 Comparison of the effective Poisson s ratio ($-\varepsilon_r/\varepsilon_z$) of cartilage in axial tension for one-step ramp loading.

contact conditions in axial tension: for frictionless conditions, the ratio slowly changed from 0.6 toward the Poisson s ratio of the nonfibrillar matrix; for the adhesive contact conditions, it did not change monotonically.

IV. Conclusions

The present study was intended to investigate the dependence of the material properties of articular cartilage on the combination of the collagen fiber network structure and the distributed chondrocyte structure. In experiments, the investigation illustrates that the variations in the computed ground deformations depend on the degree of stiffness anisotropy (including effects of Poisson s ratio) and the relative magnitudes of horizontal and vertical stress change.

References

[1] Donzelli P., Spilker R. and Mow, V.C. (1999) Contact analysis of biphasic transversely isotropic cartilage layers and correlations with tissue failure. J. Biomech. 32: 1037-1047.

[2] Garcia J., Altiero N. and Haut, R. (1998) Approach for the stress analysis of transversely isotropic biphasic cartilage under impact load. ASME J. of Biomech. Eng. 120: 608-613.

[3] Guilak F., Ratcliffe A. and Mow V.C. (1995) Chondrocyte deformation and local tissue strain in articular cartilage: a confocal microscopy study. J. Ortho. Res. 13: 410- 421.

[4] Holmes M. and Mow V.C. (1990) Nonlinear characteristics of soft gels and hydrated connective tissues in ultrafiltration. J. Biomech. 23: 1145-1156.

[5] Huang C.Y., Mow, V.C. and Ateshian G.A. (2001) The role of flow-independent viscoelasticity in the biphasic tensile and compressive responses of articular cartilage. ASME J. of Biomech. Eng. 123: 410-417.

F. Ibrahim, N.A. Abu Osman, J. Usman and N.A. Kadri (Eds.): Biomed 06, IFMBE Proceedings 15, pp. 576-580, 2007
www.springerlink.com ' Springer-Verlag Berlin Heidelberg 2007

[6] Jones W., Ting-Beall H., Lee G., Kelley S., Hochmuth R. and Guilak F. (1997) Mechanical properties of human chondrocytes and chondrons from normal and osteoarthritic cartilage , Trans. of Orthop. Res. Soc. 22(1): 199.
[7] Khalsa P.S., and Eisenberg S.R. (1997) Compressive behavior of articular cartilage is not completely explained by proteoglycan osmotic pressure. J. Biomech. 30: 589-594.
[8] Kwan M., Lai W.and Mow V.C. (1990) A finite deformation theory for cartilage and other soft hydrated connective tissues. J. Biomech. 23: 145-155.
[9] Lee, K.M. and Rowe R.K. (1989) Deformations caused by surface loading and tunneling: the role of elastic anisotropy. Geo-technique 39(1): 125-140.

Corresponding author:

Author: Assoc.Prof. Boonyong Punantapong
Institute: King Mongkut s Institute of Technology North Bangkok
Street: Piboolsongkram Rd., Bangsue
City: Bangkok 10800
Country: Thailand
E-mail: bpp@kmitnb.ac.th

F. Ibrahim, N.A. Abu Osman, J. Usman and N.A. Kadri (Eds.): Biomed 06, IFMBE Proceedings 15, pp. 576-580, 2007
www.springerlink.com ' Springer-Verlag Berlin Heidelberg 2007

Forward Simulation of Cardiac Excitation Propagation and ECG Patterns Using an Anisotropic Heart Model – a Toolbox

B. Pfeifer[1], M. Seger[1], F. Hanser[1], C. Hintermüller[1], G. Fischer[1], H. Mühlthaler[2] and B. Tilg[1]

[1] University for Health Sciences, Medical Informatics and Technology (UMIT), Institute of Biomedical Engineering, Hall i.T., Austria
[2] Innsbruck Medical University, Department of Vascular Surgery, Innsbruck, Austria

Abstract— **In the year 1960 Hoffman and Cranefield have published the book "Electrophysiology of the Heart". Since then a lot of research has been done, which makes it nearly impossible to integrate all discovered knowledge in one handy book for studying the nature of ECG. The relationship between the electrical excitation in the human heart and the body surface potential (BSP) is known as forward problem of electrocardiography. To enable the simulation of the electro anatomical function we coupled a cardiac model consisting of ventricles and atria. For studying the nature of ECG for the sinus beat, arrhythmias, ischemia and infarction this model can be used, and, furthermore, the model was used for developing and verifying electrocardiographic inverse approaches. The simulation toolbox was implemented in AmiraDev 3.0™, which is mainly a visualization-tool that can be expanded with self-developed plug-ins.**

Keywords—**Cardiac Imaging, Forward Problem, ECG simulation**

I. Introduction

A lot of research has been done during the last decades in order to enable the simulation of the electrocardiogram (ECG) and the body surface potential (BSP). The mechanisms of spatiotemporal pattern formation in biology are a key for understanding organs, cells, cell interactions and the causes of irregular function. Today s computer power and the available knowledge about cardiac electrophysiology enable the development of high-precision three-dimensional models for simulation, which can be used for cardiovascular diagnosis and therapy, but also for getting a deeper understanding in arrhythmias. In this paper a ventricular and atrial model, developed over the last 15 years by our group, is presented which uses the bidomain source-field formulation. This approach is used in the electrocardiographic forward and inverse approach, and validation was done for the inverse formulation in 45 patients. The patient data is derived for each patient from magnetic resonance imaging (MRI), the fibre architecture in the ventricles and anatomical features in the atria are considered based on literature data. By using the toolbox it is possible to calculate the de- and repolarisation of the potential pattern throughout the entire heart muscle and volume conductor, and can be used for better understanding the nature of the ECG in normal beat, for different arrhythmias, for ischemia and infarction.

II. Forward problem

A. Volume Conductor Modeling

A volume conductor model, consisting of the compartments chest, lungs, atrial and ventricular myocardium, and the blood masses, is the basis for the electrocardiographic forward and inverse problem. The morphological image data required for volume conductor modeling were acquired using a Magnetom Vision 1.5 Tesla scanner, from Siemens Medical Solutions (Erlangen, Germany). For torso and lung shape modeling an axial T1-flash mode, non-contrasted scan with 10mm spacing was used. For cardiac modeling oblique short axis, cine-gated scans with 4mm (atria) and 6 mm (ventricles) spacing were used. By using the volume conductor segmentation pipeline [1, 2] the label sets are extracted semi-automatically, and are then meshed. Figure 1 is showing a generated volume conductor model, which is be used for the forward problem formulation.

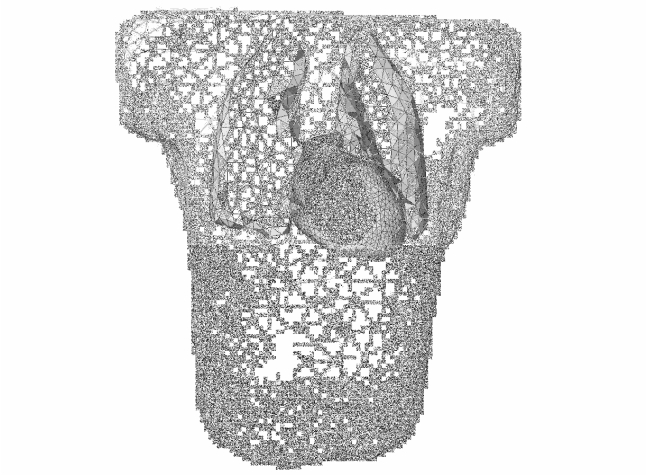

Fig.1. Patient individual volume conductor model

F. Ibrahim, N.A. Abu Osman, J. Usman and N.A. Kadri (Eds.): Biomed 06, IFMBE Proceedings 15, pp. 581-584, 2007
www.springerlink.com ' Springer-Verlag Berlin Heidelberg 2007

B. Cellular Automaton

For computing the cardiac activation sequences a cellular automaton (CA) was developed [3]. Therefore, after the patient individual segmentation approach different types of tissue were assigned to the cardiac model. These types are the endocardium, epicardium and the myocardium. Further, the sinus node, crista terminalis, Bachmann bundle, fossa ovalis, pectinate muscles, coronary sinus, isthmus, the bundle of His, left and right bundle branch and the Purkinje fibre system have to be defined. These tissue types have to be parameterized by applying the refractory period and the parameters for the transmembrane potential distribution, and, furthermore, the fibre geometry needs to be applied. The fibre structure assigned to the model is described in the literature [4, 5].
An important factor for the CA computation is the effective refractory period (ERP) defined for a heart cycle length (CL) of 700ms (ERP_{700}). ERP is defined to be the time period, in which a heart muscle cell can not be excited by a stimulus. The run time ERP at the CL is calculated by:

$$ERP(CL) = ERP_{700} + A + B \cdot \frac{CL - 700}{1000} - D \cdot (\frac{C - CL}{C})^2 \quad (1a)$$

if CL < C and

$$ERP(CL) = ERP_{700} + A + B \cdot \frac{CL - 700}{1000} \quad (1b)$$

if CL ≥ C, respectively. A is the offset value, B the slope of the function, C is a predefined CL, and D is a coefficient for the quadratic decrease. These parameters have to be defined for each tissue type individually. The chosen values for the defined tissue types are described in [3].

C. Activation Time Computation

Before the activation time computation can be started, an arbitrary number of tetrahedrons (nodes) on the cardiac model with an arbitrary time instant for starting the excitation process need to be selected. Each node in the cellular automaton model can take three different states: excitable (**e**), refractory (**R**) and waiting (**W**, which was introduced due to algorithmic needs). By selecting the node with the earliest excitation time the simulation starts. The status of this node is then set from **e** to **R**. The possible excitation times of the excited neighbors of the node are calculated according to the distance between the center of masses and conduction velocities for each connection, and are then stored in **W**. In the next step the tables are searched for the node with the lowest excitation time, which is the next node to be excited and stored in **R** and cleared in the corresponding table **W**. If more than one node have the same starting or possible excitation time one of them is chosen. The others become source nodes of the subsequent calculation. The propagation is calculated as described above, but three cases may occur which are handled the following way. If a neighboring node is in status **e** the possible excitation time is stored in **W**, which means that the nodes status is changed into awaiting excitation. If the node is already in the status waiting and the calculated value is higher than the stored value, then the possible excitation time is changed to the lower value, otherwise no changes are made. The third case is that if a node is in status **R**, then no value is stored for this point in **W**.
The computation is finished when there are no more starting nodes left and **W** is empty, or when the excitation time of the current source node is higher than the chosen upper limit predefined by the user.

D. Transmembrane Potential Computation

The extended Wohlfahrt formula [3] is used for modeling the different shapes of ventricular / atrial action potentials:

$$\varphi_m(t-\tau) = \alpha(t-\tau) \cdot \beta(t-\tau) \cdot \gamma(t-\tau) + K_{10}[mV] \quad (2)$$

The parameter t describes the current simulation time interval, □represents the computed activation time, □(.) describes the shape of the depolarization, □(.) the phase from the beginning of the repolarisation to the plateau shape, and □(.) describes the repolarisation process.

E. Maxwell's Equations applied to biological systems

The general Maxwell s equations in differential form are:

$$\begin{aligned} &div(D) = \rho && \text{Coulomb's law} \\ &rot(H) = j + \frac{\partial D}{\partial t} && \text{Ampers's law} \\ &rot(E) = \frac{\partial B}{\partial t} && \text{Faraday's law} \\ &div(B) = 0 && \text{Absence of magnetic monopoles} \end{aligned} \quad (3)$$

D describes the electrical displacement, H the magnetic field, E the electrical field, ρ the electrical charge volume density, and j the current surface density. For cardiac modeling following assumptions are made [6, 7]:

- Electrical field strengths are not too high
- Capacitive as well as inductive effects can be neglected because biological tissue can be described to be purely resistive
- Due to low frequency a quasi-static approximation of Maxwell s equation can be used

F. Ibrahim, N.A. Abu Osman, J. Usman and N.A. Kadri (Eds.): Biomed 06, IFMBE Proceedings 15, pp. 581-584, 2007
www.springerlink.com ' Springer-Verlag Berlin Heidelberg 2007

Therefore, the Maxwell s equations lead finally to

$$\begin{aligned} &div(D) = \rho \\ &rot(H) = j \Rightarrow div(j) = div[rot(H)] = 0 \\ &rot(E) = 0 \Rightarrow E = -grad(\varphi) \\ &div(B) = 0 \end{aligned} \qquad (4)$$

The equations can therefore be rewritten and so the fundamental equation for biological tissue can be derived:

$$div[\sigma\, grad(\varphi)] = div(j^{imp}) \qquad (5)$$

Equation (5) is valid for the active regions (the heart), whereas equations (5) for regions having only passive properties (lungs, torso) leads to a Laplace s equation:

$$div[\sigma\, grad(\varphi)] = 0 \qquad (6)$$

Therefore, the resulting differential equations to be solved are

$$div[\kappa_b grad(\varphi)] = -div[\sigma_{in} grad(\varphi_m)] \qquad (7)$$

for the cardiac region and

$$div[\kappa_c grad(\varphi)] = 0 \qquad (8)$$

for all other compartments of the volume conductor model. The tensor κ_b is the bulk conductivity, i.e. the sum of the electrical effective extracellular and effective intracellular conductivity σ_{in}. The potential φ describes the extracellular, φ_m the transmembrane potential. The tensor κ_c holds the electrical conductivities for all other compartments.

By applying the finite element method (FEM), considering the volume conductor model and the related boundary conditions [8], the equations (7) and (8) result in a system of algebraic equations:

$$R\phi = S\phi_m \qquad (9)$$

The matrices **R** and **S** are the so-called stiffness matrices, the matrix ϕ describes the potentials in all nodes of the tetrahedral volume conductor mesh, and the matrix ϕ_m contains the transmembrane potentials in all source nodes of the heart. The transmembrane potentials are computed by the cellular automaton for discrete time steps. For inverting **R** (equation (9)) the matrix **R** has to be modified as this matrix is positive semi definite due to the Neuman s boundary condition on the torso surface. Thus, the Wislon Central Terminal (WCT) is used to define the reference potential of the torso surface [9] to reveal a positive definite matrix R. The inversion of R is performed by the conjugated gradient method. This leads to the desired potentials in all nodes of the volume conductor model:

$$\phi = R^{-1} S\phi_m. \qquad (10)$$

F. Implementation

The environment chosen to implement the forward problem is amiraDev 3.0 (TGS Europe Inc.). Amira is a visualization-tool, which allows preprocessing tasks, such as segmentation, triangular or tetrahedral mesh generation. The functionality of Amira can be expanded by self developed modules, so called plug-ins. Because of the Amira API (application programming interface) the chosen programming language was C++. Thus, the forward simulation toolbox is implemented as different plug-in modules, which are coupled together using Amira .

III. Results

As described above, the prime reason of implementing the forward toolbox was to enable a wide, nearly unlimited range of simulating ECG patterns. Therefore, in this section an infarction is simulated to outline the possibilities of the given toolbox.

Figure 2 shows the infracted area of the heart which was drawn in using a forward toolbox Amira plug-in.

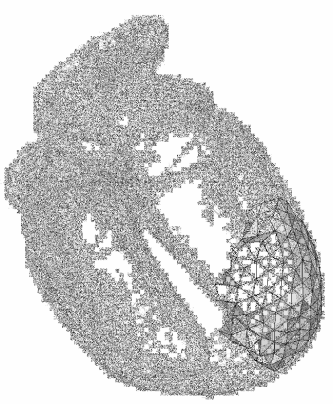

Fig.2. Heart with an infracted and on the infarction boundaries ischemic area which was used for the simulation. The cardiac model is superimposed by a tetrahedron mesh representing the infarcted region.

The modified model depicted in figure 2 was taken, and the tissue type sinus node was stimulated at 0ms in order to simulate a sinus rhythm on the infarcted model.

The simulated ECG shown in figure 3 has a definite Q wave and an enhanced ST-segment elevation, which is typically for a myocardial infarction.

F. Ibrahim, N.A. Abu Osman, J. Usman and N.A. Kadri (Eds.): Biomed 06, IFMBE Proceedings 15, pp. 581-584, 2007
www.springerlink.com ' Springer-Verlag Berlin Heidelberg 2007

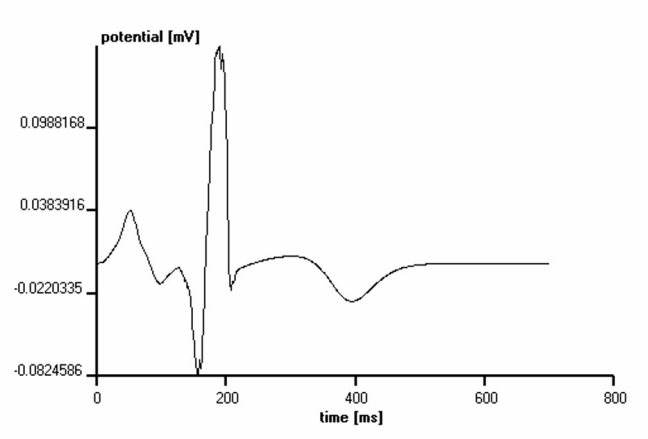

Fig.3. V3 lead of the infarction forward ECG simulation

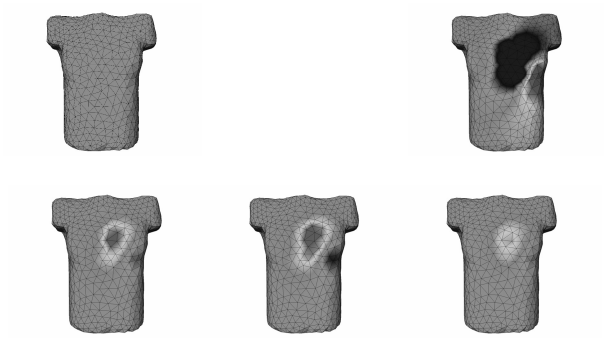

Fig.4. Body surface potential maps at times 0ms, 80ms, 220ms, 240ms, 350ms (reading direction: from left upper to right lower subfigure)

Figure 4 depicts the time series showing the spread of electrical activation and the associated body surface potentials.

IV. Conclusion

In this paper we presented an in silico model environment for simulation of cardiac de- and repolarisation as well as of the three dimensional potential pattern throughout the entire volume conductor. A cellular automaton and a bidomain based source field numerics are the fundamental basics for this approach. Amira qualified as simulation environment because of its plug-in concept. Because of this fact it was possible to develop a toolbox that can be used to study different ECG patterns without having to know details about the internal modeling, about FEM and the techniques behind. Limitations are given because of the relatively course spatial discretisation and because of not considering heart muscle contraction. Hence, microscopic cardiac propagation effects can not be simulated, but mostly the interest is about the macroscopic source-field relationship, and therefore, this fact can be neglected. As a result of not modeling contraction the simulated T-wave patterns have to be considered as fully synthetic. Beside these limitations, the presented approach enables various applications for the study of the nature of the ECG pattern in space and time.

Acknowledgment

This research study was funded by the START Y144 program granted by the Austria Federal Ministry of Education, Science and Culture (bm:bwk) in collaboration with the Austrian Science Fund (FWF).

References

1. B. Pfeifer, Model-based segmentation techniques for fast volume conductor generation , UMIT, 2006. PhD Thesis
2. B. Pfeifer, M. Seger, C. Hintermueller, G. Fischer, H. Mühlthaler, R. Modre-Osprian, and B. Tilg, AAM based segmentation for imaging cardiac electrophysiology, Methods of Information in Medicine, 2006 in press
3. Killmann R., Three-dimensional numerical simulation of the excitation and repolarisation process in the entire human heart with special emphasis on reentrant tachycardias. PhD thesis, Graz University of Technology, 1990.
4. Rijcken J., B. M., Schoofs A. J., van Campen D. H., and Arts T., Optimization of cardiac fiber orientation for homogeneous fiber strain during ejection, Annals of Biomedical Engineering 27(3), pp. 289 297, 1999.
5. Nielsen P. M. F., LeGrice I. J., Smaill B. H., and Hunter P. J., Mathematical model of geometry and fibrous structure of the heart, American Journal of Physiology 260(4.2), pp. H1365 H1378, 1991.
6. Malmivuo J. and Plonsey R. Bioelectromagnetism. Oxford University Press, Oxford, 1995.
7. Roth B. J. Electrical conductivity values used with the bidomain model of cardiac tissue. IEEE Transactions on Biomedical Engineering, 44(4):326 328, 1991.
8. Seger M., Fischer G., Modre R., Messnarz B., Hanser F., and Tilg B., Lead field computation for the electrocardiographic inverse problem finite elements versus boundary elements, Computer Methods and Programs in Biomedicine 77(3), pp. 241 252, 2005.
9. Fischer G., Tilg B., Wach P., Modre R., Hanser F., and Messnarz B. On modelling the wilson terminal in the boundary and finite element method. IEEE Transactions on Biomedical Engineering, 49(3):217 224, 2002.

Address of the corresponding author:

Author: DI Dr. Bernhard Erich Pfeifer
Institute: biomed
Street: Eduard Wallnöfer Zentrum 1
City: Hall i.T.
Country: Austria
Email: Bernhard.pfeifer@umit.at

F. Ibrahim, N.A. Abu Osman, J. Usman and N.A. Kadri (Eds.): Biomed 06, IFMBE Proceedings 15, pp. 581-584, 2007
www.springerlink.com ' Springer-Verlag Berlin Heidelberg 2007

Haptic Pulse Simulator Training Module for Disease Diagnosis

Shriram Raghunathan[1], Raja Tamilarasan[1], Praneet Jayaram[1] and Manivannan Muniyandi[2]

[1]Department of Electrical Engineering, Anna University, Chennai, India.
[2]Biomedical Engineering Division, Indian Institute of Technology, Madras, India.

Abstract– **Ayurveda is an ancient form of Indian medicine. One of the techniques used for diagnosis of various diseases in this system is the '3-point pulse' technique. A training module is proposed which simulates these three pulse points on a dummy arm. An electro-mechanical setup is developed using DC motors. Frequency and Amplitude characteristics of the human pulse are accurately reproduced by the simulator. A calculated input to the motors is provided through a micro-controller based GUI front end. Application extensions for telemedicine and remote patient monitoring are also discussed.**

I. Introduction

The art of pulse diagnosis based on the 3 Pulse Ayurvedic system of Indian medicine is a highly efficient tool in the early identification of several physical ailments. Over 330 different diseases can be diagnosed by a trained practitioner. As this technique is a highly subjective one, it requires experience on the part of the practitioner to accurately identify rare disease conditions. It is aimed to accelerate this learning process by the development of a haptic device that simulates the human pulse pattern on a prosthetic arm. An electro-mechanical setup is implemented using DC motors. The simulation works on the principle of controlling the motors at desired frequency and amplitude levels and converting rotational motion to linear motion using an appropriate mechanical setup. This linear up-down movement of the motor shaft is suitably padded and felt as the pulse. A calculated input to the motors is provided through a micro-controller based GUI front end, where individual scroll bars are provided to control amplitude and frequency levels

II. Pulse diagnosis

The three principal pulses are felt in the wrist region along the radial artery. The place for feeling the pulse is on the lateral aspect of the right forearm, 2cm up from the wrist. The index, middle and ring fingers are used to feel the three pulses in their respective order. An experienced practitioner reads these pulses by placing his fingers on the radial artery. Pressure is applied on one finger after the other and it alternates on every other finger. Based on the dominant pulse among the three and the direction in which the pulse motion is felt, a trained practitioner identifies over 350 different disease conditions.

The study of the relationship between these pulse patterns is the key to identification of the ailment. Healthy human subjects have the three pulse amplitudes in the ratio of 4:2:1 respectively. However, this ratio is believed to follow seasonal variations and changes with parameters such as time of the day, temperature and humidity of the skin. The right arm of male subjects and left arm of female subjects is used to read the pulse.

III. Validation, testing and results

a. Device Standardization

The device was standardized at the Central Research Institute for Siddha, Chennai, India, where 3-pulse diagnosis technique is used in order to diagnose diseases. A set of 7 isolated ailments was configured on the device by adjusting the various frequency and amplitude levels via the GUI. Details of the same can be found in Table 1. The device was configured by a senior research officer at the institute.

b. Testing

Using Pulse sensors, the pulse reading of a healthy human subject were obtained. Following this, the pulse pattern of a healthy subject was simulated on the device, and by placing the same sensors on top of the prosthetic arm, the pulse reading of the device was obtained. A visual comparison of the readings obtained from the first pulse (vatha) of the human subject (Fig 1) and that of the device is shown.

Using the device, a frequency of 80 bpm and an amplitude level of 200 was set for the Vatha pulse. In order to corroborate whether the frequency and amplitude values set from the GUI front end were being accurately translated at the mechanical end, the frequency and amplitude of the output waveform was recorded. Figure 2 shows the obtained waveform.

F. Ibrahim, N.A. Abu Osman, J. Usman and N.A. Kadri (Eds.): Biomed 06, IFMBE Proceedings 15, pp. 585-587, 2007
www.springerlink.com ' Springer-Verlag Berlin Heidelberg 2007

Table 1
Standardization results

Ailment	Vatha		Pitha		Kapha	
	Freq (bpm)	Amp (levels)	Freq (bpm)	Amp (levels)	Freq (bpm)	Amp (levels)
Healthy	80	200	80	100	80	50
Diabetes	100	100	80	100	80	50
Sinusitis	80	220	80	100	80	124
Bronchial Asthma	65	220	66	100	64	10
Ischemic heart disorder	90	230	66	176	64	10
Liver disorder	60	120	80	150	80	50
Diarrohea	95	97	95	150	80	50
Hyper tension	80	206	67	222	60	50

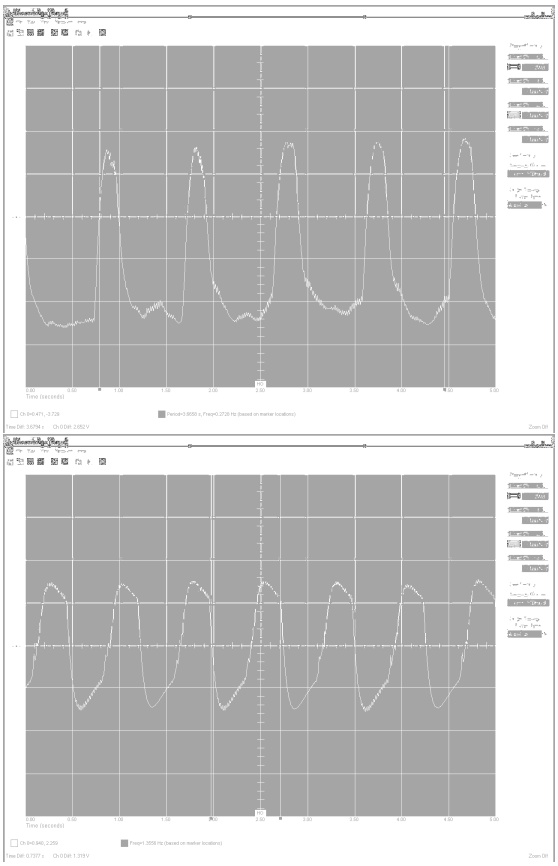

Fig. 1 Comparison of waveform of Vatha pulse obtained from human subject (top) and the simulator (bottom)

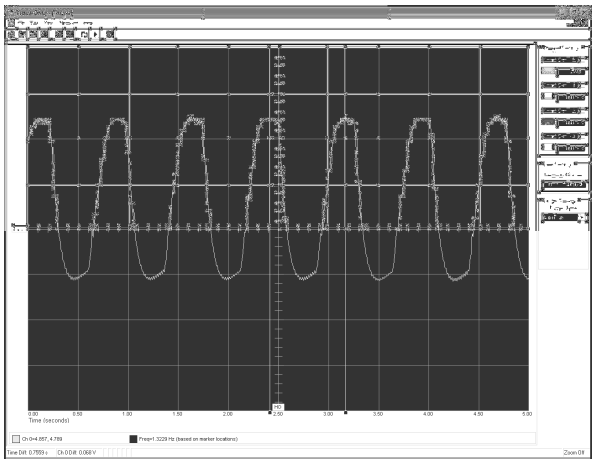

Fig. 2 Generated Pulse waveform

c. Results

Frequency set: 80 bpm
To translate x bpm into Hertz, the following relation is used.
Frequency in Hz = $x \div 60$
Thus, $80 \div 60 = 1.33Hz$
Frequency obtained: 1.3553 Hz

Thus,
$1.3553 \times 60 = 81bpm$
Accuracy: 98.75 %

Amplitude set: 144 levels = 8.01 V
To translate y amplitude levels to Volts, the following relation is used.
z = Binary(y)

$$Vo = Vref(\frac{z7}{2} + \frac{z6}{4} + ... + \frac{z0}{256}) + 5.20 \text{ V}$$

Where Vref = 5V and 5.2 V is provided by the adder circuit.
Thus,
z = Binary (144)
z = 10010000

$$Vo = 5(\frac{1}{2} + 0 + 0 + \frac{1}{6} + 0 + 0 + 0 + 0) + 5.2 = 8.01$$

Amplitude obtained: 7.8 V
Accuracy: 97.37 %

IV. Conclusions

This haptic training module, meant to aid practitioners of the Indian system of medicine finds application in areas such as telemedicine and remote-diagnosis. An extension of the device

F. Ibrahim, N.A. Abu Osman, J. Usman and N.A. Kadri (Eds.): Biomed 06, IFMBE Proceedings 15, pp. 585-587, 2007
www.springerlink.com ' Springer-Verlag Berlin Heidelberg 2007

could simulate the human pulse fed directly from a subject s arm (obtained via the pulse sensor setup) in place of the graphic front-end developed. With the use of more precise and sensitive motors such as Piezoelectric motors, it is possible to obtain highly accurate results.

REFERENCES

[1] Sergio Franco , Design with Operational Amplifiers and Analog Integrated Circuits- Third edition , McGraw Hill Higher Education, 2002 ISBN: 0-07-232084-2

[2] Janice Gillispie Mazidi, Muhammad Ali Mazidi, The 8051 Micro-controller and Embedded Systems , Prentice Hall, 1999 ISBN:0138610223

[3] Max A. Gonz alez-Palacios, Jorge Angeles, The Novel Design of a Pure Rolling Transmission to convert Rotational into Translational Motion , Proceedings of DETC 2000, 2000 ASME Design Engineering Technical conferences, September 10-14, 2000, Baltimore, Maryland, USA

[4] Sedra, Adel S. Microelectronic Circuits- Fifth Edition , Oxford University Press, ISBN 0-19-514252-7

[5] Sarvadeva Upadhyaya, Nadi Vijnaaa , First Edition, Vedic Life Sciences Pvt. Ltd, 1986

[6] www.healthmantra.com/siddha- Available on 25th January, 2006

Address of the corresponding author:

Author: Shriram Raghunathan
Institute: Department of Electrical Engineering, Anna University
City: Chennai
Country: India

F. Ibrahim, N.A. Abu Osman, J. Usman and N.A. Kadri (Eds.): Biomed 06, IFMBE Proceedings 15, pp. 585-587, 2007
www.springerlink.com ' Springer-Verlag Berlin Heidelberg 2007

In Vitro Modeling for Bioelectrical Impedance Measurement in Compartmental Syndrome

Rosidah Ab. Lazid[1], S. Anandan Shanmugam[2] and Md.Razif Md.Ali[3]

[1] University Malaya/Department of Biomedical Engineering, Kuala Lumpur, Malaysia
[2] University Malaya/Department of Medicine, Kuala Lumpur, Malaysia

Abstract— **Bioimpedance measurement was performed in vitro on a compartment model as part of the investigation for a non invasive procedure in diagnosing a compartmental syndrome (CS). A model was constructed to mimic the body compartment of a lower leg. The cellular fluid of potassium ion (K^+) of different concentration was prepared in vitro. The model was filled with K^+ solution and protein substances. Prior to the impedance measurement; pressure was applied within the compartment. This setup was to demonstrate physiologic events during CS. The impedance of the compartment at various concentration of K^+, protein and pressure were measured with a commercial tetra polar bioimpendance analyzer. The results obtained from this investigation had shown positive correlation as predicted.**

Keywords—**Compartmental Syndrome, Non invasive, bioelectrical impedance and physiologic events.**

I. Introduction

Compartmental Syndrome (CS) is a condition that occurs when fluid accumulates in unyielding fibro-osseous body compartment due to injury which results in an increase of interstitial tissue pressure that in turn reduces the arteriolar perfusion pressure ultimately causing cellular ischaemia and cell death [1].

Current objective diagnostic method involves invasive compartment pressure measurement procedures as described by Whitesides or using a commercially available portable manometer from Stryker Corp, USA.

More often, the syndrome is diagnosed clinically based on a high index of suspicion and through symptoms and signs that may not be conclusive. It is often that this condition is undiagnosed or diagnosed at a late stage when the ischaemia and tissue death is too advanced resulting in limb amputation to help salvage the patient from serious life threatening sequelae.

The current situation has placed challenge for researchers to provide improvement on the technique of diagnosing CS. Bioimpedance measurement method is one of the options for this improvement and it involves a non invasive procedure which is the objective for this investigation.

The physiologic events during the course of compartmental syndrome are summarized by the diagram below [2]. It is an important step to understand these physiologic changes and their causes for planning in setting up the protocols for measurements of impendence in a non-invasive environment.

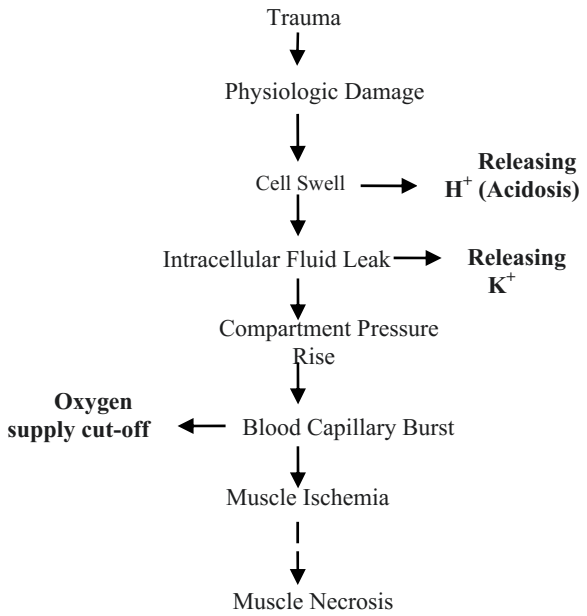

II. Materials and Methods

A. Bioimpedance and Electrolytes

A model was constructed using two cylindrical shapes container. An elastic material was used for the compartment wall. The compartment model was connected to the pressure meter. The simulation of inter-compartment pressure was carried out by applying pressure to the plunger. As a result, the compartment elastic wall expanded, and inter compartment pressure was measured by the pressure meter. At that time, the tetra polar electrodes were attached to the four conductor stubs for measuring the impedance.

F. Ibrahim, N.A. Abu Osman, J. Usman and N.A. Kadri (Eds.): Biomed 06, IFMBE Proceedings 15, pp. 588-590, 2007
www.springerlink.com ' Springer-Verlag Berlin Heidelberg 2007

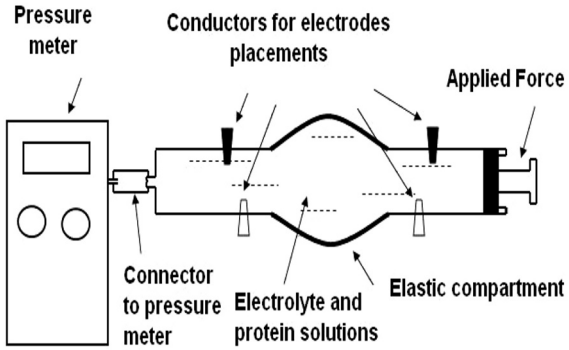

The basis for impedance measurements were determined based on the CS physiologic changes inside the compartment. The initial testing was conducted to investigate the impedance correlation of in vitro potassium ions (K^+) and protein in K^+ solution at various concentrations as indicators of CS. A tetra polar multi frequency bioimpendance analyzer from Xitron was used in the test. The distance between electrodes during measurements was 15 cm apart. If the placements of electrodes are too close with each others, the impedance measurement found to be inconsistence. The test was repeated at least for ten times for each concentration of electrolyte and protein. The impedance values obtained at 50 Hz were averaged and used to plot the graph [3], [4]. Figure 1 represented the result obtained.

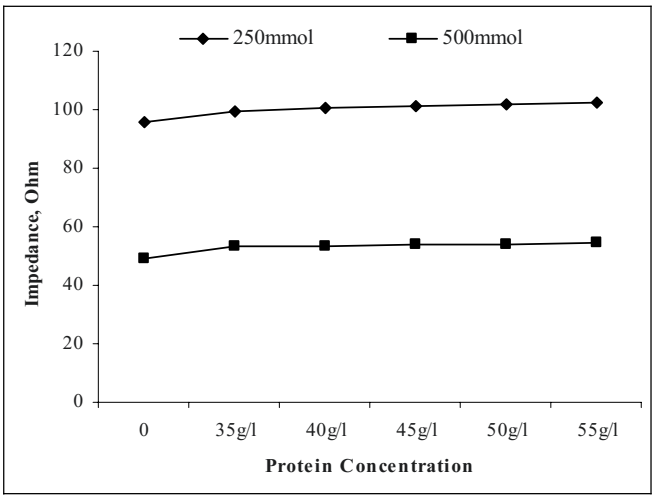

Fig. 1 Impedance measurements at various K^+/protein concentration

Early results had shown immanent correlation between impedance, K^+ and protein, as predicted by the Ohm s law. As the concentration of K^+ ion increases, the fluid inside the compartment becomes more conductive and provides less resistance for current to flow across. The presence of protein in the K^+ ionic solution in the other hand had caused resistance for the current.

$$V = IR \quad (1)$$

The positive result obtained provides a step forward in the investigation of trailing the CS events that may lead to a critical condition. In the next phase of investigation, study on the effect of pressure towards impedance was conducted.

B. Bioimpedance and Pressure

In the current technique of diagnosing CS, inter compartment pressure is the most familiar indicator of CS used by the clinicians. Hence, we have included the investigation on the effect of pressure to the impedance measurement under similar condition as in the initial testing.

The investigation of impedance versus pressure is conducted by increasing the hydrostatic pressure in the model compartment containing K^+ ions and protein to simulate CS in the lower limb compartment. The clinician refers to 30mmHg (4 Kpa) of diastolic pressure to confirm on the presence of CS [5]. Any measurements above 4 Kpa indicate severe clinical condition that requires immediate surgery to release pressure built up inside the compartment to stop further damage.

Therefore, the study of pressure versus impedance can be considered as vital for this research.

In the study of pressure versus impedance, pressure was applied to the compartment from 1 Kpa to 10 Kpa. Impedance was measured at every 1 Kpa increment and at various protein concentrations (gram/liter) in K^+ solution of 250mmol. The test was repeated at least for ten times for each pressure increment and concentration of electrolyte and protein. The impedance values obtained at 50 Hz were averaged and used to plot the graph. The result is tabulated in Table 1 and Figure 2.

F. Ibrahim, N.A. Abu Osman, J. Usman and N.A. Kadri (Eds.): Biomed 06, IFMBE Proceedings 15, pp. 588-590, 2007
www.springerlink.com ' Springer-Verlag Berlin Heidelberg 2007

Table 1 Impedance and Pressure

Pressure (Kpa)	Protein in 250mmol			
	No protein (Ω)	40g/l (Ω)	45g/l (Ω)	50g/l (Ω)
1	49.26	53.49	53.82	53.91
2	49.22	53.44	53.77	53.84
3	49.18	53.43	53.73	53.80
4	49.17	53.42	53.65	53.72
5	49.16	53.38	53.64	53.71
6	49.10	53.34	53.61	53.66
7	49.07	53.30	53.60	53.65
8	49.06	53.26	53.55	53.63
9	49.04	53.23	53.49	53.57
10	49.03	53.19	53.47	53.49

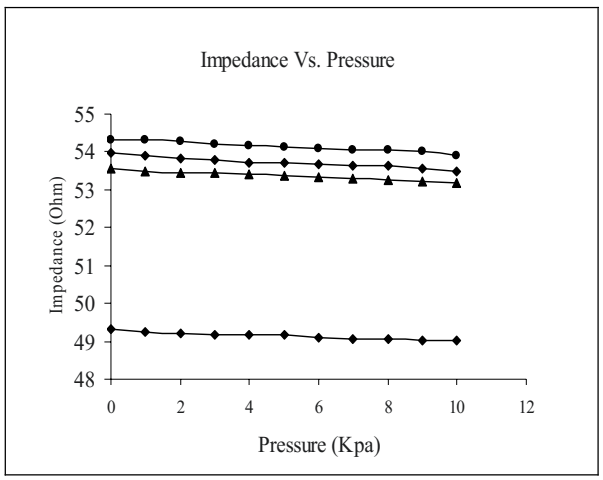

Once again, the results demonstrated a direct correlation of pressure and impedance. The test was repeated with 50mmol K+ solution with the same variation of protein s concentrations at various pressures with 1Kpa of increment. The result had shown the same trends.

Under the influence of pressure, ions in the body fluid solutions are closer with each others and current flows across with less resistance. Protein in the body fluid in the other hand created a resistance for current to flow normally and resulted in higher impedance measurements.

III. Conclusions

The study conducted in vitro indicated a correlation between bioimpendance and CS physiologic changes as predicted by the Ohm s law. The changes of inter compartment fluid composition and pressure can be detected by bioimpendance analyzers.

Monitoring of the changes in K+ concentration and pressure was decided based on the progress of CS. These events can be considered as early indicators of CS. and important for measurement before progressing to the next level of CS in which clinical intervention could be very invasive.

By capturing these events with impedance measurements and use them with reference to other clinical symptoms, clinicians may be able to assess the early state of CS by non invasive pressures. There are more investigations still required to strengthen these findings and their effectiveness, reliability and safety.

However, the findings stated have supported the theory of measuring CS electrolytes accumulation and pressure. This at least provide a positive insight for further investigation and development in the future.

References

1. Randall Swain, David Ross (1999) Lower Compartment, Post Graduate Medicine Online, Vol. 105/No. 3
2. Mulvey M, Bullock B (2000) Fluid, Electrolyte, and Acid-Base Balance, Focus on Pathophysiology , Philadephia Lippincott pp. 158-188
3. Munna Khan, Reggie O Hara, et al, (2005) Multi Dimension Application of Bioelectrical Impedance, JEPomline vol. 8
4. Cornish BH, Jacobs, A, Thomas BJ, et al (1999), Optimizing Electrode Sites for Segmental Bioimpedance Measurements, Physiology Measure 20:241-250
5. Mubarak SJ, Hargens AR, Owen CA, et al (1976), Journal of Bone & Joint Surgery, American Volume, 58(7):1016-29

Address of the corresponding author:

Author: Rosidah Ab. Lazid
Institute: University Malaya
City: Kuala Lumpur
Country: Malaysia
Email: roshida@ecri.org

F. Ibrahim, N.A. Abu Osman, J. Usman and N.A. Kadri (Eds.): Biomed 06, IFMBE Proceedings 15, pp. 588-590, 2007
www.springerlink.com ' Springer-Verlag Berlin Heidelberg 2007

Optical detection of ferromagnetic and fluorescently labeled microparticles, simulation of a magnetic trap

M. Brandl[1], M. Mayer[1,2], C. Fabian[2] and D. Falkenhagen[1]

[1]Danube University Krems/Center for Biomedical Technology, Krems, Austria
[2]University of Applied Science, St. Poelten, Austria

Abstract **A microsphere-based detoxification system (MDS) [1,2] is an adsorption system, whereby microadsorbent particles having diameters of 1--20 µm circulate in an extracorporeal filtrate circle. A thin-wall hollow-fiber membrane filter separates the microparticle-plasma suspension from the bloodstream. For patient safety, it is necessary to have a means to detect membrane ruptures that could lead to a release of microparticles into the patient's bloodstream, causing critical side effects. A non invasive optical detection system was developed to monitor the extracorporeal venous bloodstream for the presence of released microparticles. For detection purposes, polymeric microspheres, both ferromagnetic and fluorescently labeled, are suspended with the adsorbent particles. In the case of a membrane rupture, the labeled particles would be released together with the microadsorbent [2]. A high effective magnetic trap collect the ferromagnetic marker beats in the focus of an optical fluorescence detection device where the signal output is proportional to the trapped amount of labeled particles. A simulation model based on fluidic, gravitational and magnetic forces was developed to analyze the motion and sedimentation of the marker particles in the magnetic trap. The simulation results show excellent accordance to the laboratory experiments.**

Keywords—**Magnetic trap, Simulation, Ferromagnetic particles, Blood purification**

I. Introduction

In the adsorption system MDS (Microspheres based Detoxification System), high specific micro adsorbent particles in the size of 1-20 micrometers circulate in an extracorporeal filtrate circle. The MDS is especially used for acute liver dysfunctions. The system consists of two circuits: An extracorporeal blood circuit including a hollow fiber plasma filter and a secondary filtrate circuit with suspended high specific adsorbent microparticles. The fluid exchange through the membrane filter between the blood circuit and the filtrate circuit is depending on the circuit transmembrane pressure. To avoid particle contamination of the patient in case of a broken filter membrane (i.e. too high transmembrane pressure) or a broken filter embedding we add a small amount of labeled marker particles to the micro adsorbent circuit. The used marker particles are commercial monodisperse and ferromagnetic polystyrene microparticles, covered with polyurethane and covalently labeled with the fluorescence dye cresylviolet. In case of a filter rupture, the labeled marker beats are released together with the microadsorbent and can be detected by a high sensitive optical sensor including a magnetic trap. The magnetic trap consists of two permanent magnets which accumulate and focus the ferromagnetic marker beats in the optical beam of the fluorescence detector device. The fluorescence detector illuminates the control volume of the magnetic trap with light at the absorption band of the dye label. In case of trapped marker particles, the fluorescence dye emit light shifted to the fluorescence wavelength.

To optimize the accumulation of the marker beats in the magnetic trap, we have developed a mathematical model, to simulate all relevant acting forces to the particle.

II. Methods

For our investigations, we have developed a model including fluidic, gravitational and magnetic forces to the ferromagnetic particle.

A. Velocity field for streaming liquids

Fluidic forces for incompressible viscose liquids are described by the Navier-Stokes equation defined as:

$$\rho \frac{\partial \vec{u}}{\partial t} = -\vec{\nabla} p + \left(\vec{u} \cdot \vec{\nabla}\right)\vec{u} + \nu \Delta \vec{u} + \vec{f}$$
$$\vec{\nabla} \cdot \vec{u} = 0 \qquad (1)$$

From eq. 1 the velocity field $\vec{u}$ can be calculated under consideration of the specific density ρ, the local pressure p, the kinetic viscosity ν and the local force density $\vec{f}$ from external sources. For incompressible fluids, the divergence of the velocity vector field $\vec{u}$ is zero.

B. Magnetic forces

The magnetic trap consists of two rare earth permanent magnets generating an inhomogeneous magnetic field to

F. Ibrahim, N.A. Abu Osman, J. Usman and N.A. Kadri (Eds.): Biomed 06, IFMBE Proceedings 15, pp. 591-593, 2007
www.springerlink.com ' Springer-Verlag Berlin Heidelberg 2007

deflect the ferromagnetic marker beats. Substituting the local material equation

$$\vec{B} = \mu_0\left(\vec{H} + \vec{M}\right) \quad (2)$$

to the well known Maxwell equations, the magnetic field distribution can be calculated by solving

$$\vec{\nabla}\times\left(\frac{1}{\mu}\vec{\nabla}\times\vec{A} - \vec{M}\right) = \vec{0} \quad (3)$$

for the magnetic vector potential $\vec{A}$. The magnetic field density $\vec{B}$ can be easily calculated from the magnetic vector potential $\vec{A}$ using

$$\vec{B} = \vec{\nabla}\times\vec{A}. \quad (4)$$

For isotropic media ($\vec{B}$ is parallel to the particle magnetization $\vec{M}$), the acting magnetic force to the ferromagnetic beats is given by [2]

$$\vec{f}_m = M\vec{\nabla}B \quad (5)$$

C. Gravitational forces

For small particles in liquid, lift forces can not be neglected and must be considered in opposite to the acting gravitational force. The resulting force depends on the mass difference of equal particle and fluid volumes.

$$\vec{f}_g = \left(m_p - m_f\right)\vec{g} \quad (6)$$

III. Results:

To simulate the deflection and sedimentation of the labeled marker particles in the magnetic trap, the Lagrange equation for moving particles must be solved.

$$\rho_p V_p \frac{d\vec{u}_p}{dt} = -C_D \frac{\rho_f A_p}{2}\left|\vec{u}_f - \vec{u}_p\right|\left(\vec{u}_f - \vec{u}_p\right) + \vec{F} \quad (7)$$

The Lagrange equation describes the movement of the particles under influence of all acting forces summarized in $\vec{F}$ except of the fluidic forces which are part of the equation itself. The indices f and p stand for fluid and particle, where ρ is the specific density, V the volume, A the cross-section area, C_D the flow resistance, $\vec{u}$ the velocity vector field and $\vec{F}$ the sum of all acting external forces. For our model, we have calculated the flow resistance by the well known formula [3]

$$C_D = \frac{24}{\mathrm{Re}} \quad (8)$$

where **Re** is the Reynolds number. For spherical particles with radius r_p Re is defined as

$$\mathrm{Re} = \frac{2r_p\left|\vec{u}_f - \vec{u}_p\right|}{\nu}. \quad (9)$$

We run our simulations with the described mathematical model, using the software COMSOL multiphysics. The model geometry is shown in fig. 1 using a tube with diameter 4.8mm, and two disc magnets with a remanence B_r=1.2 tesla. For the simulation, we used water as liquid inside the tubing with a flow speed of 250 ml/min. The ferromagnetic particles in the practical experiment and in the simulation are spheres with a diameter of 30µm and a magnetic permeability of 5.

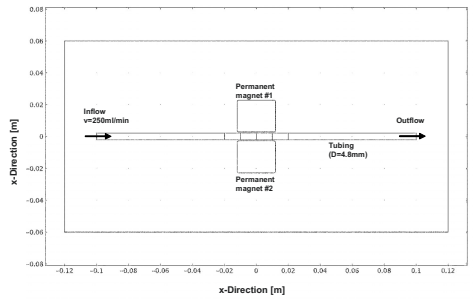

Fig. 1 Two dimensional model geometry of the magnetic trap

The particle sedimentation in the magnetic trap is shown in fig. 2 after a simulation time of t=30 sec.

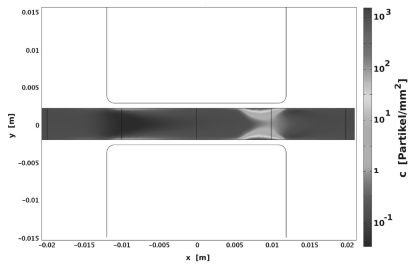

Fig. 2 Accumulation of the ferromagnetic particles in the magnetic trap

F. Ibrahim, N.A. Abu Osman, J. Usman and N.A. Kadri (Eds.): Biomed 06, IFMBE Proceedings 15, pp. 591-593, 2007
www.springerlink.com ' Springer-Verlag Berlin Heidelberg 2007

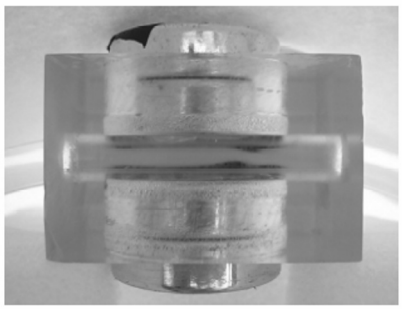

Fig. 3 Laboratory experiment of the magnetic trap (t=30sec)

The good accordance between our simulation and the laboratory experiments (fig. 3) validate the physical model.

Acknowledgment

The authors would like to thank the government of Lower Austria for financially supporting our activities.

References

1. Weber C, Rajnoch C, Loth F, Schima H, Falkenhagen D (1994) The Microspheres based Detoxification system (MDS) A new extracorporeal blood purification technology based on recirculated microspherical adsorbent particles. *Int J Artif Organs* 17:595 602
2. Falkenhagen D, Schima H, Loth F. Arrangement for removing substances from liquids in particular blood. European Patent: 94926169.7, Japanese Patent: 501083/97; U.S.Patent 5.855.782/5 Jan 99
3. Rosensweig R (1986) Ferrohydrodynamics. University Press, Cambridge
4. Schlichting H, Gersten K (2000) Boundary Layer Theory. Springer, 8th Edition
5. Hartmann J, Schildboeck C, Brandl M, Falkenhagen D (2005) Particle leakage in extracorporeal blood purification systems based on microparticle suspensions. *Blood Purif* 23:282 286
6. Brandl M, Hartmann J, Posnicek T, Aussenegg FR, Leitner A, Falkenhagen D (2005) Detection of fluorescently labeled microparticles in blood. *Blood Purif* 23:181 189

Address of the corresponding author:

Author: Dr. Martin Brandl
Institute: Danube University Krems, ZBMT
Street: Dr. Karl Dorrek Str. 30
City: Krems
Country: Austria
Email: mbrandl@donau-uni.ac.at

F. Ibrahim, N.A. Abu Osman, J. Usman and N.A. Kadri (Eds.): Biomed 06, IFMBE Proceedings 15, pp. 591-593, 2007
www.springerlink.com ' Springer-Verlag Berlin Heidelberg 2007

Temperature Modeling of Therapeutic Ultrasound: A Preliminary Finding

N.A. Kadri[1], A.R. Ahamad[1], E.N. Abdul-Latip[1], C.A. Azlan[2], M.G. Raha[1], N.F. Mohd-Nasir[3]

[1] Department of Biomedical Engineering, University of Malaya, Kuala Lumpur, Malaysia
[2] Department of Biomedical Imaging, University of Malaya, Kuala Lumpur, Malaysia
[3] Biomedical Electronics Engineering Program, Northern Malaysia University College of Engineering, Perlis, Malaysia

Abstract—**The temperature model of therapeutic ultrasound for human tissue is important in order to design an accurate instrumental assessment and calibration of therapeutic ultrasound device. The focus of this study is to verify temperature effects of ultrasound on tissues and explore the possibility of proposing a preliminary temperature model. A series of experiment had been conducted to clarify the relationship between output intensity and site of target tissue with temperature change in a phantom-tissue model for 10 minutes exposure of 3 MHz therapeutic ultrasound. It was found that 3 MHz ultrasound provided effectual heating at the superficial tissue, which is 1 cm from surface. It was also found that the experimental data had provided the necessary evidence for the development of preliminary temperature model. The temperature model had been produced by selecting suitable trend line for the graph of experimental data particularly for the temperature change at site of 1 cm from tissue surface. In conclusion, the preliminary finding of this study is the temperature effect of therapeutic ultrasound in homogeneous phantom-tissue model has a suitable pattern to be modeled into a simple mathematical equation. This study also proposed further study to develop more reliable and holistic evidence-based temperature model.**

Keywords—**Temperature modeling, therapeutic ultrasound**

I. Introduction

The investigation of thermal and non-thermal effects of directing ultrasonic energy through biological tissues has led to the discovery of therapeutic ultrasound which then extended into many medical areas, including guided surgery [1], treatment of cancer cells by hyperthermia using focused ultrasound [2], lithotripsy for non-invasive treatment of kidney stones [3] and non-invasive surgery ultrasonic liposuction [4]. In dentistry, ultrasound is used to remove dental plaque [5] and minor dental surgery [6]. In physiotherapy, therapeutic ultrasound has been used for the treatment of various soft tissue injuries and other pathological conditions [7,8].

With loads of application of therapeutic ultrasound in medical treatment, an issue arises about the need of treatment dosage and temperature modeling of the therapeutic ultrasound. Appropriate treatment dosage is needed to effect the various biophysical changes in the target tissues and to consistently deliver the required amount of energy to the target tissues [9].

An important stage prior to developing the treatment dosage and temperature modeling of the ultrasonic energy is to clarify the relationship of the ultrasonic frequency, output intensity, and duration of exposure on the amount of heating at various target tissue depths. There are a few studies investigating the relationships but incomplete for at least one or more factors. For example, a study had investigated only one output intensity, which was 1.5Watt/cm^2 for five minutes [10] whereas another study investigated two intensities, 1.0 and 1.5 Watts/cm^2, for ten minutes [11].

The hypothesis for this study was that a 3-MHz-ultrasound treatment with higher output intensity, greater exposure time and at more superficial site, will contribute to a greater change in temperature. However, the rate of temperature change and pattern of the change should vary between different parameters.

II. Methodology

A. Preparation of phantom-tissue model

A solid phantom-tissue model had been developed according to the invention by Madsen et al. from Wisconsin Alumni Research Foundation, Madison, Winconsin [12]. This phantom has the speed of sound and ultrasonic attenuation characteristics of human tissue, with very low ultrasonic scatter levels. The ultrasonic speed is approximately 1,538 m/s, which is very near to the mean ultrasonic speed of human tissue, 1,540 m/s. The ultrasonic attenuation characteristic of the solid phantom is also consistent with the ultrasonic characteristic of human tissue as its attenuation coefficient is 0.46 dB/cm/MHz while the range for human soft tissues is 0.3 to 0.7 dB/cm/MHz. The backscatter coefficient is approximately 40 dB below the backscatter level of human liver tissue and essentially negligible.

The component of this phantom is a filtered aqueous mixture of large organic water-soluble molecules and emulsion of fatty acid esters. This mixture is based on a combination of evaporated whole milk and water (Figure 1). The materials also include a hydroxyl compound (n-propanol) to control the ultrasonic speed of propagation through the

F. Ibrahim, N.A. Abu Osman, J. Usman and N.A. Kadri (Eds.): Biomed 06, IFMBE Proceedings 15, pp. 594-597, 2007
www.springerlink.com ' Springer-Verlag Berlin Heidelberg 2007

material. Thimerosal is also added for prevention of bacterial contamination. Finally, pure agarose gel is added to form a solid material.

B. Instrumentations

The instruments had been arranged so that the desired treatment procedure as stated in Table 3.2 could be applied. The ultrasound therapy unit used as the source of the ultrasonic energy throughout this study was Sonopuls 590 (Enraf Nonius B.V., Netherlands). The temperature measurement was done using HH309 Four Channel Thermometer which was connected to four needles that were then placed at different distance from surface (1cm, 2cm, 3cm, 4cm, and 5cm). The room temperature was maintained within the range of 25°C to 26°C throughout the study.

C. Experimental procedure

The phantom-tissue model was always stored at room temperature (25”℃-26”℃). Distances of 1, 2, 3, 4 and 5 cm from surface were marked on the phantom container. Holes were made (3 mm diameter) at these locations to allow the needle thermistors of the thermometer to be inserted to measure the temperature during ultrasound exposure. Three sets of holes were created to simulate a variety of treatment area. The distance between these sets of holes were 5 cm.

In this study the ultrasound frequency was fixed to 3 MHz while the output intensity was varied from 0.5 to 1.0 and 1.5 Watt/cm^2. The temperature measurement was conducted in 10 minutes during the exposure and 5 minutes after the exposure with data collections made at 1-minute intervals.

The transducer was applied in direct contact with the ultrasound gel. The angle of application was 90” from the surface of the phantom-tissue model. Size of treatment area was two times of the effective radiation area (2x ERA) and the movement of transducer was maintained at 120 beats/min, which means only two movements per second or a set of forward and backward movement per second. These procedural techniques were determined according to recommendations made by previous studies.

D. Data analysis

Data from the experiments were analyzed by considering the change in temperature as the dependent variable rather than the actual temperature measured. The data were analyzed using Microsoft Excel (Microsoft Inc., Redmond, WA) and Sigma Plot Version 8.02 (Systat Software, Inc., San Jose, CA) to generate graphs and equations for the temperature model. Paired sample tests were performed using SPSS 13.0 for Windows (SPSS Inc., Chicago, IL) to compare the effects of varying output intensity and duration of exposure at five tissue depths on the increase in tissue temperature (dependent variable). The factors were identified as significantly different if the p-value is less than 0.05.

The temperature model was produced using Microsoft Excel, which is based on graphs that were obtained from the experiment data. Suitable trend lines closest to the experiment data were chosen and appropriate equations were generated to be the thermal model for any particular intensity.

Fig. 1 Materials used for preparing the phantom-tissue model

III. Results and Discussion

Figure 2 shows the increase in temperature of the phantom-tissue model during the exposure; while Figure 3 shows the dispersion of temperature increase. It may be seen that the temperature increased as the duration of ultrasound exposure increased for the three output intensities (0.5, 1.0 and 1.5 Watts/cm^2). The magnitude of increase was also related to the depth of the target tissue and the output intensity, with peak temperatures decreasing as the depth increased and as the output intensity decreased. The most

F. Ibrahim, N.A. Abu Osman, J. Usman and N.A. Kadri (Eds.): Biomed 06, IFMBE Proceedings 15, pp. 594-597, 2007
www.springerlink.com ' Springer-Verlag Berlin Heidelberg 2007

superficial site, that is 1 cm below the surface, shows a rapid increase as the duration increases.

For the post-exposure phase (11 to 15 minutes), the same pattern is also applied to the different depth of measurement sites but oppositely. The temperatures at 1cm below the surface decreases rapidly while the other measurement sites have a little temperature increase (less than 1℃) over the 5 minutes post-exposure. The heating pattern could be considered as consistent and unaffected by the output intensity, although the peak temperatures reached for each intensity value appeared to depend on the site of the target tissue.

A. Intensity

For the output intensity factor, the mean temperature increased almost logarithmically with the increases in intensity, which was from 0.5 to 1.0 and 1.5 Watts/cm^2. Significant effects of the temperature increase ($p<0.05$) when varying the intensity (0.5, 1.0 and 1.5 Watts/cm^2) measured at different depths (1 cm, 2 cm, 3 cm, 4 cm and 5 cm) were observed.

B. Sites of target tissue

For the site of the target tissue factor, the mean temperature change diminished exponentially as the distance from the surface increased. The most superficial site, i.e. 1 cm from tissue surface, demonstrated the greatest heating during the exposure phase and consequently the greatest cooling during the post-exposure phase. There were significant effects of the temperature increase ($p<0.05$) when varying the site of the target tissue (1 cm, 2 cm, 3 cm, 4 cm and 5 cm from tissue surface) at different intensity values (0.5, 1.0 and 1.5 Watts/cm^2).

C. Temperature modeling

As the site of 1 cm from surface experienced the greatest heating during the 3 MHz ultrasound exposure, the temperature model only considered the data at that particular site. According to Figure 4, the proposed model for intensity values of 0.5, 1.0, and 1.5 Watts/cm^2, respectively is as follows:

$$y_{0.5} = 0.602\ln(x) - 0.2488 \quad (1)$$

$$y_{1.0} = 1.206\ln(x) - 0.3007 \quad (2)$$

$$y_{1.5} = 0.3227\ln(x) - 0.4909 \quad (3)$$

The temperature model proposed in this study was practically simple and included only the relevant parameter in the equation representation, as suggested by Goh [9]. However, the data employed in the model development were limited. In addition, only a single experimental data set was used. Therefore, it is paramount that further study involving additional datasets be conducted, as to acquire a more reliable model.

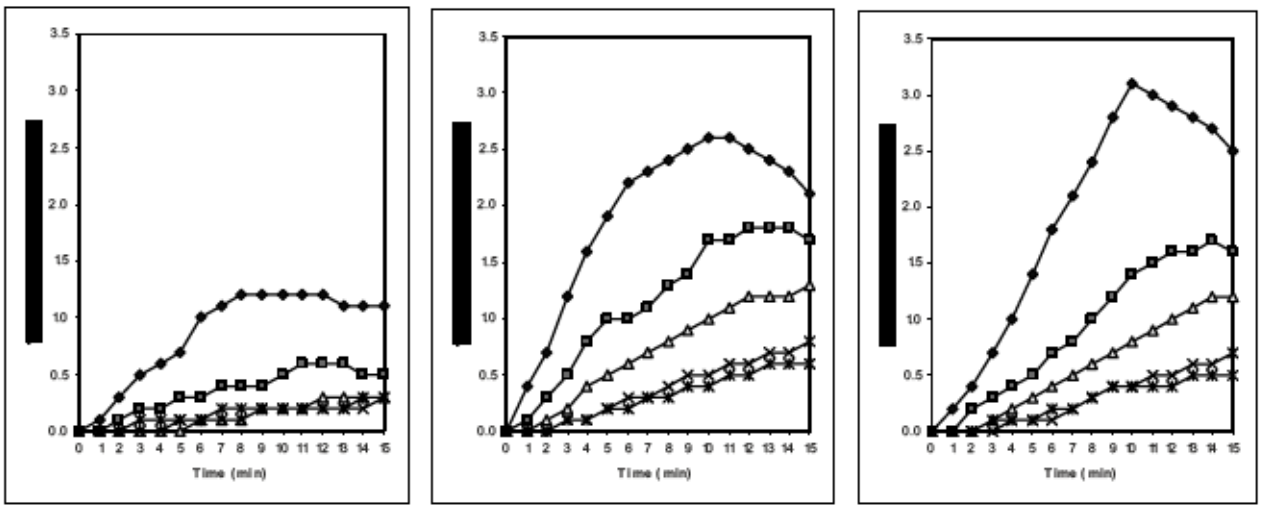

(a) (b) (c)

Fig. 2 The increase in temperature for 10 minutes exposure and 5 minutes post-exposure to therapeutic ultrasound using a) 0.5, b) 1.0 and c) 1.5 Watts/cm^2. The exposure was conducted at 120 beats/min of transducer movement for 2x ERA treatment area for 3 MHz frequency at 1cm (♦), 2cm (□), 3cm (Δ), 4cm (×) and 5cm (*) below the surface.

F. Ibrahim, N.A. Abu Osman, J. Usman and N.A. Kadri (Eds.): Biomed 06, IFMBE Proceedings 15, pp. 594-597, 2007
www.springerlink.com ' Springer-Verlag Berlin Heidelberg 2007

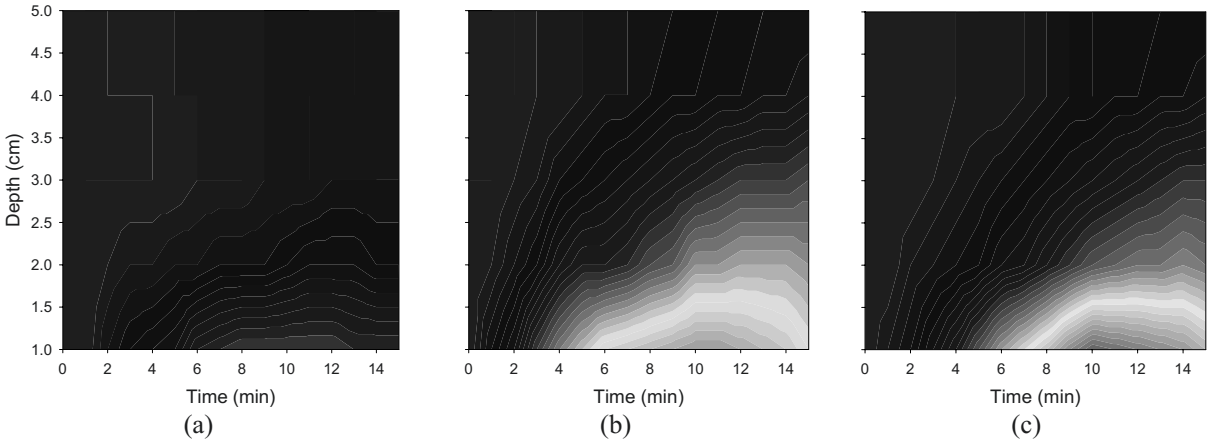

Fig. 3 The dispersion of temperature increase for 10 minutes exposure and 5 minutes post-exposure to therapeutic ultrasound using a) 0.5, b) 1.0 and c) 1.5 Watts/cm^2. The exposure was conducted at 120 beats/min of transducer movement for 2x ERA treatment area for 3 MHz frequency at 1cm, 2cm, 3cm, 4cm and 5cm below the surface.

IV. Conclusion

The results have provided the necessary evidence for development of preliminary temperature model. The temperature effects of therapeutic ultrasound in homogeneous phantom-tissue model have produced a suitable pattern to be mathematically modeled. Nevertheless, additional experimental datasets are required in order for a more reliable and robust model to be developed. This is particularly important, as the model may be used clinically as a means of enhancing the validity and reliability of the assessment and calibration of the therapeutic ultrasound device.

References

1. McGahan, J.P. (1990). Interventional Ultrasound. 1st ed. Williams & Wilkins.
2. Barkman, C.A., Almquist, L.O., Kirkhorn, T., et al. (1999). Thermotherapy: feasibility study using a single focused ultrasound transducer. Int J Hyperthermia. 42(1). pp. 63-76.
3. Demirkessen, O., Yaycioglu, O, Onal, B., et al. (2001). Extracorporeal shockwave lithotripsy for stones in abnormal urinary tracts: analysis of results and comparison with normal urinary tracts. J Endourol. 15(7). pp. 681-685.
4. Cooter, R., Babidge, W., Mutimer, K., et al. (2001). Ultrasound-assisted lipoplasty. ANZ J Surg. 71(5). pp. 309-317.
5. Harpenau, L. (2000). Clinical comparison of plaque removal and gingival bleeding reduction by two different brush heads on a sonic toothbrush. J Clin Dent. 11(2). pp. 29-34.
6. Smith, B.J. (2001). Removal of fractured posts using ultrasonic vibration: an in-vivo study. J Endod. 27(10). pp. 632-634.
7. Falconer, J., Hayes, K.W., Chang, R.W. (1990). Therapeutic ultrasound in the treatment of musculoskeletal conditions. Arthritis Care & Research. 3(2). pp. 85-91.
8. Feine, J.S., Lund, J.P. (1997). An assessment of the efficacy of physical therapy and physical modalities for the control of chronic musculoskeletal pain. Pain. 71(1). pp. 5-23.
9. Goh, A.C. (2003). An evidence-based model for determining treatment dosages in therapeutic ultrasound using thermometry: an in-vitro investigation using post-mortem pig tissue. PhD Thesis. Curtin University of Technology.
10. Lehmann, J.F., deLateur, B.J., Warren, C.G., et al (1967). Heating produced by ultrasound in bone and soft tissue. Arch Phys Med Rehabil.47. pp. 397 401.
11. Levine, D., Millis, D.L., Mynatt, T. (2001). Effects of 3.3 MHz ultrasound on caudal thigh muscle temperature in dogs. Vet Surg. 30(2). pp. 170-4.
12. Madsen, E.L., Frank, G.R. (1997). Very Low Scatter Liquid and Solid Tissue Mimicking Material for Ultrasound Phantoms and Method of Making the Same. United States Patent Document. U.S. Pat. No. 5,625,137.

Address of the corresponding author:

Author: Nahrizul Adib Kadri
Institute: University of Malaya
City: Kuala Lumpur
Country: Malaysia
Email: nahrizuladib@um.edu.my

F. Ibrahim, N.A. Abu Osman, J. Usman and N.A. Kadri (Eds.): Biomed 06, IFMBE Proceedings 15, pp. 594-597, 2007
www.springerlink.com ' Springer-Verlag Berlin Heidelberg 2007

The Alcohol Detection Using Heart Rate Variability and Bioimpedance

Chien-Hung Chen[1], Cheng-Yu Chen[1], Min-Wei Huang[1,2] and Kuo-Sheng Cheng[1]

[1] Institute of Biomedical Engineering, National Cheng Kung University, Tainan, Taiwan, ROC
[2] Department of Psychiatry, Chia-Yi Veterans General Hospital, Chia-Yi, Taiwan, ROC

Abstract— **In the study of physiological effect influenced by alcohol, the measurement of alcohol concentration is one important part of the researches. The efficient, accurate and convenient measurement tools are relatively under consideration. In this study, the regular blood tests, respiratory type alcohol examines, and Heart Rate Variability (HRV) were used to compare with the bioimpedance data in human body. The feasibility study was applied to record the ECG data from the human body with the analysis of the LabView 7.1 (National Instruments) and DAQPad 6020E (National Instruments). The bioimpedance data measured from the from left hand to right hand was recorded and analyzed by our bioimpedance measuring system and the MATLAB software version 6.5. All the electrophysiological parameters were analyzed with statistic software. In the result, the Heart Rate Variability (HRV) was significantly different in some subjects after alcohol consumption. However, there were no significant different in the bioimpedance measurement.**

Keywords— **Alcohol, Biompedance, Heart rate variability**

I. Introduction

Drunk driving is a serious problem in the car accident. The level of alcohol in the blood is the usual indicator for depriving the car-driving. Some studies revealed that the alcohol concentration would affect the central nervous system, so as to suppress the human auditory, visual, and behavioral control in a varied degree[1][2]. The contingency usually happened due to alcohol effect, especially the traffic accident. Therefore the measurement tools of alcohol concentration became more important. The accuracy and convenience of measurement also became important factors. The concentration of alcohol in the blood can be measured and quantified accurately by regular blood test, but the procedure was invasive and time-consuming. The other measurement tool is respiratory type alcohol test. Based on Henry s low,it was measurable with different alcohol transfusion to lung by breathing. But the recording device was necessary to be calibrated each day for data accuracy. The Heart Rate Variability (HRV)[3][4] has been widely applied in alcohol test. The Heart Rate Variability (HRV) was calculated by standard deviation of R-R interval data derived from original ECG data. It is difficult to get the useful ECG data in the short time. In this paper, we tried to verify the feasibility of the bioimpedance measurement in alcohol concentration test. The technology of bioimpedance measurement has been widely applied in many biomedical applications. There were some advantages of quickly analysis, convenient measurement and easily integrated design in bioimpedance measurement.

II. Materials and Methods

A total of 20 subjects (eighteen males and two females) with the age ranging from 20 to 30 years old (mean=24) are recruited in the study after the given informed consents All the subjects are not alcoholic. It is also approved by the IRB.

A. Experimental Design

The ECG and bioimpedance are measured during all the experiment before and after drinking the wine with 35% of alcohol. The experimental framework is depicted in Fig 1. The test started after feasting 1 or 2 hours. First, the subject sat comfortable on the chair with some light music on the background. Each subject had drunk 40 gm of alcohol within very short time. The physiological parameters of ECG and bioimpedance were recorded each half hour after alcohol consumption.

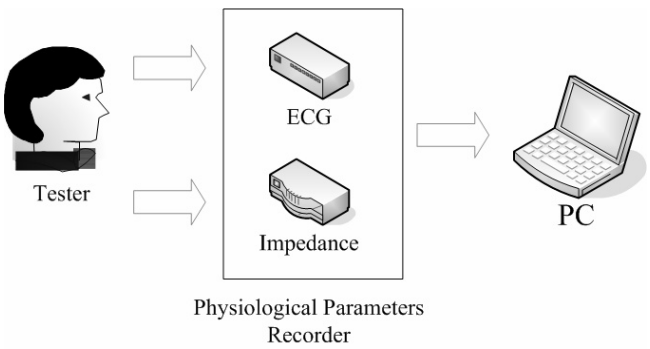

Fig. 1 System hardware

F. Ibrahim, N.A. Abu Osman, J. Usman and N.A. Kadri (Eds.): Biomed 06, IFMBE Proceedings 15, pp. 598-601, 2007
www.springerlink.com ' Springer-Verlag Berlin Heidelberg 2007

B. Physiological Parameters

During the reproductive and transferred phase, the ECG and bioimpedance were recorded using Ag/AgCl electrodes. The Lead one of ECG was obtained by ECG 100C Device (BIOPac Systems, Inc.). The data were filtered with low-pass filter 1Hz, highpass filter 35Hz, notch filter 60Hz, and amplify gain 5000. The LabView 7.1 (National Instruments) and DAQPad 6020E (National Instruments) were designed as data acquisition program.

The system block diagrams of bioimpedance measurement are depicted in Fig. 2. The basic components include (1) a microcontroller (2) a current generator (3) a voltage controlled current source (VCCS). Based on Ohm s law Eq. (1), the voltage was recorded while the current crossed over human body. The position of left hand was the input current electrode and the right hands was the output voltage electrode. Furthermore, the current pathway in the tissues was different from the varied frequency.[5][6] Fixed frequency (1k) sine wave was applied in our experiment. The another principle can be followed as ------ [7].The proposed waveform current source and digital millimeters for the bioimpedance measuring system were shown in Fig. 4.

$$R = \frac{V}{I} \tag{1}$$

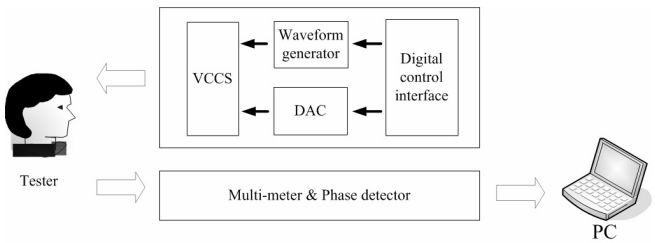

Fig. 2 Impedance system blocks

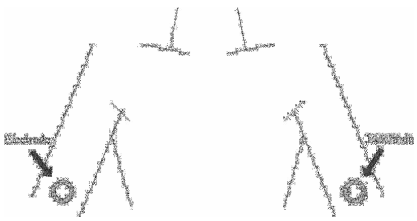

Fig. 3 Electrodes placement

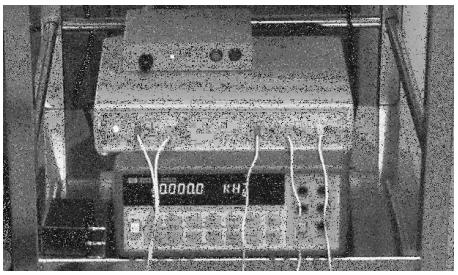

Fig. 4 Impedance system

C. Data Analysis

The software MATLAB version 6.5 was used to simulate the framework on ECG data analysis. The noise was removed by finite impulse response (FIR) filters. The Heart Rate Variability (HRV) was calculated in ECG data during all the experiment. Whereas the Equation [2] indicated the ECG standard deviation derived from the original ECG R-R interval

$$s = \left(\frac{1}{n} \sum_{i=1}^{n} (x_i - \bar{x})^2 \right)^{\frac{1}{2}} \text{ where } \bar{x} = \frac{1}{n} \sum_{i=1}^{n} x_i \tag{2}$$

In the bioimpedance, the mean value of impedance data was obtained from Equation [3].

$$\overline{X} \equiv \frac{X_1 + X_2 + \cdots + X_n}{n} = \frac{\sum_{i=1}^{n} X_i}{n} \tag{3}$$

D. Statistics

In order to estimate and analyze the parameter of recording, the biostatistics was used to verify physiological parameter influenced by alcohol. All the parameters collected from the Heart Rate Variability (HRV), bioimpedance , alcohol respired concentration and alcohol concentration from blood test were analyzed with the independent students T-test by the software SPSS version 12. The standard deviation, mean value, and P value were shown in the table.

III. Results

The measurement of respiratory type alcohol recording device was compared with the alcohol concentration in blood test. The result was shown in Fig 5(a). The Blood alcohol content (BAC) and breathe alcohol content (BrAC) were displayed proportionally each 30 minutes. In our ex-

F. Ibrahim, N.A. Abu Osman, J. Usman and N.A. Kadri (Eds.): Biomed 06, IFMBE Proceedings 15, pp. 598-601, 2007
www.springerlink.com ' Springer-Verlag Berlin Heidelberg 2007

periment, the respiratory type alcohol test was easily substituted for blood test for the perfect match in the concentration decay curve. The HRV result was shown in Fig 5(b), the R-R interval and standard deviation of ECG were analyzed with MATLAB version 6.5. The parameters of bioimpedance, HRV, and BrAC values were shown in Fig 5(c) where the alcohol consumption data was shown after 180 minutes(the 7th point shown in cross axle). It was obvious that the HRV relative value changed more variable than the bioimpedance relative value did.

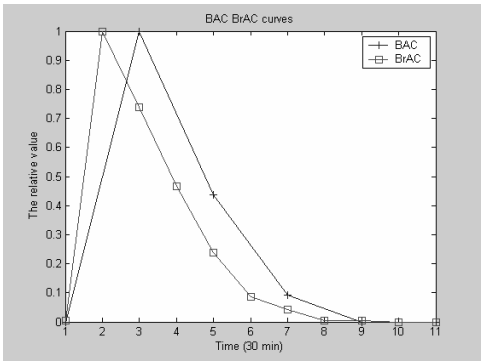

(a) BAC BrAC correct curves

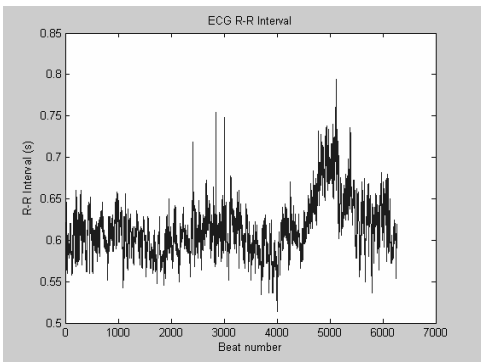

(b) ECG R-R interval

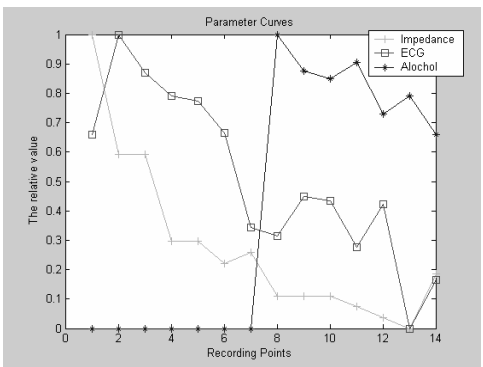

(c) Recording data curves

Fig. 5 Result of parameter data

The independent students T-test was applied for discriminate the difference between the 18 subjects. The descriptive analyzed results of parameter were listed in Table 1. The standard deviation divided by the mean value of bioimpedance changed from 51.1% to 35.9 % between befor and after alcohol consumption, whereas the standard deviation divided by the mean value of HRV value changed from 37.6% to 52.3 % between before and after alcohol consumption . The result showed the difference between befor and after alcohol consumption in HRV value was valuable for further evaluation in alcohol study. The table 2 showed the paired students T-test results between before and after alcohol consumption in the HRV and bioimpedence study. Obviously, the HRV value was easily influenced by alcohol rather then the bioimpedence value ($p<0.05$).

Table 1 Statistics of parameters

	Mean	N	Std. Deviation	Std. Error Mean	Std. Deviation / Mean
Impedance Before Drink	1.391635	18	.7117	.1677	51.1%
Impedance After Drink	1.278019	18	.4588	.1081	35.9%
HRV Before Drink	4.42E-02	18	1.6617E-02	3.92E-03	37.6%
HRV After Drink	3.34E-02	18	1.7474E-02	4.12E-03	52.3%

Table 2 Statistics of paired simples test

	Paired Differences					Sig.(2-tailed)
	Mean	Std. Deviation	Std. Error Mean	95% Confidence Interval of the Difference		
				Lower	Upper	
Impedance Before Drink - Impedance After Drink	.1136	.29371355	6.92E-02	-3.2E-02	.2567	.119
HRV Before Drink - HRV After Drink	1.09E-02	2.0169E-02	4.75E-03	8.54E-04	2.09E-02	.035

F. Ibrahim, N.A. Abu Osman, J. Usman and N.A. Kadri (Eds.): Biomed 06, IFMBE Proceedings 15, pp. 598-601, 2007
www.springerlink.com ' Springer-Verlag Berlin Heidelberg 2007

IV. Disscussion and Conclusion

In this paper, the respiratory type of alcohol detector and Heart Rate Variability (HRV) were used to verify the feasibility of the human bioimpedance. However, the result showed that the difference of HRV value between before and after alcohol consumption was significant while the no difference of bioimpedance value between before and after alcohol consumption. The result showed that the bioimpedance detection was not suitable in alcohol concentration experiment. However, the single frequency of current source was performed in this paper instead of the multi-frequency of current source probably made the worthlessness in alcohol concentration experiment detected by bioimpedance. The further modification and improvement of bioimpedance measurement technology would be anticipated in the further.

Acknowledgment

The authors would like to thank volunteers in this experiment in the Institute of Biomedical Engineering, National Cheng Kung University, Taiwan, Taiwan, ROC.

References

1. Naranjo CA, and Bremner KE, Behavioural correlates of alcohol intoxication, Addiction. Vol. 88(1), 1993, pp 25-35.
2. Tagawa M. Kano M. Okamura N. Itoh M. Sakurai E. Watanabe T. Yanai K. Relationship between effects of alcohol on psychomotor performances and blood alcohol concentrations. Japanese Journal of Pharmacology. Vol. 83(3), 2000, pp 253-260.
3. Malpas SC, Whiteside EA, Maling TJ. Heart rate variability and cardiac autonomic function in men with chronic alcohol dependance. Br Heart J Vol.65(2), 1991, pp 84-88.
4. Rossinin J, Vitasalo M, Partanen J, et al. Effects of acute alcohol ingestion on heart rate variability in patients with documented coronary artery disease and stable angina pectoris. Am J Cardiol Vol. 79, 1997, pp 487 491.
5. A. De Lorenzo**,** A. Andreoli**,** J. Matthie**,** and P. Withers**,** Predicting body cell mass with bioimpedance by using theoretical methods: a technological review, J. Appl. Physiol. Vol. 82, pp. 1542-1558, 1997.
6. Grimnes S and Martinsen ØG, *Bioimpedance and Bioelectricity Basics,* Academic Press, 2000.
7. Holder DS, *Electrical Impedance Tomography, Methods, History and Applications,* Institute of Physics Publishing, 2005

Address of the corresponding author:

Author:	Kuo-Sheng Cheng
Institute:	National Cheng Kung University, Institute of Biomedical Engineering
Street:	No.1, University Road
City:	Tainan
Country:	Taiwan, ROC
Email:	kscheng@mail.ncku.edu.tw

F. Ibrahim, N.A. Abu Osman, J. Usman and N.A. Kadri (Eds.): Biomed 06, IFMBE Proceedings 15, pp. 598-601, 2007
www.springerlink.com ' Springer-Verlag Berlin Heidelberg 2007

Visualizing Collaborative Time-Varying Scientific Datasets

J. M. Sharif [2], M. S. S. Omar [1], M. S. A. Latiff [2] and M. A. Ngadi [2]

[1]Bioinformatics Research Lab, Faculty of Science, University Technology of Malaysia, Johor, Malaysia
[2]Department of Computer System & Communication, University Technology of Malaysia, UTM Skudai, 81310, Malaysia
Email: johan@fsksm.utm.my, shahir@bio.fs.utm.my, shafie@fsksm.utm.my, asri@fsksm.utm.my
Telephone: (+607) 5532384 Fax: (+607) 5565044

Abstract— **Our perceptive of the scientific datasets has largely relied on numerical and statistical analysis of data from experimental dimension and computer simulation result [4][14][11][12][13]. In particular, we consider a simulated 3D time-varying model of scientific datasets and examine the temporal correlation among datasets. Our goal is to contrive effective visual representations to assist scientists in ascertaining temporal correlation among intricate and apparently chaotic scientific datasets. We propose a hybrid application with combination of streamline, global and local color scale and opacity scheme for spatio-temporal collaborative depiction. We illustrated also few images that can offer an effective tool for visually mining 3D time-varying scientific datasets.**

Keywords— **scientific data, visualization, hybrid scheme, coding theory, color scale, time-varying data, spatio-temporal visualization, molecular dynamics, visual representation**

I. Introduction

A spatio-temporal data set is a collection of data where data values vary in both space and time. Abstractly, such a data set can be considered as a (continuous and discrete) specification of a function, $F : \mathbb{E}^d \times \mathbb{T} \rightarrow \mathbb{R}^n$, where $\mathbb{E}^d$ denotes d-dimensional Euclidean space, $\mathbb{T} = \mathbb{R}^* \cap \{\infty\}$ the domain of time, and $\mathbb{R}^n$ an n-dimensional scalar field. Examples of such data sets include time-varying simulation results, films and videos, time-varying medical scans, geometrical models with motion or deformation, meteorological measurements and many more.

For lower dimensional spatio-temporal data sets, it is common to visualise to such data sets using line graphs, bar charts or other pictorial representations of a similar nature. For more complex spatio-temporal data sets, such as time varying geometrical models, it is common to render a visualization of spatial data at each time step, and display a series of visualization in a temporal order as animation. However, viewing animation or movies in general, is a time-consuming and resource-consuming process.

In *visual data mining*, viewing movie in order to extract meaningful information also relies on viewer s ability to remember characteristics of specific visual features in the movies as well as their skills interpreting various changes of these features correctly, often within a very a small window of time. Hence, the effectiveness of viewing usually declines rapidly when viewing period extends.

It is therefore highly desirable to use visualization to summarize meaningful information in higher dimensional spatio-temporal data sets. With a carefully prepared visualization which convey both spatial and temporal features, the human vision systems, perhaps the most intelligent vision system, may be able to interpret spatio-temporal features in the visualization.

For example, in physics the existence of spatio-temporal collaborative in ion trajectories in glasses was suggested by experimental results. However, any detailed observation of such collaboration character is not possible at moment. Meanwhile, our understanding of the structure of the glass and the ion trajectories has been enhanced with computer simulation followed by statistical analysis. However due to the size and complexity of the time-varying data generated, the details of the structure-transport relationships in the data were usually overlooked in favour of ensemble average in statistical analysis. Many scientific puzzles associating with the collaborative phenomena in ion trajectories remain unsolved and challenge the visualization technology to help uncover the spatio-temporal relationship between glass structure and ion trajectories.

During analysis, some of the data sets could be very big such as Beazleay and Lomdahl [1] were presented the method that can be used for very large scale molecular dynamic simulation. Meanwhile, Zhu et al. [16] were presented a grid technology and parallel rendering approach for visualizing a massive molecular datasets. Bulatov and Grimes [3] used a video visualization technique called MPEG-based method to generating a video clips that depict the animated movement of atoms. However, viewing animation or movie in general is a time-consuming and resources-consuming process.

To extract meaningful datasets, Imada et al. [8] introduced automated histogram filtering (AHF) for time complexity analysis on protein structure elucidation. This technique most closely to the statistical clustering technique [5] [9] [10] that had been used for analysis of molecular dynamic trajectories. While, Best and Hege [2] developed a

F. Ibrahim, N.A. Abu Osman, J. Usman and N.A. Kadri (Eds.): Biomed 06, IFMBE Proceedings 15, pp. 602-606, 2007
www.springerlink.com ' Springer-Verlag Berlin Heidelberg 2007

method called planar map. Basically, they constructed a 2D map of the trajectory that can reveal conformational ensembles and applied a cluster analysis procedure that allows for the automatic identification of the cluster. They used a line to connect all the points in 2D-dimensional map and they combine some of the point to form ellipsoid. This method will modify some of the interesting point in our works which is the main objective to visualise a timeline events of ion trajectories.

Instead of clustering or grouping the trajectories, Huitema and van Liere [7] filter out uninteresting atom motion from the larger concerted motions. Same with Wiley et al. [15], they used a similar approach with fourier and hilbert method for filtering a frequency of sample trajectory. Horiuchi and Go [6] also used a similar approach on molecular dynamic trajectories to extract the lowest frequency mode from the simulation data. The method shown by Huitema, Horiuchi and Wiley will remove some of the interesting trajectory which is critical to our main purpose to visualise a timeline of trajectories.

The objective of this work is to develop effective visual representation and visualization techniques to help scientists extract meaningful spatial and temporal information from spatio-temporal datasets. In this paper, we propose a hybrid scheme that uses streamline for orientation, color scale and color number coding scheme for depicting a timeline events and zooming effect with transparency scheme for probability of collaboration. With a collection of visual examples, we demonstrate that this scheme can offer an effective tool for visually mining 3D time-varying datasets. We show that the visualization not only confirm the presence of collaborative phenomena in ion dynamics but also help identify the dynamic patterns and trigger events of such movements. This enables scientists involved to develop more elegant and comprehensive hypotheses about scientific datasets.

The ability to convey temporal as well as spatial information is critical in our particular application, where the scientists need a visual representations that can effectively highlight the correlation between different ions in their motions among seemingly chaotic trajectories especially in collaborative events. This particular challenging requirement provided this work with the principal motivation.

In the rest of this paper, we will describe the application concern and scientific background in Section 2. In this section, we will first examine the methods that can convey orientation information to viewers. We will devote most of our focus to the visualization of temporal information in order to confirm and identify the time series activities in the data sets. In Section 3, we will present some results of visual data mining process on glassy ion trajectories if there is a collaboration events, which will be followed by our concluding remarks in Section 4.

II. Visualizing ion dynamics

In this section, we will first examine the more challenging task for visualizing temporal information in order to identify the series of events and collaborative events. We will discuss the use of glyph, color and opacity in our visual representations and present the methods for constructing and rendering composite visualization that convey a rich a collection of indistinguishable visual features for assisting in a visual data mining process.

A. Orientation

Given an ion trajectory as a series of $n + 1$ points, $p_0, p_1, \ldots, p_n$, we have nconsecutive vector segments, $v_1, v_2, \ldots, v_n$, where $v_i = (p_i - p_{i-1})$. One can visualise such a trajectory using streamlines or vector glyphs.

In Figure 1, even though each conical glyph, which represents a vector segment, depict the instantaneous velocity at a given time interval with its length and the direction of the motion with its pointer but its does not much help to visualise a time series events and collaborative issues in ion dynamic without the combination of color scale. In the next section, we will shows the color scale can give more understandable about time series events in ion dynamics.

Fig. 1. A trajectory of sodium #169

B. Temporal Information

When using visualization to summarise a series of events along a timeline, perhaps the most difficult task is to associate a particular event with a precise moment on the

F. Ibrahim, N.A. Abu Osman, J. Usman and N.A. Kadri (Eds.): Biomed 06, IFMBE Proceedings 15, pp. 602-606, 2007
www.springerlink.com ' Springer-Verlag Berlin Heidelberg 2007

timeline. This is useful not only determine the time of an event but also for the identification corresponding parties involved in collaborative, but collaborative events is not included at moment.

1) Global Color Scale: In order to shows the global time-line of events on streamline, we introduced *Global Key Colors* Scale. In this scheme, we use a small set of color, $c_1, c_2, \quad , c_k$ ($k > 1$), then we assigned a colors to specific vector in the vector series:

$$\begin{array}{ccccccc} v_1 & v_u & \ldots & v_v & \ldots & v_n \\ c_1 & c_2 & \ldots & c_i & \ldots & c_k \end{array}$$

where indices such as u and v are pre-determined. For each vector that has not assigned a color we obtain a color by interpolating the two nearest neighbours with the specified key colors in each direction. This scheme allow a viewer to determine a time frame at a global scale with the help of key colors. In Figure 2, we chosen seven key color which from rainbow color to visualise global scale of time series. At local level the interpolation can make different vector segment indistinguishable. Moreover, it is possible to have the same or similar interpolated colors between different sets of consecutive key colors.

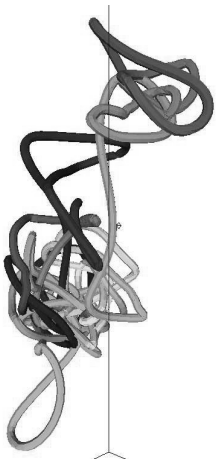

Fig. 2. Seven Key Colors for trajectory of sodium #169

2) Local Color Scale: In order to correlate each vector segment with the timeline more accurately and hence to improve the differentiation of different vector segments, we introduce a Color Number Coding Scheme in our visualization.

Given a small set of key colors, $c_1, c_2, \quad , c_k$ ($k > 1$) and distinctive interval-color (e.g., while, black or grey depending on the background color), we code a group of consecutive mvectors as a k-nary number, terminated by a vector in the interval-color. Given nas the total number of vectors and we always assign the interval-color to the first vector, we need to find the smallest integer mthat satisfies Equation 1;

$$((m + 1)\, k^m) \geq n \tag{1}$$

For instance, when $n = 1000$, using two key colors, say red and green, we need in $m = 7$ color digits. We have $m = 5$ for $k = 3$, $m = 4$ for $k = 4$, and $m = 2$ when k reaches 19. The selection of mand kneeds to address the balance between a smaller number of colors or a smaller number of color digits in each group of vectors. The former ensures more distinguishable colors in visualization, and the alter reduces the deductive effort for determine the temporal position of each vector. Figure 3 shows a quaternary color coding scheme for ion tracks with 1000 vectors.

III. Collaborative ion dynamics

When collaborative events is takes place between ions in the simulation results then the possible method that we could used is opacity scheme. But the details of this scheme, implementation and result will become the future works of this study. Even in this paper we are not focusing on collaborative events but we extended a brief regarding transfer function that could be possible in our application.

By combining all the above methods, we provide an effective visual representation for visualizing collaborative ion dynamic. Figure 4 shows the example of collaborative events in ion dynamics.

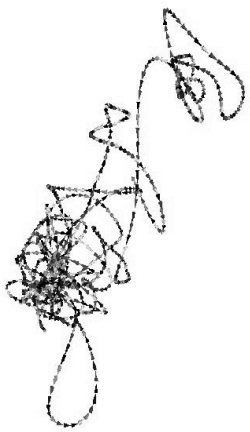

Fig. 3. Quaternary Color Coding Scheme on sodium #169 trajectory.

F. Ibrahim, N.A. Abu Osman, J. Usman and N.A. Kadri (Eds.): Biomed 06, IFMBE Proceedings 15, pp. 602-606, 2007
www.springerlink.com ' Springer-Verlag Berlin Heidelberg 2007

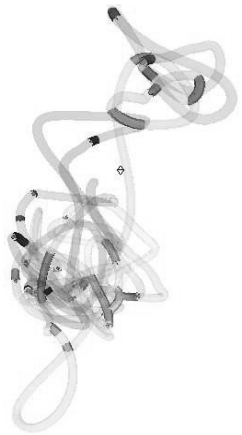

Fig. 4. Combination of visualization collaborative ion dynamics

The main objectives of this task is to discover if collaboration is exhibited between ions in the simulation results. As described previously, there is not well-defined description about collaboration events, although experiments suggested the existence of collaboration phenomena. We, including the physicists involved, did not know in what form a collaborative event may display, in what way ions may cooperate with each others or what event may cause ions entering in or disengaging from collaboration. Therefore we have introduced a variable, ψ, representing the probability of collaboration. Given a set of m hypothesized criteria of collaboration, we have:

$$\psi = \omega_1\psi_1 + \omega_2\psi_2 + \quad + \omega_m\psi_m \tag{2}$$

where ω_i is the weight of criterion i, and $\psi_1 + \psi_2 + \quad + \psi_m = 1$. In this work, we have considered three such criteria, namely (1) the ability for two or more ions to maintain similar orientation, (2) the ability for two or more ions to maintain similar velocity, and (3) the ability for two or more ions maintain constant gap between them.

Given two corresponding vector segments, $v_{a,i}$ and $v_{b,i}$, belonging to two different ion trajectories, we have:

$$\psi_1 = \left(\frac{1}{2}\left(\frac{v_{a,i} \bullet v_{b,i}}{\left|v_{a,i}\right|\left|v_{b,i}\right|} \right) \right)^{D_1} \tag{3}$$

where $D_1 \geq 0$ is de-highlighting factor. The larger the D_1 is, the less probable a vector is considered being involved in collaboration. With ψ_1, $v_{a,i}$ and $v_{b,i}$ are considered to be in collaboration, if they follow a similar direction.

Once we have computed $\psi \in [0,1]$, we can highlight or dehighlight the corresponding vector segments. Two different methods of highlighting the probability of collaboration are shown in Figure 5. We chosen a small sample because it is easy for clarification purpose. In (a), we apply an opacity of tube around the glyphs with a high ψ value, which in effect defines the opacity of the tube. In (b), we use the value of ψ to modify an opacity of the corresponding tube and vector segment . When, if there is a high probability of collaboration, the tube and vector glyphs are fully opaque and if there is a low probability, they are almost totally transparent. The second method seems to convey information with more certainty to human observer.

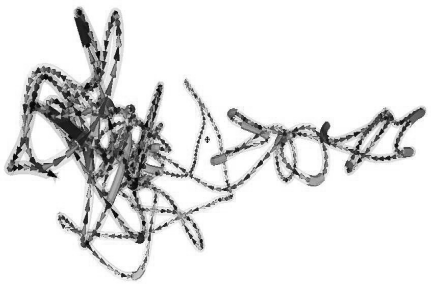

(a) direction, method 1

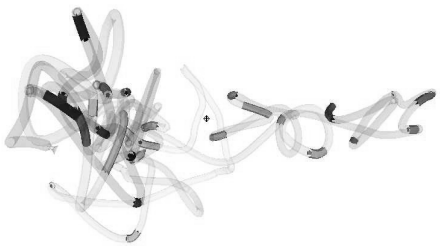

(b) direction, method 2

Fig. 5. The possible collaboration between Na #211 and Na #106, when ψ was computed with ψ_1 (only #106 is shown)

In Figure 5, (a) and (b) show the probability computed using ψ_1 between each of the ion trajectories Na #106 with Na #211. From this visual examples, the scientists would be able to trigger the collaborative events effectively. Without highlighting and de-highlighting based on ψ, it would be difficult to observer this phenomena directly.

By combining some above-mentioned methods together, we provide an effective visual representation for visualizing spatio-temporal collaboration. With the help of global color scale, the scientists can determine the global time frame of the events, for example, $t = 0$ can be easily found between two consecutive color. For more details, local color scale will help to determine which corresponding ions in collaboration. These will give such an idea to our future works to enhance the capability in helping the scientists to determine the corresponding parties involved in collaboration issues.

F. Ibrahim, N.A. Abu Osman, J. Usman and N.A. Kadri (Eds.): Biomed 06, IFMBE Proceedings 15, pp. 602-606, 2007
www.springerlink.com ' Springer-Verlag Berlin Heidelberg 2007

IV. Conclusion

We have developed an effective visual representation, which have combined from several schemes including streamlines for orientation, color scale for time series events and opacity scheme for collaborative events. Again, all these schemes can be beneficial also in another field of study like biophysics, biological, bioinformatics or any collaboration events especially in time-varying events. In the future works, we plan to extend the works in conveying temporal information in a high degree of certainty before we go further on visualizing collaborative events in ion dynamics.

References

[1] D. M. Beazley and P. S. Lomdahl. Lightweight computational steering of very large scale molecular dynamics simulations. In *Conference on High Performance Networking and Computing*. IEEE, 1996.

[2] C. Best and H.-C. Hege. Visualizing and identifying conformational ensembles in molecular dynamics trajectories. In *Computing in Science and Engineering*, pages 68 74, 2002.

[3] V. L. Bulatov and R. W. Grimes. Visualization of molecular dynamics simulations. In *Eurographics UK Chapter*, 1996.

[4] K. Funke. Jump relaxation in solid electrolytes. *Progr. Solid State Chem*, 22:111 195, 1993.

[5] H.L. Gordon and R.J. Somorjai. Fuzzy cluster analysis of molecular dynamics trajectories. volume 14, pages 249 264, Oct 1992.

[6] T. Horiuchi and N. Go. Peojection of monte carlo and molecular dynamics trajectories onto the normal axes: human lysozyme. In *Proteins*, volume 10, pages 106 116, 1991.

[7] H. Huitema and R. V. Liere. Interactive visualization of protein dynamics. In *Proceedings of Conference on Computer Graphics (VISUALIZATION 2000)*, pages 465 468. IEEE, Oct 2000.

[8] J. Imada, P. Chapman, and S.M. Rothstein. Recognizing patterns in high-dimensional data: automated histogram filtering for protein structure elucidation. In *19th International Symposium on High Performance Computing Systems and Applications, 2005. HPCS 2005*, pages 238 243. IEEE, May 2005.

[9] M.E. Karpen, D.J. Tobias, and C.L. Brooks. Statistical clustering techniques for the analysis molecular dynamics: Analysis of 2.2-ns trajectories of ypgdv. volume 32, pages 412 420, Jan 1993.

[10] S.L. Kazmirski, A. Li, and V. Daggett. Analysis methods for comparison of multiple molecular dynamics trajectories: Applications to protein unfolding pathways and denatured ensembles. volume 290, pages 283 304, Jan 1999.

[11] K. L. Ngai. Analysis of nmr and conductivity-relaxation measurements in glassy li_2s-sis_2 fast-ion conductors. *Physical Review B*, 48, 1993.

[12] K. L. Ngai, G. N. Greaves, and C. T. Moynihan. Correlation between the activation energies for ionic conductivity for short and long time scales and the kohlrausch stretchting parameter b for ionically conducting solid and melts. *Phys. Rev. Lett*, 80:1018 1021, 1998.

[13] K. L. Ngai, Y. Wang, and C. T. Moynihan. The mixed alkali effect revisited : importance of ion interactions. *Journal of Non-Crystalline*, 307-310:999 1011, 2002.

[14] W. Smith, G. N. Greaves, and M. J. Gillan. Computer simulation of sodium disilicate glass. *Journal Chemical Physics*, 103, 1995.

[15] Adrian P. Wiley, Martin T. Swain, Stephen C. Phillips, Jonathan W. Essex, and Colin M. Edge. Parametrization of reversible digitally filtered molecular dynamics simulations. In *Journal of Chemical Theory and Computation*, volume 1, pages 24 35, Feb 2005.

[16] Huabing Zhu, Tony Kai Yun Chan, Lizhe Wang, Wentong Cai, and Simon See. A prototype of distributed molecular visualization on computational grids. In *Future Generation Comp. Syst*, volume 20, pages 727 737, 2004.

F. Ibrahim, N.A. Abu Osman, J. Usman and N.A. Kadri (Eds.): Biomed 06, IFMBE Proceedings 15, pp. 602-606, 2007
www.springerlink.com ' Springer-Verlag Berlin Heidelberg 2007

Development of a steerable cochlear implant electrode array

B.K. Chen[1], H.N. Kha[1] and G.M. Clark[2]

[1] Monash University/Department of Mechanical Engineering, Melbourne, Australia
[2] Bionic Ear Institute, Melbourne, Australia

Abstract— **Development of a new steerable electrode array with embedded nitinol shape memory alloy actuators is described in this paper. The risk of damaging the basilar membrane during insertion of electrode array into the human cochlear is expected to be significantly reduced with the ability to redirect the tip of the electrode array at the critical hook region. The final position of this electrode array can also be adjusted to lie beneath the basilar membrane inside the scala tympani for delivery of neurotrophins (growth factors). The bending behaviour of the steerable electrode array and its trajectories during insertion into the scale tympani were predicted using a 3D finite element model. Results from the model have shown that the new electrode array can be steered through the critical 'hook' region and be accurately positioned for delivery of neurotrophins.**

Keywords—**cochlear implant, electrode array, residual hearing, basilar membrane, neurotrophins. Critical hook region.**

I. Introduction

A cochlear implant system works using an electrode array which is inserted into the scala tympani (the lower tubular space of the cochlea) to transmit electrical signals converted from external sound. The signals can stimulate the auditory neurons connected to the inner ear (cochlea) which provides hearing to patients. A large number of patients with significant hearing impairment have had their hearing restored to near-normal levels. However, those with less significant hearing impairment or with some residual hearing have not benefited from cochlear implants because the potential risks of causing damage during insertion may outweigh improvements to their hearing [1,2]. Studies [3-7] have shown that the critical hook region which is about 10-12 mm from the round window is where damage to the basilar membrane and the spiral ligament is most likely to occur. Damage occurs by perforation of the basilar membrane by the tip of the electrode array or/and by shearing of the spiral ligament. If the tip of the electrode array can be redirected away from the basilar membrane or the spiral ligament, then the electrode array can pass the critical hook region without causing damage.

Research is being done to determine methods for delivering neurotrophins (growth factors) into the scala tympani to regenerate auditory neurons that are progressively due to the sensorineural deafness [8] and due to insertion-induced damage to the basilar membrane [9]. It is desirable to locate the electrode array close to the central position which is beneath the basilar membrane inside the scala tympani (Fig. 1 Position A) so that the neurotrophins delivered to the neurons close to the this cochlear structure are not wasted [10].

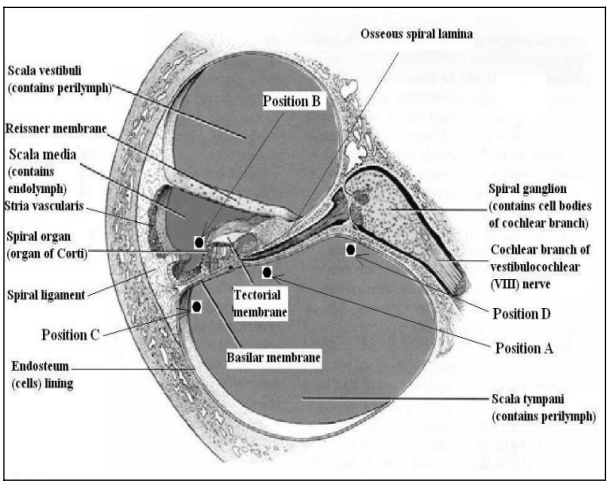

Fig. 1. Anatomy of the cross-section of cochlear pathways [11].

The steerable electrode array overcomes two major hurdles. Firstly, by reducing the risks of insertion-induced damage in the critical hook region and secondly, by providing a means of optimizing the final placement of for delivery of neurotrophins. The steering ability of the electrode array is made possible by the use of three 6mm nitinol shape memory alloy actuators which are embedded in the electrode array (Fig. 2). The first actuator which is located close to the tip of the electrode array is used to steer the tip through the critical hook region while the remaining two actuators are used to attain an optimal resting position of the electrode array for delivery of neurotropins. The nitinol shape memory alloy actuators have been shown to be biocompatible by Mineta et al. (2002) [12]. Each actuator has a memorized pre-curved shape which can be straightened at room temperature. The first straight actuator is embedded close to the front end (2-8mm from the tip) of the Nucleus standard straight array, while the second and the third actuators are embedded further from the front end (8-14mm and 14-20mm from the tip) of

F. Ibrahim, N.A. Abu Osman, J. Usman and N.A. Kadri (Eds.): Biomed 06, IFMBE Proceedings 15, pp. 607-610, 2007
www.springerlink.com ' Springer-Verlag Berlin Heidelberg 2007

the electrode array (Fig. 2). The ends of each actuator are connected with two platinum lead wires which extend to the rear end of the electrode array. When the electrode array is inserted up to the critical hook region , heating the first actuator from room temperature to 37^0C using a small current allows it to return to the memorized shape which bends the tip of the electrode array away from the basilar membrane. The insertion of the electrode array can then continue safely. After the electrode array is fully inserted into the scale tympani, the remaining two actuators are activated which cause the electrode array to move from position C (Fig. 1) to a more favourable position A.

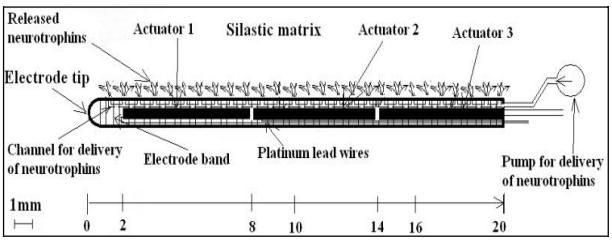

Fig. 2. Illustration of the electrode array embedded with three nitinol actuators and wires along the length.

This paper describes the use of a finite element model to predict bending behaviour of the new electrode array embedded with the nitinol actuators. The model was used to evaluate a number of design options of the steerable electrode array, e.g. the number of actuators, their locations along the length of the electrode array, their size and curvatures [13]. The modeling approach for designing the electrode array overcomes a number of limitations associated with the use of costly and time consuming experimental models to study the insertion behaviour of new electrode arrays as well the use of human temporal bone models [5,6] which have low reproducibility and the use of silicone rubber scala tympani model [14] which does not accurately represent material properties of the scala tympani.

II. Methods

Details of the finite element model used for predicting bending behaviour and insertion trajectories of an electrode array as well as final position of the electrode array have been described by Kha et al. (2006) [13]. The mesh for the electrode array and the scala tympani was constructed using FEMAP and NE/NASTRAN 8.32 was used to undertake the analysis. Flexural bending experiments were performed to determine the stiffness of the electrode arrays for the Nucleus standard straight array and the stiffness of the embedded segments was calculated using the rule of mixture [15]. Experimental values of friction coefficient between the electrode array and the endosteum lining covering the interior wall of the scala tympani for the Nucleus standard straight array were used in the finite element model [16].

Boundary conditions were applied to model the insertion of the electrode array and the bending behaviour of the actuators:

1. Insertion of the electrode array up to the critical hook region . The back end of the electrode array was constrained and a 12mm displacement was applied.
2. The first actuator at the tip of the electrode array was activated which caused the tip of the electrode array to curve away from the basilar membrane and the spiral ligament.
3. Insertion of the electrode array was continued. Another 13 mm displacement was applied to the back end.
4. The two remaining two actuators were activated and the final position of the electrode array was determined.

Forces exerted by the actuators (to recover their memorized pre-curved shapes) on the electrode array were calculated using Equation 1. Deflection (δ) of the segment of electrode array embedded with a nitinol bending actuator could be determined using Equation 2 [17].

$$F = \frac{3E_N I_N \delta_N}{L_N^3} \quad (1)$$

where

Young s modulus of elasticity of the nitinol actuator: $E_N = 28$GPa (martensite phase)

Moment of inertia of the nitinol actuator:

$$I_N = \frac{tw^3}{12} = \frac{0.035 \times 0.1^3}{12} = 2.92 \times 10^{-6} (mm^4)$$

(t is thickness and w is width of the actuator)

Deflection of actuator: $\delta_N = 2.18$mm [12]

Length of the actuator or embedded segment: $L_N = 6$mm

$$\delta = \frac{FL_N^3}{3E_{EA} I} \quad (2)$$

F. Ibrahim, N.A. Abu Osman, J. Usman and N.A. Kadri (Eds.): Biomed 06, IFMBE Proceedings 15, pp. 607-610, 2007
www.springerlink.com ' Springer-Verlag Berlin Heidelberg 2007

where

E_{EA} = average value of Young s modulus of elasticity of the electrode array segment before embedment (MPa) [15].

I = moment of inertia of the embedded segment = $\pi d^4/64$ (mm^4); (d = diameter of the embedded segment = 0.45-0.7mm).

III. Results and discussion

Figure 3a shows position of the electrode array at the critical hook region (i.e. 12mm from the round window) which was predicted using the 3D FE model. The tip of the electrode array appears to impinge the basilar membrane. Further insertion of the electrode array beyond this point may result in damage to the basilar membrane outweighing any benefits from electrical stimulation. Therefore, in patients with residual hearing, a Short-Electrode approach has been adopted in which the electrode array is extended only 10mm into the cochlea [2]. According to the authors, the short electrode array makes use of a combination of acoustic and electrical stimulation which preserve near normal music appreciation for the patients. The technique of partially inserting the electrode array into the cochlea was also confirmed by Skarzynski et al. (2004) [1] as the first step towards the treatment of partial deafness.

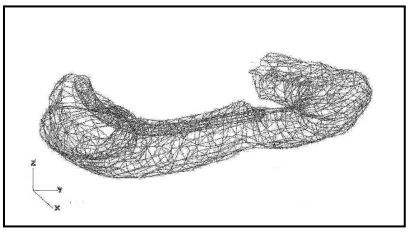

(a) Before activation

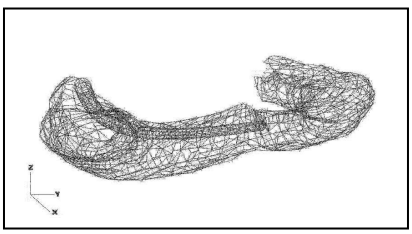

(b) After activation

Fig. 3. The electrode array at the critical hook region (before and after activation of the first actuator).

However, if the risk of damage to the basilar membrane at the critical hook region can be substantially reduced, it would be safe to insert the electrode array further into the cochleae of patients with residual hearing to fully exploit electrical stimulation. To minimize the risks, the first actuator at the tip of the electrode array was activated which caused the tip to bend downwards and away from this sensitive structure (Fig. 3b) enabling the electrode array to be safely inserted a further 13mm into the cochlea (Fig. 4a). The final position of the electrode array is attained by activation of the remaining two actuators which locates the electrode array close to the central position (Fig. 4b) for delivery of neurotrophins.

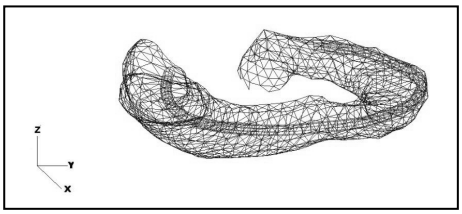

(a) Before activation

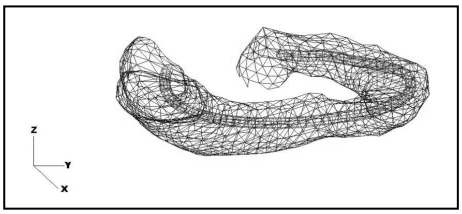

(b) After activation

Fig. 4. The electrode array at the final position (before and after activation of the remaining two actuators).

Refinement of the steerable electrode array is made possible with the use of magnetic resonance imaging (MRI) techniques [18,19] to validate the predicted positions of the electrode array before and after activation of the nitinol actuators and allows predicted and experimental trajectories of the electrode arrays to be compared. The MRI technique has also been found to be more reliable than the computer tomography in differentiating between endocochlear fluid and fibrotic occlusions [20] and is thus useful for identifying relative positions of the electrode array to the basilar membrane.

IV. Conclusions

Development of a new steerable electrode array with embedded nitinol shape memory alloy actuators has been described in this paper. The risk of damaging the basilar membrane during insertion of electrode array into the human cochlear is expected to be significantly reduced with the use

F. Ibrahim, N.A. Abu Osman, J. Usman and N.A. Kadri (Eds.): Biomed 06, IFMBE Proceedings 15, pp. 607-610, 2007
www.springerlink.com ' Springer-Verlag Berlin Heidelberg 2007

of this steerable electrode array. A 3D finite element model was used to predict the bending behaviour of the steerable electrode array and its trajectories during insertion into the scale tympani. Coupled with MRI techniques, the design of the steerable electrode array can be optimized for both passing safely through the critical hook region and for attaining the final placement for delivery of neurotrophins.

References

1. Skarzynski H, Lorens A, Piotrowska A (2004) Preservation of low-frequency hearing in partial deafness cochlear implantation, International Congress Series (Elsevier) vol. 1273, 2003, pp 239-242
2. Turner C, Gantz B (2004) Preservation of residual acoustic hearing in cochlear implantation, International Congress Series (Elsevier) vol. 1273, 2003 pp 243-246
3. Johnsson L, House W, Linthicum F (1982) Otopathological findings in a patient with bilateral cochlear implants. Annals of Otology, Rhinology & Laryngology 91:74-89
4. Galey F (1984) Initial observations of a human temporal bone with a multi-channel implant. Acta Oto-Laryngologica 38-44
5. Shepherd R, Clark G, Pyman B, Webb R (1985) Banded intracochlear electrode array: Evaluation of insertion trauma in human temporal bones. Annals of Otology, Rhinology & Laryngology 94:55-59
6. Tykocinski M, Saunders E, Cohen L, Treaba C, Briggs R, Gibson P, Clark G, Cowan R (2001) The Contour electrode array: safety study and initial patient trials of a new perimodiolar design. Otology Neurotology 22**:**33-41
7. Wardrop P, Whinney D, Rebscher S, Roland J, Luxford W, Leake P (2005) A temporal bone study of insertion trauma and intracochlear position of cochlear implant electrodes I: Comparison of Nucleus banded and Nucleus Contour™ electrodes. Hearing Research 203:54-67
8. Richardson R, Wise A, O'Leary S, Hardman J, Casley D, Clark G (2004) Tracing neurotrophin-3 diffusion and uptake in the guinea pig cochlea. Hearing Research 198:25-35
9. Malgrange B, Rigo J, Thomas R, Staecker H, Moonen G, Lefebvre P (1999) Growth factor therapy to the damaged inner ear: clinical prospects. International Journal of Pediatric Otorhinolaryngolog 49:19-25
10. Clark G, Wallace G (2004) Bionic ears: their development and future advances using neurotrophins and inherently conducting polymers. Applied Bionics and Biomechanics 1:67-89
11. Tortora G, Grabowski R (1993) Principles of Anatomy and Physiology. Addison Wesley Longman, Inc. Boston
12. Mineta T, Mitsui T, Watanabe Y, Kobayashi S, Haga Y, Esashi M (2002) An active guide wire with shape memory alloy bending actuator fabricated by room temperature process. Sensors and Actuators A 97-98:632-637
13. Kha H, Chen B, Clark G, Jones R (2006) Finite element modeling of final placement and insertion depth of new cochlear implant electrode array embedded with nitinol shape memory alloy actuators, The 2006 International Conference on Modeling, Simulation and Visualization Methods (MSV 06), 26-29 June 2006, in press
14. Rebscher S, Talbot N, Bruszewski W, Heilmann M, Brasell J, Merzenich M (1996) A transparent model of the human scala tympani cavity. Neuroscience Methods 64:105-114
15. Kha H, Chen B, Clark G, Jones R (2004) Stiffness properties for Nucleus standard straight and Contour electrode arrays. Medical Engineering and Physics 26:677-685
16. Kha H, Chen B (2006) Determination of frictional conditions between electrode array and endosteum lining for use in cochlear implant models. Journal of Biomechanics 39:1752-1756
17. Gere J, Timoshenko S (1997) Mechanics of Materials. International Thomson Publishing, PWS Publishing Company. Washington
18. Jappel A, Baumgartner W, Robinson S, Czerny C, Hamzavi J, Frei K (2004) Clinical application of magnetic resonance imaging in fifty cochlear implanted patients, International Congress Series (Elsevier) vol. 1273, 2003, pp 387-389
19. Risi F, Saldanda A, Leigh R, Gibson P (2004) Magnetic resonance imaging safety of Nucleus 24 cochlear implants at 3.0T, International Congress Series (Elsevier) vol. 1273, 2003, pp 394-398
20. Klein H, Bohndoff K, Hermes H, Schutz W, Gunther R, Schlondorff G (1992) Computer tomography and magnetic resonance imaging in the preoperative work-up for cochlear implantation. Journal of Radiography 15:89-92

Address of the corresponding author:

Author: Dr Bernard Chen
Institute: Monash University
Street: Wellington Road
City: Melbourne
Country: Australia
Email: bernard.chen@eng.monash.edu.au

F. Ibrahim, N.A. Abu Osman, J. Usman and N.A. Kadri (Eds.): Biomed 06, IFMBE Proceedings 15, pp. 607-610, 2007
www.springerlink.com ' Springer-Verlag Berlin Heidelberg 2007

An Automatic Lower Limb Training Machine for Monoplegia Patients

Soohong Kim, Jongman Cho, Junghyeon Choi and Taewoo Nam

Department of Biomedical Engineering, Inje University, Gimhae, Republic of Korea

Abstract— **This machine is developed to replace a conventional ankle stretching device (ASD) consisting of wooden wedges with a microcontroller-controlled electro-mechanical actuators. An ASD has been used for lower limb rehabilitation treatment system for training of monoplegia (hemiplegia) patients for a long time. The developed training machine can control the angle between foot and calf (AFC), holding time, and the number of repetition. The machine consists of an embedded control unit (ECU) and a main control unit (MCU). The application program running on the MCU controls the overall operation of the system, it sends commands to the ECU to get proper functions, and receives status of the ECU. The ECU consists of two clinometers, a 12-bit serial ADC, a low-pass filter with cut-off frequency of 1Hz, microcontroller, RS-232 serial interface with the MCU and electro-mechanical actuators. It can reduce the work of physical therapist and improve the effect of rehabilitation exercise.**

Keywords— **lower limb training, monoplegia, clinometer, rehabilitation, electro-mechanical actuator**

I. Introduction

Recently, efficient and systematical treatment and necessity of lower limbs training system are required for the fast increase of walking disabled people like hemiplegia patients. This is not only the indication to estimate the recovery of motor functions of lower limb of hemiplegia patient but also the goal of rehabilitation therapy [1]. Therefore, an automatic lower limb training machine can help for rehabilitation therapy.

The conventional rehabilitation therapy for lower limb monoplegia patients is insufficient because it has used very simple methods so that it cannot provide quantitative and scientific therapy. In addition, a physical therapist must take part in the process of therapy during the exercise. Nevertheless, research about this kind of rehabilitation therapy is deficient [1]. Therefore it is needed to design and develop an automatic training machine that satisfies the purpose of the treatment and can provide the patient with various treatments to supplement the shortcoming of the conventional devices.

II. Methods

A. Functional blocks

The designed machine in this study is divided into three units depending on functions; the angle measurement unit for monitoring of current AFC, the display unit for displaying of various parameters and status of machine, and the control unit for controlling of electro-mechanical actuators according to the commands. The configuration of these three units is shown in Fig. 1.

The current AFC value for each foot is measured by clinometer (SA1, DAS), low-pass filtered to eliminate spike noises. The output of clinometer is analog voltage signal proportional to the angle. The low-pass filtered AFC values are converted into digital form by dual channel 12-bit serial analog-to-digital converter (MCP3203, Microchip). The converted AFC values are processed by the microcontroller (AT89C51, Atmel). When the AFC from the clinometer sensor is obtained, these results show very sensitive changing rate between voltages. Therefore, we tried to produce low pass filter (2^{nd} order Butterworth) which has 1Hz cut-off frequency in order to get rid of noise of high frequency.

The processed 12-bit AFC value from the ECU is transmitted to the MCU via RS-232 serial communication interface and the application program on the MCU sends commands to the ECU after comparing the current AFC value with the preset AFC value.

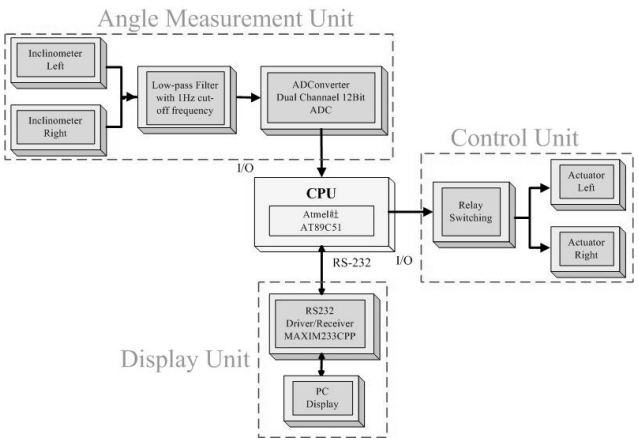

Fig. 1 Block diagram of hardware system

After receiving commands the ECU turns on or off the electro-mechanical actuators (JC35, Chang Won Gi Jeon) to get the target AFC. The actuator used in this machine is driven by 24V DC and has 10mm/sec maximum speed.

F. Ibrahim, N.A. Abu Osman, J. Usman and N.A. Kadri (Eds.): Biomed 06, IFMBE Proceedings 15, pp. 611-614, 2007
www.springerlink.com ' Springer-Verlag Berlin Heidelberg 2007

B. Application software

1. Program of the ECU

The program of the ECU was implemented by using the microcontroller compiler (μVision, Keil) and burned on 8-bit microcontroller with 4K bytes flash. MCU program is interrupted and get changed value from microcontroller when the AFC is changed. Therefore electro-mechanical actuator is operated by the commands of the ECU from the MCU.

2. Program of the MCU

Fig. 2 is a MFC program applied for ASD on the PC. It shows that it received the current AFC and compared with setting data via RS-232 serial communication interface. Finally, we can operate the electro-mechanical actuator by MCU.

This application program is based on Visual C++ 6.0 of Microsoft Visual Studio and used computer with Windows XP OS system, Pentium 4 and 1GB RAM.

C. Flow chart

1. Flow chart of the ECU

Fig. 3 shows the development of the algorithm and flow chart for the ECU.

Acquired AFC is saved in buffer of microcontroller and the header of data is analyzed. The AA header comes from the left clinometer and the CC header comes from the right clinometer. The current AFC value is transmitted to the MCU via serial communication interface when any changing has been occurred. The electro-mechanical actuator is operated with the results of data processing in the MCU.

2. Flow chart of the MCU

Fig. 4 shows the development of the algorithm and flow chart for the MCU.

The ASD is initialized with getting AFC after starting of program. The machine is operated and compared with the entering value at real-time, in addition, displayed in application window. The training is finished when the current value is satisfied with destination value. It can be stopped by therapist or patient when emergency status even though in the middle of training.

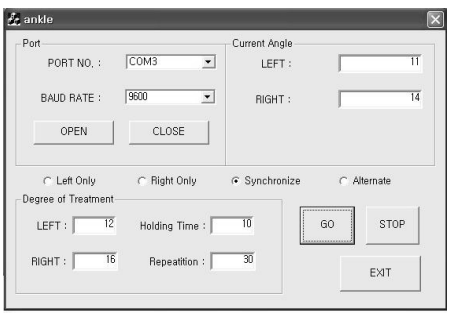

Fig. 2 User interface window of the MCU

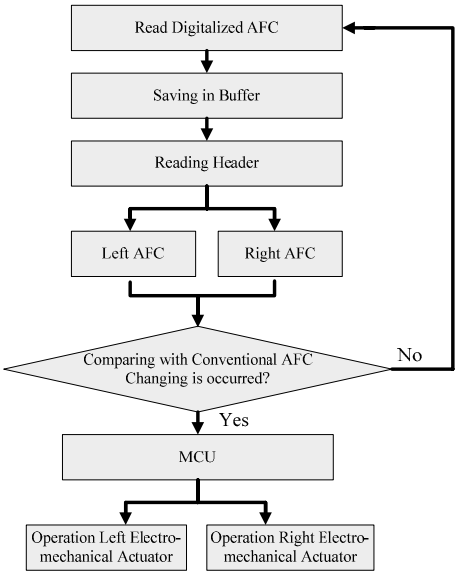

Fig. 3 Flow chart of the ECU

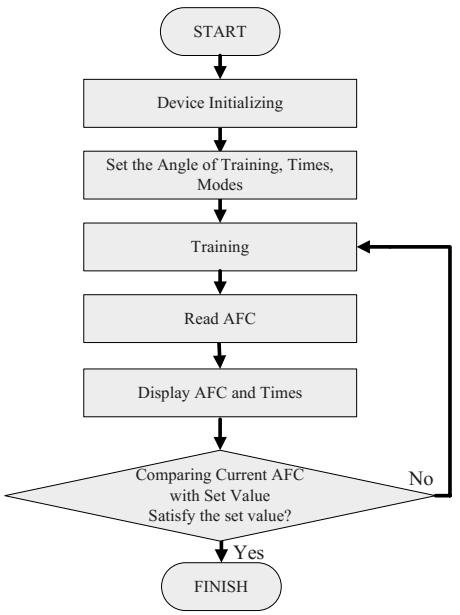

Fig. 4 Flow Chart of the MCU

D. Mechanical design

Fig. 5 shows the ankle of patient and the mechanical diagram of the ASD. (a) is the status before operation and (b) is the status after operation. Electro-mechanical actuator is used for safety operation and safety guard is made to prevent sliding down. Clinometer which is getting the current AFC is attached to each sideward of force plates.

F. Ibrahim, N.A. Abu Osman, J. Usman and N.A. Kadri (Eds.): Biomed 06, IFMBE Proceedings 15, pp. 611-614, 2007
www.springerlink.com ' Springer-Verlag Berlin Heidelberg 2007

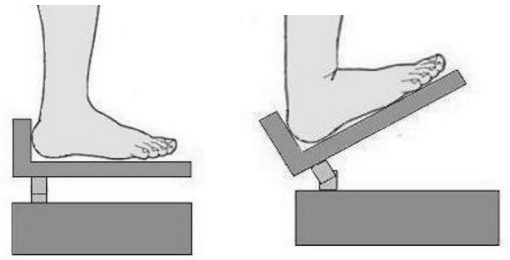

(a) Before operation (b) After operation

Fig. 5 Mechanical diagram of ASD

Fig. 6 The developed ASD (Ankle Stretching Device) system

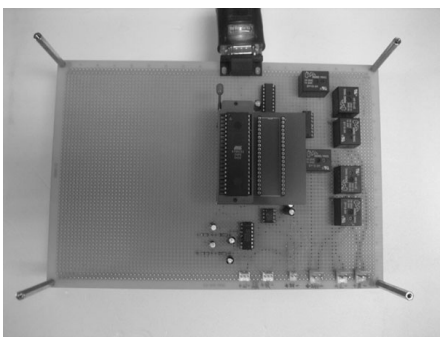

Fig. 7 ECU (Embedded Circuit Unit) of ASD system

III. Results and discussion

To improve the ability of moving the patient s weight towards the part of injured leg is one of our aims in rehabilitation treatment. The treatment which is improved the ability of supporting weight is preceded a walking training. Also, it performed a variety of postures and degree. [2]

As a result in this study, we developed the ASD system and studied the algorithm of automatic training system for monoplegia, to be exact, hemiplegia patients.

Fig. 6 shows a patient posture when the patient is under medical treatment. In order to support the patient s weight and prevent from losing the balance, a backstop is helping them during the treatment. The force plate is divided into two parts for easier control due to various kinds of patients including the hemiplegia patient. To operate the force plate, and electro-mechanical actuator is applied. The training is performed under the advance degree setting in the MCU.

Fig. 7 shows the main circuit to operate the ASD. Results measured by clinometers are get into the CPU the 12-bit dual channel serial ADC. Then the results are processed in the CPU of ECU and compared with setting data via RS-232 serial communication. After an arithmetic operation, instructions are given to the electro-mechanical actuator and then electro-mechanical actuator can be operated by switching the relay.

The ASD system can develop patient s muscle by the dynamic balance of training [3], if they are stimulated from outside or they move themselves. Moreover, hemiplegia patients caused by lose their nerve especially motor and sensor, so that they disturb their selective movement and standing up [4]. Therefore, this developed ASD can increase the available AFC and be treated to kind of these patients automatically.

IV. Conclusions

We have developed the useful ASD system for this study. However, this ASD must use with connected PC and couldn t verify with clinical demonstration. So it is recommended that for future researchers to develop better ASD after a clinical demonstration with reliability of medicine. Also, we need to develop ASD using RF communication or USB interface without connected PC in a more effective way instead of the conventional PC based ASD. Moreover, to prevent from increasing postural sway from external rotation, it needs to develop the ASD which can provide variety of degrees and directional ankle movement algorithm [5].

References

1. Jae Young Lee et al, (2004) Development of gait analysis algorithm for hemiplegic patients based on accelerometry, 41, 231-238
2. Dickstein R et al, (1984) Platform training and postural stability in hemiplegia, Arch Phys Med Rehail, 65, 588-592
3. Ragnarsdottir M. (1996) The concept of balance, Physiotherapy, 82, 368-375

F. Ibrahim, N.A. Abu Osman, J. Usman and N.A. Kadri (Eds.): Biomed 06, IFMBE Proceedings 15, pp. 611-614, 2007
www.springerlink.com ' Springer-Verlag Berlin Heidelberg 2007

4. Bohannon RW and Tinti Wald D. (1991) Accuracy of weightbearing estimation by stroke versus healthy subjects, Percept Mot Skills, 72, 935-941
5. Dong-wook Lee et al. (2003) Influence of standing balance with external rotation angle of the hemiplegia leg, Korean Society of Physical Therapy, 15, 503-512

Address of the corresponding author:

Author: Soo Hong Kim
Institute: Department of Biomedical Engineering, Inje University
Street: Obang-dong 607
City: Gimhae
Country: Republic of Korea
Email: ksh98@bse.inje.ac.kr

F. Ibrahim, N.A. Abu Osman, J. Usman and N.A. Kadri (Eds.): Biomed 06, IFMBE Proceedings 15, pp. 611-614, 2007
www.springerlink.com ' Springer-Verlag Berlin Heidelberg 2007

An Intelligent Tilt Table for Paralytic Patients

Soo Hong Kim[1], Jongman Cho[1], Jae Hong Lim[1], Tae Woo Nam[1] and Sang Il Park[2]

[1]Department of Biomedical Engineering, Inje University, Gimhae, 621-749, Korea
[2]2117-4 Samrak-dong Sasang-gu Busan Korea, Kwang Won Meditec Co.

Abstract - **Due to damaged vertebrae nerves, serious disease and aging, patients who have to lie down for long period of time need to exercise to maintain up-right standing position and recover their paralytic leg. This study describes a development of an intellectual tilt table which can provide a patient with rehabilitating condition. This can be possible by measuring and displaying the knee bent angle and pressure for each foot during exercise in real time. It is expected that the patient's exercising effect can increase by monitoring these two values during exercise.**

Keyword - **tilt table, paralytic leg, real-time monitoring system**

I. Introduction

On this account of medical development, the number of saving human lives have increased and made longer. This fact kept pace with increasing rehabilitating patients. Due to damaged vertebrae nerves, serious disease, and aging, patients who have to lie down for long period of time need to exercise to maintain up-right standing position and recover their paralytic legs. But for these patients, staying in up-right standing position is such a difficult matter.

Therefore, a tilt table has been used in many hospitals to support patient s standing-up position for the course of rehabilitating program. However, this method has few problems.

First one is that the tilting angle is adjusted by a manual way or simple electrical motor.

Secondly, the medical doctors or physical therapists should stick with a patient to observe patient s physical condition and record the data. Therefore, patients can expect their time-efficiency and progressive rehabilitation if they can manage their leg-remedial-exercise by themselves with a real-time monitoring system.

The monitoring system proposed in this study collects knee bent angle (KBA) and load of each paralytic leg (LPL) during rehabilitation training. The collected data are analyzed and displayed on a patient monitor in real-time so that a rehabilitant can recognize and do his/her most suitable rehabilitation. It is expected that a patient will try to put more load on the paralytic leg during exercise by observing his/her real-time loading status for each foot and it will improve the training effect noticeably.

II. Methods

A. Control of a tilt table

An electro-mechanical cylinder has been widely used for controlling tilting angle of a tilt table so far because it is low price and simple to control. However, it is easy to break down if tilting operation is occurred frequently and a tilt table is overloaded. In this study an oil-hydraulic cylinder driven by AC motor is used to overcome this problem. It was proven that an oil-hydraulic cylinder was easy to control tilting speed and accurate tilting angle of a tilt table.

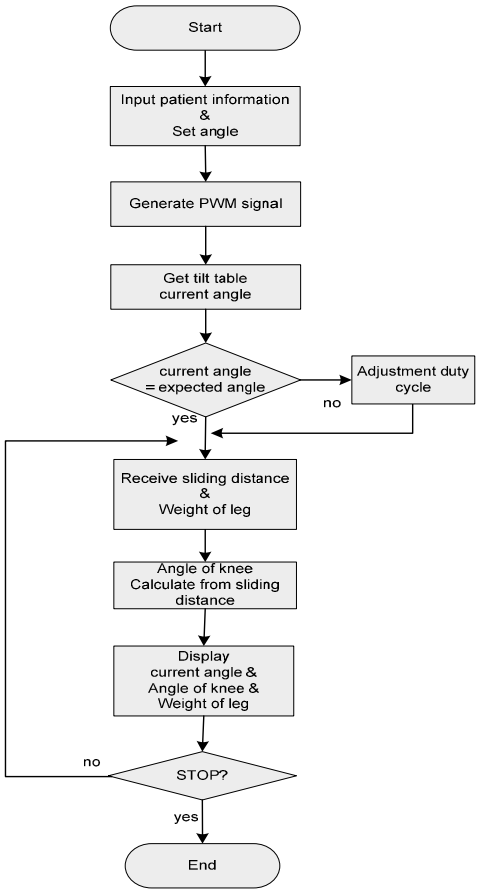

Fig. 1 Flowchart for the entire controlling process for the proposed tilt-table

F. Ibrahim, N.A. Abu Osman, J. Usman and N.A. Kadri (Eds.): Biomed 06, IFMBE Proceedings 15, pp. 615-617, 2007
www.springerlink.com ' Springer-Verlag Berlin Heidelberg 2007

The microcontroller resided in the control unit starts the AC motor of an oil-hydraulic cylinder until the tilt table reaches preset target tilting angle value. Figure 1 shows a flow for the entire controlling process for the proposed tilt table and Figure 2 depicts the developed system consisting of a tilt table which is controlled by an oil-hydraulic cylinder and patient monitor which displays KBA and LPL.

Fig.2 Developed system consisting of a tilt table and patient monitor.

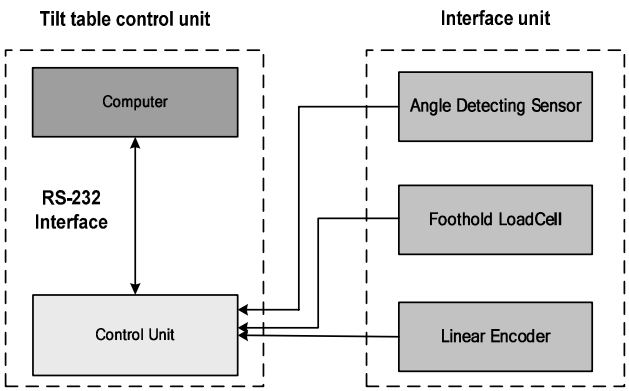

Fig. 3 Block diagram for the control unit of the developed system

B. Measurement of tilting angle

Figure 3 shows a functional block diagram for the control unit of the developed system. The incremental inclinometer (T2, USdigital Inc.) and 24-bit multi-mode counter were used to measure tilting angle and it provides 3,600 codes/revolution and the measured angle value is transmitted to a PC via a RS-232 serial interface.

C. Estimation of KBA

The KBA is estimated indirectly by measuring the moving distance of the sliding table and a linear encoder which has 0.1mm resolution was used for measuring the distance. The linear encoder consists of linear strip marked 0.05 mm scale and LED lenses. The output of the linear encoder is counted by 24-bit multi-mode counter and the actual distance is sent to PC where it is displayed on the patient monitor.

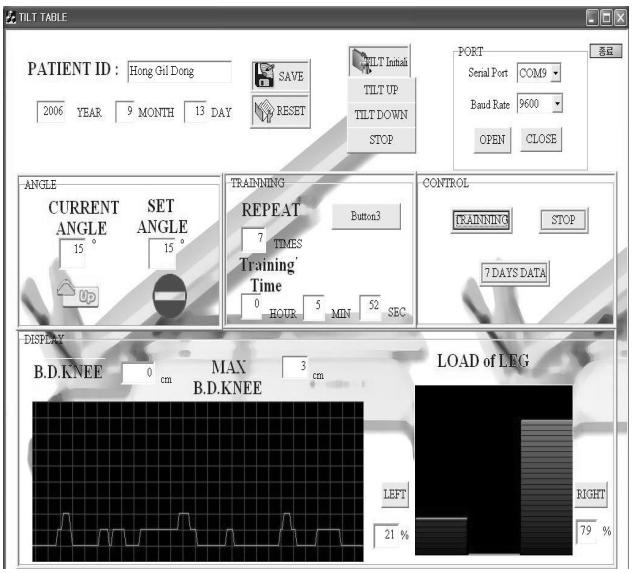

Fig. 4 Implemented monitoring software

D. Measurement of LPL

A load cell of 0.5g resolution is mounted on the each foothold to measure load (foot pressure) of rehabilitant's each leg during exercise. The output of each load cell is filtered, amplified, converted into digital form by an analog-to-digital converter (MCP 3202, Microchip technology Inc), and sent to PC for display on the patient monitor with KBA.

E. Monitoring software

An application program of monitoring system is implemented using Microsoft C++ 6.0 and it is running on a PC with Windows XP OS system, Pentium 4 and 1GB RAM. The KBA and LPL data were obtained from the control unit via RS-232C serial interface and theses data are stored on disk and displayed on the patient monitor at the same time. Figure 4 shows the implemented monitoring software.

F. Ibrahim, N.A. Abu Osman, J. Usman and N.A. Kadri (Eds.): Biomed 06, IFMBE Proceedings 15, pp. 615-617, 2007
www.springerlink.com ' Springer-Verlag Berlin Heidelberg 2007

Table 1 The data which is bending degree of knee and a load of paralytic leg to the gradient of the tilt-table

	Sliding distance(cm)				**Load of paralytic leg (%)**			
	5°	10°	15°	20°	5°	10°	15°	20°
Without Monitoring System	2.0	2.3	2.5	2.9	21.3	20.1	19.9	19.7
With Monitoring System	2.3	2.6	3.0	3.5	22.0	20.9	21.0	20.9
	+0.3	+0.3	+0.5	+0.6	+0.7	+0.8	+1.1	+1.2

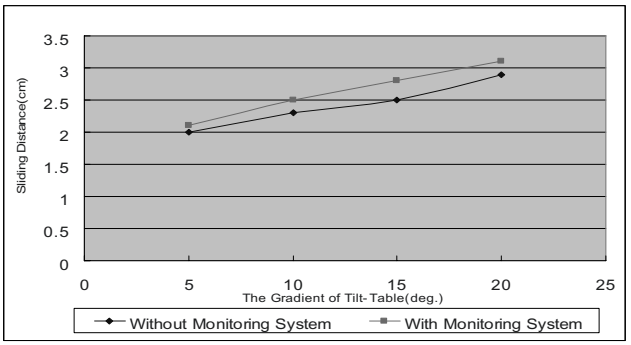

Fig. 5 The difference of sliding distance

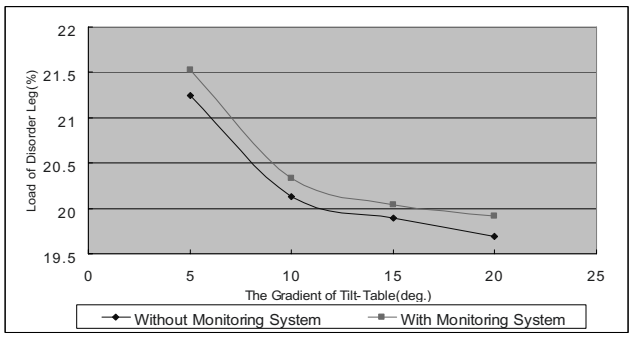

Fig. 6 The load will rate of affected leg depends of the gradient of the tilt table.

III. Results

Figure 5 shows average KBA values for three patients.

The sliding distance and KBA could not be measured under 20 degree because of injury consciousness.

The sliding distance was 2.0cm ~ 2.9 cm when the monitoring system was not used and 2.3cm ~ 3.5cm when the monitoring system was used. Figure shows this difference.

Figure 6 compares the percentage of the load for paralytic leg when the monitoring system was used and was not used. The load rate of a patient's paralytic leg was 21.3 ~ 19.7% in the rehabilitation movement when the monitoring system was not used and was 22.0 ~ 20.9% when the monitoring system was used.

Table 1 shows overall effects for rehabilitation exercise of paralytic leg with and without the monitoring system.

IV. Discussion and conclusion

This study shows the monitoring system which can provides a patient with status of the rehabilitation movement.

The results showed that the monitoring system gives good effects in the rehabilitation exercise. The paralytic leg bent degree of knee and load rate can be improvement by using this system. In addition, it can provide rehabilitants with the recognition of their movement and customized training. Also, it allows medical doctors to plan the efficient treatment for each patient. However, the KBA was not measured directly but estimated indirectly by measuring the moving distance of the sliding table. The direct measurement of KBA will provide more accurate information for treatment.

References

1. Jung Hee Oh: Rehabilitation medicine ; Dae Hak Seo Rim Inc; 1997; p268~269
2. Olaf Oldenberg, MD et al; Ambulatory Norepinephine Treatment of Severe Autonomic Orthostatic Hypotension , International journal of cardiology; vol. 52 no. 1; p 85~88.
3. S.W. Parry, R.A. Kenny; Tilt table testing in the diagnosis of unexplained syncope , Q J Med; 1999; 92; p 623□629
4. Lee, Hea Young, R.N; Biomechanical Analysis on the Shift of Gravity Line in Hemiplegic Patients. ; The journal of korean society of physical therapy vol.11, no, 1 pp 63~70,1999
5. Tilt Table Study ; Community Health care Inc.; 2001; pe-cvi 900-12-21
6. jung-gyn Yoon, Myung-hoon Kim, Dong-won Yook "The Effect of Self-Controlled Learning on Balance in Hemiplegics" PTK Vol.12 No.1 2005

Address of the corresponding author:

Author: soohong Kim
Institute: Inje University
Street: 607 Eobang-dong
City: Gimhae
Country: Korea
Email: ksh98@bse.inje.ac.kr

F. Ibrahim, N.A. Abu Osman, J. Usman and N.A. Kadri (Eds.): Biomed 06, IFMBE Proceedings 15, pp. 615-617, 2007
www.springerlink.com ' Springer-Verlag Berlin Heidelberg 2007

Application of a Novel Integrated Pointing Device Apparatus for People with Severe Disability

Chia-Ling Chen[1], MD, PhD, Hsieh-Ching Chen[2], PhD, Ching-Yi Wu, ScD[3], Huang-Chung Chen[1], MD, Shih-Wei Chou[1], MD, PhD, Simon Fu-Tan Tang[1], MD, Alice May-Kuen Wong[1], MD

[1]Department of Physical Medicine and Rehabilitation, Chang Gung Memorial and Children Hospital, Chang Gung University, Taiwan
[2]Department of Industrial Engineering and Management, Chaoyang University of Technology, Taiwan;
[3]Department of Occupational Therapy, Chang Gung University, Taiwan

Abstract **Background: To improve the computer operation for people with severe disabilities, more flexible pointing devices are required. This study investigates the effectiveness of a new developed Integrated Pointing Device Apparatus (IPDA), that can integrate numerous commercial pointing devices, for people with severe disabilities.**

Methods: We collected 20 children with quadriplegic cerebral palsy (CP) and 25 people with high cervical spinal cord injuries (SCI). People with disabilities were classified into 2 groups based on pointing device used: group A1 (SCI) or A2 (CP), who used standard mice, and group B1 (SCI) or B2 (CP), who were unable to use standard mice (IPDA combinations). All subjects received clinical severity and three specific mouse-operating efficiency assessments (continuous clicking, target-acquisition, drag-and-drop tasks). The efficiency of the people with disabilities in each mouse-operation task was expressed as a percentage of that for able-bodied subjects (%NL). The level of statistical significant was set at a value of *P* less than .05.

Results: Group B1 or B2 displayed similar operational efficiency in performing the drag-and-drop tasks to group A1 or A2, although they exhibited worse efficiency than group A1 or A2 in performing the continuous-clicking tasks (*P*<.05). The use of pointing devices was associated with American Spinal Injury Association Impairment Scale of people with SCI, and Gross Motor Functional Classification System (GMFCS) of children with CP (*P*<.05).

Conclusion: The IPDA could help most people with severe disabilities who could not utilize commercial mice to achieve acceptable operational efficiencies. Pointing devices were assigned based on the underlying severity.

Keywords— **Computer mouse, efficiencies, pointing devices, cerebral palsy, spinal cord injuries**

I. Introduction

People with severe physical disabilities often require special devices to aid in performing everyday tasks such as mobility, communication, environmental control and computer operation.(1) Cerebral palsy (CP) and spinal cord injury (SCI) are common causes of disability. Most people with upper limb disabilities encounter difficulties during certain learning activities, especially writing-based activities.

In meeting the individual needs of children with different physical disabilities, standard human-computer interfaces, such as the keyboard and mouse, were modified or alternative electronic techniques were applied in the development of special devices.(2) Such special human-computer devices comprise head-controlled interfaces built with optically or ultrasonically controlled techniques,(3-6) eye-controlled interfaces employing optically controlled techniques,(7,8) force-controlled interfaces activated by pressure sensor,(9,10) or foot-controlled interfaces that are position-controlled techniques.(11) However, these special devices are typically expensive and custom-made to suit individual needs.

This study presents a novel flexible apparatus, Integrated Pointing Device Apparatus (IPDA) that can be configured in various combinations to suit individual needs by integrating different currently available commercial pointing devices. This study evaluates the use of this novel apparatus by people with disabilities who are otherwise unable to operate standard pointing devices.

II. Methods

A. Subjects

Twenty children with CP, aged from 5 to 12 years, and 25 people with SCI, aged 20-50 years, from rehabilitation department at our hospital were enrolled in the study. The inclusion criteria of children with CP were as follows: (1) severe spastic CP with quadriplegia or athetoid CP with quadriplegia; and (3) no active infection such as pneumonia. The inclusion criteria of people with SCI were as follows: (1) high cervical (C6 or above) SCI with tetraplegia and (2) absence of active infection such as pneumonia. All subjects are able to manipulate the devices used in this study, understand the commands, had good cooperation during examination and good vision after visual correction. People with disabilities were classified into 2 groups based on pointing device used: group A1 (SCI) or A2 (CP), who used standard mice, and group B1 (SCI) or B2 (CP), who were unable to use standard mice (IPDA combinations).

F. Ibrahim, N.A. Abu Osman, J. Usman and N.A. Kadri (Eds.): Biomed 06, IFMBE Proceedings 15, pp. 618-621, 2007
www.springerlink.com ' Springer-Verlag Berlin Heidelberg 2007

Another 30 age-matched healthy subjects, with no known history of brain lesions, visual or hearing impairment, or orthopedic or neuromuscular disorders were selected as the control group for comparison of motor control assessments. The institutional review board at our hospital approved this study.

B. Experimental setup

Subjects sat in an upright position, their elbows resting on the table and flexed to 90 degrees, and with their eyes at a distance of 80 cm from the computer screen. The screen size was 14 inches with 0.35 mm/pixel resolution with screen resolution set at 1024*768. The experiment assessed three key operational performances of pointing device: continuous-clicking, target-acquisition, and target drag-and-drop tasks. Each task was repeated 3 times. A 3-min rest period between each task and 1-min rest period between each repetition were enforced. Subjects were allowed practice trials to familiarize themselves with the experimental setup.

The assessment software was programmed in Visual Basic and run on an IBM portable computer (IBM Think Pad, Ultra base 570E). The software was developed to assess a basic level of mouse operation: continuous-clicking, target-acquisition, and drag-and-drop tasks. A test was defined as a failure if the total time taken to complete a single target-acquisition or drag-and-drop task exceeded 5 minutes. Task timing started when the cursor moved away from its home position and stopped when all targets were successfully acquired in the target-acquisition tests or were dragged and dropped into a central box in the drag-and-drop tests.

(1) Continuous clicking

Subjects were asked to click as fast as possible for 10 seconds in a large square box displayed on the screen. The box area covered half of the screen to avoid the cursor exceeding the test area. The total number of clicks was recorded as an index of efficiency.

(2) Target-acquisition

The target-acquisition task takes into account moving distances, target sizes, and moving directions.[20] Each target-acquisition task trial was designed by randomizing a sequence that combined different moving directions, distances, and target sizes. There were total of 16 different combinations comprised of 8 directions, 2 distances (150 and 300 pixels), and 2 rounded target sizes (30 and 90 pixels in diameter). In each trial, the participant was asked to move the cursor to the target and click on it as rapidly as possible. The next target appeared once the target was captured. A target-acquisition trial was not completed until all 16 targets were successfully captured or total time exceeded 5 minutes. A total 3 different trials were tested to reduce the practice effects. The completion time of each trial was recorded for further analysis.

(3) Drag-and-drop

In the drag-and-drop task, subjects were asked to individually select 12 objects surrounding a box and drag each object into the box. The 12 targets were evenly distributed on a circle with the box located at its center. The distance from the surrounding objects to the central box was 7 times the size of the targets. The subjects were required to randomly choose a target and drag-and-drop it into the central box until all 12 objects were removed or total time exceeded 5 minutes. The completion time was recorded for further analysis.

C. Instrumentation

The IPDA, built with a circuit board and a microprocessor, provides two PS/2 input connectors for commercial pointing devices (Fig 1).[12] Each pointing device can be reconfigured by setting a 10-digit dip switch. The control codes from two connected pointing devices are converted and integrated into the control code of a single pointing device by the microprocessor according to their respective switch settings. The integrated control code is then connected to a personal computer via a USB interface. The IPDA also has a pair of external switches that serve as the left and right buttons on a conventional computer mouse. The IPDA conforms to standard USB interface specifications and has been confirmed to be compatible with all Logitech mice and trackballs and variety of commercial mice with PS/2 connectors.

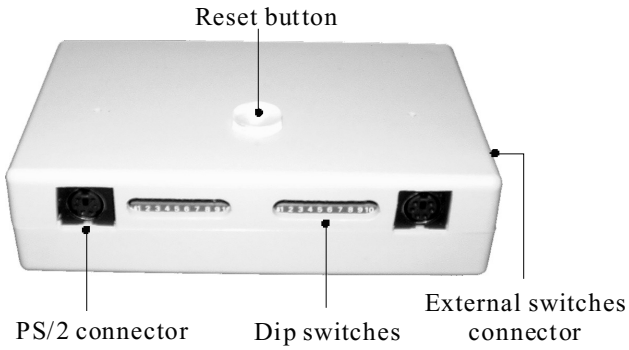

Figure 1. The Hardware in the Integrated Pointing Device Apparatus

The design goal of the IPDA is to develop an economical apparatus, which can flexibly integrate commercial computer mice and trackballs thereby tailored to individual needs, to enhance individual performance and reduce cost

F. Ibrahim, N.A. Abu Osman, J. Usman and N.A. Kadri (Eds.): Biomed 06, IFMBE Proceedings 15, pp. 618-621, 2007
www.springerlink.com ' Springer-Verlag Berlin Heidelberg 2007

and improve the maintainability of special equipment. Subjects were allowed to operate pointing devices/switches with one body part or any two body parts, such as hands, wrists, chin, etc., that facilitated better controllability. For instance, with IPDA, children with CP could operate a computer using bilateral hands with one hand controlling a trackball and the other hand controlling an external switch (Fig 2). The design of the IPDA allows users to select the most suitable combination of pointing devices and thereby improve the operational performance of children with different disabilities..

Fig 2. One Child with Cerebral Palsy Operates the Mouse via an Integrated Pointing Device Apparatus. He Used One Mouse for Cursor Control with Dominant Hand and Used an External Switch for Click Control with the other Hand Simultaneously

D. Assessment Procedures

All subjects received clinical severity and three specific mouse-operating efficiency assessments (continuous clicking, target-acquisition, drag-and-drop tasks). The efficiency of the people with disabilities in each mouse-operation task was expressed as a percentage of that for able-bodied subjects (%NL). Subjects could operate the mouse with one hand only or with bilateral hand via the integration of the IPDA. Some subjects (groups A1 or A2) could use one hand to operate the standard mouse and accomplish all tests. However, the other subjects (groups B1 or B2) could not accomplish the target-acquisition or drag-and-drop tasks with one hand only. These subjects needed bilateral hands simultaneously for operating a mouse and an external switch to accomplish all tests. Each subject underwent an operative efficiency evaluation of pointing devices, based on software developed for this study. People with disabilities also received clinical severity assessments. Severity was measured with gross motor functional classification scale (GMFCS)[13] for CP and American Spinal Injury Association (ASIA) Impairment Scale[14] scale for SCI

E. Data analysis

The operational efficiencies of the subjects for the three tasks were derived from the recorded data. The continuous-clicking efficiency was defined as total number of clicks within 10 seconds. The target-acquisition or drag-and-drop efficiencies were defined as the number or targets acquired and the number of targets dropped, respectively, divided by the total test time. For each task, the average efficiency of healthy children was taken as 100% and the efficiency of people with disabilities in each corresponding task was expressed as percentage of healthy performance (%NL) in each corresponding task.

Differences between groups were tested using an independent t-test or a Chi-square test or Fisher s exact test. The Mann-Whitney test was applied to test the differences of clinical severity assessment between groups. A repeated measures ANOVA was used to test operational efficiencies of three tasks (continuous clicking, target-acquisition, and drag-and-drop tasks) between groups. A value of $p < 0.05$ was considered statistically significant.

III. Results

The use of pointing devices was associated with ASIA Scale of people with SCI and GMFCS scale of children with CP ($P<.01$)

Operational efficiency of pointing devices

Both SCI groups exhibited worse operational efficiencies in all tasks than control subjects. Group B1 displayed worse efficiency in performing continuous clicking and target acquisition than group A1 ($P<.05$). However, group B1 demonstrated similar operational efficiency in the drag-and-drop tasks (30% NL) to group A1.

All CP groups demonstrated worse operational efficiencies in all tasks than control subjects. Group A2 showed better efficiencies in performing continuous-clicking tasks than group B2 ($p < 0.05$). However, group B2 had similar operational efficiency in the target-acquisition (approximate 30%NL) and drag-and-drop tasks as group A2.

IV. Discussion And Conclusions

The flexibility of IPDA allowed this device to meet the needs of most people with SCI and CP who are unable to operate common computer mice and trackballs alone. This apparatus allows for flexible adjustments and a combination

F. Ibrahim, N.A. Abu Osman, J. Usman and N.A. Kadri (Eds.): Biomed 06, IFMBE Proceedings 15, pp. 618-621, 2007
www.springerlink.com ' Springer-Verlag Berlin Heidelberg 2007

of two commercially available computer-pointing devices to fit a user s control functions for two body parts.

This apparatus not only enables these people to operate a computer via commercial pointing devices, but also improves their operational efficiency and posture by operating pointing devices with their better functioning body parts. It may cause secondary damage to users with disabilities if ergonomically unsound workstations or pointing devices are utilized, or if they overuse and operate the mice while sitting in awkward postures.[15-16] Cook and his colleagues argued that mouse usage may contribute to musculoskeletal injury of the neck and upper extremities.[15] Some specialized devices, including head-mounted controllers, may increase the risks of cervical lesions resulted from to repetitive impact on the cervical spine in some people.

In this study, groups B1 and B2 which used the IPDA had similar operational efficiency in drag-and-drop tasks as groups A1 and A2 which had ability to use a standard mouse, even though groups B1 and B2 were unable to complete the target-acquisition and drag-and-drop tasks with a standard mouse alone. Therefore, the IPDA could provide some people with severe physical disabilities, who could not otherwise control standard mice, to operate the cursor movement with acceptable efficiency in basic mouse-operated functions. Trewin and Pain[17] identified that users with motor disabilities had difficulties with all aspects of mouse operation, particularly the dragging task. Radwin et al.[18] determined that the average movement time was longer if healthy subjects used a lightweight ultrasonic head-controlled pointing device compared with standard mouse.

The novel IPDA design presented in this study demonstrated the following advantages: flexibility, low cost, and acceptable efficiency. The proposed IPDA is inexpensive (less than 30 USD), and compatible with numerous commercial pointing devices. The IPDA accommodated flexible combinations of devices by integrating two common computer-pointing devices controlled by two different body parts. The IPDA could provide some people with severe physical disability, who could not control a commercial mouse, achieve acceptable efficiency in basic mouse operational functions. The choice of mouse-operated ways for people with disabilities could be based on underlying motor control capability. Based our experiences, the IPDA used in this study not only can be used by people with CP or SCI, but also by people with severe upper limb disabilities caused by traumatic brain injury, or amputation, etc. The people with severe disabilities can thus utilize this apparatus to integrate a variety of commercially available pointing devices and to improve their control during computer operation.

References

1. Hawley MS, Cudd PA, Cherry AD. Implementation of a PC-based integrated control system for children. Med Eng Phys 1994;16:237-42.
2. Shein GF, Treviranus J, Brownlow ND, Milner M, Parnes P. An overview of human-computer interaction techniques for people with physical disabilities. Int J Ind Ergonom 1992;9:171-81.
3. Gottschalk M. Optical pointer helps disabled use computers. Des News 1993;48:93-4.
4. Harwin WS, Jackson RD. Analysis of intentional head gestures to assist computer access by physically disabled people. J Biomed Eng 1990;12:193-98.
5. Betke M, Gips J, Fleming P. The camera mouse: visual tracking of body features to provide computer access for people with severe disabilities. IEEE Trans Neural Syst Rehabil Eng 2002;10:1-10.
6. Chen YL, Chen WL, Kuo TS, Lai JS. A head movement image (HMI)-controlled computer mouse for people with disabilities. Disabil Rehabil 2003;25:163-67.
7. Gravil N, Griffiths PA, Potter R, Yates A. Eye control of microcomputer. Comput Bull Serial 1985;13:15-6.
8. Park KS, Lee KT. Eye-controlled human/computer interface using the line-of-sight and the intentional blink. Comput Ind Eng 1996;30:463-73.
9. Berardinis LA. Magnetic sensors for light-touch operators. Mach Des 1996;68:38.
10. Gerpheide G. Touchpad pointing device. Sci Am 1998;279:118.
11. Springer J, Siebes C. Position controlled input device for handicapped: Experimental studies with a footmouse. Int J Ind Ergonom 1996;17:135-52.
12. Chen HC, Liu YP, Chen CL, Chen CY. Design and application of integrating apparatus of computer pointing devices. Tw J Phy Med Rehab 2005;33:161-70.
13. Palisano R, Rosenbaum P, Walter S, Russell D, Wood E, Galuppi B. Development and reliability of a system to classify gross motor function in children with cerebral palsy. Dev Med Child Neurol 1997;39:214-23.
14. Bednarczyk JH, Sanderson DJ. Comparison of functional and medical assessment in the classification of persons with spinal cord injury. J Rehabi Res Dev 1993;30:405-11.
15. Cook C, Burgess-Limerick R, Chang S. The prevalence of neck and upper extremity musculoskeletal symptoms in computer mouse users. Int J Ind Ergonom 2000;26:347-56.
16. Karlqvist L, Bernmark E, Ekenvall L, Hagberg M, Isaksson A, Rostö T. Computer mouse and track-ball operation: Similarities and differences in posture, muscular load and perceived exertion. Int J Ind Ergonom 1999;23:157-69.
17. Trewin S, Pain H. Keyboard and mouse errors due to motor disabilities. Int J Hum-Comput Stud 1999;50:109-44.
18. Radwin RG, Vanderheiden GC, Lin ML. A method for evaluating head-controlled computer input devices using Fitts' law. Hum Factors 1990;32:423-38.

Address of the corresponding author:

Author Chia-Ling Chen, MD, PhD
Institute: Department of Physical Medicine and Rehabilitation, Chang Gung Memorial and Children Hospital.
Street: 5 Fu-Hsing St
City: Kwei-Shan, Tao-Yuan 333
Country: Taiwan
Email:*clingchen@gmail.com*

F. Ibrahim, N.A. Abu Osman, J. Usman and N.A. Kadri (Eds.): Biomed 06, IFMBE Proceedings 15, pp. 618-621, 2007
www.springerlink.com ' Springer-Verlag Berlin Heidelberg 2007

Conceptual Design of an Isokinetic Functional Electrical Stimulation (FES) Leg Stepping Trainer for Individuals with Neurological Disability

N.A. Hamzaid[1], C. Fornusek[1], A. Ruys[2] and G.M. Davis[1]

[1] Rehabilitation Research Centre, School of Exercise and Sport Science, The University of Sydney, Australia
[2] School of Aerospace, Mechanical and Mechatronic Engineering, The University of Sydney, Australia

Abstract— **People with neurological disabilities that affect their lower limbs are usually less active and have reduced aerobic fitness compared to their able-bodied cohorts. For this population to increase their functional capacity, proper training regimes have to be prescribed, which suit the nature of their injury and maximize their exercise capacity. One popular technique is to use functional electrical stimulation (FES) leg exercise for the weak or paralysed muscles. This paper describes the conceptual design of a new isokinetic FES leg stepping trainer for individuals with neurological disability. The combination of seated elliptical-motion stepping, FES and isokinetic exercise has the potential to improve rehabilitation outcomes in persons with lower limb paresis or paralysis. The proposed exercise machine can offer safe and intense training that is relevant to walking.**

Keywords— **Rehabilitation, Neurological Disability, Functional Electrical Stimulation, Leg Stepping Trainer, Isokinetic**

I. Introduction

Individuals with neurological disabilities suffer damage to their central nervous system, which leads to loss of manipulative functions or the ability to move. The disabilities may include stroke and spinal cord injury (SCI). People with thoracic spinal cord injury, or paraplegia, and stroke patients, usually still retain their upper body functions, and are able to perform many independent activities.

One common exercise for individuals with neurological disabilities is FES-evoked cycling. A new approach to such exercise is FES elliptical stepping.

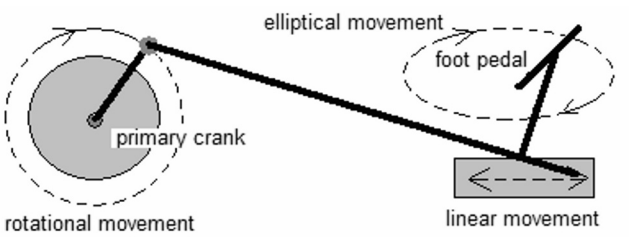

Fig. 1 Joint and linkages of an elliptical stepper

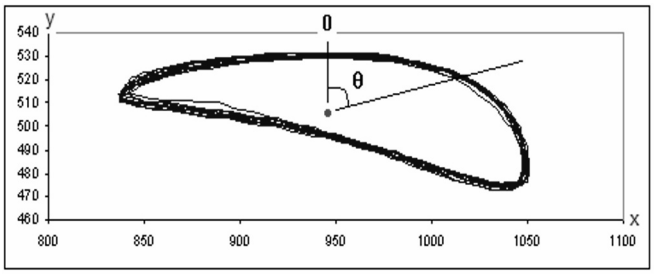

Fig. 2 Elliptical movement trace of the right pedal during an elliptical stepping movement.

Hamzaid and colleagues (unpublished) compared voluntary cycling to elliptical stepping in able-bodied subjects, and suggested that the latter activated the quadriceps muscles for a longer duration and at a higher intensity. The authors reasoned that this was due to the linear component of the movement (Figure 1).

Their study also revealed differences in hip, knee and ankle extension angles between the two exercise modalities. Leg movements on an elliptical stepping trainer produced less hip and knee angle excursions, while the ankle angle excursion was greater. The leg movements in elliptical stepping closely resembled those observed during gait. Furthermore, the foot movement projection of elliptical stepping (Figure 2) mimicked the foot movement during walking. Therefore, when the exercise is desired to improve walking ability in SCI, elliptical stepping might provide greater potential benefits compared to cycling.

II. System design

Background: Isokinetic exercise has been proven safe for the joints and is an effective form of strength training [1]. Additionally, being able to control the movement speed means that the exercise parameters can be precisely controlled. An isokinetic, or constant velocity system, requires a feedback-controlled driving mechanism that maintains its velocity regardless of the variation in the applied foot force.

The applied force is produced from the electrically stimulated muscles, which if not resisted, will alter the rotational

F. Ibrahim, N.A. Abu Osman, J. Usman and N.A. Kadri (Eds.): Biomed 06, IFMBE Proceedings 15, pp. 622-624, 2007
www.springerlink.com ' Springer-Verlag Berlin Heidelberg 2007

velocity. This approach was applied to an isokinetic FES leg cycle ergometer (iFES-LCE) by Fornusek *et al.* [2].

The proposed system includes a speed-controlled driving mechanism, which comprises an angular encoder on the primary crank, and an FES stimulator system, recruiting appropriate leg muscle contractions based on the crank angle. Since the movement of the primary crank and the resulting pedal movement are not directly related the relationship between the crank angle and leg positions must be resolved.

The proposed driving mechanism consists of a DC motor and/or an alternator. A DC motor is suitable for low speed and low power output, while an alternator is suitable for high speed high power output. When the subjects are unable to produce any power during the beginning of motion, the DC motor could initiate the movement. In addition, when the muscles eventually experience fatigue and can no longer produce enough power to sustain the exercise, the DC motor will be able to maintain the leg movements, and thus the driving speed.

On the other hand, an alternator is able to withstand a greater cycling velocity and force, and is able to maintain isokinetic exercise at higher power outputs. Once the initial momentum of stepping is overcome, the stepping velocity can be kept constant through the alternator.

Muscle stimulation: The power output will be measured, and leg muscles performance is controlled by modulating the current pulse width or the intensity of the muscle stimulation. The muscles used during FES leg cycling, i.e. quadriceps, hamstrings and gluteus, are a good selection for FES leg stepping. Including the adductor muscles might constrain unwanted leg adduction and eliminate the need for a knee brace on the subjects legs, while simultaneously recruiting additional muscle mass.

The subjects leg will be mechanically constrained with ankle foot orthoses on the pedals. No shank muscles are stimulated even though they might produce additional contraction and force. This is because the leg movement is a single degree of freedom, and from previous experience during FES cycling, the shank muscles are often inadvertently stimulated by the upper thigh stimulation. This is also to avoid recruitment redundancy when multiple muscle groups producing the same movements are stimulated.

Integrated system design: The control diagram of the proposed iFES-LST is illustrated in Figure 3. This diagram shows the main components of the system, comprising an elliptical stepper, a driving mechanism, a control unit, and a FES stimulator unit. The components are integrated to produce velocity feedback-control, to ensure the appropriate interaction between stimulation level and power production.

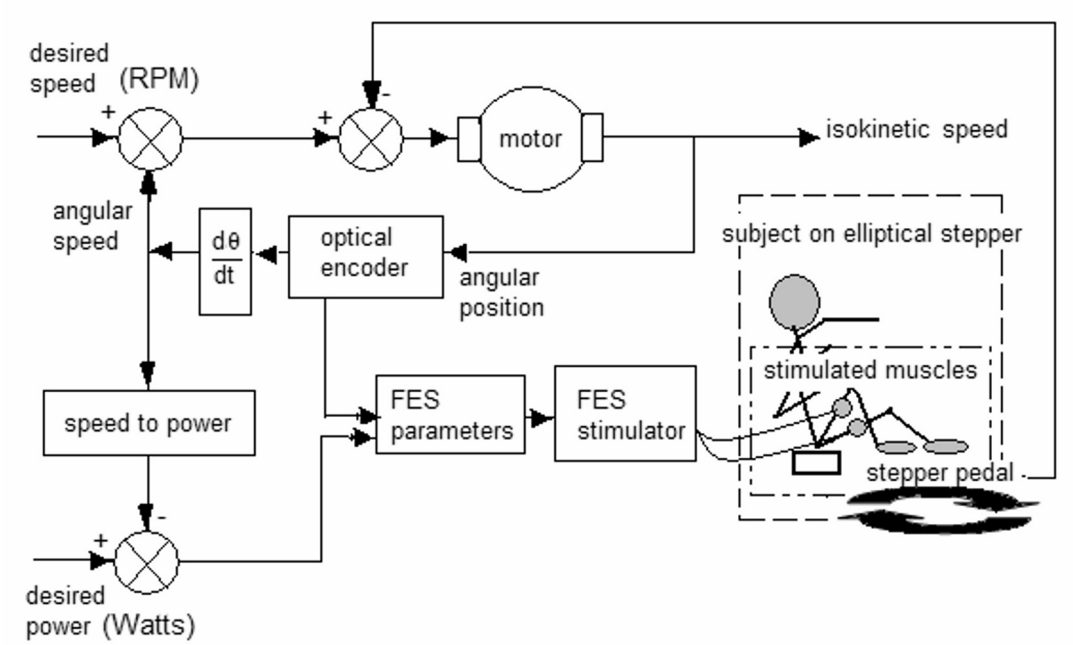

Fig. 3 Proposed iFES-LST system

F. Ibrahim, N.A. Abu Osman, J. Usman and N.A. Kadri (Eds.): Biomed 06, IFMBE Proceedings 15, pp. 622-624, 2007
www.springerlink.com ' Springer-Verlag Berlin Heidelberg 2007

A. 'Conscious Effort Free' versus 'Active Rehabilitation'

There are two paradigms of rehabilitation activity conscious effort free exercise and active rehabilitation. Conscious effort free exercise employs feedback-control to maintain the stepping cadence even when the stimulated muscles become fatigued and produced little or no power.

Another strategy is to make use of the power from upper body effort to drive the stepper, and thereby maintain the exercise activity when the stimulated muscles become fatigued. Such hybrid exercise allows the person to be as physically active as possible. This active rehabilitation may be useful as it facilitates coupling of the upper and lower limb muscles [3]. Nevertheless, an exercise activity that is highly dependent on the conscious effort may become less attractive for the inactive population in the long run.

B. Embedded Inter-limb Coordination Feature

The mechanical structure of the proposed exercise system is the BioStep Semi Recumbent Elliptical by Biodex Medical System Inc. with mechanically coupled handles and pedals (Figure 4) [4]. The strapped handle, for upper body exercise, cross-returns with the adjacent legs, which resembles a natural walking pattern. This creates the prospect of inter-limb coordination activity to train whole body movement. Passively driven movements of the arms can still potentially be advantageous as it maintains the conscious effort free exercise and promotes neural coupling while increasing whole body activity.

Fig. 4 BioStep Semi Recumbent Elliptical by Biodex Medical System Inc.

In addition, people with incomplete paraplegia or stroke may benefit from this coordination training to potentially regain their functional ability.

III. Conclusions

The ability of an isokinetic FES leg stepping trainer to provide the essential benefits of pre-walking training creates a potentially advanced version of FES cycling. While the driving mechanism concept may be somewhat similar to iFES-LCE, the mechanical setup of the proposed iFES-LST system will allow movements which better resemble walking. By integrating the stimulator and driving mechanism control, the exercise routine will be safer, more practical and beneficial for the disabled population.

Acknowledgment

The primary author received funding from a JPA Malaysian Government Scholarship. This project was funded by a Program Grant from the NSW Ministry for Science and Medical Research.

References

1. McArdle WD, Katch FI, Katch VL (1986) Exercise physiology. Lea &Febiger
2. Fornusek C, Davis GM (2004) Maximizing muscle force via low-cadence functional electrical stimulation cycling. J Rehabil Med 36, no. 5, 232-237
3. Ferris DP, Huang HJ, Kao PC (2006) Moving the arms to activate the legs. Exerc Sport Sci Rev 34, no. 3, 113-120
4. Franklin BA (2006) Semi recumbent elliptical. BioStep News, pp. 1-4.

Address of the corresponding author:

Author: Nur Azah Hamzaid
Institute: Rehabilitation Research Centre,
School of Exercise and Sport Science,
The University of Sydney
Street: P.O. Box 170 East Street
City: Lidcombe, 2141, NSW
Country: Australia
Email: nham0064@mail.usyd.edu.au

F. Ibrahim, N.A. Abu Osman, J. Usman and N.A. Kadri (Eds.): Biomed 06, IFMBE Proceedings 15, pp. 622-624, 2007
www.springerlink.com ' Springer-Verlag Berlin Heidelberg 2007

Design of a Wireless Heart Rate Monitoring System for Rehabilitation Patients

T.W. Nam, J.M. Cho and H.J. Noh

Department of Biomedical Engineering, Inje University, Gimhae, Republic of Korea

Abstract— **A development of a wireless heart rate monitoring system for rehabilitation patients who are taking physical therapy inside a rehabilitation center is discussed in this paper. The purpose of this study is to develop a monitoring system that can monitor patients' heart rates so that it gives physical therapist early warning if necessary. The whole system consists of the patient's side device (PSD) and central monitoring system (CMS). The PSD was designed to be wearable and low power consumption. The CMS was designed to monitor multiple patients simultaneously and generate a warning signal if necessary. The CMS and PSDs are linked by a wireless network proposed in this study.**

Keywords— **Wireless heart rate monitoring system, Rehabilitation, PSD (patient's side device), CMS (central monitoring system)**

I. Introduction

Nowadays, the average lifespan has increased, due to the improvement of medical care, resulting in an increase of the disabled population. Also, due to social development, the number of disabilities as a result of various diseased or due to accidents is increasing. So the needs for a rehabilitation system to assist patients in developing their physical, mental, social ability and independence increased.

And it is common that rehabilitation patients vital signs are not monitored during physical therapy in a rehabilitation center. The purpose of this study is to develop a monitoring system that can monitor heart rates of rehabilitation patients who are taking physical therapy inside a rehabilitation center so that it gives physical therapist early warning if necessary.

This system transmits the patient's heart rate to the CMSs PC through wireless communication. Therefore, patients are not restricted in their movements during treatment.

II. Materals and methods

A. System Architecture

The whole system consists of the patient s side device (PSD) and central monitoring system (CMS) as shown in Fig. 1.

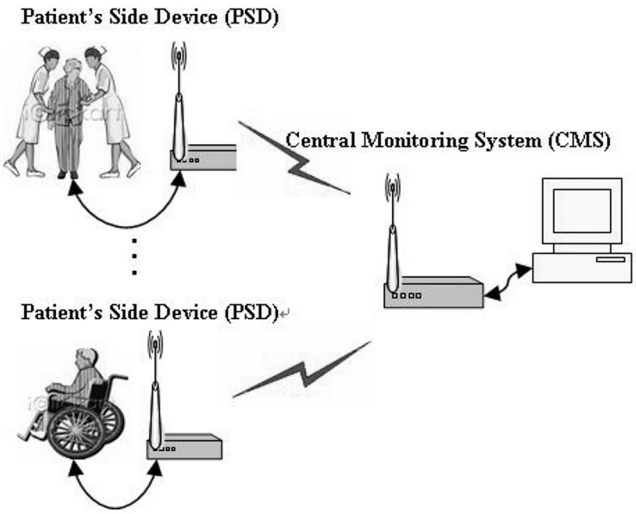

Fig. 1 Configuration of the whole system

The PSD was designed to be wearable so that a rehabilitation patient can take physical therapy without constraint and consume low power. It consists of a contact-type microphone to detect patient's heart sound, a signal processing hardware for signal conditioning of heart sound and calculating heart rate, an radio-frequency (RF) transmitter and receiver module to communicate with the CMS periodically. A small foot-print microcontroller with a built-in analog-to-digital converter (ADC) and low-power consumption was incorporated in the PSD. The heart sound signal captured a contact-type microphone is filtered by a band-pass filter and amplified to the level which corresponds to a full-scale input voltage range of the ADC built-in a microcontroller.

The CMS was designed to monitor multiple patients simultaneously and generate a warning signal if necessary. It consists of an RF transmitter and receiver module to communicate with all PSDs periodically and a Microsoft Windows-based personal computer (PC). The heart rate information for each patient are collected by an RF module and transferred to monitoring software in the PC that displays the heart rates for all patients and generates warning signal if the heart rate is out of pre-defined range.

F. Ibrahim, N.A. Abu Osman, J. Usman and N.A. Kadri (Eds.): Biomed 06, IFMBE Proceedings 15, pp. 625-627, 2007
www.springerlink.com ' Springer-Verlag Berlin Heidelberg 2007

The RF module is based on the Nextronics's NEX-AR_3A (receiver) and NEX-AT-3A (transmitter) [3]. The operating current is 1mA~2mA and frequency is 315 MHz.

The data transmitting rate is 1200bps. The dimensions of the RF module are very small. The receiver's dimensions are 15.3mm*9.8mm*2.5 and the transmitter's dimensions are 20mm*11.5mm*5.2mm. The antenna's length is 22.6Cm. The patient wears this system around on their waist.

B. Communication Protocol

The CMS and PSDs are linked by a wireless network proposed in this study. Each PSD is calculating its heart rate continuously and updating its internal variable which holds its heart rate while the RF module monitors receiving polling signal from the CMS. Each has its own predefined identification number (ID). The CMS polls each PSD continuously in order with predefined request message which has PSD s ID. Each PSD responds only to the polling signal from the CMS when it receives its own ID. It sends its heart rate value stored in the internal variable to the CMS with its own ID. The received heart rate information at the CMS is transferred to the PC via an RS-232C serial interface. Fig. 2 shows the flow chart of system.

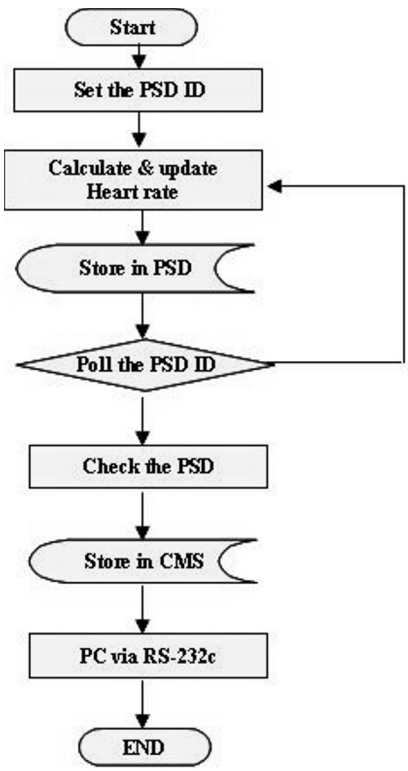

Fig. 2 Flow chart of the system

The transmitted data is divided in three parts. (Fig 3) The first part consists of a predefined signal (preamble) used as a marker. The second part contains the heart rate data and the IP. The last part is a single pulse to mark the end of the data transmission.

Receiver inspects communication protocol whether the data is correct or not [3].

C. Prototype Unit & Acquisition method

Fig. 4 shows the transmitting circuit of RF module. RF module is way of communications using RF pulse and is composed a part of transmission and receiver.

The transmission has a microphone (Type4948) to detect a heartbeat. An analog signal getting from the microphone is proceed by microcontroller (ATTINY13, Atmel). And the results from proceeding change properly output signal (10V) by using voltage converter (MAX680, MAXIM) signal provides –10V outputs from a +5V input voltage.

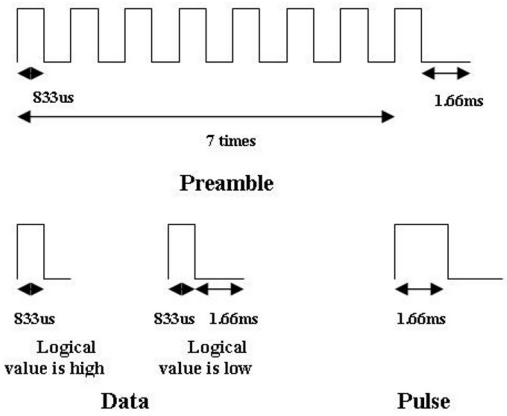

Fig. 3 Communication Protocol

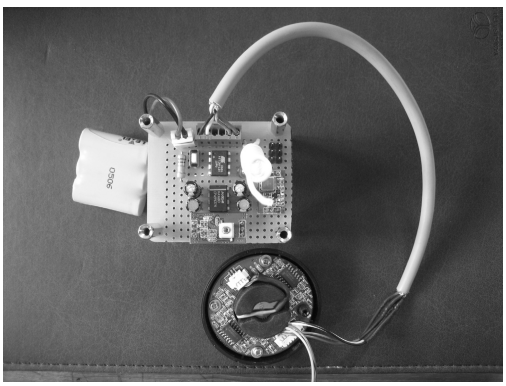

Fig 4 Transmission Circuit of RF Module

The operating voltage of transmission circuits use 4.5V battery and antenna to transmit signal in the receiver.

F. Ibrahim, N.A. Abu Osman, J. Usman and N.A. Kadri (Eds.): Biomed 06, IFMBE Proceedings 15, pp. 625-627, 2007
www.springerlink.com ' Springer-Verlag Berlin Heidelberg 2007

The receiver sends ECG signal to PC via RS-232 using microcontroller (ATMEGA128, Atmel).

III. Results

Fig. 5, 6 shows the result of experiment and processing the data. Fists subject is a male, 25 year-old, 175cm, 70 kg. Second subject is a male, 26 year-old, 180cm, 78 kg.

Both of figures show the same result. Graph (a) is a raw data measured from ECG. Graph (b) shows the absolute value due to find out value of p peak. Graph (c) is acquired from setting the value of threshold to 0.04. Finally, Graph (d) extract the square root using the result of graph c.

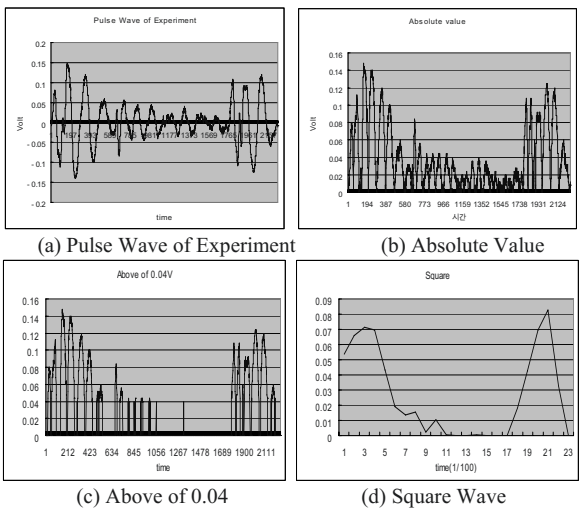

(a) Pulse Wave of Experiment (b) Absolute Value

(c) Above of 0.04 (d) Square Wave

Fig. 5 Acquired Value of heartbeat (M1, 25, 175cm, 70kg)

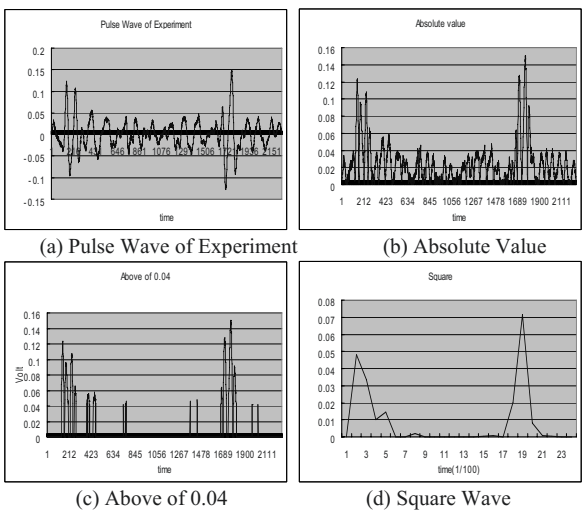

(a) Pulse Wave of Experiment (b) Absolute Value

(c) Above of 0.04 (d) Square Wave

Fig. 6 Acquired Value of heartbeat (M2, 26, 180cm, 78kg)

IV. Discussion

A prototype of this RF module has been designed and tested. It is experimented in transmitting patients' heart rate data to CMS. It would be beneficial for a better quality care of the patient. [2]

In this test, it is expected that it takes about 2-4 seconds to collect heart rate information for 50 PSDs and the maximum distance between the PSD and the CMS is about 50m.To verify that the received data is correct, the communication of protocol is both cases are compared. The data is checked by repeating the communication protocol.

Moreover, it is found that the communication speed is too low so it needs to reduce the preamble part of the communication protocol from 24 pulses to 8 pulses. Also the designed device can measure ECG signal simultaneously. Finally, it is checked the patient's heart rate.

V. Conclusion

The purpose of this study is to monitor the rehabilitation of patients more efficiently to improve treatment. With this system, the physical therapists can more concentrate on their patients.

In the future study, we will acquire heart rate data while the patient is moving without noise. Also we will transmit ECG data and patient's temperature as well as various kinds of vital signals. Moreover, we can produce one chip with microcontroller instead of the mobile heart rate module of receiver. As a result, it will be expected to reducing size and produced more advance one. Eventually, this study will contribute to improving the quality of rehabilitation treat-ment.

References

1. Mienkovic M, Jovanov E, Chapman J, Raskovic D, Price J An Accelerometer-Based Physical Rehabilitation System. ECE Dopt., University of Huntsvile, Alabama Department of Electrical Engineering & Comp.Eng. University of Alabama in Huntsvile Huntsvile,AL 35899 USA.
2. Lin Y.H.; Jan I.C; Ko, Chen Y.Y, Wong J.M, Jan G.J. (2004) A Wireless PDA-Based Physiological Monitoring System for Patient Transport Information Technology in Biomedicine, IEEE Transactions on Volume 8, Issue 4, Page(s):439 447
3. RF Modules http://nextronics.co.kr

Address of the corresponding author:

Author: Hee-Jung Noh
Institute: Department of Biomedical Engineering, Inje University
Street: 607, Obang-dong
City: Gimhae
Country: Republic of Korea
Email: ntw99@bse.inje.ac.kr

F. Ibrahim, N.A. Abu Osman, J. Usman and N.A. Kadri (Eds.): Biomed 06, IFMBE Proceedings 15, pp. 625-627, 2007
www.springerlink.com ' Springer-Verlag Berlin Heidelberg 2007

Development of Prosthetic Hand – A preliminary study

S. Yahud and N.A. Abu Osman

University of Malaya/Biomedical Engineering Department, Kuala Lumpur, Malaysia

Abstract— **The purpose of the study is to develop a prosthetic hand that able to perform the four essential tasks: cylindrical grasp, key pinch, pulp to pulp pinch and tripod pinch. The human hand could be considered as a linkage system of the intercalated bony segments. Therefore, prosthetic fingers and thumb were often modeled as a planar three-link open chain each, whose plane of motion was defined by yaw at the base joint. All the four fingers were modeled the same exclude for the lengths of each segment, and arranged parallel to one another on the *xy*-plane. All fingers maintain the same size due to assumptions that normal hands maintain similar anatomical structure and dimensional proportion, regardless of their sizes. The hand was modeled so that it will form an equiangular motion path and reach an optimum working space to meet the objective of the study. An experiment to observe the fingertip trajectory and stability of movement for each finger was carried out using motion analysis equipment available in the Motion Analysis Laboratory, Department of Biomedical Engineering, University of Malaya.**

Keywords—**Prosthetic hand, linkage system, fingertip trajectory**

I. Introduction

Human hand is a very complex and malleable tool connected to the most powerful and complicated controller, the brain. Hand is made up from wrist, palm and fingers. First finger is the thumb followed by index, middle, ring and little finger. Skeleton of the hand can be divided into three segments; the carpus or bones of the wrist, the metacarpus or bones of the palm and the phalanges or bones of the finger. Each finger consists of three phalanges (distal, middle and proximal phalanx) and one metacarpal and the thumb comprises of two phalanges (distal and proximal phalanx) and one metacarpal. And all the bones are connected at three joints. The first joint that connects proximal phalanx and metacarpal of each respective finger is the metacarpophalangeal (MCP) joint. This is where the finger joins the hand. The second joint is proximal interphalangeal (PIP) joint, which connects the proximal phalanx to the middle phalanx. The third joint is distal interphalangeal (DIP) joint, which connects the middle and distal phalanx together. Thumb is composed of three bones; first metacarpal, proximal phalanx and distal phalanx. The first metacarpal connected to the bone of the wrist at carpometacarpal (CMC) joint. Proximal phalanx of the thumb connected to the first metacarpal at the MCP joint and the distal phalanx connected to the proximal phalanx at the interphalangeal (IP) joint.

Losing a hand is tragic for every individual human being. Individual without a limb is known as amputee. The major challenged faced by every amputee is difficulty to perform several activities of daily living (ADL) such as dressing, feeding, toileting and some other basic activities. Amputation occurs due to many reasons such as war, accidents, diseases, and congenital anomalies. Study in the area of prostheses has been carried out to find an artificial substitute for the missing hand or known as prosthetic hand. Development of prosthetic hand was inspired by the beauty and complexity of the human hand.

The objective of the study is to develop a prosthetic hand that able to perform the four basic tasks required by human hand: cylindrical grasps, key pinch, pulp to pulp pinch and tripod pinch. The model of prosthetic hand should reach a maximum range of motion, in order for the hand to perform flexible tasks.

II. Methodology

Model of prosthetic hand

The human hand can be considered as a linkage system of the intercalated bony segments [1]. Therefore, artificial fingers and thumb were often modeled as a planar three-link open chain each, whose plane of motion was defined by yaw at the base joint. The model was developed with two assumptions [2] (i) yaw axis intersected the axis of rotation at the knuckle orthogonally, (ii) translations at the joints are negligible. In the proposed design of the prosthetic hand, the MCP joint at each finger defined as 1 DOF joint. The base joint of the prosthetic finger and thumb are the MCP and CMC joint respectively.

The prosthetic finger was modeled as a chain of rigid links connected by joints as mention earlier. All the four fingers were modeled the same exclude for the sizes of each segment, and arranged parallel to one another on the *xy*-plane. All fingers maintain the same size due to assumptions that normal hands maintain similar anatomical structure and dimensional proportion, regardless of their physical size [1]. In the kinematics model of the prosthetic hand, the centre of MCP joint of the index finger is chosen as the reference coordinate, (Ix_0; Iy_0; Iz_0). All the four fingers flexed only in *xy*-plane. Figure 1 shows the model of four prosthetic fin-

F. Ibrahim, N.A. Abu Osman, J. Usman and N.A. Kadri (Eds.): Biomed 06, IFMBE Proceedings 15, pp. 628-631, 2007
www.springerlink.com ' Springer-Verlag Berlin Heidelberg 2007

gers aligned on *xz*-plane and the side view of the index finger. Position of each link could be determined with respect to the fixed coordinate system. The only transformation that allowable at each joint was rotation.

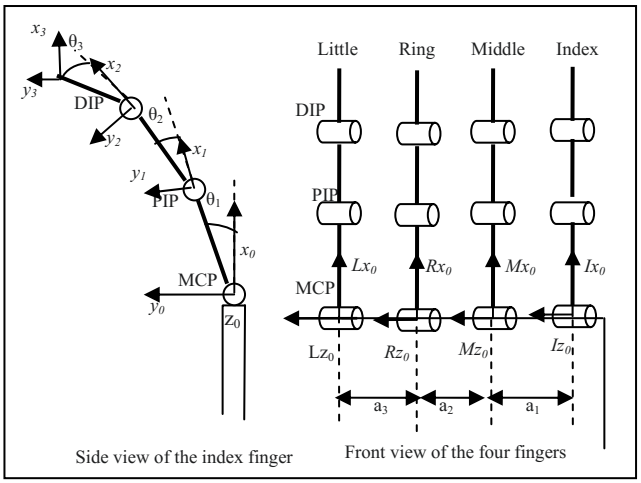

Fig. 1: Kinematics model for prosthetic finger

The prosthetic finger has the three joints MCP, PIP and DIP and each rotating at $(x_0; y_0)$, $(x_1; y_1)$ and $(x_2; y_2)$ about its respective z-axes. The fingertip was defined at $(x_3; y_3)$ coordinate. Whereas θ_1, θ_2 and θ_3 are the relative rotational displacement angles between phalanges at the MCP, PIP and DIP joint accordingly. Fingertip coordinates could be determined by successive transformations from the MCP joint to PIP and DIP joint. Transformation process that occurred at each joint was the rotation about the z-axes. Referred to side view of the index finger in figure 1, showed the rotation matrices corresponding to a rotation through an angle θ about the z-axes accordingly. The concept of homogenous coordinates was introduced in deducing the fingertip coordinate [3].

An example of homogenous transformation matrix of the index finger from fingertip to MCP joint is shown as follow:

$$I_0^3 = \begin{pmatrix} \cos(\theta_1+\theta_2+\theta_3) & -\sin(\theta_1+\theta_2+\theta_3) & 0 & l_3\cos(\theta_1+\theta_2+\theta_3)+l_2\cos(\theta_2+\theta_3)+l_1\cos\theta_3 \\ \sin(\theta_1+\theta_2+\theta_3) & \cos(\theta_1+\theta_2+\theta_3) & 0 & l_3\sin(\theta_1+\theta_2+\theta_3)+l_2\sin(\theta_2+\theta_3)+l_1\sin\theta_3 \\ 0 & 0 & 1 & 0 \\ 0 & 0 & 0 & 1 \end{pmatrix}$$

The orientation and position of the fingertip for the index finger with respect to the base could be determined from the I_0^3 matrix. The 3 x 3 submatrix in the upper left corner describe the orientation of the fingertip, i.e. the rotation of each joint with respect to the MCP joint. Elements in the 3 x 1 column matrix in the upper right corner are the coordinates of the fingertip with respect to the base. Therefore the other fingertips could be determined from the similar methods with translation along the z-axes accordingly. The value of l_1, l_2 and l_3 and θ_1, θ_2 and θ_3 are differs for each finger accordingly. Distance among metacarpal joint for other fingers are define as a_1, a_2 and a_3, i.e. middle-index finger, ring-middle finger and little-ring finger accordingly.

Hence, the instantaneous position of the fingertip for each finger can be calculated;

$$x_i = l_1 \cos\theta_1 + l_2 \cos(\theta_1+\theta_2) + l_3 \cos(\theta_1+\theta_2+\theta_3) \text{ -(1)}$$
$$y_i = l_1 \sin\theta_1 + l_2 \sin(\theta_1+\theta_2) + l_3 \sin(\theta_1+\theta_2+\theta_3) \text{ -(2)}$$

To get the function of the fingertip trajectory, equation (1) is divided by equation (2) and rearranged to yield;

$$y_i = x_i \frac{[l_1 \sin\theta_1 + l_2 \sin(\theta_1+\theta_2) + l_3 \sin(\theta_1+\theta_2+\theta_3)]}{l_1 \cos\theta_1 + l_2 \cos(\theta_1+\theta_2) + l_3 \cos(\theta_1+\theta_2+\theta_3)} \quad (3)$$

Thumb is important in determining the success of the four pre-determined task; cylindrical grasp, key pinch, tip pinch and tripod pinch. The thumb was modeled as a planar three-link open chain, whose plane of the motion was determined by the rotation at the CMC joint. It is important to include the circumduction movement of the thumb, so that the tip of the thumb will be able to oppose the other fingertip.

Figure 2 shows the kinematics model of the prosthetic thumb, θ_0 was referring to the circumduction angle from the initial position, where θ_4, θ_5 and θ_6 are the displacement angle of CMC, MP and IP joints respectively and l_4, l_5 and l_6 was representing the length of CMC-MP, MP-IP and IP-tip accordingly. Finally, *h, d* and *e* are the distance of the CMC joint coordinate from the base coordinate, the MCP joint of the index finger.

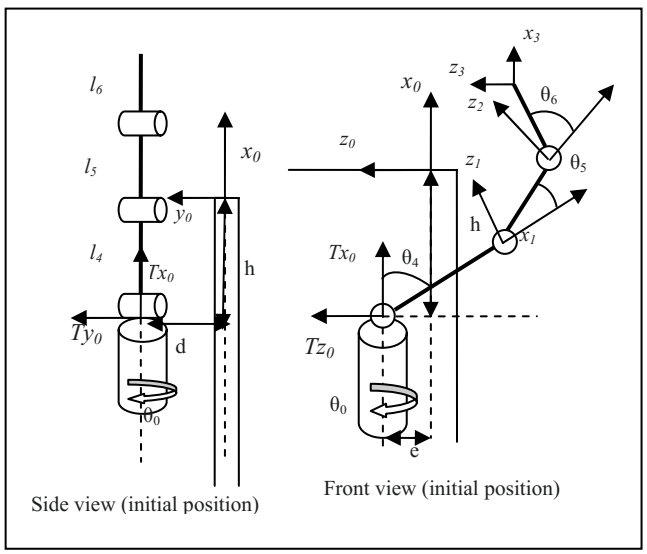

Fig. 2: Kinematics model of prosthetic thumb

F. Ibrahim, N.A. Abu Osman, J. Usman and N.A. Kadri (Eds.): Biomed 06, IFMBE Proceedings 15, pp. 628-631, 2007
www.springerlink.com ' Springer-Verlag Berlin Heidelberg 2007

The homogenous transformation matrix is demonstrates as follow:

$$T_0^4 = \begin{pmatrix} \cos\theta_0\cos(\theta_4-\theta_5-\theta_6) & 0 & -\sin\theta_0(\theta_4-\theta_5-\theta_6) & l_6\cos\theta_0\cos(\theta_4-\theta_5-\theta_6)+l_5\cos\theta_0\cos(\theta_4-\theta_5)+l_4\sin\theta_0-h \\ -\sin\theta_0\sin(\theta_4-\theta_5-\theta_6) & \cos\theta_0 & -\sin\theta_0\cos(\theta_4-\theta_5-\theta_6) & -l_6\sin\theta_0\sin(\theta_4-\theta_5-\theta_6)-l_5\sin\theta_0\sin(\theta_4-\theta_5)+l_4\sin\theta_0\sin\theta_4+d \\ \cos\theta_0\sin(\theta_4-\theta_5-\theta_6) & \sin\theta_0 & \cos\theta_0\cos(\theta_4-\theta_5-\theta_6) & l_6\cos\theta_0\sin(\theta_4-\theta_5-\theta_6)+l_5\cos\theta_0\sin(\theta_4-\theta_5)-l_4\cos\theta_0\sin\theta_4+e \\ 0 & 0 & 0 & 1 \end{pmatrix}$$

The orientation of the thumb is determined by the value of θ_0, rotation about the *x*-axis. Flexion of each joint for the thumb is about the *y*-axis. Hence the orientation of the thumb could be defined as in 3 x 3 submatrix in upper left corner of the T_0^4 homogenous matrix. The position coordinate of the thumb tip relative to the base is determined at 3 x 1 column matrix at the upper right corner of the homogenous transformation matrix. The thumb tip coordinates are demonstrated as follow:

$$x_3 = l_6\cos(\theta_4-\theta_5-\theta_6)+l_5\cos(\theta_4-\theta_5)+l_4\sin\theta_4-h \quad \text{- (4)}$$

$$y_3 = -l_6\sin\theta_0\sin(\theta_4-\theta_5-\theta_6)-l_5\sin\theta_0\sin(\theta_4-\theta_5)+l_4\sin\theta_0\sin\theta_4+d \quad \text{- (5)}$$

$$z_3 = l_6\cos\theta_0\sin(\theta_4-\theta_5-\theta_6)+l_5\cos\theta_0\sin(\theta_4-\theta_5)-l_4\cos\theta_0\sin\theta_4+e \quad \text{- (6)}$$

The value of θ_0 is varied depending on tasks to be performed by the hand. In the cylindrical grasp the value of θ_0 is depending on the size of the grasp object, for the tip and tripod pinch position the value of θ_0 is approximately 90° and during key pinch position the value of θ_0 is zero.

Theoretical trajectory and locus

The estimated fingertip trajectory and locus could be established from an equation 3 for each finger, by substituting value for angle and length of each segment respectively. The theoretical trajectory for the index finger is established in figure 3. This figure is achieved using equation 1 and 2,

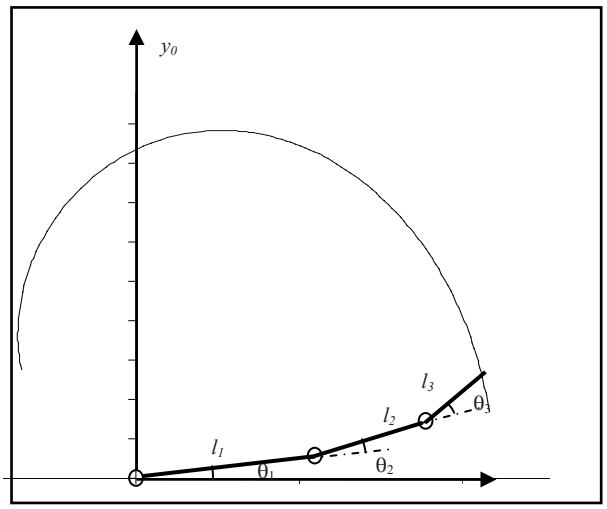

Fig. 3: Theoretical trajectory and locus for index finger

flexion angle for each joint is made within $5° \leq \theta_{1,2,3} \leq 90°$, and length of the each segment are as followed: $l_1 = 51$ mm, $l_2 = 35$ mm and $l_3 = 24$ mm. Length of each segment used in this study was adopted from author s hand herself and confirmed the selections based on Fibonacci sequence and theory introduced by Hamilton et. al. [4] and Park et. al. [5].

The optimum motion path for each finger could be reached by applying the maximum displacements angle proposed by Becker and Thakor [6]. Integration of motion path for all fingers creates a working space for the prosthetic hand.

III. Result/Discussion

An experiment to study a motion path followed by the prosthetic hand was conducted in the Motion Analysis Laboratory, Department of Biomedical Engineering, Faculty of Engineering, University of Malaya. Motion path of an individual finger was captured using video camera and analyzed using Peak Motus 7 motion analysis software. Results showing the 2D trajectory obtained for three fingers are presented below in figure 4. Whereas, figure 5 show an example of result attained in 3D motion analysis for an index finger.

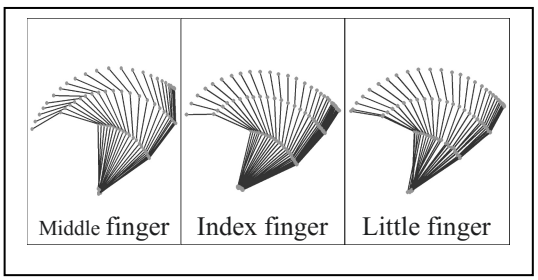

Fig. 4: Example of trajectory path for three fingers

The motion path of one finger is in equiangular form of motion and the path of fingertip trajectory for each prosthetic finger is similar to Guo s trajectory [7]. Maximum flexion angles for each joint are varied but approaching the value suggested by Thakor et. al [6]. From the result obtained in fig. 5, stability of movement made by each finger could be observed. The smoothness of the trajectory line explained the stability of each joint during motion, i.e. absence of wobbling and jerking effect. However, trajectory of each joint may result in errors due to poor digitizing process performed. To avoid errors, reflective marker should be made prominent compared to the background of the placement.

The prosthetic hand is able to pose the four desired tasks without having to reach the maximum angle of each joint. This is because the range of motion for the four tasks is in

F. Ibrahim, N.A. Abu Osman, J. Usman and N.A. Kadri (Eds.): Biomed 06, IFMBE Proceedings 15, pp. 628-631, 2007
www.springerlink.com ' Springer-Verlag Berlin Heidelberg 2007

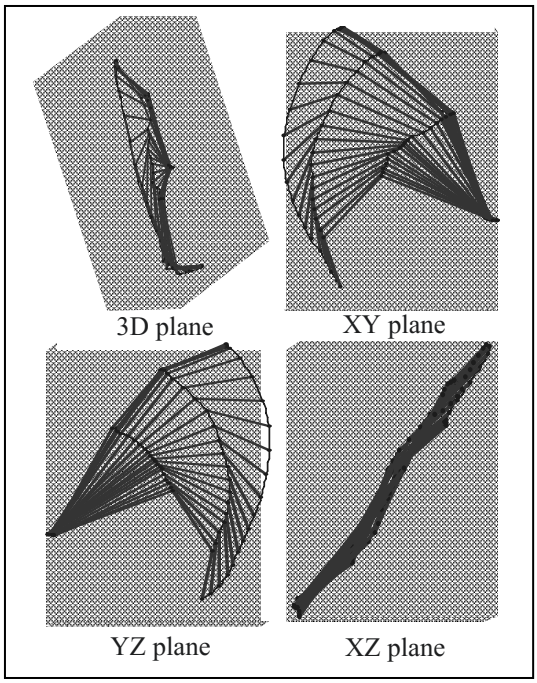

Fig. 5: Trajectory of an index finger in 3D plane

the working space of the developed model [1]. The four tasks identified in the study are basic functional activities commonly performed by human hand: cylindrical grasp, key pinch, pulp to pulp pinch and tripod pinch.

IV. Conclusion

A prototype of prosthetic hand was successfully fabricated and assembled. The hand was modeled so that it will perform an equiangular motion path. The prosthetic hand has fulfilled the objective of the study and performed within the range of motion predicted in theory. The fingertip and joint trajectory could be improved to provide wider range of motion and promote better dexterity.

Acknowledgment

I would like to thank Institute of Research Management and Consultancy, University of Malaya for the research grant code (F0233/2005B).

Rereferences

1. Chao, E.Y. Biomechanics of the hand: a basic research study , World Scientific, 1989.
2. Wright, A.K.; Stanisic, M.M. Kinematic Mapping between the Exos Handmaster Exoskeleton and the Utah/MIT Dextrous Hand , *IEEE Int. Conf. on Systems Engineering,* pp. 101-104, 9-11 Aug, 1990.
3. Per-Ake Jansson and Ragnar Grahn, Engineering mechanics, vol.2. Dynamics , Prentice Hall Int. (UK) Limited 1995.
4. R. Hamilton, R. A. Dunsmuir, Radiographic Assessment of the Relative Lengths of the Bones of the Fingers of the Human Hand , *The Journal of Hand Surgery*, vol. 27B No. 6 December 2002.
5. Andrew E. Park, MD, John J. Fernandez, MD, Chicago, IL, Karl Schmedders, PhD, Evanston, IL, Mark S. Cohen, MD, Chicago, IL The Fibonacci Sequence: Relationship to the Human Hand , *The Journal of Hand Surgery*, vol. 28A No. 1 January 2003.
6. Becker, J.C., Thakor, N.V., A study of the Range of Motion of Human Fingers with Application to Anthropomorphic Designs , *IEEE Trans. on Biomedical Engineering,* pp. 110-117, vol. 35, No.2 February 1988.
7. C.S. Lovchik., M.A. Diftler., The Robonaut Hand: A Dexterous Robot Hand for Space, *Proc. of the 1999 IEEE Int. Conf. on the Robotics & Auto.,* vol. 2, pp. 907-912, May 1999

Address of the corresponding author:

Author: Shuhaida Yahud
Institute: University of Malaya
City: Kuala Lumpur
Country: Malaysia
Email: yshuhaida@yahoo.com

F. Ibrahim, N.A. Abu Osman, J. Usman and N.A. Kadri (Eds.): Biomed 06, IFMBE Proceedings 15, pp. 628-631, 2007
www.springerlink.com ' Springer-Verlag Berlin Heidelberg 2007

EEG Based Brain Machine Interface for Rehabilitation: A Guided Tour

Hema C.R., Sazali Yaacob, R. Nagarajan, Abd. Hamid Adom, Paulraj M.P

Robotics and Intelligent Control Research Group, School of Mechatronic Engineering,
Northern Malaysia University College of Engineering, Perlis, Malaysia

Abstract- **Brain machine interfaces provide a digital channel between the brain and the physical world. Electrophysiological signals such as EMG, EEG, and EOG of the brain can provide a non muscular channel to control external devices. In this paper we present a survey on Electroencephalogram [EEG] based brain machine interfaces [BMI] and the feasibility of a brain interface to control wheel chairs. With the advent of noninvasive electrodes, research in EEG has been directed towards development of brain machine interfaces to replace damaged motor nerves. Restoring complex motor functions like reaching and grasping still remains a major challenge. This paper presents a preliminary study on using EEG signals for rehabilitation and the current research on EEG based BMI.**

Keywords **-EEG, Brain Machine Interfaces, Rehabilitation Robots, Bio-robotics.**

I. Introduction

Brain Machine Interfaces [BMI] using EEG signals is one of the growing research fields in recent years. The brain communicates with the physical world through the nervous system; when a part of the nervous system is damaged like motor nerves, (e.g. paralysis) then functions of movement are affected. Emerging technology is poised to change this scenario by opening up a digital link between the brain and the physical world. BMI enables the use of the brain to directly control machines and devices in the absence of the biological system.

BMI can be broadly classified into two types, Sensory and Motor. Sensory BMI are designed to replace a damaged organ such as retinal prosthesis to help the blind and cochlear implants for the deaf. The Motor BMI, on the other hand, seeks to translate electrical brain activity that represents intent to move into useful commands to external devices. Sensory BMI requires very accurate placement of a few tiny electrodes that stimulate the appropriate site in the brain, and the device s job is to simulate the role of the appropriate sensory organ as accurately as possible. In motor BMI, the electrodes are placed anywhere in the appropriate cortex area and their number is much higher. The decoding problem for motor BMI is much harder, since there is little knowledge of how the motor cortex encodes information, and also due to only a small fraction of the cells is being probed [1]. There are two basic types of motor BMI: non-invasive and invasive. Research on non-invasive BMI started in the 1980s by measuring brain electrical activity over the scalp.

Brain computer interfaces [BCI] have been developed to move computer cursors. Through training, subjects can learn to control their brain activity in a predetermined fashion that is classified by a pattern recognition algorithm, and converted into one of several discrete commands usually cursor actions (up/down, left/right) on a computer display. The computer presents a set of possibilities to the users, and they choose one of them through these cursor actions, until a task is completed. This approach, requiring only signal amplification and classification is known as a brain computer interface. BCI classification algorithms combine machine learning techniques with biomedical domain knowledge [1].

II. Electroencephalography

EEG is a technique that reads scalp electrical activity generated by brain structures. The EEG is measured directly from the cortical surface. When brain cells or neurons are activated, the local current flows are produced. EEG measures mostly the currents that flow during synaptic excitations of the dendrites of many pyramidal neurons in the cerebral cortex. Only large populations of active neurons can generate electrical activity recordable on the head surface; weak electrical signals detected by the scalp electrodes are to be massively amplified. The cortex is a dominant part of the central nervous system. The highest influence of EEG comes from electric activity of cerebral cortex due to its surface position [2].

III. Eeg research history

The existence of electrical currents in the brain was discovered in 1875 by an English Physician Richard Caton. In 1924 Hans Berger a German neurologist amplified these electrical signals using ordinary radio equipment and coined the term *electroencephalogram* to describe brain electric potentials in humans. In 1934 Adrain and Mathews published a paper verifying the concept of human brain wa-

F. Ibrahim, N.A. Abu Osman, J. Usman and N.A. Kadri (Eds.): Biomed 06, IFMBE Proceedings 15, pp. 632-636, 2007
www.springerlink.com ' Springer-Verlag Berlin Heidelberg 2007

ves [or EEG] and identified regular oscillations around 10 to 12 Hz which they termed as alpha rhythm. Brain waves have been categorized into four basic groups: beta (>13 Hz); alpha (8-13 Hz); theta (4-8Hz); delta (0.5 -4 Hz) [2]. Until early 1990s, most of the researches on EEG were focused on analyzing brain related disease and sleep patterns. The early 1990s witnessed a rapidly growing body of research involving detection of human brain responses and putting these techniques to appropriate uses to help disabled people. Most of the research during this period involved surgically implanting electrodes to acquire the signals. With the introduction of external electrodes during the turn of the century [2000] EEG has initiated the development of BCI to control the cursor of computers. Currently this research has been directed towards producing BMI which can control a prosthetic arm or a wheelchair [1].

IV. International 10-20 System

To perform consistent testing of EEG recordings a system called the International 10-20 electrode placement system was developed [3]. This system created a method of labeling electrode locations to be used worldwide. The EEG electrodes are placed on the scalp at 10 and 20 percent of a measured distance. Figure 1 shows the international 10-20 Electrode placement positions [3].

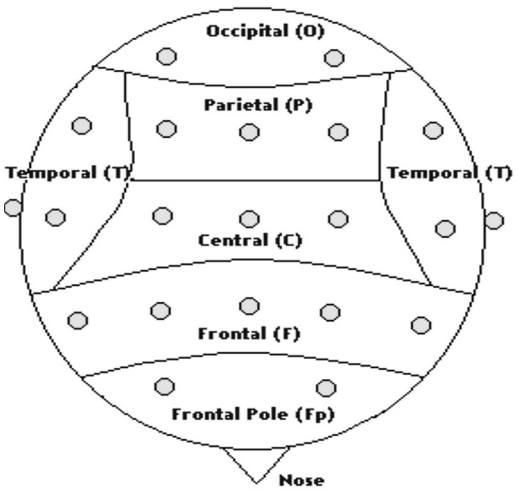

Fig. 1 International 10-20 Electrode Placement System

V. Brain machine interface: tecniques

Five main techniques are adopted in designing brain computer interface [4].

a. P300 Detection

The P300 component is a positive going evoked response potential (ERP) in the EEG with a latency of about 300ms following the onset of a rarely occurring stimulus the subject has been instructed to detect. Detecting the P300 response reliably requires averaging the EEG response over many presentations of the stimuli.

b. EEG mu-rhythm Conditioning

Subjects mu-rhythm [Appears at 9-11 Hz this activity appears to be associated with motor cortex [5]]. Amplitudes are detected while training them to move a computer cursor up and down on the screen. Results also implied that frequency bands other than mu and beta ranges may contain useful information.

c. Visual Evoked Potential Detection

Electrodes are placed over the visual cortex to detect changes in evoke potentials when the subject concentrates on a particular block out of the 64 blocks on a computer screen.

d. EEG Pattern Mapping

In this technique the EEG patterns are detected and classified for a particular action. Readiness potentials or EEG patterns are studied during experiments such as moving joystick in four directions.

e. Detecting lateral hemisphere differences

Induced lateral differences in relative brain hemisphere activation are studied during experiments where subjects hear arguments through left, right or both headphones.

VI. Need for brain machine interfaces

EEG Signals are being studied to rehabilitate people with motor disorders. About 10 million people [2 million in USA alone] all over the world suffer from neurodegenerative diseases such as cerebral palsy or amyotrophic lateral sclerosis [locked-in people], stroke and paralysis [6]. These diseases impair their ability to control their muscles and are unable to grasp objects, work with appliances or communicate in any way except through their brains. In Malaysia the increase of stroke and paralytic patients is of major concern, modern life support technology allows these individuals even those who are locked in, to live long lives, so that the personal, social and economic burdens of their disabilities are prolonged and severe.

F. Ibrahim, N.A. Abu Osman, J. Usman and N.A. Kadri (Eds.): Biomed 06, IFMBE Proceedings 15, pp. 632-636, 2007
www.springerlink.com ' Springer-Verlag Berlin Heidelberg 2007

There is a growing concern in the community today to help these disabled people and improve their living conditions. The Malaysian government has implemented many social welfare schemes such as rehabilitation and independent living policies to improve the conditions of these patients through rehabilitation service and by provision of assistive and rehabilitative devices.

VII. Motor disabilities and restoring options

Many disorders can disrupt the neuromuscular channels through which the brain communicates with and controls its external environment. Amyotrophic lateral sclerosis, brain stem stroke, brain or spinal cord injury, cerebral palsy, muscular dystrophies, multiple sclerosis and numerous other diseases impair the neural pathway that controls the muscles themselves.
Restoring these motor functions can be done depending on the severity of the impairment. In case of partial impairments, restoration can be done by increasing capabilities of remaining pathways, such as substituting muscles under control for paralyzed muscles, namely eye movements in the case of brainstem impairment and hand movements in the case of severely dysarthric patients. One other option is by rerouting around the neural breakaways that control muscles, for example using EMG signals from areas above the level of nervous break to restore useful movements. When the above two options are not possible the only solution to restore motor function is to provide a non muscular control channel directly from the brain to devices such as wheelchairs. Patients with diseases like locked-in syndrome and partial paralysis are not able to produce any type of movement. Independent to this the sensory and cognitive functions of the brain are not or partially affected. These patients are very much aware of their environment but are not able to communicate through speech or eye movements. Though many physiological signals such as EMG, fMRI, MEG and PET are available, research has proved that only EEG signals and related methods which have short time constants, can function in most environments and require relatively simple and inexpensive equipment that offer the possibility of a new non-muscular channel for a practical BMI [7].

The development of BMI to control wheel chairs is still under proof of concept stage. The next section analyses some of the research efforts and studies towards developing a BMI for motor movement and subsequent control of a powered wheel chair.

VIII. Brain machine interfaces and rehabilitation

EEG based BCI/BMI has been under study since the early nineties. BCI only provide interface between brain and computer, so far BCI have been developed to control computer cursors on the other hand BMI are more focused towards developing interfaces between brain and devices like prosthetic arms , wheelchairs etc.. BMI are used to replace impaired motor nerves and to provide an alternative communication channel to control devices like a wheelchair. Research studies have been conducted to study the EEG signals evoked by motor movements and recognition of these signals towards developing interfaces. Most research studies on EEG are currently focused on developing algorithms for classification of EEG signals related to movement. A review of the literature shows that three methods have been adopted in extracting the EEG feature data, namely Autoregression, Independent Component Analysis and Neural Networks. This section reviews some of these research studies.

A DSLVQ classifier for feature selection of EEG signals was proposed by Pregenzer et al [8]. Two different types of experiments are used to show that DSLVQ is an appropriate feature selector for a BCI. The first experiment employs DSLVQ to select the most distinct electrode positions from a large number of possible positions. The second experiment uses DSLVQ to analyze the importance of 1-Hz bands of EEG power spectra for the prediction of three different types of movement. The conclusions of this study show that the most important electrode position and frequency bands are not identical for all subjects.

Pfurtscheller and et al [9] have studied the separability of left and right motor imagery using autoregressive parameters. Four subjects were used in the experimental process and EEG, EMG and EOG signals are recorded from electrodes overlapping sensory motor area. Subject specific frequency components are selected using the DSLVQ classifier. Due to the laterality of the EEG patterns, the side [left or right] of the imagined movement can be determined with an online error between 10 to 31.8 %. The online classification of subject specific frequency bands were analyzed by a neural network. An overall improvement of classification was achieved using the off-line adaptive autoregressive model [ARR]. However the ARR method is found to be sensitive to artifacts, therefore artifacts must be controlled.

Guger and et al [10] use Common Spatial Pattern (CSP) filters to analyze real-time EEG signals. Experiments involved three subjects. Twenty seven EEG electrodes overlaying the whole primary and senorimotor cortex are used. The method proposed uses covariance to design common spatial patterns and is based on simultaneous diagonalization of two covariance matrices. The decomposition of the EEG leads to new time series which is optimal for discrimination of two populations. The patterns are designed such that signals resulting from filtering with CSP have maximum variance for left trials and minimum variance for right

F. Ibrahim, N.A. Abu Osman, J. Usman and N.A. Kadri (Eds.): Biomed 06, IFMBE Proceedings 15, pp. 632-636, 2007
www.springerlink.com ' Springer-Verlag Berlin Heidelberg 2007

trials and vice versa. The research demonstrates that CSP can be used to anise EEG signals in real time in order to give feedback to subjects as classification accuracy improved with few days of trials.

Haselsteiner and Pfurtscheller [11] have compared two different neural network topologies to classify a single trial EEG data from a BCI. The classifiers are the MLP and the FIR MLP. The static weight of the standard MLP is replaced with finite impulse response filters in the FIR MLP. The study shows that FIR MLPs performed better can standard MLP with lesser error rates.

Mahalanobis distance-based classifiers are analyzed by Babiloni et al [12], to classify the diagonal and full covariance matrix features of the EEG signals. EEG data are recorded from four electrodes placed in the C3, P3, C4 and Imagined hand movement recognition using Low Resolution Surface Laplacian and Linear P4 position of International 10-20 system. These classifiers were able to detect imagination of hand movements with a classification accuracy of 98%.

Another imagined hand movement recognition using Low Resolution Surface Laplacian and Linear Classifier is proposed by Cincotti et al [13] which use nine electrodes; the classifiers have an accuracy of 90%.

Neural network based classifiers of EEG features have been investigated by some researchers [14, 15]. Back propagation neural classifiers have also been used to analyze the EEG signals related to mental tasks.[16]

IX. Conclusions

BMI is still at the proof-of-concept stage, currently this work is undertaken by bio and neuroscience researchers. The contributions from computer engineers, psychologists and mathematician are essential to take this to the next stage. The developments of more accurate data models that carry more spatio-temporal information from the spikes in the motor cortex are required. The signals are non-gaussian and no stationary, so they are very difficult to model well with present algorithms [1].

So far, control BMI has focused on cursor movements, applying this concept to a mechanical hand or a device such as a wheelchair will prove to be more challenging. Although the theoretical and technical problems are difficult, BMI research is at a very exciting phase, thanks to the tight integration of research in computer science, engineering, and neuroscience. There is optimism about impacting the daily lives of paraplegics in the same way that sensory BMIs benefited hearing impaired patients [1].

The non-invasive BMI has potential applicability beyond the restoration of lost movement and rehabilitation in paraplegics and would enable normal individuals to have direct brain control of external devices in their daily lives. Therefore, the impact of BMI on our society promises to surpass that of any earlier digital technology.

References

[1] JOSE PRINCIPE,(2005). Brain Machine Interfaces: Mind over Matter. http://www.ece.ufl.edu/publications/Archives/inthenews/2005/brainmachine.html

[2] MICHAL TEPLAN.(2002). Fundamentals of EEG Measurement. Measurement Science Review, Volume 2, Section 2.

[3] D.G. DOMENICK. (1998). International 10-20 Electrode Placement System for Sleep. http://members.aol.com/aduial/1020sys.html

[4] RICHARD H.C. SEABROOK . (1994). The Brain Computer Interfaces : techniques for Controlling Machine. http://www.cs.man.ac.uk/aig/staff/toby/research/bci/richard.seabrook.brain.computer.interface

[5] BEN & HUGH,(2004) EEG Biocontrol Technology and Applications, http://www/biocontrol.com/eeg.html

[6] NATIONAL INSTITUTE OF BIOMEDICAL IMAGING AND BIOENGINEERING, (2004)Catch a Brain Wave, online article, http://www.nibib.nih.gov/eAdvances/102104.htm

[7] JONATHAN R WOLPAW, NILES BIRBAUMER, DENNIS J MCFARLAND, GERT PFURTSCHELLER, THERESA M. VAUGHAN. (2002). Brain-computer interfaces for communication and control. Elsevier Clinical Neurophysiology Transactions. 113(2002), 767-791.

[8] M. PREGENZER AND G. PFURTSCHELLER . (1995) . Distinction Sensitive Learning Vector Quantization (DSLVQ) Application as a Classifier based Feature Selection Method for a Brain Computer Interface. In the Proceedings of the Fourth International Conference on Atrificial Neural Networks, 433 -436.

[9] GERT PFURTSCHELLER, CHRISTA NEUPER, ALOIS SCHLOGL AND KLAUS LUGGER. (1998). Separability of EEG Signals Recorded During Right and Left Motor Imagery Using Adaptive Autoregressive Parameters. IEEE Transactions on Rehabilitation Engineering Vol.6 No. 3. 316-325.

[10] C.GUGER, H.RAMOSER AND G.. PFURTSCHELLAR. (2000). Real-Time EEG Analysis with Subject-Specific Spatial Patterns for a Brain-Computer Interface (BCI). IEEE Transactions on Rehabilitation Engineering, Vol 8, No.4. 447 456.

[11] ERNST HASELSTEINER AND GERT PFURTSCHELLER. (2000). Using Time Dependent Neural Networks for EEG Classification. IEEE Transactions on Rehabilitation Engineering Vol.8.No.4. 457-463.

[12] FABIO BABILONI,LUIGI BIANCHI, FRANCESCO SEMERARO, JOSE del R MILLAN, JOSEP MOURINO, ANGELA CATTINI, SERENELLA SALINARI, MARIA GRAZIA MARCIANI AND FEBO CINCOTTI, (2001) Mahalanobis Distance-Based Classifiers are able to Recognize EEG Patterns by using Few EEG Electrodes., Proceedings of the 23rd Annual EMBS International Conference, Istanbul Turkey.

[13] FEBO CONCOTTI, LUGI BIANCHI, JOSE DEL R MILAN, JOSEPH MOURINO, SERNELLA SALINARI, MARIA GRAZIA MARCIANI AND FABIO BABILONI, (2001), Brain Computer Interface : the use of Low Resolution Surface Laplacian and Linear Classifiers for the Recognition of imagined Hand Movements, Proceedings of 23rd Annual EMBS International Conference, Turkey , pp 655-658.

F. Ibrahim, N.A. Abu Osman, J. Usman and N.A. Kadri (Eds.): Biomed 06, IFMBE Proceedings 15, pp. 632-636, 2007
www.springerlink.com ' Springer-Verlag Berlin Heidelberg 2007

[14] TORSTEN FELZER AND BERND FREISLEBEN (2003), Analyzing EEG Signals Using the Probability Estimating Guarded Neural Classifier, IEEE Transactions on Neural Systems and Rehabilitation Engineering Vol. 11, No.4 2003. pp 361-371.

[15] DAMIEN COYLE, GIRESH PRASAD AND

THOMAS M MC.GINNITY (2004) , Extracting Features for a Brain Computer Interface by Self Organizing Fuzzy neural Network based Time Series Prediction, 26th Annual International Conference of IEEE EMBS , USA , pp 4371- 4374.

[16] C.W. ANDESON, S.V DEVULAPALLI AND E.A.STOLZ,(1994) EEG as a means of Communication: Preliminary experiments in EEG analysis using Neural Networks, Proc. 1st Annual ACM Conference on Assistive Technologies, pp 141-147.

Address of the corresponding author:

Author: Hema C.R.
Institute: Robotics and Intelligent Control Research Group, School of Mechatronic Engineering, Northern Malaysia University College of Engineering
City: Perllis
Country: Malaysia

F. Ibrahim, N.A. Abu Osman, J. Usman and N.A. Kadri (Eds.): Biomed 06, IFMBE Proceedings 15, pp. 632-636, 2007
www.springerlink.com ' Springer-Verlag Berlin Heidelberg 2007

Development of Articulation Training System with Speech Recognition Based Automatic Pronunciation Detection Mechanism

Yeou-Jiunn Chen and Jing-Wei Huang

Department of Electrical Engineering, Southern Taiwan University of Technology, Tainan County, Taiwan, R.O.C.

Abstract —**The deficiency of expressing symbol ability of the spoken language for articulation disorder will leads to the difficulty of verbal expression and communication. In the clinical protocol, language therapist subjectively utilizes the clinical experience to individually test and treat articulation disorder. The manpower of language therapist and the computer based assistant instructions are also insufficient. In this paper, an articulation training system with automatic pronunciation detection mechanism is proposed to assistance in the program of language treating for language therapist. The articulation errors in phonetic level are analyzed and modeled by clinical linguist. According to the articulation errors, a speech recognition based automatic pronunciation detection algorithm is developed to effectively acquire use's pronunciation characteristic. Speechreading based feedback responses are designed and applied to improve the efficiency of training program. Preliminary results reveal the practicability of our proposed method and system.**

Keywords—**Articulation Disorder, Pronunciation Detection, Speech Recognition, Articulation Training System, and Speechreading Feedback**

I. Introduction

The deficiency of expressing symbol ability of the spoken language for articulation disorder, which generates different degrees of the abnormality in articulation, will leads to the difficulty of verbal expression and communication. It will seriously affect person s interpersonal communication, personality, social adaptive capacity, and learning ability. Recently, researches had been focused on the articulation test and the design of speech testing materials [1-4]. For the sequence of therapy, language therapist subjectively utilizes the clinical experience to individually evaluate and treat articulation disorder [4-6].

In Taiwan, the rate of language disorder was about 10% [7]. Moreover, the rate of language disorder of 4 years to 15 years children was 2.64%; amount them 43.36% was articulation disorder [8]. Sheng Hua shown that the population of language disorder was about 2.5 million and the linguistic therapist worked in hospital was about three hundred people [9]. It is clear that the manpower for linguistic therapist is insufficient. In Taiwan, Augmentative and Alternative Communication had been proposed by National Science Council and Ministry of the Interior to help language disorder [10]. However, the assistive technology device is deficient in training procedure of articulation disorder. Glassman applied spectral parameters such as filter bank information to separate fourteen pair of consonants [11]. Neural network had been used to detect the articulation error types [12]. However, the articulation errors in phonetic level could not be effectively detected by those approaches.

In this paper, an articulation training system with automatic pronunciation detection mechanism was proposed to help linguist therapist in the process of language treatment and shown in Fig. 1. Base on the knowledge of language therapist, the words and corresponding speechreading feedback message are designed and used to evaluate the articulation errors. Moreover, the articulation errors in phonetic level are also modeled as rules. In the sequence of therapy, a prompt is shown on the screen and the user is asked to pro-

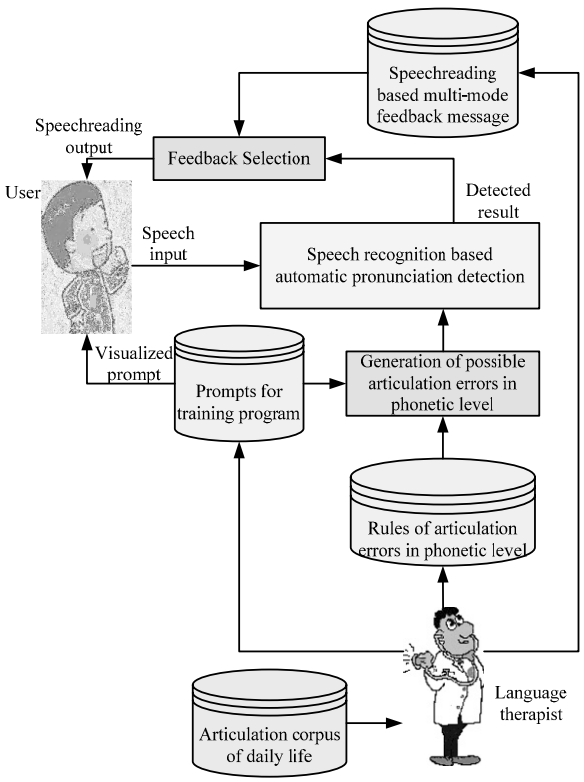

Fig. 1 System architecture of articulation training system

F. Ibrahim, N.A. Abu Osman, J. Usman and N.A. Kadri (Eds.): Biomed 06, IFMBE Proceedings 15, pp. 637-639, 2007
www.springerlink.com ' Springer-Verlag Berlin Heidelberg 2007

nounce it. According to the prompt, the possible pronunciation of articulation error is generated by the rules of articulation errors. The speech recognition based automatic pronunciation detection algorithm is adopted to find the articulation error of user s speech signal. According to the detected result and prompt information, a speechreading feedback response is selected to provoke user in articulation training.

II. Materials and methods

A. Articulation error analysis

The conversional speech of pre-school children in daily life is recorded and transcribed into text by linguistic therapist. Consequently, the language ability of pre-school children can be analyzed and used to design the prompts for language treatment. The corresponding speechreading feedback responses are also recorded. Besides, the relationship between phonemes and production model can modeled by the linguist and shown in Table 1. The types of articulation errors are also analyzed and modeled as substitutions, distortions, omissions, and additions. Moreover, the articulation errors in phonetic level can be effectively established and modeled in rules, which are shown in Table 2.

B. Automatic pronunciation detection

In the training program of language treating, a prompt, W_p, is selected and rules of articulation errors in phonetic level are also applied to generate the corresponding possible phoneme sequences. Base on those information, the grammar is established as finite state machine and used to guide the search mechanism of speech recognition.

The speech signal of user s response named observation sequence, $O=o_1o_2...o_T$, is parameterized as mel-frequency cepstrum coefficient (MFCC) to capture the acoustic characteristic and reduce the dimension of input signal. o_i is the *i-th* frame of speech signal and T is the total number frames of input speech.

Using the grammar of a prompt W_p, the Viterbi algorithm is employed to find the most likely prompt W_l, where

$$W_l = \arg\max_i L\left(O|W_i\right) \tag{1}$$

and $L(O|W_i)$ is the likelihood of the observation sequence O give prompt W_i[13]. The prompt can be treated as a sequence of subsyllable units in Mandarin and shown as

$$W_i = s_1^i s_2^i \cdots s_N^i \tag{2}$$

where N is the total number of subsyllables. For each subsyllable s, an Hidden Markov Model (HMM) is built and

Table 2 The Relationship of Phonemes and Production Model

(a) Consonants

		Bilabial	Labio-dental	Dento-alveolar	Alveolar	Retroflex	Alveo-palatal	Velar
Stops	Un-aspirated	b(ㄅ)			d(ㄉ)			g(ㄍ)
	Aspirated	p(ㄆ)			t(ㄊ)			k(ㄎ)
Affricative	Un-aspirated			zi(ㄗ)		zhi(ㄓ)	j(ㄐ)	
	Aspirated			ci(ㄘ)		chi(ㄔ)	q(ㄑ)	
Fricative	Voiceless		f(ㄈ)	si(ㄙ)		shi(ㄕ)	x(ㄒ)	h(ㄏ)
	Voiced	m(ㄇ)				ri(ㄖ)		
Nasal					n(ㄋ)			
Lateral					l(ㄌ)			

(b) Vowels

	Kaikouhu	Quchihu	Hekouhu	Cuokouhu
Mono-Vowel		yi(ㄧ)	wu(ㄨ)	yu(ㄩ)
	a(ㄚ)	ya(ㄧㄚ)	wa(ㄨㄚ)	
	o(ㄛ)	yo(ㄧㄛ)	wo(ㄨㄛ)	
	e(ㄜ)			
	e(ㄝ)	ye(ㄧㄝ)		yue(ㄩㄝ)
	er(ㄦ)			
Composed-Vowel	ai(ㄞ)	yai(ㄧㄞ)	wai(ㄨㄞ)	
	ei(ㄟ)		wei(ㄨㄟ)	
	ao(ㄠ)	yao(ㄧㄠ)		
	ou(ㄡ)	you(ㄧㄡ)		
Nasal-Vowel	an(ㄢ)	yan(ㄧㄢ)	wan(ㄨㄢ)	yuan(ㄩㄢ)
	en(ㄣ)	yin(ㄧㄣ)	wen(ㄨㄣ)	yun(ㄩㄣ)
	ang(ㄤ)	yang(ㄧㄤ)	wang(ㄨㄤ)	
	eng(ㄥ)	ying(ㄧㄥ)	weng(ㄨㄥ)	yung(ㄩㄥ)

Table 2 Parts of articulation errors in Mandarin

Types of Phoneme	Target Phonemes	Articulated Phonemes
Consonant	f, d, t, n, l, g, k h, j, q, x	NULL
	zhi, chi, shi, ri, zi, ci, si	NULL
	p	b
	t	d
	k	g
	chi, shi	zhi
	ci, si	zi
	zi, ci, zhi, chi, si, shi	d, t
Vowel	ai, ao, an, ang	a
	yai, yao, yan, yang	ya
	yin, ying	yi
	wai, wan, wang	wa
	yuan	yua

F. Ibrahim, N.A. Abu Osman, J. Usman and N.A. Kadri (Eds.): Biomed 06, IFMBE Proceedings 15, pp. 637-639, 2007
www.springerlink.com ' Springer-Verlag Berlin Heidelberg 2007

estimated to optimize the likelihood of the training set of subsyllable s and shown as

$$\lambda_s=(A_s, B_s, \pi_s) \quad (3)$$

where A_s, B_s, and π_s are the state transition probability distribution, the observation symbol probability distribution, and the initial state distribution, respectively [13].

According the prompt W_p and the most likely prompt W_l, the articulation error can be detected. Moreover, the enhanced correction prompt with the articulation error is selected as the speechreading output.

III. Preliminary results

For the parameters of speech signal, a 26-dimension feature vector, including 12 MFCCs, 12 delta MFCCs, delta log energy, and delta delta log energy was extracted. In Mandarin speech, all syllables are monosyllabic and each syllable can be phonetically decomposed into two parts: an INITIAL and a FINAL. The INITIAL of a syllable is optional and comprises a single consonant if it exists. The FINAL comprises a vowel or diphthong nucleus preceded by an optional medial and followed by an optional nasal. Thus, 94 right context-dependent INITIAL and 38 context-independent FINAL HMMs were constructed in the automatic pronunciation detection. Each INITIAL HMM consists of 3 states and each FINAL HMM consisted of 5 states, each with 10 Gaussian mixture densities.

2676 sentences (29 males, 25 females) in the database TCC300 were used as the training corpus and used to estimate the optimum parameters of HMMs. The testing speech database was pronounced by 39 children and the average age of those children was 5. For the testing database, 2412 and 1482 sentences were recorded for correct and incorrect in articulation, respectively. The users give mean opinion scores (MOS) on a scale of 1 to 5, i.e., 5 for excellent level, 4 for good level, 3 for fair level, 2 for poor level, and 1 for unsatisfactory level. The average MOS was 4.13 and the detection rate could achieve 82.7%.

IV. Conclusions

In this paper, an articulation training system with automatic pronunciation detection mechanism was proposed to assistance in the program of language treating for language therapist. Moreover, the patients with articulation disorder can be trained for language ability at home. Base on the modeled articulation errors, a speech recognition based automatic detection algorithm is developed to effectively detect user s pronunciation characteristic. Besides, speech-reading feedback responses can improve the efficiency of articulation training system. Preliminary results show the practicability of our proposed method and system.

Acknowledgment

The authors would like to thank the National Science Council, R.O.C., for its financial support of this work, under Contract No. NSC95-2221-E-218-002-MY2.

References

1. Hegde MN (1991) Introduction to communication disorders. Austin, Texas: PRO-ED.
2. Lin BG and Lin XM, (1993) Appraisal of language disorder for preschool children.
3. Yang HM, Wu JL, Lin SL, Lin YH (2004) Mandarin monosyllabic lexical neighborhood nest: Interlist equivalancy and lexical effect. Cochlear Implant Int. 201-203.
4. My GJ (1998) The strategy of language evaluation and treatment for children with language and articulation disorder. The Speech-Language-Hearing Association of the Republic of China, pp 29-35.
5. Lai XJ (1987) Articulation disorder. The Magazine of Hearing and Language, The Speech-Language-Hearing Association of the Republic of China, vol. 4, pp 70-73
6. Van Riper C and Emerick L (1984) Speech correction: An introduction to special pathology and audiology. N.J. : Prentice-Hall.
7. Department of Statistic, Ministry of the Interior at http://www.moi.gov.tw/stat/english/index.asp
8. Lin BG (1994) Language disorder and treatment. Wunan Book Co., Ltd.
9. Sheng H et al. (2001) Report of the police recommendation for manpower of linguistic therapist. The Magazine of Hearing and Language, The Speech-Language-Hearing Association of the Republic of China, vol. 16, pp 76-91
10. Center for Information Assistive Technology, Ministry of the Interior at http://ciat.moi.gov.tw
11. Glassman MS and Starkey MB (1988) Speech therapy using computer based minimal consonant pair discrimination. IEEE Proc., Engineering in Medicine and Biology Society, Nov 1988, pp 1421 1422
12. Chen YQ (1995) Apply neural network to detect articulation error type of chidren. Master Thesis, Department of Engineering Science, National Cheng Kung University
13. Rabiner L (1993) Fundamentals of Speech Recognition. Prentice Hall PTR

Address of the corresponding author:

Author: Yeou-Jiunn Chen
Institute: Department of Electrical Engineering, Southern Taiwan University of Technology
Street: No. 1, Nan-Tai Street
City: Yung-Kung City, Tainan County
Country: Taiwan, R.O.C.
Email: chenyj@mail.stut.edu.tw

F. Ibrahim, N.A. Abu Osman, J. Usman and N.A. Kadri (Eds.): Biomed 06, IFMBE Proceedings 15, pp. 637-639, 2007
www.springerlink.com ' Springer-Verlag Berlin Heidelberg 2007

Exercise Technology after Spinal Cord Injury: Functional Electrical Stimulation Leg Cycling

N.A. Hamzaid and G.M. Davis

Rehabilitation Research Centre, School of Exercise and Sport Science, The University of Sydney, Australia

Abstract— **Functional electrical stimulation (FES) is the use of electrical currents to artificially evoke muscle contractions, thereby producing human limb movements. FES is widely used amongst people with paralysis either as an exercise strategy or for daily functional applications. This paper presents an insight into one FES application – FES evoked cycling for people with spinal cord injury (SCI). Published research and peer opinions are presented to provide an understanding about the topic and to identify the benefits, technological aspects, as well as the limitations and challenges of FES cycling after SCI.**

Keywords— **Rehabilitation, Spinal Cord Injury, Functional Electrical Stimulation, Exercise Technology, Leg Cycling**

I. Introduction

Spinal cord injury (SCI) leads to significant health consequences, including muscle atrophy and reduced aerobic fitness levels. In this paper, the focus will be on low level spinal cord lesion, paraplegia, involving paralysis of the abdomen and lower limbs.

At the beginning of the 20th century, people suffering from paralysed lower limb, usually ended up in wheelchairs and seldom were prescribed with further health maintenance. However, more recently, technology has provided innovative methods to maintain the intact spinal cord nerve tracts and enrich their overall quality of life.

FES-evoked exercise has been well researched and documented for over 20 years. External electrical currents elicit muscle contractions, thus force and movement. When applied to the paralysed lower limbs to produce cycling movements, it is called FES cycling. Research on FES cycling has reported that it is one of the most popular exercise strategies for the SCI population. Other FES-evoked exercise paradigms include FES knee extension, standing, stepping, and rowing.

This paper outlines some general benefits of FES cycling, and discusses the technological aspects of such exercise. Technical insights allow greater understanding of these FES systems, and may induce greater benefits by further development of the system s efficiency and effectiveness.

II. Health and fitness benefits of FES cycling

The spinal cord has the ability to produce and modulate normal movements by receiving sensory information from the external environment. After SCI, the spinal cord looses some or all of this ability. Using FES, intact neuromusculature below the lesion can be recruited via electrical stimulation, which speaks its language , for muscles to maintain their function [1].

As the legs have a significant portion of the body muscles mass, movement of the legs greatly affects the health, fitness and performance. Muscle atrophy, a significant reduction of normal blood circulation, and altered psychosocial adaptations are all negative sequelae of leg paralysis.

With FES, the muscles can be turned on to elicit contractions. While FES cycling is not a cure for paralysis, it provides a means for maintaining normal body composition and the person s health. The physiological and psychosocial advantages of FES cycling include increased metabolic demand, cardio-respiratory fitness, promotion of blood circulation, greater muscle fibre size and volume, increase in functional exercise capacity such as strength and endurance, and likely increase in bone mineral density, as well as improved psychosocial adaptations.

David Prast [2], an Australian paraplegic, reported his personal experience of FES cycling. He observed that FES cycling eliminated his need to take anti-spasm medications, while increasing his fluid output. It also reduces the swelling of his feet, which are usually caused by blood pooling due to poor circulation. The cycling movement also provided him with pressure relief and improved digestion. Other paraplegics confirmed that FES cycling makes them feel good , and increases their stamina.

III. Basic technical aspects of FES cycling

Application of FES to produce a cycling motion requires the stimulation electrodes be placed over three primary muscle groups of each leg; quadriceps, hamstrings and the gluteal muscles. When the legs are placed on the crank cycle, the angular position of the crank can be measured.

F. Ibrahim, N.A. Abu Osman, J. Usman and N.A. Kadri (Eds.): Biomed 06, IFMBE Proceedings 15, pp. 640-642, 2007
www.springerlink.com ' Springer-Verlag Berlin Heidelberg 2007

This angular position is interpreted by a computer to turn the muscle groups on and off with pre-specified timing in order to produce the cycling motion. The result of the stimulation pattern on the three muscle groups is a cycling motion.

The stimulation controller is normally external, but can also be implanted. In this paper, we will describe an external stimulation controller and skin surface electrodes. Two surface electrodes are required for each muscle groups to provide current flow. Current through the electrodes evokes muscle contractions, which are otherwise produced by electrical impulses within the intact spinal cord.

Varying the sequential frequency affects the speed, or cycling cadence. Controlling cadence requires alteration in timing sequence of the stimulation pattern, but the general pattern is unchanged. Higher cadence promotes aerobic fitness, while slower cadence provides strength and endurance training for the leg muscles.

The stimulation current is produced in pulses, with variable frequency and/or amplitude. By externally stimulating the leg muscles, the muscles become easily fatigued. Therefore, the same level of stimulation will result in reduced force. This requires constant increase in stimulation amplitude, depending on the force and power production of the muscles. Stimulation intensity can be increased by increasing the amplitude of the current or by modulating the pulse width.

When the muscles becomes fully fatigued, even maximum stimulation produces no contraction force. This is unlike the physiologically natural muscle contraction, where the muscle fibers are selectively stimulated depending on the required force and task.

IV. Technological advance of FES cycling

One technique in dealing with muscle fatigue during FES cycling is to control the cadence. Feedback-control is implied to maintain the pedaling speed even when the stimulated muscles produce little or no power output [3]. This is referred to as passive cycling.

A FES cycling control system relies on several factors, such as seating position, conditions of surface stimulation and pedaling rate, all influence FES cycling capacity [4]. To facilitate exercise, the cycling cadence and leg power output can be controlled in an integrated manner by controlling the driving mechanism of the exercise system as well as the stimulation current supplied to the legs [5].

Apart from the electrical perspective, the mechanical structure of the cycling machine should also be considered. The seat-to-pedal distance must be safe to prevent knee hyperextension, while considering the effective range of cycling movements. The cycle itself must also be safe and ergonomically comfortable for the individual.

Careful attention has to be placed on the efficiency of the stimulation. At best, electrical stimulation and the resulting muscle contraction should be tightly related and optimized. To ensure the electrical stimulation is tightly related to the leg muscle force production, the ankle joint must be fixed, or the power production of electrical stimulation will be less [6]. The power output production however may depend on the system s efficiency.

Recently, FES cycling system design has been moving towards mobility, i.e. from a stationary indoor activity towards mobile outdoor recreational exercise. Through this technique, paraplegics can perform outdoor FES cycling and when their muscles get eventually fatigued after a period of time, the motorized cycle continues to drive the cycle passively to reach the final destination [5]. There is an increasing need to ensure the whole system is more compact, mobile and flexible.

One way of increasing FES system flexibility is by deploying a multipurpose FES system that can facilitate protocol sharing and interchanging of sensors and user interfaces [7]. Also, besides cycling on an exercise machine, paraplegics could use their electrically-stimulated legs to propel their wheelchair to increase the lower limbs activity [8].

V. Limitation and challenges

Currently, there is not enough evidence of interdisciplinary approach towards the technological advancement of functionality and health maintenance for people with SCI. There is a need to fully understand the nerve system itself as well as the technical aspects to emulate the systems properties and performance. We also need to find ways to selectively stimulate the muscle fibres to increase the muscle endurance to FES.

Meanwhile, FES cycling is one of the externally evoked exercise strategies that could maintain paraplegics fitness level. Its benefits are well proven by researches and it could be a stepping stone towards the more challenging FES standing and walking activities.

The efficiency of FES cycling can be increased through interdisciplinary approach. This requires technical experts to look into the physiological responses of people with spinal cord injury. Technical experts then need to translate their knowledge into practice for the benefit of optimal health maintenance and possibly a future for functional restoration.

F. Ibrahim, N.A. Abu Osman, J. Usman and N.A. Kadri (Eds.): Biomed 06, IFMBE Proceedings 15, pp. 640-642, 2007
www.springerlink.com ' Springer-Verlag Berlin Heidelberg 2007

VI. Concluding remarks

FES cycling is a promising way to maintain the paraplegics health and fitness. Even though FES cycling system is widely accepted and is gaining its reputation, there is still a need to further advance the technical aspects of the system. This will increase the systems efficiency and performance to optimize its benefits. This requires interdisciplinary expert approach of neurologist, technologist and health practitioners.

Acknowledgment

The primary author received funding from a JPA Malaysian Government Scholarship. This project was funded by a Program Grant from the NSW Ministry for Science and Medical Research.

References

1. Bartlett P, Field-fote E, Mackay-sim A, Keast J, Middleton J and Knott J (2006) Panel discussion, Re:connections Forum, Sydney
2. Prast D (2006) A paradigm for spinal cord injury recovery, Re:connections Forum, Sydney
3. Fornusek C, Davis GM (2004) Maximizing muscle force via low-cadence functional electrical stimulation cycling, J Rehabil Med 36, no. 5, 232-237
4. Gfohler M, Lugner P (2004) Dynamic simulation of FES-cycling: Influence of individual parameters, IEEE Trans Neural Syst Rehabil Eng 12, no. 4, 398-405
5. Hunt KJ, Stone B, Negard NO et al. (2004) Control strategies for integration of electric motor assist and functional electrical stimulation in paraplegic cycling: Utility for exercise testing and mobile cycling, IEEE Trans Neural Syst Rehabil Eng 12, no. 1, 89-101
6. van Soest AJ, Gfohler M, Casius LJ (2005) Consequences of ankle joint fixation on fes cycling power output: A simulation study, Med Sci Sports Exerc 37, no. 5, 797-806
7. Popovic MR, Keller T (2005) Modular transcutaneous functional electrical stimulation system, Med Eng Phys 27, no. 1, 81-92
8. Stein RB, Chong SL, James KB et al. (2001) Improved efficiency with a wheelchair propelled by the legs using voluntary activity or electric stimulation, Arch Phys Med Rehabil 82 no. 9, 1198-1203

Address of the corresponding author:

Author: Nur Azah Hamzaid
Institute: Rehabilitation Research Centre,
School of Exercise and Sport Science,
The University of Sydney
Street: P.O. Box 170 East Street
City: Lidcombe, 2141, NSW
Country: Australia
Email: nham0064@mail.usyd.edu.au

F. Ibrahim, N.A. Abu Osman, J. Usman and N.A. Kadri (Eds.): Biomed 06, IFMBE Proceedings 15, pp. 640-642, 2007
www.springerlink.com ' Springer-Verlag Berlin Heidelberg 2007

Prosthetic Hand for the Brain-computer Interface System

S. Yahud and N.A. Abu Osman

University of Malaya/Biomedical Engineering Department, Kuala Lumpur, Malaysia

Abstract— **The objective of the study is to develop a prosthetic hand for the usage of Brain-computer Interface (BCI) system. In the proposed BCI system the prosthetic hand was introduced as an external device controlled by the system. This hand is required to perform four essential tasks of the human hand: cylindrical grasp, key pinch, pulp to pulp pinch and tripod pinch. The hand was inspired by the perfection and complexity of the human hand. This hand consists of palm and 5 fingers with a total of 16 degrees of freedom (DOF). The phalanges of each finger was modeled as three link open chain joined at the metacarpal joint (MCP), proximal joint (PIP) and distal joint (DIP). Phalanx was made from two identical parallel aluminum plates and connected to the other segment using a bolted spacer acting as hinge joint. The Length of each segment was made such that it will form an equiangular motion path during trajectory. Each joint is actuated by its individual actuator. Two mechanisms were proposed in this study. The first mechanism is the tendon drive; used terelyne string to pull each segment to flexion. The second mechanism is a spring return; a stored resistive force in torsion spring will kick the segment to its initial position. The hand was equipped with potentiometers and force sensors for control purposes. The prototype of the prosthetic hand was tested with BCI system, in order to meet its initial objective and additional tests were carried out to evaluate its performance. An experiment to test the performance of the prosthetic hand was carried out successfully. Strength of each tendon was measured using a proof ring method and motion images were captured using video camera and analyzed using Peak Motus 7 Motion Analysis software.**

Keywords— **Prosthetic hand, Brain-computer Interface (BCI)**

I. Introduction

A. Brain-computer Interface

A brain-computer interface (BCI) is a communication system in which messages or commands convey from an individual to external device without passing through a brain's normal output pathways of peripheral nerves and muscles. A BCI use the recorded electroencephalogram (EEG) rhythms from the electrodes on scalp and translated to the external device. The BCI application is useful for people with severe motor disabilities and in worst case for a completely paralyzed or locked-in patient that unable to communicate by any way. BCI application is wide and can be varied depending on the need of the user such as communication, controlling the environment, or moving prosthetic limb. Wolpaw *et. al* has used BCI to restore communication for locked-in subject by moving a cursor in one or two dimension to choices on computer screen [1]. Birch and Mason [2] has used the LF-ASD to allow user to navigate a maze by making, turning decisions at intersection which could be implement for wheelchair control. Graz-BCI [3] is used by tetraplegic patient to control the opening or closing of a hand orthosis. In this study, the BCI is used to control a prosthetic hand. Figure 1 shows the block diagram of the BCI proposed in this study.

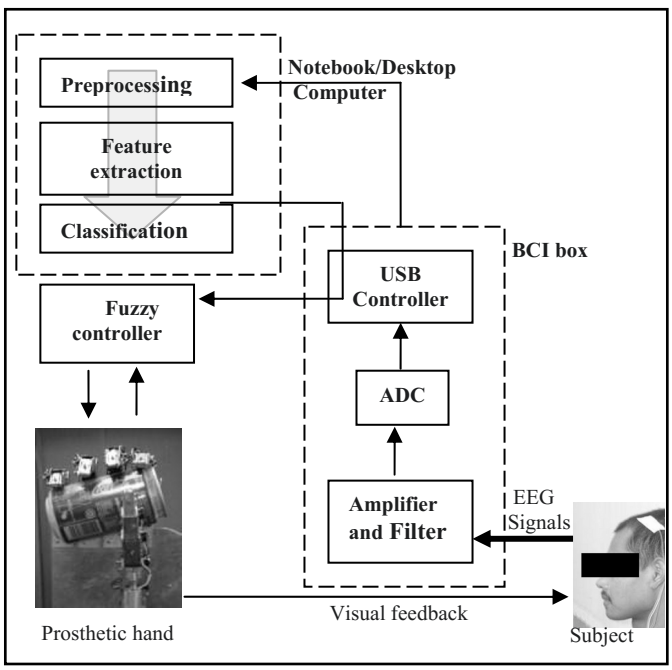

Fig. 1 Block diagram for the proposed BCI system

B. Prosthetic Hand

Prostheses can be classified into; body powered and externally powered. Most of the ancient below-elbow prosthetics known are body powered and apparently relied on the contralateral hand or relative motion between the shoulder, upper arm and forearm for the operation. Body powered below-elbow prosthetics usually consist of split hook

F. Ibrahim, N.A. Abu Osman, J. Usman and N.A. Kadri (Eds.): Biomed 06, IFMBE Proceedings 15, pp. 643-646, 2007
www.springerlink.com ' Springer-Verlag Berlin Heidelberg 2007

or five fingers, socket and harness. This type of prosthetic hand only provide open and close hand action, and due to this limitation study are carried out to overcome it by switching to the externally powered prosthetic hand.

The current trend in prosthetic hands is externally powered. An externally powered prosthetic hand is actuated by external actuators such as DC motors, ultrasonic motors, pneumatic cylinder, hydraulic cylinder and shape memory alloy material (SMA). Robotic technology has been helpful in improving the control and design of prosthetic hand. There are close relationship between robotics and prosthetic hand since both provide human like motion and prehension. In robotic hand the main focus is to imitate the human hand and enhance the performance. Thus, in robotic application two fingers are sufficient, however three fingers are needed to perform dexterous tasks in an unstructured environment and to achieve full grasp of two-dimensional object [4]. Whereas, prosthetic hands are inspired by the need to replace the function of the human hand and try the best to resemble the human hand both functionally and structurally. In general prosthetic hands have benefited from the development of the robotic technologies.

II. Methodology

In this study the primary concern is to develop a prosthetic hand that able to perform the four essential tasks using a BCI system. In order for the hand to perform the four tasks, the hand should possess the maximum number of the DOFs. As a result, the proposed design should yield a total of 16 DOFs with each finger has 3 DOFs and thumb has 4 DOFs. The design of the finger has the following characteristics; (i) each finger has a total of three joints with three DOFs, (ii) thumb has similarly three joints but with four DOFs, (iii) each DOF is actuated by one actuator, (iv) each joint has installed a torsion spring within it for return mechanism, and (v) each joint is equipped with potentiometer for control.

For every DOF of movements, it is driven by its individual actuator, thus the hand used up to 16 units of actuator. Actuator used in this design is DC micromotors type 1331 with gearhead reduction series 14/1 manufactured by Faulhaber Group. The actuator is then connected to its respective segment using a terelyne string. The string will pulled the segment as the actuator rotates, the angle and speed of the flexion is depending on the output of the actuator. Flexion of each segment is accomplished when the string being pulled by the actuator and reset to its original position when string releases. The reset mechanism is, attain with the used of torsion spring at the joint. The stored resistive force on the torsion spring will reset segment to its original position. The string will act as a flexor digitorum profundus tendon of the human hand.

The basic unit of the prosthetic hand is the prosthetic finger. Each prosthetic finger is said to maintain the same anatomical structure and dimensional proportion, regardless of their size. The three phalanx; distal, middle and proximal phalanges are denoted as ***L3***, ***L2*** and ***L1*** accordingly and connected to form a finger as shown in fig. 2. Each phalanx is made from 2-parallel aluminum plate of 1.5mm thickness and join using a brass spacer bolted with 2mm diameter stainless steel screw. DC motors with the combination of reduced gear heads are used to actuate finger segments.

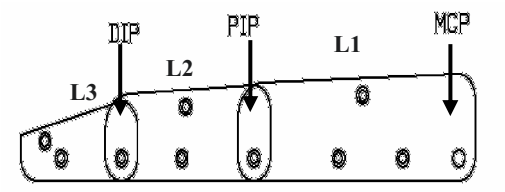

Fig. 2 Prosthetic finger

Process of determining the length of the phalanx acquired the implementation of the Fibonacci sequence. Fibonacci sequence in application to the human hand stated that; the difference between the length of the next phalanx and the sum length of the two prior phalanges must equal to zero. The sum of the distal phalanx and the middle phalanx should be equal to the length of the proximal phalanx. However, Park et al [5] in his work has showed that the bone lengths of the finger does not follow the Fibonacci relationship but the motion paths of the digits still form an equiangular spiral path. Therefore to achieve the equiangular spiral motion path the respective length that representing each segment should include the absolute bone length and functional length (radius of the joint). Length of each segment was referred to author s hand herself and using the Hamilton s ratio [6] to verify that the chosen length is sufficient to form an equiangular spiral motion.

All the fabrication and machining process was done in the mechanical workshop in the Department of Mechanical Engineering, University of Malaya, Malaysia. The precise machining was carried out using a CNC (computer numerical control) wire EDM (electrical discharge machining) machine Sodick, available in the Department of Manufacturing and Design, University of Malaya, Malaysia.

III. Result

A prototype of prosthetic hand was successfully fabricated and tested for functionality, performance and strength. Figure 4 shows the flow diagram of a BCI system to control prosthetic hand developed by Biomedical Engineering BCI group, University of Malaya. A fuzzy controller is used to

F. Ibrahim, N.A. Abu Osman, J. Usman and N.A. Kadri (Eds.): Biomed 06, IFMBE Proceedings 15, pp. 643-646, 2007
www.springerlink.com ' Springer-Verlag Berlin Heidelberg 2007

control the prosthetic hand. Input for controller is fed from the BCI box. EEG signals acquired from subject is amplified and converted to digital signal. The signal is further process and classified before send to fuzzy controller. The prosthetic hand then acted according to the subject intent. The proposed BCI system was effectively controlled the prosthetic hand. The prosthetic hand is capable of performing the four essential tasks: cylindrical grasps, key pinch, pulp to pulp pinch and tripod pinch as shown in figure 3.

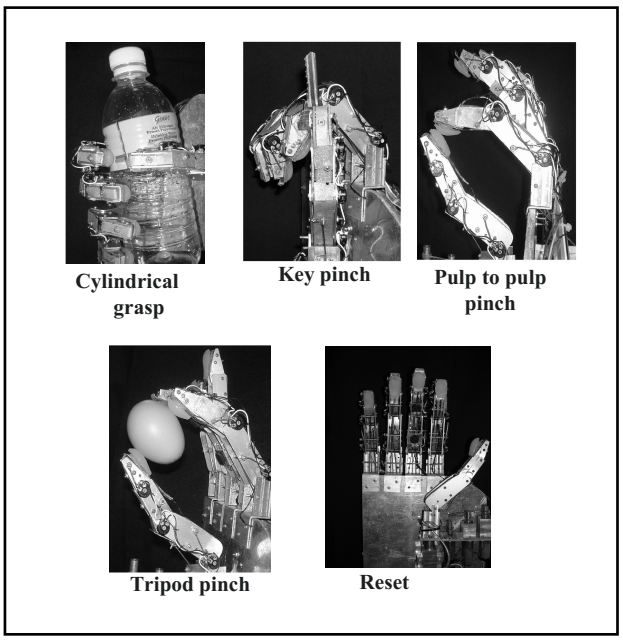

Fig. 3 The four desired tasks and reset position

Strength for each joint was measured using proof ring method. Maximum loads used for calibration of the proof ring is 1.2 kg. Figure 6 shows the graph obtained form the proof ring calibration test. A LabVIEW program was developed to capture voltage changes as the ring experienced tension. In the test the ring was placed between actuator and measured joint of the prosthetic finger. LabVIEW program will capture value of strain gages during flexion and steady state. Each joint was tested for flexion angle ranging from 10° to 90°. The collected results shows that the value do not exceed the calibration range, (0-6.5V).

Value acquired for each potentiometer shows degree of flexion made from respective joint. The reading was taken at chosen angle; 10°, 45° and 90° in fuzzy GUI (graphical user interface) controller box. Figure 4 shows a sample of collected data for three potentiometers on index finger at; metacarpal joint (MCP), proximal joint (PIP), and distal joint (DIP) accordingly.

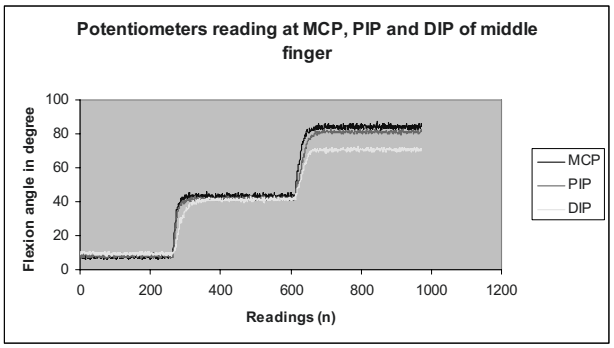

Fig. 4 Potentiometers reading at MCP, PIP and DIP joints of middle finger

IV. Discussion

Design of prosthetic hand emphasize on simple mechanism and robustness. The prototype employed simple pulling tendon mechanism for flexion and resistive torsion spring for return mechanism. Structural design of the prosthetic hand is made simple for easy assemble and dissemble without destructing any of components. Ample area in every phalanx of the finger provides space for future modification. Selection of material based on availability, cost and strength. Design and mechanism of the hand is simple if compared with other available prosthetic hands [7][8][9][10]. However, size and weight of the prosthetic hand could be reduced and skin could be added into the design to give more humanlike impression. Functional strength on each joint is depending on the tendon s material. Terelyne string is used as tendon and able to withstand a maximum functional weight of 45 kg. Therefore, the prosthetic hand is capable of handling functional weight more than required by human hand [11].

The path of fingertip trajectory for each prosthetic finger is similar to Guo s trajectory [12]. Maximum flexion angles for each joint are varied but approaching the value suggested by Thakor et. al [13]. The prosthetic hand is able to pose the four desired tasks without reaching a maximum angle of each joint.

The four tasks focused in the study are basic functional activities commonly performed by human hand. The selection of hand tasks can be observed in experiment to investigate functional strength of the hand by Chao et. al [12]. The proposed BCI system is able to control the prosthetic hand, during online experiment. Subject however has to be trained in order for him/her to control the prosthetic hand. Performance of prosthetic hand in BCI environment is very much depending on factors such as subject s EEG control ability, system performance, feedback delay and 50 Hz interference. As far as the author is concern, there is no experimental work done to demonstrate the actual performance of BCI controlling a prosthetic hand.

F. Ibrahim, N.A. Abu Osman, J. Usman and N.A. Kadri (Eds.): Biomed 06, IFMBE Proceedings 15, pp. 643-646, 2007
www.springerlink.com ' Springer-Verlag Berlin Heidelberg 2007

V. Conclusion

The prototype of a prosthetic hand has fulfilled the objective of the study. A total 16 DOFs is considered sufficient however it can be increase for better dexterity. Increasing the number of DOFs could result in different and complicated mechanism. Thus it will add complexity to the design and controller. The major contributor to the total weight of current prosthetic hand is DC motors. In future build in actuators could be considered to replace DC motors.

The prosthetic hand in this study was developed specifically for BCI application. Application of BCI technology in controlling a prosthetic hand is a promising method to restore communication of locked-in with external environment. To date, experiment to test ability to control prosthetic hand was carried out on healthy subject. The possibility of implementing the technology to locked-in patient is yet to be discovered.

Acknowledgment

I would like to thank University of Malaya for giving me an opportunity to complete this project as a fulfillment of my master degree.

References

1. J.R. Wolpaw, D.J. McFraland, T.M. Vaughan, G. Schalk, The Wordsworth Center Brain-Computer Interface (BCI) Research and Development Program. IEEE Trans. on Neural Systems and Rehab. Eng., 2003, vol.11, No.2, 204-207.
2. G.E. Birch, S.G. Mason. Brain-Computer Interface Research at the Neil Squire Foundation. IEEE Trans. on Rehab. Eng. 2000, vol. 8, No.2, 193-195.
3. C. Guger, W. Harkam, C. Hertnaes, and G. Pfurtscheller., Prosthetic control by an EEG-based brain-computer interface (BCI). Proc. AAATE 5th European Conference for the Advancement of Assistive Technology, 1999.
4. S. Nahavandi and A.Z. Kouzani, Artificial Hand From a Robotic Perspective. Seventh Australian and New Zealand Intelligent Info. Sys. Conf., 2001, 37-42,
5. Andrew E. Park, MD, John J. Fernandez, MD, Chicago, IL, Karl Schmedders, PhD, Evanston, IL, Mark S. Cohen, MD, Chicago, IL, The Fibonacci Sequence: Relationship to the Human Hand. The Journal of Hand Surgery, 2003, vol. 28A No. 1. 157-160.
6. R. Hamilton, R. A. Dunsmuir, Radiographic Assessment of the Relative Lengths of the Bones of the Fingers of the Human Hand. The Journal of Hand Surgery, 2002, vol. 27B No. 6, 546 - 548
7. R. Tomovic and G. Boni, An Adaptive Artificial Hand. IRE Trans. on Automatic Control, 1962, vol. 7, issue 3, 3-10.
8. Peter J. Kyberd. Colin Light, Paul H. Chappell, Jim M. Nightingale, Dave Whatley and Mervyn Evans.. The design of anthropomorphic prosthetic hands: A study of the Southampton Hand. Robotica (2001), 2001, Vol. 9, 563-600
9. S. Schulz, C. Plyatiuk and G. Bretthauer, A New Ultralight Anthrpomorphic Hand. Proc. of the IEEE Int. Conf. on Robotics and Auto., 2001, vol. 3, 2437-2441
10. M. Carozza, B. Massa, S. Micera, R. Lazzarini, M. Zecca and P. Dario, The development of a novel prosthetic hand ongoing research and preliminary results. IEEE/ASME Trans. on Mechatronics, 2002, vol. 7, no. 2, 109-114
11. Chao, E.Y; Biomechanics of the hand: a basic research study ; World Scientific; 1989, 97-129.
12. Gongliang Guo, William A. Gruver, and Xikang Qian., A new Design for a Dextrous Robotic Hand Mechanism. IEEE Int. Conf. on Systems, Man, and Cybernetics, 1992. 35-38
13. Becker, J.C., Thakor, N.V. A study of the Range of Motion of Human Fingers with Application to Anthropomorphic Designs. IEEE Trans. on Biomedical Engineering, 1988, vol. 35, No.2, 110-117

Address of the corresponding author:

Author: Shuhaida Yahud
Institute: University of Malaya
City: Kuala Lumpur
Country: Malaysia
Email: yshuhaida@yahoo.com

F. Ibrahim, N.A. Abu Osman, J. Usman and N.A. Kadri (Eds.): Biomed 06, IFMBE Proceedings 15, pp. 643-646, 2007
www.springerlink.com ' Springer-Verlag Berlin Heidelberg 2007

Quadraplegic Communicator for Spinal Cord Injury Patient

C.F. Soon[1], S.Y. Leong[1] and Nicholas Tan[2]

[1] Kolej Universiti Teknologi Tun Hussein Onn, Batu Pahat, Johor, Malaysia
[2] Akrab Meditech Sdn. Bhd., Petaling Jaya, Malaysia

Abstract— **Quadriplegic Communicator is designed to provide a communication tool between the quadriplegic patients and their care provider. The system is developed based on user-friendly concept and involved hardware and software integration. The acquisition circuit is able to capture rapid signal response from eye and send signal to the computer through a parallel port. The eye-blinking signal which was received in the reflective sensor will be amplified, filtered, generate a TTL signal to be acquired by the computer and able to be detected through Visual Basic program. Since this tool is expected to be used for Malaysia's citizen, the software GUI is designed in three languages selection. This system will be able to display the message that is selected from user and play the related message in sound.**

Keywords— **Quadriplegic, communicate, Visual Basic, parallel port, eye blink, sensor**

I. Introduction

Quadriplegia is caused by damage to the spinal cord (nerve damage). It is usually the result of an injury to the spinal cord. The most common causes of damage to the spinal cord are trauma's such as motor vehicle accidents, motor bike accidents, falls, sports injuries (particularly diving into shallow waters), gunshot wounds, assault and other injuries; and disease such as poliomyelitis [1].

Quadriplegics are limited in their motion and need some device to help them to communicate with the surrounding people [2]. The Quadriplegic Communicator will take input from the patient and make selection on Graphical User Interface provided. The aim of the Quadriplegics Communicator is serve as tool for quadriplegic care provider to understand the quadriplegics basic daily needs [3,4, 5].

The phototransistor reflective object sensor is used to detect the blinking eye signal from the user. The light will reflect to receiver of sensor when there is blinking eye signal from user and fed into passive high pass filter and voltage comparator. The transistor switching is connected to parallel port which will send the TTL signal to computer. The developed GUI program will respond to signal send from the hardware. The block diagram for project is defined as shown in Fig. 1

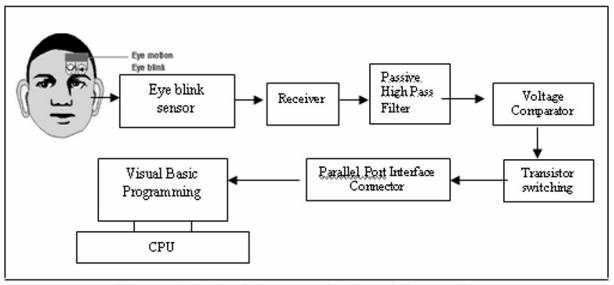

Fig. 1 Block diagram of the communicator

II. Methodology

A. Design specification

The Quadriplegic Communicator is developed based on user-friendly concept and involved hardware and software integration. It consists of eye blink sensor, hardware, parallel port connector and software. The Quadriplegic Communicator s specification is summarized in Table 1.

B. Sensor positioning

The angle of sensor holder from the spectacle is approximately 35^0 . This angle is chosen due to the reason that this angle will not disturb the user vision and available for sensing eye blink signal. The small clip is used for fixing the adjustment of sensor as shown in Fig. 2.

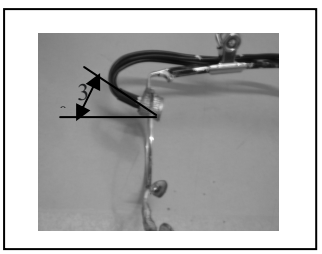

Fig. 2 The angle of sensing holder in Spectacle

The circuit block diagrams functions in Fig. 3 will be explained as follow:

F. Ibrahim, N.A. Abu Osman, J. Usman and N.A. Kadri (Eds.): Biomed 06, IFMBE Proceedings 15, pp. 647-650, 2007
www.springerlink.com ' Springer-Verlag Berlin Heidelberg 2007

Table 1 The Quadriplegic Communicator Specification

Eye blink Sensor	o Phototransistor reflective object sensor which consists of infra-red LED and phototransistor o The angle of sensor holder is approximately 35^0 from the spectacle
Hardware	o Capable to generate square wave to transmit through eye blink sensor o Capable to receive the signal and filter the signal o Consists of LED and buzzer to indicate the eye blink signal o Capable to send TTL signal to parallel port
Parallel Port Connector	o 25 pins o data pins :TTL level output o pin18-25 are ground o 5 input pins(10,11,12,13,15) o 8 output pins(2-9)
User interface	o User friendly o Provide 3 language version o Capable to provide option of the basic needs of quadriplegic patients o Capable of playing sound system

C. Sensor Driver Circuit

By referring to Fig. 1, the reflector sensor is actually driven by pulsating signal generated by a astable multivibrator. Trains of 137.9 Hz square wave from the non-symmetrical astable multivibrator is injected at the base of a transistor. The transistor can drive an infrared LED to transmit its pulsating light wave.

D. Receiving Part

Infrared beam detected by a sensitive phototransistor which is in one compact package of the sensor. The received signal needs to be conditioned before it can be send to PC. In the circuit, zener diode is applied to maintain constant voltage, regardless of varying current flow.

E. Passive High Pass Filter and Amplifier

Passive high-pass filter is used to filter the noise. The filter attenuates frequency below 159Hz and passes frequencies above that frequency. The amplifier is used to amplifier the receiving signal. A 560 gain in the inverting amplifier is multiplied to the received signal from the sensor. The output amplified signals is a clean square wave signal with minimum noise and distortion.

F. Voltage Comparator and Delay

There are two voltage comparators in the circuit. Voltage comparator is used to generate a difference voltage when there is a signal send from amplifier and passive high pass filter. The first voltage comparator will receive signal after filtering. The charging and discharging action of a capacitor is applied as a delay in this project. It is a need to have a 0.6 seconds delay between two voltage comparator because the eye-blinking signal is a fast signal response. When there is a voltage across the capacitor, it will take around 0.6 seconds to discharge the capacitor. While in the charging action of capacitor, capacitor will be charged instantly.

G. Alarm and Interface part

The buzzer will be activated and LED will be ON each time when there is an output from voltage comparator (eye blinking is detected). The signal from hardware will be send to computer through the parallel port.

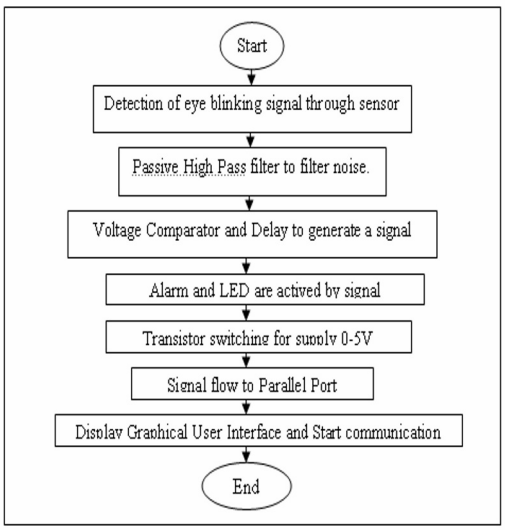

Fig. 3 Quadriplegic communicator hardware signal flow

H. Software Design

The program was written with Visual Basic program and it is divided into main menu and three submenus as shown in Fig. 4. Submenus are available in 3 languages; they are the language of the three main nations in Malaysia.

F. Ibrahim, N.A. Abu Osman, J. Usman and N.A. Kadri (Eds.): Biomed 06, IFMBE Proceedings 15, pp. 647-650, 2007
www.springerlink.com ' Springer-Verlag Berlin Heidelberg 2007

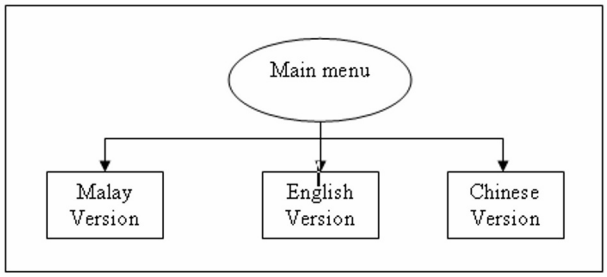

Fig. 4 Main menu and Submenu structure

a) Variable Declarations

The first part of source code for each menu is to declare the variables that will be used in the rest programming.

b) Programming of Checking Eye Blink Signal by Timer Check (TmrCheck)

Next, come to programming of checking eye blink signal which send from hardware. Due to pin 11 is the pin of parallel port which send the signal to computer, the logic AND operation is applied to 128 (the specific value for pin 11) and Inp (&H379)(input pin 11 which is at parallel port in hex) reading from hardware. When both conditions are fulfilling, it will run the following instruction.

c) Programming of Delay by Timer Message Delay (TmrMsgDly)

In order to keep the pre-programmed message to be display on the screen, one timer has to use for this purpose.

d) Programming of Sequence by Timer Sequence (TmrSeq)

It will control the sequence of pre-programmed message in submenu and running the selection of language in main menu.

e) Programming of Start and Stop button (cmdStop and cmdStart)

The start button will enabled the entire timer except timer delay and will clear the entire previous programmed message on the screen. The stop button will stop the entire timer and terminated all the programming

I. Setup program

In order to setup an application from the Visual Basic, the Visual Basic software has a good tool for this purpose: the Package and Deployment wizard.

III. Result and Analsysis

The user friendly Quadriplegic Communicator has a hardware and software as shown in Fig. 5. The timer activates the selection of each menu and the user is expected to blink when the running selection stops at the desired language on the computer screen. Then, this will lead user to the submenu. The submenu will run the pre-programmed message selection .After user make a selection, the message will be displayed and the message in sound will be played as well. Many trials has been made to find the best timer running speed to suit the responsiveness of a sick patient.

The software seems to be running well. However, the accuracy and efficiency of the hardware needs to be improved because the response of the sensor is rather slow and caused false selection. We will make a further study on the size of different patient forehead that requires adaptable sensor attachment for optimum sensor detection.

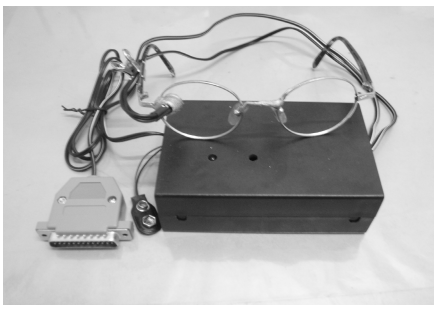

(a)

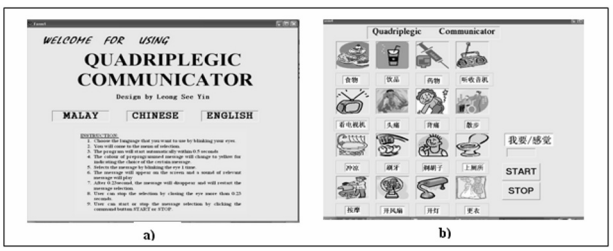

(b)

Fig. 5 (a) Prototype of the Communicator (b) Main and submenu of the GUI

F. Ibrahim, N.A. Abu Osman, J. Usman and N.A. Kadri (Eds.): Biomed 06, IFMBE Proceedings 15, pp. 647-650, 2007
www.springerlink.com ' Springer-Verlag Berlin Heidelberg 2007

IV. Conclusions

This project has been successfully prototype with a software and hardware device powered by 9V battery. The visual Basic software will respond to signal send from the hardware. In addition, the installer of Quadriplegic Communicator program can be setup and distributed to various computers. Overall of the product is quite easy to be used as a plug-and-play device. Our future work is to further improve the sensing device design and conduct clinical trial in hospital.

References

1. American Spinal Association [ASIA](1996). ASIA Standards Teaching Package , Atlanta .
2. Rod R.Seeley, PhilipTate& Trent D.Stephens (1998). Anatomy &Physiology United State of America: McGraw-Hill.pp229-240
3. Thomas E.Hutchinson,Ivy, Va.(1987) Eye Movement Detector (United states Patent 4,836,670)
4. Marcel P. J. M. Dijkers, (2005). Quality of life of individuals with spinal cord injury: A review of conceptualization, measurement, and research findings . Journal of Rehabilitation Research & Development .vol.42, Number3, pp87-110.
5. Anthony D.C.Macknight,John J.Bray, Patricia A.Cragg, Roland G.Mills(1999). Lecture Notes On Human Physiology ,4th Edition.United Kingdom: The Blackwell Science ,pp 65-102
6. Bruce Newby, (1994). Electronic Signal Conditioning .Great Britain :Butterworth-HeinemannLtd, pp105.

Address of the corresponding author:

Author: Madam Soon Chin Fhong
Institute: Kolej Universiti Teknologi Tun Hussein Onn
Street: Locked Beg 101, 86400 Pt Raja, Batu Paht Johor.
City: Batu Pahat, Johor
Country: Malaysia
Email: soon@kuittho.edu.my

F. Ibrahim, N.A. Abu Osman, J. Usman and N.A. Kadri (Eds.): Biomed 06, IFMBE Proceedings 15, pp. 647-650, 2007
www.springerlink.com ' Springer-Verlag Berlin Heidelberg 2007

Theoretical Determination of Lubrication Regimes in Two-Piece First Metatarsophalangeal Prostheses

T.J. Joyce

Center for Rehabilitation and Engineering Studies, School of Mechanical and Systems Engineering, Newcastle University, Claremont Road, Newcastle upon Tyne, NE1 7RU, UK

Abstract— **The key joint of the forefoot during gait is the first metatarsophalangeal joint. It is subject to high loads and plays an important role in propelling the human form. Unfortunately the first metatarsophalangeal joint can be subject to a number of diseases, such as rheumatoid arthritis, hallux rigidus and hallux valgus, all of which can lead to replacement of the natural joint with a prosthesis. Most commonly, a silicone spacer might be implanted but other designs are available which more closely try to match the natural joint by employing a two-piece ball and socket arrangement. Such designs are available with a range of biomaterial couples including ceramic-on-ceramic, metal-on-metal and metal-on-polymer. Calculation of predicted lubrication regimes applicable to these implant designs was undertaken. Modeling the ball and socket implant as an equivalent ball-on-plane model and employing elastohydrodynamic theory allowed the minimum film thickness to be calculated and in turn the lambda ratio to indicate the lubrication regime. Boundary lubrication is indicated for lambda less than 1, mixed lubrication for lambda between 1 and 3, and fluid film lubrication for lambda greater than 3. The calculations were undertaken for a 10 to 1500N range of loading values, a 0 to 30mm/s range of entraining velocities, and a 3 to 15mm radius ranger of sizes. Calculations showed that, for the range of loads, sizes and entraining velocities considered, the ceramic-on-ceramic and metal-on-metal implants could operate under fluid film lubrication, whereas the metal-on-polymer combination operated in the boundary lubrication regime. It was also recognized that manufacturing capabilities are critical to the radial clearances and values of surface roughness that can be achieved, and thus the predicted lubrication regime. Inevitably, a range of factors need to be considered when designing or choosing an implant for the first metatarsophalangeal joint.**

Keywords— **metatarsophalangeal, lubrication regimes, metal-on-metal, ceramic-on-ceramic, metal-on-polymer**

I. Introduction

Currently, there is a debate in the orthopedic literature regarding the potential long-term success of metal-on-metal (MoM) resurfacing hip prostheses [1-3]. These implants tend to employ relatively large articulating diameters of the order of 55mm and use cobalt chrome femoral heads rubbing against a matched cobalt chrome acetabular cup. This arrangement is in contrast to a conventional Charnley hip prosthesis which would have a stainless steel femoral head of 22.225mm diameter which articulates inside an ultra high molecular weight polyethylene (UHMWPE) acetabular cup. While the short term (to 5 years) results of the MoM resurfacing hip prostheses have been excellent [4, 5], it remains to be seen if they will match the long term success of the Charnley and similar designs [6, 7].

One of the theoretical advantages of the MoM resurfacing hip prostheses is that, due to their relatively large diameter and materials employed, they can operate with fluid film lubrication [8]. During fluid film lubrication, the articulating surfaces are separated by a film of fluid, so that wear and friction should be minimized. This prediction is in contrast to that for the Charnley and similar hip prostheses which are forecast to operate in the boundary lubrication regime. Here, surface interaction is expected with the potential of wear and increased friction.

Equally it has been shown through in vitro experiments that ceramic-on-ceramic (CoC) designs of total hip replacement can also operate in the full fluid film mode. Although of a smaller diameter (typically 28mm) than resurfacing designs, such lubrication is achieved as an excellent surface finish on the articulating surfaces can be obtained alongside a small radial clearance.

The first metatarsophalangeal (MTP) joint is the key joint of the forefoot during gait. It is subject to high loads and plays an important role in propelling the human form. Unfortunately the first MTP joint can be subject to a number of diseases, such as rheumatoid arthritis, hallux rigidus and hallux valgus, all of which can lead to replacement of the natural joint with a prosthesis.

Historically, such prostheses have tended to be single-piece double-stem designs manufactured from silicone. The most common is the Swanson implant which can give good results [9, 10]. However, concerns exist over such silicone implants due to their design [11] and possible material problems due to silicone synovitis [12, 13].

Due to such concerns, and in an attempt to apply positive experience from larger total replacement joints, a number of two-piece articulating designs for the first MTP joint have been proposed. These designs include those with spherical bearing surfaces in a ball and socket arrangement. These designs have used a range of biomaterial couples including

F. Ibrahim, N.A. Abu Osman, J. Usman and N.A. Kadri (Eds.): Biomed 06, IFMBE Proceedings 15, pp. 651-655, 2007
www.springerlink.com ' Springer-Verlag Berlin Heidelberg 2007

CoC, MoM and metal-on-polymer (MoP) [14]. With such articulating joints, wear of the bearing surfaces becomes critical, as it is widely recognized from experience with artificial hip joints that prosthetic wear debris can provoke osteolysis and the eventual failure of the replacement joint [15].

The aim of this paper was to compare the predicted lubrication regimes in the application of a first MTP prosthesis for these various biomaterial couples.

In terms of specific MTP implants, a CoC prosthesis is currently produced by Moje [16]. It employs zirconia as its material and has given acceptable short-term clinical results [17] although a catastrophic failure has also recently been described [18]. A MoM design of MTP implant, manufactured from cobalt chrome, has been implanted but clinical results were disappointing [19]. Metal-on-polymer designs include the Kenetik Great Toe Implant and the Bio-Action [20]. Both of these implants articulate a cobalt chrome metatarsal component against an UHMWPE phalangeal component.

II. Materials and methods

Modeling the ball and socket implant as an equivalent ball-on-plane model and employing elastohydrodynamic theory [21] allowed the minimum effective film thickness (h_{min}) to be calculated from:

$$\frac{h_{\min}}{R_x} = 2.80\left(\frac{\eta u}{E^* R_x}\right)^{0.65}\left(\frac{w}{E^* R_x^2}\right)^{-0.21} \quad (1)$$

Where R_x is the equivalent radius (m), η is the viscosity of the lubricant (Pa s), u is the entraining velocity (m/s), E* is the equivalent elastic modulus (Pa), and w is the load (N). In turn, given that R_a is the surface roughness and assigning subscript 1 to the ball (metatarsal component) and subscript 2 to the socket (phalangeal component) of the MTP prosthesis under consideration, then the lambda ratios were calculated from:

$$\lambda = \frac{h_{\min}}{\left[(R_{a1})^2 + (R_{a2})^2\right]^{1/2}} \quad (2)$$

This allowed the lubrication regime to be identified, as $\lambda<1$ indicates boundary lubrication, $\lambda>3$ designates fluid film lubrication, and between these values mixed lubrication is indicated [22].

Before these calculations could be undertaken, the equivalent radius (R_x) was calculated from:

$$\frac{1}{R_x} = \frac{1}{R_1} - \frac{1}{R_2} \quad (3)$$

Where R refers to the radius of the component and subscript 1 refers to the ball and subscript 2 to the socket of the MTP prosthesis. The equivalent modulus of elasticity was determined from the equation:

$$\frac{1}{E^*} = 0.5\left(\frac{1-\nu_1^2}{E_1} + \frac{1-\nu_2^2}{E_2}\right) \quad (4)$$

Again, E refers to the Young s modulus of the component and again subscript 1 refers to the ball and subscript 2 to the socket of the MTP prosthesis, similarly for the two Poisson s ratios (ν).

Clearly, the natural first MTP joint will encounter a range of loads during a lifetime and similarly the joint will move at a range of speeds. In terms of loading, values in the range of 0.8-1 x body weight have been suggested by researchers [23, 24]. For a person of 70kg this would equate to a load across the first MTP joint of some 590N [23]. Additionally it has been shown that the loading across the first MTP joint can doubled by the wearing of high heels [25]. Therefore a 10 to 1500N range of loading was chosen for the calculations of lubrication regime.

If an average speed during gait of 1Hz is taken, for a typical first MTP joint of 13mm radius (r) [23] moving through an arc of 32° during gait [26] then an average entraining velocity of 14mm/s can be calculated from:

$$u = r\omega/2 \quad (5)$$

Where ω is the angular velocity [8]. This value of 14mm/s was taken as a constant when the different load calculations were undertaken. Again allowing for higher frequencies and larger sizes of joints gave an estimated upper limit of 30mm/s for this series of calculations involving entraining velocity. The minimum speed was taken as zero and was incremented in 5mm/s steps. A constant load of 590N was assumed when the different entraining velocity calculations were undertaken.

A third set of calculations were undertaken where the radius of the prosthesis was varied between 3mm and 15mm. These values were based upon the fact that the Moje prosthesis comes in a range of sizes from 5mm to 10mm radius of the head of the metatarsal component [16]. The Moje sizes were extended so that all possible sizes of first MTP prosthesis could be considered.

Radial clearances were taken to be 30μm for the MOM [27] and CoC [28] combinations and 50μm for the MoP combination [29].

Roughness values for the zirconia were taken as 3nm for the ball and 6nm for the socket [30, 31]. For cobalt chrome they were taken as 3nm and 10nm respectively [27] while the UHMWPE cup was taken to have a roughness of

F. Ibrahim, N.A. Abu Osman, J. Usman and N.A. Kadri (Eds.): Biomed 06, IFMBE Proceedings 15, pp. 651-655, 2007
www.springerlink.com ' Springer-Verlag Berlin Heidelberg 2007

1.29μm [32]. A viscosity of the synovial fluid lubricant of 0.005Pa s was assumed [33]. Other relevant values such as Young s moduli and Poisson s ratios were taken from the literature [27, 31] and a summary is given in Table 1.

Table 1 Material Properties and Values Used in the Analysis

Item	Value or range
Load	10-1500N
Entraining velocity	0-30mm/s
Viscosity of lubricant	0.005Pa s
Radial clearance CoC and MoM	0.030mm
Radial clearance MoP	0.050mm
Young s modulus cobalt chrome	210GPa
Poisson s ratio cobalt chrome	0.3
Young s modulus zirconia	198GPa
Poisson s ratio zirconia	0.29
Young s modulus UHMWPE	1GPa
Poisson s ratio UHMWPE	0.4

III. Results

By varying the entraining velocity from 0 to 30mm/s, the resultant changes in lambda ratio are given in figure 1. As can be seen, under the chosen test conditions, for most of these velocities a CoC implant would operate in the fluid film lubrication mode (λ>3). A MoM implant would function in the fluid film lubrication regime above approximately 12mm/s entraining velocity, while a MoP implant would operate in the boundary lubrication regime (λ<1).

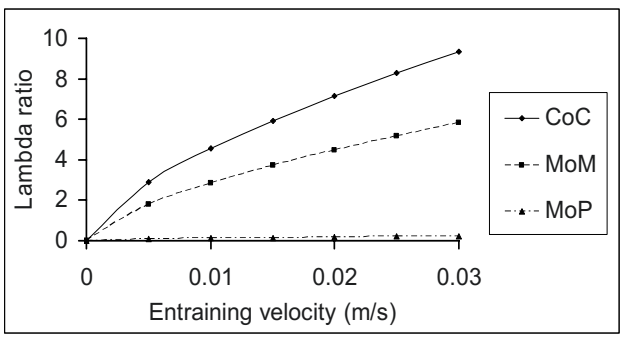

Fig. 1 Variation of lambda ratio with entraining velocity

When the prosthesis radius was varied between 3mm and 15mm the greatest values of lambda ratio were seen with CoC, followed by MoM and finally MoP, as shown by figure 2.

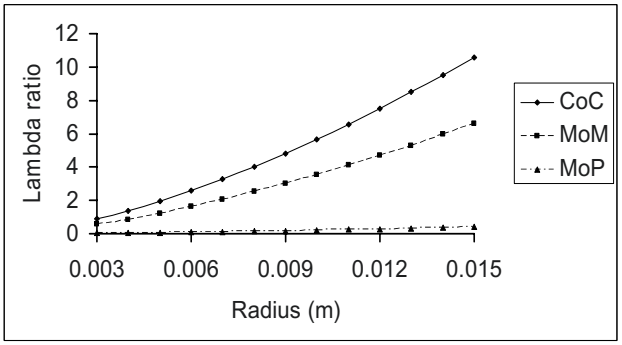

Fig 2: Variation of lambda ratio with prosthesis radius

Figure 3 offers the lubrication regime results when the various load calculations were undertaken. Again, the order from enhanced lubrication to more difficult operating conditions is CoC, MoM and MoP.

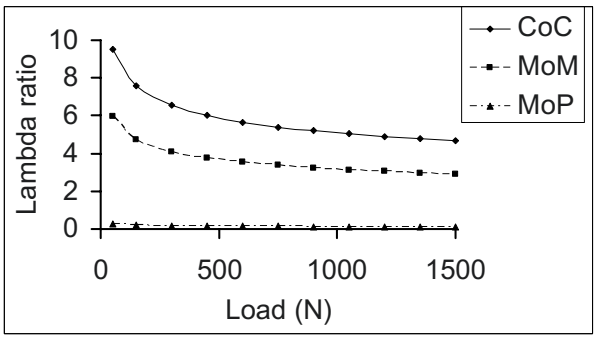

Fig. 3 Variation of lambda ratio with load

IV. Disscussion

Ceramics provide a hard, scratch resistant surface which is likely to retain its low roughness values during operation. However catastrophic in vivo fracture of a CoC first MTP prosthesis has recently been reported [18]. The MoM combination often achieved fluid film lubrication (λ>3) but this situation is reliant on maintaining excellent values of surface finish.

It has been shown that the MoP combination will operate in the boundary lubrication regime (λ<1). However, it is recognized that most MoP hip prostheses operate in the boundary lubrication regime [33] and while wear does occur and is a concern, the majority of patients are provided with a functional and successful prosthesis [34]. In addition the positive results for CoC and MoM need to be set against recognition that, when the toe is not moving, the entraining velocity is zero and so surface contact will occur, with a concomitant potential for wear.

F. Ibrahim, N.A. Abu Osman, J. Usman and N.A. Kadri (Eds.): Biomed 06, IFMBE Proceedings 15, pp. 651-655, 2007
www.springerlink.com ' Springer-Verlag Berlin Heidelberg 2007

Two key manufacturing factors that should be considered are the surface finish that can achieved and the radial clearance. The values used in this analysis, of the order of 0.003μm Ra for the metatarsal component, 0.010μm Ra for the phalangeal component and 30μm radial clearance for MoM and CoC, were taken from the literature regarding hip prostheses of a comparable articulating diameter [27]. These implants are generally produced by manufacturers who have many years of experience and produce relatively high volumes of these products. Such a situation may not always apply to first MTP prostheses, which may be produced in smaller numbers and to less strict tolerances. Increasing the surface roughness and the radial clearance will have a dramatic influence on the theoretical lubrication regime. For example, roughness values of 0.030μm for the metatarsal component, 0.063μm for the phalangeal component, and a radial clearance of 100μm were measured for an explanted MoM first MTP prosthesis [19]. When the theoretical analysis reported in this paper was repeated with these values, it was found that boundary lubrication was predicted. Clearly this is in contrast to the theoretical achievement of full film lubrication noted in this paper, when optimum surface finishes and radial clearances were input. Therefore the analysis reported in this paper needs to be appreciated in the light of such manufacturing concerns.

V. Conclussions

Lubrication theory indicates that, for the material combinations considered for application to two-piece MTP prostheses, MoM and CoC designs could operate with fluid film lubrication, while MoP designs are likely to operate in the boundary lubrication regime. However, it should be recognized that other factors may come into play when choosing a particular implant and material combination for the first MTP joint.

References

1. Villar R. (2004) Resurfacing arthroplasty of the hip. J Bone Jt Surg 86B:157-158
2. Hungerford DS. (2005) Metal-on-metal resurfacing arthroplasty: no way under the sun!--in the affirmative. J Arthroplasty 20:68-69
3. Schmalzried TP. (2005) Metal-on-metal resurfacing arthroplasty: no way under the sun!--in opposition. J Arthroplasty 20:70-71
4. Back DL, Dalziel R, Young D et al. (2005) Early results of primary Birmingham hip resurfacings: an independent prospective study of the first 230 hips. J Bone Joint Surg Br 87-B:324-329
5. Treacy RBC, McBryde CW, Pynsent PB. (2005) Birmingham hip resurfacing arthroplasty: a minimum follow-up of five years. J Bone Joint Surg Br 87-B:167-170
6. Older J. (2002) Charnley low-friction arthroplasty. A worldwide retrospective review at 15 to 20 years. J Arthroplasty 17:675-680
7. Wroblewski B, Siney P, Fleming P. (2002) Charnley low-frictional torque arthroplasty in patients under the age of 51 years. Follow-up to 33 years. J Bone Joint Surg Br 84-B:540-543
8. Udofia IJ, Jin ZM. (2003) Elastohydrodynamic lubrication analysis of metal-on-metal hip-resurfacing prostheses. J Biomech 36:537-544
9. Hanyu T, Yamazaki H, Ishikawa H et al. (2001) Flexible hinge toe implant arthroplasty for rheumatoid arthritis of the first metatarsophalangeal joint: long-term results. J. Orthop. Sci. 6:141-147
10. Bommireddy R, Singh SK, Sharma P et al. (2003) Long-term follow-up of silastic joint replacement of the first metatarsophalangeal joint. Foot 13:151-155
11. Granberry WM, Noble PC, Bishop JO et al. (1991) Use of a hinged silicone prosthesis for replacement arthroplasty of the first metatarsophalangeal joint. J. Bone Jt. Surg. 73A:1453-1459
12. Minimikawa Y, Peimer CA, Ogawa R et al. (1994) In vivo experimental analysis of silicone implants used with titanium grommets. J. Hand Surg. 19A:567-574
13. Peimer C, Taleisnik J, Sherwin F. (1991) Pathologic fractures: a complication of microparticulate synovitis. J. Hand Surg. 16A:835-843
14. Joyce TJ. (2005) Implants for the first metatarsophalangeal joint and prospective considerations. Expert Rev Med Devs 2:453-464
15. Harris WH. (1995) The problem is osteolysis. Clin. Orthop. Rel. Res. 311:46-53
16. Burger_Medical: Moje MTP Implant, http://www.burgersmedical.com/
17. Hassan K, Poornachandra C, Walters S et al. (2006) Short-term follow-up of ceramic press fit first metatarso-phalangeal joint arthroplasty. Foot 16:142-144
18. Pavier J. (2005) A catastrophic failure of a first MTP joint ceramic implant. Foot 15:47-49
19. Joyce TJ. (2006) Metal-on-metal metatarsophalangeal prosthesis retrieval study and comparison with predicted lubrication regimes. J Biomechanics 39:S525
20. Olms K, Dietze A. (1999) Replacement arthroplasty for hallux rigidus. Intl. Orthop. 23:240-243
21. Hamrock BJ, Dowson D. (1978) Elastohydrodynamic lubrication of elliptical contacts for materials of low elastic modulus. I: fully flooded conjunction. Trans ASME. J Lubn Tech 100:236-245
22. Johnson KL, Greenwood JA, Poon SY. (1972) A simple theory of asperity contact in elastohydrodynamic lubrication. Wear 19:91-108
23. Jacob HAC. (2001) Forces acting in the forefoot during normal gait - an estimate. Clin. Biomech. 16:783-792
24. Stokes IAF, Hutton WC, Stott JRR. (1979) Forces acting on the metatarsals during normal walking. J. Anat. 129:579-590
25. McBride ID, Wyss UP, Cooke TDV et al. (1991) First metatarsophalangeal joint reaction forces during high-heel gait. Foot Ankle 11:282-288
26. Nawoczenski DA, Baumhauer JF, Uberger BR. (1999) Relationship between clinical measurements and motion of the first metatarsophalangeal joint during gait. J. Bone Jt. Surg. 81A:370-376
27. Smith SL, Dowson D, Goldsmith AAJ. (2001) The lubrication of metal-on-metal total hip joints: a slide down the Stribeck curve. J Engng Tribology 215:483-493
28. Scholes SC, Unsworth A. (2000) Comparison of friction and lubrication of different hip prostheses. J Engng Med 214:49-57
29. Saikko V, Ahlroos T, Calonius O et al. (2001) Wear simulation of total hip prostheses with polyethylene against CoCr, alumina and diamond-like carbon. 22:1507-1514
30. Scholes SC, Unsworth A, Goldsmith AAJ. (2000) A frictional study of total hip joint replacements. Phys Med Biol 45:3721-3735
31. Pylios T, Shepherd DET. (2004) Prediction of lubrication regimes in wrist implants with spherical bearing surfaces. J. Biomech. 37:405-411

F. Ibrahim, N.A. Abu Osman, J. Usman and N.A. Kadri (Eds.): Biomed 06, IFMBE Proceedings 15, pp. 651-655, 2007
www.springerlink.com ' Springer-Verlag Berlin Heidelberg 2007

32. Scholes SC, Unsworth A, Hall RM et al. (2000) The effects of material combination and lubricant on the friction of total hip prostheses. Wear 241:209-213
33. Jalali-Vahid D, Jagatia M, Jin ZM et al. (2001) Prediction of lubricating film thickness in UHMWPE hip joint replacements. J Biomech 34:261-266
34. Nercessian OA, Martin G, Joshi RP et al. (2005) A 15- to 25- year follow-up study of primary Charnley low-friction arthroplasty: a single surgeon series. J Arthroplasty 20:162-167

Address of the corresponding author:

Author: Dr T Joyce
Institute: School of Mechanical and Systems Engineering
Street: Claremont Road
City: Newcastle upon Tyne
Country: United Kingdom
Email: t.j.joyce@ncl.ac.uk

F. Ibrahim, N.A. Abu Osman, J. Usman and N.A. Kadri (Eds.): Biomed 06, IFMBE Proceedings 15, pp. 651-655, 2007
www.springerlink.com ' Springer-Verlag Berlin Heidelberg 2007

Design of Web-based Tele-ultrasound Consultation System over Digital Subscriber Lines

Kee-Deog Kim [1], Sun K. Yoo[2] , D.K. Kim[3] and E.-K. Kim[4]

[1] Human Identification Research Center, Dept. of General Dentistry, Yonsei Univ.
[2] Centre for Emergency Medical Informatics, Dept. of Medical Eng., Yonsei Univ.
[3] Signal Processing Research Center, Yonsei Univ.
[4] Dept. of Diagnostic Radiology, Yonsei Univ. College of Medicine, Seoul, Korea

Abstract - **In this paper, the prototype of the tele-ultrasound consultation system has been designed and evaluated over digital subscriber lines including ADSL and VDSL. The ActiveX control, and software-based MPEG-4 and H.320 CODECs (Coder and Decoder) allowed low-cost, flexible, Web-based, and real-time implementation for interactive teleconsultation through general Web browser. Specifically, the features of designed sysem are usablity of the MPEG-4 coding of full-resolution ultrasound video, accessibility via Web browser, combined transmission of ultrasound video with video conferencing in real-time, and operability over cheap ADSL, and VDSL lines. The quality of ultrasound images in terms of compression ratio and frame rate were measured using patients' data to evaluate the performance of the designed system over DSL lines, and to demonstrate usability for practical use.**

I. Introduction

Managing large amount of dynamic moving images in real-time is a major technical challenge in the tele-ultrasound system. Some tele-ultrasound systems, running over the fiber-optic connection with the maximum bandwidth of 45 Mbps such as DS3 fiber, can achieve the high-quality ultrasound images, but they are impractical because of their high communication cost. Other tele-ultrasound systems used multiple ISDN lines from 384 Kbps to 2 Mbps to compromise the tradeoff between image quality and network bandwidth (transmission rate) [1]-[3]. The higher the bandwidth, the better the video image quality (the more expensive the communication cost). However, particularly in Korea, the ISDN is obsolescent as well as the communication cost for multiple ISDN lines are more expensive than high speed commercial lines including ADSL (Asymmetric Digital Subscriber Line), and VDSL (Very high speed Digital Subscriber Line).

The coding methods can also influence on both required network bandwidth and the image quality. Although either video-conferencing (H.320/H.323) or MPEG-1 is generally employed in tele-ultrasound systems [3]-[7], they cannot support full spatial resolution of the ultrasound because of their limited resolution of 320 by 240. Moreover, operability over the Internet through the Web-browser is another important issue necessary for the wide-spread use of the tele-ultrasound system [8].

In this paper, we designed web-based real-time tele-ultrasound consultation system operable over inexpensive, high-speed commercial lines including ADSL, and VDSL. It supports full-resolution of ultrasound video (640 X 480) and combines MPEG-4 video ompression of the ultrasound with video conferencing, as well as operates on the Internet via Web-browser using active-X controls.

II. Materials and methods

A. The Hardware

The design of the hardware system is based on the cost-effective implementation, full-resolution support of ultrasound moving images and auxiliary video conferencing capability. Especially, the hardware CODECs (Coder/Decoder) for the compression of ultrasound moving images and video conferencing were excluded for cost-effective implementation. The prototype system (Figure 1), consisting of transmitting and receiving units, was configured by the personal computer (Pentium III with 256 Mbytes RAM). The equipments at the transmitting site include ultrasound scanner (SonoAce 6600, Medicine Inc., Korea), PCI interfaced video capture board (ATI Radeon 7000, ATI Technologies Co, Canada), Ethernet LAN card (10 and 100 Mbps), microphone, speaker, and USB (Universal Serial Bus) interfaced video conferencing camera. The video capture board produces the ultrasound video images of 640 X 480 resolution with 30 frames/sec (NTSC video). The receiving unit is simpler than the transmitting unit. The USB interfaced video conferencing camera and LAN card are only required at the receiving unit for Internet connection and video conferencing.

F. Ibrahim, N.A. Abu Osman, J. Usman and N.A. Kadri (Eds.): Biomed 06, IFMBE Proceedings 15, pp. 656-659, 2007
www.springerlink.com ' Springer-Verlag Berlin Heidelberg 2007

B. The Software

The software configuration is based on the operability over the Internet through Web browser (Figure 1). ActiveX control is used to interface the Web browser (Internet Explorer 3.0 or higher, Microsoft Co., USA). The software modules are designed as the COM (Component Object Module) under DirectX framework (including DirectShow and DirectDraw) to control and display audio and video streaming data. The MPEG-4 and H.320 software modules perform the compression/decompression of the moving ultrasound images and video conferencing, respectively. H.320 video conferencing module designed as DirectShow filter produces the audio and video bit stream with constant bit rate of 128 Kbps. MPEG-4 is chosen as a compression method for ultrasound moving images, because MPEG-4 is the standard suitable for both high quality and low bit rate. The DivX (Digital Digest Co.) composes MPEG-4 software module, while the WEBREUS application adjusts the frame rate and the bit rate of the MPEG-4 module.

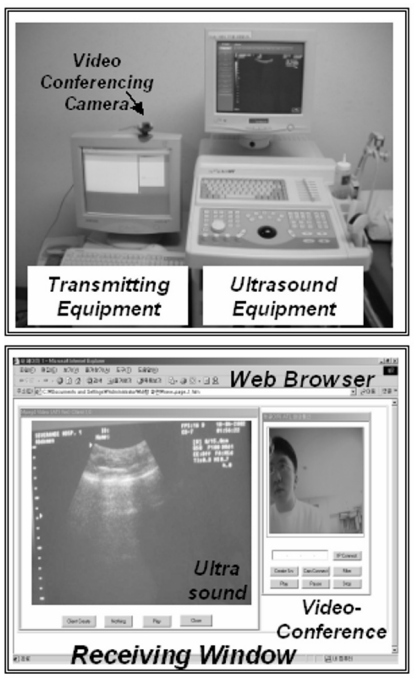

Fig. 1 Web-based real-time tele-ultrasound consultation system: Transmitting unit and receiving window (simultaneous display of moving ultrasound images and video conferencing via web browser interface).

C. Testing Network

In order to consider different transmission rates associated with upstream and downstream of external communication lines (xDSL), and to compromise possible tele-consultation situations, two kinds of testing configuration were composed using three communication lines: hospital LAN with 100 Mbps Fast Ethernet switching HUB, ADSL, and VDSL. One is small hospital configuration corresponding to upstream measurement. The transmitting unit used xDSL (either ADSL or VDSL) for internet connection, while the receiving unit was connected to the hospital LAN. Small hospital configuration corresponds to the situation, where the consulting specialists are located at the tertiary hospital, while the ultrasound examinations are performed at the primary care clinic. The other is the large hospital configuration corresponding to downstream measurement of xDSL. The transmitting unit was connected to the hospital LAN, while the receiving unit used external xDSL lines. In indirect configuration, ultrasound examinations are performed at hospital, whereas the specialists are located at home.

III. Results

The prototype system designed was evaluated using 16 patients data with 6 abnormal liver, 4 abnormal renal, 4 hemangioma, and 2 Gallbladder stone patients. Each patient data was compressed as diverse MPEG-4 formatted streams with different compression ratio (from 0.2 Mbps to 8 Mbps) and frame rate (from 10 frames/sec to 30 frames/sec). The PSNR (Peak Signal to Noise Ratio) between the uncompressed and compressed file was measured to indirectly quantify the objective image quality of received ultrasound images in terms of frame rate and compression ratio.

Table 1. The PSNRs in terms of bit rates and frame rates

Frame rate/sec	30	15	10
Bit rate (Mbps)	PSNR (dB)	PSNR (dB)	PSNR (dB)
0.2	38.70	38.62	38.53
0.6	39.19	38.96	38.83
1.0	39.40	39.16	39.04
4.0	39.51	39.51	39.51
8.0	38.51	39.51	39.51

F. Ibrahim, N.A. Abu Osman, J. Usman and N.A. Kadri (Eds.): Biomed 06, IFMBE Proceedings 15, pp. 656-659, 2007
www.springerlink.com ' Springer-Verlag Berlin Heidelberg 2007

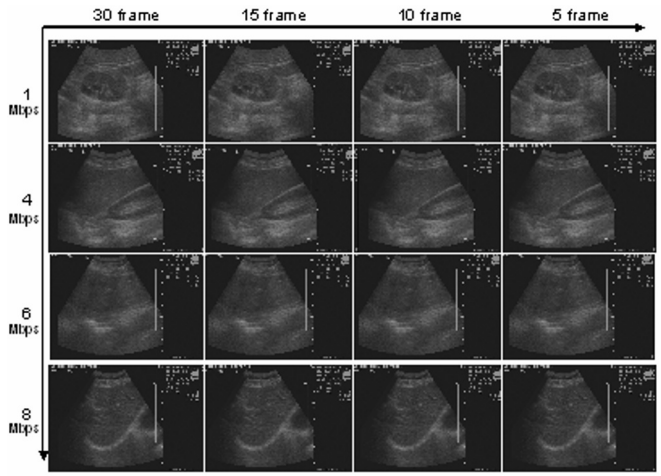

Fig 2 The image quality in terms of bit rate and the frame rate.

The PSNR increases, with increases in the bit and frame rates. The image quality was proportional to the PSNR, i.e., better image quality, after decompression, can be obtained as the bit rate increases (Figure 2). In particular, the PSNR difference between the full frame rate (30 frames/sec) and the dropped frame rate (one of 15, 10, and 5 frames/sec) gets larger as the bit rate increases. Hence, frame dropping at high bit rates should be avoided, and should only be used at low bit rates (low bandwidth line) due to the relatively small PSNR difference at a low bit rate.

The bit rate thresholds, indicators of significant difference (p-value < 0.05) between the original and the compressed video images, were 0.6Mbps, 0.7Mbps, 1 Mbps and 5 Mbps for frame rates of 30, 15, 10 and 5 frame/sec, respectively. In other words, a transmitting rate greater than bit-rate threshold can maintain high-quality ultrasound images, with no recognizable difference between the original and compressed images. The dropped frame shows a lower PSNR (higher quality) than the full frame for a given bit rate, as well as severely deteriorating the continuity of the ultrasound moving images. Hence, the dropped frame disrupts the radiologist when inspecting the received ultrasound images. As a consequence, a transmission rate of more than 0.6 Mbps, with full frame, was suggested as the bit rate threshold for maintaining the diagnostic image quality during a tele-consultation.

The upstream rates, measured at ADSL and VDSL, ranged from 0.48 to 0.62 Mbps and 4.91 to 7.31 Mbps, respectively. The measured upstream rates correspond to the performance of the small hospital configuration. For the VDSL, the measured minimum upstream rate of 4.91 Mbps was much higher than the bit rate threshold of 0.6 Mbps. With the ADSL, the maximum upstream rate of 0.62 Mbps was slightly higher than the bit rate threshold, but the minimum upstream rate of 0.48 Mbps was lower than the bit-rate threshold. Hence, the ADSL was insufficient for use as the transmitting line. The measured PSNRs, with respect to the mean transmission rates for ADSL (0.51 Mbps) and VDSL (6.15 Mbps), were 37.5 and 39.2 dB, respectively. Throughout the experiments the VDSL can carry the MPEG-4 compressed ultrasound video, with high quality (without recognizable difference comparing to the original), but the ADSL was inappropriate. When the ADSL was employed, the dropped frame was inevitable for the compromised measured minimum rate of 0.48 Mbps.

The measured downstream rates corresponded to the large hospital configuration. The downstream rates measured at ADSL and VDSL, ranged from 0.95 to 1.32 Mbps and 7.56 to 9.13 Mbps, respectively. All lines maintained minimum downstream rates greater than the bit rate threshold of 0.6 Mbps. The measured PSNRs, with respect to the mean transmission rates for ADSL (1.12 M Kbps) and VDSL (8.37 Mbps), were 38 and 39.45 dB, respectively. Hence, as the receiving line, the VDSL can maintain the high quality of the received ultrasound images, while the ADSL can maintain a satisfactory quality.

IV. Discussion

The successful implementation of the tele-ultrasound is closely related to its communication cost. There are many wired lines available in Korea to transmit ultrasound images in real-time. The flat rates for month are \$2.000-\$2,500 for T1(1.5 Mbps), \$2,500-\$3,000 for E1 (2 Mbps), \$3,000-\$3,500 for DS3(45 Mbps), \$25-\$30 for ISDN (128 Kbps), \$20-\$40 for ADSL and \$40-\$50 for VDSL. The communication costs for variable bandwidth lines (ADSL, and VDSL) are much cheaper than those for fixed bandwidth lines (T1, E1, DS3, and ISDN). The use of multiple ISDN lines, similar to previous methods, are especially uneconomical, as the number of ISDN lines increases for the achievement of a high transmission rate [1]-[3], [6]. Hence, the use of variable bandwidth lines are a practical choice due to their communication cost.

Another important factor affecting the quality of ultrasound images is the transmission rate of the communication line[2],[5],[6]. With regard to the video quality, the VDSL, for both the transmitting and receiving units, was comparable to that of the DS3, as a MPEG-4 compression greater than 3 Mbps (measured minimum bandwidth) cannot recognize the difference between the compressed and original video images [9]. Nevertheless, as discussed, the communication costs of the VDSL in Korea, are extraordinarily cheaper than that of the DS3. The ADSL, for the receiving unit, can be useful for situations where slight degradation of the received ultrasound video

F. Ibrahim, N.A. Abu Osman, J. Usman and N.A. Kadri (Eds.): Biomed 06, IFMBE Proceedings 15, pp. 656-659, 2007
www.springerlink.com ' Springer-Verlag Berlin Heidelberg 2007

(satisfactory quality) is permissible. However, the ADSL, for transmitting unit, can only be used in off-line situations, where store-and-forward transmission is employed, as they mostly cannot maintain the bit rate threshold.

Internet operability, by means of a Web browser, is also important for easy access of the tele-ultrasound system at any place, whenever remote consultation is needed. Instead of dedicated execution programs, the WEBREUS use the Active-X controls to embed the designed software modules onto the Web browser [11]. This Internet accessibility is particularly useful when the consulting doctor is not located at the hospital.

V. Conclusion

In conclusion, a web-based real-time tele-ultrasound consultation system has been designed using Active X control, MPEG-4 and H.320, and was evaluated over high-speed, variable bit rate commercial lines, including ADSL and VDSL. Compared to the previous tele-ultrasound systems, it has distinct features: MPEG-4 coding of full-resolution ultrasound video (640X480 matrix with 30 frame/sec), accessibility via a Web browser, combined transmission of ultrasound video, with video conferencing in real-time, and operability over extraordinarily cheap commercial lines, particularly in Korea. The image qualities of the ultrasound video images, in terms of the compression ratios and frame rates, were measured using the data from 16 patients to evaluate the performance and demonstrate its clinical feasibility. For a measured bit rate threshold, the VDSL was applicable for both the transmitting and receiving units, while the use of the ADSL was limited to the receiving unit in case of full frame rate.

Acknowledgment

This study was supported by a grant of the Korea Health 21 R & D Project, Ministry of Health & Welfare, Republic of Korea (02-PJ3-PG6-EV08-0001)

References

1. Burgul R., Gilbert FJ., and Nudrill PE. (2000): 'Methods of measurement of image quality in teleultrasound', *British journal of Radiology*, **73**, pp.1306-1312
2. Chan FY. et al. (1999) : 'Minimum requirements for remote realtime fetal tele-ultrasound consultation', *Journal of Telemedicine and Telecare*,**5**, pp.171-176
3. Chan FY., Soong B., Lessing K., Watson D., Cincota R., Baker S., Smith M., Green E., and Whitehall H. (2000): 'Clinical value of real-time tertiary fetal ultrasound consultation by telemedicine: Preliminary evaluation', *Telemedicine Journal*, **6(2)** , pp.237-242
4. Finley JP. et al. (1997): 'Paediatric echocardiography by telemedicine-nine years experience', *Journal of Telemedicine and Telecare* , **3**, pp.200-204
5. Matani A., Yagi H., Umeda T., and Chihara K. (1999): 'A compression and transmission system of ultrasonic image sequence for telemedicine', *Telemedicine Journal*, **5(4)** , pp.385-389
6. Mehta AR., Wakefield DS., Kienzle MG., and Scholz TD. (2001): 'Pediatric tele-echocardiography: evaluation of transmission modalities', *Telemedicine Journal and e-Health,* **7(1)** , pp.17-25
7. Poon WS. et al. (2001): 'The comparative impact of video-consultation on neurosurgical health services', *International Journal of Medical Informatics* 2001; **62**: 175-180
8. Yoo SK et al. (2004): 'Performance of a Web-based, real-time, tele-ultrasound consultation system over high-speed commercial telecommunication lines, *Journal of Telemedicine and Telecare* , **10**, pp.175-179

Address of the corresponding author:

Author: Sun K. Yoo
Institute: Yonsei University College of Medicine
Street: Sudaemoon-gu Shinchon-dong 134
City: Seoul
Country: Korea
Email: sunkyoo@yumc.yonsei.ac.kr

F. Ibrahim, N.A. Abu Osman, J. Usman and N.A. Kadri (Eds.): Biomed 06, IFMBE Proceedings 15, pp. 656-659, 2007
www.springerlink.com ' Springer-Verlag Berlin Heidelberg 2007

Development of a Mobile Telemedicine System with Multi Communication Links for Urban and Rural Areas in Indonesia

Ediana Sutjiredjeki[1,2], Soegijardjo Soegijoko, Tati Latifah R. Mengko and Suhartono Tjondronegoro[1]

[1] Biomedical Engineering Research Group, School of Electrical Engineering and Informatics, ITB
[2] Department of Electrical Engineering, POLBAN

Abstract – **This paper is a progress report on the development of a mobile telemedicine system with multi communication links. The system design goal is to provide patient monitoring during the prehospital transport and to offer health services, for people who lives in underserved areas. Therefore, medical information transmission becomes very crucial, since there is no a transmission link stability guarantee. To deal with this issue, multi communication links, which including VHF radio, internet, GSM/CDMA mobile phones, and GPRS are applied for the system. Selection of the communication links depends on the availability of the local communication infrastructure.**

To implement the system functions, a functional unit called a telemedicine arbiter is being designed. This unit consists of a medical information concentrator module and a communication manager module. Communication link selection scheme is developed based on the result of the signal quality survey in a target location. To provide the scheme, a dedicated software is developed.

Currently, the research is focused on the development of a software for data transaction which is based on a client-server model. Moreover, an enhancement of the telemedicine arbiter unit is also being conducted. Finally, a number of test fields to transmit medical information has been implemented as well. The results are promising, although some improvements are still required, in particular to alleviate a problem in no signals coverage areas.

Keywords– **Mobile telemedicine system, multi communication links, telemedicine arbiter, medical information transmission, selection of communication links**

I. Introduction

As a number 4th biggest population in the world, Indonesia is struggling in spreading health services, specially for people lives in remote and or underserved areas. Indonesia has a population more than 220 millions which are spread out all over the country. One of the crucial problem to deliver health services in Indonesia is the geography, and the availability of needed infrastructure. For that reason, a mobile telemedicine system will be demanding because a fixed system is difficult to be reached by patient who lives in rural area so he or she can not be given a proper health services

In order to alleviate these problems and support different growing application of telemedicine, a development of a Mobile Telemedicine Systems with Multi Communication Link is very important. The proposed system will exploit the advantage of wireless technology and combine it with other communication technologies such as VHF radio to meet different locals and geographic requirements.

The rest of the paper is organized as follow. In Section 2 the overview and architecture of mobile telemedicine system with multi communication links is presented . Section 3 discuss the system design includes the design consideration and the design implementation. Finally, Section 4 describes the future works to be conducted in the research as a closing remarks.

II. System architecture

The aim of this research is to design and to implement a working prototype of a mobile telemedicine system with multi communication links. The architecture of the mobile telemedicine system which is being developed is depicted in figure 1. The system consists of two main units, namely a Mobile Telemedicine unit that is placed in an ambulance, and a Base unit or Hospital unit. The Mobile Telemedicine unit is responsible for collecting medical information that includes biosignals and image from the patient and display the critical signals, e.g. ECG signal, blood pressure (BP) and fetal heart rate (FHR). The unit must also be able to write and to record the data, and support the data transaction with variety of communication links. Furthermore, the unit should be able to transmit the patient s biosignals to the base unit automatically. To support the functions, the mobile telemedicine unit is provided with a telemedicine arbiter and a processing unit.

Telemedicine arbiter is a functional unit that consists of a medical information concentrator module and a communication manager module [2]. The arbiter is responsible for polling biosignals which is done bya con centrator module.

F. Ibrahim, N.A. Abu Osman, J. Usman and N.A. Kadri (Eds.): Biomed 06, IFMBE Proceedings 15, pp. 660-663, 2007
www.springerlink.com ' Springer-Verlag Berlin Heidelberg 2007

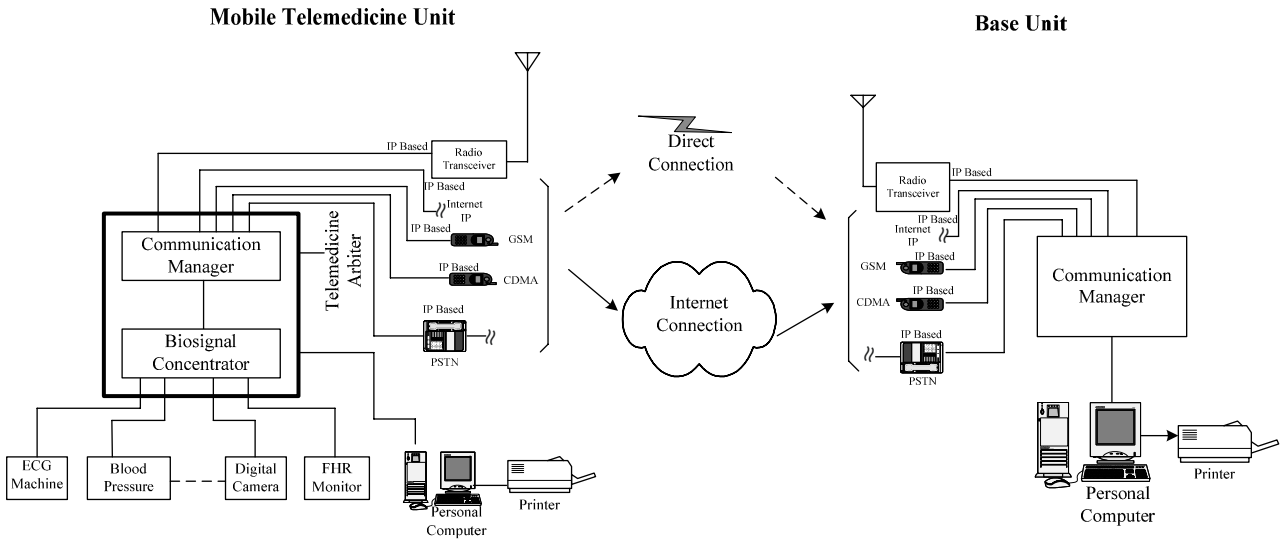

Fig. 1. The Architecture of Mobile Telemedicine System with Multi Communication Links

Basically a concentrator is an interface to be connected to each medical devices. To manage data interchange within the system is implemented by a communication manager module. This module is a modem array that comprises of mixture a number of GSM, CDMA, radio, GPRS, and satellite (optional) modems. The specification of the module is independent zone, and able to select a most suitable communication link to transmit the data.

In conjunction with the Mobile Telemedicine unit, the Base unit is located at a hospital or CHC (Community Health Centres). In this research, the base unit will be placed at RSUD R. Syamsudin, SH in the city of Sukabumi. This unit is equipped with a personal computer (PC) to display incoming signals from the Mobile unit, and a communication manager module that functions as a transceiver. This module will implement a continuous scanning to monitor incoming information and responds to them as soon as possible. In addition, a hospital data base that contains of patient information record will be integrated to the unit. All information relating to the case handled must be recorded into the data base. The information includes the patient history such as past illness, present illness, treatment details, etc. and patient demographics, i.e. patient identity. Data may be transmitted to a base unit within a reference hospital or CHC which enables the doctor or medical staffs to diagnose or monitor the patient s condition in real time.

The data interchange is conducted using TCP/IP network protocol TCP/IP network protocol. It is expected that the system will be *bandwidth independent*. To achieve this objective, the system will be provided with options of variety communication links from ordinary telephone lines, both GSM and CDMA mobile phones, GPRS, and VHF radio. Depending on the geographic location, a user can determine the mode of communication that suits her or his requirement.

A special purpose software will be developed as a protocol for data interchange by applying TCP/IP network protocol, that allows operation over several communication means. The telemedicine software must be able to acquire information concerning to the patient, store and display data of the patient, maintain and control connection between the Mobile Telemedicine unit and the Base unit, schedule doctor appointments, and capture image/other data from the output of the medical equipments. Furthermore, the software can also support Patient Information Record (PIR), because PIR is a part of acquisition data process.

III. System design

A. Design Consideration

The system application services and the availability of communication infrastructures are the most important aspects to be taken into account for designing the Mobile Telemedicine system with multi communication links. According to the most needed
requirement of health services in Indonesia, the design of the system is focused on applications for: 1) recording and reporting; 2) telediagnostic; 3) teleconsultation; and 4) distance education.

As the main design goal of the system is to provide patient monitoring during the prehospital transport and to pro-

F. Ibrahim, N.A. Abu Osman, J. Usman and N.A. Kadri (Eds.): Biomed 06, IFMBE Proceedings 15, pp. 660-663, 2007
www.springerlink.com ' Springer-Verlag Berlin Heidelberg 2007

vide health services for people in rural areas, the system designing should fulfil medical requirements. Depending on the condition of the patient and the severity of the disease, the time requirements of the monitoring vary significantly. Such monitoring may be needed periodically or may involved on-demand continuous monitoring. In such a case the method of vital signal transmission may vary, since a vital body sign has different time requirements in patient monitoring. Another challenge in designing of a mobile telemedicine system is the quality of communication networks within the target location. A transmission link stability becomes a serious problem to overcome. Although, competition in business cellular throughout the country is resulting in many cellular providers in most areas, but all connected phones may be dropping simultaneously when travelling through blank spot in network coverage. Therefore, the system should be able to cope with transferring from one network cell into another without any disconnection in communication lines. To alleviate this issue, a hybrid communications architecture with overlapping network coverage is employed [1].

B. System design implementation

The research will be conducted within two years, starting from July 2005. The design implementation of the system covers both hardware and software. The system hardware development is designing the medical information concentrator that consists of BP interface, FHR interface, and ECG interface.

The main problem to be solved in implementation of the concentrator are the integration of these interfaces, and the data sizing. Data sizing is required to optimize the bandwidth. Since the medical information does not only consists of biosignals but also patient personal information, it needs a different channel capacity for data transmission. To support this feature, we develop a dedicated program to manage the operation of the medical information concentrator.

A number of surveys to evaluate availability and mobility of communication infrastructures in the target location i.e. Sukabumi areas, has been conducted as well. The surveys cover measurements of signal strength of GSM and CDMA communication technologies, as well as line of sight distances which refers to a local hospital, namely RSUD R. Samsudin as the gateway. Figure 2 depicts the result of signal strength measurement of GSM communication. The signal quality is indicated by a number of bars. The range of bars varies between (0 5) unit. In this measurement, a maximum signal strength is five bars, and a minimum is one bar. The measurements are taken in the city and the rural areas.

In general, the availability and the mobility of GSM communication technology in these locations may satisfy the requirement for medical information transmission. Though, in a number of locations there is a constraint of transferring communication from one network cell into another. Furthermore, there are also some places which is no network. coverage Refers to Figure 2, wireless technology that can be used for mobile telemedicine in rural areas mostly is GSM. While at the moment, CDMA communication technology only covers city areas. In fact, application of radio in some Sukabumi areas is promising, particularly in areas which have a direct line of sight with the Base unit (RSUD Samsudin).

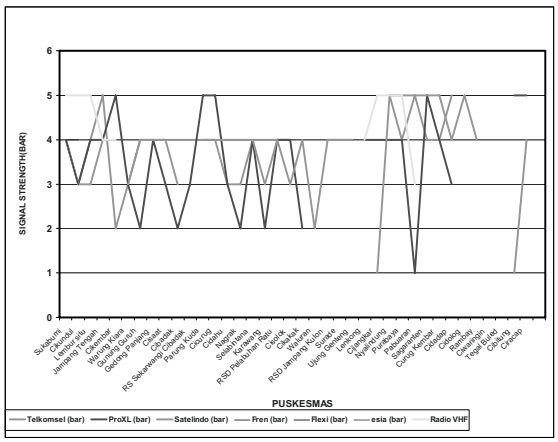

Fig. 2 . Result of signal strength measurement

Refers to Figure 2, wireless technology that can be used for mobile telemedicine in Indonesia rural areas mostly is GSM. In addition VHF radio may be employed for voice communication as well, even though a number of repeaters are still needed for certain locations. Data transmission quality is also determined by the availability of the bandwidth in the channel. Furthermore, the speed of the mobile unit will impact on the quality of the data transaction.

In designing the mobile telemedicine system, we define that if the signal strength is less than three bars, the routing program has to find an alternative link. Additionally, if the signal strength is less than two bars, the connection will be interrupted. Figure 3 shows a flow chart of routine for setting communication links.

The system applies a client-server architecture, at which the mobile telemedicine unit acts as a client, and the base unit functions as a server. Hence, the design of the software is based on a client-server protocol. Figure 4 shows the software architecture for the system. It is applied for data transaction in particular recording and reporting, telediagnose and teleconsultation

F. Ibrahim, N.A. Abu Osman, J. Usman and N.A. Kadri (Eds.): Biomed 06, IFMBE Proceedings 15, pp. 660-663, 2007
www.springerlink.com ' Springer-Verlag Berlin Heidelberg 2007

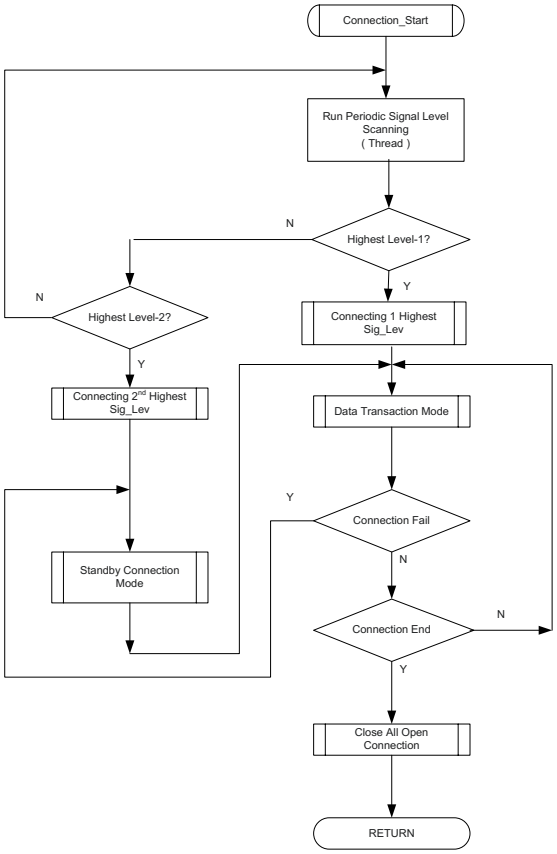

Fig. 3 . Routine for setting communication links

IV. Closing remarks

The research is still progressing. In fact developing the mobile telemedicine system with multi communication links is very challenging. We have to put a big effort while designing both hardware and software for the system, because of their complexity. Since the system is intended to serve many applications, the development of the operating system software becomes very crucial.

Principally, the software consists of two main parts, i.e. a control communication software and application software. The communication software is used to control the medical information transaction and to select a communication link. Based on the result of signal strength measurement, seems that a hybrid communication architecture is an unavoidable. This results another problem on controlling functionalities in communication systems. Whereas, to a avoid collision in service request, we define an application priority. In addition we also have to design the electronic medical record and the graphic user interface to be placed in the hospital side. Currently, we are focusing on the development of a software for data transaction. A number of medical data transmission test have been conducted. The result is promising, also some improvement are still required.

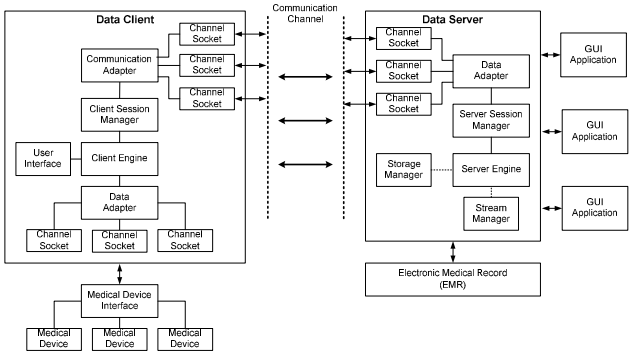

Fig. 4. Software architecture for a Mobile Telemedicine System with Multi Communication Links

Acknowledgment

The research described in this paper is partly funded by PAN ASIA ICT R&D Grants Programme. The authors would like to thank the support of ITB and Dr. Suherman, the Director of RSUD Samsudin SH as the partner in the research.

References

1. Gagliano D.M (1998) Final Report Mobile Telemedicine Testbed, Health Applications for the National Information Infrastructure, National Library of Medicine, Project NO-1-LM-6-3541.
2. Sutjiredjeki E, Soegijoko S (2006) Development of A Communication Arbiter for Mobile Telemedicine System with Multi Communication Links, to be presented at WC2006, Seoul, Korea

Address of the corresponding author:

Author: Ediana Sutjiredjeki
Institute: Biomedical Engineering Research Group,
School of Electrical Engineering and Informatics, ITB
Country: Indonesia

F. Ibrahim, N.A. Abu Osman, J. Usman and N.A. Kadri (Eds.): Biomed 06, IFMBE Proceedings 15, pp. 660-663, 2007
www.springerlink.com ' Springer-Verlag Berlin Heidelberg 2007

Managing and Organizing Plant Identification Keys for Easy Retrieval

N. Sharifalillah[1], M.B. Sapiyan[2] and I. Khairuddin[3]

[1] Faculty of Information Technology & Quantitative Sciences, University Technology MARA, 40450 Shah Alam, Selangor, Malaysia
[2] Faculty of Computer Science& Information Technology, University of Malaya, 50603 Kuala Lumpur, Malaysia
[3] Institute of Biological Sciences, University of Malaya, 50603 Kuala Lumpur, Malaysia

Abstract—**Most biologists keep data in separate databases created themselves. These databases are not well-structured. Plant identification keys are among such data. They are used to identify various plant species. The way the data is kept often requires the species identification to be done linearly. Done manual, this is very time consuming.**

Information extraction (IE) is a process of selecting information such as names, terms, or phrases, from a natural language text documents. This information is then structured into a specified template for easy retrieval. This method is applied to plant identification keys kept by the biologists. We illustrate the processes using an example from a database and discuss ways to reorganize the identification keys.

Keywords— **Plant identification keys, information extraction, information organization, ontology.**

I. Introduction

Malaysia has a vast collection of biodiversity and conservation information. The Rimba Ilmu Herbarium, a reference library of preserved plant specimens of University of Malaya for example, maintains approximately 70,000 biological plant specimens. It is the largest university collection in Malaysia. This biological information is a priceless heritage of the country that will never be outdated.

The first challenge in biological informatics is to identify a plant species. Plant species identification is important as it provides valuable information on plant characteristics. This information is the knowledge source for other various fields, such as medicine, food industry and agriculture.

The ability to identify plant species also helps in determining the plant population and its distribution. This is necessary in the effort of recognizing the species that is about to extinct.

Biologists have a lot of data. However, to get useful information from the data is very time consuming since the data have to be interpreted manually. To alleviate this difficulty, a computer application that automates the extraction of new information would help.

II. Identification Keys for Specimen Identification

Identification keys also known as dichotomous keys. They identify plant characteristics. They are represented as pair statements. To identify a species, one of the pair statements is selected before proceeding to the next level of pair statements. The process is repeated until the plant successfully identified. This is illustrated below.

Table 1 displays the fraction of identification keys taken from *Checklist System for Rutaceae*. It presents an example of one identified species, *Zanthoxylum nitidum* shown by keys *1a*, *2b*, and *3a*. We use the same species example for discussion in the next section.

Table 1 Checklist System for Rutaceae

Key	Description	Target
1a	**Woody climbers never shrubs or trees, with recurved hook like spines.**	**2**
1b	Shrubs or trees, never climbing.	4
2a	Leaves simple, shortly staled. Flowers solitary or in axillary clusters 4-5 -merous. Fruits globose or obovoid smooth to rough, sometimes obed; without pulp vesicles. Seeds few.	27
2b	**Leaves pinnate.**	**3**
3a	**Leaves with 5-9 leaflets. Twigs and leaf stalks prickly. Fruits dry, splitting.**	**Zanthoxylum nitidum**
3b	Leaves with 3 leaflets, leaf stalks not winged. Without prickles, often with long axillary staight or curced nooks. Flowers in dense axillary racemes or panicles. Fruits globose to ellipsoid, mucilaginous, without pulp vesicles. Seeds 1-3.	Luvunga borneensis
4a	Shrub of mangrove fringe. Fruits. Fruits 3 (or 4) chambered, like a 3-sided lemon. Seeds very large (large known in Orange subfam.) Leaves simple. Spines. Spines single or paired	Merope angulata
4b	Don not have character as 4a.	5

F. Ibrahim, N.A. Abu Osman, J. Usman and N.A. Kadri (Eds.): Biomed 06, IFMBE Proceedings 15, pp. 664-667, 2007
www.springerlink.com ' Springer-Verlag Berlin Heidelberg 2007

Plant identification keys are prepared by taxonomist themselves. Different taxonomist may have different styles of writing. Hence there is no standard representation of the keys.

The plant identification system is linear and rigid. As illustrated by the above example, to identify a species, a user has to go through the pairs one after another following the pointers indicated. Since this sequence can vary from one species to another, the structure of the identification keys are not well organized for easy retrieval. The representation may be improved using an ontological approach.

III. Ontology-based extraction and organization

The idea of IE is not new. IE project has started before 1970 [1]. Many works have been done to date covering multiple domains.

The idea of information extraction from unstructured documents and regenerating of information into a relational database is applied to car advertisements and computer job listings, on the newspaper taken from the Web [2].

Plant identification keys contain description of plant species. This is illustrated in Table 2.

Table 2 shows the species description of the previous example. The description contains the terminologies or keys used to describe the plant. The keys are illustrated by the highlighted words.

Table 2 Plant Description for Zanthoxylum nitidum

Species: Zanthoxylum nitidum
Woody climbers never shrubs or trees, with recurved hook like spines. Leaves pinnate. Leaves with 5-9 leaflets. Twigs and leaf stalks prickly. Fruits dry, splitting.

Plant taxonomy is hierarchical in nature. Therefore, the way plant description is recorded should have the same consideration. We have to organize the keys to ease the retrieval process.

There are two main processes involved to reorganize the identification keys:

- Extract the information from species description.
- Reformulate the information into a relation database.

IV. Methods

There are a number of processes required to extract the keys from species description and regenerating the information as a relation. The processes are as follows:

A. Indexing

Species description is data-rich sentence containing the plant identification terminologies. They are also known as keys. Before pattern matching can be applied, the description in the database has to be preprocessed. However the description is quite brief and not necessarily in complete and grammatically correct sentences. Hence the preprocessing requirement is not as extensive as usual.

Before extracting the keys from species description, for each word, it is necessary to find their root words. This process is known as preprocessing or indexing. The steps are as follows:

- Tokenization

In this step, every word is treated as a single item, shown in Table 3. This step prepares the word for the next process i.e. pattern matching.

Table 3 Tokenization

Woody	recurved	Leaves	stalks
climbers	hook	With	prickly
Never	like	5-9	.
shrubs	spines	Leaflets	Fruits
or	.	.	Dry
Trees	Leaves	Twigs	,
,	Pinnate	And	splitting
With	.	Leaf	.

- Stemming

The next step deals with the morphological aspect of the words. The word used in the description may not be the same with the common keys, but comes from the same root word. E.g. the word *prickly* in the description is an adjective while *prickle* in the common keys is the noun.

To solve the problem, we performed word stemming. It is a process of reducing the word into its root word. By reducing the morphological variance of the word, we can improve the pattern matching process.

B. Pattern Matching

The second process is pattern matching. The indexed words are match with the common keys that is used to describe the plant. The common keys are taken from [3]. We shall refer the common keys as our system dictionary.

Table 4 shows a small part of the dictionary. Based on the previous example, there are only three words in the description which match with the common keys in the dictionary.

F. Ibrahim, N.A. Abu Osman, J. Usman and N.A. Kadri (Eds.): Biomed 06, IFMBE Proceedings 15, pp. 664-667, 2007
www.springerlink.com ' Springer-Verlag Berlin Heidelberg 2007

Table 4 Plant Identification Terminologies

Leaf – Division	Stem – Part	Stem - Type
Abruptly pinnate	Lenticel	Stool
Bifoliate	Meristem	Sucker
Bipinnate	Node	Sympodium
Biternate	Phloem	Thorn
Compound	Pith	Tiller
Odd-pinnate	Prickle	Trunk
Palmate	Sapwood	Tuber
Pinnate	Stele	Turion
Simple	Trunk	Twig
Tendril-pinnate	Twig	Vine

There are two aspects to take into consideration:

- Key category

There is a situation where the category to which a key belongs to is not stated in the phrase. E.g. in the phrase *twigs and leaf stalks prickly*, the category of the plant parts is not attached with the key *twigs*. Thus, it is difficult to construct the rules.

To solve the problem, matching is based on comparing the word with the listed words in the dictionary ignoring the category to which the key belongs to.

- The co-occurrence a key in more than one category

There is a case where the key may occur twice or more in different category. E.g. the word *twig* occurs in two different categories i.e. the part of the stem and the type of the stem.

To solve the problem, only major categories to which the keys belong are referred. Based on the example given, *twig* falls under the same major category i.e. stem. Hence *twig* is referred to the stem.

C. Ontology Rule-based

The final process is to generate rules based on the results from the matching process. The rules contain the characteristics of the plant parts according to their categories. This is demonstrated in Table 5.

Table 5 Rules for Zanthoxylum nitidum

IF
Stem twig AND
Stem prickle AND
Leaf pinnate THEN
Species is Zanthoxylum nitidum

Take note that plants are grouped hierarchically based on their similarities. This organization offers efficient retrieval of the information. Through this arrangement, identification can be directed freely based on the relationship between the plant parts.

Table 6 shows the example of the hierarchical arrangement discussed above. We shall refer this concept as ontology rule-based.

Table 6 Ontology Rule-based

Root1	Stem1.1	Leaf1.1.1	Flower 1.1.1.1	Species(a)
		Leaf1.1.2	Flower1.1.2.1	Species(b)
			Flower1.1.2.1	Species(c)
	Stem1.2	Leaf1.2.1	Flower 1.2.2.1	Species(d)
			Flower1.2.2.2	Species(e)
Root2	Stem2.1	Leaf2.1.1	Flower2.1.1.1	Species(f)

V. IMPLEMENTATION

In this section we present the implementation of the prototype. Given a specimen that the stem is *twig*, the identification processes are as follows.

- Figure 1 shows the main menu of our system. There are a few options to start the identification i.e. the root, the stem, the leaf, or, the flower. This example, the user chooses to start the identification using the plant stem.
- Once the category is chosen, the user can choose one of the two available methods to proceed:
  a. Using the search engine provided. This is done by key-in the known keys for search, or
  b. Choosing one of the keys provided. This is shown in Figure 2(A) where the user selects alphabet *T*.
- Figure 2(B) shows list of the stem keys starting with *T*, and *twig* is selected.
- If any of the keys is selected, the system provides two options, shown in Figure 2(C), for the user to choose. The options are:
  a. The definition of the key, shown in Figure 2(D).
  b. The relationship between the selected key with other keys, shown in Figure 2(E). This is the fundamental component of the system. Biologists use this information for species identification as well as the interpretation of biological data.

F. Ibrahim, N.A. Abu Osman, J. Usman and N.A. Kadri (Eds.): Biomed 06, IFMBE Proceedings 15, pp. 664-667, 2007
www.springerlink.com ' Springer-Verlag Berlin Heidelberg 2007

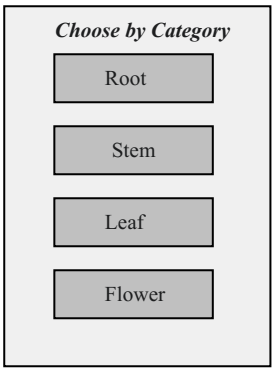

Fig. 1 Main Menu of the System

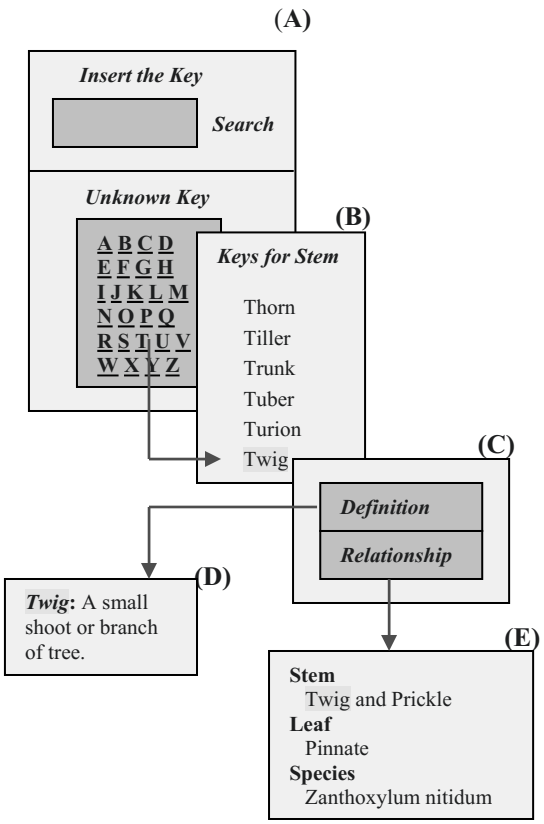

Fig. 2 Selections of Menu

VI. Discussion

We have discussed the approach to reorganize plant identification keys to provide easy retrieval. An example was used to illustrate the process and to demonstrate the approach using the developed prototype.

Nevertheless, there are two aspects to take into consideration:

- Not all the keys are matched with the common keys. This will limit the production of the rules.
- Sometimes the rules may not be representative because there is insufficient information to represent the species characteristics.

To improve the production rules, there are two factors that we can be considered:

- The natural language aspect
- The text understanding aspect

VII. Conclusions

In this paper we presented the concept of managing and organizing the information from data-rich documents. We discussed a few aspects that we need to consider in organizing the documents. Based on the prototype given, it is clearly shown that the ontological approach proposed can overcome the limitations of earlier identification system which implements a linear algorithm. The improvements made are as follows:

- The retrieval of the information is easier and faster.
- The interrelation between the keys is well defined.

Further research is being carried out to implement and validate the proposed concept.

References

1. Cowie J, Lehnert W (1996) Information Extraction. Communication of the ACM. 39(1):80-91
2. Embley D W, Campbell D M, Smith R D et al. (1998) Ontology-based extraction and structuring of information from data-rich unstructured documents, Proceedings of the 7th International Conference on Information and Knowledge Management, CIKM 98, New York, USA, 2003, pp 52 59
3. Harris J G, Harris M W (2004) Plant Identification Terminology: An Illustrated Glossary. Utah, USA

Address of the corresponding author:

Author: Sharifalillah Nordin
Institute: Faculty of Information Technology & Quantitative Sciences, University Technology MARA
City: Shah Alam
Country: Malaysia
Email: ifanordin@perdana.um.edu.my

F. Ibrahim, N.A. Abu Osman, J. Usman and N.A. Kadri (Eds.): Biomed 06, IFMBE Proceedings 15, pp. 664-667, 2007
www.springerlink.com ' Springer-Verlag Berlin Heidelberg 2007

Weight Control and Conversations in an Online Health-Community on Overweight

sa Smedberg

Department of Computer and Systems Sciences, Stockholm University/KTH, Kista, Sweden

Abstract— **This paper presents the results from a two month-long study of a group of people participating in an online health-community on overweight. The relation between their contributions in the community and their experienced weight change was investigated. The results show a tendency towards that the greater weight loss the community members experienced the more active they were in the conversations. When focusing on the online discussions more specifically concerned with learning problems, this relation was even more evident.**

Keywords— **Communication, online, learning, weight loss**

I. Introduction

The increasing number of overweight and obese people has become a challenge to primary care of today [1]. A widely used type of treatment for obese people is behavioral treatment [2]. A problem for the health-care is that treatments only have a short-term effect. Studies show that most of the patients regain weight after finishing the treatment programs [2]. Factors that inhibit successful weight loss include failure to achieve weight goals, dissatisfaction with the weight achieved, a tendency to judge self-worth in terms of weight and shape and to eat in order to reduce negative moods [2]. While underweight people tend to eat less when experiencing negative emotions, overweight people eat more [3]. Social support is one factor of importance for overweight people to lose weight and to keep a healthy lifestyle [1].

When interacting with others, online communication can be a good complement to face-to-face meetings. A study of obese adults showed that weekly online counseling had a positive impact on their weight loss [4]. Also, for many people with different health conditions, online communities have become a complementary way to interact with others who have similar problems and difficulties. By using the online health-communities people are able to share experiences and give advice on how to cope with different physical and emotional conditions [5]. Social interaction and emotional support have become key ingredients in many online communities [5]-[6], even though it has shown to be differences between different groups of people [7]. Besides the online health-communities on different diseases, there are also communities that focus on bad habits or patterns of unhealthy behavior, such as eating problems, smoking, and alcohol and drug problems.

Previous studies have been made in order to find out about how the online communities work. One often used approach has been to classify the community messages as consisting of information, being friendly or hostile, e.g. This is important when investigating the level of empathy and understanding in the community. However, in order to come closer to understand the impact that the community has on the participants, we need to make further analyses. What remains unsolved is to what extent the online communities enable people to communicate in order to learn together.

II. Method

The case study presented in this paper was made of an open and non-moderated online community for people with overweight in the Swedish Net Doctor site, netdoktor.passagen.se. The time period was October to November 2005. The target group of the study was 17 community members who had participated in a community challenge to lose weight during October and November. A starting point of the study was therefore the conversations about weight goals and weight change that the target group engaged in during the period of the study. The conversational patterns of these community members were then investigated thoroughly during the time of the study. The collected data were analyzed both quantitatively and qualitatively.

III. Results from case study

A. Weight change and communication

Total number of issues raised in the online health-community on overweight during October and November 2005 was 87. These issues were met by 556 responses, which make a total number of 643 posted messages during the two months.

Both in the beginning of October and in the beginning of November, there were issues about a common challenge to lose weight; the goal was a two kilos weight loss in October and one kilo in November. 17 of the community members reported

F. Ibrahim, N.A. Abu Osman, J. Usman and N.A. Kadri (Eds.): Biomed 06, IFMBE Proceedings 15, pp. 668-671, 2007
www.springerlink.com ' Springer-Verlag Berlin Heidelberg 2007

back about their weight results. All together, the 17 community members lost about 26 kilos during the two months. The results from the study showed that they had posted 135 messages to different conversations in the online community, and they had received 132 responses from other members.

Table 1 below shows the weight change for each of the 17 community members. The presentation is made in ascending order, starting with the community member who experienced the most weight loss and ending with the one with most weight gain. The table also shows the number of messages that each community member posted and the number of responses each one of them received.

Table 1 Weight Change, Posted and Received Messages

Community Member	Weight change	Number of posted messages	Number of responses from other members
CM1	-7.7	13	3
CM2	-5.2	5	0
CM3	-3	6	38
CM4	-2.3	17	7
CM5	-2.3	7	0
CM6	-2.2	2	1
CM7	-1.8	13	4
CM8	-1.6	5	9
CM9	-1.4	4	0
CM10	-0.5	3	0
CM11	-0.5	3	1
CM12	-0.1	2	0
CM13	0	35	56
CM14	0	1	0
CM15	0	8	9
CM16	1	9	4
CM17	1.5	2	0
SUM	**- 26.1**	**135**	**132**

The weight change spanned from a gain of 1.5 kilos to a loss of 7.7 kilos. About 70% of the members in the study, or 12 of the members, managed to lose weight, while about 18% or three of the members did not experience any weight change at all and 12% or two members experienced some weight gain. From the results, we can detect a certain, but weak, relation between weight change and the number of posted messages, while the responses from other members were more randomly distributed.

The number of posted messages was almost seven times as high for the one with the best result in comparison with the one with the lowest result. The most common was that the number of posted messages did not exceed ten. Only four of the members in the study posted more than ten messages; three of them lost weight and one of them experienced no weight change. The community member who experienced most weight loss was one of these four.

Regarding the responses from other community members, the largest number of responses was directed to one of the members who did not change weight during the period of study, while the second highest number of responses was sent to one who had lost three kilos.

The results also show that one community member deviates a lot from the rest of the group. In the table it is shown that CM13 wrote 35 messages and got 56 answers from the other community members. These are the highest numbers of the study. At the same time, this member did not lose any weight at all during the time of the study. When searching for more information about this member, a conversation from the 6th of October 2005 with the title Why are we ashamed of our weight? was found. In this conversation, some community members declared their present weight and also some progress information from the past. Two of the 17 members of the study participated in this conversation, CM13 and CM7 . While CM7 declared that her weight at that point was 71 kilos and that she had a height of 155 cm, CM13 said that her weight was 68.2 kilos and that her height was 164 cm. Additionally, CM13 also declared that her weight was as high as 102.8 kilos in the summer of 2004, which means that she had managed to lose more than 34 kilos during a time period of less than 1.5 years. To think that she would be able to meet the challenges and continue to lose weight appears difficult considering this background information. The information makes it easier to understand the extreme deviation seen in the case of CM13 .

B. Weight change and learning conversations

Up to this point, we have looked at the total number of messages sent and received by the 17 community members in the study group. However, when investigating the content of the conversations, different kinds of conversation subjects were seen, and also a slightly different activity rate.

One type of issue was related to personal problems on how to learn a new behavior. Issues of this type included questions about how to deal with temptations, how to manage to turn a weight gain, anxiety about having eaten too much during some days, requests for coaching, how to stop eating too fast, etc. Other issues dealt with more neutral questions and information about diets, food content, exer-

F. Ibrahim, N.A. Abu Osman, J. Usman and N.A. Kadri (Eds.): Biomed 06, IFMBE Proceedings 15, pp. 668-671, 2007
www.springerlink.com ' Springer-Verlag Berlin Heidelberg 2007

cise programs, tools for measuring BMI, etc., and also issues without any relation to weight problems at all, such as those about literature recommendations, congratulations on birthdays and technical issues, e.g.

In general, most of the conversation issues in the online community were of the more neutral kind or issues that lied outside overweight problems. Out of all issues raised in the community during October and November 2005, there were 25 that related to personal problems on learning a new behavior, while 62 did not. Regarding the 17 members in the target group, the distribution of their posted messages was more in favor of learning conversations; 78 of their messages were posted to learning conversations, while 57 addressed other issues.

After having filtered out the messages on learning issues in the target group, the relation between weight change and posted messages was more clearly revealed. In fig. 1, below, the relation between the number of posted messages to these conversations and the weight changes can be seen. The results are presented for each of the 17 community members.

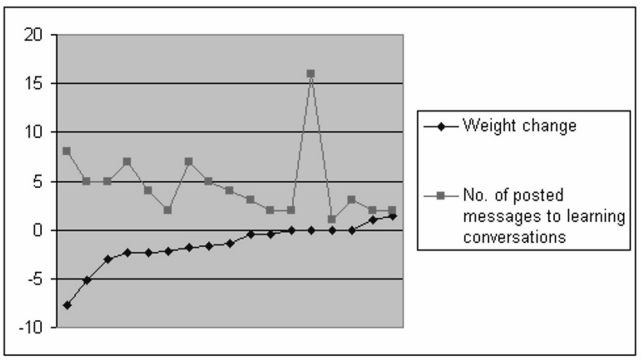

Fig. 1. Participation in online learning conversations in relation to weight change

Of those members who experienced a weight loss, half of them had posted five or more messages to conversations on learning issues. Out of those who experienced no weight change or weight gain, all but one of them posted three messages or less.

Fig. 1 shows a tendency; the number of messages seems to decrease as the weight change is getting less and less successful. However, the pattern is broken at some instances. As for the results presented in the previous section, CM13 causes a deviation from the pattern, in this case by having posted 16 messages.

C. Three categories of learning conversations

Since the goal of the community members is to learn a new life-style, a new behavior, the conversations on personal learning problems were found to be the most interesting to study. Even though communication on other issues can help the members establish friendship, learning together calls for conversations on learning-related issues.

When looking more closely into the community conversations on personal learning issues, three different categories could be seen: setbacks, obstacles and incentives. In the following paragraphs, we will shortly describe the characteristics of the three categories, and give examples from the online community conversations.

Setbacks*:* The conversations on setbacks in the online community focused on personal experiences of breakdowns and mistakes, such as problems concerning efforts to change lifestyle, to develop exercising habits, etc. One of the community member explained that s/he found it difficult to give up chocolate bars, and that s/he felt sad due to a weight gain of three kilos. Another one explained that:

I try to exercise and to eat healthy, but it seems like my body refuses to let me lose weight. [...] I would really appreciate some advice.

Descriptions of crises were often followed by expressions of disappointment and sadness. One of the members wrote:

So now, there aren t any clothes that fit me, and it makes me very depressed. I want to lose weight but HOW?

Obstacles*:* Regarding the obstacles that stand in the way for weight loss, there were conversations of seen or foreseen difficulties that the community members needed to overcome. One example was the conversation about difficulties concerned with eating slowly; another one was concerned with how to get rid of an addiction to sugar. One member wrote:

Is there anyone else out there who has experienced that you have had too little to eat according to recommendations but still suffer from overweight? [...] How did you manage to change this? [...] It is difficult when you have lived on chocolate bars and sandwiches all your life.

Incentives: Incentives induce action or motivate effort, due to the fear of punishment or the expectation of reward. Conversations on incentives in the online community were concerned with motivational factors, value systems, i.e., those things that were of importance for the members struggle to lose weight, change lifestyle, etc. The purpose of some of the conversations was to challenge the other members to achieve a certain weight loss. In the start-up message, the author encouraged the others to accept the challenge and to report back their results. Other issues raised were about how to get motivated to continue the struggle, doubts about underlying

F. Ibrahim, N.A. Abu Osman, J. Usman and N.A. Kadri (Eds.): Biomed 06, IFMBE Proceedings 15, pp. 668-671, 2007
www.springerlink.com ' Springer-Verlag Berlin Heidelberg 2007

reasons for engaging in weight reduction activities, reward systems, etc. One of the community members wrote:

I wonder if there are any specific strategies for increasing your motivation to migrate to a healthier life. What gives you the energy to succeed?

Regarding the distribution of messages posted to the different learning conversations, the 17 members of the target group engaged most frequently in conversations on incentives (65 messages), secondly in conversations about setbacks (12 messages) and least frequently on obstacles (1 message).

IV. Conclusions

The case study was made of a target group of 17 members who participated in an online community on overweight during October and November 2005. Results of the study indicate that there is a correlation between active participation in conversations on learning issues and weight loss.

However, to verify the results and to understand more about the relation between participation in online communities and changed behavior, further studies need to be done. Through in-depth studies of the way overweight people engage in online health-communities and their weight change over time, we will be able to increase our knowledge and understanding of this field.

References

1. K. Baughman, E. Logue, K. Sutton, C. Capers, D. Jarjoura, W. Smucker, Biopsychosocial characteristics of overweight and obese primary care patients: do psychosocial and behavior factors mediate sociodemographic effects? , *Preventive Medicine*, No. 37, 2003, pp 129-137, Academic Press.
2. S. Byrne, Z. Cooper, C.G. Fairburn, Psychological predictors of weight regain in obesity *, Behaviour Research and Therapy*, 2004, No. 42, pp 1341-1356.
3. A. Gelibter, A. Aversa, Emotional eating in overweight, normal weight, and underweight individuals *, Eating Behaviors*, *2003,* No.3, pp 341-347.
4. S. Fox, Internet Health Resources *, Pew Internet & American Life Project*, 16 July 2003.
5. J. Preece, *Online Communities – Designing Usability, Supporting Sociability*, 2000, Wiley & Sons, Ltd.
6. J. Preece, Empathy communities: Reaching out across the web *, ACM*, Vol. 5, Issue 2, March-April 1998, pp 32-43.
7. D.C. Andrews, Audience-specific online community design , *ACM*, Vol. 45, No. 4, April 2002.

Address of the corresponding author:

Author: sa Smedberg
Institute: DSV, Stockholm University/KTH
Street: Forum 100
City: Kista
Country: Sweden
Email: asasmed@dsv.su.se

F. Ibrahim, N.A. Abu Osman, J. Usman and N.A. Kadri (Eds.): Biomed 06, IFMBE Proceedings 15, pp. 668-671, 2007
www.springerlink.com ' Springer-Verlag Berlin Heidelberg 2007

Biodegradable composite of poly ε-caprolactone/hydroxyapatite 3-D scaffolds for bone tissue engineering

S.J. Heo[1], S.E. Kim[2], Y.T. Hyun[2], D.H. Kim[1], H.M. Lee[3], J.W. Shin[1], Y.M. Hwang[1], J.W. Shin[1]

[1] Team of BK21/Department of Biomedical Engineering, Inje University, Gimhae, Gyeongnam, Korea
[2] Department of Future Technology, Korea Institute of Machinery and Materials, Changwon, Gyeongnam, Korea
[3] School of Material Science and Engineering, Pusan National University, Busan, Korea

Abstract— **Utilizing salt leaching method, a composite material of PCL (Poly ε-caprolactone) and HA (Hydroxyapatite) particles was suggested as a potential scaffold for bone tissue engineering. For this, composite materials were prepared with various HA contents (20wt%, 40wt%, 60wt%). To ensure the potential for the scaffolds, porosity, mechanical stiffness, proliferation tests were conducted along with SEM observations. The addition of HA particles enhanced proliferation of MG-63 during the test. Also, the mechanical stiffness was increased as HA particles were added. Even the porosity was decreased as the contents of HA particles was increased, the porosity of the composite with the highest contents of HA was still adoptable (~85%). From the study we conducted, addition of HA particles to PCL showed promising results. However, further studies are needed such as long term tests for osteoconductivi-ties, regeneration of extracellular matrices, and differentiation utilizing BMSC (bone marrow stromal cell) with animals.**

Keywords— **Poly ε-caprolactone, hydroxiapatite, scaffold, bone tissue engineering**

I. Introduction

Repair of bone damages and defects, especially in case of trabecula bone, has been a challenge in bone tissue engineering. Especially, for the treatment of large defect bone substitutes are needed. Various methods or methodologies have been investi-gated and applied for the treatments of large defect utilizing autografts, allografts, or even xenografts[1-3]. However, those still have their own limitations and left much to be improved. The major problems due to the allografts and/or xenografts are biocompatibility, donor and donor-site scar-city and immune rejection problems. Bone regeneration by autogenous cell would eliminate those problems. The cells obtained from the patient can be expanded in culture and seeded on a 3D scaffold. The 3D scaffold is the necessary for the cells to proliferate, maintain their differentiation functions. PCL is known to be one of the good candidates for bone scaffolding application. PCL (Poly ε-CaproLac-tone) can take several years to degrade in vivo and is a biocompatible material. PCL is more stable in surrounding conditions, moreover it is less expensive and is easily available in large quantities[4-7]. However, pure PCL scaffolds have poor mechanical properties (strength) and osteoconductivity. To overcome this problems, many researchers have been studied to the modification of pure PCL scaffolds[8-10]. For this, Hydroxyapatite (HA) particles were added to pure PCL. HA is a synthetic calcium phosphate that resembles bone mineral. It has osteoconduc-tive and bioactivity characteristics[11-14]. In this study, PCL 3D scaffolds combined with HA particles were fabricated by gas foaming/salt leaching process with different HA volume. For the evaluations, the cell viability and proliferation of the scaffolds were measured with osteoblast-like cell.

II. Materials and methods

A. Fabrication of scaffold

Poly ε-caprolactone (PCL) pellets (Sigma Aldrich, Mw 65000, USA) were dissolved into 10ml of chloroform by stirring for several hours (~4 hrs.) at room temperature. Then ammonium bicarbonate (NH_4HCO_3) particles (size range: 212-300μm) were added to the PCL solution. The weight ratio of salt to PCL was controlled at 7:1. After homogeneous mixing of salt with PCL solution, HA particles(~10μm, Sigma Aldrich, USA) were added to the solution at room temperature. Four samples were made: 0wt%(Control), 20wt%, 40wt%, and 60wt% of HA particles in weight. Slurry of PCL/HA/salt was put into a disc type teflon mold of 8mm and 3mm in diameter and thickness, respectively. Before the materials were fully solidified, they were pulled out from the teflon mold and immersed in citric acid solution (40%w/v) at room temperature to lead gas foaming and salt leaching simultaneously. To eliminate all the remaining salt contents, samples were immersed in distilled water (~ 2 days). Then the samples were kept in a dry-oven until the experiments.

B. Physical properties of scaffolds

The porosity of PCL/HA scaffolds was measured using mercury intrusion porosimetry (Auto-pore IV 9500, Micromeritics Instrument Corporation, Norcross, GA). In addition, bulk density and apparent density were evaluated.

F. Ibrahim, N.A. Abu Osman, J. Usman and N.A. Kadri (Eds.): Biomed 06, IFMBE Proceedings 15, pp. 672-675, 2007
www.springerlink.com ' Springer-Verlag Berlin Heidelberg 2007

The compressive mechanical properties of the scaffolds were evaluated (n=5 for each group) with an Micro load System (Microload system, R&B Inc, Korea) at room temperature. The displacement rate was set to be 0.5 mm/min. Surface area was measured using image processing software (HLimage 97++; Western Vision Software) to convert compressive loads into compressive stresses. The compressive modulus was determined from the initial porous response region from 0% to 30% strain. Five samples were testes for each group and the average and standard deviation were calculated for statistical analyses.

C. Seeding cell and MTT assay

MG-63 osteoblast- like cells (American Type Culture Col-lection, No. CRL-1427, USA) were used for experiments on scaffolds. The culture medium to have enough number of cells was Dulbecco's Modified Eagle Medium (DMEM, Gibco, USA) with 10% fetal bovine serum (FBS) and 1% Penicillin/Streptomycin (P/S Hyclone, USA). The scaffolds were pre-wetted in the culture medium for over 24h and placed in well plate. After the second passage, cells were seeded on PCL/HA scaffold at 10^4 cells/scaffold. The cell/scaffold were cultured in a incubator at 37 °C with 5% CO_2. The medium was changed everyday To determine the cell viability and proliferation on the scaf-folds, we carried out a MTT(3-[4,5-dimethylthiazol-2-yl]-2,5-diphenyl tetrazolium bromide) assay (Cell Proliferation Kit I, Boehringer Mannheim, Mannheim, Germany). Cells in the scaffolds were incubated with 0.5mg/ml of MTT for 4h at 37°C. MTT assay was carried with an absorbance microplate reader (ELISA, Synergy HT, Bio-Tek Instruments, Inc, Winooski, VT, USA) at 1 and 4 days. The
wavelength to measure absorbance was 595nm. The number of the specimens in each group was five(5).

D. Surface morphology

Scaffolds were removed from culture plate. Afterwards, the cells were rinsed twice with PBS. The cells were fixed by 4% formalin in PBS (pH 7.4). After being washed twice with PBS, the specimens were dehydrated in series with various concentration of ethanols (50%, 70%, 80%, 90%, 100%). Surface and cross-sectional morphologies were observed by a FE-SEM (Hitachi Ltd., S-4300SE x250, 5kV) with palladium gold coating.

E. Statistical analysis

The data in this study are presented as mean values ± SD. Statistical analysis was performed using a one-way analysis of variance(ANOVA) at a significance lever of p=0.05. Commercial SPSS software (Ver. 11.0, Standard Software Package Inc., USA) was used with the Fisher s LSD method.

III. Results and discussion

Porous PCL/HA composite scaffolds were successfully fabricated via gas foaming/salt leaching process(Fig.1). Porosity of each group was tabulated in Table 1 and the range was found to be 84~90%. Adding HA particles into PCL caused slight decrease in porosity. However, the lowest porosity of 84.49% could be still acceptable[7]. Apparent density increased as the amounts of HA particles in PCL increased, while bulk density slightly decreases. The stiffness measured based on the compressive elastic modulus was increased up to more than 3 times when more HA particles were added as shown in Fig. 2. Apart from the improvement of physical properties of scaffolds, the addition of HA particles is promising as HA particles are known to be biocompatible and provide osteoconductive environment.

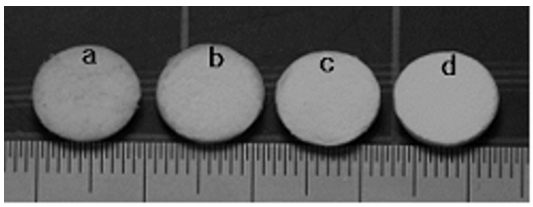

Fig. 1 A macroscopic image of four types of scaffolds
(a: PCL alone, b: PCL/20wt%HA, c: PCL/40wt%HA, d: PCL/60wt%HA)

SEM images obtained from surfaces and cross sections are shown in Fig. 3 and 4, respectively. Uniform distribution of HA particles were observed.

Table 1 Porosimetric analysis

PCL/HA weight Ratio	% Tot. Porosity	Apparent Density(g/mL)	Bulk Density(g/mL)
100/0	90.85	1.218	0.111
80/20	87.69	1.112	0.135
60/40	87.62	1.001	0.130
40/60	84.49	0.779	0.121

Even porosity was reduced in higher amounts of HA particles, the holes in the scaffolds are still large enough for the cells to penetrate(~250 μm). Also, the morphology of the cross section still looks like that of spongy bones.

F. Ibrahim, N.A. Abu Osman, J. Usman and N.A. Kadri (Eds.): Biomed 06, IFMBE Proceedings 15, pp. 672-675, 2007
www.springerlink.com ' Springer-Verlag Berlin Heidelberg 2007

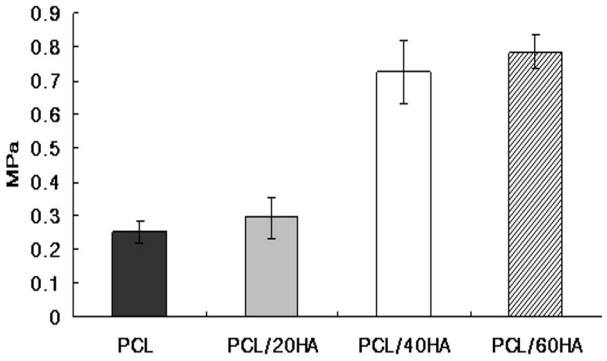

Fig. 2 Compressive modulus of four type scaffolds

An excellent penetration of the cells was observed even under short culture periods (4 days). This suggested that addition of HA particles does not provide any obstacles to cell penetration.

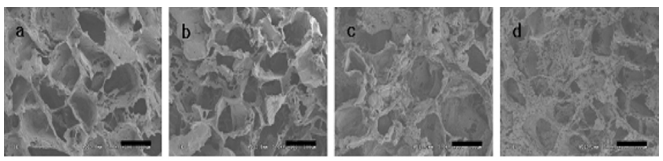

Fig. 3 SEM images, top surfaces of four type scaffolds , Bar = 250 μm
(a: PCL alone, b: PCL/20wt%HA, c: PCL/40wt%HA, d: PCL/60wt%HA)

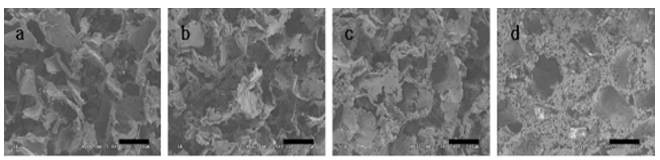

Fig. 4 SEM images, cross sectional surfaces of four type scaffolds, Bar= 250 μm
(a: PCL alone, b: PCL/20wt%HA, c: PCL/40wt%HA, d: PCL/60wt%HA)

In specialty, the cross sectional image of PCL/60wt%HA showed that only for 4 days, the cell rapidly penetrated downward over 1mm into the scaffolds. It is showed that HA affected proliferation of cells(Fig. 5).

The results of MTT assay for up to 4 days of culture are shown in Fig. 6. On the first day of seeding, the specimen of PCL/60wt%HA showed lower value. This suggests that PCL/60wt%HA did not provide preferable environment for cell adhesiveness. However, on the day 4, a great increase of proliferation in PCL/60wt%HA was observed regardless of poor initial attachment.

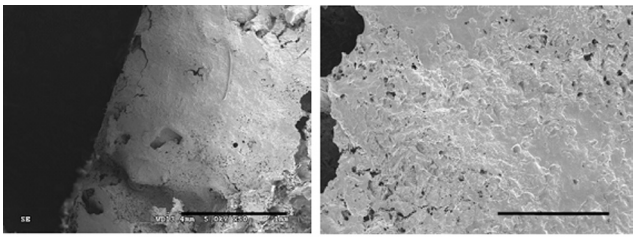

(a) (b)

Fig. 5 SEM images, cross sectional surfaces of PCL/60wt%HA with cells
(a: x50 , bar = 1mm b: x 250, bar = 250 μm)

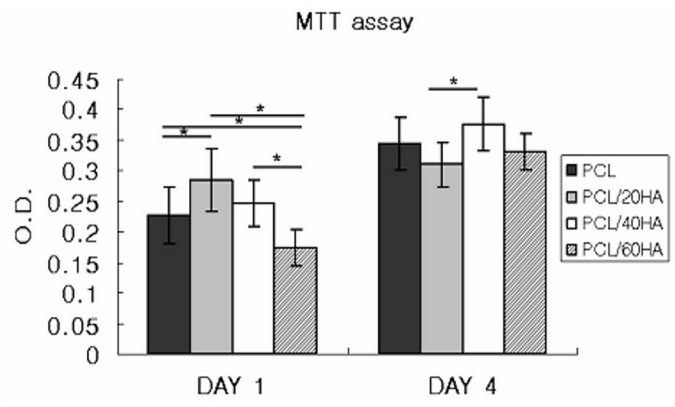

Fig. 6 MTT assay for PCL/HA scaffolds(*p<0.05)

IV. Conclusions

From the study, the various tests on composite materials of PCL and HA particles showed promising results for bone tissue engineering. However, further study should be carried out such as long term experiments utilizing other cells such as BMSC with animals. Especially, the initial attachments and strength of the materials should be improved.

Acknowledgment

This study was partially supported by Korea Science and Engineering Foundation (No. R01-2004-000-10164-0) and Korea Institute of Machinery and Materials.

References

1. Perry CR. (1999) Bone repair techniques, bone graft, and bone graft substitutes. Clin Plast Surg. 360:71-86
2. Kneser U, Schaefer DJ, Polykandriotis E et al. (2006) Tissue engineering of bone: the reconstructive surgeon s point of view. 10:7-9

F. Ibrahim, N.A. Abu Osman, J. Usman and N.A. Kadri (Eds.): Biomed 06, IFMBE Proceedings 15, pp. 672-675, 2007
www.springerlink.com ' Springer-Verlag Berlin Heidelberg 2007

3. Gazdag AR, Lane JM, Glaser D et a.l (1995) Alternatives to autogenous bone graft: efficacy and indication. J Am Acad Orthop Surg. 3:1-8
4. Rezwan K, Chen Q, Blaker J et al. (2006) Biodegradable and bio active porous polymer/inorganic composite scaffolds for bone tissue engineering. Biomaterials. 27:3413-3431
5. Yang S, Leong KF, Duz et al. (2001) The design of scaffolds for use in tissue engineering. Part I. Traditional factors. Tissue Eng 7:679-689
6. Rich J, Jaakkola T, Tirri T et al. (2002) In vitro evalution of poly([var epsilon]-caprolactone-co-DL-lactide)/bioactive glass composites. Biomaterials 23:2143-2150
7. Kim SS, Park MS, Jeon O et al. (2006) Poly(lactide-co-glycolide)/hydroxyapatite composite scaffolds for bone tissue engineering. Biomaterials 27:1399-1409
8. Palola T, Anna T, et al. (2004) In vitro mineralization of bioresorbable poly(3-caprolactone)/apatite composites for bone tissue engineering: a vibrational and thermal investigation. Journal of Molecular Structure 744-747:135-143
9. Taddei P, Di FM et al (2006) In vitro bioactivity of poly(epsilon-caprolactone)-apatite (PCL-AP) scaffolds for bone tissue engineering: the influence of the PCL/AP ratio. Int J Artif Organs 29(7):719-25
10. Kim HW, Jonathan C et al (2003) Hydroxyapatite/poly(-caprolactone) composite coatings on hydroxyapatite porous bone scaffold for drug delivery. Biomaterials 25:1279-1287
11. Marra KG, Szem JW, Kumta PN et al (1999) In vitro analysis of biodegradable polymer blend/hydroxiapatite composites for bone tissue engineering. J Biomed Mater Res 47:324-335
12. Komlew VS, Barinov SM, et al (2002) A method to fabricate porous spherical hydroxyapatite granules intended for time controlled drug release. Biomaterials. 23:3449-34454
13. Sivakumar M, Rao KP. (2002) Preparation and characterization and in vitro release of gentamicin from coralline hydroxyapatite-gelatin composite microspheres. Biomaterials 23:3175-3181
14. Rizzi SC, Heath DJ, Coombes AG et al. (2001) Biodegradable polymer/hydroxyapatite composites: surface analysis and initial attachment of human osteoblast. J Biomed Master Res 55:475-86

Address of the corresponding author:

Author: Jung-Woog Shin
e-mail: sjw@bme.inje.ac.kr
Institute: Inje University
City: Gimhae
Country: South Korea

F. Ibrahim, N.A. Abu Osman, J. Usman and N.A. Kadri (Eds.): Biomed 06, IFMBE Proceedings 15, pp. 672-675, 2007
www.springerlink.com ' Springer-Verlag Berlin Heidelberg 2007

Biodegradable Scaffolds for Tissue Engineering Fabricated by Surface Selective Laser Sintering

V.K. Popov[1], E.N. Antonov[1], V.N. Bagratashvili[1], J.J.A. Barry[2], A.L. Ivanov[1], A.N. Konovalov[1] and S.M. Howdle[2]

[1] Institute of Laser and Information Technologies, Russian Academy of Sciences, Pionerskaya 2, Troitsk, Moscow Region, Russia.
[2] School of Chemistry, University of Nottingham, University Park, Nottingham, NG7 2RD, UK.

Abstract— **Novel Surface Selective Laser Sintering (SSLS) technique enable precise fabrication of complicated 3D composite biodegradable scaffolds from thermosensitive polylactic and polylactic-co-glycolic acids and even retain bioactivity of incorporated enzymes. The presence of carbon black (CB) nanoparticles in SSLS structures raised concerns about their toxicity and biocompatibility. In present paper we studied this by diverse *in vitro* analysis using 3T3 fibroblasts, ovine meniscal chondrocytes and C2C12 myoblast cell cultures. All cells "readily" attached to and proliferated on CB containing surfaces. The abundance of live cells spreading out and covering the entire SSLS porous structures confirms their high biocompatibility. Moreover, C2C12 cells in the presence of morphogenetic protein rhBMP-2 have shown strong shift in differentiation pathway from myoblastic to osteoblastic type. These promising results encouraged us to further development of SSLS methodology targeted to custom-designed biodegradable scaffolds and implant fabrication.**

Keywords— **Tissue engineering, scaffolds, cytotoxicity, biocompatibility.**

I. Introduction

Treatment of the bone and cartilage defects caused by trauma, tumor ablation or congenital malformations still remains the complex problem in contemporary surgical practice. Tissue engineering (TE) is the newer approach which will enable to overcome the limitations of conventional methodologies [1]. Scaffold-guided tissue regeneration is one of the key technologies for the emerging field of TE [2]. It involves seeding highly porous biodegradable scaffolds with donor cells and/or growth factors, culturing and then implanting the scaffolds to induce direct growth of a new tissue. The manufacturing of such scaffolds still presents a serious problem. Imperfection of the current techniques (e.g. mold casting, injection molding, foaming, particulate leaching, etc.) has encouraged the development and use of Rapid Prototyping (RP) approach for reliable fabrication of scaffolds with desired architecture satisfying the range of requirements related to their strength and toughness, osteoinductivity and osteoconductivity, controlled rate of biodegradation and inflammatory response [3].

In our previous studies we have developed a new Surface Selective Laser Sintering (SSLS) technique [4, 5] enabling precise fabrication of TE scaffolds even from thermosensitive biodegradable polymers like polylactic and polylactic-co-glycolic acids (PLA and PLGA). In SSLS we can fuse the polymer particles which do not absorb near infrared laser radiation together by controllable melting of the particle surface only. It can be achieved by homogeneous distributing a small amount ($\leq$ 0.1 wt.%) of carbon black (CB) nanoparticles (having strong absorption at the laser wavelength) onto polymer particle surface by simple mixing. By melting of the particle surface only one can prevent significant overheating of their internal domains. We have demonstrated that this sintering process does not damage the polymer chemical structure. Moreover, it was shown with a model enzyme (ribonuclease A) incorporated into individual PLA particles that the most of enzyme activity (up to 80%) was retained after SSLS processing [5]. However, the presence of CB nanoparticles has raised concerns about the toxicity and biocompatibility of these materials [6], particularly bearing in mind that up today there were very limited data to confirm or disprove this hypothesis [7, 8]. We have focused present study on evaluation of the toxicity of SSLS scaffolds by diverse *in vitro* analysis using 3T3 fibroblasts, ovine meniscal chondrocytes and C2C12 myoblast cell cultures.

II. Materials and methods

A. Fabrication of SSLS scaffolds

Poly (D,L)-lactic acid (Alkermes Medisorb , low inherent viscosity (IV), M_w = 108 kDa, polydispersity = 1.4) was ground to a fine powder at dry ice temperature using a pestle and mortar. The particles had a broad size distribution with a mean diameter ca. 100μm. CB was obtained from Gubkin Oil and Gas Institute (Moscow, Russia) and had a surface area $\approx 100 m^2/g$. CB particles mean size (ca. 350nm) was determined using scanning electron microscopy (SEM). A small amount (ca. 0.1 1.0wt.%) of CB was added to the PLA powder by thorough mixing. Practically, each PLA particle was covered with a small amount of CB. Hydroxy-

F. Ibrahim, N.A. Abu Osman, J. Usman and N.A. Kadri (Eds.): Biomed 06, IFMBE Proceedings 15, pp. 676-679, 2007
www.springerlink.com ' Springer-Verlag Berlin Heidelberg 2007

pol™ - monodisperse (ca. 1μm) hydroxyapatite ($Ca_{10}(PO_4)_6(OH)_2$) powder produced by "Polystom Ltd." (Moscow, Russia) was used in some samples both as bioactive and reinforcing mineral filler.

Continuous wave (CW) radiation from the fibre diode laser (LS-097, IRE-Polus Ltd , Moscow, Russia) emitting at λ=0.97μm with an average power up to 20 W was delivered to the PLA/CB powder through a quartz fiber inserted into the beam delivery system of the computer controlled X-Y stage. 80mm focal distance quartz lens provided 500μm diameter laser spot onto the polymer particles enabling their fusion during the scanning process. PLA has very low (σ<0.1cm^2) absorbance at the laser wavelength (0.97μm). CB particles do absorb the light and initiate PLA surface melting followed with powder fusion. It was possible to achieve polymer sintering without significant temperature increase in the bulk of the particles optimizing laser intensity and scanning speed. The threshold laser intensity ($\mathbf{I_t}$) to melt the polymer surface without CB at scanning speed 3mm/s was about $\mathbf{I_t}$≈120–10W/cm^2. It has been decreased significantly to $\mathbf{I_t}$≈4–1W/cm^2 by adding to PLA powder just 0.1wt.% of CB.

After sintering all samples (disks, 1mm thickness and 5mm in diameter with honeycomb ca. 500x500μm structure Fig.1) were sterilised in PBS (phosphorous buffered solution) supplemented with 250units/ml of antibiotic/ antimycotic overnight. The structures were then removed and soaked in sterile PBS prior to be being seeded.

The ability of the scaffolds to support cell adhesion, proliferation and differentiation was measured by Alamar blue and alkaline phosphatase assays and analysed by optical, fluorescent and scanning electron microscopy.

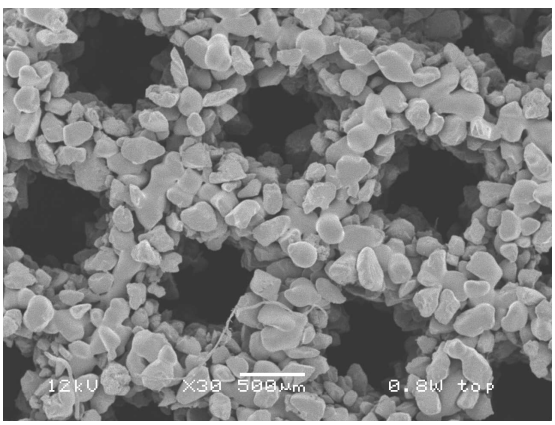

Fig. 1 SEM image of SSLS scaffold microstructure.

B. 3T3 Fibroblast cell culture

Fibroblasts were cultured in DMEM (containing 10% Newborn Calf Serum (Heat inactivated), 5% Sodium Bicarbonate 2% sodium pyruvate, 1% glutamine and 100 units/ml penicillin/streptomycin) and were passaged using 0.2% trypsin (1% HEPES). For culturing on discs the cells were seeded at a density of 1x10^4 cells per well in Falcon 96 well tissue culture plates for 24 hours.

C. Ovine meniscal chondrocytes (OMCs)

Meniscal cartilage was isolated from stifle joints taken from 4 month old sheep. OMCs were obtained by enzymatic digestion and cultured in DMEM (supplemented with 10% FCS, 1% L-glutamine, 1% non-essential amino acids, 1% antibiotic/antimycotic solution, 0.18 g/L ascorbic acid-2-phosphate and 0.046 g/L L-proline) in tissue culture flasks with a surface area of 175 cm^2. When cells were 80-90% confluent, a cell suspension was obtained by enzymatic digestion with trypsin/EDTA in PBS. Cells were split 1 in 2 and cultured to a maximum of passage 10. The cells were washed by centrifugation (1200rpm) and diluted to a concentration of 1x10^7 cells per mL in culture medium. Prior to seeding with cells, scaffolds were soaked in culture medium containing 10% foetal calf serum for at least 12 hours. Cell suspension was pipetted through each scaffold ten times (200μL per scaffold, equivalent to 2x10^6 cells per scaffold) in order to encourage cell attachment and the plate transferred immediately to a humidified incubator (37℃, 5% CO_2) and cultured statically for 4 hours.

D. C2C12 myoblast culture

The C2C12 myoblast is a cell line that differentiates forming contractile myotubes and producing proteins characteristic to muscle. Treatment with bone morphogenic protein 2 (BMP-2) causes a shift in the differentiation pathway from myoblastic to osteoblastic [9]. We have used 1x10^6 cells per well in Falcon 96 well tissue culture plates and cultured C2C12 cells on our SSLS scaffolds in the absence/presence of rhBMP-2 (500ng/ml). We analysed cells activity and differentiation using Alamar blue and alkaline phosphatase assays.

E. Alamar Blue assay

The Alamar blue assay designed to measure the mitochondrial activity of cells. At the required time point in cell culture, the culture medium is aspirated and the cells/discs

F. Ibrahim, N.A. Abu Osman, J. Usman and N.A. Kadri (Eds.): Biomed 06, IFMBE Proceedings 15, pp. 676-679, 2007
www.springerlink.com ' Springer-Verlag Berlin Heidelberg 2007

washed with PBS. Alamar Blue (100µl made up from 1:10 dilution of 10x stock solution of Alamar Blue (Serotech) was added to each of the wells containing cells and they were incubated for 60 minutes at 37°C. Following this 100µl aliquots were drawn off and transferred to a 96 well plate (Falcon). This solution was then read on the fluorescence plate reader (Cytofluor, Perceptive Biosystems) at 530nm excitation and 590nm emission.

F. Scanning electron microscopy (SEM).

Specimens were fixed overnight in 3% glutaraldehyde in PBS at 4°C and subsequently rinsed in 0.1*M* PO_4 buffer. Samples were then treated with osmium tetroxide 1% for 2hours and rinsed with distilled water. They were then dehydrated in an increasing ethanol concentration series, washed with hexamethyldisilizane (HMDS) and air-dried. After that all samples were sputter coated with gold for 4 minutes under an argon atmosphere in a Balzers SCD 030 sputter coater unit. Coated samples were examined with a Phillips 505 scanning electron microscope operating at an accelerating voltage of 15 kV.

III. Results and discussion

The variety of scaffolds sintered at different laser intensities $\mathbf{I_s}$ and containing CB in the range of 0 ÷ 1.0wt.% and/or hydroxyapatite (up to 20 wt.%) is listed in Table 1.

Table 1. SSLS samples fabricated for cytotoxicity study.

№	Sample composition	Laser intensity (W/cm^2)
1	PLA + 0.1wt.% CB	8.6
2	PLA + 0.1wt.% CB	14.5
3	PLA + 0.4wt.% CB	8.6
4	PLA + 0.4wt.% CB	14.5
5	PLA + 1.0wt.% CB	8.6
6	PLA + 1.0wt%CB	14.5
7	PLA + 0.4wt.% CB + 20wt.% HA	24.9
8	PLA + 0.4wt.% CB + 20wt.% HA	58
9	PLA + 0.4wt%CB + 20wt.% HA	120
10	PLA + 20wt.% HA	147
11	Pure PLA	152

The fibroblast cellular activity was assessed using Alamar blue on days 1, 3 and 5.

In some cases, PLA/CB samples sintered at $\mathbf{I_s}$ less then 14.5W/cm^2 became unstable and started to decay into the cell cultures reflecting their poor initial mechanical integrity. This degeneration of the materials did not affect the cell activity. Samples processed at $\mathbf{I_s}$=14.5 W/cm^2 or higher appeared to be much more stable retaining their shape and structure throughout the whole set of experiments. Disks sintered without CB additives seemed to be rather unstable, regardless their processing at higher laser intensities targeted to their better mechanical properties.

There are no dramatic differences in fibroblasts activity was found for all tested samples. HA incorporation to the disks might reduce slightly cellular activity by possible microparticles physical interaction causing damage to the cell membrane as it was reported previously elsewhere [10, 11]. However, what is rather more important, laser intensity $\mathbf{I_s}$ increase (from 14.5 to 120 W/cm^2) leads to a noticeable gradual decrease in cells activity from samples №7 to №9. This phenomenon can be explained by densification of the scaffolds structure and smoothing of their surfaces (i.e. porosity diminution, which affect the primary cell adhesion and proliferation) due to the deeper melting of PLA particles. However, for the disks sintered without CB particles (samples №10 and №11) even at $\mathbf{I_s}$ = 147 W/cm^2 cells activity was higher compare with the samples №№7-9, because of their porosity has been found similar to the samples №№2 6.

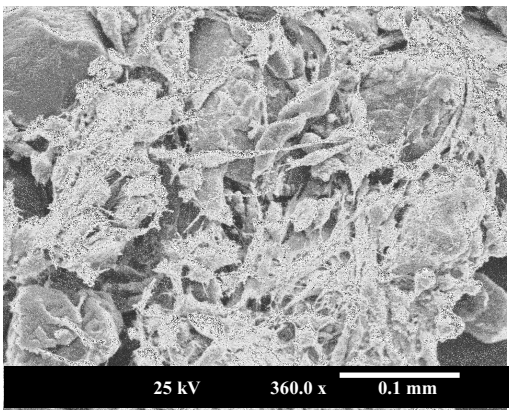

Fig. 2. SEM images of SSLS disks surfaces (sample №2) after 5 days in 3T3 fibroblast cultures.

SEM analysis (Fig. 2) of SSLS samples after 5 days in 3T3 fibroblast cultures shows enhanced cellular activity on the surfaces containing CB particles compare with the surfaces containing HA, where cell attachment and proliferation were found rather low. Surface topography plays an important role in this process as well. The cells attached more favorably to the rougher surfaces as compared with the smooth surface created by intensive polymer melting.

Alamar blue assay and SEM visualisation demonstrated high ability of the scaffolds to support ovine meniscal chondrocytes cell adhesion and colonisation. In excess of

F. Ibrahim, N.A. Abu Osman, J. Usman and N.A. Kadri (Eds.): Biomed 06, IFMBE Proceedings 15, pp. 676-679, 2007
www.springerlink.com ' Springer-Verlag Berlin Heidelberg 2007

85% of cells adhered to the scaffold and were metabolically active. SEM analysis after 24 hrs of culturing the cells on the scaffolds recorded rafts of cells covering approximately 50% of the scaffold surface (Fig. 3).

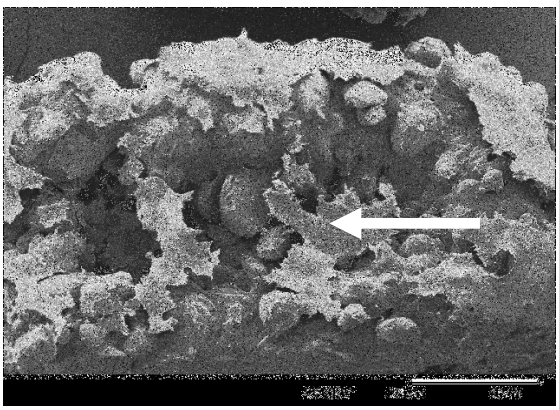

Fig. 3. SEM image of ovine meniscal chondrocytes seeded onto scaffolds. Arrow highlights examples of cell rafts.

C2C12 cells cultured on SSLS scaffolds without HA (samples №№1-4) during 7 days in presence of rhBMP-2 demonstrated high activity and strong shift in the differentiation pathway from myoblastic to osteoblastic type forming osteogenic cells (Fig. 4).

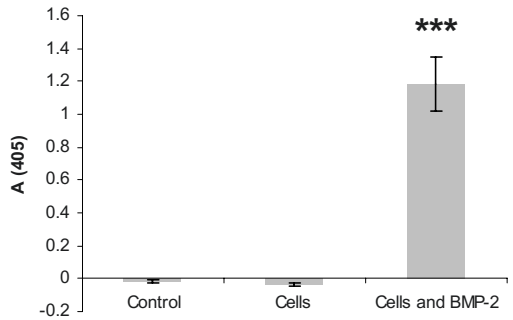

Fig. 4. Alkaline phosphatase production for C2C12 cells in the absence (Cells)/ presence of BMP-2 (Cells and BMP-2). TCP (tissue culture plates) was used as control.

IV. Conclusions

The results of our study unambiguously demonstrate that all SSLS samples were apparently non-toxic. All types of cells readily attached to CB containing surfaces confirming their high biocompatibility. It was shown *in vitro* the acceptable growth and proliferation activity in presence of carbon black at concentration range 0.1÷1.0wt.%. This allowed us to manifest the positive role of CB for cellular activity, which would augment the regenerative potential of these new sintered materials. These promising results encouraged us to further development of SSLS methodology targeted to custom-designed biodegradable scaffolds and implant fabrication.

Acknowledgment

The authors would like to acknowledge the financial support of The Wellcome Trust (CRIG № 073913 and Russian Foundation of Basic Research (Grants №№ 04-02-16933, 04-02-08109). SMH is a Royal Society Wolfson Research Merit Award Holder.

References

1. Vacanti J, Lander R (1993) Tissue engineering. Science, 260:920-925
2. Hutmacher D (2000) Scaffolds in tissue engineering bone and cartilage. Biomaterials, 21:2529-2543
3. Sachlos E, Czernuszka J (2003) Making tissue engineering scaffolds work. Review on the application of solid freeform fabrication technology to the production of tissue engineering scaffolds. European Cells and Materials, 5:29-40
4. Popov V, Antonov E, Bagratashvili V, et al. (2004) Selective laser sintering of 3-D biodegradable scaffolds for tissue engineering. Proc. MRS Fall Meeting, Boston 2003, USA, V.EXS-1, pp.F5.4.1-3
5. Antonov E, Bagratashvili V, Howdle S, et al (2005) 3-D bioactive and biodegradable scaffolds fabricated by selective laser sintering. Advanced Materials, 17:327-330
6. No small matter! Nanotech particles penetrate living cells and accumulate in animal organs , ETC CommuniquØ Issue 76, May-June 2002.
7. Allen M, Butter R, Chandra L, et al (1995) Toxicity of particulate silicon carbide for macrophages, fibroblasts and osteoblast-like cells *in vitro*. Biomed. Mater. Eng., 5:151 159
8. Price R, Waid M, Haberstroh K, et al (2003) Selective bone cell adhesion on formulations containing carbon nanofibers. Biomaterials, 24:1877-1887
9. Katagiri T, Yamaguchi A, Komaki M, et al (1994) Bone morphogenetic protein-2 converts the differentiation pathway of C2C12 myoblasts into the osteoblast lineage. J Cell Biol., 127:1755-66
10. Evans E (1991) Toxicity of hydroxyapatite *in vitro*: the effect of particle size. Biomaterials, 12:574-579
11. Sun J, Tsuang Y, Chang W, et al (1997) Effect of hydroxyapatite particle size on myoblasts and fibroblasts. Biomaterials, 18:683-690

Address of the corresponding author:

Author: V.K. Popov
Institute: Institute of Laser and Information Technologies, Russian Academy of Sciences
City: Moscow
Country: Russia
Email: popov@laser.ru

F. Ibrahim, N.A. Abu Osman, J. Usman and N.A. Kadri (Eds.): Biomed 06, IFMBE Proceedings 15, pp. 676-679, 2007
www.springerlink.com ' Springer-Verlag Berlin Heidelberg 2007

Characterization of Collagen/PEO 600K for Tissue Engineering Scaffold

N.F. Mohd Nasir[1], S.I. Sahidan[2], M. Rampado[2], M.G. Raha[2], N.A. Kadri[2], N. Mohd. Zain[2]

[1] Biomedical Electronics Engineering Program, School of Mechatronics,
Northern Malaysia University College of Engineering, Kangar, Malaysia
[2] Department of Biomedical Engineering, Faculty of Engineering, University Malaya, Kuala Lumpur, Malaysia

Abstract— **In this study, a new material which is collagen/ poly (ethylene oxide) (PEO) blend was developed to determine its possibility as a promising material for tissue scaffold. PEO with average molecular weight of 600,000 and collagen originated from calf skin were dispersed in 0.1 M acetic acid to prepare a concentration of 1 wt% for PEO and 0.15 wt% for collagen. The collagen-PEO600K blend film was then obtained by solution casting method. The morphology and the phase structure of the blends were studied using SEM and XRD. SEM results shown that by having certain ratio of collagen and PEO, the membrane began to developed porous structures which are possible to assist tissue attachment on the scaffold. The X-ray diffractograms demonstrate PEO 600K influences on the blend thus enhancing crystallinity of collagen which explained the membrane morphological structure. Therefore, we concluded that the crystallinity of PEO in the blend is crucial to produce desirable morphological structure of the membrane which is required for a reliable tissue scaffold.**

Keywords— **collagen, PEO, tissue scaffold, SEM, XRD**

I. Introduction

Collagen is readily available, non-toxic and has the fibril architecture in natural tissues. Thus, collagen provides an excellent basis for biomaterials, such as arterial prostheses and artificial skin [1, 2]. The main amino acids in collagen are glycine, proline, hydroxypropline and alanine. The ordered triple helical structure of collagen is stabilized by both interchain hydrogen bonds and by structural water molecules [3-7].

Collagen can be desorbed into the body, is non-toxic, induces only minimal immune response (even between different species), and is excellent for attachment and biological interaction with cells. Collagen may also be processed into a variety of formats, including porous sponges, gels, and sheets, and can be cross linked with chemicals to make it stronger or to alter its degradation rate [8].

Collagen and PEO do not exist together as blends in nature, but specific properties of each may be used to produce synthetic blends that make unique structure and mechanical properties. The miscibility of PEO and collagen with other synthetic polymers and the properties of the blends have been studied previously [9]. However, specific study which directed to develop a product from this material has not been carried out yet.

Thus, this study is aiming to produce scaffold for tissue engineering application. An ideal scaffold should possess following characteristics for desirable biologic response [5]: (i) three-dimensional and highly porous with an interconnected pore network for cell/tissue growth and flow transport of nutrients and metabolic waste, (ii) biodegradable or bioresorbable with a controllable degradation and resorption rate to match cell/tissue growth *in vitro* and/or *in vivo*, (iii) suitable surface chemistry for cell attachment, proliferation and differentiation, (iv) mechanical properties to match those of tissues at the site of implantation, and (v) be easily processed to form a variety of shapes and sizes [10].

Therefore, we intend to correlate the membrane surface to their phase structure of collagen/PEO blend membranes which is important in developing a tissue scaffold. This objective is hoped to be achieved through the characterization of the collagen/PEO blend membranes using Scanning Electron Microscopy (SEM) and X-Ray Diffraction (XRD) techniques.

II. Materials and Methods

Preparation of Collagen, PEO and Collagen/PEO Blend Membranes: Collagen, PEO and collagen/PEO blend membranes were prepared by solution cast method. Collagen (calf skin) from Sigma Aldrich and PEO of molecular weight of 600,000 (Fluka) were dispersed in 0.1 M acetic acid aqueous solution to have a concentration of 0.15wt% for collagen and 1wt% for PEO. The solutions were continuously stirred with a magnetic stirrer for about 1 hour at room temperature. Blends were prepared by mixing both polymers in 4 different ratios: 1:0, 1:1, 3:1, and 0:1.

Table 1 Ratio of Samples

Collagen	Poly(ethylene oxide)
1	0
1	1
3	1
0	1

F. Ibrahim, N.A. Abu Osman, J. Usman and N.A. Kadri (Eds.): Biomed 06, IFMBE Proceedings 15, pp. 680-683, 2007
www.springerlink.com ' Springer-Verlag Berlin Heidelberg 2007

Dispersions were cast on a Petri dish and allowed to dry at atmospheric pressure and room temperature to obtain collagen/PEO blend film. Samples were allowed to evaporate slowly at room temperature until a film form on the Petri dish. When the films have dried, the films were peeled according to the size needed for the XRD and SEM.

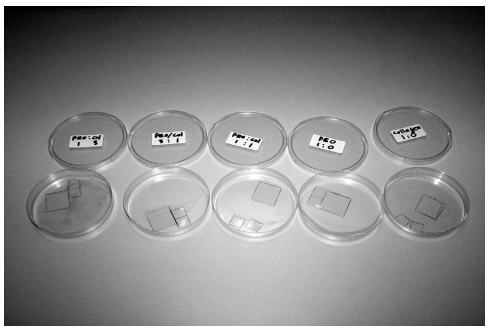

Fig 1. Collagen/PEO blend samples on Petri dish

Scanning Electron Microscope (SEM): Morphological properties of the membranes such as surface porosity, roughness and texture were studied. In this study, dried collagen/PEO blend membrane was mounted on a standard SEM sample holder and fixed to the base. The sample was then sputtered coated with gold coating using a SEM coating system before viewed under EDAX scanning electron microscope with accelerating voltage of 10kV.

X-Ray Diffraction (XRD): Identification and quantitative determination of the various crystalline compounds known as phases were studied using XRD. Thus, the existing phases of developed pure and blend membranes were studied. X-ray diffraction measurements on the membranes were performed.

III. Results and discussions

Scanning Electron Microscope (SEM): The morphologies of pure poly (ethylene oxide) 600K and pure collagen are featured in the figure 2 and figure 3.

The micrograph shows that PEO 600K has crystalline flat lamellae with leave like shape. This feature dominated the morphology of pure PEO membrane. Large spaces between the leave like structure are available through out the surface membrane. The crystalline structure was able to form due to longer evaporation time taken which enabled it to crystallize.

Meanwhile, for the scanning electron micrograph of pure collagen, it is obvious that the surface is rough and uneven. This feature dominated the surface of pure collagen membrane. However, the membrane is poor in porosity.

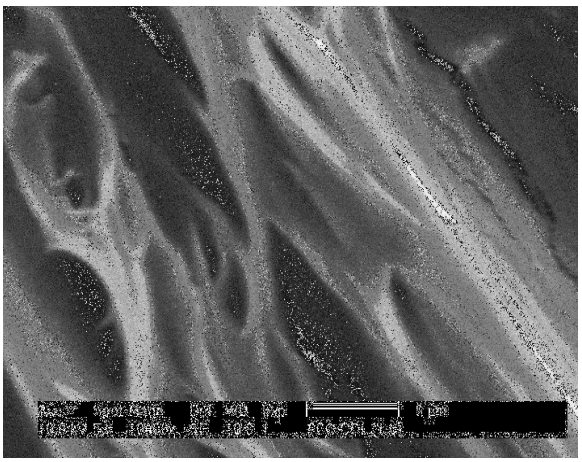

Fig 2. SEM image of pure PEO 600K membrane

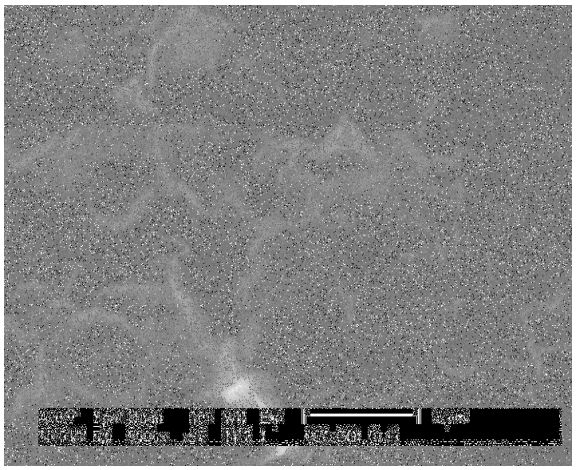

Fig 3. SEM image of pure Collagen

For the membrane with collagen/PEO blend ratio 1:1, a much plainer texture could bee seen from figure 4. We hope that the crystallinity of PEO could improve the porosity of collagen. However, the image shown had proven that equivalent amount of PEO and collagen in the blend does not contribute to the increment of porosity at the membrane surface.

F. Ibrahim, N.A. Abu Osman, J. Usman and N.A. Kadri (Eds.): Biomed 06, IFMBE Proceedings 15, pp. 680-683, 2007
www.springerlink.com ' Springer-Verlag Berlin Heidelberg 2007

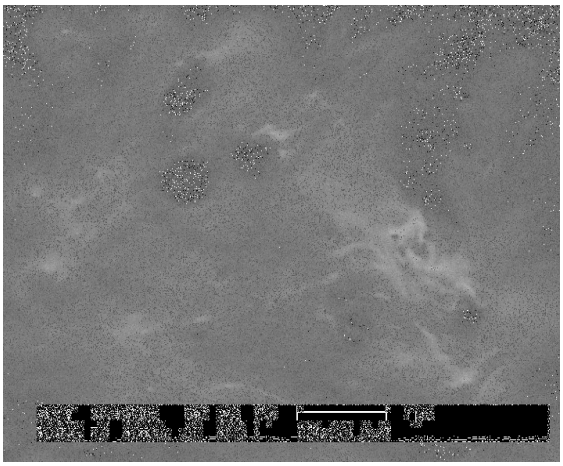

Fig 4. SEM image of Collagen/PEO 1:1 blend membrane

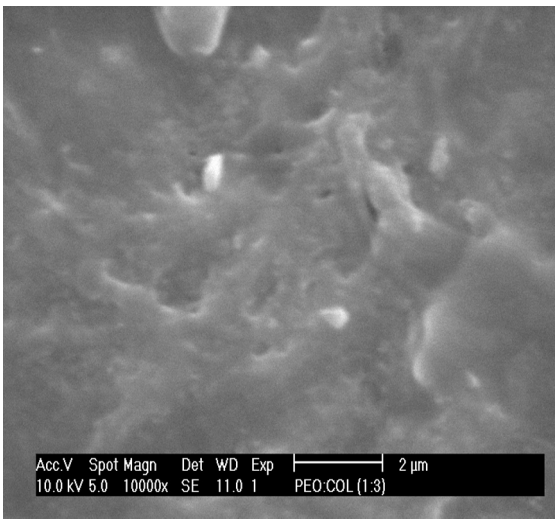

Fig 5. SEM image of Collagen/PEO 3:1 blend membrane

The micrograph for the collagen/PEO blend membrane with 3:1 ratio shows a better improvement in porosity compared to the previous ratio. Few porous structures began to develop among the uneven structure. The uneven structure is more obvious here compared to the pure collagen surface. Thus, the addition of PEO at the right ratio has improved the morphology of collagen. The porosity of the membrane could be attributed to the membrane s higher degree of crystallinity.

X-Ray Diffraction (XRD): The X-ray diffractograms for collagen, PEO and collagen/PEO blend membranes are shown in figure 6. Pure PEO 600K membrane exhibits a sharp and intense peak diffractograms at $2\theta=19^{o}$ and 23^{o} which indicates its high crystallinity. For pure collagen, there is a broad diffraction pattern appeared at $2\theta= 10^{o}$ and a characteristic peak which exist at $2\theta=23^{o}$. This broad pattern and characteristic peak indicates a typical diffraction pattern for collagen.

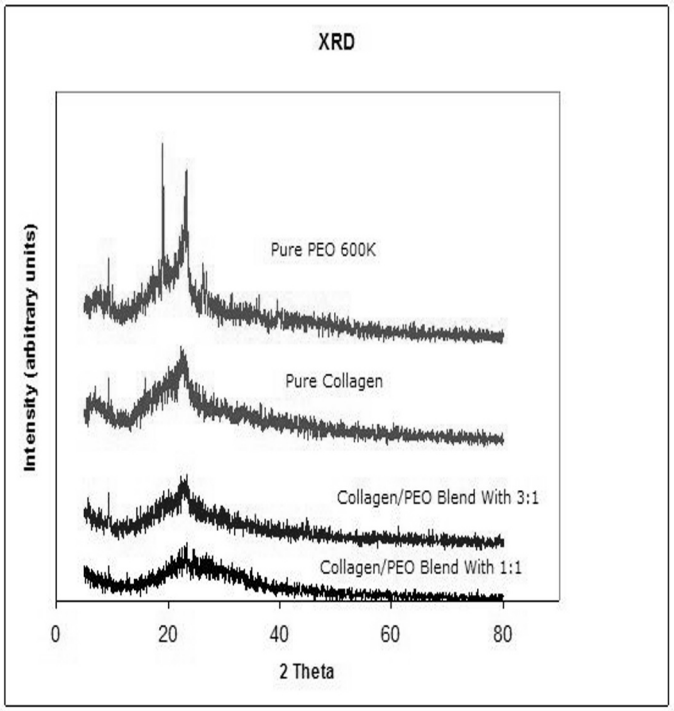

Fig 6. X-ray diffractograms of pure PEO 600K, pure collagen and collagen/PEO 600K blend membranes

Collagen/PEO blend membrane with 1:1 is still highly amorphous although we expect that equivalent amount of PEO blended with collagen will increase the crystallinity of the membrane.

For the diffractograms of collagen/PEO blend with 3:1, the peak at $2\theta=23^{o}$ is more intense and steeper than the peak observed in the previous blend. This indicates that the crystallinity of the membrane has increased.

From the X-ray diffractograms, it is proven that the morphological characteristic of the membrane has direct relationship with the phase structure of the material.

IV. Conclusions

Experimental results showed that, by blending certain amount of PEO 600K to collagen, the porosity of collagen has improved. The beginning of the formation of pores at the surface of the collagen/PEO 3:1 membrane is resulted from the complexation of two materials. The porosity and the existence of uneven structure at the membrane surface

F. Ibrahim, N.A. Abu Osman, J. Usman and N.A. Kadri (Eds.): Biomed 06, IFMBE Proceedings 15, pp. 680-683, 2007
www.springerlink.com ' Springer-Verlag Berlin Heidelberg 2007

were increased maybe due to the blend membrane s higher crystallinity character. Therefore, we concluded that the correlation of the phase structure with the porosity discovered in this research is important to understand the properties of collagen/PEO blend as a promising tissue engineering scaffold.

Acknowledgment

The authors would like to thank Faculty of Engineering, and Faculty of Science of the University of Malaya for providing facilities and permission to carry out the work. The author is also grateful to the Dean of Mechatronics School, Northern Malaysia University College of Engineering (KUKUM), Prof. Dr. Sazali Yaacob and the Head of Department of Biomedical Engineering, University of Malaya, Dr. Noor Azuan Abu Osman for their continuous support.

References

1. Huc A (1985) Collagen biomaterial characteristics and applications. J. Am. Leather Chem. Assoc. 80:195-212
2. Matsumoto K, Nakamura T, Shimizu Y, Ueda H, Sekine T, Yamamoto Y, Yiyotami Y, Takomoto Y (1999) A novel surgical material made from collagen with high mechanical strength: A collagen sandwich membrane. OSAIO J. 45(4): 288-292
3. Bailey AJ, Paul RG (1998) Collagen-is not so simple protein. J. Soc. Leather Technol. Chem.82: 104-108
4. Van der Rest R, Garrone M (1991) Collagen family of proteins. FASEB J.5:2814-2823
5. Ellis DO, AcGavin S (1970) The structure of collagen-on X-ray study.J. Ultrastruct. Res.32:191-211
6. Prockop J, Fertala A (1998) The collagen fibril: The almost crystalline structure. J. Struct. Biol.122:111-118
7. Speer DP, Chvapil M, Eskelson CD, Vlreich J (1980) Biological effects of residual glutaraldyde in glutaraldehyde-tanned collagen biomaterials. J.Biomed.Mater. Res. 14:753-764
8. Cascone MG, Sim B, Downes S (1995) Blends of synthetic and natural polymers as drug delivery systems for growth hormone. Biomaterials 16:569-574
9. Sionkowska A (2006) Photochemical stability of collagen/PEO blends. J. Photochem.&Photobio: Chem. 177:61-67
10. Marovdas NG (1973) Chemical &mechanical requirements for fibroblast adhesion, Nature 244:353

Address of the corresponding author:

Author: Nashrul Fazli Bin Mohd Nasir
Institute: Biomedical Electronics Engineering Program,
School of Mechatronics, Northern Malaysia University
Colege University
Street: Jalan Kangar-Arau
City: Jejawi, Perlis
Country: Malaysia
Email: nashrul@kukum.edu.my

F. Ibrahim, N.A. Abu Osman, J. Usman and N.A. Kadri (Eds.): Biomed 06, IFMBE Proceedings 15, pp. 680-683, 2007
www.springerlink.com ' Springer-Verlag Berlin Heidelberg 2007

Effect of TGF-β and β-Estradiol on Extracellular Matrix Secretion in Articular Chondrocyte Culture

Sharaniza Ab-Rahim[1], T. Kamarul[1], Azlina A. Abbas[1] and L. Selvaratnam[2]

[1] Department of Orthopaedic Surgery,
[2] Department of Anatomy, Faculty of Medicine, University of Malaya, Kuala Lumpur, Malaysia

Abstract— **Articular cartilage extracellular matrix (ECM) plays a crucial role in regulating chondrocyte functions via cell-matrix interaction, cytoskeletal organization and integrin-mediated signaling. The effects of transforming growth factor-β (TGF- β) and β–estradiol on extracellular matrix have remained controversial in chondrocyte studies though it has been proven that cartilage responds to these factors *in vivo*. In our study, we examined the effect of these factors on modulating glycosaminoglycan secretion. Articular chondrocytes from rabbits were cultured, and the effects of supplementing 10ng/ml of TGF-β, 10nM of β-estradiol, and a combination of both factors were compared. The synthesis of sulphated glycosaminoglycan (GAG) was shown to be enhanced in the TGF-β treated cultures and when TGF-β and β-estradiol were both used. However, β-estradiol does not appear to affect GAG deposition.**

Keywords— **Chondrocytes, Glycosaminoglycan, Extracellular matrix (ECM), Collagen type II**

I. Introduction

Articular cartilage, a flexible and semi-rigid connective tissue, offers limited intrinsic repair once damaged or injured. This is due to its poor healing ability and regeneration related to its avascularity and lack of nerve supply. Lesions occurring within the articular cartilage substance are almost always associated with pain, stiffness, altered function of the joint and, in most instances, progress to secondary osteoarthritis [1].

Articular cartilage extracellular matrix (ECM) plays a crucial role in regulating cell functions via cell-matrix interaction, cytoskeletal organization and integrin-mediated signaling. ECM also plays a critical part in binding cells of the tissue in place and is very tissue specific. Thus, poor secretion of extracellular matrix can be attributed to cell disorientation and low level of collagen synthesized compare to native cartilage. Studies have also demonstrated that by adding factors such as transforming growth factor (TGF-β) and β-estradiol can also affect the synthesis of extracellular matrix [2, 3]. However, the effects of both factors on extracellular matrix have remained controversial in chondrocyte studies though it has been proven that cartilage responds to these factors *in vivo* [4].

In this study, cells were allowed to grow and divide *in vitro* using cell culture techniques. Although numerous cells can be generated using this technique, weeks of *in vitro* culture is required to expand them to attain sufficient population density and differentiated phenotype to be effective for clinical applications. Thus, we applied a growth factor(s) in our chondrocyte cultures to determine their effects on extracellular matrix synthesis and the quality of chondrocytes produced.

II. Materials and methods

A. Chondrocyte Isolation

Primary chondrocytes were isolated from articular cartilage of adult New Zealand White Rabbits. Cartilage from knee, hip and shoulder joints were removed from the underlying bones and subsequently digested with collagenase type II (0.25%) at 37°C and 250 rpm for overnight. The digested tissues were then centrifuged at 1200 x g for 10 minutes. A supernatant layer produced following centrifugation was discarded and the pellet was then cultured in DMEM/Ham s F-12 Nutrient Mixture supplemented with 10% fetal bovine serum (FBS) and ascorbic acid (25 μg/ml). Cells were maintained in the growth medium as monolayer cultures at 37°C and 5% CO_2 for 3 weeks. The growth medium was changed every other day.

B. Seeding of Monolayer Culture

Confluent cells were released from monolayer using 0.05% trypsin-EDTA. After centrifugation and removal of the supernatant, chondrocytes were counted using a haemacytometer.

Cells harvested were resuspended in growth medium and seeded into 6-well culture dishes and 4-chamber culture slides. Cultures were then maintained for 24 hours.

C. Culture Treatment

The monolayer cultures were divided into 4 groups with identical growth medium (DMEM/Ham s F-12, 10% FBS

F. Ibrahim, N.A. Abu Osman, J. Usman and N.A. Kadri (Eds.): Biomed 06, IFMBE Proceedings 15, pp. 684-687, 2007
www.springerlink.com ' Springer-Verlag Berlin Heidelberg 2007

and 25 μg/ml ascorbic acid). Group I was nourished with growth medium without any other additives. Group II was nourished with the same growth medium supplemented with 10 nM of β-estradiol. Group III was supplemented with 10 ng/ml TGF-β and Group IV was supplemented with both 10 nM of β-estradiol and 10 ng/ml TGF-β.

Cultures were treated for 48 hours prior to collection of the culture medium and stored at -20°C until further analysis.

D. Protein Assay

Protein content of the cell lysate was determined using a Bio-Rad DC protein assay kit (Bio-Rad Laboratories, USA). Lysed cells were mixed with Bradford reagents and absorbance read at 750 nm. Standards were prepared from bovine serum albumin (BSA).

E. Quantitative Assay for Glycosaminoglycans

The glycosaminoglycans (GAG) content in the monolayer culture media was determined using a Blyscan Glycosaminoglycan Assay kit (Biocolor, UK). This assay is based on the precipitation and resolubilization of GAG/1,9-dimethylmethylene blue complex [5]. The absorbance at 656 nm was measured on the spectrophotometer and compared to a plot of standards prepared from purified 4-chondroitin sulphate (derived from bovine trachea) to determine GAG content.

F. Immunohistochemistry

Immunohistochemistry was carried out using a Dako immunostaining kit (DakoCytomation, USA) to verify the presence of type II collagen in the culture. Briefly, slides were washed with TBS buffer and treated with 0.03% hydrogen peroxide containing sodium azide prior to incubation with collagen type II primary antibody or PBS alone (negative control) for 1 hour. Slides were then incubated with horseradish peroxidase (HRP) conjugated goat anti-mouse secondary antibody IgG for 30 minutes. The samples were stained with diaminobenzidine (DAB kit, DakoCytomation, USA) according to the protocol of the manufacturer.

III. Results

Quantitative Analysis: Values for quantitative GAG analysis were normalized to protein content (μg GAGs/mg protein) to determine which sample group accumulated GAG with greater efficiency.

GAG accumulation comparisons between different treatment groups are shown in Table 1. The TGF-β treated group demonstrated significantly greater GAG accumulation per mg protein (p<0.05) compared to the untreated group (Figure 1). Co-incubation with TGF-β and β-estradiol also showed significant GAG accumulation compared to the untreated group (p<0.05). However no statistically significant difference in GAG accumulation was observed in the β-estradiol treated group.

Table 1 Total GAGs accumulated per mg protein produced by monolayer chondrocyte culture treatment groups. Values are presented as means – standard deviation.

Treatment	GAG Content (g GAGs/mg protein
Untreated	0.435 – 0.18
β-Estradiol (10 nM)	0.480 – 0.13
TGF-β (10 ng/ml)	0.879 – 0.36
β-Estradiol (10 nM) + TGF-β (10 ng/ml)	0.796 – 0.25

n=9

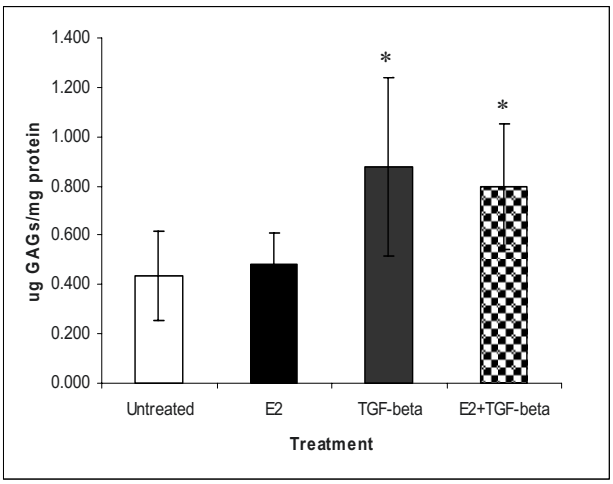

Fig. 1 Expression levels of glycosaminoglycan produced by chondrocyte culture in different treatment. Significance level between control and treatment at p<0.05 (E2: β-estradiol)

Immunohistochemistry: Immunostaining of monolayer chondrocytes cultured on chamber slides was positive for intracellular type II collagen (Fig. 2a). Monolayer chondrocytes cultured with β-estradiol, TGF-β and combination of both β-estradiol and TGF-β demonstrated comparable positivity of type II collagen deposition (Fig. b, c and d). However, the intensity of the collagen type II expression at pericellular level differed, with TGF-β treated cultures exhibiting more intense staining compared to untreated and β-estradiol treated cultures.

F. Ibrahim, N.A. Abu Osman, J. Usman and N.A. Kadri (Eds.): Biomed 06, IFMBE Proceedings 15, pp. 684-687, 2007
www.springerlink.com ' Springer-Verlag Berlin Heidelberg 2007

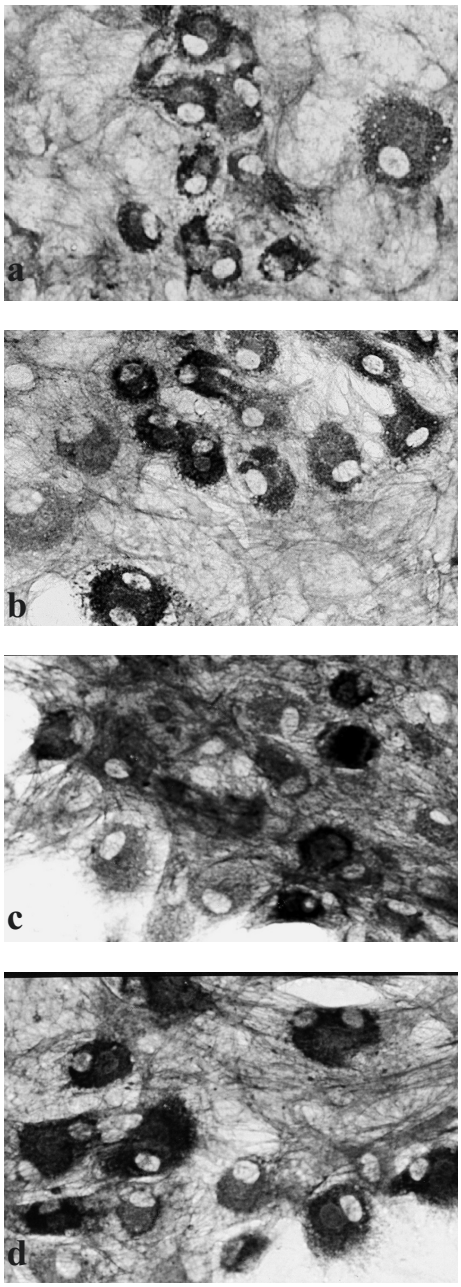

Fig. 2 Immunohistochemical staining for collagen type II in monolayer chondrocyte cultures. (a) Untreated monolayer chondrocyte culture, (b) Monolayer chondrocyte culture treated with β-estradiol, (c) TGF-β treated culture and (d) co-incubation of β-estradiol and TGF-β.

IV. Discussion

This study was conducted to investigate the influence of TGF-β and β-estradiol on chondrocyte extracellular matrix secretion. Earlier studies have shown that chondrocytes behave and respond differently to TGF-β, including at various stages of chondrocyte differentiation and in different culture models [6, 7]. In our study, TGF-β treated cultures demonstrated significantly greater GAG accumulation ($p<0.05$) compared to the control group. This was further verified by immunostaining data which showed high levels of collagen type II expression in TGF-β treated culture compared to other treatments. These findings are consistent with previous studies which have shown that the effect of TGF-β is dependant on distribution of surrounding matrix [4]. On the other hand, the amount of GAG accumulation did not appear to be affected by β-estradiol despite histological examination which demonstrated the presence of increased collagen type II expression in the culture. However, the staining intensity of collagen type II in β-estradiol treated cultures was not as strong as in TGF-β treated cultures. This could explain lower GAG accumulation in β-estradiol cultures compared to TGF-β treated cultures which is in consistent with a previous hypothesis that the effect of TGF-β is related to the presence of pericellular matrix [8]. Co-incubation of β-estradiol and TGF-β showed a GAG secretion comparable with treatment with TGF-β alone. This data suggest that β-estradiol could act synergistically with TGF-β and up-regulate GAG accumulation since TGF-β alone enhanced both GAG accumulation and type II collagen. On the other hands, β-estradiol seems to only enhanced type II collagen but not as strong as TGF-β. With combination of both factors, the synthesis of collagen type II in the culture was increased, and this effect could trigger β-estradiol receptors, thus enhance the GAG accumulation in the culture. This data suggested that effect of TGF-β and β-estradiol is not only related to up-regulation of all components of pericellular matrix but most likely to be specific to regulating collagen type II level.

V. Conclusion

The results of our study suggested that TGF-β and β-estradiol response to glycosaminoglycan synthesis are related to collagen type II levels in chondrocyte culture and may involve in collagen type II mechanism of action. However, the role of collagen type II in this process must be further elucidated.

Acknowledgment

The authors would like to acknowledge that this study was funded by a research grant from the National Biotechnology Directorate (NBD) under the 8th Malaysia Plan (06-02-02-003 BTK/ER/022).

F. Ibrahim, N.A. Abu Osman, J. Usman and N.A. Kadri (Eds.): Biomed 06, IFMBE Proceedings 15, pp. 684-687, 2007
www.springerlink.com ' Springer-Verlag Berlin Heidelberg 2007

REFERENCES

1. Brittberg M et al. (1996) Rabbit articular cartilage defects treated with autologous cultured chondrocytes. Clinical Orthopaedics and Related Research 326:270-283
2. Van Beuningen HM et al. (1994) Transforming growth factor-1 stimulates articular chondrocyte proteoglycan synthesis and induces osteophyte formation in the murine knee joint. Laboratory Investigation 71(2):279-290
3. Wluka AE et al. (2001) Users of oestrogen replacement therapy have more knee cartilage than non-users. Ann. Rheum. Dis. 60:332-336
4. Luyten FP et al. (1994) Recombinant bone morphogenetic protein-4, transforming growth factor-beta1, and activin A enhance the cartilage phenotype of articular chondrocytes in vitro. Experimental Cell Research 210:224-229
5. Farndale RW, Buttle DJ and Barrett AJ (1986) Improved quantitation of sulfated glycosaminoglycans by use of dimethylene blue. Biochim. Biophys. Acta 883:173-177
6. Van der Kraan P et al. (1992a) Differential effect of transforming growth factor β on freshly isolated and cultured articular chondrocytes. J. Rheumatol 19: 140-145
7. Hauselmann HJ et al. (1994) Phenotypic stability of bovine articular chondrocytes after long-term culture in alginate beads. J. Cell Sci. 107:17-27
8. Van Osch GJVM et al. (1998) Effect of transforming growth factor-β on proteoglycan synthesis by chondrocytes in relation to differentiation stage and the presence of pericellular matrix. Matrix Biology 17:413-424

Address of the corresponding author:

Author: Sharaniza Ab. Rahim
Institute: Department of Orthopaedic Surgery, Faculty of Medicine, University of Malaya
Street: Jalan Pantai Bharu
City: 50603, Kuala Lumpur
Country: Malaysia
Email: sharaniza_abrahim@yahoo.co

F. Ibrahim, N.A. Abu Osman, J. Usman and N.A. Kadri (Eds.): Biomed 06, IFMBE Proceedings 15, pp. 684-687, 2007
www.springerlink.com ' Springer-Verlag Berlin Heidelberg 2007

Human Adipose Precursor Cells Seeded on Hyaluronic Scaffolds: a Pilot Clinical Trial

F. Stillaert[1], C. Di Bartolo[2], J. Hunt[3] and P. Blondeel[1]

[1] Department of Plastic and Reconstructive Surgery, University Hospital Ghent, Gent, Belgium
[2] Fidia Advanced Biopolymers s.r.l., Abano Terme, Padova, Italy
3 University of Liverpool, UK Centre for Tissue Engineering, Liverpool, United Kingdom

Abstract— **Introduction: Treatment of soft tissue defects requires the generation of a long-term stable tissue construct which resides in an equilibrium with adjacent anatomical structures. Histioconductive approaches use biocompatible and –degradable scaffolds seeded with tissue- and host-specific precursor cells which are implanted at desired loci. Those scaffolds act as a temporarily nutritional extracellular matrix which guide tissue formation by ensuring cell-cell and cell-matrix interactions. We investigated whether hyaluronic acid scaffolds could be used as biocompatible scaffolds to generate an adipose tissue construct in vivo.**

Materials and Methods: Twelve volunteers (20 to 35 years) were included. Lipoaspirate was obtained with consent through the Department of Plastic Surgery with approval from the Human Ethics Committee. Isolated preadipocytes were expanded and seeded (0.5×10^6 cells) on hyaluronic acid-based biodegradable polymeric scaffolds (HYAFF11®). Four days later the engineered bio-hybrid (ADIPOGRAFT®), seeded with autologous preadipocytes, and a cell-free control scaffold were implanted subcutaneously. Three time courses (2, 8 and 16 weeks) were set up with each group consisting out of four volunteers. Harvested specimens were analyzed using standard histology and immunohistochemistry.

Results: There were no adverse effects with both cell-seeded and non-seeded scaffolds being well tolerated. Considerable volume loss of the non-seeded scaffolds was observed compared to the cell-seeded group, indicating progressive integration and biocompatibility of the latter within the host.

However, histological analysis showed no consistent or clear differences between the adipograft samples and the HYAFF11® unseeded scaffolds. Implanted materials were incompletely infiltrated with cells at 2 weeks but by 8 weeks all void spaces were filled with cells with considerable deposition of extracellular matrix.

Conclusion: This clinical trial concludes that hyaluronic acid scaffolds are biocompatible, stable cell-carriers to be used for tissue engineering purposes in humans. Further research will identify crucial cues which need to be considered to enhance preadipocyte survival with subsequent differentiation.

Keywords— **Preadipocytes, hyaluronic acid, scaffold, biocompatibiliy**

I. Introduction

Tissue engineering is a multidisciplinary endeavour with the aim of generating new tissues for clinical uses such as transplantation and reconstruction, or repair of congenital or acquired tissue defects. In particular, adipose tissue engineering aims to create autologous, long-term stable fat constructs for soft tissue contour repair. The everyday practice of free fat grafting is *in se* a reversed approach as terminally differentiated, isolated and vascular disrupted adipocytes are relocated into a matrix-deficient recipient bed. Progressive cell necrosis and resorption due to delayed neo-vascularization results in fibrotic tissue deposition with subsequent volume loss. A supportive extracellular matrix (ECM) or scaffold is mandatory to enhance or guide cell survival, migration, proliferation and differentiation.

Tissue engineering research convergence biological and engineering sciences and identifies basic functions of biological systems and points of cellular control. Translation of this knowledge results in the manufacturing of biomaterials which could offer therapeutical alternatives when approaching soft tissue loss or damage.

II. Materials and Methods

A. Scaffolds

Sponges of HYAFF 11, a linear derivative of hyaluronic acid modified by complete esterification of the carboxylic function of glucuronic acid with benzyl groups [1], were supplied by Fidia Advanced Biopolymers (Abano Terme, Italy). The structure of these sponges shows open, interconnecting pores with pore size varying between 30 and 340 μm. HYAFF 11 biomaterial is spontaneously degraded and resorbed. During this process, hyaluronic acid is released. The ADIPOGRAFT bio-hybrid is engineered by seeding autologous preadipocytes onto the biocompatible HYAFF 11 scaffold.

F. Ibrahim, N.A. Abu Osman, J. Usman and N.A. Kadri (Eds.): Biomed 06, IFMBE Proceedings 15, pp. 688-691, 2007
www.springerlink.com ' Springer-Verlag Berlin Heidelberg 2007

B. Adipose tissue harvest

Twelve healthy volunteers, aged 20-35 years, were included in this trial according to specific inclusion criteria. Lipoaspirate material was obtained (5-10 ml) through a liposuction under local anaesthesia (Xylocain 1% without adrenalin) with consent through the department of Plastic Surgery of the University Ghent and with approval from the Human Research Ethics Committee. Fat tissue was aspirated through a Coleman ASP I (2.5 mm) liposuction cannula connected to a luer-lock disposable syringe (10 ml). Donor sites were the lower lateral abdominal areas in all cases. Without further processing the syringes with the lipoaspirate were stored in a special cooled foamy kit.

C. Cell culturing and bio-hybrid engineering

Lipoaspirate was immediately sent off to Fidia Advanced Biopolymers Laboratories where it was washed 1:1 with PBS (3*) and digested 1:1 at 37°C with a sterile filtered collagenase solution (collagenase Type I 500 U/ml, 8% FCS, 0.02M Hepes and 0,02IU-0,02mg/ml Pen/Strep, in DMEM:F12) for one hour. Prior to the clinical trial experiments demonstrated that 0.15 M-0.2 M cells/ml of fat are usually recovered after collagenase digestion. As 5-8 ml were digested, cell recovered were in the range of 0.75- 1.6 millions. After centrifugation and removal of the supernatant, cells were resuspended in a preadipocyte culture medium (DMEM:F12 supplemented with 10% FCS, 1nM bFGF, 0,02IU-0,02mg/ml Pen/Strep) to obtain a final volume of 100-200 µl. The cell suspension was seeded onto an hemi-cylindrical HYAFF®11 sponge (diameter =1 cm, height= 0.4 cm) which has been hydrated previously for 24 hrs in a preadipocyte culture medium and vacuum dried. Cell seeding was performed by moving the cell-suspension containing pipette on all surfaces of the sponge ($0.5 * 10^6$ cells). The seeded hemi-cylindrical HYAFF®11 sponge is now called ADIPOGRAFT .

Considering a 10% cell loss during the seeding procedure (evaluated during experiments on cell seeding efficiency), cells seeded on each semi-cylindrical ADIPOGRAFT sponge were between 0.67 M and 1.4 M.

Seeded and non-seeded HYAFF®11 sponges were incubated and supplied with preadipocyte culture medium after 3 hours of incubation. The medium was changed after 24 hours. Sponges were washed with PBS 48 hours later and stored in an appropriate vacuum sealed double sterile package ready for transport. Before packaging, LAL test was performed on the medium submerging the sponges to check for bacterial endotoxines.

D. Scaffold implantation

Four days after the initial liposuction the ADIPOGRAFT bio-hybrid and a non-seeded control HYAFF®11 scaffold were implanted. The implantation was performed under local anaesthesia. Blunt dissection through a 1cm median sub-umbilical incision created two paramedian subcutaneous pockets (1.5 by 1 cm), the right and left paramedian areas being the recipient sites for the ADIPOGRAFT and HYAFF 11 control scaffolds respectively (Fig. 1). Seeded and non-seeded sponges were unpacked and immediately implanted avoiding any trauma to their fragile consistency. The implants were not weighed before implantation. The wound was closed with resorbable subcutaneous Vicryl 5/0 (Ethicon) sutures and a running intracuticular non-resorbable Ethilon 6/0 suture.

Three time courses (2, 8 and 16 weeks) were included with each group consisting out of four volunteers which were followed on an outpatient basis.

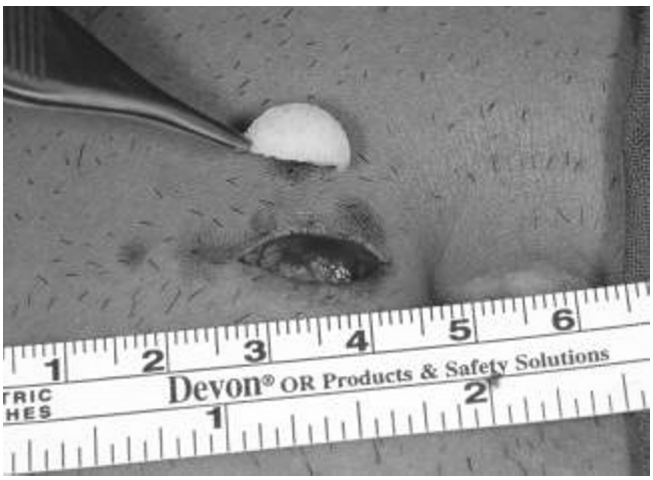

Fig. 1: HYAFF 11 sponge prior to implantation in a surgically created subcutaneous pocket.

E. Harvest and histology

At the specific time points the tissue specimens were harvested under local anaesthesia through the same incision. Careful microsurgical dissection excised a margin of surrounding fat tissue to ensure complete removal of the scaffolds which were easily identified peroperatively. Specimens were not weighed due to the presence of native and fibrotic tissue which are influencing the final weight.

F. Ibrahim, N.A. Abu Osman, J. Usman and N.A. Kadri (Eds.): Biomed 06, IFMBE Proceedings 15, pp. 688-691, 2007
www.springerlink.com ' Springer-Verlag Berlin Heidelberg 2007

Harvested tissues were analyzed histologically using Hematoxylin and Eosin, Van Geison and Von Kossa staining. (20 point) between authors info and the beginning of the paper.

III. RESULTS

Despite their fragile consistency, surgical manipulation of all hyaluronic acid scaffolds appeared to be easy.

During the entire postoperative follow-up no systemic nor local adverse effects or complications occurred. Both the cell-seeded and non-seeded scaffolds were well tolerated by the volunteers and integrated completely within the surrounding subcutaneous tissue. Clinical examination of the recipient sites could easily identify both implanted scaffolds (Fig. 2).

There were no surgical complications during the explantation of the scaffolds in all groups. ADIPOGRAFT scaffolds were easily detected preoperatively and surrounded by a thin fibrous capsule separating the scaffold from surrounding tissue. HYAFF 11 scaffolds on the other hand had a more gel-like appearance at harvest time indicating disintegration and biocompatibility of the hyaluronic acid construct. Two HYAFF 11 scaffolds were not detectable at the explantation procedure at 16 weeks. Macroscopically, all ADIPOGRAFT scaffolds were more voluminous compared to their acellular control implants (Fig. 3).

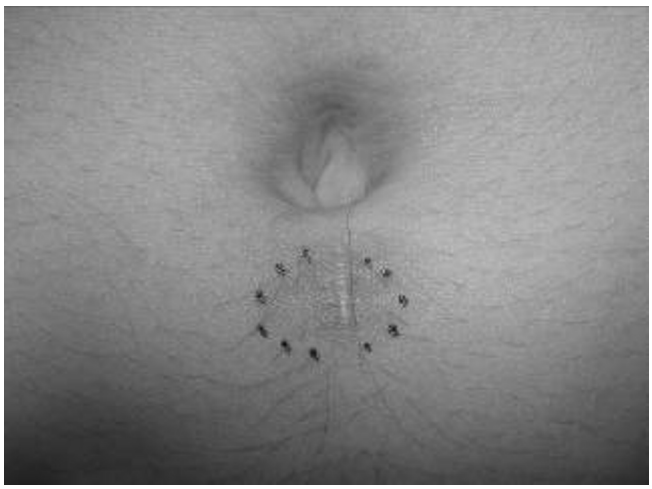

Fig. 2: Palpable implants at 8 weeks. Volume loss of the HYAFF11 control scaffold compared to the cell-seeded ADIPOGRAFT implants.

Fig. 3: Explanted ADIPOGRAFT scaffold at 8 weeks.

Histological analysis showed an incomplete cellular infiltration at 2 weeks. By 8 weeks all void spaces were filled with non-specific cells which were contained in a fibrous extracellular matrix network. Inflammatory cells were constantly observed in all specimens and there was no calcification.

Despite previous promising in vivo findings in mice [2], differentiated adipocytes were not observed indicating no proliferation or differentiation of the implanted preadipocytes. The degraded hyaluronic acid scaffold also lacked any penetration of neo-capillaries a finding for poor angiogenic induction support.

IV. CONCLUSION

Despite promising results in rodents and excellent biocompatibility and degradability characteristics hyaluronic acid scaffolds do not support preadipocyte survival and are not (adipose) tissue conductive.

The observed volume maintenance and tissue integration is promising but the deficient angiogenic penetration which compromises further organogenesis - needs to be further investigated to assess whether this histio-conductive strategy can be used in future soft tissue augmentation procedures.

ACKNOWLEDGMENT

We wish to thank the nursing staff of the Department of Plastic Surgery UZ Gent, for their assistance and patience during the surgical procedures and follow-up of the volunteers.

F. Ibrahim, N.A. Abu Osman, J. Usman and N.A. Kadri (Eds.): Biomed 06, IFMBE Proceedings 15, pp. 688-691, 2007
www.springerlink.com ' Springer-Verlag Berlin Heidelberg 2007

References

1. Rastrelli A, Beccaro M, Biviano F, Calderini G, and Pastorello A. (1990) Hyaluronic acid esters, a new class of semisynthetic biopolymers: Chemical and physicochemical properties. Clin. Implant. Mater. 9: 199.
2. Von Heimburg D, Zachariah S, Low A and Pallua N. (2001) Influence of different biodegradable carriers on the in vivo behavior of human adipose precursor cells. Plast. Reconstr. Surg. 108(2): 411-420.

Address of the corresponding author:

Author: Filip Stillaert, MD
Institute: Department of Plastic and Reconstructive Surgery
University Hospital Ghent
Street: De Pintelaan 185
City: Gent, 9000
Country: Belgium
Email: fillip.stillaert@ugent.be

F. Ibrahim, N.A. Abu Osman, J. Usman and N.A. Kadri (Eds.): Biomed 06, IFMBE Proceedings 15, pp. 688-691, 2007
www.springerlink.com ' Springer-Verlag Berlin Heidelberg 2007

Hybrid nanofiber scaffolds of polyurethane and poly(ethylene oxide) using dual-electrospinning for vascular tissue engineering

J.W. Shin[1], H.J. Shin[2], S.J. Heo[1], Y.J. Lee[1], Y.M. Hwang[1], D.H. Kim[1], J.H. Kim[1] and J.W. Shin[1]

[1] Team of BK21 / Dept. of Biomedical Engineering, Inje University, Gimhae, Korea
[2] School of Materials Science, Japan Advanced Institute of Science and Technology, Ishikawa, Japan

Abstract— **The objective of this study is to investigate the potential of dual-electrospun polymer based structure for vascular tissue engineering, especially for the medium or small size blood vessels. Polyurethane(PU), which is known to be biocompatible in this area, was electrospun along with poly(ethylene oxide) (PEO). Concentration of PU was fixed at 20wt%, while that of PEO was set from 15 to 35wt%. Morphological observation (SEM and porosity) and cellular responses were tested before and after extracting PEO from the hybrid scaffolds by soaking the scaffolds into distilled water. The diameter of PEO fibers were ranged in 200~500nm. The lower concentration of PEO tended to show beads. The porosity of the scaffolds after extracting PEO was highly increased with higher concentration of PEO as expected. Also, higher proliferation rate of smooth muscle cells was observed at higher concentration of PEO than at the lower concentration and without PEO. As conclusions, this dual electrospinning technique combined with PU and PEO is expected to overcome the current barrier of cell penetration by providing more space for cells to proliferation.**

Keywords— **Electrospinning, Polyurethane, Poly(ethylene oxide), Smooth muscle cell, Vascular tissue engineering**

I. Introduction

Cardiovascular disease is one of the significant causes of death all over the world. Especially, annual increase in coronary artery disease has been reported serious [1]. Current treatments, such as bypass graft and/or artificial prosthesis, have shown limitations. Although autologous vessels, such as saphenous vein, have been typically used for small diameter graft, most patients don t have suitable vein for use due to vascular disease, restriction of length of vessel and previous harvest [2]. To overcome current barriers as mentioned, many investigators have combined various type of natural and synthetic scaffolds to use for artificial vascular tissue engineering [3].

Various methods to process the vascular structural scaffold have been studied and introduced utilizing particle leaching, freeze drying, fiber bonding, phase separation, or rapid prototyping [4]. Among these, nanofibers manufactured by electrospinning technique have been recently paid attention. First, electrospun nanofibers show structural similarity to extracellular matrix (ECM) that plays an important role to promote tissue regeneration *in vivo* [5-8]. And thickness of electrospun scaffold can be easily controlled by adjusting various parameters. However, electrospun nanofibers still have limitations. One of them is that cells were hard to penetrate into the scaffold, even the surface characteristics are remarkable [4, 5, 9]. To solve this problem, we utilized dual-electrospinning technique of PEO and PU. Then, PEOs was subtracted from the dual-spun hybrid type scaffold. The concept of this study was shown in Fig.1.

II. Materials and methods

A. Electrospinning of PEOs

PEO solutions with various concentration ranged from 15wt% to 35wt% were spun. Each solution was contained a 10-ml syringe with a needle of 18-G. The feeding rate was set at 1ml/h by controlling a syringe pump (KD scientific, 781100, USA). The distance between the needle (anode) and a collector (cathode) was 15cm, when the electric potential was set 15kV.

B. Dual-electrospinning of PU and PEOs

In this case, 25wt% and 35wt% of PEO was simultaneously spun with 20wt% of PU. Each polymer solution was placed in a 10-ml syringe with a needle of 18-G. The feeding and other conditions were same as described in previous section. The size of collector was 15cm × 15cm, approximately.

Solution of PU (Pellethane 2102-75A; DOW Chemical Corp., MI, USA) was prepared with *N,N*-dimethylformamide (DMF; Junsei Chemical Co., Japan) at concentration of 20wt%.

C. Morphological Observations

The morphologies of electrospun nanofiber structures were observed using a scanning electron microscopy (SEM, JSM-6700F; JEOL, Japan) at an accelerating voltage of 5kV before and after extracting PEO from the dual-electrospun structures. Digital image processing technique was adopted to investi-

F. Ibrahim, N.A. Abu Osman, J. Usman and N.A. Kadri (Eds.): Biomed 06, IFMBE Proceedings 15, pp. 692-695, 2007
www.springerlink.com ' Springer-Verlag Berlin Heidelberg 2007

gate the fiber diameters utilizing image-analysis software (Image J; http://rsb.infor.nih.gov/ij/docs/index.ht-ml).

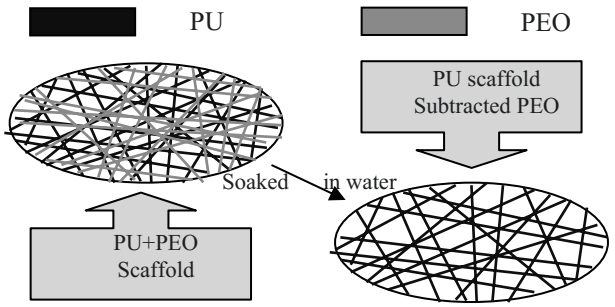

Fig. 1 Concept of this study

D. Cell isolation and culture

Enriched populations of smooth muscle cells (SMCs) were separated from femoral vein of 4-week-old New Zealand White Rabbit [10]. These were cultured in 75-cm^2 flask in culture medium containing Dulbecco s Modified Eagle medium with high glucose (DMEM-HG, Gibco BRL) supplemented 10% fetal bovine serum and 1% penicillin/streptomycin(100U/ml) at 37°C with 5% CO_2. The culture medium was changed every other day.

E. MTT assay

Cell proliferation was measured using a Cell Proliferation Kit (MTT; Roche Diagnosis Corp., IN, USA). For this, each hybrid scaffold was soaked in distilled water for 12 hours and dried in vacuum dryer for 24h. Each scaffold was cut into 1cm × 1cm. Then, SMCs were seeded (5×10^4 cells/㎠) on nanofiber scaffold for up to 7 days. Second passage SMCs were used in this study. Specimens were harvested at 1, 3 and 7 days.

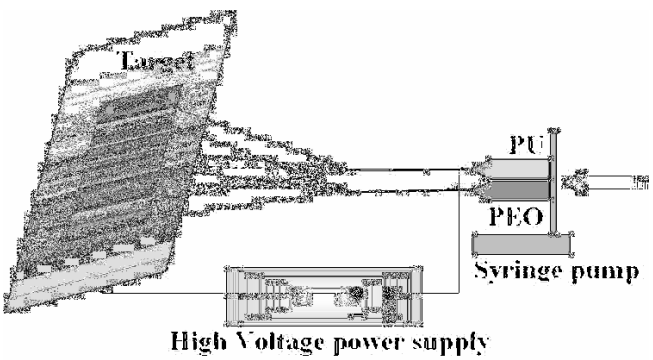

Fig. 2 Schemes of dual-electrospinning

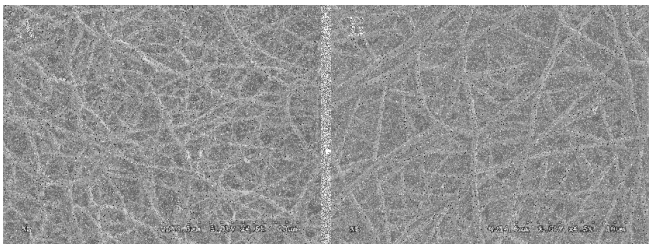

Fig. 3 Hybrid scaffolds of PU and PEO (A) Before the PEO extraction (B) After the PEO extraction in distilled water

F. Measurement of porosity

Porosity of each scaffold was deputed to Korea Chemicals Inspection & Testing Institute to measure. That was determined with the use of a mercury porosimeter.

G. Statistical analysis

The data in this study was presented as mean values –SD. Statistical analysis was performed using a one-way analysis of variance (ANOVA). When ANOVA indicated a significant difference among groups, the difference was evaluated using least significant difference (LSD). A confidence level of 95% (p<0.05) was chosen for statistical significance.

III. Results

A. Morphological characteristic of PEO nanofibers

SEM images for electrospun PEOs are shown in Fig.3. The lower concentration tends to show beads scattered on

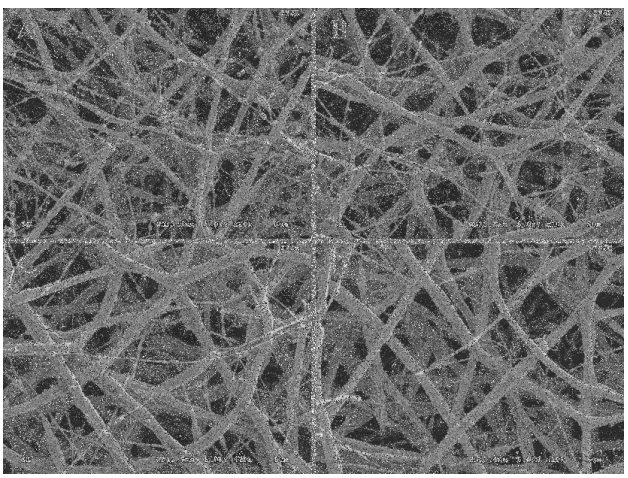

Fig. 4 PEO fibers (A) 20wt% (B) 25wt% (3) 30wt% (4) 35wt%

F. Ibrahim, N.A. Abu Osman, J. Usman and N.A. Kadri (Eds.): Biomed 06, IFMBE Proceedings 15, pp. 692-695, 2007
www.springerlink.com ' Springer-Verlag Berlin Heidelberg 2007

Table 1 Porosity of scaffolds

Group	PU only	PU(PEO) : 20(35) (not extracted PEO)	PU(PEO) : 20(35) (extracted PEO)
Porosity (%)	19.8657	26.4916	76.4005

the surface, while the others do not show. The diameter of fibers tends to increase as the concentration increases. The range of the size in diameters was 200-500nm. However, the morphology did not look different when the concentration is more than 25wt% [Fig. 5]. As the reason PEOs were spun with PU in this study was to provide affordable space for cells to proliferate, the concentration of 25 and 35wt% were chosen.

B. Characterization of dual-spun scaffolds

PEOs in hybrid scaffolds were extracted by immersing the scaffolds into distilled water. Figure 3 shows the features of PEO extraction before and after. No shrinkage was observed. Porosity was dramatically increased after PEO was extracted from the scaffold [Table 1].

C. Proliferation of SMCs

SMCs seeded on the scaffolds were propagated over time. Scaffolds spun with PEO showed higher proliferation rate than those made of PU alone. The scaffolds with higher concentration (35wt%) of PEO showed significant improvement of proliferation than those with lower concentration(25wt%) for up to 7days of culture [Fig. 6].

IV. Discussion

It is well known that extracellular environment influences cell behavior such as morphology, proliferation, functionality and cell-cell interactions. In natural tissues, cells are surrounded by extracellular matrix, which has physical structural features ranging from nanometer scale to micrometer scale. The nanometer scale architecture of ECM is believed to have great potential in the application of tissue engineering. Electrospinning, one of the fabrication methods of nanofiberous scaffolds, has been recently adopted and utilized for the fabrication of the scaffolds.

One of the key factors of tissue engineering is to provide three-dimensional biomimetic architecture. The vascular wall is composed of three basic structural layers; intima, media and adventitia. These layers consist of different cells; endothelial cells in internal layer, smooth muscle cells in medial layer and connective tissues in outer layer, respectively. Cells need porous structure, i.e., space, for proliferation and differentiation. However, the electrospun scaffold with PU alone does not show preferable space in three dimension, even the cellular responses on the surface are improved relative to the membrane type scaffolds. Therefore, to provide fully 3-dimensional structure for the cells to penetrate in regarding to natural structure of blood vessels the extraction of solvable materials from hybrid structure could be another promising technique in this area. However, the porosity should be adjusted to prevent possible leakage.

To construct affordable scaffolds which meet this condition, dual-electrospinning technique was adopted. First, the PEO was electrospun to investigate the effects of its concentration on the fiber morphology. Lower concentration did not show uniform patterns in SEM images. Based on this, we selected two types of concentration, 25 and 35wt%, for dual electrospinning. After extracting the PEO contents

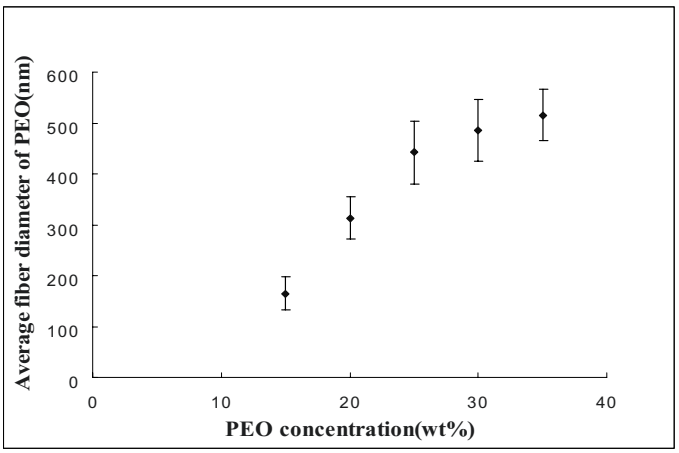

Fig. 5 PEO fiber diameter along with its concentration

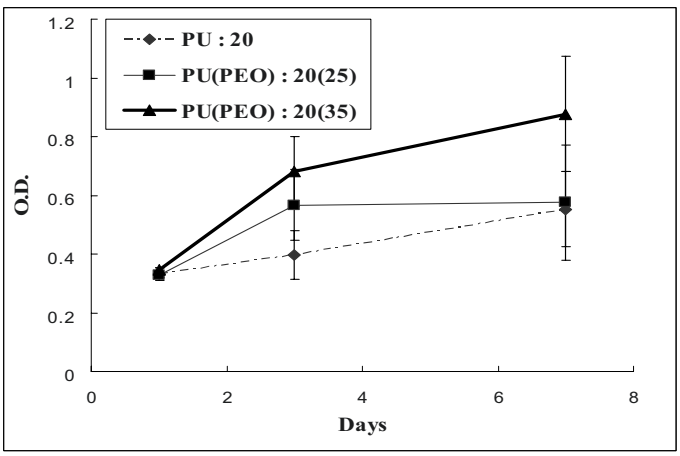

Fig. 6 Proliferation of SMCs with various scaffolds

F. Ibrahim, N.A. Abu Osman, J. Usman and N.A. Kadri (Eds.): Biomed 06, IFMBE Proceedings 15, pp. 692-695, 2007
www.springerlink.com ' Springer-Verlag Berlin Heidelberg 2007

from the dual-spun scaffolds, remarkable space was observed and measured in porosity test. In addition, the MTT assay proved that the increased space (35wt% of PEO) caused the significant increase in cell proliferation during the test periods [Fig. 6].

Some other studies suggested the blending technique with PEO and other polymers. However, we utilized dual-spinning method, instead. This dual spinning kept the structure of PU even after extracting the PEO. Also, PEO was extracted before cells were seeded, even PEO could be eventually extracted after seeding the cells. We only performed the MTT assay to investigate of proliferation of SMCs and found that there were not serious damages to the cells due to the residual PEO. However, further investigation is needed to confirm the residual PEO.

V. Conclusions

The dual-spinning of PEO and PU was successfully confirmed and its potential was confirmed by investigating morphology, cellular responses, and porosity. Then the potential of this hybrid type of scaffold was evaluated and confirmed. However, further studies are under way to optimize the fabricating conditions for hybrid scaffold using PU and PEO. Also various parameters are being studied such as differentiation, interaction of endothelial cells after being seeded onto the surface of scaffold with SMC.

Acknowledgment

This research was partially funded by Korea Science and Engineering Foundation (No. R01-2004-000-10164-0).

References

1. V. Barron, E. Lyons, C. Stenson-cox et al. (2003) Bioreactors for cardiovascular cell and tissue growth: a review. Annals of Biomedical Engineering 31:1017-1030
2. Anita C. Thomas, Gordon R. Campell, Julie H. Compbell. (2003) Advances in vascular tissue engineering. Cardiovascular pathology 12:271-276
3. Lian Xue, Howard P. Greisler. (2003) Biomaterials in the development and future of vascular grafts. J Vasc Surg 37:472-480
4. X.M. Mo, C.Y. Xu, M. Koraki et al. (2004) Electrospun P(LLA-CL) nanofiber: a biomimetic extracellular matrix for smooth muscle cell and endothelial cell proliferation. Biomaterials 25:1883-1890
5. Chencue Xu, Ryuii Inai, Masaya Kotaki et al. (2004) Electrospun nanofiber fabrication as synthetic extracellular matrix and its potential for vascular tissue engineering. Tissue Engineering 10(7/8)1160-1168
6. Chang Hun Lee, Ho Joon Shin, In Hee Cho et al. (2005) Nanofiber alignment and direction of mechanical strain affect the ECM production of human ACL fibroblast. Biomaterials 26:1261-1270
7. Wei He, ZuWei Ma, Thomas Yong et al. (2005) Fabrication of collagen-coated biodegradable polymer nanofiber mesh and its potential for endothelial cells growth. Biomaterials 26:7606-7615
8. Kent S. Haas, Steven J. Phillips, Anthony J. Comerota et al. (1991) The architecture of adventitial elastin in the canine infrarenal aorta. The Anatomical Record 230:86-96
9. H. Yoshimoto, YM shin, H.Terai et al. (2004) A biodegradable nanofiber scaffold by electrospinning and its potential for bone tissue engineering. Biomaterials 24:2077-2082
10. Soo-Hong Lee, Byung-Soo Kim, Soo Hyen Kim et al. (2003) Elastic biodegradable poly(glycolide-co-caprolactone) scaffold for tissue engineering. J Biomed Mater Res A 66(1):29-37

Address of the corresponding author:

Author: Jung-Woog Shin
Institute: Dept. of Biomedical Engineering, Inje University
Street: 607 Eu-bang Dong
City: Gimhae
Country: Republic of Korea
Email: sjw@bme.inje.ac.kr

F. Ibrahim, N.A. Abu Osman, J. Usman and N.A. Kadri (Eds.): Biomed 06, IFMBE Proceedings 15, pp. 692-695, 2007
www.springerlink.com ' Springer-Verlag Berlin Heidelberg 2007

In Vitro Augmentation of Collagen Matrix Formation - Applications in Tissue Engineering

R.R. Lareu[1,2], I. Arsianti [1], K.S. Harve[1], Y. Peng[1] and M. Raghunath[1,3]

[1]Tissue Modulation Laboratory, Division of Bioengineering, Faculty of Engineering, National University of Singapore
[2]NUS Tissue Engineering Program, Department of Orthopedic Surgery, Yong Loo Lin School of Medicine, National University of Singapore
[3]Department of Biochemistry, Yong Loo Lin School of Medicine, National University of Singapore

Abstract— **The construction of stable engineered tissue depends on the formation of a functional connective tissue produced by cells locally. A major component of connective tissue is collagen. Its deposition into a stable matrix depends on the enzymatic extracellular conversion of procollagen to collagen. This step is very slow *in vitro* and we hypothesized that this is due to a lack of crowdedness and insufficient excluded volume effect (EVE) in culture media. We used neutral (670 kDa) and negatively charged dextran sulfate (DxS, 500 kDa) to create EVE in cell cultures and to enhance *in vitro* matrix formation by accelerating procollagen conversion. Biochemical analyses in two human fibroblast lines revealed mostly unprocessed procollagen in uncrowded culture medium, whereas in the presence of DxS, procollagen conversion occurred and most of the collagen was associated with the cell layer. Immunocytochemistry confirmed DxS-related collagen deposition that colocalized with fibronectin. The large neutral dextran showed in identical concentration ranges no effects which correlated well with its smaller hydrodynamic radius as determined by dynamic light scattering. This predicted a 10 times bigger crowding power of DxS and benchmarks it as a potentially promising crowding agent facilitating the formation of extracellular matrix *in vitro*.**

Keywords— **collagen deposition, excluded volume effect**

I. Introduction

The deposition of a collagen matrix depends on the conversion of *de novo* synthesized procollagen to collagen in the extracellular space or immediately before its release into the same [1]. This limiting step for collagen matrix deposition is very slow *in vitro* both in monolayer cultures and 3D scaffolds [2]. Surprisingly, this knowledge is not widely spread in the tissue engineering field and many research groups measure the amount of collagen I in culture media, where it actually does not belong [3]. Obviously, this culture artifact represents a serious bottleneck in the creation of coherent and stable tissue structures prior to implantation or for *in vitro* systems (e.g. in drug discovery). We hypothesized that this *in vitro* deficit stems from a deficiency in crowding of standard culture media. It is well known that biological systems function as highly crowded intra- and extracellular environments. Crowding is an inevitable phenomenon that results from the large size and shape properties of the macromolecules that exclude volume they occupy, thus denying that space for other molecules [4]. Macromolecular crowding causes the excluded-volume effect (EVE) that has been appreciated to have manifold effects in biology [5]. It has been mostly characterized for the interior of cells, but this principle works also in the extracellular environment. Cells are embedded in the extracellular matrix (ECM) which consists of the largest macromolecules present in the human body. Cells isolated from tissues face a totally different situation in standard cell culture. Derived from a highly complex and dense ECM they are now bathed in large volumes of aqueous medium and have little associated ECM. The only exogenous source of macromolecules in cell culture is fetal calf serum, a crucial additive for cell survival and continued replication. It contains ~80 g/l of protein, a concentration that can cause significant crowding effects. However, used at 10% (v/v) in routine cell culture the final protein concentration reaches only ~8 g/l. Clearly, standard routine culture media are far from being crowded.

Scarce literature have indicated earlier that the addition of midsized neutral polymers like dextran T-40 (40 kDa) and small polyethyleneglycol (3.35 kDa) accelerated the processing of procollagen and its deposition [6]. The negatively charged dextran sulfate (DxS; 500 kDa) was later described to be more efficient in comparison to the above very much smaller neutral crowders [7]. These data were never followed up for biotechnical applications. Our preliminary study with two fibrogenic human cell lines significantly extend these data with regards to quantitation and immunocytochemical localization of collagen. In addition, we show for the first time dynamic light scattering data that explain the dramatic differences in the crowding potential of two differently charged but comparably sized macromolecular dextrans in our read-out system, collagen deposition.

F. Ibrahim, N.A. Abu Osman, J. Usman and N.A. Kadri (Eds.): Biomed 06, IFMBE Proceedings 15, pp. 696-699, 2007
www.springerlink.com ' Springer-Verlag Berlin Heidelberg 2007

II. Materials and Methods

A. Tissue culture

Normal embryonic lung fibroblasts (WI-38) and adult hypertrophic scar fibroblasts (HSF) were routinely cultured in Dulbecco s Modified Eagle Medium with 10% fetal bovine serum (FBS). Fibroblasts were seeded at 50,000 cells/well in 24 plates and were allowed to attach for 24 hrs. To induce collagen synthesis cells were supplemented with 100 μM of L-ascorbic acid phosphate. Macromolecular crowders were dextran sulfate (DxS) (500 kDa; pK Chemicals A/S, Koge, Denmark) and neutral dextran 670 (ND670; FlukaChemie GmbH, CH-9471, Sigma-Aldrich). Crowding treatment was for 5 days. Culture media and cell layers were harvested and digested separately with porcine gastric mucosa pepsin (2500 U/mg; Roche Diagnostics Asia Pacific) in a final concentration of 100 μg/ml. Samples were incubated at RT for 2 hrs with gentle shaking followed by neutralization with N NaOH.

B. Sodium dodecylsulfate-polyacrylamide gel electrophoresis (SDS-PAGE)

Medium and cell layer samples were analyzed by SDS-PAGE under non-reducing. Formats used were either small (Mini-Protean 3; Bio-Rad Laboratories, Singapore) or large (16 x 18 cm; SE 600; Hoefer, CA, USA). Protein bands were stained with the SilverQuest kit (Invitrogen) according to the Manufacturer s protocol. Densitometric analysis of wet gels was performed on the GS-800 Calibrated Densitometer (BioRad).

C. Protein extraction and Western blotting

Culture medium and washed cell layers were extracted with a buffer containing 150 mM NaCl, 50 mM Tris (pH 7.5), 5 mM EDTA, 1% Triton-X100 and Protease Inhibitor Cocktail Tablets. Subsequently, 20 μl of protein extract (even cell numbers) for each sample were mixed with 1x Laemmli buffer and 2 μl of β-mercaptoethanol and subjected to small format SDS-PAGE as above. Proteins were then electroblotted onto nitrocellulose membrane. Membranes were blocked with 5% non-fat milk in TBST, pH 8, for 1 hr at RT. Subsequently, the primary antibody (mouse anti-human collagen I; Monosan, Uden, The Netherlands) at a 1/500 dilution with 1% non-fat milk in TBST was incubated for 1 hr at RT. Bound primary antibody was detected with goat anti-mouse HRP (Pierce Biotechnology Inc., IL, USA) diluted 1/1000 in 1% non-fat milk in TBST for 1 hr at RT. The membrane was then incubated with Super Signal West Dura substrate (Pierce Biotechnology) and chemiluminescence was captured with an LAS-1000 Luminescent Image Analyzer (Fuji).

D. Dynamic light scattering (DLS) and viscosity measurements

Dextrans and bovine serum albumin (BSA) were prepared in HBSS, pH 7.4, in various concentrations. DLS runs were carried out for each of the single macromolecule solution using the DynaPro DLS instrument (Wyatt Technology, DynaPro™ , CA, USA) at 20°C by loading 20μl samples. Readings were obtained at 8258 Å and analyzed using the Protein Solutions™ software (Wyatt Technology). Viscosity measurements at the corresponding concentrations were done using the ARES100 FRT Rheometer. Based on the viscosity values, necessary corrections were applied for calculating the hydrodynamic radii.

III. Results

A. Dextran sulfate promotes collagen deposition in vitro

The peptic treatment of culture media and cell layers enabled us to get a clear picture of collagen distribution in both compartments by destroying non-collagenous proteins while leaving fibrillar collagens intact. Under standard (and ascorbate supplemented) conditions WI-38 and HSF fibroblast cultures showed the majority of the collagen I to be in the medium and small amounts of it in the cell layer (Fig. 1). Densitometry showed an increase of collagen I deposition (based on $\alpha_{1(I)} + \alpha_{2(I)}$ bands) by >6-fold for WI-38 and >11-fold for HSF (not shown). The DxS results were corroborated by the immunocytochemical analysis of both HSF and WI-38 cells (data not show).

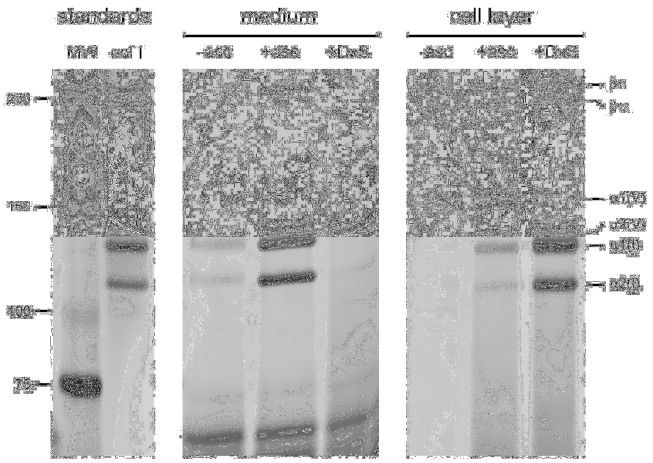

Fig. 1. Dextran sulfate promotes collagen deposition in cultured WI-38 fibroblasts.

F. Ibrahim, N.A. Abu Osman, J. Usman and N.A. Kadri (Eds.): Biomed 06, IFMBE Proceedings 15, pp. 696-699, 2007
www.springerlink.com ' Springer-Verlag Berlin Heidelberg 2007

When we tested the effects of DxS over a concentration range we found that at 10 μg/ml a significant portion of collagen was still present in the medium fraction (Fig. 2A), whereas at 500 μg/ml, collagen bands were difficult to resolve in cell layer (Fig. 2B) and medium fraction. Virtually complete collagen deposition and absence of collagen from the medium occurred only in the presence of 50 and 100 μg/ml of DxS. In separate experiments, the larger neutral dextran did not showed an effect from 100 μg/ml up to 2 mg/ml (Table 1).

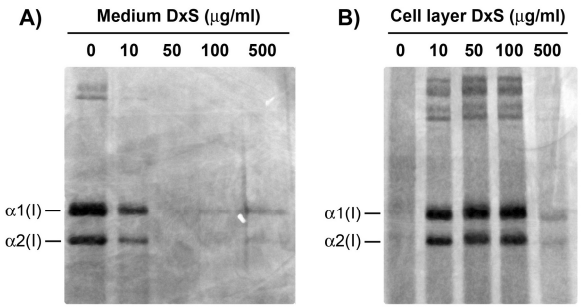

Fig. 2. Dose-dependent stimulation of collagen deposition by DxS in WI-38 fibroblast culture.

Table 1. Marginal effects of neutral dextran sulfate 670.

	Standard Culture		ND 670 (100 μg/ml)		DxS 500 (100 μg/ml)	
	M	CL	M	CL	M	CL
	25.2	3.5	17.1	0.5	1.8	14.5
ratio	7.2 : 1		34.2 : 1		1 : 8	
	2 mg/ml		16.1	0.7		
ratio			23 : 1			

B. Dextran sulfate increases collagen-related enzymatic processes in vitro

To demonstrate that the increased collagen deposition in the presence of DxS is due to correct enzymatic processing, total proteins from culture medium and cell layer fractions were analysed by immunoblotting using a collagen antibody that recognises the central portion of the molecule. Standard cultures contained collagen only in the form of procollagen in the medium, no procollagen or collagen was detectable in the cell layer (Fig. 3). In the presence of DxS, only converted collagen was detected in the cell layer, the medium was devoid of either procollagen or collagen. This could only have been the result of specific activity of procollagen C- and N-proteinases.

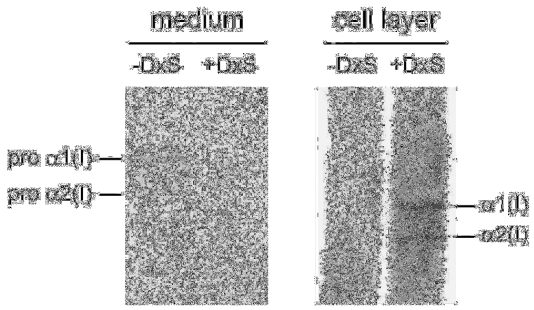

Fig. 3. Procollagen conversion is induced by DxS *in vitro*.

C. Hydrodynamic radius and viscosity measurements

DLS is a method of estimating the diffusion of macromolecules that are in Brownian motion in solution and hence their hydrodynamic radii by measuring the change in intensity of scattered light over time [8]. In physiological salt solution and at concentration of 100 μg/ml the hydrodynamic radii were 46.4 – 0.3nm (DxS 500), 21 – 0.2nm (ND670) and 4.24 – 0.05nm (BSA, 67 KDa). Viscosity of solutions were ~1 cP in all cases, equaling that of water. The data demonstrate that a negatively charged macromolecule has a much larger hydrodynamic radius than a neutral macromolecule of comparable size. This suggests a stronger crowding efficiency because the EVE is a combination of both steric repulsion and electrostatic repulsion, compared to only steric repulsion by neutral molecules [9].

IV. Discussion

Collagens are the most abundant proteins in the human body and are extremely important also in tissue engineering as adhesion and signaling matrix and creating cohesion between single cells and cell layers. The bulk of collagen is represented by the fibrillar collagen I. It is synthesized by mesenchymal cells and exported into the extracellular space as water soluble procollagen. The subsequent proteolytic removal of the C- and N-terminal propeptide converts procollagen to collagen. Only collagen can self-assemble to a water insoluble matrix (fibers). A low procollagen conversion rate is the default state of cell culture systems which means an excess of procollagen in the culture medium and poor collagen matrix formation resulting in low productivity for tissue building. We demonstrate here by applying the biophysical principle of EVE that this cell culture-intrinsic problem can be overcome. The data suggest that crowding of the culture medium with DxS (500 kDa) confined the space of molecules of comparable size and thus increased the interaction of the substrate (procollagen) with respective

F. Ibrahim, N.A. Abu Osman, J. Usman and N.A. Kadri (Eds.): Biomed 06, IFMBE Proceedings 15, pp. 696-699, 2007
www.springerlink.com ' Springer-Verlag Berlin Heidelberg 2007

enzymes for trimming (C- and N-proteinase, respectively) resulting in an increase of collagen deposited in the matrix and a massive decrease of procollagen in culture medium.

Interestingly, EVE appeared also to influence the ratios between collagen types deposited into the collagen matrix. Ascorbate supplemented fibroblasts under standard conditions showed basal deposition of collagen I and V. This suggests the presence of heterotypic fibrils with substantial collagen V content. However, in the presence of DxS collagen V was hardly detectable and collagen I become the dominant collagen type.

Initially, the increased conversion of procollagen in metabolically labelled fibroblast cultures was shown in the presence of midsized dextran T-40, and small polyethylene glycol (3.35 kDa) [6]. Although later studies suggested the very much larger dextran sulfate (500 kDa) to be more efficient than the originally introduced crowders [7], no data with similarly sized neutral dextran were generated up to now. In our direct comparison DxS 500 outperformed ND 670 dramatically in its ability to accelerate procollagen conversion. Our DLS data point to the hydrodynamic radius as a key factor to explain this phenomenon. At 100 µg/ml DxS showed a 2.21 fold larger Rh than ND670 which translates into a 10.8 fold larger volume due to charge effects and hydration. Therefore, a negatively charged macromolecule such as DxS 500 is a superior crowder compared to a neutral polymer of similar size under physiologic conditions at similar concentrations. This implies that for the same volume occupancy, far less DxS molecules are required than that for ND670 and thus lower concentrations. We would deem this advantageous because at high concentrations macromolecular solutions tend to be undesirably viscous. Looking into serum proteins as potential crowding agents we studied serum albumin (67 kDa) representing roughly 60% of serum proteins. In standard (10% FCS) culture conditions its predicted concentration would be 5 mg/ml. According to its hydrodynamic radius its volume would be 1300 times smaller than that DxS 500 and to achieve the same crowding effect as DxS 500 it would have to be present in a concentration as high as 130 mg/ml, up to almost three times higher than to be found in pure serum.

For the concentration that showed optimal procollagen conversion we have calculated an occupied volume of 5% for 100 µg/ml DxS by (i) calculating the volume of the sphere of each DxS molecule from the hydrodynamic radius and (ii) based on the number of DxS molecules present at the given concentration and the molar weight of each DxS molecule. This volume occupancy was sufficient to accelerate crucial enzymatic steps for collagen deposition and stabilization. We speculate that DxS imposed a steric exclusion effect on the proteins present in the medium resulting in their spatial confinement. This would lead to the increase in the total free energy of macromolecules in solution, as well as a much higher strength of interaction between substrates and enzymes, in this case procollagen and the respective proteinases.

V. Conclusions

We conclude that EVE is a valuable factor to be involved in tissue engineering applications and that negatively charged macromolecular crowders like DxS will have an important role to play in the construction of tissues.

Acknowledgements

The authors would like to thank Dr Phan Toan Thang (Department of Surgery, Yong Loo Lin School of Medicine, NUS) for the kind donation of HSF. MR wishes to acknowledge support by the NUS Tissue Engineering Program (NUSTEP) and the Office of Life Sciences. This work was supported by grants from the National Medical Research Council of Singapore (CPG/003/2004), the Faculty of Engineering, Office of Research FRC (R-397-000-017-112) and a start-up grant from the Office of Life Science (R-397-000-604-712) and the Provost of NUS (R-397-000-604-101). I.A. was a recipient of a graduate research scholarship from the Graduate Program in Bioengineering and the Division of Bioengineering, NUS.

References

1. Canty EG and Kadler KE (2005) Procollagen trafficking, processing and fibrillogenesis. J Cell Sci 118:1341
2. Goldberg B and Sherr CJ (1973) Secretion and extracellular processing of procollagen by cultured human fibroblasts. Proc Natl Acad Sci USA 70:361
3. Nusgens B, Merill C, Lapiere C et al. (1984) Collagen biosynthesis by cells in a tissue equivalent matrix in vitro. Collagen Rel Res 4:351
4. Hall D and Minton AP (2003) Macromolecular crowding: qualitative and semiquantitative successes, quantitative challenges. Biochim Biophys Acta 1649:127
5. Minton AP (2000) Protein folding. Thickening the broth. Curr Biol 10:R97
6. Bateman JF, Cole WG, Pillow JJ et al. (1986) Induction of procollagen processing in fibroblast cultures by neutral polymers. J Biol Chem 261:4198
7. Bateman JF and Golub SB (1990) Assessment of procollagen processing defects by fibroblasts cultured in the presence of dextran sulfate. Biochem J 267:573
8. Lanza RP, Langer R and Vacanti J (2000) Principles of Tissue Engineering. San Diego, London: Academic Press, 2nd edition
9. Prockop DJ, Sieron AL and Li SW (1998) Procollagen N-proteinase and procollagen C-proteinase: two unusual metalloproteinases that are essential for procollagen processing probably have important roles in development and cell signaling. Matrix Biol 16:399

F. Ibrahim, N.A. Abu Osman, J. Usman and N.A. Kadri (Eds.): Biomed 06, IFMBE Proceedings 15, pp. 696-699, 2007
www.springerlink.com ' Springer-Verlag Berlin Heidelberg 2007

Repair of Rabbit Focal Articular Cartilage Defects with Autologous Chondrocytes Embedded in Alginate

T. Masjudin[1], Pan-Pan Chong[1], T. Kamarul[1], L. Selvaratnam[2], S. Ab-Rahim[1] and T. Sara[1]

[1] Department of Orthopaedic Surgery, Faculty of Medicine, University of Malaya, 50603 Kuala Lumpur
[2] Department of Anatomy, Faculty of Medicine, University of Malaya, 50603 Kuala Lumpur

Abstract— **To evaluate the ability of autologous chondrocyte transplantation to repair articular cartilage defects, autologous chondrocytes embedded in alginate beads were implanted in focal cartilage defects created in 9 New Zealand white rabbits. After 4 weeks of cartilage damage, the right knee was repaired via autologous chondrocyte-alginate constructs transplantation and the left knee was left untreated (control group). The quality of cartilage tissues of both knees was then compared at 3 months following the procedure, as reflected by the quantitative analysis of glucosaminoglycan (GAG) in the cartilage and histological examination of the tissue in accordance to the Brittberg scoring scale. Macroscopic examination showed better regeneration of the defective area following chondrocyte-alginate transplantation repair compared to the non-treated site. Biochemical analysis revealed significantly higher cellular expression of GAG in the treated knee as compared to the non-treated knee [1.12 ± 0.48 µg GAGs / mg protein vs. 0.81 ± 0.17 µg GAGs / mg protein, respectively; *p*=0.008]. The mean Brittberg scores was significantly higher in the treated knee as compared to control knee [6.00 ± 1.23 vs. 1.89 ± 1.54; *p*=0.007]. This result can be explained by the fact that chondrocytes cultured in alginate gel beads retained their ability to synthesize cartilage-specific molecules. The alginate beads were perfectly biocompatible with chondrocytes and surrounding cartilage tissue. These findings also indicated that chondrocyte-alginate transplantation has shown enhanced repair results compared to the non-treated measures.**

Keywords— **Autologous chondrocyte transplantation (ACT), alginate beads, cartilage damage/defect, repair.**

I. Introduction

The ability of cartilage to repair after injury is very limited due to the absence of a neurovascular supply [1, 2]. Traditional treatment methods, such as abrasion chondroplasty and drilling, have not produced reliable and lasting cartilage repair. Recently, the more biological therapies such as autograft transplantation have produced encouraging results. Successful repair of articular cartilage lesions of the human knee by autologous chondrocyte transplantation was first reported by Brittberg *et al.* in 1994 [3].

Essentially, autologous chondrocytes were extracted from non-weight-bearing areas of an affected knee during arthroscopy and cultured in monolayer for 3 5 weeks to expand the cell population. The cultured cells were then implanted into the cartilage defect in a planned second operation and cover with a periosteal flap [3].

However, although numerous models are available for the cultivation of chondrocytes, most of these models such as monolayer or organoid (high-density) cultures, have a limited culture period and other disadvantages including poor cartilage phenotype [4, 5]. Thus, three-dimensional culture of chondrocytes within alginate beads may allow cartilage cells to maintain their differentiated status.

Alginate, a negatively charged unsulphated carbohydrate copolymer of α-L-guluronic acid and β-D-mannuronic acid, polymerises and forms a three-dimensional gel in the presence of calcium ions or other multivalent ions and can be rapidly depolymerised in the presence of a calcium chelator [6-8]. Long-term cultures of chondrocytes in alginate beads can maintain their chondrocytic phenotype [9], which allows the cells to assemble an extracellular matrix in cartilage tissue.

The aim of the present study was to investigate the efficacy of autologous chondrocytes embedded in alginate beads in reconstructing damaged focal cartilage *in vivo*. This was achieved by a comparison of the autologous alginate-chondrocyte transplantation in cartilage repair with non-treated defects.

II. Materials and methods

Nine male New Zealand white rabbits aged between 6 to 7 months and approximately 2.5 kg were used in this experiment (n=18 knees). Malaysian laws and University regulations on animal experimentation/ethics were strictly followed throughout the study as determined by University of Malaya animal ethics approval.

A. Isolation of chondrocytes

For cartilage biopsy, general anaesthesia was administered to the animal. Using a custom made chondrotome with cylindrical bevel, of 10mm diameter and 5mm laser marked depth circular, defects were created on the weight-bearing

F. Ibrahim, N.A. Abu Osman, J. Usman and N.A. Kadri (Eds.): Biomed 06, IFMBE Proceedings 15, pp. 700-703, 2007
www.springerlink.com ' Springer-Verlag Berlin Heidelberg 2007

portion of the medial femoral condyle. The remainder of the cartilage within the defective area was removed using a sharp pointed scalpel until subchondral bone was reached. Cartilage that was removed from both knees was sent for chondrocyte disaggregation and culturing. Wound closures were done with 4.0 vicryl polysorb sutures.

B. Chondrocytes culture in alginate

The isolated chondrocytes were suspended in a 1.2% low-viscosity sterile alginate solution in 0.15M sodium chloride. The cell suspension was slowly expressed through a 25-gauge needle into a 102 mM calcium chloride solution. Following 10 min of polymerization in this solution, the beads were washed three times with 0.15M sodium chloride to remove excess calcium chloride. Nine beads were transferred to each well of a 24-well culture plate and cultured with 0.4 ml of Dulbecco s modified Eagle s/Ham s F12 (1:1) medium (DMEM/F12) containing 10% fetal bovine serum (FBS), 25 μg/ml ascorbic acid, 50 μg/ml gentamicin, and 360 μg/ml L-glutamine. The cultures were maintained at 37^{o}C in a humidified atmosphere of 5%. At the end of the culture period (3-4 weeks), beads (approximately 2.5 x 10^4 cells/bead) were collected & stored at -20°C.

C. Implantation of chondrocyte-alginate constructs

A second procedure was performed 4 weeks later in only the right knees of each rabbit. The approach into the knee joint was performed using the same incision over the previous scar. The defects were either filled with 2 beads of chondrocyte-alginate (total of 5 x 10^4 cells) or left untreated (control). Antibiotics (cephalosporin) were administered to the rabbit post operatively (10 mg/kg, three times a day).

D. Harvest of specimens after 12 weeks transplantation

Specimens were biopsied after 12 weeks of in vivo implantation. Specimens were examined grossly, measured and then bisected. Half of each specimen was fixed in 10% phosphate-buffered formalin (4% formaldehyde) for histological and immunostaining examination and the other half was froze at -20°C for further biochemical analysis.

E. Histologic Examination

After being fixed in formalin for at least 24 hours, specimens were decalcified and embedded in paraffin, and sectioned at about 5μm thick. Sections were spread on slides and deparafinised in xylene and transferred in aqua dest. using decreasing concentration of ethanol. Using standard histochemical techniques, tissue sections were stained with Hematoxylin & Eosin (H&E) and Safranin-O.

F. Immunohistochemical Staining

Immunohistochemical staining was performed to verify collagen type II synthesis in the specimens. Sections were treated with protease enzyme for about 10 minutes and washed with TBS buffer prior to incubation with type II primary antibody or PBS alone (for negative control) for 1 hour. Specimens were then incubated with horseradish peroxidase enzyme (HRP) conjugated goat-anti-mouse secondary antibody (DakoCytomation kit) for 30 minutes prior to visualization using chromogen substrate diaminobenzidine (DAB). Stained slides were then mounted with DPX neural mounting medium.

G. Biochemical assay for glucosaminoglycan

The glucosaminoglycan (GAG) content in the specimens was determined using Blyscan Glucosaminoglycan Assay Kit (Biocolor, UK). Specimens were dissected into small pieces using a scalpel prior to digestion using RIPA buffer supplemented with protease inhibitor for 1 hour. Aliquots of each sample were mixed with DMMB dye and reagents from GAG assay kit. The absorbance at 656 nm was measured on the spectrophotometer and compared to a plot of standards made from shark chondroitin sulphate to determine GAG content.

H. Statistical analysis

The mean values of GAG and Brittberg scores [10] were calculated from samples of 18 separate left and right knees. The statistical significance of inter-group differences was analysed by Wilcoxon signed ranked (non-parametric) test (p<0.05).

III. Results

The defects treated with autologous chondrocytes embedded in alginate beads (right knees) showed good defect filling with the surface appearing flush and smooth. None of the cases showed obvious periosteal thickening. In the left knee, none of the untreated areas showed complete filling of the defects. In addition, in all the cases (n=9), the opposite articular surface of the tibia plateau showed some form of damage (abrasion) in the left knee. In the right knee, only 1 case showed mild abrasion on the opposing medial tibial articular surface.

F. Ibrahim, N.A. Abu Osman, J. Usman and N.A. Kadri (Eds.): Biomed 06, IFMBE Proceedings 15, pp. 700-703, 2007
www.springerlink.com ' Springer-Verlag Berlin Heidelberg 2007

In the H&E staining, chondrocytes seen within the repaired site were obviously abundant with substantial pericellular matrix. In the left knees no similar repair was noticeable. Safranin O staining indicated good proteoglycan expression within the matrix. In the repaired sites, the tissue appeared to be heavily stained whereas in the non-treated knee, staining of Safranin O was poor and uneven

Three months after implantation, the repaired sites also expressed collagen type II (Fig. 1). The repaired tissue, as compared to the surrounding native cartilage, showed an almost homogenous distribution of type II collagen expression. In the non-treated sites, weak collagen type II localisation was noted at the bottom of the empty defects or border with native cartilage (Fig. 2). However in both instances, we were unable to prove that the cartilage present there were remnants of the original biopsy procedure. However, it was obvious that there was no cartilage filling in the non-treated defect sites.

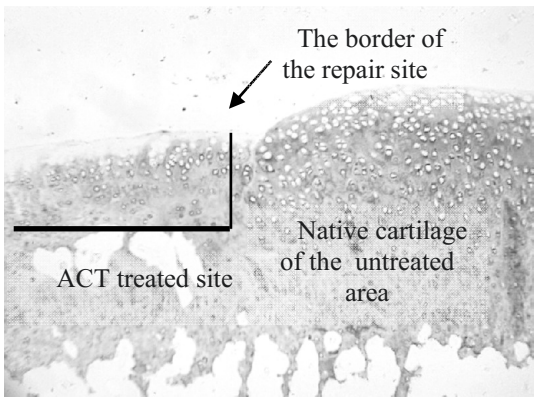

Fig. 1: Using immunohistological staining for collagen type II, we were able to see the abundance of this collagen in the repair site which was clearly expressed in this slide. Original magnification: X40.

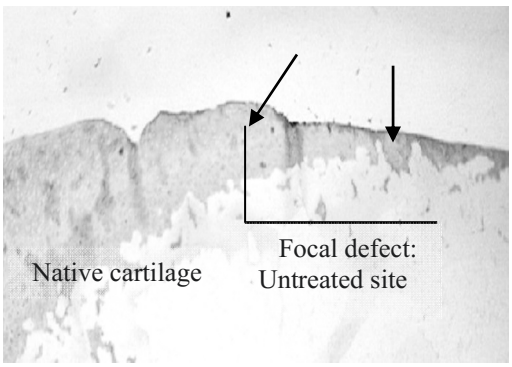

Fig. 2: In the left knee, the type II collagen demonstrated using immunohistochemical staining technique in the defective area remained only at the bottom and border of the defect (arrows). Original magnification: X10.

The mean values of GAG and Brittberg scores for the right knee were 1.12 µg GAGs / mg protein (SD= 0.48) and 6.00 (SD=1.23) respectively. In comparison to the left knee, the mean values of GAG and Brittberg scores were 0.81 µg GAGs / mg protein (SD=0.17) and 1.89 (SD=1.54) respectively. Using Wilcoxon signed ranked (non-parametric) test for both GAG and Brittberg scores, there were significant difference noted between both knees with p=0.008 for the mean comparison in GAG and p= 0.007 for the mean comparison in the Brittberg scores.

IV. Discussion

In our experiments, although not quantified, we found that the damage to the articular cartilage of the left side would result in damage to the opposing cartilage surface if left untreated. This was clearly demonstrated in all our models that were not treated surgically. As seen in our experiment involving the left knee, cartilage repair response was poor despite knowing that chondrocytes respond to tissue injury by proliferating and increasing the synthesis of matrix macromolecules near the injury [11]. This perhaps explains why the border of the left knee appeared to have ingrowth of tissue from the adjacent undamaged native cartilage. However, newly synthesized matrix and proliferating cells failed to fill the tissue defect and, soon after injury, the increased proliferative and synthetic activity ceases [11].

The chondrocyte plays a key role in regulating the composition of the extracellular matrix by modulating the synthesis and catabolism of cartilage-specific proteoglycans and collagen type II. Proteoglycans termed aggrecans are one of the major structural molecules in the extracellular matrix of articular cartilage, which forms macromolecular aggregates consisting of a large number of individual proteoglycan monomers attached to a single glycosaminoglycan (GAG) chain termed hyaluronan [6-8]. It has been shown that, if isolated chondrocytes are suspended in a three-dimensional environment, they continue to synthesis macromolecular proteoglycans typical of their chondrocytic phenotype [12]. The presence of safranin O staining also demonstrated that chondrocytes in an alginate bead culture system could produce proteoglycans even in an *in vivo* situation. Furthermore, this indicated that newly synthesised proteoglycans accumulated within the matrix in the repaired sites.

Moreover, collagen type II was heavily expressed in the transplanted sites compared to the non-treated sites. We postulated that minimal cartilage repair in the non-treated sites could have originated from the surrounding cartilage in the walls of the defect, from the calcified zone, chondrocytes in the cryptae of the irregular subchondral bone plate, or from the bone marrow of the defect in an osteochondral

F. Ibrahim, N.A. Abu Osman, J. Usman and N.A. Kadri (Eds.): Biomed 06, IFMBE Proceedings 15, pp. 700-703, 2007
www.springerlink.com ' Springer-Verlag Berlin Heidelberg 2007

defect. However, cells in the adjacent cartilage showed mitotic activity some time after injury but not sufficient for any significant repair.

It was therefore of interest to compare cartilage regeneration in a quantitative and qualitative manner between transplanted sites and the non-treated sites. Quantitatively, it appeared that the GAG content was higher in transplanted sites than the non-treated sites. This result can be explained by the fact that chondrocytes cultured in gel beads composed of alginate retained their ability to synthesize cartilage-specific matrix molecules. Qualitatively and quantitatively, the use of the Brittberg scores was a standardized accepted mean of comparing the superior quality of repaired tissue of the transplanted sites with the non-treated sites.

V. Conclusion

This current study has demonstrated that chondrocytes cultured in gel beads composed of biocompatible alginate retained their ability to synthesize cartilage-specific molecules such as proteoglycan, glycosaminoglycan and collagen type II. Thus, the use of chondrocyte-alginate constructs in autologous chondrocyte transplantation offers an improvement in current autologous cell based therapies utilized in articular cartilage repair. Although data from this short-term study in rabbits provided evidence of a superior repair with use of the chondrocyte-alginate constructs, further investigations are needed to clarify the long-term behavior of such transplantations.

Acknowledgment

The help provided by Ms. Azeera Abu Bakar, Sukanya Subramaniam, Mr. Rasanayagam and Mdm. Lim Saw Kim with the animal handling and experiments, and tissue processing is gratefully acknowledged. We also thank the National Biotechnology Directorate, Ministry of Science and Technology of Malaysia to fund this research (Research grant number: PR-06-03-01).

References

1. Petersen L, Minas T, Brittberg M, Nilsson A, Sjogren-Jansson E, Lindahl (2000) Two- to 9-year outcome after autologous chondrocyte transplantation of the knee. Clin Ortho Rel Res. 374: 212-34
2. Brittberg M (1999) Autologous Chondrocyte Transplantation. Clin Ortho Rel Res. 367:147-55
3. Brittberg M, Lindahl A, Nilsson A, Ohlsson C, Isaksson O, Peterson L (1994) Treatment of deep cartilage defects in the knee with autologous chondrocyte transplantation. N Engl J Med 331:889-895
4. Shakibaei M, de Souza P. Merker H.-J (1997) Integrin expression and collagen type II implicated in maintenance of chondrocyte shape in monolayer culture (An immunomorphological study). Cell Biol. Int. 21:115-125
5. Shakibaei M, Schroter-Kermani C, Merker H-J (1993) Matrix changes during long-term cultivation of cartilage (organoid or high-density culture). Histol Histopathol 8:463 470
6. Guo J, Jourdian GW, Maccallum DK (1989) Culture and growth characteristics of chondrocytes encapsulated in alginate beads. Connect Tissue Res 19:277 297
7. Hauselmann HJ, Aydelotte MB, Schumacher BL, Kuettner KE, Gitelis SH, Thonar EJ-MA (1992) Synthesis and turnover of proteoglycans by human and bovine adult articular chondrocytes cultured in alginate beads. Matrix 12:116 129.
8. Petit B, Masuda K, D souza AL, Otten L, Pietryla D, Hartmann DJ, Morris NP, Uebelhart D, Schmid TM, Thonar EJ-MA (1996) Characterization of crosslinked collagens synthesized by mature articular chondrocytes cultured in alginate beads: comparison of two distinct matrix compartments. Exp Cell Res 255:151 161
9. Hauselmann HJ, Fernandes RJ, Mok SS, Schmid TM, Block JA, Aydelotte MB, Kuettner KE, Thonar EJ (1994) Phenotypic stability of bovine articular chondrocytes after long-term culture in alginate beads. J Cell Sci 107:17-27
10. Mainil-Varlet P, Aigner T, Brittberg M, Bullough P, Hollander A, Hunziker E, Kandel R, Nehrer S, Pritzker K, Roberts S, Stauffer E (2003) Histological assessment of cartilage repair. J Bone Join Surg 85:45-57
11. Buckwalter J (1998). Articular cartilage: Healing and potential for healing. J of Ortho and Sports Phys Ther 28(4):192-202
12. Benya PD, Schaeffer JD (1982) Dedifferentiated chondrocytes reexpress the differentiated collagen phenotype when cultured in agarose galls. Cell 30:215-224

Address of the corresponding author:

Author: Chong Pan Pan
Institute: Department of Orthopaedic Surgery, Faculty of Medicine, University of Malaya
Street: Jalan Pantai Bharu,
City: 50603 Kuala Lumpur
Country: Malaysia
Email: pan2chong@gmail.com

F. Ibrahim, N.A. Abu Osman, J. Usman and N.A. Kadri (Eds.): Biomed 06, IFMBE Proceedings 15, pp. 700-703, 2007
www.springerlink.com ' Springer-Verlag Berlin Heidelberg 2007

Retraction Note to: A High Efficiency Optical Power Transmitting System to a Rechargeable Lithium Battery for All Implantable Biomedical Devices

Naresh Kumar Pagidimarry, Vishrut Chowdary Konijeti

Retraction Note to:
Chapter "A High Efficiency Optical Power Transmitting System to a Rechargeable Lithium Battery for All Implantable Biomedical Devices" in: F. Ibrahim et al. (eds.), *3rd Kuala Lumpur International Conference on Biomedical Engineering 2006*, IFMBE Proceedings, DOI 10.1007/978-3-540-68017-8_134

The chapter 'A High Efficiency Optical Power Transmitting System to a Rechargeable Lithium Battery for All Implantable Biomedical Devices', Biomed 06, IFMBE Proceedings 15, pp. 533-537, 2007, DOI 10.1007/978-3-540-68017-8_134 published in the book has been retracted because it contains significant parts plagiarizing another publication: 'An Implantable Power Supply with an Optical Rechargeable Lithium Battery', IEEE Transactions on Biomedical Engineering, Vol, 48, Nr. 7, July, 2001, Publisher Item Identifier S 0018-9294(01)05142-4.

The retracted online version of this chapter can be found at http://dxdoi.org/10.1007/978-3-540-68017-8_134

F. Ibrahim, N.A. Abu Osman, J. Usman and N.A. Kadri (Eds.): Biomed 06, IFMBE Proceedings 15, pp. E1, 2007
www.springerlink.com ' Springer-Verlag Berlin Heidelberg 2017

Index Authors

S

T

Index Subjects

D

E

F

G

H

I